PROCEEDINGS
OF THE
THIRD CONFERENCE
ON THE
CLIMATIC IMPACT ASSESSMENT PROGRAM

FEBRUARY 26 - MARCH 1, 1974

EDITED BY

ANTHONY J. BRODERICK

THOMAS M. HARD

DOT-TSC-OST-74-

SPONSORED BY THE U. S. DEPARTMENT OF TRANSPORTATION

HELD AT THE

TRANSPORTATION SYSTEMS CENTER
KENDALL SQUARE
CAMBRIDGE, MASSACHUSETTS 02142

Technical Report Documentation Page

1. Report No.	2. Government Accession No.	3. Recipient's Catalog No.
DOT-TSC-OST-74-15		

4. Title and Subtitle	5. Report Date
Proceedings of the Third Conference on the Climatic Impact Assessment Program	November 1974
	6. Performing Organization Code
7. Author(s)	8. Performing Organization Report No.
Anthony J. Broderick and Thomas M. Hard, Editors	DOT-TSC-OST-74-15
9. Performing Organization Name and Address	10. Work Unit No. (TRAIS)
DOT Transportation Systems Center Kendall Square Cambridge, MA 02142	R5503
	11. Contract or Grant No. PPA OS 520
	13. Type of Report and Period Covered
12. Sponsoring Agency Name and Address Office of the Secretary Department of Transportation 400 Seventh St., S.W. Washington, D.C. 20590	Conference Proceedings Feb. 26 - Mar. 1, 1974
	14. Sponsoring Agency Code

15. Supplementary Notes

16. Abstract

This volume contains the proceedings of the Third Conference on the Climatic Impact Assessment Program (CIAP), eld at the DOT Transportation Systems Center from February 26 to March 1, 1972. It includes 45 invited papers,) unscheduled presentations, and edited question-and-answer sessions following some of the papers. The conference was sentially a progress report on CIAP. Therefore, some of the papers contain new data not yet published elsewhere, and hers describe experimental equipment. Reports on work relevant to CIAP, though not sponsored by it, are also included. he subjects covered include aircraft-engine emissions, the nature of the "undisturbed" stratosphere of 1974, the nature of e "perturbed" stratosphere of 1990-2025, the possible resulting tropospheric perturbations, and the biological and onomic effects of such perturbations.

17. Key Words			18. Distribution Statement
one	atmospheric transport	NO_x	Document is available to the public through the National Technical Information Service, Springfield, Virginia 22151
issions	atmospheric modeling	climate	
T's	atmospheric dynamics	sampling	
rosols	chemical kinetics	pollutants	
st/benefit	ultraviolet radiation	stratosphere	
	plant response	photochemistry	

19. Security Classif. (of this report)	20. Security Classif. (of this page)	21. No. of Pages	22. Price
Unclassified	Unclassified	670	

rm DOT F 1700.7 (8-72) Reproduction of completed page authorized

NOTICE

The views expressed in these papers are the authors' personal opinions, and do not necessarily reflect those of any organization of which they may be members. The Department of Transportation is distributing this document in the interest of information exchange, and assumes no liability for its contents.

FOREWORD

"CIAP 3" was the third of four international conferences sponsored by the U.S. Department of Transportation for the purpose of reviewing progress on its Climatic Impact Assessment Program. Funds for this 40-month program were appropriated in 1971, and the Report of Findings will be completed in 1974. The objective of CIAP can best be stated as follows: In order to determine the regulatory controls and corrective actions necessary to ensure that future aircraft operations in the stratosphere do not result in adverse environmental effects, CIAP will assess, by a report in 1974, the impact of climatic changes resulting from perturbation of the upper atmosphere by the propulsion effluents of a world high-altitude aircraft fleet as projected to 1990.

Over two years ago, at the Survey Conference on CIAP, our primary aim was to introduce the objectives and scope of the program to domestic and foreign representatives of industry, universities, and government agencies. Most of the papers presented there were somewhat tutorial in nature. Their objective was to establish a solid basis for communications among the scientists who were to become involved in the program, since they represented a wide range of disciplines. Less than a year later, real progress was evident at the Second Conference on CIAP. Some 56 separately funded efforts had been initiated and sponsored by CIAP, and a true spirit of international cooperation was evident. Instrumentation specially developed for stratospheric measurements was nearing completion, existing data pertinent to the investigation were being analyzed, and a profitable interdisciplinary exchange of information was under way.

A few months ago, we held the Third Conference on CIAP, our last major reporting milestone prior to publication of the U.S. DOT Report of Findings. It was an extremely fruitful meeting; more than a few of the papers in this volume are real landmarks in the field of stratospheric research. We are especially grateful that the participants in CIAP have been so cooperative in heeding our admonitions to report their experimental findings with all deliberate speed. In the absence of such cooperation, progress would have been much too slow to fulfill our objectives.

On February 4th through 7th, we will sponsor the Fourth Conference on CIAP. At this time, we extend our thanks to all participants in the program, and invite you to join us for this final CIAP conference.

Samuel C. Coroniti, Program Chairman
Deputy Program Manager
Climatic Impact Assessment Program

Alan J. Grobecker, Conference Chairman
Program Manager
Climatic Impact Assessment Program

EDITORS' PREFACE

The Third Conference on the Climatic Impact Assessment Program was held at the DOT Transportation Systems Center in Cambridge, Massachusetts, from February 26 through March 1, 1974. Forty-six invited papers were read during the meeting, and seventeen unscheduled presentations were made. Except for two whose authors were unable to supply us with suitable manuscripts, edited versions of all the papers are included in this volume. Two new papers were inserted because of their particular relevance to the conference topics; replies to these papers were solicited from the scientists whose work was discussed in them. (The unscheduled and new papers appear in smaller type.) Greatly condensed transcripts of the discussions which followed many of the presentations also appear in this book.

It has taken us longer to get these Proceedings to press than we had hoped. The sheer number of papers given – many of them far more detailed in manuscript than in presentation – was probably the major factor. It was compounded by the requirement that each author have an opportunity to review galley proofs of the edited version of his paper. (It should be noted, however, that the discussions were reviewed by the speakers only as transcripts, before being edited. We have tried to be faithful to both the flavor and the technical content of these question-and-answer sessions, but it is quite possible that some errors have crept in. We apologize in advance for them.)

Most of the authors devoted considerable time and effort to the preparation of the manuscripts, and did their best to meet our requirements and deadlines. We are very much indebted to them. We are also grateful to Dr. Frederick F. Marmo of TSC, who assisted us in the technical review. Out deepest thanks, however, go to Ms. Ellen F. Rice of the Raytheon Service Company. Her task was twofold: she not only supervised the peregrinations of the various manuscripts as they moved through the production cycle, but also reviewed every paper carefully, clarifying cryptic passages and questioning inconsistencies. She deserves almost as much credit as the authors for the quality of this book.

Anthony J. Broderick
Thomas M. Hard

Transportation Systems Center
November 4, 1974

PROCEEDINGS OF THE THIRD CONFERENCE ON THE CLIMATIC IMPACT ASSESSMENT PROGRAM

U.S. DEPARTMENT OF TRANSPORTATION FEBRUARY 1974

CONTENTS

NATURAL STRATOSPHERE: WATER VAPOR AND AEROSOLS

Chairman: Rudolf Penndorf
Wellesley, Massachusetts

PERTURBED STRATOSPHERE

Chairman: George D. Robinson
Center for Environment and Man

PERTURBED STRATOSPHERE AND TROPOSPHERE

Chairman: Cecil E. Leith
National Center for Atmospheric Research

BIOLOGICAL EFFECTS OF CLIMATIC CHANGES

Chairman: Martyn M. Caldwell
Utah State University

ECONOMIC EFFECTS OF CLIMATIC CHANGE

Chairman: Ralph C. d'Arge
University of California, Riverside

PROGRESS REPORT ON THE CLIMATIC IMPACT ASSESSMENT PROGRAM

ALAN J. GROBECKER
Program Manager, CIAP
U.S. Department of Transportation
Washington, D.C.

INTRODUCTION

The United States Department of Transportation's Climatic Impact Assessment Program (CIAP), now in the 30th month of its 40-month term, has made significant progress in the compilation of data on the aircraft effluents that might perturb the stratosphere, on the natural and perturbed stratospheres, on the perturbed troposphere, and on the climatic, biologic, economic, and social consequences of increased stratospheric flight. Estimates of uncertainty of the most-likely values, caused by either the natural variability of the phenomena or by errors in estimation techniques, have also been considered.

The compiled data are being analyzed and presented in parametric form (relation of the variation in each effect to variation in its immediate cause) to permit assessments of the most likely consequences of the possible alternatives in aircraft design and operation. Examples of the parameters likely to be most sensitive to variation are given. Since the goal – that no adverse environmental effects result from the operation of aircraft in the stratosphere – is one which will require international collaboration, the study is intended to give the governments concerned the information they need to choose a prudent course of action.

In order to determine the regulatory constraints necessary to ensure that future flights in the stratosphere have no adverse environmental effects, the United States Department of Transportation initiated in 1971 a study called the Climatic Impact Assessment Program (CIAP). This study, the final results of which will be reported in 1974, assesses the impact of climatic changes which might result from the introduction of propulsion effluents into the stratosphere. The other papers presented at this Conference deal with the scientific explorations which constitute the necessary base for any analysis of such impacts. I shall use instances of the science to illustrate how the consequences of changes may be evaluated to provide a basis for future action by the international community of nations.

Nine other departments of the United States Government have collaborated in the study. Funding by the Department of Transportation has been distributed approximately equally among universities, government laboratories, profit-making organizations, and non-profit organizations. The project is international as well: major contributions have been made by scientists of the United Kingdom, France, Canada, Australia, Japan, Belgium, and the USSR, and substantial ones by a number of other countries.

CIAP DATA COMPILATIONS

The data compiled in the course of these studies have been gathered into six monographs. Monograph I, "The Natural Stratosphere of 1974", describes what we know at present about the natural stratosphere. Monograph II, "The Propulsion Effluents in the Stratosphere", describes aircraft engines, both present and future, and the routes and frequencies of the travel during which these engines would introduce emission products into the stratosphere. Monograph III, "The Stratosphere Perturbed by Propulsion Effluents", describes the perturbations of the stratosphere which may result from pollution by engine effluents. For example, one possible consequence is a change in the solar radiation transmitted to the troposphere. The content of this monograph is based strongly on computational modeling. Monograph IV, "The Natural and Radiatively Perturbed Troposphere", describes effects on the troposphere of perturbation of the stratosphere. Monograph V, "Impacts

of Climatic Change on the Biosphere", describes the effects on the biosphere of climatic and radiation changes resulting from stratospheric and tropospheric perturbations. Monograph VI, "Economic and Social Measures of Biologic and Climatic Change", describes the economic and social costs of the changes in the biosphere, as well as the costs of feasible abatement measures.

Contributions to each of the monographs have been solicited from experts in the areas indicated by the titles. These compilations of data provide the basis for constructing transfer functions by means of which the contribution to an overall answer from each of the related parts of the study may be independently estimated. Conclusions as to the overall consequences should not be drawn from inspection of any one of the several transfer functions, or from any one of the monograph compilations. A Report of Findings, to be published in December 1974, will present the results of analyses of the monograph data, carried out along the lines described in this paper.

Monograph I

Monograph I discusses the physical characteristics of the natural stratosphere, with particular attention to ozone, a species of great concern to CIAP. Figure 1 shows the mean temperature of the atmosphere as a function of altitude and as a function of latitude. The increase in temperature with altitude between about 10 and 50 kilometers inhibits the vertical mixing which is the principal means by which the stratosphere would be cleansed of pollutants introduced by aircraft. The little figures along the right ordinate indicate the flight altitudes characteristic of some stratospheric vehicles: the U.S. SST, a Boeing design stopped in 1971; the Concorde and Tupolev-144; and the Boeing 747, which sometimes flies at stratospheric altitudes.

Figure 2 illustrates some characteristic time scales for chemistry and motions in the atmosphere. One curve shows the characteristic time required for ozone photochemistry, as simply described by Chapman, to vary from about a day at about 40 km to more than 10 years at about 20 km. In contrast to this photochemical time constant, the characteristic times of diffusion due to motions in the atmosphere are shown by

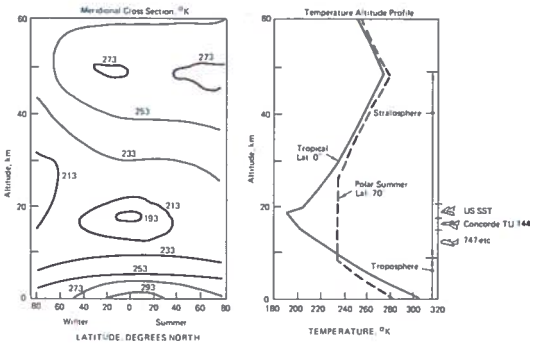

Figure 1. Atmospheric temperature variations. Note the stratospheric temperature gradient, which inhibits vertical mixing. (After R.E. Newell (1969).)

the cross-hatched band. (Since the diffusion rate is highly variable with time, the band is broad.) The residence time as determined by diffusion is great at altitudes greater than 25 km. Below 20 km, however, it is sharply reduced, and reaches values of about one week in the lower troposphere. Figure 2 also shows the ozone mass mixing ratio (the ratio of the mass of ozone to the total mass of air in a given volume), which has a maximum at about 35 km. The ozone density (ozone mass per unit volume) has its maximum at about 22 km. Since the process with the shortest characteristic time is the dominant one, it can be seen from Figure 2 that the equilibrium condition of ozone chemistry is controlled by photochemistry at altitudes above about 25 km, but by diffusion processes below that.

Figure 3 shows the variation of diffusion with latitude and altitude. The residence times below about 20 km and at latitudes lower than 30 degrees are about half the values for similar altitudes at higher latitudes.

Figure 4 indicates the variation with altitude of the molecular number density of minor species in the stratosphere. The whole air, of which these species are a small part, has a molecular number density of about 10^{24} molecules per cubic meter at an altitude of about 20 kilometers. A number of trace constituents (O_3, H_2O, CH_4, and H_2) are present in proportions of about one part per million. Other constituents (NO_2, HNO_3, NO) are even more dilute, with mixing ratios of about one part per billion. (The

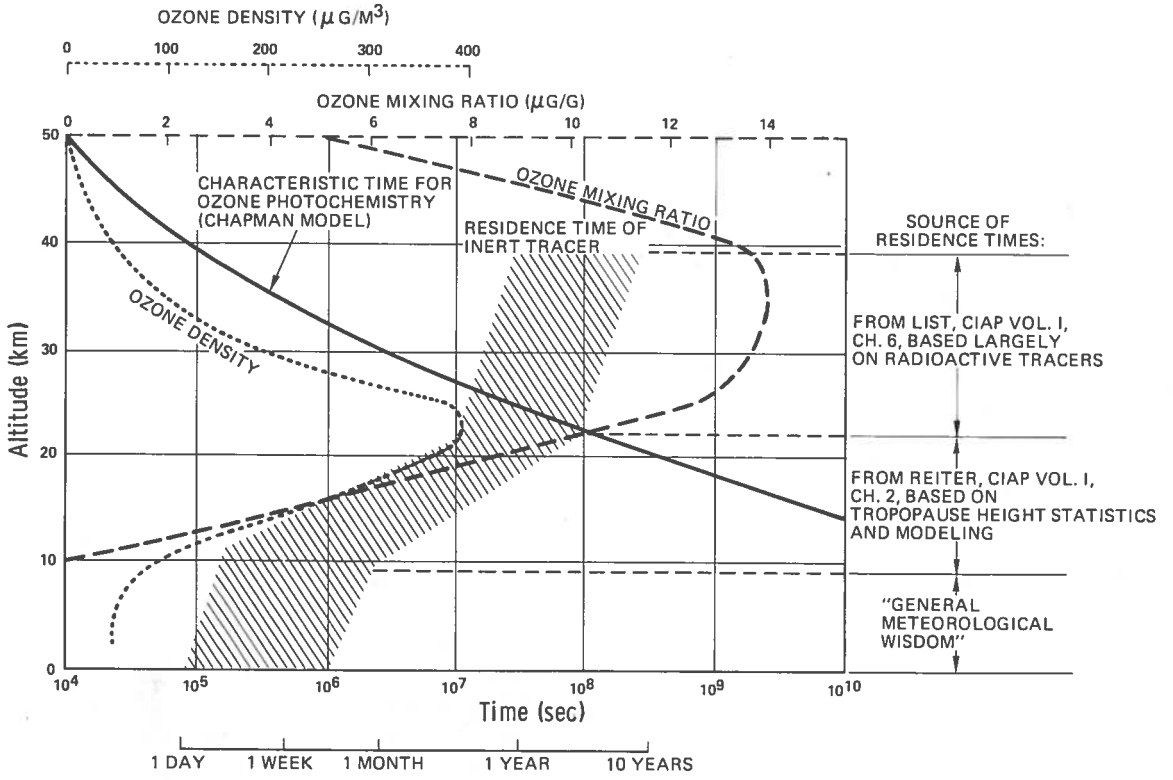

Figure 2. Characteristic time scales for chemistry and motions in the atmosphere. (After Bauer (1973).)

data on densities of CO, N_2O, NO_2, NO, and HNO_3 were acquired partly as a result of CIAP encouragement.)

Table 1 shows the budget of some of the naturally occurring stratospheric species which affect climate, either by controlling the amount of solar radiation which penetrates to the troposphere or by affecting these controlling species.

Table 1. Budget of Natural Stratospheric Species Affecting Climate

SPECIES	TOTAL SOURCE CONTENT		ANNUAL SOURCE RATE	
	Molecules	Grams	Molecules Sec^{-1}	Grams $Year^{-1}$
SO_2	$7(10)^{32}$	$7(10)^{10}$	$1\text{-}50(10)^{26}$	$0.3\text{-}16(10)^{12}$
H_2O	$6(10)^{37}$	$2(10)^{15}$	$1.3(10)^{30}$	$1.2(10)^{15}$
Aerosols		$2(10)^{11}$		$1\text{-}50(10)^{12}$
Ozone	$4(10)^{37}$	$3(10)^{15}$	$5(10)^{31}$	$1(10)^{17}$
$NO+NO_2$	$1(10)^{34}$	$1(10)^{12}$	$2\text{-}7(10)^{26}$	$4\text{-}18(10)^{11}$

A characteristic of the trace species of the natural stratosphere which must be taken into account is the great natural variability of the number densities. The total ozone column above any one place in the middle latitudes varies greatly from day to day, and also by ±25% during the year. The latitudinal variation of the total ozone column may exceed a factor of three from equator to pole. The consequences for the observer of the natural variability are illustrated by Figure 5, which shows the years of observations of total ozone column over Aspendale, Australia required to discern with 95% certainty a fractional change of total ozone per decade. Pittock (1972) finds from analysis of daily observations at Aspendale, averaged by month, that 11 years of data are required for discernment with 95% certainty of a 5% change per decade of the ozone. Satellite observations may lower the number of years of observation required to discern a given change per decade to half that shown in Figure 5.

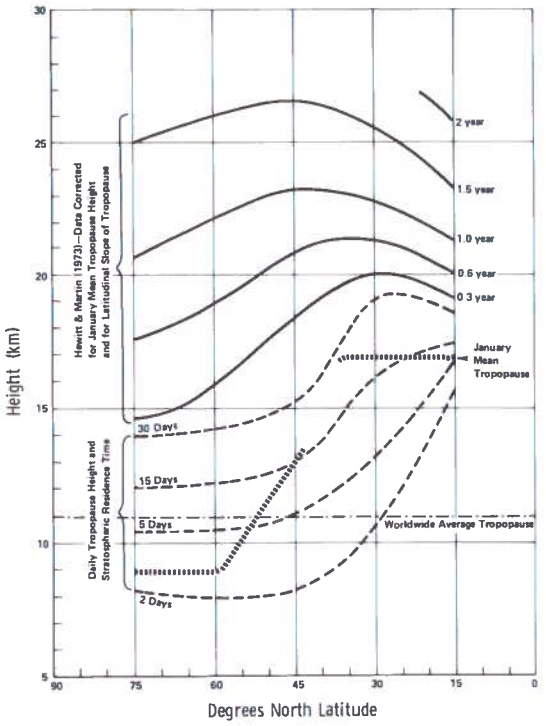

Figure 3. Mean stratospheric residence times, as a function of altitude and latitude, for January. (After Reiter (1974).)

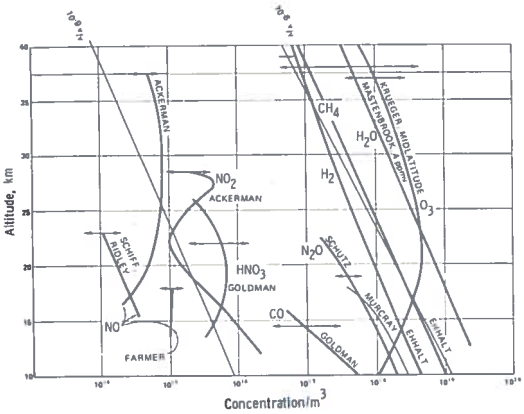

Figure 4. Concentrations of minor species in the stratosphere. (After Hard (1973).)

Monograph II

The projection into the future of number of aircraft shown in Figure 6 is derived from Monograph II. These projections, made by a number of different predictors, show a mutual

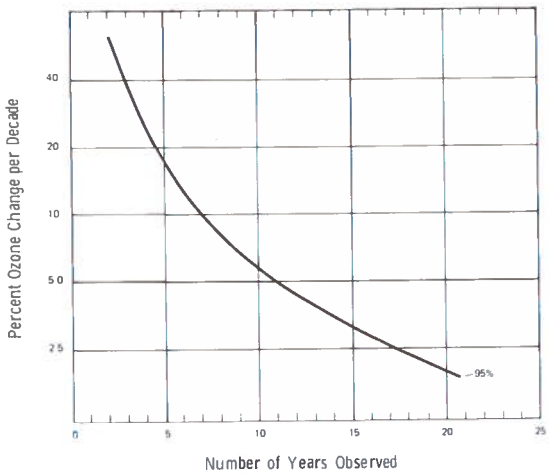

Figure 5. Years of observation required at Aspendale to discern a fractional change of total ozone per decade with 95% certainty. (After Pittock (1972).)

consistency, differing from each other by a small factor. Note the expected expansion of existing SST's, especially the UK-French Concorde and the USSR Tupolev-144. Beginning in 1985 or so, a second-generation advanced supersonic transport may be produced to meet the needs of high-speed transport. Although the numbers of stratospheric vehicles may be strongly affected by wars or other unforeseeable events, there is a striking consensus that there will be economic justification for high-speed transport vehicles which use the stratosphere.

Table 2 lists the engine emission products of interest in the CIAP study. Those which are of most concern are the nitrogen oxides, which deplete the stratospheric ozone, thus enhancing penetration to the ground of ultraviolet radiation to which the biosphere is sensitive. A second pollutant is sulfur dioxide (SO_2), which results from combustion of the sulfur in the fuel. The sulfur dioxide forms sulfuric acid which combines with water vapor to grow gradually into particles large enough to interfere with the transport of radiation in the visible and infrared bands and thus affect the climate. Other emissions, notably carbon dioxide and water vapor, appear not to be pollutants of serious concern.

The emission of two pollutants of principal concern, the nitrogen oxides and sulfur dioxide, can be greatly decreased by technological abatement measures. The emission index of nitrogen oxide, expressed as grams of nitrogen oxide per

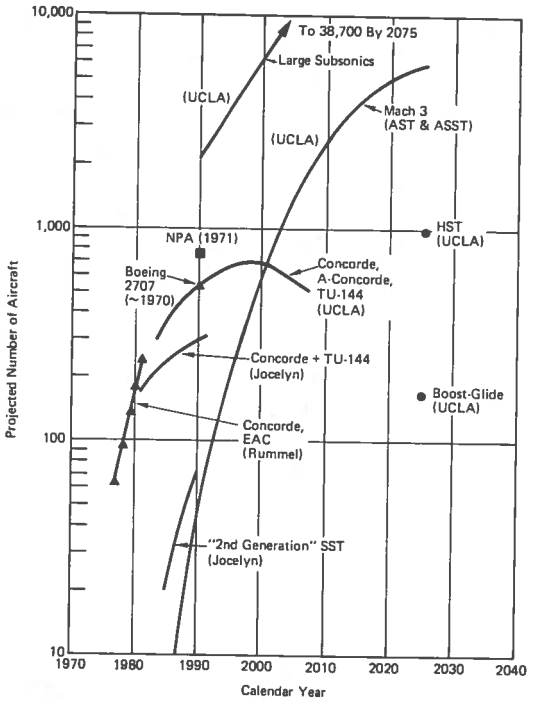

Figure 6. Projections of aircraft fleets (UCLA and others). (After English (1974).)

kilograms of fuel burned, is a function of the peak temperature in the combustor of the engine. (The gases within the combustor of most present-day gas-turbine engines are raised by combustion to temperatures exceeding 2500 K, only to be cooled again within the combustor to about 1300 K by the introduction of additional external air before the mixture of cool and burning gases is introduced into the turbine and jet exhaust.) Studies indicate that if the peak temperature in the combustor of the engine is not permitted to exceed about 1800 K, the production of nitrogen oxide is much reduced. By careful control of the combustor process, the peak temperatures of the "hot spots" of the non-uniformly burning gases in the combustor can be kept at this level or lower without diminishing the overall efficiency of the turbine and jet as a thermodynamic heat engine. In principle, a reduction of NO_x emission by one or more orders of magnitude can be achieved by this approach.

The remedy for sulfur dioxide pollution of the stratosphere is one which is already realizable with present-day refinery techniques: reduction of the sulfur content of jet fuel. A twenty-fold reduction of SO_2 emission can easily be achieved at an additional refining cost of a few cents per barrel.

Figure 7 shows estimates of the fuel which would be burned in various altitude bands by fleets of a size projected for the future by the

Table 2. Emission Products of Interest to CIAP

Emission	Interest	Current Emission Index GM/KG Fuel	Technological Remedy	Goal
CO_2	Climate	3100 Stoichiometry	Non-Hydrocarbon Fuel: H_2	
H_2O	Climate, UV	1300 Stoichiometry	None	
SO_x	Climate	20 x Percent of S = SO_2 30.6 x Percent of S = H_2SO_4	Current Fuel 0.05% Sulfur by Weight 0.01% S Fuel at 4% Price Increase 0.0025% S Fuel at 5% Price Increase	20 Fold Reduction
CO	?	4 Incomplete Combustion	Improved Combustion (Already 0.99)	
C_xH_y	Climate	0.1 – 0.2 Incomplete Combustion	Improved Combustion (Already 0.99)	
NO_x	UV	15 – 21 Time at High Temp.	Reduce Temperature Rise Above Inlet Temperature Reduce Compressor Pressures Minimize Combustion Hot Spots	10 – 100 Fold Reduction
Particulate	Climate	0.1 as C or CH Polymerization	Improved Combustion	
Heat	?		None	

UCLA study (English, 1974). The ordinate on the right-hand side of Figure 3 shows the nitrogen oxides (NO_x) which would be emitted by the aircraft fleets projected by the UCLA study if they were equipped with 1974 engines. Beginning in about the year 2000, the flux of NO_x matches the current estimates of the natural flux of nitrogen oxides into the stratosphere. A few years later the sulfur dioxide emissions of aircraft fleets of the size projected by the UCLA study, but having 1974-style engines, would also begin to match the natural flux of sulfur dioxide into the stratosphere. Clearly, such doubling of the natural flux may be expected to have significant consequences.

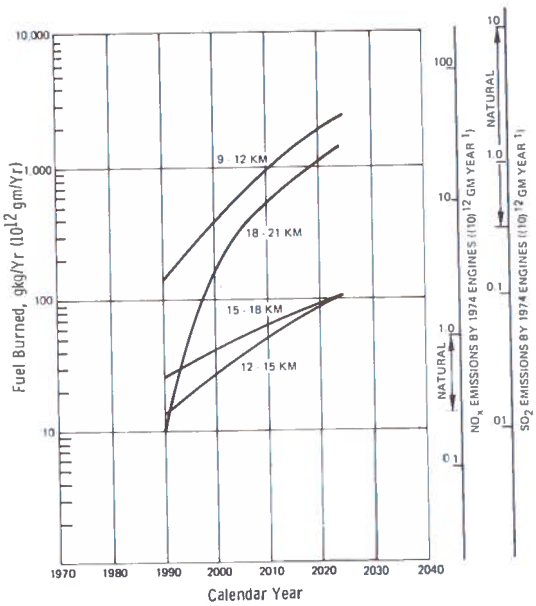

Figure 7. Fuel burned in various altitude bands: UCLA projections. Hypersonic transports and boost-guide aircraft are not included. (After English (1974).)

Monograph III

In Monograph III, the consequences of perturbing the stratosphere by the introduction of nitrogen oxides (NO_x) are projected by using computational models of the stratosphere. The depleting effect of NO_x on ozone, as estimated by eight computational models compared by J. Chang (1974) is described in Figure 8, which shows calculated reduction of vertical ozone column in terms of a uniform global rate of NO_x introduced as NO_2 at 20 km. The earliest modelers, failing to take into account the role of nitric acid as a sink for NO_x, computed larger values of reduction. The more recent models show close agreement, particularly when results are normalized to take into account the recent first measurements of the natural background levels of NO and NO_2. Small differences in the results of different models may be attributed to differences in the boundary conditions and diffusion rates assumed. Most modelers now use values of chemical reaction rates, appropriate for stratospheric-gas chemistry, which have been summarized from refereed publications evaluated by David Garvin and his group at the National Bureau of Standards.

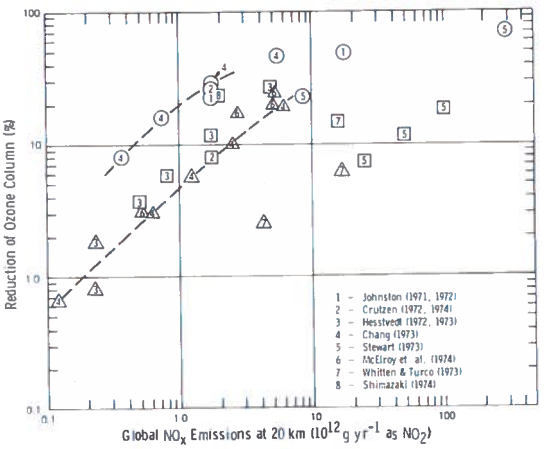

Figure 8. Calculated reduction of vertical ozone column in terms of uniform global rate of NO_x addition at 20 km. (After Chang (1974).)

Figure 9 shows the variation of ozone depletion with different altitudes of injection, as derived by one-dimensional models. The difference between ozone depletion caused by injection of nitrogen oxides at 21 km and that for injection at 17 km is about a factor of two. That is, the atmosphere is about twice as tolerant of NO_x injected at 17 km as it is of NO_x injected at the higher altitude.

Figure 10 shows the increase in direct solar ultraviolet radiation penetrating to ground level caused by depletion of stratospheric ozone, for four solar zenith angles and radiation of wavelengths between 287.5 and 322.5 nm. The heavy

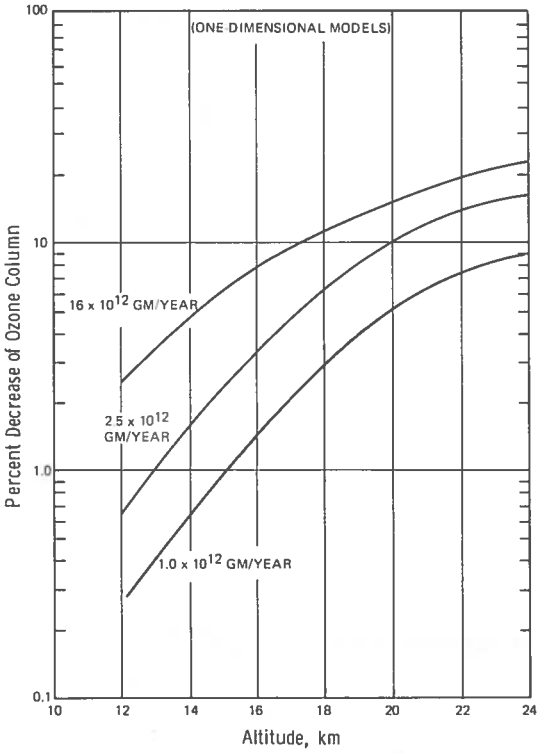

Figure 9. Effect of the altitude of injection of NO_x on depletion of ozone column. (After Chang (1974).)

line at 307.5 nm is the wavelength most nearly representative of the erythemally weighted solar ultraviolet radiation (see the section on Monograph V for discussion of this weighting). With a zenith angle of about 30 degrees, or the sun 60° above the horizon, the intensity variation of 307.5-nm solar ultraviolet at the top of the troposphere due to a 50% change in ozone is about a factor of 2. The change in intensity is much greater when the sun is closer to the horizon; however, the radiation energy which penetrates to the ground is also much smaller.

Figure 11 shows estimated changes in visible radiation at the ground due to increased aerosol loading in the stratosphere. The fractional radiation centered at about 700 nanometers and transmitted to the troposphere and ground is shown by the analytic expression in the figure. The normal optical thickness of the stratosphere at 550 nm is taken to be about 0.02, as determined by searchlight measurements by Elterman (1973). The changes in stratospheric optical thickness and in visible radiation as functions of aerosol loading rate maintained for one year's residence time in a hemispheric shell 10 km thick are shown both analytically and graphically in Figure 11.

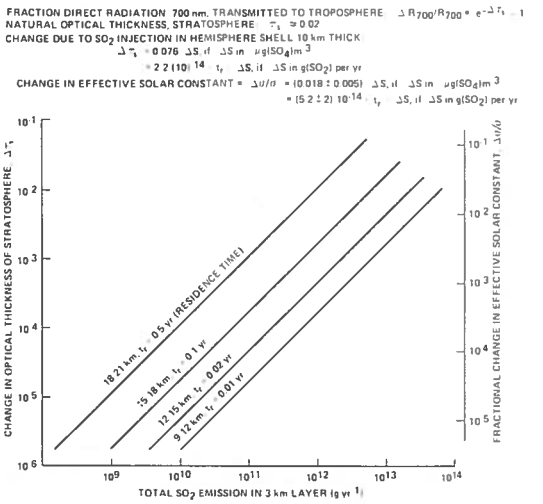

Figure 11. Change in visible radiation at ground due to increase of aerosol loading in stratosphere. (After Leith (1974).)

Monograph IV

Monograph IV describes the changes in the troposphere (called climatic changes) which would be caused by alterations in radiative transfer within the stratosphere, such as those described in Monograph III. Figure 12 shows a compilation of three different estimates of the variation in mean global surface temperature with fractional variation of ground-level solar radiation. There is a large disparity among the models of MacCracken (1974), Budyko (1971), Sellers (1973), and Manabe and Wetherald (1967). MacCracken's model (MacCracken, 1970) is two-dimensional, permitting determination of latitudinal response to changes in solar radiation.

Monograph V

Taken from Monograph V, Figure 13 shows curves of erythemal efficiency for ultraviolet radiation of various wavelengths. Erythema is the reddening of the skin due to sunburn, a trauma with which occurrence of skin cancer has been correlated. The efficiency of the radiation

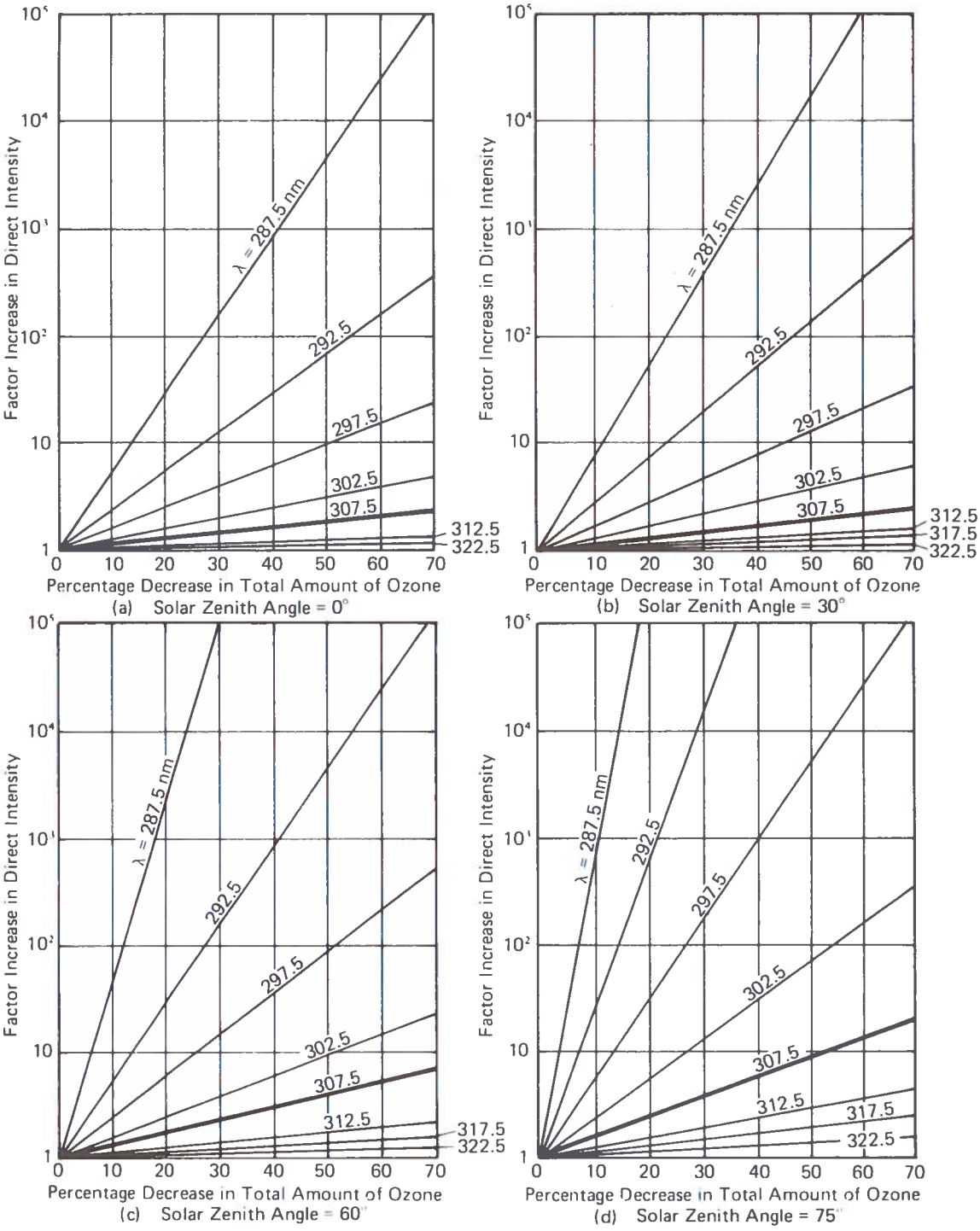

Figure 10. Relative increase in solar UV radiation for various decreases in ozone. (After Cutchis (1973).)

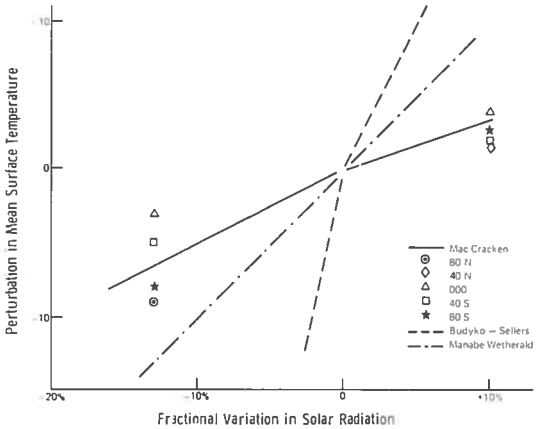

Figure 12. Change of mean surface temperature with changes in solar radiation. (After MacCracken (1974).)

causing the skin reddening, a function of wavelength, is shown by the dotted line in Figure 13. The dashed lines show the intensity of sunshine measured at Davos, Switzerland; the ultraviolet radiation received is more intense in winter, due to reflection from snow on the ground, than that in summer. The product of the erythemal efficiency and the solar intensity is the erythemally-weighted radiation, centered at about 307 nm. As the sunlight gets more intense, the center of the erythemally-weighted radiation band shifts in the direction of the shorter wavelengths.

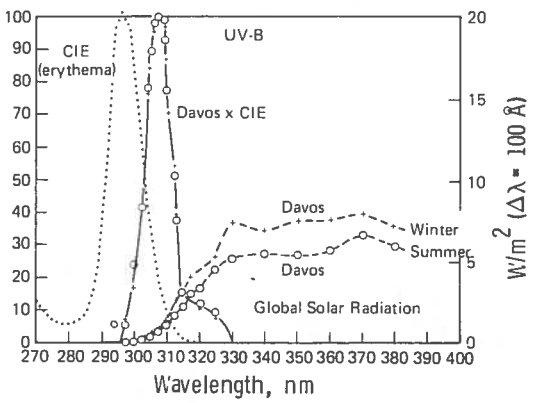

Figure 13. Curve of erythemal efficiency according to CIE (dotted line), UV global solar radiation measured in Davos by Bener (dashed lines), and their product (Davos X CIE) (solid line). (After R. Schulze and K. Grafe (1969).)

Figure 14 shows that the relationship of change in erythemally weighted radiation to change in ozone column is not algebraically linear. As the fractional decrease in the ozone column grows, so does the fractional increase of radiation which produces sunburn. This is another way of expressing the shift to the shorter wavelengths of the erythemally-weighted radiation as the radiation becomes more intense.

Studies of the incidence of skin cancer have been made by E. MacDonald in Texas, and more recently by the Third National Cancer Survey of the National Cancer Institute. Since data on the present incidence was available for Minneapolis, Minnesota, and Dallas, Texas, Cutchis (1974) has computed the increase in skin cancer incidence in those two cities expected to result from varying percentage reductions in overhead ozone.

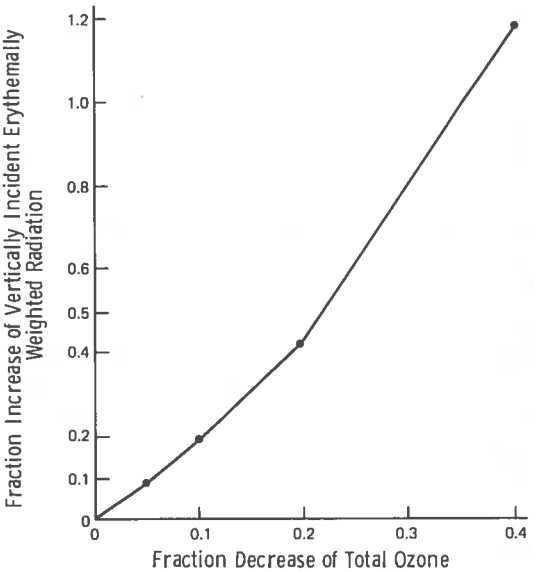

Figure 14. Relationship of change in erythemal dose to change in ozone column. (After Schulze (1974).)

As can be seen in Figure 15, the reduction in ozone which would cause a given increase in skin-cancer incidence are similar for Minneapolis and Dallas but not identical. The reason for the difference is that the mean of the erythemally weighted radiation is at a shorter wavelength in the lower latitude.

Monograph V also describes a number of biologic responses to changes in climatic vari-

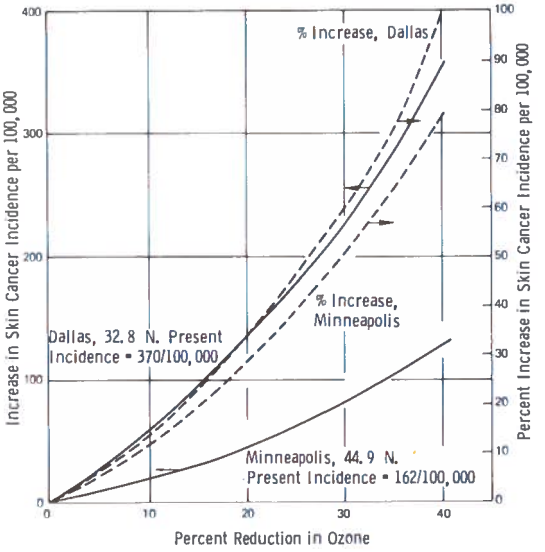

Figure 15. Increase in skin-cancer incidence for various reductions in ozone for two U.S. cities. (After Cutchis (1974).)

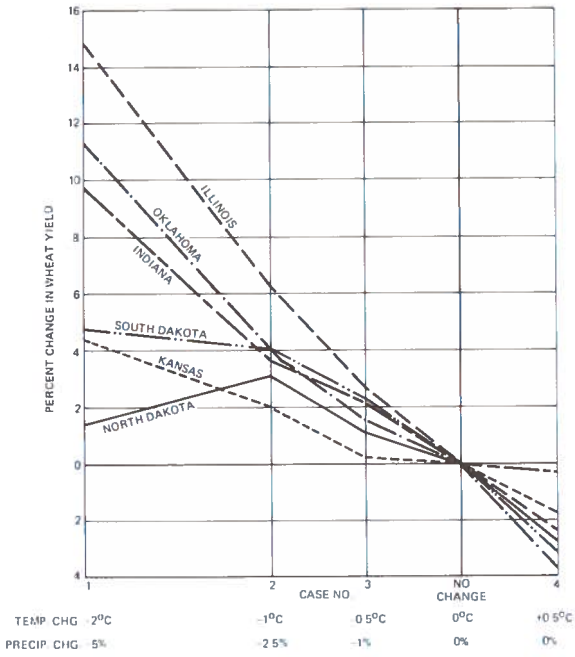

Figure 16. Effect of climatic change on wheat yield in six states. (After Ramirez et al. (1974).)

ables. Figure 16 shows the effect of four examples of climate change on wheat yield in six states in the United States. Each example, or case, represents a combination of changes from normal levels of temperature and precipitation. Since the effects of precipitation and temperature have not been separated, interpretation of Figure 16 is difficult. While temperature decrease by itself is expected to slow growth, it also reduces the rate of evapotranspiration. In the dry farming regions of the United States, the growth of wheat is largely water-limited rather than temperature-limited, so the effect of reduction of temperature in those six states is likely to be an increase in wheat yield. In countries where the temperature tolerance of the wheat crop is marginal, as in Canada and the Soviet Union, the effect of a decrease in mean temperature may be a reduction in the wheat yield, as suggested by the downward trend with cooling temperature indicated by the curve for North Dakota.

The effect of changes in light on rice yield is shown in Figure 17. Rice productivity is particularly sensitive to light intensity. A 2% change in light could in fact cause a 5% decrease in rice yield, according to the mean of the studies in question.

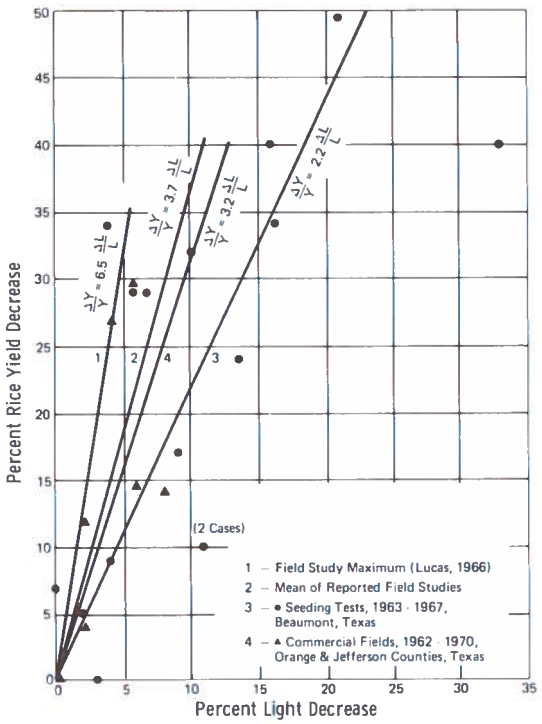

Figure 17. Effect of light on rice yield. (After Stansel (1974).)

Figure 18 shows the change in natural ecosystem productivity (measured by the difference in CO_2 productivity between photosynthesis and plant respiration processes) as a function of temperature change. The growth rates of Arctic tundra, coniferous and deciduous forests, and grassland are all strongly dependent on a temperature range near the values to which they are habituated. A decrease of temperature from that mean has an adverse effect on productivity.

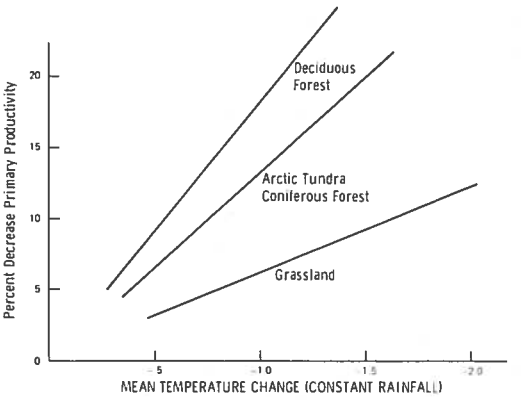

Figure 18. Change in natural ecosystem productivity with temperature changes. (After Cooper (1974).)

Monograph VI

Table 3 shows the results of Monograph VI studies of the economic sensitivity to climatic changes of agriculture, urban and physical resources, and forest and marine resources. A 1°C decrease of mean temperature might severely affect wheat production in Canada and the USSR while the production of wheat in the United States might increase. The same temperature decrease would also greatly affect the rice production of China and Korea. The impacts of a 1°C decrease in mean temperature on living expense in the U.S. may be large; forest productivity may be strongly reduced; even the

Table 3. Sensitivity of Economic Impacts to Climate Changes (after d'Arge (1974))

Area Affected	Nature of Cost For $\Delta T = -1°C$	Annual Magnitude For $\Delta T = -1°C$
Agriculture		
1. Wheat	Reduced Productivity in Marginal Areas	Very Large Cost in Canada and USSR; Slight Increase in Production in U.S.
2. Rice	Reduced Productivity in Marginal Areas	Very Large Cost in China and Korea
Human Resources	Possible Changes in Morbidity and Mortality	Unknown
Urban and Physical Resources		
1. Energy Use		
A. Residential-Commercial	Increased Space Heating	$1.60 per Capita per Year in U.S.
B. Industrial	Increased Space Heating	Very Small
2. Public Expenditures		
A. Fire Protection		
B. Sewage		
C. Highway Maintenance		$1.2 Billion per Year in U.S.
3. Macro-Regional	Locational Shifts	
Forest Resources	Reduced Productivity	
Marine Resources	Reduced Fishery Yields	

productivity of fisheries may, with some delay, be affected.

THE QUESTION OF REGULATION

Distinctly separate at the moment from the physical, biological, and economic considerations discussed so far is the legal basis for regulation of civilian stratospheric aircraft, described in Monograph VI. The review by Larsen and Faggen (1974) emphasizes three points. The first is that national sovereignty, a long-recognized international principle, authorizes regulation of SST's by each nation in its own national air space to guard against undesirable environmental effects. The second point is that United States domestic institutions for such regulation already exist; EPA is empowered to set standards for engine emissions, and the FAA to regulate the operations of national aircraft. The third point is that the International Civil Aviation Organization (ICAO) has the authority to control international stratospheric flight. ICAO is a dynamic organization which provides standards and recommends practices having to do with environmental problems of aviation. One hundred and twenty-eight nations are obligated by treaty to implement ICAO-prescribed procedures, insofar as possible.

With the expansion of civil aviation operations in the stratosphere, many nations (including the present operators of SST's) are faced with decisions concerning stratospheric pollution, since the effects of pollutants introduced anywhere in the stratosphere may be felt worldwide. Aircraft flying over Cleveland, Ohio may affect the people of Western Europe and the Soviet Union as aircraft flying over Moscow and Paris do. Figure 19 lists six choices which each nation will face in 1975. These choices are listed in order, from doing nothing to the other extreme, which is to deny the stratosphere, by international agreement, to all aircraft in the world. The consequences of each of these decision choices can be estimated to the extent that the safe side of the range of uncertainty of consequential effects can be defined. If a nation's choice includes operation of stratospheric aircraft within limits predicted to give non-discernible results by 1974 studies, and monitoring on a worldwide basis for effects subsequently reveals dangers not anticipated by the 1974 studies, the sizes of regulated fleets involved would not be hard to curtail. Meanwhile there would be a grace period of perhaps ten years for further study, to improve the data base and the modeling projection. In 1985, there should be another evaluation, on the basis of ten years of monitoring and analysis of the results, leading perhaps to a new choice, which could take into account an expanded fleet and an increased degree of regulation. In this manner the world may be kept safe from undesirable environmental consequences while the aircraft industry, which is already working on possible solutions to the environmental problems, exercises its ingenuity to adapt itself to the new requirements. In any case, an adequate monitoring system appears to be essential to the success of regulatory efforts.

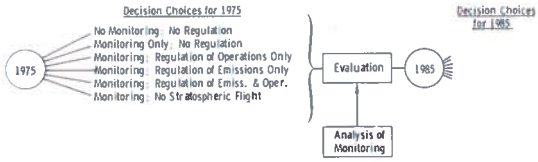

Figure 19. Decisions concerning stratospheric pollution.

Organizations which are concerned with the various functions of monitoring and regulation already exist within the United States and within the United Nations (see Figure 20). Counterparts to the United States organizations are to be found in most nations of the world. Collectively, they constitute a mechanism for implementing suitable regulation, once the needs have been definitively established.

Figure 21 illustrates a suggested basis for world regulation of stratospheric pollution. The CIAP monographs may be expected to display in a preliminary and approximate fashion the sensitivity of the natural stratospheric responses to the introduction of engine effluents, the climatic consequences of those changes (in the troposphere), and the consequent changes in the biosphere. Although the preliminary parametric sensitivities displayed in Figure 21 are at present only suggestions of form, the true values may provide a tentative basis for international regulation in subsequent years by organizations like those in Figure 20. Such data, critically scrutinized, could be used to reckon the consequences

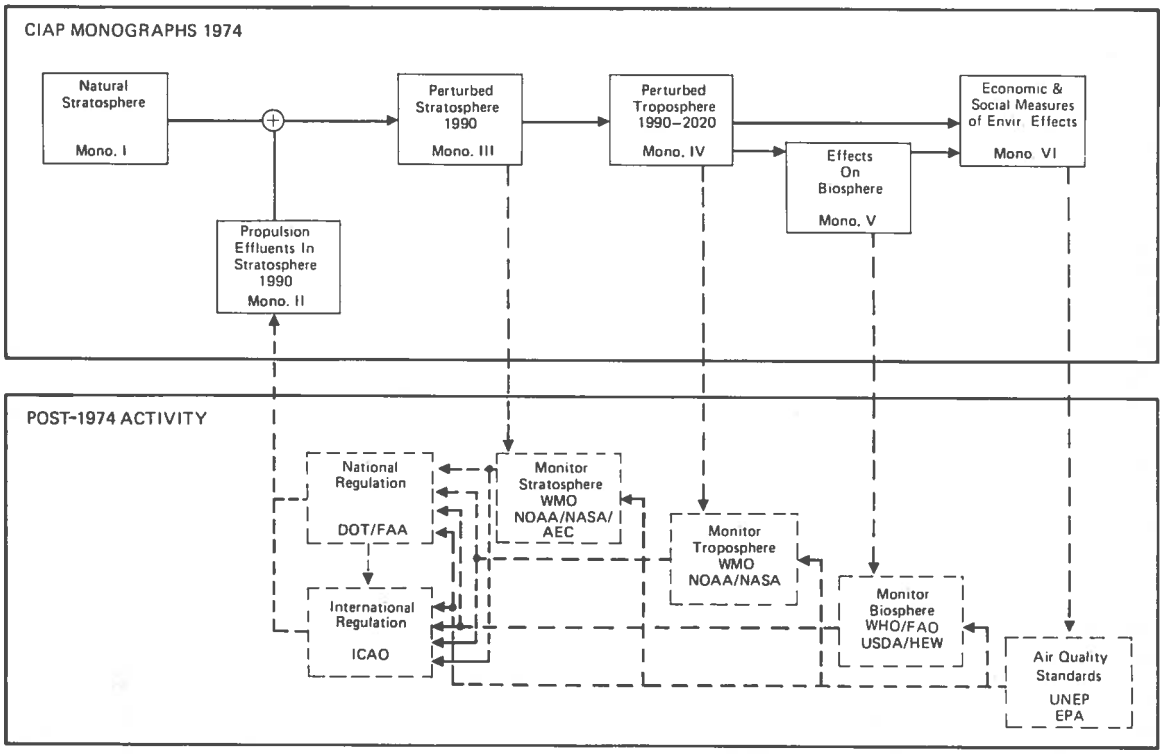

Figure 20. CIAP block diagram.

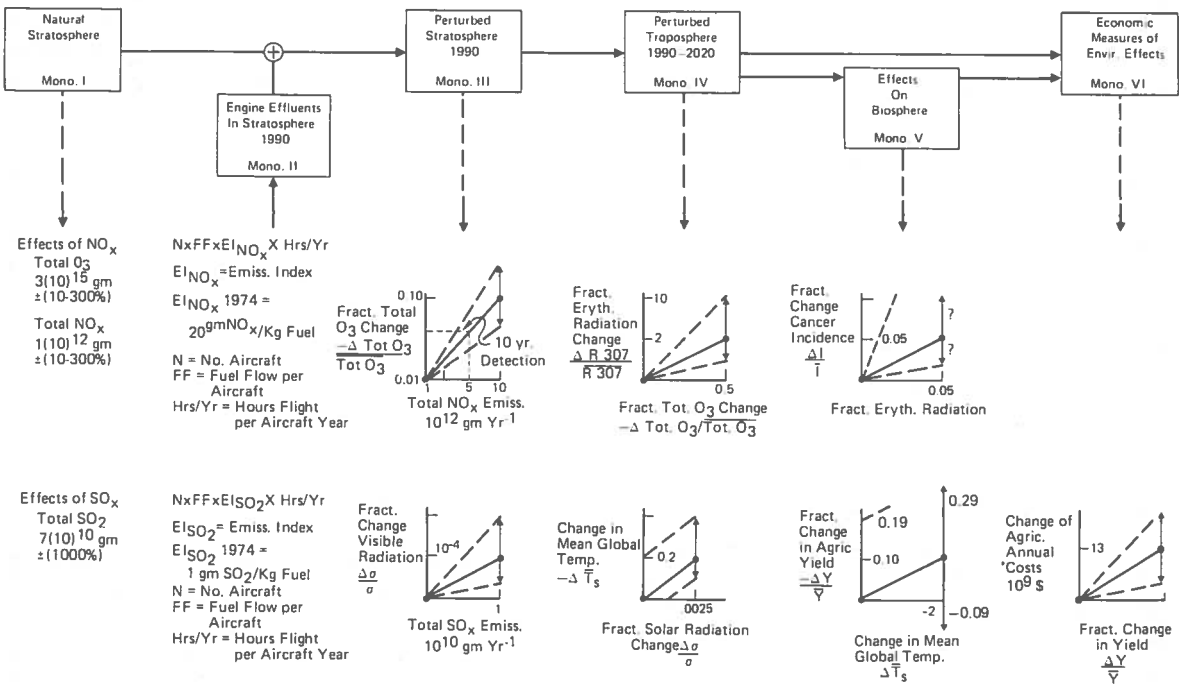

Figure 21. Basis for world regulation of stratospheric pollution.

for the projected sizes of fleets with engine emissions characteristic of 1974 engines, and for various other scenarios which may result from regulatory restrictions of pollution or of technical developments which obviate pollution.

As a preliminary estimate leading to initial regulations (subject to validation by monitoring in subsequent years) it may be useful, for each of the factors contributing to the socio-economic impacts, to work back from the smallest change which may be detected by any conceivable monitoring system. It is suggested that any change smaller than the smallest effect which could be felt or sensed would be tolerable. An alternative expression is that one can tolerate the largest effect which is too small to be discerned by any technique of monitoring.

As an example of working the problem backwards, consider a 0.5% per-year trend of observed changes in total global ozone as being the smallest trend that can be determined in ten years of observation (or, alternatively, the largest trend that cannot be reliably sensed in ten years of observation). Then the total emission into the stratosphere of NO_x which could produce this smallest discernible (or largest non-discernible) trend of global ozone could be the limit used to establish the tolerable size of the stratospheric fleet.

The formula for establishing the size of the fleet would be that the total emission in the stratosphere representing the product of the number of aircraft (N), times the fuel flow of aircraft (FF), times the engine emission index for NO_x or SO_2 (EI), should be less than the least effect that could be detected. Thus, while fleets are small, engine-emission characteristics like those of today can be tolerated. As soon as fleet sizes exceed the limiting aircraft numbers of the formula, then the tolerable engine emissions per aircraft become smaller. Such a formula provides a check so that the stratosphere can be exploited for transportation while avoiding undesirable environmental consequences. It permits the insertion of new values to allow for engine improvements or mistakes in theoretical projections discovered by monitoring systems and makes it possible to safely avoid an arbitrary, costly prohibition of stratospheric flight, which may be so important to world economics in the future.

CONCLUDING REMARKS

This report of progress concludes with a tentative outline of the Report of Findings, which will be completed at the end of this year. This Report of Findings will be based on the data in the monographs. It will review the engineering estimates that are based on the science to which you are all individually contributing. Included in the Report will be a projection of civilian traffic and the emission characteristics of engines expected to operate in the stratosphere in the future. There will also be a general discussion of physical, biological, and economic effects, with estimates of uncertainties of the estimates of each effect, attributed to uncertainties of measurements and estimation and of natural variability. The Report will describe techniques for, and limitations of, monitoring. It will summarize the legal constraints which affect the abilities of nations to regulate, and will list alternative courses of action for which scenarios are to be worked out, and their consequences. Some conclusions will be drawn from the facts, but conclusions based on value judgments will not be included, since they are not appropriate to this study.

The United States effort to anticipate undesirable environmental effects by technical design has been described in this report. To be effective, however, the effort must be an international one. I trust the international cooperation already evidenced in this study will be extended to the international implementing of safeguards against future undesirable environmental effects consequent upon the operation of a world stratospheric fleet.

REFERENCES

Bauer, E. (1973), unpublished data (Institute for Defense Analyses, Arlington, Va.).

Budyko, M.I. (1971), *Climate and Life*, Leningrad Hydrological Publishing House, Leningrad.

Chang, J.S. (1973), "Global transport and kinetic model," in "First Annual Report, DOT/CIAP Program," UCRL-51336, Lawrence Livermore Laboratory, Livermore, CA.

Chang, J. (1974b), in CIAP Monograph 3, U.S. Department of Transportation.*

Cooper, C.F. (1974), in CIAP Monograph 5, U.S. Department of Transportation.*

Crutzen, P.J. (1972), "SST's – a threat to the earth's ozone shield," Ambio 1, 41.

Crutzen, P.J. (1974), "A review of upper atmospheric chemistry," Can. J. Chem 52, 1569.

Cutchis, P. (1973), "Effect of Stratospheric Ozone Depletion on the Solar Ultraviolet Radiation Incident on the Surface of the Earth," P-922, Institute for Defense Analyses, Arlington, Va.

Cutchis, P. (1974), in CIAP Monograph 5, U.S. Department of Transportation.*

d'Arge, R. (1974), in CIAP Monograph 6, U.S. Department of Transportation.*

Elterman, L., R.B. Toolin, and J.D. Essex (1973), "Stratospheric aerosol measurements with implications for global climate," Appl. Opt. 12, 330-337.

English, J.M. (1974), in CIAP Monograph 2, U.S. Department of Transportation.*

Hard, T. (1973), unpublished data (Transportation Systems Center, Cambridge, Mass.).

Hesstvedt, E. (1972), "The effect of water vapor and nitrogen oxides upon the ozone layer, studied in a two-dimensional photochemical model with transport," presented at the International Ozone Symposium, Arosa, Switzerland.

Hesstvedt, E. (1973), "Effect of supersonic transport upon the ozone layer, studied in a two-dimensional photochemical model with transport," AGARD Conference Proceedings No. 125 (Atmospheric Pollution by Aircraft Engines), 6-1 – 6-8.

Johnston, H.S. (1971), "Reduction of stratospheric ozone by nitrogen oxide catalysts from supersonic transport exhaust," Science 173, 517.

Johnston, H.S. (1972), "Photochemistry of the oxides of nitrogen in the stratosphere," presented at the January 1972 meeting of the American Meteorological Society.

Larsen, P.B. and E.S. Faggen (1974), in CIAP Monograph 6, U.S. Department of Transportation.*

Leith, C.E. (1974), in CIAP Monograph 4, U.S. Department of Transportation.*

MacCracken, M.C. (1970), "A Zonal General Circulation Model," UCRL-50594, Lawrence Radiation Laboratory, Livermore, CA.

MacCracken, M.C. (1974), in CIAP Monograph 4, U.S. Department of Transportation.*

Manabe, S. and R.T. Wetherald (1967), "Thermal equilibrium of the atmosphere with a given distribution of relative humidity," J. Atmos. Sci. 24, 241-159.

McElroy, M.B., S.C. Wofsy, J.E. Penner, and J.C. McConnell (1974), "Atmospheric ozone: Possible impact of stratospheric aviation," J. Atmos. Sci. 31, 287.

Newell, R.E. (1969), "Radioactive contamination of the upper atmosphere," in *Progress in Nuclear Energy*, Series 12, *Health Physics*, Vol. 2, Pergamon, Oxford, 538.

Pittock, A.B. (1972), "Evaluating the risk to society from the SST," Search 3, 285-289.

Ramirez, J. et al. (1974), in CIAP Monograph 5, U.S. Department of Transportation.*

Reiter, E.R. (1974), in CIAP Monograph 1, U.S. Department of Transportation.*

Schulze, R. (1974), in CIAP Monograph 5, U.S. Department of Transportation.*

Schulze, R. and K. Grafe (1969), "Consideration of sky ultraviolet radiation in the measurement of solar ultraviolet radiation," in *The Biologic Effects of Ultraviolet Radiation (With Emphasis on the Skin)*, ed. F. Urbach, Pergamon, Oxford, 359-373.

Sellers, W.D. (1973), "A new global climatic model," J. Appl. Meteor. 12, 241-254.

Shimazaki, T. and T. Ogawa (1974), "Theoretical models of minor constituents' distributions in the stratosphere and the impacts of the SST exhaust gases," in *Proceedings of the International Conference on Structure, Composition and General Circulation of the Upper and Lower Atmosphere and Possible Anthropogenic Perturbations* (Melbourne, Jan. 14-25), pub. IAMAP, 1062-92.

Stewart, R.W. (1973), "Response of stratospheric ozone to the simulated injection of nitric oxide," presented at the fall AGU meeting, San Francisco, CA.

Stansel, J. (1974), in CIAP Monograph 5, U.S. Department of Transportation.*

Whitten, R.C. and R.P. Turco (1973), "A model for studying the effects of injecting contaminants into the stratosphere and mesosphere," AIAA paper 73-539 (Denver, June 1973).

*At present, the CIAP monographs exist only in an early draft form. They will be publicly available after completion in September 1974.

AIR TRAFFIC PREDICTIONS FOR 1990-2000

J. MORLEY ENGLISH
School of Engineering and Applied Science
University of California, Los Angeles
Los Angeles, California

ABSTRACT: An estimate of engine emissions in the stratosphere for any given time frame depends on two variables: the magnitude of the global air-transportation system and its rate of emission. Projections of the growth, altitude, speed, and geographical distribution of air transportation are made on the basis of the economic indicators of population and gross domestic product. These are related to a scenario for growth (predicated on continuation of present trends) over the next 50 years (to 2025). The influences that determine or limit growth are all assumed to be favorable, in order to establish upper-bound or worst-pollution conditions.

Engine emissions per unit of traffic will decline if enough research and development effort is directed toward improving engine characteristics. Again, however, the emissions have been assumed to be those which would occur if no unusual effort were made to reduce them, so as to establish the worst-case condition.

On the basis of these assumptions, predictions are made for global emission levels within 5° latitude and 5° longitude grid squares for each 3-km altitude band. All results should, of course, be considered as preliminary only.

INTRODUCTION

Objectives

This paper predicts aircraft emissions in the stratosphere in the 1990-2000 decade. Emissions by species, geographical location, and altitude were determined for use in the atmospheric models to be reported in the Climatic Impact Assessment Program Monographs III and IV.

A 5° latitude × 5° longitude grid was used for locating emissions so as to interface with the atmospheric models. Aircraft emissions were determined for altitude bands 3 km deep, starting at 9 km and extending to 30 km.

While some preliminary work was done to establish the tropopause height as a function of time and space, tropospheric and stratospheric flight were not directly distinguished. Altitude bands discriminate between them on a meteorological basis.

Predicted engine emissions have to be related to numbers, sizes, speeds, and altitudes of the aircraft projected to be flying. In other words, the first estimate was volume of air traffic. Directly associated with it is the amount of fuel required for propulsion. Because emissions are related to kilograms of fuel burned per hour, they can be estimated simply by multiplying the fuel times the emission index (grams of pollutant per kilogram of fuel burned) for the species in question. The studies could thus be divided into 1) the traffic prediction, with the associated fuel consumption; and 2) emission-index predictions for engines that might be in use by 1990-2000.

The study emphasized a maximum or upper-bound traffic projection rather than the most-likely level. This projected maximum traffic will materialize only if all economic conditions are favorable and no regulations are imposed on traffic.

It should also be emphasized that the study did not specifically focus on the effects of supersonic transports (SST's). While it may be true that the SST will have a relatively greater influence on climate than the subsonic jets, its main effect may be to change the altitude distribution of emissions. There unquestionably will be some coupling of supersonic traffic demand with subsonic traffic demand. An economic climate in which supersonic travel flourishes may well encourage increased subsonic travel. However, such effects were not considered.

The Philosophy of Prediction

Long-range prediction is by nature speculative. The course of the future is certain to be altered by apparently trivial events that will

trigger chain reactions. Fortunately, most of these triggering effects apply to components of the world economy and are significant in shaping the future of these components. They may not materially alter the overall course of societal evolution. Evolutionary trends have persisted over a very long time, and short of cataclysmic and totally unpredictable events, they must be presumed to continue. This persistence of trends is an important consideration, because the development of any transportation system must be viewed within the context of a projected human environment.

Most projections of transportation requirements are made by extrapolating past transportation trends into the future. Extrapolation is necessarily a divergent process; the variance of actual outcomes from expected outcomes is exponential (see Figure 1). Such projections are *forecasts*, which are statements of the future by objective and quantitative analysis of past data. Whatever system characteristics are forecast, the variance in outcome beyond 5 to 10 years into the future tends to become so large that confidence in the outcome is too low to allow for meaningful planning.

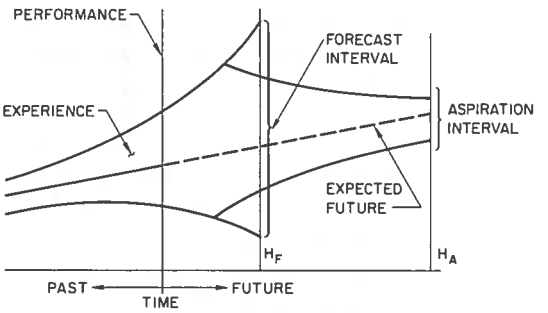

Figure 1. Prediction and aspiration levels (from English (1971)).

Predictions, on the other hand, are based on subjective expectations, which may be predicated only partly upon forecasts (Brown, 1963; de Neufville & Stafford, 1971). Expectations, aspirations, or goals (described in such broad, general terms as quality of life, prosperity, and the like) are convergent in nature (English, 1971). If the various human institutions employed to meet perceived needs do not appear to be helping to achieve the goal, they can be abandoned in favor of something else. Thus there is an adaptive feedback process that produces the desired convergence. As time passes, the goal itself may also vary, but this variance is likely to be relatively small compared with that of a particular system. In short, the process for developing technologically-based means for achieving broad social goals consists of components of a self-fulfilling prediction matrix (Jantsch, 1967). This principle indicates a need, then, to predict the *social and economic environment*. Once that has been done, a number of scenarios may be studied to see how environmental goals can be achieved. The growth factors of population, gross world product (GWP) per capita, and distributions of income are fundamental variables in the prediction of the future world environment of which any air transportation system will be a part.

Nevertheless, it is essential to consider influences that may tend to limit attainment of the postulated environment. Certain influences will operate to produce saturation effects within the economy as a whole, as well as within the component systems. For example, a significant constraining influence might be the finiteness of world energy resources.

Forecasting and Prediction

The very nature of predicting, as contrasted with forecasting, implies a longer-range objective. We must go beyond the limit of a valid forecast if we want to predict. As a consequence, we are forced to abandon dependence on past observations as guides to the trends of the future. What is left to us to rely on for underpinning our predicted outcome, then, is some concept of what we hope to have develop – in short, our aspirations.

It must of course be recognized that these cannot be defined precisely. What we now perceive to be a desirable future will undoubtedly change as events unfold. However, the variance of our aspirations as a function of futurity, if described in very broad terms, is likely to be much less than the variance of a forecast of any one component of that future environment. Furthermore, if our aspiration remains constant, we can adjust our strategy to modify our actions as necessary to make the predicted system conform to the aspiration. In other words, prediction of any system takes on a

self-fulfilling characteristic to the extent that it continues to fit (or be fitted to) one's aspiration.

This characteristic may be depicted with reference to two horizons, as in Figure 1, where H_F is the forecast-horizon and H_A is the aspiration-horizon. If no adaptive change is made in the system up to H_F, we may say with some level of confidence that the actual outcome will lie somewhere in the forecast interval. Beyond H_F, feedback effects will enable modifying actions to effect convergence to the aspiration at H_A.

An aspiration will require the prediction of the type of environment within which that aspiration is attainable. We can make some projections for the long run, particularly if our expectations are constrained by certain postulations of what will not happen. For example, it is customary to postulate that world development will not be interrupted by cataclysmic occurrences such as a worldwide nuclear war or pestilence.

Barring such catastrophes, long-term trends of population growth and increasing material standards of living may be expected to continue. On this basis we may sketch a picture of the world at time H_A and proceed to fill in details by means of a scenario.

The Scenario Approach

A scenario is a hypothesized situation that represents a plausible description of what could occur within predicted environmental constraints (Ayres, 1969). Because the scenario is set beyond the horizon of the visible future, it is not a valid prediction. It therefore gives rise to if-then questions – which, in the absence of clairvoyance, is probably the only reasonable approach.

The first consideration in picturing a scenario of the future is that of the time frame. It is desirable to go well beyond the time interval of specific interest in order to see what sort of influences may begin to emerge for the very-long-range goal to be achieved. The actual time at which an environmental goal is reached may not be very important. Just as the aspiration itself is unclear, so the time at which the scenario unfolds is highly variable. The question of concern is more one of the achievability of the postulated state, rather than the specific date of achievement. Thus we will consider the year 2025 as an arbitrary target date, and not be concerned about the possibility that the postulated environment may not be reached until 2035 or 2045.

Limits of Technology

An important advantage in using the scenario approach to prediction derives from the enforced examination of limiting technological factors. These can be upper-bound constraints on development. On the other hand, the air-transport industry will expand with evolving new technology. In most cases, where the urgency for new solutions is sufficiently strong, technical solutions will be forthcoming. Thus, recognition (manifested by sufficient funding) of a need to reduce NO_x by a significant factor will help ensure its accomplishment.

Full growth of air-traffic demand will occur only if certain technological problems are resolved. An optimistic projection of air-traffic demand implies that they will be. At the same time, it is well to recognize that certain other conditions, more often economic than technical, may provide constraints on the growth of the system. At least three such conditions need to be considered here:

a. *Energy costs.* It is entirely possible that a sharp rise in fuel prices will inhibit growth of air transport. However, it may be unwise to be concerned with the current "crisis". The fuel shortages that are now causing roll-backs of world airline scheduling are the result of short-run supply limits and political realignments rather than longer-run, physical-resource constraints. In the end, the development of other sources of energy, including synthetic fuels, may be expected to solve the problem. In the meantime, the effects could still cause a growth hiatus that might shift the growth curve a few years, but that would not necessarily affect its long-run achievement. For the purposes of this study, such aberrations were not considered.

b. *Airport capacity.* In the next 50 years air-traffic-generating population centers will not change materially from the present ones.

Many airports may be approaching capacity limits, but the development of new airports requires long lead times. Airport capacity may be limited by two problems: air traffic and ground access. The solution to the first lies in increased size of aircraft. The solution to the second must be related to improvement in urban transportation, and this is likely to proceed slowly.

c. *Public attitude to travel.* Societal values can shift quickly. At present people the world over tend to increase travel as their disposable income grows. In the future, they may shift their choice to some other form of diversion that keeps them home. However, the persistence of the past trend was assumed to continue for the purposes of this paper.

Basis of the Predictions

The fundamental predictions from which the emission rates were estimated were based on two separate levels of air-traffic forecasts, depending on the confluence of factors that might be expected to influence the outcome. These predictions were termed upper- and lower-bound predictions. Only the upper-bound prediction is addressed in this paper, and all discussion is predicated on this traffic level. The reason for selecting an upper-bound level rather than the most-likely level was the need to assess a worst-case condition. Furthermore, from the nature of long-term prediction, the variance of the actual level that may eventually occur can be expected to be very large.

On the other hand, engine emissions can be predicted with quite a high level of confidence. How engine emissions will vary depends on explicit decisions, the effects of which are known within reasonable limits. The problem of emission reductions becomes clouded only when order-of-magnitude reductions are considered. For this reason, emission predictions were based on most-likely levels, without consideration of new regulations. These most-likely emissions were coupled with the upper-bound traffic projections, thus establishing an emission level for use as a baseline for all other modeling.

Although this paper does not deal with the lower-bound prediction, the SST merits special comment. Supersonic transport may not prove a viable system and could pass from the scene altogether, in which case its lower-bound contribution would be zero. At the same time, the present SST programs in Europe and the USSR will very soon culminate in the entrance of the Concorde and TU 144 into commercial service. After the initial enthusiasm for these airplanes wears off, it will still take some years to be sure that the SST is (or is not) an economically viable system. Even if the SST is proven not to be a viable system, the aircraft already produced will be operable over their lives at the marginal cost of operation, without consideration for amortizing the sunk costs of past development expenditures. Thus even a marginally operational SST system is not likely to comprise fewer than 100 airplanes.

Energy Consumption for Propulsion

In comparing the energy requirements of different modes of transport, it is instructive to use a measure of passenger-kilometers traveled per kilogram of fuel (pk/kg), or passenger-miles per gallon, called the net propulsion-energy intensity.

The energy intensities of some typical present and proposed flight systems, based on a 50% load factor, are given in Figure 2. The energy intensity for a typical urban automobile, assuming 1.15 passengers (average utilization in the USA), is also shown for comparison. It can be noted that the first generation of jets were more energy-intensive than the DC-6, which represented the peak in piston-engine-transport efficiency. The present wide-bodied jets represent an improvement in energy intensity; they provide 10 to 12 pk/kg. Further improvements may be expected from subsonic aircraft.

On the average, there has been a 25% increase in propulsion-energy intensity between 1955 and 1970 for U.S. domestic trunk traffic (Rice, 1972). The bulk of this is due to the drop in load factor from 63.1% in 1955 to 49.7% in 1970 (CAB, 1971). It may be concluded that when the load factor is considered there has been little change in propulsion-energy intensity over this 15-year period.

It should be kept in mind that propulsion-energy intensity measures only a part of the total cost of the transport systems. In comparing air

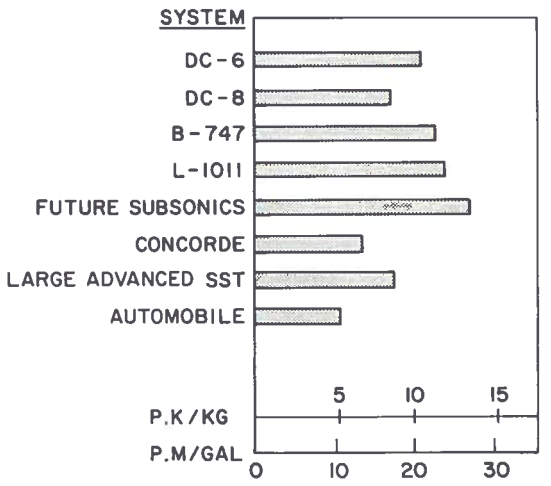

Figure 2. Net flight-system propulsion-energy intensities.

transport (which averages 12 pk/kg) with road and rail transport (which averages 70 pk/kg), other factors such as travel time and comfort must be considered. For example, over the 1955-1970 period the average fare (measured in constant dollars) dropped by 27%, while the average speed approximately doubled.

In terms of propulsion-energy intensities alone, the use of supersonic transport will represent a significant disimprovement. It is estimated that the Concorde will be slightly over twice as energy-intensive as present subsonics. Although improvements are anticipated for an advanced SST, its energy intensity will still be considerably greater than that of the generation of subsonics that will be coming into service at that time.

If propulsion-energy intensities must be improved, the most direct method would be to improve load factors. If airlines could operate at a load factor of, say, 75%, it would result in a 50% decrease in propulsion-energy intensity over present levels. Similarly, if the increase in energy intensity that will result from supersonic flight is undesirable, it could be partially alleviated by requiring SST's to operate at higher load factors than subsonics.

Passenger Fares

The effects of changing technology, growth of aircraft size, and increasing travel demand have over the years resulted in a declining fare per passenger-kilometer, as shown in Figure 3. Each new airplane development has resulted in both higher speeds and declining fares (in constant dollars). Undoubtedly, growth in demand has been partly the result of reduced costs of travel. At the same time, the amount spent on travel as a proportion of total consumer spending has risen steadily. The rising trend of spending for travel has also been characterized by availability of faster modes. The railroad gave way to the automobile, which in turn has been partly replaced by the airplane. The fact that the automobile is only partly supplanted by the airplane is largely due to the separate functions each is uniquely capable of satisfying. It is quite likely that proportional spending for the short trip by automobile will decline. Assuming that per-capita travel will continue to expand, or at least that the proportion of spending allocated to travel will remain constant, the amount spent on air travel will increase considerably. What may prove to be the limiting factor is time available for air travel. Thus, it is quite realistic to expect an increasing travel demand even in the face of rising passenger-kilometer prices.

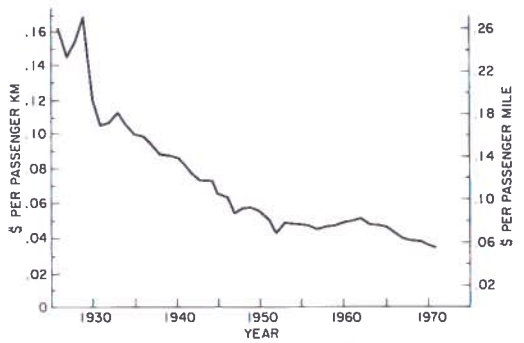

Figure 3. Average passenger revenue for U.S. domestic scheduled airlines in constant 1970 dollars (CAB, 1971).

However, such rising prices may still be some time away, even with the introduction of a premium-fare SST, operating in conjunction with a predominantly subsonic fleet. A two-speed-market demand may be satisfied with differentiated fares, even with average fares falling.

Very little is really known about the long-term price elasticity of demand. A rising-price trend will unquestionably have some depressing influence on demand growth. It may be argued that the continued growth pattern of traffic demand will be maintained if the average price of air travel is not changed in any significant way.

This, as one of the favorable economic-environment factors, is an underlying assumption of the projection.

On the other hand, the differences (if any) between subsonic and supersonic fares may be expected to have a very important influence on the proportion of the travel demand represented by an SST, or, for that matter, a hypersonic aircraft (HST). It is the consensus that SST operating costs will be higher than those of subsonic aircraft. An obvious reason is the extra fuel consumption. At the same time it is worth recalling that in the early 1950's, almost without exception, seat-kilometer costs of the subsonic jets were expected to be on the order of 20% higher than those of propeller-driven aircraft. The reason that these predictions proved to be false was the higher-than-expected productivity of the jet. A similar unexpected development should not be ruled out for the SST. One such difference could conceivably be lower, rather than the generally expected higher, fuel prices, making the cost of fuel in proportion to capital and other operating costs less significant in the overall fare structure.

Influences of Changing Technology

Technological improvements in airplane performance, as described above, are not likely to alter materially the fuel consumption per passenger-kilometer or tonne-kilometer. The potential for reducing emissions, short of constraining the growth of demand, is limited, although considerable progress can be expected in engine development.

Lowered emission indices may not improve airplane performance; in fact, some loss of efficiency might result. For this reason neither airplane companies nor engine manufacturers are likely to greet a demand for lowered emissions with much enthusiasm. Also, programs for developing clean engines may be very expensive. These costs will require corresponding fare increases.

Important technological improvements are possible for fuels. Hydrogen offers some promise for reduced NO_x, and is clean in other respects. Synthetic fuels may be manufactured that could somewhat reduce NO_x and eliminate all contaminants such as sulfur.

Air Transport versus Emissions

Emissions in the stratosphere might be limited in a number of ways. The one obvious method, that of prohibiting stratospheric flight, has not been considered in this paper. The worldwide economic cost of non-use of the stratosphere would be enormous. Furthermore, there must be some emission rate that will not result in excessive pollution of the environment, and as more knowledge is gained on the cleansing mechanisms in nature, the acceptable level might be raised. In the meantime, as emissions grow with traffic, compensating reductions can be effected by raising load factors and reducing emission indices.

Figure 4 shows two growth curves for emissions in the controlled and uncontrolled states. Curve A represents the growth of emissions for an unconstrained demand. Curve B shows a growth that might result from the determination that the permissible limit for the stratosphere is, for example, 8,000 metric tons a day.

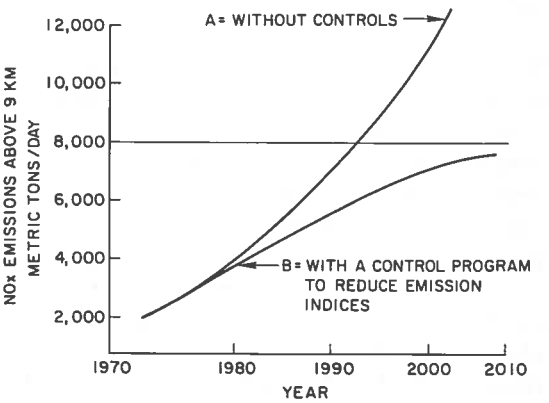

Figure 4. Growth in emissions and for different control policies.

AIR TRANSPORT DEMAND AND SERVICE PREDICTION

Scenario and Air Transport Prediction

Air traffic levels for the 1990-2000 decade are predicated on the scenario for the year 2025, described previously. It is assumed that by this time the industry will have achieved maturity.

For a prediction to be made, the economic indicators influencing the attained level must be examined.

Population

Population may reasonably be taken as the first indicator of what world travel might be. The magnitude of world population will depend on several parameters, not the least of which is the success of current efforts to control fertility rates. However, even if zero population growth (ZPG) is attained on a global basis, it is inconceivable that world population will stabilize at anything less than double its present level, and three to four times present levels is more likely. The ability of the world to support a significantly larger population at a higher standard of living than might presently be envisaged is described by Gilfillan (1972).

With population growing by a factor of four, pressures will most certainly arise for people to migrate to less populous regions. Under the most favorable circumstances, not only will these regions grow rapidly, but the growth will be accompanied by the boom characteristics always associated with rapid economic development. It is just this sort of environment that may be expected to favor rapid expansion of air transport. Furthermore, the air-transport system itself may represent a feedback phenomenon that induces economic growth. This kind of economic development may be characterized by disproportionate expansion of social overhead capital (infrastructure), along with very rapid resource exploitation. The components of the Gross Domestic Products* (GDP) represented in such activity may also be expected to be reflected in a greater growth in business travel than would be the case for already developed regions.

It must be recognized that the GDP composition will be vastly altered in 2025 from what it is at present. Increased living standards will induce significant changes not only in the less developed regions but also in the most advanced areas; people's needs will alter along with their capacities to fulfill them.

Some components of the present U.S. living standard will not be expandable to a world scale, however. Saturation of demand on certain resource capacities may be prohibitive. A notable example is the availability of suitable aircraft fuel.

Projection Backward, or Prediction by Interpolation

With the establishment of a scenario for the economic environment of 2025, along with an air transport system projection that is plausible in that context, it remains to project the developments that must take place if we are to progress from here to there (English, 1972; Tsou, 1972). The 1990 and 2000 air-transport levels may be determined by projecting backwards from 2025. This approach avoids the problem of forecast divergence, associated with extrapolation of present air-transport growth trends. However, it requires that industry produce the technology to meet needs as the perception of these needs emerges.

Furthermore, this approach may be expected to reveal inconsistencies. It may turn out that some aspects of the projected 2025 system are physically unrealizable within the postulated time frame. In particular, there is reasonable evidence that even where a very strong demand exists over a protracted period of time, growth of technology to meet that demand may be limited to about 20% per year. This tendency for new technologies to pace growth may be a phenomenon of man's organizing abilities rather than a technology-limited condition.

A second feature of the scenario approach is that one sets out to demonstrate what might occur, rather than what is most likely to occur. In this case of a world air-transportation system, it is the aim to assess the possible effects of emissions from engines in the upper atmosphere. This viewpoint ignores the decisions facing aircraft and airline industries as to capital commitment to future ventures. The industry must show a profit. We, on the other hand, are concerned with the problem of how large the system can become, given the most favorable set of environmental circumstances.

* Gross domestic product was used throughout, but Gross National Products (GNP) would have done as well. The difference represents export/import balances. However, for the world as a whole, the difference must cancel out, and for any one region it is small.

Fitting a Growth Function

Growth phenomena have been found to have the characteristics of a rapid exponential function in the early stages. As inhibiting influences arise, the growth rate slows and eventually approaches some saturation level. While various growth functions have been used for prediction, one of the most widely accepted is that of Gompertz (Burns, 1934; Gaston, 1961). The unique feature of his approach is use of a declining growth rate. The Gompertz function was used for the air-transport scenario on a region-by-region basis. For North America, as an example, the growth rate of the propensity* toward air travel is expected to decline from 8.75 to zero by 2025.

The Predicted Economic Environment of 2025 A.D.

Economic growth of the world may reasonably be expected to continue in terms of conventional measures of GDP. One of the difficulties and dangers of using GDP measures lies in the characteristics of those components of economic activity that are actually counted in GDP. In many respects GDP is a measure of increasing social and technological complexity. As a society develops, more activities are accounted for in GDP. Thus GDP growth rates actually include a component representing the rate of introduction of certain factors into the accounting system. At some point these factors of growth become stabilized with that of the GDP, and their influence on the GDP growth rate disappears. For such reasons the mature economies of the world will exhibit lower growth rates than less developed regions. In the long run this tendency leads to a more uniform worldwide distribution of GDP (which will mean a higher overall standard of living by 2025). In spite of its shortcomings, GDP may still be the best indicator of spending available for air transport.

In order to write a plausible air-transportation scenario, we must first speculate on how people will choose to allocate their spending, at both individual and societal levels. In doing this we must be cognizant of social, political, and economic customs, as well as of interactive influences of societies on one another.

In making any prediction, extrapolated trends should be treated with caution. Average world patterns tend to become quite implausible. For example, by 2025 it is predicted that GDP per capita will be higher than the USA figure for 1970. If the 2025 gross world product were related to numbers of automobiles in proportion to the USA automobile use of 1970, something on the order of 4 billion cars would be required and they would consume roughly 4×10^{12} gallons of gasoline (10^{11} barrels) per year. This number seems somewhat improbable. Traditional consumption proportions must change relatively; food expenditures may be expected to decline, and housing quality will increase as the annoyance of moving about in the congested urban setting restricts local travel. At the same time, unit costs of housing may be increasing. This inhibition of expansion of mobility within the city may result in increasing travel to more remote areas.

One factor that may translate into increased propensity for traveling is the growing difference between our expanding productive capacity and societal demands based on established consumption patterns. This difference opens up a possibility for diversionary activity. Diversionary activity is discretionary; it represents those types of activity that people perceive as desirable but non-essential (English, 1974). It may be individualized or institutionalized. For example, a company may provide well-organized travel packages for employees. The employee has the choice of accepting or rejecting them, but the attractiveness of travel options may be such that his decision is biased toward taking advantage of them.

Corporate-employee relationships in Japan, for instance, are quite different from such relationships in the USA. The more highly institutionalized Japanese business environment sponsors travel, and we see everywhere the resulting travel explosion of Japanese businessmen. Although there is a tendency for the peoples of the world to opt for similar standards of living at the same time, there are still significant differences in how they will choose to spend their time on diversionary activity. The

* Propensity toward air travel is defined in passenger-kilometers per constant dollar of GDP per capita. It is discussed in greater detail later in this paper.

USA, approaching maturity, has an already-well-established pattern of consumer demands. While there is considerable leeway for expanded diversionary activity to take the form of world travel, the relative gap between perceived essential needs and production capacity will remain smaller in the USA than it is in Japan and other developing regions where consumption demands are traditionally small.

The 2025 Air Travel Scenario

A scenario of the world air-transportation system that is possible and plausible, and that does not violate obvious physical characteristics, is as follows:

- No more than 20% of the world's population will contribute to air travel.
- A maximum of 2.5% of GDP will be spent on air travel.
- Average fares will remain constant (in constant dollars).

Given these conditions, it follows that total travel will approximate 4.1×10^{13} passenger-kilometers a year. For an average speed of 1,000 km/hr and trip length of 2,400 km, the average travel distance and time amounts to 16,000 km/yr, and 16 hours/year/air traveler. Compare this with an average of 13 hours in the air for the typical U.S. air traveler today who flies 10,000 km per year. Such a high postulated demand would have to be viewed as a maximum conceivable economic demand.

Constraining Influences

The feasibility of the predicted scenario must be examined to determine whether there are any physical constraints that will prevent its realization. While the two constraints below may pose some problems in the short run, they are not expected to seriously affect the predicted growth in air traffic in the long run.

a. *Airport constraints.* Traffic flows of the size determined by the foregoing spending levels bring into question the feasibility of accommodating them. While there are many small airports that may accommodate as much as half of the traffic, the other half will still flow through major terminals.

If there were 1,000 large airports, each would be accommodating an average of 6 million passengers, in or out, per year. Undoubtedly, the average airplane would have to be considerably larger than it is today – say 300-seat airplanes operating with a 50% load factor. This would require 10,000 operations per year, or fewer than 150 landings per day on the average. Of course, there will be many airports operating at the limits of their capacity, but what these limits will be in 2025 is difficult to say. In any case, the effect will be to distribute traffic from saturated centers to other centers. Most flights will be direct origin-destination journeys. For example, a traveler wishing to go from Wichita, Kansas to Belgrade, Yugoslavia will not make one transfer in New York and another in London, but will more likely fly non-stop.

A further effect of increasing the number of operations from each airport will be a concomitant increase in airplane capacities. Thus the large saturated airports will handle the very large airplanes, probably much larger than the present B747, while smaller centers will be served by the smaller long-range aircraft such as the DC-10-30, as well as long-range narrow-bodied airplanes.

b. *Fuel.* The predicted increase in air traffic must be considered within the context of availability of necessary fuel sources. For example, domestic trunk lines account for 3.0% of the total U.S. crude; consumption will have more than doubled by 1990 and airline needs will have increased to 6%. However, estimated world petroleum reserves at present may be expected to suffice for another 490 years, at present U.S. consumption rates (Johnson and Craig, 1973). Thus the problem of limitation of fuel resources and its effect on the growth of air traffic may not be serious for this century. (This does not imply that temporary shortages such as the present crisis of supply will not cause disruptions.)

Beyond 2000, the limitations of resources must be considered in predicting air

traffic out to the 2025 horizon. Should petroleum resources prove insufficient during this period, it is predicted that technological advances will lead to the development of alternative fuels at economic prices. Liquid hydrogen is a technically feasible fuel today, and future developments could make it competitive with petroleum fuels. Development of new synthetic hydrocarbon fuels is also a possibility.

The price of fuel, which is a function of both supply and demand, must also be considered in predicting future air-traffic levels. The growth predicted in this report is based on the assumption that there will be no significant change in the relative cost of air travel over the planning horizon. This assumption must be examined in the light of recent apparent increases in the price of jet fuel. Fortunately, a significant part of these increases may be explained by general inflation in world prices today. In the short run there may be significant price fluctuations due to inflationary forces and political factors; however, it is assumed that in the long run the price of fuel will be dictated more by the economics of supply and demand. Given the present supply and demand for petroleum fuel, there may be insufficient economic rationale for justifying significant long-run increases in the real price of jet fuel.

High-Speed Aircraft

Vehicles faster than the present subsonic jets must fly at supersonic speed and at much higher altitudes. At present, indications are that higher speeds, requiring considerably higher fuel consumption per seat-kilometer, will be economical for an average fare somewhere between 10% to 30% above present averages, provided that such a fare premium does not seriously impair demand. This does not mean, however, that posted SST air fares on scheduled high-density routes need be any higher than present scheduled coach fares. Load factor, airplane productivity, range, and the like are all considerations that enter into the optimum air-fare structure for a mix of aircraft on a world-wide transportation network. The question of elasticity of demand for the extra speed of the SST remains unresolved. Many authorities lean to the opinion that extra speed will have little value for most of the traveling public. Possibly only 10% of the total market may turn out to be suitable for SST operation. With the greater productivity of the advanced SST (a 300-passenger Mach 2.7 airplane would be roughly three times more productive than a Boeing 747) approximately 1,000 such airplanes would be needed.

World Air-Transportation Demand

The world demand of 2025 described in the scenario above provided the basis for determining traffic growth functions. Aggregate world air passenger demand was predicted in seven major regions* of the world by examining the demographic, economic, and social characteristics of the peoples of these regions. This regional demand was then distributed to grid pair routes**. Cargo demand was projected similarly.

Military traffic presented a less-well-defined problem. In the first place, there is little publicly available information on military flying on a world scale. Secondly, military flying will expand or contract in response to world tensions. On the other hand, while the numbers of aircraft are large, their utilization factors are very low compared with those of commercial operations. Thus, relatively large errors of estimation of such flying may be expected to have little influence on total traffic prediction. Finally, the upper-bound prediction for commercial traffic is realizable only in a world of extremely favorable economic conditions, which will obtain if there is a long period of generally peaceful conditions, in which case military flight would diminish.

General aviation is another segment of traffic that was deemed insignificant. Most flights may be expected to be short. If the longer-range corporate-jet component grows significantly, it will have to be at the expense of the scheduled air carrier. Therefore, it will not be an addition to but a substitution for the commercial traffic.

* Divided according to the convention of the population division of the Department of Economics and Social Affairs of the United Nations.

** The world was divided into a 5° latitude by 5° longitude grid in accordance with a CIAP specification.

Demand Prediction Model

The economic indicators of propensity to travel, population, and gross domestic product were used to predict air-travel demand.

a. *Propensity to travel.* The regional propensity to travel, a, is a convenient parameter for describing the segment of per-capita income that is allocated to air travel. It is defined as

$$a = \frac{\text{Regional annual air travel (pk)}}{\text{Regional per-capita product (\$)}}$$

Strictly speaking, propensity as an economic term is a non-dimensional parameter expressed as dollars of travel per dollar of GDP. In this context the meaning is specialized.

Propensity-to-travel data for the world regions in 1970 is given in Table 1. Note that Asia has the highest propensity to travel. This is due to the dominant effect of Japan on Asian air travel, and is also a result of the comparatively low per-capita income for this region. Europe has the next highest figure, 74.18, while the U.S. is 56.14. Propensity to travel is predicted to increase in the future and approach maturity by 2025. At maturity, continued growth in travel would be no greater than that of general economic growth. Eventually other economic and social goals may be expected to force the substitution of a new economic activity for travel, but this is not expected to be a likely development for all regions of the world before 2025.

The predicted growth rates of propensities to travel are also shown in Table 1. The growth rates for North America, Asia, Europe, and the U.S.S.R. are predicted to decline in the future according to a Gompertz function. The growth rates for Africa, Latin America, and Oceania are expected to behave differently, as the economic development patterns will vary. The growth rate in Africa is expected to increase till the end of the century due to its high potential for economic development. After 2000 the rate will decline. The growth rates for Latin America and Oceania will reach a maximum in 1990 and will then decline to reach maturity by 2025.

The declining growth rate in passenger air travel for developed countries is clearly indicated by U.S. data (CAB, 1971). Figure 5 gives revenue passenger–kilometers from 1930 to the present. The growth rate derived from this, shown in Figure 6, indicates the decline that has occurred, from 30% in 1930 to 6% in 1970.

b. *Population.* A reasonable upper bound on population was predicated on the maintenance of present growth rates to 2025 (United Nations, 1970), Table 2. An exception was made for Oceania, for which the rate was doubled on the theory that boom economic conditions associated with a rapidly expanding air-transport system would induce inordinately high immigration.

c. *Regional per-capita domestic product.* Existing forecasts (World Bank, 1971) were used in predicting upper-bound per-capita

Table 1. Predicted Rate of Passenger Propensity to Air Travel

Region	1970 Propensity $\left(\frac{pk \times 10^6}{\text{income per capita}}\right)$	Propensity Growth Rates (%) 1980	1990	2000	2025
Africa	43.11	4.5	6.5	8.5	2.75
Latin America	32.86	6.5	9.5	7.4	1.5
North America	56.14	6.25	3.5	1.75	-0.5
Asia	155.64	11.8	7.6	4.3	0.1
Europe	74.18	5.5	3.0	1.4	-0.5
Oceania	4.79	7.5	9.5	5.55	1.0
USSR	48.84	7.5	4.3	2.3	-0.3

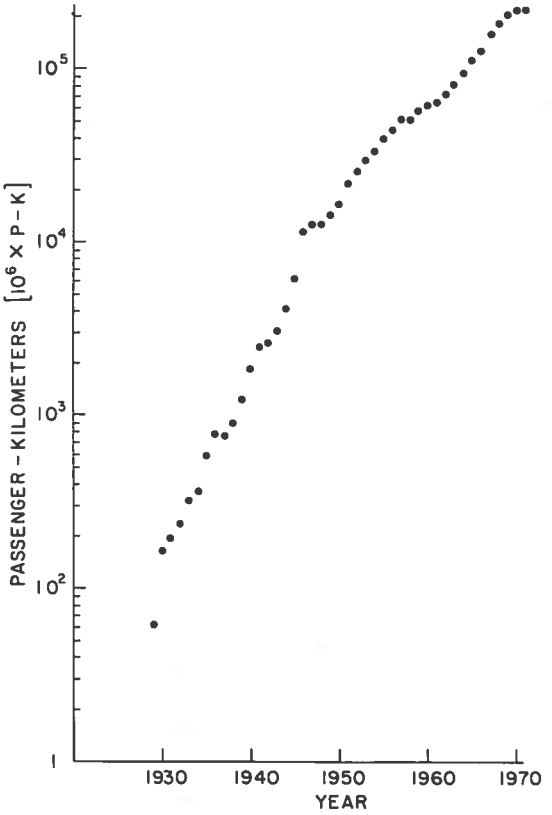

Figure 5. U.S. passenger travel by air.

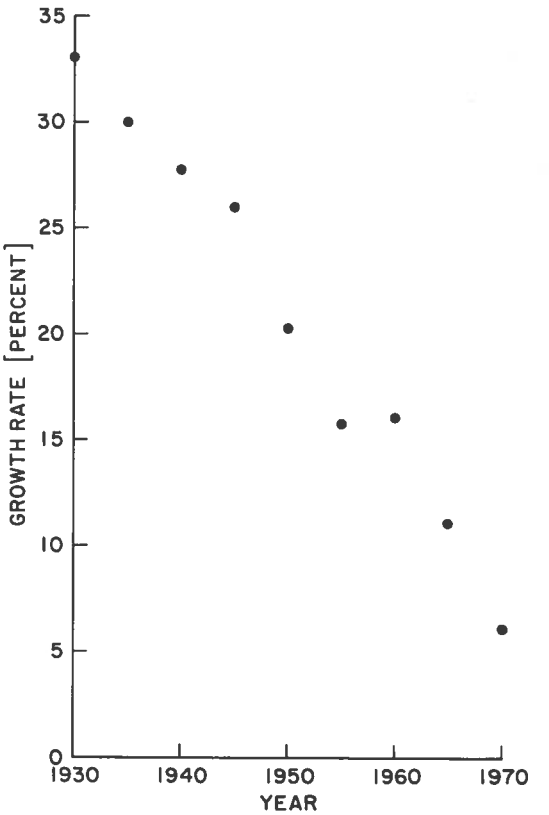

Figure 6. U.S. passenger air-traffic trend.

domestic products for the different world regions. The domestic product for each region from 1980 to 2025 is given in Table 3. These estimates were used in conjunction with the world regional population to derive the regional per-capita income data given in Table 4.

d. *Passenger demand.* Regional annual passenger demand R_t for year t, given in Table 5, was calculated as follows:

$$R_t = I_t \times a_t$$

where I_t is the regional per-capita gross domestic product and a_t the regional pro-

Table 2. World Population, Realistic Upper-Bound Prediction (millions of people)

Region	1970	1980	1990	2000	2025
Africa	344.5	463	622	836	1,751
Latin America	283.3	377	502	668	1,365
North America	227.6	262	301	345	489
Asia	2,055.8	2,632	3,369	4,312	7,994
Europe	462.1	505	553	605	756
Oceania	19.4	26	35	47	98
USSR	242.6	279	320	368	521
World	3,635.2	4,543	5,701	7,181	12,974

Table 3. World Domestic Product, Realistic Upper-Bound Prediction
(in billions of 1970 U.S. dollars)

Region	1970	1980	1990	2000	2025
Africa	73.0	129	231	423	2,142
Latin America	140.2	248	443	832	4,515
North America	1,053.7	1,560	2,309	2,418	9,111
Asia	511.8	1,007	2,075	4,276	24,315
Europe	757.7	1,223	2,088	3,567	11,514
Oceania	44.3	78	140	263	1,363
USSR	388.6	764	1,435	2,570	8,910
World	2,969.3	5,008	8,721	14,349	61,869

Table 4. Per-Capita Domestic Product, Realistic Upper-Bound Prediction
(in 1970 U.S. dollars)

Region	1970	1980	1990	2000	2025
Africa	212.0	279	371	506	1,224
Latin America	494.9	657	883	1,246	3,309
North America	4,630.1	5,964	7,683	9,896	18,636
Asia	248.9	383	616	992	3,042
Europe	1,639.6	2,419	3,777	5,900	15,222
Oceania	2,288.6	3,007	4,007	5,596	13,843
USSR	1,601.7	2,742	4,479	6,980	17,096
World	816.8	1,102	1,530	2,137	4,769

pensity to travel in year t. The propensity to travel for future periods is determined from the present figures and predicted growth rates given in Table 1.

e. *Cargo demand.* Air-cargo demand was predicted on the basis of population, income, and the propensity for shipment by air cargo. The propensity for air-cargo shipment is similar to the indicator used for passenger traffic; it is measured in tonne-kilometers of air cargo per dollar of per-capita income. The present values for air-cargo propensity and predicted growth rates are given in Table 6.

Table 5. Revenue Air Passenger Demand, Realistic Upper-Bound Prediction
(billions of passenger-kilometers per annum)

Region	1970	1980	1990	2000	2025
Africa	9.1	20	51	166	2,102
Latin America	16.3	47	163	565	4,238
North America	259.9	739	1,570	2,750	7,133
Asia	38.7	224	906	2,617	13,551
Europe	121.6	337	821	1,681	5,728
Oceania	11.0	31	107	308	1,731
USSR	78.2	289	842	1,885	6,798
World	534.9	1,686	4,459	9,973	41,281

The predicted regional cargo demand meaaured in tonne-kilometers per year is given in Table 7 for the upper-bound condition. Table 8 gives upper-bound per-capita data for both cargo and passengers. By 2025, the per-capita cargo figure will be 100 times what it is today.

World Air Routes

The regional air traffic demand was broken down into demand between individual city pairs. As a first approximation, the existing route structure today was used for the 1990-2000 decade. Air traffic demand is dictated largely by the major population centers, and these are not expected to change significantly during the prediction period. The development of major population centers is a long evolutionary process, and little change can be expected, even over 50 years.

Cultural, political, and economic ties are also important factors governing air-traffic routes, and some changes can be expected as new world patterns develop. Greater freedom of travel can be expected for the USSR and eastern European countries. A major expansion in both domestic and international travel can also be anticipated for China as ties with the outside world develop. Developing countries will make increased use of air transport, bypassing in general the use of road and rail transport modes which was the historical pattern in developed countries. In addition, these countries will cause an increase in international travel; this was accounted for by an increasing allocation of traffic to intercontinental routes as compared with domestic routes. International traffic expressed as a percentage share of total traffic for the world regions is given in Table 9. In North America, the international passenger

Table 6. Propensity to Use Air Cargo, Realistic Upper-Bound Prediction

Region	1970 Propensity $\left(\frac{\text{tk} \times 10^6}{\text{income per capita}}\right)$	Propensity Growth Rate (%) 1980	1990	2000	2025
Africa	1.08	8.5	10.5	12.5	7.8
Latin America	0.95	14.5	16.5	12.1	5.0
North America	1.30	13.5	12.6	8.7	4.25
Asia	4.05	16.6	12.1	10.0	4.5
Europe	1.86	13.5	12.6	8.7	4.0
Oceania	0.12	13.5	12.6	8.7	4.0
USSR	0.93	8.5	10.5	9.5	4.25

Table 7. Revenue Air-Cargo Demand, Realistic Upper-Bound Prediction (millions of tonne-kilometers per annum)

Region	1970	1980	1990	2000	2025
Africa	229.9	652	2,253	9,545	320,277
Latin America	468.9	2,306	13,687	66,086	996,941
North America	6,026.2	26,347	120,894	391,094	2,797,812
Asia	1,008.0	8,136	44,844	187,271	2,572,591
Europe	3,044.5	15,933	88,641	347,668	3,367,246
Oceania	269.9	1,203	5,712	20,037	186,040
USSR	1,482.4	5,478	23,206	98,113	993,279
World	12,529.7	60,055	299,237	1,119,816	11,234,185

Table 8. Per-Capita Passenger Travel and Cargo, Realistic Upper Bound

Region	Passenger-Kilometers					Tonne-Kilometers				
	1970	1980	1990	2000	2025	1970	1980	1990	2000	2025
Africa	27	42	82	198	1,201	0.7	1.3	3.3	9.7	119.4
Latin America	57	124	324	846	3,106	1.7	5.3	20.1	59.2	228.4
North America	1,142	2,828	5,223	7,964	14,590	26.5	96.0	365.7	866.8	2,823.7
Asia	19	85	269	607	1,695	0.5	2.6	8.9	21.7	82.0
Europe	263	666	1,484	2,780	7,572	6.6	27.9	118.2	320.1	1,437.5
Oceania	565	1,193	3,068	6,555	17,580	13.9	46.6	164.0	401.2	1,398.0
USSR	322	1,037	2,626	5,122	13,043	6.1	16.8	55.7	155.0	676.5
World	147	371	782	1,389	3,182	3.5	12.1	43.6	104.2	351.4

Table 9. World International Air-Traffic Prediction (international traffic expressed as a percentage of total traffic originating from that region)

Region	Passenger				Cargo			
	1980	1990	2000	2025	1980	1990	2000	2025
Africa	58	56	55	50	47	49	50	55
Latin America	48	46	45	40	52	54	55	60
North America	23	25	26	30	33	31	30	25
Asia	39	41	44	50	56	58	60	65
Europe	73	73	74	75	83	84	86	90
Oceania	42	44	45	50	57	59	60	65
USSR	31	28	26	20	50	50	50	50

traffic is anticipated to increase from 23% today to 30% in 2025. For Africa, the share is expected to drop from 58% today to 50% in 2025 due to the increased development of domestic traffic.

The most significant change to be expected in future route structure is the development of longer non-stop flights between existing population centers. This will be the result of both increased traffic demand and the introduction of long-range aircraft types.

Today, many intermediate stops on routes are required to pick up traffic. As demand increases, it will be possible to bypass intermediate stops and fly directly to the end destination. Also, airport congestion at present major world airports will dictate increased use of other airports, which will also originate their own long-distance flights. In the last two decades the average length of trip has increased at an average rate of 1.5% per year. This trend can be expected to continue for some time, but it will eventually be limited by range of aircraft and the time air travelers are prepared to spend in the air. By the end of the century, the very-long-range non-stop routes (7,000 to 11,000 km) will still be flown by subsonic aircraft. It is doubtful that subsonic aircraft for ranges longer than 11,000 km will be developed, since the number of routes on which they could be used is limited and passenger comfort requirements may limit flight times to a maximum of 11 to 12 hours.

700-km Route Cutoff

The existing route structure, which was used as an approximation of a world air-traffic network, comprised altogether 1756 routes longer than 700 km. Routes less than 700 km were excluded, since the flight profile would not enter the stratosphere. The 700-km route cutoff for

each region was estimated from present regional air-traffic data; the cutoffs are shown in Table 10.

Table 10. Percentage of Air Route Lengths Over 700 km

Region	Passenger Traffic	Cargo Traffic
Africa	45	100
Latin America	33	92
North America	70	100
Asia	80	90
Europe	30	100
Oceania	70	100
USSR	50	100

Grid Pairs

To facilitate the computation of emissions, and to interface with global modelers, the airport pairs were aggregated into 5° longitude X 5° latitude grids. Traffic was then assumed to originate and end in the mid-point of each grid. At the equator a grid is approximately 570 km square, decreasing to a rectangle 570 km in latitude by 400 km in longitude at 45°N or S latitude.

Route Structure

As a first approximation, route structure was assumed to remain unchanged, since the major population centers which dictate route structure are not expected to change significantly by 2025. The predicted passenger and cargo traffic on ten of the principal routes is given in Table 11. On the New York-London route passenger travel is predicted to approximately double each decade. The doubling period for air cargo will be significantly smaller, 5 to 6 years.

Forecast Comparisons

In this section the forecasts of passenger traffic have been grouped. The first group includes forecasts for domestic scheduled U.S. traffic, which presently comprises 36% of total world scheduled traffic. The second group includes forecasts for world scheduled and non-scheduled traffic, excluding the U.S.S.R. (The U.S.S.R. was excluded because it was commonly not included in other forecasts.) Our UCLA

Table 11. Annual Demands on Representative Transcontinental Grid-Pair Routes

	Billion Passenger-Kilometers				Billion Tonne-Kilometers			
City Pair	1980	1990	2000	2025	1980	1990	2000	2025
N.Y.-London	40.8	96.5	190.7	623.3	1.8	7.7	23.5	142.4
Frankfurt-N.Y.	14.2	33.7	66.8	219.3	2.5	14.1	56.2	570.6
Paris-N.Y.	22.2	52.5	103.8	339.0	1.4	8.2	32.6	330.8
Dublin-N.Y.	7.7	18.3	36.3	118.7	0.6	3.5	13.9	141.2
N.Y.-Amsterdam	18.9	44.9	88.8	290.7	0.7	3.0	9.2	55.7
Amsterdam-Montreal	5.8	13.9	27.4	89.7	0.5	2.6	10.4	105.9
Rome-N.Y.	18.3	43.3	85.7	280.4	0.7	3.7	14.9	151.5
Copenhagen-N.Y.	4.9	11.7	23.4	77.3	0.3	1.6	6.5	66.3
Geneva-N.Y.	16.9	40.0	79.2	259.3	0.7	3.9	15.6	158.8
Reykjavik-N.Y.	3.7	8.7	17.1	55.9	0.2	0.9	3.4	34.9
Anchorage-Tokyo	10.1	34.2	92.7	493.6	2.2	9.3	28.4	172.0
Tokyo-San Francisco	7.5	28.6	82.4	465.0	1.2	6.7	29.0	430.9
Tokyo-Los Angeles	0.4	1.9	5.7	33.8	0.5	2.6	11.1	165.6
Tokyo-Seattle	6.6	22.8	62.4	335.0	0.4	2.4	10.2	151.6
Honolulu-Tokyo	23.3	78.7	212.1	1124.7	1.3	5.8	17.7	107.4
N.Y.-Tel Aviv	2.1	4.8	8.9	26.2	0.05	0.2	0.7	4.2

world prediction was adjusted to make it directly comparable with the other forecasts.*

A comparison of world air-freight and air-mail forecasts is also provided.

a. *Background.* In comparing forecasts, several complicating factors should be borne in mind. A significant factor is the recent rapid growth in non-scheduled traffic to approximately 13% of total commercial passenger traffic. Only recently has data been available on non-scheduled traffic, and there is still some room for error, due to the reporting procedures.

Another factor hindering comparisons is the time horizon used in each forecast. Some forecasts extend only to 1980, while others go as far as 2000. No forecasts for the year 2025, which is the scenario time of this UCLA prediction, were available. It should also be remembered that the UCLA prediction was prepared as a feasible upper bound on air traffic. This condition did not obtain for the alternative forecasts.

b. *Forecast methodology.* The models used in obtaining alternative forecasts will not be described in detail here. In some cases the model used was not made explicit. Model descriptions provided were generally based on some extrapolation of past data, derived from past correlations between air travel and economic indicators. All forecasts predict increasing air traffic, but at annual growth rates which are less than in the past and declining. The differences between forecasts results from the different patterns ascribed to the anticipated declining future annual growth rate.

It is important to note that forecasts over long periods are very sensitive to changes in assumed growth rates. For example, a 2% difference in growth rates between two forecasts with a 50-year horizon will result in the higher forecast's being 2.7 times larger than the lower one. There is no basis for believing that any one forecasting model is superior to another. In retrospect, it seems that most methodologies have left considerable room for improvement.

c. *Forecasts for U.S. domestic scheduled revenue passenger-kilometers.* The forecasts of domestic U.S. scheduled traffic are given in Table 12 and Figure 7. The actual traffic from 1970 to 1972 is noted, as well as a preliminary estimate for 1973. The most recent FAA forecast (FAA, 1970) was made in 1969 and extends to 1980. Whereas in the past the FAA has had a tendency to underforecast, the most recent study has shown an over-forecast of actual air traffic to date. By 1980 the FAA forecast is 505 BRPK (billion revenue passenger-kilometers), which should be compared with the 1973 aerospace companies' forecasts (Boeing, 1971; Aureille and Norris, 1973; Lockheed, 1972), which range from 386 to 389 BRPK.

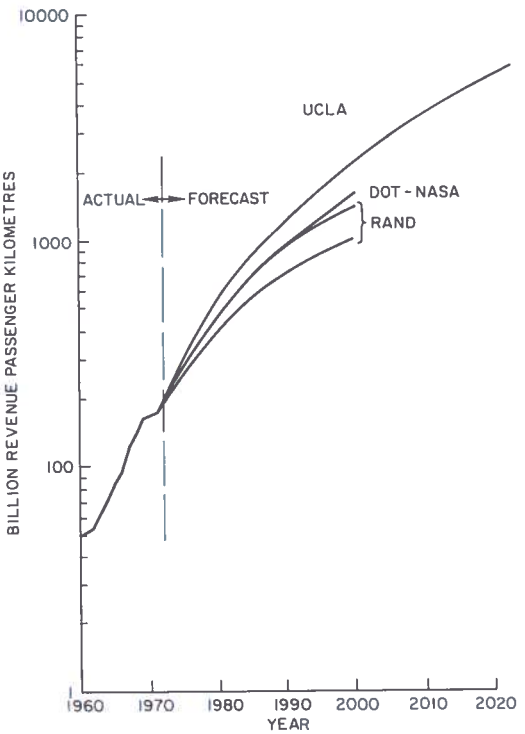

Figure 7. Forecasts of U.S. domestic scheduled revenue passenger-kilometers.

* It will be recalled that a distinction was made earlier between forecasts and predictions. The former are the methodology generally employed, where as the UCLA approach was a prediction.

Table 12. U.S. Domestic Scheduled Revenue Passenger-Kilometers (billions)

Forecast	1970	1971	1972	1973	1974	1975	1980	1985	1990	2000	2025
Actual	169	173	194	210*							
FAA	165	180	205	228	266	288	505				
ATCAC							485			1620	
ATA							487	785			
Rand (Fast Growth)							500		860	1420	
Rand (Slow Growth)							410		620	1040	
Douglas				210	230	240	386	594			
Boeing				200	216	239	389				
Lockheed				210	226	247	389	520			
UCLA							520	760	1080	1880	4800

* Estimated from preliminary data

Sources: FAA (1970); DOT-NASA (1971); Douglas (1973); Lockheed (1972); Jordan (1973); Aureille and Norris (1973); Boeing (1971)

The Rand forecasts (Jordan, 1971) are based on different assumptions of economic and population growth, and give a range of 1040 to 1420 BRPK for the year 2000. This can be compared with the DOT-NASA forecast of 1630 BRPK (DOT-NASA, 1971) and our UCLA prediction of 1880 BRPK. There are no forecasts for comparison beyond this point.

d. *Forecast of world scheduled and nonscheduled revenue passenger-kilometers.* These forecasts are given in Table 13 and Figure 8. By 1980 the range of forecasts prepared by Boeing (1971), Douglas (Aureille and Norris, 1973), and Lockheed (1972) give a range of 1200 to 1480 BRPK, compared with the UCLA figure of 1400 BRPK. In the year 2000, the divergence between forecasts has increased, with the Boeing (1971) and Douglas (Aureille and Norris, 1973) forecasts ranging from 2600 BRPK to 5750 BRPK compared with the UCLA value of 9550 BRPK. Beyond the year 2000 there are no forecasts available for comparison with the UCLA prediction of 34,500 BRPK for 2025.

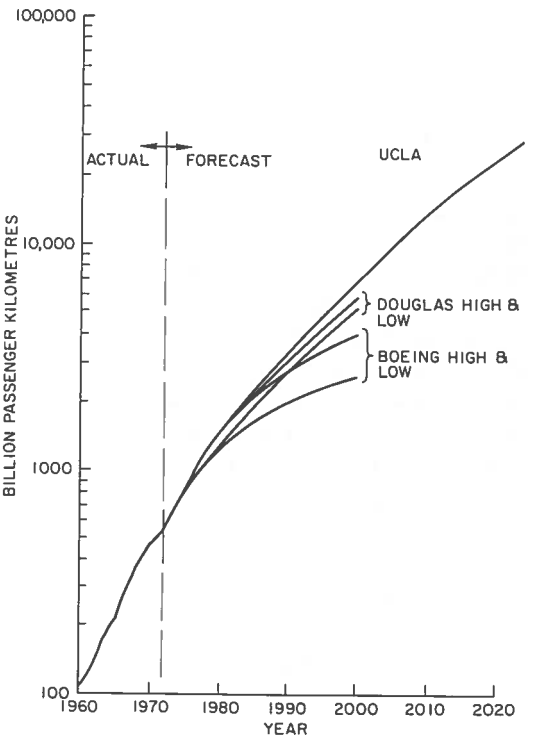

Figure 8. Forecasts of world (excluding USSR and People's Republic of China) scheduled and nonscheduled revenue passenger-kilometers (Boeing, 1971; Aureille and Norris, 1971 (Douglas)).

Table 13. World Scheduled and Nonscheduled Revenue Passenger-Kilometers* (billions)

Forecast		1972	1973	1974	1975	1980	1990	2000	2025
Boeing	High	570	630	700	785	1480	2740	4000	
	Low					1200	1900	2600	
Douglas	High	570	670	760	820	1400	2900	5750	
	Low					1250	2600	5200	
Lockheed		570	670	730	800	1370			
UCLA		570	650	740	860	1400	3620	9550	34500

* Based on ICAO (1973) estimates; excludes USSR and Peoples' Republic of China
Sources: see Table 12

e. *World scheduled and nonscheduled air freight.* The world forecasts for air freight and air mail are given in Table 14 and Figure 9.

Note that there is close agreement between the Lockheed and Boeing forecasts which extend to 1985, with the UCLA value slightly higher. No freight forecasts were available for comparisons beyond 1985.

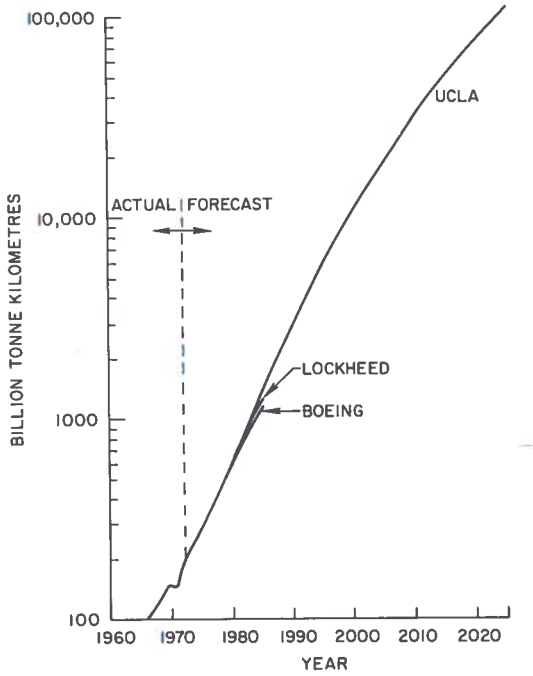

Figure 9. World scheduled and nonscheduled revenue tonne-kilometers (Lockheed, 1973; Boeing, 1971).

Comparison of Past Forecasts

A comparison of forecasts of U.S. domestic scheduled revenue passenger-miles (RPM) during the period 1944 to 1968, together with actual RPM flown, is shown in Figure 10. The growth of air traffic was predicted by English (1944) and the Curtiss-Wright Corporation (1944). Curtiss-Wright showed air traffic approaching saturation in the fifties, whereas the English prediction showed strong continued growth in the potential U.S. air-traffic market in the same period. Predictably, this market potential could not be

Table 14. World Scheduled and Nonscheduled Revenue Tonne-Kilometers (billions)

Forecast	1970	1975	1980	1985	1990	2000	2025
Actual	15						
Boeing		29	63	115			
Lockheed		30	62	128			
UCLA		27	60	138	299	1,120	11,200

Source: see Table 12

realized for about three years after the war because of unavailability of aircraft. Actual growth was intermediate between the two predictions, with the error increasing significantly with a lengthening time horizon.

Federal Aviation Administration forecasts are also shown for the years 1962, 1965, and 1968 (FAA, 1962, 1965, 1968). In earlier years the actual growth was under-forecast; more recently it has been over-forecast.

Air Transport Systems

The year 2025 will provide the potential traveler with a variety of routes and modes to reach his destination. The greater the distance of travel, the more options may be available to him. For example, a long trip may offer the possibility of high-speed train, VTOL aircraft, and HST, at a given fare and transit time. In addition, the traveler could also go by electric private vehicle and subsonic flight system at another transit time and fare. This would allow the sophisticated citizen of that era the option of traveling to suit his purpose and personality as he embraces an ever-widening region for his personal domain.

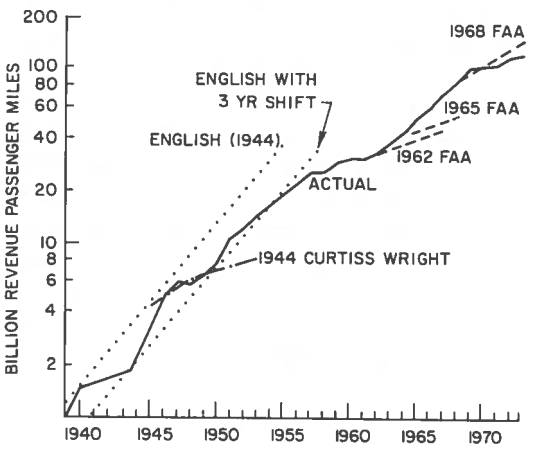

Figure 10. Comparison of past forecasts (English, 1944; Curtiss-Wright, 1944; FAA, 1962, 1965, 1968) of U.S. domestic scheduled revenue passenger-miles.

The past 50 years of air transportation have seen five distinct generations of flight vehicles. This development is expected to continue; in the next 50 years the following new generations of air transportation systems may emerge.

a. *VTOL system.* The vertical takeoff and landing short-range system will operate over distances of 95 to 700 km at speeds between 350 and 750 kph. VTOL airports will be located at many sites through large urban areas, and within all small communities. These vehicles will provide transportation service over short distances, in competition with ground-based systems. They also may provide connecting service to larger airports for long-range flights.

VTOL aircraft will vary in size, speed, and range to suit various operational environments.

b. *Subsonic systems.* In addition to present flight systems, several new subsonic flight systems will provide low-cost cargo and passenger transportation over all ranges above 750 km. Large flight vehicles will transport cargo over great distances at competitive rates. This vehicle type will also be capable of carrying up to 1,000 passengers in conjunction with the cargo. Its maximum range will be 12,000 km.

A second subsonic system will be used on lower-density routes serving the smaller urban communities. This aircraft will be profitable over both long and short ranges carrying both passengers and cargo. It may cruise at Mach number 0.92-0.95 for ranges between 750 and 12,000 km.

c. *Advanced supersonic transport.* An advanced supersonic transport will be operating at ranges between 2000 and 12,000 km. This aircraft may be capable of flying over lightly populated land areas without creating an objectionable boom, and will fly at speeds of Mach number 2.2 to 2.7 to service the major airports of the world. It

will carry 300 passengers and limited amounts of cargo at a small fare increase over coach fares. An alternative to the fare increase would be higher load factors, achieved by means of better-managed scheduling. Such scheduling might entail no fixed departure times, but departure upon reaching a given load. High levels of passenger traffic would make it possible to predict the departure fairly accurately. Electronic information signs would provide predicted departure times at approaches to the airport, within the terminals, and within the connecting transportation systems. Computer-aided, 90%-confidence departure times would also facilitate flight crews' preparations for departure.

d. *Hypersonic transport.* Hypersonic transports could provide very rapid service for ranges between 4,000 and 12,000 km. The aircraft would carry 300 passengers and a small amount of high-priority cargo at Mach 6.0 and 8.0. The HST will be economically viable at the same fare level as the SST. It will be hydrogen-fueled and will be capable of operating over lightly populated land areas (Becker and Kirham, 1971).

e. *Lighter-than-air ships.* While the rigid and non-rigid lighter-than-air type of transport was replaced by heavier-than-air craft in the 1930's, the revival of an economical lighter-than-air system in the future should be considered a distinct possibility. The economy of such a system's fuel consumption may become attractive for transporting heavy and bulky freight in a future of rising relative fuel costs. (Under such circumstances the air-freight predictions above would be adversely affected.)

Air Transportation Development

An attempt to predict the future mix of aircraft flight systems must begin by an examination of the principal parameters which will influence this mix, as to both number and type of flight systems. The state of the art in certain technical fields will exert a significant influence on the performance characteristics which will be incorporated into a new aircraft design.

The ratio of lift to drag (L/D) in fixed-wing aircraft is of great importance in determining the efficiency with which the fuel is converted into velocity and range.

An important factor in aircraft performance and profitability is the fraction of takeoff gross weight which is payload. This fraction depends to a large extent on the efficiency with which structural materials are utilized in forming the envelope for the payload and fuel. The structure must provide not only a suitable environment for the payload, but also storage for the fuel and propulsion systems, while resisting aerodynamic stresses of operation. New structural materials coming into use at the present time offer the possibility of reducing weight while maintaining service life.

Fuel is converted to thrust through the medium of a propulsion system. The efficiency with which this conversion is made is, of course, important in new aircraft development. The type of fuel used, as well as the technology of the propulsion system, will influence the aircraft configuration and its profitability. The elements of propulsion technology, and new fuels which are being considered for the future, will define the types of flight systems to be developed.

For a commercial aircraft to be purchased, the operating company must expect it to be profitable. Even if the operation need not be profitable without subsidy, as is the case with some national airlines, the flight systems which they operate must still be the most efficient available. Each type of equipment in the system will influence the operating cost. If a prediction is to be made as to the types of systems which are to be operating in the future, an attempt must be made to examine some of the more important influences on profitability. Direct operating cost represents a convenient parameter against which to measure the influence of the technical elements of the system.

Flight-System Selection Model

The servicing of the demand for passengers and cargo will require a set of flight systems. Table 15 gives the set of flight systems which are expected to be both technically and economically feasible at the operational dates shown, and describes the critical characteristics of these

Table 15. Available Flight Systems and Their Characteristics

Transport	Range (km)	Passenger Capacity	All Cargo Capacity (kg)	Secondary Cargo (kg)	Cruise Mach	Gross Weight (kg)	Operational Date
Extended small 3-jet	3,500	170	0	0	0.82	99,000	1977
Small SST	6,100	105	0	0	2.0	174,000	1975
Advanced small SST	6,300	170	0	0	2.0	226,000	1980
Large 4-jet	9,000	380	75,000	18,000	0.86	362,000	Present
Large 3-jet	5,500	295	50,000	10,000	0.83	200,000	Present
Long-range 3-jet	9,200	270	50,000	9,000	0.83	252,000	Present
Long-range traditional 4-jet	12,000	200	27,000	5,000	0.85	163,000	1979
Large 2-jet	3,500	230	0	8,000	0.82	150,000	1975
Long-range 4-jet	10,000	285	50,000	11,000	0.87	299,000	1978
Large advanced SST	7,400	295	0	0	2.7	328,000	1987
Very large 4-jet	12,000	600	100,000	13,000	0.90	408,000	1981
Advanced subsonic 4-jet	12,000	600	100,000	13,000	0.94	408,000	1985
Hypersonic	12,000	300	0	0	6.0	362,000	2015
Advanced very large	12,000	1000	150,000	23,000	0.82	544,000	2005

aircraft on the basis of the present technology of the aerospace industry and expected trends in development.

Model Background

Given a set of aircraft which might be operating during a specified time period, there remains the problem of selecting the mix of flight systems which will be purchased by the operating carriers of the world to serve the predicted demand.

The selection was made under the basic assumption that the market behavior of the world airlines can be described as if the latter were a single airline. The present market structure is essentially oligopolistic, with market shares allocated to the different domestic and international airlines. The limited competition between airlines is on the basis of service rather than price. This form of competition will tend to decrease aircraft load factors. This situation is expected to continue in the future, and the competition between airlines in the selection model was simulated by holding passenger and cargo load factors to their present levels. The fare structure also was set at present levels, with an anticipated premium for supersonic flights.

Selection Criterion

Aircraft systems were selected on their profit-generating capability on a particular route. This measure of profit differs from the conventional accounting measure of profit employed by airlines. It identifies and measures the variable costs associated with operating an aircraft system on a particular route, and excludes some of the fixed costs normally associated with operating an airline.

Selection Process

The model functions by selecting an initial aircraft from the parent set and comparing its characteristics to those of the route to be served. If the route length exceeds the range capability of the aircraft, or if the aircraft is restricted to operating only over water (like the SST) and the route is over land, the aircraft is rejected and a second is selected and tested.

Suitable aircraft are filled with passengers at

variable load factors and passenger revenue for the single route-cycle computed. If the aircraft can carry belly cargo, the cargo demand for the route is served first by carrying belly cargo in the passenger aircraft. The remainder of the route cargo demand is then served by all-cargo aircraft of the same type, if they are needed.

It is emphasized that the model attempts to serve the total route demand with its initial subset by selecting a passenger and cargo aircraft of the same type. If this fails, it selects a different cargo aircraft.

The net route profit on this flight-system subset is computed as a single value. All other combinations of passenger and cargo aircraft are then computed, and the subset with the maximum net route profit is selected to serve the route.

The number of aircraft needed to serve the route demand, considering the route flight time and the daily utilization which may be expected for each aircraft, is computed at this point. Fractional aircraft are retained to be shared with other routes which may select the same type of aircraft. Flight cycles are then computed for use by the world grid emissions model.

Model Assumptions

The basic assumptions of the model are described below. To account for transaction costs due to the introduction of new aircraft systems, the model requires that new systems generate higher net income than present systems in service.

The aircraft numbers and emission values of this report were developed with a passenger load factor of 0.5 and a cargo load factor of 0.6. These figures are in keeping with the upper-bound requirement for estimating emissions. It is highly probable that constraints on air traffic in the future will result in higher load factors.

The model imposes two types of frequency constraints upon the aircraft serving the demand. First, it is assumed that low frequency of service will cause potential passengers to choose another mode of transportation or not travel. Thus the model imposes a penalty, in the form of reduced demand for a particular type of aircraft, if the frequency of service is less than 0.7 flights per day. This causes the model to prefer a smaller aircraft, which could serve the demand for this route with a greater frequency and thus be more profitable.

Second, airport constraints which impose an upper bound on flight frequency are already beginning to appear during preferred hours at some of the larger airports. The model accounts for this by imposing a maximum flight frequency on any aircraft type, passenger or cargo. This frequency limit causes these aircraft to lose a percentage of demand, and thus profit. The model will then tend to select larger-capacity aircraft for high-demand routes, which will be more profitable because they can service all the demand.

No subsidization of the research and development costs of the supersonic or advanced subsonic aircraft was considered. Subsidization of R&D costs would result in lower capital investment and higher profits through lower annual capital recovery costs.

The data runs which contain supersonic aircraft were made with a fare increase for the supersonic aircraft of 1.4 over the normal yield for the range of the route for the 1990 period, and a 1.26 fare premium for the 2025 period. The mean value of this fare escalation over that of economy or coach fare is 1.25 for the 1990 period.

Predicted Air Fleets

A summary of the flight systems required to service the upper-bound demand is given in Table 16. The flight-system mix is determined under the assumption that the air-travel demand can be satisfied by charging a 40% premium above average fares for the supersonic flights. This would make it more profitable for airlines to operate supersonic planes, and consequently would result in a larger number of this type.

It can be noted that the dominant aircraft type in 1990 will be the medium-range jet air-bus. The second largest type will be the medium-to-long-range large-capacity jet. Three types will also be utilized for air cargo. The predicted supersonic fleet for 1990 is 1,120 aircraft, increasing to 2,320 by the year 2000. In 2025 the supersonic fleet will have decreased, due to replacement by the more productive HST.

Table 16. Upper-Bound Air Fleet

System	1980	1990	2000	2025
Extended small 3-jet and large 2-jet transports	3,360	5,940	8,800	2,640
Large, long-range, and long-range traditional 4-jet transports; large and long-range 3-jet transports	2,699	5,300	12,302	3,419
Very large 4-jet transports	0	30	523	37,684
SST's, advanced SST's, and large advanced SST's	100	1,120	2,320	734
Advanced very large transport	0	0	0	1,847
Hypersonic transport	0	0	0	846
Total	6,159	12,390	23,945	47,170

The projected air-traffic demand for the 1990-2000 time frame, and numbers of aircraft needed to service it, may seem high. On the other hand, a serious attempt was made to consider realistically (albeit optimistically) the maturing of the industry by 2025, approximately 50 years hence. Of course, these conclusions are contingent upon all economic forces' acting in a way that is conducive to air transport growth.

Production Limitations and the HST

It must be re-emphasized that the foregoing aircraft-selection models were based on the optimal mix of aircraft, without regard to availability. Production of the advanced types, particularly the hypersonic transport (HST), can be expected to be limiting.

It is conceivable that a full-scale R&D program on an advanced SST will result in a fleet operating in the 1990-2000 time frame. On the other hand, while there will not be operational HST's, there will be a few test vehicles.

Comparison of Potential Supersonic Fleet Sizes

A comparison of alternate predictions of supersonic fleets is given in Figure 11.

The Boeing (1973a) and Douglas (1973) predictions take into account both the potential market for advanced supersonic transports and also what will be feasible if it is assumed that an advanced transport will not go into service till 1985. Production-capacity constraints are also allowed for. By 1990, Boeing (1973a) predicts a total potential market of 800 aircraft, while the Douglas (1973) estimate is 250. The feasible number of advanced supersonics flying in 1990 varies from the Boeing estimate of 200 to the Lockheed (1973) forecast of 300.

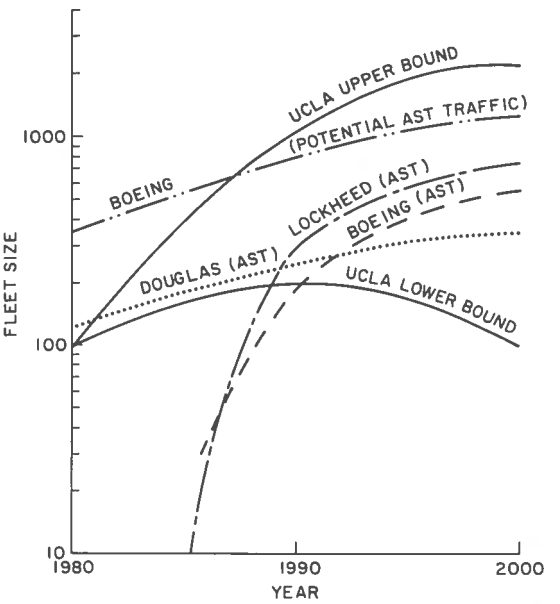

Figure 11. Forecasts of world supersonic fleet sizes.

Our UCLA upper-bound prediction of 1120 aircraft is not directly comparable, since it

includes both present European and USSR supersonics in addition to the advanced supersonic transport. The Concorde and TU 144 will number approximately 200 of the total supersonic fleet flying in 1990. It is predicted that the total fleet will have increased to 2300 aircraft by the year 2000.

It should be kept in mind that this UCLA upper-bound prediction is based on the realization of the most favorable potential market for supersonic travel, and does not take production-capacity constraints into account. The latter may tend to delay the attainment of the predicted fleet size to a date later than given here.

The lower-bound estimate, included for comparison, is based on the assumption that supersonic travel will not be economically viable, and no advanced supersonic transport will be built. The only supersonic aircraft flying in 1990 will be the European and USSR types. Production of these aircraft will have ceased before 1990 due to their unfavorable economic operation and normal attrition and probably will have reduced their number to 100 by the year 2000.

GLOBAL EMISSIONS

A computer program was used to calculate global distribution of emissions from future aircraft fleets determined in the aircraft-selection model described earlier. Emissions distributions were described by $5^\circ \times 5^\circ$ grid squares and by altitude. The stratosphere was divided into seven bands 3 km in depth, starting at 9 km altitude and extending to 30 km.

Model Description

Figure 12 gives a block diagram of the procedure used to calculate emission rates. The model inputs were the world route network, number and types of aircraft along each route, flight profiles, and emission indices.

Given a particular route, the model determines the grids through which it passes and the route length in each grid. The emission rate in tonnes/day in each grid is calculated as follows:

$$E_i = \sum_{j=1}^{4} n_j I_j F_j \times \frac{\text{Distance in grid}}{\text{Cruise speed}}$$

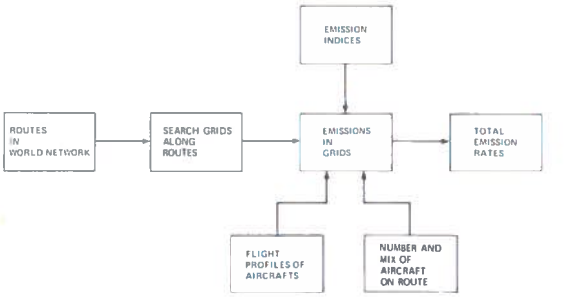

Figure 12. Block diagram of emissions-calculation model.

where

E_i = Emission rate within grid for ith emission species ($i = 1, 2 \ldots 9$)
I_j = Emission index for jth aircraft type ($j = 1, 2, \ldots 4$)
F_j = Fuel flow rate for jth aircraft type
n = number of aircraft of jth type

The emission rate was estimated for an average day during the peak traffic period, July to August. (Factors for estimating emissions for other seasons, and also for estimating the annual average, are discussed further later.)

Some simplifications and assumptions have been made in the emissions model. Routes are between grid code pairs, so the origin and destination points are assumed to be located in the middle of a grid. Also, emissions in the origin and destination grids of a route are excluded because it is assumed that aircraft will not reach stratospheric altitudes there.

Aircraft Emissions

The estimated emission indices for future aircraft engines under different assumptions of technological development have been taken from Grobman (1974). For the upper-bound emissions prediction, the indices, which were based on an assumption of normal technological progress, were used only as an example. These indices, in terms of grams of emissions species per kilogram of fuel consumed, are given in Table 17. The fuel flows used to calculate total emissions, given in Table 18, are based on estimates of future engine technology described previously.

Table 17. Engine Emission Indices for 1990 (g/kg fuel)

Species	Subsonic	Supersonic	Hypersonic
Oxides of Nitrogen (as NO_2)	8	14	17
Carbon Monoxide (CO)	3	3	–
Total Hydrocarbons (THC)	0.5	0.5	–
Soot	0.02	0.02	–
H_2O	1.25×10^3	1.25×10^3	8.9×10^3
CO_2	3.22×10^3	3.22×10^3	–
SO_2	2	2	–
Total Trace Elements	0.01	0.01	–
Lubricating Oil	0.1	0.1	0.1

Table 18. Aircraft Characteristics

Transports	Cruise Speed	Fuel Flow (kg/hr)
Advanced very large	870	20,796
Advanced subsonic 4-jet	990	14,773
Large 2-jet	835	5,909
Large 3-jet	890	7,046
Large 4-jet	900	10,909
Very large 4-jet	980	11,818
Long-range 4-jet	900	9,546
Long-range traditional 4-jet	910	4,546
Extended small 3-jet	876	3,854
SST	2,130	13,636
Advanced SST	2,130	15,909
Large advanced SST	2,876	40,909
Hypersonic	6,300	56,818

Sources: BAC (1973)
Boeing (1973b)
Douglas (1974)
NASA (1973)

Flight Profiles

The basic flight profiles used to determine the altitudes at which emissions would be injected during a flight are shown schematically in Figure 13.

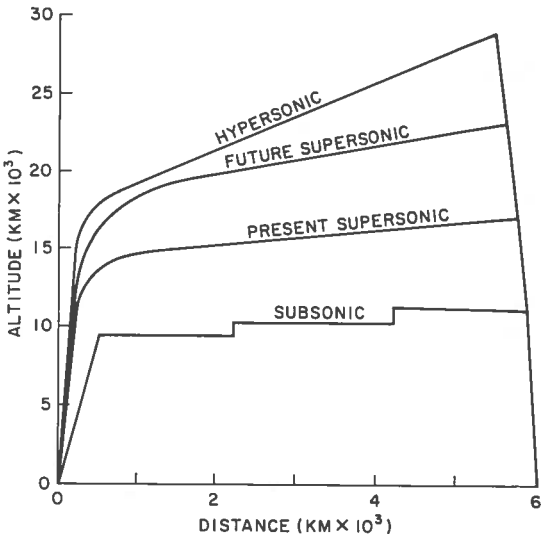

Figure 13. Representative flight profiles.

The subsonic flight profile, which has a maximum cruising altitude of 13 km (42,600 ft), is higher than that reached by present subsonic types. However, it is anticipated that succeeding generations will be certified to operate at higher altitudes than present types.

For supersonic aircraft, two flight profiles were used. The profile for present supersonic types is based on the Concorde. It will have a maximum cruising altitude of 17.5 km (57,000 ft). Future supersonic types are expected to fly higher, and a maximum cruising altitude of 23.2 km (76,000 ft) was used.

The hypersonic profile is based on a Mach 6 cruising speed and a maximum altitude of 30 km (99,000 ft).

The flight profiles were approximated by step functions for calculation of emissions. These steps, shown in Table 19, give the flight altitude as a function of distance from the origin for the four different types.

Upper-Bound Emissions

The emissions of a number of species by world grid and altitude bands for both subsonic and supersonic types were determined for the upper-bound estimates of air traffic. (These are available from the author as a computer printout or in machine-readable form.) Total world emissions for the years 1990 and 2000 are shown in Tables 20 and 21. In terms of mass, CO_2 is the

Table 19. Flight Profiles

Classification	Distance (km)	Altitude Band (km)
Subsonic	0-3000	9-12
	> 3000	12-15
Present Supersonic	0-200	9-12
	100-3000	12-15
	> 3000	15-18
Future Supersonic	0-60	9-12
	60-150	12-15
	150-1000	15-18
	1000-2000	18-21
	> 2000	21-24
Hypersonic	0-50	9-12
	50-100	12-15
	100-200	15-18
	200-2000	18-21
	2000-3000	21-24
	3000-4000	24-27
	> 4000	27-30

most significant; the lowest emission levels are for trace elements and lubricating oil. Total emissions from subsonics will be approximately double those from supersonics in 1990 and 2000.

Table 20. Summary of Total World Emissions During Peak Period in 1990 (tonnes per day)

Emission Species	Aircraft Type		
	Subsonic	Supersonic	Total
NO_2	3,792	3,841	7,633
H_2O	0.59×10^6	0.35×10^6	0.94×10^6
CO_2	1.53×10^6	0.88×10^6	2.41×10^6
Trace Elements	4.74	2.75	7.49
Lub. Oil	47.4	27.5	74.9
CO	1,426	824	2,250
CH_2	236.6	137.2	373.8
Soot	9.47	5.49	14.96
SO_2	947	549	1,496

Emissions by altitude bands for both subsonics and supersonics are given in Tables 22 and 23. Note that in both cases the highest concentration of NO_2 emissions is found in the lowest altitude band (subsonic traffic). The geographical distributions of NO_2 emissions for different altitudes of subsonic and supersonic fleets during

Table 21. Summary of Total World Emissions During Peak Period in 2000 (tonnes per day)

Emission Species	Aircraft Type		
	Subsonic	Supersonic	Total
NO_2	8.43×10^3	6.89×10^3	15.32×10^3
H_2O	1.31×10^6	0.62×10^6	1.93×10^6
CO_2	3.40×10^6	1.58×10^6	4.98×10^6
Trace Elements	10.54	4.91	15.45
Lub. Oil	105.4	49.11	154.51
CO	3.16×10^3	1.478×10^3	4.64×10^3
CH_2	525	245.7	771.7
Soot	21.11	9.84	30.95
SO_2	2111	984.2	3,095.2

the peak summer period in 1990 are shown in Figures 14 through 18. The distribution of other emission species will not differ significantly from this pattern. The representative flight profiles indicate non-overlapping of emissions of subsonic and supersonic emissions in different altitude bands. No emissions in bands higher than 24 km (79,020 ft), are expected in 1990, since the hypersonic transport will not be in service.

Table 22. Global Emissions by Altitude Band* During Peak Season for 1990 (tonnes per day)

Emission Species	9-12	12-15	15-18	18-21	21-24
NO_2	2950	842	517	784	2540
H_2O ($\times 10^6$)	4.61	1.31	4.61	7.00	2.27
CO_2 ($\times 10^3$)	1.19	3.39	1.19	1.80	5.85
Trace Elements	3.69	1.05	0.369	0.560	1.82
Lub. Oil	36.9	10.5	3.69	5.60	18.2
CO	1110	316	111	168	545
CH_2	184	52.6	18.4	28.0	90.8
Soot	7.37	2.10	0.738	1.12	3.63
SO_2	737	210	73.8	112	363

* The bands below 15 km are assumed to be all subsonic traffic; bands above 15 km are assumed to be all supersonic traffic.

The emission rate for each grid is given by an index number which is explained below each figure. To facilitate readability, only emission rates higher than 1 tonne per day are indexed. The highest emissions occurred in the zone

Table 23. Global Emissions by Altitude Band* During Peak Season for 2000 (tonnes per day)

Emission Species	Altitude (km) 9-12	12-15 Subsonic	12-15 Supersonic	12-15 Total	15-18	18-21	21-24
NO_2 (X 10^3)	6.42	2.01	0.30	2.31	1.17	1.41	4.01
H_2O (X 10^6)	1.00	0.313	0.027	0.34	0.10	0.13	0.36
CO_2 (X 10^3)	2.95	0.81	0.07	0.88	0.27	0.32	0.92
Trace Elements	8.03	2.51	0.22	2.73	0.84	1.00	2.86
Lub. Oil	80.3	25.1	2.16	27.3	8.35	16.0	28.6
CO	2.41	752	64.8	816.8	250	301	859
CH_2	401	125	10.8	135.8	41.7	50.2	143
Soot	161	5.01	0.43	5.44	1.67	2.01	5.73
SO_2	1.61	501	43.2	54.42	167	201	573

* The 9-12 km band is assumed to be all subsonic traffic; bands above 15 km are assumed to be all supersonic traffic.

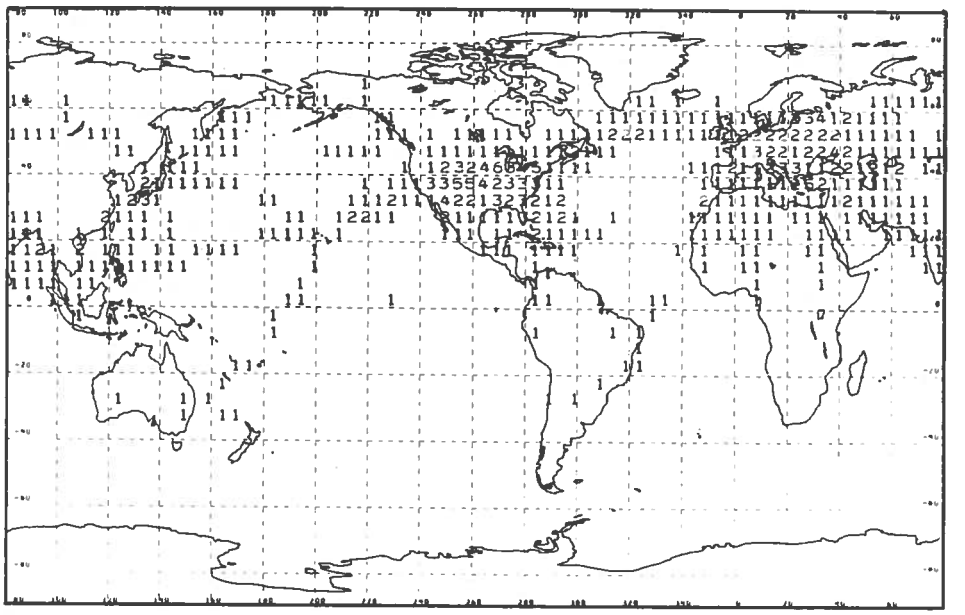

INDEX: 1: 1 to 10 5: 41 to 50 9: 81 to 90
2: 11 to 20 6: 51 to 60 A: 91 to 100
3: 21 to 30 7: 61 to 70
4: 31 to 40 8: 71 to 80

UNIT: TONNES/DAY

Figure 14. 1990 NO_2 emissions, subsonic aircraft, altitude 9 to 12 km.

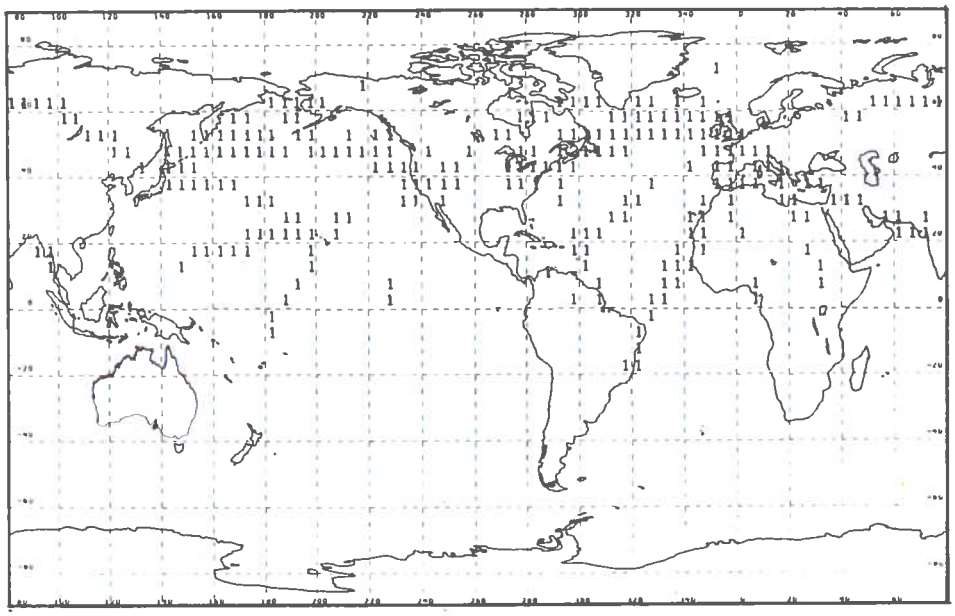

INDEX:
1: 1 to 10
2: 11 to 20
3: 21 to 30
4: 31 to 40
5: 41 to 50
6: 51 to 60
7: 61 to 70
8: 71 to 80
9: 81 to 90
A: 91 to 100

UNIT: TONNES/DAY

Figure 15. 1990 NO_2 emissions, subsonic aircraft, altitude 12 to 15 km.

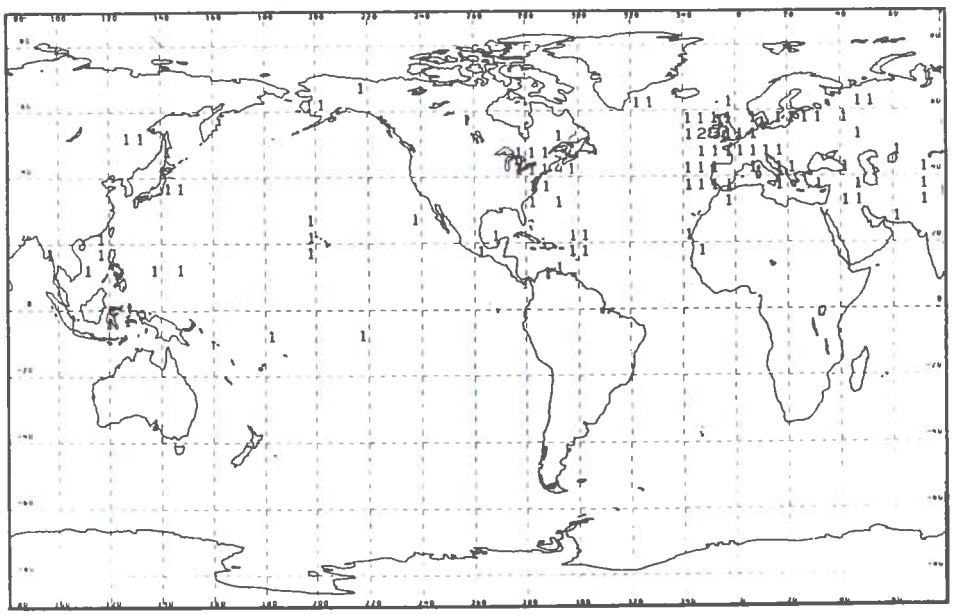

INDEX:
1: 1 to 10
2: 11 to 20
3: 21 to 30
4: 31 to 40
5: 41 to 50
6: 51 to 60
7: 61 to 70
8: 71 to 80
9: 81 to 90
A: 91 to 100

UNIT: TONNES/DAY

Figure 16. 1990 NO_2 emissions, supersonic aircraft, altitude 15 to 18 km.

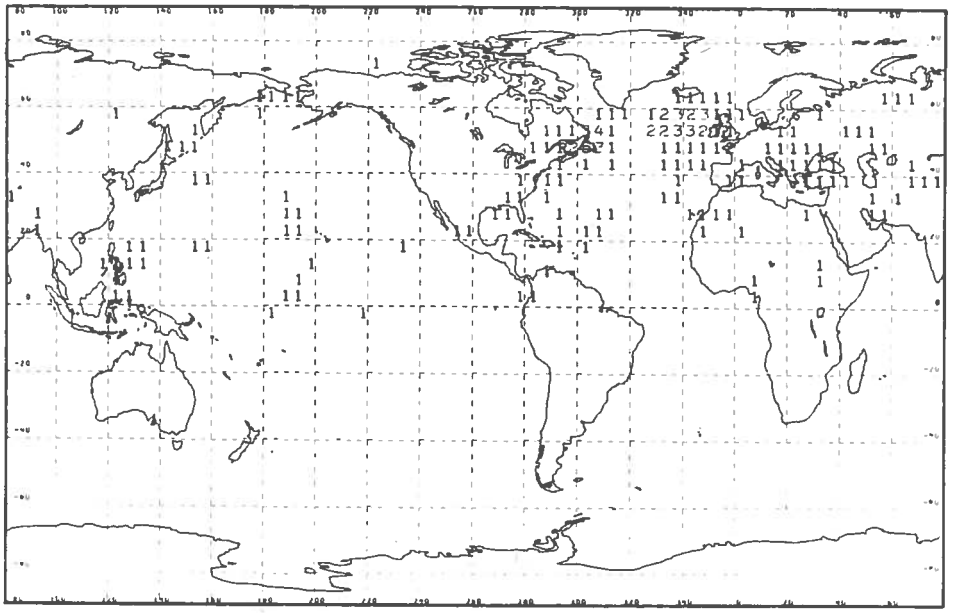

INDEX: 1: 1 to 10 5: 41 to 50 9: 81 to 90
2: 11 to 20 6: 51 to 60 A: 91 to 100
3: 21 to 30 7: 61 to 70
4: 31 to 40 8: 71 to 80 UNIT: TONNES/DAY

Figure 17. 1990 NO_2 emissions, supersonic aircraft, altitude 18 to 21 km.

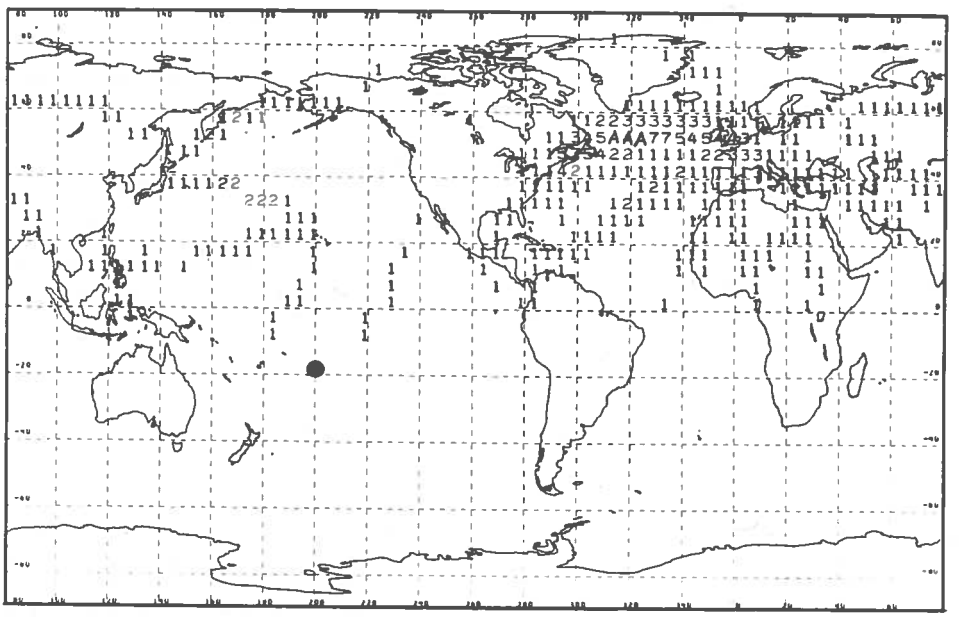

INDEX: 1: 1 to 10 5: 41 to 50 9: 81 to 90
2: 11 to 20 6: 51 to 60 A: 91 to 100
3: 21 to 30 7: 61 to 70
4: 31 to 40 8: 71 to 80 UNIT: TONNES/DAY

Figure 18. 1990 NO_2 emissions, supersonic aircraft, altitude 21 to 24 km.

defined by latitude 40°N to 60°N and longitude 80°W to 20°E. This zone, covering North America, the Atlantic Ocean, and Europe, corresponds to an area of heavy traffic routes in 1990. The southern hemisphere has few grids which have emissions higher than 1 tonne/day.

It is of interest to see that the highest subsonic NO_2 emission is 51 tonnes/day, in the 95°W, 40°N grid square (in the 9-12 km altitude band), while the highest supersonic NO_2 emission is 93 tonnes/day in the 45°W, 50°N grid square (21-24 km altitude band). It is assumed that supersonic overflights will be permitted over all continental regions except the U.S.A.

Variations in Emission Rates

The bulk of the air traffic in 1990 and 2000 will continue to be in the Northern Hemisphere, and will be dominated by the northern seasonal fluctuations much as it is today. The emission rates in tonnes per day have been calculated for an average day during the June-to-August season when air traffic is heaviest. The average emission rates for seasons other than summer and for the yearly average are obtained by multiplying the summer rates by the following factors:

Yearly Avg.	0.75
Spring	0.75
Summer	1.0
Winter	0.52
Fall	0.71

Air traffic shows considerable fluctuations within a 24-hour period. The bulk of air travel occurs during the daylight hours, with the peak number of takeoffs and landings during the evening hours. The emission rate in a grid square will also show considerable daily fluctuations, which will depend on the originating times of the aircraft passing through the grid at any time. Detailed analysis of daily fluctuation rates is presently being undertaken.

ACKNOWLEDGMENTS

The significant contribution of the project team, Professor John L. Barnes, Gerald Kernan, Gary Pan, Harold Roland, Mary W. Smith, and Dr. Peter Tsou, is gratefully acknowledged. The research was sponsored by the Climatic Impact Assessment Program of the U.S. Department of Transportation under Contract No. DOT-OS-20205.

REFERENCES

Aureille, Y.G. and C.T. Norris (1973), "Short and Long Term Forecasting Models of the U.S. Domestic and International Traffic and Forecasts to 1981" (Third Ed.), Rept. No. C1-805-3084, McDonnell-Douglas Aircraft Co.

Ayres, Robert V. (1969), *Technological Forecasting and Long Range Planning*, McGraw-Hill, New York.

BAC (1973), unpublished data supplied to DOT by the British Aircraft Corporation.

Becker, John V. and Frank S. Kirham (1971), "Hypersonic Transports," NASA Langley Research Center, Langley, Va.

Boeing Co. (1971), "Airline Traffic Forecast," Commercial Airplane Group, Seattle, AZ-6334.

Boeing Co. (1973a), "Studies of the Impact of Advanced Technologies Applied to Supersonic Transport Aircraft: Interim Summary Report. Volume 3: Market Analysis," Contract NAS 1-11938, Commercial Aircraft Group, Seattle, DG-22529-2.

Boeing Co. (1973b), unpublished data.

Brown, R.G. (1963), *Smoothing Forecasting and Prediction*, Prentice-Hall, Englewood Cliffs, NJ.

Burns, Robert F. (1934), *Production Trends in the U.S. Since 1870*, National Bureau of Economics Research, New York.

CAB (1971), *Handbook of Airline Statistics*, Civil Aeronautics Board, Washington, D.C.

Curtiss-Wright Corp. (1944), "Air Transportation in the Immediate Post-War Period," BR-69 (Buffalo, NY).

de Neufville, R. and J.H. Stafford (1971), *Systems Analysis for Engineers and Managers*, McGraw-Hill, New York.

DOT-NASA (1971), "Joint DOT-NASA Civil Aviation Research and Development Policy Study," Department of Transportation TST-10-4, National Aeronautics and Space Administration SP-265, Washington, D.C.

Douglas Corp. (1973), "Studies of the Impact of Advanced Technologies Applied to Supersonic Transport Aircraft: Task II, Market Analysis and Economic Ground Rules," Contract NAS 1-11939, McDonnell-Douglas Aircraft Corp., Long Beach, CA, MDC-J4378.

Douglas Corp. (1974), "General Performance Report," MDCJ5806/01, McDonnell-Douglas Aircraft Corp., Long Beach, CA.

English, J. Morley (1944), "Future Market for Air Travel," unpublished report prepared for the Lockheed Corporation.

English, J. Morley (1971), *Economics of Engineering and Social Systems*, Wiley, New York.

English, J. Morley (1972), "Engineering economics for the practicing engineer," internal publication, UCLA.

English, J. Morley (1974), "Economic concepts to disturb the engineer," Eng. Econ. 19(3), 141-152.

FAA (1962), "Aviation Forecasts, Fiscal Years 1963-1968," Federal Aviation Administration, Washington, D.C.

FAA (1965), "Aviation Forecasts, Fiscal Years 1966-1973," Federal Aviation Administration, Washington, D.C.

FAA (1968), "Aviation Forecasts, Fiscal Years 1968-1973," Federal Aviation Administration, Washington, D.C.

FAA (1969), "Aviation Forecasts, Fiscal Years 1970-1981," Federal Aviation Administration, Washington, D.C.

Gaston, J. Frank (1961), *Growth Patterns in Industry: A Re-examination*, National Industrial Conference Board, New York.

Gilfillan, S.C. (1972), "Environmental and population problems reconsidered," Technol. Forecast. Soc. Changes 3, 403-413.

Grobman, J. and R.D. Ingebo, "Forecast of jet-engine exhaust emissions of high-altitude commercial aircraft," in this volume.

ICAO (1973), "International civil aviation in 1972," in the May 1973 ICAO Bulletin, International Civil Aviation Organization, Montreal, Canada.

Jantsch, Erich (1967), "Technological Forecasting in Perspective," Organization for Economic Co-operation and Development, Paris.

Johnson, E. and T.R. Craig (1973), "U.S. Petroleum Supply Outlook," Boeing Commercial Airplane Co., p. 81.

Jordan, Paul (1971), Rand Corporation, unpublished work prepared for the Commission on Population Growth and the American Future.

Lockheed (1972), "World Air Travel Demand," Commercial Market Engineering and Research Division, Lockheed-California Co., Burbank, CA.

Lockheed (1973), "Studies of the Impact of Advanced Technologies Applied to Supersonic Transport Aircraft: Task II, Market Analysis," Contract NAS1-11940, Lockheed-California Co., Burbank, CA, LR-25827-2.

NASA (1973), "Advanced Supersonic Technological Concept Study, Reference Characteristics AST," National Aeronautics and Space Administration Langley Research Center, CR-132374 (work done by LTV Aerospace Corp., Hampton, VA).

Rice, R.A. (1972), "System energy and future transportation," Technology Rev. 74(3), 31-37.

Tsou, Peter (1972), "Methodology for Evaluation of Large Scale and Long Range Engineering Investments," Ph.D. dissertation, University of California, Los Angeles, CA.

United Nations (1970), "World Population Statistics," pub. UN, New York.

World Bank (1971), "World Bank Annual Report, 1970-1971," Washington, D.C.

DISCUSSION

FORNEY: Could you explain the emission levels you used?

ENGLISH: They were based on a consensus of NASA and engine manufacturers as to what we could expect for 1990 engines if no effort were made between now and then to lower them.

FORNEY: You showed a significant amount of emissions at 21 to 24 kilometers. Isn't that rather high?

ENGLISH: Well, it was originally assumed that the SST's would be flying in the 18 to 21 kilometer band. Recent discussions with the aircraft manufacturers have suggested that advanced SST's might have a slightly higher optimum cruise altitude, maybe just over 21. So our model puts them in the 21 to 24 kilometer band.

SCHAINKER: What boundary conditions did you use for your 2025 scenario? Also, have you performed any sensitivity studies with respect to changing those conditions?

ENGLISH: The scenario was as follows: 20% of the world population would contribute to world travel; that's about the percentage for the U.S. today. A maximum of 2.5 percent of gross world product would be spent on air travel; that may be high. And third, the fares would not change – in constant dollars, that is – between now and then; fares have been dropping in constant dollars, but the trend is flattening out. We then fitted our growth curve to these conditions. And no, we haven't performed any sensitivity studies yet.

L. ANDERSON: Isn't it possible that what's been driving the growth curve up all this time is the drop in fares, in terms of constant dollars?

ENGLISH: Yes, that's certainly one of the factors.

FORECAST OF JET-ENGINE EXHAUST EMISSIONS FOR FUTURE HIGH-ALTITUDE COMMERCIAL AIRCRAFT

JACK GROBMAN AND ROBERT D. INGEBO
NASA Lewis Research Center
Cleveland, Ohio

ABSTRACT: This report provides forecasts of exhaust-emission levels that may be realistically predicted for future commerical aircraft cruising within the upper troposphere and stratosphere. The forecasts are based on current knowledge of the emission characteristics of combustors and augmentors, the current status of combustion research in emission-reduction technology, and predictable trends in combustion systems and operating conditions required for jet engines that might be developed for future subsonic and supersonic commercial aircraft. Results are presented for cruise conditions in terms of an emission index, g pollutant/kg fuel. Emission forecasts include estimates for oxides of nitrogen, carbon monoxide, total hydrocarbons, particulates (soot), sulfur dioxide, total trace elements, carbon dioxide, and water. Two sets of engine-exhaust emission predictions are presented; the first is based on an independent NASA study, and the second on the consensus of an ad-hoc committee composed of industry, university, and government representatives. The consensus forecasts are in general agreement with the NASA forecasts.

INTRODUCTION

This report provides forecasts of projected levels of exhaust emissions that may be realistically applied to future commercial aircraft operating at high-altitude cruise conditions. Such predictions are needed by the Department of Transportation for the Climatic Impact Assessment Program (CIAP). The purpose of the CIAP effort is to provide an assessment, by 1974, of the potential climatic effects of perturbations of the upper atmosphere caused by the propulsion effluents of a worldwide high-altitude aircraft fleet projected to the year 1990 and beyond (Grobecker, 1973). One of the principal efforts of the overall program is the preparation of six monographs that will discuss the natural stratosphere of 1974, the nature of propulsion effluents, the perturbed stratosphere, the perturbed troposphere, biological effects, and economic effects. The engine-emission forecasts that are summarized in this report will be used as part of the input to the second monograph. These emission levels will be combined with projections of fuel-consumption rates during cruise for future aircraft, of air routes, and of frequency of travel, to determine the rate of introduction of engine effluents into the stratosphere from advanced subsonic and supersonic commercial aircraft.

Current NASA-Lewis pollutant-technology investigations, both small-scale and full-annular-combustor test efforts, are aimed at initiating and evaluating potentially attractive techniques for reducing exhaust emissions from jet aircraft (see, for example, Rudey (1972) and Jones and Grobman (1973)). These efforts will provide an estimate of the extent to which current and future combustor emission levels can be reduced. Some examples of techniques being evaluated include air atomizing, premixing, and prevaporizing fuel-injection systems; multi-zone fuel distribution; fuel staging, variable geometry for airflow, and/or fuel-distribution control; exhaust-gas recirculation, reduced reaction-zone dwell-time, rapid reaction-zone mixing; and the use of alternate fuels. In addition, engine-cycle study information is being used to forecast the operating constraints that may be imposed on the combustor. The abovementioned study elements are combined to make a NASA forecast (described in detail in Grobman and Ingebo (1974)) of practicably achievable low-emission engine technology for the time periods of 1980-1985 and 1990-and-beyond. These forecasts are made on the premise that conventional JP fuel would continue to be the only aircraft fuel that is used until the late 1990's. The use of substitute fuels such as liquefied natural gas

(LNG) and hydrogen is also considered in Grobman and Ingebo (1974) for the time period beyond the late 1990's; however, the discussion in this report is limited to JP-fueled aircraft.

Exhaust emissions predicted for the propulsion systems of future commercial jet aircraft are presented for both major and minor redesigns of the combustor using low-emission technology. In addition, theoretical minimum emission limits have been determined from chemical-kinetics calculations for a combustor burning premixed and prevaporized fuel. The emission forecasts are presented for cruise conditions in terms of an emission index, g pollutant/kg fuel. They include estimates for oxides of nitrogen, carbon monoxide, total hydrocarbons, particulates (soot), sulfur dioxide, total trace elements, carbon dioxide, and water.

Supplementary emission forecasts are presented that were prepared by an ad-hoc committee which combined the opinions of several representative engine manufacturers with the independent NASA projections. A consensus on the most likely engine cycles, combustion technology, and cruise emission levels anticipated for the time periods of 1980-1985 and 1990-and-beyond was obtained by means of a joint evaluation of the independent forecasts prepared by each of the manufacturers and by NASA. The engine manufacturers that contributed to this effort were the Detroit Diesel Allison Division of General Motors Corporation, General Electric Company, and the Pratt & Whitney Aircraft Division of United Aircraft Corporation. Each of these manufacturers prepared an independent assessment and then joined NASA in arriving at a consensus on estimated emissions. Representatives of the Department of Transportation, the Environmental Protection Agency, and the University of California, Berkeley, also served on the committee.* There was general agreement that JP or hydrocarbon-type fuels would probably be the only fuels used by commercial aircraft until far beyond 1990, so the consensus forecasts were based on the use of JP fuel only.

* The Ad Hoc Committee members were as follows: Mr. Jack B. Esgar (Chairman), NASA Lewis Research Center; Mr. Joseph N. Barney, Detroit Diesel Allison, Division of General Motors; Dr. Alan J. Grobecker, Department of Transportation; Mr. George Kittredge, Environmental Protection Agency; Mr. Donald P. Pascal, Pratt & Whitney Aircraft; Dr. William H. Roudebush, NASA Headquarters; Prof. R.F. Sawyer, University of California, Berkeley; and Mr. Morris A. Zepkin, General Electric Company.

PROJECTED ENGINE CYCLES

Both the NASA and the Ad Hoc Committee studies conclude that future commercial subsonic jet aircraft will be equipped primarily with advanced high-bypass turbofan engines. The Ad Hoc Committee study predicts that either a duct-burning turbofan or a nonaugmented (dry) turbojet may be the most likely engine for future advanced supersonic transports, whereas the NASA study selects the duct-burning turbofan engine only. Both studies conclude that JP-type fuels would probably be the only fuel used by commercial aircraft until far beyond 1990.

NASA Study

Engine designs were selected for both a subsonic and a supersonic mission that resulted in minimum values of aircraft takeoff gross weight (TOGW) for a given payload and range at a specified noise constraint. Airplane economics are improved as TOGW is reduced. Takeoff gross weight varies as the engine design parameters (turbine inlet temperature, overall pressure ratio, fan pressure ratio, and bypass ratio) and engine size are varied. The values selected for these engine design parameters were influenced by the noise constraint, which resulted in TOGW penalties. However, the values selected for these engine design parameters were not constrained by engine-exhaust emission limits; it was assumed that engine-exhaust emissions would be minimized by means of low-emission combustor technology.

A reduction in the NO_x emission index might be achieved by lowering the overall pressure ratio below the values selected in this study. A moderate reduction in overall pressure ratio might be tolerable, but a large reduction in overall pressure ratio would lead to serious TOGW penalties. Similarly, a small reduction in NO_x might also be obtained by reducing the turbine inlet temperature, but, again, not without penalizing TOGW. For the supersonic mission, NO_x might be reduced by minimizing cruise flight speed. None of these emission constraints has been considered in this study.

Tables 1 and 2 describe commercial aircraft systems and cruise operating conditions, respectively, for both subsonic and supersonic missions which are forecast for 1980-1985 and for 1990 and beyond. For the subsonic CTOL (conventional takeoff and landing) aircraft, it is assumed that production or growth versions of aircraft such as the 747 or DC-10 will continue to be in service up to 1990 at least, and that advanced turbofan engines utilizing low-NO_x combustor technology could be incorporated into these aircraft between 1980 and 1985. An Advanced Technology Transport (ATT) fueled by JP could be operational in the early 1990's. For the supersonic mission, it is forecast that the Concorde would enter service in 1975 and that growth versions of the Concorde would remain in service up to at least 1990. Detailed information is lacking on the Tupolev TU-144, which is expected to become operational in 1974; however, its operating characteristics should be similar to the Concorde's. A JP-fueled Advanced Supersonic Transport (ASST) might be operational in the early 1990's. The analytical data presented in Tables 1 and 2 for the future subsonic (ATT) and supersonic (ASST) aircraft are based on mission-analysis calculations (performed by James F. Dugan, Jr., of NASA Lewis Research Center) similar to those described in Kraft (1972) and Whitlow (1973) respectively. Although these mission analyses consider information and comments from aircraft-engine and airframe manufacturers and from airlines, they do not indicate any commitments that future aircraft and engines will match these predictions. These indicated engines and aircraft statistics are, however, the best information available to the authors at this time.

Advanced Technology Transport (ATT)

An airframe with a super-critical wing was selected. At the design cruise conditions of Mach

Table 1. Commercial Aircraft Systems

	Subsonic			Supersonic	
	Production turbofans (CTOL)		Future turbofan (ATT) - NASA study	Concorde AB turbojet	Future duct-burning turbofan (ASST) - NASA study
	747B-200	DC-10 Series 30			
Takeoff gross weight, kg	354 000	252 000	113 000	175 000	382 000
Passengers	375-500	250-380	200	128	250
Range, km	11 900	9550	5560	5900	7400
Cruise Mach number	0.85	0.85	0.85	2.0	2.7
Cruise altitude, meters	10 700	10 700	12 200	17 700	19 800
Engine make and model	P&WA JT9D-7	G.E. CF6-50	–	Olympus 593	–
Number of engines	4	3	3	4	4
Noise level, EPNdB	107	~105	96	115	108
Max power @ S.L., N (lbf)	209 000 (47 000)	227 000 (51 000)	115 000 (25 800)	170 000 (38 000)	306 000 (68 700)
SFC @ max power, $\frac{kg/hr}{N}\left(\frac{lbm/hr}{lbf}\right)$	0.037 (0.36)	0.040 (0.39)	0.056 (0.55)	–	0.078 (0.763)
Overall compression ratio @ max power	23	29.4	23.9	14.8	10
Max power @ cruise, N (lbf)	–	–	18 260 (4100)	29 650 (6666)	85 600 (19 250)
SFC @ cruise, $\frac{kg/hr}{N}\left(\frac{lbm/hr}{lbf}\right)$	–	–	0.073 (0.718)	0.121 (1.189)	0.157 (1.54)
Overall compression ratio @ cruise	–	–	26.4	–	4

0.85 and 12,200 meters altitude, the nominal lift-to-drag ratio was 20. The design range was 5560 km with a payload of 200 passengers for a transcontinental mission. An intercontinental mission with a design range of about 10,200 km has also been considered, but has not been included in Table 1, since the combustor operating conditions do not differ greatly from those of the transcontinental mission, and the exhaust emission indices would thus be similar. Takeoff gross weight of the advanced subsonic aircraft is about 113,000 kg. Three high-bypass turbofan engines are specified for the advanced subsonic mission. The engines selected resulted in a noise level of 96 EPNdB (effective perceived noise decibels) which is 10 EPNdB below the Federal Air Regulation FAR-36 requirement. The bypass ratio during cruise is 7.8. An advanced turbine-cooling scheme (full-coverage film cooling) was assumed, together with up to 13 EPNdB of fan-machinery noise suppression. The total fuel flow rate per engine during cruise is 1610 kg/hr. As shown in Table 2, at cruise operating conditions, the engine selected for the ATT has combustor inlet temperature and pressure that are slightly lower, and a combustor exit temperature that is somewhat higher, than those of a representative production turbofan engine.

Advanced Supersonic Transport (ASST)

The duct-burning turbofan engines for the ASST were selected to meet an FAR-36 sideline noise constraint (108 EPNdB). Bypass ratio and fan pressure ratio were determined by considering the jet exit velocities (and hence jet noise) of the two streams which, when added together, produce 108 EPNdB without suppression. The engines were sized for a maximum dry (i.e., non-duct-burning) takeoff with acceptable field-length and community-noise requirements (at 6.5 km, from start of roll). Turbine-inlet temperature and cooling bleed were selected as being suitable for advanced full-coverage film cooling. The airplane used in this evaluation cruised at Mach 2.7 at an altitude of 19,800 m. Initial cruise altitude was chosen to maximize the L/D (lift-to-drag ratio) over sfc

Table 2. Cruise Operating Conditions

	Subsonic		Supersonic	
	Production turbofan (P&WA JT9D)	Future turbofan (ATT) - NASA study	Concorde: AB turbojet (Olympus 593)*	Future duct-burning turbofan (ASST) - NASA study
Cruise Mach number	0.85	0.85	2.0	2.7
Cruise altitude, meters	10 700	12 200	17 700	19 800
Total airflow rate, kg/sec	304	151	83	336
Bypass ratio	4.9	7.8	0	2.36
Compressor discharge airflow rate, kg/sec	51.5	17.2	83	100
Combustor inlet temperature, K	710	661	824	810
Combustor inlet pressure, atm	9.7	7.2	6.5	4.7
Combustor exit temperature, K	1410	1540	1320	1770
Combustor fuel-air ratio	0.018	0.026	0.0141	0.0299
Combustor fuel flow rate, kg/hr	2800	1610	4200	10 750
Augmentor airflow rate, kg/sec	–	–	–	236
Augmentor inlet temperature, K	–	–	–	635
Augmentor inlet pressure, atm	–	–	–	2.6
Augmentor inlet velocity, m/sec	–	–	–	90
Augmentor exit temperature, K	–	–	–	835
Augmentor fuel-air ratio	–	–	–	0.00495
Augmentor fuel flow rate, kg/hr	–	–	–	4200
Total fuel flow rate, kg/hr (per engine)	2800	1610	4200	14 950

*Afterburner is not used for steady-state cruise.

(specific fuel consumption) quotient. An L/D of 9.9 was typical for the JP-fueled airplane. The cruise duct-burner temperature was reduced from the climb setting so that operation was near the minimum point on the sfc-versus-thrust curve. A design range of 7400 km was obtained in an all-supersonic-cruise mission (i.e., with no subsonic cruise leg) with 250 passengers. Takeoff gross weight for the ASST is about 382,000 kg. The cruise bypass ratio is 2.36. The combustor fuel flow rate per engine during cruise is 10,750 kg/hr. A small degree of augmentation is required during cruise that results in a duct-burner fuel flow rate of 4200 kg/hr. The total engine fuel flow rate during cruise is 14,950 kg/hr. As shown in Table 2, at cruise operating conditions, the engine selected for the ASST has a combustor inlet temperature and pressure that are slightly lower, but a combustor exit temperature that is much higher, than the corresponding design conditions of the Olympus 593 engine.

Ad Hoc Committee Study

The consensus forecasts are based on a general range of operating conditions for future jet engines, while the NASA forecasts are based on specific operating conditions determined from several projected engine cycles for future jet aircraft.

Subsonic Aircraft Engines

The Ad Hoc Committee agrees that many of the current turbofan engines presently being used for CTOL aircraft will continue to be in service up to at least about 1990. Aircraft engines such as the CF-6, JT9D, and RB 211 manufactured after 1978 will require modifications in order to meet proposed EPA emission standards (EPA, 1973).

Improved versions of these engines and advanced high-bypass turbofan engines for ATT aircraft would begin to enter service between 1980 and 1985. After 1990, commercial aircraft would be equipped primarily with advanced high-bypass turbofan engines. The sea-level takeoff (SLTO) thrust of these advanced turbofan engines might vary from 110,000 to 360,000 newtons (25,000 to 80,000 lbf) depending on whether they are used in short- or long-haul aircraft. (The SLTO thrust of current high-bypass turbofan engines ranges from about 180,000 to 240,000 newtons (40,000 to 53,000 lbf).) The projected values of the overall pressure ratio for the advanced engines range from about 25 to 37, compared to current values of 20 to 30. The differences in the cruise operating conditions between the advanced and current engines would result in combustor inlet pressures and temperatures, and exit temperatures, ranging from current to modestly higher values.

Supersonic Aircraft Engines

The Concorde and Tupolev TU-144 or improved versions of these aircraft will probably continue to be in service in the 1980-1985 time period; however, advanced supersonic transports (ASST's) of greater size and range would be expected to enter service in the time period beyond 1990. The selection of an engine for an advanced supersonic transport will be significantly influenced by noise constraints. Either a duct-burning turbofan or a nonaugmented (dry) turbojet could be considered as a candidate for this application. An advanced supersonic transport would be expected to cruise within a Mach-number range of 2.2 to 2.7.

The sea-level takeoff (SLTO) thrust of these advanced engines could range from 220,000 to 370,000 newtons (50,000 to 82,000 lbf). The SLTO thrust of the Olympus engine used for the Concorde is about 170,000 newtons (38,000 lbf). The projected overall pressure ratio (SLTO) could range from 12 to 25 with a turbine inlet temperature as high as 1600 to 1800 K.

PROJECTED EMISSION-REDUCTION TECHNOLOGY

Each study considers several categories of advanced combustor technology to attain varying degrees of NO_x emission reductions. In addition, the NASA study predicts a theoretical minimum NO_x emission level, based on chemical-kinetics calculations, for a combustor burning a premixed and prevaporized fuel.

NASA Study

Along with emission controls, there are a number of critical performance factors that must

be considered in the design of any aircraft gas-turbine combustor: for example, combustion efficiency, total pressure loss, durability, exit temperature profile, and altitude relight. Combustor size and weight are important because they influence the overall weight of the engine. Combustor length affects the turbine shaft length and the bearing requirements. Reducing combustor length also reduces the amount of air required to cool the combustor liner by reducing its surface area; it may also be desirable for reducing NO_x emissions by reducing reaction-zone dwell time.

Proposed Federal regulations designed to control noise limits and air quality are expected to have a significant impact on the design of future aircraft engines (Beheim et al., 1971). To offset the economic penalties of low noise, engines must be lighter and more efficient, which further emphasizes the requirement for compact engine components such as combustion systems.

Proposed regulations on aircraft emissions include limits on gaseous pollutants (CO, total hydrocarbons, and NO_x) which are produced during a defined landing-takeoff cycle (EPA, 1973). This cycle covers all aircraft operations below an altitude of 915 meters (3000 ft). A limit on smoke emissions sets a maximum value on the SAE smoke number. Meeting these aircraft emission regulations requires that improvements be made in combustor design to reduce hydrocarbons and carbon monoxide during engine idle and taxi, and to reduce NO_x and smoke during takeoff. Many of the techniques being investigated to reduce NO_x during takeoff are also applicable to the reduction of NO_x during cruise; however, the techniques being studied to reduce CO and THC at engine idle by improving combustion efficiency during idle are generally not required for cruise conditions, since combustion efficiency is already near 100 percent at cruise. Some of the techniques used to minimize CO and THC pollutants at idle may enhance the formation of NO_x or smoke at higher power conditions; therefore, future combustor designs might require variable geometry for the control of primary airflow distribution and/or fuel distribution to minimize pollutant formation over a wide range of engine operating conditions.

All of the above factors must be considered in arriving at the combustor-technology requirements for the projected engine cycles included in Table 2. The combustion efficiency during cruise of future combustors designed for either ATT or ASST aircraft should be virtually the same as for present production combustors, which is very near 100 percent. It may be feasible to design either turbojet afterburners or turbofan ductburners with combustion efficiencies near 100 percent during cruise by means of effective fuel atomization and fuel-air mixing. Optimum fuel-air mixing might be attainable by variable geometry to control airflow and/or fuel flow distribution.

Satisfactory reignition capabilities are required to allow startup of the engine in the event of a flame blowout at altitude. The technique of leaning-out the primary zone to minimize NO_x may adversely affect altitude relight; therefore, special procedures may be necessary to regain relight capabilities lost due to design changes for reduced emissions.

The discussion of combustor design techniques will accentuate those concepts which may effect a reduction in NO_x emissions during cruise operation. Two levels of combustion-system design changes for reducing cruise emissions are considered: Class 1, minor retrofits to existing production engines or minor improvements to growth versions of these production engines, such as an improved fuel injector; and Class 2, major redesign (advanced state-of-the-art emission-reduction technology) based on current experimental emission-reduction programs such as the NASA Experimental Clean Combustor Program. For comparative purposes, lower emission limits determined by chemical-kinetics calculations for a premixing/prevaporizing combustor are also included. The two levels of design improvement represent, in turn, increasing design complexity and a greater departure from conventional design methods, and the theoretical minimum represents a goal to strive for in practical combustor design by approaches that have not yet been determined.

The technology required for a Class 1 modification to a JP-fueled combustor should be available within one or two years; however, an additional three to five years would be required for implementing the modification and obtaining

the necessary engine certification. Approximately three to five years should be required to evolve the technology for a Class 2 modification to a JP-fueled combustor. An additional four to five years should be required to implement this modification into an advanced engine design.

The projected combustor technologies that might be utilized in the advanced propulsion systems listed in Tables 1 and 2 are based on a projection of the emission-reduction technology summarized in Grobman and Ingebo (1974). The predicted levels of design improvement or "class change" are discussed below.

Class 1 Engine Modification

The simplest modification to the combustor that can be envisioned would be a retrofit or redesign of the fuel-injection system to improve the atomization and carburetion of the fuel. Air atomization, discussed in Ingebo and Norgren (1973), may be capable of providing a more uniform fuel-air mixture than is possible with the conventional pressure-atomized fuel injector. Air-atomizing fuel injectors are currently under evaluation in several engine-development programs. Further research on air-atomizing fuel injectors is required to evolve designs that operate well over a wide range of fuel flows, demonstrate good durability, and satisfy altitude relight requirements.

Class 2 Engine Modification

A "Class 2 Change" is defined as a major redesign of the combustor, based on advanced emission-reduction technology. Projections for the Class 2 change will be based on the multizone (swirl-can) combustor concepts described in Jones and Grobman (1973), which provide uniform reaction-zone temperature and a relatively quick quenching of the reaction by the dilution air. The emissions of oxides of nitrogen (NO_x) for two different multizone combustors (one a swirl-can and the other a double annular) are shown in Figure 1. Also shown on this figure are data from a single-annular combustor (Wear et al., 1970). The NO_x emission index (grams of NO_2 produced per kilogram of fuel burned) is shown as a function of the combustor exit average temperature. The test conditions (pressure, inlet-air temperature, and reference velocity) were the same for all three combustors. The number of fuel-injection sources for each combustor is indicated in the figure. Increasing the number of fuel-injection sources, which spreads the combustion more uniformly throughout the combustor, appears to be a very effective way of reducing the emission of NO_x. The techniques of premixing fuel and air and rapid quenching of the combustion reaction, both incorporated into the swirl-can approach, are also considered to be a principal factor in producing the lower NO_x emissions of these combustors. Figure 2 compares the NO_x emission levels for the three combustor types with increasing inlet-air temperature and a constant exit temperature of 1500 K. The trend with increasing inlet-air temperature is an exponential increase in NO_x emission index; at an inlet-air temperature of 750 K the swirl-can combustor produces only about 60% as much NO_x as the more conventional single-annular combustor.

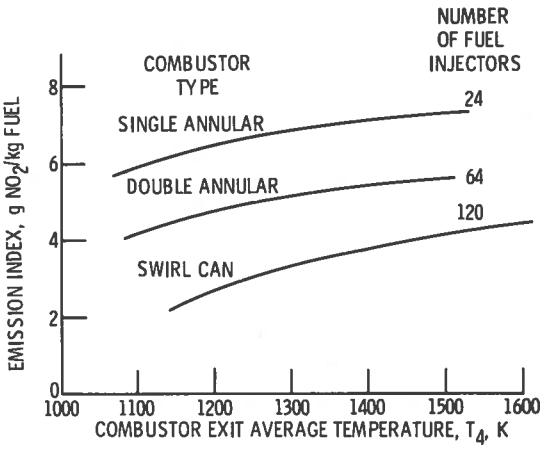

Figure 1. Variation of oxides-of-nitrogen emission index with combustor exit average temperature for single-zone and multizone combustors. Combustor inlet total temperature, T_3, 590K; combustor inlet total pressure, P_3, 6 atmospheres; reference velocity, V_r, 32 m/sec.

The swirl-can combustor is just one of the concepts being evaluated in the NASA Experimental Clean Combustor Program described in Jones (1973). The goal of this program is to develop and demonstrate technology for decreasing pollutant emissions of modern gas-turbine engines. This technology is applicable mainly to advanced CTOL aircraft with engine-compressor

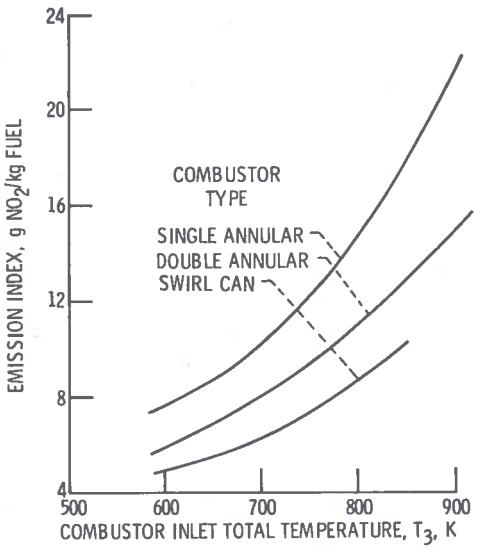

Figure 2. Variation of oxides-of-nitrogen emission index with combustor inlet total temperature for single-zone and multizone combustors. Combustor inlet total pressure, P_3, 6 atmospheres; combustor exit average temperature, T_4, 1500K.

pressure ratios of approximately 20 to 35. However, it will also be applicable to engines for supersonic aircraft. The program will be conducted in three phases. Contracts for the first phase were awarded by the NASA Lewis Research Center to both General Electric and Pratt & Whitney Aircraft. In this first phase of the program, both contractors will conduct experiments in combustor test facilities to screen combustor concepts for reducing emissions. Each contractor will evaluate the NASA-Lewis swirl-can concept in addition to several of its own concepts. The primary emphasis of these contracts will be on demonstrating a reduction in NO_x emissions to approximately one-fourth of the current levels for production engines. There is also a requirement to significantly reduce emissions at engine idle conditions. Addendums to this program have also been included for investigating ways to reduce the NO_x emission index to a level of 5 g NO_2/kg fuel during cruise for supersonic commercial aircraft.

In the second phase of the program, further tests will be conducted to implement the best designs of Phase I and to demonstrate satisfactory combustor performance, including uniformity of exit temperature profile, altitude ignition capabilities, and durability. In the third phase, the best combustor concepts will be evaluated in a high compressor-pressure-ratio engine-demonstration test. This technology may be available to engine designers during the 1980-1985 time period. Other types of low-NO_x combustor concepts being investigated in this program, as described in Jones (1973), may prove to be as attractive as or even better than the "swirl-can" concept.

Minimum Engine Emissions

Experimental research is just beginning on an attempt to evolve combustor concepts that may significantly lower the NO_x emission index, to levels on the order of a factor of ten below the current goals of the Experimental Clean Combustor Program. The NO_x emission projections for the premixing/prevaporizing combustor presented herein will be based on the analytical calculations described below. The results of these calculations should be interpreted cautiously for three reasons: (1) the analytical model used is an extreme simplification of the combustion process, (2) additional improvements in the chemical-kinetics equations used may be warranted as new chemical-kinetics data become available, and (3) the degree to which these theoretical results may be approached by practical combustor hardware is uncertain. Many problems may be envisioned in the evolution of premixing/prevaporizing combustors, including the design of a satisfactory vaporizer of JP fuel, and the control of flashback.

The theoretical flame temperature is shown plotted against equivalence ratio, ϕ, for JP fuel in Figure 3. Equivalence ratio is defined here as the ratio of the fuel-air ratio in the primary (reaction) zone to the stoichiometric fuel-air ratio. These data were obtained from the computer program of Gordon and McBride (1971) for combustor inlet conditions (800 K, 5 atm) simulating supersonic cruise. The theoretical flame temperature for JP reaches a peak at an equivalence ratio of about 1.1. For these inlet conditions, the maximum flame temperature of JP is 2560 K. Nitrogen oxide formation may be minimized by maintaining the lowest flame temperature possible in the reaction zone. Because of the lean flammability limit, the minimum flame temperature for a uniform mixture of fuel and air is shown to be about 1900 K ($\phi = 0.5$) for the specified inlet conditions.

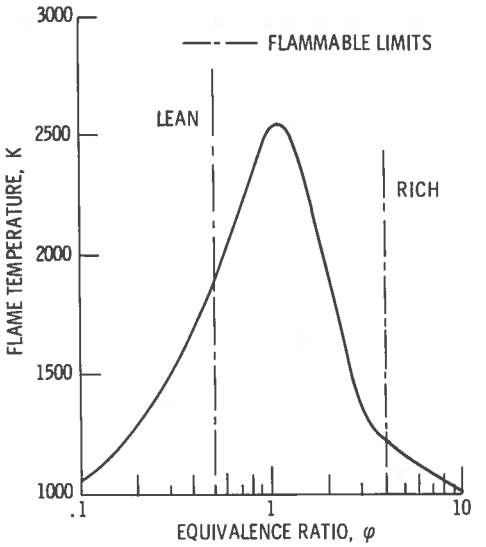

Figure 3. Theoretical flame temperature. Combustor inlet total temperature, T_3, 800K; combustor inlet total pressure, P_3, 5 atmospheres.

NO_x emission indices for a premixing/prevaporizing combustor were determined from an Equilibrium Hydrocarbon Model by using a modification of the chemical-kinetics computer program given in Bittker and Scullin (1972), described in detail in Grobman and Ingebo (1974). In this model, concentrations of all species of combustion products were assumed to be initially at equilibrium, and only the kinetics of the nitrogen-oxygen reactions were considered. Results from computations at a combustor inlet temperature and pressure of 800 K and 5 atmospheres respectively, and a reaction dwell time of 2 milliseconds, are shown in Figure 4, in which NO_x emission index is plotted against equivalence ratio in the primary (reaction) zone. Recent experimental results (unpublished data of David N. Anderson, NASA Lewis Research Center) obtained at the same operating conditions with a laboratory burner using premixed-prevaporized propane (described in Anderson (1973)), and limited calculations based on a theoretical well-stirred reactor model (Boccio et al., 1973), which includes the kinetics of the combustion reaction, are also shown in Figure 4 for comparison.

The two theoretical models agree well with experimental results near an equivalence ratio of 1.0. At lower equivalence ratios, the Equilibrium Hydrocarbon Model predicts NO_x values an

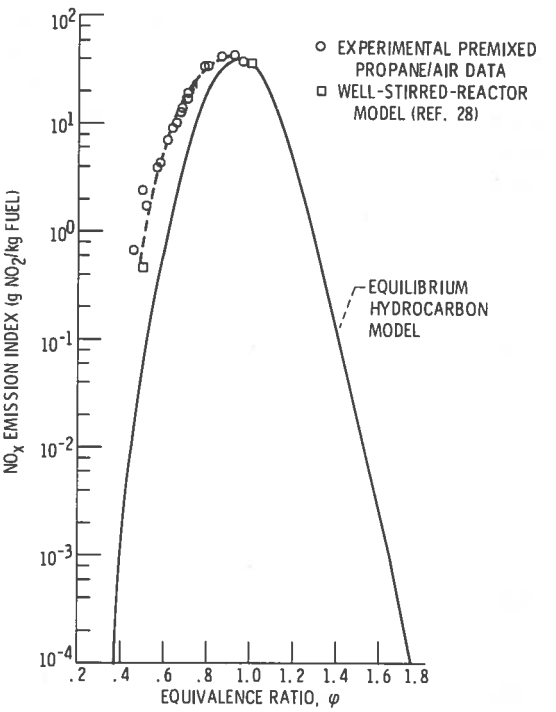

Figure 4. Theoretical NO_x emission index for a combustor burning premixed/prevaporized hydrocarbon fuel. Inlet temperature, 800K; inlet pressure, 5 atmospheres; dwell time, 2 milliseconds.

order of magnitude below the experimental results, whereas the single data point from Boccio et al. (1973) is in good agreement with experimental results at an equivalence ratio of 0.5. Thus, the Equilibrium Hydrocarbon Model may not be applicable at low equivalence ratios.

Within the reaction zone, the concentration of oxygen atoms can overshoot the equilibrium value by several orders of magnitude at low temperatures (Edelman and Exonomos, 1971). Because the oxygen atom is an important part of the nitric-oxide-producing scheme, the Equilibrium Hydrocarbon Model which assumes equilibrium values for combustion products may not predict nitric oxide concentrations accurately. Also, a recent study of premixed hydrogen flames showed that measured values of NO_x concentrations were higher than predicted when equilibrium levels for the oxygen-atom concentration were assumed (Homer and Sutton, 1973). Thus, this assumption can lead to as much as an order of magnitude difference between measured and computed NO_x concentrations at low equivalence ratios.

In applying Figure 4 to predictions of the lower NO_x emission limit presented in the next section, the curve faired through the experimental data and the data from the theoretical kinetics model of Boccio et al. (1973) will be used. These results provide only a preliminary indication of the lower limit for NO_x emissions. In actual practice, combustor performance limits such as combustion stability, degree of mixing, and uniformity of reaction-zone temperature may significantly alter these estimates.

Ad Hoc Committee Study

The present belief is that the state-of-the-art low-emission combustor technology available by the 1980-1985 time period will be motivated by the need to meet the proposed 1979 EPA emission standards (EPA, 1973). These emission standards presently pertain only to subsonic aircraft, but additional standards for supersonic aircraft are anticipated. In addition, the proposed standards are currently applicable only to aircraft operations below 900 meters (landing-takeoff cycle). Many of the concepts being investigated to reduce NO_x for the proposed EPA landing-takeoff cycle would also be effective in reducing NO_x during cruise. However, if the EPA NO_x regulation cannot be achieved by combustor redesign alone, it may become necessary to obtain a portion of the NO_x reduction through the use of water injection. This approach would not be practical for NO_x reduction at cruise because of the severe TOGW penalty due to the added weight of the water. Research programs such as the NASA Experimental Clean Combustor Program described previously are applying low-emission technology to combustor redesign. The representative engine manufacturers are also engaged in independent research efforts aimed at the development of low-emission combustors that would comply with the proposed EPA standards. It is conceivable that the necessary combustor redesign may require staged combustion or variable geometry for the control of airflow and/or fuel flow in order to obtain low emissions at both low power (idle) and high power (takeoff) conditions.

After the required low-emission combustor technology has been developed, a substantial amount of development time and testing will be required to translate this experimental technology into production technology that fulfills the safety, reliability, and economic requirements of a commercial aircraft.

A possibility exists that NO_x might be reduced to levels lower than the proposed EPA limits by means of a more advanced technology based on the evolution of a premixing/prevaporizing combustor. However, the probability of translating this more advanced concept into production technology by the 1980-1985 time period is considered to be relatively low, and it probably would not be achieved until beyond 1990.

PROJECTED EMISSIONS

NASA Study

The projected engine-exhaust emissions at cruise conditions are based on the advanced subsonic ATT and advanced supersonic ASST missions described in the engine-cycle section and Table 2. Projected emission levels are presented in terms of an emission index, grams of constituent per kilogram of fuel burned.

Emissions Affected Solely by Fuel Composition

The emission levels for constituents that are affected primarily by the composition of the fuel used are listed in Table 3. In general, the emission indices for these constituents are independent of engine operating conditions. Despite the lack of quantitative data, the quantity of carbon in the exhaust during cruise should be quite small. The estimate for carbon was obtained from Williams (1973). The estimate for SO_2 was obtained from Brines (1971), and is based on the current sulfur composition of commercial jet fuels. Total trace elements are defined to include metallic elements in the fuel, in addition to a relatively smaller quantity of eroded metal from engine components. The estimates for total trace elements, and for the quantity of lubricating oil lost from the engine lubricating system, were also obtained from Brines (1971).

Table 3. Estimated Emission Indices at Cruise Conditions with JP Fuel

Constituent	Emission index, g/kg fuel
H_2O	1.25×10^3
CO_2	3.22×10^3
Soot (as carbon)	0.1
SO_2	1-2
Total trace elements	0.01
Lubricating oil	0.1

Emissions Affected By Engine Operating Variables

The CO, total hydrocarbons, and NO_x emission forecasts presented herein for future commercial jet aircraft are based on the projected combustor technology described earlier. As noted previously, these forecasts are divided into two categories of advanced combustor technology, representing different degrees of NO_x emission reductions. The first level, designated as a "Class 1 Engine Modification", assumes a moderate change or retrofit to existing combustion system designs. Emission forecasts for a Class 1 change are based on current emission-reduction research data for air-atomizing and vaporizing fuel injectors described in Ingebo and Norgren (1973) and Norgren and Ingebo (1973). The second level, designated as a "Class 2 Engine Modification", assumes a complete redesign of the combustion system. Emission forecasts for a Class 2 change are based on current experimental data for the multizone combustors (swirl-cans) described earlier. In addition, a theoretical NO_x emission level is predicted that represents an estimate of the lower limit. Theoretical minimum emissions are based on theoretical kinetics calculations for a premixing/prevaporizing combustion system, assuming a reaction-zone dwell time of 2 milliseconds. A Class 1 change represents the least alteration to the engine design, a moderate reduction in emissions, and the highest probability of being technically feasible without penalizing combustor performance. A Class 2 change represents a major redesign of the engine's combustion system, a significant reduction in emissions, and a medium probability of being technically feasible without penalizing combustor performance. To approach theoretical minimum emissions would entail both an extremely innovative redesign of the combustion system and a very low probability of being technically feasible without penalizing combustor performance.

For each level of change, the major motivation for the indicated modifications to the engine's combustion system is the reduction of nitrogen oxides. Except for the case of the ASST duct-burner, no reductions in the combustor's CO and total-hydrocarbon emissions are projected below the best levels currently being observed for production engines; these emissions levels are already quite low during cruise, and it is difficult to envision improvements in the combustion efficiency of the core combustor, which is already as close to 100 percent as can be measured experimentally.

Procedures for NO_x Emission-Index Data Extrapolations

In many cases, it was necessary to extrapolate available experimental emission data for NO_x to the combustor or augmentor operating conditions specified for the advanced engines described in Table 2. These extrapolations were performed to correct for the proper inlet and exit temperatures, and inlet pressures, for the engines in Table 2 by using the data-correlation methods described in Niedzwiecki and Jones (1973). Inlet pressures are adjusted to the proper levels by applying a square-root correction. An exponential adjustment is applied to the inlet temperature by using the correlating parameter $\exp(T/T_d)$, where T is the inlet temperature (in K) and T_d is a constant correlation factor evaluated at 288 in Niedzwiecki and Jones. Variations in exit temperature are adjusted by applying a linear correction. Velocity or dwell-time corrections were not used because the combustor velocities of the experimental data available were judged to be representative of the requirements for the combustion systems of Table 2.

No attempt was made to correct for differences in inlet-air humidity between test-facility conditions and conditions at cruise altitude. Marchionna et al. (1973) indicates that the NO_x emission index increases with decreasing inlet-air humidity at a constant exponential rate of e^{19H} (where H is the humidity, g (H_2O)/g dry air). Typical values of inlet-air humidity for combustor test facilities vary from 0.007 to 0.006

g (H_2O)/g dry air; thus the application of combustor test data to a near-zero humidity at cruise altitude results in an underestimation of the cruise NO_x emission index of from 1 to 12 percent.

Baseline Production Engines

The NASA exhaust-emission estimates during cruise for representative production engines for both a subsonic and supersonic commercial aircraft are listed in Table 4. The cruise emission estimates for the JT9D engine are extrapolated from average JT9D takeoff emission indices given in Bogdan and McAdams (1971). The JT9D takeoff emission indices for CO and total hydrocarbons are judged to be representative of cruise emissions because combustor inlet pressure and temperature for either condition is high enough for the combustion efficiency to be independent of operating conditions (Grobman and Ingebo, 1974). These emission indices for CO and total hydrocarbons are also used to characterize combustor emissions for the advanced engines tabulated in Table 5. Emission estimates for the Olympus 593 engine were obtained from Williams (1973). The Olympus 593 engine does not use afterburning during steady-state cruise.

Table 4. Exhaust Emission Estimates (g/kg fuel) for Production Propulsion Systems at Cruise Conditions (NASA study)

	JT9D*	Olympus 593**
Oxides of nitrogen (as NO_2)	16-23	18-19
Carbon monoxide (CO)	0.2-0.8	1-5
Total hydrocarbons (as CH_2)	0.1-0.3	<1
Combustion efficiency, percent	≈100	99.9

*Based on Bogdan and McAdams (1971), p. IV-311.
**Based on Williams (1973).

Class 1 Engine Modification

The NASA emission forecasts for a Class 1 change for both an ATT and ASST mission are tabulated in Table 5. The Class 1 emission forecasts indicated for the ATT using JP are related to the operating requirements of the advanced turbofan engine (Table 2), but should also be applicable to retrofitted production engines.

A reduction in the NO_x emission index of 30 percent below the baseline levels for the JT9D and Olympus 593 engines (Table 4) is based on the assumed availability of improved air-atomizing fuel-injector technology similar to that described in Ingebo and Norgren (1973). The

Table 5. Exhaust Emission Indices (g/kg fuel) Forecast for Future Propulsion Systems at Cruise Conditions with JP Fuel (NASA study)

	Turbofan - Advanced CTOL (ATT)			Duct-burning turbofan (ASST)								
				Combustor (core engine)			Augmentor (duct-burner)			Overall engine emissions		
Changes*	Class 1	Class 2	Minimum	Class 1	Class 2	Minimum	Class 1	Class 2	Minimum	Class 1	Class 2	Minimum
Oxides of nitrogen (as NO_2)	9-13	4-6	0.2-2**	13-15	5-9	0.7-7**	3	1	0.1-0.7	10-11	3-7	0.7-7**
Carbon monoxide (CO)	0.2-0.8	0.2-0.8	0.2-0.8	0.2-0.8	0.2-0.8	0.2-0.8	60	30	0.2-0.8	17.4	8.7	0.2-0.8
Total hydrocarbons (as CH_2)	0.1-0.3	0.1-0.3	0.1-0.3	0.1-0.3	0.1-0.3	0.1-0.3	5	2.5	0.1-0.3	1.5	0.9	0.1-0.3
Combustion efficiency, %	≈100	≈100	≈100	≈100	≈100	≈100	98	99	100	–	–	–

*Class 1: Minor combustor modification.
Class 2: Major combustor modification.
Minimum: Theoretical limit from chemical-kinetics calculations.
**Upper and lower limits represent minimum primary-zone equivalence ratios of 0.6 and 0.5, respectively.

NO_x emission estimates shown in Table 5 have also been corrected for differences in operating conditions (inlet pressure and temperature, and exit temperature) between the baseline and the advanced engines. This correction for differences in combustor operating conditions results in an additional NO_x decrease of about 21% for the ATT combustor, and a NO_x increase of 8% for the ASST combustor (core engine) relative to baseline conditions. This reduction in NO_x for the ATT is mainly due to the lower projected values for combustor inlet temperature and pressure (Table 2). The increase for the ASST is mainly due to the higher projected value for combustor exit temperature. Thus, the net reduction of the NO_x emission indices for the Class 1 ATT and ASST combustors relative to the baseline engines is about 45 and 24 percent, respectively, as can be seen by comparing Table 4 with Table 5.

The NO_x emission indices for the ASST augmentor (duct-burner) are estimated from the data of Figures 1 and 2 for a single annular primary combustor (corrected to duct-burner operating conditions). This approach is considered justifiable because the combustion characteristics of a duct-burner would be expected to be similar to those of a primary combustor running at the same operating conditions. The predicted NO_x emission index for the augmentor is significantly lower than that for the combustor, because the inlet temperature and pressure, and exit temperature, for the augmentor are much lower (Table 2). The predicted NO_x emission index (overall) for the ASST engine, calculated from the independent emission indices and fuel flow rates for the combustor and augmentor, is about 43% lower than that for the corresponding baseline engine.

The ASST augmentor (duct-burner) combustion efficiency was estimated to be about 98% at the cruise operating conditions of Table 2, by means of a correlation with operating conditions presented in Branstetter et al. (1971), and by assuming that duct-burner performance would be similar to that of the experimental full-scale duct-burner described in the same report. Under these assumptions the duct-burner's contribution to CO and total hydrocarbons is significantly greater than the contribution from the primary combustor in the core engine.

Class 2 Engine Modification

The NASA NO_x emission forecasts for making a Class 2 change in either the ATT or ASST engines as tabulated in Table 5 are based on present swirl-can combustor data (Figures 1 and 2) and goals set for the NASA Experimental Clean Combustor Program. A NO_x emission index of 6 was calculated for the ATT combustor using JP fuel by correcting values obtained from Figures 1 and 2 to cruise operating conditions. This represents about a 45% reduction in the NO_x emission index as compared with "Class 1" engines (69% reduction compared with present "baseline" engines). On the basis of the NASA Experimental Clean Combustor Program goal of reducing NO_x emission indices by about one-fourth that of the "baseline" engines, a forecast value of 4 was obtained. Thus, a NO_x emission index between 4 and 6 is forecast for the ATT combustor. Similar calculations were made for the ASST combustor, which gave a NO_x emission-index forecast between 5 and 9. The NO_x emission prediction for the ASST augmentor was also based on the swirl-can combustor data of Figures 1 and 2. The predicted NO_x emission index (overall) for the ASST engine was calculated to be between 3 and 7, representing an average reduction of about 73 percent compared to the baseline engine.

An improvement in duct-burner combustion efficiency for the "Class 2" ASST engine from 98% to 99% is arbitrarily judged to be attainable by the introduction of variable geometry to control airflow and/or fuel flow distribution.

Minimum Engine Emissions

The minimum NO_x emissions forecast for the premixing/prevaporizing ATT or ASST combustor (given in Table 5) are obtained from the kinetics data of Figure 4, which include the effect of "oxygen overshoot" as discussed earlier under emission-reduction technology. These data were also corrected to the proper cruise operating conditions. The upper value shown in Table 5 represents a more conservative estimate of the minimum attainable NO_x emission index for an assumed minimum primary-zone equivalence ratio of 0.6 and an assumed reaction-zone dwell time

of 2 ms. The lower NO_x estimate (Table 5) might be attainable by operating with a minimum primary-zone equivalence ratio of 0.5. In any event, as mentioned earlier, these preliminary analytical results should be interpreted cautiously. Minimum NO_x emission indices could conceivably be estimated more accurately when more realistic computer models are evolved and when more fundamental experimental data of the type reported in Anderson (1973) becomes available.

The ASST duct-burner emission indices for CO and total hydrocarbons are assumed to be equal to the emission levels for the primary combustor.

Effect of Variations in Cruise Altitude and Mach Number

The emission forecasts presented in Table 5 are based on the constant cruise operating conditions for the projected engines given in Table 2. These forecasts may be adjusted to a varying cruise flight envelope, such as those presented in Forney (1973) and Broderick et al. (1973), by applying corrections for variations to combustor or duct-burner operating conditions. In general, the CO and total-hydrocarbon emission indices for either the ATT or ASST primary combustor are not sensitive to normal variations in combustor operating conditions during cruise, such as those presented in the above two papers. Significant increases in the CO and total-hydrocarbon emission indices for the ASST duct-burner may occur during transonic acceleration because of lower inlet temperature and pressure; however, the quantity of fuel consumed during transonic acceleration is considered to be relatively small in comparison to the total quantity of fuel used during cruise. If required, the duct-burner combustion-efficiency predictions presented in Table 5 may be corrected for varying operating conditions by using the correlation of Branstetter et al. (1971).

Projected NO_x emission indices may be corrected for varying cruise operating conditions by applying the corrections described in the section "Procedures for NO_x Emission-Index Data Extrapolation." The largest correction to the NO_x emission index would be required by variations in flight Mach number. The projected NO_x emission indices would be expected to decrease exponentially with decreasing inlet temperatures as flight Mach number is reduced. Because of the large uncertainty of the forecasts presented in Table 5, it is doubtful that cruise-altitude and Mach-number corrections would necessarily improve the accuracy of these emission-index projections; however, large variations in cruise fuel flow rates will result in proportionate variations in the projected emission rates.

Ad Hoc Committee Study

The consensus exhaust emissions achievable using projected technology are summarized in Table 6. The emission indices listed for "Current

Table 6. Consensus of Estimated Jet-Aircraft Exhaust Emissions (g/kg fuel) Possible Using Projected Technology. (Cruise operating conditions, JP fuel. Ad Hoc Committee Study.)

	Current technology			CTOL/ turbofan		Nonaugmented ASST (dry) turbojet		ASST/ duct-burning turbofan	
	CF6, JT9D, RB211	Olympus 593, NK-144	JT3D, JT8D	1*	2*	1	2	1	2
Oxides of nitrogen (as NO_2)	16	18	6-8	8	3	14	3	12	3
Carbon monoxide (CO)	4	3.5	4	3	3	3	3	30	15
Total hydrocarbons (as CH_2)	0.1	0.2	0.1	0.5	0.1	0.5	0.1	10	3
Soot (C)	0.1	0.1	0.1	0.02	0.02	0.02	0.02	0.02	0.02

*1 Anticipated emission-reduction technology.

*2 Advanced emission-reduction technology.

Technology" engines would be characteristic of existing production engines manufactured prior to 1979 that would continue to be in service during 1980 to 1985. These engines would not be required to meet the proposed 1979 EPA emission limits, since this regulation would apply only to engines either manufactured or certified after 1978.

Two emission estimates are shown for both CTOL and ASST aircraft engines representative of either retrofitted engines or advanced engines entering service after 1978. The first estimate, designated as "Anticipated Emission-Reduction Technology", assumes that the low-NO_x combustor technology generated to meet the proposed 1979 EPA emission standards covering the landing-takeoff cycle for CTOL aircraft could be applicable to the reduction of emissions during cruise for both CTOL and ASST. It is understood that this estimate assumes that the NO_x reduction will be obtained by means of combustor redesign. The NO_x emission index for the ASST engine should generally be higher during supersonic cruise than at takeoff because combustor inlet temperature increases with increasing cruise Mach number to a level exceeding the inlet temperature at takeoff conditions. Expected emission standards for the landing-takeoff cycle for commercial supersonic aircraft would require a NO_x limit at takeoff but not at cruise. "Anticipated Emission-Reduction Technology" implies that technology will be evolved to reduce NO_x emissions for the ASST engine during supersonic cruise as well as at takeoff. If cruise emission standards were not established, and if water injection should be required to obtain a portion of the required NO_x reduction during takeoff, then the projected emission index for NO_x would be expected to approach a level somewhere between the value shown for "Anticipated Emission-Reduction Technology" and the value indicated for "Current Technology" engines. The second estimate, designated as "Advanced Emission-Reduction Technology", is a more optimistic projection, and is based on the evolution of a more advanced technology, such as a premixing/prevaporizing combustor, which might achieve even lower NO_x emission levels.

The NO_x emission indices shown for the two ASST engines, based on anticipated emission-reduction technology, are not much lower than the value shown for the current Olympus 593 (Concorde) or NK-144 (Tupolev TU-144) engines. This lack of substantial reduction is attributed to the expectation that future ASST aircraft will cruise at higher flight speeds than the current models. Combustor inlet temperature may be higher at the higher flight speeds; therefore, the NO_x formation rate will tend to be greater. The projected NO_x emission index for both the nonaugmented and augmented ASST, based on advanced technology, assumes that the required turbine inlet temperature will be less than about 1750 K. For advanced-technology SST engines requiring turbine inlet temperatures greater than about 1750 K, the estimated NO_x emission index might be as high as 6 for the dry turbojet and as high as 5 for the duct-burning turbofan.

The projected emission index for carbon monoxide for both CTOL and the nonaugmented SST are somewhat higher than the lowest levels that might be achieved because of the assumption that efforts to reduce NO_x by means of both fuel-lean combustion and reduced dwell time may result in increased carbon monoxide levels. The CO emission index based on advanced technology could be reduced to as low as 0.5 if allowances were made for a somewhat higher NO_x level; however, one engine manufacturer stated that a CO emission index of 1 could be attainable for a corresponding NO_x emission index of 3 using advanced technology.

The projected emission index for total hydrocarbons, based on anticipated emission-reduction technology, is as great as about five times current values to allow for the expected tradeoff necessary to obtain reduced NO_x; however, two manufacturers believe that this value could be reduced to about 0.1. The estimated emission index for soot is based on the accumulated mass of all particles in the exhaust that are greater than about 0.1 micron.

The Ad Hoc Committee study considered two categories of emission-reduction technology, "Anticipated" and "Advanced"; the NASA study considered two categories of emission-reduction technology, Class 1 (minor combustor modification) and Class 2 (major combustor redesign), in addition to a theoretical minimum based on chemical-kinetics calculations for a completely

premixing/prevaporizing combustor. NO_x emissions predicted for the NASA "Class 2" (major combustor redesign) fall within the range of the consensus predictions designated as "anticipated" and "advanced" emission-reduction technology. The NASA emission-index predictions for total hydrocarbons are in good agreement with the consensus predictions, and those for carbon monoxide are somewhat below the consensus predictions. The consensus study did not consider a category comparable to the NASA "Class 1" (minor combustor modification) because it was felt that minor combustor modification would not be sufficient to meet proposed clean-air standards. Also, the consensus forecast did not include predictions of theoretical minimum emission levels, since they were not within the scope of the Ad Hoc Committee study of practicably achievable emission-reduction technology.

CONCLUDING REMARKS

Forecasts were made in this study by predicting technological advances in reducing exhaust emissions of future commercial aircraft operating at high-altitude cruise conditions. Emission characteristics were determined for future jet engines that were selected for both subsonic and supersonic missions on the basis of minimization of the aircraft take-off gross weight for a given payload and range and at a specified noise constraint. High-bypass turbofan engines were specified for an advanced subsonic aircraft, and duct-burning turbofan or dry turbojet engines were specified for an advanced supersonic aircraft.

It is anticipated that improved versions of many present-day aircraft will continue to be in service up to at least 1990, and advanced engines utilizing low-NO_x combustor technology could be incorporated into the design of these aircraft between 1980 and 1985. Advanced subsonic and supersonic aircraft could become operational in the early 1990's. It appears quite probable that JP-type fuels will remain the main energy source for commercial jet aircraft until at least the late 1990's.

Minor combustor modifications implemented by technological advances made within the next 4 to 7 years could reduce the NO_x emission index by approximately 30%. However, greater reductions will be needed in order to meet proposed clean-air standards. It is anticipated that major combustor redesigns to reduce NO_x emission indices by as much as 75% below those of current production engines might require 7 to 10 years for development and engine certification. Minimum emission limits determined from chemical-kinetics calculations for a combustor burning premixed/prevaporized fuel predict that even lower NO_x emission levels are theoretically possible. This theoretical minimum actually represents a goal to be approached in practical combustor design.

REFERENCES

Anderson, David N. (1973), "Effect of Premixing on Nitric Oxide Formation." NASA Technical Memorandum X-68220.

Beheim, Milton A., Robert L. Cummings, James F. Dugan, Jr., Charles E. Feiler, Jack S. Grobman, and Warner L. Stewart (1970), "Subsonic and supersonic propulsion," in "Vehicle Technology for Civil Aviation: The Seventies and Beyond," NASA SP-292, 107-156.

Bittker, David A. and Vincent J. Scullin (1972), "General Chemical Kinetics Computer Program for Static and Flow Reactions with Application to Combustion and Shock Tube Kinetics," NASA Technical Note D-6586.

Boccio, J.L., G. Weilerstein, and R.B. Edelman (1973), "A Mathematical Model for Jet Engine Combustor Pollutant Emissions," General Applied Science Labs GASL-TR-781 (NASA CR-121208).

Bogdan, Leonard and H.T. McAdams (1971), "Analysis of Aircraft Exhaust Emission Measurements," Cornell Aeronautical Lab. Inc. CAL-NA-5007-K-1, SPTD-0851 (PB-204879).

Branstetter, J. Robert, Albert J. Juhasz, and Peter W. Verbulecz (1971), "Experimental Performance and Combustion Stability of a Full Scale Duct Burner for a Supersonic Turbofan Engine," NASA Technical Note D-6163.

Brines, G.L. (1971), "Recommended Guidelines for Limiting Trace Element Emission," prepared by Pratt & Whitney for NASA Contract NAS-3-15550.

Broderick, A.J., J.M. English, and A.K. Forney (1973), "An initial estimate of aircraft emissions in the stratosphere in 1990," AIAA Paper No. 73-508.

Clements, T.R. (1973), "Effect of Fuel Zoning and Fuel Nozzle Design on Pollution Emissions at Ground Idle Conditions for a Double-Annular Ram-Induction Combustor," Pratt & Whitney Aircraft, Research & Development Center, FR-5295 (NASA CR-121094).

Edelman, Raymond and Constantino Exonomos (1971), "A mathematical model for jet engine combustor pollutant emissions," AIAA Paper 71-714.

"EPA Aircraft Emission Standards for Control of Air Pollution" (1973), *Federal Register*, Vol. 38, No. 136, Part 2, July 17, 19087-19103.

Forney, A.K. (1973), "Engine Exhaust Emissions Subprogram," in *Proceedings of the Second Conference on the Climatic Impact Assessment Program* (November 14-17, 1972), ed. A.J. Broderick, U.S. Department of Transportation, DOT-TSC-OST-73-4.

Gordon, Sanford and Bonnie J. McBride (1971), "Computer Program for Calculation of Complex Chemical Equilibrium Compositions, Rocket Performance, Incident and Reflected Shocks, and Chapman-Jouquet Detonations," NASA SP-273.

Grobecker, Alan J. (1973), "Chairman's address," in *Proceedings of the Second Conference on the Climatic Impact Assessment Program* (November 14-17, 1972), ed. A.J. Broderick, U.S. Department of Transportation, DOT-TSC-OST-73-4.

Grobman, Jack and Robert D. Ingebo (1974), "Jet Engine Exhaust Emissions of High Altitude Commercial Aircraft Projected to 1990," proposed NASA Technical Memorandum.

Homer, J.B. and M.M. Sutton (1973), "Nitric oxide formation and radical overshoot in premixed hydrogen flames," Comb. and Flame **20**(1), 71-76.

Ingebo, Robert D. and Carl T. Norgren (1973), "High Pressure Combustor Exhaust Emissions with Improved Air-Atomizing Fuel Nozzles," NASA Technical Note D-7154.

Jones, Robert E. (1973), "Advanced Technology for Reducing Aircraft Engine Pollution," NASA Technical Memorandum X-68256.

Jones, Robert E. and Jack Grobman (1973), "Design and Evaluation of Combustors for Reducing Aircraft Engine Pollution," NASA Technical Memorandum X-68192.

Kraft, G.A. (1972), "Optimization of Engines for a Commercial Mach 0.85 Transport Using Advanced Turbine Cooling Methods," NASA Technical Memorandum 68173.

Marchionna, Nicholas R., Larry A. Diehl, and Arthur M. Trout (1973), "Effect of Inlet-Air Humidity, Temperature, Pressure, and Reference Mach Number on the Formation of Oxides of Nitrogen in a Gas Turbine Combustor," NASA Technical Note D-7396.

Niedzwiecki, Richard W. and Robert E. Jones (1973), "Parametric Test Results of a Swirl-Can Combustor," NASA Technical Memorandum X-68247.

Norgren, Carl T. and Robert D. Ingebo (1973), "Effects of Prevaporized Fuel on Exhaust Emissions of an Experimental Gas Turbine Combustor," NASA Technical Memorandum X-68194.

Rudey, Richard A. (1972), "Aircraft Engine Pollution Reduction," NASA Technical Memorandum X-68129.

Wear, Jerrold D., Porter J. Perkins, and Donald F. Schultz (1970), "Tests of a Full-Scale Annular Ram-Induction Combustor for a Mach 3 Cruise Turbojet Engine," NASA Technical Note D-6041.

Whitlow, John B., Jr., Richard J. Weber, and Kestutis C. Civinskas (1973), "Preliminary Appraisal of Hydrogen and Methane Fuel in a Mach 2.7 Supersonic Transport," NASA Technical Memorandum X-68222.

Williams, M.R. (1973), "Emission levels of the Olympus 593 engine at the supersonic cruise conditions of the Concorde aircraft," in *Proceedings of the Second Conference on the Climatic Impact Assessment Program* (November 14-17, 1972), ed. A.J. Broderick, U.S. Department of Transportation, DOT-TSC-OST-73-4.

DISCUSSION

STEWART: Please explain why the NO_x emission-index reductions projected by Dr. Grobecker in his presentation are, in general, much greater than those projected in yours.

GROBMAN: Two sets of engine exhaust-emission predictions were included in my presentation. The first was based on an independent NASA study, and the second on the consensus of an ad-hoc committee composed of industry, university, and government representatives. Each study considered several categories of advanced combustor technology that might be used to attain varying degrees of NO_x emission reductions. These projections represent an engineering judgment of the technology that is practicably achievable within the next two decades, on the basis of the present status of emission-reduction technology and the technical effort that would be required to translate this experimental technology into production technology that fulfills the safety, reliability, and economic requirements of a commercial aircraft.

GROBECKER: My number might be considered an upper limit to possible improvements. It is based on simplistic physics, rather than estimates by manufacturers who actually have to deliver a product. I suspect the truth lies somewhere between the optimistic figures I quoted, and the conservative ones of the manufacturers.

PARTICLES IN HIGH-ALTITUDE AIRCRAFT EXHAUST

ANTHONY J. BRODERICK
DOT Transportation Systems Center
Cambridge, Massachusetts

INTRODUCTION

We have made measurements in an altitude-simulation test cell on an afterburning turbojet engine to determine the nature and size distribution of particulate emissions under supersonic cruise conditions. The engine employed in these tests was a YJ93-GE-3 model, which was used in the XB-70 and is the chronological and technological forerunner of the GE-4 engine planned for use in the B-2707 SST. The tests were conducted by personnel from ARO, Inc., who operate the Engine Test Facility at the USAF Arnold Engineering Development Center near Tullahoma, Tennessee. Figure 1 shows schematically the engine installation in Test Cell J-2 at AEDC. A water-cooled sampling probe was placed just behind the exit plane of the exhaust nozzle, as shown in Figure 2.

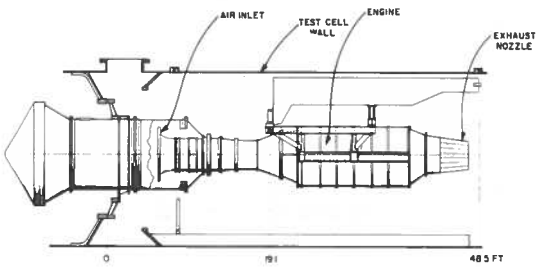

Figure 1. Schematic of installation of YJ93-GE-3 engine in J-2 test cell.

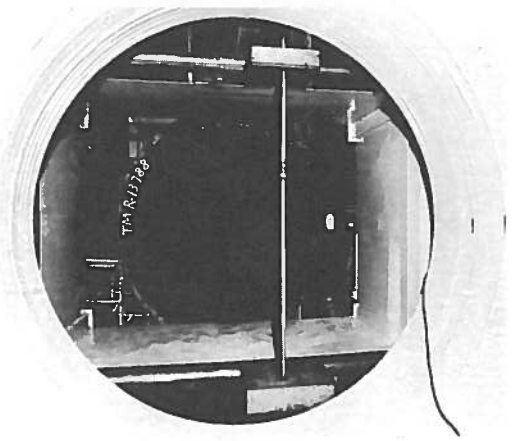

Figure 2. Sample probe, mounted on vertical support, viewed looking upstream into J93 afterburner.

INSTRUMENT

The instrumentation used for these measurements was a point-to-plane electrostatic precipitator assembled at the Transportation Systems Center. It is a modified version of the unit reported by Billings and Silverman (1962), and is fully described in Broderick et al. (1974). As-yet-unpublished results of one calibration of this device show it to be uniform in relative collection efficiency over the size range of interest by comparison to a thermal precipitator. Figure 3 shows an interior view of the assembled system. It formed a small part of the exhaust-emission measurement system described by Neely and Davidson (1973).

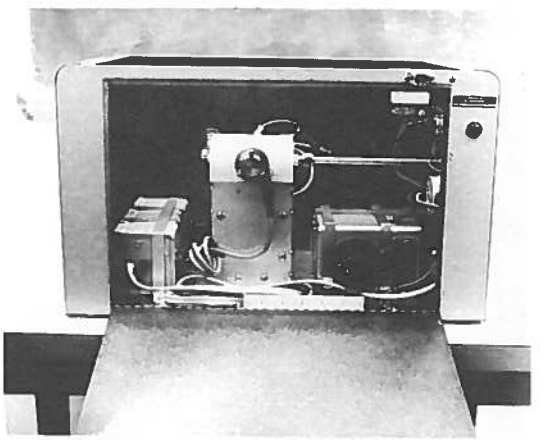

Figure 3. TSC aerosol sampler.

RESULTS

Figure 4 presents typical electron micrographs obtained in the course of our analysis. It can readily be seen that the vast majority of this unaged aerosol consists of carbon particulates much smaller than one micron in diameter. Figure 4a shows two common artifacts encountered in the analysis: the filmy one is a part of the substrate which drifted loose and resettled during either sample collection or examination; the large agglomerate is probably a piece of carbon from the sampling-line wall. Figure 4b is one of our most successful attempts to graphically portray the manner in which the particulates seem to be "built up" from small carbon spheres on the order of 50 A or so in diameter. (This side view was obtained by momentarily overheating and curling the collection substrate in the microscope's electron beam.)

a. ×6000.

b. ×36,000.

Figure 4. Samples taken at military power, Mach 2, 55,000 ft., 20 inches below exhaust centerline.

A summary of the data we analyzed is shown in Figure 5. All of these data were taken with the engine operating at military power (maximum non-afterburning thrust), at the simulated altitudes and flight speeds indicated. Note that the particle size is defined as the diameter of an equal-area circle. The data point corresponding to the largest diameter includes all particles larger than that size; that corresponding to the smallest diameter includes all smaller particles observable (down to a few A in diameter). There is a large variance in median particle size, depending on the specific engine operating parameters, from about 400 A to well below 100 A. The solid line shows the unweighted average of all the samples and indicates that a typical median particle is only just over 100 A in diameter. It is important to stress that, due to the small sample size, we do not at this time ascribe any relevance to the relationships indicated between engine operating conditions and particle size distribution. The within-sample variance of these data is on the order of the variance between samples.

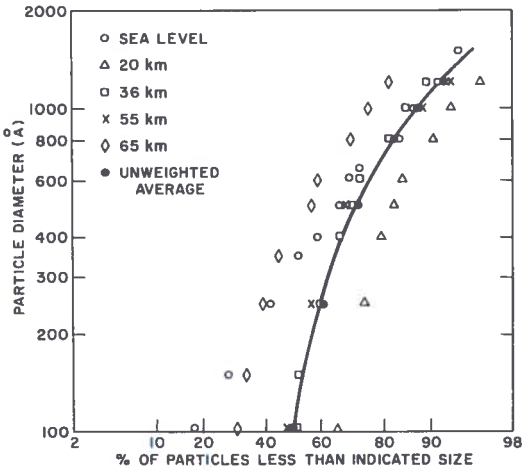

Figure 5. Summary of size distributions obtained at several simulated altitudes.

DISCUSSION

As an academic exercise more than anything else, we replotted the same data as shown in Figure 6. Here

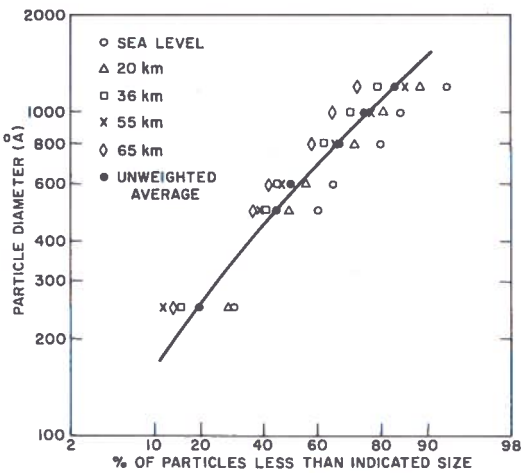

Figure 6. The distributions of Figure 5, replotted without the smaller particles.

we have eliminated all particles in the smallest size category (<100 Å). Obviously the indicated median size of our new distribution is substantially larger, varying between 400 and 700 Å, with the unweighted average median diameter being about 600 Å. These contrasting figures are presented here because it seems to me that too many workers in this field fail to acknowledge the dependence of the results of particle-size determination on the analysis techniques employed. Figure 7 shows how this can be misleading. The dots represent a size distribution reported by Palcza (1972); the crosses represent a size distribution obtained by us under very similar engine operating conditions; the dashed line represents a theoretical curve based on considerations of plume visibility as reported by Stockham and Betz (1971). There is reasonably good agreement between the theoretical curve and Palcza's results, and neither agrees very well with our data. The open circles, however, represent a replotting of our data with no account taken of particles below the range reported by Palcza. In other words, this last curve simulates the results we would have obtained had we been limited by the resolution of a scanning electron microscope, as was the case with Palcza. Thus, despite the good agreement between the two "resolution-limited" sets of data and the theoretical prediction of Stockham and Betz, I submit that these data are systematically biased, and their resulting reported median size is larger than it is in actuality.

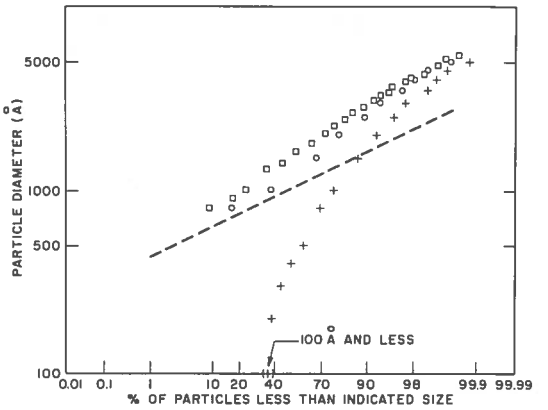

Figure 7. Comparison of results obtained by different techniques. □: 36,000 ft, military power, Mach 1.4, TF30 engine. +: 35,000 ft, military power, Mach 1.3, YJ93 engine. ○: 35,000 ft, military power, Mach 1.3, YJ93 engine, no particles below 800 Å. – – –: theoretical curve for J57 engine, military power, sea-level static.

ACKNOWLEDGMENT

This work was supported by the Office of the Assistant Secretary of Transportation for Systems Development and Technology as part of the Climatic Impact Assessment Program. Special thanks are due to Maurice Dumais and James Morris of the Transportation Systems Center, and to the employees of ARO, Inc. and AEDC who cooperated in the performance of these tests.

REFERENCES

Billings, C., and L. Silverman (1962), "Aerosol sampling for electron microscopy," J. Air Pollut. Cont. Assoc. **12**, 586.

Broderick, Anthony J., Michael J. Scotto, and Joseph C. Sturm (1974), "Particulates in jet aircraft exhaust: instrumentation and initial results," in *Recent Advances in Air Pollution Control*, AICHE Symposium Series, Vol. 70 (137), 287-293.

Neely, James and Donald L. Davidson (1973), "Emission level of the YJ93-GE-3 engine, an SST-like engine," in *Proceedings of the Second Conference on the Climatic Impact Assessment Program* (Nov. 14-17, 1972), ed. A.J. Broderick, US Dept. of Transportation DOT-TSC-OST-73-4.

Palcza, J. Lawrence (1971), "Study of Altitude and Mach Number Effects on Exhaust Gas Emissions of an Afterburning Turbofan Engine," Federal Aviation Administration Report FAA-RD-72-31.

Stockham, John and Howard Betz (1971), "Study of Visible Exhaust Smoke from Aircraft Jet Engines," Federal Aviation Administration Report FAA-RD-71-22.

DISTRIBUTION OF EMISSIONS IN THE STRATOSPHERE FROM PRESENT AND FUTURE HIGH-ALTITUDE AIRCRAFT

J.F. LEACH, M.S. MORRIS, AND P. WARDMAN
Commercial Aircraft Division
British Aircraft Corporation Ltd.
Filton, Bristol, England

ABSTRACT: From previously published assessments of existing scheduled, non-scheduled, and cargo air traffic, and forecasts for the growth of these quantities, estimates have been made of the fuel burned and oxides of nitrogen emitted by high-altitude aircraft.

The estimates have used an assumed distribution of aircraft by flight level and a previously forecast increase in average cruise altitude to predict distributions of fuel burned and oxides of nitrogen emitted by latitude and altitude for the years 1980 and 1990.

INTRODUCTION

Attention has been drawn to the meteorological aspects of aircraft engine emissions in the stratosphere by the reports of SCEP (1970) and SMIC (1971); subsequent studies by Beckwith (1972), Jocelyn et al. (1973), and Levine (1973) have considered the problems suggested and made the first calculations to quantify the chemical species involved. Papers by English (1974) and by Grobman and Ingebo (1974) at this conference take the studies a stage further.

In this paper we have sought to extend the earlier work in order to show the distribution of the engine emissions with both altitude and latitude, so that modelers may have an input of emission data for their computer programs.

While some small improvements in data have been achieved since earlier papers, notably in measurements of emission index of oxides of nitrogen, it must be admitted that we still have considerable reservations regarding the quantitative conclusions, particularly with respect to the military and Russian engine emissions. The continuing problems of oil supply present a further factor of uncertainty.

TRAFFIC AREAS CONSIDERED

U.S. Domestic

Since only medium-to-long-range aircraft reach the tropopause for a significant proportion of their flights, we have assumed a minimum flight length of 800 km for the routes considered in this survey.

Approximately 1000 routes were analyzed from ABC World Airways Guide (1973), covering North America from 50°N (so as to include the populated areas of Canada) down to 35°N (where the height of the tropopause makes subsonic stratospheric flight unlikely). The area was subdivided into two latitude bands, 35° - 40°N and 40° - 50°N.

Although there are many types of aircraft in service, in order to simplify calculations, they were reduced to four basic categories, depending on type of engine.

Boeing 727/Douglas DC9 (JT 8D)
Boeing 707/Douglas DC8 (JT 3D)
Boeing 747 (JT 9D)
Lockheed 1011/Douglas DC10 (RB 211/CF6)

(Propeller-driven aircraft now represent a negligible proportion of the overall medium-to-long-range aircraft movements.)

The actual cruise altitudes of the different types of aircraft depend on many variables, so only an approximate cruise-altitude distribution may be estimated. The distribution used in this paper was based on a North Atlantic jet-traffic survey made by National Air Traffic Control Services (1968), but modified after Beckwith (1972) to make allowance for the different operational requirements of US domestic traffic. Figure 1 shows the assumed distribution of aircraft type with flight level; the original (Wardman, 1973) ATC distribution will be shown in Table 1 further on.

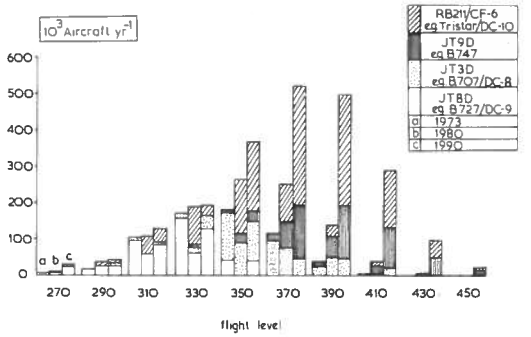

Figure 1. Assumed distribution of aircraft type with flight level for 1973, as derived from Table 1 and modified after Beckwith (1972), for the years 1980 and 1990.

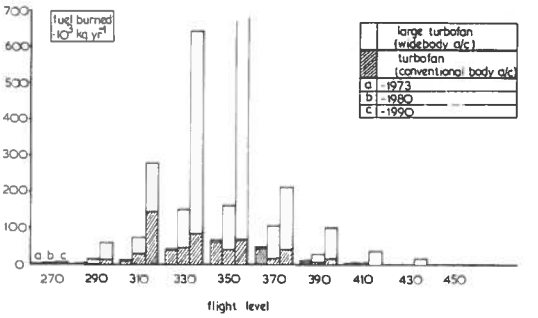

Figure 2. Distribution of fuel burned by flight level for US domestic civil subsonic traffic for the years 1973, 1980 and 1990, for latitudes 35° to 40°N and 40° to 50°N.

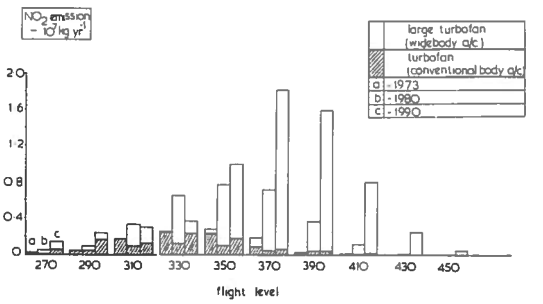

Figure 3. Distribution of NO_x emitted by flight level for US domestic civil subsonic traffic for the years 1973, 1980 and 1990, for latitudes 35° to 40°N and 40° to 50°N.

The gradual increase of average cruise altitude, due to traffic density at lower altitudes and the need to conserve fuel (predicted by Chandler and Davis (1972) and assumed by Jocelyn et al. (1973) to be a 0.6 km increase by 1980 and 1.6 km by 1990), was applied to our estimated traffic distributions for the years 1980 and 1990.

Lockheed (1972) reports an expected growth in world scheduled passenger traffic of 10.6% per year for the period 1970-1980, from 38×10^{10} passenger-km in 1970 to 105×10^{10} in 1980. While in 1970 the US domestic scheduled traffic represented 44% of the ICAO world scheduled traffic (excluding the USSR), by 1980 this figure will have fallen to 39%. Non-scheduled traffic, on the other hand, is expected to show a significant rise, from 24% of US domestic scheduled traffic in 1970 to 40% by 1980.

If we assume load factors for scheduled services to be 60% of those for the non-scheduled, we can expect that unscheduled traffic on an aircraft-movement basis will increase from 14.3% of US domestic scheduled traffic in 1970 to 23.6% in 1980.

Ray and Ray (1972, 1973) show that cargo traffic in the period 1972-73 was 2% of total scheduled traffic, while in the papers by Ciesla (1973) the Civil Aviation Authority forecasts a world cargo-traffic increase of 19.6% for 1970-80. If we assume a similar figure for the USA we can expect the US domestic cargo traffic to be 7% of US domestic scheduled traffic by 1980 and perhaps 11.5% by 1990.

The resulting distributions of fuel burned and NO_x emitted by flight level are shown in Figures 2 and 3 respectively. Since it appeared that the distributions for each of the two latitude bands chosen were the same, these two bands are conveniently shown on the same figure. Aircraft of categories A and B are grouped together for simplicity, as are those of C and D.

Europe

Levine (1973) has drawn attention to the need to consider European aircraft fuel burnup in the stratosphere; consequently, a survey similar to that made for US domestic traffic was carried out for the traffic of European airlines, excluding the USSR.

Estimates were made for 1980 and 1990 on the basis of 11.5% growth in passenger-km predicted by McDonnell-Douglas (1972) for scheduled traffic. In the period up to 1980, non-scheduled passenger-km should be increasing at 16.5% per year according to Douglas, and cargo traffic by 20% per year according to Ciesla (1973).

Aircraft were put into categories similar to those of US domestic traffic, and the numbers of

aircraft of each type at each flight level were assessed for latitude bands 40° - 50°N and 50° - 60°N. Figures 4 through 7 give the distribution of fuel burned and NO_x emitted for the various flight levels in the two latitude bands.

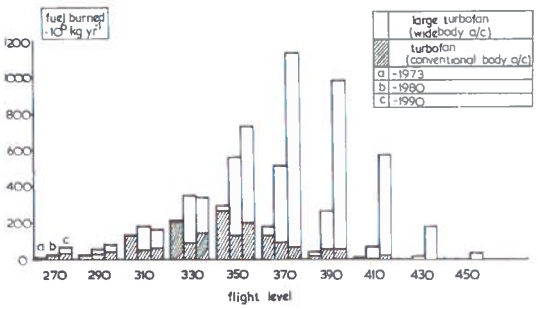

Figure 4. Distribution of fuel burned by flight level for European civil subsonic traffic for the years 1973, 1980 and 1990, for the latitude band 40° to 50°N.

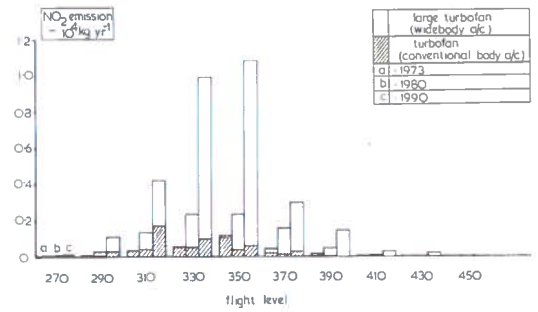

Figure 5. Distribution of NO_x emitted by flight level for European civil subsonic traffic for the years 1973, 1980 and 1990, for the latitude band 40° to 50°N.

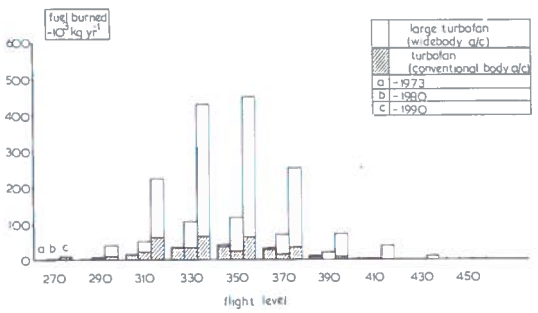

Figure 6. Distribution of fuel burned by flight level for European civil subsonic traffic for the years 1973, 1980 and 1990, for the latitude band 50° to 60°N.

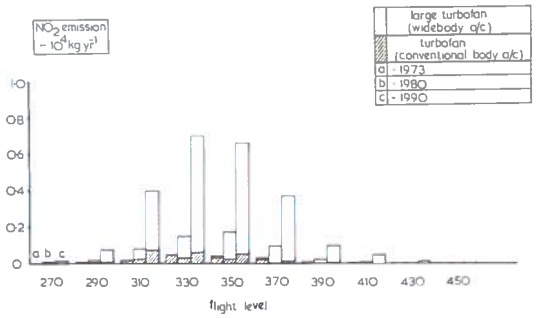

Figure 7. Distribution of NO_x emitted by flight level for European civil subsonic traffic for the years 1973, 1980 and 1990, for the latitude band 50° to 60°N.

Soviet Russia

Of all the areas of aircraft operation considered (except perhaps military operations) this is probably the most uncertain, not only from the point of view of estimating future growth but also from that of obtaining reliable information on present traffic levels and engine emissions.

The ABC World Airways Guide (1973) was used to assess the scope of Aeroflot services and their distribution within the USSR, but of course this is not necessarily accurate, since Aeroflot does not operate by the same rules as Western airlines. The breakdown of types of aircraft was similar to that used for US aircraft, except that turboprop aircraft were included to allow for flights at high latitudes where the tropopause is very low.

It may not be unreasonable to assume that, for the purposes of this paper, the USSR passenger-km growth in 1970 to 1980 corresponds to US growth for the period 1960-70 at 14% per year (from Lockheed (1972)).

Cargo traffic is assumed to be 2% of scheduled traffic and to have a growth similar to that of Western nations, about 20% per annum up to and including 1990, but it is also assumed that there will be no non-scheduled traffic of any description.

In the period 1980-90 it is likely that, as with Western airlines when wide-bodied aircraft are extensively used, there will be some slowing down of traffic on an aircraft-movement basis, and the growth for this period will be approximately the same as Western traffic-growth predictions for 1970 to 1980, about 11% per year. Figures 8 through 11 give the distributions for the same conditions as for Europe.

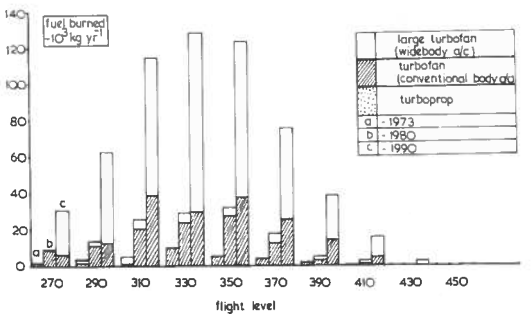

Figure 8. Distribution of fuel burned by flight level for USSR subsonic traffic for the years 1973, 1980 and 1990, for the latitude band 40° to 50°N.

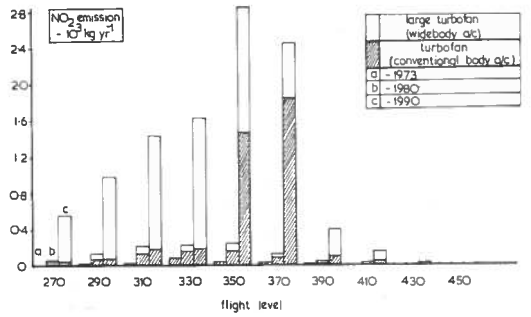

Figure 9. Distribution of NO_x emitted by flight level for USSR subsonic traffic for the years 1973, 1980 and 1990, for the latitude band 40° to 50°N.

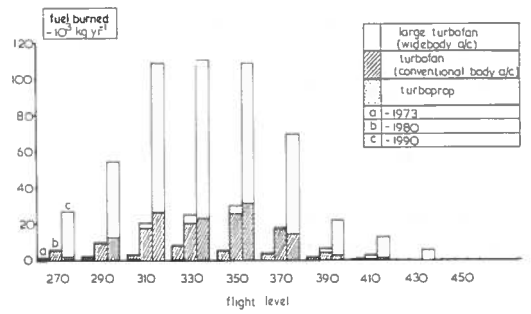

Figure 10. Distribution of fuel burned by flight level for USSR subsonic traffic for the years 1973, 1980 and 1990, for the latitude band 50° to 60°N.

North Atlantic

There are varying predictions for the annual total subsonic passenger growth rates in the period 1970-80 for this route, including McDonnell-Douglas (1972), 14%, Lockheed (1972), 12.4% and the U.K. Civil Aviation Authority (1972),

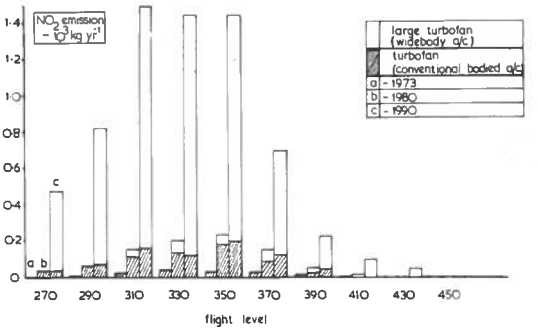

Figure 11. Distribution of NO_x emitted by flight level for USSR subsonic traffic for the years 1973, 1980 and 1990, for the latitude band 50° to 60°N.

18%. For the period 1971-75 Lockheed predicts 13%, and for 1971-76 Douglas predicts 12%.

Lockheed (1972) suggests that by 1980 the 1970 figure of 74% of total passengers carried by scheduled flights may have fallen to 62%.

Beckwith (1972) reports that the fuel burned per passenger-km is expected to drop from 0.12 kg in 1973 to 0.08 kg in 1980; hence, a 13% increase in numbers of passengers carried may correspond to a 9% growth in fuel burned.

With the above assumptions, a detailed study by Jocelyn et al. (1973), using as a basis the report by the National Air Traffic Control Services (1968) which provided a breakdown of aircraft cruise altitudes for one particular day in 1967 (see Table 1), concluded that the fuel burned in cruise above the tropopause on this route would increase by 9% per year for the period 1970-1990, and extended the study to calculate the quantities involved.

Table 1. Flight Levels in Use at 10° West, August 17, 1967

	Number of Aircraft			
Flight Level	East	West	Total	%
280	–	5	5	1.58
290	8	1	9	2.84
310	14	38	52	16.40
330	58	30	88	27.76
350	24	70	94	29.65
370	42	14	56	17.67
390	11	1	12	3.78
410	1	–	1	0.32
TOTAL	158	159	317	100.00

Wardman (1973), in an unpublished paper presented at the COVOS/COMESA seminar in Paris, used this survey to break down this calculated quantity of fuel burned by altitude and latitude; his estimates, shown in Figure 12 for 1980 and 1990, are utilized in this paper.

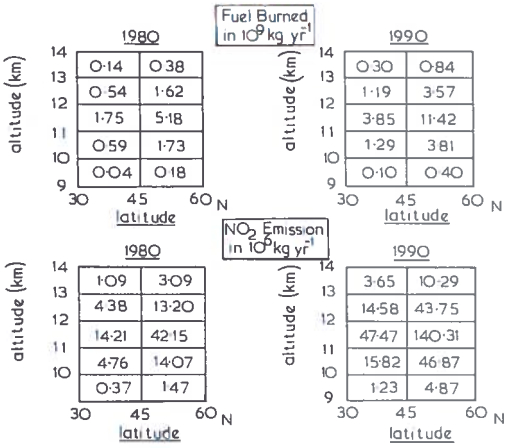

Figure 12. Estimated emission of NO_x as a function of altitude and latitude for the years 1980 and 1990 due to civil subsonic traffic on North Atlantic route as calculated by Wardman (1973).

Polar Route

The polar-route group covers flights from Europe and North America to the Far East via the North Pole. Considerations of engines and aircraft in service, and growth in traffic from 1970 on, were similar to those for the North Atlantic route, but it was assumed that the whole flight would be made above the tropopause, and an annual fuel-burnup growth rate of 10% was used. Figure 13 gives the predicted distribution of NO_x and fuel burnup for this route.

Military Operations

From the survey made by the Institute of Strategic Studies (1970), Yaffee (1972) quotes the US Department of Defense estimate of total US military fuel burnup as 1.3×10^{10} kg per year. Jocelyn et al. (1973) concluded that 15% of this fuel would be burned above the tropopause and, given the current oil-supply position, it is assumed that the world-wide consumption of oil for military purposes will remain constant during 1970-1990.

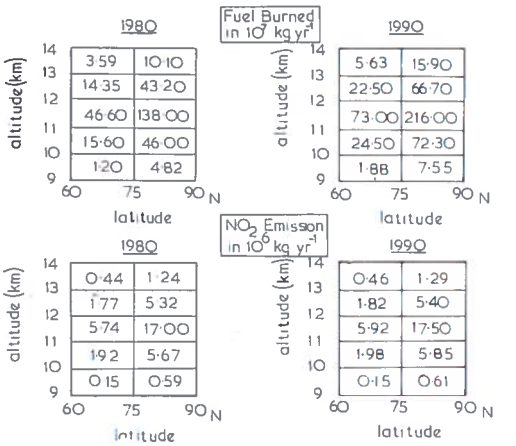

Figure 13. Distribution of fuel burnup and NO_x emitted for civil subsonic traffic on Polar route for the years 1980 and 1990.

In the absence of any helpful data, it is assumed that the military-aircraft activity for the USSR is some 50% of that of the USA, and that for Europe it is 25% of the US figure.

Since the quantities involved are not large compared with those of civil operations, the estimates would have to be in error by an order of magnitude to produce a significant inaccuracy in the 1990 values.

The traffic of the three military blocs was subdivided into the main areas of activity of the civil aircraft: i.e., the US military was assumed to operate over the USA, the North Pole, and the North Atlantic; the European military over Europe, the North Pole, and the North Atlantic; and the Russian military over the USSR and the polar regions.

The fuel burned by each bloc in each of these areas was assumed to be in proportion to that nation's civil activity in the region, except for the USSR, where the US proportions of domestic and polar activity was used. The calculated amounts were added to the relevant civil fuel burnup in each area for the final analysis, but they are not shown on the separate area distributions. The calculated amounts of fuel burned and NO_x emitted are shown in Tables 2 and 3 respectively.

Supersonic Transport Operations

Operations of these aircraft were analyzed extensively in the paper by Jocelyn et al. (1973);

Table 2. Total Military Fuel Burnup at Cruise Above 8 km (in 10^9 kg yr^{-1})

Area	1970	1973	1980	1990
United States	0.34	0.26	0.25	0.17
North Atlantic	1.24	1.47	1.54	1.78
Polar	1.46	1.32	1.21	1.06
Europe	0.16	0.11	0.14	0.17
USSR	0.36	0.34	0.37	0.32
TOTAL	3.50	3.50	3.50	3.50

Table 3. Total Military NO_x Emission at Cruise Above 8 km (in 10^6 kg yr^{-1})

Area	1970	1973	1980	1990
United States	1.76	2.70	2.70	1.88
North Atlantic	1.27	1.46	2.22	1.91
Polar	1.41	1.36	1.73	1.18
Europe	1.52	1.12	2.14	1.51
USSR	0.27	0.23	0.28	0.28
TOTAL	6.23	6.84	9.07	6.76

this analysis was subsequently used by Wardman (1973) to produce a breakdown by altitude and latitude of worldwide SST operations. It is felt unnecessary to depart significantly from Wardman's figures, except for one modification: the emission index for NO_x for the second-generation SST will be reduced to 2.5 (see the section on estimating pollutants).

Figure 14 shows Wardman's assumed SST fleet and Figure 15 his assumed percentage burnup of fuel analyzed by latitude and altitude for 1980. (It is assumed that this distribution will hold for 1990.) Figures 16 and 17 give the analyzed NO_x emissions for 1980 and 1990 respectively.

Aircraft type	Aircraft in service			
	1975	1980	1985	1990
Concorde/ TU-144	10	150	245	300
2nd generation SST	0	0	20	75

Figure 14. Supersonic-transport fleet as assumed by Wardman (1973) and used in this paper.

GENERAL CONSIDERATIONS

One general consideration will almost certainly affect all aircraft during the next few

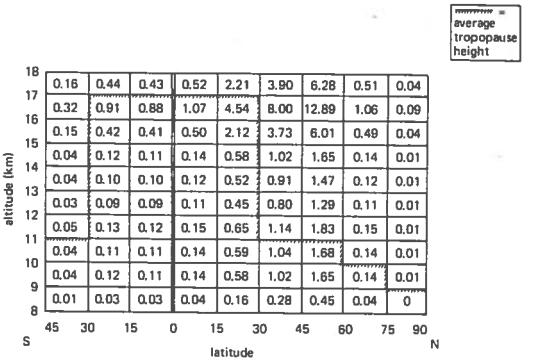

Figure 15. Percentage of fuel burned as a function of latitude and altitude for predicted fleet of first-generation supersonic-transport aircraft. It is assumed that this distribution holds for both 1980 and 1990. An arbitrary tropopause height is included to indicate proportions burned above and below tropopause.

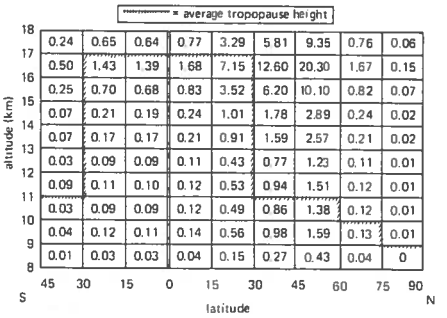

Figure 16. Predicted rate of NO_x emission by the possible 1980 supersonic transport fleet, as a function of latitude and altitude.

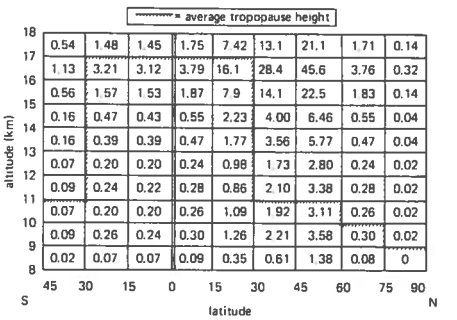

Figure 17. Predicted rate of NO_x emission by the possible 1990 supersonic transport fleet, as a function of latitude and altitude.

years, and that is the shortage of oil. It has been assumed in our calculations that this shortage will result in the elimination of the equivalent of two years' growth for both US and European airlines during the next five years, but thereafter

the growth should continue as estimated. However, this may be unduly pessimistic, since one European airline is reported to be still expecting 4% growth in 1974, whereas we have assumed at the most zero growth for this year. We have assumed that the USSR will not be affected by the oil shortages, although here we may have been optimistic.

ASSUMPTIONS USED IN ESTIMATING POLLUTANTS

Oxides of Nitrogen

At present it is commonly possible to obtain emission data for NO_x only for engines at sea-level conditions; consequently, many data for cruise conditions are extrapolations from the sea-level case.

However, recently measurements have been made in both the USA and the UK under simulated cruise conditions, both with and without the air dryers which show the effect of the ambient stratospheric humidity. Where available, these figures are now included; they tend to confirm the extrapolations of Scott (1973) and Williams (1973).

We assume from the AGARD Conference Proceedings (1973) that for engines built after 1985, technology will be available to reduce emission indices by an order of magnitude. Therefore, for the second-generation SST, which previously had a reputed NO_x emission index of 25 (which Wardman (1973) assumed could be improved to 12.5), we now assume an index of 2.5 (as NO).

Similarly, wide-bodied subsonic aircraft will also benefit from this latest technology; it should be possible to reduce their emission indices by an order of magnitude also, while still operating at the high combustor temperatures and pressures which otherwise would lead to high NO_x production.

Soviet power plants, however, remain largely a closed book to Western observers, and consequently little can be gleaned in the way of data on NO_x emissions. It must be assumed that if, as is supposed, their technology is 6-8 years behind Western technology, the emission index for NO_x for the present range of Russian engines must be similar to that of the fan engines in US aircraft of the middle 1960's.

The emission indices for NO_x used in this paper are shown in Figure 18.

SUBSONIC AIRCRAFT ENGINES				
flight levels	NO_x E.I. (g/kg fuel) as NO_2			
	JT3D	JT8D	JT9D	R211/Cr6
270	12 50	17 50	28 75	23 50
290	11 00	15 25	25 75	20 75
310	9 75	13 50	23 25	18 25
330	8 75	12 25	21 00	16 25
350	8 00	11 00	19 25	15 00
370	7 25	10 25	17 75	14 00
390	6 75	9 50	16 75	13 00
410	6 50	8 75	15 75	12 25
430	6 25	8 25	15 00	11 75
450	6 00	7 75	14 50	11 25

1st Generation SST (Olympus 593) **	
altitude km	Effective NO_x E.I. (g/kg fuel) as NO_2
8	11 0
9	11 0
10	9 4
11	9 4
12	11 0
13	20 0
14	20 0
15	19 0
16	18 0
17	17 0
18	

* Based upon Scott and Williams (1973), with re assessment of large turbofan emissions based upon unpublished data, Scott (1972)

** Wardman (1973)

Figure 18. Emission indices for NO_x used in this paper, for subsonic and supersonic engines as a function of altitude.

Water Vapor

In order to obtain the distribution of water vapor with altitude and latitude, it is only necessary to multiply the fuel burned by an appropriate factor. This factor is approximately 1.3, or an emission index of 1300.

Sulfur Dioxide

The SO_2 emission is also a direct function of the fuel burned, since the emission is due entirely to the sulfur content of the fuel; it may therefore also be calculated by means of an appropriate factor. Environmental pressure may well result in the reduction of the sulfur content of aviation kerosenes below the present average levels of about 0.05%, which give an emission index of 1.0. This pressure should accelerate the spread of hydrofining of fuel oils, leading to the production of kerosenes having an emission index on the order of 0.2 or a factor of the fuel burned of 0.02%.

OVERALL ESTIMATES OF POLLUTANTS

Figure 19 shows the final integrated fuel-burnup estimate from all sources for altitudes

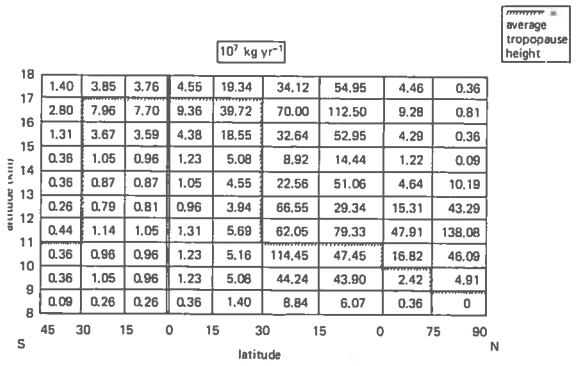

altitude (km)	45 S	30	15	0	15	30	15	0	75	90 N
18	1.40	3.85	3.76	4.55	19.34	34.12	54.95	4.46	0.36	
17	2.80	7.96	7.70	9.36	39.72	70.00	112.50	9.28	0.81	
16	1.31	3.67	3.59	4.38	18.55	32.64	52.95	4.29	0.36	
15	0.36	1.05	0.96	1.23	5.08	8.92	14.44	1.22	0.09	
14	0.36	0.87	0.87	1.05	4.55	22.56	51.06	4.64	10.19	
13	0.26	0.79	0.81	0.96	3.94	66.55	29.34	15.31	43.29	
12	0.44	1.14	1.05	1.31	5.69	62.05	79.33	47.91	138.08	
11	0.36	0.96	0.96	1.23	5.16	114.45	47.45	16.82	46.09	
10	0.36	1.05	0.96	1.23	5.08	44.24	43.90	2.42	4.91	
9	0.09	0.26	0.26	0.36	1.40	8.84	6.07	0.36	0	
8										

Figure 19. Overall integrated fuel burnup from all sources as a function of latitude and altitude for the year 1980. An arbitrary tropopause height is indicated.

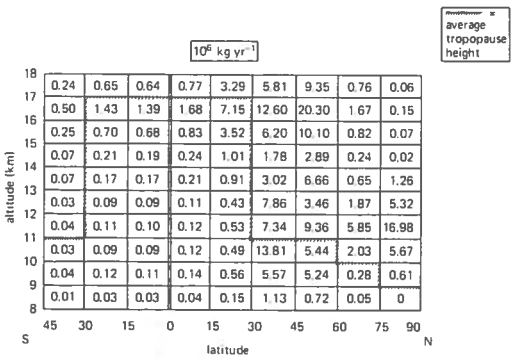

altitude (km)	45 S	30	15	0	15	30	45	60	75	90 N
18	0.24	0.65	0.64	0.77	3.29	5.81	9.35	0.76	0.06	
17	0.50	1.43	1.39	1.68	7.15	12.60	20.30	1.67	0.15	
16	0.25	0.70	0.68	0.83	3.52	6.20	10.10	0.82	0.07	
15	0.07	0.21	0.19	0.24	1.01	1.78	2.89	0.24	0.02	
14	0.07	0.17	0.17	0.21	0.91	3.02	6.66	0.65	1.26	
13	0.03	0.09	0.09	0.11	0.43	7.86	3.46	1.87	5.32	
12	0.04	0.11	0.10	0.12	0.53	7.34	9.36	5.85	16.98	
11	0.03	0.09	0.09	0.12	0.49	13.81	5.44	2.03	5.67	
10	0.04	0.12	0.11	0.14	0.56	5.57	5.24	0.28	0.61	
9	0.01	0.03	0.03	0.04	0.15	1.13	0.72	0.05	0	
8										

Figure 20. Overall integrated emission of NO_x from all sources as a function of latitude and altitude for the year 1980. An arbitrary tropopause height is indicated.

above 8 km, as a function of altitude and latitude, for 1980. Figure 20 shows the corresponding estimate for NO_x. Figures 21 and 22 show our comparable estimates for 1990.

In order to compare our estimates with those in other surveys, we note that the fuel burned above the tropopause is expected to rise from 8.3×10^9 kg yr^{-1} in 1973 to 45×10^9 kg yr^{-1} in 1990, while the NO_x (as NO_2) shows an increase from 7.2×10^7 kg yr^{-1} in 1973 to 72×10^7 kg yr^{-1} in 1990. The NO_x would be at an even higher level if it were not for our anticipated low emission characteristics of later larger turbofans and the second-generation SST engines from 1985 onwards.

It may be seen that these estimates are only slightly less than our previous estimates given in Jocelyn et al. (1973).

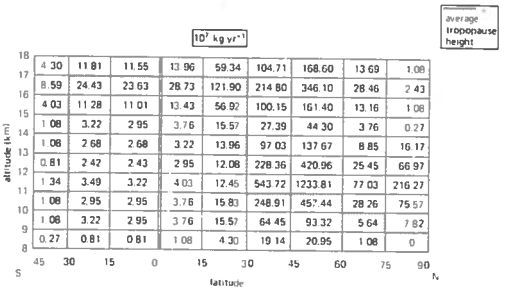

altitude (km)	45 S	30	15	0	15	30	45	60	75	90 N
18	4.30	11.81	11.55	13.96	59.34	104.71	168.60	13.69	1.08	
17	8.59	24.43	23.63	28.73	121.90	214.80	346.10	28.46	2.43	
16	4.03	11.28	11.01	13.43	56.92	100.15	161.40	13.16	1.08	
15	1.08	3.22	2.95	3.76	15.57	27.39	44.30	3.76	0.27	
14	1.08	2.68	2.68	3.22	13.96	97.03	137.67	8.85	16.17	
13	0.81	2.42	2.43	2.95	12.08	228.36	420.96	25.45	66.97	
12	1.34	3.49	3.22	4.03	12.45	543.72	1233.81	77.03	216.27	
11	1.08	2.95	2.95	3.76	15.83	248.91	457.44	28.26	75.57	
10	1.08	3.22	2.95	3.76	15.57	64.45	93.32	5.64	7.82	
9	0.27	0.81	0.81	1.08	4.30	19.14	20.95	1.08	0	
8										

Figure 21. Overall integrated fuel burnup from all sources as a function of latitude and altitude for the year 1990. An arbitrary tropopause height is indicated.

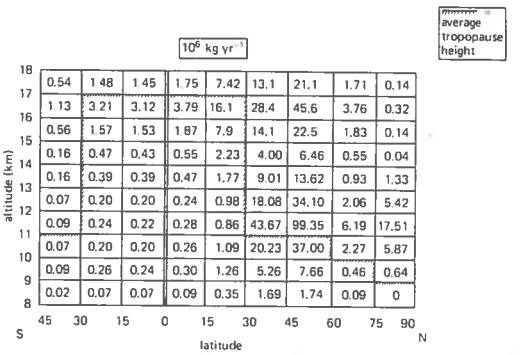

altitude (km)	45 S	30	15	0	15	30	45	60	75	90 N
18	0.54	1.48	1.45	1.75	7.42	13.1	21.1	1.71	0.14	
17	1.13	3.21	3.12	3.79	16.1	28.4	45.6	3.76	0.32	
16	0.56	1.57	1.53	1.87	7.9	14.1	22.5	1.83	0.14	
15	0.16	0.47	0.43	0.55	2.23	4.00	6.46	0.55	0.04	
14	0.16	0.39	0.39	0.47	1.77	9.01	13.62	0.93	1.33	
13	0.07	0.20	0.20	0.24	0.98	18.08	34.10	2.06	5.42	
12	0.09	0.24	0.22	0.28	0.86	43.67	99.35	6.19	17.51	
11	0.07	0.20	0.20	0.26	1.09	20.23	37.00	2.27	5.87	
10	0.09	0.26	0.24	0.30	1.26	5.26	7.66	0.46	0.64	
9	0.02	0.07	0.07	0.09	0.35	1.69	1.74	0.09	0	
8										

Figure 22. Overall integrated emission of NO_x from all sources as a function of latitude and altitude for the year 1990. An arbitrary tropopause height is indicated.

REFERENCES

ABC World Airways Guide (1973), ed. K. Vomhof, IPC Business Press, New York.

AGARD (1973), *Proceedings of the Conference on Atmospheric Pollution by Aircraft Engines*, CP 125.

eckwith, W.B. (1972), "Future patterns of aircraft operations and fuel burnouts, with remarks on contrail formation over the United States," in *Proceedings of the International Conference on Aerospace and Aeronautical Meteorology* (May 22-26, 1972, Washington, D.C.), American Meteorological Society, 422.

Chandler, C.L. and J.T. Davis (1972), "The case for high design cruise altitude for advanced transports," in *Proceedings of the International Conference on Aerospace and Aeronautical Meteorology* (May 22-26, 1972, Washington, D.C.), American Meteorological Society, 397.

Ciesla, E. (1973), "Air cargo in Comecom countries," Interavia **2**, 132, and Interavia **3**, 251.

Civil Aviation Authority (U.K.) (1972), "North Atlantic Traffic Forecasts, 1972 to 1976, Projected to 1981," CP 11.

English, J.M. (1974), "Air traffic predictions for 1990-2000," in this volume.

Grobman, J. and R.D. Ingebo (1974), "Forecast of jet-engine exhaust emissions for future high-altitude aircraft," in this volume.

Institute of Strategic Studies (1970), *Military Balance*, London.

Jocelyn, B.E., J.F. Leach, and P. Wardman (1973), "The effect of growth in stratospheric flight operations," Water, Air and Soil Pollution **2**, 141.

Levine, H.B. (1973), "Subsonic jet aircraft contribution to NO_x in the stratospheric ozone layer 1968/90," AIAA Paper No. 73-534 (Denver, June 1973).

Lockheed Aircraft Corp. (1972), "World air traffic summary," in Interavia Air Letter No. 7510 (Geneva).

McDonnell-Douglas (1972), "Douglas forecast traffic," Flight International **102** (3308), 146.

National Air Traffic Control Services (1968), "A Study of North Atlantic Jet Traffic, July and August 1967," Note No. 1/68 (NATCS, Board of Trade/ Ministry of Defence, London).

Ray and Ray (1972), "Airline traffic," Aviat. Wk. Space Tech. **97** (12), 35; **97** (20), 37; **97** (21); 51.

Ray and Ray (1973), "Airline traffic," Aviat. Wk. Space Tech. **98** (7), 36; **98** (11), 29; **99** (3), 36.

'SCEP' (1970), *Man's Impact on the Global Environment: Assessment and Recommendations for Action*. Report of the study of critical environmental problems (SCEP), MIT Press, Cambridge, Mass.

Scott, C.J. (1972), private communication.

Scott, C.J. and M.R. Williams (1973), "Stratospheric cruise emissions of nitrogen oxides from supersonic and subsonic transport aircraft – measurements and predictions," presented at the COVOS/ COMESA seminar, March 22-23, 1973, Paris.

'SMIC' (1971), *Inadvertent Climate Modification: Report of the Study of Man's Impact on Climate* (SMIC), MIT Press, Cambridge, Mass.

Wardman, P. (1973), "Chemical effects of emission in the stratosphere from present and future high-altitude aircraft," presented at the COVOS/ COMESA seminar, March 22-23, 1973, Paris.

Williams, M.R. (1973), "Emission levels of the Olympus 593 engine at the supersonic cruise conditions of the Concorde aircraft," in *Proceedings of the Second Conference on the Climatic Impact Assessment Program* (November 14-17, 1972), ed. A.J. Broderick, U.S. Department of Transportation, DOT-TSC-OST-73-4.

Yaffee, M.L. (1972), "DOD and airlines face energy crisis," Aviat. Wk. Space Tech. **97** (21), 54.

DISCUSSION

DOWNIE: You indicated quite a bit of travel at 41,000 and 43,000 feet. In the domestic U.S. there's almost nothing, except maybe military, at 43,000, and very little at 41,000.

LEACH: We are anticipating that cruise altitudes will be forced to rise as traffic at the present levels increases.

SCHAINKER: Could you and Professor English discuss the differences between your forecasting techniques, and summarize some of your different assumptions?

LEACH: Well, we simply used the growths projected in surveys by Douglas, Lockheed, and Boeing.

ENGLISH: All those forecasts were based principally on extrapolation of air-traffic trends, with little regard for economic factors, though Lockheed did look at willingness to pay a premium for speed. I looked at the most favorable conditions, having no guide in such questions as air-transportation demand elasticity, and came up with a scenario for 2025, and then said, "Now, how do we get there?" I used much the same approach for a projection in 1944, and it's worked out pretty well.

(UNIDENTIFIED): How much difference is there in your NO_x predictions for 1990?

ENGLISH: Ours is around 7000 tonnes a day.

LEACH: We have 720 kilotons a year, so the difference is more than a factor of three.

ENGLISH: I think one of the most important factors in this difference is our much larger projected number of aircraft. Mind you, I don't expect that number to be realized, since it would require unrealistically rapid production of SST's. Remember that the UCLA projections are *demand* projections, not forecasts of number of aircraft.

THE WINTERTIME MEAN MERIDIONAL CIRCULATION IN THE STRATOSPHERE OF THE SOUTHERN HEMISPHERE

ELMAR R. REITER
Colorado State University
Fort Collins, Colorado

The asymmetry in the seasonal ozone distributions of the northern and southern hemispheres (Figure 1), if taken as being characteristic of a stratospheric tracer, lets us surmise that the stratospheric circulations in the two hemispheres behave differently too. Adler (1974) has recently been able to compute vertical-motion patterns in the stratosphere for typical winter months, using NIMBUS 3 SIRS (Satellite Infrared Radiometer Spectrometer) data. The calculation results were adjusted in magnitude to vertical motion patterns observed from standard National Meteorological Center data in the northern hemisphere. The same adjustments were applied to the SIRS data in the southern hemisphere, allowing, however, for the different radiation fluxes in the two hemispheres.

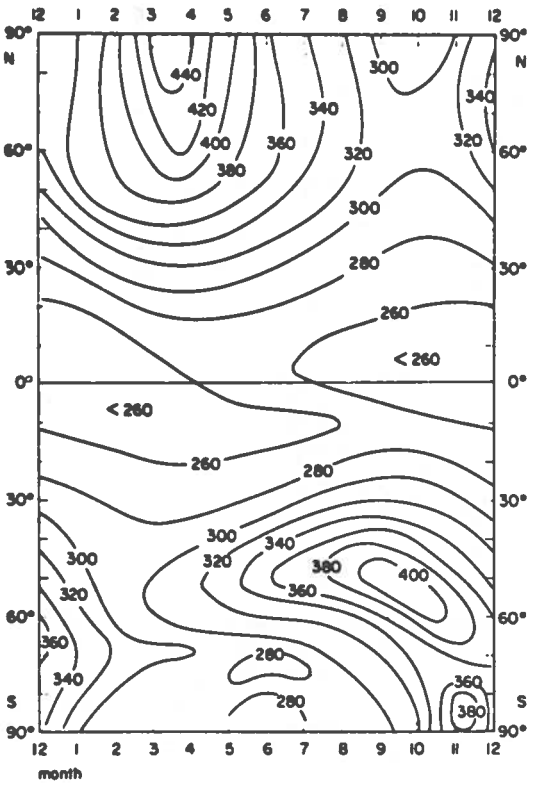

Figure 1. Total ozone as function of season and latitude in both hemispheres. (From Dütsch, 1971.)

Monthly mean vertical motions (in units of millibars per day) are shown in Figures 2 and 3 for January 1970 and July 1969, and for the northern and southern hemispheres, respectively. In Figure 2 the "unadjusted" and "adjusted" vertical motions from SIRS data can be compared to those derived from the NMC data.

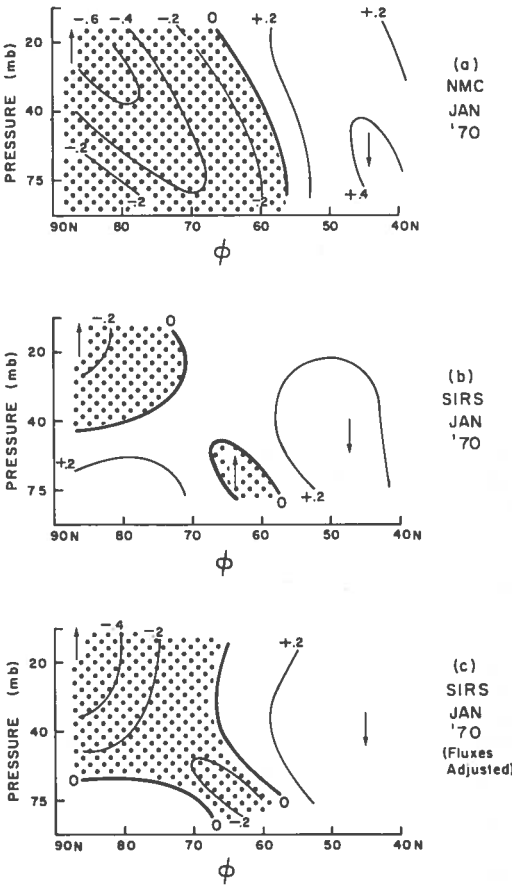

Figure 2. Zonally averaged vertical motions for the northern hemisphere, January 1970, in mbar/day. Regions with ascending motions are shaded. (a) Motions based on NMC data. (b) Motions based on SIRS data. (c) Motions based on SIRS data but adjusted to fluxes observed with NMC data. (From Adler, 1974.)

In the northern hemisphere we find a two-cell pattern with rising motions in the tropics and in the polar regions, and sinking motions in middle latitudes (see also Teweles (1964), Mahlman (1966), and Reiter (1969)). The southern hemisphere, on the other hand,

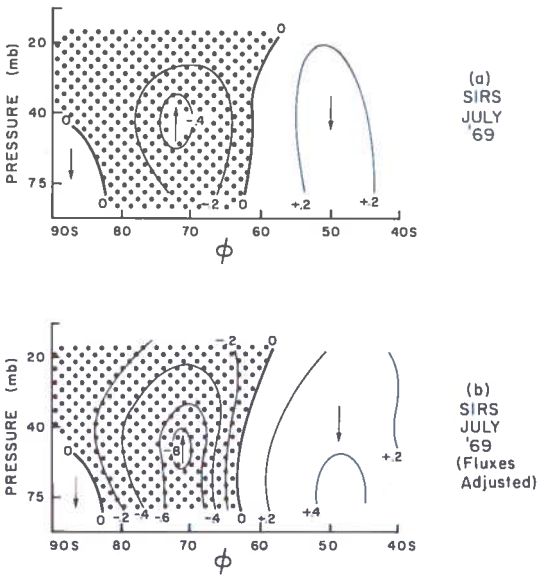

Figure 3. Zonally averaged vertical motions for the southern hemisphere, July 1969, in mbar/day. (a) Motions based on SIRS data. (b) Motions adjusted to fluxes observed with NMC data. (From Adler, 1974.)

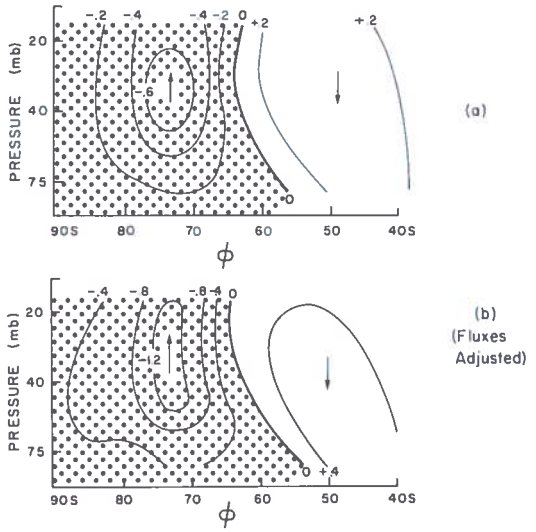

Figure 4. Zonally averaged vertical motions for the southern hemisphere, for period 1-10 July, 1969 in mbar/day. (a) Motions based on SIRS data. (b) Motions adjusted to fluxes observed with NMC data. (From Adler, 1974.)

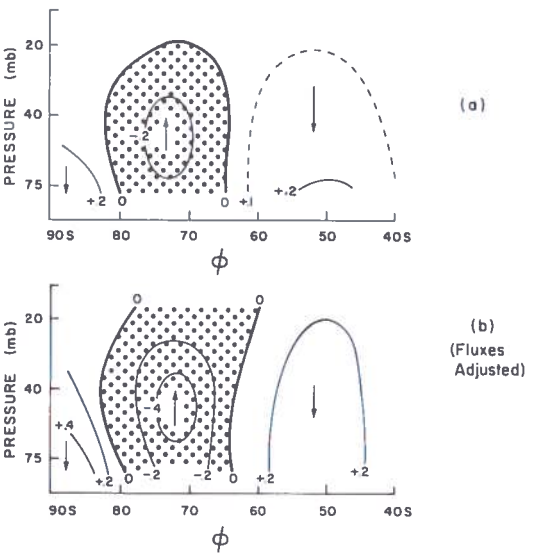

Figure 5. Zonally averaged vertical motions for the southern hemisphere, for period 18-27 July, 1969 in mbar/day. (a) Motions based on SIRS data. (b) Motions adjusted to fluxes observed with NMC data. (From Adler, 1974.)

reveals a three-cell pattern in the mean monthly motions of the lower stratosphere, with a sinking motion over the pole. We thus suspect that this sinking motion over the pole is caused by the katabatic outflow of cold air near the earth's surface along the slopes of the Antarctic highlands (see Reiter (1969, 1971)). This outflow, coupled to the sinking motion in the troposphere and stratosphere, also leads to the observed winter maximum of ozone at the earth's surface.

Within the month of July 1969 Adler investigated two 10-day periods, the first one (July 1-10) being characterized by a "minor stratospheric warming" event that did *not* lead to a breakdown of the polar vortex, but showed the presence of a significant planetary-wave pattern. The vertical motions in the stratosphere during this period closely resemble those normally observed in the northern hemisphere during winter (Figure 4). The undisturbed vortex period (July 18-27), on the other hand, clearly reveals the previously described three-cell pattern (Figure 5). Poleward heat fluxes, shown in Figure 6, are more than a factor of two larger during the disturbed period than during the undisturbed period. A similar difference should be expected for the poleward ozone transport.

From these vertical motion analyses we can draw the following conclusions:

1. The mean meridional circulation of the stratosphere depends strongly on the amplitude of planetary waves, and therefore should not be considered as a separate, absolute entity.
2. Planetary waves are highly efficient in transporting heat, ozone, and so on from low to high latitudes. The cyclone waves of middle latitudes fulfill an important function in large-scale horizontal and vertical mixing. However, they apparently do not effect the rapid transfer of trace constituents, such as O_3, from low to polar latitudes, that we observe during late winter and spring in the northern hemisphere.

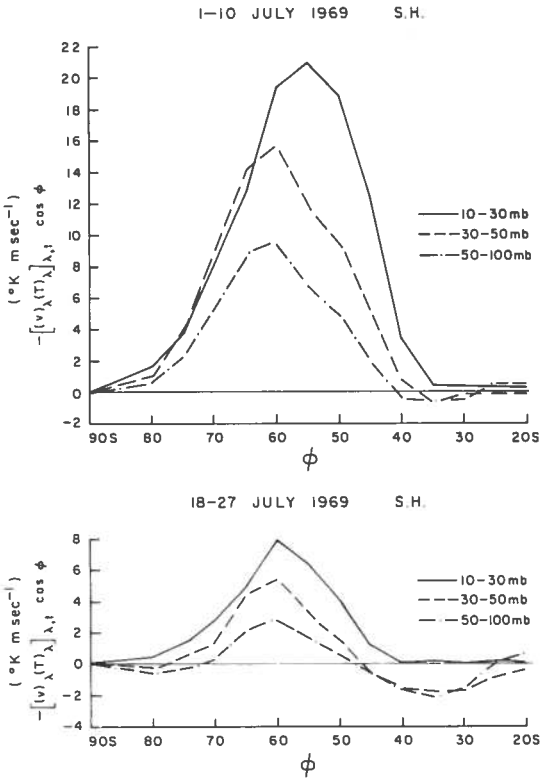

Figure 6. Poleward heat fluxes in the southern hemisphere for the periods indicated. (From Adler, 1974.)

3. There are extended periods when planetary-wave activity is suppressed even in the northern hemisphere. Such a conclusion can be drawn from the great interannual variability of the northern-hemisphere mean polar-vortex behavior during March (Figure 7) (Reiter and Macdonald, 1973). It should not be surprising, therefore, if occasionally one found a three-cell pattern in the mean meridional circulation of the stratosphere even in the northern hemisphere. Such a pattern would characterize periods of reduced meridional transport processes.
4. Large-scale horizontal (and vertical) transport processes undergo significant variations in their magnitudes over relatively short time periods. So do small-scale turbulence and diffusion processes, as is evident, for instance, from the sporadic occurrence of severe clear-air turbulence. This variability in the effectiveness of small- and large-scale mixing processes will have to be viewed in the context of the time scales of photochemical reactions in the stratosphere. Thus, in analogy with conditions in the lower troposphere, the environmental impact of pollutants released by a fleet of SST's will depend strongly on the prevailing flow patterns in the stratosphere.

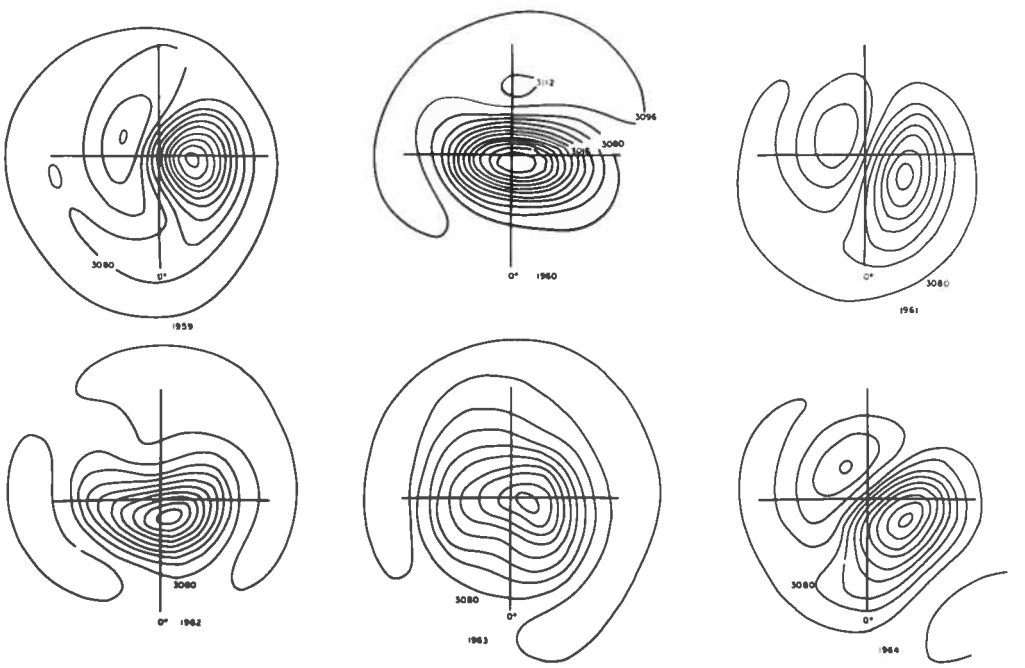

Figure 7. Configuration of mean stratospheric vortex at 10 mbar for the month of March in different years. (From Reiter and Macdonald (1973), based on data from the Tägliche Höhenkarten, published in the Meteorologische Abhandlungen, Freie Universität Berlin.)

REFERENCES

Adler, R.F. (1974), "A Comparison of the Structure and Flow Characteristics of the Upper Troposphere and Stratosphere of the Northern and Southern Hemispheres," Colorado State University, Dept. of Atmospheric Science, Ph.D. Dissertation.

Dütsch, H.U. (1971), "Photochemistry of atmospheric ozone," Adv. in Geophys. **15**, 219-322.

Mahlman, J.D. (1966), "Atmospheric General Circulation and Transport of Radioactive Debris," Colorado State University, Atmospheric Science Paper No. 103, USAEC Report C00-1340-7.

Reiter, E.R. (1969), "Atmospheric Transport Processes, Part 1: Energy Transfers and Transformations," AEC Critical Review Series, TID-24868, 253.

Reiter, E.R. (1971), "Atmospheric Transport Processes, Part 2: Chemical Tracers," AEC Critical Review Series, TID-25314, 382.

Reiter, E.R. and B.C. Macdonald (1973), "Quasi-biennial variations in the winter-time circulation of high latitudes," Archives Met. Geoph. Bioclim., Ser. A. **22** (2-3), 145-167.

Teweles, S. (1964), *Stratospheric-Mesospheric Circulation*. Research in Geophysics, Vol. 2, ed. H. Odishaw, Massachusetts Institute of Technology Press, Cambridge, Mass., 509-528.

METHODS FOR DERIVING A TWO-DIMENSIONAL TRANSPORT MODEL

E.F. DANIELSEN AND DENNIS DEAVEN*
National Center for Atmospheric Research
Boulder, Colorado

ABSTRACT: For predictions of the concentrations of trace constituents in the stratosphere, a two-dimensional transport model based on reliable observations of atmospheric motion is presently in demand. Previously developed two-dimensional transport models are subject to criticism because the methods used to obtain the motion field are indirect. The inability to measure the small but important vertical velocities has hindered the development of reliable transport models. For this reason, an analysis method has been developed that produces the three-dimensional velocity field over the northern hemisphere at points which are uniformly distributed in space and time, directly from observations. The three components of the velocity are obtained from isentropic trajectories that are centered at each of the regularly spaced grid points. With this complete data set we can test the applicability of eddy-diffusion-coefficient theory by utilizing the potential vorticity as a quasi-conservative scalar. We propose to evaluate the flux vector, gradient vector, and the Reynold's stress tensor to determine whether K theory is applicable.

INTRODUCTION

The growing interest in predicting the concentrations of trace constituents in the stratosphere places a premium on a reliable transport model. Numerical models in three dimensions are being improved, but they are not well suited to complicated chemical calculations. Two-dimensional (2-D) models, obtained by zonal time averaging, have the advantage of reducing the number of computations by several orders of magnitude; therefore, a reliable 2-D model is in demand.

Deriving a 2-D model from the radiosonde data is difficult, because radiosondes do not measure the all-important vertical velocities, and reliable hemispheric analyses of the geopotential and horizontal winds are hampered by the non-uniform distribution of stations. One alternative approach was used by Davidson et al. (1966), who developed a 2-D diffusion model by comparing numerical solutions to the observed average distribution of man-made radioactive isotopes. Another approach was used by Reed and German (1965), who used eddy heat-flux calculations to derive the components of the eddy-diffusion tensor. Gudiksen et al. (1968) included mean meridional circulations, and Luther (1973) refined the eddy-diffusion coefficients by computing monthly rather than seasonal means.

Although the 2-D transport models listed above have been developed with considerable care, they are subject to criticism because their models are necessarily indirect. The difficulty stems from the inability to measure the small but very important vertical velocities. If the three velocity components were known at the latitude, longitude (ϕ, λ) grid points, the mean circulations could be computed directly by zonal time averaging of the velocity components. Then, after the mean velocities had been subtracted from the grid-point values, the zonal time correlations between the velocity deviations could also be computed directly. These correlations produced by the large-scale eddies are primarily responsible for the turbulent transport in a 2-D model.

Our inability to measure vertical velocities does not prevent us from computing them by several diagnostic or predictive methods. During the past decade we have obtained what we believe to be the most representative values from isentropic trajectories (Danielsen, 1961, 1966). These results were obtained from case studies over a limited area (North America or Asia) and involved both hand analyses and machine methods. In this paper we present a completely automated program applied to the entire northern hemisphere. The analysis program is elaborate and complicated; it has to be, to meet our standards and our needs. It is also an efficient program, however, because we intend to apply it to at least a decade of synoptic data.

* This paper was presented by Jean-François Louis of NCAR.

The basic mathematical formulae for the transport model are shown in Figure 1. An over-bar denotes a longitudinal-time mean, while a tilde denotes a density-weighted mean. Local deviations from the density-weighted mean are identified by a prime. If χ is a quasi-conservative atmospheric scalar (for example, the mass mixing ratio of a trace gas) then the time rate of change of $\tilde{\chi}$ is produced by advection of $\tilde{\chi}$ with the mean wind $\tilde{V}$ and by the divergence of the eddy flux of χ, which depends upon correlations between χ' and V'. In general, the local time derivative would depend also upon the sources and sinks for χ, but these are neglected in this presentation.

$$(\bar{\ }) = \frac{1}{2\pi\tau}\int_{t-\tau}^{t+\tau}\int_{0}^{2\pi}(\ )\,d\lambda\,dt \qquad (\tilde{\ }) = \frac{1}{\bar{\rho}\,2\pi\tau}\int_{t-\tau}^{t+\tau}\int_{0}^{2\pi}\rho(\ )\,d\lambda\,dt$$

$$\overline{\rho\chi} = \bar{\rho}\tilde{\chi} \qquad \chi' = \chi - \tilde{\chi} \qquad V' = V - \tilde{V}$$

CONTINUITY EQUATION

$$\frac{\partial}{\partial t}(\rho\chi) = -\nabla\cdot(\rho\chi V)$$

AVERAGED EQUATION

$$\frac{\partial}{\partial t}\tilde{\chi} = -\tilde{V}\cdot\nabla\tilde{\chi} - \frac{1}{\bar{\rho}}\nabla\cdot\overline{(\rho\chi'V')}$$

K THEORY

$$\begin{bmatrix}\overline{\rho\chi'u'}\\ \overline{\rho\chi'v'}\\ \overline{\rho\chi'w'}\end{bmatrix} = -\bar{\rho}\begin{bmatrix}K_{xx} & K_{xy} & K_{xz}\\ K_{yx} & K_{yy} & K_{yz}\\ K_{zx} & K_{zy} & K_{zz}\end{bmatrix}\cdot\begin{bmatrix}\frac{\partial}{\partial x}\tilde{\chi}\\ \frac{\partial}{\partial y}\tilde{\chi}\\ \frac{\partial}{\partial z}\tilde{\chi}\end{bmatrix}$$

$$\text{LET} \quad K = \frac{1}{\bar{\rho}}\begin{bmatrix}\overline{\rho u'u'} & \overline{\rho u'v'} & \overline{\rho u'w'}\\ \overline{\rho v'u'} & \overline{\rho v'v'} & \overline{\rho v'w'}\\ \overline{\rho w'u'} & \overline{\rho w'v'} & \overline{\rho w'w'}\end{bmatrix}\tau$$

SOLVE FOR τ

Figure 1. Basic equations for two-dimensional transport model.

In K theory – the simplest turbulence closure approximation with possible large-scale applicability – the eddy fluxes are assumed to be proportional to the negative gradient of $\tilde{\chi}$. The coefficients of proportionality form a symmetric tensor, a diffusion tensor whose K_{ij} components must be evaluated. For a zonal time-averaged model only K_{yy}, K_{yz}, and K_{zz} must be evaluated, since $K_{zy} = K_{yz}$ and the K_{xj}'s do not contribute.

To evaluate the K_{ij}'s, and at the same time to test the applicability of K theory, we propose to evaluate the flux vector and the gradient vector by choosing as a quasi-conservative scalar χ, the potential vorticity.* Furthermore, if we represent the K tensor by a characteristic time τ times the Reynolds-stress tensor, τ will be overdetermined. We can evaluate τ separately from each component of the flux vector. If these τ's are in reasonable agreement, K theory is applicable; if they disagree, we conclude that a higher-order closure is required.

The velocity deviations at the ϕ, λ grid points are computed from

$$V' = V^* - \tilde{V}^* \qquad (1)$$

where V* is derived from isentropic trajectories. From each ϕ,λ grid point a 12-hr trajectory is computed both backward and forward in time. After the ϕ,λ,z coordinates have been determined at t + 6 hr and t – 6 hr, the components of V* are computed as shown in Figure 2. The Z's represent the mean of two values. One is obtained by interpolating in space from values interpolated in time. The other is obtained by interpolating in time from values interpolated in space.

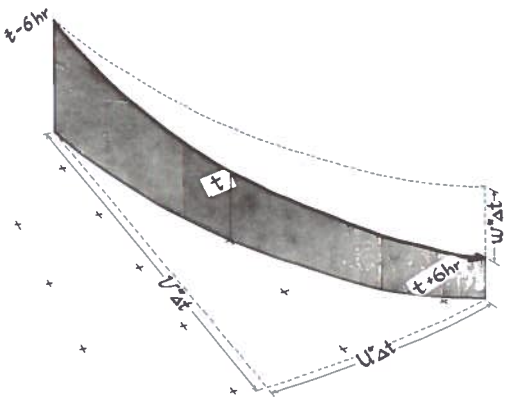

Figure 2. Isentropic trajectory to determine u*v*w* at ϕ,λ grid points.

To facilitate zonal or meridional averaging we use a polar grid separated by 5° in ϕ and 5.62° in λ. The latter is an odd value which results from dividing 360° into 64 intervals (a power of two to permit use of the fast Fourier transform). One quarter of the grid is shown in Figure 3. The complete grid from pole to equator includes 1153 points. Figure 3 also includes one quarter of the National Meteorological Center's (NMC) i,j octagonal grid. This grid includes 1977 grid points from the North Pole to about 15°N.

* The definition of potential vorticity is given in Equation (10).

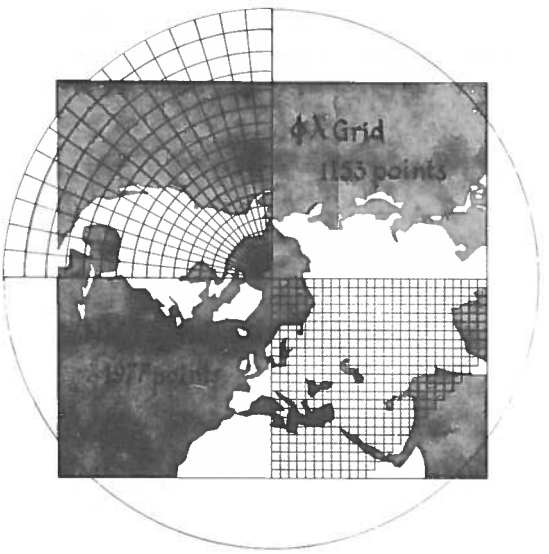

Figure 3. φ,λ grid and NMC (i,j) grid over northern hemisphere.

We begin our northern-hemisphere analyses by interpolating the heights and temperatures given at i,j grid points on the NMC analysis tapes to the φ,λ grid points. These NMC constant-pressure analyses are used to take full advantage of their time continuity. Over the ocean areas where data are sparse, the NMC analyses are strongly influenced by the NMC's predictions. The predictions provide a first-guess field which is then tuned or refined by the radiosonde, aircraft, and satellite observations.

However, the NMC analyses are restricted to 7 pressure levels between 850 and 100 mb and to the octagonal grid. Also, they do not include analyses of water vapor. The Danielsen·Deaven analysis method, outlined in Figures 4 and 5, is used to extend these analyses from 1000 to 20 mb and to the equator.

To extend the NMC's time continuity into the stratosphere, we analyze for the thickness from 100 to 70, 50, 30, and 20 mb, rather than at the heights at these lower pressure levels. The heights are obtained by adding the thickness fields to the 100-mb height field; the heights therefore differ from, but are related to, the 100-mb heights.

The first guess for the φ,λ grid points is the zonal mean. We compute separately the zonal means from the radiosonde observations and from the satellite data. We found this to be necessary because the two sets of data produce different means at low latitudes. The computer compares the two mean values as a function of latitude and adjusts the satellite values to agree with the radiosonde values. At low latitudes the satellite data yield temperatures which are too high (thicknesses which are too large) in comparison to the radiosonde values.

We take advantage of the winds by assuming geostrophic balance. To the left of each wind vector we create a fictitious station and assign it a height deviation as specified in Figure 4. These heights are treated as observed heights, so in effect the number of stations is doubled.

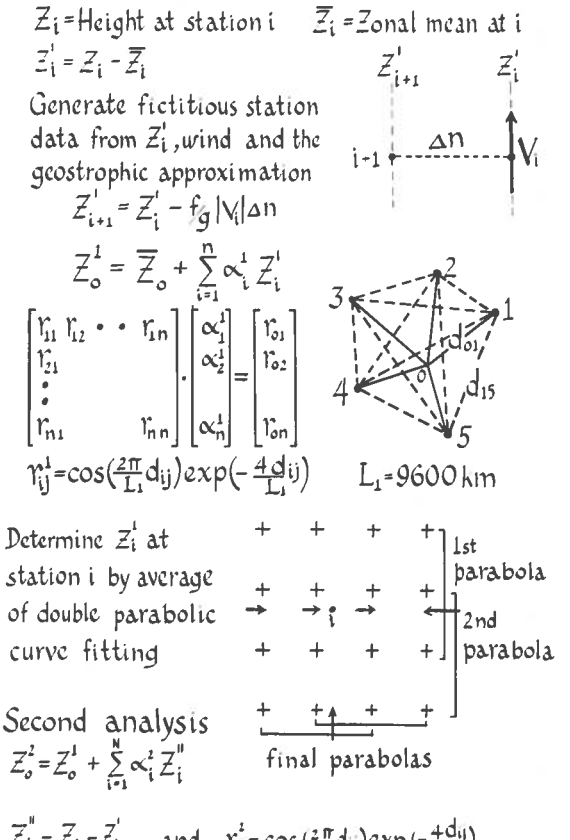

Figure 4. Danielsen·Deaven analysis method.

The grid-point values are a weighted sum of the values at eight surrounding stations, a technique introduced by Eddy (1967). The weights are obtained from solution of the matrix

equation shown in Figure 4. Eddy determined the correlation function r_{ij} from the statistics of the deviations themselves. We prefer to specify the correlation function as a damped cosine whose angle $(2\pi d/L)_{ij}$ depends upon the distance between stations i and j and upon a wavelength L. On the first pass we set $L_1 = 9600$ km.

On the first pass the computer assigns a height at each ϕ,λ grid point. These constitute the first analysis. The second analysis is based on the deviations of the heights at the stations from the heights implied by the first grid analysis. We interpolate the heights at the stations from the heights at the 16 surrounding grid points as shown in Figure 4, by forming the mean of two parabolas along each coordinate.

On the second pass we set $L_2 = 4800$ km. In regions where new height deviations Z'' are still correlated, more resolution is introduced. Where the deviations are uncorrelated, the analysis is unaltered. The resulting analysis is quite good with respect to the large-scale gradients, but it also includes short-wavelength oscillations which are either spurious or not accurately resolved.

To filter out these unwanted short waves we use double Fourier filtering in ϕ,λ coordinates. Sixty-four grid points (2^6) are used in the longitudinal direction to permit use of the fast Fourier transform. The northern-hemisphere analyses are reflected at the equator, with a zero north-south slope at the equator. The analyses then extend over the complete surface of a sphere, and so the latitudinal wave number

$$n = \frac{40{,}000 \text{ km}}{L_n} \tag{2}$$

and the longitudinal wave number

$$m = \frac{40{,}000 \text{ km} \cos\phi}{L_m} \tag{3}$$

We want to filter out all waves shorter than 2500 km, so we truncate the Fourier transform at $n = 16$ and $m = 16 \cos\phi$ (closest integer). At each latitude the grid values are obtained by inverting the truncated transform, with m ranging from 16 at the equator to 3 at 85°. The information content of the filtered analyses is high because they retain between 90 and 99% of the variance at the stations.

Figures 5-7 show how these objective analyses compare to hand analyses. Figure 5 is the initial hand analysis of the 100-50 mb thickness. The unfiltered objective analysis, Figure 6, is similar to but noisier than the hand analysis. In Figure 7 the hand analysis is smoothed subjectively to remove short wavelengths, but to preserve the area enclosed by each contour. The objective analysis after double Fourier filtering, Figure 8, compares very favorably to the smoothed hand analysis. The differences are small and occur in data-sparse regions where it would be difficult to judge which analysis is the better.

The successive steps in the analysis method and coordinate transformations are outlined in Figure 9. The NMC analysis tapes supply i,j grid values of Z, T and θ on seven pressure surfaces from 850-100 mb. The double parabolic interpolation method is used to obtain values on the ϕ,λ grid.

The radiosonde tapes and the Danielsen-Deaven analysis methods are then used to extend the 850-100 mb analyses to the equator, to extend the analyses upward to the 20-mb level, to extend the analyses downward to 1000 mb, and to analyze the relative humidity from 1000-300 mb. Knowing the temperature and relative humidity, we compute the water-vapor mixing ratio X_v. Then we compute the virtual temperature

$$T_v = T(1 + 0.62\, X_v) \tag{4}$$

and the potential virtual temperature

$$\theta_v = T_v \left(\frac{P_0}{P}\right)^{0.286} \tag{5}$$

where $P_0 = 1000$ mb, the reference pressure level.

We now know θ_v, T_v, χ_v, and Z at 12 pressure levels for each ϕ,λ grid point. If we were to plot θ_v versus $P^{0.286}$ and connect the successive θ_v's with straight lines, we could construct a sounding at each grid point. But we also know the height Z at each P surface, so we can add more resolution to the grid-point soundings. The height difference $Z_2 - Z_1$, the thickness between pressure surfaces 2 and 1, implies a

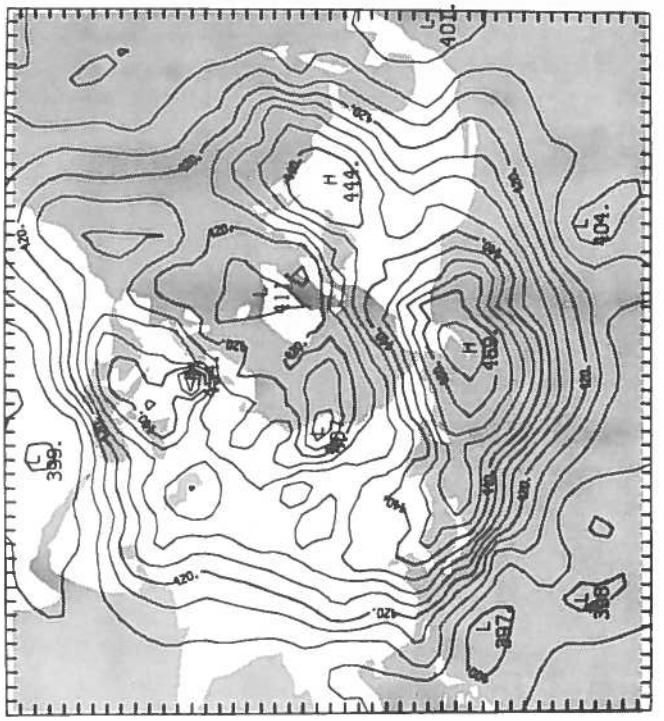

Figure 6. Objective analysis of 100-50 mb thickness, contoured in hundreds of meters.

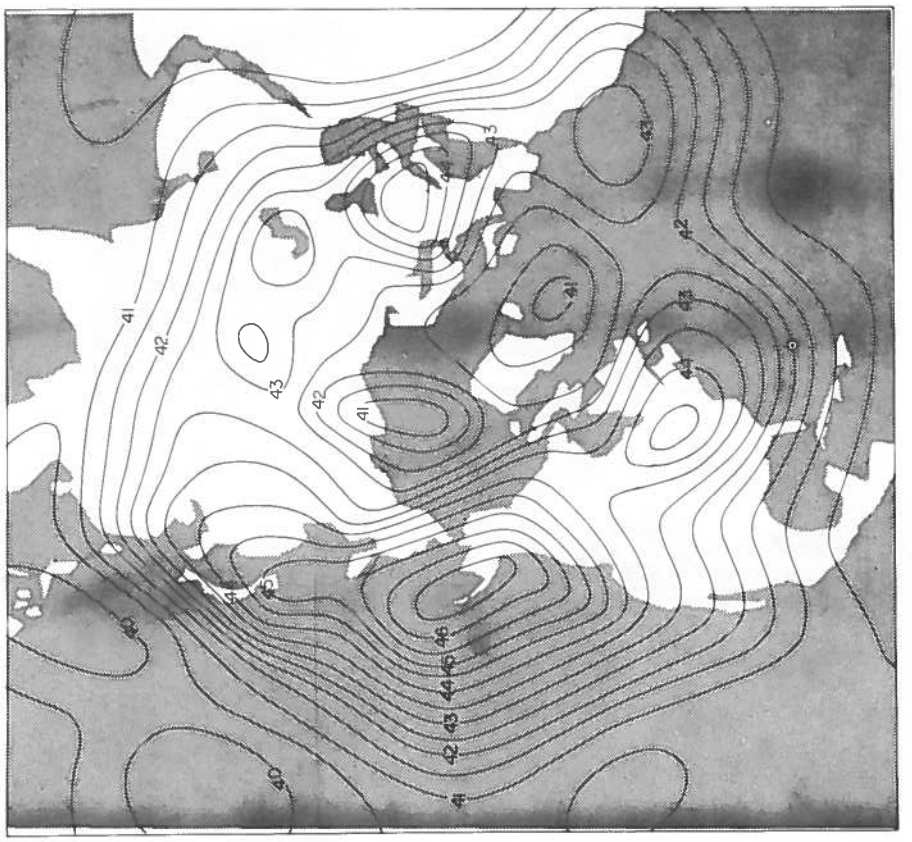

Figure 5. Hand analysis of 100-50 mb thickness, contoured in hundreds of meters.

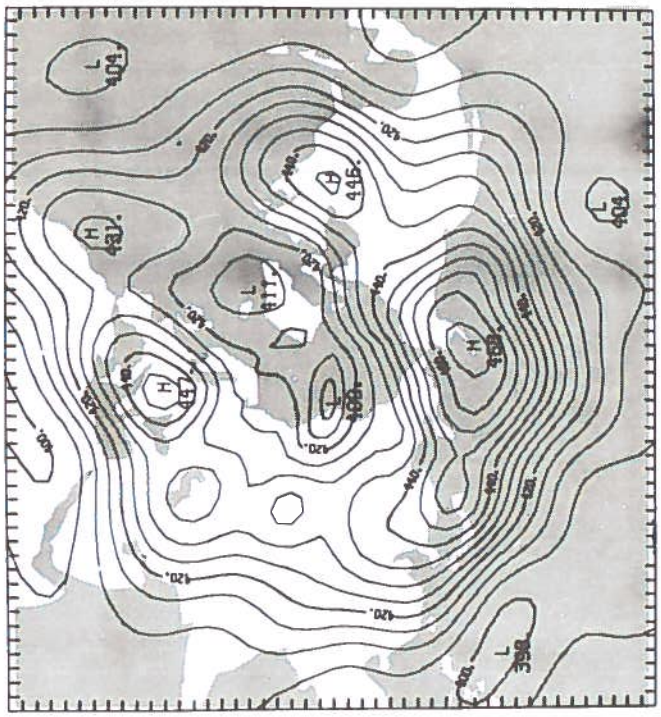

Figure 8. Double-Fourier-filtered analysis derived from Figure 7.

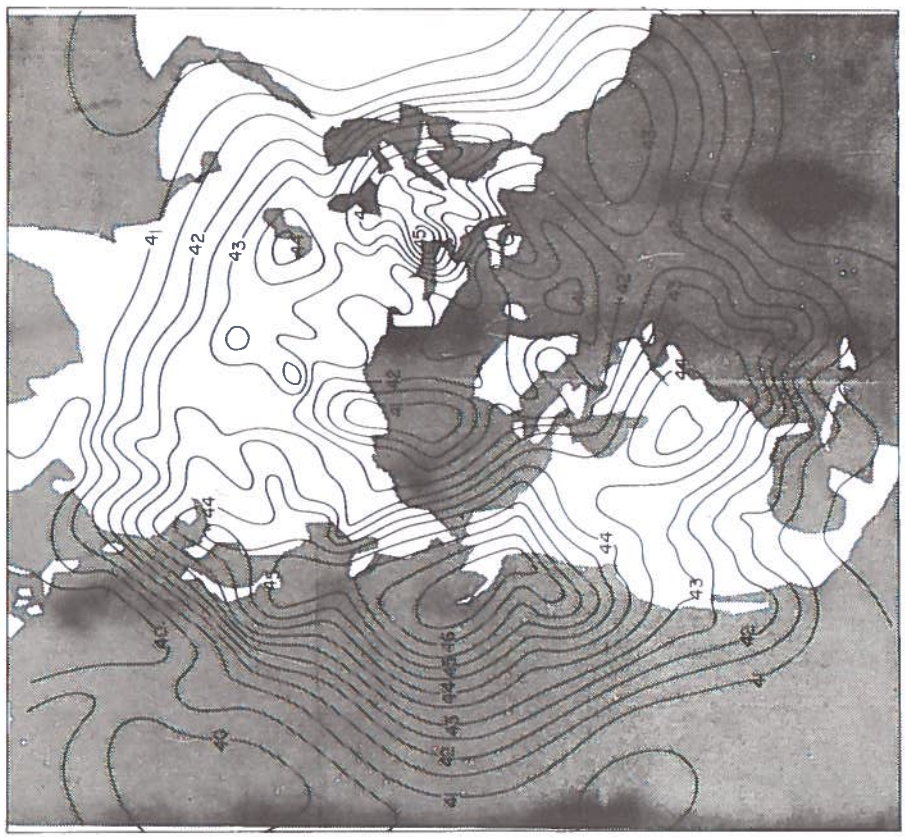

Figure 7. Hand-smoothed analysis derived from Figure 6.

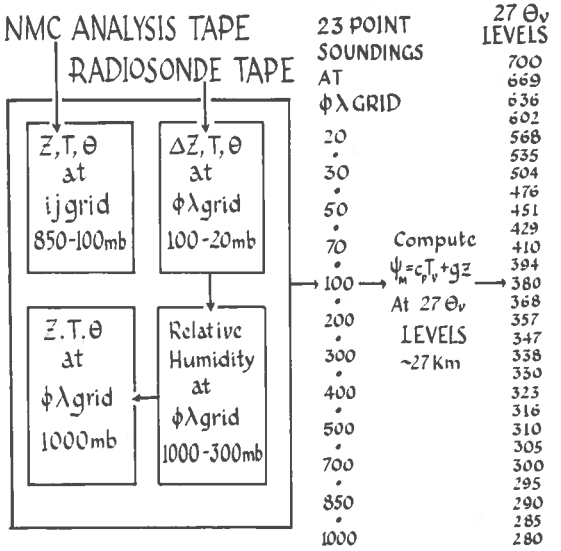

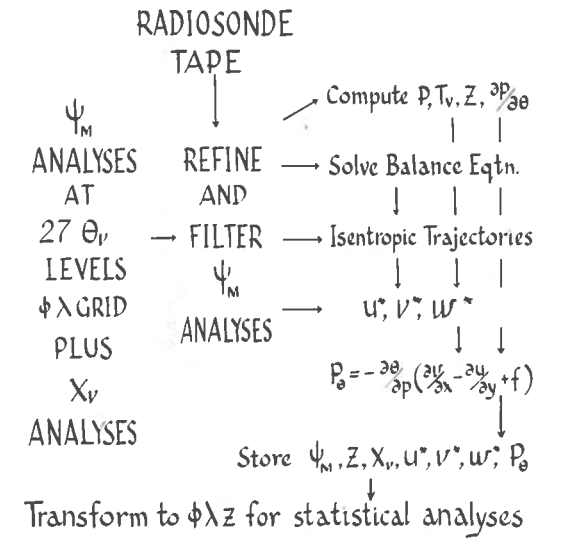

Figure 9. Outline of data processing and analysis on isobaric and isentropic surfaces.

mean θ_v which must be between θ_{v_2} and θ_{v_1}. If we assume that θ_v varies linearly with $P^{0.286}$ from θ_{v_1} to $\overline{\theta}_v$ and then changes to another linear variation from $\overline{\theta}_v$ to θ_{v_2} the pressure at which the change must occur is given by

$$Z_2 - Z_1 = \frac{c_p}{gP_0^{0.286}}\left[\theta_{v_2}\left(P^{0.286} - P_2^{0.286}\right) + \theta_{v_1}\left(P_1^{0.286} - P^{0.286}\right)\right] \qquad (6)$$

where c_p is the specific heat at constant pressure and g is the acceleration of gravity.

Successive solutions of (6) yield 11 additional points for each sounding. The result is a 23-point sounding which passes through the θ_v's and the $\overline{\theta}_v$'s as required by the Z's. We use these grid-point soundings to transform to constant θ_v analyses.

The θ_v levels have been chosen to correspond to a 1-km height interval in a standard atmosphere. In winter, we use 29 levels from 270 to 700°K; in summer, 27 levels from 280 to 700°K. At each θ_v level, the Montgomery stream-function

$$\psi_M = c_p T_v + gZ \qquad (7)$$

is computed from the 23-point soundings. These ψ_M values at the ϕ,λ grid points are treated as the first analysis in ϕ,λ,θ_v coordinates. We tune or refine these analyses by making a second analysis with the Danielsen·Deaven method using the ψ_M values computed from the radiosonde observations at the stations. The final step in these analyses is, of course, the double Fourier filtering.

The refined and fi .ered ψ_M values form the basic data set from which all of the other atmospheric variables are derived. For example, the pressures on the θ_v surfaces are computed from

$$\frac{\partial \psi_M}{\partial \theta} = c_p\left(\frac{P}{P_0}\right)^{0.286} \qquad (8)$$

The virtual temperatures are computed from θ_v, P and (5), and the heights from ψ_M, T_v and (7).

Next, we solve the non-linear balance equation in θ_v coordinates, which determines the stream-function ψ from the ψ_M field. In the computation, 21 grid-point values are used in the finite-difference approximations of the vorticity and deformations at each grid point. The horizontal velocity is then given by

$$\mathbf{V} = \mathbf{k} \times \nabla\psi \qquad (9)$$

where $\mathbf{k}$ is a unit vertical vector. This velocity is non-divergent. It closely approximates the large-scale wind at middle and high latitudes, but is less reliable at low latitudes. We still lack a means

for deriving the divergent component of the velocity.

The horizontal velocities derived from (9) are used to construct isentropic trajectories centered at each ϕ,λ grid point on all of the isentropic surfaces. From each of these trajectories we determine u*, v* and w*.

Finally, we compute the potential vorticity

$$P_\theta = -\frac{\partial \theta_v}{\partial P}\left(\frac{\partial v}{\partial x} - \frac{\partial u}{\partial y} + f\right)_{\theta_v} \qquad (10)$$

where $\partial P/\partial\theta$, the stability, is derived from the second derivative with respect to θ_v of ψ_M. In (10) f is the vertical component of the earth's vorticity,

$$f = 2\omega \sin\phi \qquad (11)$$

where ω is the angular velocity of the earth.

As mentioned previously, P_θ is the quasi-conservative scalar which will replace χ in the continuity equation. We will use P_θ to evaluate the eddy fluxes and to test the applicability of K theory.

The output from each northern-hemispheric analysis will be stored on magnetic tape. At each ϕ,λ point on the 27 θ_v levels we will store $\psi_M, \chi_v, Z, u^*, v^*, w^*$ and P_θ.

After several years of synoptic data have been processed we will study the statistics of the meteorological data in isentropic coordinates and in constant-height coordinates. The 2-D zonal time-averaged transport model will be derived from the data after it has been transformed to constant-height coordinates. We also intend to derive a 2-D meridional time-averaged transport model which will permit us to model the flow across the mean continents and oceans.

REFERENCES

Danielsen, E.F. (1961), "Trajectories: isobaric, isentropic and actual," J. Meteor. **18**, 479-486.

Danielsen, E.F. (1966), "Research in Four-Dimensional Diagnosis of Cyclonic Storm Cloud Systems," Scientific Report No. 1 and No. 2, Contract No. AF19(629-4762), The Pennsylvania State University, 53 pp.

Davidson, B., J.P. Friend, and H. Seitz (1966), "Numerical models of diffusion and rainout of stratospheric radioactive material," Tellus **18**, 301-315.

Eddy, A. (1967), "Statistical objective analysis of scalar data fields," Appl. Meteor. **6**(4), 597-609.

Gudiksen, P.H., A.W. Fairhall, and R.J. Reed (1968), "Roles of mean meridional circulation and eddy diffusion in the transport of trace substances in the lower stratosphere," J. Geophys. Res. **73**, 4461-4473.

Luther, F.M. (1973), "Monthly Mean Values of Eddy Diffusion Coefficients in the Lower Stratosphere," UCRL-74616, Lawrence Livermore Laboratory.

Reed, R.J., K.E. German (1965), "Contribution to the problem of stratospheric diffusion by large scale mixing," Mon. Wea. Rev. **93**, 313-321.

DISCUSSION

ELLSAESSER: Did you have any trouble with ellipticity in the lower latitudes?

LOUIS: Yes. We don't think that the balance equation will work very well below 20 or 25 degrees latitude, though we don't know yet.

Professor Blamont's paper was not available for publication in these *Proceedings*.

STRATOSPHERIC TURBULENCE AND VERTICAL EFFECTIVE DIFFUSION COEFFICIENTS

N.W. ROSENBERG AND E.M. DEWAN
Air Force Cambridge Research Laboratories
L.G. Hanscom Field
Bedford, Massachusetts

ABSTRACT: We have obtained an estimate of residence times in the stratosphere in terms of an effective diffusion coefficient, K_e. Our approach is based on the hypotheses that (1) CAT (clear-air turbulence) is the major source of vertical transport, and that (2) almost all CAT is caused by the Kelvin-Helmholtz shear instability. According to the best current evidence, turbulent instability occurs whenever the Richardson number (Ri) is less than approximately 0.25.

Our calculations used velocity data from a NASA report of 200 rocket smoke-trail wind profiles at 25 m resolution. Our analysis of stratospheric shears as a function of altitude from this sample (30,000 data points) revealed that about 2% of the altitude consists of thin sporadic layers of high shear, separated by large regions of low shear. Richardson numbers and turbulence frequencies were computed from these shears on the basis of a standard temperature profile.

A model for vertical transport by such intermittently-occurring turbulent mixing zones, separated by regions of negligible mixing, was generated using the turbulence statistics. It leads to a value of K_e which is approximately 0.3 m^2/s between 12-18 km, when data at 25 m resolution is used. When 100-m resolution is used, the diffusion estimates are slightly smaller. These results agree with other methods of measuring diffusivity (radioactive fallout, CH_4 loss) and seem to indicate that CAT plays a prominent role in vertical transport in the stratosphere.

INTRODUCTION

In this paper we report computations of the observed frequency distribution of the magnitudes of vertical shears of horizontal winds between 5 and 20 km altitude. We then derive the probability distribution of turbulent layers for various values of vertical thickness, on the basis of accepted relationships between shear and turbulence. An effective vertical-diffusion coefficient, K_e, is estimated from a simple model using this empirical turbulence probability distribution.

Specifically, we calculate the effect of clear-air turbulence (CAT) upon vertical transport, using a model consisting of a vertical column of thin, randomly-spaced mixing (turbulent) layers separated by thick non-mixing atmospheric layers. The turbulent layers correspond to the intermittent sporadic CAT "blini" described in the literature (Bretherton, 1969). We also assume that essentially all CAT is due to shear instability of the Kelvin-Helmholtz type, which can occur in stratified fluids. This assumption is shown to have wide experimental support in the current literature. Our results lead to an estimated diffusion coefficient of approximately 0.3 m^2/s in the stratosphere. This is roughly consistent with vertical diffusivities estimated from radioactive fallout, which have values ranging from 0.1 m^2/s to 1.0 m^2/s for tropical and polar stratospheres respectively (Junge, 1963).

CLEAR-AIR TURBULENCE AND KELVIN-HELMHOLTZ BILLOWS

In order to clarify our model, it seems appropriate to briefly review the main background information concerning the Kelvin-Helmholtz (K-H) instability, as well as the evidence that CAT, at the altitude of interest, is almost always due directly to the K-H phenomenon.

The K-H Instability

Kelvin's original paper (Kelvin, 1910) on this phenomenon treated the influence of wind on water waves. Helmholtz was the first, however, to discuss the instability of surfaces separating

fluids which have different velocities. Subsequent literature assigns their names to the more general instability which occurs when there are vertical shears of horizontal velocities across finitely thick layers of vertically stratified fluids. This instability frequently occurs in both the ocean and the atmosphere. Whenever a horizontal layer is buoyantly stable but has a sufficiently high velocity-shear across it, a small perturbation will result in a growing wave which eventually breaks and generates a patch of turbulence. Such breaking "gravity waves" are usually organized in clusters and result in horizontally wide but vertically thin turbulent layers. The criterion for instability is given in terms of Richardson number, Ri, which is defined as

$$\mathrm{Ri} = -g(\partial\rho/\partial z)/[\rho(\partial u/\partial z)^2]$$
$$= (-g/T)\,((\partial T/\partial z) + \Gamma)/(\partial u/\partial z)^2 \qquad (1)$$

The first form on the right is often used in oceanography, and the second form in atmospheric physics. g is the acceleration gravity, ρ is the fluid density, z the vertical coordinate, u the horizontal velocity, T the temperature in °K, and Γ the adiabatic lapse rate (dry air assumed) (Monin and Yaglom, 1971).

The criterion for stability is that Ri be > 0.25 everywhere in the flow (Taylor, 1931; Goldstein, 1931; Miles, 1961; Hazel, 1972; Turner, 1973). This is a general result which has been accepted (within certain restrictions). This criterion does not mean, however, that instability and turbulent breakdown occur whenever and wherever $\mathrm{Ri} < 0.25$; it simply means that $\mathrm{Ri} < 0.25$ is a *necessary* condition for turbulence to occur. The physical reason for the value 0.25 is that, for this value of Ri (Ludlam, 1967; Businger, 1969a), the available kinetic energy due to the velocity difference across the layer is equal to the work which must be done against buoyancy forces in order to exchange fluid parcels across the layer. Once the energy is available, a perturbation may result in a growing nonlinear oscillation of the layer, in the form of a wave. When turbulence has started (after the wave breaks), mixing can occur *within* the layer. Businger (1969) has shown that in this case, Ri = 1 represents equality between potential energy and available kinetic energy (thus explaining Richardson's original Ri = 1 criterion for the instability threshold). Once a layer has become turbulent, then, one would expect it to continue to be "fed" energy until Ri has increased to 1. This occurs when the layer thickens enough to sufficiently lower the shear across it. After such a point, turbulence would be damped by the forces of stable buoyancy.

Internal K-H billows below the ocean surface have been investigated by oceanographers. One simple model for such observations has been given by Woods (1969). He assumed that Ri = 0.25 is also a *sufficient* condition for turbulence. Experimental evidence to date seems to indicate that a value of Ri around 0.25 is indeed a sufficient condition in the free ocean and atmosphere (away from boundaries and in the absence of obliquely-shearing oblique winds, etc. (see Hines, 1971). Woods also assumed that Ri = 1 was the "cutoff" condition for turbulence. He thus postulated a "hysteresis effect" that would give a stable layer until $\mathrm{Ri} < 0.25$, and would then become turbulent until the layer thickened enough to make Ri = 1.

Figure 1 (based on his report) shows the sequence of events he observed by means of dye tracers. The initially stable layer goes into oscillation. A wave builds up until nonlinear effects predominate, causing a characteristic "roll-up." Finally there is turbulent breakdown and layer spread until Ri = 1. He assumed that the density (ρ) and velocity (V) gradients were zero outside the layer, but that ρ and V at the top and bottom layer surfaces remained constant. Under these assumptions, the transition from Ri = 0.25 to Ri = 1 causes the layer to thicken by a factor of 4. At Ri = 1 the turbulence subsides and the layer becomes stable.

The original (and now famous) paper which first described this "roll-up" effect was by Rosenhead (1931); it showed a numerically-generated billow effect. This effect has also been beautifully reproduced in the laboratory by Thorpe (1973), who generated K-H billows by inducing a shear between two initially stable liquids of different densities. His measurements indicated that the actual "cutoff" for turbulence is more like 0.4 ± 0.1 rather than the overly simple theoretical value mentioned above, so Ri = 0.4 is known in the literature as the Thorpe number (Garrett and Munk, 1972).

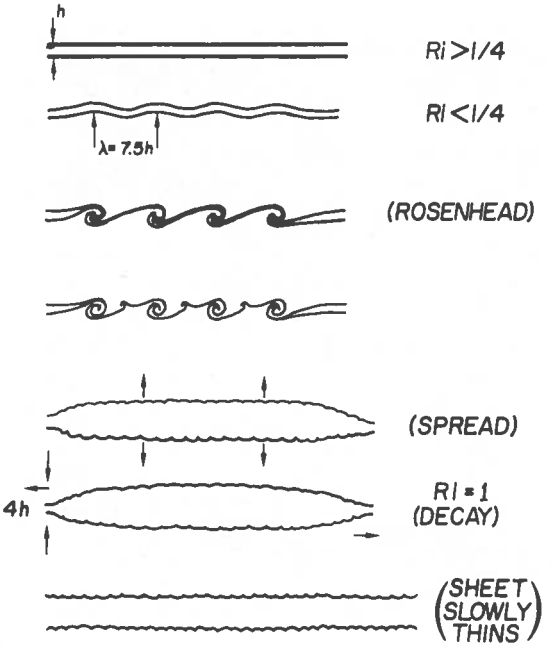

Figure 1. Development of an underwater Kelvin-Helmholtz-type instability and subsequent roll-up, breakdown, spread and decay. (After Woods, 1969.)

According to Woods and Wiley (1972) such K-H mixing and spreading events constitute the principal mechanism for vertical mixing throughout the World Ocean. Their work has been enlarged upon by others (e.g., Garrett and Munk, 1972). In view of the hypothesis that CAT is due to K-H billow events, it seems eminently reasonable to hypothesize that it also plays the dominant role in vertical mixing of the upper atmosphere.

CAT and K-H Billow Events

Radar observations of CAT by Richter and Gossard (see Battan, 1973) clearly show the K-H billow shape. In fact, the entire sequence observed by Woods has also been seen in CAT; it is illustrated by Browning and Watkins (1970) with the schematic shown in Figure 2 (see also Atlas, 1970). The spreading shown appears to be negligible in contrast to what is seen in the ocean. Earlier work of Ludlam (1967) also showed similar structures in clouds. When Browning (1971) analyzed seventeen K-H events by means of simultaneous radar and balloon soundings, he found that almost all of these events were preceded by a period of time in which Ri was around 0.25. The events themselves lasted approximately 500 sec. on the average, and the condition Ri < 0.25 was often maintained for over one-half hour prior to the K-H events in the figures he gave. This and other evidence reviewed by Dutton (1971, 1973) make a convincing case that CAT is most likely due to the K-H phenomenon. Thorpe himself refers (1973) to underwater K-H as "underwater CAT."

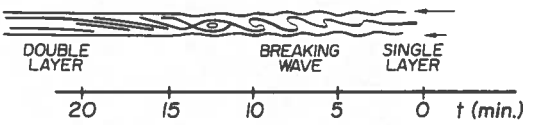

Figure 2. Schematic of a K-H billow event in the atmosphere as detected by means of radar. (After Browning and Watkins, 1970.)

WIND-PROFILE DATA AND THE STATISTICAL SPATIAL STRUCTURE OF CAT

The experimental data base for our calculation was a series of reports containing 200 vertical profiles of horizontal winds measured from smoke trails by Miller, Henry, and Rowe* (1959-1962, 1965, 1968). They gave wind velocity vectors as a function of height at 25-m intervals with a precision of 0.1 m/s. Figure 3 shows a typical smoke trail. This montage shows the progressive distortion due to shears. In all there were 90,000 data points: 50,000 below 12 km, 30,000 between 12 and 16 km, and 10,000 above 16 km. From these, shears were calculated as $[(\Delta V_x/\Delta_z)^2 + (\Delta V_y/\Delta Z)^2]^{1/2}$, where V_x and V_y represent the horizontal wind components.

Figure 4 shows the cumulative frequency distribution for component shears measured at 25-m spacing, where the ordinate is given in units of standard deviations. The linear portions of these curves (the central 90%) correspond to a Gaussian distribution with a standard deviation of 0.014 s^{-1} in both components at both altitudes. However, high shears occur more

* All profiles were obtained in beautiful weather, and this selection aspect of the method of data collection must be kept in mind.

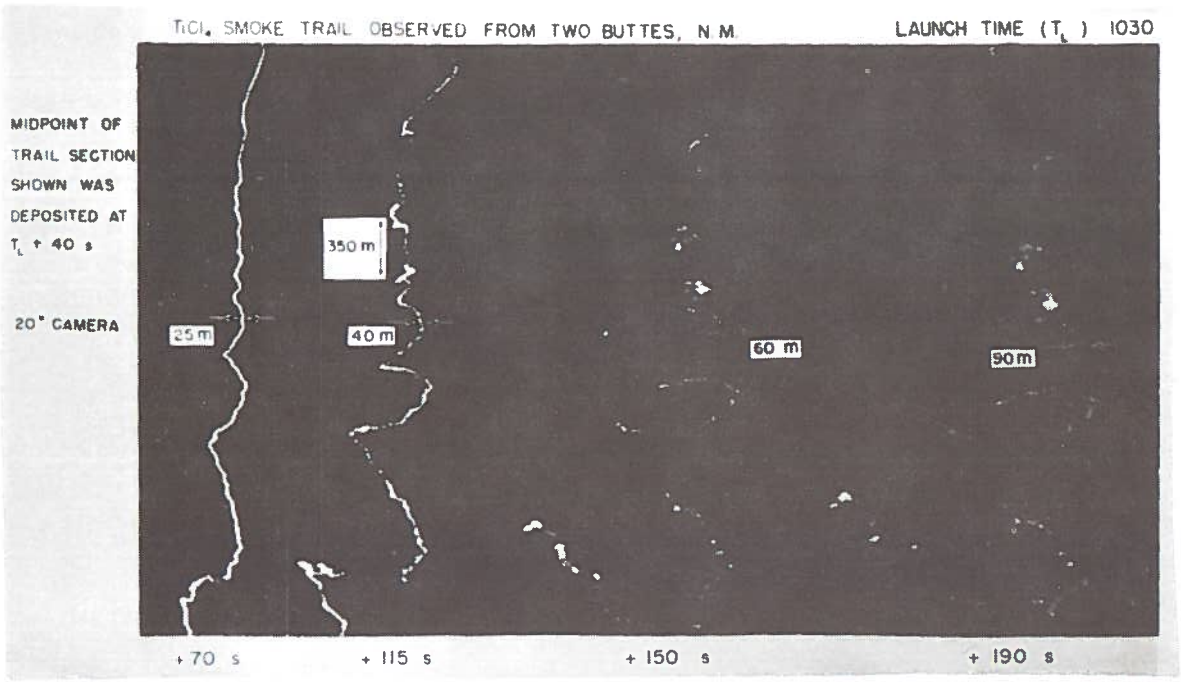

Figure 3. Typical smoke-trail profile showing the distortion due to wind shears.

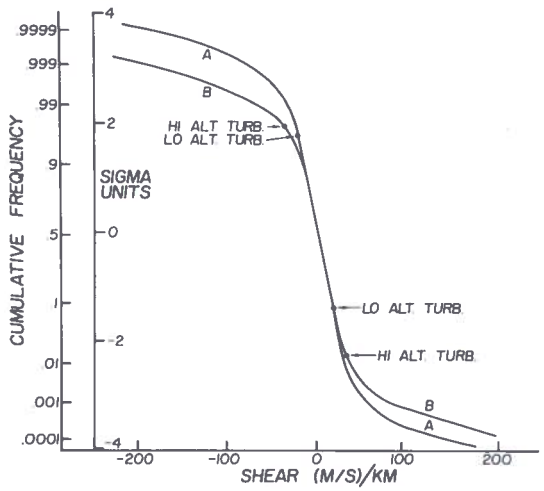

Figure 4. Cumulative frequency distributions for component shears. A is based on tropospheric winds while B represents stratospheric shears. The threshold shears for turbulence are indicated by dots. Note that distributions become non-Gaussian (actually log-normal) for supercritical shears. Observe also the asymmetry about the vertical axis.

predict. When the non-Gaussian portions of these curves were plotted with a log-normal scale for the ordinate, they became linear. According to Gibson, Stegen, and Williams (1970), who referred to predictions of Kolmogoroff, Obukhoff, and Yaglom, there is now good evidence that the probability distributions of velocity derivatives are log-normal, provided that these velocities are part of an inertial-range turbulent velocity field. This raises a very interesting question: Why should the high shears which would *bring about* turbulence have the log-normal statistics which would be expected from the turbulent process itself? One might speculate that the high shears (of horizontal and presumably *laminar* winds) have their origin in a much larger scale of turbulence. We will not discuss this phenomenon further in this paper, but simply note that it seems to be of interest.

The critical shear was computed from $Ri = 0.25$, but since temperature measurements made simultaneously with the wind data were not available, we used U.S. Standard Atmosphere mean temperature gradients of -6°/km in the troposphere and 0°/km in the stratosphere, with a -9.8°/km adiabatic lapse rate. This led to a

frequently than a Gaussian distribution would critical shear, S_c, of 0.025 s^{-1} in the 5-12 km region (troposphere), while for the 12 km - 19 km region (stratosphere), S_c was 0.045 s^{-1}. The latter higher value, of course, reflects the higher stability of the stratosphere. Figure 4 shows that many of the above-threshold shears are in the log-normal portion of the curves, especially for the stratosphere.

Using the above values for S_c, we obtained the cumulative frequency distribution, $P_I(L)$, for finding turbulent layers of thickness L or greater. Note that only 2% of shears at 25 m resolution exceed threshold in Figure 4. $P_I(L)$ is related to the probability P(L) of finding a layer having a thickness between L and L + dL by

$$P_I(L) = 1 - \int_0^L P(L')dL' \qquad (2)$$

We can therefore derive P(L) from our data by calculating the difference between $P_I(L)$ for neighboring values of L.

$$(dP_I(L))/dL = P(L) \qquad (3)$$

Figure 5 shows a plot of $P_I(L)$ vs. L. We used the empirical results of Miller et al. (1965) directly in our calculations. An extrapolation was made for L = 0 by a least-squares fit of the form $P_I(L) \propto \sqrt{L}$ on available points.

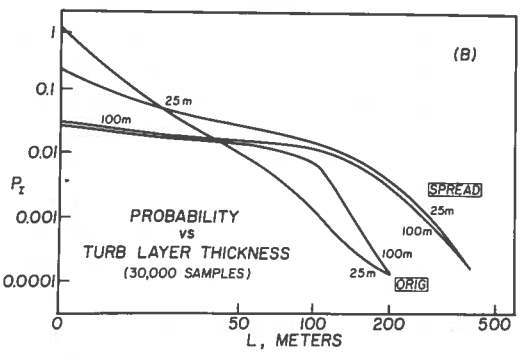

Figure 5. Cumulative frequency distributions ($P_I(L)$) for various lengths L of unstable layers.

THE VERTICAL-STACK DIFFUSION MODEL

A one-dimensional model relating effective vertical diffusivity K_e to $P_I(L)$ is derived below. In other words, the vertical structure of CAT layers is determined from wind-shear data, using the criterion Ri < 0.25, and this structure is then used to determine the vertical transport by means of the model.

Assumptions

First we shall assume that there is no vertical transport between turbulent layers: in other words, all such transport is assumed to take place within CAT mixing layers. Second, we shall assume that the horizontal rearrangements of the layers and material being transported will have no effect on the vertical transport. This type of assumption is not unusual in oceanography and allows the use of a simple one-dimensional model (Garrett and Munk, 1972).

Model

The fundamental definition of the coefficient of diffusivity provides the basis for the derivation of our model. Figure 6 shows a horizontal slab through which material (or heat, in the general case) diffuses vertically. Suppose that the concentration C of the material is held to a constant at the top of the slab by means of an infinite reservoir, and assume that the downward diffusion is steady-state. Assume that all material reaching the bottom of the slab drops into an infinite sink at zero concentration. The profile of C would then be a straight line as indicated.

The definition of the coefficient of diffusivity, K, is

$$K = (dn/dt)/(dc/dz) \qquad (4)$$

where dn/dt is the number of moles of material flowing out through a unit of surface area at the bottom of the slab per unit of time, and dc/dz is the constant gradient of the concentration with respect to the altitude, z. When vertical motion is not due to molecular transport effects, but is instead due to turbulence of some sort, this motion can be expressed in terms of effective diffusivity, K_e.

To simulate stratospheric vertical motion, we imagine a series of thin horizontal mixing

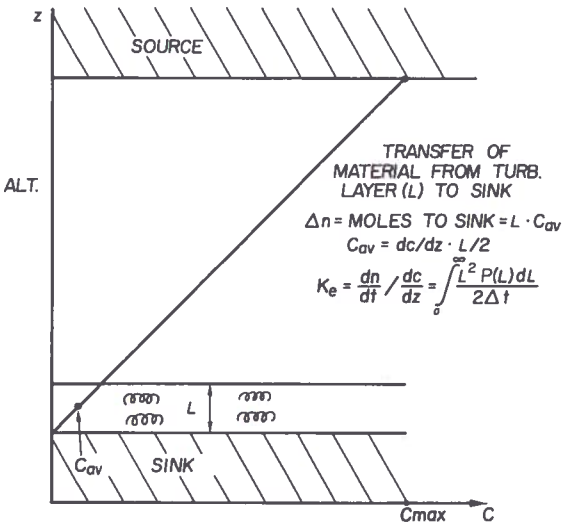

Figure 6. Diagram for K_e model relating wind-profile statistics (P(L)) to vertical transport.

layers which are randomly arranged vertically and vary randomly in their thickness. We suppose that within each layer there is complete mixing and that after a time interval t, the entire profile is replaced by a different one from an ensemble of statistically similar profiles. In reality the CAT layers will appear sporadically and intermittently, but we shall assume that our "time step" approach will not affect the results. Whenever a mixing layer occurs at the bottom of the stack, material will flow out to the sink. This would happen only occasionally, after a large number of time steps, each of duration Δt. Due to the assumed steady-state random nature of the process, the *average* concentration gradient will remain constant. In Figure 6, when a mixing layer of thickness L occurs at the bottom of the slab, the volume of material involved is L times the unit of area, and the average concentration within this volume is (L/2) (dc/dz) leading to Δn (moles transferred) = L(L/2) (dc/dz). If we know the probability P(L) that a layer of thickness L will occur at the bottom in the interval Δt, we can obtain

$$Ke = (\Delta n/\Delta t)/(dc/dz) = \int_0^\infty P(L)L^2 dL/(2\Delta t) \quad (5)$$

which takes into acount all possible layer thicknesses.

Since we assume that the random nature of our turbulent layers will ensure that vertical transport will be, on the average, diffusive in nature, we can assume that K_e also satisfies the diffusion equation:

$$K_e \nabla^2 C = \partial C/\partial t \quad (6)$$

From this we can calculate the residence time for a layer of pollution. Assuming an initial Gaussian distribution, Eq. (6) leads to

$$C(z,t) = \frac{1}{\sqrt{t}} \exp(-z^2/4 K_e t) \quad (7)$$

(Korn and Korn, 1968). The residence time t_R, i.e., the time needed for the Gaussian radius (one-dimensional) to reach a distance (z) = H, is therefore

$$t_R = H^2/4 K_e \quad (8)$$

In order to calculate K_e from Eq. (5) and t_R from Eq. (8) we need to have an estimate of Δt, and this will be discussed in the next section.

GROWTH AND DECAY TIME, Δt, FOR A K-H BILLOW EVENT

The Δt in our model does not correspond to the duration of turbulence, but rather to the time needed for a K-H event to develop after Ri has descended below 0.25. Thus Δt, or the time between profiles in the model, corresponds to the interval between $Ri < 0.25$ and the time when turbulent breakdown makes $Ri > 0.25$.

We shall estimate Δt directly from some observations by Browning (1971) of 17 K-H events. He made measurements simultaneously by radar and balloon soundings. Figure 2, taken from Browning and Watkins (1970), shows that in a typical event, the build-up and breakdown can take place in a period of approximately 1000 seconds. In Browning (1971), information on Δt times was available for 6 of the 17 K-H events. The time elapsed between $Ri < 0.25$ and the end of a billow event ($Ri > 0.25$) varied between approximately 1000 seconds and 5000 seconds, averaging about 3000 seconds, and the average duration of the 17 billow events themselves is

approximately 500 seconds. (The exceptional case of a 4-hour billow event was omitted in the calculation of this average.) In view of the above, we chose $\Delta t \simeq 3{,}000$ sec for the 5-12 km altitude region which was studied by Browning.

The value of Δt for the stratosphere would differ from the above values. From Rosenhead (1931) it can be seen that Δt is proportional to λ/U, where λ is the most unstable wavelength $\approx 7h$ and where h is the layer thickness (Turner, 1973), and where U is half the difference between the velocities on each side of the layer. Thus

$$\Delta t \propto 7h(du/dz)^{-1}\,(h/2)^{-1} \propto du/dz^{-1} \qquad (9)$$

where we take du/dz to be S_c. Since the stratospheric S_c is approximately twice the size of the tropospheric S_c, Δt in the stratosphere would be 1,500 sec, if we accept 3,000 seconds as the tropospheric Δt.

The turbulence should start to decay when Ri exceeds 0.4, the Thorpe number mentioned above. As we have seen from the data of Browning, the duration of a billow is about 500 sec on the average, which presumably is the time needed to raise the Ri above the threshold once turbulence has commenced.

RESULTS

Figure 7 summarizes our main findings. The relation

$$P(L) = 1 - \int_0^L P(L')dL'$$

was explained earlier, and illustrated in Figure 5. We have also explained how the effective diffusion coefficient, K_e, can be obtained from

$$K_e = \frac{1}{2\Delta t} \int_0^L P(L')(L')^2 dL' \qquad (10)$$

Figure 7 shows K_e as a function of the upper limit of integration L. Among the 30,000 atmospheric shears, 60 were found with a thickness greater than 200 m ($P_I(L) = 0.002$), but none with a thickness greater than 300 m ($P_I(L) = 0$). A comparison of Figures 5 and 7 shows how $P_I(L)$ affects the shape of $K_e(L)$.

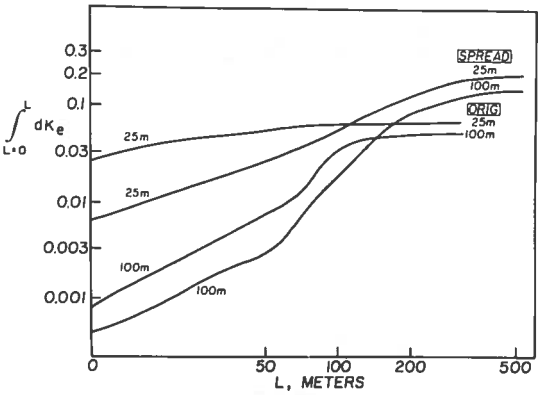

Figure 7. Diffusion coefficient K_e vs. turbulent-layer thickness, showing results at 25 m and 100 m resolution, and the effects of layer spreading on them.

Figure 7 indicates that $K_e = 0.068\ m^2/s$ for data at 25 m resolution. We were also interested in the effect of data resolution on K_e. A four-point moving average was used to smooth component velocity profiles to simulate 100-m resolution. Figure 7 shows that this results in no significant change in the final value of K_e, although the dependences of P_I and K_e on L have been markedly altered ($K_e \approx 0.054$).

Next we consider the effect of vertical spreading of turbulence upon our estimate of K_e. As was discussed earlier, once turbulence has been initiated in regions of high shear, it spreads vertically until the mean shear decreases so much that the increasing Richardson number reaches the "extinction" value of about 0.4.

Figure 8 shows "original" 25-m and 100-m resolution shear profiles. It also shows what happens if we allow turbulence spreading to bring supercritical shears down to their critical values (Ri = 0.25).

Figure 9 demonstrates how the spreading was computed. The left side shows a jagged profile of shear vs. altitude, and the right side a hodograph (showing the velocity profile as seen from above). When a supercritical shear is encountered at an altitude z (e.g., altitude 16.50 km in Figure 9, between point 7 and 8 in the hodograph), a search is made to find the maximum height separation, centered at z, which is still supercritical ($Ri < 0.25$). It is assumed that the profile will take on a constant shear between those two altitudes, with the excess energy going into turbulence. Thus we joined heights 16.30 km and 16.65 km with a constant shear, and the

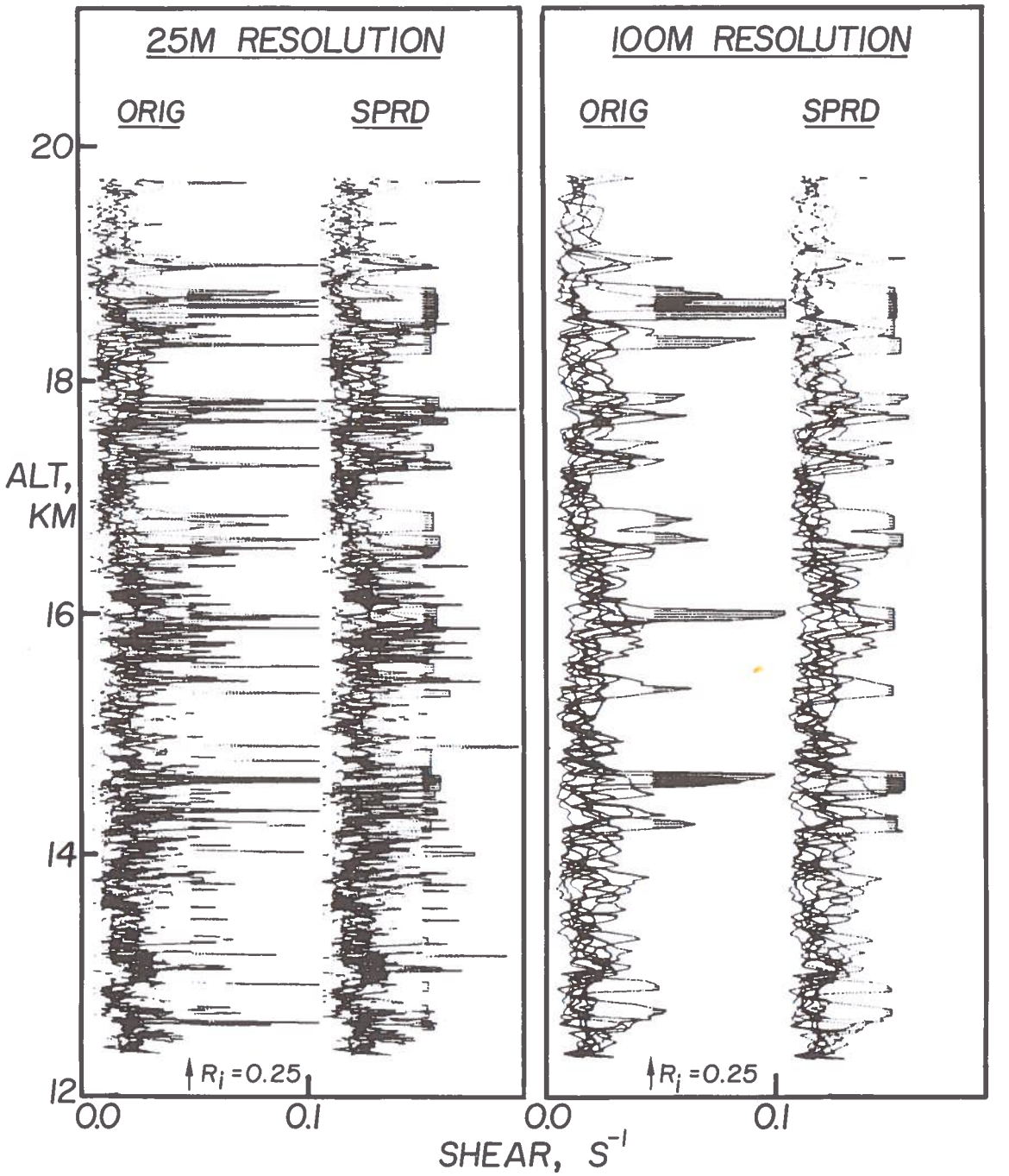

Figure 8. Effects of resolution and layer spreading of supercritical shear layers. The curve on the right side of each box shows the profile after spreading. These profiles consist of a superposition of 8 trails.

hodograph between these points with a straight-line vector.

Figures 5 and 7 show the effects of spreading on $P_I(L)$ and $K_e(L)$ at 25 m resolution. The K_e estimate has been raised to 0.21 m^2/s because of the thickened layers. A decrease in resolution to 100 m is seen to decrease estimated K_e to 0.15 m^2/s. From this we would expect that, if the resolution were improved beyond 25 m, one might find a larger value for K_e. Trails

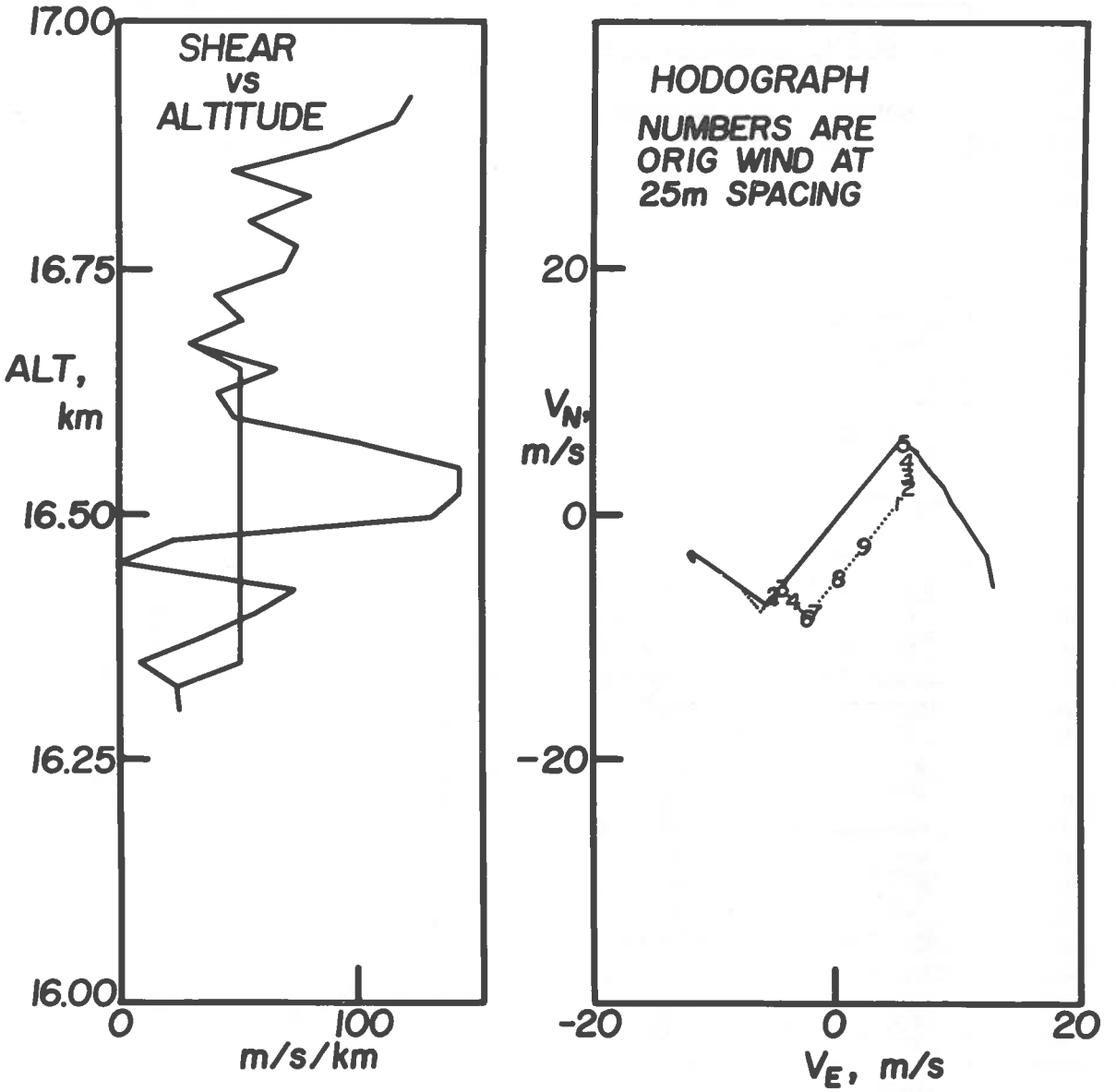

Figure 9. Shear profile and velocity hodograph before and after spreading.

with such higher resolution (10 m) are currently being analyzed in our laboratory. If the spreading were allowed to continue until Ri = 0.4, K_e would be increased. The spread which would account for a change in Ri from 0.25 to 0.4 is found from

$$\mathrm{Ri} = -g\left(\frac{\theta'}{\overline{\theta}}\right)\frac{1}{(u')^2} = -\frac{g\theta' h^2}{\overline{\theta}(\Delta u)^2} \qquad (11)$$

where $\overline{\theta}$ is the average potential temperature in a layer, θ' is the potential-temperature gradient, h is the layer thickness, and Δu is the difference in horizontal velocity across the layer. θ' and Δu can be presumed to remain approximately constant as the layer expands; thus Ri is proportional to h^2. From this we see that h^2 would grow by a factor of (0.4/0.25) = 1.6. From Eq. (10) we see that an increase of all values of L (or h) in this way amounts to multiplying K_e by a factor of 1.6. A spread 25-m profile would then result in

$$K_e = 0.21 \times 1.6 \approx 0.3 \text{ m}^2/\text{s}.$$

In order to see whether the extremely high shears (in excess of 2 S_c) were an important factor for the value of K_e, we edited out these high shears (amounting to 0.1% of the sample) and repeated the calculations. We obtained essentially identical results, and so ignored the very high shears thereafter.

Using Eq. (8) with H = 10 km (corresponding to the growth of a Gaussian radius located at 20 km down to the tropopause at 10 km), we obtain a residence time $t_R \approx 3$ years for $K_e = 0.3$ m^2/s. Is this an overestimate or an underestimate? It is difficult to answer this question without further information on the reliability of our estimate of Δt.

CONCLUDING REMARKS

We used a statistical analysis of 200 wind profiles in conjunction with a vertical-stack diffusion model to calculate the effective vertical diffusivities to be expected from CAT in the stratosphere. (It was also necessary to use the radar and balloon soundings of Browning for these calculations.) Our results indicate that it is likely that K_e in the stratosphere is in the 0.3 m^2/s range if the spreading of turbulent layers is taken into account. Our results seem to agree with measurements of radioactive fallout (see Junge, 1963) as well as measurements of CH_4 loss (see Wofsy and McElroy, 1973). The results are also consistent with the findings of Lilly, Waco, and Adelfang (1973), who derived vertical diffusivities from turbulence spectra observed by aircraft-borne instrumentation, and with the studies discussed by Justus (1973) for the altitude range of interest.

In this way we see that one need not resort to such mechanisms as stratospheric penetration by thunderstorms, "dumping" by global circulation to the poles, aerosol "precipitation", etc. in order to explain observed stratospheric residence times. In other words, it now appears that CAT plays the same prominent role in vertical transport in the stratosphere that "underwater CAT" plays in the World Ocean.

The next steps in this research should involve (a) a careful study of the high shears and possible instrumental effects, (b) better estimates of Δt, and (c) analysis of higher-resolution velocity profiles.

ACKNOWLEDGMENTS

We thank Prof. Mark Beran of the University of Pennsylvania and Tel Aviv University, Israel for assistance in the early part of this work. We also thank S. Zimmerman and E. Good for stimulating discussions.

REFERENCES

Atlas, D., J.I. Metcalf, J.H. Richter, and E.E. Gossard (1970), "The birth of 'CAT' and microscale turbulence," J. Atm. Sci. 27, 903-913.

Battan, L.J. (1973), *Radar Observation of the Atmosphere*, University of Chicago Press, 271.

Bretherton, F.P. (1969), "Waves and turbulence in stably stratified fluids," Radio Science 4, 1279-1287.

Browning, K.A. (1971), "Structure of the atmosphere in the vicinity of large-amplitude Kelvin-Helmholtz billows," Roy. Met. Soc. Quart. J. 97, 283-299.

Browning, K.A. and C.D. Watkins (1970), "Observations of clear air turbulence by high power radar," Nature 227, 260-263.

Businger, J.A. (1969a), "On the energy supply of clear air turbulence," in *Clear Air Turbulence and its Detection*, edited by Y.H. Pao and A. Goldburg, Plenum Press, 100-108.

Businger, J.A. (1969b), "Note on the critical Richardson number(s)," Quart. J. Roy. Met. Soc. 95, 653-654.

Dutton, J.A. (1971), "CAT aviation and atmospheric science," Rev. Geophys. 9, 613-657.

Dutton, J.A. (1973), "Recent perspectives on turbulence in the free atmosphere," in N.K. Vinnichenko, N.Z. Pinus, S.M. Shmeter, and G.N. Shur, *Turbulence in the Free Atmosphere*, Consultants Bureau, N.Y.

Garrett, C. and W. Munk (1972), "Oceanic mixing by breaking internal waves," Deep Sea Research 19 (1972), 823-832.

Gibson, C.H., G.R. Stegen, and R.B. Williams (1970), "Statistics of the fine structure of turbulent velocity and temperature fields measured at high Reynolds number," J. Fluid. Mech. 41, Part 1, 153-167.

Goldstein, S. (1931), "On the stability of superposed streams of fluids of different densities," Proc. Roy. Soc. 132, 524-548.

Hazel, P. (1972), "Numerical studies of the stability of inviscid stratified shear flows," J. Fluid Mech. **51**, Part 1, 39-61.

Hines, C.O. (1971), "Generalizations of the Richardson criterion for the onset of atmospheric turbulence," Quart. J. Roy. Met. Soc. **97**, 429-439.

Junge, C.E. (1963), *Air Chemistry and Radioactivity*, Academic Press, New York, 250.

Kelvin (Sir William Thomson) (1910), *Collected Works*, Vol. 4, 362 (orig. Phil. Mag. **42**, 1871).

Justus, C.G. (1973), "Upper atmospheric mixing by gravity waves," American Institute of Aeronautics and Astronautics Paper No. 73-495.

Korn, G.A. and T.M. Korn (1968), "Mathematical handbook for scientists and engineers," second edition, McGraw-Hill Book Co., New York, 320.

Lilly, D.K., D.E. Waco, and S.I. Adelfang (1973), "Stratospheric mixing estimated from high altitude turbulence measurements," American Institute of Aeronautics and Astronautics Paper No. 73-497.

Ludlam, F.H. (1967), "Characteristics of billow clouds and their relation to clear air turbulence," Quart. J. Roy. Met. Soc. **93**, 419-435.

Miller, R.W., R.M. Henry, and M.G. Rowe (1965), "Wind velocity profiles measured by the smoke-trail method at Wallops Island, Virginia (1959-1962)," NASA TN D-2937; see also NASA TN D-4365 (1968).

Miles, J.W. (1961), "On the stability of heterogeneous shear flows, Part I," J. Fluid Mech. **10**, 496-512.

Miles, J.W. (1963), "On the stability of heterogeneous shear flows, Part II," J. Fluid Mech. **16**, 209-227.

Monin, A.S. and A.M. Yaglom (1971), *Statistical Fluid Mechanics*, Volume 1, MIT Press, 91-92.

Rosenhead, L. (1931), "The formation of vortices from a surface of discontinuity," Proc. Roy. Soc. **134**, 170-192.

Taylor, G.I. (1931), "Effect of variation in density on the stability of superposed streams of fluid," Proc. Roy. Soc. A. **132**, 499-523.

Thorpe, S.A. (1973a), "CAT in the lab," Weather, November, 471.

Thorpe, S.A. (1973b), "Experiments on instability and turbulence in a stratified shear flow," J. Fluid Mech. **61**, Part 4, 731-751.

Turner, J.S. (1973), *Buoyancy Effects in Fluids*, Cambridge University Press, Cambridge, England.

Wofsy, S.C. and M.B. McElroy (1973), "On vertical mixing in the upper stratosphere and lower mesosphere," J. Geophys. Res. **78**, 2619-2624.

Woods, J.D. (1969), "On Richardson's number as a criterion for laminar-turbulent-laminar transition in the ocean and atmosphere," Radio Science **12**, 1289-1298.

Woods, J.D. and R.L. Wiley (1972), "Billow turbulence and ocean microstructure," Deep Sea Research and Oceanic Abst. **19**, 87-121.

DISCUSSION

REITER: You've obtained diffusion coefficients on a relatively small scale. If you include synoptic disturbances, the residence times in the lower stratosphere become shorter.

ROSENBERG: Yes, this is only the vertical diffusivity; if other processes contribute, each will have to be weighted accordingly.

VERTICAL DISPERSION NEAR 20 KM

H. PANOFSKY AND W. HECK
Pennsylvania State University
University Park, Pennsylvania

ABSTRACT: Vertical-mixing coefficients are being determined from HICAT data. Preliminary estimates of average K-values at 20 km suggest 10^2 cm^2 sec^{-1} or less. Some consequences are discussed.

Subsynoptic vertical-exchange coefficients are being derived from HICAT (high-altitude clear-air turbulence) observations, by a method similar to that used by Lilly et al. (1973), but with fewer assumptions.

The equations used are:

$$\kappa_h = \frac{-\overline{w'T'}}{\gamma_d - \gamma}$$

$$\kappa_m = \frac{-\overline{u'w'}}{\frac{\partial u}{\partial z}} = \frac{-\overline{v'w'}}{\frac{\partial v}{\partial z}}$$

where κ_h is the eddy conductivity, κ_m the eddy viscosity, w the vertical velocity, u and v the horizontal velocity components, T the temperature, γ_d the adiabatic lapse rate, and γ the prevailing lapse rate. A bar denotes an average over a turbulent patch, and a prime a deviation from the average.

The numerators are evaluated after removing the low frequencies by cross-spectral analysis in order to eliminate random effects and the influence of gravity waves.

Only a few cases have been analyzed, and these had rather strong turbulence, leading to mixing coefficients on the order of 10^4 cm^2 sec^{-1}. Since turbulence is intermittent, average subsynoptic mixing coefficients must be on the order of 10^2 cm^2 sec^{-1}. These values agree well with the estimates by Lilly et al., and are significantly lower than the total vertical coefficients inferred from total transports, which are commonly given as 5×10^3 cm^2 sec^{-1}. Therefore, the transport must be due to large-scale (synoptic) vertical motions.

This large difference between small-scale and large-scale mixing coefficients accounts for the fact that individual layers with peculiar concentrations of ozone and dust can sometimes be identified for a year. Small-scale mixing is so ineffective that the vertical width of such layers even after a year is a kilometer or less.

Therefore, it is suggested that a plume from an individual airplane track will spread very little vertically, but will broaden horizontally, primarily because of wind shear, and take on the general shape of a pancake. Other planes' exhaust plumes may be exposed to different large-scale conditions, and the pancakes may have different mean upward and downward motions. After a while, the pancakes will be torn up by horizontal shears. Still, a sounding at a given point will be characterized by minima and maxima, the distance between which is on the order of 1 km. The total thickness of the polluted air layer will be governed by the synoptic mixing coefficient, 5×10^3 cm^2/sec.

This stratified structure produced is, of course, typical for all variables in the stratosphere, and is due to the smallness of subsynoptic mixing coefficients.

REFERENCE

Lilly, D.K., D.E. Waco, and S.I. Adelfang (1973), "Stratospheric mixing estimated from high altitude turbulence measurements," AIAA paper 73-497.

DISCUSSION

BLAMONT: I think the dominant diffusion mechanism is neither small-scale turbulence nor large-scale motion, but something in between, such as gravity waves. I've seen an isentropic balloon go up and down two kilometers four times a day near the equator.

ROSENBERG: I think that the turbulence associated with thick turbulent layers can be easily measured with aircraft. On the other hand, such measurements are probably less sensitive to smaller-scale activity than the smoke-trail technique, and this may account for the difference between our estimates of effective vertical diffusivity.

(UNIDENTIFIED): We are ultimately concerned with global-scale pollution effects. Is there a sudden discontinuity in diffusion coefficient on the length scale, or is it a gradual change in magnitude?

PANOFSKY: There are two kinds of diffusion involved. Richardson diffusion is very slow. Taylor diffusion is a garden-hose effect in which successive parcels go in different directions, governed by the motions of all the different scales, and it is much faster. I think the eddy-diffusion coefficients on the global scale represent Taylor diffusion.

THE STRATOSPHERIC RESIDENCE TIME OF ODD NITROGEN AND THE EFFECT OF THE SST, STUDIED IN A TWO-DIMENSIONAL MODEL DERIVED FROM HIGH-ALTITUDE SAMPLING OF RADIOACTIVE DEBRIS

P. FABIAN* AND W.F. LIBBY
Institute of Geophysics and Planetary Physics
University of California, Los Angeles
Los Angeles, California

ABSTRACT: A two-dimensional time-dependent stratospheric model for tracer studies was developed. Various sets of data on eddy-diffusion coefficients, and on mean meridional and vertical velocities available from the literature, were introduced in turn while the model was tested against the stratospheric distribution of radioactive debris from high-yield nuclear explosions on both hemispheres.

The model which yielded the best fits of prediction to sampling data was used to assess the effect of a fleet of SST's on the stratospheric distribution of odd nitrogen, and to estimate residence times. For two extreme cases, 500 SST's equally distributed on the northern hemisphere north of 25°N and 500 SST's cruising within a latitude belt 10 degrees wide around 40°N, perturbations were studied for four flight altitudes between 18 km and 24 km.

The stratospheric residence time of odd nitrogen was estimated to be 1.5, 1.8, 2.0, and 2.3 years at 18, 20, 22, and 24 km altitude, respectively.

INTRODUCTION

Odd-nitrogen species, i.e., NO, NO_2, and HNO_3, are natural minor constituents of the atmosphere. Their global distribution, which depends on natural sources and sinks as well as on transport processes, plays an important role in the ozone photochemistry, since it is well established that oxides of nitrogen reduce ozone (Crutzen, 1971; Johnston, 1971).

In the lower stratosphere the main production of odd nitrogen most likely results from the oxidation of N_2O by O (^1D), which is a product of photodissociation of ozone by UV radiation. N_2O emanates from the soil as a product of microbiological action.

The initial product NO reacts rapidly with ozone, forming NO_2; the balance between NO and NO_2 is maintained through the photodissociation of NO_2, which yields NO and O. Moreover, hydrogen compounds convert NO_2 to nitric acid, the balance between HNO_3 and NO_2 being maintained through photodissociation of HNO_3.

According to Isaksen and Hesstvedt (1973), equilibrium times for the NO-NO_2-HNO_3 cycle increase from 1 day at 30 km to about 10 days at 15 km altitude. Thus, regarding seasonal variations of average daytime number densities of NO, NO_2, and HNO_3, one can assume photochemical equilibrium at least for altitudes above 15 km. Below about 27 km HNO_3 is the dominating component, while NO and NO_2 are more abundant above 30 km (Isaksen and Hesstvedt, 1973).

There is evidence for a minor source of odd nitrogen in polar regions. Cosmic rays at latitudes beyond 60° are a significant source of ions, and subsequently NO, at high latitudes (Warneck, 1972).

The only major sink for odd nitrogen identified so far is rainout and washout of soluble species in the troposphere.

Thus, the natural cycle of odd nitrogen in the lower atmosphere most likely consists of formation of NO (source), rapid interconversion within the NO-NO_2-HNO_3 cycle, and rainout or washout of NO_2 and HNO_3 in the troposphere (sink), in which atmospheric motions play an important role.

Since Johnston (1971) and Crutzen (1971) first pointed out that additional injection of NO by a future fleet of SST's might reduce the ozone

* P. Fabian is also with the Max Planck-Institut für Aeronomie, Lindau, West Germany.

layer, there have been several attempts to assess this effect. However, because of the complexity of the problem, the models involved were mostly confined to handling the photochemical reaction scheme, while the stratospheric dynamics was reduced to one-dimensional eddy diffusion or two-dimensional steady-state approaches (see, for instance, Hesstvedt, 1973; Isaksen and Hesstvedt, 1973; Crutzen, 1973; Johnston, 1974). On the other hand, three-dimensional dynamical models are too elaborate at present to include the complete photochemical reaction scheme (Mahlman, 1973).

Thus, the most realistic compromise at present for simulating the stratospheric distribution of various minor constituents, and its disturbance by future SST activities, is time-dependent two-dimensional models, including mean meridional circulation and eddy diffusion. However, parameterization of eddy diffusion is a crucial point, since the eddy diffusion coefficients used among the scientific community vary over wide ranges, and adjustments of theoretical predictions to observed cross-sections reveal unsatisfying arbitrariness. Fission products from nuclear explosions in the atmosphere, however, provide an excellent tool for testing various models for their capability of reproducing realistic tracer distributions in the stratosphere, since no photochemistry is involved.

We, therefore, developed a two-dimensional model and tested it against the stratospheric distribution of radioactive debris from single events of nuclear shots. We used radioactivity data from the high-altitude quarterly sampling program (HASL) along the 80-degree meridian, and applied each of the different sets of eddy diffusion coefficients and mean meridional and vertical velocities available in the literature, thus comparing model prediction and sampling data. The model yielding the best fit was used to assess the effect of a fleet of SST's on the stratospheric distribution of odd nitrogen, and to estimate residence times as a function of altitude.

Two extreme cases were studied for a fleet of 500 SST's: all aircraft equally distributed on the northern hemisphere north of 25°N, and all SST's cruising within a latitude circle 10 degrees wide around 40°N.

A TWO-DIMENSIONAL STRATOSPHERIC MODEL FOR TRACER STUDIES, DERIVED FROM RADIOACTIVE-FISSION-PRODUCT DISTRIBUTIONS

Fission Product Data

During 1967 to 1971, 10 high-yield nuclear bomb tests were performed by the Chinese (at 40°N) and French (at 22°S), causing single injections of radioactive material into the stratosphere of both hemispheres. The fission products were sampled in the stratosphere approximately every three months by the HASL program between about 70°N and 50°S along the 80°W meridian.

Eighteen two-dimensional decay-corrected cross-sections of Zr-95 (65-day half-life), sampled after the various shots, were kindly provided by K. Telegadas (1973). The activity ratio of Zr-95 to Ce-144 (285-day half-life) was used to distinguish between Chinese and French explosions' fission materials.

In some cases partial mixing occurred of debris from the northern hemisphere and that from the southern hemisphere, mainly in equatorial regions. These mixing data were not used for the tracer experiments. Thus, in some of the Zr-95 cross-sections (presented in Figures 2 through 5 as dashed lines) data gaps occur at low latitudes.

Basic Concept of the Model

The prevailing zonal motion of the atmosphere justifies the application of a two-dimensional model with meridional and vertical transports, in which quantities like mixing ratios, velocities, and eddy diffusion coefficients are zonally averaged.

The transport equation for any constituent without gravitational vertical settling is given in the form

$$\frac{\partial c}{\partial t} = -\frac{\partial vc}{\partial y} - \frac{\partial wc}{\partial z} + \frac{\tan\phi}{a}\,vc + \frac{\partial}{\partial y}\left(K_{yy}\frac{\partial c}{\partial y}\right) + \frac{\partial}{\partial y}\left(K_{yz}\frac{\partial c}{\partial z}\right) + \frac{\partial}{\partial y}(\Gamma K_{yz}c) + \frac{\partial}{\partial z}\left(K_{yz}\frac{\partial c}{\partial y}\right) + \frac{\partial}{\partial z}\left(K_{zz}\frac{\partial c}{\partial z}\right) + \frac{\partial}{\partial z}(\Gamma K_{zz}c) - \frac{\tan\phi}{a}\left[K_{yy}\frac{\partial c}{\partial y} + K_{yz}\frac{\partial c}{\partial z} + \Gamma K_{yz}c\right]$$

wherein the following notation has been used:

c = concentration of trace substance (mass per unit volume)
v = mean meridional wind velocity
w = mean vertical velocity
y = direction towards North Pole
z = vertical direction
K_{yy} = horizontal, K_{zz} = vertical, K_{yz} = anisotropic } eddy diffusion coefficients
$\Gamma = -1/\rho\,(\partial\rho/\partial z)$
ρ = air density
ϕ = geographic latitude
t = time
a = radius of the earth

The first three terms of the equation give the change in concentration due to mean meridional circulation, while the others denote the effect of large-scale eddy-diffusion processes. This equation is numerically integrated by a finite-difference scheme with specified boundary and initial conditions.

In the latitude-altitude coordinate system used, the space between North Pole and South Pole is divided into 10-degree horizontal zones. In the vertical direction the model extends from 9 km to 28 km with height increments of 1 km. The time increment ΔT for integration was chosen as 1/360 year or $\Delta T = 8.75 \times 10^4$ sec. For simplicity's sake, every month is considered to consist of 30 "days" or $30 \times 8.75 \times 10^4$ sec. The grid points of the model are given in Figure 1.

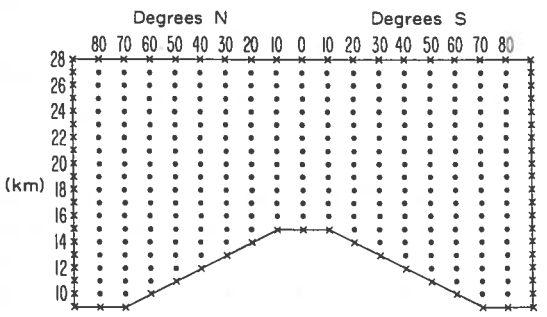

Figure 1. Schematic presentation of the grid. Inner points are symbolized by •, margin points by ×. The tropopause height varies with latitude as indicated.

Boundary Conditions

The boundary conditions depend upon which kind of tracer is to be inserted into the model. For this study we use constituents having their sink in the troposphere due to fast washout and rainout processes.

Upper boundary: We assume the mixing ratio to be constant with altitude.

Lower boundary (tropopause): Due to fast washout in the troposphere (on the order of days) of both radioactive debris and odd nitrogen, the tracer concentration at the lower margin points (Figure 1) is set at 60 percent of that at the next higher grid point after every time step, while at all tropospheric levels the concentration is kept at zero. This factor f = 60% was chosen on the basis of special experiments with the model discussed in "Model Testing" below.

Vertical boundaries (poles): The assumption of zonal symmetry requires the condition v = 0 over the poles. Furthermore, we assume that the mixing ratio is constant with latitude over the poles.

Initial Conditions

For the fission-product experiments, all of the decay-corrected Zr-95 cross-sections mentioned above were used for initial tracer distribution. By integration of the transport equation, theoretical cross-sections were obtained for the high-altitude sampling periods thereafter; they were then compared with the experimental data.

Calculation Procedure

For every month the velocities v and w and the eddy diffusion coefficients K_{yy}, K_{zz} and K_{yz}, as well as the density ρ, are computed for every grid point. A linear interpolation is used for the basic data, which are given for discrete altitudes only. For the southern hemisphere, data from the northern hemisphere are used with a time shift of 6 months, assuming hemispheric symmetry. Then for every daily time step the new tracer distribution for the inner points is computed, using a finite-difference form of the transport equation. The new values for the margin points are computed according to the boundary conditions given above.

Model Testing

The model was run with various sets of data for eddy-diffusion coefficients and mean vertical and meridional velocities, to test each set's ability to reproduce the observed stratospheric distributions.

For every comparison of theoretical and experimental tracer concentrations, a "reproducibility factor" R was computed according to the following definition: The absolute values of the differences between theoretical and sampled concentrations were summed up over all grid points where sampling data exist, and this sum was divided by the appropriate total burden of radioactivity. Thus, a model with minimal R will give the best reproducibility.

The following sets of data were used in turn:

Eddy-diffusion coefficients after:
- Reed and German (1965)
- Gudiksen, Fairhall, and Reed (1968)
- Luther (1973)
- Hesstvedt (1973).

Mean meridional and vertical velocities after:
- Murgatroyd and Singleton (1961)
- Jessen (1973)
- Gudiksen, Fairhall, and Reed (1968)
- Hesstvedt (1973).

Without exception all tracer experiments led to lowest values of R, and thus best reproducibility, when eddy-diffusion coefficients given by Luther (1973) were combined with velocity data after Gudiksen et al. (1968).

As the results in Figures 2 through 5 show, the agreement between theoretical and observational data was so good that this combination was used for all further experiments without variation of any of these basic parameters.

Additional tests were performed with the lower boundary condition. The factor f, defined earlier, was varied between 0.0 and 0.9 to adjust the model to a realistic decrease of the total radioactive burden with time. It turned out that for $f = 0.6$ the time constant for this decrease in the northern hemisphere was 1.15 years, which agrees well with earlier estimates based on Sr-90 fallout (Fabian et al., 1968). Moreover, in most experiments the reproducibility factor R reached its lowest values for $f = 0.6$. We, therefore, adopted $f = 0.6$ for further experiments.

Results

A total of 15 independent experiments were performed using initial radioactivity distributions from the different high-altitude sampling flights. Every experiment was run until the distribution of debris was disturbed by the following nuclear blast. The longest run was possible with the debris from the June 17, 1967, Chinese test. Using the fission-product distribution collected between October 7 and November 9, 1967 as the initial distribution, the model could be run as long as 339 days. At four sampling times (Jan. 8-21, April 1-6, May 30-June 15, Sept. 28-Oct. 6, 1968) data computed by the model were compared with the experimental cross-sections.

As Telegadas (1973) has already pointed out, it usually takes until about two months after the nuclear explosions for the fission products to become zonally mixed. This became most evident after the Chinese October 14, 1970 test. Half a month later (Nov. 2-6, 1970), radioactive debris from this shot could be detected only in the very northern portion of the sampling corridor; all other samples originated from previous tests.

While this cross-section could not be used as the initial distribution for modeling this Chinese debris (in Figure 4, C and D, only debris from the French May 31 and July 4, 1970 shots was used) the sampling 3 1/2 months later (February 22-27, 1971) gave a perfect initial distribution (Figures 5A and B).

A part of the results of our modeling experiments is demonstrated in Figures 2 through 5. Isolines of the Zr-95 concentration (units: pCi/standard cubic meter (SCM)) are plotted in a latitude-altitude grid, the theoretical predictions from the model (solid lines) being compared with the high-altitude sampling data (dashed lines). The altitudes of highest concentration, symbolized by crosses and dots for theoretical and experimental data respectively, are also given.

Figure 2 shows experiments with the June 17, 1967 Chinese test (3 MT yield). A, B, and C are based upon the initial distribution from the January 8-21, 1968 sampling, about seven

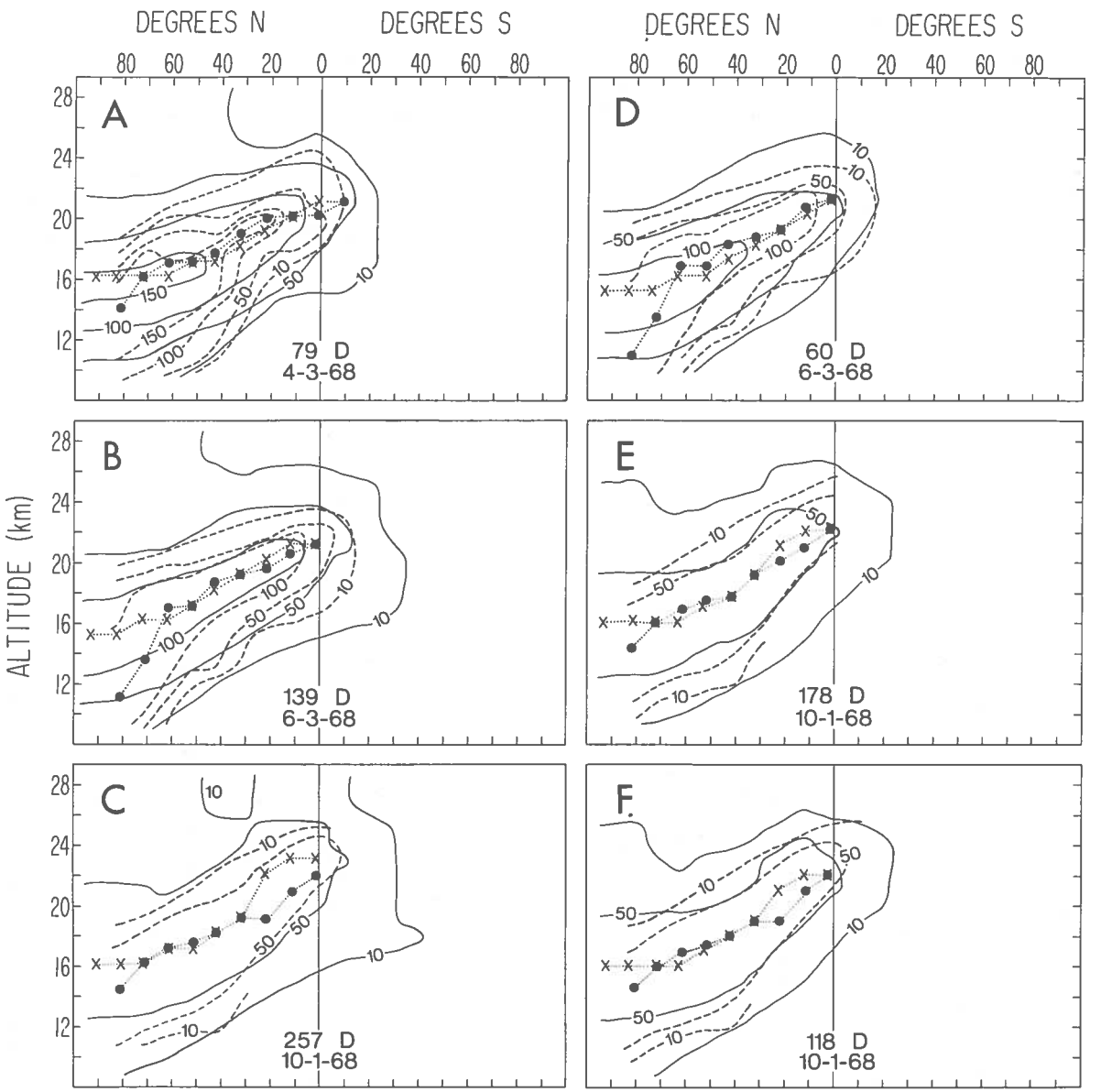

Figure 2. June 17, 1967 nuclear test, northern hemisphere (N). Distribution of Zr-95 concentration (pCi/SCM) corrected for radioactive decay to June 17, 1967. Solid lines, theoretical prediction from model; dashed lines, data from high-altitude sampling program. Altitudes of maximal concentration are indicated by X and • for theoretical and experimental data respectively. The number of days given in each graph corresponds to the integration time of the model after the respective initial distribution. Initial distributions are Jan. 8-21, 1968 (7 mos. after shot) for A, B, C; April 1-6, 1968 (9 1/2 mos. after) for D, E; and May 30-June 15, 1968 (12 mos. after) for F. (See text for more details.)

months after the shot; they compare predicted and measured tracer concentrations during the April 1-6 (A), May 30-June 15 (B), and September 28-October 6 (C) 1968 high-altitude samplings. D and E are based upon the initial distribution from April 1-6, and compare model predictions with the samples taken during the May 30-June 15 (D) and September 28-October 6, 1968 (E) flights. F compares the model prediction based on the initial distribution from

May 30-June 15, 1968 with sampling data from September 28-October 6, 1968.

On August 24 and September 9, 1968, the French detonated two bombs with a total yield of 4 MT. Debris from these shots penetrated into the northern hemisphere and mixed with part of the debris from the Chinese June 17, 1967 explosion. Thus, for the experiments given in C, E, and F no comparison between model prediction and sampling data is possible for latitudes south of 30°N.

Figures 3 A, B, and C show results based on data from the French August 24 and September 9, 1968 nuclear tests, collected during the September 28-October 6, 1968 sampling. For the sampling periods February 3-19 (A), April 6-9

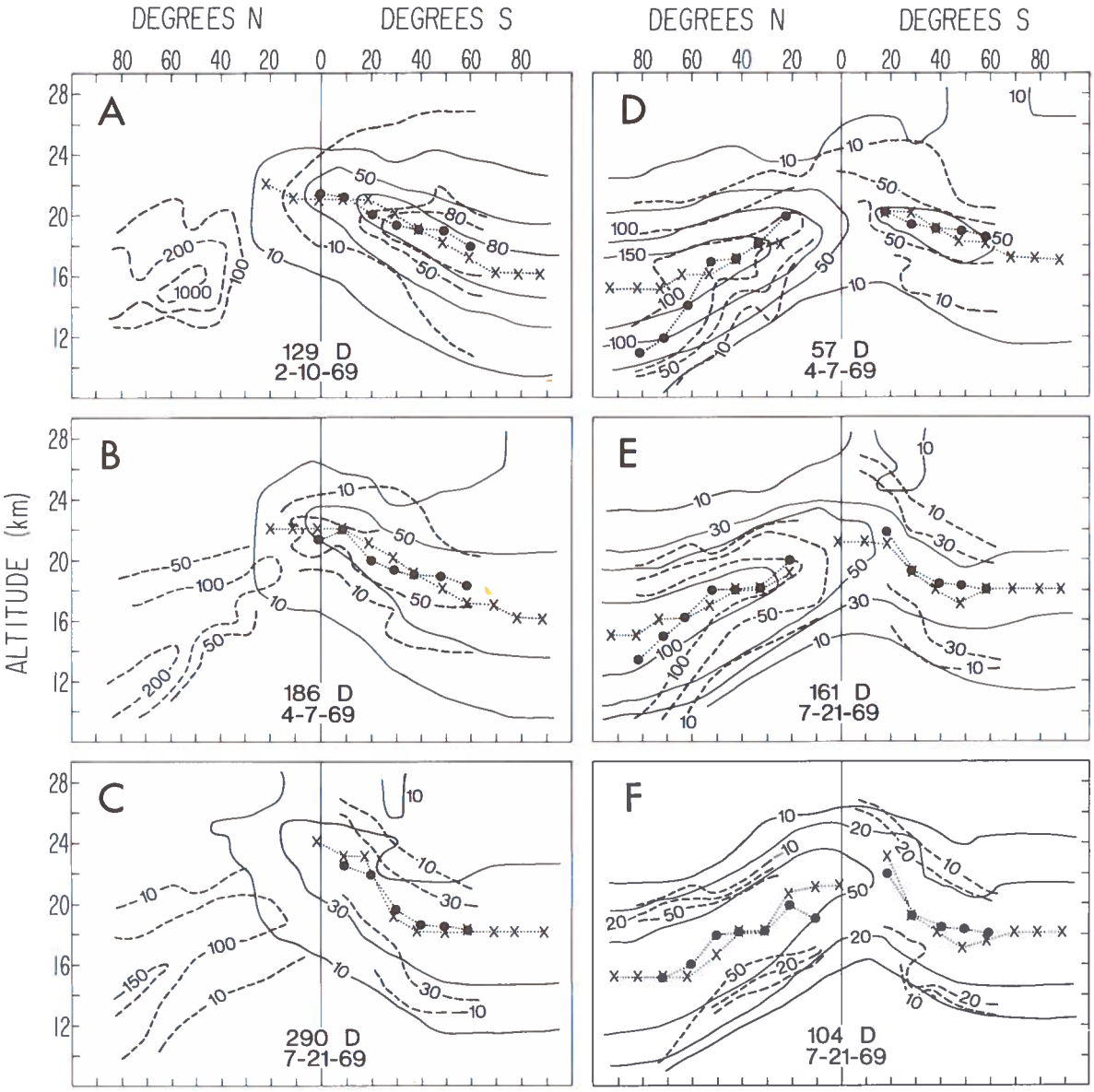

Figure 3. Aug. 24, Sept. 9 (S), and Dec. 27, 1968 (N) nuclear tests. Distribution of Zr-95 concentration (pCi/SCM) corrected for radioactive decay to Dec. 27, 1968. Solid lines, model prediction; dashed lines, HASL data. Altitudes of maximal concentration: X (theoretical) and • (experimental). Number of days given is model integration time after initial distribution. Initial distributions are Sept. 28-Oct. 6, 1968 (1 mo. after shot) for A, B, C; Feb. 3-19, 1969 (1 1/2 & 5 1/2 mos. after, respectively) for D, E; April 6-9, 1969 (3 & 7 mos. after, respectively) for F.

(B), and July 14-29, 1969 (C), predicted cross-sections were compared with observed data. Debris from another Chinese 3-MT test on December 27, 1968 mixed somewhat with the French debris in the equatorial zone. Thus, in the tropics, some of the dashed isolines are interrupted in A, B, and C. Figures 3 D, E, F show results from fission products injected into both hemispheres by the French shots of August 24 and September 9 and the Chinese shot of December 27, 1968. Based upon the initial distribution from February 3-19, 1969 samples, the predicted and measured cross-sections were compared for the April 6-9 (D) and July 14-29, 1969 (E) flight periods. F gives data from the July 14-29, 1969 sampling based on the initial distribution from April 6-9, 1969. Again, because of partial mixing of fission products from both hemispheres, some of the dashed isolines are interrupted in the tropics in D, E, and F.

Figures 4 and 5 show experiments with the fission products originating from the 1970 nuclear explosions. Based upon the initial distribution of debris from the French May 31 and July 4, 1970 shots (total yield 4 MT) collected during the August 17-22, 1970 period, Figures 4 A and B permit the comparison of predicted and sampled cross-sections for the November 2-6, 1970 (A) and February 22-27, 1971 (B) high-altitude flight programs.

As mentioned earlier, during the November 2-6, 1970 sampling time only a very small fraction of the debris produced by the Chinese October 14, 1970 shot (3 MT) had arrived within the flight corridor. Thus, for the experiments shown in Figures 4 C and D, only fission products from the earlier French tests were taken as initial distribution for the November 2-6, 1970 period. Figures 4 C and D give a comparison of predicted and sampled cross-sections for the following

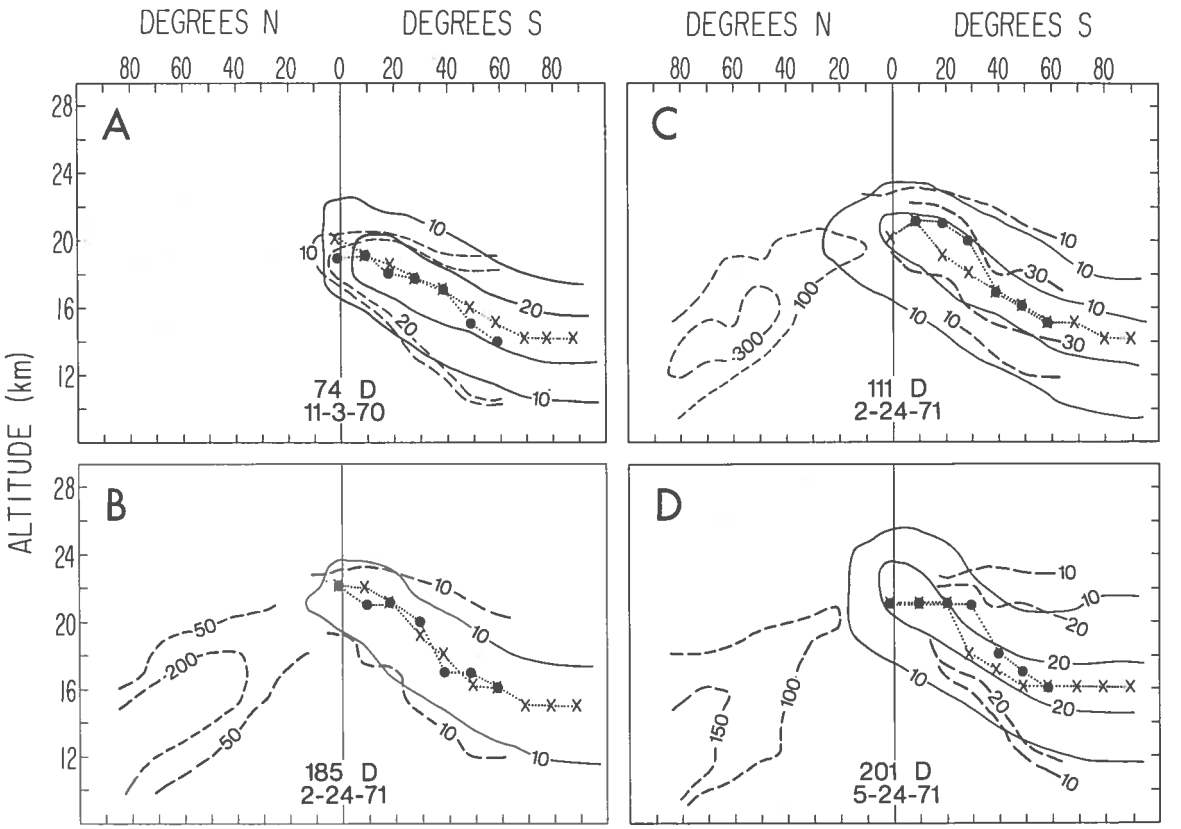

Figure 4. May 31, July 4 (S), and Oct. 14, 1970 (N) nuclear tests. Distribution of Zr-95 concentration (pCi/SCM) corrected for radioactive decay to Oct. 14, 1970. Solid lines, model prediction; dashed lines, HASL data. Altitudes of maximal concentration: X (theoretical) and • (experimental). Number of days given is model integration time after initial distribution. Initial distributions are Aug. 17-22, 1970 (2 mos. after shots) for A, B; Nov. 2-6, 1970 (4 1/2 mos. after) for C, D.

February 22-27 and May 22-28, 1971 sampling periods, respectively.

In Figure 5, starting with the initial distribution from the February 22-27, 1971 sampling program, debris from the Chinese October 14, 1970 test was also included. Figures 5 A and B give a comparison of model prediction and sampling during May 22-28 and July 19-23, 1971 respectively. Based on the initial distribution from May 22-28, 1971 sampling, Figures 5 C and D give results from the July 19-23 and October 4-6, 1971 periods, respectively.

Debris from another French explosion on June 13, 1971 (1 MT), together with the

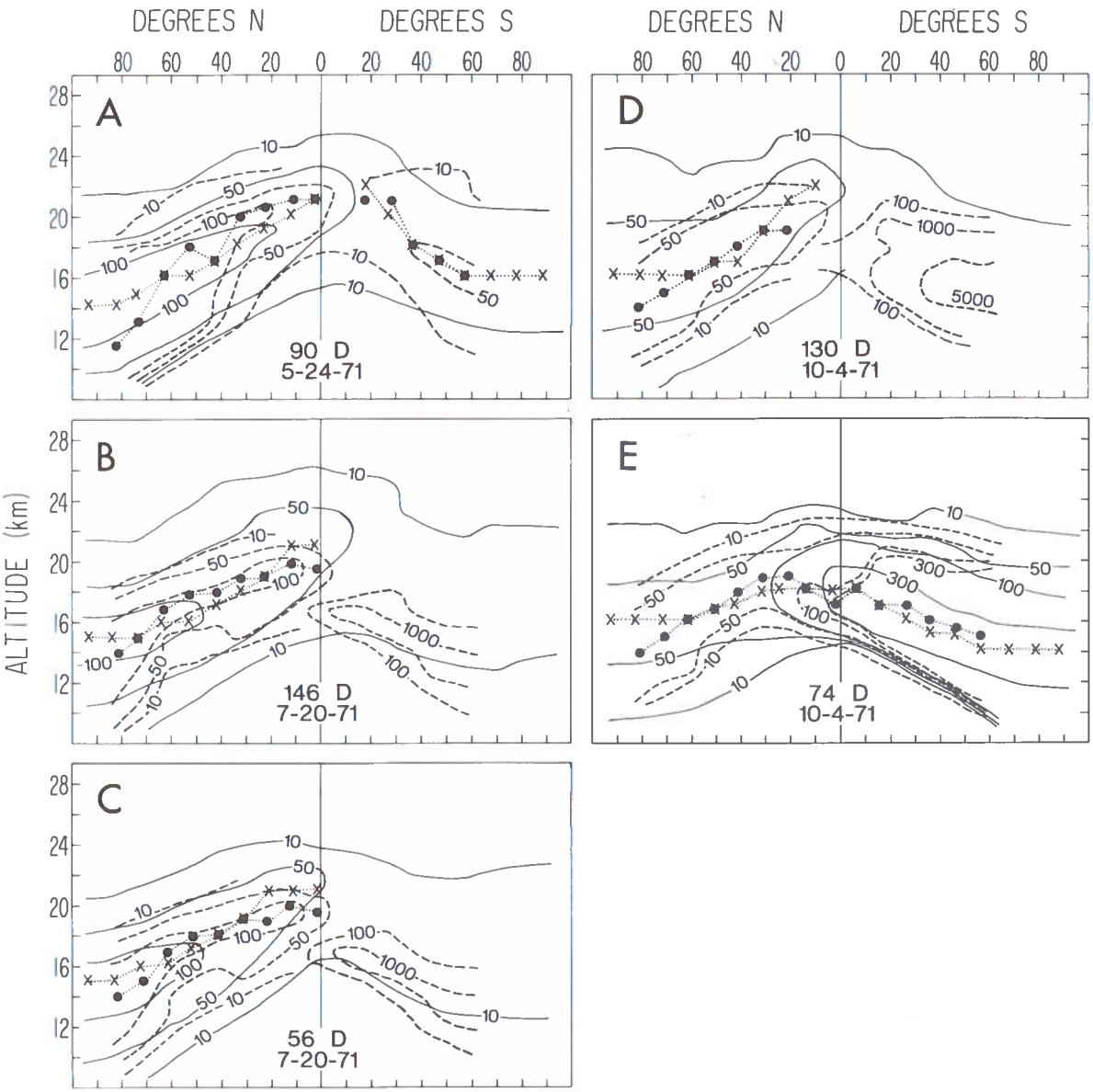

Figure 5. May 31, July 4 (S), Oct. 14, 1970 (N) and June 13, 1971 (S) nuclear tests. Distribution of Zr-95 concentration (pCi/SCM) corrected for radioactive decay to Oct. 14, 1970. Solid lines, model prediction; dashed lines, HASL data. Altitudes of maximal concentration: X (theoretical) and • (experimental). Number of days given is model integration time after initial distribution. Initial distributions are Feb. 22-27, 1971 (4 & 8 mos. after shots, respectively) for A, B; May 22-28, 1971 (7 & 11 mos. after, respectively) for C, D; July 19-23, 1971 (9 & 1 mos. after, respectively) for E.

remainders from the Chinese October 14, 1970 shot, dominated during the July 19-23, 1971 sampling period, which is taken as the initial distribution for the last experiment. Figure 5 E gives predicted and measured cross-sections for the last sampling period of this series, October 4-6, 1971. As mentioned earlier, sampling data which were classified as mixtures from different nuclear explosions were omitted.

The results show that the model described gives excellent agreement between predicted and sampled cross-sections of nuclear debris. Despite the fact that the sampling corridor does not cover the entire latitude range, especially on the southern hemisphere, and although many experimental data were omitted because of partial interference of debris from the various shots, the theoretical and sampling data fit well together, proving the model to be capable of simulating the stratospheric transport processes.

Therefore, we did not attempt to further improve the reproducibility by varying the basic parameters like eddy-diffusion coefficients or mean velocities.

THE EFFECT OF A FLEET OF SST'S ON THE STRATOSPHERIC DISTRIBUTION OF ODD NITROGEN

Basic Considerations

As mentioned in the introduction, the processes removing odd nitrogen from the atmosphere are the same that remove nuclear debris: rainout and washout in the troposphere. It is therefore reasonable to apply our stratospheric model in assessing the effect of a future fleet of SST's on the distribution of odd nitrogen. Of course, additional source terms have to be introduced in the transport equation given earlier for both the natural production of NO and the NO injected by the SST fleet.

Besides intermediate products like N_2O_5 which are not considered here, all species involved in the $NO\text{-}NO_2\text{-}HNO_3$ cycle contain only one atom of nitrogen. Thus no further photochemistry has to be included in the model when only the total odd-nitrogen distribution is concerned. Moreover, since we assume that the SST constitutes a small, continuous, constant source of NO, equilibrium can also be assumed for the disturbed odd-nitrogen cycle.

The rates of NO production from oxidation of N_2O were computed by Isaksen and Hesstvedt (1973) in a one-dimensional model with eddy diffusion. These production rates, plotted in Figure 6 as a function of altitude for different latitudes, were used for our computation. The rates of NO production by cosmic rays were taken from Warneck (1972). For the NO injection caused by a fleet of SST's, the following assumptions were made: In accordance with Johnston (1974) we consider 500 U.S.-type SST's operating for 7 hours per day, which would correspond to an average NO emission rate of 1.5×10^8 molec cm^{-2} sec^{-1} if all aircraft were equally distributed over the entire globe. (This will probably not be the case, as most flight routes are concentrated in the northern hemisphere and particularly on the transatlantic routes.)

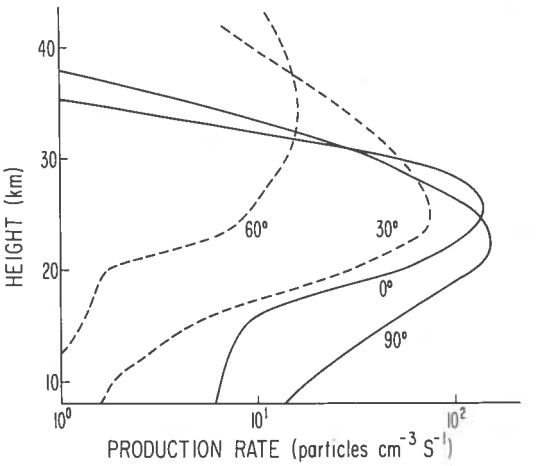

Figure 6. Rate of production of nitric oxide due to the reaction $N_2 + O(^1D) \rightarrow 2\,NO$ (after Isaksen and Hesstvedt, 1973). The rate for 90° latitude is for the summer hemisphere; the rates for 60° and 30° are for the winter hemisphere.

We therefore made experiments with two extreme situations: all 500 SST's equally distributed over the northern hemisphere north of 25°N, and all 500 SST's concentrated within a latitude belt 10 degrees wide around 40°N. The corresponding injection rates for these experiments are 5.2×10^8 molec cm^{-2} sec^{-1} and 2.3×10^9 molec cm^{-2} sec^{-1}. For both experiments, the flight level of the SST was varied between 18 km and 24 km.

Results

For each of the different flight configurations, the transport equation (with the additional source terms) was integrated, starting from an initial odd-nitrogen distribution of 10 ppb by volume throughout the stratosphere. The model was run simultaneously for both natural and natural-plus-SST sources, computing at every time step the increase of odd-nitrogen mixing ratio caused by the SST. Thus the choice of the natural NO production rate was not critical for this study, since it was merely used to produce a reference distribution of odd nitrogen which is "not too far from reality". (It turned out that these natural odd-nitrogen mixing ratios varied between 1 and 15 ppb by volume, depending on latitude and altitude.)

After three years of integration time, a quasi-stationary state was reached, and the perturbations caused by the SST's revealed only seasonal variations thereafter. The highest disturbances occur in late summer, due to the weaker vertical exchange, while in late winter the disturbances reach their annual minimum. For these extreme situations, Figures 7 and 8 show the results of the study for the two different flight configurations.

In Figure 7, all 500 SST's are equally distributed on the northern hemisphere north of 25°N. The flight altitudes are 18 km (A and E), 20 km (B and F), 22 km (C and G), and 24 km (D and H). The left half corresponds to late winter (end of February), the right half to late summer (end of August).

The influence of the flight level is quite evident. The increase in odd-nitrogen mixing ratio caused by the SST is approximately doubled for every 2 km of increase in flight altitude.

The most severe disturbance of the ozone layer would occur in the "photochemical region" above 25 km. Here the mean increase of odd nitrogen caused by 500 SST's would amount to 2, 4, 8, and 15 ppb by volume for 18, 20, 22, and 24 km flight altitudes, respectively, with only slight seasonal variations, which are more pronounced in the lower stratosphere.

Figure 8 shows analogous results for the other extreme flight configuration, all 500 SST's concentrated around 40°N. As in the previous experiment, every 2-km increase in flight altitude approximately doubles the disturbance. However, the amount of the disturbance comes out smaller than in Figure 7, for which all SST's were equally distributed north of 25°N. Only locally along the flight route does concentrating all planes around 40° cause higher disturbances in summer. The increase of odd-nitrogen mixing ratio in the "photochemical region" above 25 km amounts to about 1.5, 2.5, 5, and 10 ppb by volume for 18, 20, 22, and 24 km flight altitudes, respectively.

For the natural mixing ratios of odd nitrogen in the stratosphere, different values are given in the literature, ranging between 1 ppb and 20 ppb. The above-given increases caused by a fleet of 500 SST's are severe compared to the natural background.

However, the emission rate used for our study must be considered as an upper limit. Efforts are underway to develop engines with reduced NO emission, and a reduction by a factor of 10 or even more seems to be feasible. Thus, the disturbances given in Figures 7 and 8 will be reduced by this factor or any other which might arise from different flight conditions.

Stratospheric Residence Times of Odd Nitrogen and the NO Injection by Nuclear Explosions

Mean stratospheric residence times were estimated from the previous experiments by removing all SST's from the atmosphere after the quasi-stationary state had been reached. From the decrease of the disturbances at different altitudes, mean residence times were computed, averaging over the latitudes 20° through 80°N. The residence times defined this way turned out to be 1.5, 1.8, 2.0, and 2.3 years for 18, 20, 22, and 24 km altitudes, respectively.

There have been heated discussions about whether or not the intense nuclear explosions of 1961-62 constitute a sufficient experiment against which photochemical theories can be tested and extrapolations of the environmental impact of future SST activities can be made (see, for instance, Foley and Ruderman, 1973; Johnston et al., 1973; Goldsmith et al., 1973).

During the 1961-62 peak testing period, something on the order of 10^{34} molecules of nitric oxide were injected into the stratosphere (Johnston et al., 1973), which is equivalent to the emissions of 500 U.S.-type SST's during one

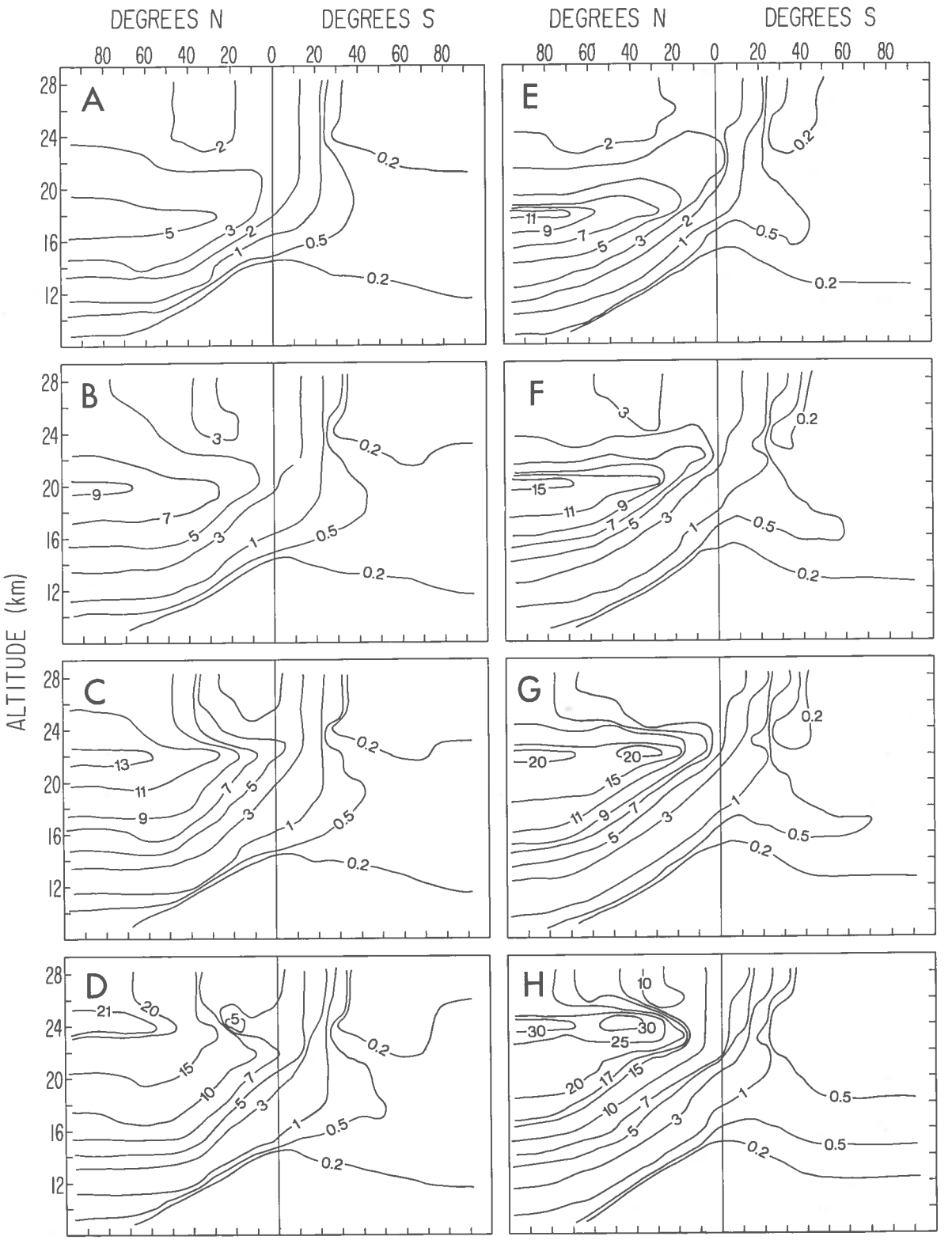

Figure 7. Increase in odd-nitrogen mixing ratio caused by a fleet of 500 SST's, equally distributed over the northern hemisphere north of 25°N, for various flight levels. Units: ppb by volume. Flight levels: 18 km for A and E, 20 km for B and F, 22 km for C and G, and 24 km for D and H. Seasons: End of Feb. for A through D, end of Aug. for E through H.

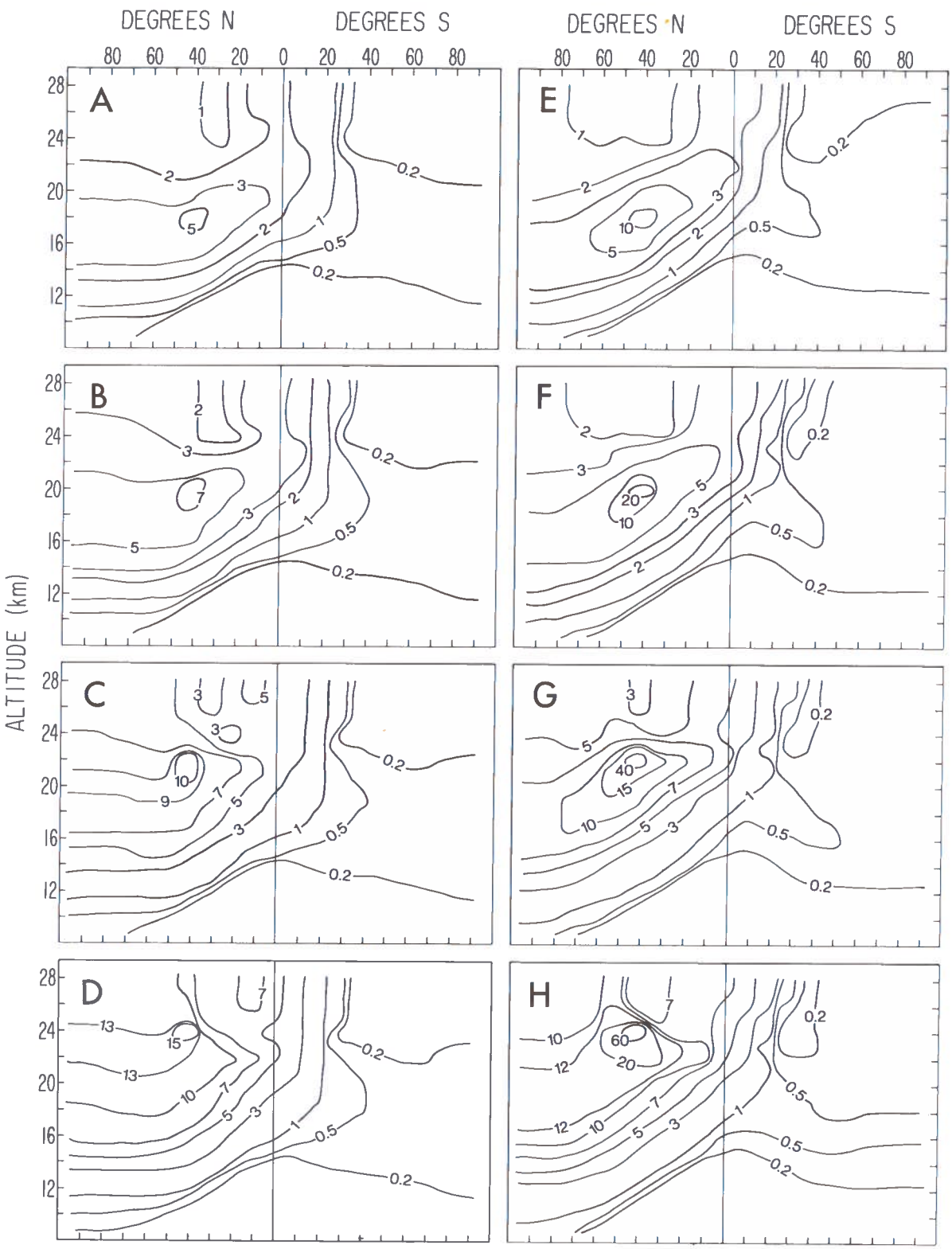

Figure 8. Increase in odd-nitrogen mixing ratio caused by a fleet of 500 SST's, concentrated within a 10-degree-wide flight corridor around 40°N, for various flight levels. Units: ppb by volume. Flight levels: 18 km for A and E, 20 km for B and F, 22 km for C and G, and 24 km for D and H. Seasons: End of Feb. for A through D, end of Aug. for E through H.

year of operation. However, most of the bomb-produced NO was injected into the lower stratosphere and at high latitudes, thus affecting the ozone layer less. Moreover, only a few ozone stations were operating before 1960 to detect an ozone decrease, if there was any.

While Foley and Ruderman (1973) and Goldsmith et al. (1973) claim that there was no effect on the ozone layer at all, Johnston et al. (1973) and Johnston (1974) give evidence for a slight ozone decrease between 1960 and 1962. However, the contention that the well-established ozone increase between 1962 and 1970 in the northern hemisphere (Komhyr et al., 1971) is due to the stratosphere's returning to normal after the addition of nitric oxide by bombs during the test period prior to 1962, which would require stratospheric residence times of odd nitrogen on the order of 8 to 10 years, can be ruled out. According to our estimates, residence times as long as this are very unlikely to occur.

ACKNOWLEDGMENTS

This work has been supported in part by the Climatic Impact Assessment Program, Contract DOT OS-30027, Office of the Secretary, United States Department of Transportation.

REFERENCES

Crutzen, P.J. (1971), "Ozone production rates in an oxygen-hydrogen-nitrogen oxide atmosphere," J. Geophys. Res. **76**, 7311-7327.

Crutzen, P.J. (1973), "A discussion of the chemistry of some minor constituents in the stratosphere and troposphere," Report AP-12, Inst. of Meteorology, University of Stockholm.

Fabian, P., W.F. Libby, and C.E. Palmer (1968), "Stratospheric residence time and interhemispheric mixing of Strontium-90 from fallout in rain," J. Geophys. Res. **73**, 3611-3616.

Foley, H.M. and M.A. Ruderman (1973), "Stratospheric NO production from past nuclear explosions," J. Geophys. Res. **78**, 4441-4450.

Goldsmith, P., A.F. Tuck, J.S. Foot, E.L. Simmons, and R.L. Newson (1973), "Nitrogen oxides, nuclear weapon testing, Concorde and stratospheric ozone," Nature **244**, 545-551.

Gudiksen, P.H., A.W. Fairhall, and R.J. Reed (1968), "Roles of mean meridional circulation and eddy diffusion in the transport of trace substances in the lower stratosphere," J. Geophys. Res. **73**, 4461-4473.

Hesstvedt, E. (1973), "Effect of supersonic transport upon the ozone layer, studied in a two-dimensional photochemical model with transport," presented at AGARD meeting, London.

Isaksen, S.A. and E. Hesstvedt (1973), "The distribution of odd nitrogen in the lower stratosphere and possible perturbations caused by stratospheric air transport," preprint.

Jessen, W. (1973), "Ein Rechenmodell zur Beschreibung des stratosphärischen Ozonkreislaufs," Mitteilungen aus dem Max Planck-Institut für Aeronomie, Report No. **50** (Springer-Verlag, Berlin).

Johnston, H. (1971), "Reduction of stratospheric ozone by nitrogen oxide catalysts from supersonic transport exhaust," Science **173**, 511-522.

Johnston, H., G. Whitten, and J. Birks (1973), "Effect of nuclear explosions on stratospheric nitric oxide and ozone," J. Geophys. Res. **78**, 6107-6135.

Johnston, H. (1974a), "Reduction of stratospheric ozone by supersonic transports," preprint.

Johnston, H. (1974b), "Photochemistry in the stratosphere – with applications to supersonic transports," preprint (Astronautica Acta).

Komhyr, W.D., F.W. Barrett, G. Slocum, and H.K. Weickmann (1971), "Atmospheric total ozone increase during the 1960's," Nature **232**, 390-391.

Luther, F.M. (1973), "Monthly mean values of eddy diffusion coefficients in the lower stratosphere," Lawrence Livermore Laboratory, preprint.

Mahlman, J.D. (1973), "A three-dimensional stratospheric point-source tracer experiment and its implications for dispersion of effluent from a fleet of supersonic aircraft," AIAA Paper No. 73-528.

McConnell, J.C. and M.B. McElroy (1973), "Odd nitrogen in the atmosphere," J. Atmos. Sci. **30**, 1465-1479.

Murgatroyd, R.J. and F. Singleton (1961), "Possible meridional circulations in the stratosphere and mesosphere," Quart. J. Roy. Met. Soc. **87**, 125-135.

Reed, R.J. and K.E. German (1965), "A contribution to the problem of stratospheric diffusion by large scale mixing," Mon. Wea. Rev. **93**, 313-321.

Telegadas, K. (1973), "The radioactivity distribution in the stratosphere from high yield Chinese and French nuclear tests (1967-1970)," manuscript.

Warneck, P. (1972), "Cosmic radiation as a source of odd nitrogen in the stratosphere," J. Geophys. Res. **77**, 6589-6591.

DISCUSSION

GREENSTONE: You pointed out that residence time varies with altitude, but didn't mention whether it varies with latitude.

FABIAN: It does vary slightly with latitude, but I hesitate to go into specifics because the residence times are only rough estimates, critically dependent on certain definitions.

GOLDBURG: What are the values of the eddy-diffusion coefficients you used?

FABIAN: They are in between the Reed and German data and those of Gudiksen, Fairhall, and Reed.

SCHAINKER: What are the values of the reproducibility factors for the data you used in validating the model of nuclear data?

FABIAN: They vary between 20 and 100 percent, depending on the data set.

THE REMOTE MEASUREMENT OF TRACE ATMOSPHERIC SPECIES BY CORRELATION INTERFEROMETRY

HAROLD W. GOLDSTEIN AND M.H. BORTNER
Space Sciences Laboratory
General Electric Company
Philadelphia, Pennsylvania

ABSTRACT: A correlation interferometer has been developed for the measurement of carbon monoxide and methane at 2.35 μm in the troposphere and in the stratosphere. This instrument has been used in laboratory tests, solar-looking outdoor tests, and downward-looking airplane-based tests. The aircraft tests were flown on a Falcon provided by the Canada Centre for Remote Sensing over both polluted and unpolluted regions of North America. The results of these various tests are discussed and compared with simultaneous measurements made by other techniques. Since the results obtained for carbon monoxide and methane were good, a study was undertaken to investigate the feasibility of measuring stratospheric nitric oxide and sulfur dioxide using the correlation-interferometric technique. It has been determined that an instrument having a filter centered at 1900 cm^{-1} with a half-width of 20 cm^{-1} at 50% transmission would have the sensitivity necessary to measure nitric oxide concentrations of 0.4 and 0.04 ppb with measurement errors of less than 10 and 50% respectively. In the case of sulfur dioxide, the correlation interferometer would have a filter centered at 1370 cm^{-1} with a half-width of 20 cm^{-1} at 50% transmission. This instrument would have sufficient sensitivity to measure 0.04 and 0.009 ppb of sulfur dioxide with errors of 10 and 50% respectively.

A correlation interferometer has been developed which measures the concentration of carbon monoxide in the troposphere and in the stratosphere using absorption in the 2.35-μm region. Methane is also measured simultaneously. On the basis of these positive results, a study was undertaken to determine the feasibility of using this instrument for measuring a large variety of atmospheric trace gases. This study will be discussed in detail after a brief description of the instrument and presentation of the results of downward-looking measurements made on flights aboard a Falcon jet, and of the results of sunward-looking measurements made from the ground.

The 2.35-μm band of CO was chosen because in the non-thermal infrared region most of the upwelling radiation observed is sunlight reflected from the earth's surface. Thermal emission from absorbing molecules is negligible, and thus independent of altitude, so the interpretation of the data is simpler than in the thermal IR, For sunward-looking measurements, on the other hand, this advantage is not as useful. But since it is not always possible to find suitable absorption bands in the non-thermal IR, thermal IR bands must sometimes be used. This is the case for three of the gases examined in the multi-gas analysis given below.

The heart of the interferometer is shown schematically in Figure 1. Note that both the mirrors in the instrument are fixed, and variation in the path-length difference is achieved by the oscillation of the compensating plate. For the results given below, a 13° oscillation was used, giving a path-length difference of 2.7 to 3.95 mm. A spectral filter having a half-width at half-height of approximately 10 cm^{-1} is used.

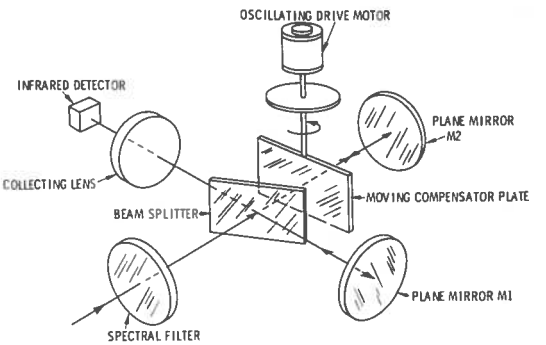

Figure 1. COPE correlation interferometer.

Figure 2 shows the spectrum of carbon monoxide in this region and the corresponding interferogram. Since the spectral lines have a

separation of about 3 cm^{-1}, the interferogram has a peak at 1/3 cm^{-1}, or about 3 mm. The correlation interferometer uses only this section of the interferogram, since that is where most of the information on CO is contained (2.7 to 3.95 mm). The instrument operates directly on this section rather than transforming it into a spectrum. (Indeed, a spectrum obtained from the transformation of a portion of an interferogram would have little meaning.)

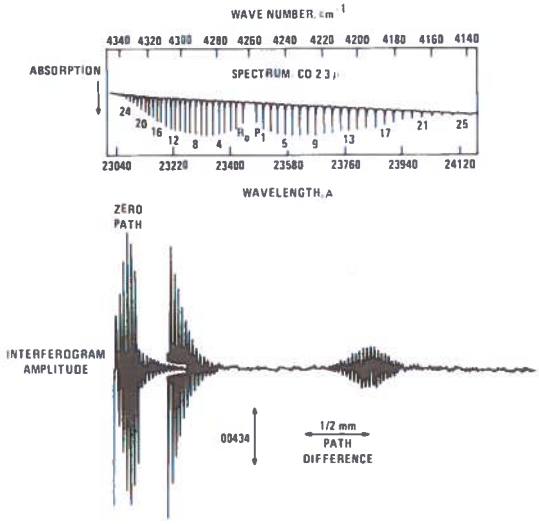

Figure 2. Interferogram and spectrum of CO.

The inside of the actual instrument is shown in Figure 3. The oscillating plate can be seen below the drive motor. The frame is made of Corning ULE material, which has the lowest expansion coefficient of any construction material. A CO-containing standard cell with its own light source is used to test for any instrument changes. The instrument is shown on the Falcon mounted over a downward-looking window in Figure 4.

During aircraft flights, data were recorded both on a magnetic-tape recorder and with a NOVA mini-computer with a teletypewriter. The latter provides a method for checking the instrument and data during flight. The magnetic-tape recorder permits other data to be recorded simultaneously with the interferogram.

Flights were made over Ontario in May 1973, and the results given in Table 1 are reasonable. This was the first successful use of the correlation interferometer on an airborne platform.

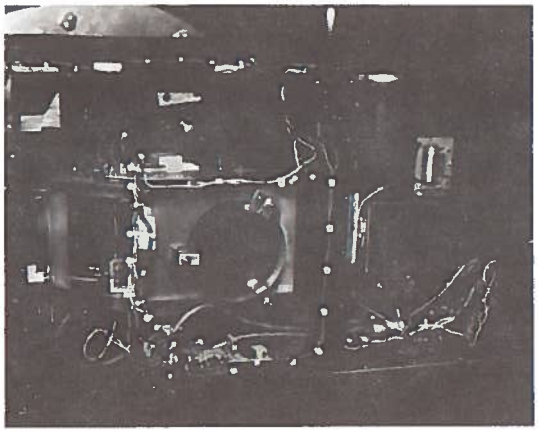

Figure 3. The engineering model correlation interferometer.

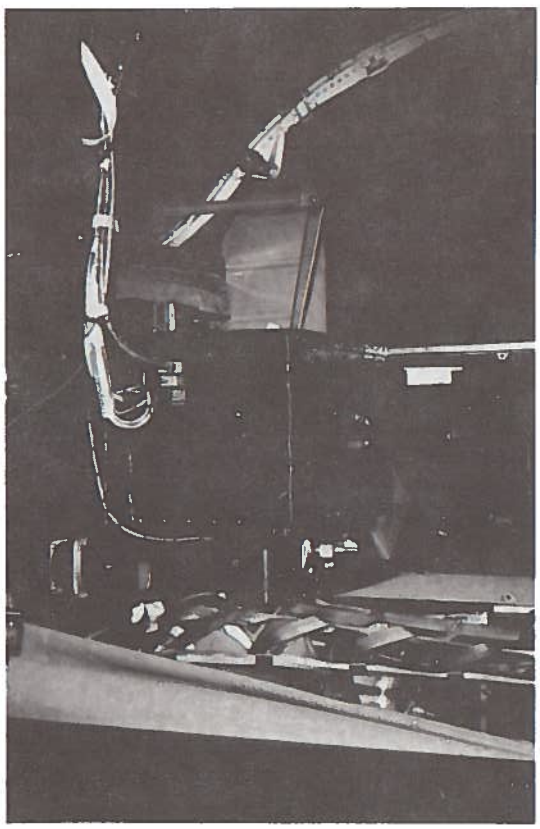

Figure 4. The correlation interferometer on the Falcon.

Measurements were also made outside our laboratory in Valley Forge, Pennsylvania. Simultaneously, similar measurements were made with an 0.1-cm^{-1}-resolution Idealab IF-6 interferometer-spectrometer at 4.6 μm. In addition, cells

Table 1. Flight Measurements of CO and CH_4 Over Canada, May 24, 1973

Location	CO atm-cm	CO ppm	CH_4 atm-cm	CH_4 ppm	Condition
Petawawa	0.074		1.50		80% cloud cover*
North Bay	0.176		1.45		40% cloud cover
Sudbury	0.216	0.141	1.43	0.84	10% cloud cover
Georgian Bay	0.091	0.060	1.09	0.71	Over water
Owen Sound	0.275	0.180	1.63	1.07	
Perth	0.148	0.094	1.62	1.03	
Cornwall	0.486	0.307	2.53	1.59	
Montreal area	0.479	0.296	2.08	1.28	Some water
Ottawa area	0.149	0.104	1.38	0.96	Descending
Ottawa	0.389	0.288	1.72	1.27	
Alfred	0.431	0.315	1.63	1.19	

*Clouds at 8000 ft.

containing various amounts of carbon monoxide could be placed in the path. Results for CO are shown in Table 2. Similar results for CH_4 are shown in Table 3. The accuracies appear to be approximately 10% for CO and 5% for CH_4.

Table 2. Corroborative Measurements of Carbon Monoxide. Solar-Looking Experiment, June 14-15, 1973

Actual CO (atm-cm)	CO by Interferometer (atm-cm)
0.082 ± 0.020	0.082, 0.108
0.084 ± 0.020	0.084
0.085 ± 0.020	0.049, 0.085
0.088 ± 0.020	0.076
0.095 ± 0.020	0.124, 0.144
0.100 ± 0.023	0.063, 0.100
0.122 ± 0.033	0.112
0.124 ± 0.033	0.156
0.155 ± 0.040	0.167
0.202 ± 0.045	0.260
0.220 ± 0.045	0.265
0.267 ± 0.045	0.235, 0.250
0.583 ± 0.020	0.552
0.584 ± 0.020	0.591
0.593 ± 0.020	0.558, 0.616
0.605 ± 0.023	0.620
0.630 ± 0.035	0.680
0.667 ± 0.044	0.658, 0.681
0.682 ± 0.045	0.657
1.08 ± 0.016	0.991
1.09 ± 0.016	1.06, 1.06
1.58 ± 0.020	1.56, 1.57, 1.57

In order to determine the detectability of a number of atmospheric trace gases (both naturally-occurring and pollutant) in situations simulating their optical thicknesses in the atmosphere, a systematic study was carried out which

Table 3. Corroborative Measurements of Methane. Solar-Looking Experiment, June 14-15, 1973

Actual CH_4 (atm-cm)	CH_4 by Correlation Interferometer (atm-cm)
1.02 ± 0.16	0.93, 1.02, 1.03, 1.07, 1.11
1.09 ± 0.18	0.87, 0.91
1.34 ± 0.23	1.22
1.40 ± 0.23	1.25
1.68 ± 0.18	1.38, 1.46, 1.54, 1.68
2.08 ± 0.20	2.08
2.55 ± 0.20	2.45, 2.46, 2.55
3.07 ± 0.18	2.90
3.31 ± 0.20	2.82
3.80 ± 0.20	3.90
4.03 ± 0.20	4.09, 4.22
4.50 ± 0.22	4.25
5.27 ± 0.23	5.24
6.73 ± 0.23	6.70

simulated the performance of the correlation interferometer in the qualitative measurement of optical thicknesses of these gases.

Each calculation was comprised of the following steps:

1. Spectra with 0.5 cm^{-1} resolution were obtained for individual gases at specific optical thicknesses, using a Digilab FTS-14 interferometer-spectrometer and ratioing to the background spectrum.
2. By use of computer techniques, spectra of various combinations of gases were obtained with appropriate optical filters.

3. From each spectrum, an interferogram was generated.
4. For each gas of interest an interferogram for the combination of interferent gases with that gas was compared with an interferogram for the combination of the interferent gases without that gas. The difference is the effect of the gas of interest in the presence of those interferents.

The gases studied were:

Methane (CH_4)
Carbon monoxide (CO)
Carbon dioxide (CO_2)
Water (H_2O)
Ammonia (NH_3)
Nitric oxide (NO)
Nitrogen dioxide (NO_2)
Nitrous oxide (N_2O)
Sulfur dioxide (SO_2)
Ethane (C_2H_6)
Ethylene (C_2H_4)

Table 4 lists the spectra which were obtained, arranged in order of increasing wavelength.

In addition to the spectra listed, spectra of water were desired. Since it was not practical to obtain spectra for atmospheric amounts of water (for which a path length of several kilometers is needed), these were obtained by computation from data in NBS tables. All spectral regions in which water is a significant interferent in the spectra of Table 4 were covered. The amount of water used was 2150 atm-cm, as given by Gutnick;* multiples of this from 0.1 to 10 were also used.

Various combination spectra were generated, from which the corresponding interferograms were obtained. For these calculations a Lorentzian filter was assumed, with half-width at half-maximum of 1/2 to 1% of the wavenumber at line center.

The interferograms with and without the gases of interest (the gases to be measured) are shown in Figures 5 through 8 for the atmospheric burdens of CO, CH_4, NO, and SO_2 respectively. (Similar results have been obtained

* Gutnick, M. (1962), AFCRL Interim Note on Atmospheric Properties No. 22, Air Force Cambridge Research Laboratories, Bedford, Mass.

Table 4. Spectra Used for Interferogram

$\nu(cm^{-1})$	Gas	Optical Thickness (atm-cm)
5156 - 4900	CO_2	250
	NH_3	0.036, 0.36
5048 - 4792	CO_2	250
	NH_3	0.0036*
4538 - 4282	CH_4	5.4
	CO	0.36
	NH_3	0.0036*, 0.036, 0.36
	NO_2	0.014*
	N_2O	0.9
4358 - 4102	CH_4	5.4
	CO	0.36
	NO_2	0.014*
3778 - 3522	CO	0.36
	CO_2	250
	NH_3	0.0036*
	NO	0.016*
	N_2O	0.9
3578 - 3322	CO_2	250
	NH_3	0.0036*
	NO_2	1.08*
	N_2O	0.9
3416 - 3160	NH_3	0.036
	N_2O	0.9
3116 - 2860	CH_4	5.4
	NO_2	0.014, 0.14
	N_2O	0.9
	C_2H_6	0.00162, 0.00288, 0.00405, 0.0120, 0.0205, 0.102, 0.507
	C_2H_4	0.0206, 0.0615, 0.1850
3038 - 2782	CH_4	5.4
3800 - 2700	C_2H_6	0.013, 1.3, 13, 99
	C_2H_4	99.8
3600 - 2700	C_2H_4	0.013, 1.3
	C_2H_4O	0.026, 0.13, 45.4
	$C_2H_6O_2$	0.013, 0.59
	$\alpha C_{10}H_{16}$	0.012, 0.5
	$\beta C_{10}H_{16}$	0.012, 0.36
2668 - 2412	CH_4	5.4
	N_2O	0.9
	SO_2	0.072
2598 - 2342	SO_2	0.072
2286 - 2030	CO	0.36
	CO_2	250
	N_2O	0.9
2018 - 1762	CO_2	250
	NH_3	0.0036*, 0.036
	NO	0.004, 0.016
1810 - 1554	NH_3	0.0036
	NO_2	0.014
1506 - 1250	CH_4	5.4
	NO_2	0.014*
	N_2O	0.9
	SO_2	0.0036

*No significant absorption.

for the other gases listed above.) The effect of the gas of interest is shown by the difference in the two interferograms. Since the sensitivities and accuracies attainable for the measurement of CO and CH_4 are known from the results of experimental studies described above, they can be related to the differences in the appropriate pairs of interferograms (Figures 5 and 6, respectively). That is, the differences between the two interferograms are attributable to CO, and CO measurements under atmospheric conditions are made with an accuracy of about 10% and a sensitivity of .04 atm-cm. With this cause-and-effect information, similar differences in any other pair of interferograms (such as those of Figure 7 for NO or Figure 8 for SO_2) can be used to estimate the accuracy and sensitivity to be expected for the gas causing those differences. On the basis of this reasoning (assuming the same signal strength as for CO), the sensitivity to be expected for each of the gases studied was obtained from a pair of interferograms and is given in Table 5. Clearly, the correlation interferometry can be very useful for the stratospheric and tropospheric measurement of these important trace atmospheric species.

Table 5. Estimated Detection Sensitivities Relative to CO (assuming source intensity to be independent of wavelength)

Species	Filter Center Frequency (cm)	(μm)	Delay Range (mm)	Sensitivities Relative to CO = 0.04 atm-cm
CH_4	4280	(2.39)	5.5 - 6.4	5
			All other	2
CO	4280	(2.39)	2.3 - 3.5, 5.6 - 6.3, 7.4 - 9.4	1
CO_2	4835	(2.07)	5.0 - 6.0	2
			6.0 - 8.0	125
			All other	1250
H_2O	3465	(2.89)	All	1250
NH_3	4500	(2.22)	2.6 - 4.0	5
			6.3 - 7.5	10
N_2O	3465	(2.89)	3.0 - 3.6	5
			8.5 - 9.7	0.5
NO*	1900	(5.26)	2.8 - 3.7	0.2
			5.8 - 7.0	0.08
			9.0 - 9.5	0.08
NO_2*	1630	(6.13)	0.5 - 4.0	0.06
			All other	0.08
SO_2*	1370	(7.30)	~ 2.0	0.03
			2.5 - 4.0	0.2
			4.5 - 5.7	0.2
			8.0 - 9.5	0.3
C_2H_4*	2988	(3.35)	1.0 - 4.0	0.5
			4.5 - 5.5	0.2
			6.0 - 8.5	0.5
C_2H_6	2988	(3.35)	1.0 - 4.0	0.02
			5.0 - 7.5	0.008
			7.5 - 9.2	0.02

*Detector with a $D^* \simeq 3 \times 10^{10}$ cm $Hz^{1/2}$ W^{-1}; all other species assume detector with a $D^* \simeq 10^{11}$ cm $Hz^{1/2}$ W^{-1}.

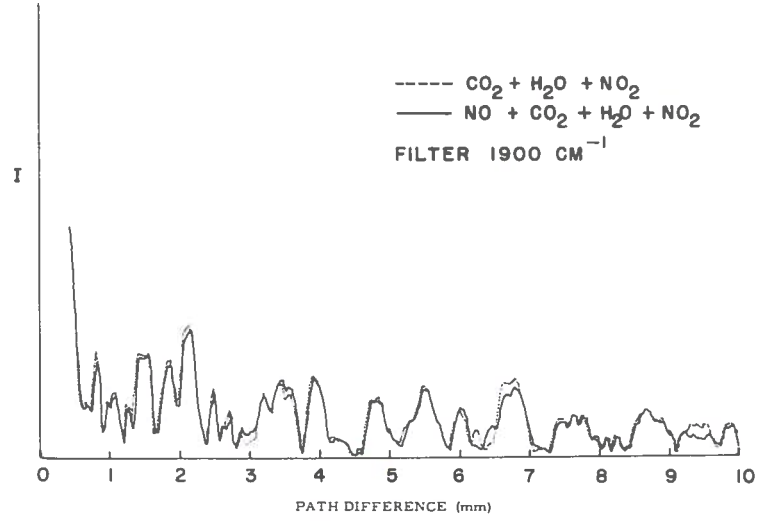

Figure 5. CO effect on interferogram.

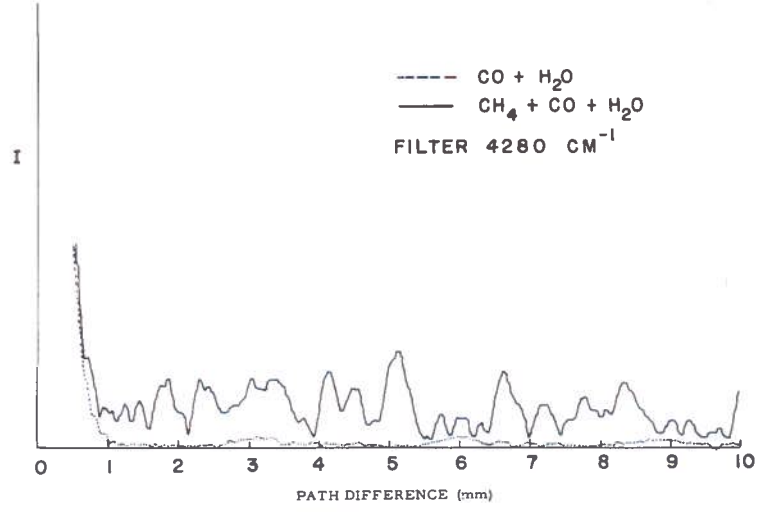

Figure 6. Methane effect on interferogram.

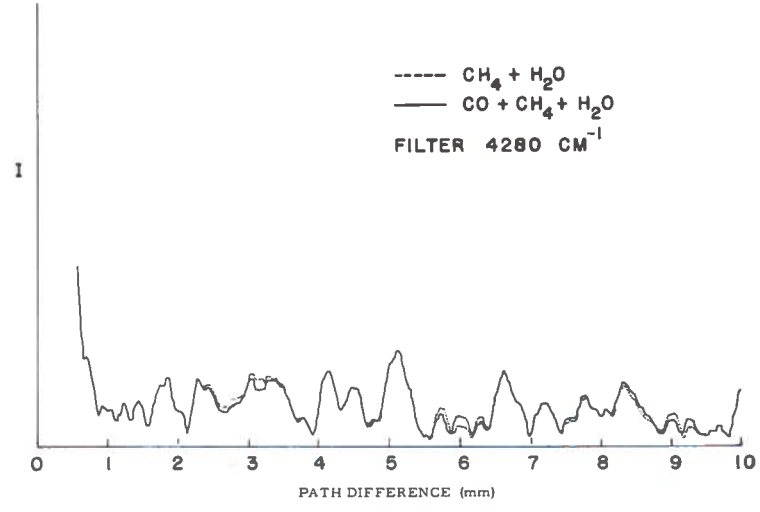

Figure 7. NO effect on interferogram.

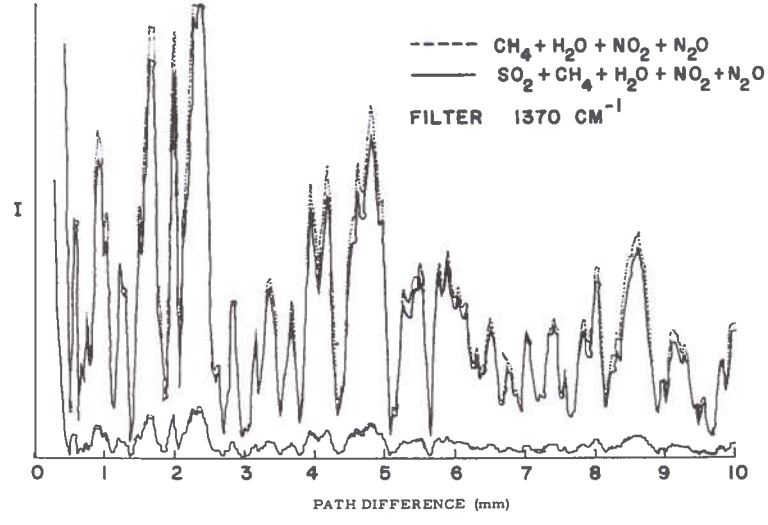

Figure 8. SO_2 effect on interferogram.

DISCUSSION

GREEN: When you defined your error as between five and ten percent, were you talking about the upper bound? Or were you really talking about a one-sigma error?

GOLDSTEIN: When we take a cell with a known concentration of gas and add a known amount of gas to it, the measurement we get back is within five percent of the expected value.

(UNIDENTIFIED): Did you say your detection was theoretically limited?

GOLDSTEIN: At present we are detector-limited.

A TUNABLE UV LASER PROBE FOR MAKING ATMOSPHERIC MEASUREMENTS OF THE FREE RADICAL OH

D.D. DAVIS, P. HOGAN, AND A. MORIARTY
Chemistry Department
University of Maryland
College Park, Maryland

ABSTRACT: Reported on is a new tunable UV laser probe which has been designed to detect the free radical OH under atmospheric conditions at concentrations as low as 3×10^5 cm^{-3}. Also discussed are recent results from a smaller, prototype laboratory system, which has been used to determine the sensitivity of the laser-induced fluorescence technique under simulated atmospheric conditions. This same system has been employed to examine several important spectroscopic features of the OH radical. These include lifetimes for several K′ levels in the $v' = 1$ manifold of the $A^2\Sigma$ state, branching ratios from the $v' = 1$ state, and quenching cross-sections for the $A^2\Sigma$ state.

INTRODUCTION

Although there is no direct evidence for the existence of OH in the stratosphere, the presence of this species has been widely accepted by aeronomists. It is also well accepted that the OH radical plays a key role in controlling the chemistry of the atmosphere, and hence the concentration of a large number of minor gases.

Among the many pivotal reactions in which this species participates are the following:

$OH + CH_4 \rightarrow CH_3 + H_2O$
(primary step in the oxidation of CH_4 to CO)

$OH + CO \rightarrow CO_2 + H$
(principal reaction responsible for converting CO to CO_2 in the atmosphere, and a major source of atomic hydrogen)

$OH + NO_2 + M \rightarrow HNO_3 + M$
(a major source of nitric acid in the stratosphere)

$OH + O_3 \rightarrow HO_2 + O_2$
(a significant loss mechanism for ozone in the stratosphere)

$OH + H_2O_2 \rightarrow H_2O + HO_2$
(a major loss mechanism for hydrogen peroxide in the stratosphere)

$OH + SO_2 + M \rightarrow HSO_3 + M$
(a key atmospheric process responsible for initiating the conversion of SO_2 to more complex sulfur compounds such as H_2SO_4 and sulfate aerosol)

In addition to these six key reactions, there are several other reactions in which OH is believed to be important. These have been summarized in the schematic reaction diagram of Figure 1.

In general, the stratospheric OH concentration has been calculated from various models; hence, its values as a function of altitude have depended on a mechanistic scheme with an accompanying set of gas-kinetic and photochemical rate constants. Direct concentration measurements of OH would establish a new set of reference points in the atmosphere. This would impose a very important new set of constraints on existing models, which should result in their further refinement.

EXPERIMENTAL APPARATUS AND TECHNIQUE

The basic technique which has been utilized at the University of Maryland in building a highly sensitive probe for OH is that of resonance fluorescence – more specifically, in this case, laser-induced resonance fluorescence. The operating principle of this method of detection is quite simple; it involves pumping a free-radical species to its lowest spin-allowed excited electronic state, using a resonance-line excitation source. The resulting fluorescence radiation is then monitored at right angles to the pumping source. The signal-to-noise ratio in this type of system (noise being defined as scattered radiation) is optimized by using highly collimated

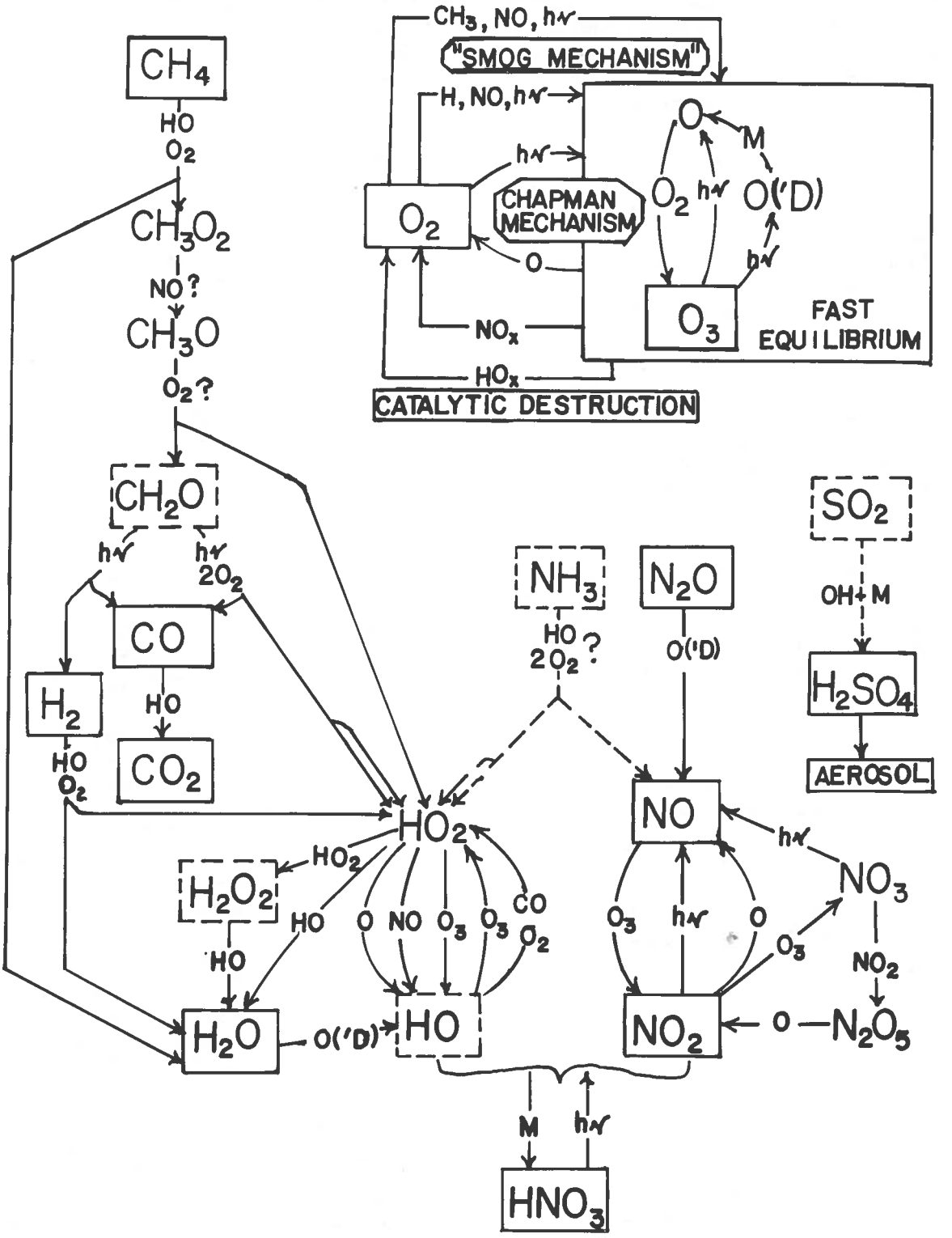

Figure 1. Schematic diagram of atmospheric reactions.

beams of incident resonance radiation, small fluorescence-sampling apertures, and large scattering chambers equipped with appropriate light traps.

In the case of free-radical species, such as OH, additional sensitivity can be achieved by sampling the fluorescence signal at wavelengths longer than those used in the initial excitation process. This is true because of the several vibrational levels in the ground electronic state that a given excited electronic state can reach by fluorescence.

An energy-level diagram for OH is shown in Figure 2. The longest wavelength capable of exciting fluorescence in OH is 306.4 nm, corresponding to the transition $A^2\Sigma - X^2\pi$ (0,0). The fluorescence would then be observed at ≈ 340 nm, which corresponds to the (0,1) transition. A second convenient transition which could be pumped is the (1,0), occurring at $\approx$ 282 nm. Observation in this case would take place at ≈ 310 nm. Although both pumping frequencies could be used, the greater stability of the dye lasing medium used in producing 282-nm radiation (i.e., Rhodamine 6G dye) make the latter pumping frequency somewhat more desirable. In addition, a consideration of the Franck-Condon factors for both the pumping of OH and the sampling of fluorescence indicates a sensitivity for (1,0) pumping with (1,1) sampling which is higher by a factor of four or five than that for (0,0) pumping with (0,1) sampling.

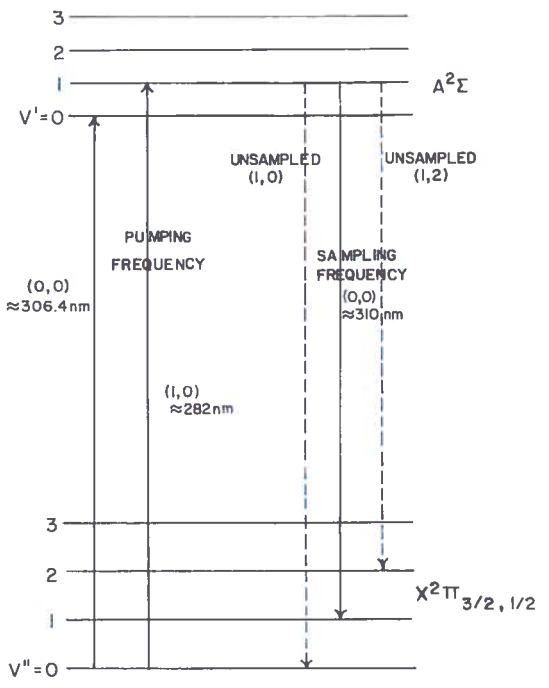

Figure 2. Energy-level diagram for OH.

The basic components of a system capable of detecting OH concentrations in the 10^5 radicals/cm^3 range are shown in Figure 3. This system consists of a dye-laser oscillator-amplifier which is driven by a frequency-doubled ruby laser at 345 nm. The fundamental output from the dye laser, using Rhodamine 6G dye as the lasing medium, is in the 564-nm region, and this output is frequency-doubled to ≈ 282 nm. In this spectral region several OH transitions can be excited which correspond to rotational states for OH of k = 1, 2, and 3, which is where most of the Boltzmann population is found at low temperatures.

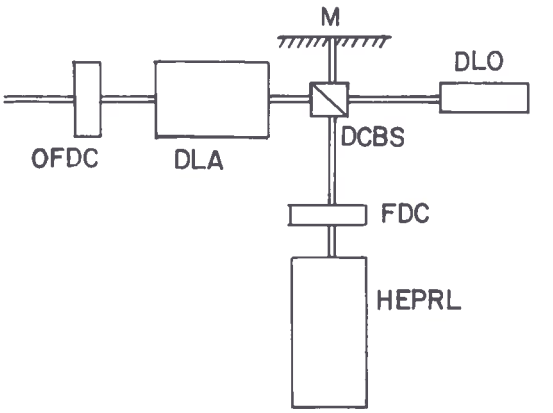

Figure 3. Schematic diagram of a tunable UV laser probe for detecting OH.

OFDC	Output-Frequency-Doubling Crystal
DLA	Dye-Laser Amplifier
M	Mirror
DCBS	Dielectric-coated Beam-Splitter
DLO	Dye-Laser Oscillator
FDC	Frequency-Doubling Crystal
HEPRL	High-Energy Pulsed Ruby Laser

In the system illustrated in schematic form in Figure 3, approximately 90% of the total ruby-laser pump energy is deflected into the dye-laser amplifier, and 9% is then used to drive the oscillator. The oscillator in this case consists of a multi-element Fabry-Perot system which is capable of producing laser linewidths as narrow as 0.002 nm. Since the energy of the oscillator

must be kept low to prevent damage to the tuning elements, the energy and the narrow linewidth necessary for detecting very low concentrations of OH is achieved by injecting the TEM_{00} mode of the oscillator into the highly energized dye-laser amplifier. Under these conditions, good mode structure, narrow linewidths, and high energies can all be realized. Further increases in sensitivity can be obtained by operating the laser system at higher repetition rates and longer integration times. The system shown in Figure 3 could be operated at pulse rates as high as 1 per second.

RECENT RESULTS AND FUTURE EXPERIMENTS

At present a prototype system similar to that shown in Figure 3 has been assembled and is fully operational in the laboratory. This prototype system, however, does differ in two important respects from the previously described system: (1) the dye laser is driven by a frequency-doubled neodymium-glass laser operated at approximately 1/6 the energy of the previously described ruby laser (1.2 J); and (2) the laser linewidth of the laboratory system is significantly greater. There are fewer Fabry-Perot tuning elements in the laboratory system, so linewidths on the order of 0.02 nm are generated, rather than those of 0.002 nm for the system in Figure 3. Since the linewidth of an OH rotational transition is on the order of 0.0015 nm, it is readily apparent that the prototype system is down in sensitivity by approximately a factor of 60. Even so, this system has shown very high sensitivity in detecting OH.

To date, for example, the prototype OH laser probe has been coupled to a 3-liter resonance-fluorescence chamber, which in turn has been coupled to a high-intensity cw continuum light source. When this chamber has contained gas mixtures consisting of 1 mtorr of O_3, 3 mtorr of H_2O, and N_2 as a diluent gas, OH steady-state concentrations in the 10^7 cm^{-3} range have been detected. As indicated earlier, the increased energy and narrower linewidth of the ruby-driven laser system should significantly improve this sensitivity (by about a factor of 60) and allow measurements of OH in the 10^5-10^6 range.

In addition to the atmospheric OH simulation test just described, a considerable effort has been made with the laboratory OH probe to better define the spectroscopy of OH. Among the many important problem areas in which new information is still required are: (1) measurements of lifetimes of specific K states in both the $v' = 0$ and $v' = 1$ vibrational states of the $A^2\Sigma$ electronic level; (2) experimentally determined branching ratios for transitions out of the $v' = 0$ and $v' = 1$ vibrational states; (3) very precise electronic cross-sections for quenching of the $A^2\Sigma$ state of OH by gases such as He, Ar, H_2O, N_2, and O_2; and (4) reliable rotational and vibrational relaxation cross-sections, again for the $v' = 0$ and $v' = 1$ manifolds in the $A^2\Sigma$ electronic state. This kind of information will both facilitate the selection of ideal conditions for maximizing the sensitivity of the OH atmospheric probe, and help to establish a reliable basis for calibrating the instrument under actual flight conditions.

Thus far some 20 transitions in the $v' = 1$ manifold of the $A^2\Sigma$ state have been selectively reached by tuning the laboratory neodymium-driven dye laser. The ground-state ($v'' = 0$) rotational levels from which pumping occurred ranged from $K = 1$ to $K = 5$. A comparison of the measured intensities for these 20 transitions with those predicted from calculated transition probabilities and from a Boltzmann distribution for rotational states showed excellent agreement. From the sampled set of 20 transitions, it has been possible to selectively examine the lifetimes of several rotational states in the $v' = 1$ manifold of the $A^2\Sigma$ state. These include $K' = 0$, 1, 2, 3, and 4. In each case, only one rotational quantum state was excited. Initial lifetime measurements for these states have ranged from 728 to 800 ns. Experimental measurements of the branching ratios from the $v' = 1$ state have also been made for the first time. Those transitions examined were (1,2), (1,1) and (1,0). Their respective intensities were 0.02 : 1.00 : 0.28. At present, studies are under way to determine precise electronic cross-sections for quenching of the $v' = 1$ state by several of those gases previously mentioned.

Paralleling the continuing laboratory studies on OH will be the completion of the ruby-driven

dye-laser system. This system has been specifically designed to interface with the National Center for Atmospheric Research's Sabreliner jet. This aircraft will permit this laser system to measure OH in both the lower stratosphere and the lower and upper troposphere. With other instruments on the aircraft, several trace gases directly related to OH through chemistry will also be sampled, including CO, O_3, H_2O, and CH_4.

UV FLUX LEVEL AND OZONE OVERBURDEN FROM LATITUDES 60°N to 60°S

BACH SELLERS AND FREDERICK A. HANSER
Panametrics, Inc.
Waltham, Massachusetts

ABSTRACT: The Panametrics UV Spectrophotometer provides an omnidirectional (up to 75° from the vertical) measurement of the solar flux in the 200 to 400 nm region. This spectrophotometer uses a UV diffuser, a movable filter wheel containing 10 bandpass filter sets, and a UV photomultiplier. Intensity can be measured as much as four orders of magnitude down from the unattenuated solar flux. Comparison of measured flux values with those computed for an ozone-free atmosphere allows the ozone overburden to be calculated. UV-flux and ozone-overburden results are most accurate at high altitudes, where the response to Rayleigh-scattered light is small compared to the response to direct sunlight.

Measurements made during the CIAP Airstream flights are reported over the latitude ranges: 5°N to 35°N in June 1973, at 50 to 60 kft altitude; 69° to 35°N in September 1973, at 45 to 60 kft altitude; and 35°N to 46°N, and 55°N to 60°N, in November 1973, at 40 to 55 kft. Flux measurements show the obvious dependence on solar elevation angle, and the cutoff below 300-320 nm due to ozone absorption. At altitudes above 50 kft, and for high solar-elevation angles, a measurable flux was observed at 210 ± 10 nm. For altitudes near 60 kft and the sun near the zenith the 210-nm flux was 1 to 2 × 10^{-9} W/(cm^2-nm), when the ozone overburden (above 60 kft) was about 0.2 cm STP. Ozone overburdens calculated from the flux measurements at 40 to 60 kft are generally less than those calculated from ground-based measurements, with the difference usually being in agreement with the expected ozone content at lower altitudes.

INTRODUCTION

One of the potential climatic effects of the operation of a worldwide SST fleet is change in the UV flux level at the earth's surface and in the lower atmosphere, due to modification of the earth's high-altitude ozone layer. Thus, as discussed by Grobecker (1972), measurement of the solar UV flux in the atmosphere is one of the important questions to be addressed by CIAP.

Figure 1 shows the proposed Standard Solar Spectrum at 1 A.U. from Thekaekara (1970), as well as the ozone absorption coefficients measured by Inn and Tanaka (1953) and the O_2 absorption coefficients given in Green (1966). Since the ozone layer is generally equivalent to 0.2 cm STP or more, it effectively blocks all radiation at wavelengths much less than 300 nm, and most of the variation in solar UV fluxes is in the range of 280 to 330 nm. As discussed in Shotkin and Thompson (1973) and Smith (1973), this is also the region of the solar UV spectrum that has the most biological effect at the earth's surface, so monitoring of this wavelength interval is most important.

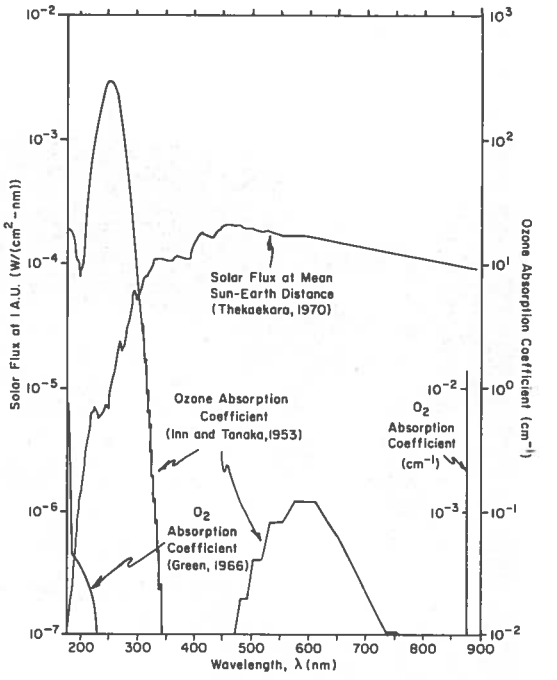

Figure 1. Unattenuated solar spectrum, and ozone and O_2 absorption coefficients.

At high altitudes the dip in ozone absorption coefficients at 210 nm produces a measurable flux at this wavelength. Absorption by O_2 reduces the 210-nm flux intensity to negligible values for altitudes much below 50 kft. For calculations of the chemistry of the ozone layer, which is concentrated above 50 kft, measurement of the 210-nm flux is desirable, however.

The Panametrics UV Spectrophotometer is designed to measure the solar UV flux over the range 200 to 400 nm. It has an omnidirectional response (to more than 75° from the vertical) and thus requires no mechanical aiming. Thus far solar UV data have been obtained from a number of CIAP Airstream flights, and portions of the data from these flights are presented in this paper.

DESCRIPTION OF UV SPECTROPHOTOMETER

A picture of the Panametrics UV Spectrophotometer (UVS) and the associated test console appears in Figure 2. The UVS is basically a bandpass-filter-wheel photometer with seven narrowband filters (≈ 2 nm) in the 280-330 nm region, one wideband filter (≈ 15 nm) at 210 nm, and two wideband filters (≈ 30 nm) in the 330-400 nm region. Thus, narrowband filters are used in the region where most solar-flux variation is expected. The arrangement of the protective outer quartz plate, the diffuser, the bandpass filters, and the UV photomultiplier is shown in Figure 3, while a picture of the internal structure of the UVS, showing the twelve-position filter wheel, is given in Figure 4. The UVS is mounted in the fuselage of a WB-57F just forward of the tail, as shown in Figure 5. A summary of the UVS characteristics is given in Table 1.

The output of the UV photomultiplier goes to a 5-decade logarithmic amplifier (0 to 5 volt output), and filter collimators are set so that the maximum expected signal is somewhat below the 5-volt output limit. Thus UV flux can be measured to more than four orders of magnitude below the unattenuated solar flux. For the narrowband filters (2 nm) the leakage flux between 330 and 400 nm limits accurate measurements to about three orders of magnitude below the 330-400-nm-region flux intensity. Typical bandpass-filter transmission curves are shown in Figure 6. The 2-nm-passband filters are used in pairs to reduce the signal from the

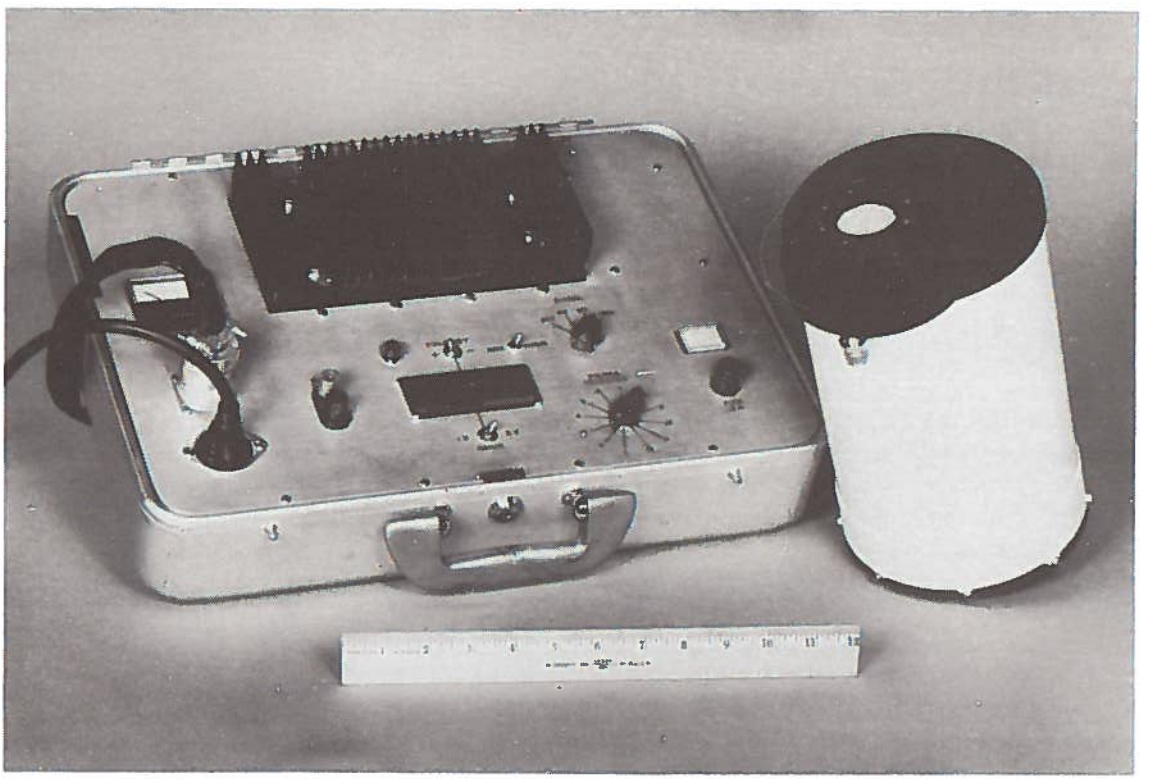

Figure 2. UV spectrophotometer and ground checkout test console.

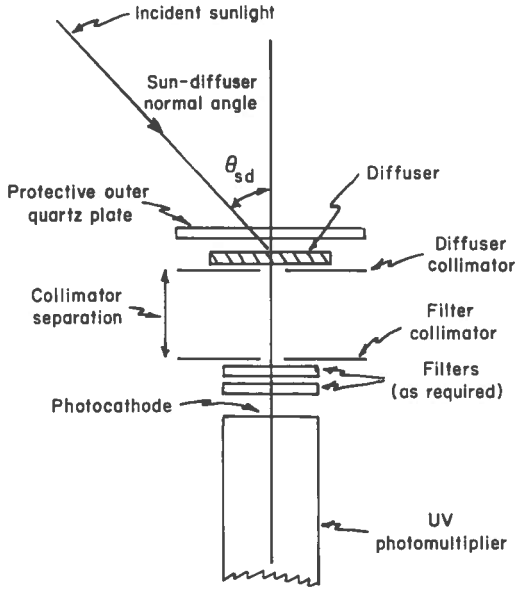

Figure 3. General arrangement of spectrophotometer diffuser, filters, and photomultiplier.

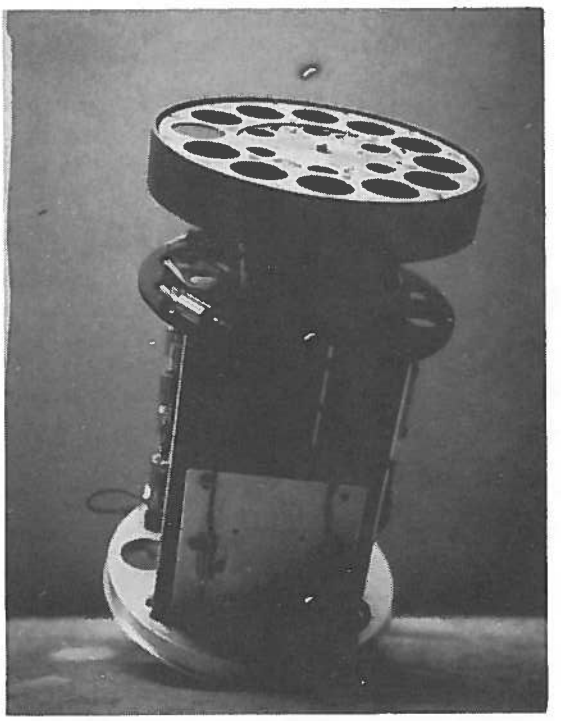

Figure 4. View of UV spectrophotometer with housing removed (showing filter wheel on top, electronics on bottom).

leakage flux at longer wavelengths. The 210-nm measurement uses three 214-nm filters with a 28-nm passband. The actual response at high

Table 1. Spectrophotometer Characteristics Summary

Measurement technique: Omnidirectional measurement (up to 75° from vertical) by a diffuser, movable wheel containing bandpass filters, and special UV photomultiplier. Intensity measured up to 4 orders of magnitude down from the unattenuated solar flux. Wheel has 12 positions sampled at 1 position/sec.

Position	Central Wavelength (nm)	Effective Bandwidth (nm)
1	210	15
2	287	2
3	291	2
4	298	3
5	305	2
6	310	2
7	319	2
8	329	2
9	363	26
10	393	28
11	Calibration checks	
12	Blank - for photomultiplier dark-current measurement.	

Power Consumption: (From +28 V)	Electronics	20 W
	Heaters*	50 W
	Max. Total	70 W

Weight: 10.5 lb

Size: Cylinder, 6″ diameter × 10″ deep

* Temperature is controlled at +20°C, with external temperature as low at -70°C. Heater power is, therefore, 50 W at -70°C and 0 W at +20°C external temperature.

altitudes is modified by the attenuation of the solar spectrum by ozone and O_2. The expected spectral responses to the unattenuated solar flux, and to the solar flux attenuated by 0.2 cm ozone and 1×10^4 cm O_2, are shown in Figure 7. Since the latter conditions correspond to those at about 60 kft altitude, the effective response at 210 nm is thus appropriate for most aircraft measurements. The 210-nm response has a threshold of about 1×10^{-10} W/(cm^2-nm), set by the leakage flux from $>$ 300 nm.

The UVS is periodically calibrated with a Standard of Spectral Irradiance (SSI), traceable to the NBS. The SSI is calibrated from 250 nm to 2500 nm, and is accurate to 7% at 250 nm, improving to about 4% at 400 nm. The measured

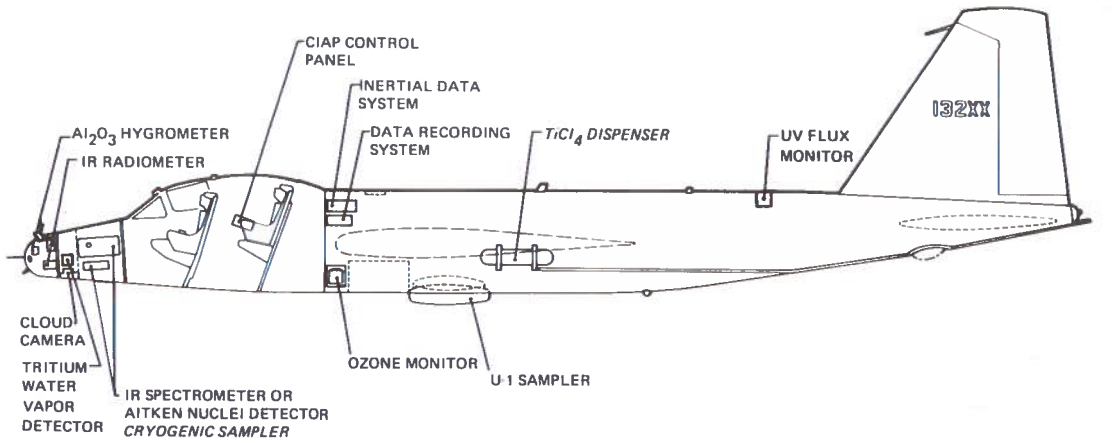

Figure 5. CIAP WB57F instrumentation, fuselage-mounted. Italicized equipment not in prime aircraft as of 1 September 1973.

UVS flux values from 280-400 nm thus have an absolute accuracy of about 5%. For the 210-nm filter the SSI spectrum is extrapolated, using a blackbody spectrum, and this is estimated to result in a 50% absolute accuracy for the 210-nm flux measurements.

A more complete discussion of the UVS is given in an earlier paper (Sellers et al., 1973).

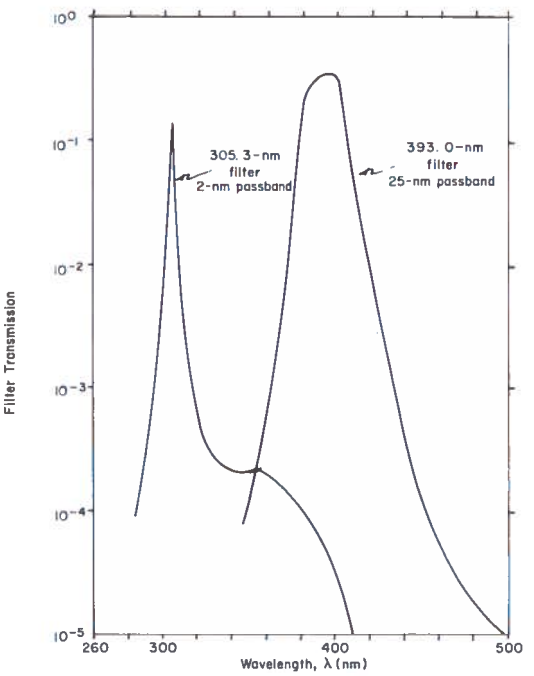

Figure 6. Typical measured transmission curves of bandpass filters.

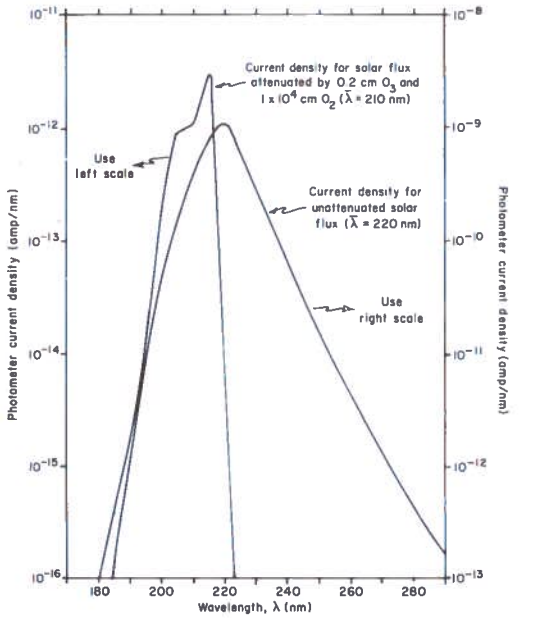

Figure 7. Photometer current density vs. wavelength for 214-nm filters with unattenuated and attenuated solar flux. Calculations are for 1 cm^2 effective collection area, and a photomultiplier gain of 10^6.

RESULTS

The UVS solar-UV-flux results presented here come from three CIAP Airstream flight series, made in June, September, and November 1973. Table 2 lists the date, latitude range, altitude, and time span of useful flux data from these flights. Because of problems with a switch used to turn on a calibration light, only about

85% of the maximum possible amount of data was obtained. (This malfunction has since been corrected.) The percentages obtained for each flight series are: June – 85%; September – 75%; and November – 100%.

Table 2. Summary of UVS Data Available From the First Three CIAP Airstream Flight Series

Date (mo/day/yr)	Latitude Range (deg. N)	Approximate Altitude (kft)	Approximate Amount of Data (minutes)
June 1973 series			
6/2/73	24 to35	60	170
6/3/73	6 to 9	60	145
6/4/73	9 to 11	50	40
6/5/73	9 to 17	55-60	210
6/6/73	5 to 9	55	110
6/7/73	9 to 35	55	335
Sept. 1973 series			
9/5/73	26 to 29	50	30
9/7/73	-8 to -1	50	60
9/7/73	-20 to -12	55-60	70
9/9/73	-34	45	30
9/9/73	-69 to -40	45-55	200
9/10/73	-36 to -33	60	80
9/12/73	-33 to +2	50-60	300
9/23/73	9 to 34	55	325
Nov. 1973 series			
11/1/73	35 to 46	55	125
11/2/73	64 to 73	40	140
11/3/73	65 to 75	40	110
11/4/73	65 to 70	55	120
11/5/73	55 to 64	40	140

The analysis procedure used is that described in Sellers et al. (1973), except that it has been improved to take into account the angular distribution of the Rayleigh-scattered light. Basically, the flux components and angular distributions calculated by Dave and Furukawa (1966) are used to find the fraction of the UVS response due to direct sunlight, and this in turn is used to calculate the total downward UV flux from the measured photometer current and SSI calibration.

A north-south sample of UV flux measurements is given in Table 3. Figure 8 is a plot of the data in Table 3 along with the unattenuated solar spectrum from Thekaekara (1970). The ozone overburden calculated from the 305- and 310-nm flux measurements is also given in Table 3, along with the 11-year averages (1960-1970) from Wu (1973). For the southern-hemisphere measurement a comparison is made with the July 1969 measurements from the NIMBUS 3 satellite (Wu (1973) and references cited therein), since the 10-year-average ground-based measurements of Wu (1973) are only for the northern hemisphere. The ratio of the high-altitude to the ground-based ozone overburden is also listed, along with the same ratio calculated from the model ozone profile of Dave and Furukawa (1966). Since Dave and Furukawa use a mid-latitude model, some deviation is to be expected. The pressures listed in Table 3 were calculated from the Inertial Data System (IDS) altitude and the appropriate atmosphere from the U.S. Standard Atmosphere Supplements (1966).

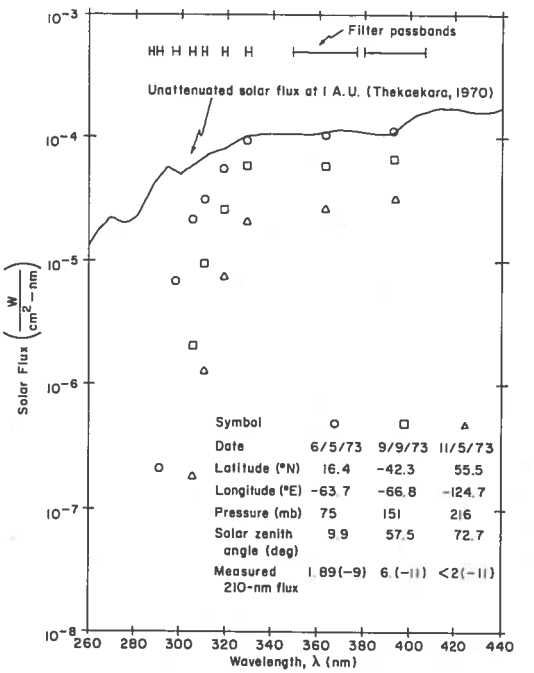

Figure 8. A north-south sample of measured fluxes.

The results in Table 3 and Figure 8 show the effect of the increasing ozone-overburden thickness on the solar flux north and south of the equatorial zone, although the larger solar zenith angle also has a strong effect. Fluxes are shown only when the leakage flux from longer wavelengths is not significant. The fluxes are organized, in tabular form, to provide the desired baseline UV flux and ozone-overburden geographical/seasonal variations for monitoring purposes.

Table 3. A North-South Sample of UV Flux Measurements

Date (mo/day/yr)	11/5/73	6/5/73	9/9/73
GMT (min)	1276	940	1125
Latitude (deg N)	55.6	16.4	-42.3
Longitude (deg E)	-124.7	-63.7	-66.8
Solar zenith angle (deg)	72.7	9.9	57.5
Pressure level (mb)	216	75	151
Measured downward UV flux ($W/(cm^2\text{-}nm)$) at given wavelength (nm):			
393.0	3.15(-5)	1.14(-4)	6.77(-5)
363.0	2.64(-5)	1.05(-4)	5.95(-5)
329.2	2.09(-5)	9.31(-5)	5.95(-5)
319.3	7.41(-6)	5.61(-5)	2.63(-5)
310.3	1.28(-6)	3.16(-5)	9.59(-6)
305.3	1.85(-7)	2.17(-5)	2.08(-6)
297.8	–	6.94(-6)	–
290.7	–	2.09(-7)	–
210.0	<2(-11)	1.89(-9)	6.(-11)
Ozone overburden (cm STP)	0.271	0.211	0.270
Ground level ozone (11-yr. avg.) (Wu, 1973)	0.325	0.295	0.340*
Ozone overburden ratio (pressure level/ground)	0.83	0.72	0.79
Ratio calculated from model of Dave and Furukawa (1966)	0.91	0.76	0.88

*July 1969

estimated to be accurate to 5-10%, except for the 210-nm fluxes, which have an error of about ±1 × 10^{-10} $W/(cm^2\text{-}nm)$ and a 50% absolute uncertainty. The 280 to 400 nm accuracy is limited by the accuracy of the NBS Standard, while the 210-nm accuracy is expected eventually to be improved to 10-20%. The thickness of the ozone overburden above flight altitude is estimated to be accurate to 0.02 cm STP.

Table 4 shows three flux measurements made at 15 to 30°N latitude in June and September 1973. The ozone-overburden measurements are consistent with the measurements in Table 3. when the different pressure levels and latitudes are taken into account. Table 5 shows a series of measurements at about 10°N latitude and a number of solar zenith angles. Here the calculated ozone overburden shows no strong dependence on solar zenith angle, although the UV fluxes do. The remainder of the UVS data is consistent with the samples shown here, with a gradual increase in ozone overburden away from the equator, and the expected dependence of the UV flux on solar elevation angle.

Tables and plots of the complete data are available to those who desire them, for the flights listed as well as later flights. Results are also available for the January 1974 Airstream flight series, for which at least 75% of the maximum possible amount of data was obtained. Data will generally be presented in about 2-minute averages, although finer resolution (to 12 seconds) is possible, as shown by the filter-wheel cycle time listed in Table 1.

CONCLUSIONS

The omnidirectional filter-wheel UV Spectrophotometer has given us much useful data from several CIAP Airstream flights. Ozone overburdens calculated from the UV flux measurements are consistent with ground-based measurements when account is taken of the higher altitude of the UVS data. The resulting UV flux data are accurate to 5-10%, limited prinicpally by the accuracy of the available calibration standard, and will be provided to all interested CIAP experimenters. The data also will be

Table 4. A Sample of UV Flux Measurements at 15 to 30°N Latitude

Date (mo/day/yr)	6/5/73	9/5/73	6/2/73
GMT (min)	877	1175	1280
Latitude (deg N)	16.3	27.8	27.7
Longitude (deg E)	-65.2	-95.5	-94.6
Solar zenith angle (deg)	24.9	27.3	41.8
Pressure level (mb)	107	117	75
Measured downward UV flux (W/cm^2-nm)) at given wavelengths (nm)			
393.0	1.07(-4)	1.09(-4)	8.75(-5)
363.0	9.85(-5)	1.05(-4)	7.76(-5)
329.2	7.95(-5)	9.50(-5)	7.08(-5)
319.3	5.06(-5)	5.03(-5)	4.10(-5)
310.3	2.64(-5)	2.99(-5)	1.88(-5)
205.3	1.69(-5)	1.25(-5)	1.06(-5)
297.8	4.89(-6)	5.53(-6)	3.31(-6)
290.7	1.22(-7)	2.22(-7)	6.35(-8)
210.0	3.0(-10)	3.5(10)	7.(-11)
Ozone overburden (cm STP)	0.224	0.223	0.212
Ground level ozone (11-yr. avg.) (Wu, 1973)	0.295	0.275	0.300
Ozone overburden ratio (pressure level/ground)	0.76	0.81	0.71
Ratio calculated from model of Dave and Furukawa (1966)	0.82	0.84	0.76

Table 5. A Sample of UV Flux Measurements at 10°N Latitude

Date (mo/day/yr)	6/7/73	6/4/73	6/5/73
GMT (min)	929	785	760
Latitude (deg N)	11.0	9.7	10.4
Longitude (deg E)	-80.8	-78.1	-77.3
Solar zenith angle (deg)	29.3	60.0	64.9
Pressure level (mb)	96	105	104
Measured downward UV flux ($W/(cm^2$-nm)) at given wavelength (nm)			
393.0	1.05(-4)	6.31(-5)	4.94(-5)
363.0	9.56(-5)	5.64(-5)	4.32(-5)
329.2	8.80(-5)	4.82(-5)	3.70(-5)
319.3	5.06(-5)	2.38(-5)	1.81(-5)
310.3	2.79(-5)	9.34(-6)	5.97(-6)
305.3	1.63(-5)	3.54(-6)	1.87(-6)
297.8	4.97(-6)	1.27(-6)	8.22(-7)
290.7	1.46(-7)	–	–
210.0	5.6(-10)	<1(-11)	<1(-11)
Ozone overburden (cm STP)	0.206	0.222	0.218
Ground level ozone (11-yr. avg.) (Wu, 1973)	0.290	0.285	0.290
Ozone overburden ratio (pressure level/ground)	0.71	0.78	0.75
Ratio calculated from model of Dave and Furukawa (1966)	0,80	0.82	0.82

organized, in tabular form, to provide the desired baseline UV flux and ozone-overburden geographical/seasonal variations for monitoring purposes.

ACKNOWLEDGMENTS

The successful operation of the UV Spectrophotometer has depended on the work of many peopel. Mr. Jean L. Hunerwadel of Panametrics, Inc. carried out the electronics design, and Mr. Anthony J. Broderick of the DOT Transportation Systems Center provided substantial assistance during both the design and the data-processing phases. Dr. Ronald J. Massa and Mr. Fritz Ostherr of Dynatrend, Inc. provided the necessary liaison between Panametrics and Los Alamos Scientific Laboratory (LASL), the organization responsible for the actual flight program. The continuous effort of Mr. Paul Guthals, the LASL Technical Manager, and his staff is also appreciated.

REFERENCES

Dave, J.W. and P.M. Furukawa (1966), "Scattered Radiation in the Ozone Absorption Bands at Selected Levels of a Terrestrial, Rayleigh Atmosphere," Meteorological Monographs, Vol. 7, No. 29, American Meteorological Society.

Green, A.E.S. ed. (1966), *The Middle Ultraviolet: Its Science and Technology*, Wiley, New York.

Grobecker, A.J. (1972), "Assessment of climatic changes due to flights in the stratosphere," AIAA Paper No. 72-658 (presented at AIAA 5th Fluid and Plasma Dynamics Conference, Boston.)

Inn, E.C.Y. and Y. Tanaka (1953), "Ozone absorption coefficients in the visible and ultraviolet regions," J. Opt. Soc. Am. 43, 870-3. (Also in Adv. in Chem. Ser. No. 21, 263-8.)

Sellers, B., F.A. Hanser, and J.L. Hunderwadel (1973), "Design, Fabrication and Flight of an Ultraviolet Interference-Filter Spectrophotometer Aboard a WB57F High Altitude Aircraft," Report PANA-UVS-1, Panametrics, Inc., Waltham, Mass.

Shotkin, Louis M., and John F. Thompson, Jr. (1973). "Uncertainties in Determining the Effective UV Radiation at Various Altitudes," AIAA Paper No. 73-102.

Smith, Kendric C. (Chairman of Ad Hoc Panel) (1973), "Biological Impacts of Increased Intensities of Solar Ultraviolet Radiation," PB 215 524, available from NTIS, U.S. Dept. of Commerce.

Thekaekara, M.P. (1970), "Proposed standard values of the solar constant and the solar spectrum," J. Environ. Sci. 13, 6-9.

U.S. Standard Atmosphere Supplements (1966), U.S. Government Printing Office, Washington, D.C.

Wu, Mao-Fou (1973), "Observation and analysis of trace constituents in the stratosphere," Report No. ERT P-93, DOT-TST-74-7.

DISCUSSION

(UNIDENTIFIED): Do you correct your data for water vapor?

SELLERS: No.

(UNIDENTIFIED): Did you take measurements on a relative basis?

SELLERS: No, we based the ozone measurements on absolute attenuation measurements.

ELLSAESSER: What type of calculation did you use for the diffuse flux?

SELLERS: We don't calculate the diffuse flux as such. We have a set of tables which give the Rayleigh scattering components. Our instrument sees the Rayleigh components due to both the direct and the ground-reflected radiation, and we take them into account in getting the total downward flux. The values are always small compared with the total direct flux.

ELLSAESSER: Is the difference accounted for by what we might call the underburden of ozone?

SELLERS: Our numbers were eighty to ninety percent of the total overburden. We think the difference is reasonably accounted for by the low-level ozone.

HANSER: I'd like to amplify that. We used the model calculations of Dave and Furukawa from an AMS publication. The ozone profile of their mid-latitude model shows about ten percent ozone below the fifty-to-sixty-kilofoot level we used. We usually agree quite closely with their ratio, though of course a number of our flux measurements are made in the southern hemisphere or near the equator, and in various seasons.

Since our instrument has omnidirectional response, it isn't good at ground level, where much of the light is Rayleigh-scattered. But up at 50 or 60 kft, only about ten percent of the light is Rayleigh-scattered, which would make only about a one-percent difference to our total measured flux. Our flux is total flux per square centimeter downward over the upper hemisphere, and includes both the direct sunlight and the Rayleigh-scattered components.

BALLOON MEASUREMENTS OF SOLAR FLUXES BETWEEN 1960 Å AND 2300 Å

P. SIMON
Institut d'Aéronomie Spatiale de Belgique
Brussels, Belgium

ABSTRACT: New observational data in the 1960 - 2300 Å wavelength range have been obtained by means of a balloon-borne spectrometer. Ultraviolet spectra for different zenith angles were recorded with an equivalent slit width of 6 Å. Extrapolation to zero air mass leads to extraterrestrial solar fluxes lower than the values measured previously. The present results give an apparent blackbody temperature of the sun on the order of 4700°K at 2000 Å.

INTRODUCTION

From the point of view of aeronomy, knowledge of the spectral distribution of the ultraviolet solar fluxes reaching the atmosphere is fundamental to determining the photodissociation rates of atmospheric constituents. For instance, in the stratosphere, solar radiation in the wavelength range from 1800 to 2400 Å photodissociates O_2 to form O_3. Minor constituents such as N_2O, HNO_3, and H_2O_2 are also photodissociated in that wavelength range (see, for example, Nicolet (1972, 1973)); the most recent measurements of solar flux for these constituents are those reported by Ackerman et al. (1971) and by Broadfoot (1972). The data obtained at wavelengths shorter than 1880 Å by Parkinson and Reeves (1969), and confirmed at 1700 Å by recent rocket observations (Ackerman and Simon, 1973; Rottman, 1973) and by satellite experiments (Heath, 1973), show the need for new determinations in the 2000-Å atmospheric window.

This paper reports new measurements of absolute ultraviolet solar fluxes between 1960 and 2300 Å, obtained by means of a balloon-borne spectrometer integrated into a sun-pointing gondola.

INSTRUMENTATION

The instrument is a modified version of the spectrometer used aboard rockets by Ackerman and Simon (1973). A coarse-ground quartz window, used as a diffuser, was placed in front of the entrance slit to integrate the radiation over the whole solar disk. Spectral scanning was achieved by rotation of a 26 × 26 mm plane grating (Bausch and Lomb 35-53-04-020) ruled at 1200 grooves per mm and blazed at 2000 Å. The diffracted light was received by a solar-blind photomultiplier (EMR 542 P-09-18) with a RbTe photocathode. The slit width of the spectrometer was equivalent to a triangular slit function with a full width at half maximum of 6 Å. The analog output signal was telemetered to the ground after measurement and amplification by a solid-state electrometer. The flight instrument was aligned with fine sun sensors which pointed the balloon gondola at the sun to better than 30 arcseconds. The instrument alignment accuracy was on the order of 5 arcminutes. (A more detailed description is given in Simon (1974).)

The absolute calibration of the spectrometer is referenced to the 1956 International Pyrheliometric Scale. Using a Reeder thermopile as a transfer standard, the irradiance of a low-pressure mercury lamp was measured at 2537 Å. The spectrometer was directly and absolutely calibrated against this lamp before and after each flight. The relative sensitivity curve of the spectrometer was determined by comparison with a sodium-salicylate-coated photomultiplier, using a monochromatic beam emerging from a McPherson 30-cm-focal-length monochromator (model 218).

An electroless discharge lamp filled with $SiCl_4$ (emitting silicon atomic lines in the 1800-2600 Å wavelength range) and a deuterium lamp were used as light sources. The final accuracy of the flight-instrument calibration is estimated to be ± 10%.

The resulting absolute sensitivity curve of the instrument is shown in Figure 1.

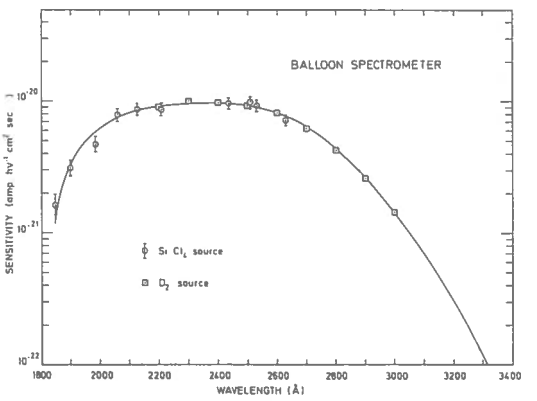

Figure 1. Absolute sensitivity curve of the flight instrument versus wavelength.

OBSERVATIONS AND RESULTS

The two flights were carried out on September 23, 1972 and May 16, 1973, at Aire sur l'Adour in France. On the first flight, the balloon (Raven, 3×10^5 m^3) reached an altitude of 41.5 km. The main purpose of this flight was the measurement of the stratospheric absorption of the solar radiation (Simon, 1974), so this experiment was performed at large solar zenith angles. The observation period extended from 1630 to 1840 GMT. Ultraviolet spectra between 1900 and 2300 A were obtained for zenith angles increasing from 78° to 88°.

On the second flight, the balloon (Winzen, 3×10^5 m^3) reached an altitude of 39 km. In this case, the main purpose of the flight was to determine the ultraviolet solar fluxes, so measurements were made at relatively smaller solar zenith angles. Spectra were recorded from 1600 to 1722 GMT. The corresponding zenith angles were 54° and 70°. Figure 2 shows one of the recorded spectra.

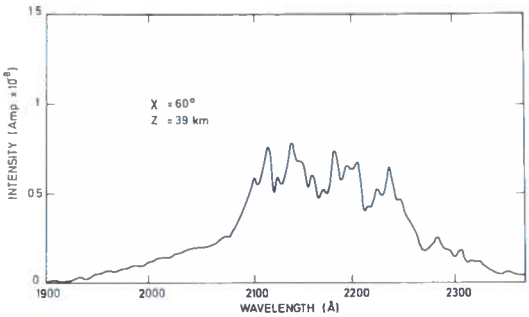

Figure 2. Stratospheric solar spectrum recorded during the second flight from 1900 Å to 2400 Å, obtained by means of the balloon-borne spectrometer, for a solar zenith angle of 60° and an altitude of 39 km.

The classical Langley method was used to determine the optical depth and the extraterrestrial solar fluxes. Some examples of extrapolation to zero air mass are given in Figure 3.

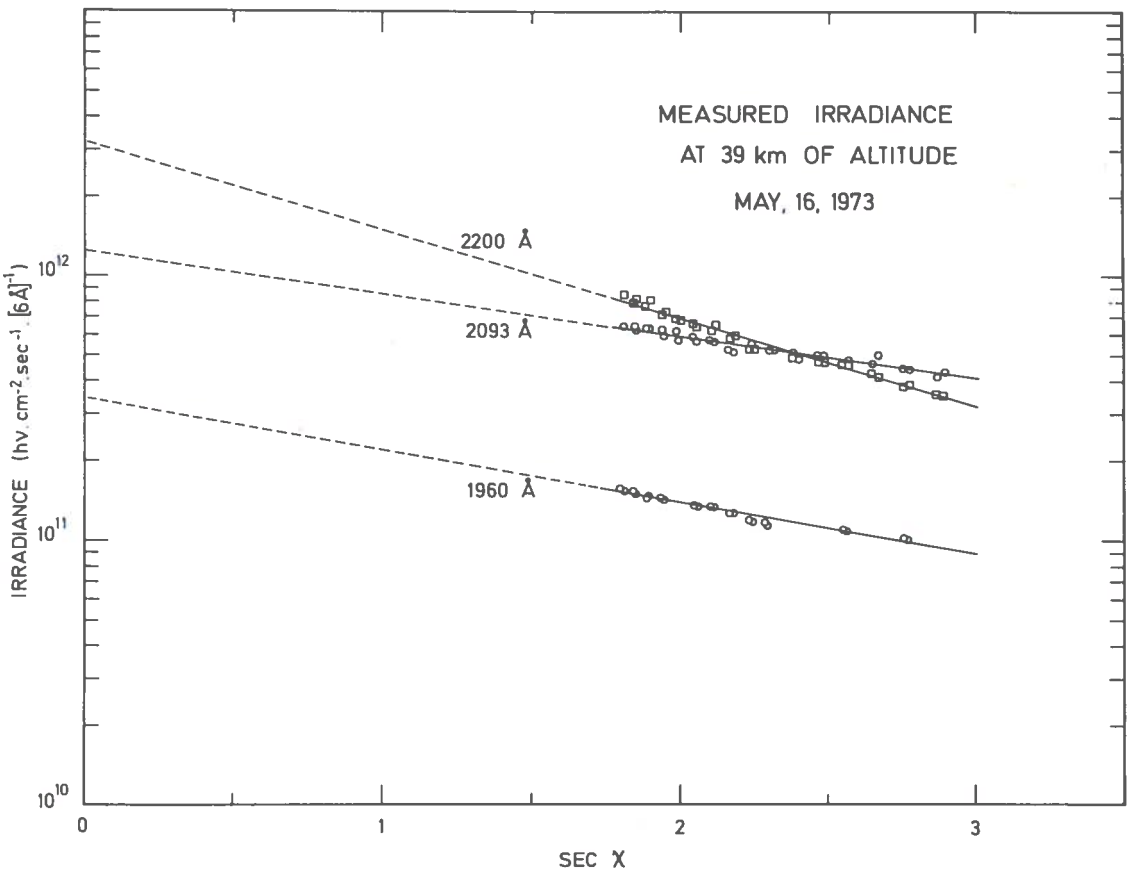

Figure 3. Measured solar irradiances versus the secant of the solar zenith angle, at three wavelengths.

For the first flight, the air masses were calculated using the approximation for large zenith distances given by Swider and Gardner (1967). Since in the wavelength range considered there are two different absorbing constituents, oxygen and ozone, with different scale heights, the contributions at each wavelength of the two absorbers in the air-mass calculation were taken into account. The oxygen and ozone column densities were deduced from pressure measurement and from absorption data around 3000 Å, respectively. Using the ozone absorption cross-sections measured by Inn and Tanaka (1953) and the oxygen absorption cross-sections published by Ackerman (1971), the optical depth was calculated for a pure oxygen-ozone atmosphere between 1900 and 2400 Å. The Rayleigh-scattering extinction was also taken into account. Figure 4 shows the good agreement between experimental optical-depth values and those of the oxygen-ozone absorption model.

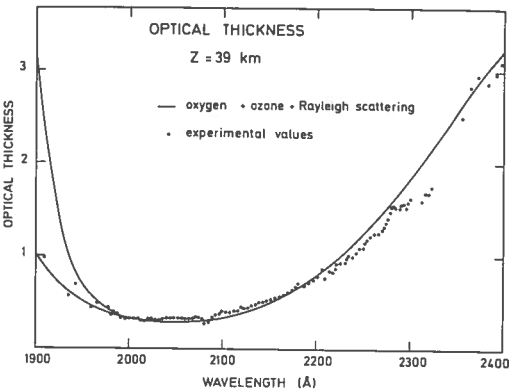

Figure 4. Experimental optical thickness (dots) and a pure oxygen-ozone atmospheric absorption curve in the wavelength range from 1900 to 2400 Å. The full curve was calculated for an ozone content of 4×10^{17} molecules/cm^2 and an oxygen content of 1.48×10^{22} molecules/cm^2. The splitting of this curve below 2000 Å corresponds to the lowest and the highest values of the oxygen cross-section in the Schumann-Runge band system.

The solar-flux results of the two flights are shown in Figure 5. The best-fitting curve is reproduced in Figure 6 for comparison with other determinations of solar fluxes in the 1700-2400 Å wavelength interval. The new values are roughly 40% lower than the previous measurements of Ackerman et al. (1971). They are in good agreement with Broadfoot's values for wavelengths

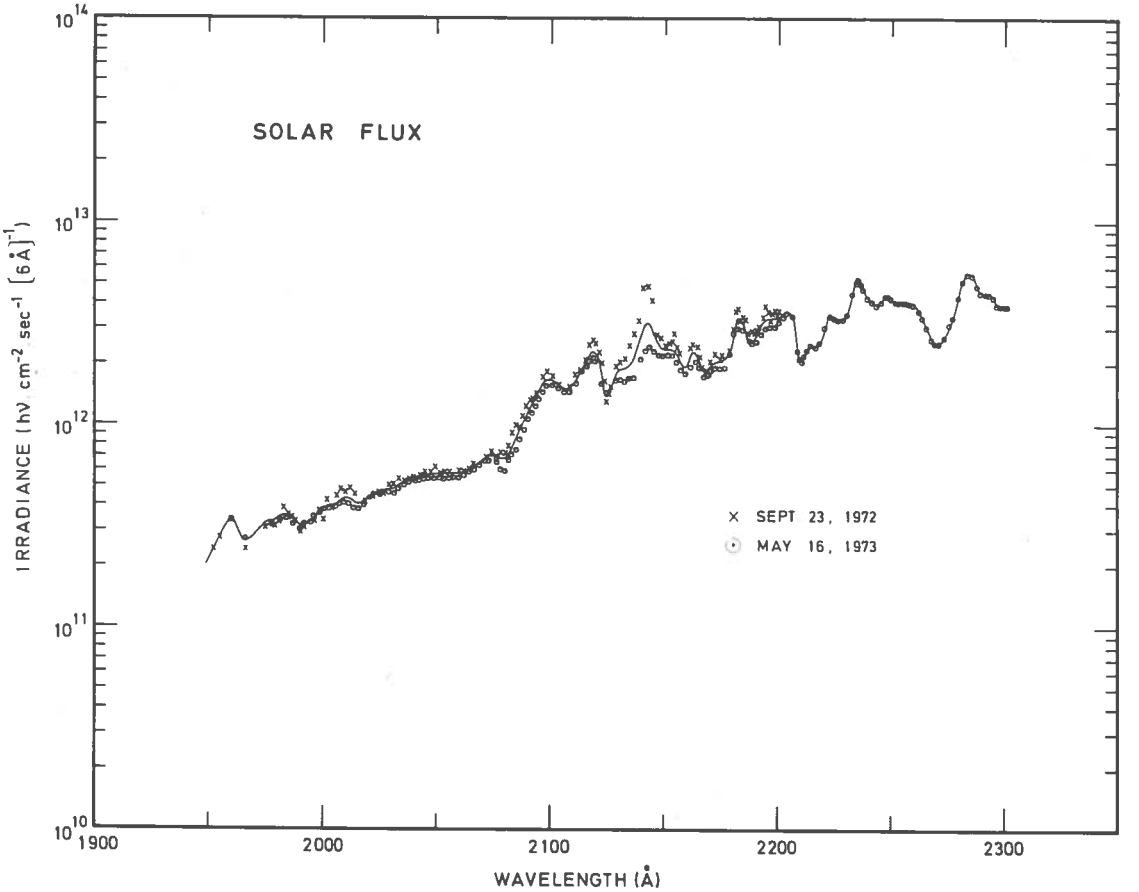

Figure 5. Solar fluxes versus wavelength at one astronomical unit, deduced from the two balloon flights.

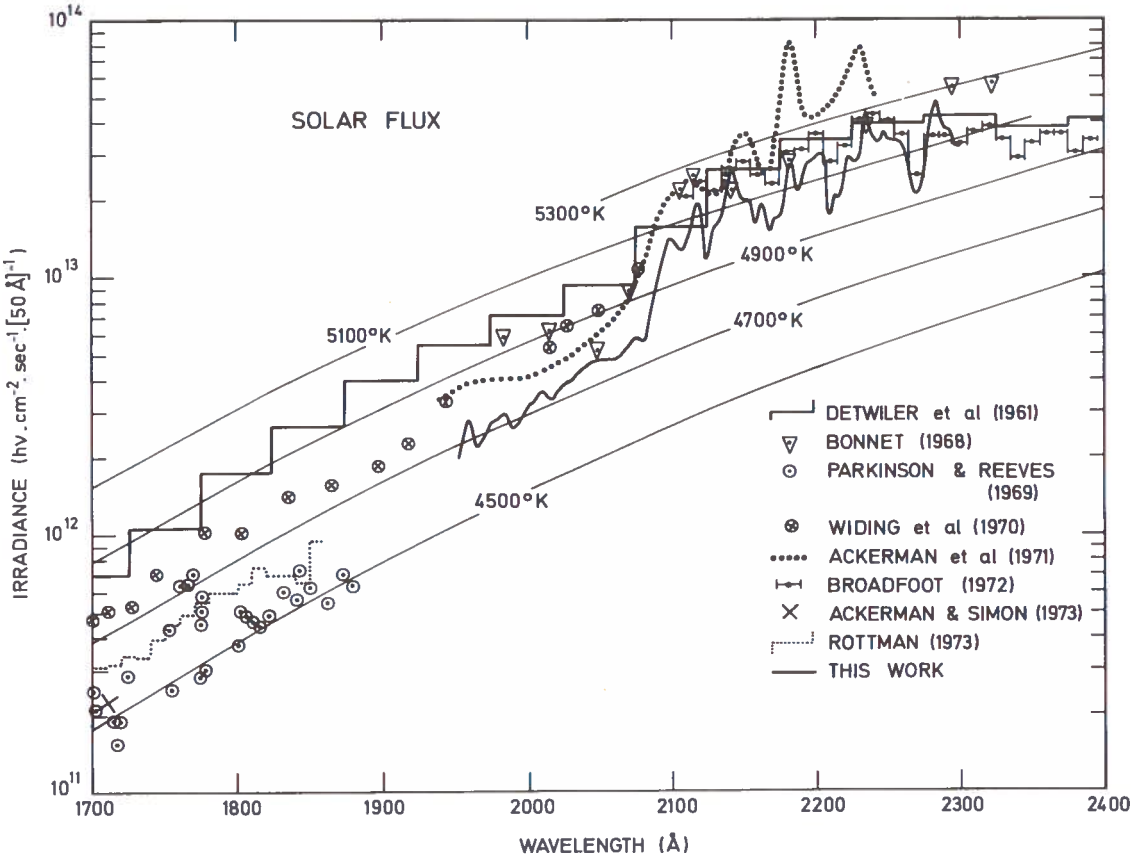

Figure 6. Comparison of ultraviolet solar fluxes reported by various experimenters from 1700 to 2400 A. Fluxes for different blackbody temperatures are also shown.

longer than 2250 A, but are lower at the shorter wavelengths. Table 1 and Figure 7 compare the new values with those published by Ackerman (1971) which are generally used in photodissociation-rate calculations. The agreement is fairly good for some wavelength intervals defined in Table 1.

Table 1. Comparison Between the Solar Flux Measurements Reported Here and the Values Published by Ackerman (1971)

Wavelength interval (A)	Flux ($h\nu$ cm^{-2} sec^{-1}) This work	Flux ($h\nu$ cm^{-2} sec^{-1}) Ackerman (1971)	Ratio of Ackerman's flux to this work's
1961 - 1980	1.01×10^{12}	1.39×10^{12}	1.38
1980 - 2000	1.20	1.53	1.27
2000 - 2020	1.44	1.60	1.11
2020 - 2041	1.80	1.74	0.97
2041 - 2062	2.08	2.31	1.11
2062 - 2083	2.45	4.20	1.71
2083 - 2105	5.09	7.30	1.43
2105 - 2128	7.12	9.42	1.32
2128 - 2150	9.23	1.06×10^{13}	1.15
2150 - 2174	8.42	1.34	1.59
2174 - 2198	1.20×10^{13}	1.32	1.10
2198 - 2222	1.22	1.73	1.42
2222 - 2247	1.77	1.80	1.02
2247 - 2273	1.60	1.82	1.14
2273 - 2299	1.96	2.26	1.15

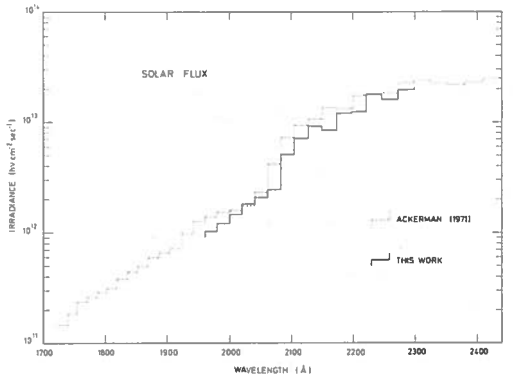

Figure 7. Comparison of solar fluxes reported here with values published by Ackerman (1971). The wavelength intervals are defined in Table 1.

Since the flux values of Parkinson and Reeves (1969) between 1400 and 1900 Å have recently been confirmed by Ackerman and Simon (1973), Heath (1973), and Rottman (1973), the apparent blackbody temperature of the sun appears to be close to 4550°K at 1900 Å. The present results indicate a decrease of only 150°K from 2000 Å down to 1900 Å. The intensity change from 2080 Å to 1700 Å could be nearly exponential, as suggested by Donnelly and Pope (1973).

ACKNOWLEDGMENTS

I would like to express my thanks to Prof. M. Nicolet for his interest in this work, and to Dr. M. Ackerman for his advice in the preparation of the experiment and for the data reduction. I am also indebted to Dr. R. Pastiels, who calibrated the reference source in the IPS 1956 scale, and to Mr. Lippens for his computer-programming assistance.

This work has been sponsored in part by the CIAP office of the U.S. Department of Transportation through the Office of Naval Research under contract N0014-73-C-0076.

REFERENCES

Ackerman, M. (1971), "Ultraviolet solar radiation related to mesospheric processes," in *Mesopheric Models and Related Experiments*, ed. G. Fiocco, D. Reidel Pub., Dordrecht, Holland, 149.

Ackerman, M., D. Frimout, and R. Pastiels (1971), "New ultraviolet solar flux measurements at 2000 Å using a balloon borne instrument," in *New Techniques in Space Astronomy*, eds. Labuhn and Lust, D. Reidel Pub., Dordrecht, Holland, 251.

Ackerman, M. and P. Simon (1973), "Rocket measurement of solar fluxes at 1216 Å, 1450 Å and 1710 Å," Solar Phys. **30**, 345.

Bonnet, R.M. (1968), "Stigmatic spectra of the sun between 1800 Å and 2800 Å," Space Res. **8**, 458.

Broadfoot, A.L. (1972), "The solar spectrum 2100-3200 Å," Astrophys. J. **173**, 681.

Detwiler, C.R., D.L. Garrett, J.D. Purcell, and R. Tousey (1961), "The intensity distribution in the ultraviolet solar spectrum," Ann. Geophys. **17**, 9.

Donnelly, R.F. and J.H. Pope (1973), "The 1-3000 Å Solar Flux for a Moderate Level of Solar Activity for Use in Modeling the Ionoshpere and Upper Atmosphere," NOAA Technical Report ERL 276-SEL 25.

Heath, D.F. (1973), "Space observations of the variability of solar irradiance in the near and far ultraviolet," J. Geophys. Res. **78**, 2779.

Inn, E.C.Y. and Y. Tanaka (1973), "Absorption coefficient of ozone in the ultraviolet and visible regions," J. Opt. Soc. Amer. **43**, 870.

Nicolet, M. (1972), "Aeronomic chemistry of the stratosphere," Planetary Space Sci. **20**, 1671.

Nicolet, M. (1974), "An overview of aeronomic processes in the stratosphere and mesosphere," Can. J. Chem. **52**, 1381.

Parkinson, W.H. and E.M. Reeves (1969), "Measurements in the solar spectrum between 1400 and 1875 Å with a rocket-borne spectrometer," Solar Phys. **10**, 342.

Rottman, G.J. (1973), in R.F. Donnelly and J.H. Pope, "The 1-3000 Å Solar Flux for a Moderate Level of Solar Activity, for Use in Modeling the Ionoshpere and Upper Atmosphere," NOAA Environmental Research Laboratories Technical Report ERL 276-SEL 25.

Simon, P. (1974), "Observation de l'absorption du rayonnement ultraviolet solaire par ballons stratosphériques," Bull. Acad. Roy. Belgique, Cl. Sci., in press.

Swider, W., Jr. and M.E. Gardner (1967), "On the Accuracy of Certain Approximations for the Chapman Function," AFCRL-67-0468 (Environmental Research Papers, No. 272), Air Force Cambridge Research Laboratories, Bedford, Mass.

Widing, K.G., J.D. Purcell, and G.D. Sandlin (1970), "The UV continuum 1450-2100 Å and the problem of the solar temperature minimum," Solar Phys. **12**, 52.

DISCUSSION

KRUEGER: What is the total absorption of the atmosphere above the flight altitude?

SIMON: The optical depth at 2050 Å is 0.2 for the first flight (41.5 kilometers altitude) and 0.3 for the second one (39 kilometers altitude).

(UNIDENTIFIED): Did you attribute the lower values to instrument problems or to shorter flights?

SIMON: Calibration techniques are the most difficult experimental problem in absolute ultraviolet spectrometry. Unfortunately, the difficulties increase in the vacuum ultraviolet wavelength range, which would explain the disagreement between the solar flux measurements.

Dr. Tohmatsu's paper was not available for publication in these *Proceedings*.

INVESTIGATIONS OF THE STRATOSPHERIC AEROSOL

K.YA. KONDRATYEV, L.S. IVLEV, AND G.A. NIKOLSKY*
Leningrad University
Leningrad, U.S.S.R.

ABSTRACT: Experimental investigations of the vertical concentration profile, the size distribution, and the composition of the stratospheric aerosol are reviewed. The effect of aerosol on the radiation regime of the stratosphere is considered. The results of detailed investigations of the stratospheric aerosol carried out at Leningrad University are discussed. An analysis of the available data permitted the authors to draw conclusions about space/time variations of the structure of the stratospheric aerosol, as well as its optical properties and their influence on the radiation regime of the surface/atmosphere system. These conclusions indicate the need for extension of such investigations of the atmospheric aerosol, and particularly of its optical properties.

Increasing interest in recent years in the problem of climate and its changes (particularly those due to the industrial activity of man) is reflected in the recognition of the problem of climate as second only to the problem of short-term weather forecasting in the Global Atmospheric Research Program. The investigation of the causes of contemporary climatic changes requires the consideration of a number of physical factors such as an increase in the carbon dioxide concentration and pollution of the atmosphere in general, change in the characteristics of the underlying surface, and industrial heat production. One of the very important factors is undoubtedly the aerosol content of the stratosphere and its influence on the radiation budget of not only the stratosphere but the surface/atmosphere system as a whole. In this connection it is interesting to examine the current status of the problem of stratospheric aerosol. We shall start with a short review of the available results, and then discuss aerosol and radiation measurements carried out by a group of co-workers at Leningrad University.

BRIEF REVIEW OF THE FIELD

One important fact is that the aerosol content of the stratosphere is greater than that of the upper troposphere. This was first detected by Junge with the help of direct balloon and aircraft measurements of the concentration of large aerosol particles and Aitken nuclei (Junge, 1963). Attention of scientists was drawn to this finding for two reasons: 1) the stratosphere serves as a reservoir for artificial pollutants, and 2) a greater aerosol content considerably changes the radiation budget of the atmosphere. It is significant that the aerosol not only may absorb solar radiation but also may destroy the ozone which absorbs short-wave solar radiation. Several theories explaining the greater aerosol content in the stratosphere have been put forward. All these theories took into account such factors as a) accumulation of space dust, b) injection of dust and sulfur dioxide during volcanic eruptions, and c) penetration of the tropospheric aerosol into the stratosphere through the tropopause breaks (Junge, 1963; Meinel and Meinel, 1967; Martell, 1966). Measurements by Mossop (1965) and Friend (1966) showed that the microstructure of the aerosol particles in the stratosphere differed considerably from that of the tropospheric particles: the particle size distribution in the stratosphere has a maximum for particles whose radius is about 0.3 μm, the particles being either entirely sulfate or enveloped in a sulfate shell.

Optical measurements also detected the existence of the layer of increased optical turbidity which is nearly always present at altitudes of 17 to 20 km (Kondratyev et al., 1969; Murcray et al., 1969a; Sholokhova and Fedorova, 1971). However, in most cases the aerosol content as derived from optical measurements was found to be much higher than that as derived from direct microphysical measurements. Particularly large discrepancies between the microphysical and optical data were found in the case of optical measurements in the infrared spectral region. This may be easily explained if we suppose that giant particles, with a radius greater than 1 μm, were not taken into account by the measurements of Junge (1963), Mossop (1965), Friend (1966), and Kondratyev et al. (1969).

In recent years a large amount of new and important data on the vertical profiles of the concentration, microstructure, and composition of the stratospheric aerosol has been obtained. This advance is connected, first of all, with the development of lidar sounding techniques (Grams and Fiocco, 1967; Schuster, 1970; Grams et al., 1972; Collis et al., 1973). An important contribution has been made by the investigations sponsored by the Climatic Impact Assessment Program (Friend, 1973; Cadle, 1972; Poppoff, 1972), and particularly by the investigations at the University of Wyoming (Rosen et al., 1973; Hoffman et al., 1972a,b). Of great importance were the achievements made in the electron-microscopic and chemical analysis of aerosol samples collected at high altitudes (Bigg et al., 1970; Shedlovsky, 1971; Reiter, 1973), and the investigations of the vertical profile of the atmospheric aerosol concentration from manned spacecraft (Gray et al.,

*This paper was presented at the conference by John Gille of NCAR.

1971; Cunnold et al., 1972; Kondratyev, 1972). Results of the lidar soundings of the stratospheric aerosol have been discussed and analyzed by a number of authors, e.g. Zuev et al. (1973). The most important findings derived from the lidar measurements of the stratospheric aerosol content were the detection of a) a distinct change in the vertical profile of the stratospheric aerosol with latitude; b) a pronounced layered structure of the aerosol, c) a rapid temporal changeability of the vertical aerosol profile, and d) a sharp decrease of the aerosol backscattering coefficients at altitudes above 25 km.

Variations of the vertical profile of stratospheric aerosol with latitude are related to the change in temperature stratification of the atmosphere, and to the attenuation of convection in high latitudes. The higher the latitude, the less pronounced and the lower in altitude is the stratospheric aerosol layer.

The rapid variability of the vertical profile of the stratospheric aerosol illustrated in the paper of Grams and Fiocco (1967) is confirmed by the data of a searchlight sounding (Elterman et al., 1969). This variability may be due to a number of factors, viz., turbulence, condensation, coagulation, and advection of air masses. The last factor, which also implies the existence of a small-scale horizontal nonuniformity of the stratospheric aerosol, seems most plausible.

Rather interesting is the large decrease in the backscattering coefficient at altitudes corresponding to higher values of relative humidity. This decrease could lead to a change in the aerosol size distribution, viz., to formation of more compact particles and change in their refractive index, which causes a decrease in the backscattering coefficient (Ivlev and Yanchenko, 1972). The results of simultaneous measurements of the aerosol vertical profiles with the lidar and the photoelectric counter (see Ward et al. (1973)) showed an appreciable difference in the aerosol concentration obtained by these methods, at altitudes of 24 to 28 km. It is possible, however, that the values of the stratospheric aerosol concentration measured in this region by lidar are underestimated because of the technique used in processing laser measurements.

Of great interest are those investigations of the stratospheric composition (Rosen et al., 1973; Hoffman et al., 1972a,b; Ward et al., 1973) which are designed to carry out simultaneous measurements of three interacting components: the aerosol, ozone, and water vapor. Unfortunately, the small number of simultaneous measurements of this kind does not permit any definite conclusions to be drawn about the character of the interaction of the above components. It is clear, however, that the interaction process is rather complicated, especially since at the altitudes considered a continual mixing of air masses takes place. It is interesting to note, for example, that there is no definite relationship between the decrease in ozone concentration and the increase in aerosol concentration, i.e., the ozone-destroying effect of aerosol particles is probably not the factor determining the ozone content of the stratosphere.

The application of photoelectric counters and the development of aerosol radiosondes permitted the authors of the latter four papers to obtain extensive data on the space-time structure of the stratospheric aerosol concentration and on the variability of vertical aerosol profiles. The measurement technique made it possible to determine the ratio of the concentration of particles with a diameter greater than 0.25 μm to that of particles with a diameter greater than 0.50 μm. In all cases this size ratio changed noticeably with altitude; in the lower stratosphere a decrease in this ratio to minimum values of about 3 or 4 was almost always observed. In a number of cases a decrease in the size ratio was observed at higher altitudes.

An analysis of the dependence of the vertical aerosol profiles on geographical conditions leads, in general, to the same conclusions as the lidar soundings. Of interest in this connection are the results of the measurements over Antarctica, which show that the stratospheric aerosol in the summer hemisphere is less abundant and consists of smaller particles.

The comparison between the results of measurements made with a photoelectric counter between 1963 and 1972 showed that the aerosol content in the atmosphere changed considerably from year to year. The largest aerosol content was observed in 1963 after the eruption of the volcano Agung.

The results of recent analyses of the chemical composition of samples of the stratospheric aerosol differ considerably from the earlier data (Cadle, 1973; Shedlovsky, 1971; Ward et al., 1973). First of all, it should be noted that the compounds containing $SO_4^{=}$ are not always the main components of aerosol particles. The content of Ca^{++} and of other elements in the samples turned out to be rather high. Weight concentrations of the aerosol matter exceeded those in Junge's data by about two orders of magnitude.

The results of Bigg et al. (1970) indicate that there are many particles of nonphotochemical origin in the stratosphere. Those found at altitudes of about 25 km are particles of a coarse structure similar to that of the smokes of metals. Some of the particles investigated were enveloped in some other substance, the largest part of which evaporated under the effect of the electron beam.

Measurements from manned spacecraft permitted us to estimate the global variability of the stratospheric aerosol (Gray et al., 1971; Cunnold et al., 1972; Kondratyev, 1972). The principal conclusions of these measurements agree well with the data of balloon, aircraft and lidar measurements of the stratospheric aerosol, particularly the detection of an aerosol layer at altitudes of 40 to 50 km during the measurements from manned spacecraft.

In the period from 1962 to 1972, Leningrad University investigators performed balloon launches of an instrumentation package in mid-latitudes of the European part of the USSR. One of the purposes of these launches was to study the concentration distribution, particle size distribution, and optical properties of the stratospheric aerosol. The main sources

of the information were a) actinometric measurements of direct solar radiation (25 flights), b) impactor measurements of the vertical profile of number density and of particle size distribution at various altitudes (23 flights), c) filter measurements of the chemical composition and size distribution of the stratospheric aerosol (2 flights) and d) spectral measurements of the attenuation of direct solar radiation (3 flights) (Kondratyev et al., 1969; Kondratyev and Nikolsky, 1970; Ivlev, 1972).

Moreover, some conclusions have been drawn from simultaneous measurements with radiation instruments and an ozonometer (10 flights), from spectral measurements of sky brightness and of the attenuation of direct solar radiation made by Fedorova's group (Sholokhova, 1971; Fedorova et al., 1973) in the same latitudes, and from the processing of Murcray's data (Kondratyev et al., 1963, 1971; Fedorova et al., 1973; Andreev et al., 1972). The main results of this data analysis are discussed below.

VERTICAL PROFILE OF THE STRATOSPHERIC AEROSOL CONCENTRATION

The vertical profile of the coefficient of aerosol attenuation of solar radiation and of aerosol number density has a rather complicated and variable layered character. An analysis of the occurrence of the aerosol, inversion, and isothermal layers shows that the aerosol layers are most frequently observed above and below the inversion and isothermal layers, which are at 10-13 km, 17-18 km, and 22-23.5 km. The centers of the aerosol layers are most often located at altitudes of 13.5 km, 16.5 km, 19.2 km, 21.8 km and 24 km. At these altitudes the values for the coefficients of aerosol attenuation in the visible spectral region reach 0.01-0.03 km^{-1}, and the values for the number density for particles with radii $\geqslant 0.2$ μm are 0.1 to 1.0 cm^{-3}. Incomplete agreement is observed between the vertical aerosol profiles obtained from the optical and microphysical measurements of the number density, which suggests the variability of the size spectrum of aerosol particles with altitude. In most measurements, particularly those made in summer, it was observed that the Junge layer was divided into two layers, which may be related to the existence in these latitudes of two tropopauses (polar and tropical).

In the measurements made in winter and late fall, a decrease in the thickness of the aerosol layers and their "blurring" were observed (σ_{aer} decreased to 0.005 km^{-1} for H between 18 and 20 km). A unique correspondence with the vertical ozone profile was not observed, which apparently may be explained both by the ozone-destroying effect of aerosols and by the photochemical formation of aerosols in the presence of ozone.

One of the indications of the variations of the stratospheric aerosol is the variability of the transparency of the entire atmospheric thickness from the data of surface measurements at the "background" stations (i.e., the stations intended for estimating the variability of global turbidity of the atmosphere).

The results of systematic observations of twilight phenomena and the data from measurements made at the "background" stations show that the atmospheric turbidity varies considerably. Figure 1 illustrates temporal variations of turbidity and relative transmission of the atmosphere using the data of actinometric observations from the high-altitude station at Mauna Loa (Ellis and Pueschel, 1971; Peterson and Bryson, 1968). As can be seen, a sharp increase in turbidity took place in 1963 due to the eruption of the volcano Agung, though a tendency toward increased turbidity was observed in 1960-1962. This increase preceding the Agung eruption is evidently connected with the numerous nuclear explosions in the atmosphere between 1959 to 1962. In fact, a careful study of the variation of relative transmission and of the increase of the turbidity coefficient in 1962 shows that an appreciable increase in turbidity began in the middle of 1962, i.e., a year before the eruption of Agung.

The variation of relative transmission prior to 1962 indicates that the turbidity of the upper troposphere and stratosphere has a pronounced seasonal character related to the large-scale circulation. Recent data from other "background" stations confirm that the atmospheric turbidity exhibits latitudinal and seasonal variation (Volz, 1972; Cronin, 1971). Observations of twilight phenomena over many years show that the stratospheric turbidity in the Northern Hemisphere has an annual periodicity with a maximum in October-November and a minimum in April-May, with a general tendency towards an increase in transparency between 1964 and 1970. But even in recent years the autumn-winter turbidity maxima have reached fairly large values, as has been confirmed by balloon soundings of the attenuation of solar radiation in the atmospheric layer above 30 km in a winter period (December-January) in 1967, 1968, 1970 and 1971 (Ellis and Pueschel, 1971; Cunnold et al., 1973).

Between 1964 and 1970 the general tendency towards a clearing of the atmosphere after the Agung eruption was often contravened. In Figure 1 it can be seen that numerous cases of increased atmospheric turbidity with a subsequent rapid clearing took place during this period. Several strong volcanic eruptions occurred in the equatorial region during this time (Taal (1965), Fernandina (1968), etc.), the products of which were injected immediately into the stratosphere. A number of the surface and atmospheric nuclear tests in China also caused pollution of the upper troposphere and stratosphere. In the Arctic the eruptions of several volcanoes also took place in this period: Trident (April 1963), Surtsey (November 1963), Redoubt (1966) and Hekla (1970). We know that during the eruptions of the Arctic volcanoes the volcanic dust and gases propagated only within the atmosphere of the Northern Hemisphere. On the other hand, a considerable part of the volcanic products from the eruptions in the equatorial belt also reached the atmosphere of the temperate latitudes of the Northern Hemisphere.

During the volcanic eruptions, along with the ash and sulfur gases, a considerable amount of water vapor

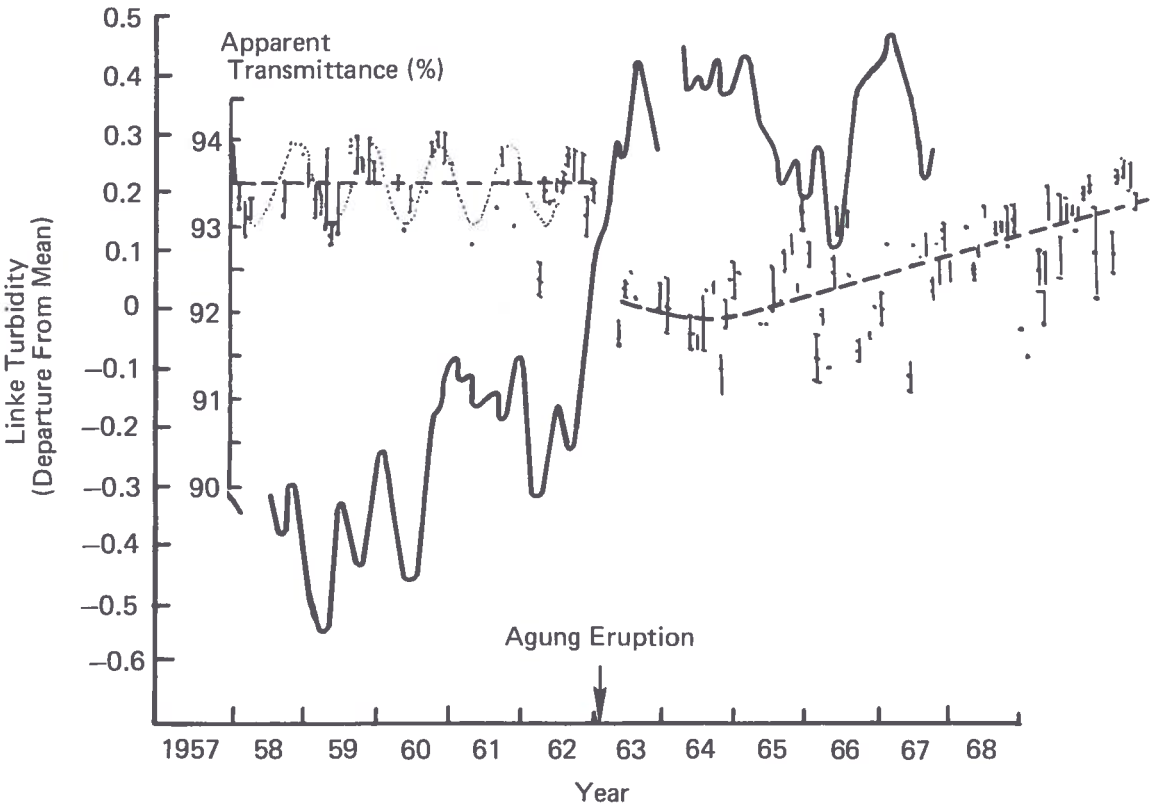

Figure 1. Deviation of the turbidity coefficient from the mean value, and the variation of the relative transmission of the atmosphere during 1958-1968.

reaches the stratosphere, particularly in the case of the submarine and coastal eruptions. Thus, according to Volz (1972), it is possible to say that during the decade 1960-1970 the products of volcanic eruptions and nuclear tests were much more abundant in the Northern Hemisphere than in the Southern Hemisphere. The transport of these products by seasonal circulation of the stratospheric air masses manifests itself, at mid-latitudes, in rather high values for the autumn-winter maximum of turbidity. The origin of the aerosol layer observed by a number of investigators at an altitude of about 48 km is probably related to the presence at such altitudes of volcanic gases and water vapor.

CHEMICAL COMPOSITION AND SIZE DISTRIBUTION OF THE STRATOSPHERIC AEROSOL

The data given above have partially characterized the chemical composition of the stratospheric aerosol. It should be noted that our measurements, as well as Cadle's latest measurements (Cadle, 1973), indicate a more complicated and changeable chemical composition of the stratospheric aerosol than that obtained by Junge (1963) and Friend (1966). Ammonium sulfate is not always the main and prevalent component of the stratospheric aerosol. A considerable contribution is made by the mineral component, which may be due in part to both volcanic ash and the products of meteorite disintegration in the upper atmosphere. We may agree with Newkirk's (1967) estimate of the latter's contribution as 10-20% if we assume that the annual fallout of material from space onto the earth reaches approximately 10^5 tonnes and that the lifetime of the stratospheric aerosol particles is on the order of one year.

The aerosol mixing ratio for the stratosphere probably varies between 10^{-11} g/g to 10^{-8} g/g. Rather high values of the mixing ratio, equal to 0.5×10^{-8} g/g, were obtained during drift flights at an altitude of 30-31 km in the summer of 1968 (Ivlev et al., 1973).

Investigation of the stratospheric aerosol size distribution confirmed that the particle size spectrum of the aerosol varies with altitude and the time periods of measurement. It should be mentioned that particle size distributions similar to those obtained by Friend (1973) have not been observed in our flights. The reason becomes clear if one bears in mind that there were no strong volcanic eruptions immediately prior to the launches of our microphysical experiments. However, in the particle size spectra of the stratospheric aerosol, deviations from the Junge distribution were distinctly seen for particles with radii of 0.3-0.5 μm and 1.7-2.3 μm (see Table 1).

Table 1. Size Distribution of Aerosol Particles in the Stratosphere, Averaged Over the Period 1966 to 1969

r_i-r_k μm	$\frac{\Delta N_{(r_i-r_k)}}{\sum_{r_i=0.2}^{r_i=10} \Delta N}$ 10-17 km	17-24 km	24 km
0.20-0.25	0.561	0.476	0.547
0.25-0.375	0.157	0.178	0.177
0.375-0.50	0.130	0.178	0.180
0.50-0.75	0.056	0.076	0.060
0.75-1.00	0.044	0.035	0.014
1.00-1.25	0.024	0.019	0.0085
1.25-1.50	0.014	0.013	0.0073
1.50-1.75	0.0080	0.0070	0.0095
1.75-2.00	0.0062	0.0090	0.0085
2.00-2.25	0.0050	0.0023	0.0060
2.26-2.50	0.0011	0.0020	0.0032
2.50-3.00	0.0006	0.0014	0.0014
3.00-3.50	0.0006	0.0003	0.0008
3.50-4.00	–	0.00007	0.0008

Particularly interesting are the data obtained with the polyvinylchloride filters during the drift phase of balloon flights at an altitude of 31 km (Ivlev and Surikov, 1968), because when the samples are collected with these filters the particle-size distribution function is nearly undistorted. A chemical analysis of the filters showed a satisfactory agreement between the chemical composition of the stratospheric aerosol and that of meteorite dust. A maximum for particle sizes between 1.5 μm and 2.25 μm was revealed. This maximum was also observed in a number of cases during the impactor measurements. The following transformation of size spectrum with altitude is typical. Relative maxima of size distribution for the particles with radii of 0.5 μm and 1.75 μm or more are more pronounced in the layer at 17-24 km than in the lower layers. In samples, the presence of particles ≥ 3 μm is characteristic of the altitudes above 24 km. Since the lifetime of these particles at such altitudes cannot be long, it is reasonable to postulate the existence of a powerful source of these particles more constant in its activity than the volcanoes. It would be most natural to suppose that these particles are of space origin. It should be mentioned that the real lifetime of aerosol particles in the stratosphere may be much longer than calculated (3-6 months for particles ≤ 1 μm) because of their coarse structure.

The stratospheric content of finely-dispersed aerosol is much lower than that of the troposphere. In the stratosphere, therefore, relatively less particle growth by coagulation occurs. For this reason, the different fractions of the stratospheric aerosol may behave nearly independently and their chemical composition may be different. The deviations from the Junge distribution become understandable if there are several different sources producing various particle size spectra.

We can suggest three principal processes for the formation of stratospheric particles:

1. Particle growth on ions: finely-dispersed fraction;
2. Formation of sulfate particles with maximum radius of about 0.5 μm;
3. The breakup of the larger particles (those with a maximum ≥ 1 μm).

The particles formed according to the third process may be of volcanic and space origin; in the latter case, most of the particles over 2 μm must burn up upon entering the earth's atmosphere.

It is likely that a similar situation exists in the case of the tropospheric aerosol, whose particle number density is small when the coagulation mechanism is weak.

An electron-microscopic analysis of the atmospheric aerosol samples shows the diversity of the nature of stratospheric particles. Figure 2 illustrates the different types of stratospheric particles: the homogeneous dense particle (2a); the aggregate of comparably sized spheres, probably produced by combustion products of space dust (2b); the compact particle (2c) more uniform in density than that in 2a; the aggregate of small crystals of ammonium sulfate enclosed in a sphere of very low density (2d); the group of small particles, possibly of terrestrial origin (2e); and the giant particle with a large number of small particles stuck to it (2f).

Of most interest is the aggregate of sulfate particles. Patterns of this kind were often obtained earlier on the substrate of a colloid film. The shell of the nucleus was usually attributed to the dried residue of a liquid solution. In this particular case, the particles were captured by the polyvinylchloride filter EPP-15, which was then washed in xylene. One may suppose that the photo (2d) reflects the real structure of sulfate particles in the stratosphere. Small sulfate particles/crystals make up coarse unstable aggregates, inside which are microcapillaries which absorb water even at a comparatively low relative humidity. The water makes the aggregate stable and facilitates its further growth by coagulation. Such a mechanism is pronounced at not very high values of relative humidity (between 30% and 70%) when sulfate particles are incompletely dissolved.

A similar mechanism may be also at work in the coagulation growth of the particles made up of less hygroscopic substances, depending on the solubility of these substances. The optimal growth conditions for the different particles will correspond to various values of relative humidity. At increased humidity the giant particle aggregate may be transformed into a droplet, and fall into the lower atmospheric layers, which behavior agrees well with the experimentally observed fact of a strong instability of the vertical profile of the stratospheric aerosol.

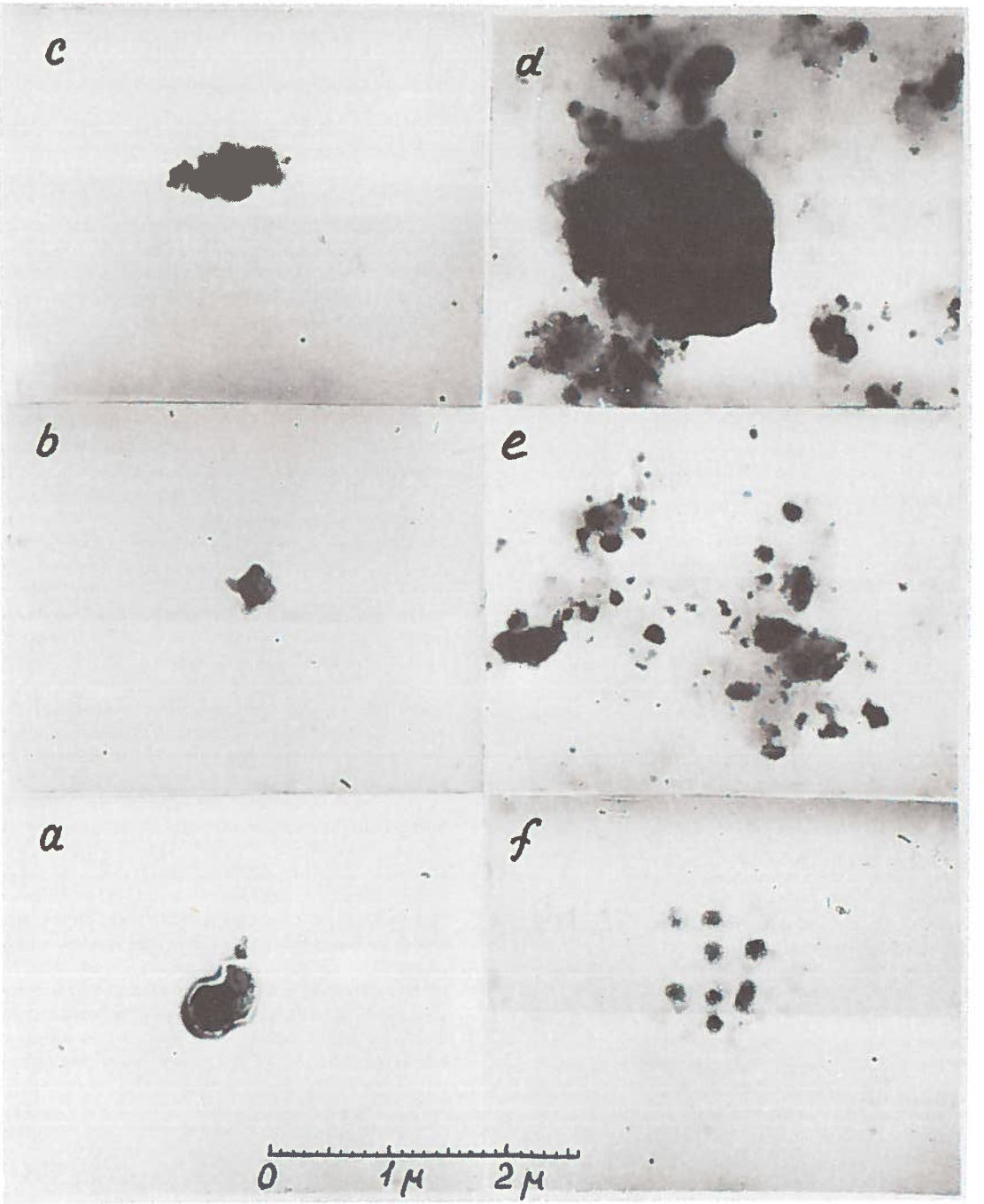

Figure 2. Electron-microscopic photographs of various types of aerosol particles collected in the stratosphere at an altitude of 30-31 km. (See text for discussion.)

OPTICAL PROPERTIES OF THE STRATOSPHERIC AEROSOL

Noticeable bands of attenuation of radiation by the stratospheric aerosol have not been detected in the visible spectral region. It is likely that aerosol absorption of radiation has an almost neutral character.

In the infrared spectral region, the bands of radiation attenuation corresponding to liquid water and ice, and ammonium sulfate, are strong, which suggests

the presence of these components in stratospheric aerosol particles.

The stratospheric absorption bands near 5.3 μm reported by Kiselyova et al. (1971) and attributed to nitrogen oxides may belong to nitrates. The presence of nitric acid in the stratosphere was detected with the help of optical measurements by Murcray et al. (1969b).

Now we shall present some examples of the effect of aerosols on the radiation budget of the stratosphere. Table 2 shows the values for aerosol absorption of shortwave radiation (cal $cm^{-2}min^{-1}$) from the data of three balloon soundings. Radiative heating due to aerosol absorption of direct solar radiation in summer conditions at altitudes of 15 to 20 km was about 0.01-0.03 K/hr.

Figure 3 presents vertical profiles of the radiation balance for the visible (0.35-0.7 μm), near-infrared (0.7-3.0 μm) and total short-wave (0.35-3.0 μm) spectral regions for winter sounding (the underlying surface was snow and there was light cloud cover).

In the troposphere, up to altitudes of 8 to 9 km, the considerable increase in shortwave radiation balance with height is related to the variability of radiation characteristics of the surface below the balloon trajectory, whereas in the stratosphere it is mainly due to absorption of solar radiation by the optically active components. This is confirmed by the isothermal air-temperature profile at altitudes of 16 to 20 km and by the presence of inversions at altitudes of 10 to 12 km and 26 to 30 km.

The value of the radiation-balance vertical gradient for the visible spectral region is considerably smaller than that for the near-infrared region. It is evident that in this case the component of the balance for the near-infrared spectral region exerts a determining influence on the vertical profile of the total shortwave radiation balance.

Balloon soundings of the vertical profile of the shortwave albedo over underlying surfaces with large albedo values (snow or cloud layers) show that upper-tropospheric and stratospheric turbidity leads to a noticeable decrease in the values of the surface-atmosphere system albedo (up to 10-15%). This effect can, to a certain degree, compensate (on a planetary scale) for the increase in the system albedo due to the increased

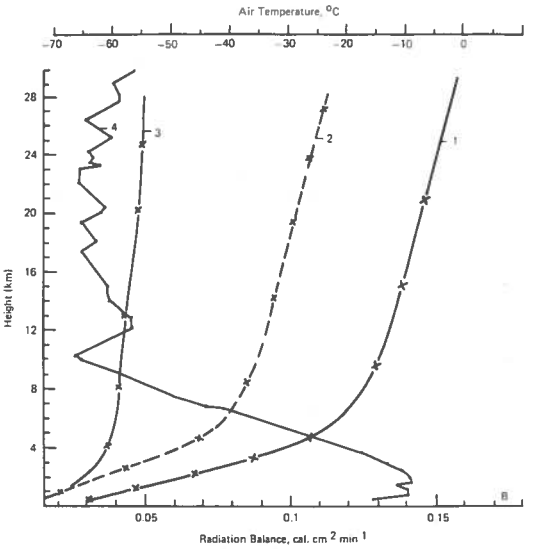

Figure 3. Vertical profiles of the short-wave radiation balance for: (1) the total short-wave region (0.35-3.0 μm), (2) the visible region (0.35-0.7 μm), and (3) the near-infrared region (0.7-3.0 μm). (4) is the vertical profile of the air temperature during the ascent of the balloon.

aerosol concentrations, in the case of small values of the albedo of the underlying surfaces. Hence, we must conclude that in estimating the influence of aerosol on the earth's albedo as a whole it is very important to take into account the ratio of the areas of the underlying surfaces with different albedos.

CONCLUSION

Although our investigations of the stratospheric aerosol are still at the initial stage, we now have rather extensive information on the concentration field, size distribution, and chemical composition of aerosol particles. The main problem now is to continue and extend detailed investigations of the stratospheric aerosol, particularly of its optical properties. Only in

Table 2. Absorption of Short-Wave Radiation by the Stratospheric Aerosol (cal $cm^{-2}min^{-1}$)

Atmospheric Layer (km)	Aerosol Absorption	Total Attenuation	Method	Solar Elevation (deg)	Season
10-30	0.035	0.218	Direct solar radiation	33.5-38.9	Summer
9-17	0.09	–	Shortwave balance	15-12	Autumn
9-17	0.08	–	Shortwave balance	11-13	Autumn

this way will it be possible to obtain sufficient experimental data on the conditions of formation and destruction (sources and sinks) and the properties of the stratospheric aerosol, and on the effect of the aerosol on the radiation budget of the stratosphere and of the surface-atmosphere system. This is extremely important, not only for an understanding of the processes occurring in the stratosphere, but also for determining the possible role of the stratospheric aerosol as a climate-regulating factor.

REFERENCES

Andreev, S.D., L.S. Ivlev, and E.L. Yanchenko (1972), "Some problems of the vertical profile of the aerosol attenuation coefficient in the atmosphere in the wavelength range of 0.5-6 μm," Izvestia Vuzov, Fizika, 5, 98-103.

Bigg, E.K., A. Ono, and W.J. Thompson (1970), "Aerosols at altitudes between 20 and 27 km," Tellus 22, 550-563.

Cadle, R.D. (1973), "Composition of the stratospheric 'sulfate layer'," in *Proceedings of the Survey Conference* (Feb. 15-16, 1972), Climatic Impact Assessment Program, U.S. Department of Transportation, DOT-TSC-OST-72-13, 130-139.

Collis, R.T.H., W. Viezee, E.D. Hake, Jr., and P.B. Russell (1973), "Lidar measurements of the variability of stratospheric particulates," AIAA Paper 73-520.

Cronin, J.F. (1971), "Recent volcanism and the stratosphere," Science 172 (27), 847-849.

Cunnold, D.M., C.R. Gray, and D.C. Merritt (1972), "Stratospheric aerosol layer detection," in *Proceedings of the International Radiation Symposium* (Sendai, Japan, May 26-June 2, 1972), 192-204.

Cunnold, D.M., C.R. Gray, and D.C. Merritt (1973), "Stratospheric aerosol layer detection," Pure Appl. Geophys. 106-108, 1264-1271.

Ellis, H.T. and R.F. Pueschel (1971), "Solar radiation: abscence of air pollution trends at Mauna Loa," Science 172 (21), 845-847.

Elterman, L., R. Wexler, and D.F. Chang (1969), "Features of tropospheric and stratospheric dust," Appl. Opt. 8 (5), 893-903.

Fedorova, E.O., I.S. Reshetnikov, and O.V. Nefedova (1973), "The altitude change of brightness phase functions and of the angular variation of the degree of polarization of the daylight sky in the 27 μm O_2 emission band," Izvestia Akad. Nauk USSR, Fizika Atm. i Okeana 9 (2), 195-197.

Friend, J.P. (1966), "Properties of the stratospheric aerosols," Tellus 18 (2-3).

Friend, J.P. (1973), "Trace material composition of the lower stratosphere," in *Proceedings of the Survey Conference* (Feb. 15-16, 1972), Climatic Impact Assessment Program, U.S. Department of Transportation, DOT-TSC-OST-72-13, 71-79.

Grams, G.W. and G.J. Fiocco (1967), "Laser measurements of stratospheric aerosols during 1964-1965," J. Geophys. Res. 72, 3523-3542.

Grams, G.W., J.H. Blifford, Jr., B.G. Schuster, and J. DeLuisi (1972), "Complex index of refraction of airborne fly ash determined by lasar radar and collection of particles at 13 km," J. Atm. Sci. 29 (5), 27.

Gray, G.R., H.L. Malchow, D.C. Merritt, and R.E. Var (1971), "Aerosol monitoring by satellite horizon scanning," AAIA Paper No. 71-1111 (Palo Alto, Nov. 8-10, 1971).

Hofmann, D.J., J.M. Rosen, and J.L. Kroening (1972a), "Global Monitoring of Stratospheric Aerosol, Ozone and Water Vapor," Progress Report, Contract No. 00014-70-0266-0005, Univ. of Wyoming.

Hofmann, D.J., J.M. Rosen, T.J. Pepin, and J.L. Kroening (1972b), "Global Measurements of Stratospheric Aerosol, Ozone and Water Vapor by Balloon-Borne Sensors," Progress Report GM-3, Univ. of Wyoming.

Ivlev, L.S. (1972), "Some results of balloon measurements of the atmospheric aerosol," in "Problems of Atmospheric Physics," No. 10, Leningrad Univ. Press, 92-103.

Ivlev, L.S. and O.M. Surikov (1968), "Balloon measurements of the vertical distribution of the atmospheric aerosol," in "Problems of Atmospheric Physics," No. 6, Leningrad Univ. Press, 59-63.

Ivlev, L.S. and E.L. Yanchenko (1972), "Backscattering of radiation by the atmospheric aerosol," in "Problems of Atmospheric Physics," No. 10, Leningrad Univ. Press, 128-132.

Ivlev, L.S., B.J. Ogorodnikov, and A.Yu. Semova (1973), "Determination of the content of some chemical elements in the stratospheric aerosol," Trudy IPG No. 19.

Junge, C.E. (1963), *Air Chemistry and Radioactivity*, Academic Press, New York.

Kiselyova, M.S., I.N. Reshetnikova, G.E. Sinelnikova, and E.O. Fedorova (1971), "Band of atmospheric absorption about 5.3 μm," Izv. Akad. Nauk USSR, Fizika Atm. i Okeana 7 (5), 552.

Kondratyev, K.Ya., ed. (1972), *Investigation of the Environment from Manned Orbital Stations*, Gidrometeizdat, Leningrad.

Kondratyev, K.Ya., G.N. Gaevskaya, and G.A. Nikolsky (1963), "Experimental investigation of the radiation balance in the free atmosphere," in "Problems of Atmospheric Physics," No. 1, Leningrad Univ. Press, 17-31.

Kondratyev, K.Ya., G.A. Nikolsky, I.Ya. Badinov, and S.D. Andreev (1967), "Direct solar radiation up to 30 km and stratification of attenuation components in the stratosphere," Appl. Opt. 6 (2), 197-207.

Kondratyev, K.Ya., I.Ya. Badinov, L.S. Ivlev, and G.A. Nikolsky (1969), "Aerosol structure of the troposphere and stratosphere," Izvestia Akad. Nauk USSR, Fizika Atm. i Okeana 5 (5), 408-493.

Kondratyev, K.Ya. and G.A. Nikolsky (1970), "Direct solar radiation up to altitudes of 30 km and the solar constant; results of the investigations from the International Geophysical Projects," Meteorological Investigations No. 17, Moscow, 23-33.

Kondratyev, K.Ya., G.A. Nikolsky, D.G. Murcray, and J.J. Kosters (1971), "The solar constant from data of balloon investigations in the USSR and the USA," COSPAR XI, Space Research XI, Akademie-Verlag, 695-703.

Martell, E.A. (1966), "The size distribution and interaction of radioactive and natural aerosols in the stratosphere," Tellus **18** (2-3), 486-498.

Meinel, A.B. and M.P. Meinel (1967), "Volcanic sunset-glow stratum: origin," Science **155**.

Mossop, S.C. (1965), "Stratospheric particles at 20 km altitude," Geochim. Cosmichim. Acta **29** (2), 201-207.

Murcray, D.G., T.G. Kyle, J.J. Kosters, and P.R. Gast (1969a), "The measurement of the solar constant from high-altitude balloons," Tellus **21** (5).

Murcray, D., T. Kyle, F. Murcray, and W. Williams (1969b), "Presence of HNO_3 in the upper atmosphere," J. Opt. Soc. Amer. **59** (9), 1131-1134.

Newkirk, G.A. (1967), "Meteoric dust in the stratosphere determined by optical scattering techniques," Symp. on meteor orbits and dust, Smiths. Contrib. Astroph. **11**, 4.

Peterson, J.T. and R.A. Bryson (1968), "Atmospheric aerosols: increased concentrations during the last decade," Science **162**, 120-121.

Poppoff, I.G. (1973), "The measurements of minor stratospheric constituents using high-altitude aircraft," in *Proceedings of the Survey Conference* (Feb. 15-16, 1972), Climatic Impact Assessment Program, U.S. Department of Transportation, DOT-TSC-OST-72-13, 217-225.

Reiter, E.R. (1973), "Trace gases, aerosols and solar radiation in the stratosphere: explored and unexplored problem areas," AIAA Paper No. 73-509.

Rosen, J.M., D.J. Hofmann, and T.J. Pepin (1973), "An optical model for stratospheric aerosols, in *Proceedings of the 15th Conference on Laser Radar Studies of the Atmosphere* (June 4-5, 1973, Williamsburg, Va.), 24.

Schuster, B.G. (1970), "Detection of tropospheric and stratospheric aerosol layers by optical radar," J. Geophys. Res. **75**, 3123-3132.

Shedlovsky, J.P. (1971), "Chemical composition of stratospheric aerosols," in "Particle Models, Their Validity and Application," ed. I.H. Blifford, NCAR-TN/PROC 68, National Center for Atmospheric Research, 221-226.

Sholokhova, E.D. and E.O. Fedorova (1971), "Determination of the atmospheric scattering coefficients in the individual spectral regions from 1.2 to 2.2 μm at altitudes to 18-20 km," Izvestia Akad. Nauk USSR, Fizika Atm. i Okeana 7 (6), 678-680.

Volz, F.E. (1972), "Return of normal stratospheric turbidity and new short dust event during October 1971," in *Proceedings of the International Radiation Symposium* (Sendai, Japan, May 26-June 2, 1972).

Ward, G., K.M. Cushing, R.D., McPeters, and A.E.S. Green (1973), "Atmospheric aerosol index of refraction and size-altitude distribution from bistatic laser scattering and solar aureole measurements," Appl. Opt. **12** (11), 2585-2592.

Zuev, V.E., L.S. Ivlev, and K.Ya. Kondratyev (1973), "New results of investigations of the atmospheric aerosol," Izvestia Akad. Nauk USSR, Fizika Atm. i Okeana 9 (4), 371-385.

DISCUSSION

FRIEND: I think this paper is an important contribution, in that it provides recent particle size distributions. I'd be interested in seeing individual data. It seems that in earlier measurements of particle size distribution we were observing mostly ammonium sulfate. In the last ten or so years, the composition of the stratospheric aerosol has changed considerably; the indications are that now there is a high proportion of sulfuric acid, which of course would have a size distribution considerably different from ammonium sulfate.

GILLE: I'd like to make one comment on the last section. Absorption by particles in the near-infrared is quite plausible if one accepts a high concentration of sulfuric acid. A year ago, it was suggested that the aerosol absorption of solar radiation in the visible part of the spectrum would be rather small, but would get larger beyond one micron wavelength.

VERTICAL PROFILES OF CH_4, H_2, CO, N_2O AND CO_2 IN THE STRATOSPHERE

D.H. EHHALT, L.E. HEIDT, R.H. LUEB, AND N. ROPER
*National Center for Atmospheric Research**
Boulder, Colorado

ABSTRACT: On 9 September 1973 a newly developed cyrogenic sampling system was flown aboard a balloon to 30 km altitude over Palestine, Texas. Stratospheric air samples of 5 to 10ℓ STP were collected at eight different altitudes. These large samples allowed measurement of the CO, N_2O, and CO_2 concentrations, in addition to those of CH_4 and H_2. The resulting vertical profiles of these trace gases are reported and discussed.

INTRODUCTION

Over the past year we have made a number of balloon flights, using a grab-sampling system to collect vertical profiles of eight stratospheric air samples. The samples were then analyzed by gas chromatography for their H_2, CH_4, and Ne content. However, this grab-sampling system is useful only up to 35 km; above that altitude the recovered samples become so small (less than 21 cm^3 STP) that the detection sensitivity drops. In addition, contamination from sample-container surfaces, a problem for H_2 and particularly for CO, increases relative to the amount of sample as the altitude increases. We decided therefore to use a cryogenic sampling system which would allow the collection of large samples (about 10ℓ STP) at any altitude. The system consists of nine 200-ml pressure tanks made of stainless steel, cooled by liquid Ne contained in a dewar and kept at 0.5 atm above ambient pressures. The tanks are opened and closed at sampling altitudes by motor-driven high-vacuum valves made of stainless steel. As for the grab-sampling system, all internal surfaces were electropolished, and the system is evacuated and baked for several days prior to launch. In fact, the system is pretty much operated the same way as the grab-sampling system, except that the collection times for 10ℓ STP vary between about 30 min at 30 km altitude to about 1 min at 15 km. Correspondingly, since sampling is done during descent at a rate between 30 and 50 m/min, the uppermost sample is taken over a height interval of 1 km, and the lowest over about 100 m. The fact that the cryogenic sampler provides much bigger samples opens up the possibility of measuring other trace gases besides H_2, CH_4, and CO. At present we are set up to measure CO_2 and N_2O. CO_2 is measured manometrically. The N_2O concentration is obtained from the N_2O-to-CO_2 concentration ratio, determined in an Atlas M86 mass spectrometer. Measurements of other trace gases will be added in the future. The new cryogenic system was flown for the first time on 9 September 1973 from Palestine, Texas. The flight was successful; vertical profiles of H_2, CH_4, CO, CO_2, and N_2O were obtained, and are reported below.

RESULTS

Figure 1 shows the vertical CO_2 profile (it also shows the stratospheric temperature profile from a radiosonde launched the same day). Obviously the measured CO_2 mixing ratios vary little in the lower and middle stratosphere; they lie between 314 and 321 ppm. The average is 318 ppm, about 2 ppm lower than the present tropospheric average of 320 ppm. In contrast, the tropospheric CO_2 mixing ratio shows large variations, having high values close to the ground and a maximum with a very high peak of 426 ppm at 12.2 km altitude. Similar tropospheric maxima also occurred for CO and H_2. CO_2, CO, and H_2 are produced in combustion engines, and we suspect that those samples were collected within a flight corridor to the Greater Southwest Airport and are contaminated by exhaust from commercial aircraft. Our plane flew a triangular

* The National Center for Atmospheric Research is sponsored by the National Science Foundation.

course between Waco, Palestine, and Ft. Worth which brought it fairly close to the airport. There is another possible explanation: on 5 and 6 September, Hurricane Delia moved into Texas. It persisted as a surface low-pressure region through 7 September. However, the 200-mb chart shows a high-pressure region at high altitudes over the full area which persisted through 10 September. Thus air which was swept upward by the hurricane from the surface, and therefore had high concentrations of CO_2, CO, and H_2, could have been kept circulating in the upper troposphere over the Gulf area through 10 September. However, the measured concentrations of CO and CO_2 at 12 km are so high that they would have to have come from a rather polluted surface area. Also, the width of the concentration maximum is far too shallow to correspond to the outflow layer of a hurricane. Thus we consider the first explanation to be more likely, at least for CO and CO_2.

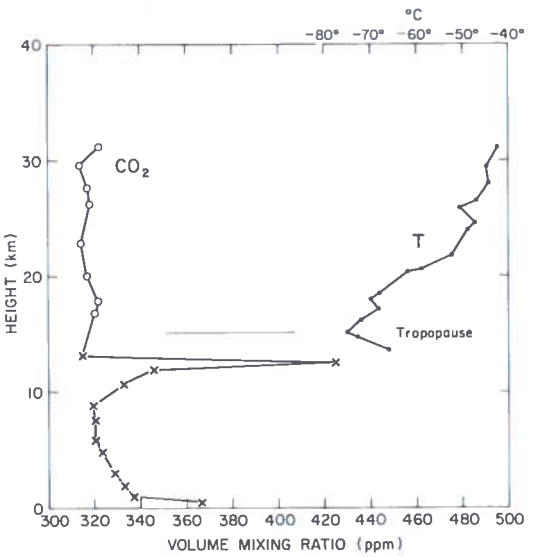

Figure 1. Vertical profiles of CO_2 mixing ratio and temperature. Open circles represent balloon samples collected over eastern Texas on 9 September 1973. Crosses represent samples from NCAR Sabreliner flight around Palestine, Texas, on 10 September 1973. The temperature data are from a radiosonde launched from Ft. Worth, Texas, on 9 September 1973, 00Z.

Figure 2 shows the vertical distribution of the trace gases H_2, CH_4, N_2O, and CO. Again the balloon data are indicated by the circles; the aircraft samples which were collected a day later are indicated by the crosses. The tropopause on 9 September was at 15 km altitude. The H_2 profile shows no unusual variation with altitude except the already mentioned tropospheric maxima. The stratospheric H_2 concentrations are not significantly higher, nor do they show a maximum above 25 km as had been observed on some of our earlier flights.

The stratospheric CH_4 profile shows more variation. The CH_4 concentration drops rapidly above the tropopause, then remains constant at about 1 ppm over a 7-km-deep layer, and drops rapidly again above 28 km. Such a sharp upper drop had not been observed in any of the previous profiles. In fact, the concentration of 0.60 ppm at 31 km measured here is the lowest we have observed at that altitude.

It is interesting to compare the CH_4 profile with the N_2O profile. It is obvious that their stratospheric portions are quite well correlated. Like CH_4, N_2O shows a sharp drop above the tropopause, a 7-km-deep layer of nearly constant concentration, and a steep decrease above that. This similarity is very gratifying. CH_4 and N_2O have a similar distribution of sources and sinks in the stratosphere: the tropopause acts as a source; destruction takes place slowly in the lower stratosphere and rapidly in the upper stratosphere. Thus, regardless of the transport pattern the distributions of N_2O and CH_4 should be parallel – just as they are in the present case.

The tropospheric part of the N_2O profile is also quite interesting. It shows the highest N_2O concentration we have found so far. Usually the vertical profiles show very little variation with altitude and remain around 0.25 ppm. On 10 September, however, we observed very high surface values and a broad maximum extending from the high troposphere into the low stratosphere. N_2O is not associated with pollution, and one wonders whether Hurricane Delia might have been responsible for the peculiar distribution. N_2O is produced in the soil; the concentrations there are one to two orders of magnitude higher than in the atmosphere (Schütz et al., 1970). Passage of a low-pressure system would tend to increase the rate of N_2O exhalation into the atmosphere, producing high concentrations in the surface air, and thus could explain the gradient of N_2O away from the surface. Also, N_2O would be swept upward by the hurricane,

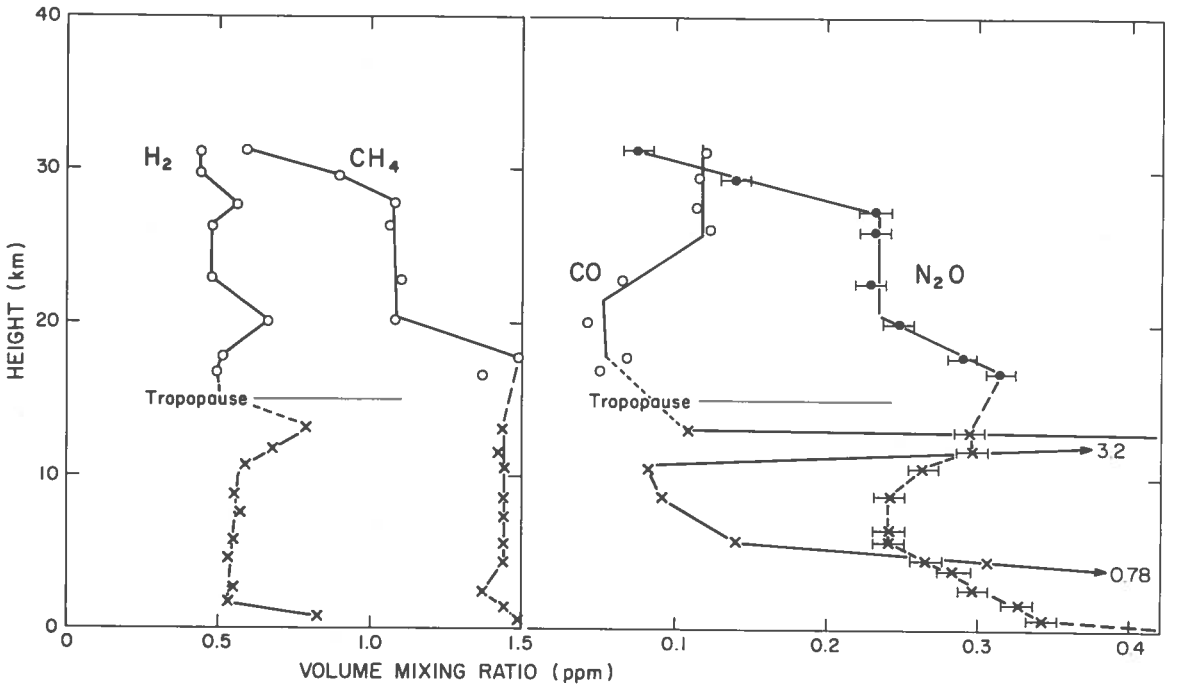

Figure 2. Vertical profiles of CH_4, H_2, CO, and N_2O mixing ratios over eastern Texas. Circles represent balloon data collected on 9 September 1973. Crosses represent samples from an aircraft flight on 10 September 1973. Except for N_2O and CO, the measurement errors are about the size of the symbols.

which should produce higher N_2O concentrations in the outflow layer of the hurricane. However, it is difficult to see how the increased local exhalation could fill such a deep vertical column of the atmosphere with increased N_2O concentrations, unless it were rather confined horizontally. More careful analysis of the weather situation and air flow pattern will be needed to decide this question.

Next we consider the CO profile. The average CO concentration in the northern troposphere is 0.15 ppm. Thus, the undisturbed part of our tropospheric profile (i.e., disregarding the maximum at 12 km as polluted) indicates a decrease of the CO concentration beginning in the troposphere. This decrease continues into the stratosphere to a concentration of about 0.04 ppm at 20 km altitude. This decrease agrees well with the predictions made by chemical models. The upper part of the stratospheric CO profile, however, does not agree at all with model predictions. The CO concentrations measured on 9 September exhibit a rather strong increase between 22 and 26 km and a constant value of 0.1 ppm above 26 km, whereas chemical models predict a much weaker increase which reaches a concentration of 0.1 ppm only at 50 km altitude, as we shall see below.

Needless to say, one-dimensional modeling cannot fit the measured profiles of CH_4 and N_2O either. To reproduce the observed deep layer of constant mixing ratio, unrealistically large eddy-diffusion coefficients in the lower stratosphere would be required. Obviously advection and mean vertical motion must be responsible for the shape of these measured profiles. So far we have had no opportunity to analyze the stratospheric flow pattern on 9 September, and the explanation of the details of the vertical trace-gas profiles will have to wait for future studies.

It is of course not unexpected that measured trace-gas profiles should differ from those predicted by a one-dimensional chemical model. A one-dimensional model packs all of the stratospheric dynamics into one parameter, the vertical eddy-diffusion coefficient. Furthermore, it is usually a steady-state model, which is to say it describes a mean state of the atmosphere which is averaged geographically as well as in time. By contrast, a measured profile is taken during a

single day, at one specific geographic location, and in a particular meteorological situation. The observed situation is thus not necessarily in a steady state, and horizontal advection and mean vertical motion might be quite important. This is especially true for trace gases with long chemical lifetimes whose concentrations do not adjust quickly to the new photochemical environment into which they have been transported. Thus, for CH_4, H_2, N_2O, and CO it makes sense to compare predicted profiles only to the mean of many measured profiles, and this will be done below.

COMPARISON WITH OTHER MEASUREMENTS

First we consider the CH_4 and H_2 profiles averaged over all our balloon data from Palestine, Texas (cf. Ehhalt and Heidt, 1973). These are shown in Figure 3. In averaging the data the height has been counted from the height of the tropopause, which averaged 15 km. The error bars given represent the standard mean deviation due to natural variation of the mixing ratios in the individual profiles. In addition to the balloon data, the results of two rocket flights from White

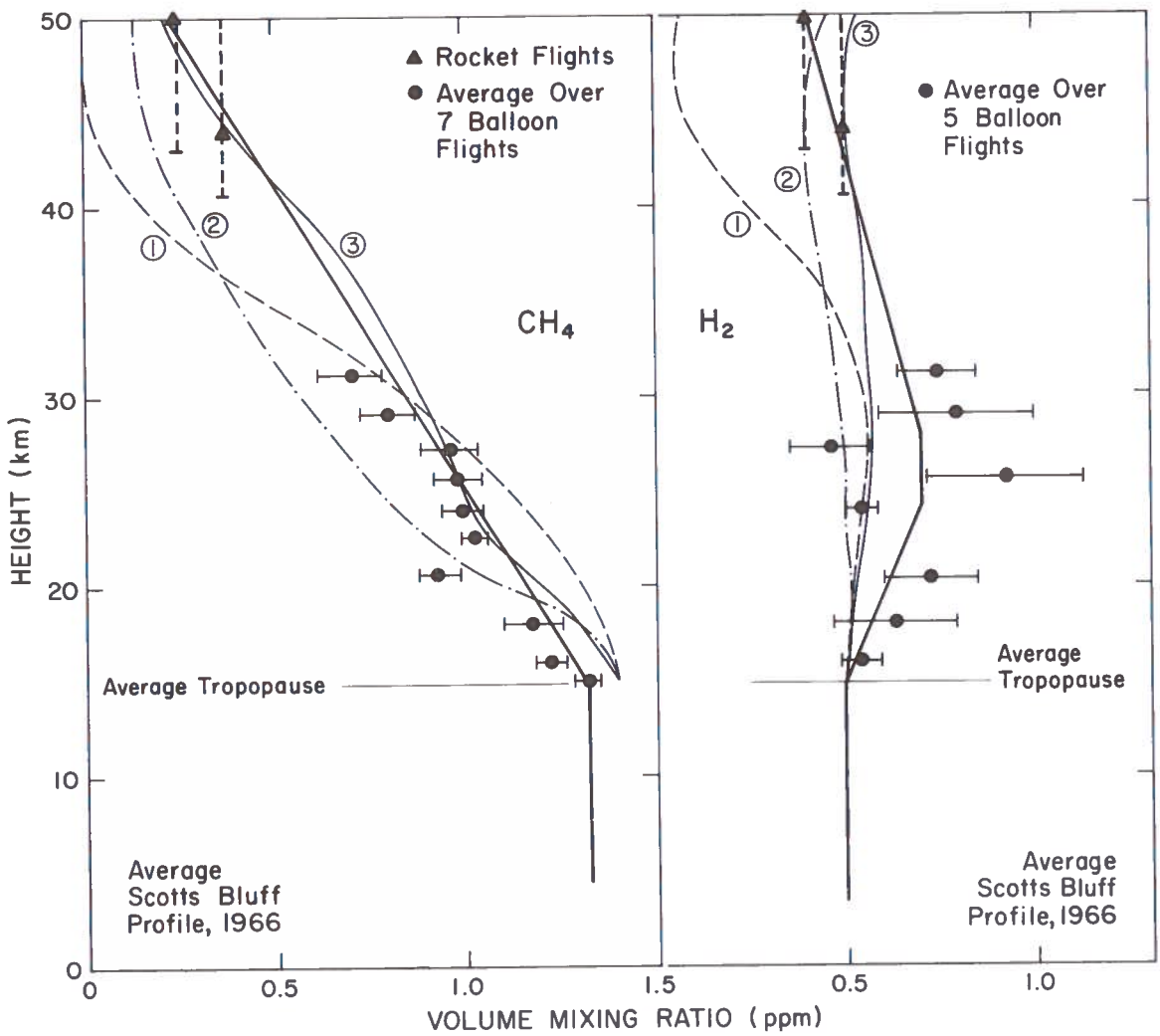

Figure 3. Average vertical profiles of CH_4 and H_2 mixing ratios over eastern Texas. Thin lines (1), (2), and (3) represent mixing-ratio profiles predicted by chemical-model calculations for different k_z profiles (see text).

Sands, N.M. are included. The earlier one, flown on 4 September 1968, collected an integrated sample between 44 and 62 km altitude. This corresponds to a weighted mean altitude of 50 km. The data obtained during this flight have been published previously (Scholz et al., 1970; Ehhalt et al., 1972; Ehhalt, 1974). The other flight, flown on 23 May 1973, collected a sample between 40 and 50 km, mean altitude 44 km. The data obtained during this flight will be published soon.

The average CH_4 data also indicate somewhat more rapid decreases immediately above the tropopause and above 28 km, with a relatively weak decrease in between. However, because of the variance of the data we prefer to represent the profile by a straight line, as indicated in the figure. The H_2 data exhibit a much larger variance. The average H_2 profile increases in the lower stratosphere, reaches a maximum of 0.7 ppm at about 25 km, and seems to decrease slowly above 28 km, reaching about 0.4 ppm at 50 km. The heavy curve represents a running average of the data points. Also included in the figures are the results of model calculations represented by the thin lines (1), (2), and (3). All these calculations were made with P. Crutzen's (1974) steady-state one-dimensional chemical model, leaving the chemistry unaltered and only varying the profile of the eddy-diffusion coefficient in the vertical. Profile (1) was calculated for Crutzen's original choice of eddy-diffusion coefficient profile, $k_z = 10^4$ cm^2/sec between the tropopause and 50 km, and an exponential increase above that to 3×10^6 cm^2/sec at 95 km. Profile (2) used a k_z profile which was essentially profile "C" of Wofsy and McElroy (1973). Profile (3) used a k_z profile obtained by trial and error to optimally fit the measured CH_4 profile. Like the k_z profile of Wofsy and McElroy, this profile introduces a barrier of relatively low eddy diffusion in the lower stratosphere, but assumes a $k_z = 10^5$ cm^2/sec between 30 and 50 km, and an exponential increase above. Our k_z values are thus about a factor of two higher than Wofsy's profile below 40 km, and somewhat lower above.

It is obvious from Figure 3 that Crutzen's original k_z profile does not provide enough CH_4 at 40-50 km, i.e., transport is too slow relative to the chemistry, and $k_z = 10^4$ cm^2/sec is too small. In fact, it was from the relatively high CH_4 value of 0.25 ppm at 50 km that Wofsy and McElroy concluded that the previously used vertical eddy-diffusion factors must be too small (at least for one-dimensional models), and proposed much higher k_z values in the middle and upper stratosphere. Theoretical profile (2), which is based on their k_z profile "C", does indeed explain the average CH_4 profile better. Still, that fit can be improved, and if our k_z profile is used the model predicts profile (3), which is in quite good agreement with the measured CH_4 profile.

Of course, any given concentration profile can be fitted by a suitably chosen k_z profile. To test their usefulness, we will have to check how well the same k_z profiles serve to predict the concentration profiles of H_2, CO, and N_2O as well. In the case of H_2, profile model (1) again provides too small a transport to compensate for the H_2 destruction between 40 and 60 km and allows a deep minimum to develop, which is not observed experimentally. Profiles (2) and (3) reproduce the measured H_2 profile pretty well, although both fail to explain the observed maximum around 25 to 28 km; profile (3) shows a very slight maximum, (2) none at all. (In fact, none of the k_z profiles we tried made the model reproduce the full maxima, which suggests the possibility that the chemistry is not quite correct.)

The profiles published so far for CO and N_2O are few, and differ so greatly in character from each other that averaging is not attempted, and the individual measurements are given. Figure 4 shows the CO data. Again all heights are given with respect to the tropopause. The full curve represents the measurements of Seiler et al. (1972), who found a constant value in the troposphere, a very steep transition across the tropopause, and constant but much lower concentrations of 0.04 in the lowest kilometers of the stratosphere. By contrast, the data of Goldman et al. (1973) show a decrease already begun in the troposphere and continuing into the stratosphere without obvious transition. This was also observed on our flight on 9 September, except that there the concentrations increased again above 22 km. Another bit of information was provided by our second rocket flight, which gave a CO mixing ratio of 0.05 ppm at 44 km. If we disregard the high CO values above 26 km

found on 9 September and shift the boundary value for the model calculations from 0.15 to 0.1 ppm, all model profiles would overlap reasonably well with the experimental data points in the lower stratosphere. Because of the scatter of the experimental data in the lower stratosphere and the lack of CO data in the middle and upper stratosphere, it is presently impossible to use the CO profiles to distinguish between the different k_z profiles.

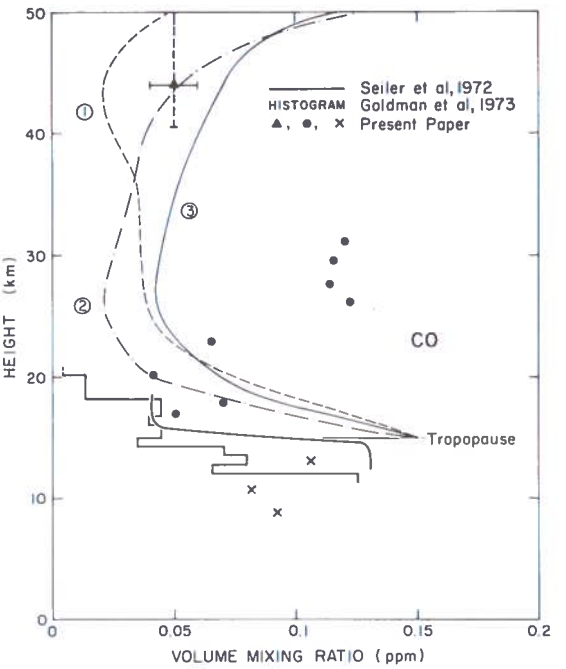

Figure 4. Measured profiles of CO mixing ratio by various authors compared to CO profiles (1), (2), and (3) predicted by chemical-model calculations for different k_z profiles (see text).

The same is true for the N_2O profiles shown in Figure 5. Although the N_2O profile we found on 9 September does not agree too badly with the data of Murcray et al. (1973) (the histogram), or with the data taken by Schütz et al. (1970) (the open squares), there is sufficient scatter in the lower stratosphere to make it difficult to distinguish between the different theoretical profiles. In the upper stratosphere the rocket data indicate very low concentrations above 44 km (Ehhalt, 1974). All three model profiles would cover the experimental data reasonably well, if the boundary value at the tropopause were raised from 0.25 ppm to the higher values observed on our flight or Murcray's. In sum, it is presently impossible to use the N_2O data to distinguish between the three different k_z profiles.

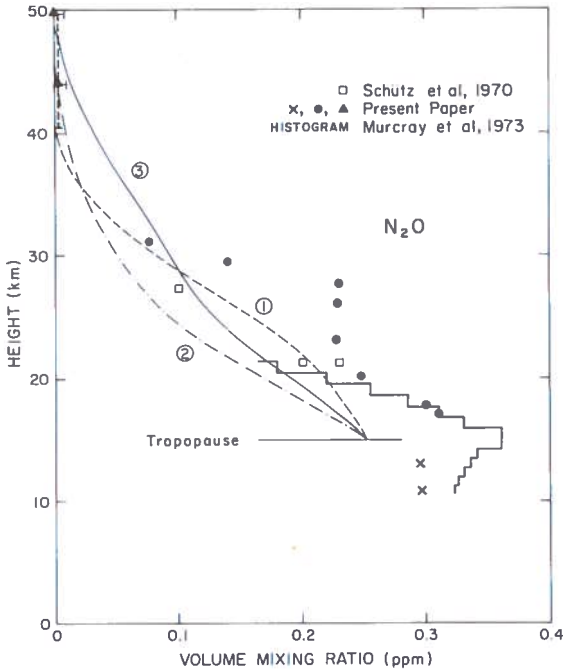

Figure 5. Measured profiles of N_2O mixing ratio by various authors compared to N_2O profiles (1), (2), and (3) predicted by chemical-model calculations for different k_z profiles (see text).

CONCLUSION

One obvious conclusion is that we need to measure more profiles of N_2O and CO, preferably at different latitudes, to obtain an average stratospheric profile which can be compared in detail with the predictions of one- or two-dimensional models. It should be added that the agreement between predictions and observed profiles is not too bad for H_2, CH_4, N_2O, and CO. Another obvious conclusion is that it is advantageous to measure several trace gases simultaneously. In that way incidents of pollution become more obvious, and since the profiles tend to confirm each other, effects of horizontal transport and vertical mean motion can be discerned more easily. With the large samples the cryogenic sampler provides we hope to be able to add a few more trace gases to our list, such as H_2O and odd nitrogen.

Finally, the comparisons made here between experimental and theoretical profiles confirm the

conclusion of Wofsy and McElroy (1973) that large vertical eddy diffusions are required to explain the vertical CH_4 profile. However, a word of caution seems to be in order. The comparisons have been made with a one-dimensional model in which all of the transport must be provided by vertical diffusion. A two-dimensional model which provides other modes of transport, like meridional cells with mean vertical motions, will reduce the need for such large k_z values. Thus, the k_z values derived depend on the dimensionality of the model, and it is quite conceivable that the true stratospheric profiles of the vertical eddy-diffusion coefficient are considerably smaller than those quoted here.

REFERENCES

Crutzen, P. (1974), "A review of upper air chemistry," Can. J. Chem. **52** (8), 1569.

Ehhalt, D.H., L.E. Heidt, and E.A. Martell (1972), "The concentration of methane between 44 and 62 kilometers altitude," J. Geophys. Res. **77**, 2193.

Ehhalt, D.H. and L.E. Heidt (1973), "The concentration of molecular H_2 and CH_4 in the stratosphere," Pure Appl. Geophys. **106-108**, 1352.

Ehhalt, D.H. (1974), "Sampling of stratospheric trace constituents," Can. J. Chem. **52** (8), 1510.

Goldman, A., D.G. Murcray, F.H. Murcray, W.J. Williams, J.N. Brooks, and C.M. Bradford (1973), "Vertical distribution of CO in the atmosphere," J. Geophys. Res. **78**, 5273.

Murcray, D.G., A. Goldman, F.H. Murcray, W.J. Williams, J.N. Brooks, and D.B. Barker (1973), "Vertical distribution of minor atmospheric constituents as derived from airborne measurements of atmospheric emission and absorption infrared spectra," in *Proceedings of the Second Conference on the Climatic Impact Assessment Program*, November 14-17, 1972, ed. A.J. Broderick, U.S. Department of Transportation, DOT-TSC-OST-73-4.

Scholz, T.G., D.H. Ehhalt, L.E. Heidt and E.A. Martell (1970), "Water vapor, molecular hydrogen, methane, and tritium concentrations near the stratopause," J. Geophys. Res. **75**, 3049.

Schütz, K., C. Junge, R. Beck and B. Albrecht (1970), "Studies of atmospheric N_2O," J. Geophys. Res. **75**, 2230.

Seiler, W. and P. Warneck (1972), "Decrease of the carbon monoxide mixing ratio at the tropopause," J. Geophys. Res. **77**, 3204.

Wofsy, S.C. and M.B. McElroy (1973), "On the vertical mixing in the upper stratosphere and lower mesosphere," J. Geophys. Res. **78**, 2619.

DISCUSSION

ELLSAESSER: Can you explain why your vertical N_2O profile shows considerable variations in the troposphere?

EHHALT: Yes, we think we can. The balloon was launched about three days after a hurricane had moved through Texas. Now, N_2O is produced in the soil and released to the atmosphere. A low-pressure region moving in would be expected to accelerate the exhalation rate, which would partly explain the high above-ground values. The hurricane would tend to carry the high-N_2O air upward in its center, and its outflow layers would then have high N_2O values – which is what we apparently have, though we haven't done a detailed analysis.

(UNIDENTIFIED): Why do we have to use eddy-diffusion coefficients? Couldn't transport be explained by other processes?

EHHALT: There's no way to include the other processes in the one-dimensional model we used. Nonetheless, the experimental profile I showed clearly indicates mean motion.

WARNECK: When you averaged your data, did you use averages for each altitude, or only for those above the tropopause?

EHHALT: We averaged the data in altitude intervals above the tropopause.

SCHAINKER: What is the definition of your error bar?

EHHALT: For methane and hydrogen, the one-sigma error is the size of the dot on the graph. In the figures showing averages, the error bar given is the mean standard deviation based on the observed variation. I think the errors for methane and hydrogen are small enough that the experimental and theoretical data can be compared. We can't do that for CO and N_2O, however, because the few profiles we have scatter too much.

ACKERMAN: It seems from the data you showed that you think there is not more than a factor-of-two decrease in the mixing ratio of methane between 30 and 50 kilometers.

EHHALT: Not really. The slide that showed the methane mixing ratio of only 0.5 ppm at 30 kilometers was an individual profile. If we average all the profiles you get a value of 0.7 or 0.8 for 30 km. The rocket value of 0.25 at 50 km was also an individual measurement.

PROGRESS REPORT ON DISTRIBUTION OF STRATOSPHERIC NITRIC ACID

A.L. LAZRUS AND B.W. GANDRUD
*National Center for Atmospheric Research**
Boulder, Colorado

ABSTRACT: Some of the major findings to date on NCAR's program of measurements of nitric acid in the stratosphere are as follows:

- Nitric acid is concentrated in a layer beginning at about 20 km and extending to 27 km and above, depending on latitude.
- The concentrations increase from equatorial to poleward latitudes.
- The present data suggest higher concentrations in winter and spring than in summer and mid-fall.
- The nitric acid does not appear to be significantly associated with natural stratospheric sulfate aerosol.
- The rate of removal of nitric acid from the stratosphere corresponds well with the estimated rates of production of odd-nitrogen molecules.

INTRODUCTION

This paper is a preliminary report on the measurement of nitric-acid vapor (HNO_3) in the stratosphere by means of direct sampling from balloons and aircraft (Lazrus et al., 1972). From these measurements we have obtained information on the spatial variability of the nitric-acid layer, and, to a lesser extent, on its seasonal fluctuations. Evidence is also presented to indicate the effect of transport on nitric-acid distribution in the lower stratosphere, the extent to which HNO_3 is associated with stratospheric aerosol, and the rate at which it is transported into the troposphere. Values of the nitric-acid-vapor content of tropical tropospheric air are also given.

The existence of nitric acid in the stratosphere has important implications for estimating the climatic impact of increased stratospheric flight. The nitrogen oxides generated by these aircraft are capable of catalytically diminishing ozone in the stratosphere, thereby increasing the intensity of ultraviolet light reaching the earth's surface (Crutzen, 1972). Nitrogen dioxide is readily converted by hydroxyl radicals to nitric-acid vapor. Hydroxyl radicals are formed by reactions involving water vapor in the ozone layer. Thus, the nitrogen oxides may be converted to nitric acid rapidly enough that their influence on the ozone layer would be reduced. Though nitric-acid vapor is itself photodissociated back to nitrogen dioxide and is also destroyed by hydroxyl radicals (Johnston, 1973), these latter reactions are sufficiently slow that the concentration of nitric-acid vapor exceeds the concentrations of the nitrogen oxides in the lower stratosphere. Thus it is believed that nitrogen oxides are ultimately removed from the lower stratosphere in the form of nitric acid. This hypothesis is tested here for naturally occurring nitrogen oxides and nitric-acid vapor in the stratosphere. The source of these substances is primarily nitrous oxide, formed biogenically at the earth's surface and converted to nitric oxide when attacked by excited atomic oxygen in the stratosphere (Crutzen, 1971).

Another possibility is that the nitrogen oxides will react with compounds in aircraft exhaust (e.g., SO_2), form an aerosol, and thereby be removed by washout. (The reaction of SO_2 and NO_2 under the influence of ultraviolet light to form a solid aerosol has been studied (Urone, 1970).) Furthermore, since SO_2 is most likely the precursor of naturally occurring sulfate aerosol in the stratosphere, it might also be expected to form a stable aerosol with NO_x.

* The National Center for Atmospheric Research is sponsored by the National Science Foundation.

Data are given in this report regarding the extent to which nitrate is associated with naturally occurring stratospheric aerosols.

EXPERIMENTAL

In both the aircraft and balloon experiments, the samples are collected by adsorption on IPC 1478 filters, 41 cm in diameter. This filter, composed of cellulose fibers impregnated with dibutoxyethyl pthalate, is first subjected to a pretreatment to remove water-soluble impurities (Gandrud and Lazrus, 1972). Comparative field tests on WB57F aircraft indicated that the pretreatment introduces no loss in collection efficiency for either aerosols or nitric-acid vapor. This was further confirmed for aerosols in the environmental test chamber of the Health and Safety Laboratory of the Atomic Energy Commission, which was cooperating in the study.

Sampling on both IPC 1478 and polystyrene filters make it possible to distinguish between particulate nitrate and nitric-acid vapor. While sulfate-particle collections were similar for the two types of filter, nitrate particles were almost completely absent on the polystyrene filter (see Table 1). Laboratory simulation of the sampling showed that the polystyrene filter papers did not adsorb nitric-acid vapor, whereas the impregnated IPC filters did (Lazrus et al., 1972). The measurements of nitric-acid vapor by this technique are in agreement with both theoretical predictions and infrared radiometry, as will be shown later.

The sampling was done through the AEC's aircraft and balloon programs for stratospheric monitoring. The WB57F aircraft sampled between tropopause height and 63,000 ft along the track indicated in Figure 1. The aircraft are equipped with tubular airfoils situated outside the fuselage. A remotely operated sample changer sequentially lowers a filter into the airfoil for the chosen sampling period, and then returns it to a sample folder which is isolated from the foil by duct seals. The filters are thus exposed to ambient air only during sampling. On each flight, two filters were exposed for only 5 seconds each to provide contamination control blanks. Typical sampling periods were about 30 minutes.

Figure 1. Track for aircraft sampling of the stratosphere in the AEC's Project Airstream.

During balloon sampling, air flow through the filters was maintained at the higher altitudes by either turbine pumps or air-ejector systems. On each balloon flight an additional sample was included as a contamination control blank.

In the aircraft sampling, the control filters generally did not contain nitrate above our detection limit. In the balloon sampling, however, the contamination correction averaged 8% of the sample size. The detection limits ranged from 3 to 7 X 10^{-9} g m^{-3} depending upon altitude and sampling time.

Details of the sampling and chemical analysis are described elsewhere (Lazrus et al., 1972).

CONCENTRATION AND DISTRIBUTION

The latitude distributions of nitric acid obtained by aircraft are shown in Figures 2-4, along with the balloon data. Though aircraft

sampling along the Airstream track can be completed within a few days, balloon sampling requires several months; the balloon flights at a given location generally require several days. It should therefore be borne in mind that although all the data are indicative of a given season, they have not been obtained simultaneously.

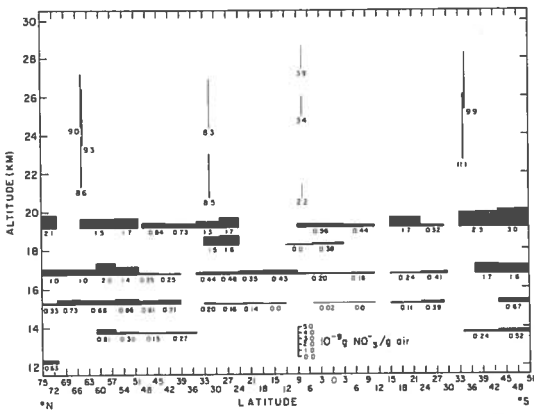

Figure 2. Spring 1971 (northern hemisphere) nitric-acid concentrations from aircraft and balloon sampling. Concentrations (ppbm) are indicated by the height of the bars. The lower edge of the bar represents the altitude at which the sample was taken. Width of the bar at 19.3 km and below represents the latitude range over which the sample was collected by the WB57-F aircraft.

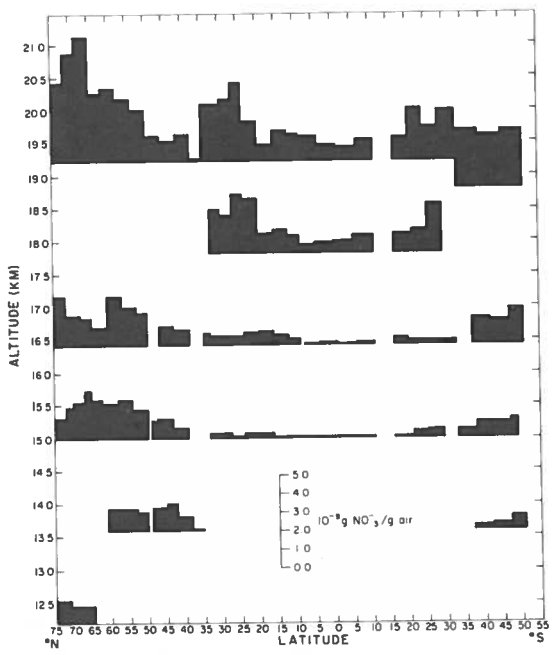

Figure 3. Fall 1971 nitric-acid concentrations determined from aircraft sampling.

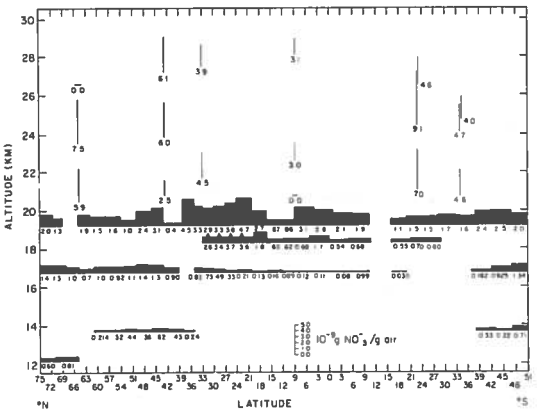

Figure 4. Spring 1972 nitric-acid concentrations determined from aircraft and balloon sampling.

The samples collected at 15.3 km during spring 1971 indicate that the values must have been below the detection limit in subtropical tropospheric air. This is not surprising, since HNO_3 is removed by rainout or washout in tropospheric air. Accordingly, the concentration gradients become quite steep between 19 and 21 km, with most of the nitric acid existing above this altitude. Steep concentration gradients have also been observed by infrared spectrometry (Murcray et al., 1972). The latitude distribution at the higher altitudes is more clearly seen in the vertical profiles of Figures 5-7, drawn from balloon and aircraft data. The data during the northern-hemisphere spring of both years indicate low concentrations over the equator with values increasing with increasing latitudes.

A concentration profile for nitric-acid vapor, not taking into account seasonal or meridional variability, has been computed by Crutzen (1973). It is included in Figure 6 for comparison with the experimental data. It can be seen that the observed profiles are similar to the theoretical.

Given the extent of the variability observed, the results are in reasonable agreement with those obtained by infrared irradiance measurements (Murcray, 1972).

The nitric-acid profile at 65°N diminished to below our detection limit at altitudes of 26 to 27

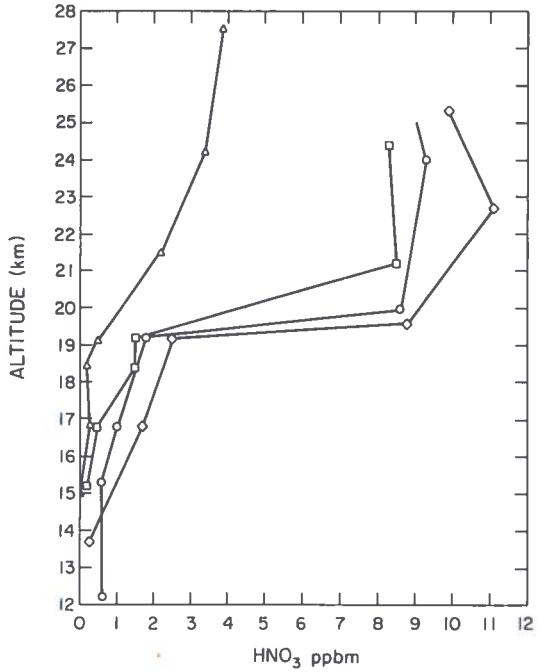

Figure 5. Vertical profiles of HNO_3, spring 1971. Δ – 8°27′N; □ – 31°26′N; ○ – 64°39′N; ◊ – 34°12′S.

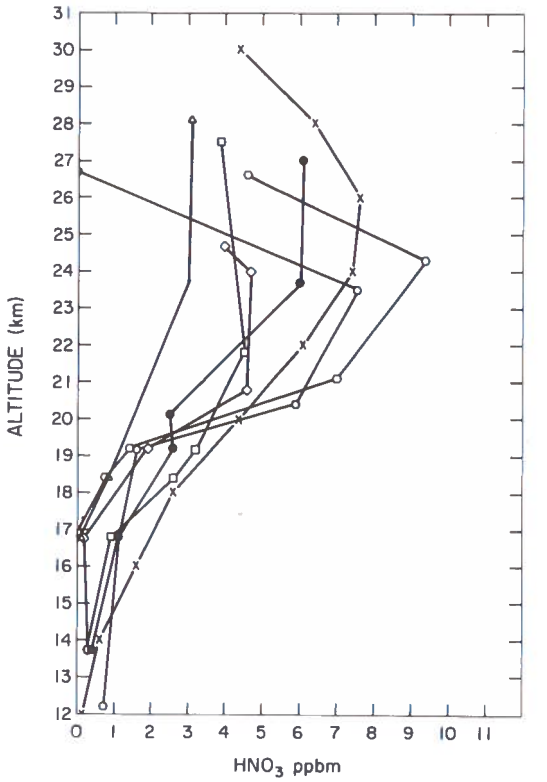

Figure 6. Vertical profiles of HNO_3, spring 1972. Δ – 8°27′N; □ – 32°51′N, ● – 42°30′N; ○ – 64°39′N; ◊ – 34°12′S; O – 23°26′S; X – theoretical (Crutzen, 1973).

kilometers in spring 1972. Recent data collected during April 1973 at 33°N and 34°S have extended our observations to 37 km, as shown in Figure 6. The nitric-acid vapor is still present at small but measurable concentrations at this altitude. The curve suggests that nitric-acid concentrations are very low above 40 km at these latitudes. The data indicates, as might be expected, that the top of the layer decreases in height as latitude increases.

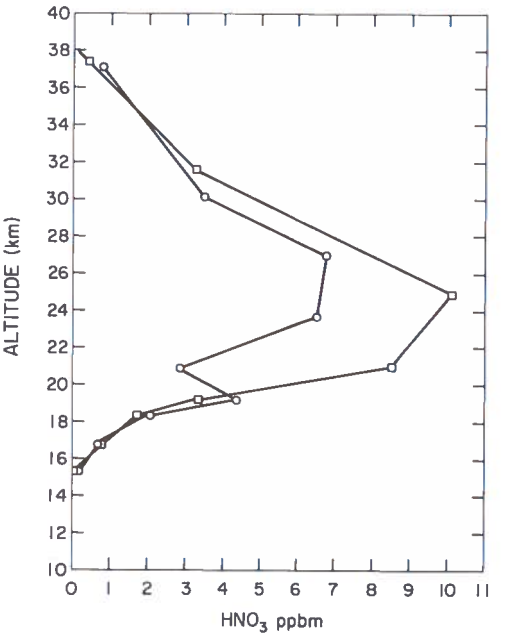

Figure 7. Vertical profiles of HNO_3, spring 1973. □ – 32°51′N; ○ – 34°12′S.

It is interesting to note that in Figure 6, as in the earlier data, the amount of nitric-acid vapor observed is larger in spring than in mid-fall.

The southern-hemsiphere values corresponding to late fall tend to be higher than the northern-hemisphere spring values. Balloon flights were made during each season only at 34°S. Fortunately, as can be seen from Figure 8, these samples give us some idea of possible seasonal effects. Indeed, the data suggest a tendency for concentrations to be higher during winter and spring than in summer and mid-fall. The two southern-hemisphere profiles with high concentrations were both determined in late fall. Though the amount of data is not sufficient to be conclusive, it does suggest seasonal and geographical HNO_3-concentration trends analogous to those of ozone (Dütsch, 1971).

Nitrogen oxides in the stratosphere are oxidized to nitric acid, which is relatively inert in the

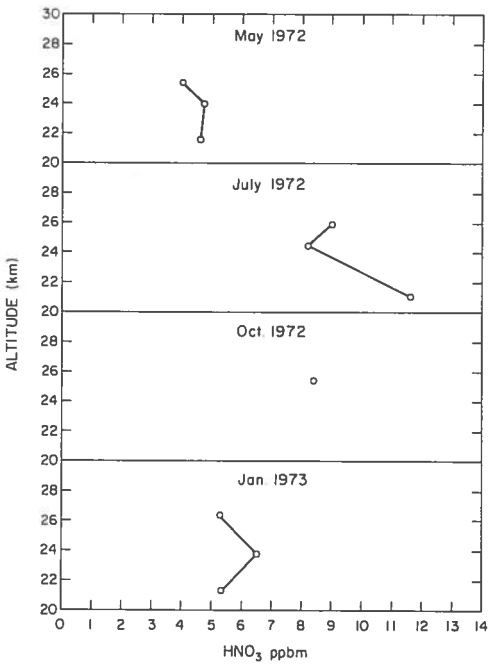

Figure 8. Seasonal variations of nitric-acid concentrations in southern hemisphere, 34°12'S.

lower stratosphere (Johnston, 1971; Crutzen, 1971). It is therefore believed that most oxidized nitrogen is removed from the stratosphere as nitrates, as either nitric-acid vapor or an aerosol. From the data summarized in Table 1, it is apparent that only a small fraction of the nitrate is removed in aerosol form. Using a quasi-empirical atmospheric-transport model successfully tested with radioactive aerosols (Krey, 1970), an annual flux of 2×10^5 tons of stratospheric sulfate aerosol across the tropopause has been computed. The average ratio of nitrate to sulfate found on the polystyrene filters (0.054), indicates that only 10^4 tons of nitrate are transported from the stratosphere as aerosol.

The remaining nitrate is most likely removed through air exchange into the troposphere, as nitric-acid vapor.* Although nitric acid and sulfate occur primarily in separate phases (vapor and aerosol respectively), the correlation coefficient between concentrations of nitrate and sulfate measured in our samples collected below 19.3 km was 0.90 and 0.77 in spring and fall 1971, and 0.84 in spring 1972. The similarity in their distribution pattern is illustrated by hand-drawn concentration isopleths in Figure 9. It seems reasonable to suggest that this similarity results from concentration control by diffusive processes in the lower stratosphere, and that the nitric-acid vapor is transported into the troposphere much as stable and radioactive aerosols are. If this is so, Krey's model, which is derived quasi-empirically from radioactive aerosol data, can be applied to the observed nitric-acid-vapor concentrations. This yields a calculated transport of $1.4 \pm 0.7 \times 10^6$ tons of stratospheric nitric acid vapor into the troposphere annually. Thus, only about 1% of the nitrate removed from the stratosphere annually is transported as an aerosol.

Current chemical models yield several estimates of odd-nitrogen production in the natural

* Nitric-acid vapor enters the troposphere in regions of stratospheric subsidence such as the cyclonic side of jet streams and the South Pole. Indeed, it has been known for some time that snow and soils in the region of the South Pole contain anomalously high concentrations of nitrate and sulfate (Wilson and House, 1965; Claridge and Campbell, 1968).

Table 1. Nitrate Data from Stratospheric Sampling

Date	Altitude (Km)	Latitude (N)	Longitude (W)	$NO_3^-/SO_4^=$ Wt. Ratio	NO_3^- Mass Mixing Ratio (ppb)
4 December 1969	17	34°30′	102°55′	0.00	0.00
4 December 1969	17	37°20′	102°30′	0.00	0.00
4 December 1969	18	46°30′	101°30′	0.00	0.00
4 December 1969	18	47°48′	101°45′	0.00	0.00
4 December 1969	18	33°30′	102°40′	0.00	0.00
4 December 1969	18	34°20′	103°35′	0.00	0.00
17 October 1970	18	33°30′	101°05′	0.34	0.30
17 October 1970	19	34°20′	91°10′	0.00	0.00
30 August 1973	18	33°30′	101°05′	0.15	0.093

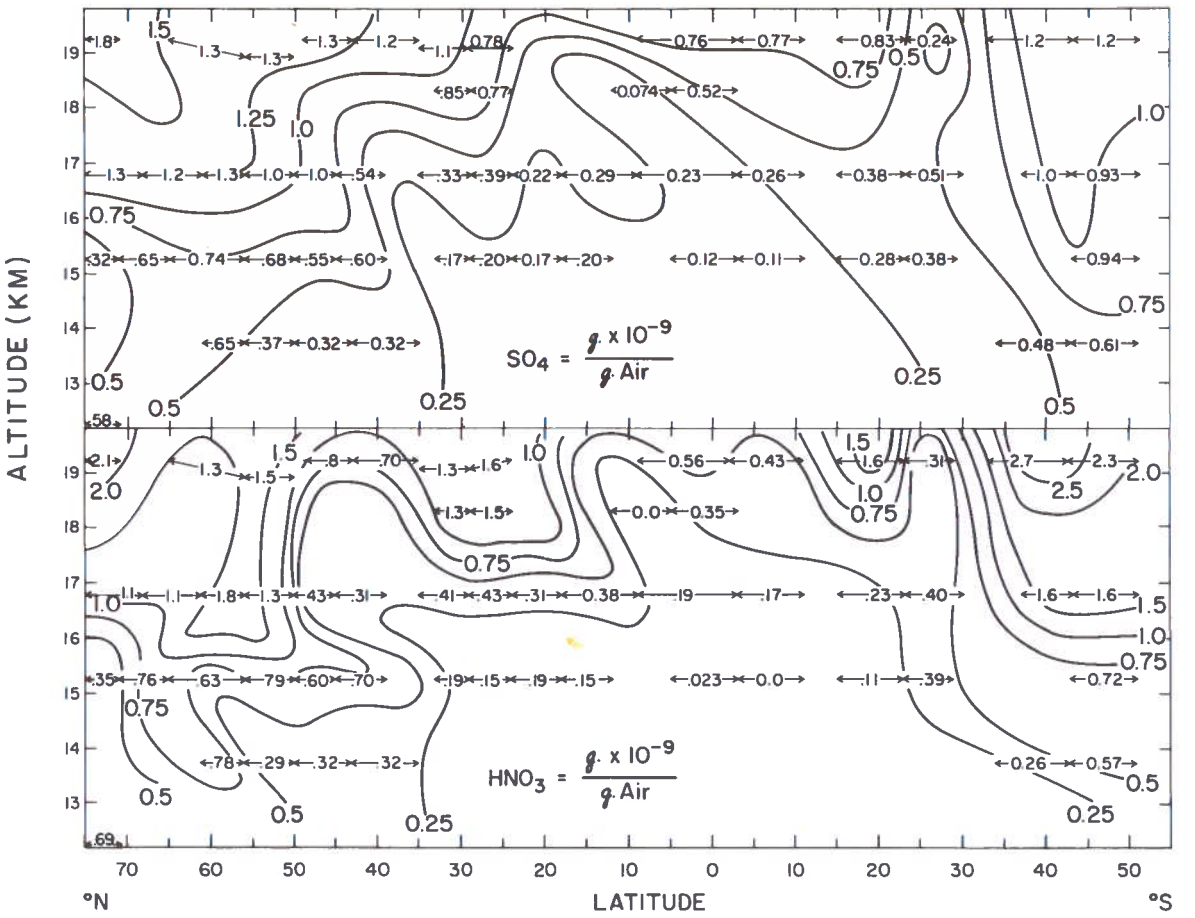

Figure 9. Hand-drawn concentration isopleths for nitric-acid vapor and sulfuric-acid aerosol based on aircraft data of spring 1971.

stratosphere. Nitric oxide (NO) production from nitrous oxide (N_2O), both by photodissociation and by reaction with electronically excited oxygen atoms ($O(^1D)$), has been estimated as 0.3 to 0.9×10^8 molecules cm^{-2} sec^{-1} (McElroy and McConnell, 1971), with photodissociation making the smaller contribution. This source strength corresponds to $1 \pm 0.5 \times 10^6$ tons of nitric acid removed annually from the stratosphere to maintain a quasi-steady-state concentration of odd-nitrogen molecules. A second model (Nicolet and Peetermans, 1972) estimates the nitric oxide production from the reaction of nitrous oxide with atomic oxygen as $1 \pm 0.5 \times 10^8$ molecules cm^{-2} sec^{-1}. This corresponds to $1.6 \pm 0.8 \times 10^6$ tons of nitric acid transported from the stratosphere annually. The good agreement of the estimates for production of odd nitrogen in the natural stratosphere from N_2O with our calculated value of $1.4 \pm 0.7 \times 10^6$ tons of nitrate removed annually lends considerable credence to the models involved. It further tends to confirm the belief that the odd nitrogen in the stratosphere is removed primarily as nitric-acid vapor.

ACKNOWLEDGMENTS

This work is part of a cooperative project with the Division of Biomedical and Environmental Research of the Atomic Energy Commission and with the Climatic Impact Assessment Program of the Department of Transportation.

REFERENCES

Claridge, G.G.C. and I.B. Campbell (1968), "Origin of nitrate deposits," Nature **217**, 428-430.

Crutzen, P.J. (1971), "Ozone production rates in an oxygen-hydrogen-nitrogen oxide atmosphere," J. Geophys. Res. **76**, 7311-7327.

Crutzen, P.J. (1972), "SST's – a threat to the earth's ozone shield," Ambio **1**, 41-51.

Crutzen, P.J. (1973), "A review of upper atmospheric photochemistry," Canad. J. Chem. **52**, 1569-1581.

Dutsch, H.V. (1971), "Photochemistry of atmospheric ozone," Adv. in Geophys. **15**, 219-322.

Gandrud, B.W. and A.L. Lazrus, (1972), "Design of system for removing water soluble materials from IPC 1478 filter paper," Environ. Sci. Tech. **6**, 455-457.

Johnston, H.S. (1971), "Reduction of stratospheric ozone by nitrogen oxide catalysts from SST exhaust," Science **173**, 517-522.

Krey, P.W. and B. Krajewski (1970), "Comparison of atmospheric transport model calculations with observations of radioactive debris," J. Geophys. Res. **75**, 2901-2908.

Lazrus, A.L., B. Gandrud, and R.D. Cadle (1972), "Nitric acid vapor in the stratosphere," J. Appl. Meteor. **11**, 389-392.

McElroy, M.B. and J.C. McConnell (1971), "Nitrous oxide: A natural source of stratospheric NO," J. Atmos. Sci. **28**, 1095-1098.

Murcray, D.G., A. Goldman, F.H. Murcray, W.J. Williams, J.N. Brooks, and D.B. Barker (1972), "Vertical distribution of minor atmospheric constituents as derived from air-borne measurements of atmospheric emission and absorption infrared spectra," in *Proceedings of the Second Conference on the Climatic Impact Assessment Program*, (November 1972), ed. A.J. Broderick, U.S. Dept. of Transportation, DOT-TSC-OST-73-4, 86-98.

Nicolet, M. and W. Peetermans (1972), "Production of nitric oxide in the stratosphere by oxidation of nitrous oxide," Ann. Geophys. **28**, 751-761.

Urone, P., W.H. Schroeder, and S.R. Miller (1971), "Reaction of sulfur dioxide in air," in *Proceedings of the Second International Clean Air Congress* (Washington, Dec. 6-11, 1970), ed. Englund and Beery, Academic Press, N.Y., 370-375.

Wilson, A.T. and D.A. House (1965), "Chemical composition of south polar snow," J. Geophys. Res. **70**, 5515-5518.

COUNTING OF CONDENSATION NUCLEI AT LOW PRESSURES: ITS APPLICATION TO PHOTOLYSIS OF GASEOUS IMPURITIES IN THE STRATOSPHERE

J. BRICARD
Laboratoire de Physique des Aérosols
Université de Paris
Paris, France

and

P. DELATTRE AND G. MADELAINE
Centre d'Etudes Nucléaires
Fontenay-aux-Roses, France

ABSTRACT: The field of application of the continuous-flow nuclei counter is extended to pressures below 760 torr, down to 60 torr. A drop in the counting efficiency at decreasing pressures was noticed, and a practical solution to this problem is presented.

The equipment used to study the formation of particles by photolysis of the gaseous impurities of the air at low pressure is described and the early results are given.

INTRODUCTION

Numerous authors have demonstrated that the action of solar radiation upon the gaseous impurities normally found in the atmosphere leads to the formation of particles at normal pressure and temperature. Our aim was to carry out a similar study under temperature and pressure conditions corresponding to those prevailing in the stratosphere.

During preliminary work we developed a continuous-flow counter for condensation nuclei, which will be briefly described.

CONTINUOUS-FLOW CONDENSATION-NUCLEI COUNTER

This instrument makes it possible to count the number of those particles in suspension in the air being studied whose radius is greater than a few units of 10^{-7} cm, and whose concentration ranges between 10 particles and 10^5 particles per cc. (A schematic drawing of the counter appears in Figure 1.) It works as follows (Bricard et al., 1972):

Air containing the nuclei first passes through a vapor saturator, which is a sealed enclosure provided with a heated internal lining made of spongy fabric whose lower end is immersed in n-butanol. The gas is then fed through a nozzle suitably cooled by means of the Peltier effect, which provides the supersaturation of n-butanol necessary to cause its condensation on the condensation nuclei, and to obtain drops with radii between 0.5 μm and 1.5 μm, which are readily detectable visually.

The drops thus formed are passed through a measuring chamber illuminated by a laser beam. The measuring volume, defined by the diaphragms D_1 and D_2, is of such dimensions that the probability of finding only one particle is equal to 0.95.

The light diffused by each droplet as it passes through the measuring chamber is caught by a photometer fitted with a photomultiplier. The resulting pulses are counted with a counting circuit, and their amplitudes can be measured. Knowing the velocity of the air flowing through the measuring volume, the volume's cross-section in the flow direction, and the pulse frequency, one can obtain the concentration of the droplets coming out of the nozzle, and from it the concentration of the condensation nuclei in the air.

If, when the incoming air is at normal temperature and pressure, the temperature difference ΔT between the nozzle and the saturator is increased, one finds that, for a given aerosol, the number of particles counted in a given air volume first increases rapidly (curve 1, Figure 2), then shows a discontinuity in slope at A for a value $\Delta T_1 = 16°C$ (the value depends on the characteristics of the counter), then increases very slowly up to a value ΔT_2, corresponding to point B, above which the increase becomes very fast again. This last ΔT_2 value corresponds to the onset of homogeneous nucleation in the vapor.

It must be noted that the temperatures we measure are, on the one hand, that of the spongy fabric impregnated with n-butanol in the saturator and, on the other hand, that of the cooled nozzle. Neither temperature represents exactly that of the vapor in these same locations; the difference between the actual vapor temperatures and those quoted depends on the nature and geometry of the components of the apparatus. However, for a given apparatus, we have checked that the observed values were reproducible within the allowance for experimental errors.

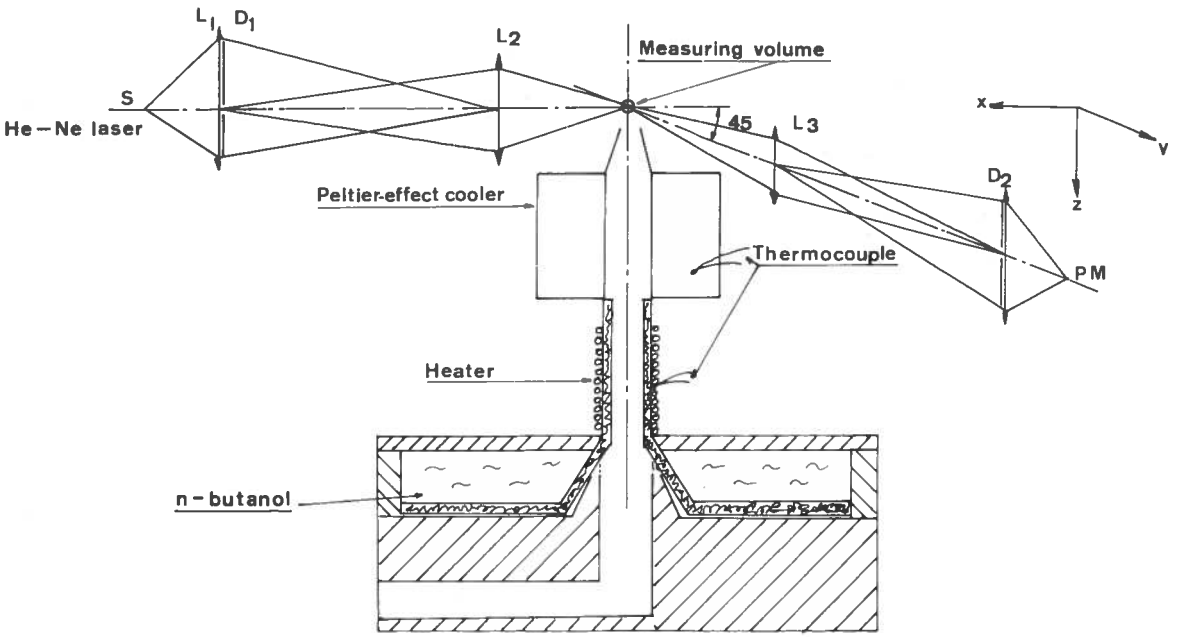

Figure 1. Schematic of continuous-flow condensation nuclei counter.

According to nucleation theory, in the case of n-butanol, the supersaturation which would be required under these conditions for nucleation to proceed at an appreciable rate should be higher than 470%; this would correspond in our experimental conditions to ΔT_2 = 36° ± 1°C, which agrees well with the foregoing results (Figure 2).

We think that the counting increase corresponding to the AB segments can be assigned to small drops formed on very small nuclei that are inactive at low supersaturations. This feature is revealed by the use of a photomultiplier with low background noise, and was partly overlooked at the beginning of our experiments (Bricard et al., 1974).

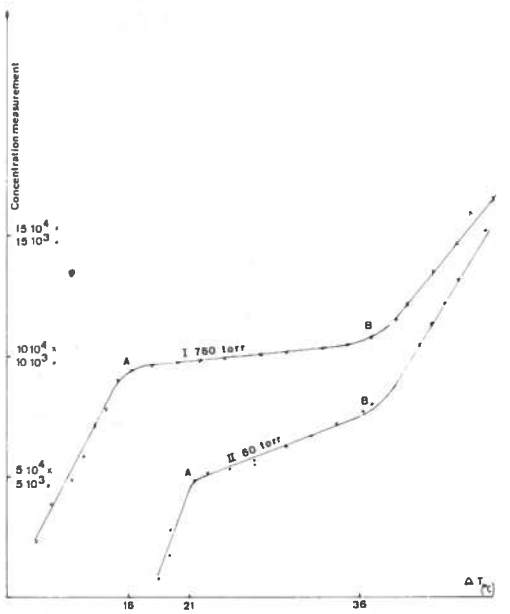

Figure 2. Concentration of nuclei vs. Δt of the condensation nuclei counter.

In order to count the maximum number of nuclei with this type of counter, one should choose conditions in the vicinity of point B and take $\Delta T \approx 35°C$. If one chooses the conditions at A, one makes an absolute error in the case of atmospheric aerosol, amounting to a defect of 10% of the total number of nuclei.

If we use a General Electric condensation-nuclei counter instead of the apparatus in Figure 1, we note that the counting variation as a function of the expansion ratio, i.e., of the cooling ΔT, is similar to that of Figure 2. In the case of the G.E. counter operating with n-butanol, the expansion rate is such that the calculated cooling is on the order of 12°C, i.e., a supersaturation of 2.3 (the temperature before expansion being that prevailing in the laboratory). In order to maintain comparable conditions in the experiments which are described below, we fixed our operating conditions in the vicinity of point A, which corresponds to a ΔT of about 17°C. This experimental ΔT value is about 5° above the actual ΔT value.

USE OF THE COUNTER AT LOW PRESSURES

The apparatus used is shown in Figure 3. It consists of:

- A stainless-steel reaction chamber of 200-liter capacity, whose internal wall was specially treated in order to reduce the absorption of gaseous impurities as much as possible. This

vessel is fitted with a quartz window transparent to radiations of wavelength longer than 0.27 μm.

- A two-stage pumping unit: a primary pump and a cryogenic pump, allowing a vacuum of 10^{-6} torr, required for degassing the walls and bringing the chamber to a low pressure.
- A device for introducing reconstituted air containing low concentrations of sulfur dioxide and nitrogen oxide (from a few pphm to 1 ppm).
- An irradiating device consisting of a high-pressure mercury-vapor lamp.
- Various samplers for gas analyses and for measuring the concentrations and sizes of particles inside the test chamber.

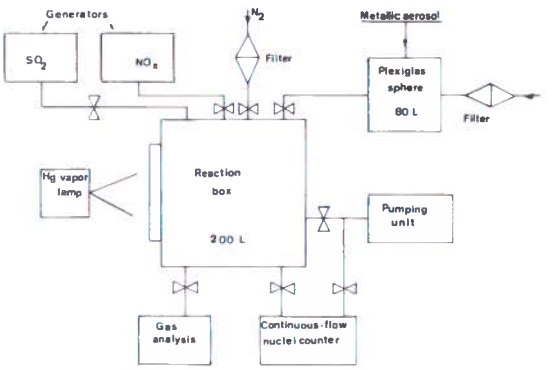

Figure 3. Apparatus for generating condensation nuclei at low pressure.

The particles eventually formed are counted by the continuous-flow condensation-nuclei counter described earlier.

The chamber and counter are interconnected by means of a pipe, 3 cm long and 2 cm in diameter.

The reaction chamber is evacuated and then filled to atmospheric pressure p_0 with air taken from the outside, containing the natural atmospheric aerosol. Counting is carried out under the following conditions. Let c_0 be the particle concentration found. Pressure within the reaction chamber is then reduced to the value p by pumping. Let c'_p be the particle concentration level which is then measured.

Note (Pollak and Metniecks, 1960) that c'_p is systematically lower than $c_p = c_0\, p/p_0$, the value which would be expected if the aerosol particles follow the air flow during pumping.

If pressure within the reaction chamber is again brought to p_0 by the addition of filtered nitrogen, it is found that the concentration of particles becomes c_p. The counting defects noticed at low pressure are thus ascribable neither to evaporation, nor to diffusion losses towards the wall, nor to particle coagulation. It can thus be concluded that some particles, although present at low pressure, are not counted at that pressure. Curve I of Figure 4 shows, as a function of pressure the counting losses $(c_p - c'_p)/c_p$ obtained during three different sequences of measurements, expressed as a percentage. It can be seen that the counting loss increases gradually as pressure diminishes, and becomes equal to 100% at a pressure of 60 torr. These results agree with those obtained previously with expansion counters by Junge et al. (1961), Pollak and Metniecks (1960, 1961), and Schlarb (1940).

Curves II and III in Figure 4 correspond to similar experiments in which the atmospheric aerosol has been replaced by aerosol obtained by filling the reaction chamber with atmospheric air which has been filtered and then irradiated with the mercury-vapor lamp (photolysis aerosol, curve II), and with an aerosol obtained by the vaporization of a platinum wire (curve III). The counting loss is more accentuated with the photolysis aerosol, whose particles are finer than those of the platinum aerosol, than with the atmospheric aerosol, whose particles are coarser; the losses are in the order I < III < II, whereas the particle sizes are in the order II < III < I.

ELIMINATION OF THE COUNTING LOSS

Oscilloscope measurement of the signals sent by the photomultiplier shows that their amplitude, which is substantially proportional to the square of the radius of the droplets, diminishes as pressure decreases, and drops on the average from 10 mV at 760 torr to 1 mV at 260 torr; after this point, they are no longer distinguishable from the background noise at lower pressures, and cannot be measured with accuracy. Thus, it is as if, at low pressure, a certain number of droplets are unable to grow sufficiently, and the diffused light therefore becomes too weak to be detected by the photomultiplier.

We compensated for the decrease in the growth rate of the droplets at low pressures by increasing the supersaturation in the counter. This was accomplished by heating the saturator, while holding the temperature of the cooling nozzle constant and equal to 0°C ± 1°C. (The various temperatures are determined by means of thermocouples.)

The experiments represented in Figure 2 were repeated with a saturator thus modified. We determined the changes in the number of nuclei counted for a given time period as a function of the temperature difference ΔT maintained between the cooling nozzle and the saturator for various pressures between 60 and 760 torr. We noticed that the ΔT_1 value for which the number of nuclei counted undergoes a first change in slope (point A, Figure 2) increases gradually as pressure decreases, varying from $\Delta T_1 = 16° \pm 1°C$ at atmospheric pressure with an atmospheric aerosol to $\Delta T_1 = 21°C \pm 1°C$ at 60 torr. If we increase ΔT beyond ΔT_1, we find that, whatever the pressure, the number of particles counted increases very slowly, and then undergoes a new change of slope for $\Delta T = \Delta T_2 = 36° \pm 1°C$, this ΔT_2 value being independent of pressure. These results are expressed by the various curves on Figure 2.

The experiments shown in Figure 4 were repeated at varying pressures between 760 and 60 torr, ΔT being fixed at a value just below $\Delta T_2 = 36°C$. As shown in the following table, the experimental values of c'_p were

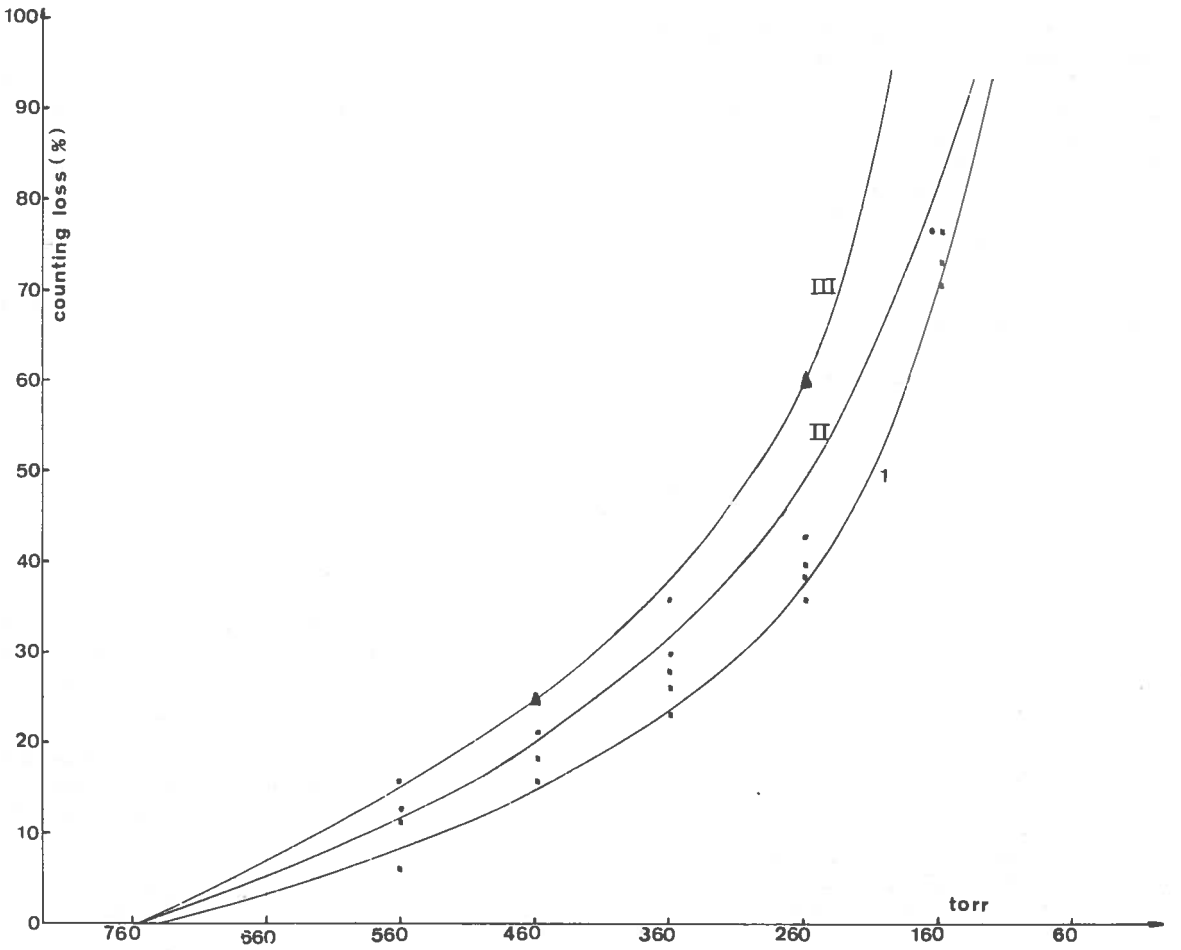

Figure 4. Counting loss vs. pressure.

Table 1. Condensation-Nuclei Concentrations at Various Pressures

p, Torr	760	560	360	260	160	60	760
Concentration as measured	87,000	53,000	27,000	15,000	4,500	800	5,000
Concentration as calculated	–	64,000	41,000	30,000	18,000	5,200	5,200
Loss, %	–	17	31	50	73	100%	–
Concentration as measured by heating the alcohol bath	87,000	63,000	40,000	30,000	18,000	5,000	5,000

found respectively equal to the c'_p values obtained after the atmospheric pressure had been re-established, within the experimental errors. This modification of the apparatus therefore allows us to eliminate the counting errors arising at low pressures.

PRODUCTION OF PARTICLES BY LOW-PRESSURE PHOTOLYSIS

With the above-described apparatus the particle diffusion to the wall, at least in the case of the

atmospheric aerosol, is not appreciable. We shall tentatively assume that this is true also for the aerosol resulting from photolysis of gaseous impurities of the air, although the resulting particles are of smaller size.

During a study which we consider to be preliminary, we have explored the photolysis of gaseous impurities in the air as follows: natural air is first cleared of all particles through "absolute filtration", and is then fed into the reaction chamber at atmospheric pressure. A check made with the condensation-nuclei counter as the air is fed in shows that the number of particles is nil. Irradiation is then begun, and the evolution of the concentration of nuclei formed is followed for about 2-3 hrs. For reduced-pressure experiments, the value of the desired pressure is obtained by pumping before starting the irradiation.

Figure 5 shows the changes in nuclei concentration per cc, versus time. The shape of the curves can be explained as follows:

- Increasing part: This corresponds to particle formation, first by homogenous nucleation, when vapor pressure of the nucleogenous substance (sulfuric acid in SO_2 photolysis) is sufficient to start the process, then later by vapor condensation and coagulation; when particles attain a radius of about 10^{-7} cm they are detected by the counter.
- Decreasing part: This corresponds to the evolution of an aerosol cloud in a closed container ruled by the laws of coagulation and Brownian diffusion, after the air has passed through an equilibrium state. Under continuous irradiation, the vapor formed can either condense directly onto the pre-existing particles, or give rise to new nuclei which, due to their very high mobility, settle onto the coarser particles previously formed. After a time period that depends on the rate of particle production, an equilibrium state is reached.

It can thus be seen that the low pressures do not prevent the formation of particles by photolysis. Further experiments will be necessary in order to define this phenomenon with greater precision, however, especially in controlled atmospheres with known concentrations of gaseous impurities.

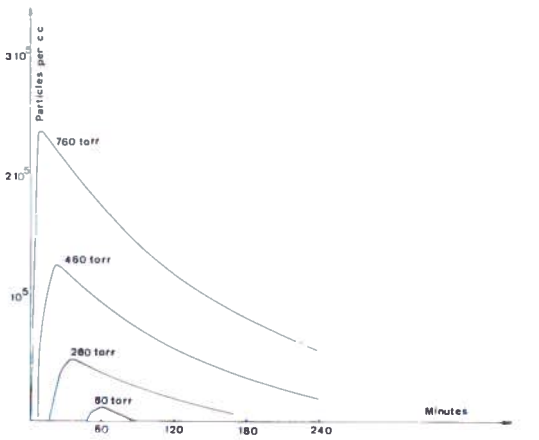

Figure 5. Nuclei concentration vs. time, for trace-gas photolysis.

REFERENCES

Bricard, J., G. Madelaine, P. Reiss, and P.-Y. Turpin (1972), "Compteur de noyaux de condensation à flux continu," C.R. Acad. Sc. Paris 275, Series B, 387.

Bricard, J., P. Delattre, G. Lebaupain, and G. Madelaine (1974), "Comptage des noyaux de condensation à pression réduite," C.R. Acad. Sc. Paris 278, Series B, 191.

Junge, C.E., C.W. Chagnon, and T.E. Manson (1961), "Stratospheric aerosols," J. Met. 18, 181.

Pollak, L.W. and A.L. Metniecks (1960), "The effect of pressure on the counting of condensation nuclei," Geophys. Pur. Appl. 47, 123.

Pollak, L.W. and A.L. Metniecks (1961), "The influence of variations in pressure on the calibration of a photoelectric nucleus counter," Geophys. Pur. Appl. 50, 17.

Schlarb, G. (1940), "Untersuchungen über Kondensationskerne und Leichtionen in künstlich klimatisierten Räumen," Bioklim. Beiblätter 7, 86.

ASPECTS OF LABORATORY STUDIES IN HIGH-RESOLUTION INFRARED SPECTROSCOPY

K. NARAHARI RAO
Department of Physics
The Ohio State University
Columbus, Ohio

ABSTRACT: Laboratory research in high-resolution infrared spectroscopy has witnessed a period of technological advances and consolidation during the past quarter of a century. Therefore, it is vitally important that one develop a proper perspective when using the spectral data and parameters which have become available in this period. Since some aspects of spectroscopic results are becoming increasingly important to atmospheric scientists and astrophysicists, specific experiments are being conducted. Spectra of CO are here discussed in greater detail to illustrate what modern research is capable of; the importance of these laboratory results to the interpretation of solar data is elaborated. Work is still in progress on the spectra of CO_2, H_2O, N_2O and NO in the 5.3-μm region; the current status of the results is described briefly. Some aspects of the ν_3 band of NO_2 are mentioned.

INTRODUCTION

Laboratory investigations of the infrared spectra of small molecules are becoming increasingly important to numerous fields, most notably to atmospheric and astrophysical studies. The improved technology which became available during the past two decades, combined with the vast amount of human effort which took place in different laboratories around the world, has resulted in phenomenal refinements to some aspects of the information that can be obtained in the infrared; in other areas, however, work remains to be done. It is therefore important to develop a broad perspective on the field, in order to appreciate not only the precision achieved but also the limitations of the data which have accumulated, especially during the period of technological advancement and consolidation. Since the experimental spectroscopist is interested in improving spectral resolution, achieving precision in spectral positions, and determining unambiguous values for the intensities of spectral lines, a brief discussion will first be presented of some of the developments in these areas. It will be followed by a description of spectra of a few of the molecules specifically of interest to stratospheric studies. In this paper, attention will be confined mainly to work done with grating spectrographs.

TECHNOLOGY

Spectral Resolution

At present, large precision gratings having ruled areas of 16 in. X 8 in. (40 cm X 20 cm) are available for work in the infrared (Rao 1972); with them as the main dispersing elements in spectrographs it has been possible to achieve working spectral resolution* of about 0.015 cm^{-1} (see Figure 1, taken from Rao (1973), and also Figure 5 later in this paper). A schematic of the optical arrangement of the 10-m-focal-length Czerny-Turner spectrograph with which these spectra were obtained is shown in Figure 2.

Precision in Spectral Positions

The importance of obtaining precise values for spectral positions needs no emphasis here. For identifying the molecular species responsible for the transitions, for determining the structural parameters of molecules, and also in making experiments involving intensity measurements, having accurate values available for spectral positions allows us to reach meaningful conclusions.

* By spectral resolution, we mean measured full width, in cm^{-1} at half maximum, of well-resolved spectral lines.

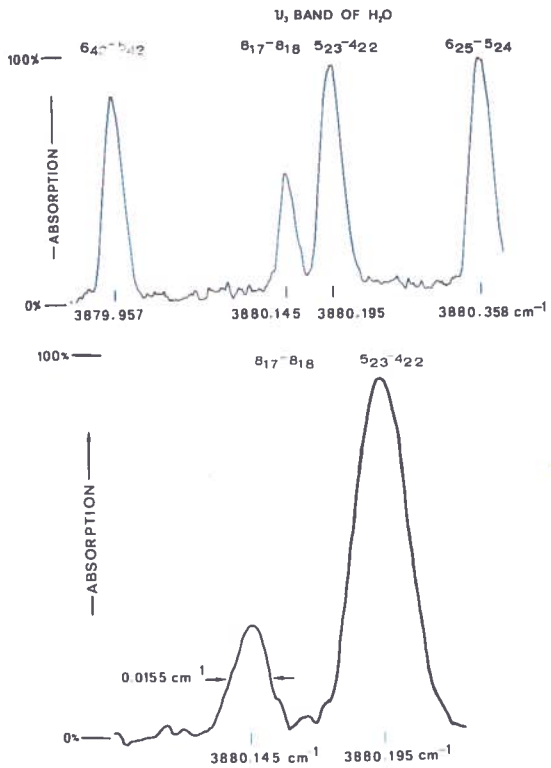

Figure 1. Resolution test with the 10-m-focal-length Czerny-Turner spectrograph. Grating: 79 grooves/mm, 16 in. X 8 in. echelle in double-pass. Detector: PbS cooled to 193K. Source: carbon furnace operating at 300 A. Path length: 124 m. Pressure: 0.08 torr. Amplifier: PAR model HR-8; time constant, 1 sec. (NOTE: Drs. Arlan W. Mantz, Bruce D. Alpert, and J.A. Vigil participated in the construction and initial testing of this spectrograph.)

Much work has been done in the past in both setting up infrared standards and establishing procedures for the actual recording and measurement of infrared spectra. Since molecular structural studies in the infrared have been based mostly on investigations of absorption spectra, it was proposed in 1950 that absorption standards, especially of the lines of the carbon monoxide molecule, be used as secondary standards for wavelength measurements. Much has happened since then. As may be seen from the listing below, even as recently as July 1973 new experiments were conducted for refining the wavenumbers of the rotational structure of the first overtone band of the carbon monoxide molecule.

- Infrared CO bands as secondary standards in the infrared (Rao, 1950)
- Highly precise wavelengths in the infrared (HCN, N_2O, and CO) (Rank et al., 1961)
- Wavelength standards in the infrared (Rao et al., 1966)
- New near-infrared wavenumber standards (2-0 band of $^{12}C^{16}O$) by high-resolution Fourier spectroscopy in vacuum (Guelachvili, 1973)

In making use of these infrared standards, it is important to impress a wavenumber scale on the infrared spectrum while it is being scanned. That has been done by a variety of procedures:

- Use of interference fringes with a Fabry-Perot etalon
  - NRC, Ottawa (Douglas and Sharma, 1953)
  - NBS, Washington, D.C. (Plyler and Tidwell, 1956)
  - Michigan State (in Rao et al., 1966)
- Use of atomic lines of neon and thorium
  - Ohio State (Rao et al., 1959; Copen, 1964; Rao et al., 1966)
  - NBS, Washington, D.C. (Maki and Thibault, 1968)
- Use of a Michelson goniometer
  - Paris (Henry, 1973)
  - Ohio State (Rao, ongoing)
- Use of an optical encoder
  - NOAA NESS (Fridovich and Champion, 1974)

One of the earliest of these procedures was proposed in 1953; it involved the recording of Fabry-Perot interference fringes simultaneously with the recording of infrared spectra. Again, many novel methods have been explored since then. In 1973-74, the use of Michelson goniometers and optical encoders has contributed much to progress in this area. This diversity of experiments will not merely satisfy a pedagogic curiosity, but is necessary to provide independent verification of results. Such verification is

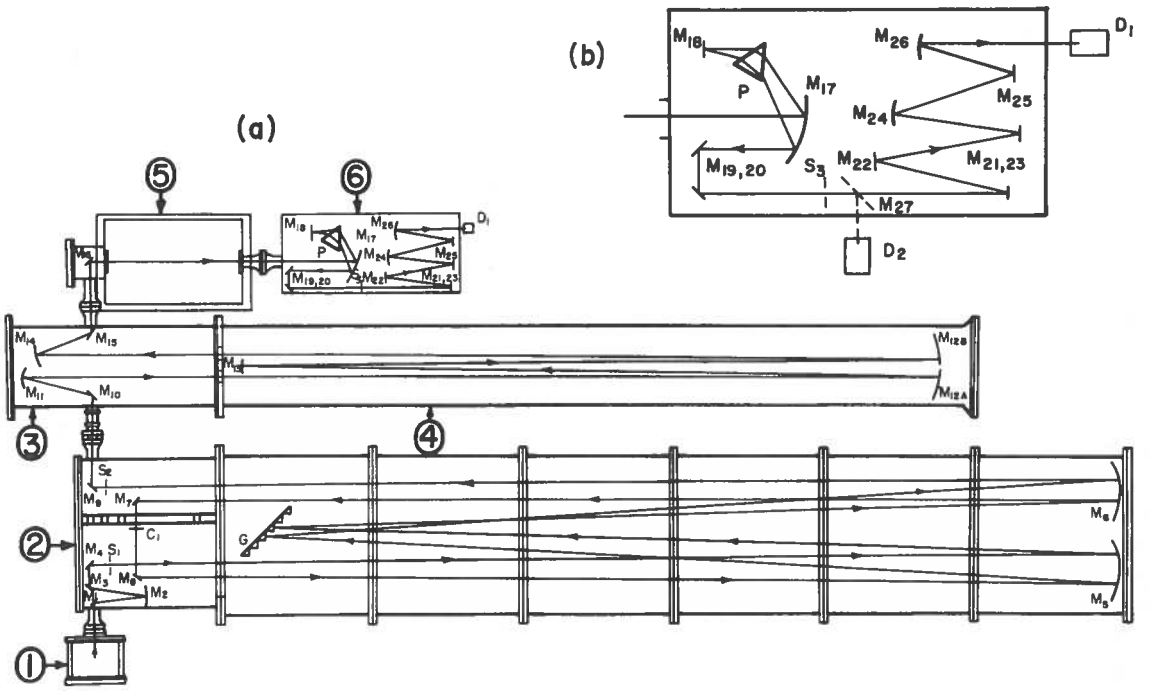

Figure 2. (a) Optical diagram of the 10-m-focal-length Czerny-Turner vacuum grating spectrograph at The Ohio State University. (b) Enlarged view of chamber 6 to show the placement of the movable mirror, M_{27}, and the arrangement of the two detectors, D_1 and D_2. (See Pugh et al. (1973) for details on the use of two detectors as indicated in (b).)

particularly important when the results are applicable to other areas.

To summarize: over two decades numerous efforts have been made to devise a series of methods which would lead to precision in spectral positions. Consequently, we now have a measure of agreement and confidence in wavenumber data emanating from different laboratories.

Intensity Measurements in Infrared

As far as the experimental values for intensity parameters are concerned, the interest in these quantities has strengthened in the latter part of the 1960's. Due to efforts currently underway in different laboratories, we should be on firmer ground in this matter in the next few years. The somewhat unsettled state of affairs at present becomes evident if we examine the following list, which shows examples of some of the different units in which the strengths of the spectral lines are being reported.

$cm^{-1}\ (cm\ atm)^{-1}$

$cm^{-1}\ (cm\ atm)^{-1}_{STP}$

$cm^{-1}\ (m\ atm)^{-1}$

$cm^{-1}\ (km\ atm)^{-1}$

$cm^{-1}\ (km\ amagat)^{-1}$

$cm^{-1}\left(\frac{molecules}{cm^2}\right)^{-1}$

or

$cm^{-1}\left(\frac{molecules}{cm^3} \times cm\right)^{-1}$

$cm^{-1}\left(\frac{grams}{cm^2}\right)^{-1}$ or $cm^{-1}\left(\frac{grams}{cm^3} \times cm\right)^{-1}$

Wavenumbers per molecule per cm^2*

* While we recognize the need to discuss and adopt the most appropriate unit for the line strength parameter S, it should be noted that this last usage is the consequence of an unfortunate trend to consider the word "wavenumber" synonymous with cm^{-1}.

EXAMPLES OF MOLECULAR DATA

Spectrum of Carbon Monoxide Molecule (CO)

Somewhat detailed discussions will be presented for the spectrum of CO because it is one of the few molecules for which excellent laboratory measurements are available. Furthermore, CO is of interest to a broad range of fields. For example, its occurrence in the spectra of Venus and Mars has been established by Fourier-transform spectroscopic techniques (Connes et al., 1968; Kaplan et al., 1969); not long ago, it was identified in interstellar space as one of the more abundant of the molecules having non-hydrogenic atoms (Wilson et al., 1970); and knowledge of the atmospheric abundance of this molecule has been important ever since it was first detected as a constituent of the earth's atmosphere (Migeotte and Neven, 1950; Migeotte, 1959; Locke and Herzberg, 1953).

A brief review of laboratory studies of the infrared spectrum of CO will first be presented, and the significance of the experimental results to some of the more recent solar measurements will be discussed.

The vibration-rotation fundamental of CO at 4.7 μm is easy to study by absorption techniques. An absorption path of only about 2 cm-atm is required for observation. The spectrum presents a simple appearance, and the spacing between the successive lines in its rotational structure (3-4 cm^{-1}) is such that, as mentioned earlier, CO lines are useful in calibrating infrared spectra in the day-to-day work of a laboratory. The third overtone band of CO (the 4-0 band) occurs in the photographic infrared (Herzberg and Rao, 1949), and one needs an absorption path of nearly 800 meters at a pressure of 1 atmosphere to observe it. Obviously, such absorption studies allow us to obtain information for only a very small portion of the potential energy curve (see Figure 3). However, in the spectrum of a CO laser we observe $\Delta v = 1$ transitions between energy levels up to $v = 37$. All the observed laser lines have now been measured by means of a vacuum grating infrared spectrograph (Roh and Rao, 1974), employing

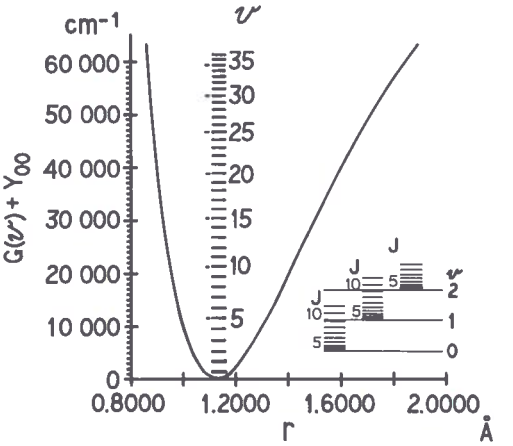

Figure 3. Potential energy curve for $^{12}C^{16}O$.

some of the techniques listed earlier. The observational data were fitted to the vibrational-rotational term-value expression given below:

$$
\begin{aligned}
T(v,J) &= G(v) + F_v(J) \qquad (1)\\
&= \omega_e(v+1/2) - \omega_e x_e(v+1/2)^2\\
&+ \omega_e y_e(v+1/2)^3 - \omega_e z_e(v+1/2)^4\\
&+ \omega_e a_e(v+1/2)^5 - \omega_e b_e(v+1/2)^6 + \ldots\\
&+ J(J+1)\,[B_e - \alpha_e(v+1/2) + \gamma_e\\
&\times (v+1/2)^2 - \delta_e(v+1/2)^3 + \ldots]\\
&- J^2(J+1)^2\,[D_e - \beta_e(v+1/2)\\
&+ \pi_e(v+1/2)^2 - \ldots]\\
&+ J^3(J+1)^3\,[H_e - \eta_e(v+1/2) + \ldots]\\
&- J^4(J+1)^4\,L_e + \ldots
\end{aligned}
$$

The molecular constants evaluated are summarized in Table 1. The error limits quoted for each constant are the standard deviations. In evaluating these molecular constants, using least-squares techniques, other measurements in the infrared (Rank et al., 1957 and 1965; Weinberg et al., 1965) and in the microwave (Rosenbloom et al., 1958; Cowan and Gordy, 1957; Helminger et al., 1970) regions have been included by weighting the data proportionally to $(\Delta\nu)^{-2}$, where $\Delta\nu$ is the estimated uncertainty of measurement.

Table 1. Molecular Constants of $^{12}C^{16}O$, in cm^{-1}

	SET I		SET II		SET III	
ω_e	2169.817346	± 0.000670	2169.816461	± 0.000517	2169.814986	± 0.000962
$\omega_e x_e$	13.289545	± 0.000280	13.289234	± 0.000214	13.289120	± 0.000404
$\omega_e y_e$	1.06521×10^{-2}	$\pm 0.00350 \times 10^{-2}$	1.06270×10^{-2}	$\pm 0.00296 \times 10^{-2}$	1.06298×10^{-2}	$\pm 0.00559 \times 10^{-2}$
$\omega_e z_e$	-5.037×10^{-5}	$\pm 0.197 \times 10^{-5}$	-5.127×10^{-5}	$\pm 0.175 \times 10^{-5}$	-5.085×10^{-5}	$\pm 0.332 \times 10^{-5}$
$\omega_e a_e$	1.1486×10^{-6}	$\pm 0.0510 \times 10^{-6}$	1.1314×10^{-6}	$\pm 0.0460 \times 10^{-6}$	1.1436×10^{-6}	$\pm 0.0871 \times 10^{-6}$
$\omega_e b_e$	3.3124×10^{-8}	$\pm 0.0484 \times 10^{-8}$	3.2996×10^{-8}	$\pm 0.0441 \times 10^{-8}$	3.3113×10^{-8}	$\pm 0.0835 \times 10^{-8}$
B_e	1.931283656	$\pm 484 \times 10^{-9}$	1.931282629	$\pm 292 \times 10^{-9}$	1.931279851	$\pm 381 \times 10^{-9}$
α_e	1.751003×10^{-2}	$\pm 0.000110 \times 10^{-2}$	1.750780×10^{-2}	$\pm 0.0000540 \times 10^{-2}$	1.750207×10^{-2}	$\pm 0.0000759 \times 10^{-2}$
γ_e	1.7214×10^{-6}	$\pm 0.0260 \times 10^{-6}$	1.2466×10^{-6}	$\pm 0.00936 \times 10^{-6}$	0.998×10^{-6}	$\pm 0.162 \times 10^{-6}$
σ_e		0		0		0
D_e	6.125781×10^{-6}	$\pm 0.000780 \times 10^{-6}$	6.124783×10^{-6}	$\pm 0.000692 \times 10^{-6}$	6.123804×10^{-6}	$\pm 0.00131 \times 10^{-6}$
β_e	2.927×10^{-9}	$\pm 0.437 \times 10^{-9}$	1.806×10^{-9}	$\pm 0.201 \times 10^{-9}$	1.179×10^{-9}	$\pm 0.199 \times 10^{-9}$
π_e	4.313×10^{-10}	$\pm 0.763 \times 10^{-10}$	2.466×10^{-10}	$\pm 0.162 \times 10^{-10}$	1.690×10^{-10}	$\pm 0.248 \times 10^{-10}$
H_e	7.723×10^{-12}	$\pm 0.749 \times 10^{-12}$	6.396×10^{-12}	$\pm 0.310 \times 10^{-12}$	8.418×10^{-12}	$\pm 0.456 \times 10^{-12}$
η_e	3.364×10^{-13}	$\pm 0.772 \times 10^{-13}$	2.192×10^{-13}	$\pm 0.158 \times 10^{-13}$	2.352×10^{-13}	$\pm 0.264 \times 10^{-13}$
L_e		0		0		0

SET I: Roh and Rao (1974)
SET II: Includes 2-0 region sunspot data in addition to data in Set I
SET III: Includes 7-6 region sunspot band in addition to data in Set II

Solar CO *Data*

Recently, measurements of solar CO lines were reported in the fundamental vibration-rotation band region of the CO molecule at 4.7 μm in the infrared (Hall, 1973). This was a continuation of studies made in the first-overtone region at 2.3 μm (Hall, 1970). It should be pointed out that the solar data were not included in the least-squares program for determining molecular constants given in set I of Table 1, since there was no clear indication of the observational uncertainties ($\Delta\nu$) of the solar data. The constants are sensitive to the weighting of observational data which, as stated earlier, is considered to be proportional to $(\Delta\nu)^{-2}$. As may be seen from Table 2, the values calculated for the 7-6 band lines by using constants in set I of Table 1 do not agree with the solar measurements at the high J values.

To examine this problem further, the molecular constants were re-evaluated by including the solar data in the 2.3-μm region

Table 2. Wavenumbers (expressed in vac cm^{-1}) for the 7-6 Band of $^{12}C^{16}O$

R(J)	Solar Data	Calculated	Difference
R 65	2140.930	2140.913	0.017
66			
67	2142.811	2142.796	0.015
68	2143.688	2143.669	0.019
69			
70			
71	2146.056	2146.018	0.038
101	2146.361	2146.119	0.242
102			
103	2144.929	2144.552	0.377
104	2144.156	2143.692	0.464
105	2143.336	2142.781	0.555
106			
107			
R108	2140.603	2139.738	0.865

(Hall, 1970); this resulted in the constants reported in set II of Table 1. In these calculations, the observational uncertainty was arbitrarily assumed to be ±0.005 cm^{-1}. The standard deviations are slightly better in set II

constants than in those in set I. Set III was obtained by including the solar data at 4.7 μm (Hall, 1973), in addition to all the data used for set II. The standard deviations are worse in this case. Again, the 7-6 band lines were calculated by using molecular constants given in sets II and III of Table 1; a comparison with the observational data is presented in Table 3. Even with the molecular constants in set III, the differences between the observed and the calculated values are still very much outside the measurement errors for the higher J values. Incidentally, the 7-6 band forms a head, and the lines R(101) - R(108) are lines in the returning branch. When the observational uncertainties in the solar data are clarified, it should be possible to include the latter also in the evaluation of the molecular constants for $^{12}C^{16}O$.

Molecular Spectra at 5.3 μm

Recent efforts to detect the NO molecule in the stratosphere were made in the region of about 5.3 μm in the infrared (see, for instance, Toth et al. (1973) and Ackerman et al. (1973)). This is precisely the spectral region where, among others, some of the vibration-rotation bands of H_2O, CO_2, CO, and N_2O also occur. Therefore, the laboratory studies at The Ohio State University were directed toward mapping the spectra of several molecular species of interest to atmospheric problems and determining their spectroscopic parameters. A Michelson goniometer was used in calibrating these data relative to CO standards. The final values for spectral positions, molecular constants, and line strengths will appear in future publications from this laboratory. Some sample data are presented in this section.

$H_2{}^{16}O$: A tracing of the spectrum of water vapor is reproduced in Figure 4; the spectral positions of the lines observed are listed in Table 4.

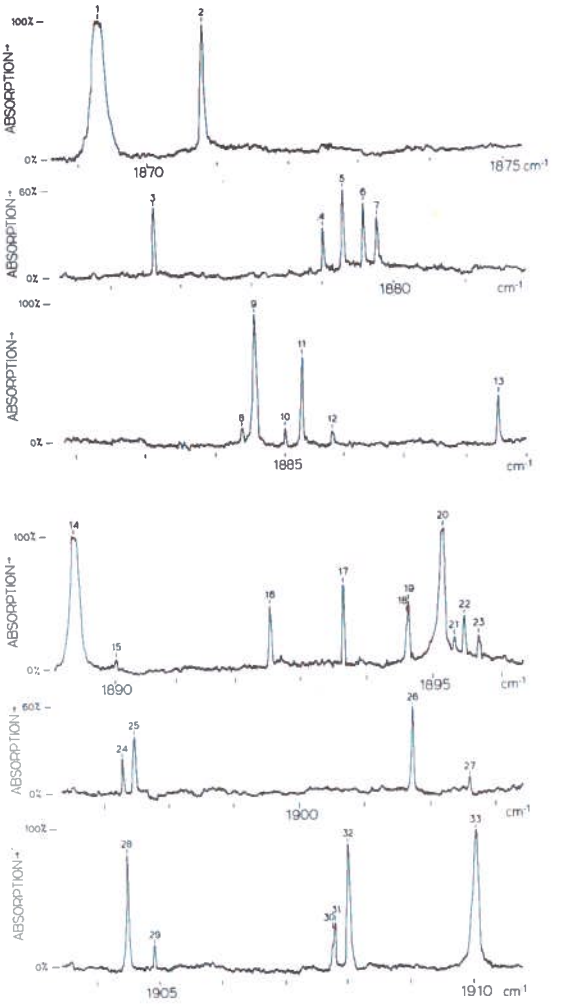

Figure 4. Spectrum of water vapor at 5.3 μm.

Table 3. Wavenumbers (expressed in vac cm^{-1}) for the 7-6 Band of $^{12}C^{16}O$

R(J)	Sunspot (7-6)	Calculated*	Difference	Sunspot (7-6)	Calculated†	Difference
R 65	2140.930	2140.930	0.000	2140.930	2140.930	0.000
67	2142.811	2142.816	-0.005	2142.811	2142.818	-0.007
68	2143.688	2143.692	-0.004	2143.688	2143.695	-0.007
71	2146.056	2146.047	0.009	2146.056	2146.054	0.002
101	2146.361	2146.337	0.024	2146.361	2146.537	-0.176
103	2144.929	2144.795	0.134	2144.929	2145.025	-0.096
104	2144.156	2143.948	0.208	2144.156	2144.194	-0.038
105	2143.336	2143.050	0.286	2143.336	2143.314	0.022
R108	2140.603	2140.050	0.553	2140.603	2140.373	0.230

* Using molecular constants in set II of Table 1.

† Using molecular constants in set III of Table 1.

Table 4. Measurements of Some of the Water-Vapor Lines at 5.3 μm

Serial Number (as in Fig. 4)	Wavenumber (vac cm^{-1})	Serial Number (as in Fig. 4)	Wavenumber (vac cm^{-1})
1	1869.348_9	18	1894.647_6
2	70.808_3	19	94.680_7*
3	76.628_7	20	95.195_9*
4	79.013_7	21	95.378_0
5	79.296_1*	22	95.512_3
6	79.597_2	23	95.741_9
7	79.782_1	24	97.370_7
8	84.384_4	25	97.516_6*
9	84.564_1	26	1901.756_1*
10	85.017_4	27	02.606_8
11	85.298_0	28	04.355_5
12	85.765_9	29	04.762_5
13	88.795_1	30	07.688_5
14	89.569_9*	31	07.715_2
15	91.348_1	32	07.959_0*
16	92.593_8	33	09.967_3*
17	93.711_8*		

* Dr. Lucien Henry, Paris, France, has also measured these lines; these data agree excellently with his measurements (Henry, 1973).

$^{12}C^{16}O_2$: More extensive measurements were made for the carbon dioxide bands occurring in this spectral region. Figure 5 illustrates the type of observational data obtained, displaying the spectral resolution for a few of the lines of the CO_2 bands. Some of the main features of the bands studied are discussed below.

The rotational structure has been well resolved for the $3\nu_2{}^1(\Pi - \Sigma)$ band and the $4\nu_2{}^2 - \nu_2{}^1$ $(\Delta - \Pi)$ "hot" band. At the absorption path of about 120 m-atm, we observed the weak Q branch of the $4\nu_2{}^0 - \nu_2{}^1$ $(\Sigma - \Pi)$ "hot" band but none of its P and R structure. A search was also conducted, with no success, to locate the Q branches of the $3\nu_2{}^1$ bands of $^{13}C^{16}O_2$ and $^{12}C^{16}O^{18}O$. Using the available "F factors" for these bands (Garing and McClatchey, 1973), and assuming that in atmospheric carbon dioxide $^{13}C^{16}O_2$ is 1.1% abundant and $^{12}C^{16}O^{18}O$ is 0.4% abundant, it is possible to calculate the line-strength parameters, S, for these bands. These calculations suggest that we should have observed the Q-branches of the

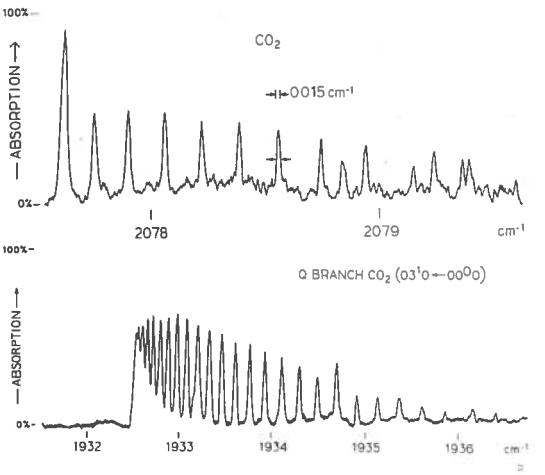

Figure 5. Samples of CO_2 spectra at 4.8 μm and 5.2 μm.

carbon-13 and oxygen-18 isotopic species, particularly with our absorption path of 120 m-atm. It would therefore seem desirable to conduct laboratory studies using enriched isotopic samples of carbon dioxide and determining experimental values for the "F factors" of the

isotopic varieties before we come to conclusions about the limits within which these parameters* are currently known.

N_2O: The N_2O bands occurring in this region have been scanned. Some new features have been observed, and work is still in progress in this phase of the laboratory studies. In selecting spectral regions for NO detection in the stratosphere, it would be advantageous to have available a composite map of the CO_2, N_2O, and H_2O bands in this region. That is one of the principal goals of the program of research in this laboratory.

Infrared Bands of NO_2

The locations of several of the infrared bands of this molecule are indicated in Figure 6 in relation to atmospheric transmission sketched for a 1000-ft horizontal airpath at sea level. Very recently, work was completed in interpreting the rotational structure of the ν_2 and ν_3 fundamentals† of this molecule (Hurlock et al., 1973; Hurlock et al., 1974). In the publication related to the ν_3 band, the spectrum was not reproduced. In view of the interest in this band for atmospheric studies (see, for instance, Goldman et al. (1970) and Ackerman and Muller (1972)), a composite tracing was made of this band; it is reproduced in Figure 7. The serial numbers on this figure are the same as those appearing in the assignments table of the article by Hurlock et al.

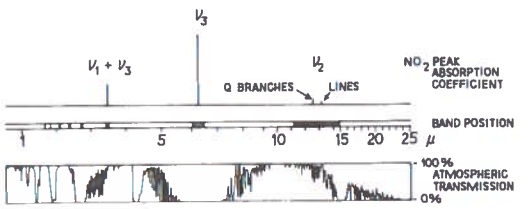

Figure 6. Location of NO_2 bands relative to atmospheric transmission sketched for 1000 ft. horizontal airpath at sea level.

* See Appendix A for explanation of the intensity parameters.

† Mr. Sidney M. Kirschner has developed new computer techniques for interpreting the ν_3 spectrum. His results agree with the work of Hurlock et al. (1974). Such independent verifications are necessary, especially when complex computations, based on involved theoretical relations, have to be performed.

(1974). Further studies, based on improved laboratory spectra and intensity measurements, are in progress.

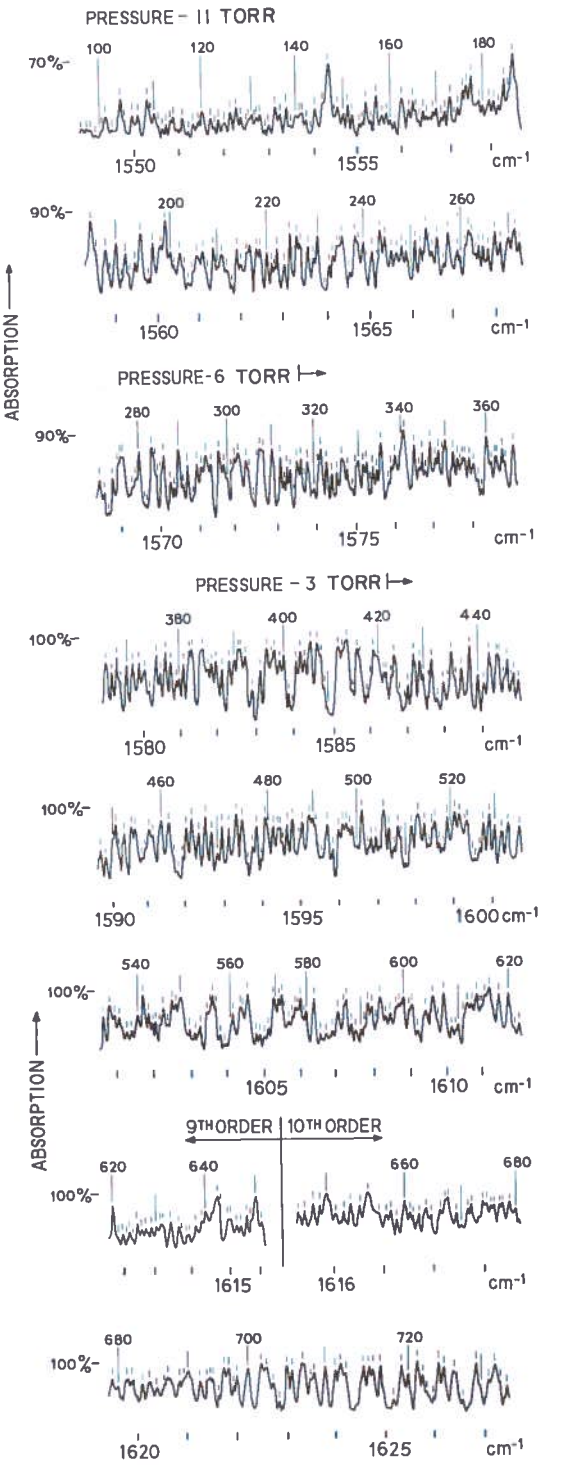

Figure 7. ν_3 band of $^{14}N^{16}O_2$: Path length used: 1 meter. See S.C. Hurlock (1970).

CONCLUDING REMARKS

For many years, investigations in high-resolution infrared spectroscopy were important only to a spectroscopist whose interests were confined primarily to the determination of structural parameters of molecules and to the correlation of experimental results with theory. More recently, research in this field has expanded in numerous directions, as outlined below, each with exciting possibilities.

- Molecular structure: molecular geometry, internuclear distances, and force fields
- Planetary and stellar spectra (explored since 1962 by Fourier spectroscopy (Connes, 1969))
- Molecular laser emissions (Rao and Mantz, 1972), important because absorption spectroscopy does not give transitions between levels that can be reached in lasers
- Photochemistry of the stratosphere: O_3, H_2O, NO_2, CH_4, N_2O, HNO_3, CO, NO, etc. (NO_2 and HNO_3 identified in 1968)
- Laser Stark spectroscopy (e.g., Johns and McKellar, 1973), for high-resolution and high-precision data
- Heterodyne measurement techniques (e.g., Freed et al., 1974, or Eng et al., in press)
- Tunable lasers (e.g., Nill et al., 1972 a, b)

The future of the field is full of promise, and it is hoped that the human effort which is so important for success will continue with unabated vigor.

ACKNOWLEDGMENTS

The work reported in this paper was done with the participation of Dr. Larry A. Pugh, Dr. Stephen C. Hurlock, Dr. Won B. Roh, Mr. Da-Wun Chen, Capt. Jerry Perrizo, Capt. William Heath, and Mr. Sidney Kirschner, who have all spent long and arduous hours conducting experiments in the laboratory and interpreting the data.

APPENDIX A

DEFINITION OF INTENSITY PARAMETERS

The strength of a spectral line arising from the transition $(v', J', \ell') - (v'', J'', \ell'')$ can be written (Penner, 1959) as

$$S = \frac{8\pi^3}{3hc} \cdot \frac{N_v''}{Q_R} \cdot g'' \cdot \nu \cdot \exp([-F''(J)]\ hc/kT) \cdot$$

$$|< v', J', \ell' |\underline{\mu}| v'', J'', \ell'' >|^2$$

where

N_v'' = number of molecules per unit volume in the lower vibrational state
Q_R = lower-state rotational partition function
ν = wavenumber of transition (cm^{-1})
$F''(J)$ = rotational term value of lower state (cm^{-1})
$\underline{\mu}$ = dipole moment of molecule
g'' = statistical weight of lower state.

We can write, in a manner analogous to that of Herman and Wallis (1955),

$$|< v', J', \ell' |\underline{\mu}| v'', J'', \ell'' >|^2 = L \cdot |< v' |\underline{\mu}| v'' >|^2 \cdot F$$

$$= L \cdot |R_0|^2 \cdot F$$

where

L = rigid-rotor line strength
R_0 = rotationless dipole-moment matrix element
F = factor which takes into account interaction between rotation and vibration.

Defining the quantity S_0, which depends only on the vibrational quantum numbers, as

$$S_0 = \frac{8\pi^3}{3hc} \cdot N_v'' \cdot |R_0|^2 \cdot \nu_0$$

where

$$\nu_0 = G(v') - G(v'')$$

we can write

$$S = S_0 \cdot L \cdot g'' \cdot \left(\frac{\nu}{\nu_0}\right) \cdot \left(\frac{1}{Q_R}\right) \cdot$$

$$\exp([-F''J]\ hc/kT) \cdot F$$

The F-factor can be written (Toth, 1974), in the case of a perpendicular band for a molecule like CO_2, in the form

$$F = (1 + \xi n)^2$$

where

$$n = n(J'', \ell'')$$

REFERENCES

Ackerman, M. and C. Muller (1972), "Stratospheric nitrogen dioxide from infrared absorption spectra," Nature **240**, 300.

Ackerman, M., D. Frimout, C. Muller, D. Nevejans, J.C. Fontanella, A. Girard, and N. Louisnard (1973), "Stratospheric nitric oxide from infrared spectra," Nature **245**, 205.

Connes, Pierre (1970), "High resolution Fourier spectroscopy," in *Optical Instruments and Techniques*, Oriel Press, London, England.

Connes, P., J. Connes, L.D. Kaplan, and W.S. Benedict (1968), "Carbon monoxide in the Venus atmosphere," Astrophys. J. **152**, 731.

Copen, D. (1964), "The Use of Atomic Thorium Spectra for Calibrations in the Infrared," M.S. thesis, The Ohio State University.

Cowan, M. and W. Gordy (1957), "Submillimeter wave spectroscopy: DCl," Bull. Amer. Phys. Soc. **2**, 212.

Douglas, A.E. and D. Sharma (1953), "Rotation-vibration spectra of diatomic and simple polyatomic molecules with long absorbing paths. IX. The spectra of the HCN and DCN molecules from 2.5μ to 0.5μ," J. Chem. Phys. **21**, 448.

Eng, R.S., H. Kildal, J.C. Mikkelsen, and D.L. Spears "Determination of absolute frequencies of $^{12}C^{16}O$ and $^{13}C^{16}O$ laser lines" (to be published in 1974).

Freed, C., A.H.M. Ross, and R.G. O'Donnell (1974), "Determination of laser line frequencies and vibrational-rotational constants of the $^{12}C^{18}O_2$, $^{13}C^{16}O_2$, and $^{13}C^{18}O_2$ isotopes from measurements of cw beat frequencies with fast HgCdTe photodiodes and microwave frequency counters," J. Mol. Spectrosc. **49**, 439.

Fridovich, B. and E. Champion (1974), private communication (NOAA NESS).

Garing, J.S. and R.A. McClatchey (1973), "Atmospheric absorption line compilation," Appl. Opt. **12**, 2545. (Also private communication from R.A.M., 1974.)

Goldman, A., D.G. Murcray, F.H. Murcray, W.J. Williams, and F.S. Bonomo (1970), "Identification of the $\nu_3 NO_2$ band in the solar spectrum observed from a balloon borne spectrometer," Nature **225**, 443.

Guelachvili, G. (1973), "New near infrared wavenumber standards ($2 \leftarrow 0$ band of $^{12}C^{16}O$) by high resolution Fourier spectroscopy in vacuum," Optics Communications **8**, 171.

Hall, D.N.B. (1970), "Observations of the Infrared Sunspot Spectrum Between 11 340 Å and 24 778 Å," Ph.D. dissertation, Harvard University.

Hall, D.N.B. (1973), "Detection of the ^{13}C, ^{17}O, and ^{18}O isotope bands of CO in the infrared solar spectrum," Astrophys. J. **182**, 977.

Helminger, P., F.C. De Lucia, and W. Gordy (1970), "Extension of microwave absorption spectroscopy to 0.37-mm wavelength," Phys. Rev. Lett. **25**, 1397.

Henry, Lucien R. (1973), private communication (Faculté des Sciences, Paris).

Herman, R. and R.F. Wallis (1955), "Influence of vibration-rotation interaction on line intensities in vibration-rotation bands of diatomic molecules," J. Chem. Phys. **23**, 637.

Herzberg, G. and K. Narahari Rao (1949), "Rotation-vibration spectra of diatomic and simple polyatomic molecules with long absorbing paths. II. The spectrum of carbon monoxide below 1.2μ," J. Chem. Phys. **17**, 1099.

Hurlock, Stephen C. (1970), "High Resolution Absorption Spectra of the Isotopic Modifications of Nitrogen Dioxide and Other Small Molecules," Ph.D. dissertation, The Ohio State University.

Hurlock, S.C., K. Narahari Rao, L.A. Weller, and P.K.L. Yin (1973), "High resolution spectrum and analysis of the ν_2 band of $^{14}N^{16}O_2$," J. Mol. Spectrosc. **48**, 372.

Hurlock, S.C., W. Lafferty, and K. Narahari Rao (1974), "Analysis of the ν_3 band of $^{14}N^{16}O_2$," J. Mol. Spectrosc. **50**, 246.

Johns, J.W.C. and A.R.W. McKellar (1973), "Stark spectroscopy with the CO laser: The ν_2 fundamentals of H_2CO and D_2CO," J. Mol. Spectrosc. **48**, 354.

Kaplan, L.D., J. Connes, and P. Connes (1969), "Carbon monoxide in the Martian atmosphere," Astrophys. J. **157**, L187.

Locke, J.L. and L. Herzberg (1953), "The absorption due to carbon monoxide in the infrared solar spectrum," Can. J. Phys. **31**, 504.

Maki, A.G. and R. Thibault (1968), "Analysis of some perturbations in the ν_4 band of methyl chloride," J. Chem. Phys. **48**, 2163.

Migeotte, M. (1959), "The fundamental band of carbon monoxide at 4.7μ in the solar spectrum," Phys. Rev. **75**, 1108.

Migeotte, M. and L. Neven (1950), "Détection du monoxyde de carbone dans l'atmosphère terrestre, à 3580 mètres d'altitude," Physica **16**, 423.

Nill, K.W., F.A. Blum, A.R. Calawa, and T.C. Harman (1972), "Observation of A-doubling and Zeeman splitting in the fundamental infrared absorption band of nitric oxide," Chem. Phys. Letters **14**, 234; and "Observation of nuclear hyperfine splitting in the infrared vibration-rotation absorption spectrum of the NO molecule," Chem. Phys. Letters **15**, 144.

Penner, S.S. (1959), *Quantitative Molecular Spectroscopy and Gas Emissivities*, Addison Wesley Publishing Co., Reading, Mass.

Plyler, E.K. and E.D. Tidwell (1956), "The precise measurement of the infrared spectra of molecules of the atmosphere," in "Les Molécules dans les Astres," Septième Colloque International d'Astrophysique, 426-429.

Pugh, L.A., T. Owen, and K. Narahari Rao (1973), "$3\nu_3$ band of $^{12}CH_4$ at 1.1μ," J. Chem. Phys. **59**, 1243.

Rank, D.H., A.H. Guenther, G.D. Saksena, J.N. Shearer, and T.A. Wiggins (1957), "Tertiary interferometric wavelength standards from measurements on lines of the 2-0 band of carbon monoxide and derived wavelength standards for some lines of the 1-0 band of carbon monoxide. The velocity of light derived from a band spectrum method: IV," J. Opt. Soc. Amer. **47**, 686.

Rank, D.H., D.P. Eastman, B.S. Rao, and T.A. Wiggins (1961), "Highly precise wavelengths in the infrared. II. HCN, N_2O, and CO," J. Opt. Soc. Amer. **51**, 929.

Rank, D.H., A.G. St. Pierre, and T.A. Wiggins (1965), "Rotational and vibration constants of CO," J. Mol. Spectrosc. **18**, 418.

Rao, K. Narahari (1950), "The infra-red CO bands as wave-number standards in the infra-red region," J. Chem. Phys. **18**, 213.

Rao, K. Narahari (1972), "Large plane gratings," in *Molecular Spectroscopy: Modern Research*, K. Narahari Rao and C.W. Mathews, eds., Academic Press, Inc., New York.

Rao, K. Narahari (1973), "Expanding frontiers of research in high-resolution infrared spectroscopy," Ann. New York Acad. Sci. **220**, 17-54.

Rao, K. Narahari, T.J. Coburn, J.S. Garing, K. Rossmann, and H.H. Nielsen (1959), "Wavelength calibrations in infrared. Part II. Use of atomic lines from a hollow cathode discharge tube with neon as carrier gas," J. Opt. Soc. Amer. **49**, 221.

Rao, K. Narahari, C.J. Humphreys, and D.H. Rank (1966), *Wavelength Standards in the Infrared*, Academic Press, New York.

Rao, K. Narahari and A.W. Mantz (1972), "Molecular laser emissions in the infrared," in *Molecular Spectroscopy: Modern Research*, K. Narahari Rao and C.W. Mathews, eds., Academic Press, Inc., New York.

Roh, W.B. and K. Narahari Rao (1974), "CO laser spectra," J. Mol. Spectrosc. **49**, 317.

Rosenbloom, B., A.H. Nethercot, Jr., and C.H. Townes (1958), "Isotopic mass ratios, magnetic moments and the sign of the electric dipole moment in carbon monoxide," Phys. Rev. **109**, 400.

Toth, Robert A. (1973), private communication (Jet Propulsion Laboratory).

Toth, R.A., C.B. Farmer, R.A. Schindler, O.F. Raper, and P.W. Schaper (1973), "Detection of nitric oxide in the lower atmosphere," Nature Phys. Sci. **244**, 7.

Weinberg, J.M., E.S. Fishburne, and K. Narahari Rao (1965), " 'Hot' bands of CO at 4.7 microns measured to high J values," J. Mol. Spectrosc. **18**, 428.

Wilson, R.W., K.B. Jefferts, and A.A. Penzias (1970), "Carbon monoxide in the Orion nebula," Astrophys. J. **161**, L43.

DISCUSSION

(UNIDENTIFIED): Intensity information from laboratory infrared spectra is urgently needed for the quantitative measurement of atmospheric abundances. Could you expand a little on your capabilities for making accurate intensity measurements?

RAO: We are making them right now. Our technical abilities are adequate, and a year from now we should be in a better position to make definitive statements.

(UNIDENTIFIED): Could you comment on the quality of the spectral intensities that are now available?

RAO: There has been no systematic evaluation of intensity measurements made with high-precision spectrographs, so it is difficult to make accurate estimates. Incidentally, one must be cautious in making intensity calculations from reproductions of spectra appearing in the literature, especially when such reproductions were furnished only to identify the observed rotational structure.

RECENT RESULTS OF STRATOSPHERIC TRACE-GAS MEASUREMENTS FROM BALLOON-BORNE SPECTROMETERS

D.G. MURCRAY, A. GOLDMAN, W.J. WILLIAMS, F.H. MURCRAY, J.N. BROOKS, J. VAN ALLEN, R.N. STOCKER, J.J. KOSTERS, AND D.B. BARKER
Department of Physics and Astronomy
University of Denver
Denver, Colorado

and

D.E. SNIDER
Ballistic Research Laboratories
Aberdeen Proving Ground, Maryland

ABSTRACT: Atmospheric absorption and emission infrared spectra are analyzed in terms of mixing ratios of trace gases in the lower stratosphere. The emission technique is applied to recent observations of H_2O spectra in the 25-μm region and to HNO_3 spectra in the 11.3-μm region. The sunset technique for determining mixing-ratio profiles from absorption spectra is discussed and applied to H_2O and NO_2 in the 6-μm region.

INTRODUCTION

Many of the minor constituents of current stratospheric interest have strong absorption bands in the infrared. The concentrations of a number of these are quite small, so even though the absorption bands are strong, long atmospheric paths are required in order to obtain measurable absorptions for many of the molecules. One method of obtaining such paths is to use the sun as the source for the spectrometer, and to study the variation of the solar spectrum with altitude. Further enhancement in the atmospheric path can be achieved by taking data at large solar zenith angles. This technique is particularly useful for initial detection of a molecule. However, a slight change in the portion of the sun used as the spectrometer source can cause a significant change in the air mass and a resulting uncertainty in mixing ratio. An additional limitation is that data can be obtained only during sunrise or sunset.

With the development of more sensitive infrared detectors, it has become possible to obtain information concerning the distribution of many minor species by studying atmospheric emission spectra. In most wavelength regions the intensity of the emitted atmospheric radiation is many orders of magnitude less than the corresponding solar radiation, so the instrumentation problems are quite different. While the resolution in this case is significantly less than in the absorption spectra, many bands, such as the HNO_3 emission in the 11.3-μm region, are easily identified. These HNO_3 emissions, when observed in the lower stratosphere at an elevation angle of $\approx 45^\circ$, correspond to absorptivities of from ≈ 0.001 to ≈ 0.01. This increased sensitivity makes it possible to measure the variation in atmospheric emission as the instrumentation platform rises through the atmosphere, so in the determination of a mixing-ratio profile the uncertainty due to the optical path is not as great as in the case of the sunset spectral technique.

During the past few years, our group at Denver University has used both techniques, with balloon-borne spectrometers and radiometers, to study stratospheric H_2O, CO_2, O_3, CH_4, N_2O, CO, HNO_3, NO_2, and NO. Recent results from our measurements and analysis are discussed below.

METHODS OF ANALYSIS

The analysis of the emission and absorption data obtained with solar zenith angles smaller than 90° is based on successive layer-by-layer calculations. Homogeneous atmospheric layers are defined by the actual altitudes of observations $h_1, h_2, \ldots, h_N$, where h_1 is the highest

altitude. The basic equations are similar for both emission and absorption spectra. The equations for emission spectra are (Goldman et al., 1973a):

$$R(\nu,h_1) = E(\nu,1)\, B(\nu,1), \quad (1)$$

$$R(\nu,h_n) = T(\nu,n)\, R(\nu,h_{n-1}) + E(\nu,n)\, B(\nu,n), \quad (2)$$

$$n = 2, \ldots, N,$$

where $R(\nu,h_n)$ is the infinite-resolution radiance at $\nu(cm^{-1})$ observed at altitude h_n, $B(\nu,n)$ is the black-body radiance of layer n, and $E(\nu,n)$ and $T(\nu,n)$ are its infinite-resolution emissivity and transmittance respectively. The corresponding equations for absorption spectra are (Goldman et al., 1973b):

$$A(\nu,h_1) = E(\nu,1), \quad (1a)$$

$$A(\nu,h_n) = T(\nu,n)\, A(\nu,h_{n-1}) + E(\nu,n), \quad (2a)$$

$$n = 2, \ldots, N,$$

where $A(\nu,h_n)$ is the infinite-resolution absorption observed at h_n. The infrared atmospheric emissivity is determined by the gas amounts, the atmospheric temperature and pressure profiles, and the vibration-rotation and pure-rotation spectral lines of the various molecular species. Equations (1) and (2) represent successive equations for $R(\nu,h_n)$ and $A(\nu,h_n)$, where each step below h_1 involves two consecutive layers, and thus can yield concentrations of atmospheric constituents as a function of altitude.

The applications of Equations (1) and (2) with the line-by-line method and the band-model method to the derivation of stratospheric mixing-ratio profiles have been described recently (Goldman et al., 1973a; Goldman et al., 1973b; Murcray et al., 1973). In the present work more recent results, obtained by using similar methods, are reported for H_2O and HNO_3.

New results for NO_2 are derived here from high-altitude solar spectra obtained at solar angles larger than 90°. The quantitative determination of mixing-ratio altitude profiles from such spectra requires accurate determination of the optical path. When the zenith angles are larger than 90°, refraction effects can become significant, depending on the observation altitude and the zenith angle. This can be seen in Table 1, which shows typical results for the traversed air mass for optical paths from an altitude of ≈ 40 km with various zenith angles. The air mass traversed and the minimum altitude reached by the optical path for various solar zenith angles and various observer altitudes can be seen in Figures 5 and 6 of a previous paper by Murcray et al. (1969). It is apparent that small variations

Table 1. Optical Parameters for "Setting Sun" Technique for a Balloon at 40.0-km Float Altitude

Tangent Altitude (km)	Apparent Zenith Angle (deg.)	Astronomical Zenith Angle (deg.)	Refraction (min. of arc)	Air Mass	Effective Pressure (torr)	Tangent Height Pressure (torr)
---	86.00	86.00	0.03	0.03	1.4	---
40.0	90.00	90.00	0.10	0.09	1.6	2.2
36.1	92.00	92.01	0.35	0.29	2.8	3.6
31.2	93.00	93.01	0.84	0.69	5.5	7.4
24.4	94.00	94.04	2.66	2.11	15.0	21.4
15.4	95.00	95.21	12.60	9.76	64.2	91.3
13.3	95.20	95.49	17.33	13.89	90.9	130.1
11.1	95.40	95.75	21.22	19.29	127.7	182.4
8.8	95.60	96.04	26.51	26.33	179.5	260.69
6.4	95.80	96.35	32.94	35.59	249.1	362.7
3.8	96.00	96.72	43.18	48.50	344.2	494.4

1.0 air mass $\equiv 2.149 \times 10^{25}$ molec/cm^2.

in pointing to the center of the sun can lead to significant variations in the derived air mass traversed.

The optical-path results discussed above were obtained from a ray-tracing computer program (written by R. Harter, on the basis of the work by Treve (1964)). In principle, the ray-tracing procedure can be used to extend the line-by-line/layer-by-layer method (Goldman et al., 1973a; Goldman et al., 1973b), developed for balloon spectra at zenith angles smaller than 90°, to the line-by-line analysis of sunset spectra. This has been deferred to future work, and only a one-layer line-by-line analysis has been carried out here.

The ray-tracing program has been used to derive an effective pressure, P_e, according to $P_e = \int Pdm / \int dm$, where P is the atmospheric pressure and m is the atmospheric mass being traversed. The effective pressure along the optical path is consistent with the Curtis-Godson approximation for constant temperature and constant mixing ratio along the path. Table 1 also shows the derived P_e values, which can be compared with the atmospheric pressures at the observer altitude and at the minimum altitude of the path.

The one-layer line-by-line analysis is used here with the P_e defined above. This is a good approximation for the analysis of spectra obtained with zenith angles significantly larger than 90°, when most of the absorption takes place in a few-km layer above the minimum altitude of the ray. It should be noted that whereas such a one-layer approximation is more valid for the larger zenith angles, the determination of the optical path for such angles is less reliable.

RESULTS

H_2O

Samples of data obtained with the spectral radiometer system in the 16 to 30-μm region can be seen in Figure 1 of Goldman et al. (1973a). The presence of emission due to HNO_3 in the 20- to 24-μm region is clearly evident on the lower-altitude records. There is a group of strong water-vapor lines around 25 μm, while both sides of this region are relatively free of atmospheric emission. Hence, this region was used to determine the amount of water vapor present in the stratosphere. Profiles A and B in Figure 1 below were determined from emission data obtained from Holloman AFB, New Mexico. During the 7 December 1967 flight the absorption in the 6.3-μm region was measured during sunset. These data have also been reduced to water-vapor mixing-ratio values, the derivation of which will be described in the discussion on NO_2.

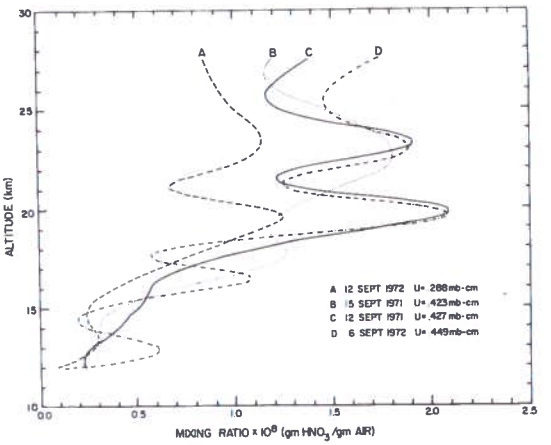

Figure 1. Mixing-ratio profiles of water vapor. Curves A and B were derived from spectral radiometer data obtained from Holloman AFB. Curve C was obtained from Fairbanks, Alaska. The points denoted by circles were derived from transmittance measurements made from Holloman AFB during sunset.

Stratospheric water-vapor measurements continue to be the subject of considerable controversy. Any measurement that does not yield a uniform mixing ratio of 2.0×10^{-6} g H_2O/g air is suspected of being contaminated. Each of the profiles discussed above shows an indication of a layer in the 20-25 km region. The techniques used in these measurements should minimize the effects of local contamination. The emission measurements were made using a liquid-nitrogen-cooled spectral radiometer, and there should be no contamination from this instrument. The solar spectra obtained during sunset should also be insensitive to any contamination effect, since the analysis is based on significant changes in absorption in a very short time period; local contamination should not change that rapidly. In the case of the emission spectra, the data taken during ascent and descent agree very well. In addition, the data taken while the balloon was at float altitude showed no significant change.

Figure 1 also shows a similar water-vapor profile (C) determined from atmospheric emission data obtained from a balloon flight made from Fairbanks, Alaska. Note that this profile does not show any evidence of the layer observed at Holloman AFB.

HNO_3

The major atmospheric emission in the 11.3-μm region in the lower stratosphere is due to HNO_3. This can be used to measure the HNO_3 altitude profile by using a sensitive filter radiometer with a filter passing radiation from 10.6 to 11.6 μm (Murcray et al., 1973). Such nondispersed emission data have advantages over the spectral data in that they are obtained more rapidly and the instrument has greater sensitivity. These two factors make possible a much finer determination of the variation of the mixing-ratio profile with altitude. The observed data show some scatter due to atmospheric and instrumental noise. The data are therefore smoothed using a least-squares/spline technique combined with a requirement that the curve be monotonically decreasing with altitude. Data from a number of balloon flights have been reduced in this manner. HNO_3 profiles determined from several flights made from Holloman AFB can be seen in Figure 7 of Murcray et al. (1973). The main variability appears to be in the altitude of the bottom of the layer. This is also reflected in the total amount of HNO_3 in a vertical path. Figure 2 shows more recent results, for balloon flights made from Fairbanks, Alaska; however, Alaska data are available only for September. Most of the Alaska data indicate that at the higher latitude the layer is lower in altitude, and that the total column density of HNO_3 is greater at the high latitudes. In general, the altitude of the HNO_3 layer is correlated with the altitude of the tropopause.

NO_2

The presence of NO_2 in the lower stratosphere was tentatively identified by Murcray et al. (1968) and then confirmed by Goldman et al. (1970). The NO_2 identification was made from observations of the solar spectrum in the ν_3 NO_2 region near 1617 cm^{-1}. The solar spectra were

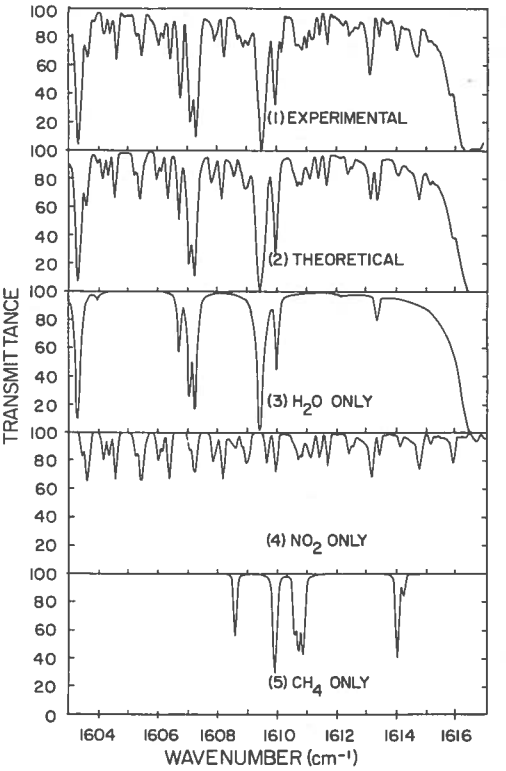

Figure 2. Mixing-ratio profiles of HNO_3 and total HNO_3 amounts as derived from balloon flights made from Fairbanks, Alaska.

obtained from a balloon-borne grating spectrometer, at an altitude of 30 km, during sunset, with solar zenith angles larger than 90°. The spectra have a resolution of ≈ 0.5 cm^{-1} and show a number of NO_2 features among the H_2O lines.

More recently, Ackerman et al. (1973) reported high-resolution (≈ 0.1 cm^{-1}) observations of the ν_3 NO_2 band in the solar spectrum. The spectra were obtained by using a grid spectrometer developed by Girard (1963), which was flown in the Concorde at an altitude of 16 km and at solar zenith angles from 88° to 91°. The spectrum presented by Ackerman et al. (1973) shows a number of NO_2 and CH_4 features among the H_2O lines. The three distinct NO_2 features observed near 1613 cm^{-1} in the balloon spectra (Goldman et al., 1970) are resolved by Ackerman et al. (1973) to a number of components.

In the present work the ν_3 NO_2 balloon and Concorde observations mentioned above have been used to derive NO_2 mixing-ratio values in

the lower stratosphere. It should be noted that quantitative analysis of the balloon spectra has been made previously by Ackerman and Muller (1973). However, the method of reducing the observational data to transmittance values has since been revised, as will be described here, and a re-analysis was deemed worthwhile. The quantitative analysis of the atmospheric ν_3 NO_2 data has been delayed due to difficulties encountered in the spectroscopic analysis of this band. A successful rotational analysis of this band was accomplished only recently by Hurlock et al. (1974), who derived accurate upper-state constants.

Individual line parameters, positions, intensities, and ground-state energies were generated for the ν_3 $^{14}N^{16}O_2$ band with J up to 60 and K up to 12. The energy levels were computed according to the constants derived by Hurlock et al. (1974). Rigid-rotor line intensities were assumed here, and the total band intensity was normalized to the value of 2059 cm^{-2} atm^{-1} at 25C as determined by Guttman (1962). The derived line intensities at 298K are shown in Figure 3 as a function of ν. A number of K sub-bands can be seen on the linear intensity scale, as well as a number of Q branches which are spread over the spectrum, with no distinct central Q branch. Spin splitting in the ν_3 NO_2 band has been observed, but not included in the rotational analysis (Hurlock et al., 1974). It was also not taken into account in the present calculations. The observed solar spectra indicate that "hot" bands and isotopic bands are not significant for analysis of the present data. A halfwidth of 0.06 cm^{-1} atm^{-1} at 300K has been assumed here for all lines, on the basis of a theoretical estimate by Tejwani (1972).

The derived line parameters were first used for comparisons of line-by-line calculations with the experimental spectrum published by Guttman (1962). The comparison is shown in Figure 4, where a 10 cm^{-1} resolution has been assumed in the calculated spectrum. The agreement between the two spectra is quite good. It is interesting to note that the calculated spectrum is practically insensitive to the value of the halfwidth used, and that doubling the path results in doubling the integrated absorption. This indicates that the spectrum is in the linear region of the curve of growth.

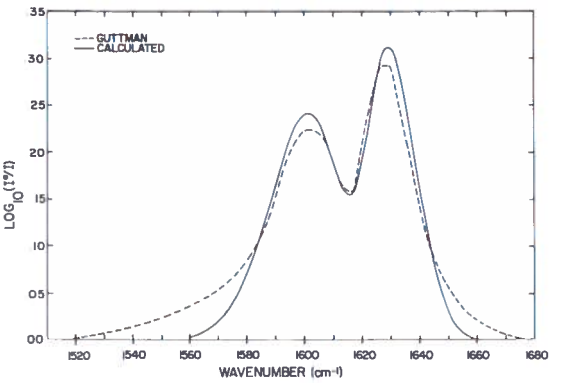

Figure 4. Comparison of theoretical and experimental (Guttman, 1962) spectra of the 1618 cm^{-1} band of NO_2 at 25C, 1.18 atm pressure, and 0.0495 cm cell. A resolution of 10 cm^{-1} was used in the calculated spectrum.

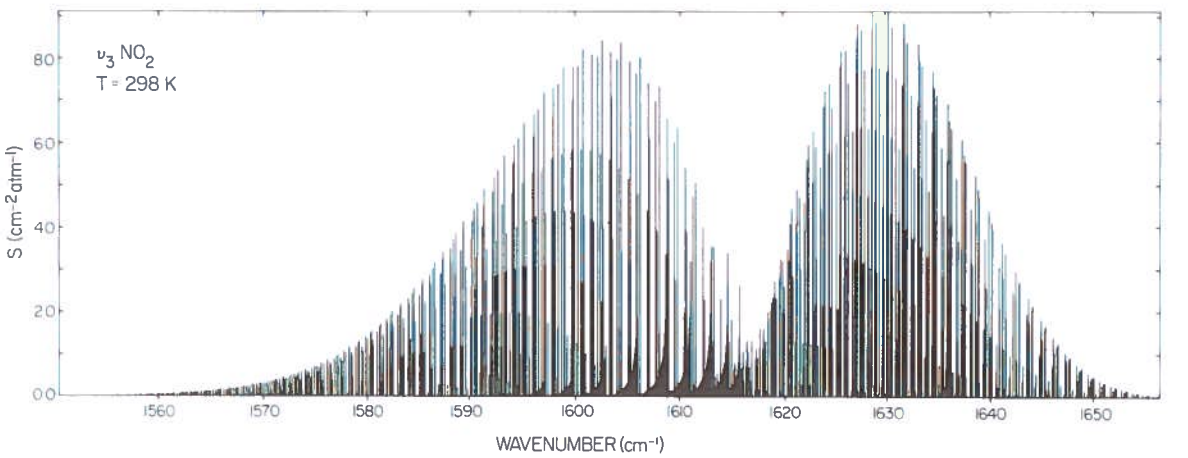

Figure 3. Line intensities of the ν_3 $^{14}N^{16}O_2$ band at 298K.

Comparisons of experimental and calculated spectra obtained recently are shown in Figures 5 and 6. Good agreement is seen between the experimental and the calculated spectra. These spectra have a resolution of ≈ 0.5 cm^{-1} and are in the intermediate region of the curve of

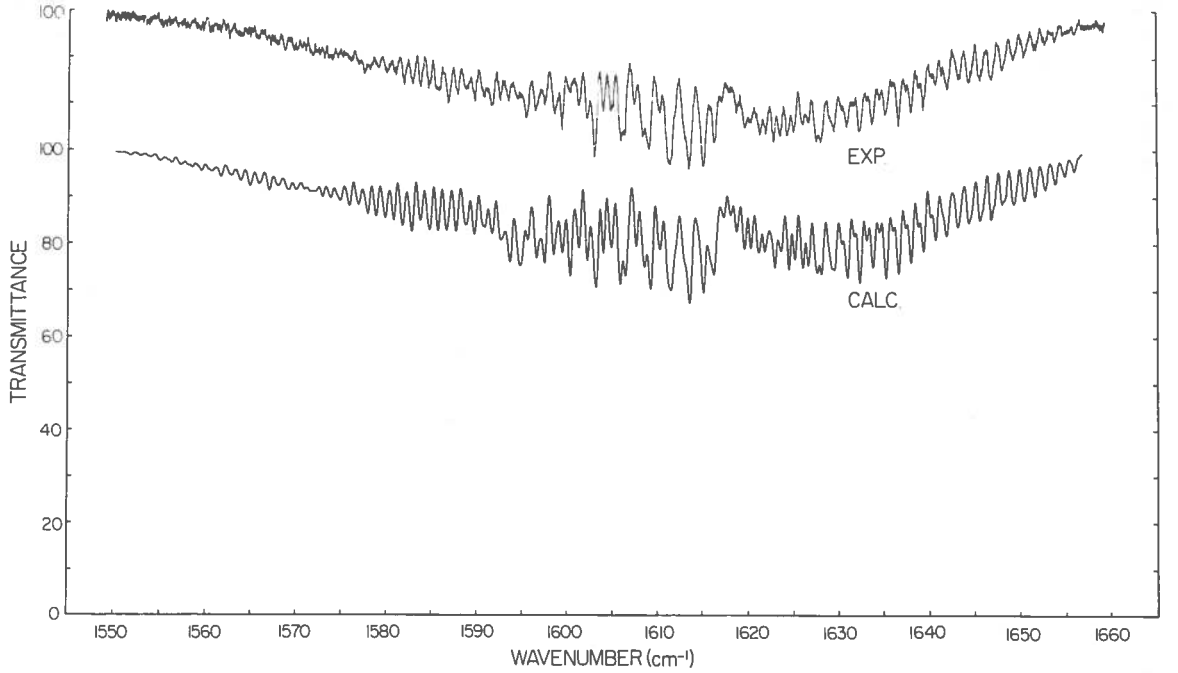

Figure 5. Comparison of theoretical and experimental spectra for the 1618 cm^{-1} band of NO_2 at 42C, 3.3 torr, and 9.94 cm cell. Resolution is 0.5 cm^{-1}. The 100% line is displaced by 30% for clarity.

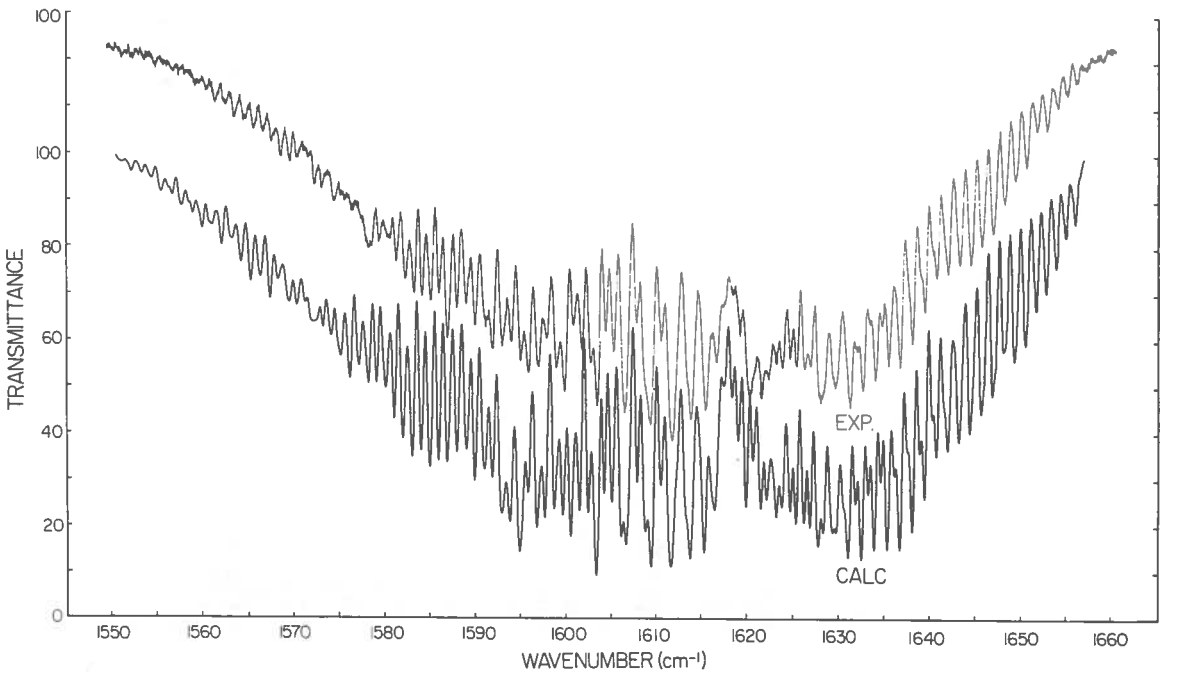

Figure 6. Comparison of theoretical and experimental spectra for the 1618 cm^{-1} band of NO_2 at 42C, 30 torr, and 4.96 cm path. Resolution is 0.5 cm^{-1}. The 100% line is displaced by 30% for clarity.

growth. With the 0.06 cm^{-1} halfwidth adopted here, it was necessary to increase Guttman's (1962) band intensity by a factor of 2, which seems contradictory to the agreement obtained between the calculated spectrum and Guttman's spectrum (see Figure 4). The source of the disagreement may be due to differences between Guttman's and the present determinations of the amounts of gas in the absorption cells. The current measurements at Denver University cover a large region of the curve of growth for Voigt lines, which will allow the determination of the total band intensity and halfwidth values for line groups across the band. It is suspected that significant deviation from Guttman's band intensity may result. In the line-by-line analysis, the transmittance is a function of the product of the amount of gas and the line intensities. Therefore, a change in the band intensity yields a corresponding inverse change in the gas amount.

The currently generated ν_3 NO_2 line parameters were combined with the atmospheric line parameters as compiled by McClatchey et al. (1973) for the analysis of the sunset balloon spectra (Goldman et al., 1970). The 1503-1531 cm^{-1} region, which shows practically no contribution from CH_4 or NO_2, was first used to determine H_2O mixing-ratio values by fitting a one-layer line-by-line calculation to each of the observed records. The optical-path parameters and the resulting H_2O mixing ratios are shown in Table 2. The H_2O mixing ratios are compared in Figure 1 with recent H_2O mixing-ratio profiles determined from atmospheric emission spectra (see discussion on H_2O).

Note that the 1616 cm^{-1} H_2O line occurs at the center of the ν_3 NO_2 band, where practically no NO_2 absorption is expected on the balloon spectra. Thus, with the H_2O mixing ratios derived above, the 1616 cm^{-1} line has been used to reconstruct the vacuum envelope of the data in the NO_2 region; this resulted in enhanced amounts of NO_2 absorption. One-layer line-by-line calculations were then fitted to the spectra. Figure 7 shows the re-normalized spectra, together with the calculated spectrum for Rec 142. The NO_2 mixing ratios obtained for the various records are listed in Table 2. The balloon spectra which appear in Figure 7 show no identifiable contribution from CH_4, so no CH_4 was used in the calculations.

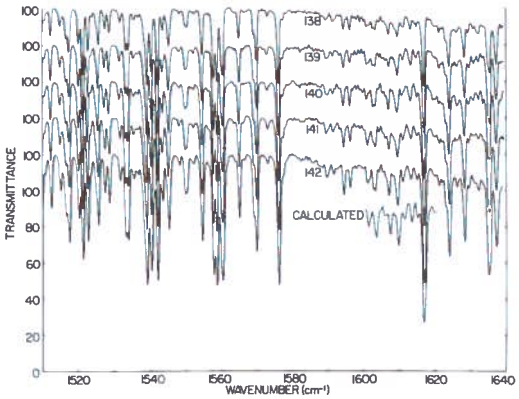

Figure 7. Experimental sunset balloon spectra (Records 138-142, from Goldman et al. (1970)) and a theoretical spectrum for Record 142. (See details in Table 2.)

The recent Concorde spectrum reported by Ackerman et al. (1973) shows the 1603-1617 cm^{-1} portion of the ν_3 NO_2 band at ≈ 0.1 cm^{-1} resolution. A number of well-resolved features of H_2O, NO_2, and CH_4 are observed. Figure 8 shows the Concorde spectrum, which has been

Table 2. H_2O and NO_2 Mixing Ratios Derived from Balloon Sunset Spectra in the 6.3-μm Region

Rec	Tangent Altitude (km)	Astronomical Zenith Angle (deg)	Apparent Zenith Angle (deg)	Air Mass	Tangent Height Pressure (torr)	Effective Pressure (torr)	H_2O Mixing Ratio (ppmw)	NO_2 Mixing Ratio (ppbv)	NO_2 Concentration (molec cm^{-3})
138	28.4	91.2	91.18	0.84	11.1	8.8	2.4	5.0	2.5×10^9
139	27.6	91.5	91.48	1.01	12.7	9.9	2.4	3.7	2.1×10^9
140	26.0	92.0	91.97	1.43	16.1	12.5	1.7	2.8	2.1×10^9
141	24.3	92.4	92.36	1.95	21.4	15.0	1.6	2.3	2.1×10^9
142	22.4	92.8	92.74	2.77	28.6	21.2	1.4	1.8	2.3×10^9

1.0 air mass $\equiv 2.149 \times 10^{25}$ molec/cm^2.

normalized by us to transmittance by drawing a zero line and a 100% line on the published data. The spectrum was obtained from 16 km at 91° solar zenith angle. For these conditions, we have derived 8.8 air masses, P_e = 75 torr, and a tangent altitude of 14.9 km. Figure 8 also shows calculated individual contributions of H_2O (0.9 ppmw), NO_2 (0.4 ppbv), and CH_4 (1 ppmv), and a combined contribution of H_2O (0.9 ppmw), NO_2 (0.4 ppbv), and CH_4 (0.05 ppmv). The various features of H_2O, NO_2, and CH_4 are well accounted for in the calculated spectra, especially in the 1603-1610 cm^{-1} region. It should be noted that the Concorde spectrum indicates a CH_4 mixing ratio significantly below 1 ppmv, which is smaller than expected at 16 km. A more critical evaluation of the absolute intensities of the weak ν_2 CH_4 lines in this region may therefore be required.

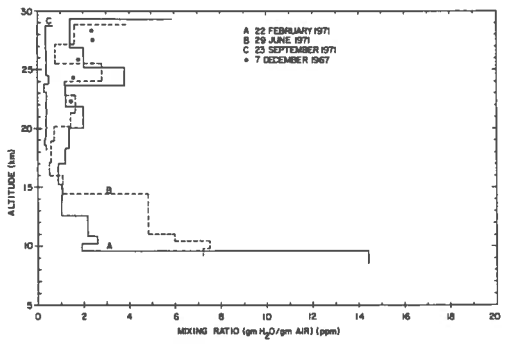

Figure 8. Experimental sunset spectrum obtained from the Concorde (Ackerman et al., 1973), theoretical spectra of individual H_2O, CH_4, and NO_2 molecules, and a theoretical spectrum of combined H_2O, CH_4, and NO_2. (See text for details.)

Figure 9 shows the present results for the NO_2 mixing ratio, derived from the balloon sunset spectra and from the Concorde spectrum. Also shown are the results of the analysis by Ackerman and Muller (1973) of the same balloon spectra analyzed here (but before re-normalization).

In addition to the ν_3 NO_2 spectra discussed above, a number of recent studies were carried out in order to determine NO_2 mixing ratios in the stratosphere. Ackerman and Muller (1973) have derived an NO_2 mixing ratio of (3.4 ± 1) ppbv at 12.5 km, with an upper limit of 2.3 ppbv at 16.1 km, from balloon sunset spectra in the region of the much weaker $\nu_1 + \nu_3$ NO_2 band, obtained at an altitude of 34 km. Harries (1973)

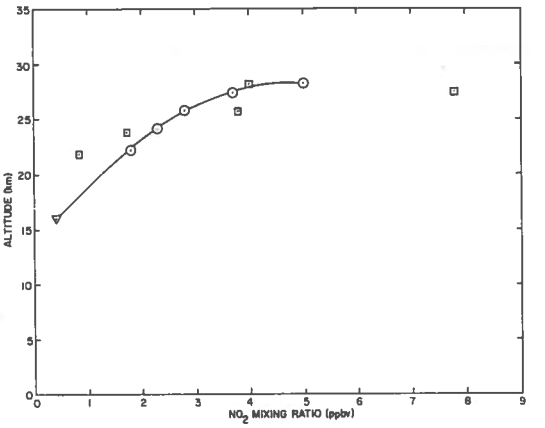

Figure 9. Mixing-ratio profile of NO_2. Circles denote the results of the present analysis of the balloon spectra taken by Goldman et al. (1970). The triangle denotes the results of the present analysis of the Concorde spectrum taken by Ackerman et al. (1973). The squares denote the results of the previous analysis of the balloon spectra taken by Goldman et al. (1970) which was made by Ackerman and Muller (1973).

reported identification of NO_2 rotational lines in the 20-30 cm^{-1} region from emission spectra measured from the Concorde with a zenith angle of 90° and ≈0.07 cm^{-1} resolution. An average mixing ratio of ≈20 ppbv was estimated and recently revised to ≈2.5 ppbv (Harries, 1974). Farmer (1974) reported the detection of two features due to the $\nu_1 + \nu_3$ NO_2 band from the Concorde-borne interferometric spectra, with a resolution of ≈0.2 cm^{-1}. A tentative mixing ratio was derived as (1.8 ± 0.5) ppbv over the 15 to 20-km range.

Harrison et al. (1972) reported an attempt to detect NO_2 from stellar spectra in the 388-515 nm region at ≈0.24 nm resolution. No evidence could be found for NO_2 absorption by the earth's atmosphere, establishing an upper limit of 10 ppbv. An unpublished and also unsuccessful attempt to detect atmospheric NO_2 in the visible solar spectrum reflected by the moon has been made by Murphy (1972). More recently, Brewer et al. (1973) reported detailed NO_2 mixing-ratio profiles, from the ground up to ≈50 km, as determined from absorption measurements near 444.8 nm with ≈0.3 nm resolution. The profiles show considerable diurnal variation. Profiles obtained during sunset show NO_2 mixing-ratio values from 1 ppbv to 10 ppbv in the 14 to 27-km range.

The results reported in the present work are within the same order of magnitude as the recent studies mentioned above. However, a detailed comparison between the various results is not yet available.

ACKNOWLEDGMENTS

This research was supported in part by the Advanced Research Projects Agency, monitored by the Air Force Cambridge Research Laboratories, and in part by the National Science Foundation – Department of Transportation (Climatic Impact Assessment Program) Grant GA-26228.

Acknowledgment is made to the National Center for Atmospheric Research, which is sponsored by the National Science Foundation, for computer time used in this research.

The authors are indebted to S.C. Hurlock, W.J. Lafferty, and K. Narahari Rao for making their ν_3 NO_2 analysis available. C. Bauer, W. Cochran, T. Dow, and J.R. Starkey have made their valuable contributions. Thanks are also due to A. Ozolins and the Computer Support Division of the Ballistic Research Laboratories for assistance with many of the calculations necessary for the NO_2 analysis.

REFERENCES

Ackerman, M., and C. Muller (1973), "Stratospheric methane and nitrogen dioxide from infrared spectra," PAGEOPH **106-108**, 1325.

Ackerman, M., J.C. Fontanella, D. Frimout, A. Girard, L. Gramont, N. Louisnard, C. Muller, and D. Nevejans, "Recent stratospheric spectra of NO and NO_2," Aeronomica Acta, A120-1973, Institut d'Aéronomie Spatiale de Belgique, 3 Avenue Circulaire, B-1180, Bruxelles, Belgium.

Brewer, A.W., C.T. McElroy, and J.B. Kerr (1973), "Nitrogen dioxide concentrations in the atmosphere," Nature **246**, 129.

Farmer, C.B. (1974), "Infrared measurements of stratospheric composition," Canad. J. Chem., **52** (8), 1544.

Girard, A. (1963), "Spectromètre à grilles," Appl. Opt. **2**, 79.

Goldman, A., D.G. Murcray, F.H. Murcray, W.J. Williams, and F.S. Bonomo (1970), "Identification of the ν_3 NO_2 band in the solar spectrum observed from a balloon-borne spectrometer," Nature **225**, 443.

Goldman, A., D.G. Murcray, F.H. Murcray, W.J. Williams, and J.N. Brooks (1973a), "Distribution of water vapor in the stratosphere as determined from balloon measurements of atmospheric emission spectra in the 24-29-μm region," Appl. Opt. **12**, 1045.

Goldman, A., D.G. Murcray, F.H. Murcray, W.J. Williams, J.N. Brooks, and C.M. Bradford (1973b), "Vertical distribution of CO in the atmosphere," J. Geophys. Res. **78**, 5273.

Guttman, A. (1962), "Absolute infrared intensity measurements on nitrogen dioxide and dinitrogen tetroxide," J. Quant. Spectrosc. Radiat. Transfer **2**, 1.

Harries, J.E. (1973), "Measurements of some hydrogen-oxygen-nitrogen compounds in the stratosphere from Concorde 002," Nature **241**, 515.

Harries, J.E. (1974), private communication.

Harrison, H., N. Laulainen, and T. Washington, "Attempt to Detect NO_2 in Stellar Spectra," Project ASTRA Publication No. 17, June 1972, University of Washington, Seattle, Washington 98195.

Hurlock, S.C., W.J. Lafferty, and K. Narahari Rao (1974), "Analysis of the ν_3 band of $^{14}N^{16}O_2$," J. Mol. Spectrosc. **50**, 246.

McClatchey, R.A., W.S. Benedict, S.A. Clough, D.E. Burch, R.F. Calfee, K. Fox, L.S. Rothman, and J.S. Garing, "AFCRL Atmospheric Absorption Line Parameters Compilation," AFCRL-TR-73-0096, 26 Jan. 1973, Environmental Research Papers No. 434.

Murcray, D.G., T.G. Kyle, F.H. Murcray, and W.J. Williams (1968), "Nitric acid and nitric oxide in the lower stratosphere," Nature **218**, 78.

Murcray, D.G., T.G. Kyle, F.H. Murcray, and W.J. Williams (1969), "Presence of HNO_3 in the upper atmosphere," J. Opt. Soc. Amer. **59**, 1131.

Murcray, D.G., A. Goldman, A. Csoeke-Poeckh, F.H. Murcray, W.J. Williams, and R.N. Stocker (1973), "Nitric acid distribution in the stratosphere," J. Geophys. Res. **78**, 7033.

Murphy, R.E., unpublished, 1972, Institute for Astronomy, University of Hawaii, Honolulu, Hawaii.

Tejwani, G.D.T. (1972), "Calculation of pressure-broadened linewidths of SO_2 and NO_2," J. Chem. Phys. **57**, 4676.

Treve, Y.M. (1964), "A new method for calculation of the atmospheric refraction and the optical air-mass," unpublished paper.

IN-SITU MEASUREMENTS OF NO IN THE STRATOSPHERE USING CHEMILUMINESCENCE

B.A. RIDLEY AND H.I. SCHIFF
York University
Downsview, Ontario, Canada

and

A. SHAW AND L.R. MEGILL
Utah State University
Logan, Utah

ABSTRACT: In-situ measurements have been made of the NO mixing ratios in the stratosphere at Holloman Air Force Base, New Mexico, in four balloon flights over the altitude range 17-30 km. Evidence is presented to indicate that no serious sampling errors occurred from contamination of the sampled air or from NO removal in the inlet to the instrument. Results are also reported for measurements taken in the 50-60 kft range on two RB-57F flights as part of the Airstream mission.

BALLOON FLIGHTS

At the second CIAP conference we described an instrument (Ridley et al., 1973a), which utilized the chemiluminescence method, that was suitable for in-situ measurements of NO in the stratosphere. The instrument was designed to operate automatically from either balloon or aircraft platforms and was provided with on-board calibration. Its detection limit was 0.02 ppbv.

We have reported (Ridley et al., 1973b, 1974) measurements with this instrument taken from a balloon over the altitude range 17-23 km. The NO mixing ratio was found to be close to 0.1 ppbv. Since this number was nearly an order of magnitude smaller than those predicted by the fashionable models of the day and those derived from early, 'remote-sensing', twilight absorption measurements in the infrared, we gave considerable attention to the possibility of contamination and sampling errors in our measurements.

Since that time we have completed two additional balloon experiments at Holloman Air Force Base, New Mexico, in which the measurements were extended to an altitude of 30 km. Both during the flights and in the laboratory, tests were made for contamination and sampling errors. The first sampling error considered was the possibility of contamination by the balloon and/or the flight packages. Balloon flight No. 2 was programmed to take measurements during several sequences of ascent, float, and descent. The absence of any detectable differences among the results obtained during these three flight conditions indicated that no major contamination was being encountered from outgassing or absorption from the balloon or payload.

The second possibility considered was self-contamination. The O_3 used to produce the chemiluminescence is exhausted with the sampled air through a 2.4-m length of tubing attached upward from the flight package, and so might have reduced the NO concentration in the incoming sampled air. Again, the absence of differences in the amount of NO detected during ascent and descent suggested that such contamination was negligible, in agreement with predictions based on simple diffusion calculations. More direct evidence was obtained during balloon flight No. 3 from a Komhyr ozonesonde mounted next to the sampling side of the NO instrument. The ozone profile obtained, shown in Figure 1, is perfectly normal. No unexpected changes in this profile occurred when the NO instrument was turned on during ascent or off during descent. The O_3 flow to the NO instrument was also interrupted for two 10-minute intervals, once near the beginning (open circles) and once near the end (closed circles) of the two-hour period during which the balloon was floating at its maximum altitude. The lack of any

change in the ambient O_3 readings of the ozonesonde confirms that the sampled air is not contaminated by the O_3 exhausted from the NO instrument.

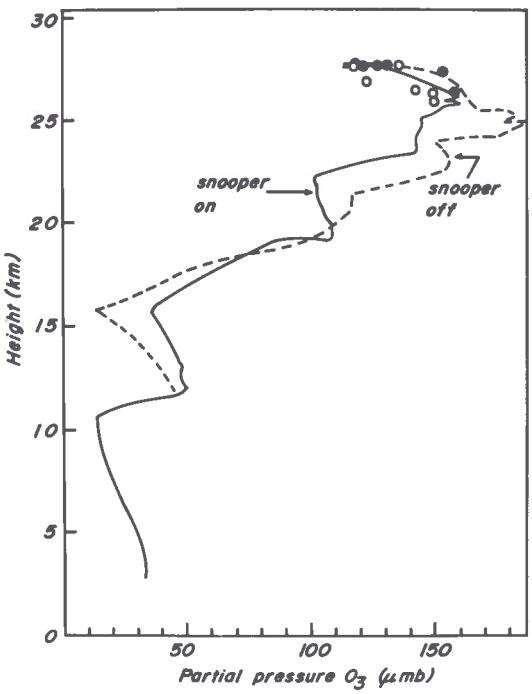

Figure 1. Vertical ozone distribution obtained during ascent and descent for the balloon flight of 22/6/73 (Komhyr ozonesonde).

Finally, we considered the possibility that the NO content of the sampled air was reduced by passage through the 2.6-m inlet tube, either by absorption on the inner aluminum surface of the tube or by heterogeneous reactions between the ambient NO and O_3 on the surface. Laboratory experiments were performed under conditions of pressure, temperature, and NO and O_3 concentrations similar to those which obtain in the stratosphere. These experiments showed differences of less than 10% when 0.2 ppbv of NO was introduced at the front and at the back end of the inlet tube. These differences were close to those which we calculated for homogeneous reaction of NO with O_3 in the tube and applied routinely to correct our raw data.

An in-situ test was made for this effect during balloon flight No. 4 on November 13, 1973. Measurements were taken for a period of several hours with the balloon floating at 30 km. Then, by ground command, half of the 2.6-m inlet tube was cut off. No significant change in the NO signal was detected.

On the basis of these tests, we now feel confident that our in-situ measurements do not involve any serious sampling or contamination errors.

Figure 2 shows the NO mixing ratios and Figure 3 the NO number densities obtained from both these balloon measurements and the aircraft measurements described in the next section. The

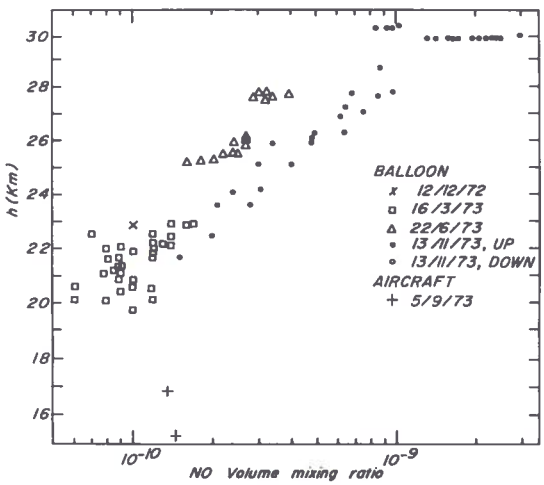

Figure 2. Vertical nitric oxide volume-mixing-ratio profiles obtained during the four balloon and one aircraft flight. The aircraft flight data was averaged from Figure 5.

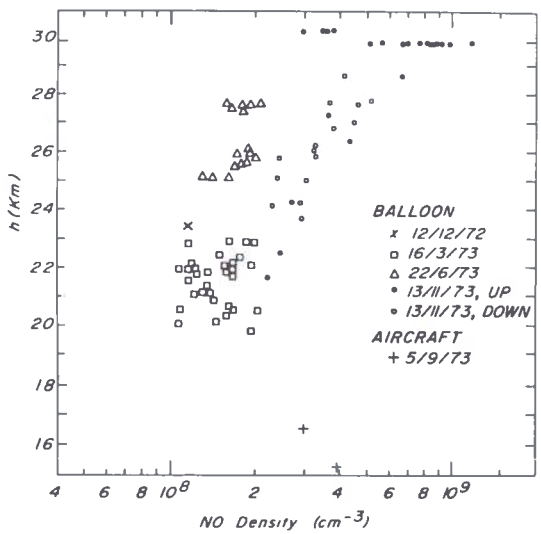

Figure 3. Vertical nitric oxide number-density profiles obtained during the four balloon and one aircraft flight. The aircraft flight data was averaged from Figure 5.

accuracy of these measurements is believed to be better than 50%.

RB-57 FLIGHTS

Instrument

The instrument used for aircraft measurements of NO in the stratosphere differs from that used on balloons only in the method used to generate the air flow. On the balloon a blower is used to draw sample air through the instrument; on the aircraft the ram of the forward motion of the aircraft is used.

Since the air-flow system for the aircraft has not been described in detail before, we will do so briefly here. As can be seen in Figure 4, sample air enters through the inlet, and most of it is diverted into the pod. An iris in front of the instrument sets the approximate flow; fine control is achieved by a servoed valve in the bypass line, which is adjusted to give constant flow (as measured near the instrument output). Since most of the sample air bypasses the instrument, high flow in the input tube is maintained, and the residence time in this tube is short.

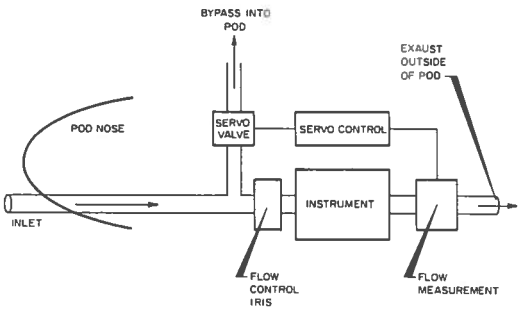

Figure 4. Schematic representation of aircraft flow system.

Measurements

Two successful series of aircraft measurements of NO taken on the RB-57F, a high-altitude sampling aircraft, are described here. The first series was taken on a flight between Albuquerque, New Mexico and Howard Air Force Base, Panama. The first half of the flight was made at 50,000 feet, the second half at 55,000 feet. Figure 5 shows the observed NO concentration during the flight (as a function of approximate local time), together with the altitudes. Each point on the curve is actually an average over approximately two minutes. There was a two-minute dead interval between measurements, and a longer dead time of six minutes every fourth measurement.

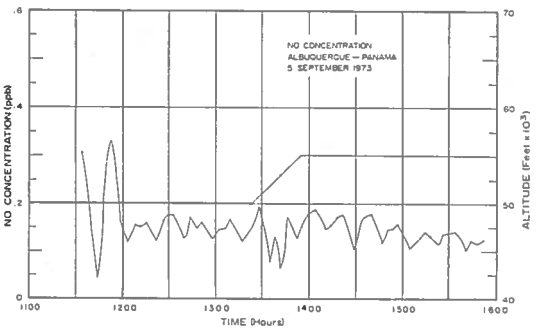

Figure 5. NO measurements made on Albuquerque-Panama flight, 5/9/73. The top curve indicates altitude; the bottom curve connects the NO data points.

In these measurements, the NO concentration in the sample air is compared to a NO/N_2 sample of known NO concentration (calibration gas). The accuracy of the results thus depends directly on the accuracy of the assay of the calibration gas. Unfortunately, there was a difference of a factor of four in the concentrations of NO in the calibration gas before and after the flight. The lower value (measured after the flight) has been used in the data presented here. This gives results consistent with other measurements that have been made. However, there still exists the possibility that the values given in Figure 5 are low by as much as a factor of four.

The second series of measurements was taken on a flight from Fairbanks, Alaska northward to a latitude of 75°N and back to Fairbanks. The results for this series of measurements are plotted in Figure 6, along with the approximate altitude. This plot is interesting in that nightfall occurred during the flight. In fact, a general decrease in NO concentration could be seen throughout the flight, ending with a sudden decrease to almost zero. The gradual decrease may be due to the prolonged twilight which occurs at high latitudes; the abrupt decrease to near zero is due to sundown. Only a few points are shown after sunset. Data taken after 1800 hours were noisy, and so were not completely analyzed, but continued to indicate near-zero NO concentrations.

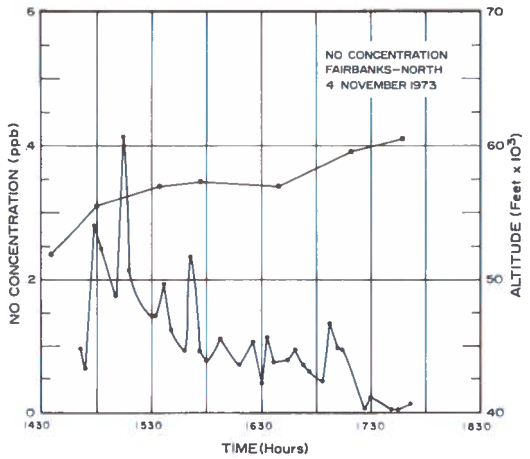

Figure 6. NO measurements made on the Fairbanks-north flight, 4/11/73. The top curve indicates altitude; the bottom curve connects NO data points.

The aircraft measurements reported here complement the balloon measurements made at higher altitudes. As was shown in Figure 2, the results of both types of measurement are consistent.

REFERENCES

Ridley, B.A., K.H. Welge, H.I. Schiff, L.R. Megill, and A.W. Shaw (1973a), "Instrumentation for NO measurement in the stratosphere," in *Proceedings of the Second Conference on the Climatic Impact Assessment Program* (Nov. 14-17, 1972), ed. A.J. Broderick, U.S. Dept. of Transportation, DOT-TSC-OST-73-4, 146.

Ridley, B.A., H.I. Schiff, A.W. Shaw, L. Bates, C. Howlett, H. LeVaux, L.R. Megill, and T.E. Ashenfelter (1973b), " 'In-situ' measurements of nitric oxide in the stratosphere between 17.4 and 22.9 km," Nature **245**, 310.

Ridley, B.A., H.I. Schiff, A.W. Shaw, L.R. Megill, L. Bates, C. Howlett, H. LeVaux, and T.E. Ashenfelter (1974), "Measurement of nitric oxide in the stratosphere between 17.4 and 22.9 km," Planet. Space Sci. **22**, 19.

DISCUSSION

SCHAINKER: What could have caused the concentration of the calibration gas to change between the beginning and the end of the flight?

SCHIFF: Keeping a sample of calibration gas standard is a fairly common problem in environmental testing. You can fill a cylinder and monitor it, and the level will gradually decrease and then appear to stabilize. Then all of a sudden one day it'll change. It's the first time we've seen it happen like that, though.

(UNIDENTIFIED): It seems to me, from the results presented at Melbourne that used a sensitivity study, that discrepancies in NO measurements of a factor of 10 should not be surprising. NO is such a local variable, and is so involved with other diurnal species, that models using a daily average should not be expected to give absolute NO concentrations any closer than a factor of 2.

STUDIES OF STRATOSPHERIC H_2O, O_3, HNO_3, N_2O, AND NO_2 FROM AIRCRAFT

J.E. HARRIES, J.R. BIRCH, J.W. FLEMING, N.W.B. STONE, D.G. MOSS, N.R.W. SWANN AND G.F. NEILL*
National Physical Laboratory
Teddington, Middlesex, United Kingdom

ABSTRACT: We have performed measurements of the submillimeter-wave emission spectrum of the stratosphere for a number of atmospheric conditions and experimental configurations, and data have been obtained during a period of 20 months, over a number of areas of the world.

This paper presents a current summary of the way in which several species have been observed to be distributed with height, latitude, season, and time of day. Of course, it is now important to obtain information on the real variabilities of these gases in order to approach an understanding of the ozone-destruction problem.

In addition, comparisons are made with other workers' results so as to give as complete a picture as possible of the constitution of the stratosphere.

INTRODUCTION

In a number of recent publications (Harries, 1972; 1973a, b, c; 1974; Harries et al., 1972) we have described aspects of our work on the use of the submillimeter spectral region to study stratospheric composition. This spectral region contains the pure-rotation spectra of many light dipolar molecules. The wavelengths involved are between 100 and 1000 μm. The advantages and disadvantages of this spectral region have been discussed in the past (Harries, 1972, 1973a; Farmer, 1974). In the main the advantages center on the relative coarseness of the instrumental tolerances necessary for making measurements at such long wavelengths, and the consequently low cost, size, weight, and general robustness of apparatus needed. When Fourier spectroscopic methods are used, these instrumental advantages are maximized. The chief disadvantages, on the other hand, are the characteristically low signal-to-noise ratios achievable in the far infrared (problems associated with both weak sources and insensitive detection), and the spectroscopic assignment problems caused by the superposition of spectra – the spectra are not, of course, separated as well as they are in the near- and mid-infrared, where vibrational frequencies are often well isolated. It should be noted that the former disadvantage (poor signal-to-noise ratio) is partly overcome by the use of helium-cooled crystal detectors.

Our work over the past five years has shown that submillimeter techniques are capable of producing valuable quantitative measurements, and they are a worthy contender in many areas of atmospheric measurement.

The technical progress which our group has managed to achieve in this period has taken place mainly in two areas: instrumental development and spectroscopic study. In the former case, we have already mentioned the use of cooled detectors; it was this, coupled with the incorporation of phase modulation (Chamberlain, 1971; Harries et al., 1972) into the apparatus that led to rapid improvement in the quality of results obtained. We have previously indicated (Harries et al., 1974; Harries, 1973b) that a large fraction of our effort has had to go into developing our understanding of the spectrum, and this has involved us in laboratory measurements and in calculations of theoretical spectra, line strengths, half-widths and so on. These efforts will be discussed further below.

The techniques we used have been discussed previously (Harries, 1972, 1973a) and so need no further mention here, other than a review of

* Messrs. Harries, Birch, Stone, Swann, and Neill are with the Division of Electrical Science; Messrs. Fleming and Moss are with the Division of Materials Applications.

general features. A Michelson interferometer with phase modulation has been used, together with a liquid-helium-cooled InSb detector (Rollin type). So far nearly all our observations have been from aircraft (Comet 2E, Concordes 002 and 001) but further work on balloons is planned. Earlier work was carried out at a fixed observation zenith angle, but in the last year we have developed a limb-scanning technique which can produce information on vertical distributions, as well as on total amounts of gas. Throughout the work we have observed in emission, as opposed to absorption, for reasons previously stated (Harries, 1972, 1973a).

We are also developing in our program a simple filter radiometer for operation between 9.6 μm and 100 μm, to observe emission from stratospheric O_3, H_2O, and other species. This work is not yet far advanced so no results are yet available. However, the radiometer has had one successful flight, carrying a single ozone channel, and is currently being modified for further flights.

This paper includes a discussion of our laboratory spectroscopy program; a brief discussion of the sky spectrum itself; a review of our measurements of total abundance of H_2O, O_3, HNO_3, and N_2O above 15 km in many areas of the world; a report on our more recent vertical distribution measurements; and a view of future work and some conclusions.

NEW LABORATORY SPECTRA

At the start of this work, the laboratory data on the submillimeter spectra of most of the gases that were of interest were limited mainly to the work of Gebbie and Stone (Stone, 1964) and Hall and Dowling (Dowling, 1967). A program was therefore begun at the NPL to obtain improved spectra, particularly in the longer wavelength region beyond $\lambda = 250$ μm, using a phase-modulated Michelson interferometer and a Rollin detector. Some preliminary spectra have already been presented (Harries, 1973b; Harries et al., 1974), but here we wish to present new spectra of HNO_3, NO_2, and N_2O in this region.

Figure 1 presents a spectrum of a mixture of HNO_3 and NO_2. The results, together with more details on the apparatus used, will be published in due course. For the present, this spectrum is useful for two reasons. First, note that all NO_2 lines are marked by arrows. We observe the relatively very strong Q-branch of NO_2 at about 37.78 cm^{-1}, which we have been using in recent work to obtain a value of the stratospheric column density of NO_2. It is clear why, as a result of its greater strength, a more accurate result is expected from this Q-branch than from the individual pure-rotation lines at lower wavenumbers. Second, the appearance of the HNO_3 band (HNO_3 is an accidentally symmetric top — see Fleming (1974) and Harries et al. (1971)), makes it obvious why the region of the far-infrared spectrum we are using (centered at about 20 cm^{-1} — or $\lambda = 500$ μm) is ideal for observations of HNO_3, and why at higher wavenumbers (Baluteau and Bussoletti, 1973) (for $\tilde{\nu} > 40$ cm^{-1} or so) it is not possible to observe HNO_3, particularly since the HNO_3 band is temperature-shifted to lower wavenumbers at stratospheric temperatures (≈ 220 K).

Figure 2 shows part of a spectrum of (pure) NO_2, again showing the Q-branch at 37.78 cm^{-1} and the other, weaker, pure-rotation lines at lower wavenumbers. NO_2 has a very complicated spectrum, and we are currently comparing our results with a calculated spectrum produced for us by C.B. Farmer and F.W. Taylor at Jet Propulsion Laboratory. Other calculations by G. Duxbury at Bristol University will also be used to this end.

Finally, in Figure 3 we show a spectrum of N_2O, a linear molecule with evenly spaced lines. As with HNO_3, it again is evident that observations above about 40 cm^{-1} (Baluteau and Bussoletti, 1973) will be very unlikely to observe N_2O in the stratosphere. The same is also true of a number of other gases, including NO. Moreover, these problems at higher wavenumbers are exaggerated by the increase in optical depth with increasing wavenumber, due to water vapor, which further adds to the difficulties of observing weak lines of species such as HNO_3 and N_2O.

These and other data have been used to provide accurate line positions, together with information on line strengths and widths. Further observations are continuing with measurements of the important ozone spectrum.

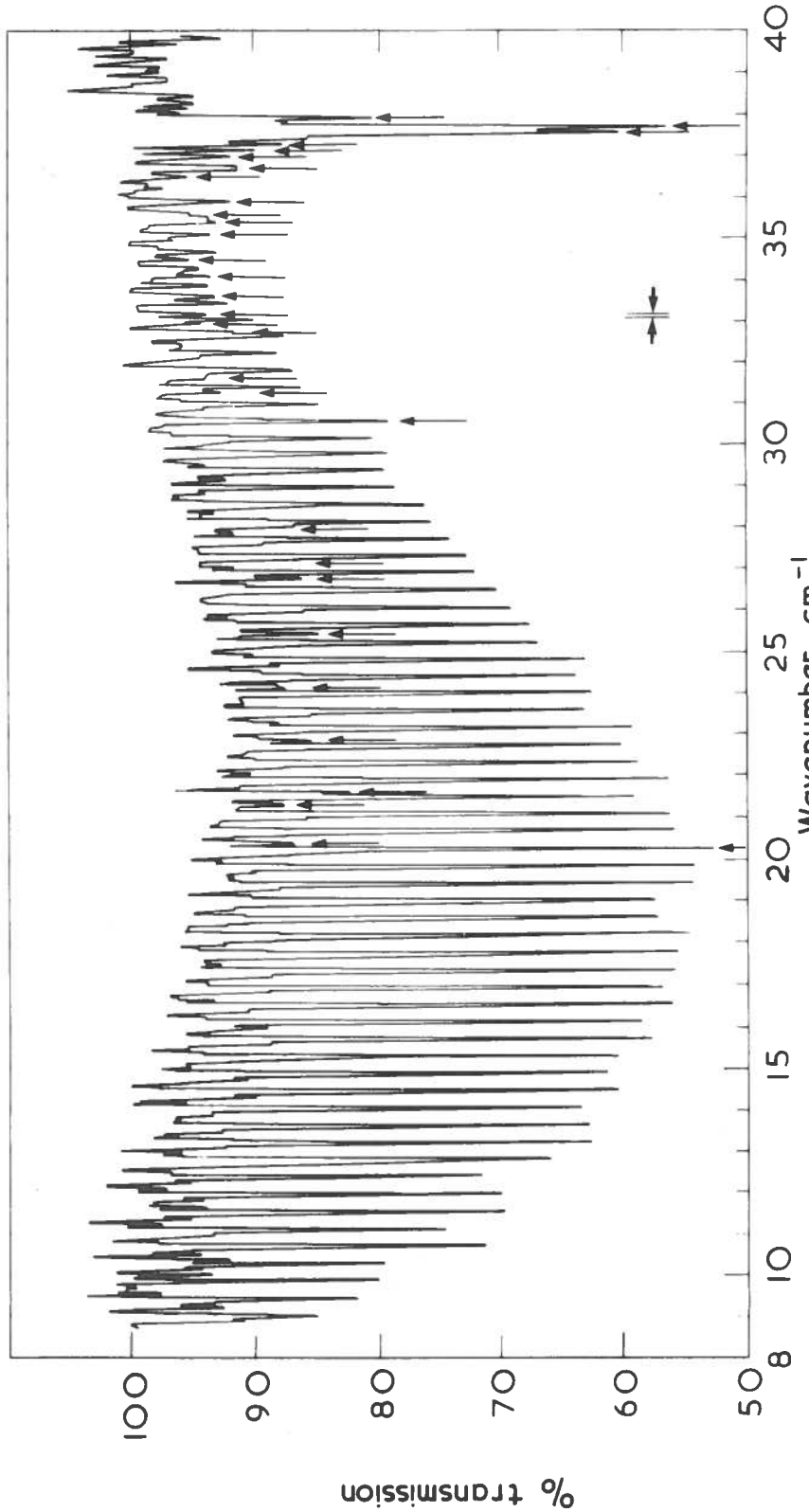

Figure 1. The spectrum of a mixture of NO_2 and HNO_3 at a (nominal) total pressure of 100 torr. The path length was 203 mm and the temperature 300 K. Arrows designate NO_2 lines. See the text for discussion. Resolution is 0.05 cm^{-1}.

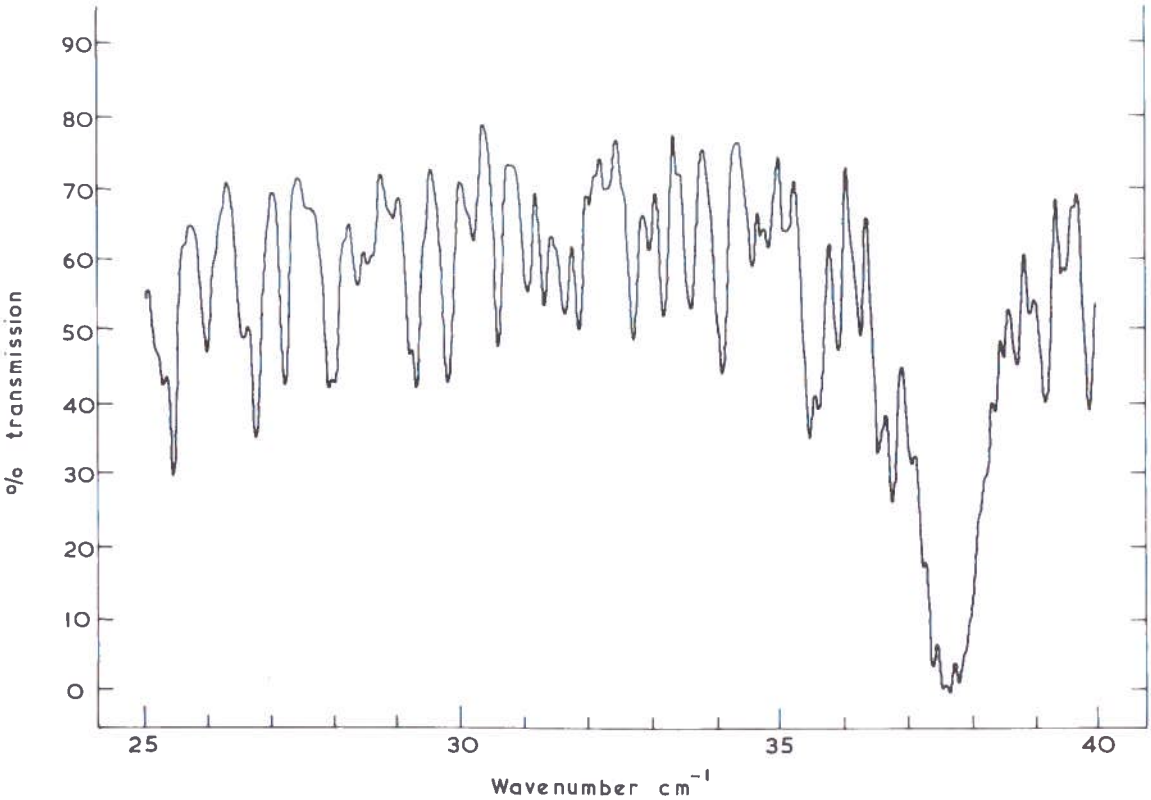

Figure 2. The spectrum of pure NO_2 near the pseudo-Q_2 branch at 37.78 cm^{-1}; pressure 400 torr, path length 903 mm, temperature 300 K. See text for discussion. Resolution is 0.05 cm^{-1}.

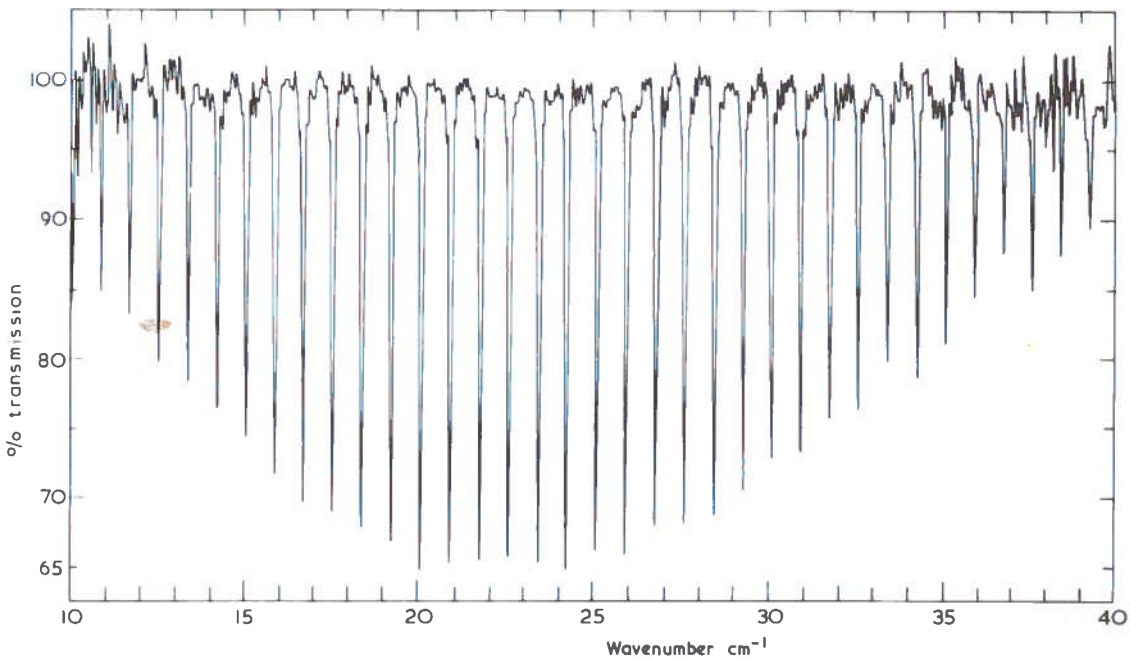

Figure 3. The spectrum of pure N_2O. Pressure 200 torr, path length 203 mm, temperature 300 K. See text for discussion. Resolution is 0.05 cm^{-1}.

THE STRATOSPHERIC EMISSION SPECTRUM

The preceding section leads us naturally to the sky spectrum itself. We have published spectra, taken previously under a variety of conditions, and so we wish to present only two examples of spectra to illustrate different points. First, to emphasize the problem of spectroscopic assignment, let us consider Figure 4, which shows a stratospheric spectrum (top curve) obtained on the Comet 2E at 12 km altitude. The lower curve, given in sections for comparative purposes, shows a spectrum for ozone calculated using the data given in a paper by Gora (1959). As we have mentioned before, it was new work on the ozone spectrum (Harries et al., 1972; Beckman and Harries, 1974) that identified the possibilities of this spectral region, since before that time only the strongest lines seen in Figure 4, due to H_2O, O_2, and O_3 (see Harries et al. (1972) and Harries (1973a)), had been identified.

Once the ozone spectrum had been assigned it only remained to consider the outstanding observed features in terms of emission from other species, such as HNO_3, N_2O, NO_2, NO, SO_2, CO and so on. This is a rather extensive topic, and for details we refer to other publications (Harries, 1972, 1973a) and to papers to appear in the next year or so (e.g., Beckman and Harries (1974)) in which we hope to provide a detailed spectroscopic analysis of the spectrum. For the present we will only give a current list of assignments. These appear in Appendix A in terms of line number, which may be identified in the spectra given in Harries (1973a).

Second, to illustrate results from our limb-scanning observations, we show Figure 5, which (though rather hastily prepared) contains portions of two spectra recorded in October 1973 in the limb-scanning aircraft experiment. The results from these measurements, which were made over the Bay of Biscay area, have still to be analyzed, but the diagram shows the way in which the spectral lines of the various species grow with increase of zenith angle. The top curve is taken at 15 km, at a zenith angle of 84° (elevation angle +6°), and the lower curve at 15 km and a zenith angle of 91° (elevation angle -1°). Other zenith angles between 84° and 93° were also used.

TOTAL ABUNDANCE ABOVE 15 KM: GEOGRAPHICAL DISTRIBUTIONS

In order to discuss our measurements of the total abundance of a number of stratospheric constituents, we present diagrams summarizing all the results so far evaluated, the fruits of some five years of observation from 1969 through 1973. Only measurements of H_2O and O_3 were made until late 1971, at which time the achievable resolution was increased to allow observation of the other species mentioned in the preceding section. Our spectroscopic studies have indicated that HNO_3 and N_2O both have several emission lines free from blending so that quantitative measurements may be obtained. For NO_2, blending presents a far more serious problem. In the case of SO_2, there appears to be only one line strong enough, and sufficiently free of blending, to permit a rather tentative measurement. For other species, such as CO and NO, no measurement is possible, because the weak emission lines of these species are heavily overlaid by those of other gases.

The measurements up to and including those of November 1971 were made on the Comet 2E aircraft. From May 1972 on, observations were made from Concordes 002 and 001.

The total abundance has been obtained as follows (Harries et al., 1974; Harries, 1973d). From radiosonde or satellite data a mean temperature for the lower stratosphere has been adopted. We should note that, since the submillimeter region is in the Rayleigh-Jeans region of the Planckian curve at normal atmospheric temperatures, emission power is directly proportional to absolute temperature. In general, the assumption of a mean temperature was inaccurate to much less than ±10% in the region 10-30 km. For any reasonable vertical distribution of gas, such as constant mixing, or layered as for ozone, the major line-forming region is from the flight level up to about 20-25 km. Typically, variability of temperature in the line-forming region was less than ±5%. This uncertainty therefore carries through linearly to uncertainty in emitted power.

The emission spectra are intensity-calibrated by laboratory sources, and also by the strong oxygen lines that appear in the spectra (see Table 1 in Harries (1972)). Removing the temperature

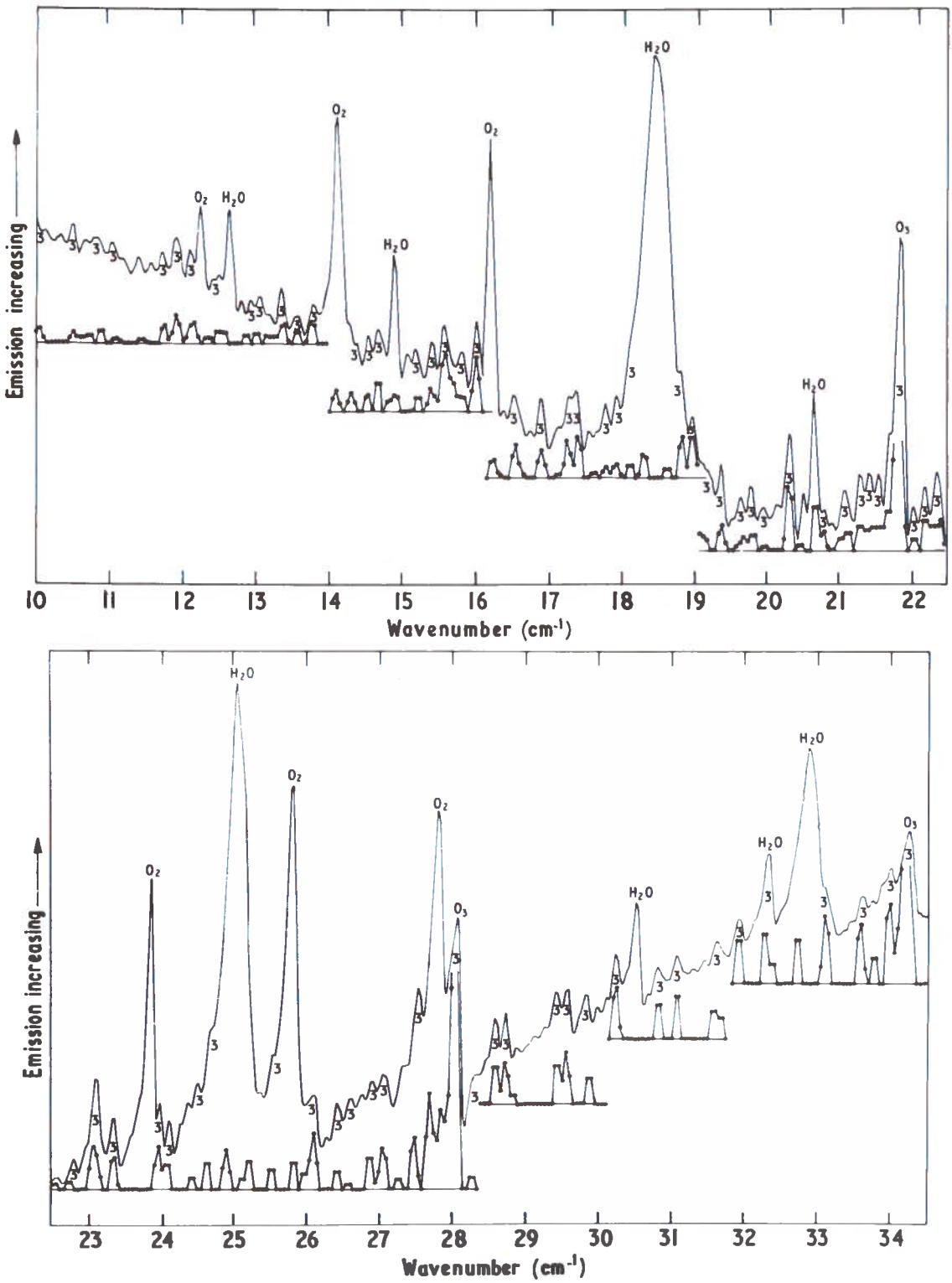

Figure 4. The average of two sky emission spectra (top curve) recorded at 12 km altitude and a zenith angle of 80°. Ozone lines are identified by 3's. Resolution is 0.067 cm^{-1}. The lower curve is a theoretical spectrum, smoothed to the experimental resolution, for ozone emission.

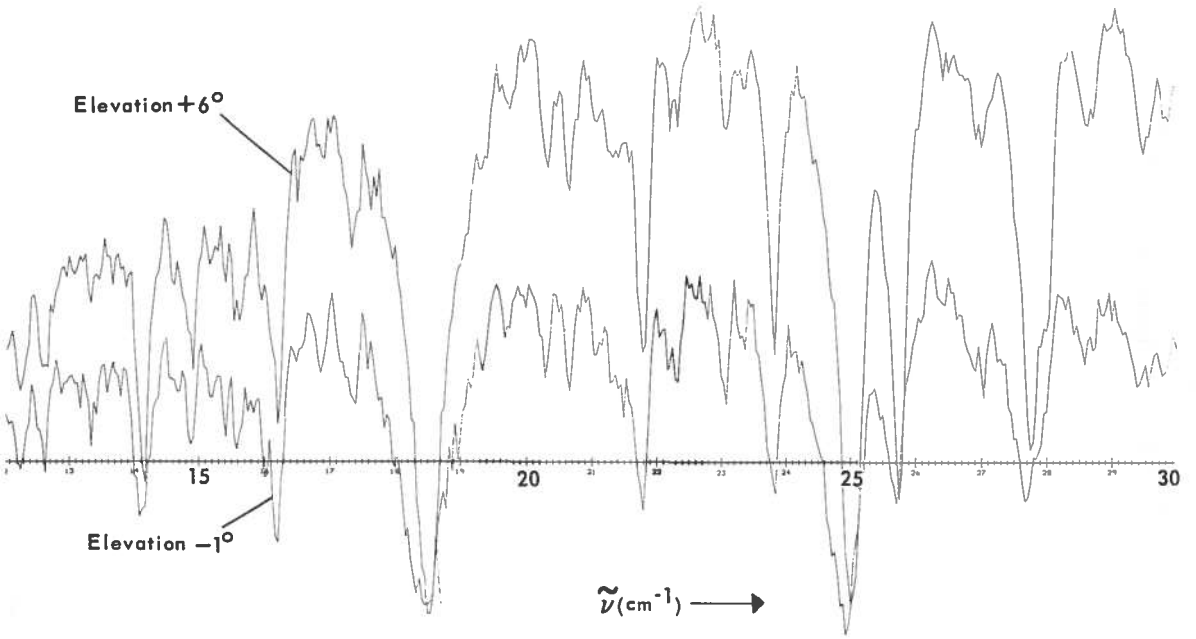

Figure 5. Examples of spectra obtained in the limb-scanning mode of the experiment. The top spectrum was obtained at a zenith angle of 84°, the bottom at 91°. Altitude was 15 km, and spectral resolution is 0.05 cm^{-1}.

dependence as a 'constant' Planck term leaves an integrated area (or equivalent width) for the measured line, which may then be interpreted as being due to a certain total number of molecules. In this way we obtain a column number density (the number of molecules in a vertical column of unit cross-section). We have in the past converted this number to a volume mixing ratio by assuming constant mixing, i.e., by dividing it by the vertical air-column density. In the present section, however, we restrict ourselves to column number density (molecules cm^{-2}) in order to avoid the confusion that some authors feel with such a change of units.

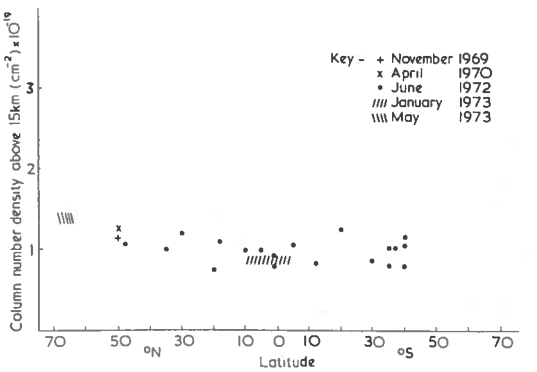

Figure 6. The column number density (molecules cm^{-2}) of ozone above 15 km measured as a function of latitude. The observation periods are labeled in the diagram.

Ozone

Figure 6 gives a summary of our results to date for ozone. It should be borne in mind that many other data exist which have yet to be analyzed (this applies to all species, of course) and so at the end of our program there should be considerably more data available than are shown here.

In the case of the Comet observations (marked + and X) results have been corrected from 12 to 15 km by assuming constant mixing. Though this may be of questionable accuracy, this is the only way to compare these results with those from the Concorde. Since it is mainly H_2O and O_3 which were measured in the Comet flights, it is likely that the greatest error is incurred for O_3, which of course does not have constant mixing in this region of the atmosphere. A brief study shows that we are likely to be underestimating the column density for typical O_3 distributions by less than 20%. This is not

considered too serious for the few Comet data included in Figure 6.

The solid circular points represent measurements made during the tour of Concorde 002 to the Far East and Australia in June 1972. The right-hatched measurements over the equator were made in January 1973 when 002 was returning from South Africa, and the left-hatched area at 65-70°N shows the results of measurements in the Arctic in May 1973 on 002. Other observations, on Concorde 001 in July 1973, and Concorde 002 in October 1973, have yet to be reduced and are not shown.

In general we have found rather good agreement between our values of total ozone and those measured by the meteorological networks, though because of the sparseness of the latter it is usually impossible to obtain data very close to our flight paths. We are endeavoring to obtain data from the Nimbus BUV (backscatter ultraviolet) experiment to assist in our work. The measurements (May 1973) at 65° to 70°N appear to have observed the large spring maximum in ozone; in addition, the vertical profile obtained in the 15-km region (see the next section) indicates rather high mixing ratios, which again accords with what might be expected for conditions during the spring increase (Craig, 1965). On the other hand, it is somewhat surprising that in the June 1972 data a larger increase between the equator and 40°S was not detected, though the few measurements of total ozone we could obtain from the meteorological network for comparison appeared to confirm our measurements. Low equatorial values of ozone were quite definitely obtained in the overflight of January 1973.

Thus, our observations fit in fairly well with the known latitudinal and seasonal variations of total ozone. The lowest column number density in Figure 6 corresponds, in more usual units, to about 0.27 cm atm NTP, and the highest to about 0.42 cm atm NTP.

Water Vapor

Figure 7 gives some of our results for H_2O. A brief inspection of Figure 4 will show that it is impossible to record a spectrum without observing a number of strong H_2O lines from which humidity data may be extracted, and so

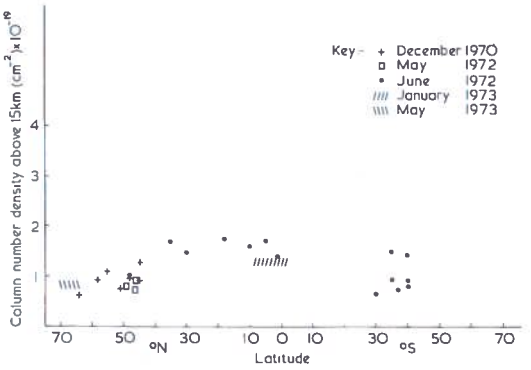

Figure 7. The column number density (molecules cm^{-2}) of water vapor above 15 km measured as a function of latitude. The observation periods are labeled in the diagram.

vast quantities of water data exist on our stored tapes which have yet to be analyzed. A specialized technique for extracting the water concentration, using the oxygen emission lines as a standard, has been described elsewhere (Harries, 1973c; Burroughs and Harries, 1970).

As for ozone, results dated November 1971 and before were obtained on the Comet 2E at 12 km altitude, and again it has been necessary to adjust the column density to a value at 15 km, assuming a constant mixing distribution, in order to compare them with the Concorde results. This is valid, as long as the lower observations (12 km) were within the stratosphere, since the mixing-ratio distribution with height is generally constant, as has been demonstrated by many workers' results (Murgatroyd et al., 1955; Mastenbrook, 1971; Harries, 1973c) and is discussed further on.

In general a dry stratosphere has been observed in our measurements, with volume mixing ratios in the mid-latitude stratosphere of about 3×10^{-6} ($\approx 2 \times 10^{-6}$ by mass).

The apparent rise in column density above 15 km towards the equator observed in Figure 7 is almost entirely caused by the influence of the high equatorial tropopause. Data taken when the tropopause exceeded 15 km have, of course, been excluded, but our observations in the past have shown that the influence of the wet troposphere extends some distance into the base of the stratosphere, even for a well-defined tropopause.

The lowest column number density seen in the figure corresponds to a mixing ratio of about 2.3×10^{-6} by volume. The lowest value we have ever observed, which was at about 51°N in 1971, was 1.6×10^{-6} by volume. (Further information on our water-vapor measurements may be found in Harries (1973c).)

During the measurements in June 1972, mid-latitude mean mixing ratios of about 3×10^{-6} were observed in both the northern and southern hemispheres. It is of interest that the meteorological network quoted equatorial tropopause temperatures of around -83°C, which at a pressure of 100 mb for saturated air corresponds to a volume mixing ratio of about 3.3×10^{-6}, i.e., very near the mid-latitude values we observed. This fact has obvious relevance to the theory that the source of mid-latitude stratospheric water vapor is the air rising through the equatorial tropopause, where water-vapor 'freeze-out' dries the air.

Vertical distribution profiles will be discussed in a subsequent section.

Nitric Acid

Figure 8 presents our results for nitric acid, HNO_3. Apart from the one point for November 1971 (Comet 2E), all data were obtained from the Concorde. In view of the non-constant mixing distribution of HNO_3 observed by other workers and ourselves (Murcray et al., 1973; Lazrus et al., 1972; Harries et al., 1974; Harries and Stone, 1973), the November 1971 point (marked Δ) is not of high reliability, since a linear height correction has been applied to it (as described above).

In general our data illustrate quite a wide variability, but little evidence for any significant latitude variations is observed. The measurement at 70°N is the average of several individual observations, and so is of relatively high reliability; it may be significant that this value is greater than the mean of the equatorial results. The average value of the column number density corresponds to a mixing ratio of about 3×10^{-9} by volume (assumed constant), and a pressure-column density of about 2×10^{-4} cm atm. These figures agree well with determinations by Murcray et al. (1973).

In the May 1973 series of measurements both day- and night-time missions were flown,

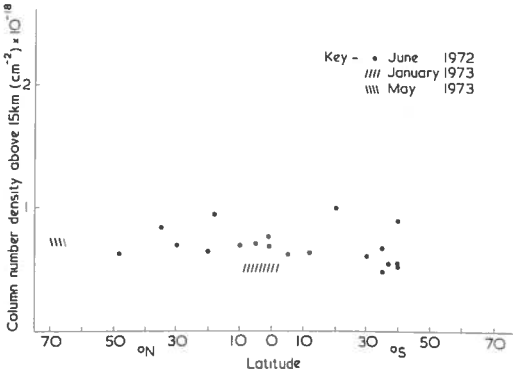

Figure 8. The column number density (molecules cm^{-2}) of nitric acid above 15 km measured as a function of latitude. The observation periods are labeled in the diagram.

but no day/night differences could be detected outside the random error of the measurements, which was about ±30%.

Nitrous Oxide

The results for N_2O are shown in Figure 9, again as column number density against latitude. For N_2O only three sets of data were used, since the other two sets (July and October 1973) have still to be analyzed.

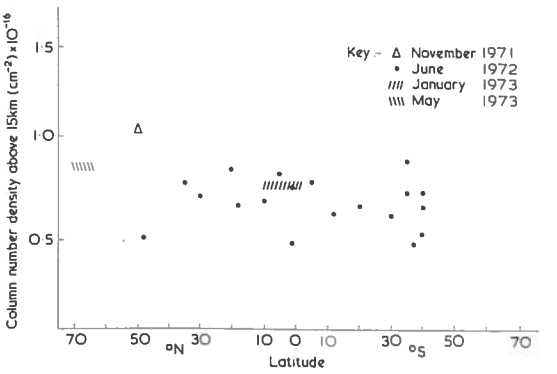

Figure 9. The column number density (molecules cm^{-2}) of nitrous oxide above 15 km measured as a function of latitude. The observation periods are labeled in the diagram.

Overall, we see a high variability of the abundance above 15 km, but no conclusive latitudinal variation. The estimated error for each individual measurement is about ±30%. As we

will see in the section on vertical distributions, there still appears to be quite a wide range of values being reported for N_2O, even though it is a well-studied species (at least in the troposphere). Murcray has obtained information (Goldman et al., 1973) from solar absorption spectra, indicating a variability of a factor of 2 in the concentration in the lower stratosphere (at about 15 km). In our results it is certain that a large part of the variability is due to experimental scatter; however, for example, the cross-hatched data at 70°N and over the equator are averages of several individual measurements, and we may expect the error in each case to be about ±10%. In this case, the difference of about 30-40% may be real, and possibly a manifestation of the large variability observed by Murcray.

VERTICAL DISTRIBUTIONS

In this section we consider data on the vertical distribution of H_2O, O_3, HNO_3, and N_2O in the lower stratosphere, which we obtained in the first of our limb-scanning experiments on board Concorde 002 in May 1973. Further limb-scanning observations in October 1973 are currently being analyzed. This limb-scanning technique has been discussed by Gille (Gille and House, 1971), by Farmer (1974), and by ourselves (Harries et al., 1974; Harries, 1973b). It views the atmosphere at angles below horizontal, to identify layers of the atmosphere for concentration measurements. It is clear, therefore, that the technique will yield, in our case, distribution data only between 15 km and some lower boundary (such as the tropopause). For gases *above* 15 km we must still consider only total abundance, not distribution. The aircraft configuration can, therefore, give valuable information on the important stratosphere-troposphere boundary layer in the 10-16 km region, as we will see.

We have previously given details of how the limb-scanning process works in our case (Harries et al., 1974), so for the present we merely note that interferograms are recorded at observational zenith angles of between 80° and 93°, with the majority taken between 85° and 93°. A layer-by-layer calculation is then carried out, using measured spectral equivalent widths evaluated at the various zenith angles, which correspond with geometrically located layers in the atmosphere. In this way a distribution is constructed, beginning with the first layer below 15 km and continuing down*.

Figure 10 shows how the radiance of a single spectral line is expected to vary with zenith angle around 90°. The curves shown are the results of a radiative-transfer calculation which uses several models of mixing-ratio distribution (Harries et al., 1974).

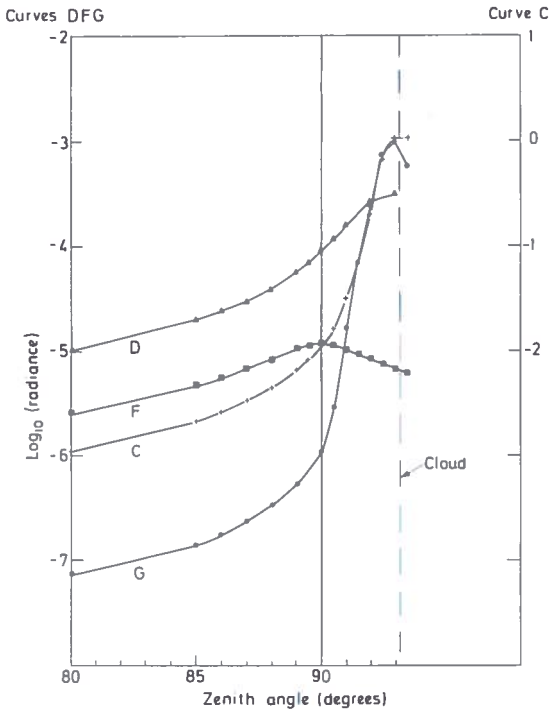

Figure 10. Radiance calculated as a function of zenith angle for several different model atmospheres. Details are given in the text.
Model C is for a strong emitting line of a constant-mixing gas.
Model D is for a weakly emitting line of a layered gas, extending above and below the flight level.
Model F is for a weakly emitting line of a layered gas, residing entirely above the observer.
Model G is for a weakly emitting line of a gas, residing almost entirely below the flight level.

It can be seen that case D is effectively the sum of the two cases F and G. The diagram

* A full description of this process will be published in due course.

illustrates the fact that information on the vertical distribution of gas is contained in such limb-scanning observations. Notice that, in principle, this information refers to both above and below the flight level (angles less than and greater than 90° respectively). However, the strongest dependence of radiance on chosen distribution occurs for layers below the flight level; for angles less than 90°, the curves are very similar in shape, and in the presence of experimental noise would be difficult to distinguish from one another.

We have seen in a previous work (Harries et al., 1974) how this information appears in practice, so it will not be repeated here.

Figure 11 is based on the first of our limb-scanning experiments, carried out in May 1973. This diagram shows the results for H_2O, O_3, HNO_3, and N_2O, as well as more tentative ones for SO_2 and NO_2, averaged for two flights made on May 16 and 16/17 (night) 1973.

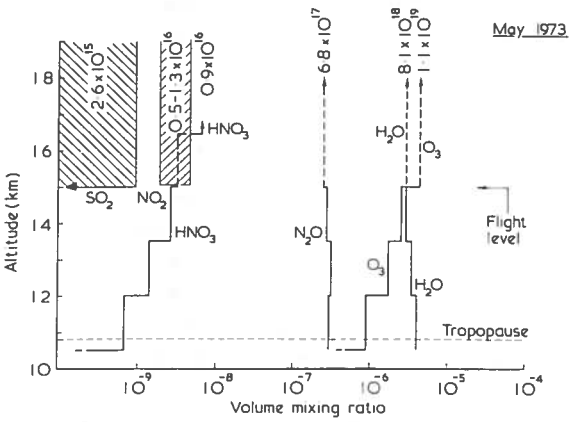

Figure 11. The vertical distributions of H_2O, O_3, N_2O, and HNO_3, measured in the limb-scanning experiment on Concorde 002, May 1973, from 15 km altitude. Below 15 km, concentrations are quoted explicitly in volume units; above 15 km, total column number densities (cm^{-2}) are quoted at the top of each curve. The curve above 15 km represents the constant volume mixing ratio equivalent to the quoted column density. At the top left the range of column densities observed for NO_2 is given, and an upper limit to the amount of SO_2.

For the reasons just mentioned we may justifiably deduce a mixing-ratio distribution profile only below the observation altitude (15 km); above this level we have quoted, as before, only the total column number density. These are the figures shown at the top of each curve, in units of molecules cm^{-2}. The values range from 10^{19} molecules cm^{-2} to less than 10^{15} molecules cm^{-2}. This range of column density is obtained from a single spectrum, demonstrating the power and dynamic range of radiative methods such as ours.

The shaded areas at the far left are for NO_2 and SO_2. In the case of NO_2 we have used the Q-branch at 37.78 cm^{-1} mentioned in the section on laboratory spectra; unfortunately, this does not yield any information below the horizon, because nearby strong H_2O lines become so intense that the NO_2 Q-branch is obscured. Thus, information on only the column density has been obtained. The box shown represents the range of values of column number density observed, which are 0.5 to 1.3×10^{16} cm^{-2} converted to an effective average volume mixing ratio (see above). Some limited evidence is available of a variation between day and night, but more evidence is necessary before a conclusion can be reached. In the case of SO_2 there is still uncertainty in our assignments, and, moreover, in the value of integrated line strength which should be used. The box shown therefore indicates that we can place an *upper limit* on the amount of SO_2 above 15 km of 2.6×10^{15} cm^{-2}, corresponding to an effective average volume mixing ratio of 1×10^{-9}. This is *not* an absolute measurement, but an upper limit; the true value could be much lower than this.

Below the 15-km level, we give mixing-ratio profiles for H_2O, O_3, HNO_3, and N_2O. The results are given as the average mixing ratio in 1.5-km-thick layers. The layer size will be reduced in future work, but was limited by the number of zenith-angle observations which were obtained.

For water vapor, the mixing ratio drops from a value of about $4 - 5 \times 10^{-6}$ at the tropopause to about 3×10^{-6} at 15 km, and appears to stay near this value above 15 km. We have previously obtained a large amount of information in this region of the stratosphere on the humidity distribution, and have invariably found similar behavior (cf. Figure 2 of Harries (1973a)).

The ozone profile yields a total amount in good agreement with the limited meteorological

network data that were available (Harries et al., 1974; Harries, 1973b) and indicates fairly high mixing ratios in the 11-15 km layer, as might be expected for polar spring maximum conditions (Craig, 1965). (This was discussed briefly in the preceding section.) We are currently analyzing similar data taken in October 1973, and hope to compare the spring and autumn profiles.

The N_2O profile is basically a constant mixing result, with some indication of a fall-off above 15 km. The average mixing ratio in the lower stratosphere is, however, approximately 300×10^{-9}, somewhat higher than the accepted value of 250×10^{-9}. The N_2O results have been replotted in Figure 12 on a linear scale of mixing ratio, and a number of other workers' results are shown for comparison. The stepped curve is the present result. The solid curve is due to Murcray and co-workers (Goldman et al., 1973), the dot-dash curve is due to Junge and co-workers (Schütz et al., 1970), the dotted curve is a past result by Murcray (Goldman et al., 1970), and the broken curve is a previous result of our own

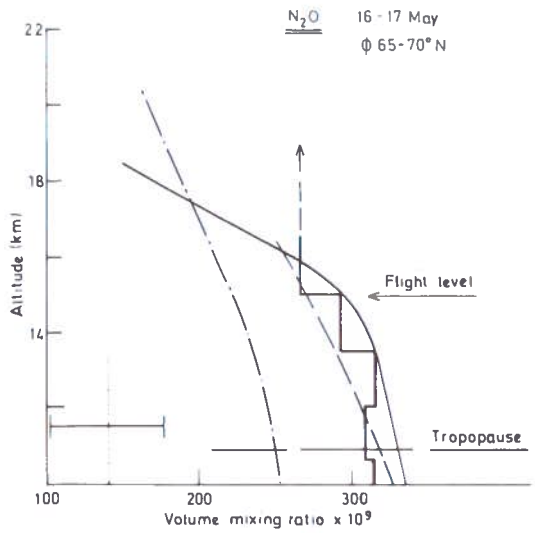

Figure 12. Results of the inversion procedure for N_2O. The stepped curve shows the present results; the broken curve gives our previous results (Harries, 1972); the solid curve, some recent results by Murcray and co-workers (Goldman et al., 1973); the dot-dash curve, results by Schütz et al. (1970); and the dotted curve some earlier results by Murcray and co-workers (Goldman et al., 1970).

(Harries, 1972). Farmer and Toth (1974) report results similar to Murcray's and our own.

Thus there still appears to be a good deal of uncertainty about the N_2O profile in the lower stratosphere, and it is a currently open question whether the observed variabilities are due to real atmospheric variations or to instrumental effects. It was not possible in the present work to obtain any information about N_2O above about 17-18 km, because the lower layers, which contain a higher mixing ratio, dominate the observed radiance. The published data (see Figure 12 for some examples) do seem to reflect as much variability above 17 km, however, as in the lower layers.

Finally, in Figure 13 we consider the mixing-ratio profile obtained for HNO_3. The mixing ratios seem significantly higher than those given in published data by Murcray (Murcray et al., 1973; Williams et al., 1972), which were for the same levels but taken at lower latitudes. However, Murcray does report higher concentrations in results he has obtained over Alaska at latitudes similar to our own (Murcray et al., 1974), and the observations may reflect an effect based on tropopause height and seasonal variations, similar to that observed for O_3.

Figure 13 shows the HNO_3 data replotted on a linear mixing-ratio scale* and compared with other results. The broken curve is a result by Murcray's group in mid-latitudes (Murcray et al., 1973), the squares represent the extreme values of a "double-layer" observed by the same group (Williams et al., 1972), and the two areas enclosed by polygons circumscribe the range of values obtained, again in mid-latitudes, by Lazrus and his co-workers (1972).

As mentioned above, we are currently analyzing data for October 1973, and we hope to compare spring and autumn results for HNO_3 in this way.

The picture emerging for HNO_3 appears to be reasonably consistent among the various groups of workers, though at the moment unexplained variations in the total amount do occur, ranging over about a factor of 2. The

* The column density above 15 km has been arbitrarily contained below 25 km in order to depict the general shape of the layer indicated by our unit-scanning observations. See Figure 11 for the corresponding column density.

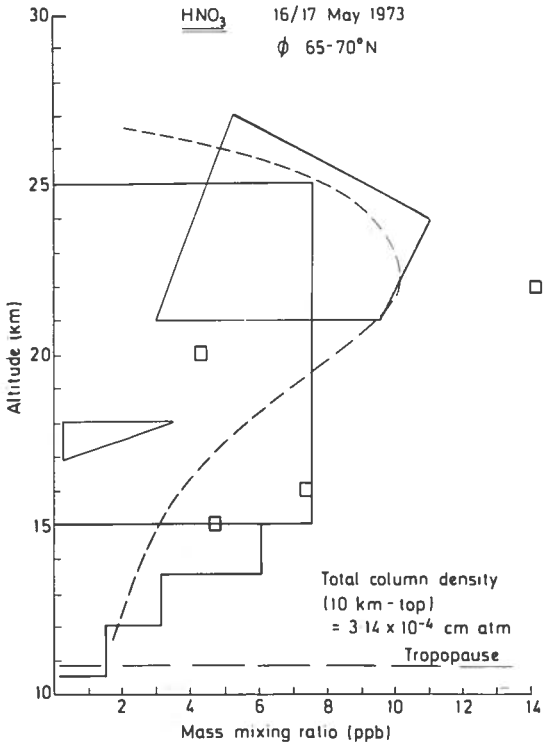

Figure 13. The results for HNO_3 compared with previous measurements. The broken curve is by Murcray et al. (1973), as are the square points (Williams et al., 1972); the light triangle and quadrangle enclose points measured by Lazrus et al. (1972).

mean pressure column density appears from Murcray's work, and our own, to be about 2.5×10^{-4} cm atm.

CONCLUSION AND PLANS FOR FUTURE WORK

Though much analysis of our data remains to be done, and other experiments are planned, we may regard this paper as a first summary of the results we have obtained on stratospheric composition in our program of research supported by COMESA, the Committee on the Meterological Effects of Stratospheric Aircraft.

There are three divisions into which our results fall. There are (a) new laboratory spectroscopic measurements, (b) geographical studies of column-density variability, and (c) studies of vertical distribution in the lower stratosphere. Details of our new laboratory spectra will be published in the near future. Our geographical observations indicate known seasonal and latitudinal variations for ozone and water vapor, and give mean levels of HNO_3 and N_2O across the globe, but show no evidence of marked latitudinal or seasonal variations in the latter two species. The vertical distribution data agree well with other results, and again for H_2O and O_3 they fit well, within accepted variations as a function of height above tropopause. Many other data have still to be added to the results, particularly from flights carried out in July and October of 1973.

Some subsections of our research program not mentioned in this paper will soon be producing new results. These are the study of theoretically generated spectra being carried out at Bristol University, the radiative-transfer calculations being performed in our group at the NPL, and the calculations of the H_2O and O_3 emission spectra at various levels in the stratosphere under way at Queen Mary College.

Our future experimental programs include flights of the lightweight mid-infrared radiometer mentioned in the introduction, flights of our high-resolution submillimeter interferometer in limb-scanning mode on a high-altitude balloon, and further geographical studies of composition in the lower stratosphere on board a Canberra aircraft, in collaboration with the Meteorological Office.

APPENDIX A

PARTIAL ASSIGNMENT LIST

Observed Lines		Assignment		Observed Lines		Assignment	
Line Number	Position (cm^{-1})	Position (cm^{-1})	Species	Line Number	Position (cm^{-1})	Position (cm^{-1})	Species
1	9.182	8.969	HNO_3	54	17.978	17.988	O_3
		9.107	O_3	56	18.516	18.573	H_2O
2	9.402	9.388	HNO_3	58	19.013	19.044	O_3
3	9.551	9.545	O_3	59	19.150	19.103	O_3
4	9.679	9.638	O_3			19.130	O_3
6	10.017	10.067	O_3	61	19.434	19.416	O_3
		10.113	O_3			19.458	O_3
7	10.181	10.217	HNO_3	62	19.566	19.566	SO_2
9	10.534	10.537	O_3	67	20.334	20.357	O_3
		10.552	O_3	68	20.528	20.503	O_3
10	10.650	10.651	HNO_3	69	20.680	20.710	H_2O
11	10.831	10.85	H_2O	70	20.811	20.868	O_3
12	11.064	11.061	HNO_3	71	20.944	20.941	N_2O
13	11.223	11.187	O_3	72	21.094	21.161	O_3
14	11.426	11.481	HNO_3	73	21.309	21.309	O_3
15	11.674	11.733	N_2O	74	21.431	21.425	O_3
16	11.767	11.752	O_3	77	21.875	Q Branch	O_3
17	11.931	11.929	O_3	79	22.191	22.202	O_3
18	12.125	12.156	O_3	80	22.341	22.340	O_3
19	12.279	12.292	O_2	83	22.900	22.890	NO_2
20 (a)	12.431	12.375	O_3	84	23.084	23.091	O_3
20 (b)	12.519	12.514	O_3	86	23.341	23.378	O_3
21	12.664	12.684	H_2O	89	23.857	23.863	O_2
22	12.817	12.917	O_3	90	23.969	23.956	O_3
		12.919	O_3	91	24.113	24.129	O_3
23	13.088	13.095	O_3	92	24.262	24.180	NO_2
25	13.381	13.345	O_3	93	24.375	24.406	HNO_3
26	13.404	13.422	O_3	94	24.500	24.496	O_3
27	13.578	13.572	HNO_3	95	24.686	24.696	O_3
28	13.806	13.817	O_3	96	25.013	25.082	H_2O
29	14.100	13.990	HNO_3	98	25.539	25.566	O_3
30	14.137	14.168	O_2	99	25.763	25.819	O_2
31	14.290	14.303	O_3	100 (b)	26.094	26.102	O_3
32	14.403	14.405	HNO_3	102	26.434	26.453	O_3
33	14.563	14.592	O_3	105	26.900	26.942	O_3
34	14.703	14.721	O_3	106	27.091	27.033	O_3
35	14.922	14.943	H_2O	108	27.531	27.546	O_3
36	15.094	15.081	N_2O	109	27.778	27.831	O_2
37	15.213	15.258	O_3	110	28.056	28.070	O_3
38	15.425	15.451	O_3	112	28.581	28.621	O_3
39	15.600	15.609	O_3	113	28.725	28.728	O_3
		15.624	O_3	117	29.381	29.457	O_3
40	15.660	15.657	HNO_3	118	29.569	29.562	O_3
42	16.030	16.035	O_3			29.588	O_3
43	16.228	16.253	O_2	119	29.720	29.624	O_3
44	16.400	16.493	HNO_3	120	29.831	29.920	O_3
45	16.547	16.552	O_3	123	30.262	30.298	O_3
		16.579	O_3			30.303	O_3
47	16.903	16.934	O_3	125	30.538	30.558	H_2O
48	17.178	17.259	O_3	127	30.852	30.859	O_3
49	17.316	17.348	O_3			30.899	O_3
50	17.400	17.454	O_3	128	31.071	31.127	O_3
51	17.593	17.593	N_2O	130	31.424	31.464	HNO_3
53	17.828	17.819	O_3	131	31.657	31.648	O_3
						31.707	O_3

Observed Lines		Assignment	
Line Number	Position (cm^{-1})	Position (cm^{-1})	Species
132	31.905	31.973	O_3
134	32.333	32.366	H_2O
136	32.886	32.951	H_2O
137	33.105	33.103	O_3
		33.170	O_3
140	33.629	33.646	O_3
141	33.738	33.824	O_3
143	34.009	34.011	O_3
144	34.238	Q Branch	O_3

N.B.: Where a line is clearly and reproducibly observed, but as a shoulder to a stronger line (e.g., line 29), the wavenumber is given to only two decimal places.

REFERENCES

Baluteau, J.P. and E. Bussoletti (1973), "High resolution spectra of the atmosphere between 30 and 200 cm^{-1}," Nature Phys. Sci. **241**, 113-114.

Beckman, J.E. and J.E. Harries (1974), "Submillimetre-wave atmospheric and astrophysical spectroscopy," to be published in Appl. Opt. in October.

Burroughs, W.J. and J.E. Harries (1970), "Direct method of measuring stratospheric water vapour mixing ratio," Nature **227**, 824-825.

Chamberlain, J. (1971), "Phase modulation in far infra-red (submillimetre wave) interferometers, I. Mathematical formulation," Infrared Phys. **11**, 25-55.

Craig, R.A. (1965), *The Upper Atmosphere*, Academic Press, New York.

Dowling, J.M. (1967), "Investigations in the Far Infrared with a Lamellar Grating Interferometer," Air Force Report No. SSD-TR-67-30, Space and Missile Systems Organization, Los Angeles Air Force Station, California.

Farmer, C.B. (1973), "Infrared measurements of stratospheric composition," Can. J. Chem. **52**, 1544-1559.

Farmer, C.B. and R.A. Toth (1974), private communication.

Fleming, J.W. (1974), to be published in Chem. Phys. Lett.

Gille, J.C. and F.B. House (1971), "On the inversion of limb radiance measurements, I: Temperature and thickness," J. Atmos. Sci. **28**, 1427-1442.

Goldman, A., D.G. Murcray, F.H. Murcray, W.J. Williams, T.G. Kyle, and J.N. Brooks (1970), "Abundance of N_2O in the atmosphere between 4.5 and 13.5 km," J.O.S.A. **60**, 1466-1468.

Goldman, A., D.G. Murcray, F.H. Murcray, and W.J. Williams (1973), "Balloon-borne infrared measurements of the vertical distribution of N_2O in the atmosphere," J.O.S.A. **63**, 843-846.

Gora, E.K. (1959), "The rotational spectrum of ozone," J. Mol. Spec. **3**, 78-99.

Harries, J.E. (1972), "Measurements of Hydrogen-Oxygen-Nitrogen Compounds in the Stratosphere from Concorde 002. Part 1," National Physical Laboratories Report No. DES 16.

Harries, J.E. (1973a), "Measurements of some hydrogen-oxygen-nitrogen compounds in the stratosphere from Concorde 002," Nature **241**, 515-519.

Harries, J.E. (1973b), "Measurements of Some Hydrogen-Oxygen-Nitrogen Compounds in the Stratosphere from Concorde 002. Part 2," National Physical Laboratories Report No. DES 21 (April).

Harries, J.E. (1973c), "Measurements of stratospheric water vapour using far infrared techniques," J. Atmos. Sci. **30**, 1691-1698.

Harries, J.E. (1973d), "Measurements of Some Hydrogen-Oxygen-Nitrogen Compounds in the Stratosphere from Concorde 002. Part 3," National Physical Laboratories Report No. DES 24 (December).

Harries, J.E., W.J. Burroughs, and G. Duxbury (1971), "Pure rotation spectrum of HNO_3 vapour," Nature **232**, 171-173.

Harries, J.E., N.R.W. Swann, J.E. Beckman, and P.A.R. Ade (1972), "High resolution observations of the submillimetre stratospheric emission spectrum," Nature **236**, 159-161.

Harries, J.E. and N.W.B. Stone (1973), "Measurements of some hydrogen-oxygen-nitrogen compounds in the stratosphere from Concorde 002," in *Proceedings of the Second Conference on the Climatic Impact Assessment Program* (November 1972), ed. A.J. Broderick, U.S. Department of Transportation, DOT-TSC-OST-73-4, 78-85.

Harries, J.E., N.W.B. Stone, J.R. Birch, D.G. Moss, N.R.W. Swann, and G.F. Neill (1974), "Submillimetre wave observations of stratospheric composition," in *Proceedings of the First International Symposium of IAMAP and IAPSO*, (Melbourne), 275-291.

Lazrus, A.L., B. Gandrud, and R.D. Cadle, "Nitric acid in the stratosphere," J. Appl. Met. **11**, 389-392.

Mastenbrook, H.J. (1971), "The variability of stratospheric water vapour," J. Atmos. Sci. 28, 1495-1501.

Murcray, D.G., A. Goldman, F.H. Murcray, W.J. Williams, J.N. Brooks, and D.B. Barker (1973), "Vertical distribution of minor atmospheric constituents as derived from air-borne measurements of atmospheric emission and absorption infrared spectra," in *Proceedings of the Second Conference on the Climatic Impact Assessment Program*, (November 1972), ed. A.J. Broderick, U.S. Department of Transportation, DOT-TSC-OST-73-4, 86-98.

Murcray, D.G., A. Goldman, W.J. Williams, F.H. Murcray, J.N. Brooks, R.N. Stocker, and D.E. Snider (1974), "Stratospheric mixing ratio profiles of several trace gases as determined from balloon-borne infrared spectrometers," in *Proceedings of the First International Symposium of IAMAP and IAPSO*, (Melbourne), 292-303.

Murgatroyd, R.J., P. Goldsmith, and W.E.A. Hollings (1955), "Some recent measurements of humidity from an aircraft up to heights of about 50,000 feet over southern England," Q.J. Roy. Met. Soc. 81, 533-537.

Shutz, K., C. Junge, R. Beck, and S. Albrecht (1970), "Studies of atmospheric N_2O," J. Geophys. Res. 75, 2230-2246.

Stone, N.W.B. (1964), "Spectroscopy of Some Gases in the Far Infrared Using a Michelson Interferometer," Ph.D. thesis, University of London.

Williams, W.J., J.W. Brooks, D.G. Murcray, F.H. Murcray, P.M. Fried, and J.A. Weinman, "Distribution of nitric acid vapor in the stratosphere as determined from infrared atmospheric emission data," J. Atmos. Sci. 29, 1375-1379.

DISCUSSION

RAO: Could you further explain your lack of NO results?

N. STONE: NO is one of the gases we cannot hope to observe in submillimeter stratospheric emission spectra; we can only give a very high upper limit. This is because the dipole is weak, and the emission intensity hence very low, and in addition the lines are heavily masked. Dr. Schiff's work clearly indicates concentrations of about one ppb, which is at least an order of magnitude less than we could detect.

(UNIDENTIFIED): Do you have any information on the vertical profile of SO_2?

N. STONE: No; all we could do was put an upper limit on its concentration above 15 kilometers, which is 2.6 times 10^{15} per square centimeter column number density.

(UNIDENTIFIED): You showed some spectra taken around 90 degrees. At those angles, did you have any problems with thermal emissions from the troposphere at your flight altitudes?

N. STONE: No, I think that all the altitudes from which we derived profile data were such that we were looking above the troposphere, and had no thermal-emission problems. You can't get useful data at lower angles anyway.

IN-SITU NO AND O_3 MEASUREMENTS IN THE LOWER STRATOSPHERE FROM A U-2 AIRCRAFT

M. LOEWENSTEIN, J.P. PADDOCK, I.G. POPPOFF, AND H.F. SAVAGE
NASA Ames Research Center
Moffett Field, California

ABSTRACT: Simultaneous in-situ measurements of nitric oxide and ozone in the lower stratosphere have been made from the U-2 high-altitude research aircraft based at the NASA Ames Research Center. Nitric oxide was measured with a chemiluminescence analyzer, and ozone was measured by means of optical absorption.

Data are presented for 18- and 21-km flight altitudes. The three sets of measurements reported were carried out in December 1973 and January 1974 along meridian 122° West between 38° and 48° North latitude. All data were gathered within ± 2 hours of local noon. The observed NO concentrations at 21 km for the three flights reported here ranged from $0.5 \pm 0.3 \times 10^8$ to $3.0 \pm 0.8 \times 10^8$ molec cm^{-3}.

INTRODUCTION

Airborne nitric oxide and ozone detectors have been carried on aircraft flights over the west coast of the United States to obtain in-situ measurements of nitric oxide and ozone at altitudes up to 21 km. Results from three flights are presented here. The flights were made on December 6, 1973 from 1100 to 1430 local standard time (1900 - 2230 UT); December 18, 1973 from 1030 to 1430 local standard time (1830 - 2230 UT); and January 22, 1974 from 1000 to 1330 local standard time (1800 - 2130 UT). The experimental platform was a U-2 aircraft employed in the NASA Earth Resources Aircraft Project at Ames Research Center, Moffett Field, California.

EXPERIMENTAL

The nitric oxide instrument is a chemiluminescence detector based on the light-emitting reaction of nitric oxide with excess ozone in a flow reactor. Light from the NO/O_3 reaction is detected by a cooled EMI 9659 photomultiplier tube. A Corning 2-62 filter which transmits wavelengths >600 nm is placed between the reactor and the photomultiplier tube. Signals from the photomultiplier are processed in the photon-counting mode by an amplifier, a discriminator, and a linear count-rate circuit having a time constant of one second. Two different flow rates from an on-board NO/N_2 calibrator of known mixing ratio provide periodic instrument calibrations. The instrument zero is periodically determined by mixing the excess ozone with the atmospheric sample upstream of the reactor. An automatic cycle timer sequences the instrument through the measure, calibrate, and zero-level modes for three minutes each.

The atmospheric mixing ratio of the nitric oxide, X_{NO}, is calculated from

$$X_{NO} = \frac{S_{atm}}{S_{cal}} \times \frac{F_{cal}}{F_{atm}} \times X_{cal}$$

where S represents the measured photon count rate from the atmospheric or calibrator nitric oxide, F is the atmospheric or calibrator gas flow, and X_{cal} is the mixing ratio of the on-board nitric oxide calibrator. The nitric oxide detector sensitivity for the measurements reported here is 0.025 parts in 10^9 by volume.

Ozone-concentration measurements were based on the absorption of the 253.7-nm Hg line in the Hartley continuum. The unattenuated mercury-lamp intensity at 253.7 nm is determined by routing the atmospheric sample flow over a catalytic reactor which removes 100% of the ozone present. The instrument operates on a 10-second cycle, 5 seconds each for the absorbed and the unattenuated beam measurements. Beer's law is applied to extract the ozone partial pressure, using an optical absorption coefficient of 306 cm^{-1} atm^{-1}; the absorption tube is 71 cm

long. Pressure and temperature corrections are applied to the instrument readout to derive the partial pressure of atmospheric ozone. The instrument is a commercial unit that was especially adapted for use in the U-2 experiment system. Its rated sensitivity is 3 nbar partial pressure of ozone.

A ram inlet port one inch in diameter brings the sample air flow into the aircraft. Flexible stainless-steel lines connect the instrumentation manifold to the inlet and outlet ports. Typical in-flight air-flow rates are 30 STP liters per minute to the nitric oxide detector and 0.3 STP lpm to the ozone detector. Motorized valves in the manifold isolate the instruments from the atmosphere and from each other up to 12 km altitude, at which point the valves are opened by the pilot and measurements commence. Thereafter the system operation is fully automatic. The environment in the experiment bay of the aircraft during data gathering is maintained at approximately 45°F and 4 psia. The aircraft's true air speed is 400 knots at the flight altitudes employed in these experiments.

Data from the ozone and nitric oxide instruments are recorded on magnetic tape once per second, and the outputs of various pressure, temperature, and flow sensors are recorded every 10 seconds. Graphic displays of the raw nitric oxide and ozone data are prepared from the magnetic tape. The data is analyzed from the graphic outputs.

RESULTS

Figure 1 shows results obtained on flights of December 6 and December 18, 1973 and January 22, 1974, at longitude 122°W and latitudes as indicated in the figure. Ozone data are plotted as partial pressures in nanobars, and nitric oxide data as the number of molecules per cm^3.

Loss of nitric oxide in the inlet flow lines has been measured and is less than 5%. No corrections have been made to the nitric oxide data for this loss. Loss of ozone in the inlet lines has been measured to be 25%, and the ozone data have been corrected by this amount. The estimated uncertainty in the ozone data is ±15%. Error limits for the nitric oxide number densities are derived from the statistical errors, as well as from estimated uncertainties in sample and calibrator flow rates, and the calibrator mixing ratio.

Our measurements of nitric oxide concentrations are in good agreement with another chemiluminescence measurement made in the same altitude range (Ridley et al., 1974). However, our measured concentrations are lower, by a factor between three and ten, than recently reported optical measurements (Ackerman et al., 1973; Toth et al., 1973).

ACKNOWLEDGMENTS

This work is part of a continuing NASA program of stratospheric research and was partially supported by the Climatic Impact Assessment Program of the U.S. Department of Transportation.

REFERENCES

Ackerman, M., D. Frimout, C. Muller, D. Nevejans, J.-C. Fontanella, A. Girard, and N. Louisnard (1973), "Stratospheric nitric oxide from infrared spectra," Nature **245**, 205.

Ridley, B.A., H.I. Schiff, A.W. Shaw, L.R. Megill, L. Bates, C. Howlett, H. LeVaux, and T.E. Ashenfelter (1974), "Measurement of nitric oxide in the stratosphere between 17.4 and 22.9 km," Planet. Space Sci. **22**, 19.

Toth, R.A., C.B. Farmer, R.A. Schindler, O.F. Raper, and P.W. Schaper (1973), "Detection of nitric oxide in the lower atmosphere," Nature **244**, 7.

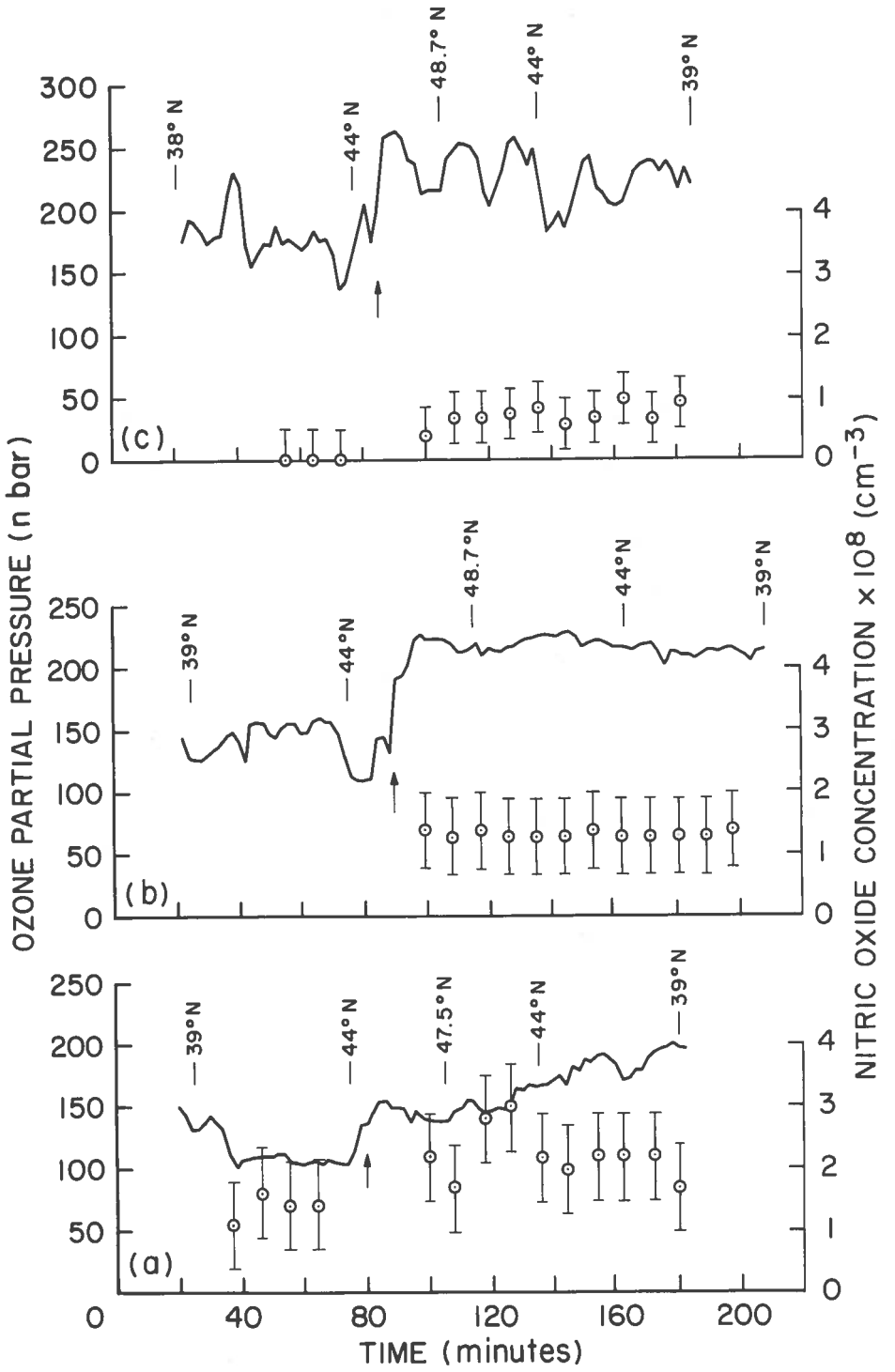

Figure 1. O_3 and NO data from flights of a) Dec. 6, 1973, b) Dec. 18, 1973 and c) Jan. 22, 1974. The solid line is the ozone data; the circled points are the nitric oxide data. Time is measured from time zero at aircraft takeoff. Data to the left of the vertical arrow are for 18 km altitude, and those to the right are for 21 km altitude.

ADDITIONAL MEASUREMENTS OF NO

H.I. SCHIFF AND B.A. RIDLEY
Centre for Research in Experimental Space Science
York University
Downsview, Ontario, Canada

We would like to report some preliminary NO measurements near the tropopause. They were obtained during a test flight of our chemiluminescence instrument modified for the NASA global atmospheric sampling program (GASP). The instrument was flown on board the NASA Convair 990 on four separate flights: one from San Francisco to Honolulu, two from Honolulu northward for 900 miles, and one from Honolulu to San Francisco. These flights were made over the period Jan. 31 to Feb. 4, 1974. Some 600 minutes of measurement were recorded, including 266 minutes at 40-41 kft, 281 minutes at 33-35 kft, and 57 minutes at 29 kft.

The NO mixing ratio was found to vary with location and altitude, and from day to day. Table 1 shows the fraction of the observation time at each altitude during which the mixing ratio was found to lie within the indicated range.

The following indications were obtained: (1) In general, the mixing ratios are low. (2) For the same location and day, the mixing ratios at 33-35 kft are higher than those at 29 or 40-41 kft. (3) For the same altitude and day there is considerable patchiness; mixing ratios at different locations can vary by a factor of 6 or more. (4) There also appears to be variability from day to day at the same location and altitude. In connection with (4), it may or may not be significant that the maximum values at 35 kft during the San Francisco-to-Honolulu flight on Jan. 31 and the maximum values at 41 kft during the return trip on Feb. 4 occurred at the same location, viz. between 135-140°W 37°N. No attempt has yet been made to correlate the results with location of commercial flight corridors, ozone concentrations, or meteorological parameters.

We must again emphasize the preliminary nature of these results, and point out that we have not had the opportunity to test the sampling system provided on the Convair 990.

Table 1. Eastern Pacific Tropopause NO Measurements

Altitude (kft)	NO Mixing Ratio (ppbv)	% of Time at Altitude
40-41	⩽ 0.05	65
	0.05-0.10	30
	0.10-0.20	5
33-35	⩽ 0.05	15
	0.05-0.10	50
	0.10-0.20	25
	0.20-0.30	10
29	⩽ 0.05	50
	0.05-0.10	50

VERTICAL DISTRIBUTION OF NO, NO_2, AND HNO_3 AS DERIVED FROM STRATOSPHERIC ABSORPTION INFRARED SPECTRA

JEAN-CLAUDE FONTANELLA, ANDRE GIRARD, LOUIS GRAMONT, AND NICOLE LOUISNARD
Office National d'Etudes et de Recherches Aérospatiales
Châtillon, France

ABSTRACT: This paper presents the results of NO, NO_2, and HNO_3 measurements made in June and July 1973 from Concorde 001. The flight altitude was about 16 km.

The results for NO are, within experimental error, in agreement with results of a previous spectrometric balloon-borne experiment conducted jointly by IASB and ONERA (14 May 1973). Nitric oxide is concentrated in stratospheric layers above the flight altitude. The integrated amount of NO along the optical path is $4 \pm 1.5 \times 10^{16}$ molec cm^{-2} for a solar elevation varying from $+2^{\circ}$ above the horizontal plane to -1°. A value of 6×10^{8} molec cm^{-3} may be derived as an upper limit for the local concentration at the flight altitude. There is no significant difference between the integrated amounts observed at sunset and at sunrise.

The measured value of NO_2 local concentration at 15.5 km is $1.1 \pm 0.2 \times 10^{9}$ molec cm^{-3} under sunset conditions. This value does not vary significantly between 15 km and 30 km.

The measured value of HNO_3 local concentration at 15.5 km is $1 \pm 0.3 \times 10^{10}$ molec cm^{-3}, increasing with altitude between 15 and 20 km. The local concentration is maximum at 20 km, where the measured value is $2 \pm 1 \times 10^{10}$ molec cm^{-3}; it seems to decrease rapidly above 20 km.

INTRODUCTION

A year ago, experimental data for NO_2 and HNO_3 were far too few, considering the major importance of these species in the photochemical processes within the stratosphere; as for NO, the total lack of stratospheric measurements left the field wide open for predictions of its effect on the ozone layer.

Considerable progress has recently been made, in large part thanks to the efforts developed in the USA, the United Kingdom, and France by CIAP, COMESA, and COVOS, respectively. The purpose of this paper is to present the contributions of ONERA on this topic and to compare them with recent data provided by several authors.

Our experimental method is based on infrared absorption spectrometry, using the sun as a source at sunset or sunrise. The value of this method has been brilliantly demonstrated by more than a decade of balloon observations reported by Murcray and his group from the University of Denver. The principle of this method and the quantitative accuracy of the interpretation of observational data have been discussed by Murcray et al. (1972) and, more recently, by Farmer (1973). Previous experimental attempts to detect NO traces in the stratosphere demonstrated an upper limit on the order of 1 ppb for NO concentration. In this concentration range, two conditions have to be fulfilled for detection by spectrometric means:

- The instrument has to be placed inside the stratosphere, both to avoid the troposphere (which is a diffusing and absorbing layer) and to have available the long optical path provided by tangential crossing of the stratospheric layers.
- Low noise ($S/N > 100$) and high resolution (much smaller than 1 cm^{-1}) are simultaneously required, but are difficult to obtain with a conventional grating spectrometer. The importance of using the highest possible resolving power will be emphasized later along with more details about NO detection.

Generally speaking, Fourier-transform spectrometry is the most powerful method available. However, for measuring trace constituents, only one or a few absorption lines for each species

have to be recorded, so the multiplex advantage of Fourier spectroscopy is not of fundamental importance; more reliable and more flexible instruments than a long-path difference interferometer can be used. In principle, the grille spectrometer (Girard, 1963) allows scanning of any narrow spectral region with a high luminosity (or "throughput"). The selection of appropriate spectral intervals, including strong and reasonably well isolated lines of the species under study, must be supported by theoretical work and high-resolution laboratory spectra. A parallel effort in both the latter fields is required for present-day stratospheric studies.

Balloon-borne and high-altitude airborne experiments sponsored by the French Committee on the Consequences of Stratospheric Flight (COVOS) have been performed by our group in the last few months. Both instruments, essentially a grille spectrometer associated with a sun tracker, have been described in previous papers (Girard et al., 1973a; Ackerman et al., 1973c). The main characteristics of the spectrometer are:

focal length: 60 cm
resolution: 0.1 cm^{-1}
grille area: 15 X 15 mm
equivalent slit width: 0.1 mm
ruled area of the grating: 64 X 64 mm
scanning rate: 0.15 cm^{-1} per second.

A vertical profile of NO (Figure 1) has been derived from the spectra obtained during a balloon-borne experiment (14 May 1973) conducted jointly by the Institut d'Aéronomie Spatiale de Belgique (IASB) and ONERA (Ackerman et al., 1973b).

This paper is devoted to some more recent results, obtained during experiments performed in June and July 1973 on board Concorde 001.

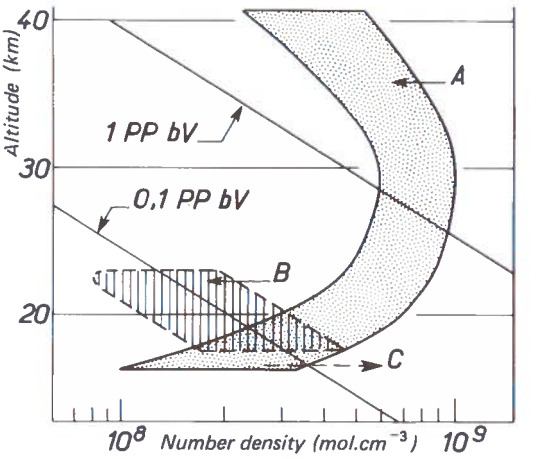

Figure 1. Number density of nitric oxide versus altitude. A. Profile deduced from previous spectrometric balloon-borne experiment (M. Ackerman et al., 1973b). B. Measured values from Ridley et al. (1973). C. Upper limit deduced from this work.

OBSERVATIONAL DATA

Observations were made during nine specific flights made on Concorde 001 during June and July 1973 at sunset (7 flights) and sunrise (2 flights). Usable spectra were obtained during all these flights. The experimental conditions for each flight are given in Table 1. (One unsuccessful sunrise experiment is not included.) Typical trajectories are represented in Figure 2; all

Table 1. Concorde Experiments

Flight No.	Date	Spectral range (cm^{-1})	Solar Elevation (°) Start	End	Species Identified*
1	June 6th	1908 - 1918	+2.50	-0.50	NO
2	July 9th	1603 - 1615	+2.50	-0.50	NO_2
3	– 11th	1323 - 1336	+3	-0	HNO_3
4	– 13th†	1885 - 1918	-1.50	+1.20	NO
5	– 17th	1603 - 1609	+7	+3	NO_2
6	– 18th	1323 - 1336	+6.50	+3	HNO_3
7	– 20th	1364 - 1330	+3	-0.50	HNO_3 ϕ
8	– 23rd	1770 - 1610	+3.50	0	NO_2

* H_2O, CO_2, CH_4, O_3, and N_2O lines are also recognizable on several spectra.

† Sunrise flight (all others sunset).

ϕ On Flight 7, SO_2 was also sought; on Flight 8, HCHO was also sought.

measurements were made between 46° and 51°N latitude. More than twenty minutes of useful data was obtained for each flight.

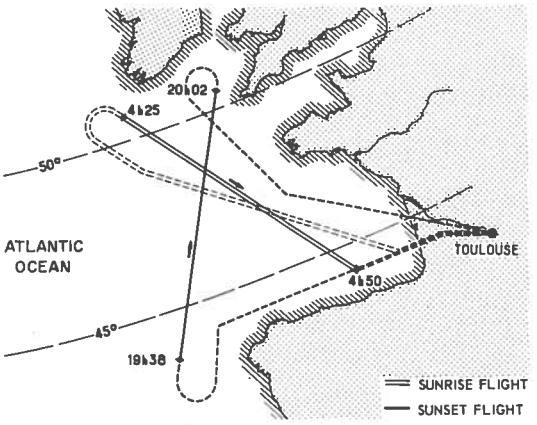

Figure 2. Concorde 001 environmental flights. Typical trajectories, June-July 1973.

Wavelength calibration was performed by interpolation from well-known H_2O, CO_2, and CH_4 absorption lines; the compilation edited by McClatchey et al. (1973) was of considerable help.

The observational data presented below are limited to NO, NO_2, and HNO_3. Besides these species, many other lines have been identified: H_2O, CO_2, CH_4, N_2O, and O_3 ($\nu_2 + \nu_3$ band near 1728 cm^{-1}, during flight No. 8, Table 1). Many lines have not yet been identified.

The change in solar elevation angle during each flight was never more than 3.5 degrees. Synthesis of a vertical concentration profile requires measurement at a wide range of solar-elevation angles. It was thus necessary to use data obtained on different days to develop the vertical profiles presented here; daily variations have been neglected. This appears to be reasonable, since good agreement was obtained for data taken at the same solar elevation on different days.

Nitric Oxide

Since they were performed one month after a successful balloon-borne spectrometric experiment devoted to NO measurement (conducted by IASB and ONERA), the airborne experiments were devoted to determination of the profiles of NO_2 and HNO_3. The main purpose of the Concorde-borne NO experiments was to compare the total NO-column values at sunset and sunrise conditions.

The laboratory spectrum of NO presented in Figure 3 was obtained with the same spectrometer used for the Concorde experiments. The spectral regions employed during flights No. 1 (6 June at sunset), No. 4 (13 July at sunrise), and during the previous balloon-borne experiment are indicated.

The choice of the spectral region employed during the balloon-borne experiment, which appeared to be quite suitable, was reinforced by a preliminary airborne experiment (5 April), made on a Caravelle.

The detection of NO in these experiments is incontrovertible: in every spectrum, appropriate

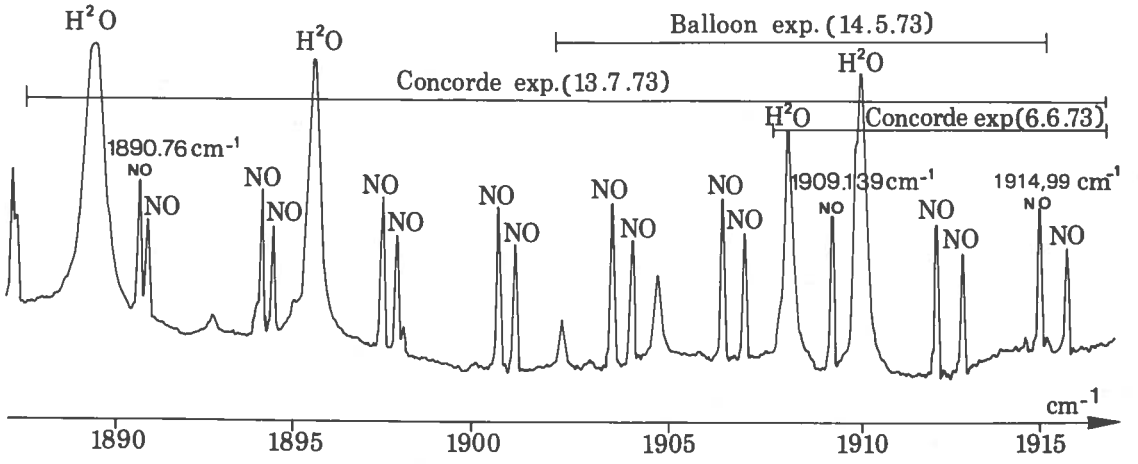

Figure 3. Laboratory spectrum of nitric oxide between 1890 and 1915 cm^{-1}

signals are observed at each expected location of an NO absorption line. But not all of the more than 250 lines are of equal significance; many are more or less contaminated, by absorption lines of other species (H_2O, CO_2, N_2O) and by solar-CO hot bands. In many cases, the contaminant is predominant. Only three lines were actually used for numerical analysis, as indicated in Figure 3: 1914.99, 1909.14, and 1890.76 cm^{-1}.

The spectra obtained near 1890.76 cm^{-1} are shown in Figure 4. The nearest line in the McClatchey compilation is the H_2O line at 1890.74 cm^{-1}, but its low strength makes its contribution negligible. Another NO line (1890.91 cm^{-1}) is also visible, and the separation of the doublet may be used as a resolution test. (Since this line may be contaminated by the N_2O line at 1890.88 cm^{-1} it was not used for analysis.) The NO doublet is bracketed by CO_2 lines (P56, 1890.33 cm^{-1}, and P54, 1891.78 cm^{-1}). The strong H_2O line is often observed from the ground.

The spectra obtained near the line at 1909.14 cm^{-1} are presented in Figure 5. A strong solar-CO line can be seen near 1908.5 cm^{-1}, and there is a very weak CO_2 line at 1909.21 which overlaps with NO. It has been carefully verified that the growth of the observed equivalent width of the CO_2 line at 1909.21 cm^{-1} is greater than that of isolated CO_2 lines. (See, for instance, the P56 CO_2 line (1890.33) in Figure 4. The evolution of the strong CO_2 lines P32 (1908.14) and P30 (1909.51) may also be observed in Figure 5.) Furthermore, synthetic spectra have been derived for this region; results are presented at the end of this paper, and a more complete discussion of this point will follow.

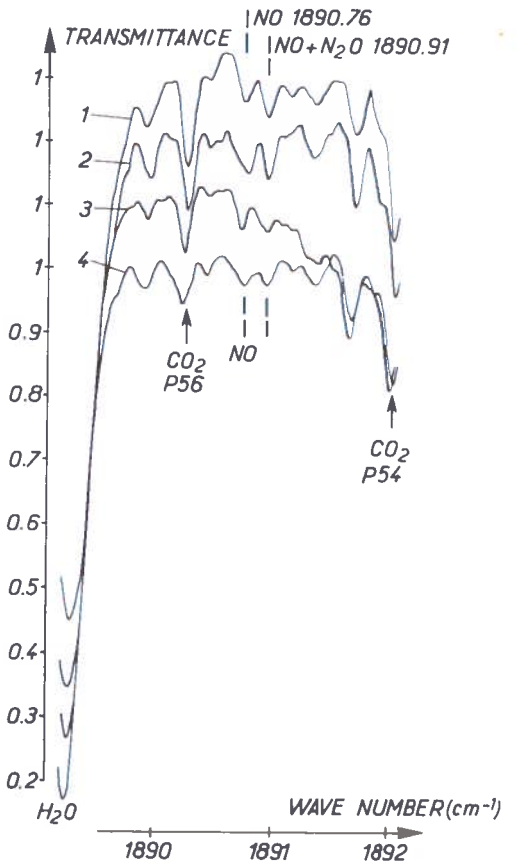

Figure 4. Solar spectra recorded from Concorde 001 near 1890 cm^{-1}. Angular solar elevations are indicated in Table 2. The nitric oxide doublet at 1890.76 and 1890.91 cm^{-1} is identified.

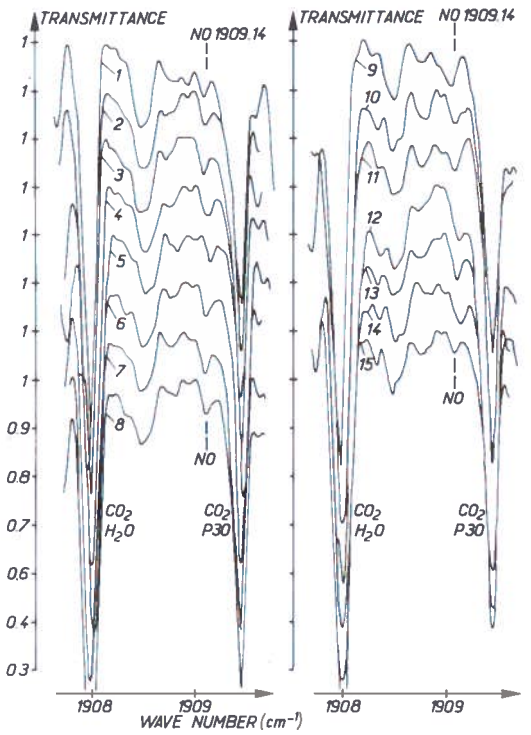

Figure 5. Solar spectra recorded from Concorde 001 near 1909 cm^{-1}. Solar-angle elevations are shown in Table 2. The nitric oxide line at 1909.14 cm^{-1} is identified.

The spectra obtained around 1914.99 cm^{-1} are presented in Figure 6. Judging from the

McClatchey compilation, there should be no risk of contamination of this NO line by any other telluric species.

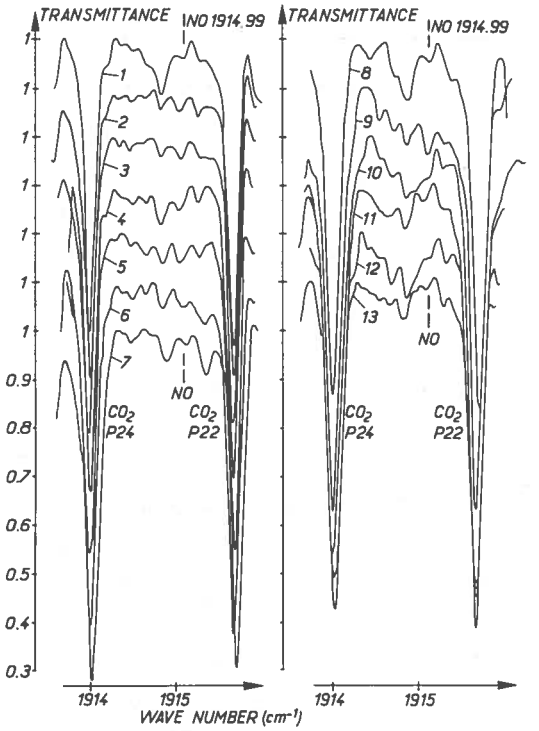

Figure 6. Spectra recorded from Concorde 001 near 1915 cm^{-1}. Angular solar elevations are indicated in Table 2. The nitric oxide line at 1914.99 cm^{-1} is identified.

Values of the solar elevation angles corresponding to spectra presented in Figures 4, 5, and 6 are given in Table 2.

Table 2. Values of Solar Elevation Angles for NO Spectra in Figures 4, 5, and 6

Spectrum number		Flight number* (Table 1)	Solar Elevation Angle (°)
Fig. 4:	1	4	-0.60
	2	4	-0.25
	3	4	0.92
	4	4	1.30
Fig. 5:	1	1	2.40
	2	1	1.90
	3	1	1.80
	4	1	1.40
	5	1	1.25
	6	1	0.75
	7	1	0.65
	8	1	0.10
	9	1	0
	10	1	-0.52
	11	1	-0.60
	12	4	-1.36
	13	4	-1.00
	14	4	0
	15	4	0.46
Fig. 6:	1	1	2.33
	2	1	1.75
	3	1	1.50
	4	1	1.10
	5	1	0.84
	6	1	0.50
	7	1	0.25
	8	1	-0.10
	9	1	-0.33
	10	4	-1.25
	11	4	-1.10
	12	4	0.10
	13	4	0.30

* No. 1 was performed at sunset, No. 4 at sunrise. Flight altitude, 15.5 km.

Nitrogen Dioxide

Figure 7 shows a typical spectrum of the 1610 cm^{-1} region, containing the ν_3 band of NO_2 in a narrow atmospheric window inside the very strong H_2O band. NO_2 lines have been identified according to the recent data of Dana and Fontanella (1973). Theoretical relative intensities (Ackerman et al., 1973c) are shown in the upper part of Figure 7. Typical spectra obtained at various solar elevations between 1604 and 1606 cm^{-1} are shown in Figure 8. The two lines used for analysis (1604.15 and 1606.14) are indicated in the Figure. Values of the solar elevation angles corresponding to the spectra presented in Figure 8 are given in Table 3.

Nitric Acid

Due to the lack of theoretical data, identification and analysis of HNO_3 lines are based on experimental work. The lines have been identified according to a set of spectra obtained at various solar elevations near 1326 cm^{-1} as presented in Figures 9a and 9b. As in the case of NO_2, identification of HNO_3 is not very difficult. Values of solar elevation angles corresponding to the spectra presented in Figure 9 are given in Table 4.

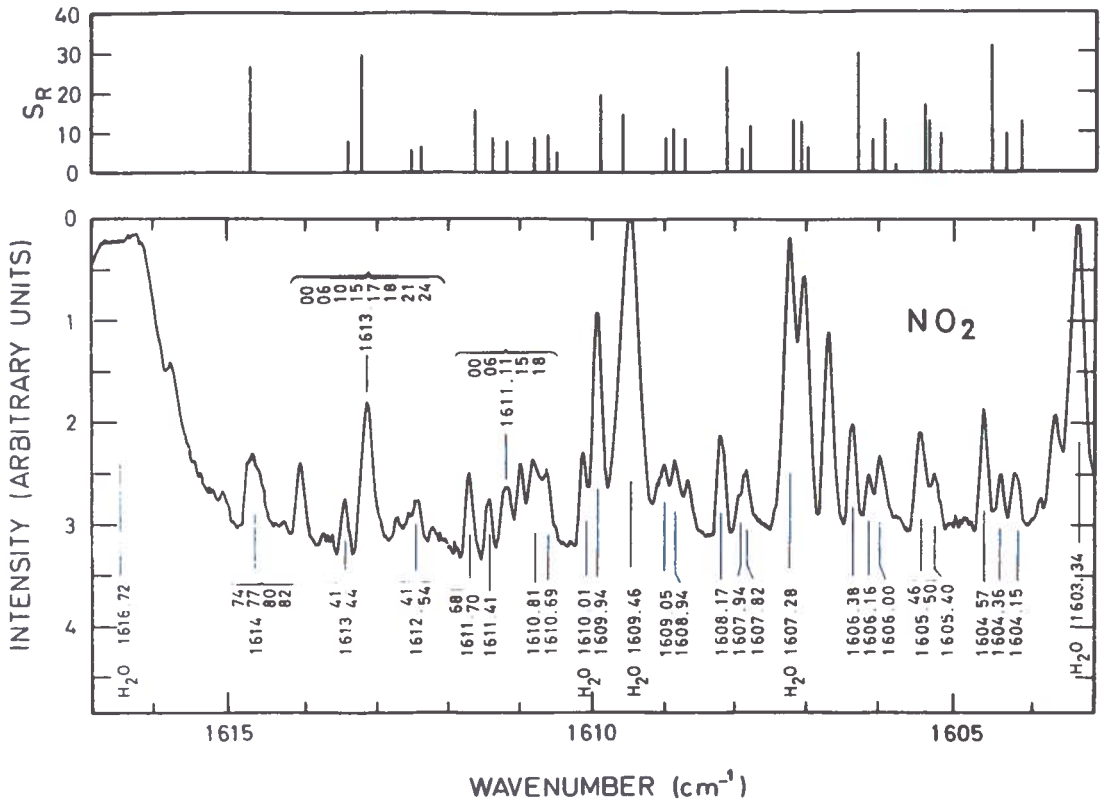

Figure 7. Solar spectrum recorded from Concorde 001 between 1603 and 1617 cm^{-1}. Solar angle is +1°. Telluric water-vapor and nitrogen dioxide lines are indicated. The computed relative intensities for NO_2 (Ackerman and Muller, 1972) are shown at the top.

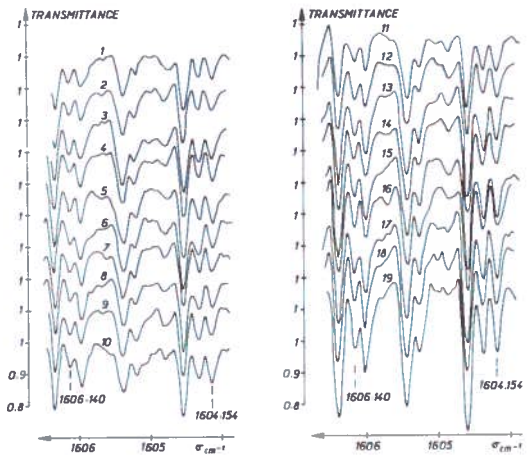

Figure 8. Solar spectra recorded from Concorde 001 near 1605 cm^{-1}. Solar angles are indicated in Table 3. The nitrogen dioxide lines at 1604.154 and 1606.140 cm^{-1} are identified.

Table 3. Values of Solar Elevation for Spectra of Nitrogen Dioxide (Figure 8). Flight altitude: 16 km.

Spectrum number	Flight number (Table 1)	Solar Elevation Angle (°)
1	5	6.20
2	5	5.85
3	5	5.50
4	5	5.15
5	5	4.70
6	5	4.40
7	5	4.00
8	5	3.70
9	5	3.40
10	5	3.10
11	2	2.50
12	2	2.30
13	2	1.60
14	2	1.40
15	2	0.75
16	2	0.60
17	2	0.05
18	2	-0.05
19	2	-0.50

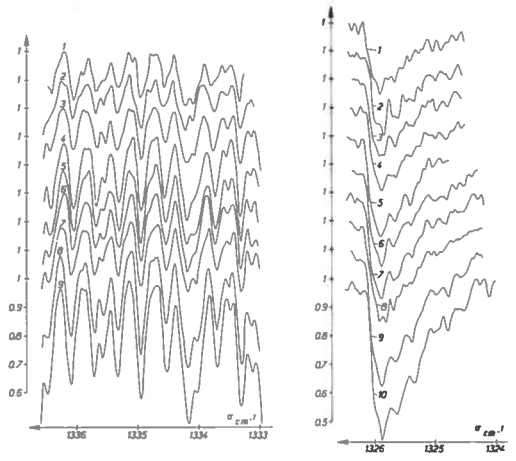

Figure 9. Solar spectra recorded from Concorde 001 near 1330 cm^{-1}. Solar angles are indicated in Table 4. Many absorption lines (at left) and a Q branch (at right) can be identified.

Table 4. Values of the Solar Elevation Angle for Spectra of Nitric Acid (Figure 9). Flight altitude: 16 km.

Spectrum number	Experiment number (Table 1)	Solar elevation (degrees) Figure 9a	Solar elevation (degrees) Figure 9b
1	6	5.90	6.10
2	6	5.80	5.63
3	6	4.95	5.10
4	6	4.80	4.67
5	6	4.10	4.25
6	6	3.90	3.80
7	6	3.30	3.47
8	7	2.85	3.03
9	7	1.15	0.95
10	7	0.65	0.85

NUMERICAL ANALYSIS

Summary of Theoretical Elements

Beer-Lambert Law

In accordance with previous discussions (e.g., Farmer (1973)), diffusion by and emission of the stratosphere may be neglected in the considered wavelength range.

The Beer-Lambert law can be expressed as

$$dL(\sigma) = -k(\sigma, T, P)\, L(\sigma)\, n\, dl \qquad (1)$$

where L = intensity at frequency σ, k = extinction coefficient, n = molecular number density, dl = atmospheric path, and T and P = temperature and pressure respectively.

Line Intensity and Line Shape

For a single line the extinction coefficient k can be shown to be

$$k(\sigma, T, P) = S(T)\, f(\sigma, T, P). \qquad (2)$$

The line intensity S is a function of T,

$$S(T) = S_0 \left(\frac{T}{T_0}\right)^{\gamma} \exp -\frac{E}{k_B}\left(\frac{1}{T} - \frac{1}{T_0}\right), \qquad (3)$$

where T_0 = reference temperature, S_0 = line intensity at T_0, E = energy of the lower state, γ = numerical coefficient equal to 1 for linear molecules, and k_B = Boltzmann constant.

The line shape is dependent on the local temperature and pressure conditions. In the lower stratosphere, the collision-broadened shape is predominant,

$$f_L(\sigma, T, P) = \frac{1}{\pi} \frac{\alpha_L}{(\sigma - \sigma_0)^2 + \alpha_L^2}, \qquad (4)$$

where σ_0 is the line-center frequency. The line half-width α_L is pressure- and temperature-dependent,

$$\alpha_L = \alpha_L{}^0 \left(\frac{P}{P_0}\right)\left(\frac{T_0}{T}\right)^{1/2},$$

where $\alpha_L{}^0$ is the line half-width under standard conditions. At higher altitudes, the line shape is determined by the velocity distribution

$$f_D(\sigma, T) = \frac{1}{\alpha_D \sqrt{\pi}} \exp -\left(\frac{\sigma - \sigma_0}{\alpha_D}\right)^2 \qquad (5)$$

where the Doppler half-width is given by

$$\alpha_D = \frac{\sigma_0}{c}\left(\frac{2 k_B T}{m}\right)^{1/2} = 3.58 \times 10^{-7} \sigma_0 \left(\frac{T}{M}\right)^{1/2}$$

and c = light velocity, M = molecular mass (g), and m = mass per molecule. Finally, the actual line shape (Voigt profile) is described by a convolution of the Doppler- and Lorentz-broadened shapes,

$$f_V = f_D \otimes f_L \,. \tag{6}$$

Transmission Function

For a given value σ of the frequency, several lines of several species may interact. The total extinction coefficient is obtained by adding values of the interacting lines, and from Eq. (1) and (2) we may derive

$$dL(\sigma) = -L(\sigma) \sum_j n_j \sum_i S_{ij} f_{ij}\, dl \,, \tag{7}$$

where S_{ij} and f_{ij} are the intensity and the shape of the ith line for the jth species and n_j is the local number density of the jth species.

The general expression for the transmission coefficient is given by integration of expression (7) along the atmospheric path,

$$T(\sigma) = \frac{L}{L_0} = \exp - \int_{l_1}^{l_2} \sum_j n_j \sum_i S_{ij} f_{ij}\, dl \,, \tag{8}$$

where n, S, and f are variable with path length. In practice, this computation is approximated by dividing the atmosphere into layers of given temperature and pressure. If l_p is the atmospheric path inside the layer p Eq. (8) is given by

$$T(\sigma) = \exp - \sum_p l_p \sum_j n_{jp} \sum_i S_{ijp} f_{ijp} \,. \tag{9}$$

l_p is given by geometrical considerations (including earth curvature) for given values of the flight altitude and solar elevation angle (Figure 10). Over the altitude range considered (above 13 km) refractive effects of the atmosphere may be neglected.

Finally, the *observed* transmission $T_0(\sigma)$ is given by a convolution of the infinite-resolution transmission spectrum $T(\sigma)$ (given by Eq. (9)), and the point-spread function $A(\sigma)$ of the spectrometer (instrument function):

$$T_0(\sigma) = T(\sigma) \otimes A(\sigma). \tag{10}$$

Synthetic spectra were computed on the basis of Eq. (1) to (10) (see "Results").

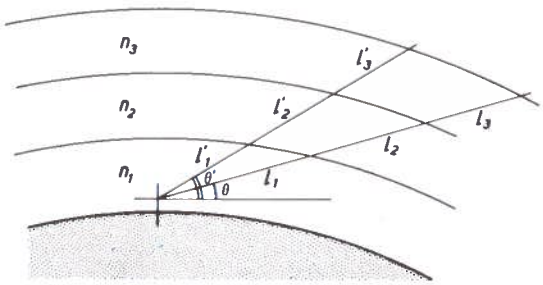

Figure 10. Notation for the layers in the stratosphere. l_i is the geometrical path inside the ith layer; n_i is the number density of a species inside the ith layer; and θ, θ' are elevation angles from the Concorde altitude.

Case of a Single Isolated Line

Eq. (10) describes a general situation. For a single isolated line, Eq. (9) may be reduced to

$$T(\sigma) = \exp - \sum_p l_p n_p S_p f_p \,. \tag{11}$$

The observed data is the equivalent linewidth, given by

$$W(\sigma_0) = \int_{\sigma_0 - \frac{\Delta\sigma}{2}}^{\sigma_0 + \frac{\Delta\sigma}{2}} [1 - T(\sigma)]\, d\sigma. \tag{12}$$

$\Delta\sigma$ is a finite spectral interval defined by the line shape; $W(\sigma_0)$ is independent of the instrument function and expresses the fraction of absorbed energy integrated over that linewidth.

In the case of a very weak line a linear approximation is valid, and from Eq. (11) and (12) we can write

$$W(\sigma) = \int_{\sigma_0 - \frac{\Delta\sigma}{2}}^{\sigma_0 + \frac{\Delta\sigma}{2}} \sum_p l_p n_p S_p f_p d\sigma$$

$$= \sum_p l_p n_p S_p \sum_p l_p n_p S_p. \tag{13}$$

In these equations, the unknown quantities are the local number densities n_p in the various atmospheric layers.

Methods for Data Treatment

Several comments should be made on the theoretical development given in the previous section.

1. The orders of magnitude of stratospheric half-width (≈ 0.001 cm^{-1} at 40 km) and instrument resolution (0.1 cm^{-1}) are such that a linear approximation is valid only for very weak lines: the absorption at the line center must be less than 3 percent.
2. Even in the case of a single isolated line, the observed linewidth is an ambiguous representation of the total column density of the absorbing molecule. The distribution of its abundance with altitude has a non-negligible effect.
3. Practical measurements of equivalent width are not quite based on objective criteria, due to the effects of lines of the same (or other) species which overlap on the wings.
4. All observational data involve all stratospheric layers, since the flight altitude is in the very low stratosphere. However, information about local number density at the flight altitude can be deduced from two measurements in the following way: For the first measurement, the sun is slightly above the local horizontal plane (i.e., solar elevation $\theta \approx 1°$). The integrated absorption thus involves the distribution of the species from the aircraft (point A_1 in Figure 11) to the outside of the atmosphere. A few minutes later at sunset (or sooner at sunrise), the sun is below the local horizontal plane ($\theta \approx -1°$); as in the first case, the integrated absorption involves, at this moment, the distribution of the species between the aircraft (point A_2, Figure 11) and the sun. Along this axis, the state of the atmosphere beyond the point B where the axis again crosses the flight altitude may be assumed to be identical to the atmosphere beyond A_1 (same altitude for A_1 and B, and solar elevation equal to $+1°$ in both cases). Consequently, the difference between the equivalent widths measured in A_1 and A_2 is due only to the path A_2B (on the order of 200 km long) in the atmospheric layer close to and just below the flight altitude. This method is valid even in the case of an evolving photochemical process along the axis beyond the points A_1 and B.
5. Above the flight altitude, the result of the inversion process becomes more and more uncertain as the altitude increases. The optical path inside each layer varies with solar elevation in a manner not very different from one layer to another; when the altitude increases, this relationship is nearer and nearer the $(1/\sin\theta)$ law, which should be valid for plane parallel layers. In other words, the 'weighting functions' (Farmer, 1973) do not present any typical maximum, so the inversion process may become ambiguous. The measurement accuracy required for ensuring a proper restitution of a vertical concentration profile is clearly higher than in the case of negative values of solar elevation, as, for instance, in subtangential observation from a balloon floating in the upper stratosphere. Nevertheless, it was possible to obtain good data for local number density in the low and middle stratosphere from observational data obtained at various solar angles.

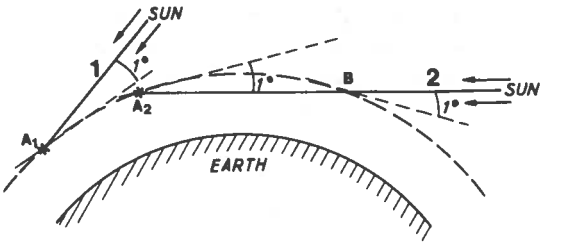

Figure 11. Optical path between the sun and the aircraft for two complementary positions of the plane. A_1, solar elevation $+1°$; A_2, solar elevation $-1°$.

Three methods have been used for data analysis. They are, in order of decreasing rigor:

1. *Computation of synthetic spectra*, on the basis of Equations (1) to (10). This method is the only one that overcomes

the drawbacks mentioned above, in particular the third one. Values of local number density of the species under study are introduced in a layer-by-layer stratospheric model and iterated until good agreement is reached between observed and computed spectra for various solar elevations. This method is at present under development, and initial results are given below for nitric oxide in the 1909 cm^{-1} region.

2. *Equivalent-width method.* The process of inverting the equivalent width of an isolated line, at solar elevation θ, to vertical profile n(h) (number density for altitude h) is non-linear. Apparently, the procedure must be based on successive iterations using a mathematical simulation over a narrow spectral range convenient for integration. On the one hand, the integrated absorption $W(\sigma_0, \theta)$ of a line is derived by ground-based measurements for various solar elevations θ. On the other hand, the integrated absorption of the same line is computed, for the same geometrical conditions (flight altitude, solar elevation), by introducing values of local number density in a layer-by-layer stratospheric model. The pressure and temperature introduced in the model are standard-atmosphere values. Other data to be introduced are the line parameters S_0, E, γ, and $\alpha_L{}^0$, and the integration range $\Delta\sigma$. Convenient values for local number density of the absorbing species are sought in order to reach agreement between computed and observed data over the range of solar elevation. This agreement is effected by successive iterations, using a computer in a conversational mode.

   This method was applied to nitric oxide and nitrogen dioxide spectra.

3. *Laboratory simulation.* Observed spectra are simulated by introducing a convenient quantity of the chosen species in a cell in front of the same spectrometer to be used for stratospheric experiments. For lack of theoretical data, this method has been used for HNO_3.

RESULTS

Nitric Acid

As mentioned in the previous section, the spectral analysis was based on laboratory simulation. Laboratory spectra obtained around 1326 cm^{-1} for various integrated amounts of HNO_3 are presented in Figure 12. Stratospheric spectra in the same spectral region are shown in Figure 9. This derivation of the extinction function provides only a crude simulation of stratospheric conditions. The laboratory spectra were obtained at room temperature, with a total pressure of 68 mb (atmospheric pressure near 20 km) within the cell, by adding dry nitrogen to nitric acid. The cell is a glass cylinder 60 mm long. The windows (calcium fluoride) are sealed with a thin layer of 'Voltalef', a fluorocarbon grease. Low-resolution spectra recorded under the same sampling conditions led to calibration values which agree well with results obtained by Murcray et al. (1969). The calibration curve deduced from the spectra presented in Figure 12 is given in Figure 13.

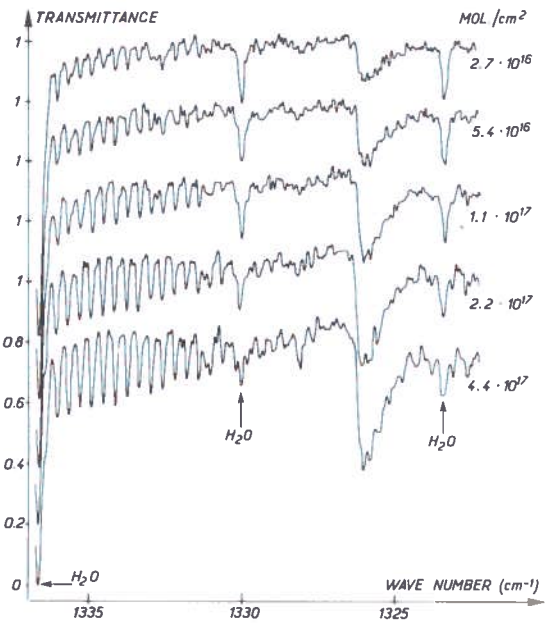

Figure 12. Laboratory spectra of nitric acid for different total amounts of molecules. Total pressure is 66 mbar.

The local number density near the flight altitude of 15.5 km, as deduced from this study, is $10 \pm 3 \times 10^9$ molec cm^{-3}, or $2.7 \pm 0.8 \times 10^{-9}$

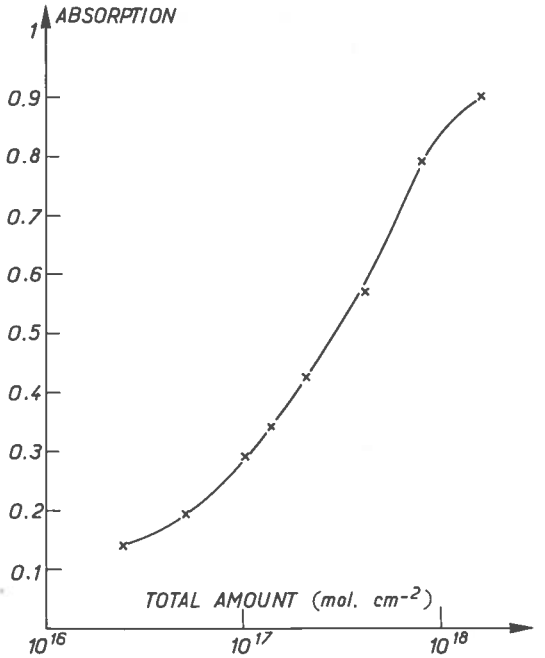

Figure 13. Maximum absorption from Q branch at 1326 cm^{-1} of nitric acid versus HNO_3 number density resulting from laboratory spectra (Figure 12).

ppmv. (This value was obtained by the method described in the previous section (Figure 11).)

Since pressure and temperature dependence of line intensity and line profile has not yet been considered for this species, the measured integrated amount $q(\theta)$, at solar elevation θ, may be described by a set of linear equations,

$$q(\theta_j) = \sum_i n_i l_{ij} \ ,$$

where n_i is the local number density for the layer number i, and l_{ij} the optical path inside the layer number i for the solar elevation θ_j (Figure 10).

A six-layer equation has been solved by the damped least-squares method; the result is shown as curve 3 of Figure 14a. On the same figure, two other vertical profiles are suggested, starting from the point of local concentration at 15.5 km: uniform mixing ratio (curve 2) and uniform number density (curve 1). Integrated amounts have been computed from these profiles for various solar elevations (Figure 14b). It can be seen that the curves deduced from uniform mixing ratio (curve 2) and uniform number density (curve 1) are not in agreement with observed data, whereas curve 3, with a maximum

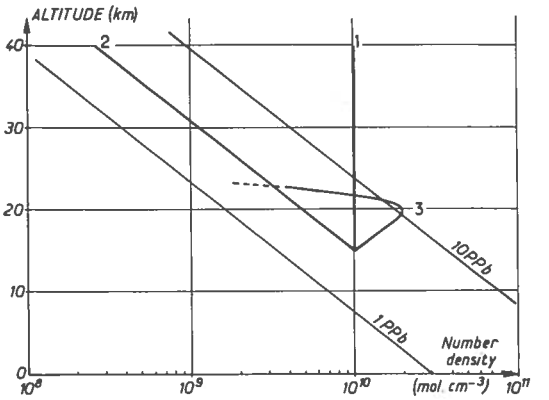

Figure 14a. Nitric-acid number density versus altitude. 1. Constant number density. 2. Constant mixing ratio. 3. Inverting experimental curve 3, Figure 14b.

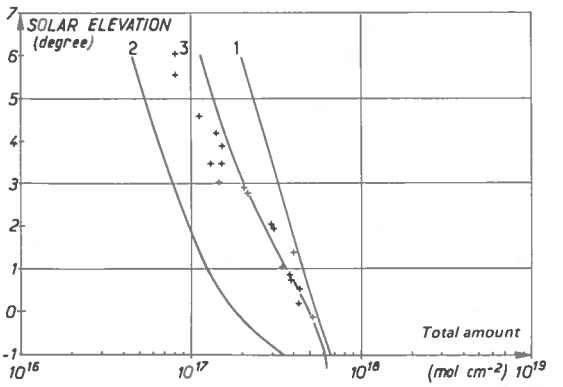

Figure 14b. Total amount of nitric acid versus solar elevation angle. 1. Constant number density of 10^{10} cm^{-3}. 2. Constant mixing ratio of 2 ppbv. 3. The best fit to experimental points (+).

at 20 km for local concentration, is in much better agreement with the measurements. A strong concentration in the layers just above the flight altitude is suggested by the relatively slow variation of the integrated amounts for low, positive values of solar elevation.

Curve 3 of Figure 14b has been compared with profiles deduced from other experimental data (Figure 15): Murcray et al. (1972) (spectrometry in emission) and Lazrus et al. (1972) (direct-sampling method). The latter have noticed large daily and seasonal variations. All these data agree on two points:

- There is a clear increase in abundance from 15 km to 20 km.
- The local concentration is maximum, in terms of number density, around 20 km.

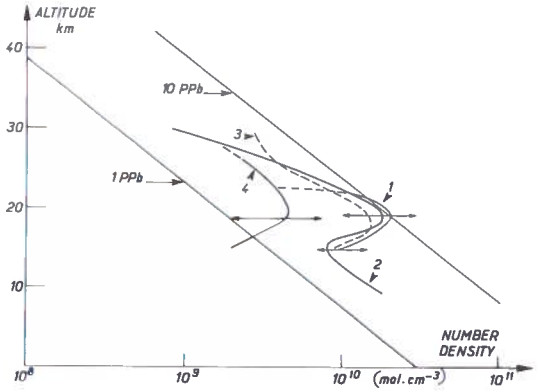

Figure 15. Number density of nitric acid versus altitude; limit of accuracy and of dispersion indicated by arrows. 1. This work. 2. Model (McElroy et al., 1973). 3. Emission measurements by Murcray et al. (1972). 4. Chemical measurement by A.L. Lazrus et al. (1972).

This maximum value is $2 \pm 1 \times 10^{10}$ molec cm^{-3} in the case of our work; a very similar value may be deduced from the data given by Murcray ($\approx 1.5 \times 10^{10}$ molec cm^{-3}). These values are higher than the numbers deduced from the data given by Lazrus ($\approx 5 \times 10^{9}$ molec cm^{-3}).

Nitrogen Dioxide

The spectra presented in Figures 7, 8a and 8b were obtained under sunset conditions. Data analysis was conducted by the equivalent-width method discussed earlier. Line strengths used in our analysis were determined by Muller (1973).

The local number density of NO_2, near the flight altitude of 15.5 km, deduced from these spectra is $1.1 \pm 0.2 \times 10^{9}$ molec cm^{-3}, or $3 \pm 0.6 \times 10^{-10}$ ppmv. This value is deduced from study of the 1604.154 cm^{-1} line. With the 1606.140 cm^{-1} line, the same treatment leads to a perceptibly higher value: $1.5 \pm 0.3 \times 10^{9}$ molec cm^{-3}. This disagreement is probably due to uncertainty in the line-strength values deduced from theoretical considerations. High-resolution laboratory measurements are now being performed by our group in order to improve these data.

Two vertical profiles are presented in Figure 16a; the equivalent widths deduced from these profiles, for various solar elevations, are compared with experimental data in Figure 16b. The main finding of this study is that the number density of NO_2 is concluded to be approximately constant between 15 and 25 km. Its value is between 1×10^{9} and 2×10^{9} molec cm^{-3}. Above 25 km, the inversion process becomes very uncertain. Nevertheless, the dashed curves shown on Figure 16b are in good agreement with our experimental data.

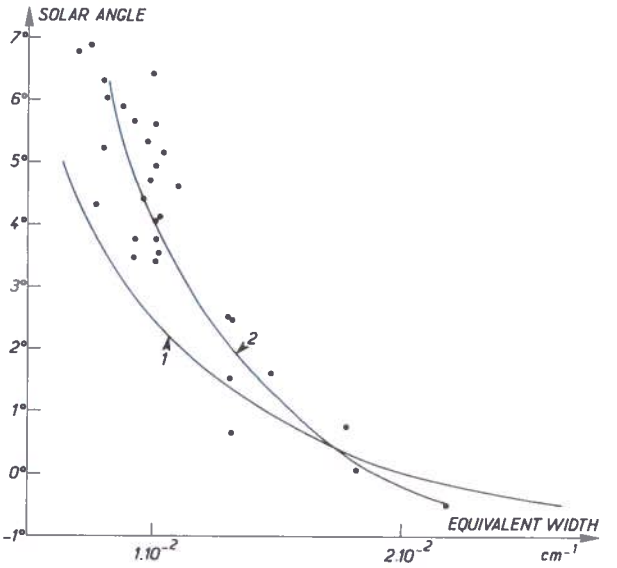

Figure 16a. Number density of NO_2 molecules versus altitude. 1. Constant mixing ratio 0.6×10^{-9}. 2. Inverted profile from 1604.150 cm^{-1} line. 3. Inverted profile from 1606.38 cm^{-1} line.

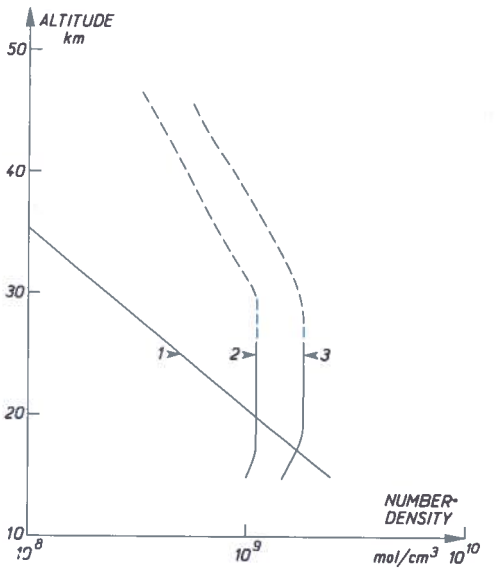

Figure 16b. Equivalent width of NO_2 absorption line (1604.154 cm^{-1}). 1. Constant mixing ratio of 0.6×10^{-9} (curve 1, Figure 16a). 2. The best fit to experimental points.

If we compare this profile with previous results (Figure 17) we see that:

1. Between 20 and 25 km our data are in good agreement with the values deduced by Ackerman and Muller (1972) from the spectra obtained by Murcray et al. (1969). In both cases, the spectral region studied is the ν_3 band near 1610 cm^{-1}.
2. Between 15 and 20 km, the values obtained by other authors are generally higher than our data. Spectrometric measurements of Ackerman and Muller (1972) and Farmer (1973) were made in the near-infrared ($\nu_1 + \nu_3$ band). However, this disagreement cannot be explained by the range of uncertainty in line strength in the ν_3 band, as deduced from recent laboratory data (Dana and Fontanella, 1973).
3. Photometric observations in the visible range (Brewer et al., 1973) lead to higher values than our data, but the shapes of both profiles are very similar: nearly constant number density between 15 and 25 km.
4. Local and seasonal variations may partially explain the measurement dispersion.

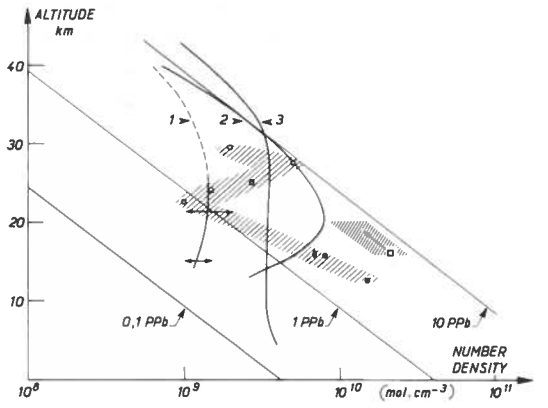

Figure 17. Number density of NO_2 molecules versus altitude. 1. Measured profile of this work. Dashed line indicates a possibility for the profile above 25 km. 2. Theoretical model (McElroy et al., 1973). 3. Measured profile of Brewer et al., 1973. Other experimental points are: ○, deduced from Murcray spectra (Murcray et al., 1969) by Ackerman and Muller (1972), with ν_3 band; ●, with $\nu_1 + \nu_3$ band. ◆, measured by Farmer et al. (1973) with $\nu_1 + \nu_3$ band. □, measured by Harries (1972) by far infrared emission.

Nitric Oxide

As stated earlier, the purposes of the Concorde NO experiments were:

- to compare the total amount of NO in sunset and sunrise conditions, and
- to study the agreement between the total amount measured at sunset from 16 km and the vertical distribution (Figure 1) derived from the spectra obtained in a spectrometric balloon-borne experiment (14 May 1973) conducted jointly by IASB and ONERA (Ackerman et al., 1973a).

In Figure 18, the values of the equivalent width from NO lines 1890.76 (spectra in Figure 4), 1909.14 (spectra in Figure 5) and 1914.99 (spectra in Figure 6) are plotted with respect to solar elevation, in accordance with Table 2. On the same figure, the curves deduced from the vertical profile (Figure 1) have been traced for the same three lines. It appears that, in spite of some erratic points, there is no disagreement

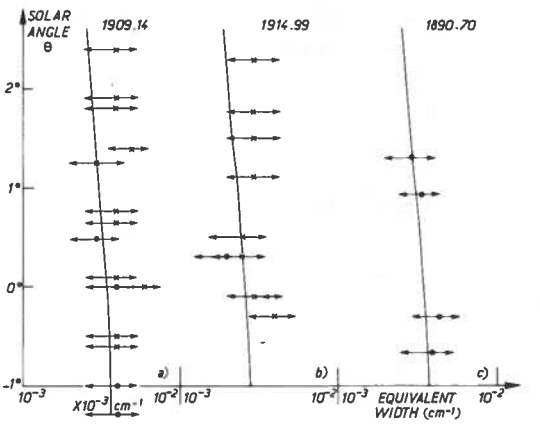

Figure 18. Equivalent width of three NO absorption lines versus solar angle as measured from stratospheric spectra. σ_1 = 1909.14 cm^{-1}, σ_2 = 1914.99 cm^{-1}, σ_3 = 1890.70 cm^{-1}. Arrows indicate experimental accuracy. X are experimental points from flight no. 4, • are experimental points from flight no. 1. Solid lines are computed values from experimental profile shown on Figure 1, curve A.

between the results of the balloon-borne experiment and those of the Concorde experiments, though, in the latter case, a tendency to slightly higher values of the total amount may be observed. In fact, within the accuracy of measurement, no significant variation may be deduced from airborne observations for solar elevations varying from +2° to -1°. This confirms that nitric oxide is concentrated in stratospheric layers above the flight altitude.

There is no significant difference in total amount of NO between sunset and sunrise conditions.

The integrated amount of NO along the optical path from 15.5 km is $4 \pm 1.5 \times 10^{16}$ molec cm^{-2} for solar elevation angles varying from +2° to -1° at sunset and at sunrise. An upper limit of 6×10^{8} molec cm^{-3} (lower than the 10^{9} value reported in Fontanella et al. (1973)) may be given for the local number density at 16 km (mixing ratio less than 1.6×10^{-10}).

The first three conclusive measurements of NO were performed within a very short time span. They are:

1. $10^{-10} \pm 60\%$ as local mixing ratio between 17.4 and 22.9 km (Ridley et al., 1973). This value is a result of a balloon-borne experiment performed on March 16, 1973 using the chemiluminescence method. Measurements were made between 10:40 and 15:05 local time.
2. $10 \pm 2 \times 10^{-10}$ for mean mixing ratio between 11 km and 26 km (Toth et al. 1973). This value is the result of an air borne experiment performed at sunrise on March 11, 1973 using infrared absorption spectrometry with the sun as source.
3. $7 \pm 3 \times 10^{-10}$ for mean mixing ratio from the altitude 11.8 km and for a horizontal sighting (Girard et al., 1973b). This value is the result of a preliminary flight performed at sunset on a Caravelle airliner on April 5, 1973, with the equipment used later on Concorde for this work.

The last two values cannot be plotted on Figure 1, since in both cases the mixing ratio was derived under the assumption of a uniform distribution in a broad altitude range. The fact that the mixing ratio increases with altitude, a major finding of the balloon experiment, explains why the mean mixing ratio measured from the low stratosphere is higher than the local value in the lower stratosphere. The values obtained for local concentration at 17 km by spectrometry (Ackerman et al., 1973b) and chemiluminescence (Ridley et al., 1973) are in good agreement. Finally, the set of present experimental data appears to be relatively coherent, within the accuracy of measurement and local and daily variations. The main problem arises from the observation, by chemiluminescence, of a tendency to a uniform mixing ratio between 17.4 and 22.4 km, which is clearly not in agreement with our spectrometric observations from balloons and the Concorde.

Figure 19 is given as a first example of the computation of synthetic spectra recently performed by our group. It involves four species: H_2O, CO_2, N_2O, and NO. The stratosphere has been divided into six layers. The vertical profile used for NO is the upper limit of the vertical profile of Figure 1.

The geometric conditions are: altitude of the observer, 16 km; angular evaluation, +1 degree. Figure 19a is the spectrum synthesized at infinite resolution; Figure 19b is the result of the convolution of the experimental instrument function (half-width 0.1 cm^{-1}) by the spectrum of Figure 19a. Figure 19c is the same as 19b, with the exclusion of NO in the model. Figure 19d is the result of the convolution of an instrument function of 0.3 cm^{-1} half-width with the spectrum of Figure 19a. Lastly, Figure 19e is an actual spectrum recorded aboard Concorde under the same geometrical conditions.

Several observations can be made:

- It appears, from a comparison of Figures 19b and 19c, that the contribution of NO to the observed absorption line around 1909.1 cm^{-1} is predominant but the effect of the CO_2 line at 1909.21 cm^{-1} is not negligible.
- The importance of high resolution is obvious from a comparison of Figures 19a, 19b, and 19d.
- The resolution in the actual spectrum (Figure 19e) is clearly higher than the resolution in the computed spectrum

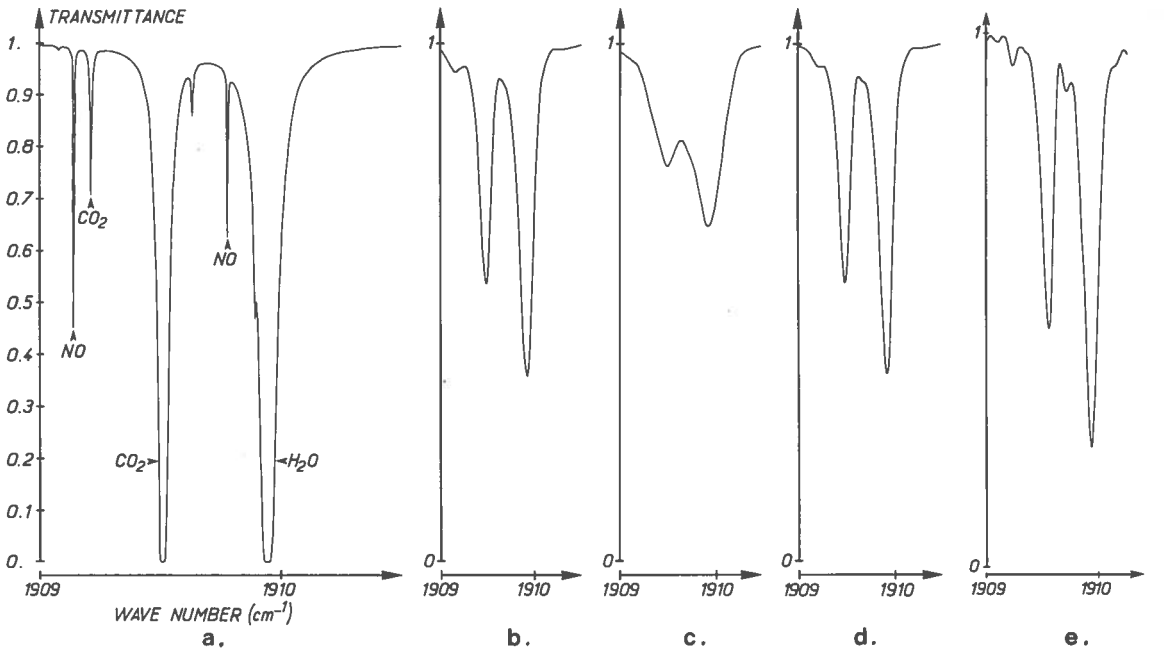

Figure 19. Synthetic spectra near 1909 cm^{-1} for an altitude of 16 km and a solar elevation of +1°. a. Assuming very high resolution. Amount of NO calculated from upper limit of the profile in Figure 1; CO_2 mixing ratio 3×10^{-4}; H_2O mixing ratio 5×10^{-6}. b. Resolution, 0.1 cm^{-1}. c. Same, without NO. d. Resolution, 0.3 cm^{-1}. e. Natural stratospheric spectrum.

(Figures 19b and 19c). This is due to the fact that the instrument function used for the computation was the experimental record of a line. It was slightly too wide, so the experimental record must be corrected for the natural width of the line under study.

The line observable on Figure 19e between the H_2O and CO_2 lines is probably a solar CO line.

The main results for NO, NO_2, and HNO_3 are plotted in Figure 20.

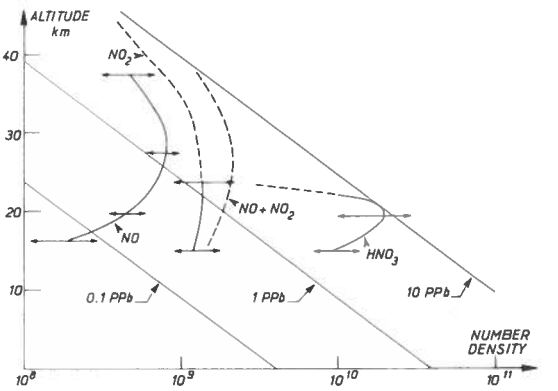

Figure 20. Number density versus altitude for NO, NO_2, and HNO_3 as measured in this work and from previous balloon experiment (Ackerman et al., 1973b).

CONCLUSION

The results presented above constitute a simultaneous set of measurements for NO, NO_2, and HNO_3 in the low stratosphere, in spring-summer, at medium north latitudes. The predominance of HNO_3 between 15 km and 20 km seems more marked than generally expected.

Two balloon-borne experiments to observe NO_2 and HNO_3 are planned in 1974; they should provide the more precise data for the high stratosphere suggested by this work.

Furthermore, several airborne experiments would permit us to complete this study in two areas: to measure the local concentrations around 12 km, with the view of improving present values introduced in the models as lower boundary conditions, and to compare results obtained under various seasonal and climatic conditions.

ACKNOWLEDGMENTS

At ONERA, J. Besson and H. Brejaut, in charge of solar pointing systems, participated in

the experiments. The contribution of P. Billebault, D. Labbe, and M. Nogues to the preparation of experiments was important. G. Gregoire and G. Fergant have contributed to the data analysis. We thank all of them.

We are grateful to C.B. Farmer and R.A. Toth, from the Jet Propulsion Laboratory, for their cooperation during the flight experiments on Concorde, in Toulouse. We also thank M. Ackerman and C. Muller, from IASB, for frequent and fruitful discussions at many stages of this work. The experiments have been made possible by Aérospatiale (SNIAS), who provided the Concorde and computed suitable trajectories, which were flown with remarkable accuracy.

This work was conducted under contract No. 73-150218 from the French Committee for the Study of the Consequences of Stratospheric Flight (COVOS).

REFERENCES

Ackerman, M. and C. Muller (1972), "Stratospheric nitrogen dioxide from infrared absorption spectra," Nature **240**, 300.

Ackerman, M., D. Frimout, C. Muller, D. Nevejans, J.C. Fontanella, A. Girard, and N. Louisnard (1973a), "Stratospheric nitric oxide from infrared spectra," Nature **245**, 205.

Ackerman, M., J.C. Fontanella, D. Frimout, A. Girard, L. Gramont, N. Louisnard, C. Muller, and D. Nevejans (1973b), "Recent stratospheric spectra of NO and NO_2," Can. J. Chem. **52**, 1532.

Ackerman, M., D. Frimout, J.C. Fontanella, A. Girard, R. Gobin, L. Gramont, and N. Louisnard (1973c), "Airborne and balloon borne spectroscopy for the study of atmospheric gas pollutants," in the Proceedings of the Second Conference on Sensing of Environmental Pollutants (Washington, 10-12 Dec. 1973).

Brewer, A.W., C.T. McElroy, and J.B. Kerr (1973), "Nitrogen dioxide concentrations in the atmosphere," Nature **246**, 129.

Dana, V. and J.C. Fontanella (1973), "Etude de l'absorption du dioxyde d'azote dans la région de 6,18," Nouvelle Revue d'Optique 4 (4).

Farmer, C.B. (1973), "Infrared measurements of stratospheric composition," Can. J. Chem. **52**, 1544.

Fontanella, J.C., A. Girard, L. Gramont, and N. Louisnard (1973), "Analyse de spectres stratosphériques de NO et de NO_2," presented at the C.R. Ac. Sc. Meeting of 29/10/73 (to be published).

Girard, A. (1963), "Spectromètre à grilles," Appl. Opt. **2**, 79.

Girard, A., J.C. Fontanella, and L. Gramont (1973a), "Détection et dosage de constituants stratosphériques minoritaires," in the Proceedings of the COVOS/COMESA Conference (Paris, 22-23 March 1973) (available through COVOS, 93 bd. du Montparnasse, 75006 Paris).

Girard, A., J.C. Fontanella, and L. Gramont (1973b), "Détection de l'oxyde azotique dans la stratosphère," C.R. Ac. Sc. **276B**, 845.

Harries, J.E. and N.W.B. Stone (1972), "Measurements of some hydrogen-oxygen-nitrogen compounds in the stratosphere, from Concorde 002," in *Proceedings of the Second Conference on the Climatic Impact Assessment Program* (November 14-17, 1972), ed. A.J. Broderick, U.S. Department of Transportation, DOT-TSC-OST-73-4.

Lazrus, A.L., B.W. Gandrud, and R.O. Cadle (1972), "Distribution of stratospheric nitric acid," J. Appl. Meteorol. **11**, 389.

McClatchey, R.A., W.S. Benedict, S.A. Clough, D.E. Burch, R.F. Calfee, K. Fox, L.S. Rothman, and J.S. Garing (1973), "Atmospheric Absorption Line Parameters Compilation," Air Force Cambridge Research Laboratories, Bedford, Mass.

McElroy, M.B., S.C. Wofsy, J.E. Penner, and L.J.C. McConnell (1974), "Atmospheric ozone: possible impact of stratospheric aviation," J. Atm. Sci. **31**, 287.

Muller, C. (1973), private communication.

Murcray, D.G., F.H. Murcray, W.J. Williams, T.G. Kyle, and A. Goldman (1969), "Variation of the infrared solar spectrum between 700 cm^{-1} and 2240 cm^{-1} with altitude," Appl. Opt. **8**, 2519.

Murcray, D.G., A. Goldman, F.H. Murcray, W.J. Williams, J.N. Brooks, and D.B. Barker (1972), "Vertical distribution of minor atmospheric constituents as derived from air-borne measurements of atmospheric emission and absorption infrared spectra," in *Proceedings of the Second Conference on the Climatic Impact Assessment Program* (November 14-17, 1972), ed. A.J. Broderick, U.S. Department of Transportation, DOT-TSC-OST-73-4.

Ridley, B.A., H.I. Schiff, A.N. Shaw, L. Bates, C. Howlett, H. Levaux, L.R. Megill, and T.E. Ashenfelter (1973), "Measurements in situ of nitric oxide in the stratosphere between 17.4 and 22.9 km," Nature **245** (3), 10.

Toth, R.A., C.B. Farmer, R.A. Schindler, O.F. Raper, and P.W. Schaper (1973), "Detection of nitric oxide in the lower stratosphere," Nature **244**, 7.

DISCUSSION

SCHIFF: I think I should point out that these measurements agree with ours for NO at 30 kilometers and at 20 kilometers, but in between there is a difference of a factor of four or five. And more important, we don't see that mixing-ratio maximum at 24 kilometers that you report.

ACKERMAN: That maximum is relatively broad.

RAO: Recently we measured NO and N_2O spectra near 1890 cm^{-1} and found some lines that aren't listed. Have you recorded N_2O with your spectrometer in the laboratory?

GIRARD: No.

(UNIDENTIFIED): Considering all the available measurements, the ratio between observed NO and NO_2 at 20 km is not in agreement with the predictions of photochemistry. Moreover, the relation between sunset and sunrise values of NO and NO_2 is likewise inconsistent.

GIRARD: We have noticed no difference greater than 20 percent in total NO between sunset and sunrise conditions.

RECENT RESULTS OF AIRCRAFT INFRARED OBSERVATIONS OF THE STRATOSPHERE

C.B. FARMER, O.F. RAPER, R.A. TOTH, AND R.A. SCHINDLER
Jet Propulsion Laboratory
California Institute of Technology
Pasadena, California

ABSTRACT: The analysis of stratospheric spectral data obtained during a series of recent flights with the JPL near-infrared high-speed stepping interferometer, on board the British prototype of the Anglo-French Concorde (002), has confirmed earlier results from high-altitude observations with the instrument, and has provided additional information on the mixing ratios for such species as NO, NO_2, N_2O, CO, CO_2, CH_4, O_3, and H_2O. The application of deconvolution techniques to the spectra from these flights has increased the spectral resolution and resulted in the determination of more accurate values for the mixing ratios of several of these trace species, as well as new upper limits for others. Finally, laboratory spectral studies made in conjunction with the N_2O data reduction have resulted in revised values for the mixing ratio of N_2O in the stratosphere. This paper shows representative spectra for many of the trace stratospheric gases, and discusses the values for the mixing ratios and their latitudinal variations for all the trace gases observed to date.

INTRODUCTION

During the past year observations of the stratospheric infrared spectrum have been made in three series of aircraft flights. The instrument used in the observations is a high-speed stepped Michelson interferometer, covering the 2 to 8 μm range at a resolution of ≈ 0.2 cm^{-1}, the spectra being taken in absorption over long optical paths by tracking the Sun close to sunrise or sunset. The instrumentation, the anticipated molecular detection levels, and details of the observational technique and its accuracy were discussed at the second CIAP conference (Farmer, 1973).

The first flight series, in the February-March period of last year, was made for the most part over the continental U.S. (covering the 30° to 76°N latitude band) from an NC 135 aircraft at observation base altitudes between 11 and 12 km. Both sunset and sunrise spectra were recorded. It was during this series that we first detected NO from lines in the 1-0 band at 5.3 μm (Toth et al., 1973). The second series of observations was made in June from the French Concorde prototype (001); we secured three of the flights in this series, each giving about 20 minutes of observation (solar tracking) time, in the 40°-50°N latitude band over the Bay of Biscay at base altitudes between 15 and 16 km. The third series was made from the British Concorde prototype (002), over the same locale and at the same altitudes; we had five successful flights in this series and had expected to continue with a few more to be made at higher latitudes, but unfortunately the aircraft's flight program was terminated after the fifth flight.

The data from the first flights (NC 135) covered the full wavelength range of the instrument at the maximum resolution, and were obtained with the use of two detectors – one InSb at liquid-N_2 temperature, the other pyroelectric at ambient temperature. For the Concorde flights, however, we restricted ourselves to the 2-5.5 μm range, using only InSb, since Girard was observing in the same flight series with an instrument of superior resolution for the longer wavelengths, in the vicinity of ν_3 NO_2 and 1-0 NO. (A report on his observations appears just before this paper.) We could therefore better utilize the limited observation time available by confining our measurements to the shorter wavelength regions, thus providing useful spectral coverage for the maximum number of molecular species of interest.

SCOPE OF THE RESULTS

For remote-sensing spectral observations made in absorption or emission, it is not possible

to derive the vertical distribution of the spectrally active species at altitudes above the observation base, without some *a priori* knowledge or assumption of the form of the distribution. For the non-uniformly mixed species, the most useful and unambiguous observations are those made at solar zenith distances of 90° and greater. For species which are approximately uniformly mixed vertically, observations made at any zenith angle which is large enough to give measurable absorptions can provide useful information for the altitude range up to roughly one pressure scale height above the observation base altitude. The limitations of remote-sensing spectral observations in determining total column abundances and their vertical distributions, for different conditions of observation, have been discussed by Farmer (1974). The present observations, taken as a whole, covered a range of base altitudes from 11 to 16 km, so that the molecular concentrations derived from them are restricted to the region between the tropopause and approximately 20 km; as was mentioned in the introduction, the latitude range covered the northern hemisphere from 30° to 76°.

A brief further comment on the observational procedure is appropriate here. Each spectrum is recorded in a time interval of between 2 and 3 minutes. For the 001 flight-period (June) observations, the trajectories chosen, together with the Concorde flight performance, resulted in apparent motion of the sun of 1/4-1/2°. For the 002 flights, which occurred in the October-November period, the characteristics of the trajectories were such that the solar effective motion during each observation could be reduced to 1/8-1/4°. For these we were able to use a diffusely reflecting mirror in the input-tracking optical system and further reduce the random fluctuation in the spectra; this improved S/N level resulted in our being able to use deconvolution techniques in the analysis of the spectra to resolve some of the spectral blending problems. This is discussed further in the following sections.

The molecular constituents which produce measurable absorptions in the frequency range covered by these measurements can be separated into two distinct groups: the "strong" species which give extended, well-defined bands, and the "weak" species which produce only a few small spectral features. The former include CO, CH_4, CO_2, H_2O, N_2O, and O_3; for these our main contribution to the investigation of stratospheric composition is to provide some new or extended information on spatial distribution, particularly the variation of mixing ratio with latitude. The "weak" or difficult species are those for which we have endeavored to maximize the quality of the spectra in order to achieve their detection or, failing this, to reduce to a minimum the upper limit which can be assigned to their possible abundances and mixing ratios.

As far as undetected molecules of interest are concerned, so far we have studied only the spectral regions where transitions of HCl and H_2CO occur; we have obtained new upper-limit concentrations for these. (Some further comments on the implications of the HCl upper limits derived from both ground-based and aircraft spectra are made in a later section.) There are also a number of other gases (for example, NH_3 and H_2O_2) for which we shall eventually be able to give improved upper limits, but these data have not yet been investigated.

In the following section the results for individual species are discussed in turn. The overall results of the several analyses of the data (as far as they have been taken to date) are summarized in Table 1, which gives the range of concentrations determined for each molecule and indicates the spatial variability where applicable. It is stressed that the results are tentative, since in many cases further work is necessary to explore the effects of possible spectral interference from other molecules. Laboratory measurements under way at present will provide the data on line frequencies and strengths required for this purpose (in particular, for CH_4 and CO_2), and final results for some of the stratospheric molecules listed in Table 1 cannot be given until these ancillary measurements and analyses have been completed.

Carbon Dioxide

Carbon dioxide absorptions appear in almost every spectral region of interest throughout the frequency range covered by our instrument. This allows them to be routinely analyzed along with the other molecules of interest to provide an independent check on the computation of the

Table 1. Summary of Provisional Results of 1973 Observations of Stratospheric Trace Gases

Species	Bands Analyzed	Relative Volume Mixing Ratio	Variation With Latitude[a]	Variation With Altitude
CO	1-0	2 to 7 × 10^{-8}	yes	yes[b]
CO_2	$3\nu_2$	3.29 ± 0.34 × 10^{-4}	no	no
CH_4	ν_3	0.6 to 1.2 × 10^{-6}	yes	no[d]
H_2O	ν_2	2.3 ± 0.4 × 10^{-6}	no[c]	no[d]
N_2O	$\nu_1 + \nu_2$, $2\nu_1$	3.6 ± 0.4 × 10^{-7}	no	no
NO	1-0	1 to 4 × 10^{-10}		yes
NO_2	$\nu_1 + \nu_3$	$1.8^{+0}_{-1.0}$ × 10^{-9} [e]		yes
HCl	1-0	$\geq 2 \times 10^{-10}$ $\leq 8 \times 10^{-10}$		f g
H_2CO	ν_1, ν_5	$\geq 2.4 \times 10^{-9}$		

[a] Latitude range 33 to 74°N.

[b] No variation observed in lower stratosphere.

[c] Possible increase in lower stratosphere at latitudes below 35°N.

[d] No apparent variation in altitude range 11 to 20 km.

[e] Uncertain; mixing ratio given as maximum value at sunset, 16 km altitude.

[f] HCl upper limit for constant mixing above 12 km over land.

[g] Uncertain detection; taken as HCl upper limit for constant mixing above 16 km over ocean.

optical path over which the absorptions are produced for each solar elevation angle and base altitude.

Assuming uniform mixing for CO_2 over the effective altitude range of the observations, the CO_2 features should yield a consistent value for the relative mixing ratio. Any observed variation of this value gives a direct indication of the errors associated with the geometrical uncertainties and the estimation of equivalent widths for relatively prominent absorption lines.

Taking the CO_2 observations as a whole, analyses based principally on the $3\nu_2$ band at 1933 cm^{-1} indicate that the volume mixing ratio lies consistently in the range 329 ± 37 ppm. We have found no systematic departure from this range of values to support any variation of the CO_2 mixing ratio with latitude or altitude, i.e., from the surface to 20 km over the northern hemisphere. This is not a tautological argument, as it might appear at first sight, since any real systematic variation in the CO_2 abundance would appear as a parallel systematic trend in apparent errors in the geometrically computed column air masses.

Carbon Monoxide

Carbon monoxide concentrations were determined from the 1-0 (2143 cm^{-1}) band, using the published strengths of Burch and Williams (1962). A portion of two spectra in the CO region are shown superimposed in Figure 1; the upper trace was recorded at 11.9 km at a solar zenith angle of 85°, and the lower at 15.2 km and 89° zenith angle. In addition to the R-branch of the 1-0 telluric CO band, the spectra show P-branch lines of the ν_3 and the "hot" $\nu_2 + \nu_3 - \nu_2$ bands of N_2O. Absorptions between the CO lines are due to solar CO and the $2\nu_3$ band of O_3.

Seiler and Warneck (1972) have obtained a considerable amount of data on the vertical mixing profile of CO from balloon flights over Northern Europe, using in-situ techniques. Their results show an initial strong decrease in the CO

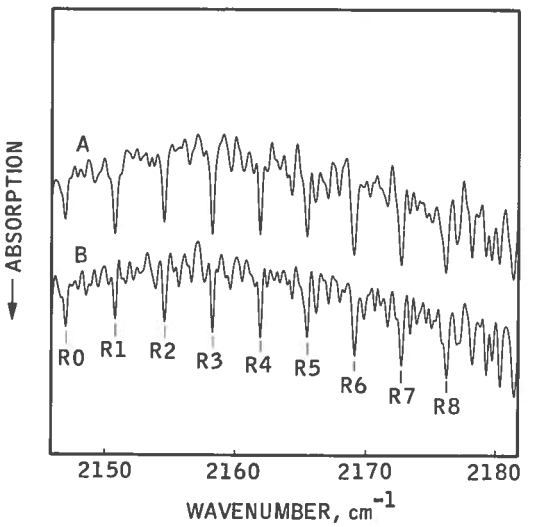

Figure 1. Portions of two spectra in the R-branch region of the 1-0 CO band. Trace A was recorded from 11.9 km at a solar zenith angle of 85°, and trace B from 15.2 km at an 89° zenith angle.

mixing ratio, from 0.15 ppmv at the top of the troposphere to a value of 0.04 ppmv at an altitude of 1 km above the tropopause, with constant vertical mixing above this altitude. All of our results were obtained from measurements made at altitudes ranging from 1.5 to 5 km above the tropopause, so on the basis of the Seiler and Warneck results they have at all times been in this region of constant vertical mixing. The values we obtained for the CO mixing ratios increased from 0.023 ± 0.005 ppmv to 0.066 ± 0.010 ppmv with decreasing latitude (see Figure 2); they are in consonance with the Seiler and Warneck results only if there is a strong latitude variation in the lower stratospheric CO abundance. It should be pointed out, nevertheless, that our data *taken alone* do not rule out a decrease in CO mixing ratio with altitude, above the tropopause, since the lowest observed values (at the higher latitudes) were obtained at the highest altitudes above the tropopause, while the measurements made closest to the tropopause (in the lower latitudes) were those which gave the highest mixing ratios. However, the measurements made at the same latitude as those of Seiler and Warneck are in close agreement with their results, and it appears more probable that the large decrease which we observed between equatorial and polar latitudes is in fact a real latitudinal variation rather than a manifestation of the decrease with altitude immediately above the tropopause itself.

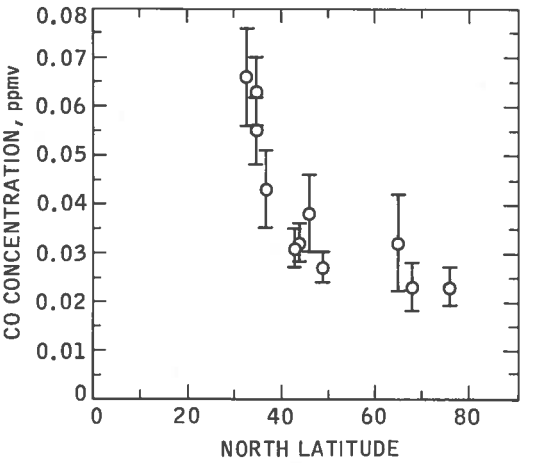

Figure 2. Variation of stratospheric mixing ratio for CO as a function of latitude, assuming constant mixing ratio in the region > 1 km above the tropopause.

Methane

The methane data are derived mainly from the ν_3 band (3018 cm^{-1}), examples of which are shown in Figure 3. The spectral region illustrated shows the strong P-branch manifolds, but the entire region is overlain by numerous features of much weaker CH_4 bands (which we are currently studying in collaboration with Hunt at Florida State University). The refinement of the basic spectral data for CH_4 in this region is of particular importance, because the region contains several narrow spectral windows between the main ν_3 manifolds which can be used in the search for several other molecules of interest, in particular HCl (1-0) and H_2CO (ν_5).

Figure 4 shows the results of the analysis of ν_3 from all of our observations to date, plotted again as a function of latitude. For this analysis we have taken the ν_3 molecular parameters from Barnes et al. (1972), Kyle (1968), and Tejwani and Varanasi (1971). The latitude dependence of methane in the lower stratosphere has also been investigated by Lowe and McKinnon (1972) using the R-branch of ν_3. The Lowe and McKinnon values are shown in Figure 4 as solid

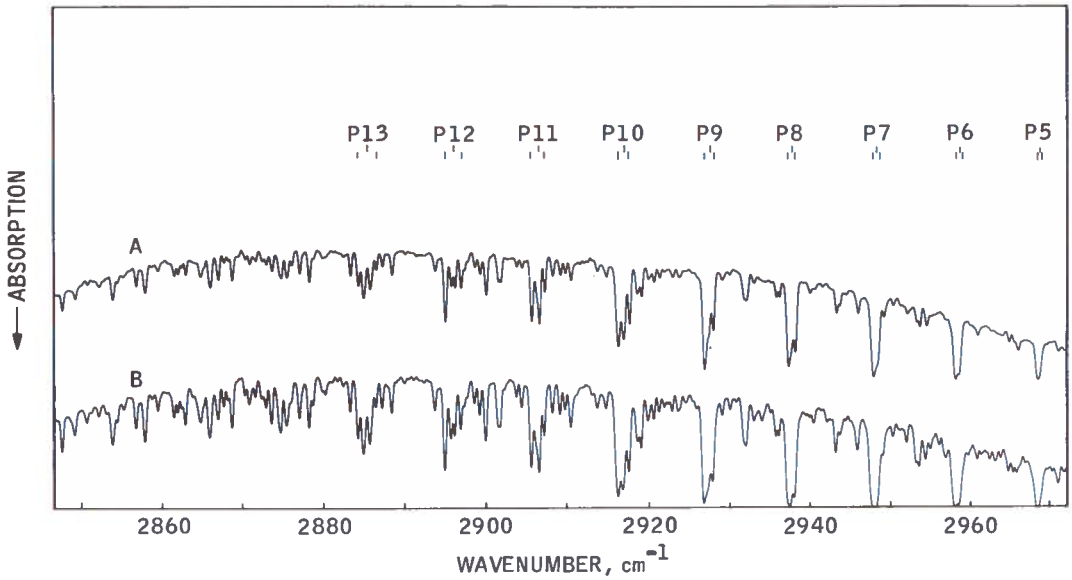

Figure 3. Portions of two spectra in the ν_3 region of CH_4, showing the strong P-branch manifolds. This region contains several small windows between the main ν_3 manifolds which can be used in the search for such molecules as HCl and H_2CO.

circles, while the present results are plotted as open circles. The somewhat smaller error bars associated with our values indicate that the CH_4 mixing ratio is not constant with latitude, while the Lowe and McKinnon data are consistent with either a distribution close to uniform mixing or the decrease with increasing latitude at the rate suggested by our results. There may of course be a variation with season and longitude, so the larger differences, especially in the tropical latitudes, may well be real. However, a decrease in the abundance of CH_4 with increasing latitudes is not unexpected, in view of its biogenic origin.

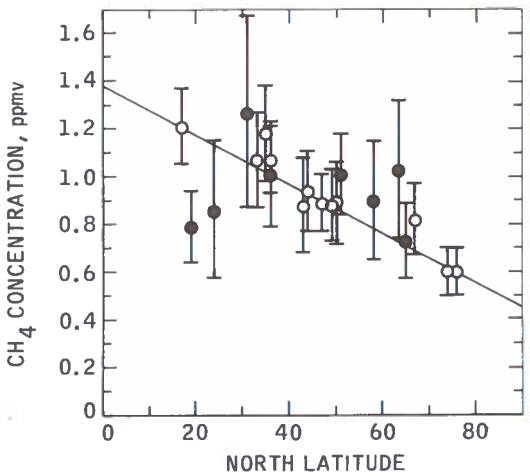

Figure 4. Variation of the stratospheric mixing ratio for CO as a function of latitude, assuming constant vertical mixing. Dark circles are the data of Lowe and McKinnon (1972).

Water Vapor

The stratospheric spectra provide an opportunity to check the relative intensities of the ubiquitous water-vapor transitions over a wide range of line strengths. For the derivation of stratospheric mixing ratios from the spectra we have used chiefly lines from the ν_2 band in the 6-μm spectra and the $2\nu_2$ band for the 3-μm region. The intensities of many of the lines used in the analysis have already been measured in the laboratory; our results are found to be generally in good agreement with the Benedict and Calfee (1967) values included in the AFCRL spectral line listing (McClatchey et al., 1973). Their application to the stratospheric spectra yields a mixing ratio of 2.3 ppmv with no variation with latitude (over the range from 33 to 76°N) or altitude (12 to 20 km), beyond a cumulative uncertainty of ± 0.4 ppmv.

Nitrous Oxide

Several bands of N_2O appear in the spectral range covered by the present measurements; three of the more prominent are ν_3 at 2224 cm^{-1}, $2\nu_1$ at 2563 cm^{-1}, and $\nu_1 + \nu_2$ at 1880 cm^{-1}. The ν_3 band produces intense absorptions in atmospheric spectra in a region where there are also strong absorptions from other molecules, principally CO_2 (ν_3 etc.). Consequently, it is often difficult to locate the continuum accurately, and the amount of N_2O producing the absorption may thus tend to be underestimated.

At the completion of the 002 flight series, and during the course of the analysis of the N_2O lines in the data, we noticed that there was an apparent difference between the relative absorptions of the different N_2O bands in the spectra and the relative intrinsic strengths of the bands themselves. For the latter we had taken the published values appearing in the AFCRL line listing. We therefore measured in the laboratory (Toth, 1974) the intensities of the two bands which were the most reliable (that is, from the standpoint of the analysis of atmospheric spectra, viz., $2\nu_1$ and $\nu_1 + \nu_2$) in an attempt to identify the source of the discrepancy.

The laboratory value for $2\nu_1$ was found to be in good agreement with Burch's value (incorporated in the AFCRL listing), whereas the value for $\nu_1 + \nu_2$ was significantly greater than the AFCRL value. Our measured value for the Q-branch of $\nu_1 + \nu_2$ is $S(Q) = 0.22$ cm^{-2} atm^{-1} at 296K (= 0.315 cm^{-2} atm^{-1} at 220K). The revised laboratory values gave consistent results for the N_2O abundances derived from different bands in the observed stratospheric spectra so they were adopted for a complete reanalysis of the spectra from all three flight series. Portions of two of the stratospheric spectra covering the $2\nu_1$ band are shown in Figure 5, and the weaker $\nu_1 + \nu_2$ band at 1880 cm^{-1} can be seen in Figure 6.

The N_2O mixing ratio derived from $2\nu_1$ is 0.33 ± 0.05 (15%) ppmv, and that derived from $\nu_1 + \nu_2$ is 0.36 ± 0.04 ppmv; there is no discernible variation with latitude or altitude over the ranges covered by the observations.

This result is somewhat higher than those given by Schütz et al. (1970) and Harries (1973) (≈0.25 ppmv).* Harries did not detect any variation with latitude between 5°S and 48°N.

* Harries' more recent results, presented earlier in this volume, are in closer agreement with the values quoted here.

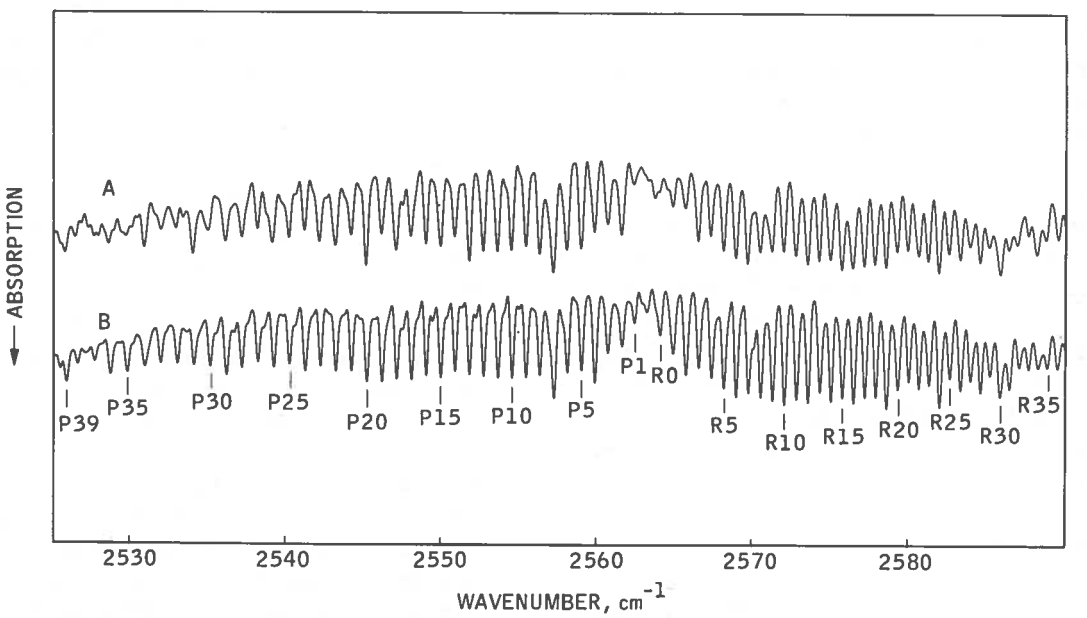

Figure 5. Portions of two stratospheric spectra covering the $2\nu_1$ band of N_2O. Trace A was recorded from 11.9 km at a solar zenith angle of 85°, and trace B from 15.2 km at an 89° zenith angle.

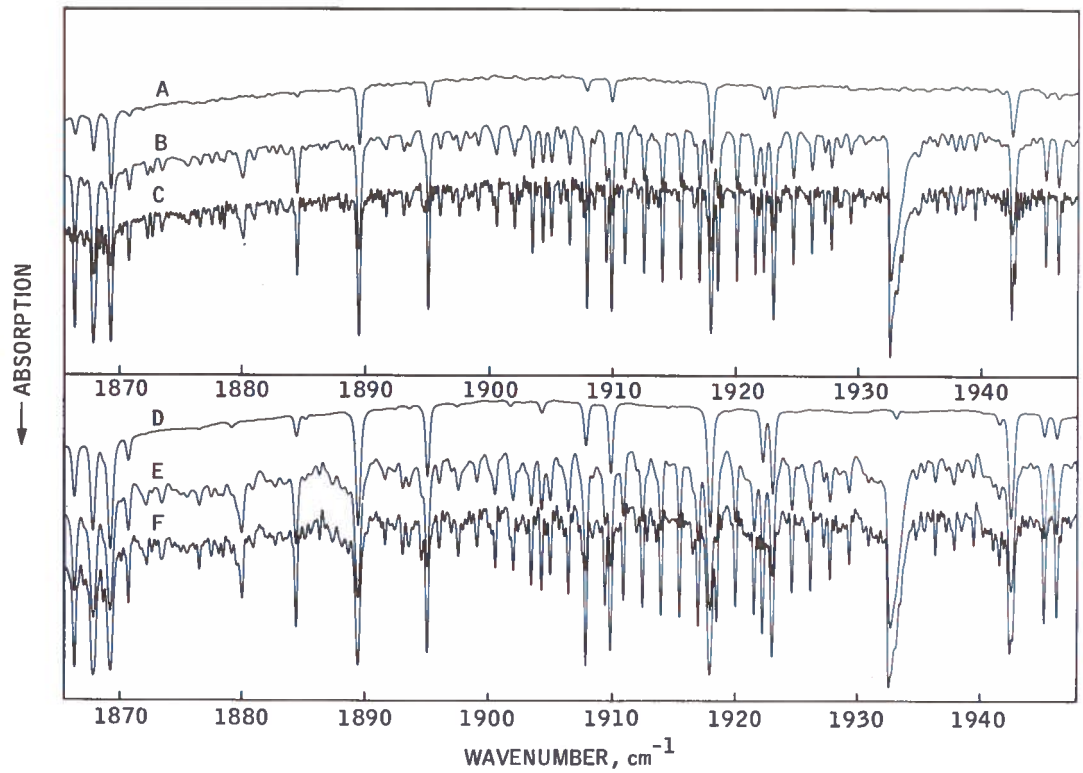

Figure 6. Two sets of spectra in the region of the 1-0 band of NO. The upper traces (A and D) are internal calibration scans, the middle traces (B and E) the unmodified solar spectra, and the bottom traces (C and F) resolution-enhanced versions of B and E, respectively.

On the other hand, Goldman et al. (1973) have given mixing ratios (from the ν_3 band) of 0.33 ppmv (tropopause) to 0.18 ppmv (18 km); these results are derived from recent (1972) observations and can be compared with their earlier (Goldman et al., 1970) value of 0.11 ppmv at 13 km altitude. It is possible that the difficulties of spectral fitting in the analysis of the strong ν_3 absorptions, alluded to above, are the cause of a systematic underestimation of the true absorption of N_2O in this region, resulting in a low estimate of the N_2O mixing ratio. Again, the data available at present are not sufficient to rule out the possibility of large (i.e., factors of 2 or 3) natural variations in the N_2O abundance in the lower stratosphere.

Nitric Oxide

The first spectra which were obtained showing NO features (from the 1-0 band in the 1900 cm^{-1} region) were recorded at a relatively low altitude (11 km); the NO absorptions were weak and close to the detection limit, so that we were unable to derive more than an estimate of the total molecular abundance over the optical path. The result, 1.0 ppbv (Toth et al., 1973), was given in terms of the *apparent* mixing ratio of NO *assuming constant mixing.* A major difficulty with the analysis of the data at the time was that we could not be sure to what extent the NO lines were blended with other very weak absorptions of CO_2, N_2O, and solar CO.

The 001 and 002 observations yielded a large number of additional spectra taken under more favorable conditions of observational geometry, covering solar zenith angles between 88 and 92°, from which the mixing ratio of NO could be determined within a more restricted altitude range close to the observation altitude ($\approx$ 16 km). In addition, the S/N ratio in the spectra from all of the flights was sufficiently high to allow deconvolution techniques to be used in the later numerical treatment of the data. By this

means sufficient resolution enhancement was achieved to resolve many of the blends between the NO lines and those of the interfering molecular species.

Figure 6 shows two sets of spectra covering the 1865 to 1945 cm^{-1} region; each of the sets consists of an internal calibration scan (upper trace), the unmodified solar spectrum (middle trace), and the resolution-enhanced version (lower trace). The region between 1870 and 1915 cm^{-1} which contains many of the stronger NO transitions is shown in more detail in Figure 7, for four separate observations, after the deconvolution process has been applied. An example of the separation of closely blended lines can be seen in the low frequency shoulder of the strong $3\nu_2$ CO_2 line (P42) at 1900.6 cm^{-1}. The weak feature closest to the center of the latter (at 1900.36 cm^{-1}) is a combination of a solar CO transition with P23 of the "hot" CO_2 band $4\nu_2{}^2 - \nu_2{}^2$. The adjacent weak line at 1900.08 cm^{-1} is the unblended R 6(½) line of NO.

While the deconvolved spectra show several NO lines which can be used in the determination of total column abundances and the mixing ratio at altitudes up to that of the observation altitude, the detailed analysis of the spectral

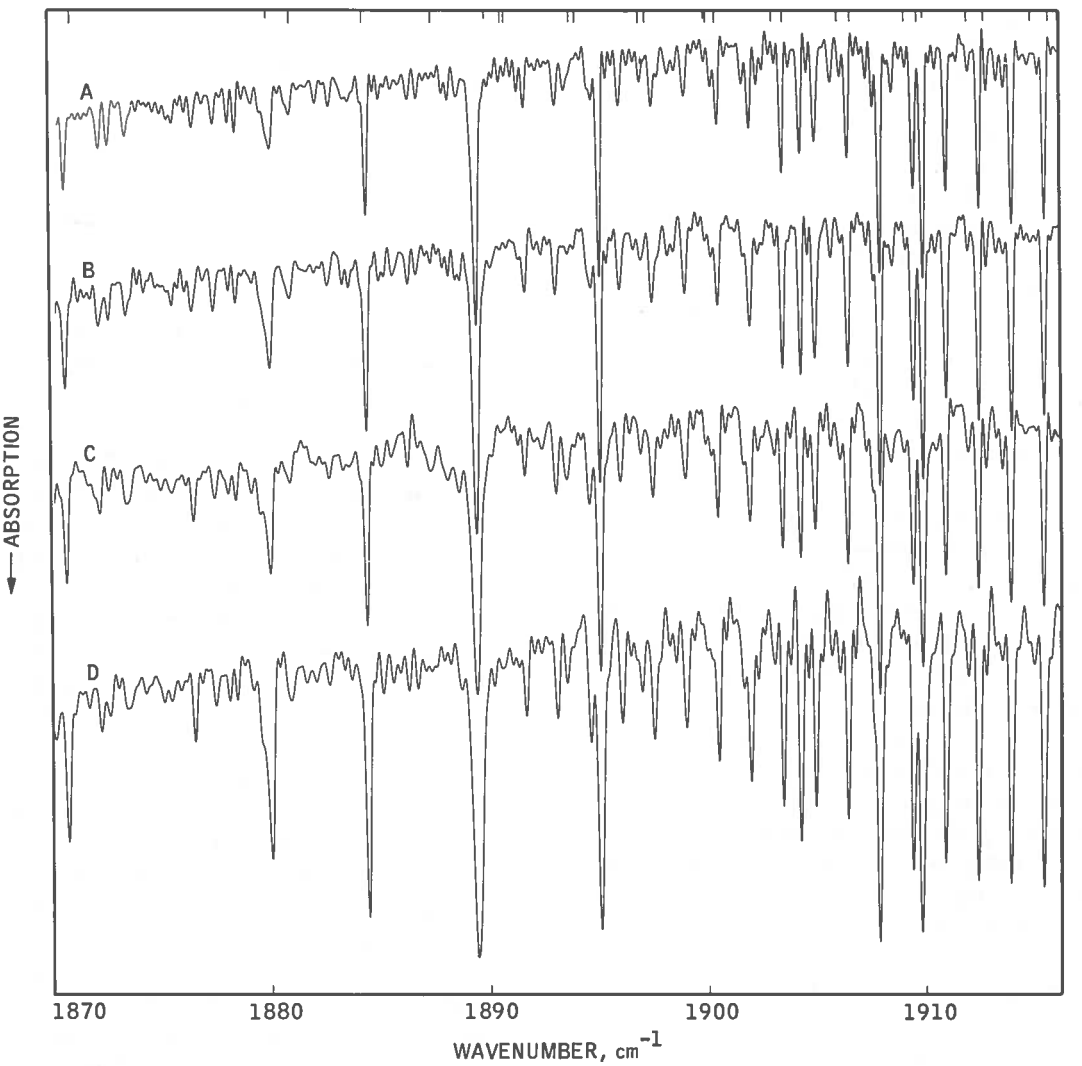

Figure 7. Portions of deconvolved spectra from four separate observations at different solar zenith angles in the R-branch region of the 1-0 NO transition. The large features in these spectra are principally due to CO_2 and H_2O.

region cannot be completed until all of the required molecular parameters for the weak interfering bands have been determined. The laboratory studies necessary for this purpose are under way at the present time; the results obtained thus far, particularly for the isotopic and "hot" bands of CO_2, indicate that the contributions from other molecules to the absorptions at the NO line frequencies do not significantly affect the derived NO abundances. The range of values for the NO mixing ratio between 11 and 16 km given in Table 1 (viz., 1 to 4×10^{-10} by volume) represents a preliminary indication only, based on the partially complete laboratory data obtained up to the present time. The final results, together with a detailed account of the analysis of the 1-0 NO region of the spectra, will be given in a later paper.

Nitrogen Dioxide

As was mentioned in the introduction, it was decided that the spectral range of the instrument during the Concorde flights should be limited to a long-wavelength cut-off at ≈ 5.5 μm, in view of the superior resolution achieved by the Girard instrument at the longer wavelengths.

As a result, only the weak $\nu_1 + \nu_3$ band (at 2906 cm^{-1}) could be used for the search for NO_2 in the spectra; it is some 30 times less intense than the ν_3 band (1617 cm^{-1}) observed by Girard (Fontanella et al., 1974). Furthermore, the $\nu_1 + \nu_3$ band is severely blended with the numerous lines of CH_4 which are present throughout this spectral region. Analysis of the very few features which can be confidently identified as NO_2 lines yields the somewhat uncertain value for the mixing ratio of NO_2 at 16 km of 1.3 ± 0.5 ppbv. The relatively large errors quoted with this value contain, in addition to the normal experimental error, an estimate of the maximum extent to which the NO_2 absorptions may be enhanced by contributions from other gases (principally CH_4). In spite of the difficulties with the analysis, the result appears to be in reasonable agreement with the new values of Fontanella et al. (1974) and Murcray et al. (1974) for the lower stratosphere.

Hydrogen Chloride

Interest in the determination of the concentration of chlorine compounds in the stratosphere has increased markedly over the past year, in view of the role which chlorine could play in the catalytic destruction of ozone, much like that of oxides of nitrogen in the very low stratosphere.

The most probable source of stratospheric chlorine is HCl, through its reaction with the hydroxyl radical

$$HCl + OH \rightarrow Cl + H_2O \qquad (1)$$

The reaction of chlorine atoms with ozone is very rapid,

$$Cl + O_3 \rightarrow ClO + O_2 \qquad (2)$$

and the chlorine atom can be regenerated by reaction of the chlorine oxide with either atomic oxygen or nitric oxide

$$ClO + O \rightarrow Cl + O_2 \qquad (3)$$

$$ClO + NO \rightarrow Cl + NO_2 \qquad (4)$$

Although the rates for these two reactions are similar, in the lower stratosphere the nitric oxide concentration is greater than that of atomic oxygen by three or four orders of magnitude, so reaction (4) is the predominant mechanism for regenerating chlorine atoms. Thus the two catalytic processes ($NO + O_3$ and $Cl + O_3$) are interconnected in the lower stratosphere, and the net effect of the presence of HCl in concentrations comparable to that of the NO is to accelerate the chain decomposition of O_3 (Wofsy and McElroy, 1974).

While chlorine compounds are known to be present at volume concentration levels on the order of 10^{-9} in the atmospheric boundary layer over the oceans (Junge, 1957; Chesselet et al., 1972) it is unlikely that this source would provide a very large contribution to the stratosphere by upward diffusion. Indeed, the relative mixing ratio has been found by in-situ methods to have fallen off considerably within 3 km of the surface. This is confirmed by the evidence from ground-based spectral observations, which suggests that the average volume mixing ratio of HCl in the troposphere (that is, averaged over the first scale volume) is less than 3×10^{-10}. The maximum scale height for HCl implied by the latter is again ≈ 3 km, so the stratospheric

concentration (at, say, 15 km altitude) for HCl originating at the ocean surface would be less than 5×10^{-11}.

Stolarski (1973) has discussed a perhaps-more-likely alternative: the injection of chlorine into the stratosphere from volcanic eruptions. If chlorine compounds were to be detected in the stratosphere, the determination of their vertical mixing profile through the troposphere and lower stratosphere would be of great help in distinguishing between these alternative sources.

The strong 1-0 fundamental band of HCl occurs at 2806 cm^{-1}, and the frequencies of several of the more intense P and R branch lines (i.e., those of low J) lie in the relatively transparent "microwindows" between the main manifolds of the ν_3 CH_4 band which dominates this region of the stratospheric spectrum. The search for these lines in the spectra thus provides a good test for HCl; if the lines are absent, an upper limit to the HCl concentration may be set. With the present instrument detection capability this limit is of the order 10^{-10} by volume. However, again as a result of the sensitivity of the window regions to contamination by weak lines of both methane and water vapor, the upper limits that can be achieved are critically dependent on detailed observation geometry. This is illustrated in Figure 3, which shows portions of two spectra covering the 2850 to 2970 cm^{-1} range. The upper trace corresponds to a solar zenith angle of 84° at an observation altitude of 11.9 km, and the lower trace to a zenith angle of 91° at 15.5 km altitude. The first three R-branch lines of HCl, which occur at 2925.9 (R1), 2544.9 (R2) and 2963.3 (R3) cm^{-1}, are located far enough away from strong absorptions to enable them to be detected at fairly small total column abundances. R2 provides the best example: on the upper curve of Figure 3, the spectral intensity over the frequency range within several resolution widths of the position of R2 reaches the continuum level, and no absorption of equivalent width greater than 2×10^{-3} cm^{-1} can be discerned in any of the spectra obtained under observation conditions similar to that reproduced in the figure. Using the line intensity values given by Toth et al. (1970) corrected to a mean stratospheric temperature of 220K, such estimates of the minimum detectable equivalent widths yield an upper limit for the total column abundance of 5×10^{15} molecules cm^{-2}. This value would be equivalent to an upper-limit mixing ratio of 1.8×10^{-10} (by volume) *if the gas were uniformly mixed.* Of course, the upper-limit value for the total column abundance does not preclude the existence of higher mixing ratios than the latter, over a limited altitude range – i.e., a stratified distribution.

For spectra recorded under conditions similar to that illustrated in the lower trace of Figure 3, however, the situation is different. In all of the spectra taken at zenith angles greater than 90° at the Concorde flight altitudes (15 to 16 km), absorptions are found to occur at the frequencies of the "detectable" strong HCl transitions. The total air mass for these observations is greater by approximately an order of magnitude than that for the previous observations (smaller zenith angle, 11.9 km altitude), so that the weak features are considerably enhanced and the "windows" correspondingly degraded. This can be seen by comparison of the two spectra reproduced in Figure 3. At present it is not known to what extent the spectra may be contaminated at the HCl line frequencies by weak lines of the other species active in the region. Consequently, it is stressed that the appearance of absorptions at the HCl line positions in the 16-km near-horizontal-path spectra cannot be interpreted as a *detection* of HCl. Detailed laboratory and theoretical studies are currently being undertaken to determine the maximum possible contributions from very weak CH_4 and H_2O transitions to the absorption at the HCl line frequencies. If these should fail to account for the observed absorption, the results for the two cases described above, taken in combination, would imply the presence of HCl in the stratosphere, in a layer close to the 16-km observation altitude. For the summary given in Table 1, the results for the 11-km (NC 135) and the 16-km (Concorde) observations are listed separately, both being given as upper limits for the mixing ratio, assuming uniform vertical mixing.

Other Species

A number of other molecules, expected to be present as trace constituents of the lower stratosphere, are of interest in current studies as

either intermediate or final products of the photochemical processes which may influence the composition of this region of the atmosphere. Several of these have bands which fall within the spectral range of the observations and which may be detectable; these include H_2O_2, H_2CO, SO_2, NH_3, N_2O_5, and NO_3, and the spectra are currently being searched for evidence of their presence. The absence of such absorptions in the spectra would allow improved upper limits to be placed on their total column densities, but here again a substantial amount of laboratory and numerical work is required, to determine line strengths for the molecules themselves and to evaluate the degree of contamination of the continuum and their nominal absorption frequencies, before minimum upper-limit values can be confidently assigned to each candidate species.

To date, this aspect of the analysis of the spectra has covered only the ν_1 and ν_5 bands of H_2CO (at 2782.4 and 2843.2 cm^{-1} respectively), for which a laboratory spectroscopic investigation was recently undertaken. Quantum assignments for a number of the lines of these bands have been made, and their transition strengths applied to the aircraft spectra suggest an upper-limit mixing ratio for H_2CO, assuming uniform vertical mixing, of not more than 2.4×10^{-9} by volume.

ACKNOWLEDGMENT

The success of an airborne measurement program of this type is critically dependent on the support provided by the aircraft personnel. For the Concorde flights in particular, optimization of the solar viewing conditions placed fairly rigid constraints on the aircraft with respect to its time of arrival at a given latitude and longitude and the specific heading at that time. The precision with which these rendezvous conditions were met by all of the Concorde flight crews was a measure of their understanding of the needs of the program and their desire to meet those needs, and made a vital contribution to the success of the measurement program. In the NC 135 series as well, the cooperation and support of the aircraft personnel in providing extended solar viewing periods and additional dedicated flights resulted in the acquisition of a great many more measurements than we had originally anticipated. We therefore gratefully acknowledge the cooperation and support provided by all of the flight crews and aircraft personnel who were involved in this program, and extend our sincere thanks for their contribution to its success. We would also like to express our gratitude to the HSI flight crew, Messrs. Harold Geise, Robert Perrin, and Robert Wilson, without whose services these measurements could not have been made.

This paper presents the results of one phase of research carried out at the Jet Propulsion Laboratory, California Institute of Technology, under Contract Number NAS 7-100, sponsored by the National Aeronautics and Space Administration, and under Contract DOT-AS-20094, sponsored by the Climatic Impact Assessment Program of the Department of Transportation.

REFERENCES

Barnes, W.L., J. Susskind, R.H. Hunt, and E.K. Plyler (1972), "Measurement and analysis of the ν_3 band of methane," J. Chem. Phys. **56**, 5160.

Benedict, W.S. and R.F. Calfee (1967), "Line Parameters for the 1.9 and 6.3 Micron Water Vapor Bands," Environmental Study Services Administration Professional Paper 2, U.S. Government Printing Office, Washington, D.C.

Burch, D.E. and D. Williams (1962), "Absorptance by nitrous oxide bands in the infrared," Appl. Opt. **1**, 587.

Chesselet, R.J., J. Morelli, and P. Buat-Menard (1972), *The Changing Chemistry of the Oceans*, Wiley Interscience, New York, 93-114.

Farmer, C.B., R.A. Toth, R.A. Schindler, and O.F. Raper (November 14-17, 1972), "Near infrared interferometric measurements of stratospheric composition to be made from the Concorde," in *Proceedings of the Second Conference on the Climatic Impact Assessment Program*, ed. A.J. Broderick, U.S. Department of Transportation, DOT-TSC-OST-73-4, 65.

Farmer, C.B. (1947), "Infrared measurements of stratospheric composition," Can. J. Chem. **52**, 1544.

Fontanella, J.C., A. Girard, L. Gramont, and N. Louisnard (1974), "Vertical distribution of NO, NO_2, and HNO_3 in the stratosphere as derived from infrared absorption spectra," in this volume.

Goldman, A., D.G. Murcray, F.H. Murcray, W.J. Williams, T.G. Kyle, and J.N. Brooks (1970), "Abundance of N_2O in the atmosphere between 4.5 and 13.5 km," J. Opt. Soc. **60**, 1466.

Goldman, A., D.G. Murcray, F.H. Murcray, and W.J. Williams (1973), "Balloon-borne infrared measurements of the vertical distribution of N_2O in the atmosphere," J. Opt. Soc. **63**, 843.

Harries, J.E. (1973), "Measurements of some hydrogen-oxygen-nitrogen compounds in the stratosphere from Concorde 002," Nature **241**, 515.

Junge, C.E. (1957), "Chemical analysis of aerosol particles and of gas traces on the island of Hawaii," Tellus **9**, 528.

Kyle, T.G. (1968), "Line Parameters of the Infrared Methane Bands," Scientific Report No. 1, prepared for Air Force Cambridge Research Laboratories, Bedford, Massachusetts.

Lowe, R.P. and D. McKinnon (1972), "Measurements of stratospheric methane over North America," Can. J. Phys. **50**, 668.

McClatchey, R.A., W.S. Benedict, S.A. Clough, E.D. Burch, R.F. Calfee, K. Fox, L.S. Rothman, and J.S. Garing (1973), "AFCRL Atmospheric Absorption Line Parameters Compilation," AFCRL-TR-0096, Environmental Research Papers No. 434, Air Force Cambridge Research Laboratories, Bedford, Massachusetts.

Murcray, D.G., A. Goldman, W.J. Williams, F.H. Murcray, T.W. Brooks, J. Van Allen, R.N. Stocker, J.J. Kosters, and D.B. Barker (1974), "Recent results of stratospheric trace-gas measurements from balloon-borne spectrometers," in this volume.

Schütz, K., C. Junge, R. Beck, and B. Albrecht (1970), "Studies of atmospheric N_2O," J. Geophys. Res. **75**, 2230.

Seiler, W. and P. Warneck (1972), "Decrease of the carbon monoxide mixing ratio at the tropopause," J. Geophys. Res. **77**, 3204.

Stolarski, R.S. and R.J. Cicerone (1974), "Stratospheric chlorine: a possible sink for ozone," Can. J. Chem. **52**, 8, 1610.

Tejwani, G.D.T. and P. Varanasi (1971), "Calculation of collision-broadened linewidths in the infrared bands of methane," J. Chem. Phys. **55**, 1075.

Toth, R.A., R.H. Hunt, and E.K. Plyler (1970), "Line strengths, line widths, and dipole moment functions for HCl," J. Mol. Spectrosc. **35**, 110.

Toth, R.A., C.B. Farmer, R.A. Schindler, O.F. Raper, and P.W. Schaper (1973), "Detection of nitric oxide in the lower atmosphere," Nature **244**, 7.

Toth, R.A. (1974), unpublished data.

Wofsy, S.C. and M.B. McElroy (1974), "HO_x, NO_x, and ClO_x. Their role in atmospheric photochemistry," Canad. J. Chem. **52**, 1582.

DISCUSSION

(UNIDENTIFIED): Do you have enough CO in the region south of 30° to get a vertical profile, to see whether the falloff in CO mixing ratio is perhaps in the upper troposphere?

FARMER: No, we don't have any data below 30° latitude. But we made very sure that we were not in the region of the sharpest falloff, just above the tropopause. I think that the falloff is much greater than Seiler and Warneck's result.

BARRETT: For our H_2 data going north at a latitude of 33°, we got about the same mixing ratio by mass, which would mean about 1.7 by volume. We're having difficulty understanding why the stratosphere should be so dry. Could you give any reason why you got such a low value? You didn't discuss the water spectrum.

FARMER: I skipped water because of our limited time here. Water is strange; everyone seems to have different values for it, which they firmly defend, so if ours is different from somebody else's that's perfectly consistent.

We have taken very great care to go through a large number of lines, and remeasure them in the laboratory, and they agree very well in general with the published strengths. We analyzed all the stratospheric data carefully, and looked at the geometry carefully, and we feel that over our latitude and altitude range that number – 2.3±4 ppmv – is correct. I don't know why this value might be different from someone else's, but there are systematic errors in each of the techniques that are used, and perhaps that's why the values appear to be at variance.

(UNIDENTIFIED): At what altitude would you apply that 2.3 figure?

FARMER: Well, we don't seem to detect much variation between about 12 and 18 kilometers. This is a rather small altitude range, but in that range there is also no significant variation with latitude between 35° and 75° north – in other words, the water vapor is uniformly mixed in the stratosphere between those spatial limits.

OBSERVATIONS OF THE SOLAR SPECTRUM IN THE 1800-2100 cm^{-1} REGION AND THE SEARCH FOR NO LINES

D.G. MURCRAY, A. GOLDMAN, W.J. WILLIAMS,
F.H. MURCRAY, J. VAN ALLEN, AND S.C. SCHMIDT
Department of Physics and Astronomy
University of Denver
Denver, Colorado

ABSTRACT: Observations of the variation with altitude of the infrared solar spectrum between 1800 and 2100 cm^{-1} are presented. The spectra were obtained with a balloon-borne grating spectrometer having a spectral resolution of ≈0.35 cm^{-1}. The spectra are interpreted in terms of solar CO lines and telluric H_2O, CO_2, and N_2O lines. Contributions from NO lines to the current spectra and to recently published solar spectra are examined. The observed absorptions attributed to NO are overlapped by features due to solar CO and telluric CO_2 or N_2O, so the quantitative analysis of the results appears uncertain. An upper limit of 1 to 3 ppbv is derived for the mixing ratio of NO in the lower stratosphere.

In a previous paper (Murcray et al., 1969a), a number of observations of the variation of the infrared solar spectrum between 1800 and 2100 cm^{-1} with altitude were presented. These observations were obtained during a balloon flight made on 23 March 1968. During a more recent balloon flight, made on 18 January 1972, a large number of new solar spectra in the 1800-2100 cm^{-1} region were obtained from various altitudes, from the ground up to 30 km. The instrumentation and the data-reduction procedures have been described in detail elsewhere (Murcray et al., 1967, 1969a). The major change made from the instrumentation described (Murcray et al., 1967) is the use of a liquid-helium-cooled Ge/Cu photodetector.

Figures 1 - 3 show three sets of transmittance samples, with four consecutive records in each set, in the 1800-2100 cm^{-1} region as obtained from various altitudes. The details of the records (i.e., altitudes, times, pressures, temperatures and sun zenith angles) have been tabulated earlier (Goldman et al., 1973a). Instrument spectral resolution is ≈ 0.35 cm^{-1}. The transmittance scale is offset by 20 percent from one record to another for clarification.

The spectra presented in Figures 1 - 3 show numerous absorption features which are due to atmospheric H_2O, CO_2, and N_2O. The dominant features of these absorbers have been discussed previously (Murcray et al., 1969a). Many of the features observed in the figures, however, do not change as a function of altitude or sun zenith angle and thus can be attributed to solar origin and ultimately interpreted as absorption lines due to CO in the solar atmosphere, similar to those observed in the 2100-2300 cm^{-1} region (Goldman et al., 1973b). The solar CO lines from the $\Delta v = 1$ bands contribute significant line structure in the 1750-2350 cm^{-1} region, on which the telluric absorption features are superimposed.

At the top of Figure 3, calculated CO line intensities at 4500K are presented; below that is a one-layer line-by-line calculated transmittance spectrum of the CO lines under the same conditions described in Goldman et al. (1973b). It can be seen that many of the solar CO lines are already well separated from the telluric lines on records obtained from ≈ 10 km, but in many instances a large solar line group coincides with a strong telluric absorption line still present at 30 km.

Recognition of the solar features is important for the interpretation of the solar spectra in terms of minor atmospheric constituents. The detection of unsuspected minor atmospheric constituents such as HNO_3 and NO_2 has been made possible by observing the solar spectrum from balloon altitudes during sunset (Murcray et al., 1968, 1969b; Goldman et al., 1970). Application of this method in the 1750-2350 cm^{-1} region is complicated by the presence of the solar lines. The complication is twofold: in the determination of the baseline envelope, and in the interpretation of weak line features.

A number of sunset spectra in the 1800-1970 cm^{-1} region were shown in Figure 10 of Murcray et al. (1969a). These spectra suggest that the 1840 to 1915 cm^{-1} region is relatively transparent and can be used for a search of lines from the NO (0-1) band, the Q branch of which occurs at 1875.8 cm^{-1}. In order to examine the interpretation of this region, Figure 4 shows several records obtained from about 30 km for both high sun (present flight) and setting sun (previous flight, (Murcray et al., 1969a)). Also shown are a one-layer line-by-line calculation of solar CO transmittance at 4500K and a two-layer line-by-line transmittance calculation, where the first layer is the previous solar CO layer, and the second layer is a horizontal atmospheric layer of five airmasses, at an effective temperature and pressure of T = 217K, P = 0.03 atm respectively, with 1 ppm H_2O, 330 ppm CO_2 and 0.2 ppm N_2O. This layer corresponds approximately to a path with sun zenith angle of about 93° at an observation altitude of about

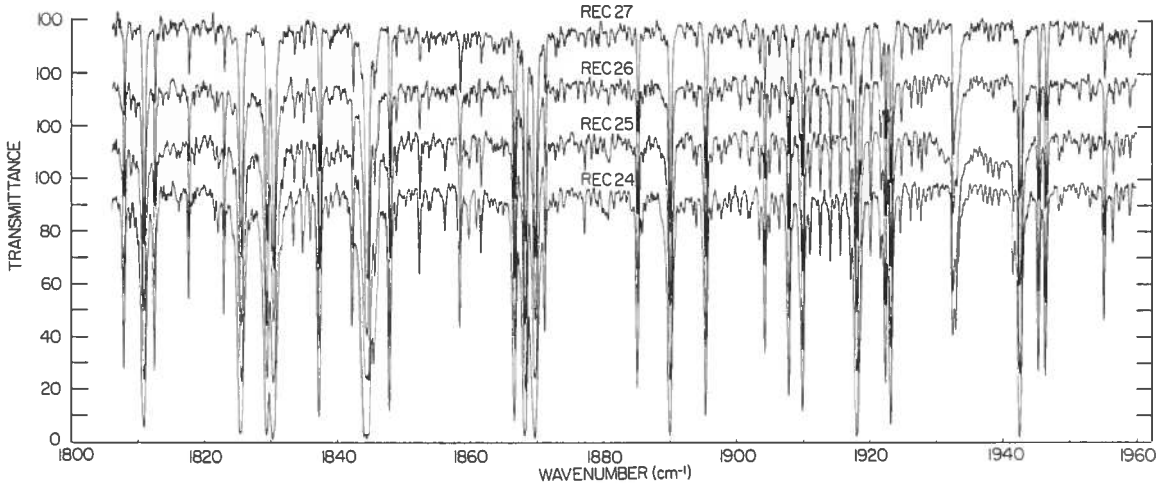

a. For the region 1800-1960 cm^{-1}

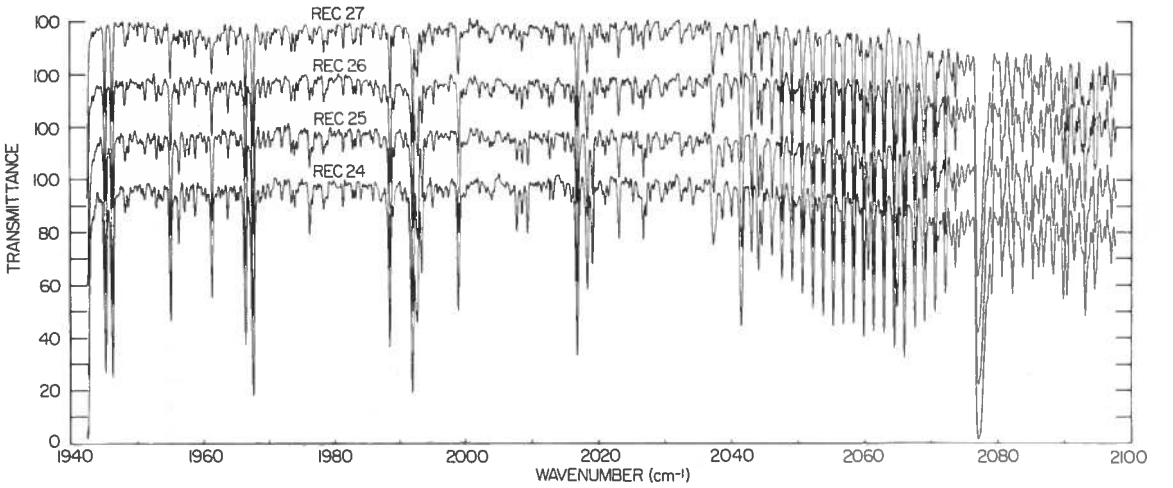

b. For the region 1940-2100 cm^{-1}

Figure 1. Observed spectral transmittance at various altitudes and solar zenith angles. Rec 24 at 8.4 km and 60.37°; Rec 25 at 9.1 km and 60.78°; Rec 26 at 9.8 km and 61.20°; Rec 27 at 10.5 km and 61.57°.

30 km. The atmospheric line parameters used were those compiled recently by McClatchey et al. (1973). The assumed resolution is 0.3 cm^{-1}.

In order to examine the data for possible contributions from NO lines, the combined effect of solar CO plus telluric H_2O, CO_2, N_2O, and NO has also been calculated. The individual line parameters of the fundamental band of NO (Goldman and Schmidt, 1974) were used in a similar two-layer line-by-line calculation with 5 ppbv NO. The results of this calculation are also shown in Figure 4. It is seen that the overall agreement with the experimental data is not changed by the addition of the NO lines. In some instances the calculations seem to accurately reproduce the weakest of the observed features, even without the NO lines, but in several cases the agreement with the weaker features is not complete. On the high-sun records many of the solar features are evident among the H_2O, CO_2, and N_2O lines. During sunset, considerable increase in the H_2O, CO_2, and N_2O absorption occurs and tends to mask significant portions of the solar features, but not always as predicted by the present calculations. The H_2O mixing ratio used here is too small, but increasing it would not improve the agreement for the weaker features. In view of the uncertainties in the line parameters of the solar CO lines (Goldman et al., 1973b), and of the telluric CO_2 and N_2O lines (McClatchey et al., 1973) in this spectral region, and the uncertainties in the approximations involved in the current two-layer transmittance calculations (Goldman et al., 1973a), the overall agreement is quite good. It is apparent that the identification of NO lines on these spectra would be rather uncertain.

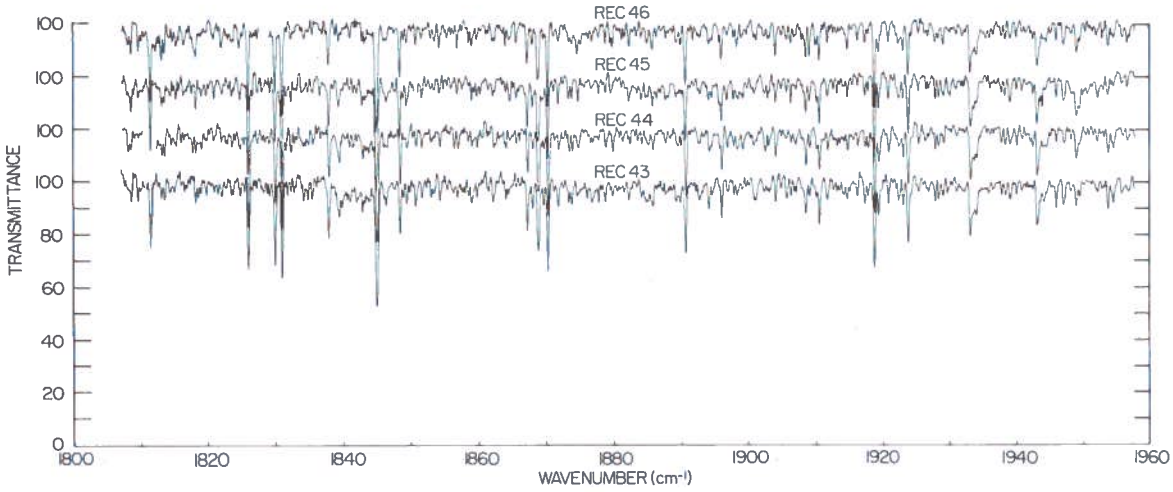

a. For the region 1800-1960 cm^{-1}

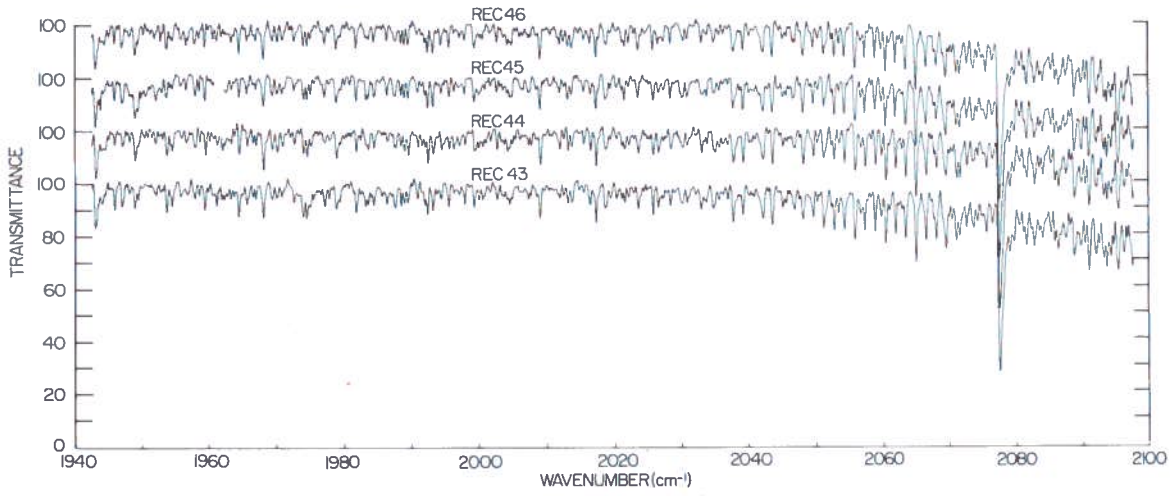

b. For the region 1940-2100 cm^{-1}

Figure 2. Observed spectral transmittance at various altitudes and solar zenith angles. Rec 43 at 18.3 km and 69.52°; Rec 44 at 18.8 km and 70.07°; Rec 45 at 19.5 km and 70.64°; Rec 46 at 19.9 km and 71.20°.

NO contributions can be suggested from a number of features, such as those near 1846.6, 1857.3, 1894.0 and 1897.0 cm^{-1}. These features are consistently enhanced on the data observed during sunset and are also enhanced when NO is added to the calculation for solar CO plus telluric H_2O, CO_2, and N_2O. Thus these observed features could be due to the P1(17/2), P1(11/2), R1(9/2) and R1(11/2) NO lines. However, similar features, but with weaker intensities, can be seen on the calculation of solar CO plus telluric H_2O, CO_2, and N_2O, and are mostly due to solar CO and telluric CO_2 with a smaller contribution from N_2O lines. Strictly, this allows only an estimate of ≈3 ppbv as an upper limit for the NO mixing ratio from the observed spectra, but the possibility of NO contributions is not ruled out.

The method of calculation used in Figure 4 can also be extended for comparisons with recent observations of the solar spectrum reported by Toth et al. (1973), by Girard et al. (1973), and by Ackerman et al. (1973a,b). These authors inferred several NO features from solar spectra obtained in the 1870-1910 cm^{-1} region and derived mixing-ratio values for NO in the stratosphere.

In order to examine the contribution of NO lines to spectra such as those presented in Toth et al. (1973), a series of calculations for solar CO and telluric H_2O, CO_2, N_2O, and NO lines in the 1870-1915 cm^{-1} region have been carried out for observations at an altitude of about 12 km. Figure 5 shows five separate one-layer calculations (curves A to E) of the individual contributions of solar CO and telluric H_2O, CO_2, N_2O, and NO

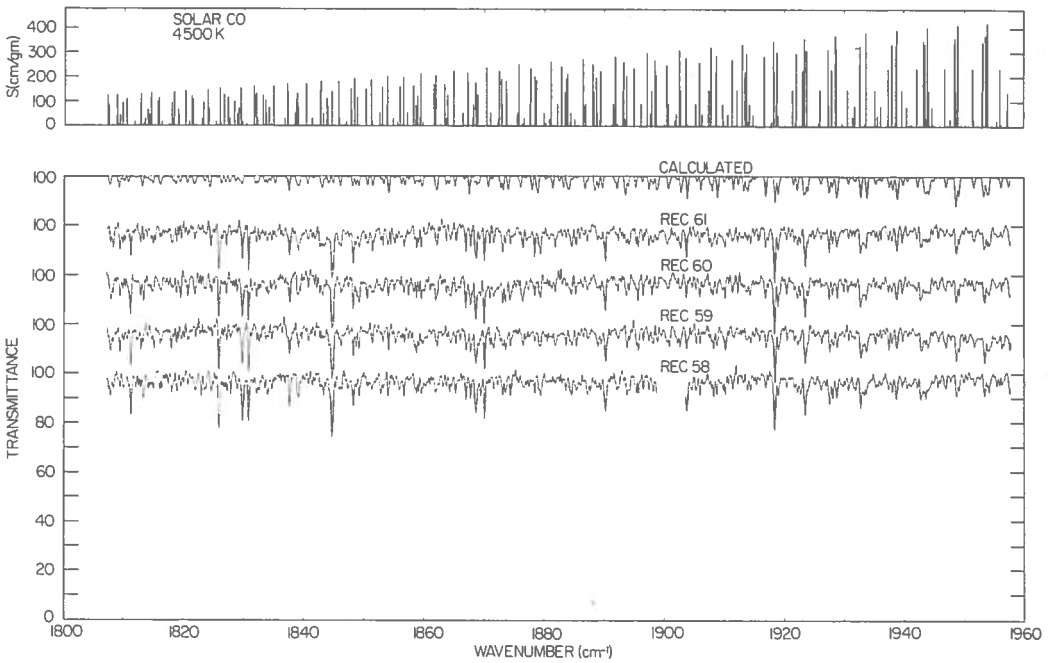

a. For the region 1800-1960 cm^{-1}

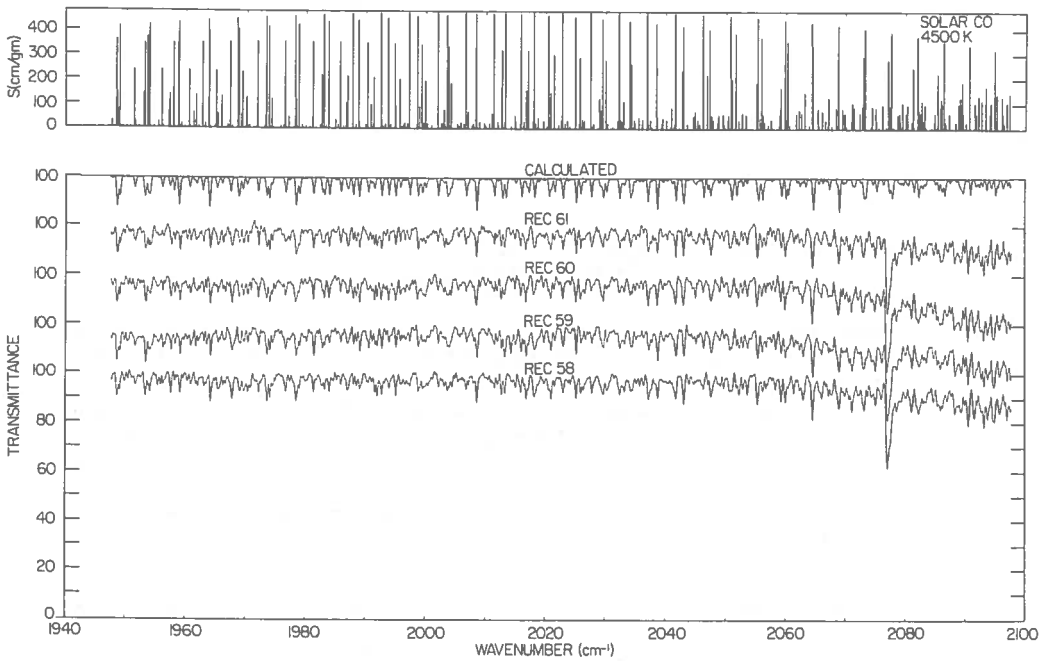

b. For the region 1940-2100 cm^{-1}

Figure 3. Lower four curves are observed spectral transmittance from various altitudes and solar zenith angles. Upper two curves are calculated solar CO line intensities and transmittance. Rec 58 at 26.6 km and 78.30°; Rec 59 at 27.2 km and 78.93°; Rec 60 at 27.7 km and 79.57°; Rec 61 at 28.3 km and 80.21°.

for 90° sun zenith angle. Curves F-G show the combined effect of solar CO plus telluric H_2O, CO_2, and N_2O in a two-layer calculation for both 90° and 70° zenith angles. For the 90° case, the combined effect of solar CO plus telluric H_2O, CO_2, N_2O, and NO is also shown (curve H).

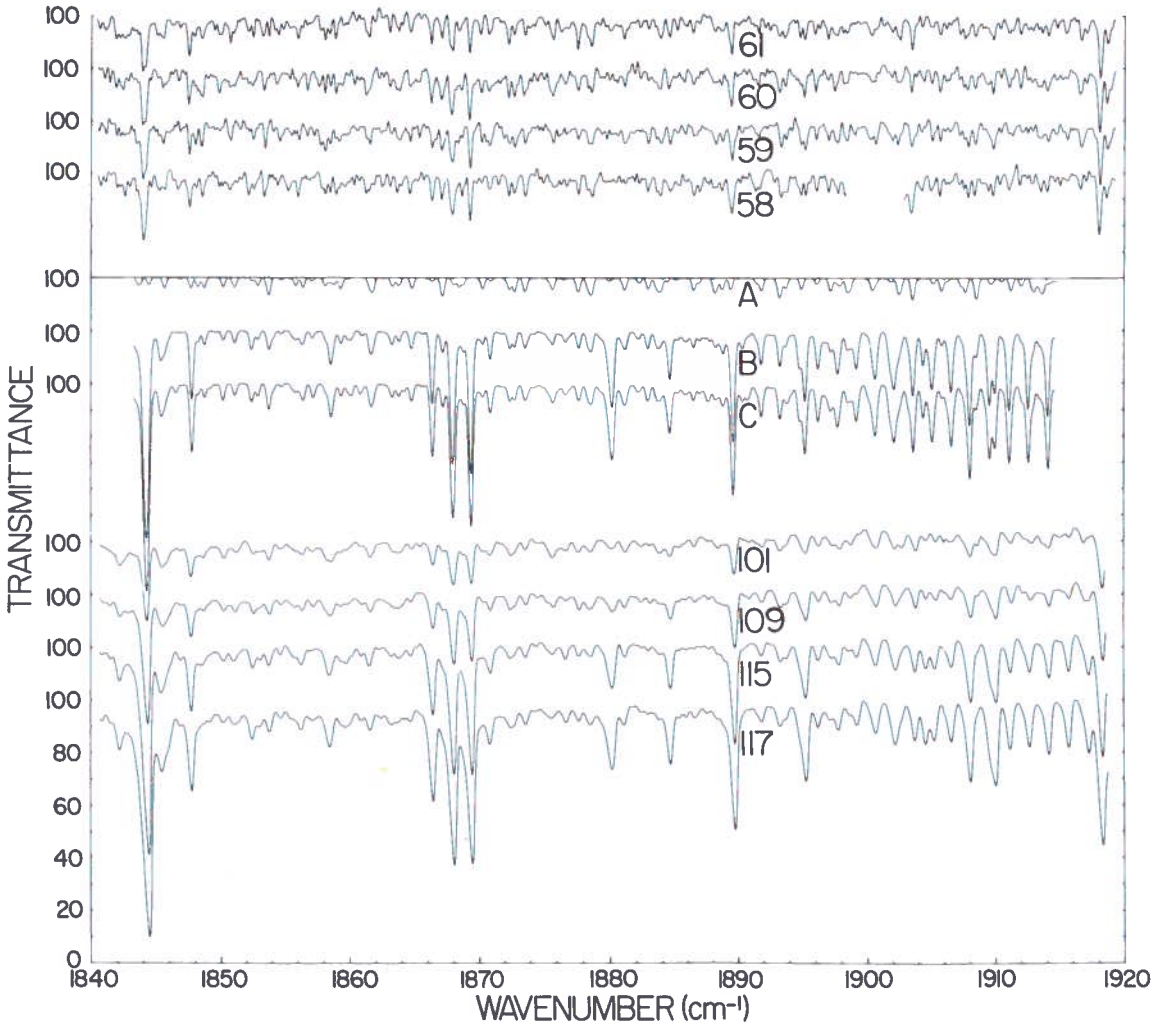

Figure 4. Upper four curves are observed spectral transmittance at various altitudes and solar zenith angles during the 18 Jan 1972 flight. Rec 58 at 26.6 km and 78.30°; Rec 59 at 27.2 km and 78.93°; Rec 60 at 27.7 km and 79.57°; Rec 61 at 28.3 km and 80.21°. Lower four curves are observed spectral transmittance obtained from 30.2 km during sunset on the 23 March 1968 flight (Murcray et al., 1969a). Solar zenith angles are 86.51°, 89.93°, 92.49°, and 93.42° for Records 101, 109, 115, and 117 respectively. Curves A to C are calculated transmittance for 30 km: A – one layer, solar CO; B – two layers, solar CO plus telluric H_2O, CO_2, and N_2O at 93°; C – two layers, solar CO plus telluric H_2O, CO_2, N_2O, and NO at 93°.

It can be seen from Figure 5 that many solar lines predicted by the calculation to be prominent at 12 km and 70° are in good agreement with the observations given in Figures 1 - 3 and in Toth et al. (1973). As expected, the enhancement by the telluric lines is significantly larger at 12 km than at 30 km. The overall agreement between the calculated spectra in Figure 5 and the observed spectra of Toth et al. (1973) is quite good, and several possibilities arise for NO identifications. The calculations show that the weak line observed at 1890.8 cm^{-1} could be largely due to NO, since none of the solar CO plus telluric H_2O, CO_2, and N_2O lines seem to occur there. The NO line near 1887.6 cm^{-1} is quite prominent on the calculated solar CO plus telluric H_2O, CO_2, N_2O, and NO spectra, but the corresponding calculation for solar CO plus telluric H_2O, CO_2, and N_2O also shows a small peak in the same region. It should be noted that the calculations show that the contribution of non-NO absorptions to the 1890.8 cm^{-1} peak is significantly smaller than their contribution to the 1887.6 cm^{-1} peak. The NO Q-branch at 1875.8 cm^{-1} is superimposed on solar CO and telluric CO_2 and N_2O lines, so the enhancement of this feature during sunset could be due largely to $CO_2 + N_2O$ lines rather

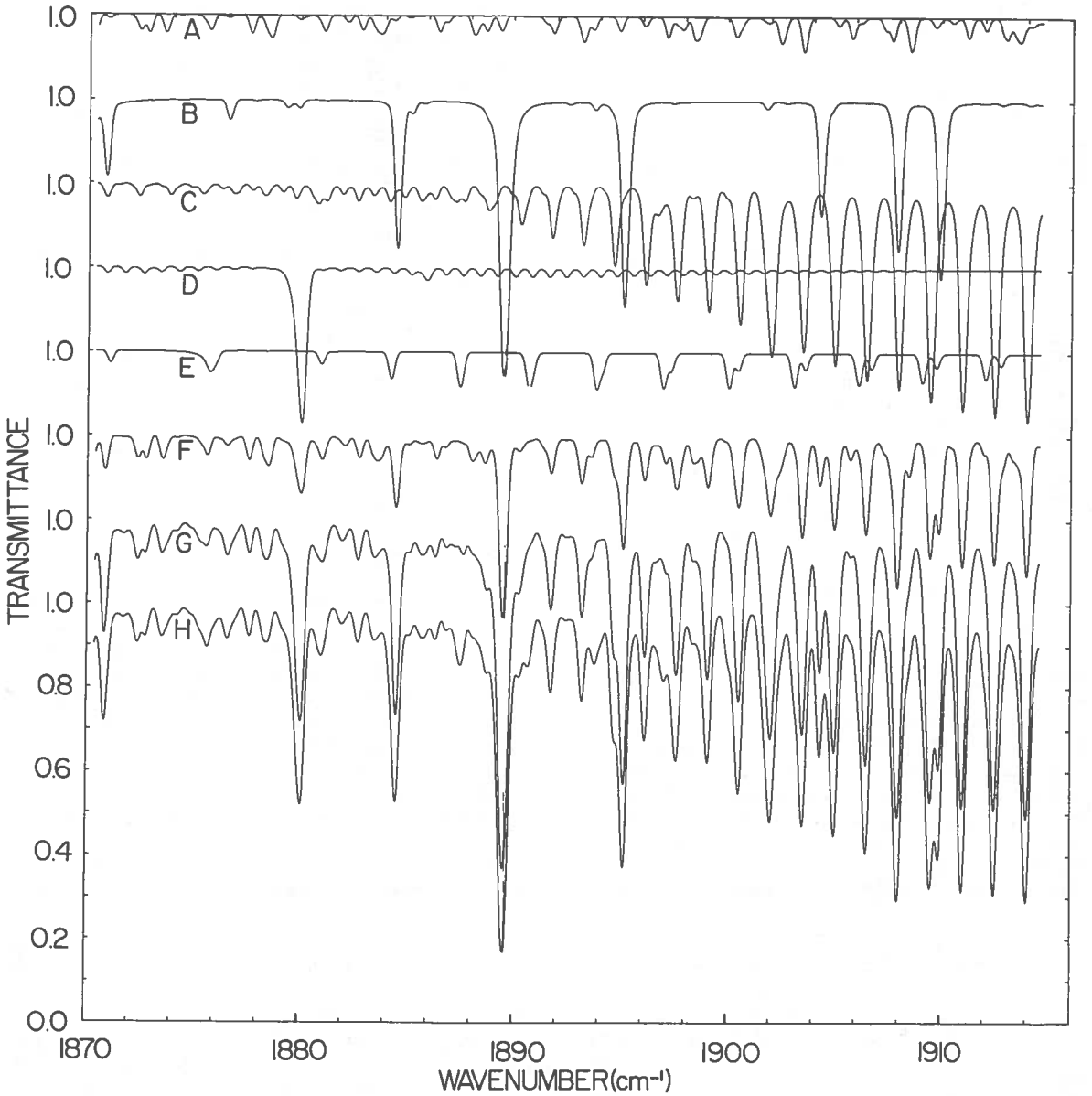

Figure 5. Curves A to E are one-layer transmittance calculations for individual molecules, at 12 km altitude and 90° sun zenith angle: A – solar CO; B – (telluric) H_2O; C – CO_2; D – N_2O; E – NO. Curves F to H are two-layer transmittance calculations for 12 km altitude: F – solar CO plus telluric H_2O, CO_2, and N_2O at 70°; G – solar CO plus telluric H_2O, CO_2, and N_2O at 90°; H – solar CO plus telluric H_2O, CO_2, N_2O, and NO at 90°. Resolution is 0.3 cm^{-1}.

than to the NO Q-branch (compare curves F, G, and H). It thus seems that while an NO contribution is possible, the determination of a (1.0 ± 0.2) ppbv NO mixing ratio (Toth et al., 1973) appears uncertain.

Since no spectra were presented in Girard et al. (1973), it is not possible at this time to make a comparison between calculated and experimental results.

For comparison with the spectra presented in Ackerman et al. (1973a,b), portions of the calculated spectra presented in Figure 4 have been recalculated with 0.1 cm^{-1} resolution. Here the 30-km, 93° path, temperature, and pressure (given above) have been used to approximate the 40-km, 94° path of Ackerman et al. The results are presented in Figure 6 for the 1896-1915 cm^{-1} region. It can be seen that the agreement with the stronger H_2O and CO_2 features of Ackerman et al. (1973a,b) is quite good. The observed solar CO lines seem weaker and more variable than predicted, but the "windows" in the solar CO spectrum near 1907 cm^{-1} and 1904.3 cm^{-1} are well reproduced by the calculation. It should be noted that on each side of the strong CO_2

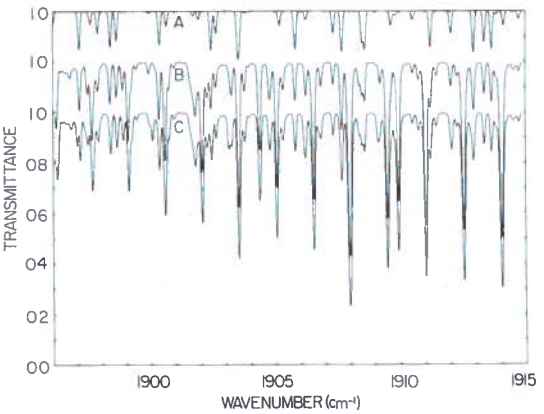

Figure 6. Curve A is a one-layer transmittance calculation for solar CO. Curves B and C are two-layer transmittance calculations for solar CO and telluric lines at 40 km altitude and 94° sun zenith angle: B – solar CO plus telluric H_2O, CO_2, and N_2O; C – solar CO plus telluric H_2O, CO_2, N_2O, and NO. Resolution is 0.1 cm^{-1}.

lines identified in Ackerman et al. (1973a,b), there is another CO_2 line whose intensity is ≈10% of the strong line. This is clearly seen from Figure 6 and the list of line parameters (McClatchey et al., 1973). The strong lines are due to the (11^102)-(00^001) transitions and the weaker lines are due to the (12^202)-(01^101) transitions (McClatchey et al., 1973). Thus the stronger 1903.545 cm^{-1} CO_2 line is accompanied by the two weaker 1903.257 cm^{-1} and 1903.774 cm^{-1} components, the 1905.031 line by the 1904.730 and 1905.297, the 1906.521 by 1906.214 and 1906.825, and the 1909.512 by 1909.212 and 1909.896. Figure 6 shows how the weaker CO_2 components overlap considerably with the NO lines marked in Ackerman et al. (1973a,b) at 1903.11, 1903.64, 1906.14, 1906.73, 1909.14 and 1909.78 cm^{-1}, and it seems that the inferred NO absorption could be largely due to these CO_2 lines. Unfortunately, laboratory data are not available for the intensity of these $\Delta\ell = 1$ CO_2 lines, and the quantitative analysis of the results is limited in accuracy.

In sum, it seems that the features attributed to NO in Toth et al. (1973) and Ackerman et al. (1973a,b) might have a measurable contribution due to NO lines. It must be concluded, however, that only an upper limit for the NO mixing ratio can be derived from the solar spectra available at this time. The comparisons of the present calculated spectra with the observed spectra presented here (Figures 1 - 4) and in Toth et al. (1973) and Ackerman et al. (1973a,b) indicate an upper limit of 1 to 3 ppbv for NO in the lower stratosphere. The recent stratospheric NO measurements by Ridley et al. (1973, 1974) using an NO-O_3 chemiluminescence technique indicate a NO mixing ratio of the order of 0.1 ppbv, which is in agreement with the upper limit deduced here.

It is evident that high-resolution spectra (better than 0.1 cm^{-1}) will allow a more detailed determination of stratospheric NO from solar spectra. Also, atmospheric emission measurements with a resolution of the order of 0.3 cm^{-1} could reveal more of the NO lines, since the problem of solar CO lines would be eliminated. This is demonstrated in Figure 7, where one-layer transmittance calculations are presented for H_2O, CO_2, and N_2O and for H_2O, CO_2, N_2O, and NO, without the contribution from the solar CO lines. It is apparent that the sensitivity to NO lines is greatly increased. The H_2O, CO_2, and N_2O lines can still play a significant role in masking the NO lines, however.

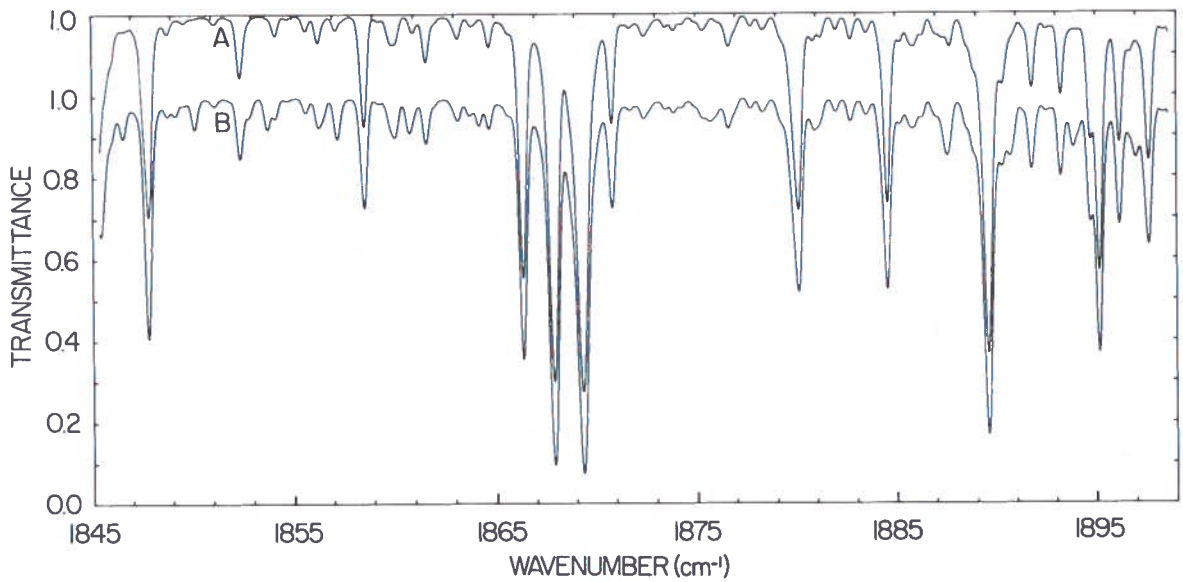

Figure 7. One-layer transmittance calculations at 30 km altitude and 93° sun zenith angle without solar CO: A – (telluric) CO_2, H_2O, and N_2O; B – CO_2, H_2O, N_2O, and NO. Resolution is 0.3 cm^{-1}.

Note added in Proof: Papers on stratospheric NO measurements presented at the Third Conference on CIAP strongly support the conclusions of the present paper. The chemiluminescence NO detector flown by Loewenstein et al. (1974) yields a mixing ratio of about 0.1 ppbv at ≈20 km. Also, a comparison of the measured and the calculated IR spectra presented by Fontanella et al. (1974) (Figures 5 and 19b and d) clearly show the dominant role of CO_2 in these spectra.

ACKNOWLEDGMENTS

Acknowledgment is made to the National Center for Atmospheric Research, which is sponsored by the National Science Foundation, for computer time used in this research.

This research was supported by the National Science Foundation, and by the Department of Transportation on the Climatic Impact Assessment Program, Grant GA-26228.

REFERENCES

Ackerman, M., J.C. Fontanella, D. Frimout, A. Girard, N. Louisnard, C. Muller, and D. Nevejans (1973a), "Observation de l'oxyde nitrique stratosphérique par spectrométrie d'absorption infrarouge en ballon," C.R. Acad. Sc., Paris, **277 B**, 33.

Ackerman, M., D. Frimout, C. Muller, D. Nevejans, J.C. Fontanella, A. Girard, and N. Louisnard (1973b), "Stratospheric nitric oxide from infrared spectra," Nature **245**, 205.

Fontanella, J.C., A. Girard, L. Gramont, and N. Louisnard, "Vertical distribution of NO, NO_2 and HNO_3 as derived from stratospheric absorption infrared spectra," in this volume.

Girard, A., J.C. Fontanella, and L. Gramont (1973), "Détection de l'oxyde azotique dans la stratosphère," C.R. Acad. Sc., Paris, **276 B**, 845.

Goldman, A., D.G. Murcray, F.H. Murcray, W.J. Williams, and F.S. Bonomo (1970), "Identification of the ν_3 NO_2 band in the solar spectrum observed from a balloon-borne spectrometer," Nature **225**, 443.

Goldman, A., D.G. Murcray, F.H. Murcray, W.J. Williams, J.N. Brooks, and C.M. Bradford (1973a), "Vertical distribution of CO in the atmosphere," J. Geophys. Res. **78**, 5273.

Goldman, A., D.G. Murcray, F.H. Murcray, and W.J. Williams (1973b), "Solar absorption in the CO fundamental region," Astrophys. J. **182**, 581.

Goldman, A. and S.C. Schmidt (1974), "Infrared spectral line parameters and absorptance calculations of NO at atmospheric and elevated temperatures for the $\Delta v = 1$ bands region," submitted to J. Quant. Spectrosc. Radiat. Transfer.

Loewenstein, M., J.P. Paddock, I.G. Poppoff, and H.F. Savage (1974), "In-situ NO and O_3 measurements in the lower stratosphere from a U-2 aircraft," in this volume.

McClatchey, R.A., W.S. Benedict, S.A. Clough, D.E. Burch, R.F. Calfee, K. Fox, L.S. Rothman, and J.S. Garing (1973)," AFCRL Atmospheric Absorption Line Parameters Compilation," AFCRL-TR-73-0096, Environmental Research Paper No. 434, Air Force Cambridge Research Laboratories, Bedford, Mass.

Murcray, D.G., F.H. Murcray, and W.J. Williams (1967), "A balloon-borne grating spectrometer," Appl. Opt. **6**, 191.

Murcray, D.G., T.G. Kyle, F.H. Murcray, and W.J. Williams (1968), "Nitric acid and nitric oxide in the lower stratosphere," Nature **218**, 78.

Murcray, D.G., F.H. Murcray, W.J. Williams, T.G. Kyle, and A. Goldman (1969a), "Variation of the infrared solar spectrum between 700 cm^{-1} and 2240 cm^{-1} with altitude," Appl. Opt. **8**, 2519.

Murcray, D.G., T.G. Kyle, F.H. Murcray, and W.J. Williams (1969b), "Presence of HNO_3 in the upper atmosphere," J. Opt. Soc. Amer. **59**, 1131.

Ridley, B.A., H.I. Schiff, A.W. Shaw, L. Bates, C. Howlett, H. LeVaux, L.R. Megill, and T.E. Ashenfelter (1973), "Measurements in situ of nitric oxide in the stratosphere between 17.4 and 22.9 km," Nature **245**, 310.

Ridley, B.A., H.I. Schiff, A.W. Shaw, L.R. Megill, L. Bates, C. Howlett, H. LeVaux, and T.E. Ashenfelter (1974), "Measurement of nitric oxide in the stratosphere between 17.4 and 22.9 km," Planet. Space Sci. **22**, 19.

Toth, R.A., C.B. Farmer, R.A. Schindler, O.F. Raper, and P.W. Schaper (1973), "Detection of nitric oxide in the lower stratosphere," Nature Phys. Sci. **244**, 7.

REPLY TO THE PAPER OF MURCRAY ET AL.

M. ACKERMAN, D. FRIMOUT, AND C. MULLER
Institut d'Aéronomie Spatiale de Belgique
Brussels, Belgium

and

J.C. FONTANELLA, A. GIRARD, AND N. LOUISNARD
Office National d'Etudes et de Recherches Aérospatiales
Châtillon, France

The preceding article by Murcray et al. (1974), entitled "Observations of the Solar Spectrum in the 1800-2100 cm^{-1} Region and the Search for NO Lines", concludes that solar spectra available at this time permit derivation of only an upper limit for the stratospheric NO mixing ratio. However, spectra taken in May, June, and July 1973 by means of balloon- and aircraft-borne spectrometers (Ackerman et al., 1973, 1974; Fontanella et al., 1974) have allowed us to determine the stratospheric abundance of nitric oxide. The sample spectrum shown in Ackerman et al. (1973, 1974) which corresponds to the tracing shown for 22.3 km in Figure 1 does not, of course, present sufficient information to permit the derivation of the published vertical distribution of NO; the whole set of spectra observed by means of the balloon-borne spectrometer flown in May 1973 was used. The spectra available to us will not be published until all the features observed have been satisfactorily interpreted. However, those pertinent to NO have been analyzed, and enable us to briefly report on the abundance of nitric oxide.

In the spectral range considered (1901.5 to 1915.2 cm^{-1}), many solar and telluric absorption lines occur; interference between several constituents is clearly a problem, particularly when relatively small absorptions have to be quantitatively interpreted. Murcray et al. (1974), considering the effect of CO_2, state that the inferred NO absorption could be largely traced to CO_2 lines of the $(12^202) - (01^101)$ transitions, whose intensity is 10% of that of the strong CO_2 lines of the $(11^102) - (00^001)$ transitions. The importance of these lines is overstated by Murcray et al., as shown below, and the comparison between the measured and the calculated IR spectra presented by Fontanella et al. (1974) for the conditions of the aircraft measurements at 15 km are not relevant to a criticism of the results published by Ackerman et al. (1973, 1974), which were obtained at 40 km. The integrated absorption cross-sections and positions of the CO_2 lines listed by MacClatchey et al. (1973) are in agreement (within experimental uncertainties) with our measurements, and have been used in our interpretation. Three NO lines, belonging to the R_{11} branch, have been used for the quantitative evaluation of NO in the optical path reported for the balloon experiment by Ackerman et al. (1973, 1974). They occur at 1903.112 cm^{-1}, 1909.139 cm^{-1} and 1914.993 cm^{-1}. They were chosen because they are the strongest components of the NO doublets considered, and are subject to the least contamination by other absorbers in the spectral range covered by the balloon-borne spectrometer. The NO line at 1903.112 cm^{-1} shows, in addition, a spectral separation from a nearby CO_2 line larger than the instrumental half-width; this can be seen in Figure 4 of the paper by Murcray et al. (1974), where, as stated by those authors, the 30-km, 93° path, temperature, and pressure have been used to approximate the 40-km, 94° path in Ackerman et al. (1973, 1974). The NO line at 1909.139 cm^{-1} is separated by only 0.10 cm^{-1} from the CO_2 line. The NO line is not, however, 10 times less intense than the main CO_2 line at 1909.512 cm^{-1}, as stated by Murcray et al. (1974), but about 70 times less intense. Its integrated absorption cross-section is more than 500,000 times smaller than the integrated absorption of the nearby NO line. For a CO_2 mixing ratio of 3×10^{-4} by volume, the CO_2 line has an absorption equal to the absorption of NO at a NO mixing ratio of the order of 6×10^{-10}. This is a value close to the published number for the altitude of 22.5 km. In addition, as shown in Figure 1a of this reply, the observation of spectra taken at successively larger solar zenith angles is very instructive. While the minimum altitude reached by the solar rays decreases, the absorption at 1909.1 cm^{-1} occurs at the same place and is progressively shifted below 25 km towards the position of the CO_2 line at 1909.2 cm^{-1}, showing the smaller and smaller contribution of NO, whose mixing ratio decreases with decreasing altitude. Above 30 km the NO absorption can be considered as uncontaminated by CO_2 and the quantitative evaluation is quite straightforward. For lower altitudes the CO_2 contribution can be evaluated specifically because the small CO_2 lines beside the main CO_2 lines occur twice as frequently in the spectrum as the NO doublets do.

Finally, no CO_2 line occurs close to the NO line at 1914.993 cm^{-1}. The evolution of this absorption feature from one spectrum to the next is shown in Figure 1b of this reply. The non-uniformly-mixed vertical distribution of NO in the stratosphere observed under the conditions of the balloon experiment is also quite obvious here, as was also concluded by Fontanella et al. (1974) (see their section on NO and Figures 4, 5 and 6).

From the experimental evidence presented here, it should be apparent that the interpretation of the data need not be restricted to setting an upper limit on the

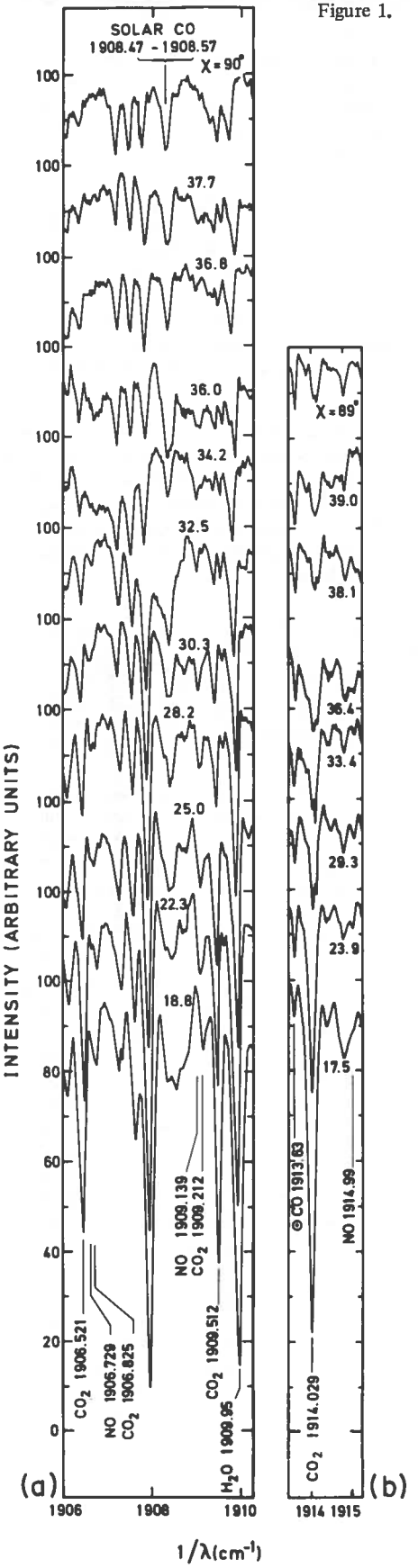

Figure 1. Intensity of solar radiation versus wavenumber recorded by means of the balloon-borne spectrometer (Ackerman et al., 1973).

a. The spectral region from 1906.0 cm^{-1} to 1910.2 cm^{-1} recorded during sunset is shown. The upper spectrum corresponds to a solar zenith angle, x, of 90°. For each of the other spectra x was larger. The minimum altitude reached by the solar radiation in the atmosphere is also indicated. Two main CO_2 lines are indicated at 1906.521 cm^{-1} and at 1909.512 cm^{-1}. Two small CO_2 lines are also marked at 1906.825 cm^{-1} and at 1909.212 cm^{-1}. According to MacClatchey et al. the integrated absorption is about 20% larger for the first one than for the second one. The first one is obviously resolved from the NO line at 1906.729 cm^{-1} that predominates at 30.3 km. The NO line at 1909.139 cm^{-1} was chosen for the evaluation already published because its integrated absorption is twice as large as that of the line at 1906.729 cm^{-1}. It can be considered as uncontaminated above 30 km, and its presence cannot be ruled out at $x = 90°$ or in the spectrum marked 18.8 km when the CO_2 contribution has been subtracted. Features remaining unchanged throughout the series of spectra are due to solar absorption. Some of them have not yet been identified; identification is in progress, using the spectra taken at higher solar elevations.

b. The spectral region from 1913.5 cm^{-1} to 1915 cm^{-1} recorded during sunset is shown. The upper spectrum corresponds to a solar zenith angle, x, equal to 89°. For each of the other spectra x was larger than 90° and the minimum altitude reached by the solar radiation in the atmosphere is indicated. The NO line observed at 1914.99 cm^{-1} is not contaminated by CO_2. It is separated by 0.45 cm^{-1} and by 0.34 cm^{-1} respectively from the two closest CO_2 lines, due to the $(12^202) - (01^101)$ transitions that occur at 1914.541 cm^{-1} and at 1915.328 cm^{-1}. This NO line has not been considered by Murcray et al. in Figure 4 of their paper, where the upper limit of the synthetic spectra is the solar CO line at 1914.73 cm^{-1}. The NO line appears clearly on the spectra at 38.1 km, 36.4 km, 33.4 km, 29.3 km, and 23.9 km, and is detectable at 39.0 km and 17.5 km. The solar CO line observed at 1913.63 cm^{-1} in this figure, and others shown in Figure 1, indicate that the solar absorptions computed by Murcray et al. (1974) under the same conditions as described by Goldman et al. (1973) are overestimated in intensity, and moreover do not represent the observed relative intensity distribution of the solar lines.

NO mixing ratio. It is evident, however, that no firm conclusion could have been derived from the observed spectral range if the resolution had been three times lower, as is the case for the experimental spectra published by Murcray et al. Their spectra yield about 10 times less information because the absorptions are three times less intense and three times less resolved. The situation would have also been less propitious if the observations had been performed from 30 km (as was the case for the experiments reported by Murcray et al.) instead of 40 km, since the geometric factors related to the shape of the earth make the method of limb observation more effective for depression angles of 3 to 5 degrees, corresponding to minimum altitudes of the solar grazing rays that are 10 to 25 km lower than the altitude at which the instrument is flown. For this reason, the availability of 11×10^6 ft^3 balloons was important.

In conclusion, we want to emphasize that it is evident from the arguments presented here that Ackerman et al. (1973) had spectra available to them that allowed the determination of stratospheric NO.

REFERENCES

Ackerman, M., D. Frimout, C. Muller, D. Nevejans, J.C. Fontanella, A. Girard, and N. Louisnard (1973), "Stratospheric nitric oxide from infrared spectra," Nature **245**, 205.

Ackerman, M., J.C. Fontanella, D. Frimout, A. Girard, L. Gramont, N. Louisnard, C. Muller, and D. Nevejans (1974), "Recent stratospheric spectra of NO and NO_2," Canad. J. Chem. **52**, 1532 (Aeronomica Acta **A-120**, 1973).

Fontanella, J.C., A. Girard, L. Gramont, and N. Louisnard (1974), "Vertical distribution of NO, NO_2 and HNO_3 in the stratosphere, as derived from infrared absorption spectra," in this volume.

Goldman, A., D.G. Murcray, F.H. Murcray, and W.J. Williams (1973), "Solar absorption in the CO fundamental region," Astrophys. J. **182**, 581.

McClatchey, R.A., W.S. Benedict, S.A. Clough, D.E. Burch, R.F. Calfee, K. Fox, L.S. Rothman, and J.S. Garing (1973), "AFCRL Atmospheric Absorption Line Parameters Compilation," AFCRL-T.R.-73-0096, Environmental Research Papers No. 434, Air Force Cambridge Research Laboratories, Bedford, Mass.

Murcray, D.G., A. Goldman, W.J. Williams, F.H. Murcray, J. Van Allen, and S.C. Schmidt (1974), "Observations of the solar spectrum in the 1900-2100 cm^{-1} region and the search for NO lines," in this volume.

SPECTROPHOTOMETRIC NITROGEN DIOXIDE MEASUREMENTS

A.W. BREWER AND C.T. McELROY
Department of Physics
University of Toronto
Toronto, Ontario, Canada

and

J.B. KERR
Atmospheric Environment Service
Downsview, Ontario, Canada

ABSTRACT: Because of the current uncertainty in the concentration of photochemically active gases in the stratosphere, a program has been established to measure the vertical profile of atmospheric nitrogen dioxide. Spectrographic measurements of NO_2 have been made both from the ground and from aircraft. The most recent series of measurements was made from the British prototype Concorde 002 during environmental flights made in October and November, 1973. These observations are added to previous measurements which were made at lower altitudes.

PRINCIPLE OF THE METHOD

Nitrogen dioxide strongly absorbs visible and near-ultraviolet light, and its absorption changes rapidly with wavelength for wavelengths between 0.43 μm and 0.45 μm, as shown in Figure 1. This characteristic permits atmospheric NO_2 to be measured by measuring its absorption of sunlight, with methods similar to those which have been used for measuring ozone for more than 50 years (Dobson, 1957). To this purpose, we have adapted a photon-counting spectrophotometer (Brewer, 1973) which was originally designed for ozone measurements.

The spectrophotometer measures intensities at wavelengths $\lambda_1 = 0.4377$ μm, $\lambda_2 = 0.4448$ μm, and $\lambda_3 = 0.4500$ μm with slit widths equivalent to about 0.3 nm. At these wavelengths, and for our slit widths, the solar spectrum is at stationary points and strong differential absorption by NO_2 is achieved. If I_1 is the measured intensity at λ_1 and so on, then after the three intensities have

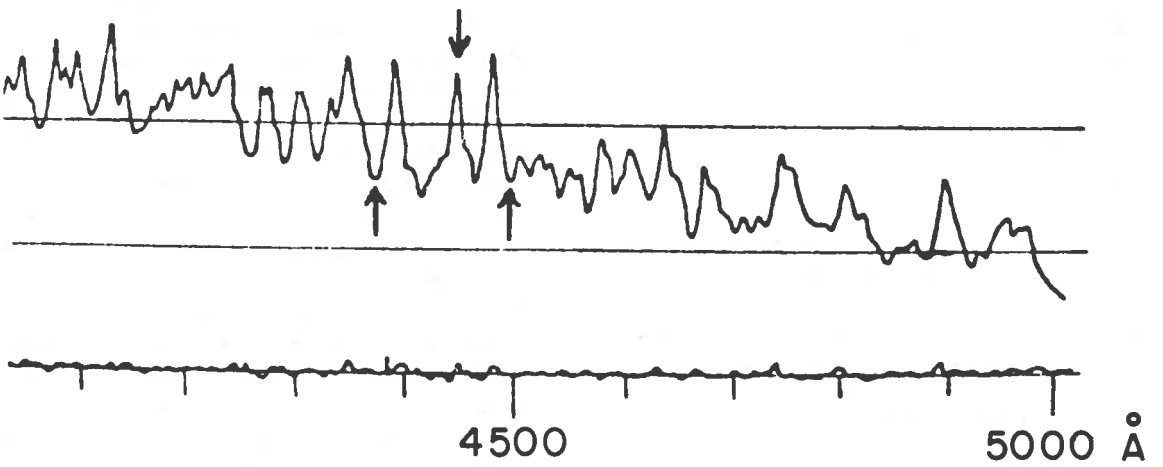

Figure 1. The absorption spectrum of NO_2 (Hall and Blacet, 1952). The three wavelengths used in this work are marked by arrows.

been measured, the function $F = \log_{10} [I_1/I_2] - 1.46 \log_{10} [I_2/I_3]$ is calculated [$1.46 = (\beta_2 - \beta_1)/(\beta_3 - \beta_2)$], ($\beta_1$ = Rayleigh scattering coefficient at λ_1, etc.). This function automatically eliminates Rayleigh scattering. Ozone absorption is reduced enough that it cannot cause interference. All effects for which the absorption at the three wavelengths is linear with wavelength, though perhaps not totally removed, are reduced so far as to be unobservable. On the other hand, a layer of NO_2 (at STP) 10 μm thick will increase this function by 0.007 (we can measure such an increase quite reliably, except when the intensities are extremely low). We do not know of any other trace gas that has enough wavelength-non-linear absorption to interfere with the measurement of NO_2 in this spectral region.

Using amounts of NO_2 comparable to those observed in the optical paths attained in the atmosphere, we have confirmed the exponential growth of absorption (see Figure 2) which has been reported by others (Hall and Blacet, 1952); we have also measured the value for the effective absorption coefficient, which is consistent with their published values. We have not determined whether temperature has a significant effect.

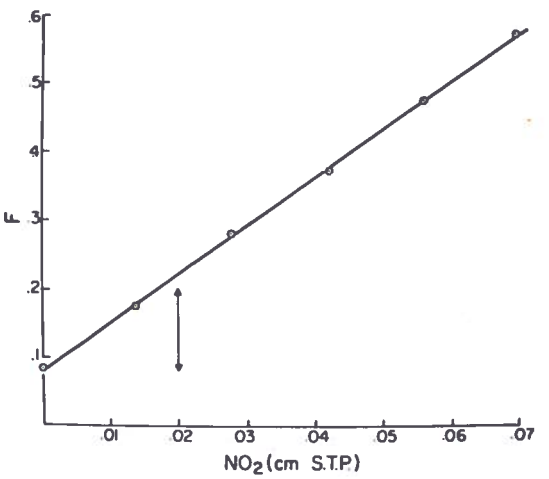

Figure 2. Growth of our function F with NO_2 amount. The vertical line indicates the largest NO_2 amount observed in atmospheric paths during this work.

As is done for ozone measurements, we have measured the three intensities in direct sunlight and also in the light scattered from the clear zenith blue sky.

Observations from the ground in southern Ontario, near Picton at 44°N, 77°W, in conditions of clear air (visibility greater than 30 km and with a cloudless sky), give measurements of which Figures 3a and 3b are typical. The differences between sunrise and sunset are persistent, and during the first half of 1973 the sky curves did not change to a detectable extent.

Sky measurements are valuable because they are equivalent to a measurement by an observer (rather diffuse) at the mean scattering height. The effective mean scattering height is shown in Figure 4. Taken together, the direct-sun and zenith-sky measurements enable us to measure the NO_2 below the scattering level. This may be seen as follows: the light from the direct sun passes obliquely through the lower layers, whose optical absorption is enhanced in proportion to the secant of the zenith angle. On the other hand, the light from the clear zenith sky is scattered downward by air at rather high levels, and it passes vertically through the low-level NO_2, whose absorption is thus not increased by obliquity. We usually assume that this low-level NO_2 is below 2 km. Deep convection may carry it upward into higher layers, but on the clear days when we take our measurements this will not usually be the case. As long as it is below 10 km it will not alter the conclusions we reach in this paper regarding stratospheric NO_2.

We can also measure the low-level NO_2 by climbing through it and observing the direct sun while we do so. We have made only two measurements of this kind. During one made at noon with a solar zenith angle of about 27°, we observed very little NO_2 in the lowest 2 or 3 km, less than we could measure with certainty, and much less than was measured at sunrise and sunset on the same day. The second measurement was made in the late afternoon with a solar zenith angle of 75°. The quantities found were less than we typically find at sunrise or sunset, but measurable. The actual concentrations found, which are assumed in the case of the observations made from the ground to be distributed through the lowest 2 km, are shown against the appropriate layer in Figure 5.

The NO_2 amount is quite variable but it is subject to a strong diurnal variation. There is very little when the sun is high. There is, on the average, about 50% more at sunrise than at sunset. Using direct moonlight, we have made

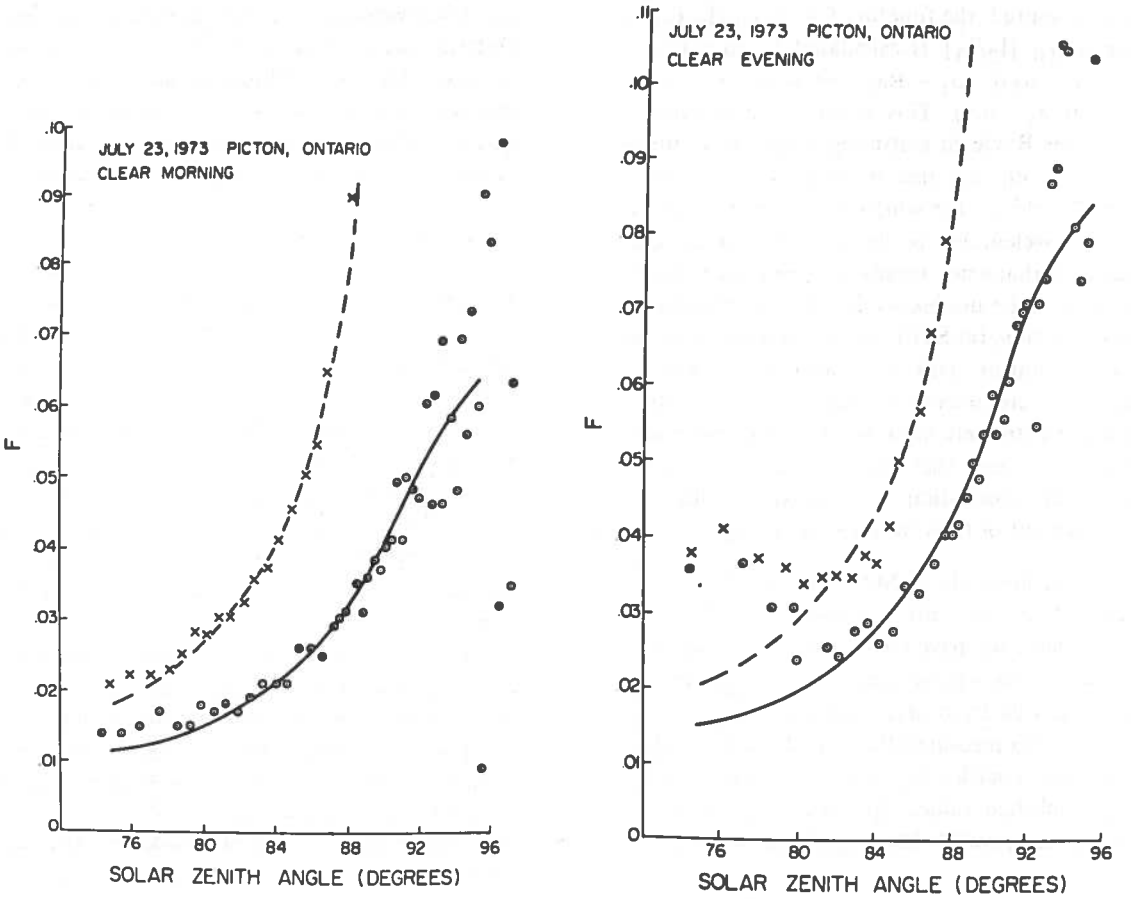

a. During sunrise.

b. During sunset.

Figure 3. Typical observation of the variation of our function F. Cloudless sky and clear air, visibility greater than 30 km. ×, observed direct sun. ⊙, observed zenith sky. - - - -, calculated direct sun. ——— , calculated zenith sky.

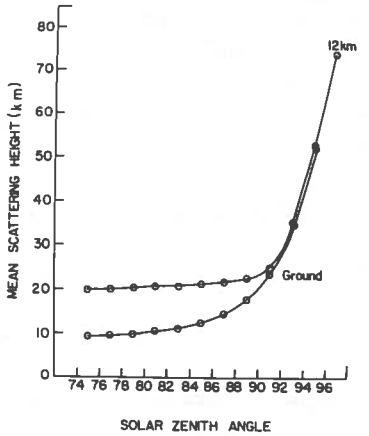

Figure 4. Calculated mean scattering height (km) in the zenith sky as a function of solar zenith angle (χ = 0.45 μm), as observed from the ground or an aircraft at 12 km. Cloudless skies and single scattering only are assumed.

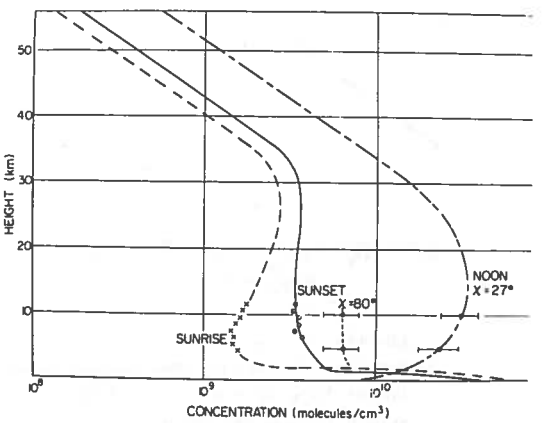

Figure 5. The vertical distribution of NO_2 concentration over southern Ontario, spring 1973, at sunset, sunrise, and high noon, as deduced from ground observations or measurements from an aircraft climbing to 10 km.

observations of NO_2 absorption; they have low accuracy but suggest that nighttime amounts of NO_2 are similar to those observed at sunrise.

NO_2 IN THE UPPER ATMOSPHERE

The upper-atmospheric distribution of NO_2 should be obtainable from the zenith-sky curves, as ozone's is from the well-known "umkehr" effect. For ozone, zenith-sky curves, such as those of Figure 3, show two turns or "umkehrs". The first occurs before sunset as the mean scattering level moves through the ozone layer, and the second occurs when the light path across the top of the ozone layer becomes important.

Except perhaps at the very end of the measurements, when the solar zenith angle is 96°, we find no umkehr. When we consider all our measurements, including the aircraft measurements which will be discussed later, we find that our measurements are best fitted if the NO_2 distributions at sunrise and sunset are as shown in Figure 5. Then, if we use a single-scattering model, which should be a good approximation at the wavelengths concerned, we get the calculated zenith-sky curves shown in Figure 3. The shape of these curves depends upon the distributions and amounts of NO_2, and their position depends both upon these and on the F_0 for our instrument, which we cannot measure directly, but which will be discussed further. (F_0 is the value of F which would be obtained when measuring sunlight with zero NO_2 in the optical path.)

It will be noticed that the fit of the calculated curves in Figure 3 is good for $\chi > 85°$, but for higher suns the observations lie above the curves, especially in the late afternoon. We interpret this as showing that there is considerably more NO_2 in the upper atmosphere during the daytime. It is decreasing during the late afternoon to the sunset values, often with a considerable collapse at $\chi \approx 80°$. More NO_2 is seen at sunset than at sunrise, and in the morning at $\chi \approx 80\text{-}85°$ the NO_2 increases again, but usually more slowly than it collapses in the evening.

F_0 is usually determined by plotting the observed value of F against the secant of the sun's zenith angle. If the amount of NO_2 were constant, this would give a straight line which would extrapolate to F_0 at sec $\chi = 0$, and its slope would be the amount of NO_2. As can be seen in Figure 6, which shows direct sun

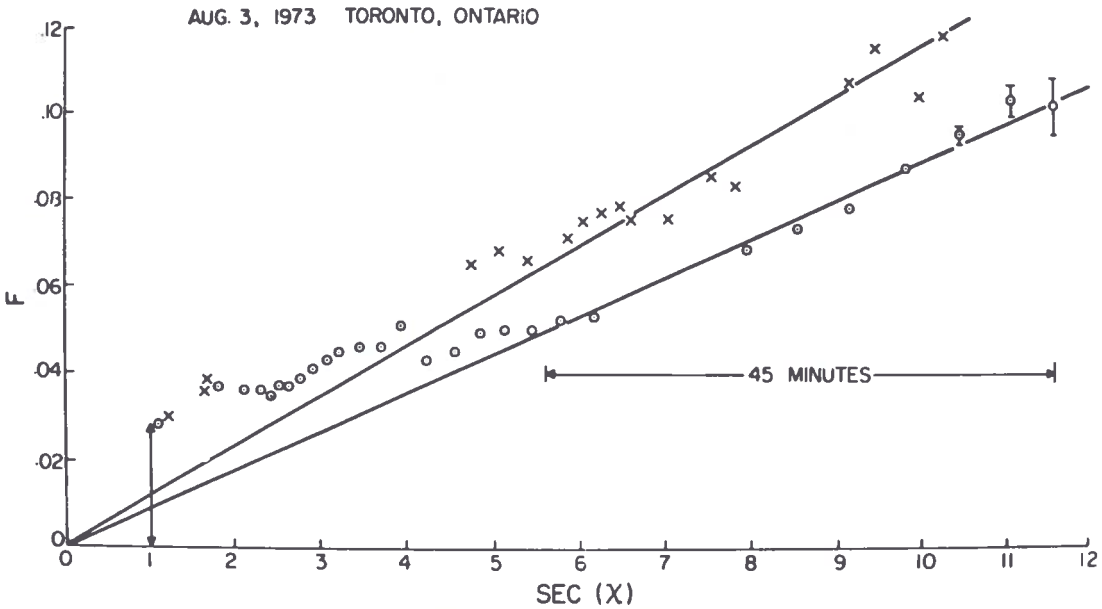

Figure 6. Observations of our function F in direct sunlight throughout one day. There were some cloud patches present and considerable haze at sunrise; visibility was greater than 20 km at noon and greater than 10 km at sunset. X, afternoon; ⊙, morning. sec (χ) is the effective secant, calculated on the assumption that the NO_2 is at an average height of 20 km. The vertical arrow corresponds to the values of F and χ expected for an overhead sun.

measurements, the measurements do not lie in a straight line, but if we use values near sunrise or sunset (when sec χ is changing rapidly) we can extrapolate the line to an F_0 which we have normalized to zero.

The high-noon NO_2 amounts are then given by the readings relative to F_0, when the value of sec χ is close to 1. This F_0 is consistent with the F_0 required to give a best fit to the sunset or sunrise umkehr curves which are discussed above. It gives a total NO_2 overhead at high noon of 3 or 4×10^{-3} atm. cm. When we combine this total amount with the concentration in the lower atmosphere which was observed by climbing through it in an aircraft, and use a curve of the same basic shape as the sunrise-sunset curve, we get the curve marked "noon" in Figure 4 as a suggested distribution for midday.

CONCORDE MEASUREMENTS

We can get good values of the NO_2 concentrations which occur at sunrise or sunset if we observe the rising or setting sun from an aircraft. The measurements of concentrations at the level of the aircraft, or below it, are independent of F_0, the uncertainty of which is a serious problem for upward-looking measurements. As the sun moves through zenith angles greater than 90°, the increases in the optical path lengths occur at the tangent height, and thus the concentration there can be observed accurately. We have made such measurements in flights at 11 km over western Quebec in June 1973, and at 15.5 km (about 100 mb) over the Bay of Biscay in Concorde 002 in October-November, 1973. Figure 7 shows one of three sunset curves and one of two sunrise curves, all measured from Concorde.

At zenith angles of 90° (when the reading of our instrument is affected by the NO_2 above the flight level) the Concorde readings were very similar to those obtained in June 1973, over western Quebec (Val d'Or). This suggests that there is very little *seasonal* variation in the NO_2 above 15 km. The evening NO_2 is a little more than that present at sunrise, so there is a small diurnal hysteresis.

For the periods when the sun was below 90° zenith angle, however, the shape of the morning curve is different from that part of the evening

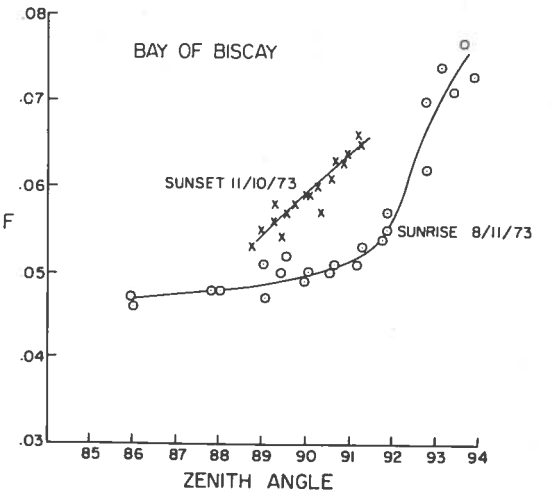

Figure 7. Direct-sun observations made from Concorde. The values of F are normalized to the F_0 derived in Figure 6.

curve which we were able to observe, and the corresponding NO_2 concentrations are consequently rather different. It seems that the difference between sunrise and sunset mainly occurs in the levels at and below 100 mb, and that at these levels there may also be a considerable seasonal variation.

A final curve of NO_2 mixing ratio versus height, including these observations, is shown in Figure 8.

At sunrise the NO_2 below 10 km was the same over the Bay of Biscay in October-November as it had been in Ontario in June, but the Concorde flights indicated low concentrations around 16 km, whereas the June flights did not, although because of the lower level of the latter flights we have no direct measurement. We did not get any low-level measurements from the Concorde evening flights because of the presence of clouds. The high-noon values shown are those deduced from measurements in June over Ontario. These noon values are subject to an uncertainty of the order of ±50%.

We may add that these regions where the hysteresis is large are those where the ozone concentration is low; in the fall particularly there is a very strong tendency for the ozone to show a minimum concentration at about 15 km (Brewer and Milford, 1960). It therefore seems reasonable to expect to find that at night the NO_2 is being removed by reaction with ozone, and that this takes longer when the ozone concentration is low.

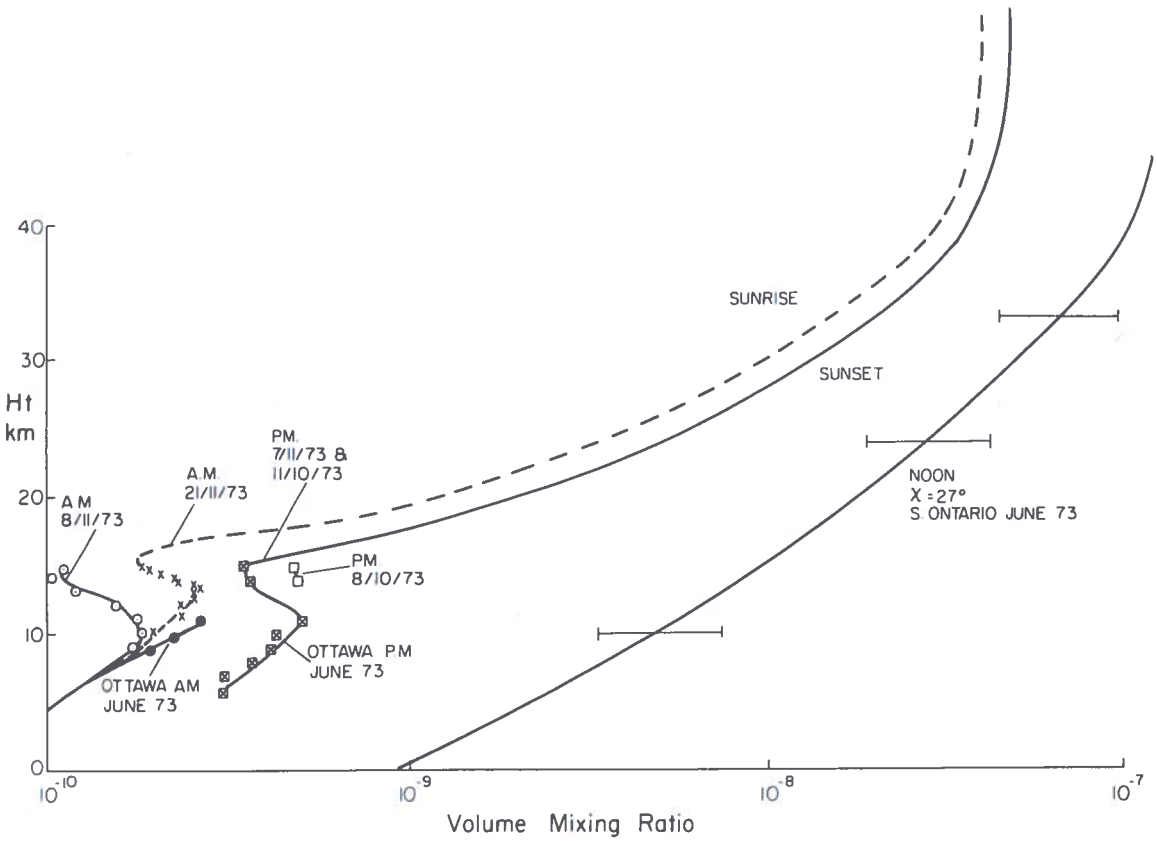

Figure 8. Suggested vertical distribution of NO_2 mixing ratio, Bay of Biscay, October-November 1973. The observed concentrations at and below flight level (15.5 km) are shown. Above the aircraft, the NO_2 amounts appeared to be very similar to those observed in June 1973 over southern Ontario. Flight dates were: sunrise 8 and 21 November 1973, sunset 8 and 11 October, and 7 November 1973.

REFERENCES

Dobson, G.M.B. (1957), "Observers' handbook for the ozone spectrophotometer," Ann. I.G.Y. **5**, 46.

Brewer, A.W. (1973), "A replacement for the Dobson spectrophotometer?", Pure and Appl. Geophys. **106-108**, 919.

Brewer, A.W. and J.R. Milford (1960), "The Oxford-Kew ozonesonde," Proc. Roy. Soc. **A256**, 470-495.

Hall, T.C. and F.E. Blacet (1952), "Separation of the absorption spectra of NO_2 and N_2O_4 in the range 2400-5000 A," J. Chem. Phys. **20**, 1745-1748.

DISCUSSION

GOLDMAN: It is well known that there is a water line in the center of the spectral region you've chosen. Did you take this into account? You didn't show us any actual atmospheric spectra.

KERR: At 4500 angstroms, we did not observe any effects of water vapor. We took observations with the spectrum shifted by 25 angstroms. This shift halves the sensitivity of our instrument's response to NO_2. We obtained the same values of NO_2 to within ±20% for the normal and shifted wavelength settings.

GELINAS: What are the values observed from the aircraft?

KERR: The aircraft climbs to about 12 kilometers, and we can measure the distribution during the climb to this height. Using our extra-terrestrial solar constant, which we have measured to the best of our ability, and using continuity in order to make the integrated amount above flight level consistent with that which was observed below flight level, we extrapolate the noon-time observations to the stratosphere. These extrapolated values are very uncertain, perhaps ±50%.

(UNIDENTIFIED): When you measured your F function, did you use one NO_2 absorption cell, or many cells? And if you used many cells, did the slope of the function depend on which cell you used?

KERR: We had one cell at STP into which we put equal increments of NO_2.

BARRETT: I don't think you intended the F_0 to represent the solar flux under particular conditions, but it is the response your instrument would have outside the atmosphere.

KERR: No, it's a weighted double ratio which would be observed in the atmosphere using sunlight and no NO_2 in the path.

ALTERNATIVE INTERPRETATION OF UMKEHR DATA FOR NITROGEN DIOXIDE

HAROLD S. JOHNSTON
Department of Chemistry and Inorganic Materials Research Division
Lawrence Berkeley Laboratory
University of California
Berkeley, California

ABSTRACT: Brewer and coworkers (1973) have successfully overcome the difficulties of observing atmospheric nitrogen dioxide by its visible absorption spectrum. They have developed a method (related to the ozone umkehr method) which should be very valuable in monitoring both tropospheric and stratospheric NO_2. The first set of data that they have published (Brewer et al., 1973) can be interpreted in two ways: (1) Brewer et al. assumed that NO_2 was constant during and shortly after sunrise and sunset, from which they deduced the vertical distribution of NO_2 and a very high column of NO_2 at midday; (2) alternatively, the data may be interpreted in terms of rapidly changing NO_2 at sunrise and sunset, a slow smooth increase during the day, and no midday maximum. The second interpretation is consistent with current chemical models of the stratosphere.

INTRODUCTION

Nitrogen dioxide (NO_2) has a strong, highly structured absorption spectrum in the visible and near-ultraviolet spectral region; a portion of this spectrum is shown in Figure 1. It would appear that this detailed spectrum could be used to observe nitrogen dioxide in the atmosphere, but several workers have reported failure to do so (informal reports and oral communications). Difficulties include Rayleigh scattering, particulate scattering, atmospheric inhomogeneities, and the highly structured solar spectrum in the same wavelength region, shown in Figure 2.

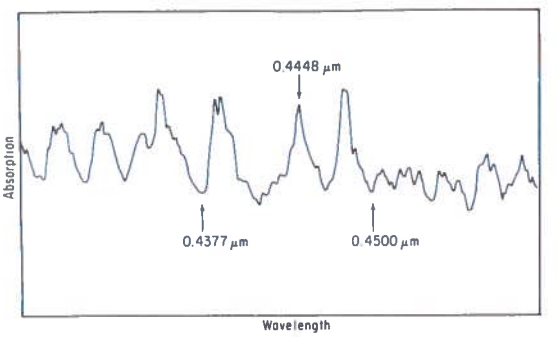

Figure 1. Portion of visible absorption spectrum of nitrogen dioxide (as observed in this laboratory) showing the three wavelengths used by BKM to define the function F.

Brewer, Kerr and McElroy (Brewer et al., 1973 (BKM); Brewer et al., 1974 (BMK)) have surmounted these difficulties by an ingenious differential method which includes a sensitive photon-counting technique. BKM used three wavelengths, at a peak and two valleys of the NO_2 absorption, where $\lambda_1 = 0.4377$ μm, $\lambda_2 = 0.4448$ μm, and $\lambda_3 = 0.4500$ μm (see Figure 1).

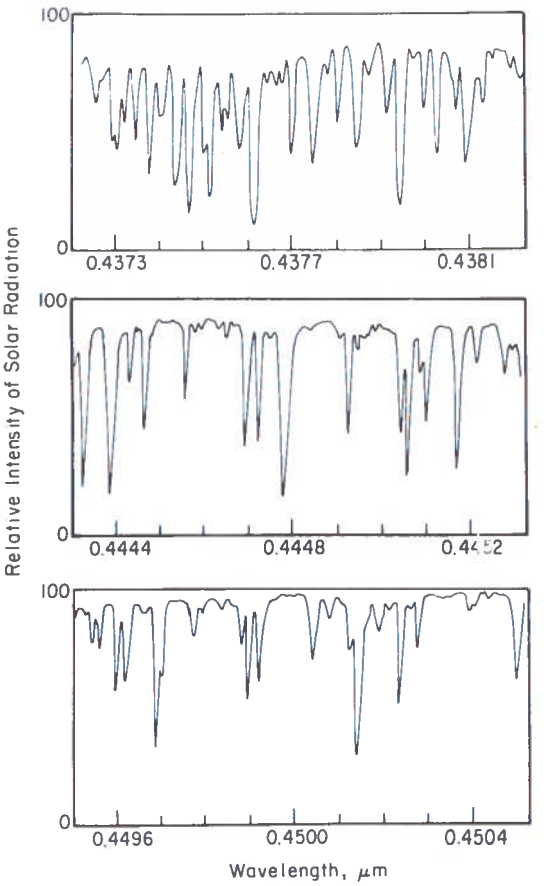

Figure 2. High-resolution display of solar spectrum as measured at the Earth's surface in the wavelength vicinity of BKM's three points. From *A Photometric Atlas of the Solar Spectrum*, Utrecht Rijksuniversiteit Sterrewacht.

They looked directly at the sun for one series of measurements and they looked at scattered light from the zenith sky for another group. Their spectral resolution was about 0.0003 μm. They defined the function F,

$$F = \log \frac{I_1}{I_2} + 1.46 \log \frac{I_3}{I_2} \quad (1)$$

The constant 1.46 was selected to eliminate (to a high degree of approximation) the effect of Rayleigh scattering. Particulate scattering changes smoothly in this wavelength region (in some cases as $\lambda^{-1.8}$ (Charlson and Ahlquist, 1969)), and the effect on log I_1/I_2 is very nearly cancelled by the opposing effect on log I_3/I_2.

Ozone also has a structured spectrum in this wavelength region, but its effect is readily calculated and is small. One assumes that NO_2 and O_3 obey the relation $I = I^0 \exp(-\sigma C^0 \sec \chi)$, where I^0 is the solar intensity above the atmosphere, σ is the laboratory-measured wavelength-dependent absorption cross-section, C^0 is the vertical column of NO_2 or O_3 in units of molecules cm^{-2}, and χ is the solar zenith angle. The function F then becomes

$$F = \log \frac{I_1^0}{I_2^0} + 1.46 \log \frac{I_3^0}{I_2^0} - 0.434[(\sigma_1 - 2.46\,\sigma_2 + 1.46\,\sigma_3)\,NO_2\,C^0_{NO_2} + (\sigma_1 - 2.46\,\sigma_2 + 1.46\,\sigma_3)O_3\,C^0_{O_3}] \sec \chi \quad (2)$$

letting

$$F_0 = \log \frac{I_1^0}{I_2^0} + 1.46 \log \frac{I_3^0}{I_2^0}$$

and using the appropriate constants, one obtains

$$F = F_0 + (3.04 \times 10^{-19}\, C^0_{NO_2} + 2.78 \times 10^{-23}\, C^0_{O_3}) \sec \chi \quad (3)$$

(Strictly speaking, sec χ should be replaced by a more complex term acknowledging the curvature of the earth for values of sec χ in excess of 8.) A vertical column of 0.33 cm (STP) of ozone gives the same values of F as a vertical column of NO_2 of 0.8×10^{15} molecules cm^{-2}, a small correction easily applied to the observed data. After this correction has been applied, there are two ways to evaluate the NO_2 vertical column from ground-based (or aircraft-based) observations. The slope of F with sec χ gives a direct, self-calibrating measure of the vertical column of nitrogen dioxide

$$C^0_{NO_2} = (dF/d \sec \chi)/3.04 \times 10^{-19} \quad (4)$$

provided that the vertical column itself does not change very much during the time interval over which dF/d sec χ is evaluated. In an alternate method, the value of F is observed over a wide range of values of sec χ for one day, extrapolated to a zero sec χ, and the value of F_0 inferred for use on that and other days. In this case every measurement of F is a direct measurement of the vertical column of NO_2,

$$C^0_{NO_2} = \frac{F - F_0}{3.04 \times 10^{-19} \sec \chi} \quad (5)$$

provided that F_0 is constant. The highly structured solar spectrum (see Figure 2) puts very great demands on the rigidity and constancy of the wavelength settings of the spectrograph; a very slight change of wavelength settings, especially for λ_2, can cause a large change in F_0.

BKM came to four conclusions: (1) Their method can overcome the difficulties of light scattering and ozone absorption to give a measure of the NO_2 column; (2) the nitrogen dioxide column increased by about a factor of 1.5 between early morning and late afternoon; (3) the nitrogen dioxide column showed a midday maximum about a factor of 3 greater than the morning value; and (4) observations of the vertically scattered zenith radiation during sunrise or sunset give information about the vertical distribution of NO_2 in the atmosphere. In this article evidence is presented in support of BKM's conclusions (1) and (2), and it is argued that the data can be interpreted to give alternatives to their conclusions (3) and (4).

EVALUATION OF F_0

BKM measured the value of F by focusing on the sun from sunrise through noon to sunset on August 3, 1973 at Toronto, Ontario, Canada. Their results are replotted and presented in Figure 3. The early-morning points do not coincide with the late-afternoon points, and thus the overhead column of NO_2 must have changed during the day. This change of the column of NO_2 during the day makes difficult and uncertain the extrapolation to a zero sec χ in order to evaluate F_0 (Equation 3). The function, sec χ, changes rapidly near sunrise and near sunset but only very slowly during the middle of the day; for example, 3 units of sec χ from 7.9 to 4.9 requires 27 minutes, 3 units from 4.9 to 1.9 requires 123 minutes, and 0.7 units from 1.85 to 1.15 requires 184 minutes. BKM reasoned that less change of NO_2 would be expected during the 45-minute interval of early morning or late afternoon (Figure 3), as opposed to the longer period needed to obtain a comparable change of sec χ during the middle of the day. Thus they graphically extrapolated the points between sec $\chi = 11.5$ and sec $\chi = 5.5$ to zero, Figure 3. This value of F_0 was used in all cases in the 1973 BKM article, and their conclusions depend critically on it.

One contention of this paper is that the extrapolation used to obtain F_0 is not precise; it is subject to considerable error and uncertainty. BKM gave several other sets of data which can be extrapolated to give F_0;

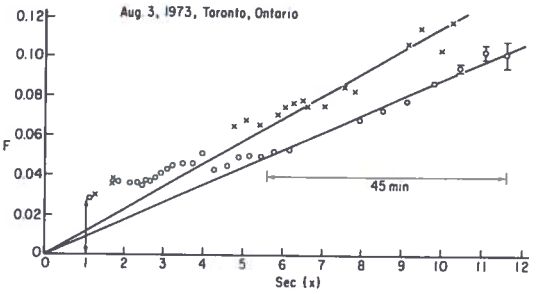

Figure 3. A replotting of data from Figure 6 of BMK (1974). The value of F_0 is obtained by extrapolation of the data in the 45-minute range identified by the arrows. August 3, 1973.

two examples are given in Figures 4 and 5. Figure 4 gives ground-based values of F for early morning of July 23, 1973, and Figure 5 gives late-afternoon data obtained from an airplane at 12 km elevation on June 13, 1973. These data cover the same range of sec χ as that used by BKM to obtain F_0 from the data of August 3. The value of F_0 can be obtained from the observed data on June 13 (PM), July 23 (AM and PM), and August 3 (AM and PM).

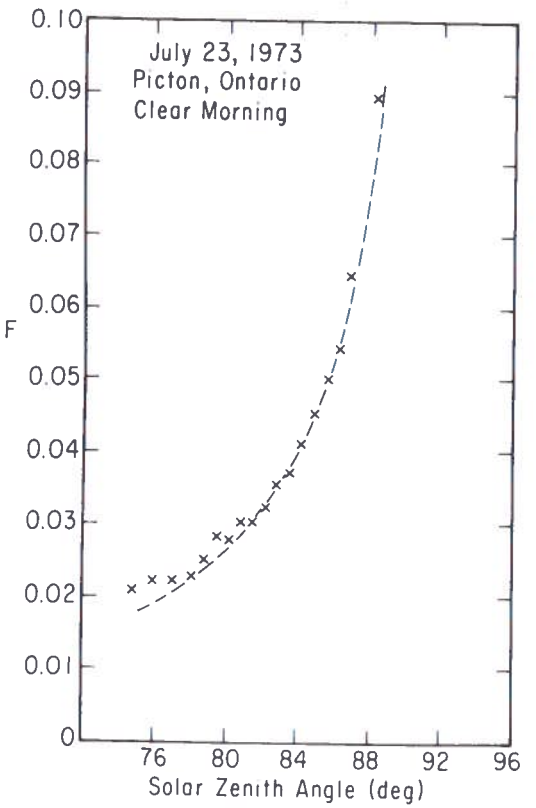

Figure 4. Data replotted from Figure 3a of BMK (1974). July 23, 1973.

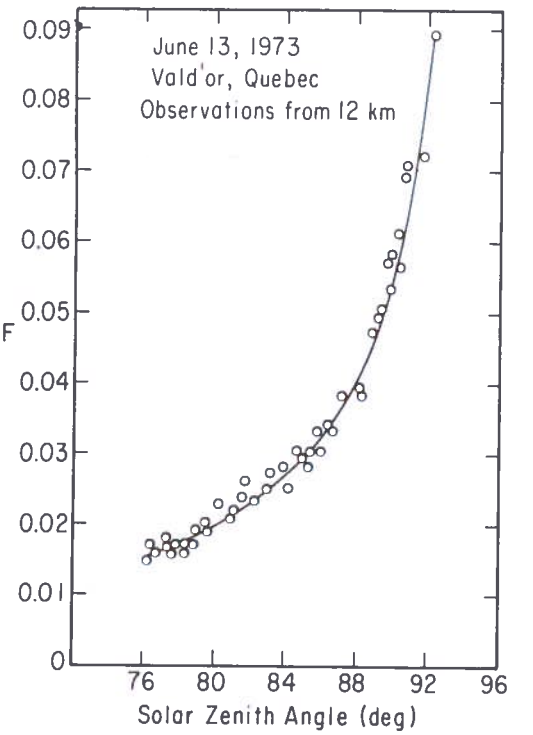

Figure 5. Data replotted from Figure 3 of BKM (1973). June 13, 1973.

These five sets of data were fitted to the equation

$$F = F_0 + K \sec \chi$$

by the method of least squares for sec χ between 5.5 and 12. The results are shown in Figure 6 and the intercepts F_0 are given in Table 1. The intercepts F_0 vary from -0.003 to 0.019. This spread is 0.022 units of F; it corresponds to a vertical column of 72×10^{15} molecules of NO_2 per square cm, which corresponds in turn to 18 parts per billion above 12 km. Thus, the uncertainty in F_0 as measured by these five cases from BKM (1973) is very large.

The effect of this uncertainty is especially great with respect to interpretation of the midday data.

The data of Figure 3 for August 3 can be extrapolated to zero in at least two different ways, each of which is plausible. One method is that used by BKM, as discussed above; another method is proposed here. Although the afternoon data in Figure 3 all lie above the morning data, the difference is attenuated by the large values of sec χ, and the absolute value of the difference is not great. The extrapolation to a zero sec χ could quite reasonably use all of the data of Figure 3. The least-squares straight line through all these August 3 data is given as curve A in Figure 7. In the units of the previous figures, the value of F_0 is 0.0186. The extrapolation used by BKM is given as lines B and C in Figure 7. The two lines D are derived from Figure 8.

Table 1. The Intercept F_0, and the Vertical Column of NO_2 Inferred from the Slope, dF/d sec χ

Observation	F_0	Vertical Column of NO_2, 10^{15} Molecules cm^{-3} From Slope	Corrected for O_3	Above 12 km
June 13, PM	+0.013	4.6	3.8	3.8
July 23, AM	+0.010	7.4	6.6	
July 23, AM	+0.019	10.2	9.4	
August 3, AM	-0.003	30.1	29.2	2.9*
August 3, PM	+0.009	33.7	32.9	6.6*

* Corrected for 0.008 F units between 0 and 12 km on basis of BKM's Figure 7.

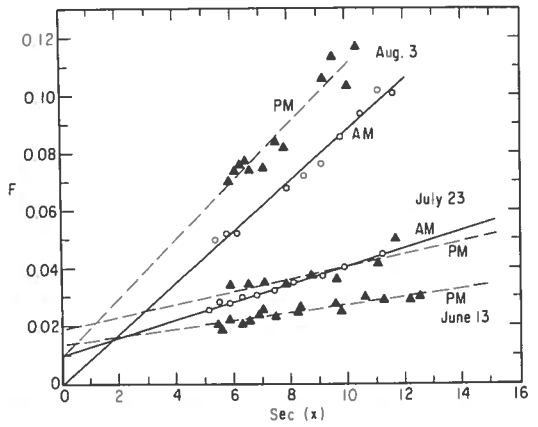

Figure 6. Evaluation of F_0 from five sets of data from BKM (1973) over the same range of sec χ as used by BKM in their extrapolation to obtain F.

The column of NO_2 calculated from Equation 5 for a given value of F depends strongly on the value of F_0 used. All of the experimental data are plotted twice in Figure 8. In one case (points represented by crosses) the value of F_0 is 0.0186, as found from extrapolation A in Figure 7. The points give a vertical column of NO_2 of about 22×10^{15} molecules cm^{-2} in the early morning, about 26×10^{15} at noon, and about 30×10^{15} in the late afternoon. The least-squares line A in Figure 7 is the horizontal line A in Figure 8. The morning points systematically lie below the line and the afternoon points systematically lie above the line. A better description of the crosses in Figure 8 is the straight line D, which slowly and linearly increases from morning to sunset. This line is used to calculate the function F with the F_0 given by curve A; the function F is then replotted as the third case, D, in Figure 7. In both Figures 7 and 8, the lines D give an excellent representation of the data.

The column of NO_2 was also calculated from each data point using the value of F_0 as obtained by BKM, and these values are the circles in Figure 8. The

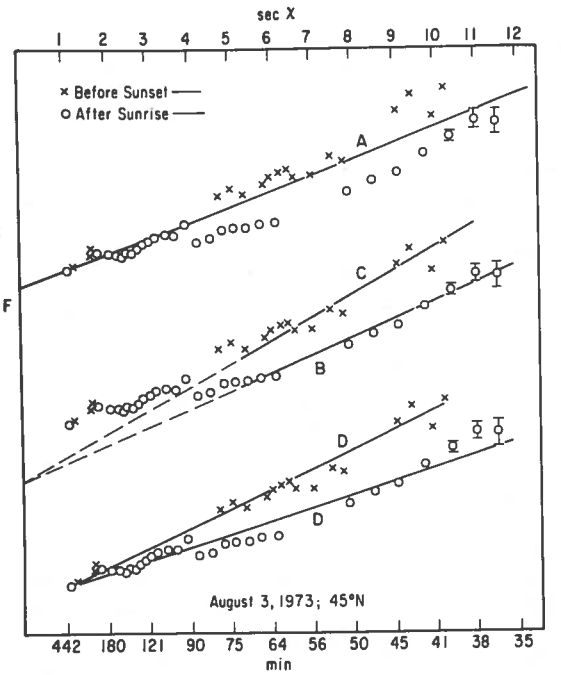

Figure 7. Three replottings of the data from Figure 6 of BMK (1974). A, extrapolation to a zero sec χ using all of the data. B and C, extrapolation to a zero sec χ as done by BMK. D, curves deduced from line D in Figure 8, based on intercept from line A above.

extrapolated lines B and C from Figure 7 are seen between 5 and 6 AM and between 6 and 7 PM. With this value of F_0, the calculated midday NO_2 increases to a high broad maximum, Figure 8, which is about three times greater than the early morning value. It should be emphasized that the circles and crosses of Figure 8 are based on the same experimental data (Figure 3). The two sets of points differ only in the value of F_0 used in Equation 5 to go from observed F to calculated NO_2 column. The evaluation of F_0 as given by line A of Figure 7 gives the crosses in Figure 8, and the evaluation

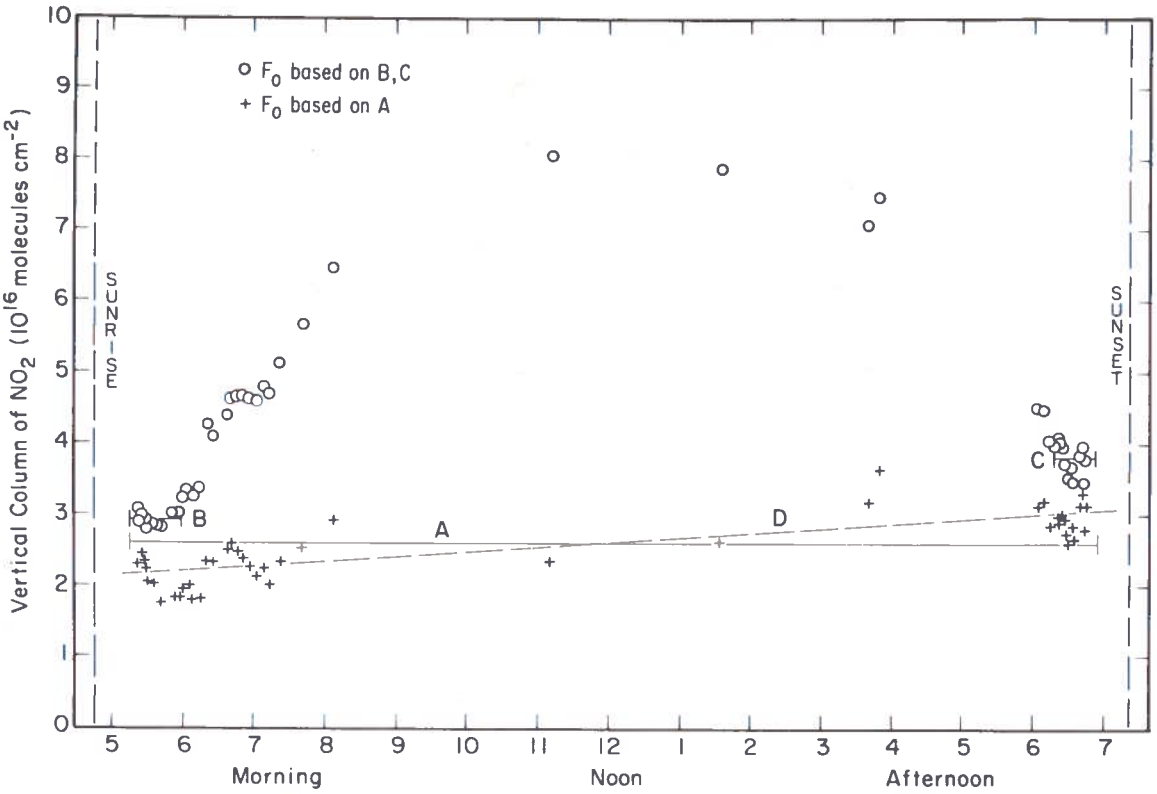

Figure 8. Computed variation of vertical column of NO_2 (August 3, 1973) during the day on the basis of two different values of F_0 (A and BC of Figure 7). These computed points are derived from the same observed values of F; they differ only as to value of F_0 used. The line D represents a linear increase of NO_2 from 30 minutes after sunrise to sunset; it gives the values of F in curves D of Figure 7 if one uses the F_0 from curve A of Figure 7.

of F_0 as given by B and C of Figure 7 gives the circles in Figure 8. Whether NO_2 goes through a midday maximum or shows a simple monotonic increase from morning to sunset depends critically on how F is extrapolated to zero sec χ, and this extrapolation shows poor precision from one case to another, as shown by Figure 6.

EVALUATION OF NO_2 FROM SLOPES

The value of the column of nitrogen dioxide can be calculated from the slope of the value of F as a function of sec χ (Equation 4). To evaluate $C^0_{NO_2}$ from Equation 4, it is necessary for the instrument to be stable for only an hour or so, whereas to evaluate $C^0_{NO_2}$ from Equation 5 one must have atmospheric and instrumental stability to give a reproducible F_0 day after day. The values of the NO_2 column inferred from the slopes of Figure 6 and Equation 4 are given in Table 1. The slopes are corrected for 0.33 cm of ozone. The values on June 13 were directly observed at 12 km. On August 3, a second instrument was put on board an airplane and F was observed up to and back down from 12 km at midday. The difference in F between 12 km and ground was about 0.008 units (BKM's Figure 7), which corresponds to 26.3×10^{15} molecules NO_2 cm^{-2}. This value was subtracted from the ground-based values found in the morning and late afternoon, and the results are entered in Table 1. These values consistently indicate stratospheric columns of NO_2 of about $4 \pm 2 \times 10^{15}$ molecules cm^{-2} with larger values in the afternoon than in the early morning. This value can be compared with the global-average nitric-acid column of 4×10^{15} molecules cm^{-2} as reported by Lazrus and Gandrud (1974). Model calculations (for example, Isaksen (1973)) show that columns of the species $HNO_3/NO_2/NO$ at 45°N in the summer occur in the ratio 4/3/3. Thus, the values of stratospheric NO_2 as inferred from slopes of BKM's F function are in good agreement with models and with observations of stratospheric nitric acid.

THE DIURNAL TREND OF NITROGEN DIOXIDE

During the day there is a dynamic balance between NO, NO_2, NO_3, N_2O_5, and HNO_3, which is brought about by photolysis and by reactions of these species

with O, O_3, HO, and HOO. At sunset, the photolysis ceases, and the species, O, HO, and HOO decrease to very small values. Nitric oxide rapidly reacts with ozone and with NO_3,

$$NO + O_3 \rightarrow NO_2 + O_2$$

$$NO + NO_3 \rightarrow 2\,NO_2$$

This conversion is virtually complete within a few minutes in the stratosphere. Nitrogen dioxide slowly reacts with ozone,

$$NO_2 + O_3 \rightarrow NO_3 + O_2$$

$$NO_3 + NO_2 \xrightarrow{M} N_2O_5$$

and depending on the temperature and concentration of ozone, roughly half of the NO_x is converted to N_2O_5 during the night (Johnston, 1971).

To provide the data for Figures 9 and 10, Dr. Gary Whitten carried out a model calculation of the diurnal variation of 12 species, including 45 elementary chemical reactions involving odd oxygen, the oxides and oxyacids of nitrogen, and free radicals derived from water. A standard distribution (45°N, spring equinox) of ozone, water, and temperature (Johnston and Whitten, 1973) was taken. The total NO_x column (NO, NO_2, NO_3, N_2O_5, HNO_3) was set at 14×10^{15} molecules cm^{-2}, and the vertical distribution of each species was derived. The distribution of sunlight was recomputed each hour of the day. The diurnal variation of these O_x, NO_x, and HO_x species was evaluated, and calculations were continued until agreement was obtained between the distributions at any time t and at t + 24 hours. The resulting vetrical column of NO_2 integrated from 15 to 50 km is given by Figure 9 for a period of 26 hours. During the night NO_2 is slowly converted to N_2O_5. At sunrise about half of the NO_2 is quickly converted to nitric oxide,

$$NO_2 + h\nu \rightarrow NO + O \xrightarrow{O_2} NO + O_3$$

$$NO + O_3 \rightarrow NO_2 + O_2$$

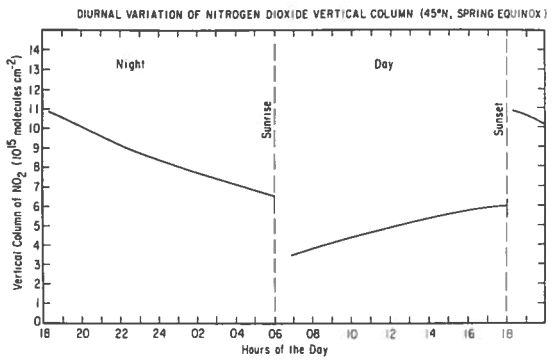

Figure 9. Diurnal variation of the NO_2 vertical column as calculated from a chemical model of 12 species (O_x, HO_x, NO_x) and 45 elementary reactions.

The relaxation times for this process vary between 30 and 90 seconds depending on elevation. During the day NO_2 is slowly formed from the photolysis of N_2O_5

$$N_2O_5 + h\nu \rightarrow 2\,NO_2 + \frac{1}{2}\,O_2 \text{ (mechanism uncertain)}$$

with a relaxation time of from about 1 hour at 40 km to about 8 hours at 15 km. For this model calculation, the vertical column of NO_2 increased from 3.5×10^{15} an hour after sunrise to 5.9×10^{15} at sunset. This calculated change is in good agreement with BKM's observations, if one uses the value of F_0 as derived from line A in Figure 7.

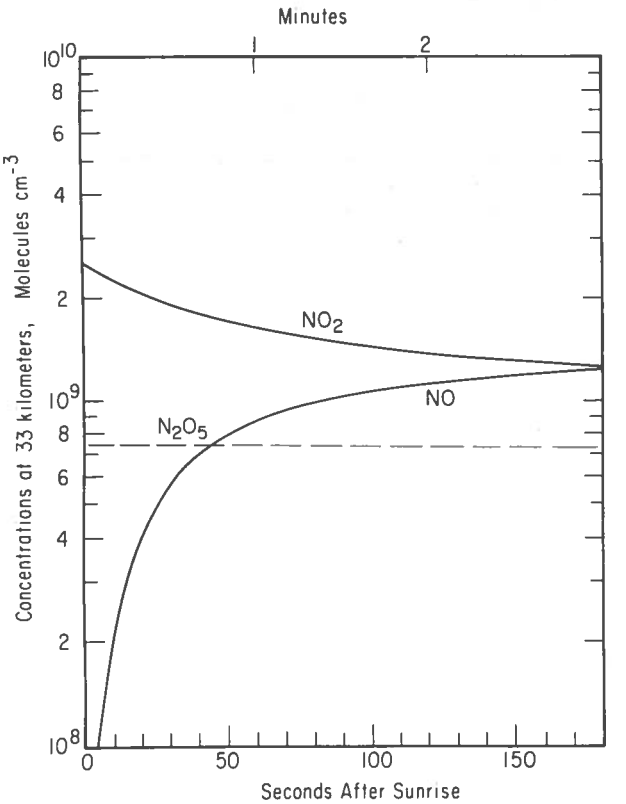

Figure 10. The calculated changes of NO, NO_2, and N_2O_5 at 33 km during three minutes after sunrise. (These fast changes after sunset and sunrise are omitted from Figure 9.)

There is a rapid change of NO_2 and NO immediately after sunrise or sunset. An example of the changes of NO, NO_2, and N_2O_5 for three minutes after sunrise is given by Figure 10 for an elevation of 33 km. BKM (1973) observed the scattered light from the zenith sky during sunrise and sunset (BKM's Figures 2A and 2B, for example). These observations were used to infer the vertical distribution of NO_2. However, as can be seen from Figures 9 and 10, it is at sunrise and sunset that NO_2 changes the most rapidly of any time of day.

The rapid decrease of NO_2 after sunrise ($NO_2 + h\nu \rightarrow NO + O$) and the rapid increase of NO_2 after sunset ($NO + O_3 \rightarrow NO_2 + O_2$) invalidate the use of scattered zenith radiation at these times as a measure of the vertical distribution of NO_2.

ACKNOWLEDGMENT

This work was supported by the Climatic Impact Assessment Program by means of an interagency agreement between the Department of Transportation and the Atomic Energy Commission through the Inorganic Materials Research Division, Lawrence Berkeley Laboratory.

REFERENCES

Brewer, A.W., J.B. Kerr, and C.T. McElroy (1973), "Nitrogen dioxide concentrations in the atmosphere," Nature **246**, 129-133.

Brewer, A.W., C.T. McElroy, and J.B. Kerr (1974), "Spectrophotometric nitrogen dioxide measurements," in this volume.

Charlson, R.J. and N.C. Ahlquist (1969), "Brown haze: NO_2 or aerosol," Atmospheric Environment **3**, 653-656.

Isaksen, I.A. (1973), "The production and distribution of nitrogen oxides in the lower stratosphere," Pure Appl. Geophys. **106**, 1438-1445.

Johnston, H.S. (1971), "Catalytic Reduction of Stratospheric Ozone by Nitrogen Oxides," UCRL-20568, 44-48.

Johnston, H.S. and G.W. Whitten (1973), "Instantaneous photochemical rates in the global stratosphere," Pure Appl. Geophys. **106-108**, 1468-1489.

Lazrus, A.L. and B.W. Gandrud (1974), "Progress report on distribution of stratospheric nitric acid," in this volume.

REPLY TO DR. JOHNSTON'S PAPER

A.W. BREWER, C.T. McELROY, AND J.B. KERR

We are indebted to Dr. Johnston for his lucid comments on our method of measurement. We had extensive experience of ozone measurement as a background to our work, and many of Dr. Johnston's explanatory notes cover ground familiar to those long versed in this method.

There is no doubt that the crux of the matter is our instrument's F_0, the value we would obtain for F if there were no NO_2 between the instrument and the sun. We have always been very conscious of the dangers of deceiving ourselves or others, and we were aware of solutions of the type which Dr. Johnston proposes, including one which gives rapid rise of NO_2 at sunset, rapid decay at sunrise, and a very low level by day.

We would like to point out the following features which caused us to make our deductions, or which cause us to keep them.

1. We almost invariably find that NO_2 at sunset is higher than at that day's sunrise. This suggests a diurnal variation with a maximum by day.
2. We have often observed decreases in our F in the afternoon in spite of rapidly increasing sec χ. (They occur at $\chi \approx 75°$-$80°$.) We interpret them as indicating a partial collapse of the NO_2.
3. Night measurements of directly transmitted moonlight are very similar to scattered-sunlight dawn ones.
4. Harries and coworkers* find that there is more NO_2 present by day. They say "for our night flight (twilight conditions) the total NO_2 abundance appears to be significantly, and consistently (i.e., using all three lines available), lower than during the daytime flights."
5. The decisive reason for our choice of F_0 has been that it enabled us to fit our observed zenith-sky curves, taken at sunrise and sunset, using a model calculation of an essentially static NO_2 distribution at sunrise or sunset. The fit can perhaps be improved slightly if we assume the NO_2 is increasing slowly during the sunrise period and decreasing slowly during the sunset period. Now, the important optical paths which occur in events at sunrise or sunset are wholly sunlit. Only some of the direct downward transmission of scattered light occurs through air which is not sunlit. If we accept the results of Dr. Johnston and Dr. Whitten's calculation, the rapid photochemical changes occur at the instant of sunrise and sunset; other changes are slow. If this is indeed so, then there is no way that our F_0 can be as high as Dr. Johnston has suggested, and there has to be a large diurnal maximum.

We may show this as follows:

At sunset (or sunrise) we can measure the NO_2 between about 15 and 27 km from the slope of the zenith-sky curve, independent of F_0 or of diurnal variations.

To interpret the slope of the zenith-sky curve, consider two observers, Ob_1 at a point where χ = 89.5°, and Ob_2 at a point where χ = 90.5°, each observing his zenith, Z_1 or Z_2 (see Figure 1). The light paths for the two observers are identical to line Ob_1Z_1, but Ob_2 has the extra horizontal path between Ob_1Z_1 and Ob_1Z_2, which is about 110 km long. If there is large and rapid change immediately after sunset, then there might be some difference in the lowest part of the vertical paths, Z_1 to Ob_1 and Z_2 to Ob_2; however, it seems reasonable to neglect this, because the dark part of the downward path is very small, or nonexistent if the observer is in an aircraft at 12 km.

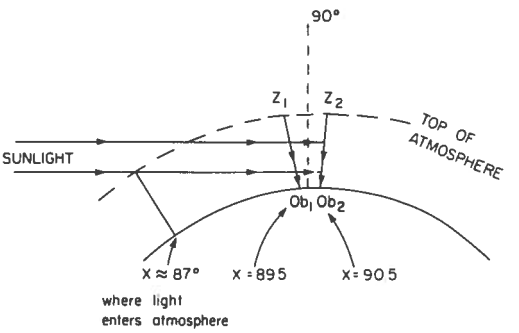

Figure 1. Geometry of NO_2 observation near sunrise and sunset.

The difference in F for the two values of χ is therefore the effect of 110 km of horizontal transmission, weighted with respect to the intensity of scattering at each level. The scattering per unit height is proportional to the product of the illumination and the air density. Calculation shows that the weighting is low below 10 km because the illumination is weak, and it is low above 35 km because the density is low. Between

* J.E. Harries, N.W.B. Stone, J.R. Birch, N.R.W. Swann, G.F. Neill, and J.W. Fleming (1974), "Submillimetre wave observations of stratospheric composition," in *Proceedings of the International Conference on Structure, Composition and General Circulation of the Upper and Lower Atmospheres and Possible Anthropogenic Perturbations* (Melbourne, Jan. 1974), IAMAP, 280.

about 15 and 27 km there is a broad maximum, and so the difference in the values of F observed by Ob_1 and Ob_2 is equivalent to the effect of 110 km of air with an NO_2 concentration equal to the average concentration between 15 and 27 km. If the atmosphere is horizontally laminated, then we may derive the differences between F at Ob_1 and F at Ob_2 as the slope of the zenith-sky curve for a stationary observer, and we may derive an NO_2 concentration, which is independent of F_0, for the instant of sunset (or sunrise).

When we do this we get values which are the same as those given in our vertical distributions obtained from much more elaborate model calculations.

We now try to use these data (which are independent of F_0) to deduce F_0 by calculating the effects of absorption in the path between the sun and Ob_1. There are two principal possibilities:

1. We can assume that in the sunlit track between the sun and Ob_1, the NO_2 is essentially the same as in the (sunlit) path between Ob_1Z_1 and Ob_2Z_2. This is equivalent to assuming no substantial change in the NO_2 during the period where χ changes from about 87° to 90.5°, all in sunlit air. In this manner we get the low value of F_0 which was used in all our published observations; clearly, however, we have very low precision for the amounts at the noon maximum.

2. On the other hand, we can assume that the NO_2 is reduced in the regions where χ lies between 87° and 88.5°. That is, we have a diurnal variation, with rapid appearance of NO_2 just *before* sunset and disappearance just *after* sunrise. This gives a high value of F_0, and it would require that all curves for the period noon $\rightarrow \chi \approx 87°$ be level and essentially featureless, since we have been obliged to assume that in air which is sunlit with χ greater than about 89° the NO_2 will be small. Examination of all our observations has caused us to reject this latter possibility.

We do not think that Dr. Johnston can obtain a totally coherent set of interpretations of our observations in terms of the diurnal variation of his and Dr. Whitten's model. We would be happy to supply any friend or critic with our raw data.

WATER BUDGET OF THE STRATOSPHERE

HUGH W. ELLSAESSER
Lawrence Livermore Laboratory
University of California
Livermore, California

ABSTRACT: Since upwelling of the Hadley cell constitutes the only significant known natural troposphere-to-stratosphere flux, stratospheric mass and mean residence time yield a reliable estimate of the Hadley flux through the tropical tropopause. This estimate, multiplied by the tropical-tropopause cold-trap saturation mixing ratio of 3.4 ppm for the H_2O influx and by the mean stratospheric mixing ratio of 2.5 ppm for the outflow, leads to an imbalance requiring a stratospheric sink specific for water vapor of about 3×10^8 tons/yr. Observational evidence indicates that the cold Antarctic winter stratosphere provides such a sink.

INTRODUCTION

From the first observations (Dobson et al., 1945) of its existence, meteorologists have been puzzled by the aridity of the stratosphere. Succeeding observations have merely proved it to be even more remarkable and more characteristic. So far no more plausible explanation has been advanced than the original one of Dobson et al. (1945), that all air entering the stratosphere is forced through the cold (water-vapor) trap of the tropical tropopause.

However, before this explanation can be given serious consideration, one must dispose of the following proposed sources of stratospheric H_2O: oxidation of solar protons, stratospheric oxidation of CH_4, thunderstorm penetrations of the tropopause, meridional circulation about the westerly jet streams (producing stratospheric injections through the subtropical tropopause gap), and upward diffusion through the polar tropopause. To date no data have been produced to unequivocally support any of these sources as a significant mechanism for troposphere-to-stratosphere transport of air or any of its constituents (and particularly H_2O) by natural atmospheric processes.

NON-HADLEY SOURCES

Despite the steep vertical gradients of H_2O in the vicinity of the polar tropopause, and saturation mixing ratios well above that of the tropical tropopause, meteorologists have long tactily admitted that upward transport of H_2O by diffusion does not occur, since otherwise the observed dryness of the stratosphere would be inexplicable. However, only recently has the logical corollary that *as H_2O goes, so go the other constituents* been acknowledged (Newell et al., 1973). Since there are no barriers to upward diffusion of H_2O vapor at the polar tropopause, the dry stratosphere, as pointed out by Brewer (1949), is physically understandable only if in the mean there is sufficient subsidence in the lower polar stratosphere to negate the upward movement, relative to air, of H_2O (and all other constituents) by diffusion. It can only be presumed that this subsidence is also sufficient to deny appreciable stratospheric residence time to H_2O injected by thunderstorm penetrations of the polar tropopause, or by tropospheric injections over the westerly jet streams through the subtropical tropopause gaps.

Several authors have noticed the frequent occurrence, poleward of 30°, of a minimum in the vertical distribution of O_3 at a height of about 15 km – a minimum which exhibits considerable regularity with regard to height, season, and latitude. A fairly close relation has also been noted between this O_3 minimum and the presence of a double tropopause in middle latitudes. In particular, the frequency of O_3 minima as a function of latitude is negligible from 0 to 20°N, shows an abrupt increase at the latitude at which double tropopauses are most frequent, and remains essentially constant poleward of this latitude. In a recent review Dobson

(1973) has suggested that these O_3 minima result from poleward migration of laminae of O_3-poor tropospheric air entering the stratosphere through the subtropical tropopause gap. He found it remarkable that the maximum frequency of the O_3 minima were found at nearly the same height (varying by less than a kilometer), from the lowest latitude at which they were observed up to that of Thule, rather than paralleling surfaces of constant potential temperature or constant potential vorticity.

If Dobson's explanation (1973) is correct, we would expect these laminae of tropospheric air to be H_2O-rich as well as O_3-poor. However, Mastenbrook's (1971) frost-point soundings near Washington, D.C. from 1964 to 1969 suggest a maximum neither in mean value nor in variability of the H_2O mixing ratio at 120 mb (≈15 km). Even if Dobson's suggestion is correct and these poleward migrating laminae are H_2O-rich, as would be expected if they are of tropospheric origin, the degree to which they maintain their altitude and O_3 mixing ratios suggests that they would not significantly alter the stratospheric H_2O mixing ratio, and therefore would not represent a significant source of H_2O to the stratosphere.

Estimates of natural sources of CH_4 range from 5 to 19 $\times$ 10^8 tons/yr, 2-30% of which penetrates the tropopause and is oxidized to form H_2O in the stratosphere. Most models indicate that the bulk of the oxidation occurs between 20 and 30 km, with the peak rate of change in mixing ratio of H_2O to be expected near 30 km. Table 1 lists rates calculated from recent studies of the change in H_2O-vapor mass mixing ratio which would be expected in the 20-to-30-km layer if all the CH_4 penetrating the tropopause were oxidized to H_2O and the H_2O remained uniformly mixed in this layer. The rates come to 0.08 to 2 ppmm/yr. Oxidation of CH_4 in the middle stratosphere is consistent with some observational evidence supporting an increase in H_2O mixing ratio with height in this region. However, due to the range of uncertainty and the small effect of all but the largest estimate in Table 1, it appears preferable at this time to regard CH_4 oxidation as, at most, a small effect well within the range of uncertainty of the major H_2O sources and sinks of the stratosphere.

THE HADLEY CELL SOURCE

From the total mass of the stratosphere of 6.67 $\times$ 10^{14} tons (average of estimates of SCEP (1970), Sissenwine et al. (1972), and Weickmann et al. (1974)), and a mass weighted mean residence time of the stratosphere of two years (SCEP, 1970), the Hadley-cell flux of air through the tropical tropopause is determined to be 3.33 $\times$ 10^{14} tons/yr. This number compares favorably with the estimates of 0.76 to 9.17 $\times$ 10^{14} tons/yr culled from the literature and listed in Table 2.

The mean vertical velocity through the tropical tropopause cannot be measured directly. As indicated by Table 2, the most direct estimates are based on the computed annual mean radiational heating rates of 0.25 to 0.3°C/day at the tropical tropopause, under the assumption that the near-constancy in tropopause temperature is maintained principally by adiabatic cooling due to the upwelling Hadley cell. The one additional parameter required is the ambient lapse rate, which almost discontinuously varies from a 200-to-100-mb average of 6°C/km below

Table 1. Rate of Change of Water Mass Mixing Ratio of 20-30 km Layer of the Stratosphere (if all water produced by stratospheric methane oxidation remained uniformly mixed in this layer)

	CH_4 Flux Through Tropopause		H_2O Mixing Ratio
Reference	Rate (molec/cm^2 sec)	Equivalent H_2O (10^8 tons/yr)	Change in 20-30 km Layer (ppmm/yr)
Wofsy et al., 1972	2 $\times$ 10^9	0.19	0.08
Nicolet & Peetermans, 1972	5 $\times$ 10^9	0.48	0.21
Ehhalt & Heidt, 1972	2.5-5 $\times$ 10^{10}	2.25-4.5	1-2
Nicolet, 1972	5 $\times$ 10^9	0.48	0.21

Table 2. Estimates of Hadley-Cell Flux through the Tropical Tropopause (using air density of 0.1828 kg/m^3)

Vertical Velocity (cm/sec) (w)	Latitudinal Extent	Mass Flux of Air (10^{14} tons/yr)	Source
0.07	27°N - 27°S	9.17	Weighted average from cross-sections of Murgatroyd and Singleton (1961) by Sissenwine et al. (1972).
0.03	17°N - 17°S	2.58	Attributed to Manabe and Hunt (1968) by Sissenwine et al. (1972).
0.02	20°N - 20°S	1.97	Vertical velocity for adiabatic balance of 0.25°C/day radiational heating computed by Rodgers (1967) at equatorial tropopause, and latitudinal extent of same (Newell et al., 1969a).
0.02	15°N - 15°S	1.5*	w as above, "assumes vertical motion occupies 30 degrees of latitude centered on the equator" (Newell et al., 1969a)
0.02	"15° latitude strip"	0.76	w as above, no reason given for reduced latitude strip (Newell 1970). Adopted by Weickmann and Van Valin (1972).
0.03	17.5°N - 17.5°S	2.62	Selected from above estimates by Sissenwine et al. (1972).
0.05	25°N - 24°S	5.94	Limits of observations whose annual temperature cycle and Rodgers' (1967) 0.25°C/day radiational heating were assumed to be balanced by adiabatic ascent by Reed and Vlcek (1968).
0.05			Attributed to Manabe and Hunt (1968) by Reed and Vlcek (1968).
0.067	22.5°N - 22.5°S	7.45	Annual average of 150 mb w and width of updraft as estimated from Kidson et al. (1969).
0.04			Attributed to Lateef (1968) by Singer (1971).
0.02			Estimated from observed rate of removal of Agung dust from equatorial stratosphere by Dyer and Hicks (1968).
0.03	25°N - 25°S	3.7	Assuming adiabatic balance of 0.25°C/day 100-mb heating rate, and its latitudinal extent as estimated from Rodgers (1967).
0.03	30°N - 30°S	4.4	Assuming adiabatic balance of 0.25°C/day tropical-tropopause heating rate, and latitudinal extent as estimated from Fig. 21 of Manabe and Möller (1961).
0.03	15°N - 15°S	2.3	Vertical velocity and latitudinal extent representative of the tropical tropopause as estimated from Fig. 7 of Manabe and Hunt (1968).
0.03	22.5°N - 22.5°S	3.3	Assuming adiabatic balance over latitudinal extent of 0.25°C/day heating of tropical tropopause as estimated from Dopplick (1970).
0.01 0.05	20°N - 20°S to 25°N - 25°S	1 - 6	Range of possible values from 100 mb, 5 years' mean vertical velocities of Oort and Rasmusson (1971).

*Newell et al. (1969a) gave 2.6 × 10^{12} g/sec (=0.82 × 10^{14} tons/yr), which they later used as a hemispheric value.

the tropopause to a 100-to-50-mb average of -3°C/km above it (Oort and Rasmusson, 1971). Such a sharp gradient is possible only if there is an equally sharp gradient in the vertical velocity.

It therefore seems appropriate to restrict the calculation to the tropopause itself, which is characterized as a thin layer having a lapse rate of 0°C/km. This appears to be the assumption made by Newell et al. (1969a), since the numbers agree with theirs within rounding, considering their allowance for cancellation of 20% of the radiational heating at the tropical tropopause by eddy transport. However, the larger vertical velocity obtained by Reed and Vlcek (1968) from the same heating rate is apparently due to the use of a tropospheric ambient lapse rate of slightly less than half the adiabatic.

The latitudinal extent of the Hadley upwelling offers additional uncertainty. Using sufficiently low frost-point measurements as the criterion, Newell et al. (1969a) adopted "30° of latitude centered on the equator" even though the basic 0.25°C/day heating rate appears to be valid from 25°N to 25°S. Later Newell (1970)

reduced this to "a 15° latitude strip" and offered no comment about the large increase in derived stratospheric residence time (2300 vs. 1000 days) when the resulting H_2O flux was divided into "the total stratospheric H_2O content above 100 mbar ($\approx 10^{15}$ g)".

Since the tropical tropopause (when identifiable) is nearly uniform in height from the equator to the jet stream of the westerlies, and since throughout most of this extent it is subject to net radiational heating, a balancing vertical velocity would appear to be valid over this much larger latitudinal range. However, at the poleward portions of the tropical tropopause the upwelling becomes a part of the meridional circulation about the jet itself, and (insofar as discernible from present data) quickly reenters the troposphere through subsidence or migrates horizontally to the pole without mixing with air having appreciable stratospheric residence time. This simply argues again in favor of using the stratospheric mass and residence time as a more objective method of estimating the tropospheric-to-stratospheric Hadley-cell flux.

The third parameter of importance is the tropical tropopause temperature. Accurate determination of this parameter is crucial, since a 4°C rise doubles, and a 15°C rise causes an order-of-magnitude increase in, the saturation vapor pressure of the cold trap (List, 1971). Table 3 contains a summary of values found in the literature. Most of these suggest that the -80°C (193.16K) commonly used is too cold to represent the annual and latitudinal average temperature of the tropical-tropopause cold trap. This is partially compensated for, since in the Northern Hemisphere the Hadley-cell upwelling is twice as strong in winter (when the tropopause is coldest) as in summer (Reed and Vlcek, 1969). Furthermore, in the regions of deep convection which make up the bulk of the Hadley-cell upwelling, the tropical tropause will tend to be higher and colder than average. Finally, mean tropopause temperatures established from individual soundings will be lower than those determined from mean soundings. Kochanski (1955) found a difference of 1 to 8°C. The difference will be even greater when mean temperatures are determined for nearby standard pressure levels, such as the 100-mb level which is frequently used to estimate the mean temperature of the tropical tropopause. The structure of the tropical tropopause is such as to maximize this difference. Accordingly, perhaps greater weight should be given to the study by Angell and Korshover (1974) based on tropopause heights and temperatures determined from individual soundings, even though this was the only such study found. In 10 years of soundings from Gan (1°S 73°E) and Singapore (1°N 104°E) they found 12-month running-average tropopause temperatures ranging from -84.5 to -81.5°C. Anyway, at this point I will accept -80°C as the cold-trap temperature, noting that, despite the Gan and Singapore data, it may tend to yield an *underestimate* of the mean annual Hadley-cell H_2O flux into the stratosphere.

Table 3. Tropical Tropopause Temperatures

Degrees K	Source
193	"Typically" (Newell, 1970).
193 – 194	Yields stratospheric frost-point mixing ratios consistent with those observed by Kuhn et al. (1972), in Weickmann et al. (1974).
192.5 – 198.8	Range of 5 yearly means for December-February (5-yr. mean 193.8) and June-August (5-yr. mean 197.1) temperatures at 100 mb from 15°N to 15°S, compiled by Kidson et al. (1969).
193.7 – 197.5	Mean January and July tropopause temperatures, 10°N to 10°S, determined from mean temperature profiles from 1957-1960 IGY data by Smith (1963).
193.4 – 197.0	5-year mean winter and summer temperatures at 100 mb from 10°N to 10°S from Oort and Rasmusson (1971).
189 – 197	Representative isotherms from January and July maps of the tropical tropopause by Makhover (1972).
188.7 – 191.7	12-month running means of tropopause temperatures determined from individual soundings at Gan (1°S 73°E) and Singapore (1°N 104°E) (Angell and Korshover, 1974).

A second reason for expecting the cold-trap temperature (saturation mixing ratio) and Hadley-cell flux to underestimate H_2O flux is the penetration of the tropical tropopause by cumulonimbus clouds. Because of the steep stratospheric

inversion (averaging 3°C/km), convection cells penetrating 1 and 2 km into the stratosphere will presumably mix with air which has saturation vapor pressures 1.6 and 3.5 times that of a -80°C cold trap. Since present data and understanding provide no believable estimates or even confirmation of such a flux of H_2O into the stratosphere, it will be ignored at this time.

For a -80°C cold trap at 100 mb, List (1971) gives a saturation mixing ratio over ice of 3.4 ppmm. With a Hadley-cell flux of 3.3×10^{14} tons/yr this yields a troposphere-to-stratosphere H_2O vapor flux of 11.3×10^8 tons/yr. Comparison of this number with the estimates listed in Table 4 and with those for total H_2O content of the stratosphere listed in Table 5 raises two questions:

a. How does the stratosphere maintain a mean mixing ratio of around 2.5 ppmm (Mastenbrook, 1971) when all air entering the stratosphere passes through a cold trap whose characteristic saturation mixing ratio is not less than 3.4 ppmm, and when there is presumptive evidence for direct stratospheric injections of additional H_2O via CH_4 oxidation, the subtropical tropopause gaps, and cumulonimbus penetrations of the tropopause?

b. Is there any connection between the above dilemma and the apparently consistently low previous estimates of influx of H_2O to the stratosphere via the Hadley cell cited in Table 4?

The second question is something that needs to be raised, but no attempt will be made to answer it here.

The first question suggests the presence of stratospheric sinks *specific* for H_2O; i.e., an outflow of air whose mixing ratio is 3.4 ppmm or less, such as through the tropopause gaps or subsidence over Antarctica and/or Greenland, cannot reduce the mean mixing ratio of the stratosphere. Presumptive evidence for three such sinks is cited in the literature: (1) photolytic decomposition above the mesopause, (2) the liquid-coated particles of the Junge layer, and (3) the stratospheric cirrostratus of the wintertime Antarctic. To balance the values so far adopted for the stratospheric H_2O budget, these sinks would have to remove from the stratosphere approximately 3×10^8 tons of H_2O per year.

Table 4. Estimates of Stratospheric Injection of Water Vapor by the Hadley Cell

H_2O Injection (10^8 tons/yr)	Basis and Source
3.28	Twice the 5.2×10^6 g/sec obtained by Newell et al. (1969a) from 2 ppm × Hadley-cell flux quoted in Table 2.
1.6*	From 5×10^6 g/sec obtained by Newell (1970) from 2 ppm × Hadley-cell flux quoted in Table 2.
2.2 – 3.2*	From 7-10 × 10^6 g/sec attributed by Singer (1971) to 10 March 1971 Congressional testimony of Newell.
2.2 – 3.3*	3-4.5 ppm × Hadley-cell flux of Newell (1970) quoted by Weickmann and Van Valin (1972).
5.76	2 ppm × Hadley-cell flux quoted in Table 2 by Sissenwine et al. (1972).
11.3	3.33×10^{14} tons/yr × 3.4 ppm (this study).

* Comparison of Newell et al. (1969a & b) and Newell (1970) indicates that these values are probably hemispheric, since the original estimate of Newell et al. (1969a) used as hemispheric was later used accidentally (or arbitrarily without explanation) as a global value.

Estimates of the photolytic destruction rate of H_2O are of the order of 10^4 tons/yr (Brinkmann, 1969), i.e., four orders of magnitude too small to be significant. Available evidence indicates that the large particles of the Junge layer are predominantly solutions of 75% H_2SO_4 and 25% H_2O, with residence times of 6 months (Junge, 1963b) to 2 years (SCEP, 1970). From the work of Elterman et al. (1973) and Grams and Fiocco (1967), the author has arrived at 5.3×10^{-7} g/cm^2 of 2 g/cm^3 particles as the approximate equivalent of an optical depth of 0.02, the value found by Elterman et al. (1973) for the normal dust loading of the stratosphere. Such a layer, uniformly covering the globe, would amount to 2.67×10^6 tons. If 25% were H_2O, this layer could account for a maximum rate of removal of H_2O from the stratosphere of 0.33 to 1.3×10^6 tons/yr. This figure could be significantly larger only if the number of stratospheric particulates has been grossly underestimated or their residence time in the stratosphere is appreciably shorter than 6 months. Thus, on the basis of present understanding of the Junge layer, it cannot play a significant role in the stratospheric H_2O budget.

Table 5. Estimates of Global Mass and Residence Time of Stratospheric Water Vapor

Water Content (10^8 tons)	Residence Time (years)	Basis and Source
15.93	1.31 - 6.6	2.5 ppm H_2O for layer from 15 to 50 km and total H_2O flux of 2.4-12.15 X 10^8 tons/yr, Weickmann et al. (1972).
12.	2.1	2 ppm H_2O for layer from 50-100 thousand ft. and Hadley-cell flux quoted in Table 2 (Sissenwine et al., 1972).
5. (1 hemisphere)	2.7*	2 ppm H_2O for layer above 100 mb over 2.5 X 10^{18} cm^2 and H_2O flux of 5.2 X 10^6 g/sec used by Newell et al. (1969a).
10.	6.3*	"Total stratospheric water content above 100 mbar (~10^{15}g)" and H_2O flux of 5 X 10^6 g/sec used by Newell (1970).
23.1		3 ppm X stratospheric mass of 7.7 X 10^{14} tons (SCEP, 1970).
16.		(Bauer, 1974).
16.7	1.5	2.5 ppm X stratospheric mass of 6.67 X 10^{14} tons/influx of 11.3 X 10^8 tons/yr (this study).

*Newell (1970) makes no comment about the doubling of the residence time resulting from dividing essentially the same H_2O flux into the stratospheric content of one hemisphere in the earlier paper and that of both hemispheres in the later paper.

That the Antarctic winter stratosphere may serve as a sink for stratospheric H_2O is suggested by the following evidence: (1) the lowest naturally occurring temperatures on Earth have been observed there, (2) persistent clouds (termed stratospheric cirrostratus) were observed there from June or July to the beginning of October in both 1950 and 1951 by Liljequist (1956) (who also stated that such clouds had been previously reported in the Weddell Sea by the *Deutschland* in the winter of 1912), and (3) available observations of stratospheric humidity show a north-to-south gradient (McKinnon and Morewood, 1970; Kuhn et al., 1972) (see Figures 1 and 2).

There are a number of reasons for believing that the Antarctic winter stratosphere should be colder than that of the Arctic, and thus more likely to reach the temperatures below -80°C required to create a sink for stratospheric H_2O vapor. Among these are:

a. The mean midsummer surface temperature of the southern hemisphere is 3°C colder than that of the northern hemisphere (Meinardus, 1934).

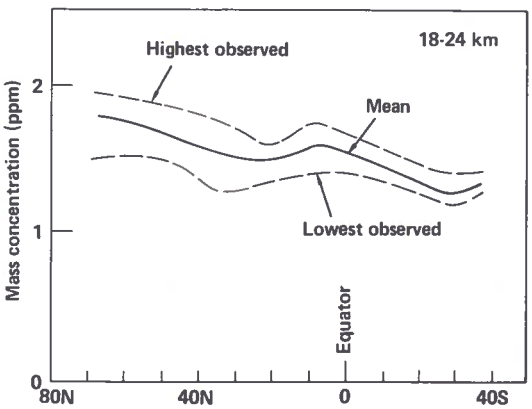

Figure 1. Mean and range of H_2O mass mixing-ratio observations at 18-24 km over North and South America, northern hemisphere winter, by McKinnon and Morewood (1970).

b. The larger and higher Antarctic ice cap is more efficient for radiating energy to space.

c. The more zonal circulation of the southern hemisphere, and the bulk of Antarctica itself, reduce eddy heat transport down the radiationally-induced latitudinal temperature gradient.

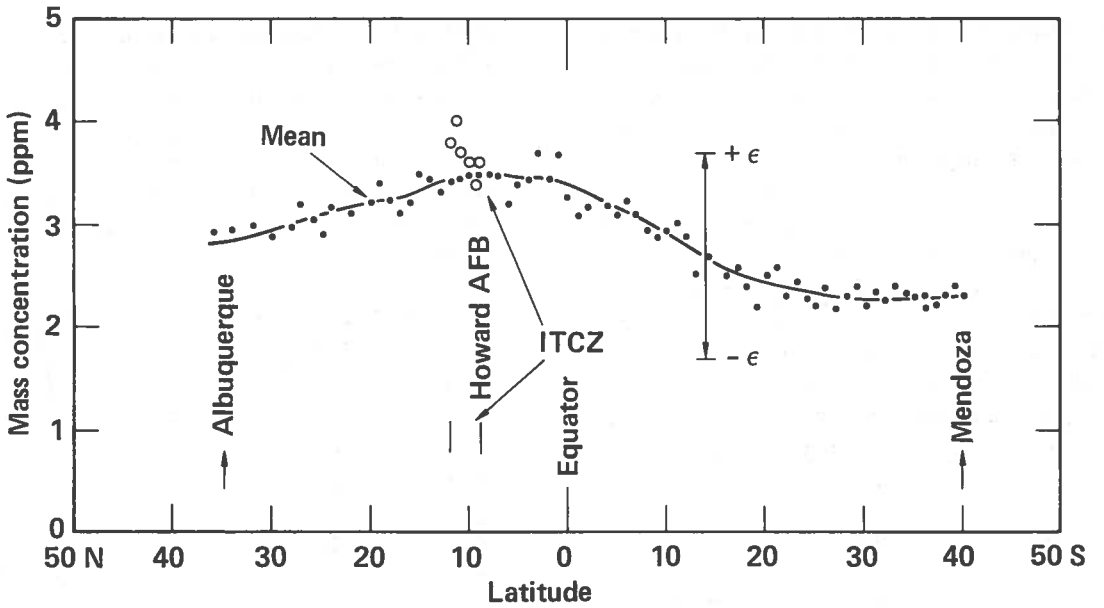

Figure 2. Project Airstream observations of H_2O mass mixing ratio at 17-19 km, October 1972 (Kuhn et al., 1972).

d. The ellipticity of the Earth's orbit causes the terrestrially received solar flux to be about 7% less at the southern-hemisphere winter solstice than at the northern-hemisphere winter solstice.

The observational data indicate even larger temperature differences between the Arctic and Antarctic winter stratospheres than the above suggest. Willett's (1968) analysis of IGY and post-IGY data spanning 4 or more years per station gave a 50-mb minimum mean monthly temperature of -86°C for August at both Halley Bay (75° 31′S) and South Pole (90°S), compared to -50°C for October at both Resolute (74° 43′N) and Alert (82° 30′N), and 50-mb extremes of -94°C at both Antarctic stations compared to -79 and -83°C for Resolute and Alert. This is confirmed by the mean rocket soundings in Figure 3, constructed by Faust (1967). With special cold-tolerance balloons, -104.6°C at 22.8 and 26-27.8 km was observed at Bird Station (80°S) on 27 July 1965 (Lovill, 1965).

The much colder Antarctic winter stratosphere is also indicated by (and rendered more understandable by) the SIRS 669.3 cm^{-1} radiance data presented by Fritz and Soules (1972). These show the southern-hemisphere radiances following a fairly smooth annual cycle

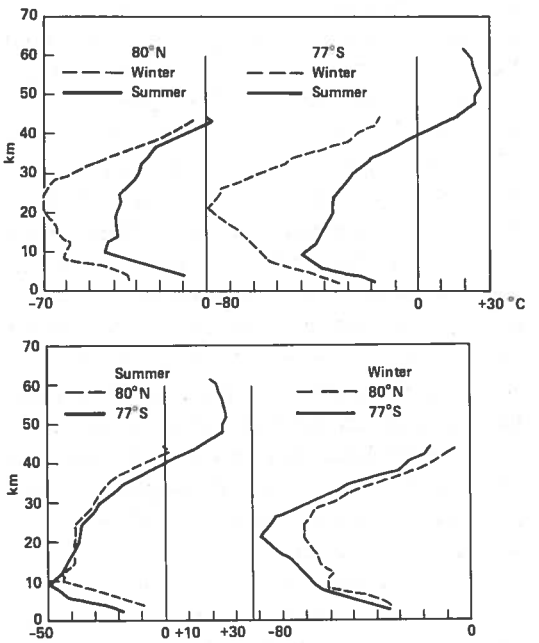

Figure 3. Rocket-data mean winter and summer temperature profiles over Franz Joseph Land (80°N) and McMurdo (77°S) (Faust, 1967).

with a winter minimum. The northern-hemisphere radiances start a similar winter decline, at a slightly higher level, but are then interrupted by a sudden stratospheric warming which both obliterates the expected minimum

and inserts a much higher radiance for a portion of the cycle. As a result, the mean winter radiance (temperature) of the northern-hemisphere is much greater than that of the southern hemisphere.

If the colder Antarctic winter stratosphere acts as a sink for stratospheric H_2O vapor, it should induce a north-to-south moisture gradient in the stratosphere. Moisture flux down the gradient should be proportional to the cross-sectional area times the diffusivity times the gradient. Through an annular ring encircling the Earth and extending 10 km above the tropical tropopause, a horizontal eddy diffusivity of 10^6 m^2/sec yields an H_2O flux:

$$\text{Flux } (10^8 \text{ tons/yr}) = 2.8\ \Delta H_2O \text{ (ppmm)}/\Delta\phi \text{ (radians)}$$

Thus a gradient of about unity (i.e., 1/2 ppm H_2O/ 1/2 radian) would be sufficient to account for the imbalance cited above. For the 1/2 radian southward from the tropical maximum, McKinnon and Morewood's (1970) data (see Figure 1) yield $\Delta H_2O \approx 0.3$ ppmm, and the Kuhn et al. (1972) data (see Figure 2) yield $\Delta H_2O \approx 1.0$ ppmm. Since the absolute values of the former are only about half those of the latter and of the generally accepted Mastenbrook (1971) data, the gradient is perhaps similarly underestimated. An underestimation of the gradient might also be expected because southern latitudes were sampled only during January, i.e., several months after the presumed sink would have entered its summer period of inactivity. Thus the available data appear to be consistent with the Antarctic winter stratosphere's serving as a sink for approximately 3×10^8 tons/yr of stratospheric H_2O vapor.

If evenly distributed over Antarctica, 3×10^8 tons of ice would produce a 21-μm layer (water equivalent); restricted to latitudes poleward of 85°S the layer would amount to 0.03 cm. Even if it all fell in the course of one month, such a snow-fall would go unnoticed. In any event, reevaporation within the troposphere would be the more likely fate of such hydrometeors.

Recently, Stanford (1973) has independently proposed that the Antarctic winter stratosphere provides a frost-trap sink for stratospheric H_2O vapor. Analyzing radiosonde data from Amundsen-Scott (South Pole) he found that the 11-year mean saturation mixing ratio at 50 mb was below 3 ppmm during June, July, and August, and that the August value reached 1 ppmm. At 100 mb it was also below 3 ppmm in July, August, and September, and at 150 mb in August and September (see Figure 4).

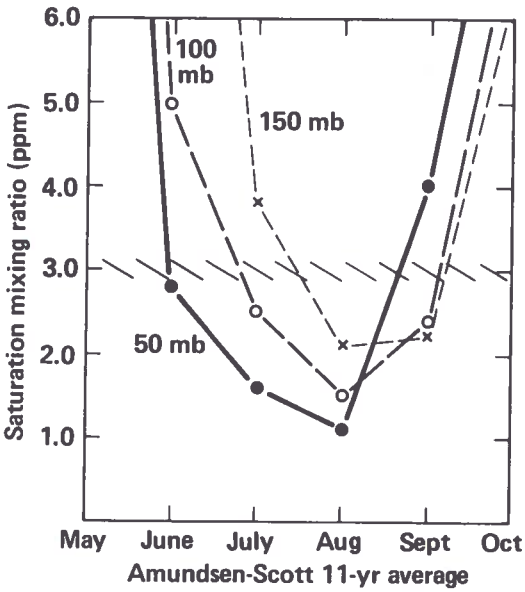

Figure 4. Winter mean monthly H_2O saturation mixing ratio determined by Stanford (1973) from 11 years of Amundsen-Scott (South Pole) soundings.

SUMMARY

The major features of the H_2O budget of the natural stratosphere are indicated in Table 6.

Table 6. Water Budget of the Stratosphere

Process	Flux (10^8 tons/yr)
Troposphere to Stratosphere	
Hadley cell (3.33×10^{14} tons of air/yr $\times$ 3.4 ppm H_2O)	11.3
Stratosphere to Troposphere	
Return Hadley cell (3.33×10^{14} tons of air/yr $\times$ 2.5 ppm H_2O	8.3
Antarctic precipitation from stratospheric cirrostratus (residual of above and $2\pi a \times K\Delta z \rho_{air} \times \Delta H_2O$(ppm)/$a\Delta\phi$ (radians)	3

ACKNOWLEDGMENTS

This work was performed under the auspices of the United States Atomic Energy Commission and was supported by the Climatic Impact Assessment Program, Office of the Secretary, Department of Transportation.

REFERENCES

Angell, J.K. and J. Korshover (1974), "Quasi-biennial and long-term fluctuations in tropopause pressure and temperature, and the relation to stratospheric water vapor content," Mon. Wea. Rev. **102**, 29-34.

Bauer, E. (1974), Chapter 1, CIAP Monograph I, E.R. Reiter (ed.), U.S. Department of Transportation.*

Brewer, A.W. (1949), "Evidence for a world circulation provided by the measurements of helium and water vapour distribution in the stratosphere," Quart. J. Roy. Met. Soc. **75**, 351-363.

Brinkmann, R.T. (1969), "Dissociation of water vapor and evolution of oxygen in the terrestrial atmosphere," J. Geophys. Res. **74** (23), 5355-5368.

Dobson, G.M.B., A.W. Brewer, and B.M. Cwilong (1946), "Meteorology in the lower stratosphere," Proc. Roy. Soc. **A185**, 155-175, Bakerian Lecture, 14 June 1945.

Dobson, G.M.B. (1973), "The laminated structure of the ozone in the atmosphere," Quart. J. Roy. Met. Soc. **99**, 599-607.

Dopplick, T.G. (1970), "Global radiative heating of the earth's atmosphere," Planetary Circulations Project Report No. 24, Dept. of Meteorology, MIT.

Dyer, A.J., and B.B. Hicks (1968), "Global spread of volcanic dust from the Bali eruption of 1963," Quart. J. Roy. Met. Soc. **94**, 545-554.

Ehhalt, D.H. and L.E. Heidt (1972), "Vertical profiles of CH_4 in the troposphere and stratosphere," 11-1, 11-11, Proc. AGU/AMS Symposium on Sources, Sinks and Concentrations of Carbon Monoxide and Methane in the Earth's Environment, St. Petersburg Beach, Fla., August 15-17.

Elterman, L., R.B. Torlin, and J.D. Essex (1973), "Stratospheric aerosol measurements with implications for global climate," Appl. Opt. **12**(2), 330-337.

* At present, these monographs exist only in an early draft form. They will be publicly available after their completion in September 1974.

Faust, H. (1967), "Stratosphärische Temperaturen im Nord- and Südpolargebiet," Meteorol. Rundschau **20**(3), 89-91.

Fritz, S. and S.D. Soules (1972), "Planetary variations of stratospheric temperatures," Mon. Wea. Rev. **100**(7), 582-589.

Grams, G. and G. Fiocco (1967), "Stratospheric aerosol layer during 1964 and 1965," J. Geophys. Res. **72**, 3523-3542.

Junge, C.E. (1963b), "Sulfur in the atmosphere," J. Geophys. Res. **68**(13), 3975-3976.

Kidson, J.W., D.G. Vincent, and R.E. Newell (1969), "Observational studies of the general circulation of the Tropics: long term mean values," Quart. J. Roy. Met. Soc. **95**, 258-287.

Kochanski, A.B. (1955), "Mean Cross Sections Along 80°W," AWS Tech. Report 105-115, Hq. Air Weather Service, Washington, D.C.

Kuhn et al. (1972), unpublished data; see Weickmann et al., 1974.

Lateef, M.A. (1968), "Vertical motion at 100 mb in the Tropics," Mon. Wea. Rev. **96**, 286-290.

Liljequist, G.H. (1956), *Norwegian-British-Swedish Antarctic Expedition, 1949-52, Scientific Results*, Vol. II, Parts 1 and 2, Norsk Polarinstitut, Oslo.

List, R.J. (1971), *Smithsonian Meteorological Tables*, 6th ed., 5th reprint, Smithsonian Institution Press, Washington, D.C.

Lovill, J. (November 1965), "Antarctic spring stratospheric warming as related to upper stratospheric ozone fluctuations" (paper presented at IAMRC/CSIRO Joint Meeting, Melbourne, Australia).

McKinnon, D. and H.W. Morewood (1970), "Water vapor distribution in the lower stratosphere over North and South America," J. Atmos. Sci. **27**(3), 483-493.

Makhover, Z.M. (1972), "Altitude and temperature of the tropopause over the Northern Hemisphere," Meteorologiya i Gidrologiya **7**, 28-35 (English translation in JPRS-57127, 30-39, NTIS, Springfield, VA, 1972).

Manabe, S. and B.G. Hunt (1968), "Experiments with a stratospheric general circulation model, I. Radiative and dynamic aspects," Mon. Wea. Rev. **96**, 477-502.

Manabe, S. and F. Möller (1961), "On the radiative equilibrium and heat balance of the atmosphere," Mon. Wea. Rev. **89**, 503-532.

Mastenbrook, H.J. (1971), "The variability of water vapor in the stratosphere," J. Atmos. Sci. **28**, 1495-1501.

Meinardus, W. (1934), "Die Niederschlagsverteilung auf der Erde," Z. Meteorol. **51**, 345-350.

Murgatroyd, R.J. and F. Singleton (1961), "Possible meridional circulations in the stratosphere and mesosphere," Quart. J. Roy. Met. Soc. **87**, 125-135.

Newell, R.E. (1970), "Water vapour pollution in the stratosphere by the supersonic transports?", Nature **226**, 70-71.

Newell, R.E., D.G. Vincent, and J.W. Kidson (1969a), "Interhemispheric mass exchange from meteorological and trace substance observations," Tellus **21**, 641-647.

Newell, R.E., J.W. Kidson, and D.G. Vincent (1969b), "Annual and biennial modulations in the tropical Hadley cell circulation," Nature **222**, 76-78.

Newell, R.E., G.J. Boer, and J.W. Kidson (1973), "Application of tropical general circulation statistics to the cycles of carbon monoxide, water and sulphate" (paper presented at CACGP Symposium on Trace Gases, Mainz, Germany, April 2-5).

Nicolet, M. (1972), "Aeronomic chemistry of the stratosphere," Planet. Space Sci. **20**, 1671-1702.

Nicolet, M. and W. Peetermans (1972), "On the vertical distribution of carbon monoxide and methane in the stratosphere" (paper presented at the AGU/AMS Conference on Sources, Sinks and Concentrations of CO and CH_4 in the Earth's Environment, St. Petersburg Beach, Fla., August 15-17).

Oort, A.H. and E.M. Rasmusson (1971), "Atmospheric circulation statistics," Professional Paper 5, NOAA, Rockville, Maryland.

Reed, R.J. and C.L. Vlcek (1969), "The annual temperature variation in the lower tropical stratosphere," J. Atmos. Sci. **26**(1), 163-167.

Rodgers, C.D. (1967), "The radiative heat budget of the troposphere and lower stratosphere," Rept. No. A2, Planetary Circulations Project, Dept. of Meteorology, MIT, Contract AT(30-1) 2241.

"SCEP" (1970), *Man's Impact on the Global Environment: Assessment and Recommendations for Action*, Report of the Study of Critical Environmental Problems, MIT Press, Cambridge, Mass.

Singer, S.F. (1971), "Stratospheric water vapour increase due to human activities," Nature **233**, 543-546.

Sissenwine, N., A.J. Kantor, and D.D. Grantham (1972), "How Dry is the Sky? A Decade Later and the SST," AFCRL-72-0294, Air Force Cambridge Research Laboratories, Bedford, Mass.

Smith, J.W. (1963), "The vertical temperature distribution and the layer of minimum temperature," J. Appl. Meteorol. **2**(5), 655-667.

Stanford, J.L. (1973), "Possible sink for stratospheric water vapor at the winter Antarctic Pole," J. Atmos. Sci. **30**, 1431-1436.

Weickmann, H.K., et al. (1974), Chapter 7, CIAP Monograph III, G.D. Robinson (ed.), U.S. Department of Transportation.*

Weickmann, H.K. and C.C. Van Valin (1972), "The sources and sinks of water vapor in the upper atmosphere," in preprint volume of the International Conference on Aerospace and Aeronautical Meteorology, Washington, D.C., May 22-26, American Meteorological Society, Boston, 186-191.

Willett, H.C. (1968), "Remarks on the seasonal changes of temperature and of ozone in the Arctic and the Antarctic stratospheres," J. Atmos. Sci. **25**(3), 341-360.

Wofsy, S.C., J.C. McConnell, and M.B. McElroy (1972), "Atmospheric CH_4, CO and CO_2," J. Geophys. Res. **77**(24), 4477-4493.

DISCUSSION

BARRETT: I'd like to point out a slight, sort of helpful, inconsistency. If you accept Kuhn's meridional H_2O profile as reasonably accurate, you should be using 3 ppm for that band between twenty degrees north and twenty degrees south, rather than Mastenbrook's 2.5. Then you wouldn't need such a strong sink.

(UNIDENTIFIED): The water-vapor distribution seems to fall off in the higher latitudes of both the northern and southern hemispheres. Could the Arctic be a sink as well?

ELLSAESSER: I did consider the possibility that even in the Arctic winter stratosphere we might reach temperatures which could dry the stratosphere somewhat. However, none of the observational data I've seen argues well for an Arctic minimum saturation mixing ratio less than 2.5 ppm.

VOLZ: I'd like to comment on the evidence for fallout of water particles in the stratosphere. The reported color of Arctic twilight striations indicates that they are not in the stratosphere. The twilight evidence for polar stratospheric clouds is weak, but there might still be a sink for water vapor in those regions.

KREY: Tritium should exchange with water vapor in the stratosphere. If there is preferential removal of water vapor over the Antarctic, one would expect an increase in the tritium in the Antarctic troposphere. But the International Atomic Energy Agency's tritium profile shows that the tropospheric distributions in the two hemispheres are quite similar.

ELLSAESSER: On the other hand, there's ozone at the surface in the Antarctic, and some people have suggested that the excess sulfate there is due to wintertime subsidence.

GLOBAL MEASUREMENTS OF THE TIME VARIATIONS AND MORPHOLOGY OF THE STRATOSPHERIC AEROSOL

D.J. HOFMANN, J.M. ROSEN, AND T.J. PEPIN
Department of Physics and Astronomy
University of Wyoming
Laramie, Wyoming

ABSTRACT: The results of over 70 balloon soundings, made over the past two years from 10 stations situated in latitude from 85°N to 90°S, are utilized in a study of the time variations and spatial distribution of the global stratospheric aerosol. From this study a number of features of the natural background aerosol, considered noteworthy in terms of the goals of CIAP, are presented.

A simple seasonal variation below 20 km altitude is observed at northern midlatitudes; it results in a maximum total aerosol loading in winter and a minimum in summer. A strong correlation with tropopause height is observed. Asymmetries in the global seasonal variation can be explained in terms of variation of the tropopause height, which affects the stratospheric volume available for aerosol formation and transport. Above 20 km, no seasonal variation is evident, and the natural production processes are almost in equilibrium with loss processes. Thus, the conclusion is drawn that the lifetime of matter injected below about 20 km will be relatively short (annual average of about 6 months), while above this altitude lifetimes could be considerably longer.

Synoptic studies in the northern hemisphere are used to construct latitudinal cross-sections of aerosol mixing ratio versus height. These profiles show the variation of the stratospheric aerosol layer with latitude, as well as the existence of other thin layers extending over a very large horizontal distance. Some of these stratospheric layers appear to be associated with transport through the tropopause gap at midlatitudes, while other (tropospheric) layers appear to be associated with volcanic activity.

INTRODUCTION

The University of Wyoming's Global Stratospheric Monitoring program has been operating for approximately the past two years. In addition to measurements of the stratospheric aerosol layer, complementary measurements of ozone, water vapor, ion density, condensation nuclei, and fine-scale temperature have also been carried out by the balloon-sounding technique. The most extensive of these measurements involves the stratospheric aerosol layer, commonly referred to as the Junge layer, i.e., those particles having diameters greater than about 0.3 μm. The time variation and global distribution of this constituent, obtained from a number of stations over the globe, are the subjects of this paper.

Figure 1 locates the stations from which routine flight operations have been conducted during the program. In addition, soundings have recently been made from Wallops Island, Virginia, and from the Sanriku balloon station in Japan. The Antarctic soundings are part of the United States Antarctic Research Program; the Australian soundings are carried out by the University of Melbourne group under the direction of Dr. Jean Laby.

From the results of over 70 soundings it is now possible to describe some of the characteristics of the "natural" stratospheric aerosol background. By "natural" is meant the non-volcanically-injected component, since no volcanic eruptions violent enough to inject large amounts of material into the stratosphere have apparently occurred during this period of measurement, although such injections have occurred within the troposphere. The contribution of volcanic activity to tropospheric gases which enter the stratosphere (and thus may form aerosol by chemical reaction) is here considered as part of the natural-background aerosol source.

DESCRIPTION OF INSTRUMENTATION

Figure 2 is a schematic drawing of the balloon-borne "dustsonde" developed by Rosen (1964) and utilized in this program. Its mode of operation is as follows. Air being sampled, on

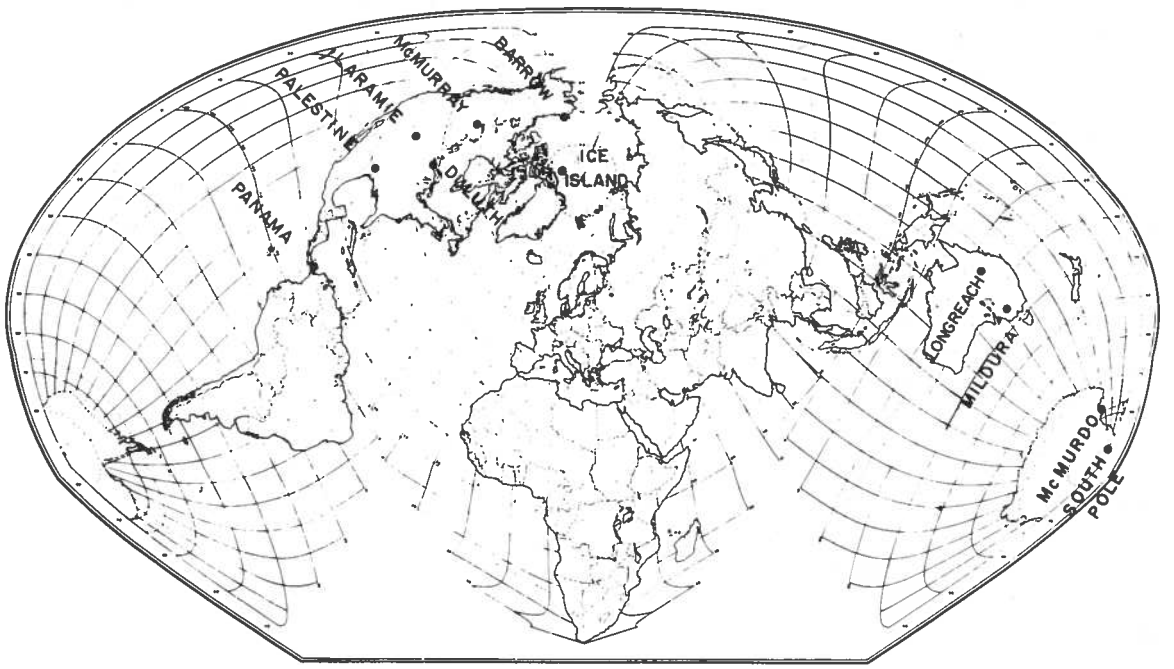

Figure 1. Locations of balloon soundings.

balloon ascent and parachute descent, is pumped at a rate of about 3/4 liter per minute in a well-defined stream through the focal point of the condenser lens in the 2500-cm^3 scattering chamber, where individual particles scatter light into the microscopes. The light pulses observed by the microscopes are amplified by photomultipliers. By pulse-height discrimination, and careful laboratory calibration with aerosol of known size and index of refraction, the integral concentration above about 0.3 μm and 0.5 μm diameter is determined routinely on each sounding. For further details of the calibration technique, see Pinnick et al. (1973).

The requirement of coincident events from the two photomultipliers enhances the signal-to-noise ratio, background noise being due mainly to Rayleigh scattering from air molecules at low altitude and to scattering from the chamber walls and cosmic ray scintillation in the photomultiplier glass at high altitude. About every 15 minutes during flight, the air sample is passed through a filter prior to measurement, to provide a background reading. For most instruments (depending on photomultiplier quality), the background rate becomes negligible above about 10 km altitude. The detector is lowered about

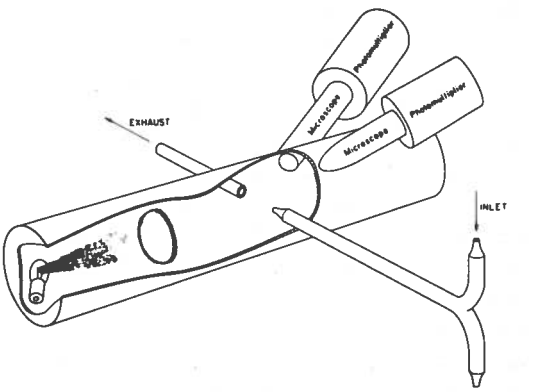

Figure 2. Schematic diagram of the aerosol detector.

90 m below the balloon following launch so as to avoid contamination by the balloon. Observations made during ascent and descent are compared for verification.

At the presently observed low stratospheric-particle concentrations (about 1 particle/cm^3 with diameter greater than 0.3 μm), the particle-counting rate of the instrument in the stratosphere is of the order of 10 counts/sec. The complete instrument, weighing 9 kg, is carried to about 27 km, with a balloon rise rate of 0.3 km/min. In order to reduce statistical fluctuations, a registration of 500 particles is utilized for

each concentration data point, so that at the current low concentrations, the average vertical resolution is about 250 m, or about 100 data points per sounding for the particles greater than 0.3 μm in diameter. Upon reaching ceiling altitude the parachute is severed from the balloon, and it descends with the detector at approximately 0.5 km/min, again sampling the atmosphere. The uncertainty in the measured concentrations, due mainly to the uncertainty in the air-sample flow rate, is estimated to be less than ±5%.

SOME GENERAL FEATURES

Although the instrument utilized here is not capable of determining the composition of the stratospheric aerosol, this information has been obtained on occasion by including in the balloon payload complement at Laramie the impactor sampler of the Australian CSIRO group (E.K. Bigg). This device is capable of determining composition through the chemical reaction which takes place on the specially prepared electron-microscope impactor grids. It found the aerosol in the lower stratosphere to be composed predominantly of sulfuric-acid droplets. Therefore, the refractive characteristics of a nonabsorbing aerosol with index 1.40 have been utilized in the size calibration of the dustsonde.

On most occasions, only two sizes are measured. This information only gives a crude indication of the character of the size distribution; more important, it can be utilized to detect variations in size distribution. The aerosol currently found in the stratospheric layer displays a globally uniform size distribution which results in a ratio of concentrations for the two sizes measured (greater than 0.3 μm and greater than 0.5 μm diameter) of about 4-5. This gives a characteristic (e-folding) diameter of about 0.15 μm for an exponential size distribution, or an exponent of about 3 for a power-law-integral size distribution. These conclusions would not change radically for other aerosol compositions if the aerosol remained nonabsorbing. Absorptive properties of the aerosol would result in a larger characteristic diameter or a smaller exponent for the same ratio of concentrations. Grossly nonspherical configurations, currently of negligible importance in the stratosphere, would obviously render these figures inappropriate.

The peak of the mixing ratio of aerosols greater than 0.3 μm in diameter, depending somewhat on season, is situated at a height of 22-26 km in equatorial regions, sloping nearly parallel to the tropopause to about 17-18 km in polar regions. At the peak, the mixing ratios are about 8-10 particles per milligram of ambient air. This is equivalent to a mass mixing ratio of about 1.3 ppb. At the tropopause, the aerosol mixing ratio may be 10 times less, depending on season. In terms of particle concentration, the peak stratospheric values occur at altitudes about 4 km lower than the peak mixing ratios, and have been in the range 0.5-1.5 cm^{-3} over the globe for the past two years.

Although the long-term changes in the aerosol layer appear small, a sizable annual cyclic variation with an average amplitude of about 10^6 particles ($>$ 0.3 μm in diameter) per cm^2 of stratospheric column is observed. Integrating this amount over the earth and over the size distribution results in a required annual aerosol production of 6.5×10^5 tons. For a 75% H_2SO_4/25% H_2O composition, as deduced by Rosen (1971), and assuming that the H_2SO_4 results from oxidation of SO_2, 3.2×10^5 tons of SO_2 per year are required. For a 75% annual stratospheric-tropospheric mass exchange (Danielsen, 1968), a SO_2 mass mixing ratio of about 0.4 ppb would be required at the tropopause.

TIME VARIATIONS AT NORTHERN MIDLATITUDES

While soundings have been carried out at most stations on a bimonthly basis, an effort has been made to make measurements from the Laramie station at 41°N latitude once a month. This frequency of soundings has proven to be satisfactory for studying the time variation of the natural aerosol background which, with the lack of significant volcanic activity, has revealed a somewhat uniform seasonal variation in the lower stratosphere.

The characteristic seasonal trends of the stratospheric aerosol layer ($>$ 0.3 μm in diameter) over Laramie are exhibited in Figures 3, 4, and 5, which show the aerosol mixing ratio (particles/mg ambient air) versus height for three periods labeled summer (July-Sept.), winter (Nov.-Feb.), and spring (Mar.-June), respectively. Certain features of the aerosol profiles suggested

this categorization. These data include soundings through December 1973. The vertical bars in the figures indicate the observed range of tropopause positions for the soundings.

Beginning with Figure 3, we find the summer aerosol layer to be highly stable, with both the upper troposphere and the lower stratosphere relatively free of particles. The high mixing-ratio features near 10 km are due to cirrus clouds; their presence can be ascertained by observing the ratio of concentrations of the two sizes of particles measured. The cirrus particles are generally characterized by a steeper size distribution (i.e., a greater ratio of small to large particles than observed in the stratosphere).

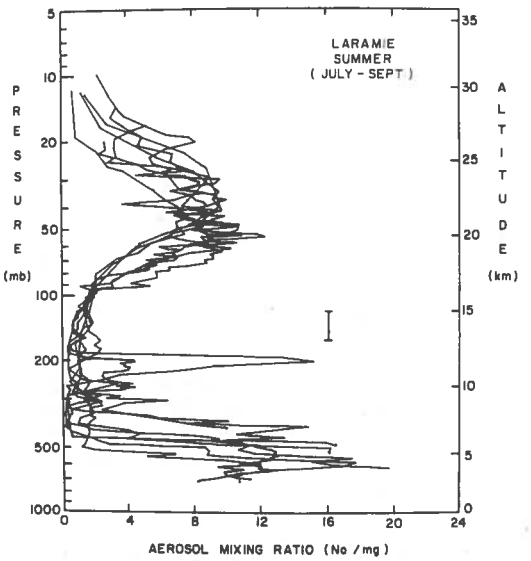

Figure 3. Summer aerosol mixing ratios versus height at Laramie, Wyoming. The vertical bar marks the observed tropopause positions.

The winter profiles, shown in Figure 4, appear less uniform, and as the tropopause decreases in altitude the particle concentration in the lower stratosphere appears to increase, generally in a layered fashion near 200 mb pressure (12 km height). Notice, however, that the upper troposphere still maintains relatively low mixing ratios.

The spring soundings, shown in Figure 5, can be characterized as somewhat variable, being highly layered; both the lower stratosphere and the upper troposphere are dominated by such laminae of relatively high mixing ratio.

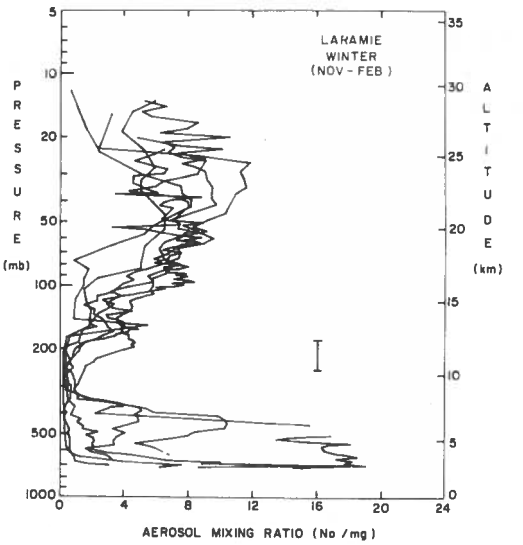

Figure 4. Winter aerosol mixing ratios versus height at Laramie, Wyoming. The vertical bar marks the observed tropopause positions.

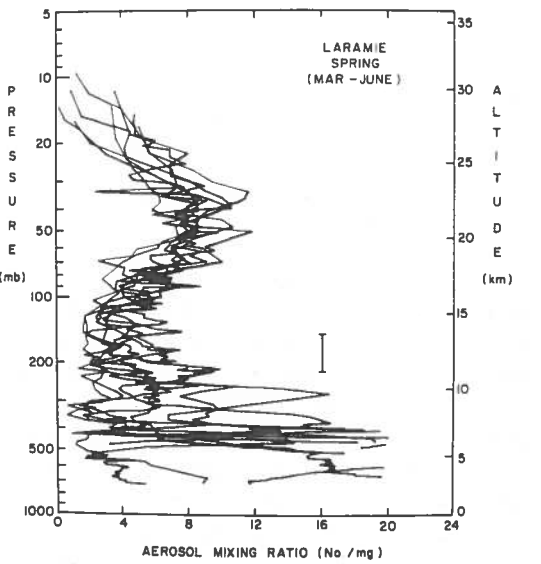

Figure 5. Spring aerosol mixing ratios versus height at Laramie, Wyoming. The vertical bar marks the observed tropopause positions.

In Figure 6, the extremes of the seasonal variation are compared, now in terms of particle (> 0.3 μm diameter) concentration versus altitude. The arrows mark the observed positions of the tropopause. The curved grid lines are lines of constant mixing ratio, in particles/mg air. With this format, the layered structure just above the winter tropopause is more pronounced, and one

observes a considerable increase in the stratospheric particle loading below about 20 km during winter. Above this height the aerosol concentration remains relatively constant.

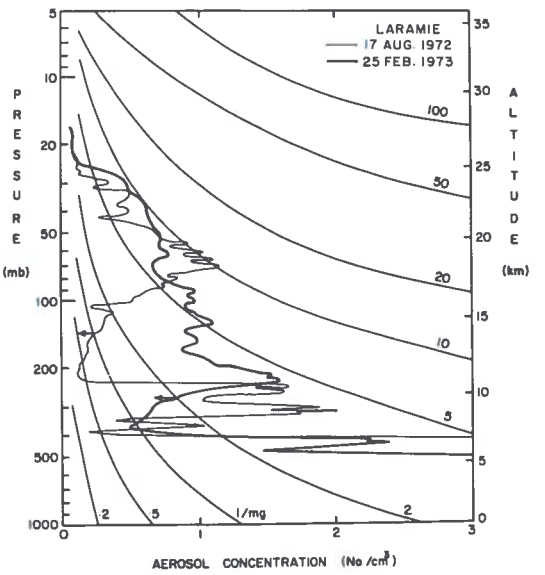

Figure 6. Summer and winter aerosol concentrations versus height at Laramie, Wyoming. The arrows mark the observed tropopause positions. The curved grid lines are lines of constant mixing ratio in units of particles per mg of air.

A useful parameter for studying the time variations of the aerosol is the area under the vertical concentration distributions. This is equivalent to the total number of particles per unit area above a specified altitude. This quantity is shown in Figure 7a plotted against time in units of 10^6 particles/cm^2-column above several different heights. In each case the upper part of the sounding has been completed by extrapolating the observed concentration to zero at 10 mb pressure (31 km altitude). The uncertainties caused by this extrapolation are estimated to be less than a few percent, and the overall uncertainty of the integrated aerosol data is estimated to be about ±5%.

Except for an apparent increase at high altitude in early 1973, the integration above 20 km shows little time variation. Above 15 km, a late-winter/early-spring maximum begins to appear, and is an obvious feature of the total aerosol loading above the tropopause, shown by the solid line in Figure 7a.

The observed tropopause heights are plotted in Figure 7b. An inverse correlation with the total aerosol loading above the tropopause is evident. In Figure 7c, the ratio of the concentrations of the two sizes measured shows a uniformity in the size distribution, at least since early 1972. There is a suggestion, though perhaps not yet statistically significant, of a long-term trend of decreases in both average concentration and average particle size.

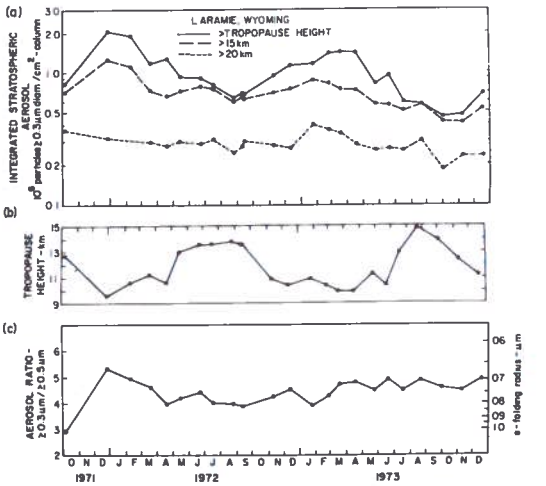

Figure 7. Time variation at Laramie, Wyoming of a) integrated aerosol above the tropopause, above 15 km, and above 20 km; b) tropopause height; and c) aerosol size ratio.

MEASUREMENTS AT OTHER LATITUDES

Although the frequency of soundings made from stations other than Laramie has been lower than one might wish, the uniformity of the current aerosol layer on a global scale allows some conclusions to be drawn from these measurements.

An example of this is the measurements from the polar regions. Figure 8 shows a comparison of three vertical aerosol-concentration distributions over the ice island T-3 (85°N), all a year apart. These measurements again include only particles with diameters greater than 0.3 μm. Above an altitude of about 15 km, little change is seen. Below this altitude the observed decrease is similar to that observed at Laramie (41°N) during this period. High concentrations of particles in the lower atmosphere (below 9

km) were observed in all soundings, although the concentrations were higher in 1971 and 1973. The average particle size below 9 km was observed to be smaller than in the stratosphere.

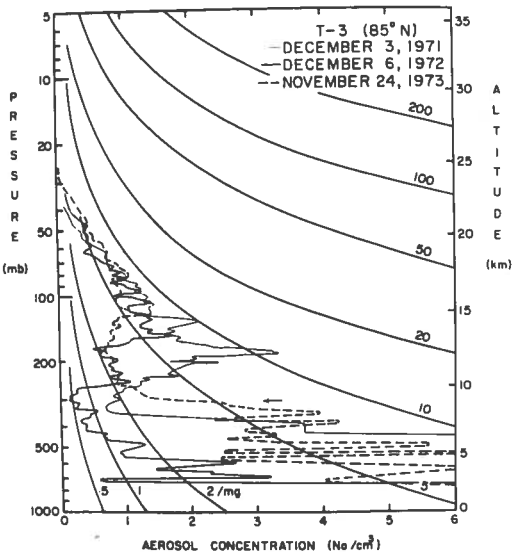

Figure 8. Aerosol concentration versus height over the ice island T-3 on three occasions, each a year apart. The arrow marks the observed tropopause position in 1971. The curved grid lines are lines of constant mixing ratio in units of particles per mg of air.

Measurements of the particles over 0.3 μm in diameter made one year apart at the South Pole are shown in Figure 9. Here one observes little if any difference in the stratospheric aerosol between the two periods. The sharply defined layer at about 3 km in the 1973 sounding was due to a low-lying cloud over the 2.8 km polar icecap. The total aerosol loading observed at the South Pole was relatively high, being at least as great as that observed at Laramie during the same time period. In view of the marked seasonal variation observed at Laramie, one might have expected that the local summer loading at the South Pole would have been considerably less than that in local winter at Laramie, if a corresponding seasonal variation was effective at the South Pole.

Figure 10 shows the total stratospheric-loading parameter, as displayed for the Laramie soundings in Figure 7a, together with the observed aerosol loading as a function of time at other latitudes. In this figure the time scales for stations in different hemispheres are shifted by 6

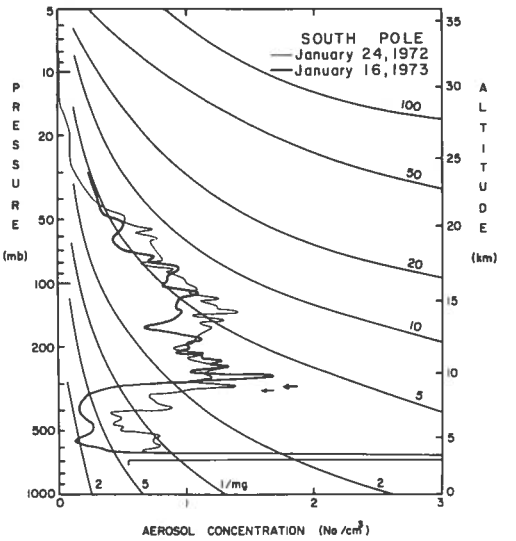

Figure 9. Aerosol concentration versus height over the South Pole on two occasions a year apart. The arrows mark the observed tropopause positions. The curved grid lines are lines of constant mixing ratio in units of particles per mg of air.

months, so that if a simple symmetric seasonal variation exists globally, all curves should be in phase. A number of features are noteworthy.

1. There appears to be a general latitudinal gradient in particle loading, with a minimum occurring in equatorial regions.
2. Data from stations at comparable latitudes in opposite hemispheres (e.g., Palestine, Texas and Mildura, Australia) suggest that there is not a great inter-hemispheric difference in aerosol loading.
3. The seasonal variation in the northern hemisphere appears to be in phase for all stations except Panama (9°N), which shows a variation 6 months out of phase.
4. The seasonal variation in the southern hemisphere appears to have the phase expected for a simple seasonal variation, except for the Antarctic stations (McMurdo and South Pole), which also may be 6 months out of phase, as suggested by comparison with the north polar data. Since measurements are available for only a single season, the

Antarctic observations might also be interpreted as being due to an in-phase variation, with a total aerosol loading considerably higher than that observed in the north polar regions. For reasons which will be discussed later, the former seems to be the more consistent conclusion.

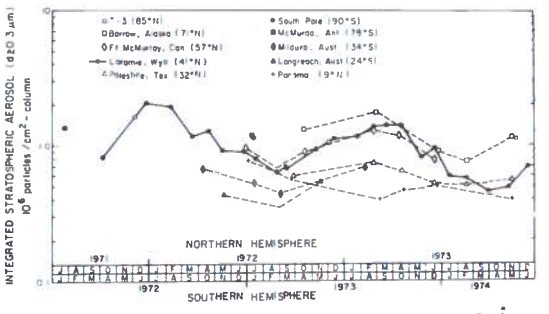

Figure 10. Integrated aerosol as a function of time for all stations. The time scales for the two hemispheres have been shifted relative to one another by 6 months.

LATITUDINAL AEROSOL DISTRIBUTIONS

A major first step in the interpretation of somewhat limited sounding data is the identification of unusual or non-typical profiles. Only after some repeatability is recognized can such differentiation begin. The Laramie flights provide the most information for this type of study. Typical seasonal profiles (Figures 3, 4, and 5) have been identified for the Wyoming location. The spring soundings showed a wide amount of variation near the tropopause level, whereas the summer profiles are all very similar. The winter profiles suggest an intermediate situation. This is what might be expected, since spring represents a time of year when atmospheric conditions are changing rapidly and are in a somewhat disturbed state. On the other hand, summer is a time of relatively static conditions. By the same reasoning, the winter soundings should show little variation, but not enough information is presently available to properly assess them. We have thus come to the conclusion that, for the present, summer is probably the best season during which to compare soundings from a large range of latitudes, because the stratospheric aerosol layer appears to be in a relatively stable and uniform configuration.

Soundings from high or low latitudes seem to show a smaller degree of variability than the midlatitude soundings. An identifiable typical profile emerged after only a few soundings at Barrow and Panama, whereas it took a much longer time for a consistent picture to become evident for the Laramie soundings. For example, the Panama profiles are almost identical if the tropopause heights are made to coincide.

Once typical profiles can be recognized for the various sites, a latitude profile can be constructed with confidence that it represents a somewhat average condition for the time at which the soundings were made. This is more-or-less possible now for the summer season, because during this time the soundings show a great deal of consistency and little variation with time. The final results therefore are not sensitive to simultaneity of the soundings.

Figure 11 shows the vertical concentration profiles of particles having diameters greater than 0.3 μm at five stations in the northern hemisphere, measured within about a week of each other in summer. The three midlatitude soundings were made on June 19, 1973, while the high-latitude and low-latitude soundings were made on June 27, 1973. The aerosol mixing-ratio latitude-height distribution constructed from these data is shown in Figure 12. The heavy barred line shows the measured height of the tropopause. As indicated earlier, this season is characterized by low aerosol mixing ratios in the lower stratosphere and upper troposphere. The region of highest mixing ratio is in the equatorial stratosphere, with the height of the maximum sloping downward to the north. For comparison, the ozone mixing-ratio distribution and the potential-temperature distribution, measured at the same time as the aerosol, are shown in Figures 13 and 14 respectively. Except perhaps near the tropopause, there is little similarity between these distributions. The aerosol distribution shows a greater height variation with latitude than do the other two quantities.

A winter series of soundings was carried out in late November, 1973, but the latitudinal aerosol distribution was not ready for presentation at this time. As a substitute, we show in Figure 15 a distribution measured during fall, which is a transitional period when the mixing ratio just above the tropopause is beginning to

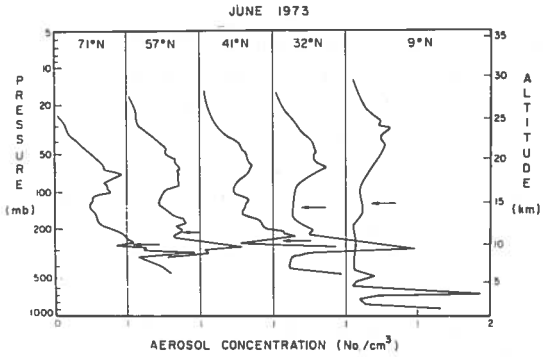

Figure 11. Individual aerosol ($d \geq 0.3$ μm) soundings in the northern hemisphere during the period 19-27 June 1973. Arrows indicate the observed tropopause positions.

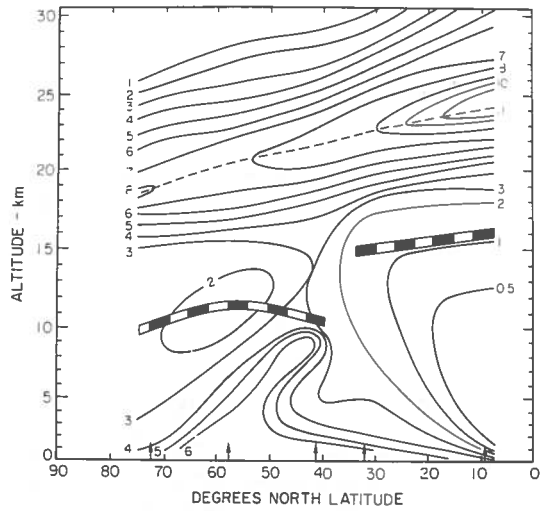

Figure 12. Isopleths of constant aerosol mixing ratio in units of particles per mg of air as a function of latitude and altitude, constructed from the data in Figure 11. Arrows indicate the sounding sites. The heavy barred line is the approximate position of the tropopause.

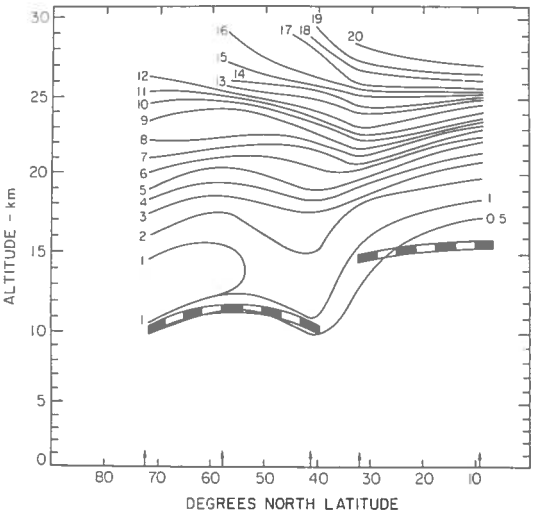

Figure 13. Isopleths of constant ozone mixing ratio in μg per g air as a function of latitude and altitude, measured concurrently with the data in Figure 12.

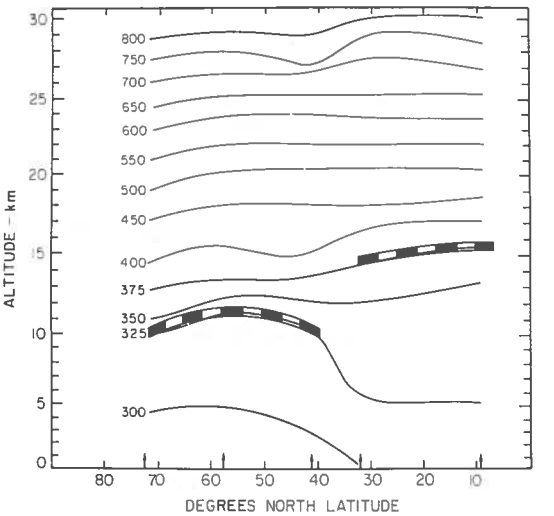

Figure 14. Potential temperature distribution measured concurrently with the data in Figure 12.

increase. Possible effects of the tropopause gap at midlatitude are suggested.

A springtime aerosol distribution is shown in Figure 16. The high degree of complexity is typical of this season. Multiple-layered structure is common, and some of the layers appear to extend over 30° of latitude. The multiple-layered structure at high altitude observed in the Barrow, Alaska (71°N) sounding during this series must be regarded as nontypical and thus makes detailed analysis of the latitudinal distribution at this time hopeless.

The amount of latitude resolution needed to obtain representative structure can be estimated from information such as that shown in Figures 12, 15, and 16. If the structure size is larger than the distance between sounding sites, then adequate resolution has probably been obtained. In

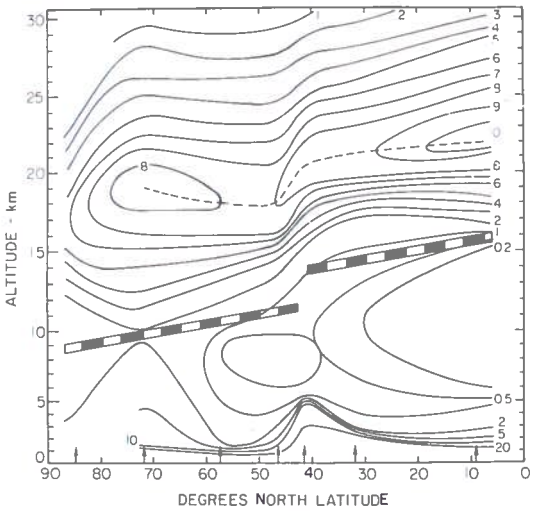

Figure 15. Isopleths of constant aerosol mixing ratio as a function of latitude and altitude during fall 1972. Arrows indicate the sounding sites. The heavy barred line is the approximate position of the tropopause.

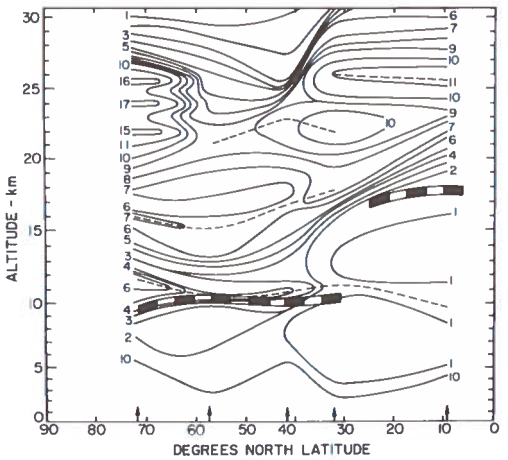

Figure 16. Isopleths of constant aerosol mixing ratio as a function of latitude and altitude during spring 1973. Arrows indicate the sounding sites. The heavy barred line is the approximate position of the tropopause.

some cases, however, especially in spring, the latitude profiles show structures whose size is on the order of the site spacing, indicating that the resolution may not be adequate. Unfortunately, the number of sites could not be increased under the existing constraints of the sampling program.

Figure 17 shows an attempt to construct an aerosol distribution in the southern hemisphere from two Australian and two Antarctic stations during the austral summer of 1972-1973. The equatorial mixing ratios were artifically generated from the tropopause height by utilizing the observation of the intimate relation between the height of the aerosol layer and that of the tropopause in equatorial regions of the northern hemisphere. Although this is admittedly a weak example of global coverage, the distribution is probably representative, since it is for the summer season. This distribution resembles that in Figure 12 enough that one may conclude that no major differences exist between hemispheres.

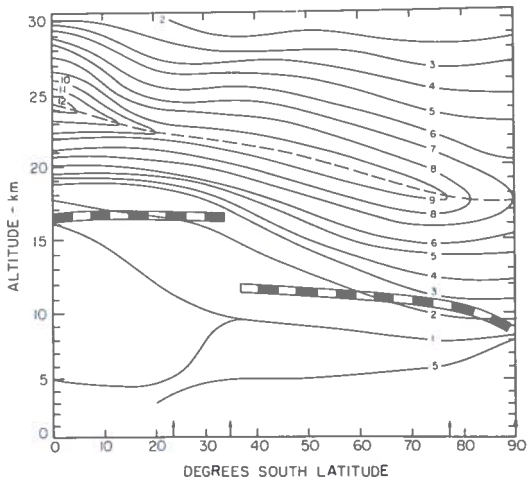

Figure 17. Isopleths of constant aerosol mixing ratio as a function of latitude and altitude during summer 1972-1973 in the southern hemisphere. Arrows indicate the sounding sites. The heavy barred line is the approximate position of the tropopause.

On occasion, extensive layers of particles have been observed in the troposphere. Examples of these are shown in Figures 18 and 19. The first of these, measured in the summer of 1972, shows two layers, one near the tropopause and another a few kilometers below it. These tropospheric layers were probably associated with a small volcanic eruption which occurred in Japan in June 1972. Its time development was measured at Laramie, and has been reported earlier (Rosen et al., 1972). No sizable effect on the stratospheric aerosol layer was evident.

A second case, shown in Figure 19, measured in April, 1973, indicates a highly extensive tropospheric layer at about 5 km. Since it is very unlikely that ordinary tropospheric features such as clouds could be this extensive, we have

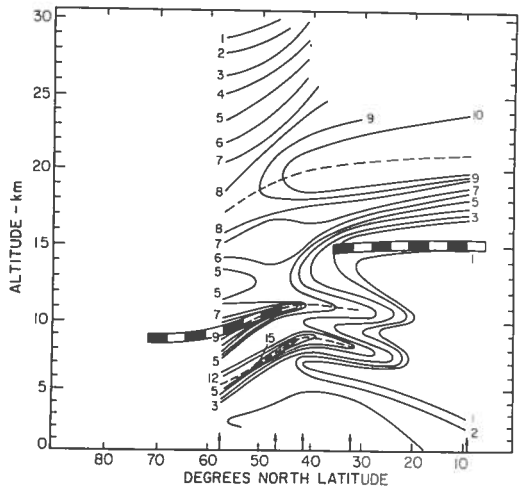

Figure 18. Isopleths of constant aerosol mixing ratio as a function of latitude and altitude during summer 1972. Arrows indicate the sounding sites. The heavy barred line is the approximate position of the tropopause.

tentatively identified it as being due to volcanic activity in Iceland during this period. The height of the eruption plumes agrees quite well with the observed height of the layer.

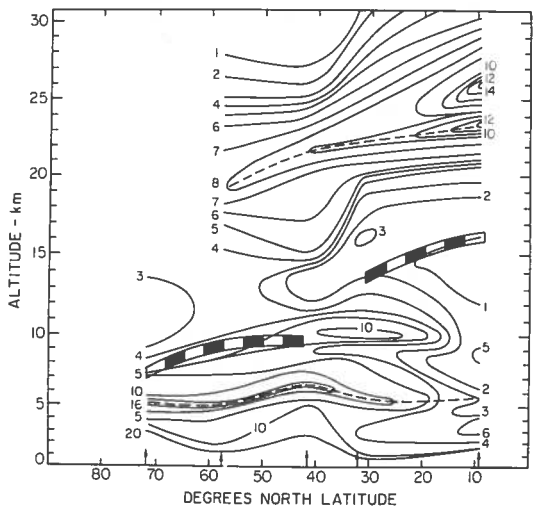

Figure 19. Isopleths of constant aerosol mixing ratio as a function of latitude and altitude during spring 1973. Arrows indicate the sounding sites. The heavy barred line is the approximate position of the tropopause.

DISCUSSION

Perhaps the most significant observations in the program to date, and thus deserving of further scrutiny, are the marked seasonal variation found at northern midlatitudes, the similarity of the north and south polar aerosol profiles, and the asymmetric nature of the apparent global seasonal variation.

The high degree of correlation between total stratospheric aerosol and the tropopause height observed at Laramie (Figure 7) can hardly be coincidental. In fact, if one studies the individual profiles, it becomes evident that the variation occurs mainly in the lower stratosphere, i.e., that region in which the tropopause exhibits its seasonal variation in height. It is thus rather clear that, at least at northern midlatitudes, the tropopause height variation is affecting the stratospheric volume available for aerosol formation and transport. This effect is not felt above about 20 km.

The similarity of the polar observations is demonstrated in Figure 20. Although the T-3 (85°N) sounding was made in local winter and the South Pole sounding in local summer, the profiles are nearly identical. This suggests either that the polar seasonal variation is unusual or that it does not exist at all. The other unusual feature of the global seasonal variation is the observation that Panama is 6 months out of phase with the other northern-hemisphere stations.

Having observed an excellent correlation between total stratospheric-aerosol loading and tropopause height at Laramie, we investigated whether such a relation was valid at other latitudes. In Figure 21 is plotted the integrated aerosol loading versus the observed tropopause pressure for all the stations. The correlation is good; it has a coefficient of 0.8. This demonstrates that the total stratospheric-aerosol loading displays a global seasonal variation which is intimately related to the height of the tropopause. This may at first seem incongruous, given the observed phase differences at some stations. This apparent difficulty is somewhat clarified by the fact that one observes the same phase differences in the tropopause height. This is shown in Figure 22, where monthly-mean tropopause heights versus latitude for the two extreme

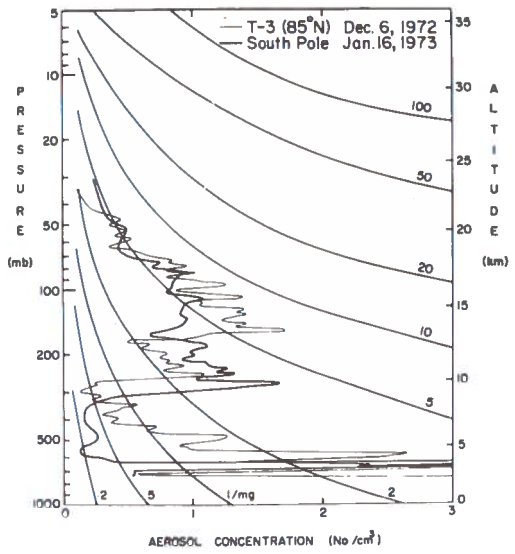

Figure 20. A comparison of the vertical distribution of aerosol particles having diameters greater than 0.3 μm over the ice island T-3 and the South Pole six weeks apart. The curved grid lines are lines of constant mixing ratio in units of particles per mg of air.

seasons are shown. These data were obtained during the IGY period 1957-1958 (Monthly Mean Aerological Cross Sections, 1961); the general features appear to be valid annually, however.

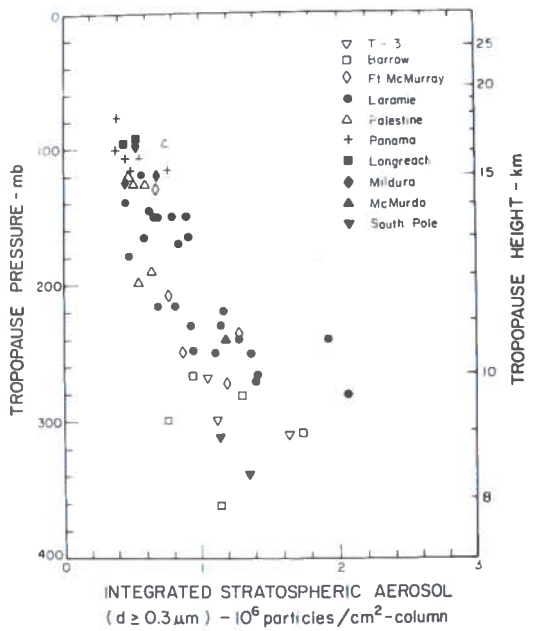

Figure 21. The global total stratospheric aerosol loading as a function of observed tropopause height.

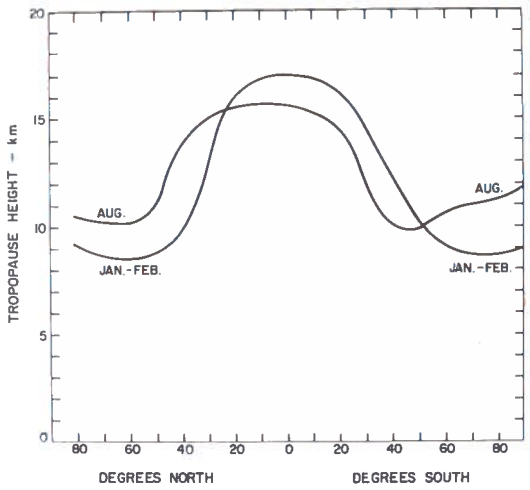

Figure 22. The location of the average tropopause as a function of latitude for the seasons when the tropopause height is at extreme values.

Figure 22 suggests that if the tropopause height is a controlling factor in the total stratospheric-aerosol loading, then Panama, at 9°N, should experience a seasonal variation in phase with the Australian stations and the two poles should exhibit in-phase seasonal variations. Both of these expectations are consistent with our observations, and it can be concluded that the height of the tropopause is a major factor in the modulation of the stratospheric aerosol.

The apparent ability of tropopause height variations to affect the aerosol loading by as much as a factor of two, when such variations seem to have only small effects on the ozone distribution, can be attributed to the apparent location of the aerosol source region. The region of maximum aerosol mixing ratio is considerably closer to the tropopause than the ozone source region, which displays a maximum ozone mixing ratio at about 35 km in equatorial regions. Thus Dütsch (1963) observed an annual-average correlation coefficient of only 0.5 between tropopause height and total ozone at Arosa, Switzerland. One concludes that the proximity of the aerosol source region, presumably fed from below rather than from above, to the fluctuating tropopause gives the latter greater control over the "effective size" of the stratosphere in terms of aerosol-formation capacity.

An obvious alternate explanation of the Panama observations is that the observed decrease in the total aerosol at Panama, at the

time when other northern-hemisphere stations are observing an increase, is due to transport from equatorial regions northward at this time. In fact this phenomenon does occur, just as there is meridional transport of ozone; nevertheless, the lowering of the tropopause during local summer at Panama appears to be associated with an increase in aerosol concentration in the lower stratosphere, so the height of the tropopause apparently affects the size of the equatorial aerosol source region. In terms of mixing ratio, a different picture emerges. The mixing-ratio profiles over Panama are essentially identical if the tropopause levels are made to coincide. Thus the maximum in the mixing-ratio profile moves up and down with the local tropopause. Even though the mixing ratio at the maximum stays relatively constant, a high tropopause will dictate less total aerosol loading. It is interesting to note that even though the equatorial tropopause, and consequently the aerosol maximum, may vary in altitude considerably from flight to flight, the ozone mixing-ratio profiles do not change appreciably. Although this observation might change somewhat if seasonal averages rather than individual soundings were compared, it is highly suggestive of an aerosol source at the tropopause which has a relatively short time constant, i.e., the depleting effects of meridional transport are continuously being counterbalanced by the aerosol source to maintain a constant mixing-ratio profile at a fixed distance from the tropopause.

The degree to which meridional transport and local production of aerosol compete in producing the observed aerosol profile at mid- and high latitudes is not yet known, and can probably be determined only through model calculations when all the necessary data, including vertical distributions of SO_2 and Aitken nuclei, are obtained. In addition, the importance of interhemispheric exchange in the stratosphere will probably have to be taken into account to accurately describe the physical situation. For example, such a process could account for the observation of similar aerosol concentrations in the two hemispheres even though the northern hemisphere is the predominant anthropogenic sulfur-producer.

Although the ingredients of the gas-phase chemistry almost surely include SO_2, more complicated sulfur compounds, such as dimethyl sulfide, which has recently been discovered in sea water (Lovelock et al., 1972), may also be important. It is possible that sulfur-bearing gases are injected into the stratosphere under certain meteorological conditions in extratropical regions, so transport from equatorial regions northward may not be the dominant high-latitude source, as it is with ozone. Injection into the stratosphere of Aitken nuclei, and coagulative production of larger aerosol, cannot yet be ruled out as a contributing mechanism.

The observation at Laramie of a highly layered aerosol structure in the region of the tropopause during spring and early summer, when the total aerosol is decreasing, suggests that horizontal transport, probably through the mid-latitude tropopause gap, is the dominant sink mechanism in the lower stratosphere.

The parameter which is perhaps best suited for identifying true long-term trends in the stratosphere is the peak aerosol mixing ratio. This quantity does not appear to be overly sensitive to meteorological parameters or altitude; it reflects what might be considered the source strength of particles. Further analysis is necessary, however, to fully determine the usefulness of this parameter.

The general complexity of the system at midlatitudes is demonstrated in Figure 23, where the aerosol mixing ratio, in units of particles ($>$ 0.3 μm diameter) per mg air, is plotted versus height and time at Laramie. A complicated stratospheric-tropospheric exchange is indicated in spring. The lines of constant mixing ratio seem to follow the tropopause height in a general manner in the lower stratosphere (where tropopause effects are felt) but not at higher altitudes. The presence or absence of meridional transfer during the winter buildup period is difficult to discern without similarly detailed histories at other latitudes to "trace" air-parcel movements.

Although the latitude survey profiles presently available are crude and perhaps somewhat inadequate, they do nevertheless suggest and illustrate some important aspects of the global distribution of aerosols. The discussion here will be limited to those conclusions best supported by the data.

Extensive aerosol layers have been observed on several occasions in the northern hemisphere. They occur in the lower stratosphere and upper

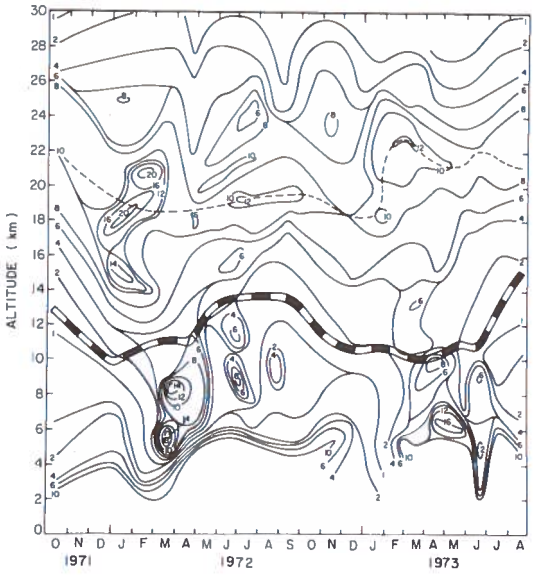

Figure 23. Aerosol mixing ratio in units of particles per mg of air as a function of height and time at Laramie, Wyoming. The observed height of the tropopause is indicated by the heavy broken line.

troposphere and in one case cover a latitude range from Barrow, Alaska, to Panama. The layers appear to be continuous, but more latitude coverage would be desirable to prove this beyond doubt. In the lower stratosphere an ozone layer generally appears with an aerosol layer, whereas in the troposphere there does not seem to be any recognizable structure in the ozone profile that can be associated with the existing aerosol layer. This suggests a different mechanism for the creation of tropospheric layers, since they cannot simply be stratospheric layers that have moved to lower altitudes.

One possible source of the tropospheric aerosol layers is volcanic eruptions. In the early summer of 1972, a Japanese volcano erupted, injecting a smoke cloud up to an altitude of about 9 km, or approximately to the level of the tropopause. Extensive dust layers throughout the troposphere were observed that summer but no unusual increase in the concentration of stratospheric aerosols was noted. It is believed that volcanic eruptions in many parts of the world can go unnoticed, and thus give rise to tropospheric dust layers that cannot be associated with any known volcanic activity. We do not believe a large enough eruption has occurred during the measurement period to enable us to fully assess the influence of volcanic activity on the stratospheric aerosol layer.

In order to better study the transport of stratospheric aerosols, latitude-height distributions of potential temperature and ozone mixing ratio have been investigated as part of each latitude cross-section survey. In regions where these three constituents are conservative their structure should be similar. There is in general not much correlation between the structures of these three quantities, except sometimes near the tropopause. The lines of constant aerosol mixing ratio are observed to be steeper than the lines of potential temperature, indicating that at least one of these quantities cannot be considered a good tracer for stratospheric motions. In view of the general lack of global-scale similarity in structure of aerosols, ozone, and potential temperature, the usefulness of these quantities as tracers for large-scale stratospheric motions is questionable.

In terms of the goals of CIAP, perhaps the most important observation is that artificial injections of material at altitudes below about 17 km in midlatitudes will have lifetimes depending on the season of injection, being influenced by seasonal fluctuations of the tropopause. The cleansing action takes place during spring and early summer, so that a maximum lifetime of about 9 months could be expected for late-summer injections. Correspondingly short lifetimes (i.e., a few months) would be expected for winter injections. Above 20 km one cannot rely on this scrubbing mechanism, and thus lifetimes of particulate matter would be determined by diffusion, sedimentation, and dynamic transport.

Our observation of little or no change in the aerosol loading above 20 km means simply that the source mechanisms (chemical and/or meridional transport) are nearly in equilibrium with diffusion, sedimentation, and coagulation of particles. Thus, until sufficient research has been carried out to pinpoint the nature and strength of the natural source, the effect and magnitude of the sink terms above 20 km (and therefore the expected lifetime of particulates injected in this region) cannot be determined.

ACKNOWLEDGMENTS

This research was supported by the Climatic Impact Assessment Program of the U.S. Department of Transportation, through the Office of Naval Research and the National Science Foundation. Dr. R.G. Pinnick and other members of the Atmospheric Research Group in the Department of Physics and Astronomy at the University of Wyoming were instrumental in carrying out the instrument preparations, field work, and data reduction. A part of this analysis was done while one of us (DJH) was on leave at the Max Planck-Institut für Aeronomie, Lindau/Harz, Federal Republic of Germany, and this opportunity as well as useful discussions there with Dr. P.G. Pruchniewicz are gratefully acknowledged.

REFERENCES

Danielsen, E.F. (1968), "Stratospheric-tropospheric exchange based on radioactivity, ozone and potential vorticity," J. Atmos. Sci. **25**, 502-518.

Dütsch, H.U. (1963), "Mittelwerte und wetterhafte Schwankungen des atmosphärischen Ozongehalts in verschiedenen Höhen über Arosa," Arch. Meteorol. Geophys. Bioklimatol., Ser. A. **13**, 167-185.

Lovelock, J.E., R.J. Maggs and R.A. Rasmussen (1972), "Atmospheric dimethyl sulphide and the natural sulphur cycle," Nature **237**, 452-453.

Monthly Mean Aerological Cross Sections (1961), U.S. Department of Commerce, U.S. Government Printing Office.

Pinnick, R.G., J.M. Rosen and D.J. Hofmann (1973), "Measured light-scattering properties of individual aerosol particles compared to Mie scattering theory," Appl. Opt. **12**, 37-41.

Rosen, J.M. (1964), "The vertical distribution of dust to 30 km," J. Geophys. Res. **69**, 4673-4676.

Rosen, J.M. (1971), "The boiling point of stratospheric aerosols," J. Appl. Meteorol. **10**, 1044-1046.

Rosen, J.M., D.J. Hofmann, T.J. Pepin and J. Kroening (1972), "Extensive dust layer in the Northern Hemisphere," Nature **240**, 347-348.

DISCUSSION

VOLZ: Your data show a very constant aerosol level. If you attribute the variations in the late summer of 1971 to a dust event on which I recently published a paper, then there are no non-seasonal variations over the last three years.

(UNIDENTIFIED): What was that you said earlier about an index of refraction?

HOFMANN: We aren't sure that that increase wasn't just an anomalous seasonal variation, as we have observed a similar one to be.

HOFMANN: I was talking about calibration of the instrument. When I say 0.3 micron in diameter, I refer to a non-absorbing aerosol having an index of refraction between 1.40 and 1.50. If there were some absorption, then the quoted diameter would have to be changed.

(UNIDENTIFIED): How much of your data is from the Antarctic night? I should think these nuclei would form ice crystals – particularly large particles – and leave you a fairly clean sky.

HOFMANN: All our South Pole measurements have been made during the summer; no one seems to want to go down there in winter. The summer aerosol seems to have concentrations and a size distribution pretty close to what we measure everywhere else. We do hope to get some winter measurements this year, though.

RECENT MEASUREMENTS OF CONDENSATION NUCLEI IN THE STRATOSPHERE

JAMES M. ROSEN, RONALD G. PINNICK, AND RICE HALL
Department of Physics and Astronomy
University of Wyoming
Laramie, Wyoming

ABSTRACT: A type of condensation nuclei (CN) counter for application at low pressures has been developed. This instrument draws ambient air through a chamber in which a given degree of supersaturation is maintained. The CN in the sampled air subsequently grow fairly large and are then counted by a photoelectric particle counter. This technique has the advantage of not requiring the usual type of calibration. The CN counter was tested in a vacuum chamber under simulated stratospheric pressures to adjust the parameters so that the efficiency would be independent of pressure. A test balloon flight was conducted on December 19, 1973, from Laramie, Wyoming; consistent data were obtained on both ascent and descent. The CN profile and concentrations agree fairly well with earlier direct measurements of CN. Typical CN concentrations in the stratosphere inferred from this first flight are about 10 per cm^3 or less.

Although there has been much discussion and debate over the concentration of stratospheric particles smaller than 0.1 μm in diameter, relatively few attempts to measure these particles have been reported. A detailed understanding of the so-called stratospheric aerosol layer cannot be reached until the role of these very small particles has been discovered. In addition, a realistic optical model of the stratosphere cannot be developed until the concentration and size distribution of the small particles has been determined. More recently, the influence of the very small particles introduced into the stratosphere in aircraft exhaust has been examined. However, it is difficult to properly assess this problem when neither the natural concentration level nor the emission index of jet engines for this particle size range is definitely known.

More stratospheric measurements of particles smaller than 0.1 μm are clearly necessary, but a repetition of previous experiments may not improve our knowledge, since the accuracy of the detectors at high altitude is in question. For this reason, a new type of counter for detecting these small particles has been designed and built at the University of Wyoming. For the purposes of this paper, particles smaller than 0.1 μm in diameter will be referred to as condensation nuclei (CN) because this name reflects the method by which the concentration was measured. Most CN detectors operate in two stages. In the first stage, a vapor (usually H_2O) is made to condense on the particles so that they grow to a relatively large size. In the second stage some type of light-scattering principle is applied to detect these larger CN. In the Wyoming instrument the CN are grown in a thermal-gradient diffusion cloud chamber (TGDCC) such as that illustrated in Figure 1. The sampled air is first drawn through a device that dilutes the concentration of the CN to a level that can easily be handled by the counter in the last stage. After dilution the sample passes into the TGDCC, whose outer wall is kept at constant temperature by an ice bath. A temperature-controlled inner rod is kept moist with a working fluid. The difference in temperature between the evaporating fluid and the outer wall produces a degree of supersaturation in the TGDCC that depends on the temperature of the inner rod. In the case of laminar flow or no flow at all, the supersaturation can be calculated at any point inside the TGDCC where equilibrium has been established. In actual practice, however, the TGDCC is so short that equilibrium is not attained by the air passing through, and in addition some degree of turbulence is present. These considerations make it impractical to theoretically determine the degree of supersaturation experienced by a parcel of air as it passes through the TGDCC. However, it is

important that the effective degree of supersaturation be known, since this factor determines the minimum CN size that will grow by condensation.

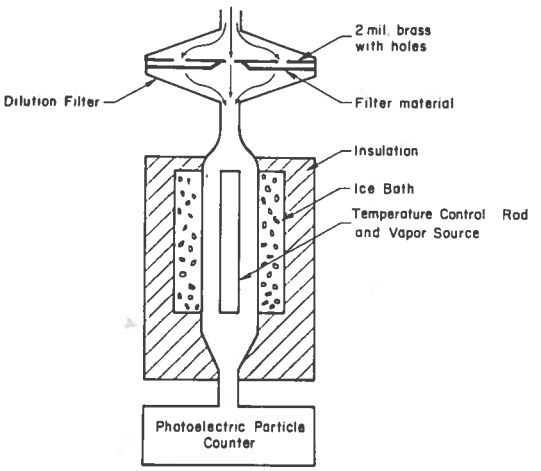

Figure 1. Schematic diagram of the Wyoming CN detector.

Experimentally, the problem has been attacked by measuring the counting rate vs. the inner-rod temperature. As the inner-rod temperature is increased, the degree of supersaturation therefore increases, and the rate at which enlarged CN are counted consequently increases until all the CN present are large enough to be counted. There is then no further increase in counting rate with an increase in inner-rod temperature. Figure 2 shows the actual results of such a measurement, clearly indicating this "plateau." (Such a plateau would not appear if the particle size distribution were continuous from CN to molecules.) However, at still higher inner-rod temperatures the counting rate begins to decrease. We attribute this to a loss in efficiency of the overall system due to the very large size of the particles at high inner-rod temperatures. Thus it is desirable to keep the inner rod at a temperature just high enough to produce condensational growth on all CN present, but no higher. By experiments like that of Figure 2 we are now determining the optimum operating parameters for many types of CN size distributions and chemical compositions, as well as for ambient pressures ranging from equivalent-sea-level to 30 km. The absolute value of the CN concentration measured at sea level is in good agreement with the values obtained from two other independent methods.

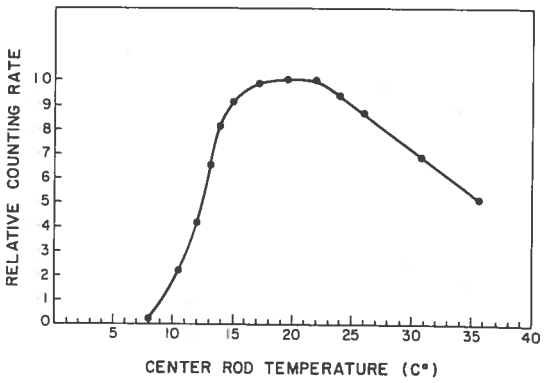

Figure 2. The dependence of measured CN concentration on the inner-rod temperature with atomized distilled deionized water as working fluid.

After the sampled air has passed through the TGDCC, the enlarged particles are detected by a photoelectric particle counter. This part of the instrument is basically the same as the Wyoming dustsonde used in the CIAP program, and as such is fully developed and operational to altitudes of 30 km. Since the instrument counts individual particles, no calibration is required for this stage of detection. However, as mentioned before, other stages of the instrument may operate at efficiencies somewhat less than 100%, and an experimental investigation will be necessary to determine the minimum size of CN detectable.

The efficiency of the instrument at high altitude has been determined from tests in a vacuum chamber with an arrangement as shown in Figure 3. The procedure involved installing the entire instrument in a large vacuum system, along with a tank to hold the CN sample. The sample tank was connected to the CN counter and also vented to the inside of the vacuum system through a filter permitting free flow. Operation was begun at atmospheric pressure and the counting rate of the instrument noted. For an ideal detector the counting rate would be proportional to the pressure as the system is evacuated, provided the CN are not volatile. When the system is slowly brought back to atmospheric pressure by adding clean air, the counting rate should be independent of pressure. Correction to the CN concentration arising from diffusive loss to the walls of the sample tank and from clean air displacing the sampled air can be estimated from the decay rate measured at

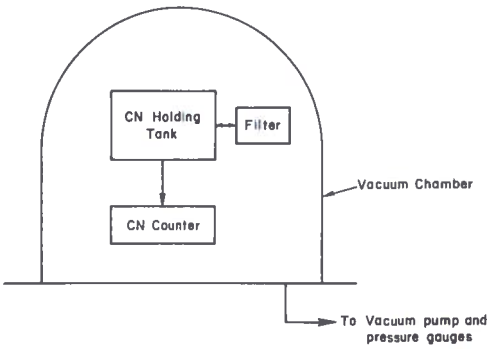

Figure 3. Schematic diagram of the apparatus used to test the Wyoming CN counter at low pressure.

several pressures covering the range of operation. At its present state of development, the CN counter will operate from ground level to 23 km altitude with an efficiency nearly equal to 1 (see Figure 4).

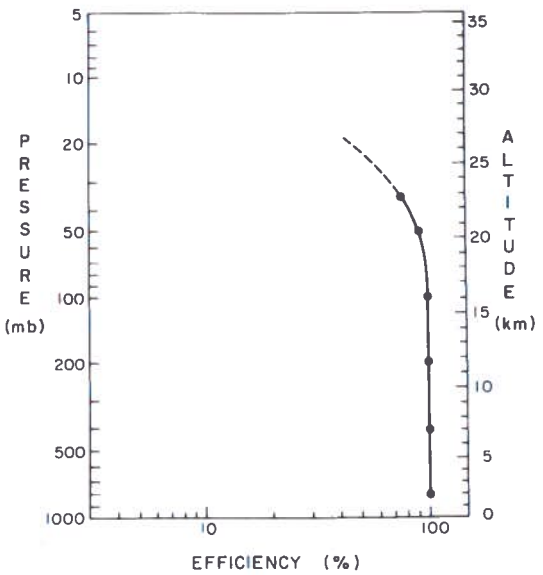

Figure 4. The efficiency of the Wyoming CN counter as a function of pressure.

Even though the CN counter is not fully developed, a test flight was conducted to assess the overall feasibility of the instrument, as well as to help determine the approximate CN concentration to be expected over the range of operating altitudes. The results, shown in Figure 5, have been corrected for efficiency and the dilution rate. Even with the dilution device the counter will not respond reliably to ambient CN concentrations of more than about 700 per cm^3. (During the latter part of the ascent a problem developed in the telemetry system and some data was lost.)

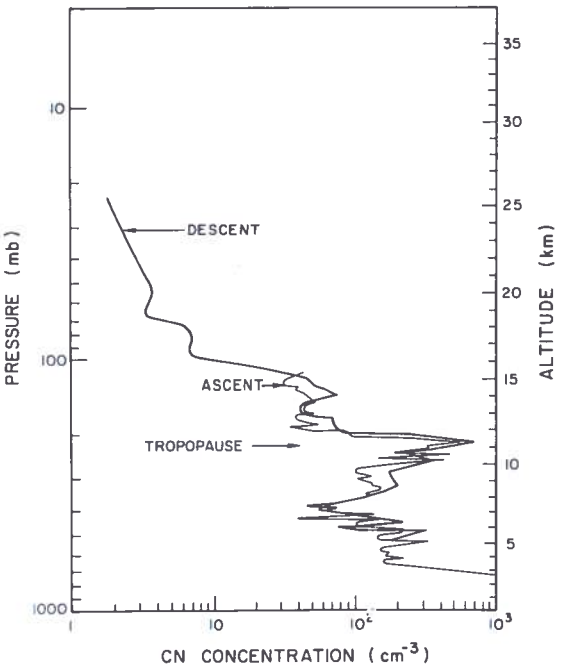

Figure 5. The vertical profile of CN concentrations obtained from Laramie, Dec. 19, 1973, using the Wyoming CN counter.

The agreement of the ascent and descent profiles implies that the instrument is at least consistent. More structure is observed on ascent since the instrument is moving more slowly. The raw data show significant variations in the CN concentration within an altitude interval of 50 meters.

The absolute values obtained during the test flight agree well with the direct measurements of Junge et al. (1961) and Hoppel et al. (1973), considering the difference in times and locations. For purposes of comparison, these other data are presented in Figure 6. Since the instrument apparently provided credible results, some comment on the meaning of the data itself seems warranted. It is noteworthy that significant layers in the upper troposphere were found in many of the soundings reported by Junge et al. (1961) as well as in this study. However, the Wyoming sounding shows a much bigger layer with a considerable amount of fine structure. The recent measurements by Hoppel et al. (1973) also provide evidence of a CN layer in the upper troposphere.

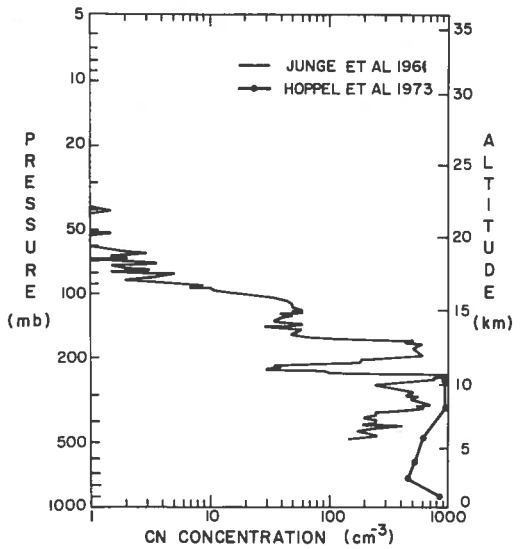

Figure 6. The vertical profile of CN concentration as obtained by other investigators by direct sampling methods. The data of Junge et al. were taken on Nov. 2, 1959, from Sioux Falls. The data of Hoppel et al. are an average of five soundings taken in June of 1972 off the East and West coasts.

We believe that these observations suggest a jet air-traffic source for the CN layer. Its apparent increase since 1959, when the measurements by Junge et al. were made, is consistent with the increase in air traffic, and the layer covers exactly the altitude range that is used by commercial jet aircraft. The fine structure in the CN profile could be due to individual exhaust trails that have not had enough time to completely diffuse. Furthermore, the amount of jet fuel being consumed in the upper troposphere is consistent with the mass budget required by the CN. The present jet-fuel consumption in the free world is about 25×10^9 gallons a year (Beckwith, 1972). The total consumption in the northern hemisphere is probably very close to this amount. About 96% of this fuel is consumed above 6 km at an average flight altitude of 11 km (Beckwith, 1972). The amount of this fuel that appears as an aerosol is determined by the emission index, which is measured in milligrams of aerosol per gram of fuel burned. The emission index has been determined from in-situ measurements as well as from tests conducted under simulated flight conditions (Rosen and Greegor, 1974; Sawyer, 1970). The results indicate that about 1 mg of aerosol per g of fuel is produced under cruise conditions. The emission index for CN, however, may be smaller than this typical value of 1. The measured size distribution of particles in the exhaust indicates that a very conservative lower value of the emission index for CN would be 0.1. Thus about 10^9 gm of CN could be injected into the region around 11 km every month. In the northern hemisphere this implies a source strength of about 1000 CN/cm^3-mo for particles 0.01 μm in diameter. Since the lifetime of aerosol at this altitude, determined by the decay rate of volcanic dust layers (Rosen et al., 1972), would be about a month, the concentration of CN produced by jet air traffic should be about 1000/cm^3 – a value very close to that observed.

If it is true that the source of CN in the upper troposphere is jet-engine emissions, then clearly a partial transfer of air traffic to the stratosphere could greatly alter the present CN concentrations at the new flight levels. At present there are apparently relatively few centers of condensation which play a role in forming the stratospheric aerosol layer. If a large number of CN were present, the formation of that layer could be prevented in much the same way that contrails are greatly reduced by the introduction of copious numbers of CN. Thus it seems possible that increased air traffic in the stratosphere may actually reduce the present concentration of optically active aerosols rather than increase it.

We hope the above discussion will be taken as a tentative suggestion rather than a definite conclusion, since parts of the argument are based on poorly known parameters.

This research was supported under the Climatic Impact Assessment Program of the United States Department of Transportation through the Office of Naval Research.

REFERENCES

Beckwith, W. Boynton (1972), "Future patterns of aircraft operations and fuel burnouts with remarks on contrail formation over the United States," in the Proceedings of the International Conference on Aerospace and Aeronautical Meteorology, May 1972, published by the American Meteorological Society.

Hoppel, W.A., J.F. Dinger, and R.E. Ruskin (1973), "Vertical profiles of CCN at various geographical locations," J. Atmos. Sci. **30**, 1410-1420.

Junge, C.E., C.W. Chagnon, and J.E. Manson (1961), "Stratospheric aerosols," J. Meteorol. 18, 81-108.

Rosen, J.M., D.J. Hofmann, T.J. Pepin, and J. Kroening (1972), "Extensive dust layer in the Northern Hemisphere," Nature 240, 347-348.

Rosen, J.M. and R. Greegor (1974), "Jet engine soot emission measured at altitude," J. Aircraft 11, 243-245.

Sawyer, R.F. (1970), "Reducing jet pollution before it becomes serious," J. Astro. and Aero. 8, 62-67.

COMPARATIVE LIDAR/AIRCRAFT MEASUREMENT OF STRATOSPHERIC AEROSOLS

PHILIP B. RUSSELL, WILLIAM VIEZEE, AND RICHARD D. HAKE, JR.
Stanford Research Institute
Menlo Park, California

ABSTRACT: Results are presented from the SRI/WB-57F comparative lidar/aircraft experiment conducted in July 1973. Good agreement between aircraft- and lidar-inferred ambient aerosol mass concentration was obtained by modeling the sampled particles as spherical droplets of aqueous sulfuric-acid solution with a specific gravity of 1.5, a real refractive index of 1.41, and the Deirmendjian Haze H size distribution. The particle composition, specific gravity, and refractive index adopted are consistent with a laboratory analysis of the aircraft-collected filter sample and the estimated ambient relative humidity. The size distribution adopted is consistent with several previous CIAP-sponsored measurements. The sensitivity to assumed particle acidity (and thus to estimated ambient humidity) of the lidar and aircraft particulate-mass values is explored, showing that the two measurements agree for any assumed H_2SO_4 mass fraction between 40 and 94%. Finally, with a model H_2SO_4 mass fraction of 60%, lidar observations were converted to a time series of stratospheric particulate optical depths for the period October 1972 through September 1973. The resulting values are approximately an order of magnitude smaller than those obtained by searchlight measurements made in 1964 and 1965, when there was a large volcanic contribution to the stratospheric aerosol.

INTRODUCTION

In late July of 1973 a comparative experiment, including aircraft sampling and lidar observations of stratospheric particulates, was conducted at Menlo Park, California. The experiment was designed to compare lidar and in-situ measurements of particulate content, as well as to obtain information on the composition of the particulate material. The joint experiment involved participation by three CIAP-sponsored groups, namely, (1) lidar observations by SRI, (2) aircraft sampling by LASL, and (3) laboratory analysis at NCAR. The experiment included one aircraft overflight and three periods of lidar observations.

This paper will present first a comparison of the aircraft and lidar measurements of particulate mass concentration, and then a time series of particulate optical depths obtained from our lidar measurements by using an *optical model of the stratospheric aerosol* which is consistent with CIAP measurements. Descriptions of the lidar's operating principle, the SRI equipment, and the method of lidar-data analysis, as well as a number of other experimental results, have been given in our previous reports (Viezee et al., 1973a,b; Collis et al., 1973; Russell et al., 1973a,b,c, 1974) and will not be included in this paper.

COMPARISON OF AIRCRAFT- AND LIDAR-INFERRED PARTICULATE MASS CONCENTRATIONS

On 26 July 1973 a CIAP-instrumented WB-57F aircraft made in-situ measurements at an altitude of 61,000 ft (18.7 km) (MSL) over the SRI lidar site at Menlo Park, California. A sample of ambient particulate material was collected by means of a wing-pod filter sampler provided by William A. Sedlacek of LASL. This sample was returned to the laboratory and analyzed for chemical composition and mass by Bruce Gandrud and Allan Lazrus of NCAR. Some of the results of that analysis are shown in Table 1.

The analysis revealed a particle composition which was essentially an aqueous sulfuric-acid solution with an ambient mass concentration of $(5.8 \pm 1.1) \times 10^{-14}$ g cm^{-3} of sulfate ion ($SO_4^{=}$). The acid/water mass ratio of the solution droplets in the stratosphere is determined by the ambient relative humidity (Toon and Pollack, 1973), data for which were not available in this experiment. Therefore, an estimate which had been used in previous CIAP experiments (Dynatrend, 1973) was adopted. This estimate gives an acid/water mass ratio of 60%/40%, and hence a particle specific gravity of 1.5. At the lidar wavelength ($\lambda = 0.6943$ μm), a solution of this specific gravity has a real refractive index of 1.41 (Gray, 1963; Neumann, 1973). The particle shape was judged to be amorphous or spherical, thus permitting scattering to be computed with the Mie theory of scattering by spheres. The particle size distribution was not measured, but the Deirmendjian Haze H distribution was assumed in our analysis because of other experimental support (including some results of the Laramie Comparative Experiment, also sponsored by CIAP). (Detailed discussion of the validity of the assumed particle size distribution and shape is given by Russell et al. (1973b).)

Lidar observations were made on two nights prior to the aircraft flight, and also on the night of the flight. Columns 8 through 10 of Table 1 compare the data obtained by the aircraft and the lidar. The aircraft-measured ion mass concentration and assumed specific gravity imply a particulate mass concentration of $(9.8 \pm 1.8) \times 10^{-14}$ g cm^{-3}. The lidar-measured particulate-backscattering coefficients can be converted to mass concentrations by using the refractive index, mass

Table 1. Comparison of Lidar Observations with Aircraft Mass Sampling Measurements

Method of Observation	1	2	Particle Characteristics					Ambient Aerosol Characteristics		
			3	4	5	6	7	8	9	10
	Date (1973)	Time (PST)	Chemical Composition	Density ($g\ cm^{-3}$)	Refractive Index	Shape	Assumed Size Distribution	Particulate Backscattering Coefficient f_A ($m^{-1}\ sr^{-1} \times 10^{-9}$)	Number Concentration, $N(cm^{-3})$*	Mass Concentration, $M (g\ cm^{-3} \times 10^{-14})$
Aircraft (filter sample, 18.7 ± 0.15 km)	26 July	0819-0906	Sulfuric acid and water solution (5.8×10^{-14} g cm^{-3} $SO_4^=$ ambient)[a]	1.5[b]	1.41[c]	Amorphous (frozen) or spherical (liquid) droplets[d]	Deirmendjian Haze H		2.1 ± 0.4[e]	9.8 ± 1.8[f]
Lidar (18.5 - 18.8 km, $\lambda = 0.69\ \mu m$)	23 July	2030-2300						2.9 ± 0.9[g]	1.6 ± 0.5[h]	7.4 ± 2.3[i]
	24 July	2100-2342						4.8 ± 0.9[g]	2.6 ± 0.5[h]	12.2 ± 2.3[i]
	26 July	2210-0030						3.7 ± 0.9[g]	2.0 ± 0.5[h]	9.4 ± 2.3[i]

*Note that N is the total number of particles (per unit volume) of all sizes. A photoelectric particle counter would measure only the fraction N_R/N of this total (see Table 2).

[a]Aircraft measurement.

[b]Inferred from aircraft measurement (chemical composition plus estimate of ambient humidity) and previous experiments.

[c]Inferred from aircraft measurement (Columns 3 and 4), using standard tabulation at 18.3°C.

[d]Inferred from aircraft measurement (Columns 3 and 4, plus ambient temperature (-61°C), plus room-temperature analysis showing no solid particles larger than instrument resolution of 0.2 μm).

[e]Computed from aircraft measurement (Column 10) using value of $\bar{m}$ (see Table 2) consistent with Columns 4, 6, and 7.

[f]Computed from aircraft measurement (Column 3) using specific gravity from Column 4.

[g]Lidar measurement.

[h]Computed from lidar measurement (Column 8) using value of $\hat{f}_A$ (see Table 2) consistent with Columns 3, 5 to 7.

[i]Computed from lidar measurement (Column 8) using value of $\tilde{f}_A$ (see Table 2) consistent with Columns 3 to 7.

density, size distribution, and shape given in Columns 3 through 7 of Table 1. This conversion requires computation of $\tilde{f}_A$, the backscattering coefficient per particulate mass per unit volume. Values of $\tilde{f}_A$ for a range of assumed particle characteristics, including those used in Table 1, are given in Table 2. By using the relation

$$M = f_A/\tilde{f}_A \qquad (1)$$

and the appropriate value (3.94×10^4 m^{-1} sec^{-1} g^{-1} cm^3) of $\tilde{f}_A$ from Table 2, the lidar-measured values of particulate backscattering coefficient f_A in Column 8 of Table 1 were converted to the ambient particulate mass concentrations M shown in Column 10 of Table 1. For all dates the lidar-inferred values are within experimental error* of the aircraft-inferred value; for 26 July the agreement is excellent.

All of the mass values can be converted to particulate number concentrations N by using the assumed particle size distribution and density; the resulting values are given in Column 9 of Table 1. Particle number concentrations may also be obtained directly from the lidar measurements of f_A by using the appropriate value (from Table 2) of $\hat{f}_A$, the backscattering coefficient per particle per unit volume, and the relation

$$N = f_A/\hat{f}_A . \qquad (2)$$

Figure 1 shows the lidar/aircraft comparison from a slightly different viewpoint. Here the aircraft-inferred mass value has been converted to a backscattering coefficient (using the inverse of Eq. (1)). Again, the agreement is seen to be good on all three dates, and very good on 26 July, the actual date of the overflight. In fact, the difference between the lidar and aircraft values for 26 July is so much smaller than the measurement uncertainties that the agreement appears to have been forced. We have therefore investigated the sensitivity of the inferred values to the assumptions made in our analysis.

For a range of reasonable particle size distributions (cf. Table 2), we have shown that the conversion of backscattering coefficient to mass is not very sensitive to assumed particle size distribution. However, both aircraft-inferred and lidar-inferred mass depend quite strongly (and oppositely) on particle specific gravity, which was obtained in this experiment only from an estimate of ambient relative humidity. In addition, changing the particle specific gravity also changes the particle refractive index (Gray, 1963; Russell et al., 1973b), and the particulate backscatter-to-mass ratio $\tilde{f}_A$ is strongly dependent on refractive index (cf. Table 2). Both refractive index and specific gravity are determined by the acidity of the droplet solution, which we originally assumed to be 60% sulfuric acid by mass.

* The stated error (uncertainty) limits are ± 1σ. The aircraft error bars result from uncertainties in measured mass of sulfate ion and computed volume of sampled air. The lidar error bars result from Poisson counting statistics, radiosonde-derived density errors, and uncertainty in the stratospheric light-extinction profile used to compute scattering ratios and backscattering coefficients. For detailed error analyses, see Viezee et al. (1973a) and Russell et al. (1973a,b).

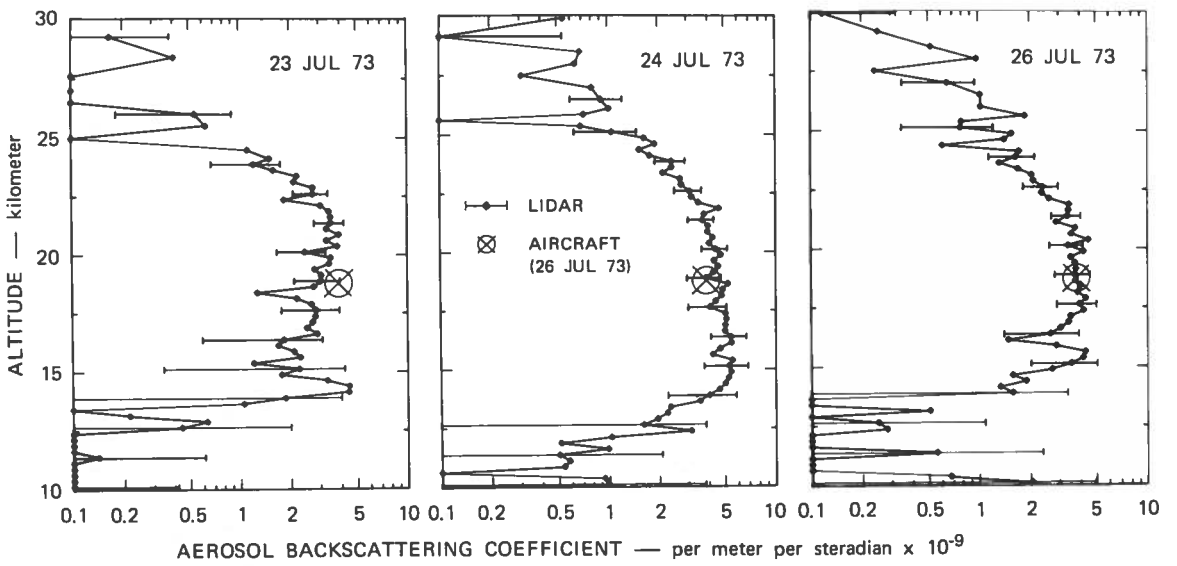

Figure 1. Comparison of lidar-measured particulate backscattering coefficients with computed value based on aircraft mass-sampler measurement. The computation assumes an aerosol mass density of 1.5 g cm^{-3}, the Deirmendjian Haze H size distribution (spherical particles), $\lambda = 0.7$ μm, and refractive index m = 1.41. See text for details.

Table 2. Light-Scattering and Other Properties Computed for Selected Aerosol Size Distributions and Refractive Indices

Size Distribution	N (cm^{-3})	N_R/N R = 0.15 μm	N_R/N R = 0.25 μm	$N_{0.15}/N_{0.25}$	$\bar{v}$ ($cm^3 \times 10^{-14}$)	ρ ($g\ cm^{-3}$)	$\bar{m}$ ($g \times 10^{-14}$)	Refractive Index	$\hat{\beta}_p$ ($m^{-1}cm^3 \times 10^{-7}$)	$P(\pi)/4\pi$	$\hat{f}_A$ ($m^{-1}sr^{-1}cm^3 \times 10^{-9}$)	$\hat{\gamma}_A$ ($m^{-1}sr^{-1}g^{-1}cm^3 \times 10^4$)
Deirmendjian Haze H	100	0.417	0.124	3.36	3.14	1.5	4.73	1.33[a]	0.988	0.01095	1.08	2.29
								1.40[b]	1.36	0.01282	1.75	3.69
								1.41	1.41[d]	0.0131[d]	1.86[d]	3.94[d]
								1.45[b]	1.63	0.01431	2.33	4.92
								1.54[a]	2.07	0.01847	3.81	8.09
Deirmendjian Haze L	100	0.474	0.236	2.01	11.7	1.5	17.55	1.33[a]	3.95	0.01002	3.96	2.26
								1.40[b]	4.47	0.01605	7.17	4.09
								1.41	4.52[d]	0.01777[d]	8.03[d]	4.58[d]
								1.45[b]	4.73	0.02465	11.66	6.64
"Junge"												
r_1 (μm)	r_2 (μm)	ν										
0.04	10.0	2.5		3.59	1.98	1.5		1.5[c]	0.290	0.049	1.39	4.68
		3.0		4.63	0.444	1.5		1.5[c]	0.101	0.039	0.390	5.86
		3.5		5.98	0.176	1.5		1.5[c]	0.407	0.034	0.140	5.30
		4.0		7.72	0.107	1.5		1.5[c]	0.0185	0.035	0.652	4.06
0.08	10.0	2.5		3.59	10.9	1.5		1.5[c]	1.63	0.049	7.80	4.77
		3.0		4.63	3.10	1.5		1.5[c]	0.797	0.038	33.02	6.49
		3.5		5.98	1.37	1.5		1.5[c]	0.448	0.032	1.45	7.06
		4.0		7.72	0.851	1.5		1.5[c]	0.279	0.031	0.859	5.67
0.04	3.0	2.5		3.59	1.03	1.5		1.5[c]	0.262	0.045	1.19	7.70
		3.0		4.63	0.347	1.5		1.5[c]	0.0977	0.035	0.369	7.07
		3.5		5.98	0.166	1.5		1.5[c]	0.0404	0.034	0.137	5.50
		4.0		7.72	0.106	1.5		1.5[c]	0.0184	0.035	0.0648	4.08
0.08	3.0	2.5		3.59	5.50	1.5		1.5[c]	1.47	0.045	6.66	8.07
		3.0		4.63	2.32	1.5		1.5[c]	0.772	0.037	2.84	8.16
		3.5		5.98	1.26	1.5		1.5[c]	0.445	0.032	1.42	7.51
		4.0		7.72	0.837	1.5		1.5[c]	0.278	0.030	0.855	6.81

Notes: $n(r)\,dr \equiv$ number of particles per unit volume with radii between r and r + dr.

$N_R \equiv \int_R^\infty n(r)\,dr \equiv$ number of particles, with radii larger than R.

$\bar{v} \equiv (1/N)(4/3)\pi \int_0^\infty r^3 n(r) dr \equiv$ mean volume per particle.

$N \equiv N_0 \equiv$ number of particles of all sizes. $\bar{m} \equiv \rho\bar{v} \equiv$ mean mass per particle.

[a]Mie scattering results taken from Deirmendjian (1969) ($\lambda = 0.7$ μm).

[b]Mie scattering results computed in this laboratory ($\lambda = 0.7$ μm).

[c]Mie scattering results taken from McCormick et al. (1968) ($\lambda = 0.6943$ μm).

[d]Obtained by interpolation of values for 1.40, 1.45 refractive index.

However, a recent publication of Toon and Pollack (1973), in agreement with a previous paper by Rosen (1971), indicates that 75% is a more likely H_2SO_4 mass fraction for the stratospheric particles, although values ranging between 40% and 80% may be possible.

We have therefore repeated the lidar/aircraft mass comparison for a range of assumed acid concentrations. The results are shown in Figure 2. The bottom horizontal scale gives solution mass percentage of sulfuric acid, and the top scale gives the corresponding specific gravity. The vertical scale is inferred particulate mass concentration. The curved line gives the aircraft value; as expected, it depends strongly on assumed specific gravity. The nearly horizontal line gives the lidar value. Its *expected* strong dependence on specific gravity is almost entirely suppressed by a compensating dependence on refractive index. One can see the close agreement obtained at an assumed H_2SO_4 mass fraction of 60%. If 75% is assumed instead, two different values are obtained, but they still agree well within error bars. In fact the lidar and aircraft measurements agree for any assumed H_2SO_4 mass fraction between 40 and 94%.

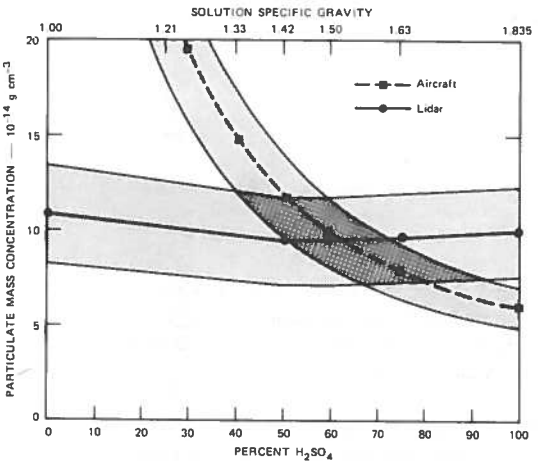

Figure 2. Dependence of lidar- and aircraft-inferred particulate mass concentration on assumed acid fraction of sulfuric-acid/water solution. Aircraft curve assumes $M(H_2SO_4) = (5.9 \pm 1.1) \times 10^{-14}$ g cm^{-3}. Lidar curve assumes $f_A = (3.7 \pm 0.9) \times 10^{-9}$ m^{-1} sr^{-1}; Deirmendjian Haze H size distribution. The shaded areas indicate the estimated uncertainties ($\pm 1\sigma$) in the respective measurements.

This type of agreement lends support to the matching method of lidar analysis (cf. Viezee et al. (1973a), Collis et al. (1973)), which assumes a "clean air" layer for calibration purposes.

PARTICULATE OPTICAL DEPTHS

The particle characteristics used in the above analysis constitute an *optical model of the stratospheric aerosol*. This model can be used to obtain values of stratospheric particulate extinction from the backscattering measurements. We have done this (assuming an H_2SO_4 mass fraction of 60%), and the results are shown in Figure 3. The results on the left are for integrated optical depth through two upper layers. They show quite a bit of seasonal variability, including a notable decrease in particulate extinction during January of 1973. This decrease coincides with a sudden stratospheric warming and the associated reversal of the local zonal wind. This coincidence has been discussed in several previous reports (Russell et al., 1973a,c, 1974). Optical depths integrated upward through the stratosphere for somewhat lower layers, including the major peak, are shown on the right. Here the seasonal variability, while significant compared to the error bars, is much less than in the upper layers. These particulate optical depths can be compared to the model values of Elterman (1968). In general, the model values are about an order of magnitude larger than the lidar measurements. This is not surprising, since the model values are based on searchlight measurements made in 1964 and 1965, when contributions from Agung and possibly other volcanoes (Cronin, 1971) were present, and when lidar measurements also indicated particulate backscattering about an order of magnitude larger than the present values. Evidently we are now in a period of small volcanic contribution to the stratospheric aerosol, and both particulate backscattering and particulate extinction are much smaller than they were in 1964-1965.

Our CIAP-sponsored lidar observations will continue until April 1974. We will make a final report in June 1974.

REFERENCES

Collis, R.T.H., W. Viezee, R.D. Hake, Jr., and P.B. Russell (1973), "Lidar measurements of the variability of stratospheric particulates," AIAA/AMS paper 73-520, presented at International Conference on Environmental Impact of Aerospace Operations in the High Atmosphere, Denver, Colorado, 11-13 June, 1973.

Cronin, J.F. (1971), "Recent volcanism and the stratosphere," Science 172, 847-849.

Deirmendjian, D. (1969), *Electromagnetic Scattering on Spherical Polydispersions* American Elsevier, New York.

Dynatrend (1973), "Laramie Comparative Experiment, Data Report and Preliminary Report of Conclusions," ed. Dynatrend, Inc. (March 15, 1973).

Elterman, L. (1968), "UV, Visible and IR Attenuation for Altitudes to 50 km, 1968," AFCRL-68-0153, Environmental Research Papers, No. 285.

Gray, D.E. (1963), *American Institute of Physics Handbook*, McGraw-Hill, New York, A-91.

McCormick, M.P., J.D. Lawrence, Jr., and F.R. Crownfield, Jr. (1968), "Mie total and differential backscattering cross sections at laser wavelengths for Junge aerosol models," Appl. Opt. 7, 2424-2425.

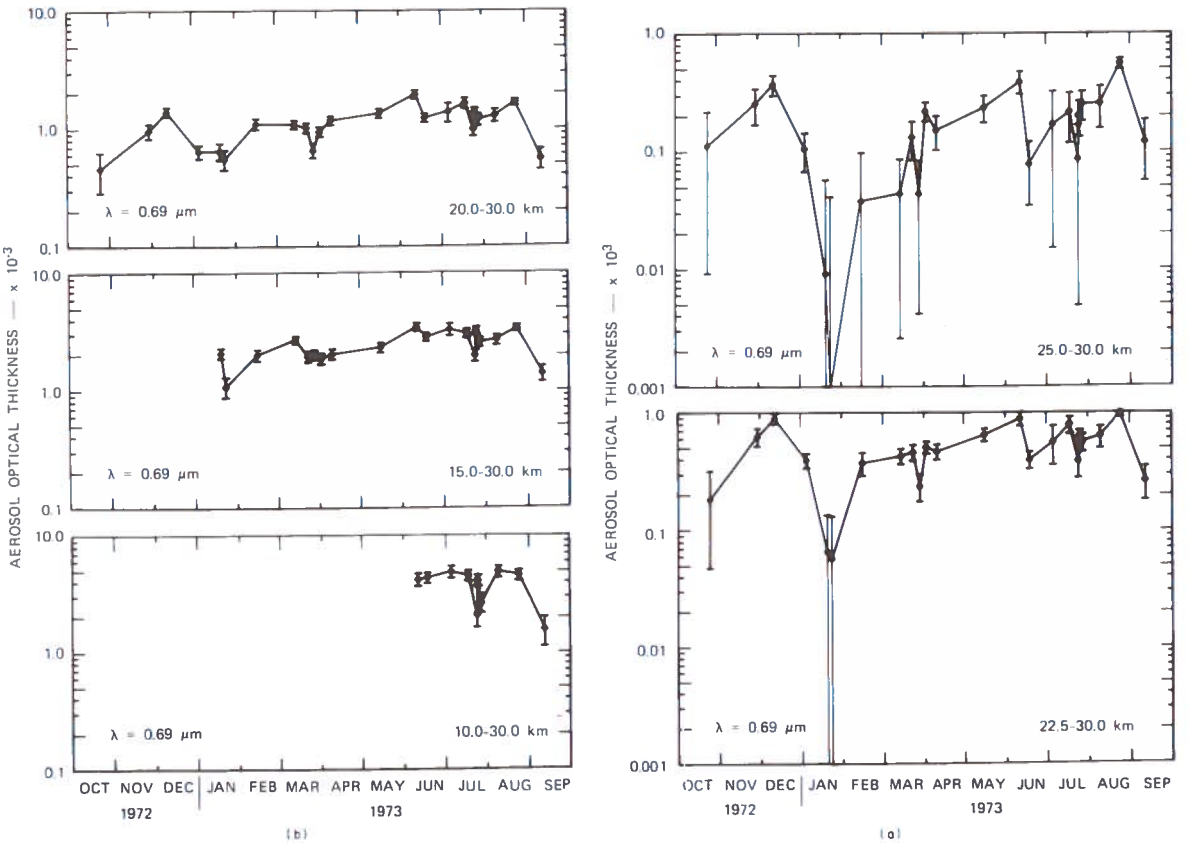

Figure 3. Time variability of particulate optical thickness for several altitude regions. Values are derived from lidar-measured backscattering coefficients by assuming the backscatter phase function $P(\pi)/4\pi = 0.0131$ (Deirmendjian Haze H size distribution, spherical particles, $\lambda = 0.7$ μm, refractive index m = 1.41). See text for discussion.

Neumann, J. (1973), "Radiation absorption by droplets of sulfuric acid-water solution and by ammonium sulfate particles," J. Atmos. Sci. 30, 95-100.

Rosen, J.M. (1971), "The boiling point of stratospheric aerosols," J. Appl. Meteor. 10, 1044-1046.

Russell, P.B., W. Viezee, and R.D. Hake, Jr. (1973a), "Lidar Measurements of the Variability of Stratospheric Particulates." First Semiannual Report 2217, Contract NAS2-7261, Stanford Research Institute, Menlo Park, California, July 1973.

Russell, P.B., W. Viezee, and R.D. Hake, Jr. (1973b), "Lidar Measurements of the Variability of Stratospheric Particulates." Second Semiannual Report 2217, Contract NAS2-7261, Stanford Research Institute, Menlo Park, California, October 1973.

Russell, P.B., W. Viezee, and R.D. Hake, Jr., and R.T.H. Collis (1973c), "Lidar Observations of Stratospheric Particulates," presented at the Fall Annual Meeting, American Geophysical Union, San Francisco, California, 10-13 December, 1973.

Russell, P.B., W. Viezee, and R.D. Hake, Jr. (1974), "Lidar Measurements of the Variability of Stratospheric Particulates." Fifth Quarterly Report 2217, Contract NAS2-7261, Stanford Research Institute, Menlo Park, California, January 1974.

Toon, O.B. and J.B. Pollack (1973), "Physical properties of the stratospheric aerosols," J. Geophys. Res. 78, 7051-7056.

Viezee, W., R.D. Hake, Jr., and P.B. Russell (1973a), "Lidar Measurements of Stratospheric Constituents." First Quarterly Report, Contract NAS2-7261, Stanford Research Institute, March 1973.

Viezee, W., R.D. Hake, Jr., and P.B. Russell (1973b), "Lidar Measurements of the Variability of Stratospheric Particulates." Second Quarterly Report, Contract NAS2-7261, Stanford Research Institute, June 1973.

DISCUSSION

CRUTCHER: Many questions have been asked about error bars. This paper is replete with error bars. Most of these error bars really ought to be multiplied by the square root of 2, or perhaps the square root of 3, because of the serial correlation. Most people assume that the bars are to be used against the normal distribution, a standard deviation giving you so many percentage points within a certain limit, in which case you must take out the serial correlation to reach independence. Your error bars as given imply a precision that I don't believe the data have.

P. RUSSELL: When you say 'serial correlation', do you mean the reproducibility in time, from one point to another?

CRUTCHER: I mean the relation between one point now, and a few seconds later, or a few minutes later, or a few hours later, whatever your time interval is.

P. RUSSELL: The error bars which I have shown are *not* based on the variance of any set of measurements made over a period of time. Instead, at the time each measurement is made, we make an estimate of the uncertainty *in that single measurement*. This estimated uncertainty is plotted as an error bar, as shown in the slides. That error bar is independent of the values measured in any previous or subsequent measurement.

Now, how do we estimate the uncertainty of a given measurement? For the lidar measurements, the uncertainty results from three sources: (1) probable statistical errors in the number of light photons received, (2) probable radiosonde errors in the density profile which we use to relate the lidar backscattering to molecular backscattering, and (3) probable error in the stratospheric light-extinction profile. These three sources of error are quadratically combined to give an overall lidar error. For the aircraft measurement of mass concentration, the two sources of uncertainty are (1) laboratory weighing error in measuring the mass of sulfate, and (2) calibration error in computing the volume of air that passed through the filter. These two errors are also quadratically combined to give an overall error in the aircraft-measured particulate mass concentration.

AEROSOLS IN THE STRATOSPHERE

GUY V. FERRY AND HOMER Y. LEM
Space Sciences Division
NASA Ames Research Center
Moffett Field, California

ABSTRACT: An aerosol-collecting instrument has been developed at NASA Ames Research Center. Aerosol particles are collected by direct impaction on 0.2-mm palladium wires. The instrument has been flown on the NASA Ames CV-990 to collect aerosol particles from the 9 to 12 km altitude range, and on a NASA Ames U-2 to collect particles at 20 km altitude.

The palladium-wire sampling surfaces were examined using a scanning electron microscope at magnifications of 3000 x and 10,000 x. Particles as small as 0.06 μm in diameter were detectable. Elemental analyses of selected particles with a diameter of 0.5 μm or larger were made. Elements of atomic number 11 (sodium) and higher were detectable.

The concentration of particles in the stratosphere at the points of collection varied greatly. Average concentrations of 10 particles/cm^3 were found, with three- or fourfold variations common. In the 9 to 12 km altitude range, only two morphological types of particles were collected: a ring-structure type composed of a central particle surrounded by large numbers of smaller particles, and a rosette type with a flat, dendritic, leaflike structure. Individual collections were always composed entirely of one type of particle.

Most of the ring-type particles appear to be solid particles coated with liquid. These particles were composed of various combinations of Al, Ca, Fe, and Si, sometimes with sulfur present and sometimes without. A few particles appeared to be all liquid, and sulfur was the only element detected in those. The rosette-type particles appeared to have been a slurry that had flattened out on collection. Only sulfur was detected in the rosette-type particles.

Collections are currently being made at 20 km altitude. Preliminary analyses of these collections indicate concentrations and variations in concentration of particles similar to those found in the 9 to 12 km altitude range. Three morphological particle types have been found: ring-structure, crystal, and irregular-solid. Elemental compositions of these particles were similar to the ring-structure-type particles found at 9 to 12 km altitude.

INTRODUCTION

Measurements of the composition of stratospheric aerosols collected by balloons were first reported by Junge et al. (1961). Electron-microprobe X-ray analysis identified sulfur as the most plentiful constituent, with traces of Al, Si, and Fe. Friend et al. (1961, 1966), using electron-diffraction methods, identified hygroscopic particles in stratospheric collections as ammonium sulfate and ammonium persulfate. Junge and Manson (1961) analyzed additional stratospheric aerosols using X-ray fluorescence methods and chemical spot tests; again, they found the elements S, Al, Si, and Fe, as well as traces of Cl, K, and Ca. Mossop (1963, 1964), examining stratospheric particles collected by U-2 aircraft, found several small insoluble particles within each larger water-soluble aggregation, and suggested they were of cosmic origin. Cadle et al. (1970) and Lazrus et al. (1971) analyzed filter samples from aircraft and balloon flights in the stratosphere. They found sulfur isotope ratios in one measurement similar to that found in the Hekla volcano plume; oxygen isotope ratios were also consistent with atmospheric oxidations of sulfur gases, implying in-situ formation of stratospheric aerosols by reactions of gases diffusing upward or injected by volcanic eruptions, in agreement with other workers' findings (Junge et al., 1961; Junge and Manson, 1961; Bigg et al., 1970).

At lower altitudes (1 to 10 km), Gillette and Blifford (1971) found the same major aerosol elements of S, Si, K, Ca, and Cl, as well as Ti, using X-ray fluorescence methods.

Although the origin of most of the stratospheric aerosol particles is thought to be volcanic, a cosmic origin has been suggested for certain types of insoluble particles in the slurry matrix (Mossop, 1963, 1964, 1965; Bigg et al., 1970, 1971). Farlow et al. (1972), using particle collections made by E.K. Bigg, CSIRO, Australia, performed X-ray emission analysis on individual particles from that collection, and found compositions very similar to those in volcanic emissions examined by others. They concluded that any cosmic-dust contributions to the collection must have been vanishingly small. To more clearly define the nature and source of stratospheric aerosols, NASA Ames Research Center has initiated a systematic experiment for stratospheric aerosol collection.

EXPERIMENT AND ANALYSIS

Aerosol particles are collected from the stratosphere by means of an instrument developed at NASA

Ames Research Center. The aerosol particles are collected by direct impaction on collecting surfaces. A wide variety of collecting surfaces can be used; in this series of experiments, 0.2-mm palladium wires were used. These thin wires provide efficient collection of particles with a diameter as small as 0.06 μm at the speeds and altitudes of the Ames Research Center's CV-990 and U-2's, which are used to carry the aerosol-sampling instrument into the stratosphere.

The aerosol-sampling instrument prevents contamination of the sampling surfaces by the use of a sealed-module concept. The modules and their components are cleaned and assembled in a clean room. Two 0.2-mm palladium wires, one of which has been lightly coated with very heavy silicon oil, are mounted in an aluminum ring. The oil coating prevents the larger aerosol particles from bouncing off the collecting surfaces on impact. The oil reduces the resolution of particles during analysis, but permits comparison of the numbers of large particles on coated surfaces and on uncoated surfaces to determine whether a complete collection has been made.

The aluminum ring with the palladium wires is installed in a standoff attached to the lid of the module. The lid is sealed to the bottom of the module by means of sealing screws. The sealed module can be removed from the clean room and installed in the sampling instrument without contamination of the collecting surfaces. During installation of the module in the sampling instrument, an arm of the instrument is fastened to the lid of the module to hold the module closed when the sealing screws are removed. At sampling altitude, the arm and lid are deployed into the free airstream outside the aircraft. After the sampling period, the arm and the lid are withdrawn from the free airstream and the module reclosed. After the aircraft lands, the sealing screws are reinstalled, the arm is removed from the lid, and the module is removed and returned to the clean room where the surfaces are removed for analysis. The instrument used on the CV-990 holds four modules, and the one used on the U-2 holds two modules; thus discrete, incremental samples can be collected at different times during a flight. The sampling instrument on the CV-990 is housed in an auxiliary pylon located on the nadir side of the CV-990 just aft of the wings. (The CV-990 is used to obtain collections from the 9 to 12 km altitude range.) On the U-2, the instrument is housed in its own pylon located about two-thirds of the way out on the starboard wing. (The U-2 is used to collect samples from 20 km altitude.) Figure 1 shows the U-2 instrument with the module lid deployed in the collecting position.

Sampling surfaces removed from the modules are examined using a scanning electron microscope at magnifications of 3000 x and 10,000 x. Photographs from the scanning electron microscope are used to identify particle types and to yield size distributions of particles on the collecting surfaces. At 10,000 x, particles with a diameter as small as 0.06 μm can be detected with this technique.

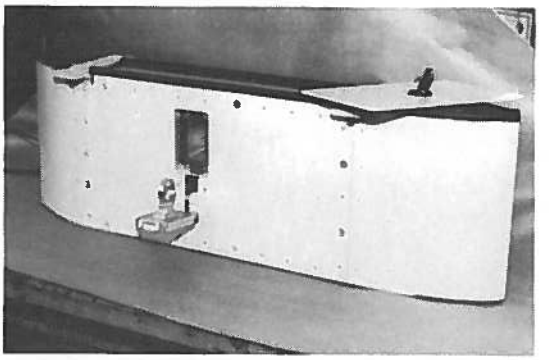

Figure 1. Aerosol sampling instrument for U-2 with module lid deployed in the collecting position.

Random areas of the front-facing surfaces of the collecting wires are selected for analysis. The rear-facing surfaces of the collecting wires are used as control surfaces to detect contamination. Collections found on uncoated collecting wires are compared with those found on the oil-coated wires. Elemental analyses using X-ray emission techniques are performed on selected particles with diameters of 0.5 μm or more. Elements with an atomic number of 11 (sodium) or higher can be detected. Elements with an atomic number lower than 11 (nitrogen, oxygen, and carbon, for instance) cannot be detected with the instrumentation used.

RESULTS

Two particle types were found on the collecting surfaces flown on the CV-990. The first particle has a ring structure. This type consists of a central, relatively large particle surrounded by many smaller particles. Figure 2 is a 10,000 x magnification of a ring-structure-type particle. The largest particle in the picture is about 0.8 μm. All particles of this type are smooth and round like a drop of liquid. Figure 3 shows a side view of a 0.7 μm particle at 10,000 x magnification. The upper portion of the particle is rounded, rather than flat as a liquid drop would be. This indicates that the particle consists of a relatively large piece of solid matter, probably coated with a liquid.

The ring-structure particle type is similar to those described by Bigg et al. (1971) and others as having a high sulfuric-acid content. A very intriguing feature of this particle type is shown in Figure 4. Here one can hardly recognize the ring structure; only the particle in the lower left-hand corner shows any indication of having a ring associated with it. This indicates that there is no interaction between ring-structure particles during or after collection. This photograph, taken at 10,000 x magnification (the largest particle is about 1 μm in diameter), is typical of a 30-minute collection. In samples, the large particle is apparently coated with a very large amount of liquid. This liquid washes the small

Figure 2. Ring-structure type particle. Magnification is 10,000 x. Largest particle in picture is about 0.8 μm.

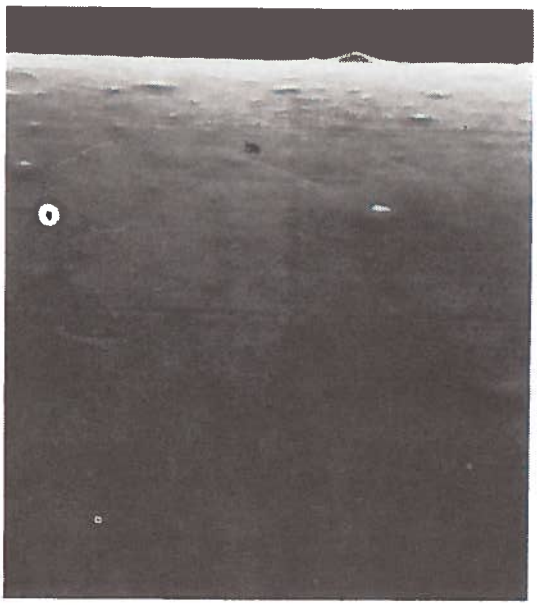

Figure 3. Side view of a 0.7-μm ring-structure-type particle at 10,000-x magnification.

particles away from the large one, leaving a well-defined circle of small particles around the large one. The sampling surface is typically darkened where the liquid has been.

Figure 4. Large collection of ring-structure-type particles. Note lack of interaction of rings from different particles. Magnification is 10,000 x. Largest particle is about 1 μm in diameter.

Ring-structure particles are found in all sizes. The structure is always the same: a relatively large particle surrounded by a large number of smaller ones. The size of the relatively large particle can decrease until it is as small as can be resolved by the scanning electron microscope, 0.06 μm. The only resulting change in structure is a decrease in the number of satellite particles with the decreasing size of the central particle.

Elemental analysis of individual ring-structure particles shows that they are composed of various combinations of Al, Ca, Fe, and Si, sometimes with sulfur present and sometimes without. A few ring-structure particles burn away under the beam of the scanning electron microscope; only sulfur is found in these particles. The typical particle, however, contains silicon with either one or two of the metallic elements, Ca, Fe, and Al. The presence of sulfur cannot be related to size, shape, or elemental composition.

The second particle type found on collecting surfaces flown on the CV-990 is a rosette. This type of particle is flat and dendritic or leaf-like. Figure 5 is a 10,000-x-magnification photograph showing rosette-type particles. The largest particle is about 7 μm in diameter, and from 0.1 to 0.2 μm thick. It appears to be a slurry that has flattened out on collection. Figure 6, a 3000-x-magnification photograph, shows the wide variety of sizes and shapes in which the rosette-type particle is found. Sulfur is the only element detected in the rosette-type particles.

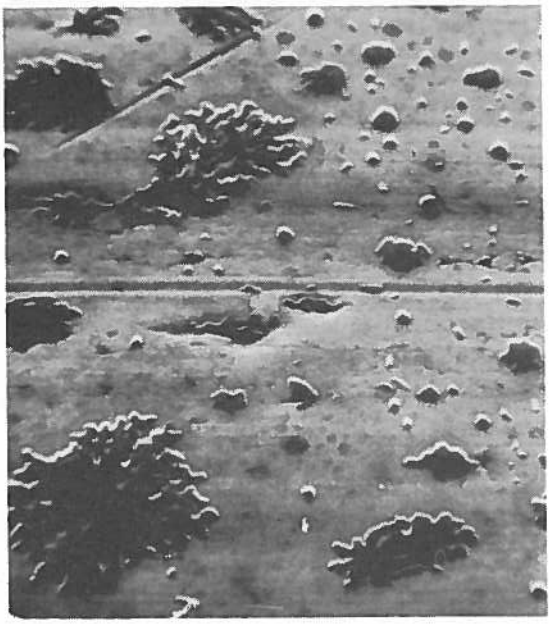

Figure 5. Rosette-type particle. Magnification is 10,000 x. Largest particle is 7 μm in diameter.

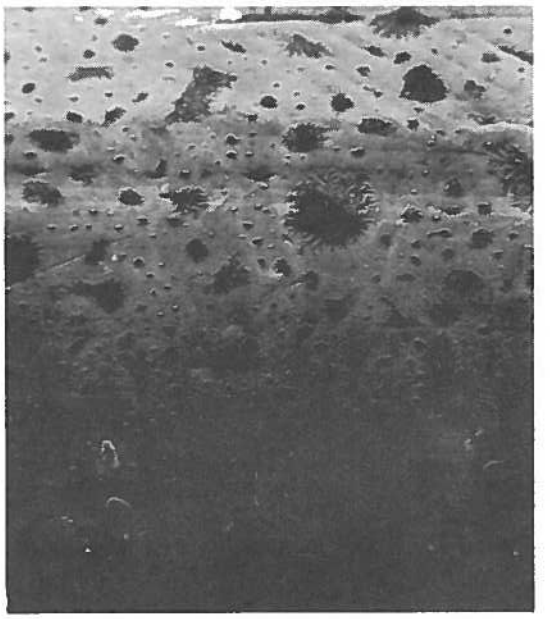

Figure 6. 3000-x magnification of rosette-type particles. Note wide variety of sizes and shapes.

Collections of particles made in January, September, October, and November 1972 are composed almost entirely of ring-structure particles, while those made in January 1973 are composed almost entirely of rosette-type particles. A very few rosette particles were found in collections made late in 1972, and a very few ring-structure particles were found in collections made in January 1973.

Data from flights made in October 1972 and January 1973 are shown in Table 1. Collections made in October 1972 were made on a ferry flight from Moffett Field, California to Cold Bay, Alaska and on flights over the Bering Sea. Collections made in January 1973 were made over the northwestern United States. Collection altitudes varied from 30,000 to 41,000 feet.

Table 1. Particle Collection Data

Sample Number	Date	Time (GMT)	Location	Altitude (x 10^3 ft)	Speed (knots)	Exposure (min)	Area Exam. (μm^2)	No. of Part.	Particle Conc. (per cm^3)	Fraction < 0.1 μm	Fraction < 0.5 μm
1	3 Oct 72	0200	42°N/128°W	31	472	30	90	528	13.2	0.78	0.99
2	3 Oct 72	0230	44°N/132°W	31	470	30	90	367	9.1	0.88	0.99
3	3 Oct 72	0300	46°N/136°W	31	470	30	90	291	7.2	0.50	0.99
4	4 Oct 72	1300	54°N/176°W	37	466	32	90	716	16.7	0.72	0.98
5	8 Oct 72	1130	55°N/169°W	33-36	456	30	90	400	10.2	0.67	0.99
6	8 Oct 72	1200	54°N/176°W	36	465	30	90	678	16.9	0.82	0.99
7	9 Oct 72	1130	58°N/156°W	32	453	30	90	47	1.2	0.98	1.00
8	9 Oct 72	1200	61°N/150°W	37	440	30	90	172	4.5	0.85	0.99
9	10 Oct 72	1000	70°N/163°W	37	484	30	90	555	13.3	0.82	0.98
10	13 Oct 72	0230	65°N/145°W	33-37	450	31	90	658	16.6	0.79	0.99
11	13 Oct 72	0300	65°N/145°W	37	455	31	90	882	21.5	0.71	0.99
12	13 Oct 72	0900	68°N/142°W	36-37	482	30	90	276	6.7	0.47	0.95
13	13 Oct 72	0930	73°N/141°W	37	480	34	90	139	3.0	0.80	0.96
14	13 Oct 72	1000	70°N/143°W	37	482	35	90	857	17.6	0.87	0.98
15	13 Oct 72	1400	65°N/146°W	37	460	36	90	799	16.6	0.68	0.98
16	16 Jan 73	0200	41°N/101°W	31-35	500	30	90	423	9.8	0.79	0.99
17	16 Jan 73	0400	38°N/115°W	40-41	488	26	90	394	10.8	0.52	0.99
18	16 Jan 73	1830	40°N/110°W	30-33	473	30	180	1030	12.6	0.70	0.99
19	18 Jan 73	2100	45°N/122°W	31-35	465	30	180	891	11.2	0.42	0.98
20	18 Jan 73	2200	45°N/122°W	35-37	475	23	180	549	8.8	0.70	0.96
21	18 Jan 73	2230	44°N/123°W	37	473	19	180	199	3.9	0.18	0.88
22	18 Jan 73	2300	42°N/122°W	37	453	19	90	313	12.7	0.68	0.96

Stratospheric particle concentrations calculated for the times of collection vary from 1 to 21 particles/cm^3 of air sampled. The average concentration found was about 10 particles/cm^3. Particle concentrations varied three- to fourfold from day to day and sometimes from flight to flight only a few hours apart.

The majority of particles found were smaller than 0.1 μm in diameter, and almost all particles were smaller than 0.5 μm in diameter. Table 1 shows the fraction of particles in each category for the collections covered in this paper. Table 2 shows a size frequency distribution for representative collections.

Table 2. Typical Size Distributions

Size Range (μm)	Sample Number 6	8	11	16	22
<0.1	555	146	627	333	212
0.1-0.2	80	17	185	27	55
0.2-0.3	13	5	61	32	21
0.3-0.4	8	1	2	21	11
0.4-0.5	8	1	4	8	3
0.5-0.6	6	0	0	1	0
0.6-0.7	2	0	0	1	2
0.7-0.8	2	0	0	0	2
0.8-0.9	0	2	1	0	1
0.9-1.0	1	0	0	0	2
>1.0	3	0	2	0	4
Total	678	172	882	423	313

Particle collections made around 65,000 feet with a U-2 indicate that particle concentrations in the stratosphere at such altitudes are of the same magnitude and variability as those found at lower altitudes with a CV-990. The size distributions of particles from those altitudes are similar also. There are some significant differences, though. There appears to be much less liquid at 65,000 feet than at lower altitudes. A few very large particles have been found at the higher altitude, and none were found at lower altitudes.

Figure 7 shows a 10-μm crystal-shaped particle containing Al, Ca, Si, and S. Figure 8 shows a 3-μm amorphous particle containing Al and S. Figure 9 shows a 5-μm cotton-ball-shaped particle containing Ca and S. Figure 10 shows a 5-μm amorphous particle, apparently surrounded by a liquid. If the electron beam of the scanning electron microscope is allowed to scan over the liquid for some time, the liquid seems to burn away, revealing a large number of particles 0.1 μm or smaller in diameter.

Figure 11 is a 10,000-x-magnification photograph showing a particle with wings that are semi-transparent to electrons. Also in Figure 11 is a typical collection of particles 0.5 μm and smaller that had apparently aggregated in a liquid drop that has since evaporated. Figure 12 shows a 6-μm rose-shaped particle like those formed by many of the wing shapes found in Figure 11. The particle contains Ca and S.

Figure 7. 10-μm crystal-shaped particle containing Al, Ca, Si, and S. Magnification is 10,000 x.

Figure 8. 3-μm amorphous particle containing Al and S.

On 25 October 1973, one collecting surface was exposed at 65,000 feet for over 5 hours, all the way from Moffett Field, California to Wallops Island, Virginia. Figure 13 is a 6000-x-magnification photograph of the result. Particles are piled on top of particles to form a mound of particles 12 μm wide. Figure 14 shows a 9

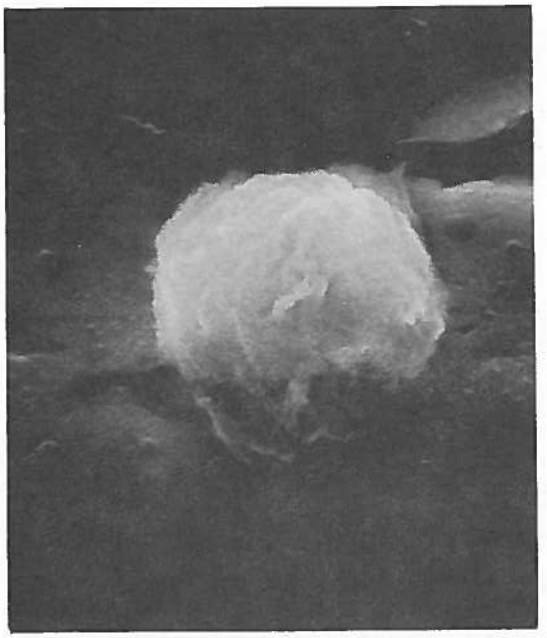

Figure 9. 5-μm cotton-ball-shaped particle containing Ca and S. Magnification is 10,000 x.

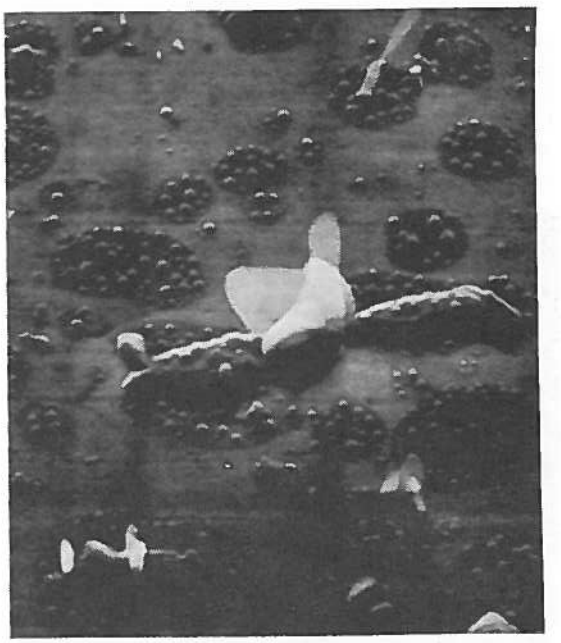

Figure 11. Particle with wings that are semi-transparent to electrons. Magnification is 10,000 x.

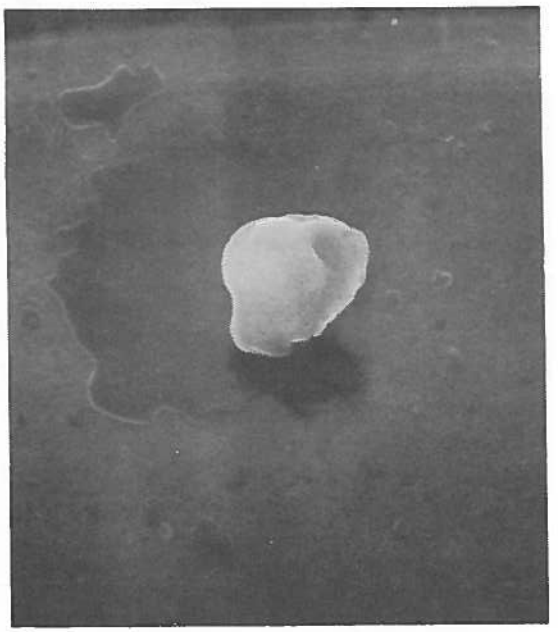

Figure 10. 5-μm amorphous-shaped particle apparently surrounded by liquid. Electron beam can burn away liquid to reveal small particles underneath. Magnification is 10,000 x.

Figure 12. 6-μm rosette-shaped particle formed from wing shapes. Contains Ca and S. Magnification is 10,000 x.

by 17 μm particle, formed by crystalline platelets, found on the collecting surface from the 25 October 1973 flight. Only sulfur was detected in this particle. Figure 15 shows a 9-μm particle composed of crystalline platelets. The background of the photograph is an even larger crystalline platelet, 44 μm in diameter.

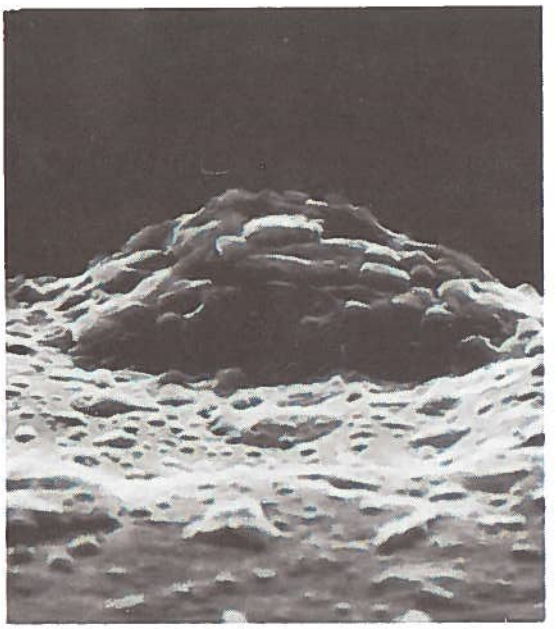

Figure 13. 6000-x magnification of a 5-hour particle collection with a U-2 at 65,000 feet. Mound is 12 μm wide.

DISCUSSION

The generally accepted bimodal distribution of particle sizes was not found in the collections made with the CV-990. There is no minimum in particle size distribution around 0.2 μm in these collections. Data from this work shows an increase in particle concentration with decreasing size down to the limit of resolution of the instrumentation used. Although it is possible that particle collections made in this series of experiments were too small to reveal the bimodal distribution, it is more likely that the minimum found by earlier investigators was due to collection-efficiency problems around 0.2 μm.

The elemental compositions of the particles from these collections are consistent with a terrestrial source. The conclusion of Farlow et al. (1973) that the amount of extraterrestrial material in stratospheric aerosol particles is vanishingly small seems to be confirmed.

The concentration of particles in the stratosphere varies greatly from day to day. However, the changes over a period of half an hour, as indicated by samples 12 to 14 and 19 to 22 in Table 1, are probably not real.

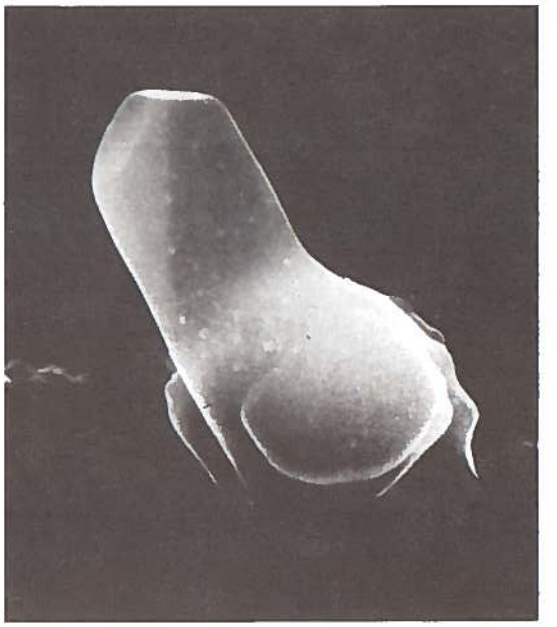

Figure 14. 9 by 17 μm crystalline particle formed on the collecting surface. Magnification is 10,000 x.

Figure 15. 9-μm crystalline platelets lying on a 44-μm platelet partially shown. Magnification is 10,000 x.

Samples 12 and 13 from 13 October 1972 indicate low particle concentrations, while sample 14, taken just a half hour later, indicates a high particle concentration. Samples 12 and 13 have smaller fractions of their particles in the small size range than sample 14. Particles in the medium and high size ranges are about the same for all three samples. This may indicate that the attitude of the CV-990, at the time samples 12 and 13 were made, affected the efficiency of the collectors for small particle sizes. On the other hand, it is possible that the depletion of small-sized particles reflects increased aggregation of small particles on larger ones at the times and places of the collection for samples 12 and 13.

The above arguments hold for samples 19 to 22. Sample 21 has very few small particles, while samples 19, 20, and 22, taken about the same time, have a greater fraction of particles in the smaller sizes. At any rate, the data indicate a precision of about 2 or 3 particles/cm^3 for the particle concentrations.

The crystalline-platelet particles found on the extended collection made on 25 October 1973 indicate that some type of reaction took place during or after the collection. The size and condition of the crystalline-platelet particles indicate that they crystallized from an aggregation of particles on the surface. This formation of a new particle type on collecting surfaces suggests the possibility that at least some of the large particles found in other collections were formed on the collecting surface. But why should these very large particles form at 65,000 feet and not at lower altitudes? More study in this area is indicated.

REFERENCES

Bigg, E., A. Ono, and W. Thompson (1970), "Aerosols at altitudes between 20 and 37 km," Tellus **22**, 550.

Bigg, E., Z. Kviz, and W. Thompson (1971), "Electron microscope photographs of extraterrestrial particles," Tellus **23**, 247.

Cadle, R., A. Lazrus, W. Pollock, and J. Shedlovsky (1970), "The chemical composition of aerosol particles in the tropical stratosphere," Proceedings of the AMS Symposium, University of Hawaii.

Farlow, N., G. Ferry, and H. Lem (1973), "Analysis of individual particles collected from the stratosphere," *Space Research XIII*, 1153, Akademie-Verlag, Berlin.

Friend, J., H. Feely, P. Krey, J. Spar, and A. Walton (1961), "The high altitude sampling program," Final Report DASA 1300, Contract DA-29-044-XZ-609, Defense Atomic Support Agency.

Friend, J. (1966), "Properties of the stratospheric aerosol," Tellus **18**, 465.

Gillette, D. and I. Blifford (1971), "Composition of tropospheric aerosols as a function of altitude," J. Atmos. Sci. **28**, 1199.

Junge, C.E., C.W. Chagnon, and J.E. Manson (1961), "Stratospheric aerosols," J. Meteor. **18**, 81.

Junge, C. and J. Manson (1961), "Stratospheric aerosol studies," J. Geophys. Res. **66**, 2163.

Lazrus, A., B. Gandrud, and R. Cadle (1971), "Chemical composition of air filtration samples of the stratospheric sulfate layer," J. Geophys. Res. **76**, 8083.

Mossop, S. (1963), "Stratospheric particles at 20 km," Nature, Lond. **199**, 325.

Mossop, S. (1964), "Volcanic dust collected at an altitude of 20 km," Nature, Lond. **203**, 824.

Mossop, S. (1965), "Stratospheric particles at 20 km altitude," Geochim. et Cosmochim. **29**, 201.

DISCUSSION

(UNIDENTIFIED): What proportion of the particles you collected were spherical?

FERRY: I don't know what shape they were when I collected them. After collection on a surface, they all have flat bottoms.

(UNIDENTIFIED): Did you coat the samples?

FERRY: No, the samples were uncoated, and in the pictures shown here the collecting wire was also uncoated. We also flew coated wires to check the collection efficiency. However, the coating degraded the image under the scanning electron microscope.

AIRBORNE LIDAR MEASUREMENTS OF THE DISTRIBUTION OF STRATOSPHERIC AEROSOLS

F.G. FERNALD AND C.L. FRUSH
*National Center for Atmospheric Research**
Boulder, Colorado

and

B.G. SCHUSTER
University of Missouri at Rolla
Rolla, Missouri

ABSTRACT: During February, March, and April of 1973, airborne lidar measurements of stratospheric aerosols were collected under a jointly sponsored NCAR/DOT program. An extensive portion of the northern hemisphere was covered on flights that ranged from 0° to 150°W and from the equator to 85°N. The results from this experimental program show a Junge layer (20-24 km) whose maximum scattering ratio varies between 1.1 and 1.2, considerably lower than measurements recorded during the 1960's. Latitudinal and longitudinal variations in the aerosol concentrations are interpreted in relation to the stratospheric temperature and wind field.

INTRODUCTION

During January, February, March, and April of 1973, NCAR's dye lidar was flown on an Air Force NC 135 aircraft as part of the CIAP program to monitor the distribution of aerosols within the stratosphere. The results of this joint NCAR/DOT experiment demonstrate the unsurpassed capabilities of airborne lidar in mapping the temporal and spatial variations in the stratospheric aerosol distributions.

Lidar measurements of stratospheric aerosols were first recorded over a decade ago. That time was characterized by relatively high stratospheric aerosol amounts associated with the 1963 eruption of Agung in Bali (e.g., Rosen, 1969). During that early period, the stratospheric dust layer could be detected easily, and one could approximate the molecular atmosphere's contribution to the net lidar return by "standard" atmospheres, since the aerosol's contribution to the net return was comparable to or greater than that of the molecular atmosphere itself in the vicinity of 20 km.

By 1971, though, stratospheric aerosol concentrations appeared to have decreased to their pre-1963 levels (e.g., Fox et al., 1973). Atmospheric density variations from the "standard" atmosphere had become comparable to the aerosol's contribution to the net lidar return, necessitating more sophisticated data-recording methods and data-reduction techniques. The success of the current experiment is a direct result of advances in these two areas at NCAR.

The lidar system used during these experiments was built around a dye laser operating at 585 nm, and is similar to that discussed by Grams and Wyman (1972). Data was recorded digitally on tape with a system designed and built at NCAR by Charles Frush. Data analyses followed the scheme outlined by Fernald et al. (1972). The molecular atmosphere was in all cases approximated from available radiosonde measurements. The attenuating properties of the aerosols themselves were ignored, but the attenuations by molecular scattering and by ozone absorption were incorporated into the solution.

Since the dye laser (wavelength of 585 nm) operates close to the peak in the Chappuis continuum of ozone, a signal loss of from 4 to 7%, due to ozone absorption, occurred during the two-way transit of the lidar pulse over the region of interest, which extended from 10 to 30 km. These figures were arrived at by using an absorption coefficient of 0.110 cm^{-1} atm^{-1} (Handbook of Geophysics, 1961), along with a series of five different ozone models supplied to the authors by John DeLuisi of NCAR.

DATA PRESENTATION

Figures 1 through 9 present the results of nine of these missions, reduced to contour diagrams of the vertical distribution of aerosol concentrations as measured along the flight paths. The scattering ratio is the total lidar signal divided by that which would be expected from an aerosol-free atmosphere (a ratio of 1.0 indicates no aerosols), and, therefore, is essentially an aerosol mixing ratio. These contours were generated from successive two-hundred-shot averages (approximately 200-nautical-mile segments along the flight path) which were smoothed both vertically and horizontally

* The National Center for Atmospheric Research is sponsored by the National Science Foundation.

before applying a standard computer contouring routine. They therefore display only relatively large-scale features of the aerosol distributions.

The largest single uncertainty in the results is due to the calibration scheme. The data are normalized by assuming that no aerosols are present in regions where the return signal is minimal relative to that expected from the actual molecular atmosphere (Fernald et al., 1972; Russell et al., 1973a). Any aerosol contamination at this level (28 to 30 km) will thus cause an overall underestimation of the true aerosol content. If this basic normalizing assumption is accepted, then the calibration for each of the 200-shot averages will usually have a standard deviation of 1%.

The additional errors associated with the radiosonde data (Russell et al., 1973b) and with the ozone correction are assumed to be on the order of 1% each. Furthermore, the 200-shot averages show standard deviations ranging from a few tenths of one percent at 12 km to 2-3% at 30 km. The net standard error from these statistically independent sources will, therefore, normally vary from 1.7% at 12 km to roughly 4% at 30 km.

Since the aerosol contribution (zero to 20% of the net return) is in many instances only a few times larger than the statistical fluctuations, inferred aerosol densities acquire relatively large errors. In general, though, these measurements are as accurate (if not more so) than most direct-sampling schemes.

DISCUSSION OF RESULTS

From Figures 1 through 9 it is apparent that the Junge layer (maximum aerosol concentration in the vicinity of 20 to 24 km) is a feature common to all the cross-sections. Scattering ratios in this region vary considerably, ranging from 1.08 to 1.20, with no marked latitudinal or meridional trends aside from the slight decrease in the elevation of this maximum with increasing latitude.

Often during the flights there were tenuous cirrus cloud layers immediately above the aircraft. Though optically thin with respect to the transmission of the laser pulse, they represented very strong backscattering targets, as evidenced by the close packing of contours in the lower portions of some of these cross-sections. Comparisons with radiosonde data show that these cirrus layers generally extend up to the tropopause. An especially interesting example of this is seen on the Honolulu-to-the-Equator flight of 7 March 1973 (Figure 2) which shows two well-marked cirrus layers over the equator. The top of the highest layer delineates the tropopause at 17 km.

Considerable variability in the stratospheric aerosol content is apparent from these results. Comparisons with meteorological data generally show that major gradients in aerosol density are associated with definite meteorological features. With assistance from Dennis Deaven of NCAR, isentropic analyses of the type described by Danielsen (1968) and Danielsen et al. (1970) have been made for flights which traversed

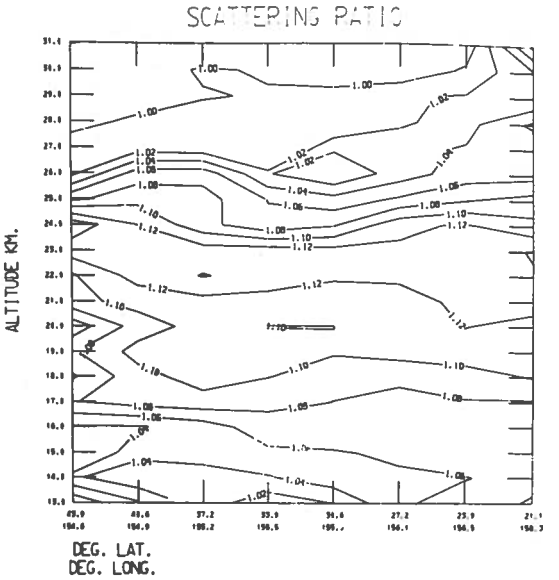

Figure 1. Scattering-ratio cross-section from the Fairbanks-to-Honolulu flight covering the time period from 0830Z to 1200Z on 7 March 1973. No data were obtained during the early portion of this flight.

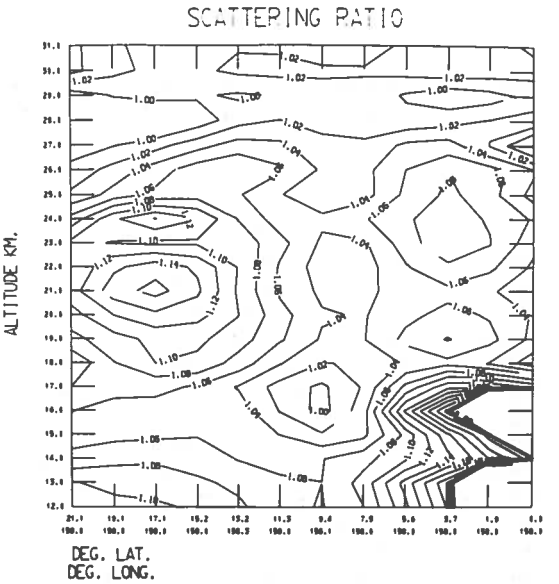

Figure 2. Scattering-ratio cross-section from the Honolulu-to-the-Equator-and-return flight covering the time period from 1100Z to 1620Z on 9 March 1973.

North America and the North Atlantic. In these papers Danielsen et al. have shown that potential vorticity, being a conservative property, acts as a tracer of stratospheric motions, and that high concentrations of

ozone and radioactive particles of stratospheric origin are positively correlated with high values of potential vorticity. A similar correlation should be apparent in these lidar results, assuming no large infusion of tropospheric aerosols into the stratosphere. In general, this is the case, although there are a few marked exceptions.

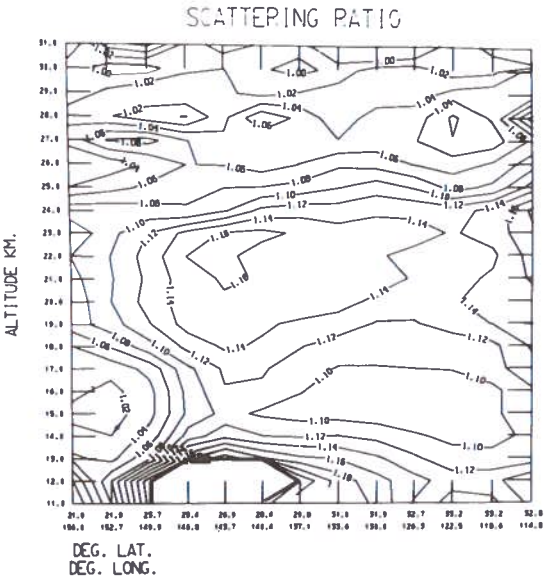

Figure 3. Scattering-ratio cross-section from the Honolulu-to-Albuquerque flight covering the time period from 0700Z to 1300Z on 11 March 1973.

The cross-section for the Albuquerque-to-Goose-Bay flight (Figure 4) shows two minima in the scattering ratio at 17 km (one centered at 38°N and 100°W, the other at 47°N and 72°W) which are correlated with minima in potential vorticity. The low scattering ratios extending over the western third of the cross-section for the Goose-Bay-to-Iceland flight (Figure 5), and the maximum centered at 60°N and 34°W, also correlate reasonably well with the respective minimum and maximum potential vorticities. The high values of the scattering ratio immediately above the tropopause at the eastern edge of this cross-section, though, coincide with relatively low values of potential vorticity immediately above the tropopause at this point. This region was southeast and downwind of the then-active Vestmannaeyjar volcano. It is tempting to speculate that this aerosol maximum resulted from tropospheric sources, possibly the volcano itself.

Two days later, though, results of the Iceland-to-Scotland flight (Figure 6) no longer showed large scattering ratios in the stratosphere over Iceland. It is assumed that this marked decrease in aerosols was associated with the major changes which occurred in the wind field at all stratospheric levels.

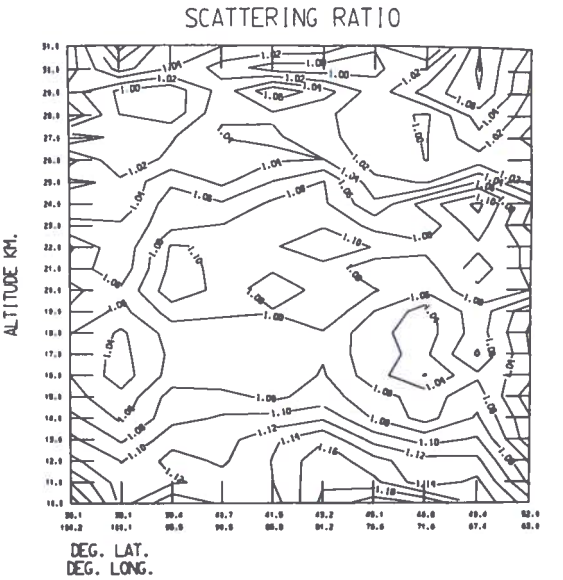

Figure 4. Scattering-ratio cross-section from the Albuquerque-to-Goose-Bay flight covering the time period from 0300Z to 0830Z on 9 April 1973.

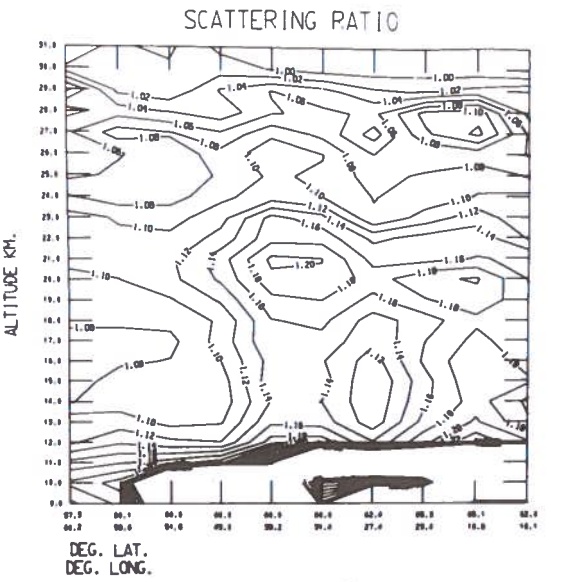

Figure 5. Scattering-ratio cross-section from the Goose-Bay-to-Iceland flight covering the time period from 0000Z to 0500Z on 10 April 1973.

Dense cirrus-cloud cover above the aircraft and an equipment malfunction precluded the collection of any useful data during the first half of the flight from Iceland to Madrid. Results from the remaining portion

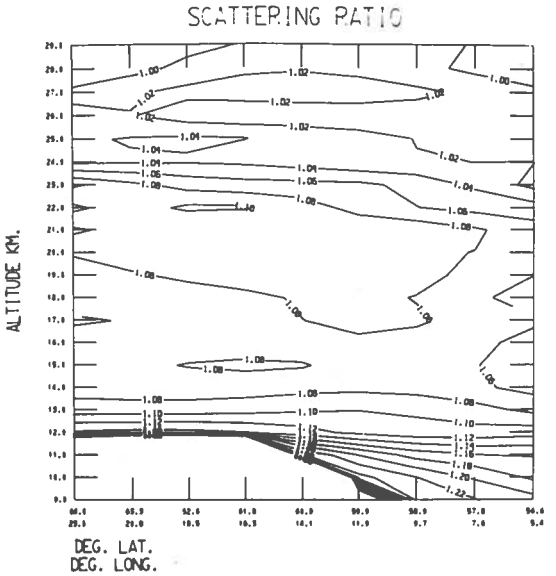

Figure 6. Scattering-ratio cross-section from the Iceland-to-Scotland and return flight covering the time period from 2200Z on 12 April 1973 to 0200Z on 13 April 1973.

of this flight, extending from England to Madrid, are presented in Figure 7. The scattering-ratio maximum at 46° to 47°N appears to be associated with a weak, "cut off" low-pressure area which was centered over the northwest coast of the Iberian peninsula.

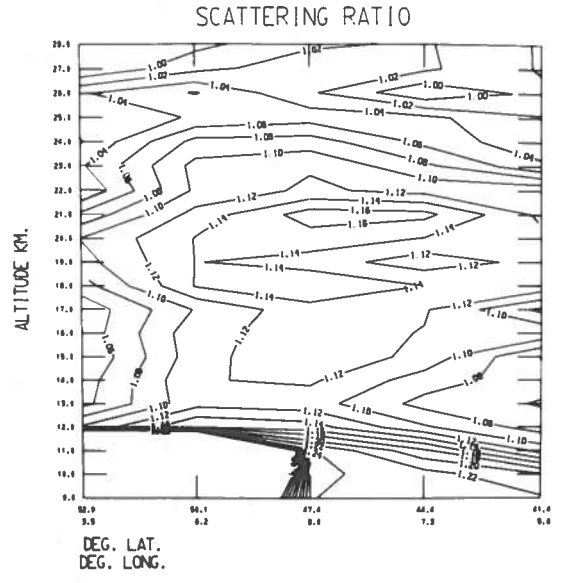

Figure 7. Scattering-ratio cross-section from the Iceland-to-Madrid flight covering the time period from 0200Z to 0400Z on 14 April 1973. No data were obtained during the early portion of this flight.

The flight from Madrid to Washington (Figure 8) produced another extremely interesting cross-section. It traversed a jet stream at 40°N and 35°W (maximum wind of 66 knots at 190° at the flight level of 9.5 km) in advance of a trough, and then intersected the same jet at 40°N and 51.5°W (maximum flight-level wind of 97 knots at 359°) on the western side of the trough. These positions (indicated by the S and N superimposed on Figure 8) agree very well with the jet cores appearing on the isentropic analyses for 00Z, 17 April 1973.

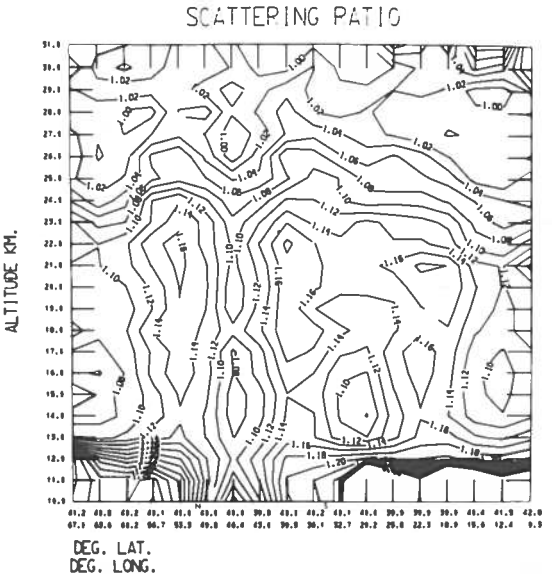

Figure 8. Scattering-ratio cross-section from the Madrid to Washington flight covering the time period from 1930Z on 16 April 1973 to 0130Z on 17 April 1973.

Cirrus clouds to the east and to the west of the two jet cores nicely define the tropopause at 12 km and 13 km, respectively. The isentropic analysis shows the tropopause dipping to 8 km in the region between the jets. The lack of a well-defined tropopause above 10 km is substantiated by the lack of any perceptible aerosol stratification in this region. The low horizontal resolution obtainable from these data precludes any attempt to detect stratosphere-troposphere exchange in regions of stratospheric folds (Danielsen et al., 1970; Reiter, 1972). The techniques developed here, though, indicate that such observations are possible; the only additional requirement would be a more powerful lidar to increase the horizontal resolution obtainable; such a lidar is well within the state of the art.

Here again maxima and minima in the scattering ratio correlate reasonably well with potential vorticity. Minima positioned at 64°W, 46°W and 12°W all coincide with potential-vorticity minima: In the vicinity of 30°W longitude (immediately east of the jet centered at 35°W) the density of the cirrus layer above the

aircraft increased noticeably, and the additional attenuation caused the net return from the stratosphere to be reduced considerably. The minimum centered at 30°W and 14 km is felt to be a spurious result caused by the extreme weakness of the signals which get through the clouds. The Washington-to-Albuquerque flight, Figure 9, again shows marked variation in aerosols, but in this case the maxima and minima are slightly out of phase with those in the potential-vorticity analysis.

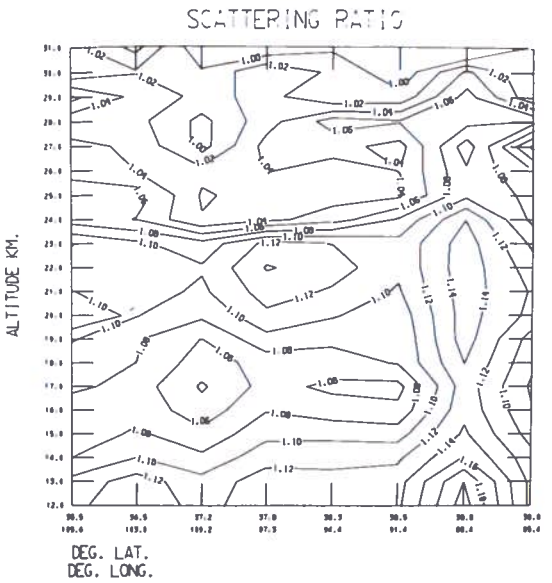

Figure 9. Scattering-ratio cross-section from the Washington-to-Albuquerque flight covering the time period from 0700Z to 1000Z on 17 April 1973.

Useful lidar data were also obtained during flights from Goose Bay to Fairbanks, from Fairbanks to 85°N and return, and during two short flights from Fairbanks to 72°N and return. These data are being analyzed and will be presented in the future.

SUMMARY

Results from the most extensive single lidar experiment performed to date have been presented. They show the distribution of stratospheric aerosols to be quite variable in space and time, but highly organized when compared with the corresponding isentropic analyses of meteorological data. Features such as these can only be revealed by experiments like this one, which are capable of sampling large portions of the globe on the synoptic time scale. Many of the features appearing on these cross-sections remain unexplained in these preliminary analyses. The final report of this project will look at a limited number of isentropic trajectories in an attempt to adequately trace the development of some of the more pronounced stratospheric aerosol maxima and minima.

While no other scheme is currently capable of recording the stratospheric aerosol distribution at the temporal and spatial resolution of lidar, this observational method is not without its critics, since lidar measures only the optical properties of the aerosols. In order to accurately interpret lidar data in terms of aerosol number densities or mass loadings, good optical models of the stratospheric aerosols are required. Russell et al. (1973b) present results of their work on this problem. More good work in this area is definitely required if the capabilities of lidar as a remote stratospheric probe are to be fully realized.

REFERENCES

Danielsen, E.F. (1968), "Stratospheric-tropospheric exchange based on radioactivity, ozone, and potential vorticity," J. Atmos. Sci. **25**, 502-518.

Danielsen, E., R. Bleck, J. Shedlovsky, A. Wartburg, P. Haagenson, and W. Pollock (1970), "Observed distribution of radioactivity, ozone, and potential vorticity associated with tropopause folding," J. Geophys. Res. **75**, 2353-2361.

Fernald, F.G., B.M. Herman, and J.A. Reagan (1972), "Determination of aerosol height distributions by lidar," J. Appl. Meteor. **11**, 482-489.

Fox, R.J., G.W. Grams, B.G. Schuster, and J.A. Weinman (1973), "Measurements of stratospheric aerosols by airborne laser radar," J. Geophys. Res. **78**, 7789-7801.

Grams, G.W. and C.M. Wyman (1972), "Compact laser radar for remote atmospheric probing," J. Appl. Meteor. **11**, 1108-1113.

Handbook of Geophysics (1961), rev. ed., USAF Air Research and Development Command, Macmillan, New York, 16-21 and 16-25.

Reiter, E.R. (1972), "Atmospheric Transport Processes, Part 3: Hydrodynamic Tracers." U.S. Atomic Energy Commission Critical Review Series, NTIS No. TID 25-731.

Russell, P.B., W. Viezee, and R.D. Hake (1973a), "Lidar measurements of the variability of stratospheric particulates," Stanford Research Institute Project No. 2217, Semiannual report (July).

Russell, P.B., W. Viezee, and R.D. Hake (1973b), "Lidar measurements of the variability of stratospheric particulates," Stanford Research Institute Project No. 2217, second semiannual report (October).

Rosen, J.M. (1969), "Stratospheric dust and its relationship to the meteoric influx," Space Sci. Rev. **9**, 58-89.

THE EFFECT OF NO_x EFFLUENTS ON OZONE

J.S. CHANG
Lawrence Livermore Laboratory
Livermore, California

and

H.S. JOHNSTON
University of California, Berkeley
Berkeley, California

ABSTRACT: The results of model calculations of the reduction of stratospheric ozone by nitrogen oxides from supersonic-transport exhausts, carried out by eight groups over the period 1971-74, are assembled here in tables and figures. The spread in calculated reductions of ozone for a given rate of input of nitrogen oxides is about a factor of ten. Some of this spread can be traced to differences in the chemistry of the models. However, the greatest source of discrepancy appears to be different treatments of eddy diffusion and boundary conditions. The eight models show a surprisingly close agreement in percent ozone reduction as a function of percent increase in the NO_x column; doubling stratospheric NO_x is calculated to reduce ozone by 20 percent.

INTRODUCTION

Since the first report on the catalytic reduction of stratospheric ozone by nitrogen oxides from supersonic-transport exhaust (Johnston, 1971), there have been several more detailed studies of the same subject (Johnston, 1972; Crutzen, 1972, 1974; Hesstvedt, 1972, 1973, 1974a,b; Chang, 1973; Chang et al., 1973; Stewart and Hoffert, 1973; Stewart, 1973; McElroy et al., 1974; Whitten and Turco, 1973, 1974; Shimazaki and Ogawa, 1974). If these results are plotted simply as number of supersonic transports versus percent reduction of ozone, there appears to be a wide discrepancy. However, such a plot overlooks several important variables: rate of fuel consumption, emission index for nitrogen oxides, height of SST flight, and the corridor effect (the local maximum over zones of high traffic density relative to world-wide average emission of exhaust gases). The primary object of this paper is to gather in one place the results from the different investigators, and to present the results in a uniform manner. The secondary purpose of this paper is to indicate reasons for agreement and disagreement between different authors; a detailed re-examination of the various models is reserved for future study, however.

THEORETICAL MODELS AND NUMERICAL EXPERIMENTS

As is well known, there is a hierarchy of three-, two-, and one-dimensional models that can be used to predict the effect of engine effluents on stratospheric ozone. Because of the relative complexity of the three-dimensional model, all of the current results come from the simpler two- and one-dimensional models. In fact, the bulk of the results has actually been obtained from one-dimensional models. The one-dimensional models are easier to study, chemically more complete, and relatively inexpensive to use. But they suffer greatly from their complete parameterization of all motions into one vertical direction, through the so-called "eddy diffusion" process. To various extents all the available results are affected by variations in the physical input parameters of each model (eddy-diffusion coefficients, boundary conditions, etc.), the computational techniques used in each model, and the choice of chemical kinetics in each model.

The required form of the source of engine effluents, denoted here as S_{NO_x}, for example, depends on the type of model. Thus, 1-D models require that the source function be a function only of altitude (i.e., $S_{NO_x}(z)$) for the altitude of each flight corridor. The 2-D models require additional resolution in the latitudinal direction, while the 3-D model requires additional resolutions in both the latitude and longitude of the flight corridors. However, the available results from the 2-D models have utilized source functions that are equivalent to those of the 1-D models by assuming a uniform global dilution of the engine effluents in the stratosphere at the altitude of the flight corridors.

This section presents a summary of all existing results from model calculations on the amount of ozone perturbation due to NO_x emissions in the stratosphere. Although the source function for 1-D models has a simple form, there is a broad range of values for the source, S_{NO_x}, depending on how the models used it in the simulation experiments. The characteristics of the source, S_{NO_x}, depend on the following parameters,

$$S_{NO_x}(z) = 8760 \times N \times E_{pi} \times f \times \dot{w}_{fe} \times EI_{NO_x} , \quad (1)$$

where $S_{NO_x}(z)$ is given in g/yr, i.e., the annual rate of introduction of NO_x (as NO_2). The terms in the right-hand side of the above expression are as follows:

8760 = number of hours in the year
N = number of airplanes (fleet size)
E_{pi} = number and type (i) of engines per airplane
f = fraction of the day that each airplane flies in the corridor
$\dot{w}_{fe}$ = fuel-flow rate per engine (kg/hr-engine)
EI_{NO_x} = emission index of NO_x (as NO_2) for the particular type of engine (g NO_2/kg fuel).

The source $S_{NO_x}(z)$ has also been stated in units of molecules/cm^3-sec, which is obtained from the expression

$$S_{NO_x}\left(\frac{\text{molecules}}{\text{cm}^2\text{-sec}}\right) = 4.15 \times 10^{14}\, S_{NO_x}\left(\frac{\text{g}}{\text{yr}}\right) \times \frac{1}{\Delta z} \times \frac{1}{A}, \qquad (2)$$

where Δz is the range of height over which NO_x is injected into the flight corridors (cm), A is the global area (cm^2), and 4.15×10^{14} is the ratio of the number of molecules per mole (6.025×10^{23}) to the product of the mass of NO_2 per mole (46 g) and the number of seconds in one year (3.15×10^7). With the foregoing expressions, it becomes possible to compare the effects of the sources that have been used in any 1-D and 2-D models.

Table 1 presents a summary of results from the following sources: Johnston (1971, 1972), Crutzen (1972, 1974), Hesstvedt (1972, 1973, 1974a,b), Chang (1973), Chang et al. (1973), Stewart (1973), Stewart and Hoffert (1973), McElroy et al. (1974), Whitten and Turco (1973, 1974), and Shimazaki (1973). The numbers with asterisks were not presented by the original author and are obtained from available data using the foregoing expressions for the source S_{NO_x}. Table 1 is presented as a source of raw data. The symbols which identify the various authors' results are used below in the analysis and interpretation of this data base.

Table 1 first shows the characteristics assumed to define the aircraft fleet in the stratosphere, i.e., its size, the type of engine (Boeing or Concorde), and the emission index. The next grouping in the table characterizes the resulting NO emissions: the assumed corridor altitude, the magnitude of the source of NO_x (as NO_2) in g/yr, and the calculated percent increase of the NO_x. The last two headings show the resulting percent reductions of the natural ozone column and some comments relevant to each result.

The results of model calculations in Table 1 are shown in several graphs. Figure 1a gives percentages of reduction of the vertical ozone column for various uniform world-wide additions of NO_x at 20 km, expressed as multiples of 10^{12} grams of NO_2 per year. The authors are identified by number as in Table 1. Figure 1b gives the same data for NO_x insertions at 17 kilometers. For a given rate of NO_x injection and at a given altitude, the models show about a factor-of-10 spread in computed ozone reduction. The more conspicuous differences between models are explored below.

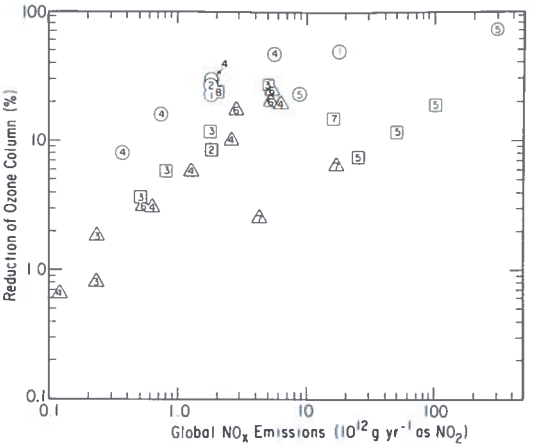

a. At 20 km.

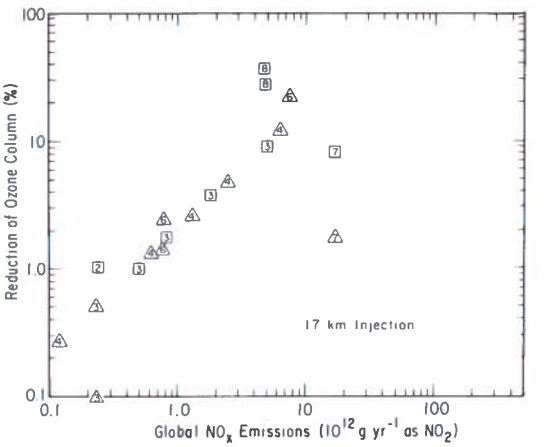

b. At 17 ± 1 km.

Figure 1. Calculated reduction of vertical ozone column in terms of uniform global rate of NO_x addition.

COMPLETENESS OF CHEMICAL-KINETICS SYSTEMS

In the development of appropriate chemical-kinetics systems for describing the ozone distribution in the stratosphere, we have gone from the oxygen-only system to O-H, O-N, and finally the present O-N-H system. There may be other reactions of varying importance yet to be discovered, but the present system seems quite adequate to describe the global ozone balance and the general structure of the minor trace constituents in the stratosphere (Vupputuri, 1974; Johnston, 1973; McElroy et al., 1973; Crutzen, 1974; and others).

Table 1. Summary of Results of Model Calculations

Supersonic Transports			NO_x Emissions			Ozone Column	
No.	Type†	Emission Index (gNO_2/kg fuel)	Elev. (km)	10^{12}g yr^{-1} (NO_2)	$\frac{\Delta NO_x}{NO_x}$ (% inc.)	$\frac{\Delta O_3}{O_3}$ (% dec.)	Comments
① JOHNSTON (1971)							
500	B	22	20	1.8	47	23	
500	B	22	20	18	470	50	10-fold "local maximum"
[1] JOHNSTON (1972)							
NOT APPLICABLE					10	2.3	1 ppb NO_x background
					33	6.0	
					100	12.8	
					330	24	
					1000	37	
					3300	48	
					3.3	1.0	3 ppb NO_x background
					10	3.2	
					33	8.0	
					100	18	
					330	31	
					1000	44	
					1	0.5	10 ppb NO_x background
					3.3	1.7	
					10	4.3	
					33	11	
					100	22	
					333	36	
② CRUTZEN (1972)							
500	B	22	20	1.8*		25	4.9 ppb NO_x
500	B	22	20	1.8*		15	15 ppb NO_x
NOT APPLICABLE					12	10	4.9 ppb NO_x background
					20	15	
					33	20	
					49	25	
					67	30	
					114	40	
					204	50	
					10	10	15 ppb NO_x background
					17	15	
					27	20	
					37	25	
					52	30	

Supersonic Transports			NO_x Emissions			Ozone Column	
No.	Type†	Emission Index (gNO_2/kg fuel)	Elev. (km)	10^{12}g yr^{-1} (NO_2)	$\frac{\Delta NO_x}{NO_x}$ (% inc.)	$\frac{\Delta O_3}{O_3}$ (% dec.)	Comments
[2] CRUTZEN (1974)							
500	B	22	20	1.8*		8.5	
200	C	22*	18	0.24*		1	
③ HESSTVEDT (1972)							
NOT APPLICABLE					10*	2.8	45° summer 20 ppb NO_x background
					100*	18	
					400*	40	
[3] HESSTVEDT (1973, 1974a) (2-dimensional)							
200	C	21	18	0.23	0.6*	0.1	30° winter
200	C	21	23	0.23	2.6*	0.8	
200	C	21	28	0.23	4.9*	2.5	
200	C	21	18	0.23	3.0*	0.5	60° summer
200	C	21	23	0.23	5.0*	1.8	
200	C	21	28	0.23	7.7*	2.4	
500	C	19	18	0.51		0.3	60° summer Model A
500	C	19	23	0.51		2.2	
500	C	19	28	0.51		5.7	
[3] HESSTVEDT (1974b) (2-dimensional)							
NOT APPLICABLE			17	0.5		1.0	Luther's K Values
			17	0.8		1.7	
			17	1.8		3.7	
			17	5.0		9	
			20	0.5		3.7	
			20	0.8		5.8	
			20	1.8		12	
			20	5.0		27	

* Derived from the author's data via equations (1) and (2)

† B = Boeing SST
C = Concorde
H = hypersonic transport
A = advanced SST

Table 1 (Cont'd)

Supersonic Transports			NO_x Emissions			Ozone Column	Comments
No.	Type†	Emission Index (gNO_2/kg fuel)	Elev. (km)	10^{12}g yr^{-1} (NO_2)	$\frac{\Delta NO_x}{NO_x}$ (% inc.)	$\frac{\Delta O_3}{O_3}$ (% dec.)	Comments
				④ CHANG (1973)			
300	C	22	20	0.37		8	Without HNO_3 or HO_x
600	C	22	20	0.74		16	
500	B	22	20	1.8		28	
500	B	66	20	5.6		47	
				△④ CHANG et al. (1973)			
38*	B	21*	20	0.12*	2.68	0.65	
188*	B	21*	20	0.62*	13.47	3.07	
380*	B	21*	20	1.24*	27.03	5.72	
760*	B	21*	20	2.5*	54.36	10.15	
1880*	B	21*	20	6.2*	137.25	19.41	
114*	C	21*	17	0.12*	1.56	0.27	
564*	C	21*	17	0.62*	7.8	1.30	
1140*	C	21*	17	1.24*	15.62	2.53	
2280*	C	21*	17	2.5*	31.30	4.80	
5640*	C	21*	17	6.2*	82.94	12.30	
				⑤ STEWART & HOFFERT (1973)			
1000	B	66	27	8.7*		23	
1000	B	66	27	322*		70	37-fold "local maximum"
				⑤ STEWART (1973)			
NOT APPLICABLE			20	25*		7.5	
			20	50*		12	
			20	100*		19	

Supersonic Transports			NO_x Emissions			Ozone Column	Comments
No.	Type†	Emission Index (gNO_2/kg fuel)	Elev. (km)	10^{12}g yr^{-1} (NO_2)	$\frac{\Delta NO_x}{NO_x}$ (% inc.)	$\frac{\Delta O_3}{O_3}$ (% dec.)	Comments
				△⑥ McELROY et al (1974)			
	C		17	0.74*	6.7*	1.4	
	C		17	0.74*	11*	2.4	
	C		17	7.4*	71*	21	
	C		16-21	0.53*	9.3*	1.9	
	A		20	0.52*	16*	3.1	
	A		20	2.8*	86*	17	Includes T feedback. Table 5 of the reference.
	A		20	5.2*	92	20	
	A		20	5.2*	155*	26	
	A		20	5.2*	155*	26	
	H		25	0.5*	20*	4.4	
	H		25	2.5*	69*	16	
	H		25	2.5*	101*	16	
12	H	210	25	0.6*		6	
37	H	210	25	1.8*		16	
74	H	210	25	3.6*		26	
100	A	21	20	0.7*		5	Figure 16 of the reference. Not included in △⑥ points in figure.
200	A	21	20	1.4*		9	
400	A	21	20	2.7*		17	
800	A	21	20	5.4*		28	
1500	C	21	17	1.4*		5	
3000	C	21	17	2.7*		9	
4500	C	21	17	5.4*		18	
				△⑦ WHITTEN & TURCO (1973)			
NOT APPLICABLE			20	4.1*	13*	2.5	
			20	16.5*	53*	6.5	
			16	16.5*	30*	1.7	
				⑦ WHITTEN & TURCO (1974)			
NOT APPLICABLE			12	16*		2.5	
			16	16*	61*	8	
			20	16*	128*	15	
			24	16*		23	
			28	16*		23	
				⑧ SHIMAZAKI (1974)			
NOT APPLICABLE			20	2.0*		24	
			16	4.9*	329*	37	
			16	4.9*	163*	27	

It is well known that individually HO_x and NO_x both destroy ozone through the appropriate reaction chains. However, when they are considered together, the HO_x species actually serve to temper the effect of NO_x on ozone. This is due principally to the transfer reaction

$$HO + NO_2 + M \rightarrow HNO_3 + M.$$

In the ambient stratosphere this reaction may be of importance only in the detailed representation of odd nitrogen, but for the perturbation calculations (from NO_x effluents) it is essential. In Figure 1a, the circled numbers are all obtained from early studies where HNO_3 was not included for various reasons. In comparing them to the more recent results (Δ and □), we note an overestimation in the early studies. This is due to the fact that part of the NO_x effluent has been converted into HNO_3, and odd nitrogen in the form of HNO_3 does not participate directly in the catalytic destruction of ozone. The effectiveness of this chemical reservoir for NO_x effluents decreases as net NO_x increases. This is illustrated in Figure 2, where we have plotted the partition ratios NO/NO_x, NO_2/NO_x, and HNO_3/NO_x as a function of net NO_x for some typical conditions in the stratosphere (≈20 km at midlatitude). It can be seen that as net NO_x increases, the partition increasingly favors NO and NO_2. Consequently, we have the strongly nonlinear relation between the percentage of reduction in ozone column and the net NO_x source as shown in Figure 1.

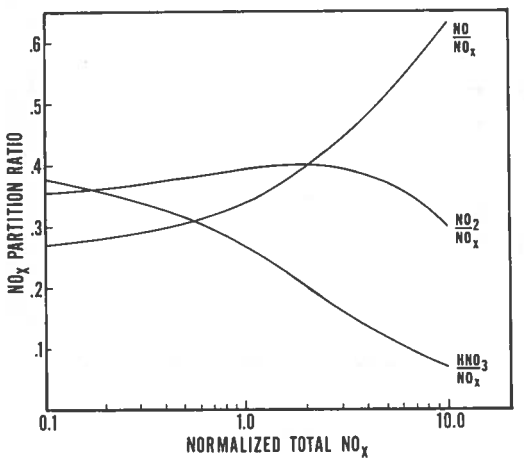

Figure 2. Calculated partition of NO_x into NO, NO_2, and HNO_3.

Figure 2 shows that HNO_3 comprises about 40 percent of the vertical column of NO_x ($NO + NO_2 + HNO_3$). Thus, omission of nitric acid from the mechanism would be expected to cause about a factor-of-two error in the NO_2 emissions of Figure 1a. The points ①, ②, and ④ in Figure 1a should be shifted about a factor-of-two to the right by virtue of the neglect of HNO_3. On the other hand, some models showed a large overestimate of stratospheric nitric acid; a comparison of observed nitric acid (Lazrus and Gandrud, 1974) with calculated nitric acid is shown in Figure 3. The critical region for ozone destruction by NO_x is between 25 and 35 km. At these elevations Stewart [5] and Whitten △7 appear to have a large overestimate of nitric acid; their points on Figure 1 should be shifted to the left, about a factor of two for △7 and almost a factor of ten for [5]. In ④ the photolysis constants were based on observed ambient ozone and not recomputed when large ozone reductions occurred. All other results in Figure 1 are based on self-consistency between computed ozone and computed photolysis constants. As shown by Johnston (1971a), there is about a factor-of-two difference between ozone reductions calculated with and without this feedback mechanism. Thus, the results of ④ should be shifted about a factor of two toward smaller ozone reductions.

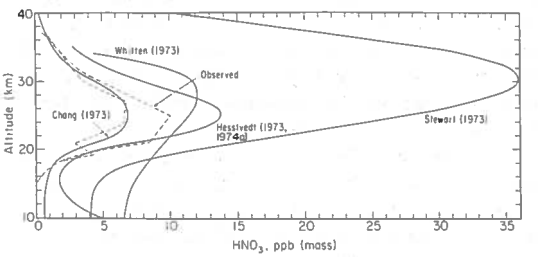

a. For Lazrus (1974).

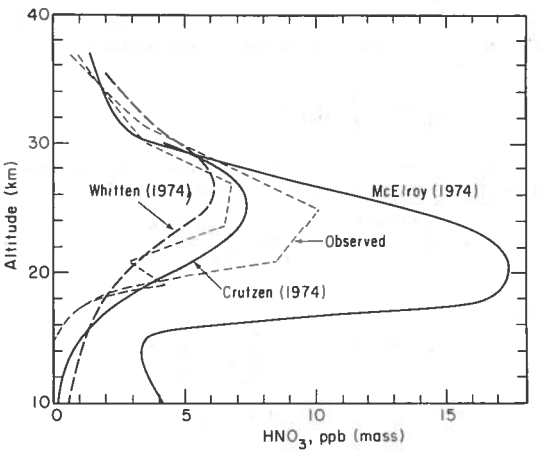

b. For Lazrus and Gandrud (1974).

Figure 3. Comparison of calculated and observed nitric acid in the natural stratosphere.

These readily identified omissions or overestimates in the photochemical models all tend to reduce the spread of results in Figure 1. Even with these corrections for nitric-acid chemistry and radiative feedback, however, there remains a fairly large spread in calculated ozone reduction from one model to another.

From the above discussions it is clear that completeness in the chemical-kinetics system will affect not only the perturbational studies but also the qualitative

understanding of the ambient atmosphere. It is strongly suggested that in the development of more complete two- and three-dimensional models, simplicity in model structure and analysis cannot be achieved at the expense of chemical kinetics if one is to understand the chemical balance of the stratosphere.

THE EFFECT OF TRANSPORT PARAMETERIZATION

We note that the difference between [7] and [7] with identical input is purely due to the difference in assumed NO_x concentrations at the lower boundary (at 10 km in this model) and the choice of associated boundary conditions. (The result corresponding to [7] is now preferable.) This illustrates the importance of boundary conditions in the simple models. The remaining differences in Figure 1 are seen to be essentially due to the differences in stratospheric residence time as determined by the choice of vertical eddy-diffusion coefficients and boundary conditions. (This has also been observed in the two-dimensional model being developed by Hesstvedt (1974b).)

For the chemical-kinetics systems under consideration, the total NO_x (i.e., $NO + NO_2 + HNO_3$) is approximately a conserved quantity, with the oxidation of N_2O as its principal source. If so, then total NO_x behaves very much like a tracer in the models. Since the parameterized transport in the one-dimensional models is a linear operator in the mathematical sense, we could assume a linear relation between net NO_x sources and the steady-state total NO_x column concentration

$$[NO_x] = \alpha_i [S_{NO_x}],$$

where α_i is model-dependent and represents the linear transport effect. Consequently, we have

$$[NO_x]^{natural} = \alpha_i [S_{NO_x}]^{natural}$$

and

$$[NO_x]^{perturbed} = \alpha_i \left([S_{NO_x}]^{natural} + [S_{NO_x}]^{SST} \right).$$

Therefore,

$$\Delta[NO_x] = [NO_x]^{perturbed} - [NO_x]^{natural} = \alpha_i [S_{NO_x}]^{SST}$$

If we take the ratio $\Delta[NO_x]/[NO_x]^{natural}$, then α_i cancels. In other words, the quantity $\Delta[NO_x]/[NO_x]^{natural}$ is to a large extent independent of the individual differences in transport parameterization. Figures 4a and 4b show the results of this rearrangement for Figures 1a and 1b respectively. The agreement between models in Figure 4 is at least a factor of ten better than the same results in Figure 1. The lines in Figure 4a correspond to a series of calculations made by Johnston (1972). They indicate onset of nonlinearity for large calculated ozone reductions.

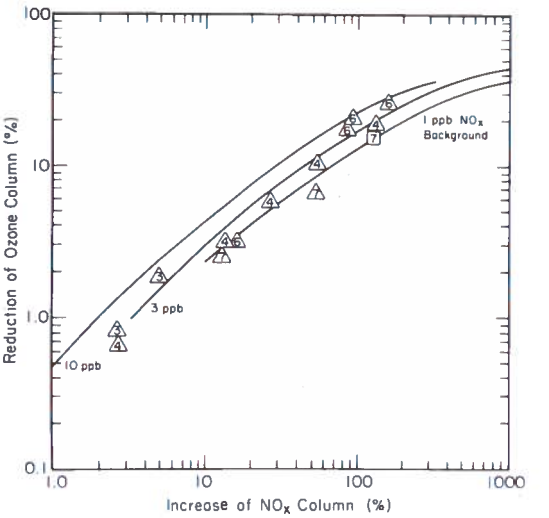

a. At 20 km. Lines are based on Johnston (1972).

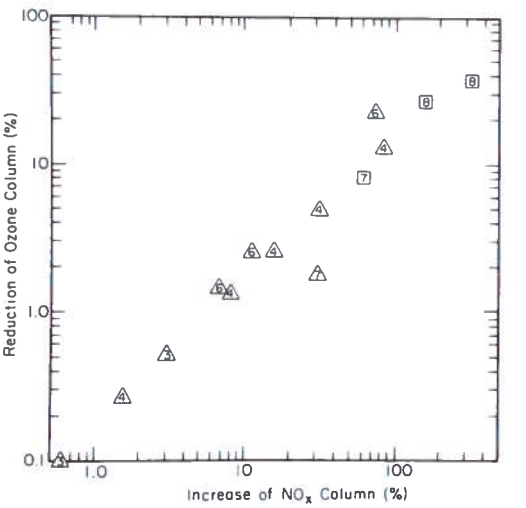

b. At 17 ± 1 km.

Figure 4. Calculated reduction of vertical ozone column in terms of relative perturbation of NO_x vertical column.

Any remaining differences are probably due to small deviations from the linearity assumptions. The level of agreement between models in Figure 4 suggests that all existing models seem to have the same chemical sensitivity to perturbation, and that the principal source of disagreement is the individual parameterization of the transport. At this point, we should point out that this sensitivity to transport parameterization is not unique to one-dimensional models. In fact, all models in which

the motions have been parameterized will exhibit similar sensitivity (perhaps not so strongly as the one-dimensional model).

It therefore seems essential to establish the proper transport parameterization for each class of simple models, i.e. one- and two-dimensional models. Since the computed ambient trace-constituent distributions are sensitive to this parameterization, we may then use agreement with experimental data as a criterion for validation. Due to the scarcity of systematic global measurements, the use of such a validation technique is not yet practical.

ACKNOWLEDGMENT

We would like to thank Drs. Crutzen, Hesstvedt, Stewart, Wofsy, Whitten, Shimazaki, and Vupputuri for making their results available either directly to us or to the CIAP office. Without their cooperation this study would not have been possible at this time.

This work was performed under the auspices of the U.S. Atomic Energy Commission and the U.S. Department of Transportation's Climatic Impact Assessment Program.

REFERENCES

Chang, J.S. (1973), "Global transport and kinetics model," in First Annual Report, DOT-CIAP Program, UCRL-51336, Lawrence Livermore Laboratory, Livermore, California. (4)

Chang, J.S. (1974), "Simulations, perturbations, and interpretations," in this volume.

Chang, J.S., A.C. Hindmarsh, and N.K. Madsen (1973), "Simulation of Chemical Kinetics Transport in the Stratosphere." UCRL-74823, Lawrence Livermore Laboratory, Livermore, California. 4

Crutzen, P.J. (1972), "SST's – a threat to the earth's ozone shield," Ambio 1, 41. (2)

Crutzen, P.J. (1974), "A review of upper atmospheric chemistry," Canad. J. Chem. 52, 1569. [2]

Hesstevdt, E. (1972), "The effect of water vapor and nitrogen oxides upon the ozone layer, studied in a photochemical model with meridional transport," paper presented at the International Ozone Symposium, Arosa, Switzerland, 1972 (also submitted to Water, Air, and Soil Pollution). (3)

Hesstevdt, E. (1973), "Effect of supersonic transport upon the ozone layer, studied in a two-dimensional photochemical model with transport," AGARD Conf. Proc. No. 125 on Atmospheric Pollution by Aircraft Engines, 6-1–6-8. 3

Hesstvedt, E. (1974a), "Reduction of stratospheric ozone from high flying aircraft, studied in a two-dimensional photochemical model with transport," Canad. J. Chem. 52, 1592. 3

Hesstevdt, E. (1974b), private communication to CIAP. [3]

Johnston, H.S. (1971), "Reduction of stratospheric ozone by nitrogen oxide catalysts from supersonic transport exhaust," Science 173, 517, (1); also "Catalytic Reduction of Stratospheric Ozone by Nitrogen Oxides," University of California, Berkeley, UCRL 20568.

Johnston, H.S. (1972), "Photochemistry of the oxides of nitrogen in the stratosphere," presented at the January 1972 meeting of the American Meteorological Society. [1]

Lazrus, A.L. and B.W. Gandrud (1974), "Progress report on distribution of stratospheric nitric acid," in this volume.

McElroy, M.B., S.C. Wofsy, J.E. Penner, and J.C. McConnell (1974), "Atmospheric ozone: Possible impact of stratospheric aviation," J. Atmos. Sci. 31, 287. 6

Shimazaki, T. and T. Ogawa (1974), "Theoretical models of minor constituents' distributions in the stratosphere and the impacts of the SST exhaust gases," in *Proceedings of the International Conference on Structure, Composition and General Circulation of the Upper and Lower Atmosphere and Possible Anthropogenic Perturbations* (Melbourne, Jan. 14-25), pub. IAMAP, 1062-92. [8]

Stewart, R.W. (1973), "Response of stratospheric ozone to the simulated injection of nitric oxide," presented at the Fall AGU Meeting, San Francisco, Calif. [5]

Stewart, R.W. and M.I. Hoffert (1973), "Stratospheric contamination experiments with a one-dimensional atmospheric model," AIAA Paper 73-531 (Denver, June 1973). (5)

Vupputuri, R.K. (1974), "The role of stratospheric pollutant gases (H_2O, NO_x) in the ozone balance and its implications for the seasonal climate of the stratosphere," in *Proceedings of the International Conference on Structure, Composition, and General Circulation of the Upper and Lower Atmosphere and Possible Anthropogenic Perturbations* (Melbourne, Jan. 14-25), pub. IAMAP, 905-932.

Whitten, R.C. and R.P. Turco (1973), "A model for studying the effects of injecting contaminants into the stratosphere and mesosphere," AIAA Paper 73-539 (Denver, June 1973). 7

Whitten, R.C. and R.P. Turco (1974), "The effect of SST emissions on the earth's ozone layer," in *Proceedings of the International Conference on Structure, Composition and General Circulation of the Upper and Lower Atmosphere and Possible Anthropogenic Perturbations* (Melbourne, Jan. 14-25), pub. IAMAP, 971-983. [7]

SIMULATIONS, PERTURBATIONS, AND INTERPRETATIONS

JULIUS S. CHANG
Lawrence Livermore Laboratory
Livermore, California

ABSTRACT: Directly and indirectly the CIAP program has stimulated the development of many so-called parameterized-transport and chemical-kinetics models of the stratosphere. The variety of parameters involved has made it necessary to understand and evaluate the possible implications of different parameterizations. This is especially important at present, since these models may constitute the major input to the study of the perturbation of the stratosphere by stratospheric vehicle operations. Working from our present understanding of these models, we shall analyze the parameterization of various physical processes simulated by the models, the perturbational studies made with these models, and the restrictions on the interpretation of simulation results.

INTRODUCTION

In their review of model-calculated effects of NO_x effluents on ozone, Chang and Johnston (1974) have suggested that several observable differences in simulation results are due to variations in the physical input parameters. Because of the lack of a uniform and complete data base, the analysis by Chang and Johnston is of necessity mostly qualitative. In fact, up to the present the emphasis of most modeling studies has been on understanding the chemical kinetics and the simulation of ambient (natural) stratospheric composition. Very little effort has been devoted to detailed analysis of the coupling of various physical and chemical processes. In this paper we shall provide an analysis of this type. It will be limited to one-dimensional models of the stratosphere because of the availability of modeling results and the cost of carrying out extensive computations. Nevertheless, much of what will be said applies equally well to two-dimensional models.

One-dimensional models are governed by the conservation equation

$$\frac{\partial c_i}{\partial t} = -\frac{\partial}{\partial z} F\left(c_i, \rho(z)\right) + P\left(c, J(z,t,c), k[T(z,t), \rho(z)]\right) - L\left(c, J(z,t,c), k[T(z,t), \rho(z)]\right) c_i + S_i(z,t) , \quad (1)$$

where

c_i = $c_i(z, t)$ is the concentration of the ith constituent;
c = $c(z, t)$ is the general representation of all constituents;
$P(\cdot)$ = production of c_i due to photochemical interactions;
$L(\cdot)c_i$ = loss of c_i due to photochemical interactions;
$\rho(z)$ = ambient air density;
$F(\cdot)$ = averaged vertical flux of the ith constituent;
S_i = any other possible sinks or sources of c_i;
$J(\cdot)$ = photodissociation coefficients;
$k(\cdot)$ = chemical-kinetics rate coefficients;
and t and z are time and altitude respectively.

Equation (1) is defined over a domain $z_B < z < z_T$ with appropriate boundary conditions at z_B and z_T. Vertical transport is parameterized by the so-called eddy-diffusion coefficient, K(z),

$$F(c_i, \rho) = - K(z)\rho(z) \frac{\partial}{\partial z} [c_i/\rho(z)] . \quad (2)$$

From the above description of the one-dimensional model we can easily identify the major physical input parameters: the physical domain of definition, boundary conditions, transport coefficients, chemical-kinetics systems, photodissociation coefficients, and other physical data. In the following sections we shall first discuss briefly how a particular parameterization of these input parameters may affect the

physical model. Then we will present some detailed results on the effect of variations in transport and chemical-kinetics coefficients on the accuracy of the simulation of the ambient and perturbed stratosphere. Finally, we will discuss some of the limitations on interpretation of the currently available modeling results.

PHYSICAL INPUT PARAMETERS

Ideally, we would like to justify the one-dimensional model as a representation of the "globally" averaged model of the stratosphere, i.e., a latitudinally and longitudinally averaged model. Unfortunately, there has been no rigorous study of the proper averaging processes required to derive Eq. (1) from the more physical multi-dimensional equations.* A pragmatic interpretation of the one-dimensional models would avoid this idealistic view completely. Instead, we should consider these models as a qualitative tool for studying the relative importance of transport and chemical-kinetics processes in the stratosphere. The physical reality resides in the accuracy of the characteristic response times of the individual processes under consideration. This provides a realistic evaluation of the overall interactive coupling of the system. The vitality of the one-dimensional model lies in the availability of extensive parameterization that permits the study of a wide range of response characteristics of the physical system. Consequently, we can indeed obtain a "global" view of the stratosphere through such simplified models. If we accept this as a reasonable interpretation of the models, we then need to consider possible parameterizations of the physical processes, their motivation and effects.

Physical Domain and Boundary Conditions

The choice of the spatial domain depends on the chemical species to be studied and on available input information for the solution of the systems. For example, the boundaries z_B and z_T are usually taken at altitudes such that we can either reliably estimate the total flux of individual species, or such that the solution's sensitivity to uncertainties at the boundary is minimal. However, the choice of lower boundary poses additional difficulties. In locating the lower boundary at the tropopause, it is difficult to observationally establish the appropriate boundary conditions, whereas in locating it at the ground, parameterization of rainout and tropospheric motions seems to be required. Furthermore, if we hold the fluxes fixed at the tropopause, any downward transport of effluents injected above it must be limited by this flux. On the other hand, if we hold the concentrations fixed, our resultant inability to raise the concentration level at the boundary would make the troposphere an infinite reservoir. In short, the former type of boundary conditions at the tropopause may underestimate the physical boundary fluxes, whereas the latter type may overestimate these same fluxes. At present it seems best to have the lower boundary at the surface. Given sufficiently large transport coefficients, the troposphere will then serve as a buffer zone where the uncertainty in boundary condition may be isolated from the stratospheric region of prime interest. By varying the tropospheric transport coefficients by orders of magnitude we can also establish the model's sensitivity to this input parameter.

Transport Coefficient

As was pointed out earlier, vertical transport in the one-dimensional model is parameterized through the so-called eddy-diffusion coefficient K(z) in Eq. (2). (The use of the name "eddy diffusion coefficient," in the context of one-dimensional models, arises more from habit than from physical reality. In the present context, it is best described as a set of coefficients suitable for approximating the net vertical motion of the minor trace constituents in the stratosphere through a diffusion process. It may be physical only insofar as it is useful in representing the characteristic transport time in the stratosphere. There is no unique approach for deriving a suitable set of eddy-diffusion coefficients.) In Figure 1 we show some representative values of

* A more detailed discussion of this can be found in Chapter 3 of CIAP Monograph 3.

K(z) used in the one-dimensional models.* This figure shows clearly why one-dimensional models are physically difficult to justify, and to what extent we must use care in interpreting any model results. Each of the investigators had his own justification for choosing a particular eddy-diffusion profile, and we shall not go into the details. It is quite interesting to note that in spite of the discrepancies in profiles every model is still valid with respect to some measurement. This strongly suggests that all models should be evaluated systematically before the simulation results are accepted.

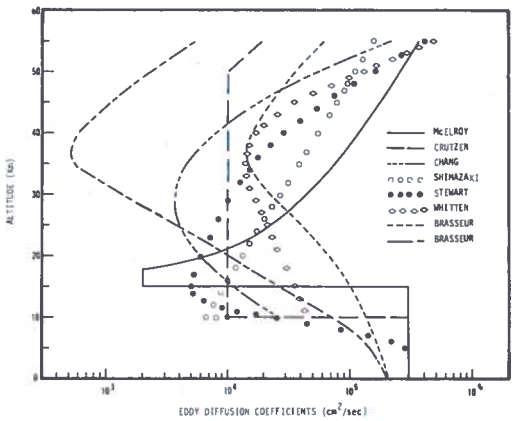

Figure 1. Representative values of K(z) used in one-dimensional models.

Chemical-Kinetics Systems

Of all models that consider some type of transport process, one-dimensional models are generally the most complete in considering photochemical kinetics. All one-dimensional models now include the essential O-N-H system, i.e., the Chapman cycle, the NO_x cycle, the HO_x cycle, and the transfer reaction involving HNO_3. The number of reactions considered ranges from 40 to more than 100. But from the study by Chang and Johnston (1974) it is clear that at least for the NO_x - O_3 question all the models behave quite similarly under the same perturbations, i.e., for a given percent increase in NO_x, the percent decrease in ozone differs by only $\approx 30\%$ from the mean. This agreement allows the simpler one-dimensional models to be used in extensive parameter studies, especially when the relative importance of particular photochemical reactions is being evaluated under a wide range of conditions.

Photodissociation Coefficients

Photodissociation processes in the atmosphere are important mechanisms for the production and destruction of many chemical species. The photodissociation rate, J (z, θ, ψ, t, c), is a complicated function of the spatial coordinates (z, θ, ψ), time (diurnal and seasonal), and constituent concentrations c = (c_i, . . . , c_j), which again are a function of z, θ, ψ, and t. Due to the complex dependence of J on the independent variables, and in particular its dependence on t, no model has yet been able to evaluate a set of photodissociation rates consistent with the supposed averaged nature of the one-dimensional model. Consequently, many approximations have been used; at this time, there exists no detailed evaluation of their relative merits. Two standard approximations are: a) fixed zenith angle and solar flux, and b) fixed zenith angle and half solar flux (half sun). Although many modelers favor the half-sun assumption, present numerical experiments indicate that as far as ozone perturbation is concerned the effect is very small, less than 1 - 2%. More exact calculations are needed to accurately assess the importance of diurnal variation in solar flux.

Other Physical Data

In most models, the ambient temperature and air-density distributions are usually taken from the available literature, such as the U.S. Standard Atmosphere (1962) and its supplement. At various times, other minor species, such as H_2O, H_2, CH_4, etc. have also been taken from published measurements. The fixed data set often changes from problem to problem depending on the purpose of the study. Since these data are either standard values or minor constituents with minimal influence on the model, there are no essential disagreements among the models.

* For the sake of brevity, we have identified only the first author of the references from which these profiles were obtained.

In order to analyze the above comments more quantitatively, we shall describe the results from a series of numerical experiments performed with a one-dimensional model at Lawrence Livermore Laboratory. This model extends from the ground to 55 km. The numerical technique used in the computations is a variant of the Gear method (Hindmarsh, 1972); its use in the one-dimensional model is described in Chang et al. (1973). In all, twelve minor constituents (O, O_3, NO, NO_2, HNO_3, N_2O, HO, HO_2, H_2O_2, N, H, $O(^1D)$) are solved for in the model. Vertical distributions of N_2, O_2, H_2O, and CH_4 are held constant throughout the calculation. Forty reactions are used in the model; they are listed in Table 1. Where possible, the original measurements are cited, as referenced in Garvin and Hampson (1974). The other reaction rates are either evaluated in Garvin and Hampson (1974) or were evaluated by previous reviews (i.e., Baulch et al. (1973), Wilson (1972), and Hampson (1973)). The solar flux and absorption cross-section data used have been described by Gelinas et al. (1973). The cosine of the solar zenith angle is kept at 0.707, except when noted to be different. On the basis of the comparative study by Chang and Johnston (1974) we believe this set of forty reactions to be adequate for describing the O-N-H system.

SIMULATIONS OF THE AMBIENT STRATOSPHERE

Using the various eddy-diffusion coefficients shown in Figure 1 in an otherwise identical one-dimensional model, we have obtained the model's sensitivity to this critical input parameter. We first note some general features in the eddy-diffusion profiles. Although the profiles are quite scattered in Figure 1, most of them have a mean value around 1-2 $\times$ 10^4 cm^2/sec, which seems to be the previously accepted average value (Seitz et al., 1968). Above 25 km the differences between profiles can be as high as two orders of magnitude (compare the Brasseur KMIN and McElroy profiles). But between 18 and 25 km the differences are down to a factor of two, and this is the region just below the ozone maximum. (This is also around the projected flight altitude (18-21 km) of the Boeing 2707 supersonic transport (SST).) A striking difference between this McElroy profile and the others is the strong minimum around 15 to 18 km. This local minimum presents a sharp barrier against the downward transport of any effluent injected above this gap. This is true for not only SST effluents, but also ambient ozone (see Figure 2). It is interesting to note that this particular profile was deduced from the CH_4 measurements of Ehhalt and Heidt (1973). Since CH_4 is an upward-moving tracer (in contrast to the downward-moving O_3), it may be more sensitive to the detailed dynamic and chemical processes in the troposphere, and in particular the detailed mixing processes around the tropopause. In any case, aside from the detailed justification of physical motivations, the present set of diffusion profiles did provide a wide range of possible vertical-transport rates.

Figures 2 and 3 illustrate typical simulation results based on these difusion coefficients. In general, above 30 km, in spite of the large differences in transport rates, all the solutions are in close agreement. This reaffirms the complete dominance of local photochemical equilibrium at those altitudes. In fact, it also verifies the minimal effect of upper-boundary conditions on these models. So long as the upper boundary is placed sufficiently within the photochemical-equilibrium region, we need not worry about the uncertainties in either the type of boundary condition or its magnitude. The sharp discontinuities in ozone at about 17 km for McElroy and at 10 km for Crutzen, Chang and Shimazaki are due to assumed discontinuities in the diffusion coefficient. This also provides some indication of the accuracy of the numerical solution (in its ability to resolve such sharp discontinuities). It is also clear from Figure 2 that in order to maintain the correct discontinuity in ozone at the tropopause, the diffusion coefficients in the region above the tropopause must not be larger than 4 $\times$ 10^4 cm^2/sec. Another indication of this latter phenomenon can be found in Figure 3, i.e., in the HNO_3 profiles corresponding to Whitten, Brasseur KMAX, and Brasseur KMIN. In these figures, we can also observe that although Chang and McElroy have essentially the same

Table 1. Table of Photochemical Reactions

Reaction	Rate Coefficient	Reference
$NO + O \xrightarrow{M} NO_2$	$3.96 \times 10^{-33} \exp(940/T)$	
$NO + O_3 \rightarrow NO_2 + O_2$	$9 \times 10^{-13} \exp(-1200/T)$	
$NO_2 + O \rightarrow NO + O_2$	9.1×10^{-12}	Davis et al. (1972)
$O + O_3 \rightarrow 2O_2$	$1.9 \times 10^{-11} \exp(-2300/T)$	
$O + O_2 \xrightarrow{M} O_3$	$1.07 \times 10^{-34} \exp(510/T)$	Huie et al. (1972)
$O(^1D) \xrightarrow{M} O$	5.85×10^{-11}	
$O_2 \xrightarrow{h\nu} O + O$	J_1	
$O_3 \xrightarrow{h\nu} O + O_2$	J_2	
$O_3 \xrightarrow{h\nu} O(^1D) + O_2$	J_3	
$NO_2 \xrightarrow{h\nu} NO + O$	J_4	
$N + NO_2 \rightarrow N_2O + O$	9×10^{-12}	
$N_2O + O(^1D) \rightarrow N_2 + O_2$	1.1×10^{-10}	
$N_2O + O(^1D) \rightarrow 2NO$	1.1×10^{-10}	
$N + O_2 \rightarrow NO + O$	$1.1 \times 10^{-14} T \exp(-3150/T)$	
$N + NO \rightarrow N_2 + O$	2.7×10^{-11}	
$N + NO_2 \rightarrow 2NO$	6×10^{-12}	
$O(^1D) + N_2 \xrightarrow{M} N_2O$	2.8×10^{-36}	
$N + O_3 \rightarrow NO + O_2$	5.7×10^{-13}	
$O(^1D) + H_2O \rightarrow 2OH$	3.5×10^{-10}	
$O(^1D) + CH_4 \rightarrow OH + CH_3$	4×10^{-10}	
$OH + O_3 \rightarrow HO_2 + O_2$	$1.6 \times 10^{-12} \exp(-1000/T)$	
$OH + O \rightarrow O_2 + H$	4.2×10^{-11}	
$HO_2 + O_3 \rightarrow OH + 2O_2$	$1 \times 10^{-13} \exp(-1250/T)$	
$NO_2 + O_3 \rightarrow NO_3 + O_2$	$1.23 \times 10^{-13} \exp(-2470/T)$	Johnston (1973)
$HO_2 + O \rightarrow OH + O_2$	$8 \times 10^{-11} \exp(-500/T)$	
$H + O_2 \xrightarrow{M} HO_2$	$2.08 \times 10^{-32} \exp(290/T)$	
$H + O_3 \rightarrow OH + O_2$	2.6×10^{-11}	
$HO_2 + HO_2 \rightarrow H_2O_2 + O_2$	$3 \times 10^{-11} \exp(-500/T)$	
$OH + HO_2 \rightarrow H_2O + O_2$	2×10^{-10}	Hochanadel et al. (1972)
$OH + NO_2 \xrightarrow{M} HNO_3$	$\frac{4 \times 10^{-11}\,[M]}{(1.12 \times 10^{18} + [M])}$	Based on Tsang (1973)
$OH + HNO_3 \rightarrow H_2O + NO_3$	1.3×10^{-13}	
$OH + H_2O_2 \rightarrow H_2O + HO_2$	$1.7 \times 10^{-11} \exp(-910/T)$	
$NO + HO_2 \rightarrow NO_2 + OH$	2×10^{-13}	
$O(^1D) + H_2 \rightarrow OH + H$	2.9×10^{-10}	
$OH + OH \rightarrow H_2O + O$	$1 \times 10^{-11} \exp(-550/T)$	
$N_2O \xrightarrow{h\nu} N_2 + O(^1D)$	J_5	
$NO \xrightarrow{h\nu} N + O$	J_6	
$HNO_3 \xrightarrow{h\nu} OH + NO_2$	J_7	
$H_2O_2 \xrightarrow{h\nu} 2OH$	J_8	
$NO_3 \xrightarrow{h\nu} NO + O_2$	J_9	

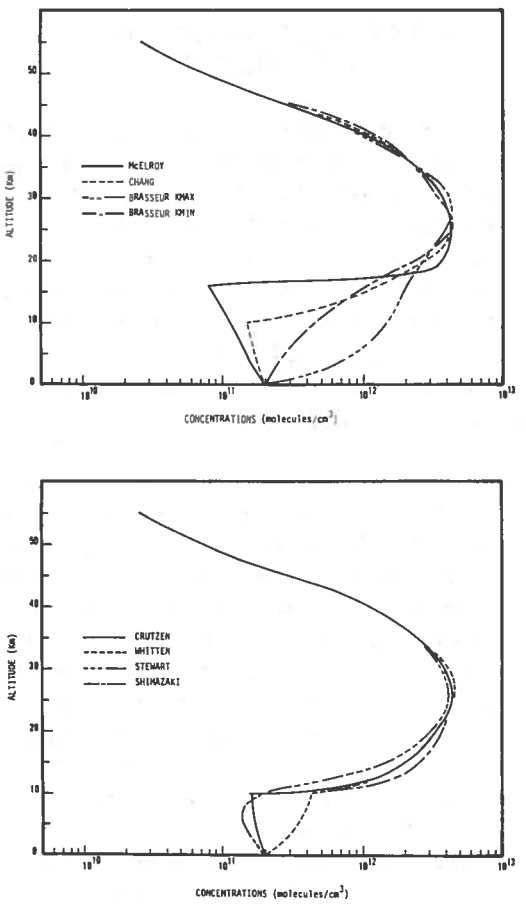

Figure 2. Comparison of theoretical vertical ozone distributions from one-dimensional models.

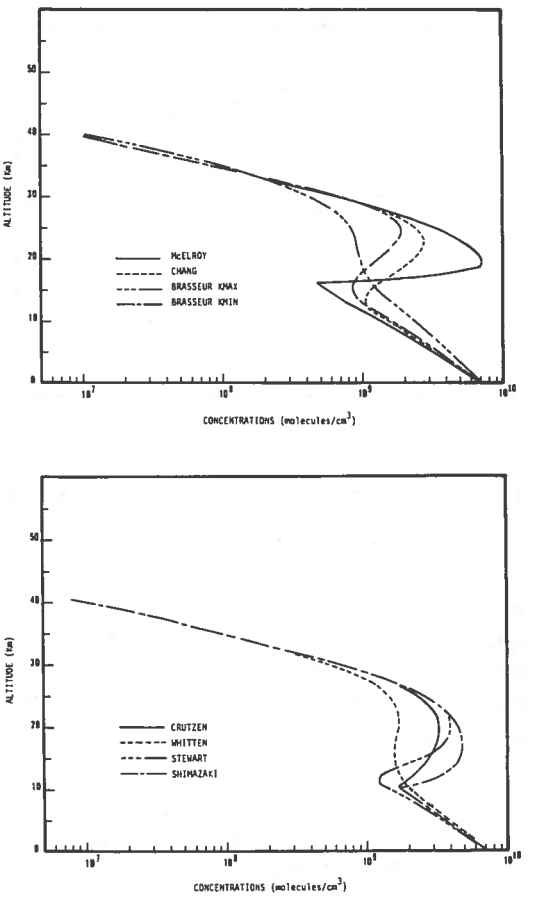

Figure 3. Comparison of theoretical vertical HNO_3 distributions from one-dimensional models.

average transport rate near the HNO_3 maximum, the HNO_3 profiles are very different. This is due to the inhibition of downward transport by the McElroy diffusion coefficient. We can also see a bulge in the ozone profile based on this McElroy diffusion coefficient, due to the same cause.

As a check on the representativeness of our calculation relative to the results in the literature, we compared our "McElroy" HNO_3 profile against the profiles published by McElroy et al. (1974). Figure 4 shows that the results agree quite well. More than half of the difference is due to differences in the rate coefficient for OH + NO_2 + M → HNO_3 + M and the assumed lower boundary values for HNO_3. (The rest of the discrepancy may be attributable to the conjectured production of odd nitrogen from tropospheric NH_3*.) Table 2 lists some of the differences in rate coefficient for this crucial transfer reaction. It partially explains the results with and without HNO_3 compared for various models in Chang and Johnston (1974). It is also important in explaining the perturbation studies in the literature and comparing them with the systematic, controlled studies in the next section. Figure 4 also illustrates the virtue of having z_B at the surface, i.e., isolation of the effect of boundary-condition uncertainty. A factor-of-4 difference in HNO_3 surface concentration produces less than a 10% change in the stratospheric concentration. Its utility is also confirmed by other more deliberate calculations, with variations in the surface concentrations of many species.

Taken together, these results demonstrate the crucial fact that many of the published

* S. Wofsy, private communication.

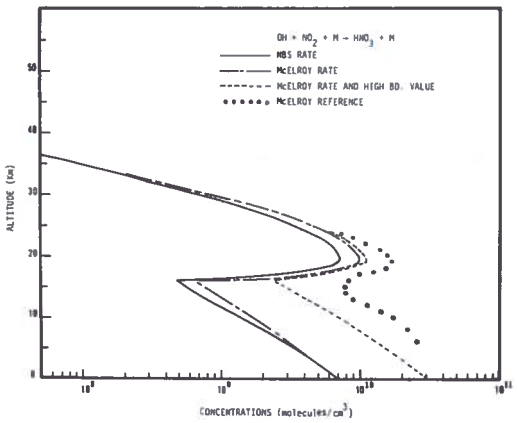

Figure 4. Effect of reaction-rate coefficient and boundary conditions on the theoretical HNO_3 distributions.

results for the chemical structure of the stratosphere are influenced more by the physical input parameters than by the assumed chemical systems, provided that all of the reactions in Table 1 are included.

Table 2. Comparison of Reaction Rates for $OH + NO_2 + M \rightarrow HNO_3 + M$ as Used by Different Authors

Altitude (km)	NBS (10^{-12})	Whitten/ Stewart (10^{-12})	McElroy (10^{-12})	Chang (10^{-12})
15	3.2	5.37	8.08	3.13
20	2.5	4.21	5.52	2.49
25	1.6	2.71	2.94	1.71
30	0.96	1.5	1.43	1.02
35	0.55	0.70	0.60	0.54
40	0.27	0.30	0.24	0.28
45	0.14	0.13	0.10	0.14

Rate Expressions:

Whitten/Stewart $$K = \frac{2.8 \times 10^{-22}\,[M]}{4 \times 10^{-11}\,[M] + 4.8T^3}$$

McElroy $$K = \frac{2.3 \times 10^{-13} \exp(880/T)\,[M]}{2.6 \times 10^{18} + [M]}$$

Chang $$K = \frac{4 \times 10^{-12}\,[M]}{1.12 \times 10^{18} + [M]}$$

OZONE PERTURBATION FROM SST EFFLUENTS

It has been suggested (Chang and Johnston, 1974) that the apparent differences among the model predictions of the ozone perturbation by SST effluents are a result of the differences in transport coefficients. Given the present set of models, in which the only difference is the diffusion coefficient, we can put these conclusions to a careful test. For each of the models we first establish its own ambient state, and then we put in various amounts of NO_x at either 20 km or 17 km. The effluents are distributed uniformly over the whole globe in a shell 1 km thick. After the system has reached a new steady-state solution, we can then compute the percent changes in ozone and total NO_x. From this data, which has been obtained in a precisely controlled way, we can then reexamine the relationship between percentage of ozone decrease and either the total global NO_x emission rate or the percent increase in total NO_x. Figures 5 and 6 show the results of these model calculations. As was first shown by Chang and Johnston (1974), the apparently large original differences in Figure 5 are reduced to approximately 30% from the mean in Figure 6. Of course, these results are exactly controlled, with identical input source functions, simulation techniques, etc. In fact, the suggested linear relation between the changes in total NO_x, $\Delta[NO_x]_{tot}$, and the total SST NO_x source rate, S_{SST}, can be established. The so-called residence time, τ, where

$$\Delta[NO_x]_{tot} = \tau S_{SST} \qquad (3)$$

was found to be constant for every model; their values are listed in Table 3. Actually, the S_{SST} in Eq. (3) should be an effective $\bar{S}_{SST}$, with a small correction due to the perturbations in N_2O and $O(^1D)$ concentrations. (A derivation of the linearity relation and the effective source rate is given in the appendix.)

The possible effect of different source-function distributions was also studied. Assuming the effluents to be injected uniformly over a vertical band 1, 2, 3, or 4 km thick produced no

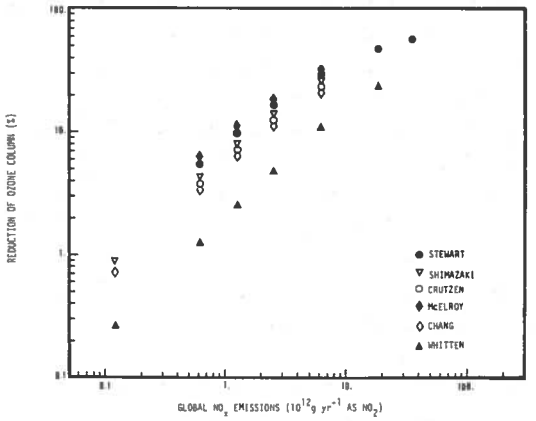

a. At 20 km.

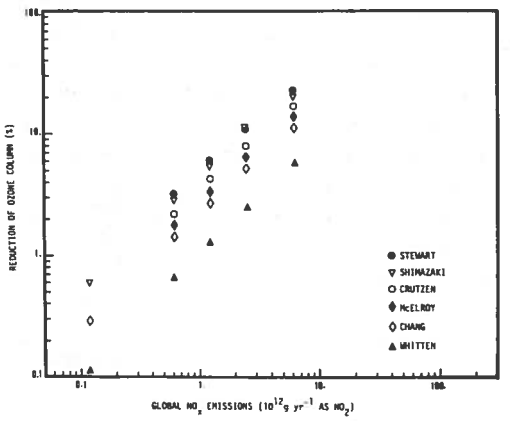

b. At 17 km.

Figure 5. Calculated reduction of vertical ozone column in terms of uniform global rate of NO_x addition.

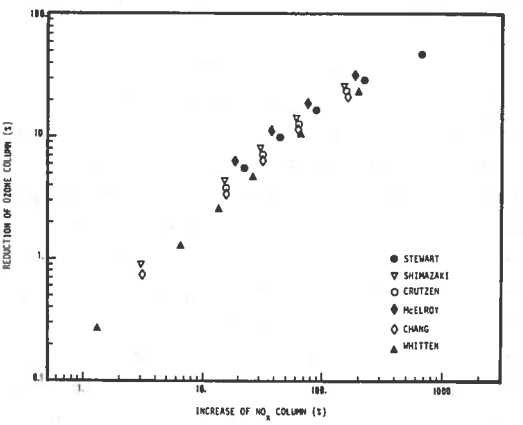

a. At 20 km.

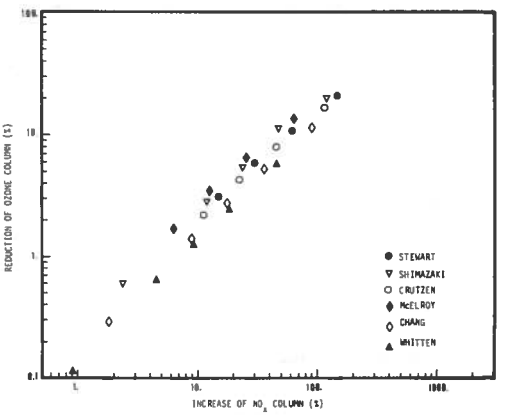

b. At 17 km.

Figure 6. Calculated reduction of vertical ozone column in terms of relative perturbation of NO_x vertical column.

real differences in their effect on the net change in the vertical ozone column density. For example, with a source strength of 2.5 X 10^{12} gm/yr (as NO_2) injected at 20 km, the percent decreases in ozone are 11.1, 10.1, 11.2, and 10.3 corresponding to 1, 2, 3, and 4-km-band source distributions respectively. The small differences are mostly due to the slight differences in centering the source function in the computer code.

INTERPRETATION OF MODEL SIMULATIONS

In the foregoing discussions, we have seen how the physical inputs to the one-dimensional models may or may not strongly influence the simulation results. It is clear that proper interpretation of any modeling result depends heavily upon our understanding of every aspect of the model. This is true not only in the perturbation studies, but also in the simulation of the ambient stratosphere. The above analysis deals mainly

Table 3. Approximate Residence Times of the 1-D Models (in years)

	Injection at 20 km	Injection at 17 km
Stewart	2.77	2.11
McElroy	2.54	0.87
Shimazaki	2.08	1.67
Crutzen	1.87	1.36
Chang	1.66	0.96
Whitten	0.61	0.43

with selected effects that seem to be explainable through a basically linear analysis. But there are other, more complex couplings which are not so open to direct analysis. An example of this is shown in Figure 7, where we have plotted the relation between total ozone and total NO_x from the same eight ambient-atmosphere models used above. The somewhat intuitive feeling that more NO_x should lead to less O_3 is not obviously borne out. Although the spread along the vertical axis is only 20%, the absence of a definite trend is nevertheless significant. It demonstrates quite clearly the complexity of the interactions and the need to examine the whole model rather than any part of it alone.

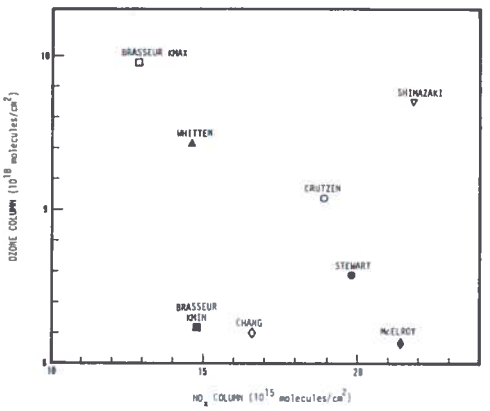

Figure 7. Comparison of the correspondence between total vertical columns of ozone and NO_x from different models.

Another yet-unmentioned component of modeling is the computation procedure. Using various assumptions, all of the existing studies dealing with ozone perturbations have made the right-hand side of Eq. (1) completely independent of time (as we have done so far). Consequently, they seek a truly steady-state solution to Eq. (1). There are two general procedures for obtaining that solution. We can set $\partial c_i/\partial t = 0$ and solve for the steady-state solution directly as a boundary-value problem (Crutzen, 1973; Brasseur, 1972; McElroy et al., 1974). Alternatively, we can solve the time-dependent equation as an initial-boundary-value problem and obtain the $t\to\infty$ asymptotic solution as the steady-state solution (Chang et al., 1973; Stewart, 1973; Whitten and Turco, 1974; Shimazaki and Ogawa, 1974). The latter approach is more general, and can be used even in the models with diurnal and/or seasonal variations in solar flux. Furthermore, this solution technique will also provide information on the transient phase of a simulation. For studies on pulsed injection of effluents into the stratosphere, such as the effect of atmospheric nuclear tests (Chang and Duewer, 1973), the time-dependent-solution technique must be used. However, it must be pointed out that although the residence times of the lower stratosphere determined by the model are less than two or three years, we still must carry the calculation up to almost three times that period in order to reach a true steady-state solution as shown in Figure 8. There are cases in the literature where this was not carried out (perhaps mostly due to the high cost of such computation). In such cases, we must interpret the results as intermediate solutions and not as the final state. This lack of time development seems to have contributed to the apparent disagreement in the published results. But because it is a transport-limited phenomenon, this effect is significant when differing results are compared, as in Figures 5 and 6.

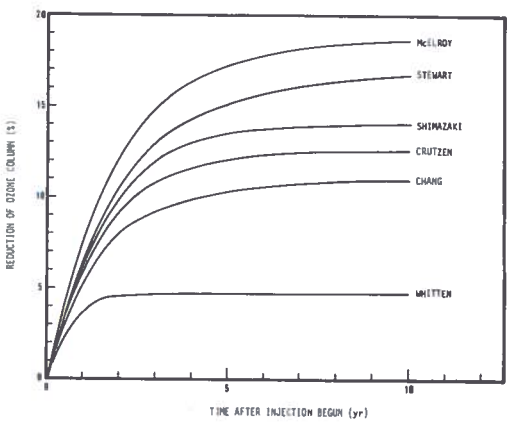

Figure 8. Examples of the time-dependent approach to steady state as determined by models with different diffusion coefficients.

Finally, there remains the question of how a truly time-dependent process, such as a seasonally varying solar zenith angle or diurnal cycle, will affect the calculations. At this time, not much is known about the effect of the diurnal cycle on perturbational studies. Because of the above-mentioned computational difficulty in reaching a true steady state, we will not be able

to assess the currently available results. We must wait for more extensive calculations. Seasonal cycles are not valid for globally averaged one-dimensional models. But we can still obtain some feeling for the seasonal-cycle response characteristic if we try a period of strong photochemical interactions followed by a period of weak photochemical interactions.

We have completed one sequence of calculations in which the cosine of the zenith angle varies seasonally from 0.2 to 0.96. After reaching a seasonally-varying equilibrium solution (after 10 years), we perform a NO_x-injection numerical experiment. Basic input parameters are as before and the details are of no importance here. What we are interested in is how the results differ from those of the constant-sun model. Figure 9 shows that for low zenith angles (large cos χ) the constant-sun model agrees well with the seasonal model, but for high zenith angles there is approximately 2% more decrease in ozone (13% vs. 11%). This difference is due to the fact that the seasonal model is not in a quasi-steady state during the period of high zenith angle because of the continuously changing seasons. In fact, there is comparatively more ozone in the ambient seasonal model during this period than is found in the constant-sun model at the corresponding zenith angle. This extra amount of ozone is not supported by local photochemical production, and consequently represents a net loss under SST perturbation. From this we suspect that the one-dimensional model will underestimate the perturbations at the mid-latitude ozone maxima by a sizable margin, because this ozone is indeed not completely supplied by local photochemistry. At the same time, the perturbations in the tropical region should be close to the one-dimensional-model results. This sensitivity to time-dependent parameters also dictates the need to fully analyze diurnal cycles.

From these analyses, we have developed an understanding of the limitations of one-dimensional models. At the same time we have also acquired a comparative tool for evaluating and analyzing the forthcoming multi-dimensional models. The most critical need at the present seems to be for the detailed evaluation of transport coefficients for one-, two- and three-dimensional models, through observations or other more detailed dynamic models such as general-circulation models. Only with such input

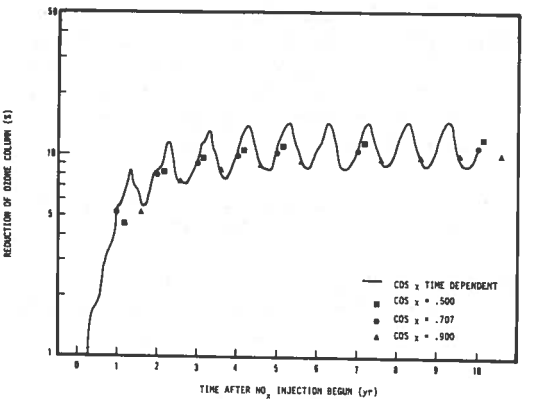

Figure 9. Comparison of ozone reduction from NO_x perturbations for seasonal-solar-flux model with constant-sun model.

can we really estimate the effects of projected stratospheric aircraft effluents with a reasonably high level of confidence.

ACKNOWLEDGMENT

The author would like to thank D. Wuebbles and R. Tarp for their valuable assistance in carrying out many of the calculations for this study. The work was performed under the auspices of the U.S. Atomic Energy Commission, and was supported in part by the Climatic Impact Assessment Program, U.S. Department of Transportation.

REFERENCES

Baulch, D.L., D.D. Drysdale, D.G. Horne, and A.C. Lloyd (1973), *Evaluated Kinetic Data for High Temperature Reactions, Vol. 2: Homogeneous Gas Phase Reactions of the* H_2-N_2-O_2 *Systems*, Chemical Rubber Co. Press, Cleveland, Ohio.

Brasseur, G. (1972), "Stratospheric chemistry," Aeronom. Acta **B41**.

Chang, J.S. and W.H. Duewer (1973), "On the Possible Effect of NO_x Injection in the Stratosphere Due to Past Atmospheric Nuclear Weapons Tests," UCRL-74480, Lawrence Livermore Laboratory.

Chang, J.S., A.C. Hindmarsh, and N.K. Madsen (1973), "Simulation of Chemical Kinetics Transport in the Stratosphere," UCRL-74823, Lawrence Livermore Lab., Livermore, Calif.

Chang, J.S. and H.S. Johnston (1974), "The effect of NO_x effluents on ozone," in this volume.

CIAP (1974), Volume 3 of the CIAP Monograph Series, U.S. Department of Transportation. NOTE: At present, these monographs exist only in an early draft version. They will be publicly available after completion in September 1974.

Crutzen, P.J. (1974), "A review of upper atmospheric chemistry," Canad. J. Chem. **52**, 1569-1581.

Davis, D.D., J.T. Herron, and R.E. Huie (1973), "Absolute rate constants for the reaction $O(^3P) + NO_2 \rightarrow NO + O_2$ over the temperature range 230-339°K," J. Chem. Phys. **58**, 530-535.

Ehhalt, D.H. and L.E. Heidt (1973), "The concentration of molecular H_2 and CH_4 in the stratosphere," Pure Appl. Geophys. **106-108**, 1352-1360.

Garvin, D. and R.F. Hampson, eds. (1974), *Chemical Kinetics Data Survey, VII. Tables of Rate and Photochemical Data for Modeling of the Stratosphere (Revised)*, National Bureau of Standards, NBSIR 74-430.

Gelinas, R.J., R.P. Dickinson, and K.E. Grant (1973), "Solar Flux and Photodissociation Calculations for LLL Atmospheric Physics Programs," Lawrence Livermore Laboratory Rept. UCRL-74944.

Hampson, R.F., ed. (1973), "Survey of photochemical and rate data for twenty-eight reactions of interest in atmospheric chemistry," J. Phys. Chem. Ref. Data **2**(2), 267-312.

Hindmarsh, A.C. (1972), "GEAR: Ordinary Differential Equation System Solver," Lawrence Livermore Laboratory Rept. UCID-30001, Rev. 1.

Hochanadel, C.J., J.A. Ghormley, and P.J. Ogren (1972), "Absorption spectrum and reaction kinetics of the HO_2 radical in the gas phase," J. Chem. Phys. **56**, 4426-4432.

Huie, R.E., J.T. Herron, and D.D. Davis (1972), "Absolute rate constants for the reaction $O + O_2 + M \rightarrow O_3 + M$ over the temperature range 200-346°K," J. Phys. Chem. **76**, 2653-2658.

Johnston, H.S. (1973), private communication to Garvin and Hampson.

McElroy, M.B., S.C. Wofsy, J.E. Penner, and J.C. McConnell (1974), "Atmospheric ozone: possible impact of stratospheric aviation," J. Atmos. Sci. **31**, 287-303.

Seitz, H., B. Davidson, J.P. Friend, and H.W. Feely (1968), "Numerical Models of Transport Diffusion and Fallout of Stratospheric Radioactive Materials," in Final Report on Project STREAK, USAEC Rept. No. NYO-3654-4.

Shimazaki, T. and T. Ogawa (1974), "Theoretical models of minor constituents' distributions in the stratosphere and the impacts of the SST exhaust gases," in *Proceedings of the International Conference on Structure, Composition and General Circulation of the Upper and Lower Atmosphere and Possible Anthropogenic Perturbations* (Melbourne, Jan. 14-25, 1974), pub. IAMAP, 1062-1092.

Stewart, R.W. (1973), "Response of stratospheric ozone to the simulated injection of nitric oxide," paper presented at the 1973 Fall AGU Meeting, San Francisco, California.

Tsang, W. (1973), "Comparison between experimental and calculated rate constants for dissociation and combination reactions involving small polyatomic molecules," Intern. J. Chem. Kin. **5**, 947-963.

Wilson, W.E., Jr. (1972), "A critical review of the gas-phase reaction kinetics of the hydroxyl radical," J. Phys. Chem. Ref. Data **1**, 535-573.

Whitten, R.C. and R.P. Turco (1974), "The effect of SST emission on the earth's ozone layer," in *Proceedings of the International Conference on Structure, Composition and General Circulation of the Upper and Lower Atmosphere and Possible Anthropogenic Perturbations* (Melbourne, Jan. 14-25, 1974), pub. IAMAP, 971-983.

APPENDIX

Here we will derive the linearity relation between the changes in total NO_x and the total source rate, S_{SST}.

If we sum up the individual differential equations for NO, NO_2 and HNO_3, we have

$$\frac{\partial [NO_x]}{\partial t} = k[N_2O]\,[O(^1D)] - \frac{\partial}{\partial z} F([NO_x]). \quad (A1)$$

The ambient $[NO_x]_A$ satisfies this equation, but the perturbed $[NO_x]_p$ satisfies the same equation with a perturbed $[N_2O]_p$ and $[O(^1D)]_p$ and a *local* source rate s_{SST} added. Consequently, the change in $[NO_x]$, $\Delta[NO_x] = [NO_x]_p - [NO_x]_A$, satisfies

$$\frac{\partial \Delta[NO_x]}{\partial t} = k([N_2O]_p\,[O(^1D)]_p - [N_2O]_A\,[O(^1D)]_A) + s_{SST} - \frac{\partial}{\partial z} F([NO_x]). \quad (A2)$$

Eq. (A2) is again a linear equation, and can be written as

$$\frac{\partial \Delta[NO_x]}{\partial t} = \bar{s}_{SST} - \frac{\partial}{\partial z} F(\Delta[NO_x]). \quad (A3)$$

If we let $G(z, z')$ be the Green's function for the steady-state equation, then the steady-state solution is

$$\Delta[NO_x] = \int_{z_B}^{z_T} G(z,z')\, \bar{s}_{SST}\, dz'$$

and the total $\Delta[NO_x]$ is

$$\Delta[NO_x]_{tot} = \int_{z_B}^{z_T} \Delta[NO_x]\, dz = \int_{z_B}^{z_T} dz \int_{z_B}^{z_T} G(z,z')\, \bar{s}_{SST}\, dz' . \quad \text{(A4)}$$

If we set

$$\bar{S}_{SST} = \int_{z_B}^{z_T} \bar{s}_{SST}\, dz$$

and define

$$\tau(z_0) = \left[\frac{\int_{z_B}^{z_T} dz \int_{z_B}^{z_T} dz'\, G(z,z')\, \bar{s}_{SST}}{\int_{z_B}^{z_T} \bar{s}_{SST}\, dz} \right]$$

we then have the linearity relation

$$\Delta[NO_x]_{tot} = \tau(z_0)\, \bar{S}_{SST}.$$

The z_0 is used to indicate the strong dependence of the double integral on the altitude of $\bar{S}_{SST}$. If the ozone perturbation is small, then $[O(^1D)]$ and $[N_2O]$ would remain essentially unchanged. This would mean that $s_{SST} \approx \bar{s}_{SST}$. From the definition of $\tau(z_0)$ we see that it is independent of the source strength if the source-function shape and its altitude of injection are unchanged. More explicitly, this means $\tau(\alpha \bar{s}_{SST}) \approx \tau(\bar{s}_{SST})$, where α is a constant source-strength factor.

ONE-DIMENSIONAL-MODEL STUDIES OF OZONE DEPLETION

R.C. WHITTEN AND W.J. BORUCKI
NASA Ames Research Center
Moffett Field, California

and

R.P. TURCO
R and D Associates
Santa Monica, California

ABSTRACT: The advantages and limitations of one-dimensional models are discussed; then various methods of solving the coupled set of reaction equations are developed and the principal characteristics outlined. Next, photoabsorption in the Schumann-Runge bands is treated from the standpoint of models that are simple enough to be run rapidly on a digital computer. The photochemistry of the various constituents is then studied. Boundary conditions are discussed, and some results obtained for two models developed by the authors are presented.

INTRODUCTION

One-dimensional (i.e., vertical) models of the photochemistry of the stratosphere have been used by numerous investigators. Because vertical transport by eddy diffusion only is included, many important effects that result from horizontal transport of minor constituents do not appear in such models. Nevertheless, one-dimensional models are valuable because they yield predictions that are usually correct qualitatively and because they can be used to optimize reaction sets for multidimensional models.

The starting point for many one-dimensional models of atmospheric photochemistry is the following set of equations that describe mass and momentum conservation:

$$\frac{\partial n_i}{\partial t} + \frac{\partial \Phi_i}{\partial z} = P_i - \ell_i n_i \tag{1}$$

$$\Phi_i = -K_e \left[\frac{\partial n_i}{\partial z} + \left(\frac{1}{H} + \frac{1}{T}\frac{dT}{dz} \right) n_i \right] - D_i \left\{ \frac{\partial n_i}{\partial z} + \left[\frac{1}{H_i} + (1+\alpha_i)\frac{1}{T}\frac{dT}{dz} \right] n_i \right\} \tag{2}$$

Here, n_i and Φ_i are the number density and flux of the ith constituent, P_i is the production rate per unit volume, ℓ_i is the loss rate, K_e is the eddy diffusivity, D_i is the binary molecular diffusivity of the ith component in nitrogen, T is atmospheric temperature, H is the mean scale height, H_i is the scale height of the ith constituent, and α_i is the molecular thermal-diffusion coefficient. Molecular diffusion is important only above 90 km, and is thus completely negligible within the stratosphere. Equations (1) and (2) for any component are coupled to those for other components through parameters P_i and ℓ_i.

The conservation equations are solved numerically by the use of techniques that lead to stability and to small truncation errors. They are of a class known as "stiff equations," the stiffness property being caused by the vastly different production and loss rates of the various photochemical reactions. Without special mathematical techniques, the solution will not converge unless time steps shorter than the characteristic time of the fastest reaction are used. Not only is this very expensive in terms of computer time, but the use of many small steps can lead to spurious sources and losses due to truncation error. In the following section, some of the mathematical techniques applicable to the problem at hand are examined.

COMPUTATIONAL TECHNIQUES

The conservation equations must be converted to finite-difference forms for numerical integration. There are numerous ways of doing

this; the simplest is the explicit technique. Here, the time derivative is

$$\frac{\partial n_i}{\partial t} \rightarrow \frac{n_i{}^{j+1} - n_i{}^{j}}{\Delta t} \tag{4}$$

where j+1 represents the time step and all other terms are evaluated at time step j. This approach is highly accurate if small time steps are used; in fact, small time steps *must* be used if stability is to be achieved (see, e.g., Ames (1969) for a complete discussion).

With the much more stable implicit method, the terms involving the space derivatives, and the production and loss terms, are evaluated at time step j+1 or at some weighted average of j and j+1.

In the semi-implicit technique, some of the terms (such as the production term P_i) may be evaluated only at the time step j. Such an approach has the advantage of decoupling the equations for the various species at time step j. The standard method for solving such equations is to march upward from the lower boundary, calculating a set of auxiliary parameters which is then used to compute the number densities by marching downward. The technique is explained in considerable detail by Ames (1969) and Shimazaki (1967).

Semi-implicit methods introduce spurious sources and losses of mass because the species number densities are obtained sequentially rather than simultaneously. Perhaps the simplest way to remove the spurious terms is by iterating the solution a number of times at a given time step. Unfortunately, excessive computer time is required for this approach; a better one is discussed later.

In his pioneering work on the photochemistry of the mesosphere and lower thermosphere, Shimazaki (1967) devised a method in which any mass lost because of the integration technique is introduced as an upward (or downward) flux $\Phi_{i\ell}$ at the lower boundary. Specifically, he integrated Eq. (1) between the boundaries so that

$$\Phi_{i\ell} = \int_{\ell}^{u} \left(\frac{\partial n_i}{\partial t} + \ell_i n_i - P_i \right) dz \tag{3}$$

where u and ℓ refer to the upper and lower boundaries, respectively, and the flux at the upper boundary has been set equal to zero. The actual integration is carried out by a rather complicated implicit method (not developed here). Shimazaki's method suffers from the fact that the correction is introduced entirely at the lower boundary; in the stratosphere, where vertical transport is slow, the matter introduced at the lower boundary cannot travel very far during a time step. It is thus desirable to introduce such corrections at all altitudes, as in the method of Whitten and Turco (Whitten et al., 1973; Whitten and Turco, 1974a,b; Turco and Whitten, 1974).

With this method, the compounds are grouped into sets, each of which is characterized by the occurrence of some element such as odd hydrogen, which is the set H, OH, HO_2, H_2O_2. The members of the set interchange rapidly with each other, but relatively slowly with compounds outside the set. The mass-conservation equations are written for each species; they are multiplied by the appropriate atom numbers, γ_i, and then summed. The large values of P_i and $\ell_i n_i$, which merely account for shuffling of species within the family, cancel; for i = hydrogen, the following equation remains:

$$\frac{\partial S_H}{\partial t} = -\frac{\partial \Phi_H}{\partial z} + \sum_H \gamma_i (P_i - \ell_i n_i) = -\frac{\partial \Phi_H}{\partial z} + P_H \tag{5}$$

where $\sum_H$ represents the sum over all odd-hydrogen species, $S_H = \sum_H \gamma_i n_i$, Φ_H is the flux of odd hydrogen, and P_H is the net production rate of odd hydrogen. For a closed chemical system, $P_H = 0$, and for many systems of aeronomic interest, P_H is a small residual net production or loss term that is much less than P_i and $\ell_i n_i$ of the individual species. The value of S_H obtained by solving Eq. (5) is then compared with the sum $S = \sum_i \gamma_i n_i$ obtained by computing the n_i values of the individual species (Eqs. (1) and (2)). The computed values of n_i are then appropriately corrected, the simplest technique being to scale each of these by a factor of S_H/S. The results obtained with this technique are similar to those procured by iterating 10 or more times at each time step.

With an implicit technique developed by one of the authors (Borucki), the entire chemical

source/loss term $P_i - \ell_i n_i$ is treated implicitly. Denoting the combined term by Q_i and omitting the transport term from Eq. (1) yields the finite-difference form

$$\frac{n_i^{j+1} - n_i^j}{\Delta t} = Q_i^{j+1} \tag{6}$$

which can be linearized by taking the first term in a Taylor series expansion of Q_i^{j+1} about Q_i^j:

$$\frac{n_i^{j+1} - n_i^j}{\Delta t} = Q_i^j + \sum_k \frac{\partial Q_i^j}{\partial n_k}\left(n_k^{j+1} - n_k^j\right) \tag{7}$$

Now the members of the set of mass-conservation equations are coupled, and it is necessary to solve a matrix equation. There are several advantages to this fully implicit method: large time steps can be used even though the mass conservation equations are very stiff; no correction scheme such as that used by Whitten and Turco is required; iteration is not needed. However, it must be emphasized that the method requires a lot of computer time. For economy's sake, large time steps are essential (Borucki et al., 1973).

Lomax and Bailey (1967) have developed an explicit multistep predictor-corrector technique with a large induced-stability boundary. Since the technique is explicit, there are no matrix inversions, so little computational time is required. Furthermore, the large induced-stability boundary allows much larger time steps to be used than can be with other techniques, such as the Euler and Runge-Kutta methods. Although the technique of Lomax and Bailey is five times faster than the second-order Runge-Kutta method and eight times faster than the fourth-order Runge-Kutta method when an eight-order stability polynomial is used, it is slower than the fully implicit technique when used on the relaxation-to-steady-state type of problem.

Finally, the Gear method (Gear, 1969) has been used by a number of investigators (e.g., J. Chang (1974)). It is an implicit, multistep, predictor-corrector method, normally used to solve systems of ordinary differential equations. The matrix of partial derivatives is reevaluated and inverted not at each time step, but only when necessary. The Gear method can be applied to the transport problem by treating the diffusion terms explicitly. Like the Lomax technique, it is significantly faster than Runge-Kutta methods.

A problem that makes particularly stringent demands on the computational technique is that of diurnal variations. The rapid changes in photodissociation that occur at sunrise and sunset make it necessary to use relatively small time steps with any method. The method used by Whitten and Turco has been successfully used to study the diurnal variations of HO_x and NO_x compounds in the stratosphere (Whitten and Turco, 1974b) with minimum time steps exceeding 200 sec. This technique is successful because, while the shuffling of species within a set occurs very rapidly, the change in the concentration of the characteristic element in the set still occurs rather slowly. For example, atomic-oxygen and ozone concentrations change rapidly, but the sum $[O] + [O_3]$ changes slowly.

The technique developed by Borucki cannot be used under twilight conditions because it is economical only if the time steps are large. However, another technique, such as that of Lomax and Bailey (1967), can be used at twilight, and then the implicit method can be used during daylight and nighttime hours.

PHOTOABSORPTION IN THE SCHUMANN-RUNGE BANDS

Molecular band absorption by molecular oxygen in the 175-205 nm spectral region is important in the photolysis of molecular oxygen, water vapor, and nitric oxide for altitudes between 60 and 90 km (Hudson et al., 1969). To accurately model the photodissociation rate of O_2 and the optical depth in the 175-205 nm spectral region, Hudson and Mahle (1972) performed a line-by-line integration of the Schumann-Runge band absorption using theoretical line profiles for column densities between 1×10^{17} and 7×10^{24} cm^{-2} and for temperatures between 150 and 300K. Interpolation constants were then found for 19 wavelength bands spanning the 175-205 nm spectral region for both the oxygen photolysis rate and the optical depth. Because the 5538 interpolation constants must be stored in computer memory, and because interpolation is required to obtain a specific value of the photodissociation rate and

optical depth, the Hudson-Mahle model is expensive to use. A much simpler and less expensive model of the Schumann-Runge band absorption has been adopted by one of the authors (Turco), who uses a band model suggested by experimental results in which the optical depth varies as the square root of the path length.

Although the model is tabulated at 0.1-nm intervals from 177.8 to 202.1 nm, it cannot be expected to be as accurate as the Hudson-Mahle model in calculating the optical depths and photolysis rates over the many decades of column density and at temperatures different from 300K (the only temperature at which 0.1-nm-resolution O_2 absorption cross-sections in the S-R band are presently available). This is because the S-R band cross-section is a very rapidly varying function of wavelength, and because the photodissociation rate depends on an exponential function of the cross-section, whereas the optical depth depends on a linear function of the cross-section. Hence, any simple band-model cross-section will not simultaneously produce the proper photodissociation rate and optical depth for every required column density. Nevertheless, the expense of using the Hudson-Mahle model makes it very desirable to find a suitable approximation.

Figure 1 compares the ratio of the S-R band photodissociation rate of the Turco model to that of the Hudson-Mahle model. For the altitude range of interest (60 to 90 km), the Turco model is always within 26% of the Hudson-Mahle model for a solar zenith angle of 0°. Part of the discrepancy between the two models is caused by the 300K cross-section used by Turco. To assess the effect of the temperature difference, the Hudson-Mahle model was used with an isothermal atmosphere at 300K. A definite improvement is evident. Thus, it appears that the difference in the results for the two models of the S-R band model would be about ±15% between an altitude of 60 and 90 km if similar temperature profiles were used. Note that below 50 km the Schumann-Runge band contribution to the O_2 photodissociation rate is always less than 20%, so a highly accurate model of the O_2 S-R band is not required for calculating the total O_2 photodissociation rate below 50 km.

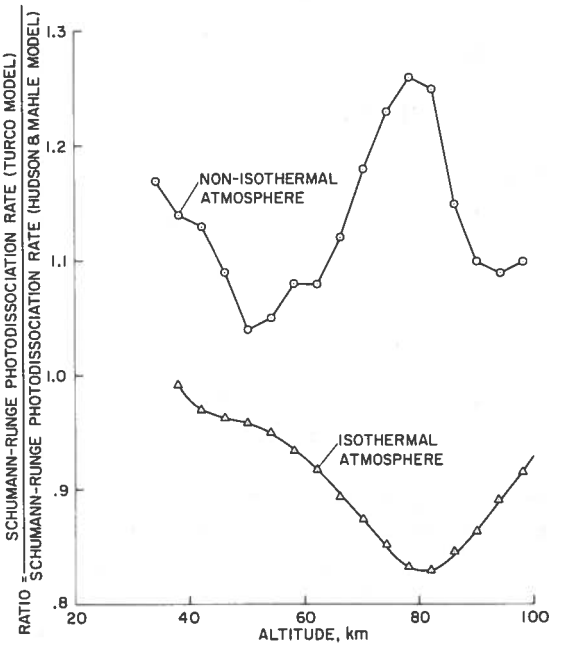

Figure 1. Molecular oxygen photodissociation rates for the methods of Whitten and Turco (1974a) and of Hudson and Mahle (1972).

PHOTODISSOCIATION RATES

The photodissociation rate of any constituent is easily determined if the solar radiation intensity at a given altitude is known,

$$q_i(z) = n_i(z) \int \sigma_i(\lambda) I_\lambda \, d_\lambda \qquad (8)$$

The difficult part of the computation is the determination of I_λ in the Schumann-Runge band region (this aspect was discussed in the preceding section). Photodissociation rates of the various minor constituents at zero optical depth are given in Appendix 1.

CHEMISTRY

The chemistry used in all models of minor constituents in the stratosphere includes at least the compounds of the oxygen-hydrogen-nitrogen system. Odd-hydrogen compounds such as H, OH, and HO_2 have a rather pronounced effect on the ozone balance through reactions such as

$$H + O_3 \rightarrow OH + O_2$$

$$HO_2 + O_3 \rightarrow OH + 2O_2$$

$$HO_2 + O \rightarrow OH + O_2$$

The odd-hydrogen compounds are formed by the decomposition of water vapor, methane, and molecular hydrogen, principally through the reaction

$$O(^1D) + H_2O \rightarrow 2OH$$

The $O(^1D)$ comes from the photolysis of ozone. Because of the abundance of water vapor in the stratosphere (10^{12} to 10^{13} cm^{-3}), the amount added by the exhaust from projected SST fleets is negligible. Hence water-vapor perturbations can be neglected in predicting the environmental effects of SST operations in the stratosphere.

This is not the case with nitrogen oxides. Crutzen (1971) and Johnston (1971) pointed out that oxides of nitrogen efficiently convert odd oxygen (i.e., atomic oxygen and ozone) to even oxygen (O_2) through the catalytic reactions

$$NO + O_3 \rightarrow NO_2 + O_2$$

$$NO_2 + O \rightarrow NO + O_2$$

Johnston (1971) predicted ozone depletion of over 50% in some cases for hypothetical SST operations. However, it was realized later that the reaction of NO_x with HO_x to form nitric acid, i.e.,

$$NO_2 + OH + M \rightarrow HNO_3 + M$$

provides an effective reservoir for NO_x compounds in the stratosphere. Murcray and co-workers (Williams et al., 1972; Murcray et al., 1973) observed HNO_3 in the stratosphere at concentrations exceeding 2×10^{10} cm^{-3}.

The chemistry used in the models of Whitten and co-workers (Whitten et al., 1973; Whitten and Turco, 1974a,b) contains the important reactions among oxygen-hydrogen-nitrogen compounds as well as those of carbon and sulphur. The set of reactions for the O-H-N system is given in Appendix 2. Other workers (e.g., J. Chang (1974) and Shimazaki and Laird (1972)) use similar sets.

BOUNDARY CONDITIONS

The boundary conditions used in one-dimensional studies are very important to the prediction of minor-constituent concentrations, particularly near the boundaries. For the upper boundary condition, some investigators (i.e., Shimazaki and Laird (1972) and Stewart and Hoffert (1974)) place the boundary sufficiently high (≈200 km) that diffusive equilibrium is an excellent approximation except for hydrogen. Whitten and co-workers (Whitten et al., 1973; Whitten and Turco, 1974a,b) place the upper boundary at only 120 km; however, diffusive equilibrium (i.e., flux = 0) is still a good approximation except for hydrogen and nitric oxide. The former has an upward flux equal to the escape flux, while the latter has a downward flux due to the production of NO in the thermosphere. In any event, the upper boundary conditions, if specified in the thermosphere, do not materially affect predictions in the stratosphere.

However, the lower boundary conditions do affect the predicted chemistry of the stratosphere. Some investigators (e.g., J. Chang (1974) and Stewart and Hoffert (1974)) extend their model all the way to the surface of the earth. The authors of the model believe the choice of surface boundary conditions does not substantially affect the predictions. However, the chemistry and transport of the troposphere must be included correctly. Other workers place the lower boundary at some point near the base of the stratosphere (Whitten et al., 1973). Whitten and co-workers do not impose strict flux or chemical-equilibrium boundary conditions on their solutions. Instead, for the technique used here, a dummy level is established near the upper and lower boundaries, and both continuity and flux equations are used to start the solution at the bottom and to terminate it at the top. If a species is dominated by chemistry, the corresponding terms will dominate the boundary condition and establish a value near the chemical-equilibrium value. At the same time, the specified flux through the boundary can affect the overall atom balance. Thus, the boundary fluxes for each constituent are still basic information for our model. When a flux-dominated constituent (e.g., O_3, H_2O) has been measured near the lower boundary, the boundary condition is set so that the measured value of the concentration is

closely maintained during the computer run. The set of lower boundary conditions used by Whitten and co-workers is given in Appendix 3.

RESULTS

In this section, only the present results are discussed in detail, but they are compared with those of several other investigators and with measurements of minor constituents in the stratosphere.

Because there is considerable disagreement in the literature as to the best profile for the eddy-diffusion coefficient, two different profiles were used (Figure 2). A comparison of the model results with the measured concentration profiles of various constituents led to the conclusion that profile 1 is more representative of the upper atmosphere than profile 2.

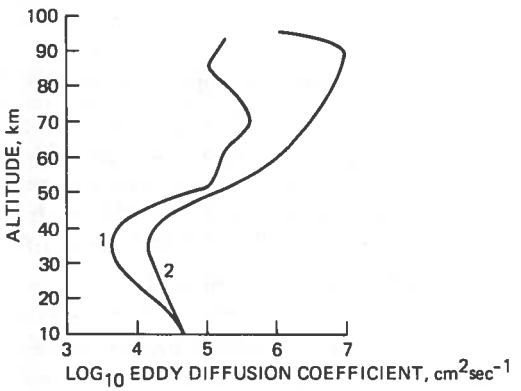

Figure 2. Profiles of eddy diffusion coefficient. (1) Hays and Olivero (1970); (2) Zimmerman (1972).

Profiles of the minor constituents computed using the Whitten-Turco model are shown in Figure 3 for eddy-diffusivity profiles 1 and 2 of Figure 2. These profiles were obtained from steady-state computations using a mean solar zenith angle of 45°. Generally, the agreement with available experimentally determined profiles is reasonably good. The computed O_3 column density is too large and the altitude of the peak concentration is too high; both features seem to be common to all results for a one-dimensional model (Stewart and Hoffert, 1974). The NO concentration at high altitudes is less than reported measurements obtained from airglow observations (Meira, 1971; Tisone, 1973). However, Strobel (1972) questioned the reliability of the latter NO measurements; from model studies somewhat similar to those presented here, he suggested mesospheric NO concentrations very close to those presented in Figure 3.

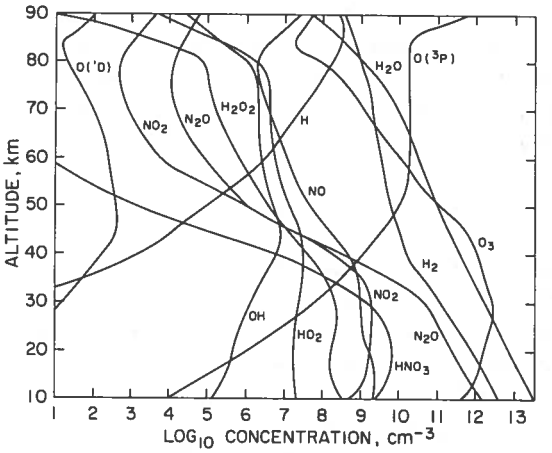

a. Profile 1.

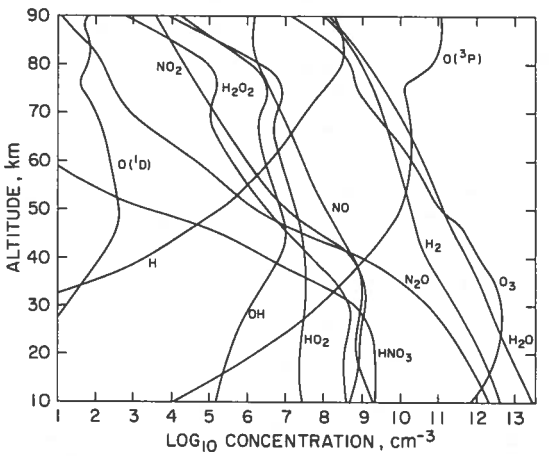

b. Profile 2.

Figure 3. Vertical distributions of various atmospheric constituents with two eddy-diffusion coefficient profiles, using the Whitten-Turco method.

Nitrogen compounds have been measured at low altitudes only recently. Using an infrared spectrometric technique, Murcray and co-workers (Williams et al., 1972) observed that the nitric-acid concentration in the stratosphere lies between 1 and 20 X 10^9 cm^{-3}, with a pronounced peak occurring near an altitude of 22 to 23 km. The HNO_3 profiles shown in Figure 3 exhibit the same magnitude and structure as the measurements, although the peak concentrations are too small; other investigators (Shimazaki and Laird, 1972) also obtain concentration values that are too small. Nitric oxide and nitrogen

dioxide have also been detected in the lower stratosphere. Schiff and co-workers (Ridley et al., 1973) observed that NO, measured by the $NO\text{-}O_3$ chemiluminescence reaction, has a concentration of about 2×10^8 cm^{-3} at 20 km, whereas Ackerman et al. (1973) obtained the larger value of 3 to 5×10^8 cm^{-3} at the same height using an infrared spectral technique. Ackerman and co-workers also obtained a height profile of NO concentration rather similar to the present results, except that their peak concentration occurs at a somewhat lower height. Loewenstein (1974) recently measured NO concentrations near an altitude of 20 km by the chemiluminescence technique and found that the concentrations decrease with increasing altitude (Figure 3).

The principal source of nitric acid in the stratosphere is the reaction of NO_2 with OH. Hence, to obtain a large concentration of HNO_3, one must have a large concentration of NO_2 (and thus NO). In this respect, the results of Ridley et al. (1973) and Ackerman et al. (1973) seem incompatible with the nitric-acid measurements, unless the rate coefficients of the important chemical reactions are substantially different from the measured values, or unless stratospheric OH concentrations are significantly larger than those currently predicted by models. At present, there is no reason to seriously doubt the rate-coefficient measurements. On the other hand, OH concentrations in the stratosphere are controlled largely by the rate of methane oxidation and of reaction of OH with HO_2, and these processes are still subject to uncertainty. Odd-hydrogen species have never been measured in the stratosphere.

The model described here can also predict the diurnal behavior of the concentrations of minor constituents. The diurnal behavior of NO, NO_2, and HNO_3 is shown in Figure 4. Diurnal variations of HO_x and NO_x compounds are discussed more fully elsewhere (Whitten and Turco, 1974b). Note that HNO_3 does not change significantly over the diurnal cycle except in the uppermost stratosphere. At night, the loss rate of HNO_3 by photolysis vanishes, but the concentrations of OH at lower altitudes decrease sufficiently that the formation of nitric acid by reaction R43 is much slower at night than during daylight hours. Hence, the production is nearly balanced by loss.

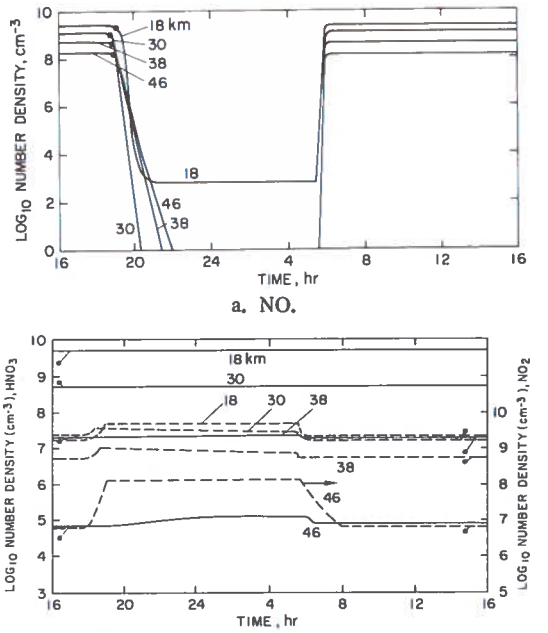

Figure 4. Diurnal behavior of various constituents at various altitudes. The symbol • denotes the steady-state concentrations for a constant solar zenith angle of 45°. The horizontal position of the circles has no meaning, since the values correspond to noon time (i.e., 45° solar zenith angle).

PERTURBED ATMOSPHERE

In Volume 2 of the Climatic Impact Assessment Program's monograph series, it is estimated (CIAP, 1974) that with present-day engines, the daily effluent of NO_x of an SST fleet flying the New York to London, Amsterdam, Frankfurt, and Paris corridor would be 28.7 metric tons in a box 500 km long, 1000 km wide, and 2 km deep. There are about 12 such boxes along the flight corridor. The corresponding daily water-vapor effluent would be about 2000 metric tons. This perturbation was simulated by assuming all NO_x to be emitted as NO and the emission to occur at a steady rate (6.6×10^3 molecules cm^{-3} sec^{-1} for NO and 4.8×10^5 molecules cm^{-3} sec^{-1} for H_2O). These data were fed into the program, which was run for a period of two years (simulated time). The water-vapor deposition was found to have no detectable effect on ozone balance, and only a very small effect on the global water-vapor distribution because of the large amount of the H_2O present in the ambient stratosphere. However, the nitric oxide emission

affects the ozone distribution; Figure 5 shows the reduction in ozone column density as a function of flight altitude. The effect of the flight altitude is evident; SST's that fly at 20 km could be expected to destroy two times more ozone than those that fly at 16 km. Diurnal variations were also inserted into the present model to evaluate their effect on the perturbed stratosphere. The computations were performed as follows: The model was run with SST flights for two years with the zenith angle fixed; the resulting perturbed concentrations were then used as initial conditions and the model was run diurnally for 60 additional days. The concentrations were then compared to the results from a study of the diurnal natural atmosphere. While the ozone concentrations were lower in the diurnal models, the percent ozone reduction with SST flights was about the same for both the steady-state and diurnal computations.

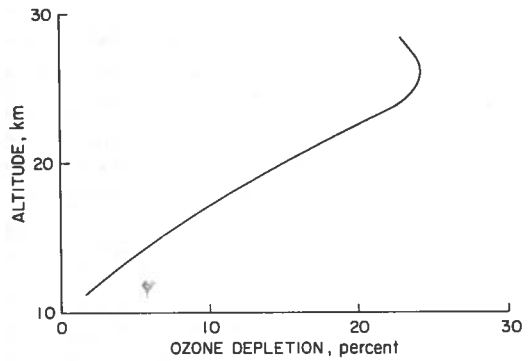

Figure 5. Percent reduction in ozone column density as a function of NO deposition altitude; deposition rate is 6.6×10^3 cm^{-3} sec^{-1}.

Although the nitric oxide was assumed to be emitted at a number of different altitudes in the present studies, the largest reduction in ozone concentration occurred near the ozone peak in every case. This point is evident in Figure 6, which shows the ambient ozone profile (A), the profile (B) when NO is injected at 16 km, and the profile (C) when NO is emitted at 20 km. The depletion occurs at the ozone peak because of the upward eddy transport of NO, NO_2 and HNO_3 (shown in Figure 7).

The ozone depletion values shown in Figure 5 are probably overestimated, since meridional spreading was confined to boxes that are only

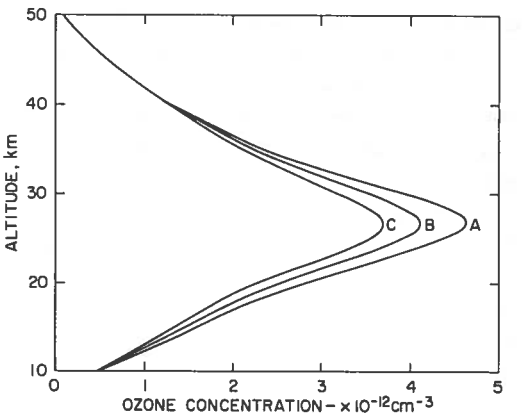

Figure 6. Ozone profiles for various assumptions about deposition altitude. (A) unperturbed atmosphere; (B) deposition at 16 km altitude, dispersion over a zone 1000 km wide; and (C) deposition at 20 km altitude, dispersion over a zone 1000 km wide.

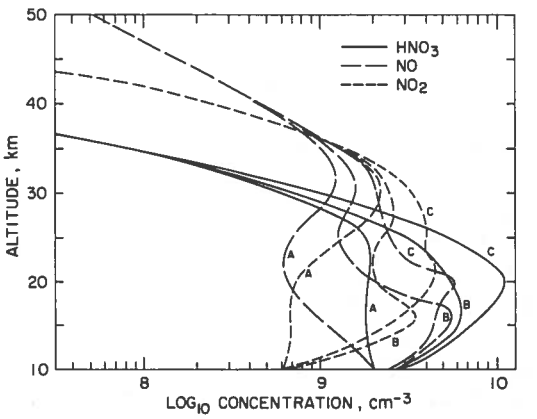

Figure 7. Vertical distribution of odd-nitrogen compounds NO, NO_2, and HNO_3. (A) unperturbed atmosphere; (B) deposition at 16 km altitude, dispersion over a zone 1000 km wide; and (C) deposition at 20 km altitude, dispersion over a zone 1000 km wide.

1000 km wide. If the boxes had been assumed to be 4000 km wide, the ozone depletion would have been only about 40% of the values shown in Figure 5. Inclusion of meridional spreading in the model can be included correctly only with a two- or three-dimensional model. (Such studies are now under way at Ames and will be reported elsewhere in the near future.) The NO emission

rates are probably much too large; probable engine improvements were not considered.

The reductions in ozone column density due to SST operations predicted by the present model are in *rather sharp disagreement* with those suggested by Johnston, who obtained reductions of as much as 50%. Although he does not give quantitative estimates, Crutzen (1971, 1972) indicates estimates of reduction in ozone column densities which are of the same order as ours. Johnston did not take transport into account, nor did he include HNO_3 as a reservoir for odd nitrogen. One of the factors underlying the small decrease in ozone is a "self-healing" effect that acts to restore the ozone after it is destroyed. Reducing the ozone column density increases the rate of photodissociation of O_2 (process J2) in the stratosphere. The atomic oxygen so released reacts with O_2 to reform ozone (reaction R3).

CIAP STANDARD PROBLEM

In August 1973, CIAP participants were sent a "standard problem" to facilitate comparison of the models being used by different investigators. This standard problem consisted of a photochemical reaction set, a vertical profile of the eddy diffusion coefficient, and calculated values of the distribution of the NO_x fluxes produced by a fleet of SST's.

The CIAP standard problem was examined by one of the authors (Borucki) with a newly developed, one-dimensional atmospheric model that uses the fully implicit numerical-integration algorithm mentioned earlier to compute both transport and photochemistry.

The CIAP photochemical reaction set consists of

$$O(^3P) + O_3 \rightarrow 2\,O_2 \qquad k_1 = 1.9 \times 10^{-11} \exp(-2300/T)$$

$$O(^3P) + O_2 + M \rightarrow O_3 + M \qquad k_2 = 1.07 \times 10^{-34} \exp(510/T)$$

$$NO_2 + O(^3P) \rightarrow NO + O_2 \qquad k_3 = 9.1 \times 10^{-12}$$

$$NO + O_3 \rightarrow NO_2 + O_2 \qquad k_4 = 9 \times 10^{-13} \exp(-1200/T)$$

$$O(^1D) + M \rightarrow O(^3P) + M \qquad \text{(assumed instantaneous)}$$

$$O_2 + h\upsilon \rightarrow 2\,O(^3P) \qquad \text{(see text)}$$

$$O_3 + h\upsilon \rightarrow O_2 + O(^3P) \qquad \text{(see text)}$$

$$O_3 + h\upsilon \rightarrow O_2 + O(^1D) \qquad \text{(see text)}$$

$$NO_2 + h\upsilon \rightarrow NO + O(^3P) \qquad \text{(see text)}$$

The calculation of the photoabsorption by O_2, O_3, and NO_2 was based on the solar fluxes and absorption cross-sections tabulated by Gelinas et al. (1973). The photodissociation of O_2 by the Schumann-Runge molecular band was computed from the data of Hudson and Mahle (1972). Because the atmospheric model used here imposes a zero-flux boundary condition at 120 km, it was necessary to extend the range of the eddy-diffusion coefficient given in the CIAP problem. The range was extended by linear interpolation from the CIAP value at 55 km to a constant value of 2×10^6 cm^{-2} sec^{-1} at 100 km and above, similar to that recommended by Shimazaki and Laird (1970). The lower boundary conditions required the number densities to be equal to those observed or calculated by others. Temperatures and number densities of the major atmospheric constituents were obtained from the U.S. Standard Atmosphere (1962). Figure 8 shows altitude-versus-number-density plots for the calculated minor constituents, both with and without an NO_x injection rate of 1.5×10^3 cm^{-3} sec^{-1}.

Figure 9 compares the calculated secular change in the vertical ozone column density at 10 km for NO_x injection rates of 1.5×10^3 cm^{-3} sec^{-1} and 6.6×10^3 cm^{-3} sec^{-1} at an altitude of 20 km and with a constant solar zenith angle of 45°. The first injection rate is that given in the CIAP standard problem; the second rate is the one used earlier. The large reductions in the computed ozone column densities disagree with those calculated earlier with a more complete photochemical reaction set. Stewart (1973) also reports that models that do not include nitric-acid photochemistry tend to show a larger reduction in ozone than those models that do. Consequently, it is suggested that the CIAP reaction set be amended to include nitric-acid

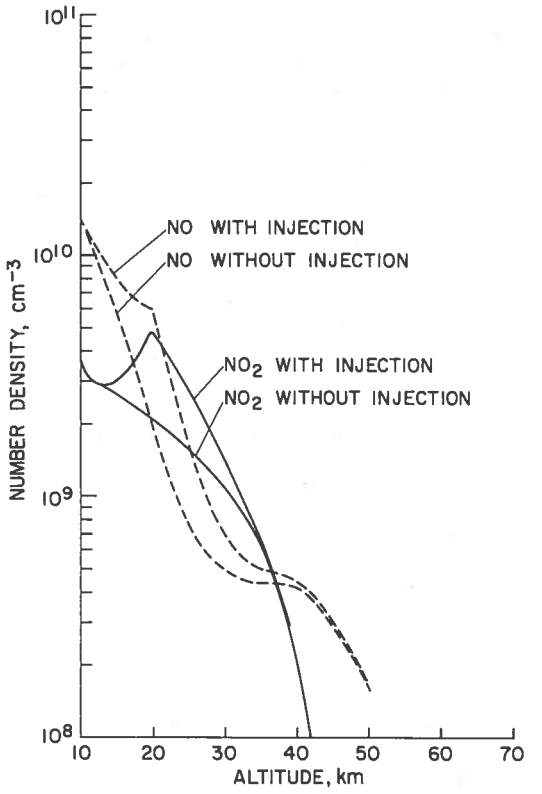

a. Odd nitrogen.

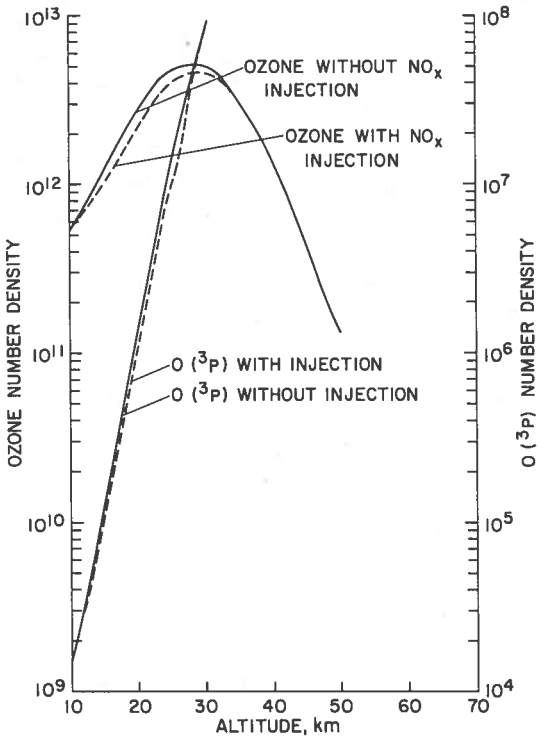

b. Odd nitrogen.

Figure 8. Vertical distributions when CIAP reaction set is used, for injection rates of 0.0 and 1.5×10^3 molecules of NO cm^{-3} sec^{-1}.

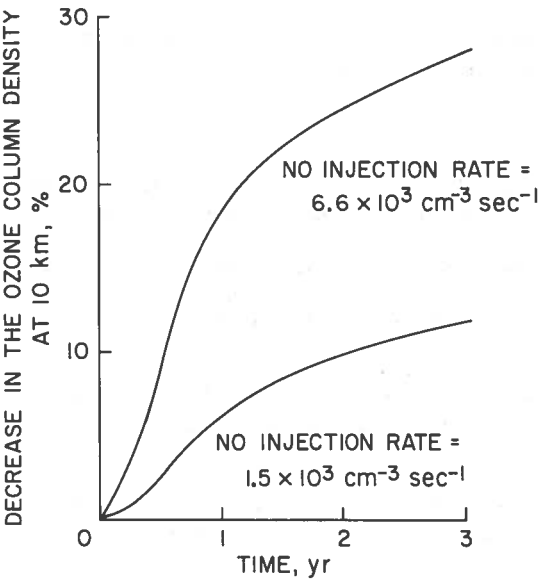

Figure 9. Percent reduction in the ozone column density as a function of time and the NO injection rate, when only the CIAP reaction set is used.

photochemistry, so that a more meaningful comparison of the models may be carried out.

CONCLUSIONS

Several techniques for numerically solving the mass and momentum conservation equations have been discussed in some detail. A general conclusion is that both the "stiffness" of the equations and computer costs must be kept in mind; the most accurate results are also the most expensive. Less expensive techniques should be considered when more approximate results are sufficient.

In a series of studies involving the simulated emission of nitric oxide by an SST fleet operating over the North Atlantic, the ozone depletion caused by the NO_x was found to be significantly less than Johnston's values, but still not negligible. Also, it was found that the degree of ozone-column destruction depends on flight altitude. Ozone depletion is less for flight altitudes below 20 km. Although one-dimensional models usually provide correct order-of-magnitude estimates of minor-constituent concentrations, neglecting horizontal transport by eddies and by circulation is a serious limitation. One-dimensional models are useful as an aid in

making the development of multidimensional models more tractable.

REFERENCES

Ames, W.F. (1969), *Numerical Methods for Partial Differential Equations*, Barnes and Noble, N.Y.

Ackerman, M., D. Frimout, D. Muller, D. Nevejans, J.-C. Fontanella, A. Girard, and N. Louisnard (1973), "Stratospheric nitric oxide from infrared spectra," Nature **245**, 205.

Borucki, W.J., A.L. Maples, and H.T. Woodward (1973), "Efficient numerical techniques for aeronomical calculations," Trans. AGU **54**, 1149.

Chang, Julius S. (1974), "Simulations, perturbations, and interpretations," in this volume.

CIAP (1974) Monograph No. 2, Climatic Impact Assessment Program, U.S. Department of Transportation. NOTE: At present, these monographs exist only in an early draft form. They will be publicly available after completion in September 1974.

Crutzen, P.J. (1971), "Ozone production rates in an oxygen-hydrogen-nitrogen oxide atmosphere," J. Geophys. Res. **76**, 7311.

Crutzen, P.J. (1972), "SST's – a threat to the Earth's ozone shield," AMBIO **1**, 41.

Gear, C.W. (1969), "The automatic integration of stiff ordinary differential equations," in *Information Processing* 68, ed. A.J.H. Morrel, North Holland Publishing Co.

Gelinas, R.J., R.P. Dickinson, and K.E. Grant (1973), "Solar Flux and Photodissociation Calculations for LLL Atmospheric Physics Programs," University of California Preprint UCRL-74944.

Hays, P.B. and J.J. Olivero (1970), "Carbon dioxide and monoxide above the tropopause," Planet. Space Sci. **18**, 1729.

Hudson, R.D., V.L. Carter, and E.L. Breig (1969), "Predissociation in the Schumann-Runge band system of O_2: Laboratory measurements and atmospheric effects," J. Geophys. Res. **74**, 4079.

Hudson, R.D. and S.H. Mahle (1972), "Photodissociation rates of molecular oxygen in the mesosphere and lower thermosphere," J. Geophys. Res. **77**, 2902.

Johnston, H.S. (1971), "Reduction of stratospheric ozone by nitrogen oxide catalysts from supersonic transport exhaust," Science **173**, 517.

Loewenstein, M., J.P. Paddock, I.G. Poppoff, and H.F. Savage (1974), "In-situ NO and O_3 measurements in the lower stratosphere from a U-2 aircraft," in this volume.

Lomax, Harvard and Harry E. Bailey (1967), "A Critical Analysis of Various Numerical Integration Methods for Computing the Flow of a Gas in Chemical Equilibrium," NASA Technical Note D-4109.

Meira, L.G. (1971), "Rocket measurements of upper atmospheric nitric oxide and their consequences to the lower ionosphere," J. Geophys. Res. **76**, 202.

Murcray, D.G., A. Goldman, A. Csoeke-Poeckh, F.H. Murcray, W.J. Williams, and R.N. Stocker (1973), "Nitric acid distribution in the stratosphere," J. Geophys. Res. **78**, 7033.

Ridley, B.A., H.I. Schiff, A.W. Shaw, L. Bates, C. Howlett, H. LeVaux, L.R. Megill, and T.E. Ashenfelter (1973), "Measurements *in situ* of nitric oxide in the stratosphere between 17.4 and 22.9 km," Nature **245**, 310.

Shimazaki, T. (1967), "Dynamic effects on atomic and molecular oxygen density; a numerical solution to equations of motion and continuity," J. Atmos. Terrest. Phys. **29**, 223.

Shimazaki, T. and A.R. Laird (1970), "A model calculation of the diurnal variation in minor neutral constituents in the mesosphere and lower thermosphere including transport effects," J. Geophys. Res. **75**, 3221.

Shimazaki, T. and A.R. Laird (1972), "Seasonal effects on distributions of minor natural constituents in the mesosphere and lower thermosphere," Radio Sci. **7**, 23.

Stewart, R.W. (1973), "Response of stratospheric ozone to the simulated injection of nitric oxide," Trans. AGU **54**, 1098.

Stewart, R.W. and M.I. Hoffert (1974), "A chemical model of the troposphere and stratosphere," J. Atmos. Sci. (to be published).

Strobel, D.F. (1972), "Nitric oxide in the D-region," J. Geophys. Res. **77**, 1337.

Tisone, G.C. (1973), "Measurements of NO densities during sunrise at Kauai," J. Geophys. Res. **78**, 746.

Turco, R.P. and R.C. Whitten (1974), "A comparison of two computational techniques for solving aeronomic problems," J. Geophys. Res. **79**, 3179.

Whitten, R.C., J.S. Sims, and R.P. Turco (1973), "A model of carbon compounds in the stratosphere and mesosphere," J. Geophys. Res. **78**, 5362.

Whitten, R.C. and R.P. Turco (1974a), "Perturbations of the stratosphere and mesosphere by aerospace vehicles," AIAA J. 12, 1110.

Whitten, R.C. and R.P. Turco (1974b), "Diurnal variations of HO_x and NO_x in the stratosphere," J. Geophys. Res. 79, 1302.

Williams, W.J., J.N. Brooks, D.G. Murcray, F.H. Murcray, P.M. Fried, and J.A. Weinman (1972), "Distribution of nitric oxide acid vapor in the stratosphere as determined from infrared atmospheric emission data," J. Atmos. Sci. 29, 1375.

Zimmerman, Samuel P. (1972), personal communication.

APPENDIX 1

Photodissociation Rates for O-H-N System (in units of sec^{-1} at zero optical depth)

Number	Process	Rate Coefficient	Reference
J1	$O_2 + h\nu \xrightarrow{\lambda < 175.9\ nm} O(^1D) + O(^3P)$	2.1×10^{-6}	1-4
J2	$O_2 + h\nu \xrightarrow{175.9 \leq \lambda < 242.4\ nm} 2\,O\,(^3P)$	3.8×10^{-8}	1-4
J3	$O_3 + h\nu \xrightarrow{\lambda < 310\ nm} O_2\,(^1\Delta g) + O(^1D)$	9.7×10^{-3}	1-4
J4	$O_3 + h\nu \xrightarrow{310 < \lambda < 611\ nm} O_2\,(^1\Delta g) + O\,(^3P)$	4.0×10^{-4}	5-7
J5	$O_3 + h\nu \xrightarrow{\lambda \leq 1180\ nm} O_2\,(^1\Sigma\bar{g}) + O(^3P)$	2.7×10^{-5}	5-7
J6	$NO + h\nu \rightarrow N + O$	1.4×10^{-5}	8
J7	$NO_2 + h\nu \rightarrow NO + O(^3P)$	1.2×10^{-2}	9-11
J8	$NO_3 + h\nu \rightarrow NO + O_2$	1.1×10^{-3}	Footnote a
J9	$N_2O + h\nu \rightarrow N_2 + O(^1D)$	2.4×10^{-6}	12-14
J10	$N_2O_5 + h\nu \rightarrow 2NO_2 + O$	6.1×10^{-4}	15,16
J11	$HNO_2 + h\nu \rightarrow OH + NO$	1.1×10^{-3}	Footnote b
J12	$HNO_3 + h\nu \rightarrow OH + NO_2$	2×10^{-4}	18,19 Footnote c
J13	$H_2O + h\nu \rightarrow OH + H$	7.1×10^{-6}	21
J14	$H_2O_2 + h\nu \rightarrow 2OH$	1.4×10^{-4}	22,23
J15	$HO_2 + h\nu \rightarrow OH + O$	1.0×10^{-3}	24,25

[a] Assumed equal to 1/10 of rate of J7.

[b] Assumed equal to 1/10 of rate of J7 (reference 17).

[c] Johnston concluded that the quantum yield of J12 is very close to unity for his measurements. Hence, the process leading to $H + NO_3$ can be ignored. Solar flux from Ackerman (reference 20).

REFERENCES FOR APPENDIX 1

1. Hudson, R.D. and S.H. Mahle, *J. Geophys. Res.*, 77, 2902-2914 (1972).
2. Ogawa, M., *J. Geophys. Res.*, 73, 6759-6763 (1968).
3. Blake, A.J., J.H. Carver, and G.N. Haddad, *J. Quant. Spectrosc. and Radiat. Trans.*, 6, 451-459 (1966).
4. Watanabe, K., E.C.Y. Inn, and M. Zelikoff, *J. Chem. Phys.*, 21, 1026-1030 (1953).
5. Inn, E.C.Y. and Y. Tanaka, *J. Opt. Soc. Am.*, 43, 870-873 (1953).
6. Griggs, M., *J. Chem. Phys.*, 49, 857-859 (1968).
7. Jones, I.T.N. and R.P. Wayne, *J. Chem. Phys.*, 51, 3617-3618 (1969).
8. Cieslik, S. and M. Nicolet, *Planet. Space Sci.*, 21, 925 (1973).
9. Hall, T.C. and F.E. Blacet, *J. Chem. Phys.*, 20, 1745-1749 (1952).
10. Nakayama, T., M.Y. Kitamura, and K. Watanabe, *J. Chem. Phys.*, 30, 1180-1186 (1959).
11. Pitts, J.N., J.H. Sharp, and S.I. Chan, *J. Chem. Phys.*, 40, 3655-3662 (1964).
12. Zelikoff, M., K. Watanabe, and E.C.Y. Inn, *J. Chem. Phys.*, 21, 1643-1647 (1953).
13. Bates, D.R. and P.B. Hays, *Planet. Space Sci.*, 15, 189-198 (1967).
14. Preston, K.F. and R.F. Barr, *J. Chem. Phys.*, 54, 3347-3348 (1971).
15. Jones, E.J. and O.R. Wulf, *J. Chem. Phys.*, 5, 873-877 (1937).
16. Johnston, H.S., R. Graham, D. Martin, and J. Girman, CIAP Quart. Rpt., Mar.-June, U.C. Berkeley (1973).
17. Johnston, H.S., Project Clean Air, Task Force No. 7, U.C. Berkeley (1970).
18. Johnston, H.S. and R. Graham, *J. Phys. Chem.*, 77, 62-63 (1972).
19. Johnston, H.S., CIAP Newsletter 72-4, U.S. Dept. of Transportation (December 1972).
20. Ackerman, M., "Ultraviolet solar radiation related to mesospheric processes," in *Mesospheric Models and Related Experiments*, Fiocco (ed.), D. Reidel, Dordrecht, pp. 149-159 (1971).
21. Watanabe, K. and M. Zelikoff, *J. Opt. Soc. Am.*, 43, 753-755 (1953).
22. Urey, H.C., L.H. Dawsey, and F.O. Rice, *J. Am. Chem. Soc.*, 51, 1371 (1929).
23. Hold, R.B., C.K. McLane, and O. Oldenberg, *J. Chem. Phys.*, 16, 225-229 (1948).
24. Hochanadel, C.J., J.A. Ghormley, and P.J. Ogren, *J. Chem. Phys.*, 56, 4426 (1972).
25. Paukert, T.T. and H.S. Johnston, *J. Chem. Phys.*, 56, 2824-2838 (1972).

APPENDIX 2

Chemical Parameters
(in units of $cm^6\ sec^{-1}$ for thermolecular reactions, $cm^3\ sec^{-1}$ for biomolecular reactions, and sec^{-1} for unimolecular reactions)

Number	Process	Rate Coefficient	Reference
1	$O + O_2 + M \rightarrow O_3 + M$	$1.1 \times 10^{-34} \exp(507/T)$	1
2	$O + O + M \rightarrow O_2 + M$	$3 \times 10^{-33} (300/T)^3$	2
3	$O + O_3 \rightarrow 2O_2$	$2 \times 10^{-11} \exp(-2410/T)$	3
4	$O(^1D) + O_3 \rightarrow 2O_2$	2.5×10^{-10}	4
5	$O(^1D) + H_2O \rightarrow 2OH$	3×10^{-10}	Footnote a
6	$O(^1D) + M \rightarrow O + M$	8×10^{-11}	5
7	$O + OH \rightarrow H + O_2$	3.8×10^{-11}	6
8	$O_3 + H \rightarrow OH + O_2$	$1.5 \times 10^{-12} T^{1/2}$	7
9	$O + HO_2 \rightarrow OH + O_2$	1×10^{-11}	8
10	$O_2 + OH \rightarrow HO_2 + O$	$3.8 \times 10^{-12} \exp(-1250/T)$	9
11	$H + O_2 + M \rightarrow HO_2 + M$	$1.9 \times 10^{-32} \exp(236/T)$	10
12	$NO + O_3 \rightarrow NO_2 + O_2$	$9 \times 10^{-13} \exp(-1200/T)$	Footnote a
13	$O + NO_2 \rightarrow NO + O_2$	9.1×10^{-12}	11
14	$NO + O + M \rightarrow NO_2 + M$	$1 \times 10^{-32} \exp(930/T)$	12
15	$OH + OH \rightarrow H_2O + O$	$1 \times 10^{-11} \exp(550/T)$	6
16	$OH + HO_2 \rightarrow H_2O + O_2$	2×10^{-10}	13
17	$H + HO_2 \rightarrow OH + OH$	$2.8 \times 10^{-10} \exp(-1000/T)$	14
18	$H + HO_2 \rightarrow H_2 + O_2$	$3.2 \times 10^{-11} \exp(-500/T)$	15
19	$H + HO_2 \rightarrow H_2O + O$	$1.6 \times 10^{-11} \exp(-500/T)$	15
20	$HO_2 + HO_2 \rightarrow H_2O_2 + O_2$	$1.7 \times 10^{-11} \exp(-500/T)$	Footnote a
21	$H_2O_2 + OH \rightarrow H_2O + HO_2$	$1.7 \times 10^{-11} \exp(-910/T)$	6
22	$H_2O_2 + O \rightarrow H_2O + O_2$	$1.5 \times 10^{-13} \exp(-2000/T)$	16
23	$H_2O_2 + O \rightarrow OH + HO_2$	$1 \times 10^{-13} \exp(-2000/T)$	16
24	$O(^1D) + H_2 \rightarrow OH + H$	1.9×10^{-10}	17
25	$O(^1D) + H_2O_2 \rightarrow H_2O + O_2$	1×10^{-10}	Footnote b
26	$O_3 + HO_2 \rightarrow OH + 2O_2$	$2.7 \times 10^{-11} \exp(-1750/T)$	Footnote c
27	$OH + OH + M \rightarrow H_2O_2 + M$	3×10^{-30}	18
28	$N_2O + O(^1D) \rightarrow NO + NO$	1.0×10^{-10}	17
29	$N_2O + O(^1D) \rightarrow N_2 + O_2$	8.0×10^{-11}	17,19
30	$N + O_3 \rightarrow NO + O_2$	$3.4 \times 10^{-11} \exp(-1200/T)$	Footnote d
31	$N + NO \rightarrow O + N_2$	$2.6 \times 10^{-11} \exp(-167/T)$	12
32	$N + O_2 \rightarrow NO + O$	$5 \times 10^{-13} T^{1/2} \exp(-3650/T)$	20
33	$N + NO_2 \rightarrow N_2O + O$	8×10^{-12}	21
34	$N + NO_2 \rightarrow 2NO$	6×10^{-12}	21
35	$N + NO_2 \rightarrow N_2 + O_2$	4×10^{-12}	21
36	$NO_2 + O_3 \rightarrow NO_3 + O_2$	$1 \times 10^{-11} \exp(-3500/T)$	Footnote a
37	$NO_2 + O + M \rightarrow NO_3 + M$	$1.4 \times 10^{-23}/(1.3 \times 10^{-12}\ [M] + 5 \times 10^7)$	Footnote e
38	$NO + NO_3 \rightarrow NO_2 + NO_2$	5.7×10^{-12} (300K)	22

APPENDIX 2 (Continued)

Number	Process	Rate Coefficient	Reference
39	$NO_2 + NO_3 + M \rightarrow N_2O_5 + M$	$1 \times 10^{-22}/(1.7 \times 10^{-10}\,[M] + 2 \times 10^{8})$	Footnote f
40	$N_2O_5 + M \rightarrow NO_2 + NO_3 + M$	$8.3 \times 10^{-8} \exp(-8300/T)$	23
41	$NO + HO_2 \rightarrow NO_2 + OH$	$1.7 \times 10^{-11} \exp(-1200/T)$	24
42	$NO_2 + H \rightarrow NO + OH$	$9.6 \times 10^{-10} \exp(-900/T)$	Footnote a
43	$NO_2 + OH + M \rightarrow HNO_3 + M$	$2.8 \times 10^{-22}/(4 \times 10^{-11}\,[M] + 4.8T^{3})$	Footnote g
44	$HNO_3 + O \rightarrow OH + NO_3$	1×10^{-14}	Footnote a
45	$HNO_3 + OH \rightarrow H_2O + NO_3$	$1.6 \times 10^{-12} \exp(-1000/T)$	Footnote a
46	$NO + OH + M \rightarrow HNO_2 + M$	$1.8 \times 10^{-32} \exp(-1135/T)$	25
47	$HNO_2 + O \rightarrow OH + NO_2$	1×10^{-14}	Footnote h
48	$HNO_2 + OH \rightarrow H_2O + NO_2$	$1.4 \times 10^{-12} \exp(-1000/T)$	Footnote a
49	$OH + H \rightarrow O + H_2$	$1.0 \times 10^{-11} \exp(-3700/T)$	26
50	$NO_3 + O \rightarrow NO_2 + O_2$	$1 \times 10^{-12} \exp(-1500/T)$	Footnote i
51	$OH + O + M \rightarrow HO_2 + M$	1×10^{-31}	27
52	$H + H + M \rightarrow H_2 + M$	8.3×10^{-33}	6
53	$N + OH \rightarrow NO + H$	5.8×10^{-11}	18
54	$NO + HO_2 + M \rightarrow HNO_3 + M$	1×10^{-33}	Footnote i
55	$O(^1D) + N_2 + M \rightarrow N_2O + M$	1×10^{-38}	Footnote j

[a] The value adopted here was suggested by the recent reviews of available rate-constant data published by the National Bureau of Standards, R.F. Hampson, ed., National Bureau of Standards Repts. NBS-10692 and NBS-10828, 1972.

[b] Order-of-magnitude estimate suggested by other $O(^1D)$ reactions.

[c] Expression is derived from an assumed 300K rate of 8×10^{-14} cm^3sec^{-1}, and an activation energy of 3.5 kcal/mole.

[d] Value of Phillips and Schiff (reference 21) at 300K and an activation energy of 2.4 kcal/mole.

[e] The equivalent pressure-dependent rate constant represents the following mechanism:

$NO_2 + O \rightarrow NO_3^*$	$K = 1.1 \times 10^{-11}$ cm^3sec^{-1}
$NO_3^* \rightarrow NO_2 + O$	$K = 5 \times 10^{7}$ sec^{-1}
$NO_3^* + M \rightarrow NO_3 + M$	$K = 1.3 \times 10^{-12}$ cm^3sec^{-1}

The rate data are taken from Klein and Herron (reference 29). NO_3^* is assumed to be in a steady state at all times. The low-pressure limit yields a rate constant 2.8×10^{-31} cm^6/sec^{-1}.

[f] The equivalent pressure-dependent rate constant represents the following mechanism:

$NO_2 + NO_3 \rightarrow N_2O_5^*$	$K = 6 \times 10^{-13}$ cm^3sec^{-1}, estimate
$N_2O_5^* \rightarrow NO_2 + NO_3$	$K = 2 \times 10^{8}$ sec^{-1} (Johnston, ref. 30)
$N_2O_5^* + M \rightarrow N_2O_5 + M$	$K = 1.7 \times 10^{-10}$ cm^3sec^{-1} (Johnston, ref. 30)

The low-pressure limit for this rate is then 5×10^{-31} cm^6sec^{-1}.

[g] The equivalent pressure-dependent rate constant is formed from data obtained from Crutzen (private communication) and Anderson and Kaufman (reference 9). The low-pressure value of 6×10^{-23} T^{-3} cm^6sec^{-1} agrees well with the recent measurement of Westenberg and deHaas (reference 25).

[h] Assumed to be the same as the rate of $HNO_3 + O$.

[i] Adopted rate constant.

[j] Simonaitis et al. (reference 31) show that $k < 7 \times 10^{-36}$ cm^6sec^{-1}; this reaction is of marginal importance (reference 31).

REFERENCES FOR APPENDIX 2

1. Huie, R.E., J.T. Herron, and D.D. Davis, *J. Phys. Chem.*, **76**, 2653-2658 (1972).

2. Campbell, I.M. and B.A. Thrush, *Proc. Roy. Soc. A*, **296**, 222-232 (1967).

3. Johnston, H.S., "Gas Phase Reaction Kinetics of Neutral Oxygen Species," Nat. Standard Ref. Data Series NBS-20, U.S. Government Printing Office (1968).

4. Gilpin, R., H.I. Schiff, and K.H. Welge, *J. Chem. Phys.*, **55**, 1087-1093 (1971).

5. Noxon, J.F., *J. Chem. Phys.*, **52**, 1852-1873 (1970).

6. Baulch, D.L., D.D. Drysdale, D.G. Horne, and A.C. Lloyd, *Evaluated Kinetic Data for High Temperature Reactions*, Vol. 1, CRC Press, Cleveland (1972).

7. Nicolet, M., *Planet. Space Sci.*, **20**, 1671-1702 (1972).

8. Kaufman, F., "Neutral Reactions," *DASA Reaction Rate Handbook*, ed. M.H. Bortner, DASA 1948, General Electric Co., Santa Barbara, Calif. (1967).

9. Anderson, J.G. and F. Kaufman, Chem. Phys. Lett. **16**, 375 (1972).

10. Kurylo, M.J., *J. Phys. Chem.*, **76**, 3518-3526 (1972).

11. Davis, D.D., J.T. Herron, and R.E. Huie, *J. Chem. Phys.*, **58**, 530-535 (1973).

12. Baulch, D.L., D.D. Drysdale, and D.G. Horne, "Critical Evaluation of Rate Data for Homogeneous Gas Phase Reactions of Interest in High Temperature Systems," *High Temperature Reaction Rate Data*, Rept. 5, Univ. of Leeds (1970).

13. Hochanadel, C.J., J.A. Ghormley, and P.J. Ogren, *J. Chem. Phys.*, **56**, 4426-4432 (1972).

14. Kondratiev, V.N., *Rate Constants of Gas Phase Reactions, Reference Book*, Izdatel'stvo "Nauka," Moscow, 1970, ed. R.M. Fristrom (transl. from the Russian), National Tech. Info. Service COM-72-10014 (1972).

15. Lloyd, A.C., "Evaluated and Estimated Kinetic Data for the Gas Phase Reactions of Hydroperoxyl Radicals," National Bureau of Standards Rept. 10447 (1970).

16. Nicolet, M., "Aeronomic reactions of hydrogen and ozone," in *Mesospheric Models and Related Experiments*, ed. G. Fiocco, D. Reidel Publ. Co., Dordrecht (1971).

17. Young, R.A., G. Black, and T.G. Slanger, *J. Chem. Phys.*, **49**, 4758-4776 (1968).

18. Wilson, W.E., *J. Phys. Chem. Ref. Data*, **1**, 535-573 (1972).

19. Simonaitis, R., R.I. Greenberg, and J. Heicklen, *Int. J. Chem. Kin.*, **4**, 497-512 (1972).

20. Wilson, W.E., *J. Chem. Phys.*, **46**, 2017-2018 (1967).

21. Phillips, L.F. and H.I. Schiff, *J. Chem. Phys.*, **42**, 3171-3174 (1965).

22. Ford, H.W. and S. Jaffe, *J. Chem. Phys.*, **38**, 2935-2942 (1963).

23. Bahn, G.S., *Pyrodynamics*, **1**, 147, 271, 335 (1964); **2**, 91, 197, 315 (1965); **3**, 245 (1965); **6**, 110 (1968).

24. Davis, D.D., W.W. Wong, S.D. Fischer, R.L. Schiff, J.O. Lephardt, J.E. Prusaczyk, W.A. Payne, L.J. Stief, R.E. Huie, and J.T. Herron (1973), "Recent kinetic measurements on the reactions of $O(^3P)$, H, and HO_2," in *Proceedings of the Second Conference on the Climatic Impact Assessment Program* (Nov. 14-17, 1972), ed. A.J. Broderick, U.S. Dept. of Transportation DOT-TSC-OST-73-4.

25. Westenberg, A.A. and N. deHaas, *J. Chem. Phys.*, **57**, 5375-5378 (1972).

26. Bascombe, K.N., "Reaction Rate Data: The Hydrogen/Oxygen System," Ministry of Aviation, E.R.D.E. Rept. 1/5/65, Waltham Abbey, U. K. (1965).

27. Peterson, H.L. and C.B. Kretschmer, "Kinetics of Recombination of Atomic Oxygen at Room Temperatures," U.S. Dept. of Commerce Rept. OTS (1960).

28. Phillips, L.F. and H.I. Schiff, *J. Chem. Phys.*, **36**, 1509-1517 (1962).

29. Klein, F.S. and J.T. Herron, *J. Chem. Phys.*, **41**, 1285-1290 (1964); erratum, ibid **44**, 3645-3646 (1965).

30. Johnston, H.S., *J. Am. Chem. Soc.*, **73**, 4542-4546 (1951).

31. Simonaitis, R., E. Lissi, and J. Heicklen, *J. Geophys. Res.*, 77, 4248-4250 (1972).

APPENDIX 3

Lower Boundary Conditions for O-H-N Compounds

Constituent	Dominant Boundary Condition	Flux Value or Equivalent[b]
$O(^3P)$	CE[a]	0
$O(^1D)$	CE	0
O_3	Flux	$[O_3]_{10} = 3 \times 10^{11}$ cm^{-3} Footnote c
NO	Footnote d	Footnote e
NO_2	Footnote d	Footnote e
OH	Footnote d	$\Phi = -1 \times 10^5$ cm^{-2}sec^{-1}
H_2O	Flux	$[H_2O]_{10} = 3 \times 10^{13}$ cm^{-3} Footnote c
H	CE	0
HO_2	Footnote d	$\Phi = -1 \times 10^5$ cm^{-2}sec^{-1}
H_2O_2	Footnote d	$\Phi = -4 \times 10^5$ cm^{-2}sec^{-1}
NO_3	CE	0
N_2O_5	CE	0
N_2O	Flux	$[N_2O]_{10} = 1.8 \times 10^{12}$ cm^{-3} Footnote c
N	CE	0
HNO_3	Flux	Footnote e
HNO_2	Footnote d	Footnote e
H_2	Flux	$[H_2]_{10} = 4 \times 10^{12}$ cm^{-3} Footnote c

[a] CE = chemical equilibrium.

[b] A positive value refers to an upward flux, a negative value to a downward flux.

[c] For certain long-lived species such as H_2O, O_3, and N_2O, which are flux-controlled, the lower fluxes at 10 km were taken to be proportional to the difference between the computed density at the lower boundary and the density indicated in the table above, which is typical of measured values.

[d] These species are very close to chemical equilibrium at the lower boundary. The material flowing through the lower boundary rapidly approaches chemical equilibrium in the stratosphere.

[e] The total mixing ratio of odd nitrogen at the lower boundary is assumed to be near 5×10^{-10} by number. Upward or downward fluxes of the species NO, NO_2, HNO_2, and HNO_3 are used to achieve this boundary condition in the manner described in footnote c, where the total odd-N flux is divided among the species according to their densities.

ATMOSPHERIC PHOTOCHEMISTRY OF N-, H-, AND Cl-CONTAINING RADICALS

STEVEN C. WOFSY
Center for Earth and Planetary Physics
Harvard University
Cambridge, Massachusetts

ABSTRACT: Sources of atmospheric odd nitrogen and hydrogen are reviewed and their role in ozone photochemistry is discussed. A model, containing few adjustable parameters, gives good agreement with observed distributions of stratospheric and mesospheric ozone. Nitric oxide emitted by aircraft flying in the stratosphere would lead to a significant reduction in the concentration of atmospheric ozone if the globally averaged source of NO exceeded 2×10^7 molecules cm^{-2} sec^{-1}. A traffic model projected by Broderick et al. (1973) for 1990 could lead to a reduction of about 2% in the column density of O_3.

Sources of atmospheric chlorine are discussed. It is argued that HCl should be the dominant form of atmospheric chlorine, and that it is produced mainly from aerosols of marine origin. The atmospheric source strength is about 2×10^8 tons per year, according to Chesselet et al. (1972). The role of chlorine compounds as a catalyst for recombination of odd oxygen is discussed and shown to be unimportant in the normal atmosphere.

An appendix is provided which discusses the importance of odd-oxygen production below 28 km, where chemical time constants are long. Chemistry below 28 km does not strongly influence NO_x-ozone interaction models, but may affect model results for ClO_x-ozone interaction.

INTRODUCTION

This paper discusses simple one-dimensional-model studies which relate to the possible perturbation of the stratosphere by future fleets of high-flying aircraft. Details of the model, including the chemical reaction scheme, have been presented by McElroy et al. (1974). Also briefly described are chemical processes as they affect the distribution of chlorine compounds in the atmosphere. The work on chlorine was motivated by concern over possible modification of the stratosphere by the space shuttle. The shuttle, now under development and scheduled for operation in the 1980's, will emit HCl as an exhaust product. A systematic study of its consequences is now in progress under the auspices of the National Aeronautics and Space Administration. This paper attempts to define the problem and focus on some of the major uncertainties and targets for future research; it follows in part the discussions of Wofsy and McElroy (1974). The chlorine problem has also been treated by Stolarski and Cicerone (1974) and by Crutzen (1974).

OZONE IN THE NORMAL STRATOSPHERE

Odd-oxygen atoms are produced in the atmosphere mainly by dissociation of O_2 in the Herzberg continuum:

$$h\nu + O_2 \rightarrow O + O \qquad (1)$$

They are removed in the stratosphere by the simple reaction

$$O + O_3 \rightarrow O_2 + O_2 \qquad (2)$$

first discussed by Chapman (1930), and by more complex reaction schemes terminating in

$$O + HO_2 \rightarrow OH + O_2 \qquad (3)$$

$$O + OH \rightarrow O_2 + H \qquad (4)$$

and

$$O + NO_2 \rightarrow NO + O_2. \qquad (5)$$

Reactions (3), (4), and (5) may be viewed as rate-determining steps in homogeneous catalytic cycles which greatly enhance the overall rate of reaction (2). The importance of HO_x in the context of the ozone problem was first recognized by Bates and Nicolet (1950). The importance of NO_x was first identified by Crutzen (1970). For present purposes, we define HO_x as $H + OH + HO_2$, and NO_x as $N + NO + NO_2 + NO_3 + 2\,N_2O_5 + HNO_2 + HNO_3$.

The major source of stratospheric HO_x is the reaction

$$O(^1D) + H_2O \rightarrow OH + OH \qquad (6)$$

with a small contribution from

$$O(^1D) + H_2 \rightarrow OH + H \qquad (7)$$

and a similar reaction with methane. NO_x is formed by oxidation of N_2O, and by dissociation of N_2 following absorption of cosmic rays.

The primary oxidation process for N_2O is

$$O(^1D) + N_2O \rightarrow NO + NO \qquad (8)$$

and this source of stratospheric NO_x has been relatively well characterized in the recent literature (Bates and Hays, 1967; McElroy and McConnell, 1971; Nicolet, 1971). Possible contribution from NH_3 oxidation remains somewhat uncertain. Measurements by Kaplan (1973) seem to indicate very low NH_3 concentration ($< .1$ ppb) above the planetary boundary layer. If such low values apply to the stratosphere, NH_3 will not play an important role in the stratospheric NO_x budget (cf. McConnell and McElroy (1973)).

Absorption of cosmic rays initiates a complex chemistry (Warneck, 1972) in which NO_x is formed by reactions such as

$$N_2^+ + e \rightarrow N + N \qquad (9)$$

$$NO^+ + e \rightarrow N + O \qquad (10)$$

$$N_2 + e \rightarrow N + N + e \qquad (11)$$

The product atoms may be released in excited states, and it is especially important to define the relative quantum yields of $N(^4S)$ and $N(^2D)$. Excess production of the former can lead to net destruction of NO_x, by reactions such as

$$N(^4S) + NO \rightarrow N_2 + O \qquad (12)$$

$$N(^4S) + NO_2 \rightarrow N_2O + O \qquad (13)$$

$$N(^4S) + NO_2 \rightarrow N_2 + O_2 \qquad (14)$$

$$N(^4S) + NO_2 \rightarrow N_2 + O + O. \qquad (15)$$

The metastable $N(^2D)$ is efficiently removed in the stratosphere, producing NO, by the reaction

$$N(^2D) + O_2 \rightarrow NO + O. \qquad (16)$$

Reaction (16) is the major source of NO in the atmosphere above 100 km. Reaction (12) is the dominant sink for mesospheric and thermospheric odd nitrogen.

The potential importance of the cosmic-ray-related source of stratospheric NO_x is emphasized in a recent paper by Ruderman and Chamberlain (1973). They point out that the cosmic-ray flux reaching the atmosphere is largest at times of low solar activity and that its effects are confined mostly to high geomagnetic latitudes. NO_x produced at high latitudes must be transported to low latitudes before it can have any significant effect on O_3. Subsequent modification of O_3 should be phase-shifted with respect to the cosmic-ray source, and Ruderman and Chamberlain (1973) make some preliminary estimates of the magnitude of this phase shift. Their estimates are in satisfactory agreement with phase shifts observed by Angell and Korshover (1973) in an analysis of ozone data taken at Tromsö and Arosa (see also Johnston (1973)). The importance of Ruderman and Chamberlain's contribution is twofold. First, it provides a reasonable mechanism to account for the much-discussed correlation of O_3 with the solar cycle, a correlation not heretofore widely accepted by the meteorological community. Second, the work implies that absorption of cosmic rays in the stratosphere may indeed lead to significant production of NO_x, which should be included in detailed attempts to model stratospheric chemistry and dynamics. A major uncertainty concerns the estimate for the rate of NO_x production by cosmic rays, for which experimental data are lacking.

Figures 1 and 2 give estimates for the concentrations of major forms of NO_x and HO_x. The results shown are intended to represent mean (24-hour average) conditions at a latitude of 30°N, for a solar declination of +12°. Vertical motion was treated by means of the expedient concept of eddy diffusion, with diffusivities chosen to reproduce observed concentrations of CH_4 and N_2O (Wofsy and McElroy, 1973), subject to the modification proposed by Cunnold et al. (1974) (i.e., increasing the vertical eddy-diffusion coefficient to 4×10^3 near the tropopause (16 km)). Residence times for stratospheric NO_x calculated by our model agree very well with those calculated by Fabian and Libby (1974). Reaction (8) is the only NO_x source considered, and transport to the troposphere is the only sink.

Considering the sparseness of the data and the crude transport simulation used in the model, agreement is quite satisfactory. In particular we note that the recent NO and NO_2 observations are adequately represented. Recent measurements of NO near 20 km evidently do not imply a strong sink for NO_x in the stratosphere. The NO density at 20 km is, however, extremely sensitive to the details of the transport model and the HNO_3-NO_2-NO interconversion mechanism (McElroy et al., 1974).

In the context of O_3 photochemistry, we are particularly concerned with concentrations of NO and NO_2 for the height range 30-50 km, and with concentrations of H and OH above 50 km. The concentration of O_3 below 30 km is controlled mainly by dynamics. Reaction (5) is the major loss process for odd oxygen below 45 km. The Chapman reaction (2) is important between 45 km and 55 km, and reactions (3) and (4) dominate above 55 km.

The concentration of NO_x in the important height range 30-50 km is determined by the balance between input associated with oxidation of N_2O (reaction (8)) and removal by vertical transport. Analyses of the various uncertainties are given by McConnell and McElroy (1973) and by McElroy et al. (1974). They concluded that the concentration of NO_x should be relatively well determined for this height range, although major uncertainties may arise at lower elevations.

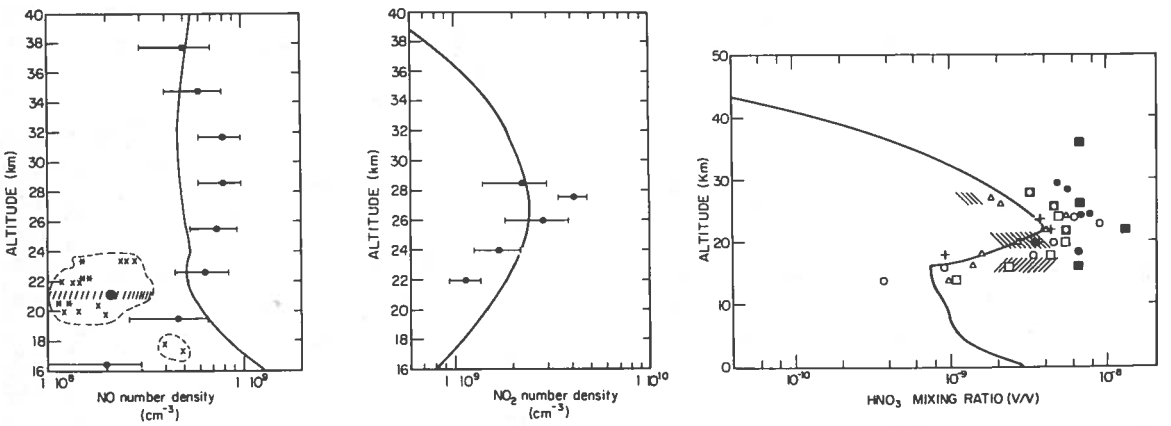

Figure 1. Calculated vertical distributions of individual NO_x constituents in the normal atmosphere, 30°N latitude, solar declination + 12°, compared with observations:

(a) nitric oxide
- ⊢●⊣ Ackerman et al. (1973)
- XXX Ridley et al. (1974) ascent
- *** Ridley et al. (1974) descent
- ///●/// Loewenstein et al. (1974)

(b) nitrogen dioxide
- ⊢●⊣ Ackerman & Muller (1972)

(c) nitric acid
For identification of points, see Figure 8 of McConnell and McElroy (1973).

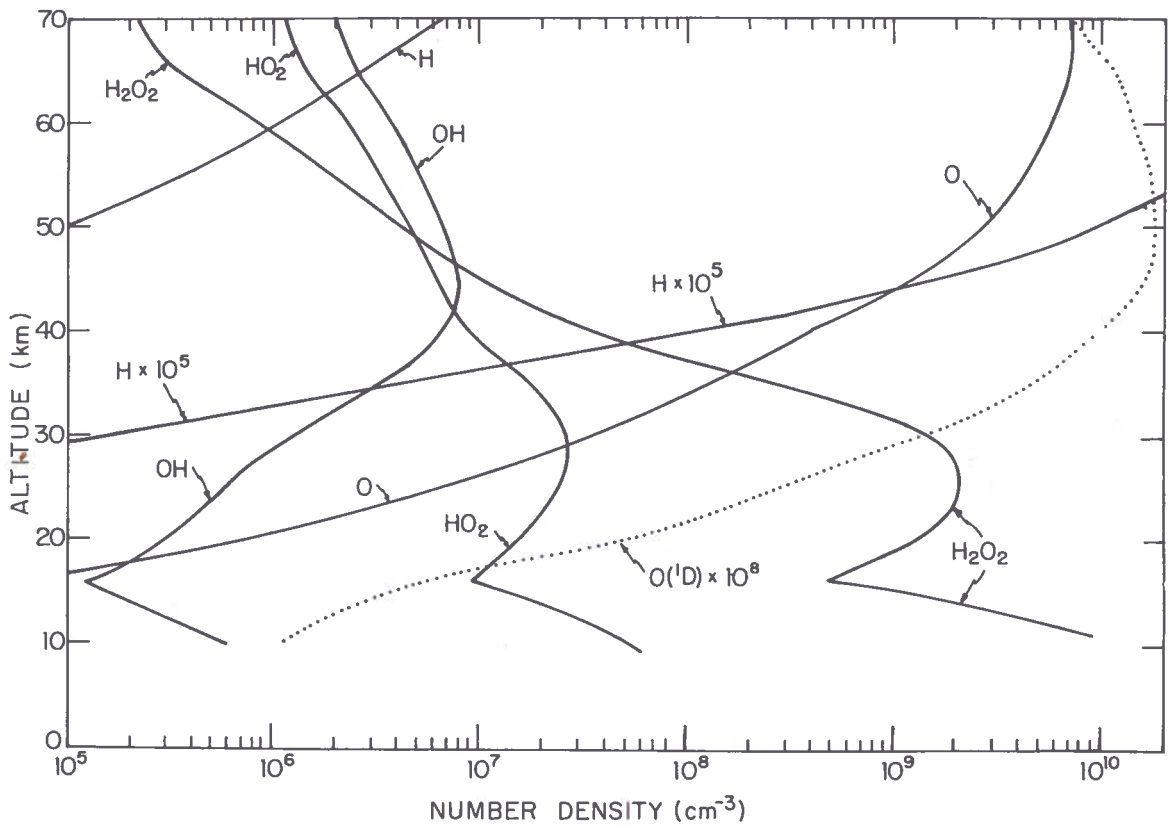

Figure 2. Calculated number densities (24-hour average) for hydrogenous radicals, H_2O_2, $O(^3P)$, and $O(^1D)$ for the normal atmosphere, 30°N latitude, solar declination +12°. The tropopause is at 16 km. From McElroy et al. (1974).

The concentrations of NO_x and HO_x given in Figures 1 and 2 were used to compute concentrations of O_3. The calculation is relatively straightforward for the atmosphere above 30 km, where photochemical processes are dominant for the odd oxygen. The results are shown in Figure 3, which includes also a comparison with observational data obtained by Johnson et al. (1952), Hering and Borden (1967), Hilsenrath et al. (1969), and Krueger et al. (1973). Theory agrees with experiment within permissible experimental error limits. The agreement is taken as a measure of the overall validity of the techniques employed to calculate NO_x and HO_x, and lends support to the general reliability of the theoretical model.

MODIFICATION OF OZONE BY SUPERSONIC AIRCRAFT

We model possible effects of NO_x introduced into the stratosphere by aircraft at cruise altitudes of 17, 20, and 25 km. The lowest altitude is appropriate for the Concorde. The intermediate value is adopted for an advanced version of the American supersonic transport (SST), and the highest value could apply for a conceptual future hypersonic transport (HST). We model the vertical distribution of NO_x input for a given aircraft with a triangular shape function centered on the appropriate altitude. The triangular function is taken to give a vertical extent of 2 km at the half-intensity point for Concorde and HST. A somewhat broader width of 4 km is adopted for the SST.

Emission rates of NO_x are of course largely unknown for the SST and HST. We adopt data given by Broderick et al. (1973) for the Concorde. From their emission rates we estimate that the Concorde, carrying 100 passengers at a cruise speed of 2.1×10^3 km hr^{-1} for approximately 7 hours per day, would emit a globally averaged quantity of NO_x equivalent to 7.74×10^4

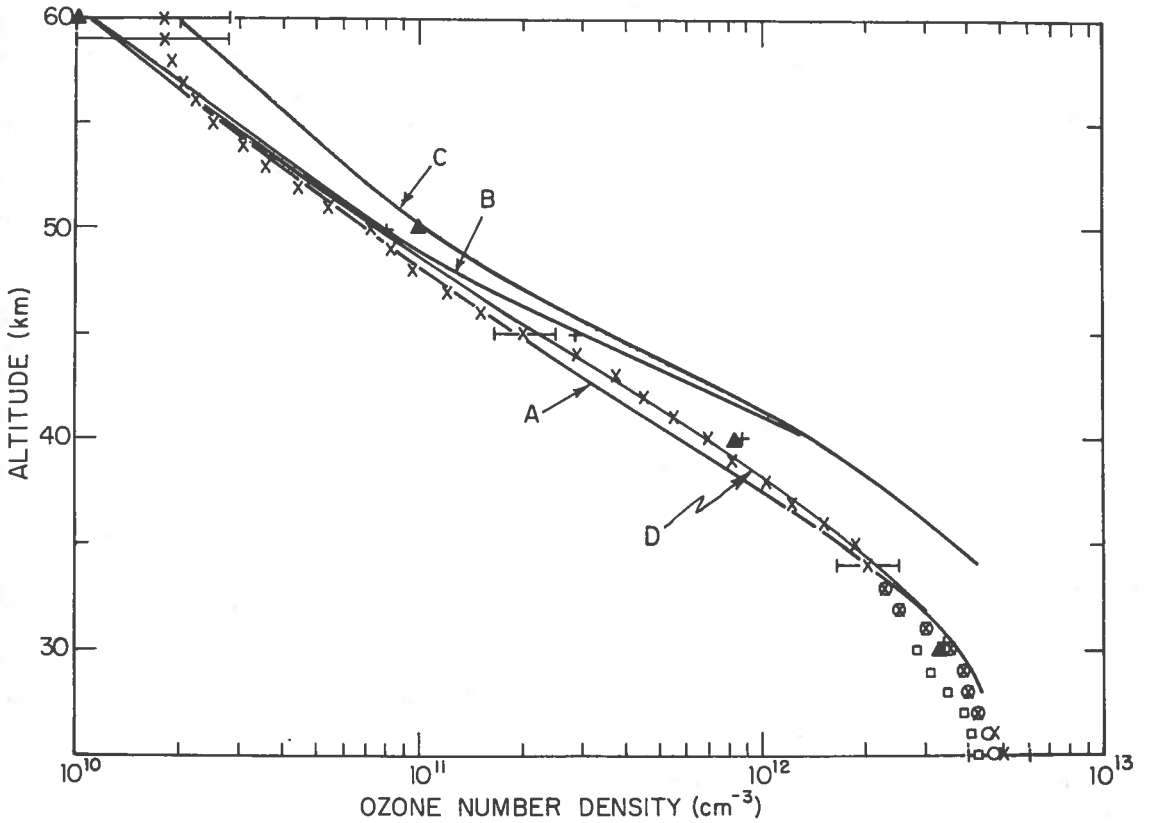

Figure 3. Calculated ozone profiles are shown for the normal atmosphere, 30°N latitude, +12° solar declination. Curve A was calculated with the complete chemical model and computed NO_x profiles; reactions involving NO_x were omitted in curve B; reactions involving NO_x and HO_x were omitted in curve C. Curve D was the same model as A, but with a slower value for the reaction rate of NO with O_3 (cf. McElroy et al. (1974)). Observations shown are as follows: Hilsenrath et al. (1969), × (with error bars), chemiluminescent rocketsonde, and ○, Mast-Brewer electrochemical balloonsonde, at Wallops Is. (38°N), Sept. 16, 1968; ▲, Johnson et al. (1952), as corrected by Evans et al. (1968), rocketsonde solar UV absorption from White Sands (32°N), June 14, 1949; +, Krueger et al. (1973), rocketsonde solar UV absorption from Pt. Mugu, California (34°N), June 18, 1970; □, Hering and Borden, Mast-Brewer balloonsondes from Tallahassee, Florida (30.4°N), 1966 summer average. Figure taken from McElroy et al. (1974).

molecules cm^{-2} sec^{-1}. Similarly, the corresponding NO_x emission rate for SST would be 5.73×10^5 molecules cm^{-2} sec^{-1}, with an assumption that the advanced SST would carry 600 passengers at a cruise speed of 3.2×10^3 km hr^{-1}, for 7 hours a day.

Figure 4 gives a summary of the various computations for O_3 in the perturbed atmosphere. In these computations we attempt to include all of the possible feedback mechanisms which occur in the perturbed atmosphere. For example, a perturbation of ozone leads to a change in the transmission of the atmosphere at ultraviolet wavelengths, with a resulting alteration in the source of odd oxygen. A change in atmospheric transmission also affects the natural source of NO_x associated with reaction (8). Reduction in the concentration of O_3 leads to a decrease in computed values for stratospheric temperature, with consequent effect on the rates of various chemical reactions. These feedback mechanisms were properly included in all computations for the perturbed environment. The consequence of thermal adjustment is shown explicitly in the figure.

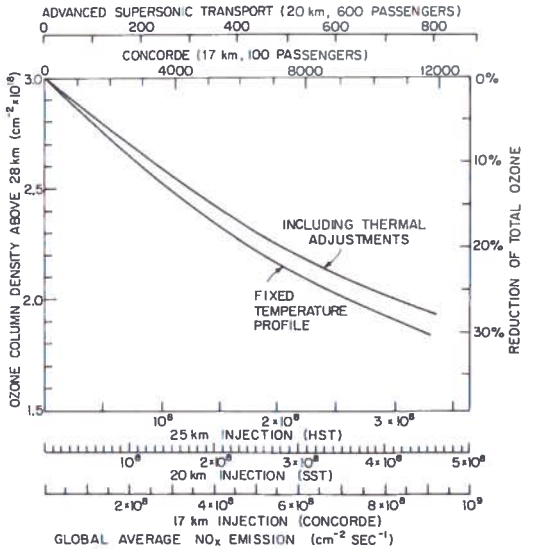

Figure 4. Perturbations in ozone by artificial injections of NO_x. A detailed discussion of the various scales is given in the text. Figure taken from McElroy et al. (1974).

The left vertical axis in Figure 4 gives the column density computed for O_3 in the atmosphere above 28 km, at a latitude of 30°N, for a solar declination of 12°. Results are shown for a variety of NO_x inputs, given by the separate scales for the bottom horizontal axis. We note that the perturbation in ozone expected for a given input of NO_x is a moderately sensitive function of the height at which injection occurs. For example, an input of NO_x equivalent to 2×10^8 molecules cm^{-2} sec^{-1} at 25 km leads to a reduction by approximately 25% in the computed column density of O_3 above 28 km. The inputs required at 20 km and 17 km to provide a similar reduction in O_3 are 2.75×10^8 cm^{-2} sec^{-1} and 5.5×10^8 cm^{-2} sec^{-1} respectively. A fleet of 775 Concordes flying for 7 hours a day at 17 km would reduce O_3 above 28 km by 3%. A traffic model projected by Broderick et al. (1973) for 1990 would provide a corresponding reduction of 2.4% for O_3 above 28 km.*

* The projected 1990 fleet would support an annual traffic volume of 5.9×10^{12} passenger-km if aircraft were assumed to fly at all times with a full complement of passengers. This figure may be compared with the present traffic of 4.4×10^{11} passenger-km per year. It is assumed that the bulk of air traffic in 1990 will be carried by current or improved versions of existing aircraft such as the B747 and DC10. The estimated NO_x emission rate adopted here for the 1990 fleet is 4.3×10^7 molecules cm^{-2} sec^{-1}, distributed over the height range 16 to 21 km.

The right vertical axis in Figure 4 shows an attempt to define the approximate change in total O_3 column due to aircraft operations. For our present purposes we assume that the atmosphere consists of two distinct regions. In one zone, chemical time constants for O_3 are short compared with time constants for transport, and the concentration of O_3 should be accurately modeled by a photochemical-equilibrium theory. In the second zone, dynamical time constants are short compared with chemical values, and the distribution of O_3 is set by the details of the atmospheric motion field. The boundary between these two zones describes a surface whose height should be an increasing function of increasing latitude. Ozone is released into the dynamical zone primarily at lower latitudes near 30 km. The low-latitude source region is clearly visible in Figure 5, which shows calculated contours of the ozone mixing ratio in a meridional plane. Figure 5 is in good agreement with the BUV satellite observations of Krueger et al. (1973).

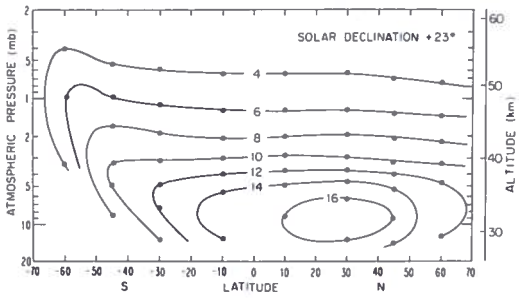

Figure 5. The calculated meridional distribution of the ozone mixing ratio (gm/gm × 10^{-6}) is shown as a function of latitude and altitude (mbar). Photochemical equilibrium has been assumed. The mixing-ratio gradients are perpendicular to the indicated contours. The gradients establish a low-latitude ozone source region near 30 km.

A reduction of O_3 at the boundary between the chemical and dynamical zones would lead to a reduction in O_3 at all locations within the dynamical zone. The reduction factor will be approximately equal to the reduction which applies in the low-latitude region of the boundary surface. Somewhat arbitrarily, we identify the boundary surface with the level at which the chemical time constant for O_3 is 15 days at 30°N latitude. Concentrations of O_3

long the boundary can then be derived with the photochemical model, and concentrations below the boundary may be reduced proportionately. The reduction factors indicated on the right-hand vertical scale of Figure 4 reflect this procedure. We believe that the procedures followed here are unlikely to lead to major error. In particular, our conclusions are relatively insensitive to the precise criterion used to define the boundary between the chemical and dynamical zones, which is discussed in detail in Appendix A.* The results shown in Figure 4 are unchanged if we include ozone in the diffusive flow calculation, rather than "scaling" it with the boundary value; these calculations will be the subject of a later publication.

ORIGIN OF ATMOSPHERIC CHLORINE

There is little doubt that the atmosphere, at least in marine environments, contains significant quantities of gaseous chlorine (here defined as all gases that contain Cl). Atmospheric chlorine was first identified by Junge (1957) and was subsequently observed by Duce et al. (1969), Buat-Menard and Chesselet (1971), and Chesselet et al. (1972). In all cases, combinations of molecular sieves and filters were used to eliminate particles with radii greater than 0.1 μm. In addition, Junge measured the concentration of Aitken nuclei and showed that at most 2% of the transmitted chlorine could be present in these particles. The mixing ratio (v/v) of total gaseous chlorine, at least for the marine atmosphere near ground level, is apparently in the range 1 to 6×10^{-9}. Junge (1957) measured gaseous chlorine compounds just above the trade-wind inversion at Hawaii and found concentrations which were approximately a factor of 2 less than values measured near the surface. Chesselet et al. (1972) observed a decrease in the concentration of gaseous chlorine carried by an air mass of marine origin as the air mass passed over land in rural France.

Wofsy and McElroy (1974) and Wofsy (1974) discussed the probability that HCl is the major form of gaseous chlorine. However, if steady-state conditions do not apply, more active forms may be important. Such a situation is conceivable for the marine environment.

No intrinsic natural sources of gaseous chlorine have been established for the stratosphere, and it has not been observed there (Farmer, 1974). Stolarski and Cicerone (1974) proposed that volcanic eruptions might inject gaseous chlorine in substantial quantity, but this suggestion is not presently supported by any experimental data. Molina and Rowland (1974) have proposed that anthropogenic chlorofluorocarbons may yield a sizable flux of Cl-atoms into the stratosphere.

Substantial sources and sinks for gaseous chlorine must exist in the troposphere. Buat-Menard and Chesselet (1971) showed that marine gaseous chlorine is probably volatilized from sea-salt aerosols. Their data indicated gas and particle covariance with wind speed, and similar covariance of the aerosol Cl/Na ratio. The results of laboratory experiments supported their analysis. They concluded that at least 3% of the particulate chlorine is converted to gas, and predicted that HCl should be the principal product. The only sink definitely identified for HCl is removal by rain (see Duce (1969)).

Table 1 collects the data we need for calculating by two methods the mean residence time, τ, for gaseous chlorine in the troposphere. First, we assume that the mean global mole fraction (f) for gaseous chlorine is known, and adopt the source-strength (s) estimates of Duce (1969) or Chesselet et al. (1971). We find

$$\tau_1 = \frac{fNH_1}{s} = 1.5 \text{ to } 9 \text{ days}, \qquad (17)$$

where N is the total atmospheric number density and H_1 is the chlorine scale height. This result may be compared to the 2- to 6-day lifetime determined by several independent methods for small hygroscopic particles, which are removed mainly by rain (Junge, 1963, 1973). The value derived for τ_1 is evidently consistent with the idea that, at least over the oceans, HCl constitutes the bulk of gaseous chlorine and is removed principally by rain.

An independent estimate for the lifetime of gaseous chlorine may be obtained if one assumes that the latter's decrease with distance from the

* The analysis given here is not sufficiently precise to allow a quantitative estimate for O_3 reduction at any particular latitude, but should be useful as a global average.

Table 1. Data for Calculating Residence Times of Gaseous Chlorine

Physical Quantity	Magnitude	References
Global source strength (s)	$2 - 6 \times 10^8$ ton/year $= 2 - 6 \times 10^{10}$ cm^{-2} sec^{-1}	Chesselet et al. (1971) Duce (1969)
Mean mixing ratio (marine) (f)	$2 - 3$ γ/m^3 $= 1 - 2 \times 10^{-9}$ (v/v)	Chesselet et al. (1971) Junge (1957)
Scale height (H_1)	3×10^5 cm	Junge (1957)
Atmospheric total number density (N)	2.5×10^{19} cm^{-3}	
Fall-off of f with distance x from seacoast	$f = f_o \exp(-\kappa x)$	Buat-Menard (1970)
κ	0.011 km^{-1}	Buat-Menard (1970)
Nominal wind velocity (v)	3 m/s	Buat-Menard (1970)

seacoast results entirely from removal via chemical reaction, as does Buat-Menard (1970). Thus the observed decay constant κ and the measured windspeed v imply

$$\tau_2 = \frac{\kappa}{v} = 0.4 \text{ days.} \tag{18}$$

τ_2 is evidently not consistent with τ_1, implying either that dilution must be responsible for the observed decrease or that gaseous chlorine must be removed by chemical reactions and aerosol formation which occur selectively in continental air.

The problem has recently been discussed by Wofsy (1974), who argued that HCl cannot be removed by aerosol formation unless either a neutralization reaction occurs or the humidity is greater than 90%. Rain is a very efficient sink for HCl, however (cf. Duce (1969)). The decrease of marine gaseous chlorine over land observed by Buat-Menard (1970) may be attributed to deeper atmospheric mixing over land, but a definite conclusion is scarcely justified in light of the present lack of data on the vertical distribution of gaseous chlorine.

INTERACTION OF ATMOSPHERIC CHLORINE COMPOUNDS WITH OZONE PHOTOCHEMISTRY

The early work of Norrish and Nevelle (1934) established that gaseous chlorine can photosensitize the recombination of O_3. Recent measurements of a variety of reactions provide many of the important rate constants (see, for example, Johnston et al. (1969)). Chlorine compounds are also known to react with other important minor constituents of the atmosphere, such as CH_4, H_2, NO, and possibly N_2O. Table 2 gives a summary of the various important reactions and rate constants. In order to investigate their possible effect on atmospheric O_3, we consider a situation in which the mixing ratio of total chlorine has the value 10^{-9}, at all altitudes. The consequent distribution of major chlorine compounds is shown in Figure 6.

The major components are HCl and ClO, at least with the particular reaction scheme adopted here. The important source reactions for HCl are

$$Cl + H_2 \rightarrow HCl + H \tag{19}$$

and

$$Cl + CH_4 \rightarrow HCl + CH_3. \tag{20}$$

The gas is removed by

$$OH + HCl \rightarrow H_2O + Cl. \tag{21}$$

Reaction of Cl with O_3 provides the dominant source of ClO:

$$Cl + O_3 \rightarrow ClO + O_2. \tag{22}$$

The major sinks are

$$ClO + NO \rightarrow Cl + NO_2 \tag{23}$$

$$ClO + O \rightarrow Cl + O_2 \tag{24}$$

Table 2. Chlorine Reactions[a]

Reaction	Rate Expression[b]	References and Remarks
$OH + HCl \rightarrow H_2O + Cl$	$2.1 \times 10^{-11} \exp(-1037/T)$[d]	Takacs and Glass (1973)
$Cl + H_2 \rightarrow HCl + H$	$2 \times 10^{-11} \exp(-2164/T)$	Galante and Gislason (1973)
$H + HCl \rightarrow H_2 + Cl$	$1 \times 10^{-11} \exp(1605/T)$	Westenberg and deHaas (1968) Benson et al. (1969)
$O + HCl \rightarrow OH + Cl$	$1.88 \times 10^{-11} \exp(-3573/T)$	Wong and Belles (1971) Balakhnin et al. (1971)
$Cl + O_3 \rightarrow ClO + O_2$	1.84×10^{-11}	Clyne and Watson (1973)[c]
$Cl + Cl + M \rightarrow Cl_2 + M$	$1.6 \times 10^{-33} \exp(800/T)$	Widman and DeGraff (1973) Hippler and Troe (1973)
$Cl + O_2 + M \rightarrow ClOO + M$	1.7×10^{-33}	Johnston et al. (1969) Nicholas and Norrish (1968)
$ClOO + M \rightarrow Cl + O_2 + M$	$1.3 \times 10^{-11} \exp(-1000/T)$	Johnston et al. (1969)
$ClO + ClO \rightarrow ClOO + Cl$	$1.3 \times 10^{-12} \exp(-1150/T)$	Johnston et al. (1969) Clyne and White (1971) Clyne and Coxon (1968)
$Cl + ClOO \rightarrow ClO + ClO$	1.44×10^{-12}	Johnston et al. (1969)
$Cl + ClOO \rightarrow Cl_2 + O_2$	1.5×10^{-10}	Johnston et al. (1969)
$ClO + NO \rightarrow Cl + NO_2$	1.7×10^{-11}	Clyne and Watson (1973)[c]
$ClO + h\nu \rightarrow Cl + O$	2.2×10^{-3}, 6.0×10^{-5}, 2.4×10^{-6}, 1.5×10^{-6}	Durie and Ramsay (1958) Pannetier and Gaydon (1948) Porter (1950) Johnston et al. (1969) Clyne and Coxon (1968)
$HCl + h\nu \rightarrow H + Cl$	2.0×10^{-7}, 1.9×10^{-8}, 0., 0.	Romand and Vodar (1948) Myer and Samson (1970)
$O + ClO \rightarrow Cl + O_2$	5.3×10^{-11}	Bemand, Clyne and Watson (1973)
$Cl_2 + h\nu \rightarrow Cl + Cl$	1.6×10^{-3}, 1.4×10^{-3}, 1.3×10^{-3}, 1.3×10^{-3}	Gibson and Bayliss (1933) Seery and Britton (1964)
$ClO + ClO + M \rightarrow Cl_2 + O_2 + M$	5×10^{-32}	Johnston et al. (1969) (net reaction)
$ClOO + h\nu \rightarrow Cl + O_2$	1.9×10^{-3}, 9.8×10^{-8}, 0., 0.	Johnston et al. (1969)
$H + Cl_2 \rightarrow HCl + Cl$	3.5×10^{-11}	Stedman et al. (1970)
$O + Cl_2 \rightarrow ClO + Cl$	$1.36 \times 10^{-11} \exp(-1560/T)$	Niki and Weinstock (1967) Clyne and Coxon (1966)
$ClO + O_3 \rightarrow ClOO + O_2$	0.	assumed
$H + ClO \rightarrow HCl + O$	1×10^{-11}	estimate
$Cl + HO_2 \rightarrow HCl + O_2$	1×10^{-11}	estimate
$ClOO + O_3 \rightarrow ClO + 2O_2$	0.	assumed
$Cl + CH_4 \rightarrow HCl + CH_3$	$5 \times 10^{-11} \exp(-1791/T)$	Clyne and Walker (1973) Davis et al. (1970)

[a] All concentrations are in units of cm^{-3}.

[b] Photolysis rates are 24-hour means and are given at 50, 30, 15, and 0 km altitudes.

[c] Preliminary results communicated by R.T. Watson.

[d] Recently J.G. Anderson (private communication, 1974) has measured this reaction at stratospheric temperatures and found $k = 2.0 \times 10^{-12} \exp(-620/RT)$. This rate is about a factor of 2 greater than that which we used to calculate the results given in Figures 6 through 9.

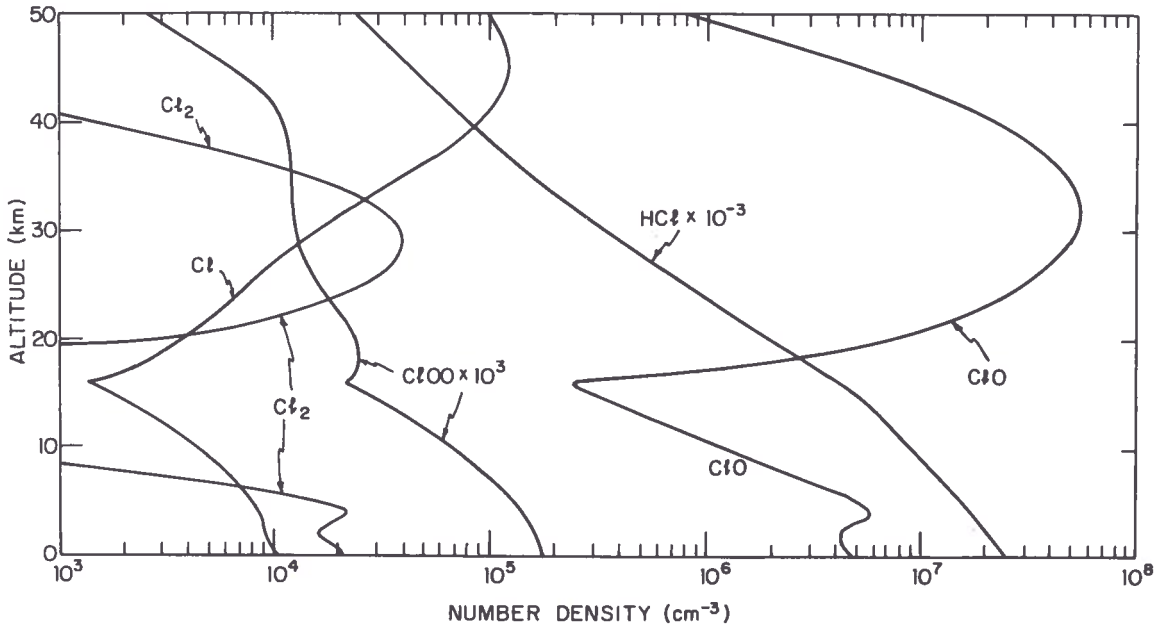

Figure 6. The distribution of gaseous chlorine constituents is shown as a function of altitude in the troposphere and stratosphere. The total mixing ratio of all gaseous chlorine compounds has been arbitrarily set at f = 1 X 10^{-9} (V/V). From Wofsy and McElroy (1974).

and

$$ClO + h\nu \rightarrow Cl + O \qquad (25)$$

with reaction (23) playing a major role in the troposphere and lower stratosphere. The rate for photolysis of ClO is not well-established. The weak near-ultraviolet absorption bands (4,0), (3,0), . . ., (0,0) were not included in the present analysis, since the upper levels were apparently observed in emission by Pannetier and Gaydon (1948) and there is no evidence for predissociation (see also Durie and Ramsey (1950)). We extrapolated data by Johnston et al. (1969) and Porter (1950) in order to estimate the contribution of longer wavelengths to the net photolysis rate. Despite these caveats, the results shown in Figure 6 should be reasonably reliable. Photolysis of ClO makes only a minor contribution (<10%) to the major chemical paths in the present model.

We omit possible formation of OClO by the reaction

$$ClO + O_3 \rightarrow OClO + O_2. \qquad (26)$$

The reaction is surely slow (cf. Clyne and Coxon (1968)) and would be followed by photolysis,

$$h\nu + OClO \rightarrow O + ClO \qquad (27)$$

although there might be some net loss of odd oxygen by the relatively slow reaction (Bemand et al., 1973)

$$O + OClO \rightarrow O_2 + ClO. \qquad (28)$$

The dominant chlorine removal of odd oxygen, however, is provided by reaction (24), and reactions involving ClOO and OClO most likely make no more than a small contribution to the total odd-oxygen removal rate. The radical ClOO is removed mainly by

$$ClOO + M \rightarrow Cl + O_2 + M \qquad (29)$$

with a small contribution due to photolysis,

$$ClOO + h\nu \rightarrow Cl + O_2. \qquad (30)$$

The possible effects of chlorine catalysis on atmospheric O_3 are summarized in Figure 7. The

results given here have been obtained following the procedures described by McElroy et al. (1974), modified to include the chlorine reactions in Table 2. Strengths of various loss processes for odd oxygen are shown in Figure 8 for an assumed total-chlorine mixing ratio of 10^{-9}. Although the effects of chlorine catalysis extend over a wide height range, their influence is generally small compared with those of reactions (3) through (5).

Figure 8 shows that the rate of the key recombination reaction (24) cuts off sharply about one scale height above the cutoff of the corresponding NO_x reaction (5). Consequently, as pointed out in the appendix, the boundary-value scaling applicable to NO_x-ozone perturbations does not adequately describe the ClO_x-ozone situation. Figure 7 should somewhat overestimate HCl-ClO_x-ozone perturbations, since boundary scaling was used. However, the rate of reaction (21) used in the present calculations is a factor of two slower at stratospheric temperatures than the recent values of Anderson (1974). This factor will be directly reflected in the sensitivity of ozone to injections of chlorine-containing gases.

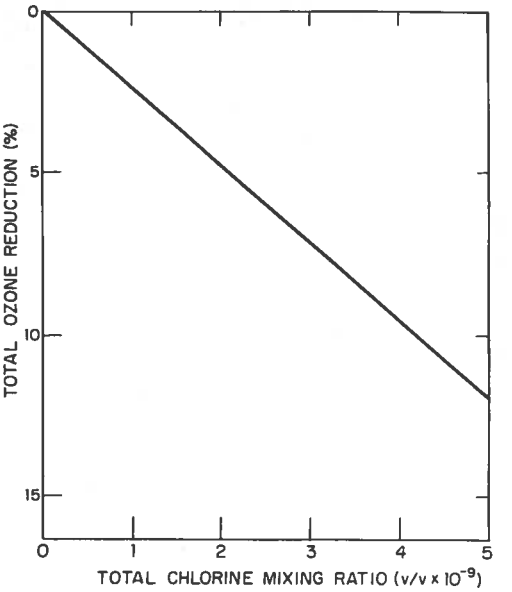

Figure 7. Catalytic reduction of ozone is shown as a function of the mixing ratio for all forms of gaseous chlorine. The ozone reduction was calculated by the method of McElroy et al. (1974). Possible modifications are discussed in the appendix. (Figure taken from Wofsy and McElroy, 1974.)

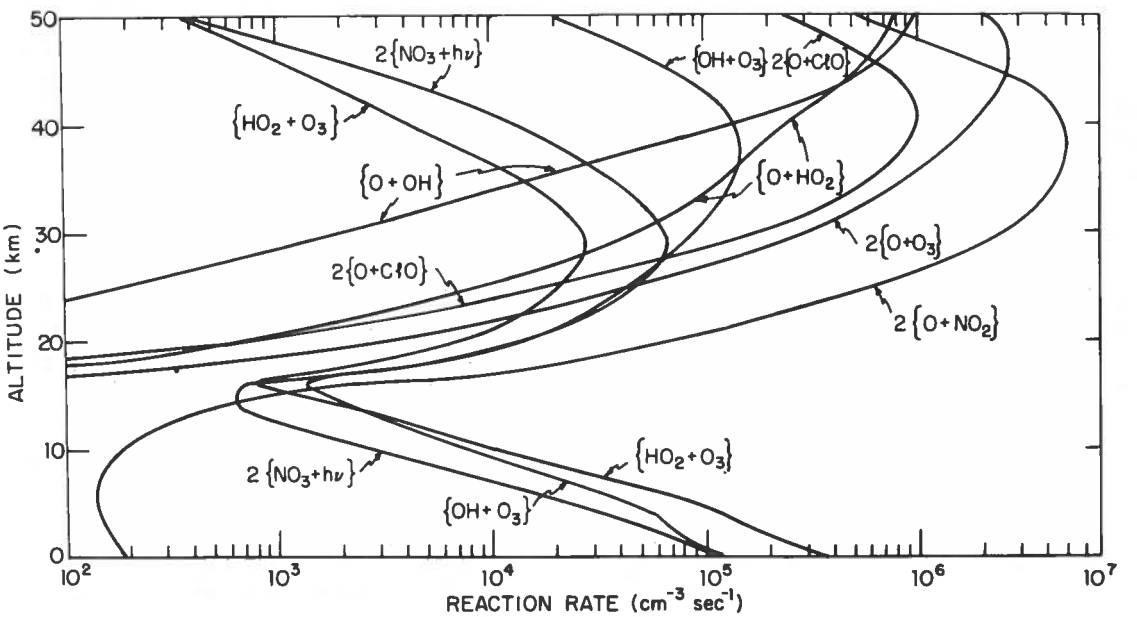

Figure 8. Recombination of O and O_3 is shown in terms of the elementary reaction rates. The mixing ratio of total gaseous chlorine has been arbitrarily chosen as $f = 1 \times 10^{-9}$ (V/V). (Figure taken from Wofsy and McElroy, 1974.)

If one accepts Farmer's (1973) upper limit for the mixing ratio of stratospheric HCl, 10^{-10}, and the results in Figure 6 which indicate that HCl is the major chlorine compound, it follows that chlorine catalysis can play at most a minor role in the normal atmosphere. It should be emphasized, however, that the various sinks for HCl which have been discussed (reaction with NH_3, rainout, washout, and heterogeneous adsorption) (Wofsy and McElroy, 1974; Wofsy, 1974) are effective only at low altitudes, below about 18 km. The space shuttle would provide a source of HCl which would extend to high altitudes, $\geqslant$40 km, where natural sources of HCl are either very small or totally absent. The effects of such high-altitude sources merit further study.

The possible injection of Cl-atoms from photolysis of chlorofluorocarbons may well introduce an appreciable amount of chlorine into the stratosphere in the near future (Molina and Rowland, 1974). Figure 7 should provide a good estimate of the sensitivity of O_3 to added chlorine. Within a factor of 50%, Figure 7 reproduces the results of more elaborate calculations in which ozone is included in the diffusive-flow calculation.

ACKNOWLEDGMENTS

This work was supported jointly by the Atmospheric Sciences Division of the National Science Foundation, and the National Aeronautics and Space Administration, under grant numbers GA 33990X and NGR 22-007-067 respectively to Harvard University. The author is indebted to Prof. M.B. McElroy for his valuable assistance and advice and to Max Havlick for indispensable technical assistance.

APPENDIX

OZONE PRODUCTION AND LOSS BELOW 30 KM

In estimating the effect of NO_x on total ozone, we have assumed a sharp boundary between the regions of the atmosphere in which the ozone density is controlled by the chemistry and the region in which ozone is dynamically controlled. This assumption was motivated by the recognition that chemical production or loss times for ozone increase exponentially with decreasing altitude below 30 km (for details, see McElroy et al. (1974)).

Fortunately, extensive data are available on the ozone distribution below 30 km, so that one may evaluate the sharp-boundary approximation using observed ozone profiles. Not unexpectedly, one finds odd-oxygen production and loss rates between 10^6 and 10^5 cm^{-3} sec^{-1} between 28 and 24 km, and between 10^5 and 10^4 cm^{-3} sec^{-1} between 24 and 16 km. When vertically integrated, these chemical terms constitute a potential source (or sink) of ozone $\approx 10^{12}$ cm^{-2} sec^{-1} in the dynamically controlled region. Since the flux of ozone out of the stratosphere is believed to be roughly 5×10^{10} cm^{-2} sec^{-1} (Dütsch, 1946; Fabian and Junge, 1970), production and loss of odd oxygen plainly cannot be ignored even in the "dynamical region" below 28 km.

The existence of important chemical activity in the dynamical region does not necessarily invalidate boundary scaling as used in the estimation of NO_x-ozone perturbations. Using a general-circulation model of the stratosphere, Mahlman (1973) produced realistic ozone distributions in a series of calculations in which ozone was treated as an inert tracer, with its mixing ratio held fixed at the 30-km level. A key fact underlies this result: the production and loss processes for odd oxygen nearly cancel each other. Moreover, in evaluating the response to a perturbation, one finds that the production and loss terms are *both* increased by artificial NO_x injections. Odd-oxygen production is increased because reduced ozone above 30 km (cf. McElroy et al. (1974)) permits penetration of more solar radiation of $\lambda \approx 200$ nm. Odd-oxygen loss is increased because the artificially enhanced NO_x provides additional loss via reaction (5), and also because (near 26-28 km) the extra UV radiation produces NO_2 at the expense of HNO_3.

Let us now examine, for a given ozone profile, the net odd-oxygen production in the stratosphere,

$$\left\langle \int_{16\text{ km}}^{28\text{ km}} (P - L)\, dz \right\rangle = \eta \qquad \text{(A1)}$$

where P and L are, respectively, production and loss of odd oxygen (cm^{-3} sec^{-1}), and $\langle\ \rangle$ denotes the summer-winter average of the integral. The calculations are performed at 30°N latitude to represent hemispheric-mean conditions. Since P and L are large terms which very nearly cancel, we know that η will be affected by small errors in the assumed ozone profile. We can evaluate this sensitivity by introducing a parameter, s, which uniformly multiplies the empirical ozone profile.

Figure A1 shows two series of calculations in which the parameter s was varied. For the "unperturbed" atmosphere, with ozone profiles taken from Krueger (1973), η has a small negative value. This is an unrealistic result, since the stratosphere would be a net sink for ozone, whose source would then lie in the troposphere. Adjustment of s shows that η can achieve

the expected value ($\approx 5 \times 10^{10}$) if the adopted ozone profiles are assumed to be too high by 10%. Alternatively, the calculated NO_x densities could be assumed to be too high by about 25%. These adjustments are well within the uncertainties of the ozone and NO_x profiles.

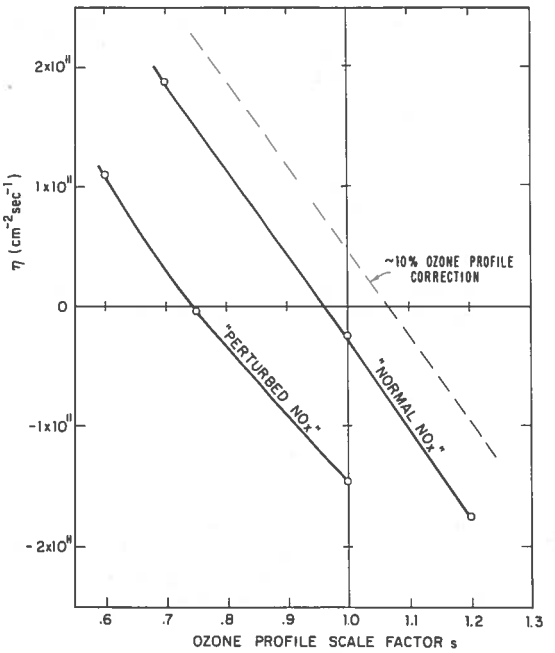

Figure A1. The net ozone production below 30 km (η) is plotted against the ozone-profile scale factor (s) for NO_x profiles corresponding to unperturbed and perturbed conditions. The perturbed calculation shown corresponds to model f of McElroy et al. (1974). This figure illustrates the sharp decrease in net production which accompanies an increase of either ozone or NO_x. The basic ozone profile is from Krueger (1973), utilizing his 30°N summer and winter observations.

The "perturbed" curve of Figure A1 shows the above calculation for model f of McElroy et al. (1974), in which a large source of artificial NO_x was included to simulate a fleet of large SST's. If the ozone profile below 30 km were assumed to be unperturbed (say s = 0.9), the artificial injection would convert the stratosphere from a source of ozone to a sink. (Note that the ozone profile *above* 30 km is adjusted to the perturbed NO_x level.) The only way to rectify the situation is to change the ozone profile below 30 km; Figure A1 shows that ozone must *decrease* in this height regime in order to restore the balance between P and L, to make the stratosphere a source for tropospheric ozone. Figure A2 shows the same result from a different point of view: addition of NO_x to the stratosphere causes a decrease in η. To summarize: *after NO_x injection, restoration of net photochemical production of ozone below 30 km requires a decrease in the ozone content below 30 km.* Ozone reduction increases P (because more UV penetrates to dissociate O_2) and decreases L (which varies roughly as $[O_3]^2$).

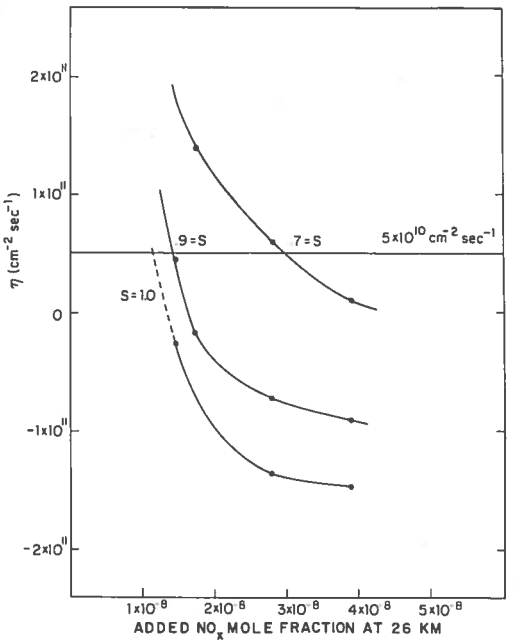

Figure A2. The net ozone production below 30 km (η) is plotted against NO_x mixing ratios for various magnitudes of perturbation of NO_x. Results are shown for several ozone profiles. The figure shows that large NO_x mixing ratios produce significant ozone loss in the dynamical region.

McElroy et al. (1974) estimated the effect of NO_x injections on ozone below 28 km by uniformly reducing the observed ozone profile in proportion to its reduced concentration at 30 km. From the above discussion, this procedure can be seen to be qualitatively correct. The resulting perturbations in total ozone (see Figure 4) are representative of the results which would be obtained from a model which included both chemistry and realistic ozone transport. As noted above, a one-dimensional "eddy diffusion" calculation for O_3 reproduces Figure 4 almost exactly.

The above result depends crucially on the extension of the important reaction (5) well below 28 km. In the case of ClO_x, however, this extension does not occur to the same extent (see Figure 8). The key reaction (24) in the chlorine catalytic cycle decreases rapidly below 40 km. The importance of this effect is shown in Figure A3. Perturbations of stratospheric chlorine strongly reduce ozone above 30 km, but have relatively little effect on ozone at 30 km. Below 30 km, odd-oxygen loss is not affected by injections of gaseous chlorine compounds. Ultraviolet insolation is increased,

however, due to the reduced ozone column above 30 km. Consequently a very strong *increase* in net photochemical production occurs at 38 km and below, in response to chlorine injections into the stratosphere.

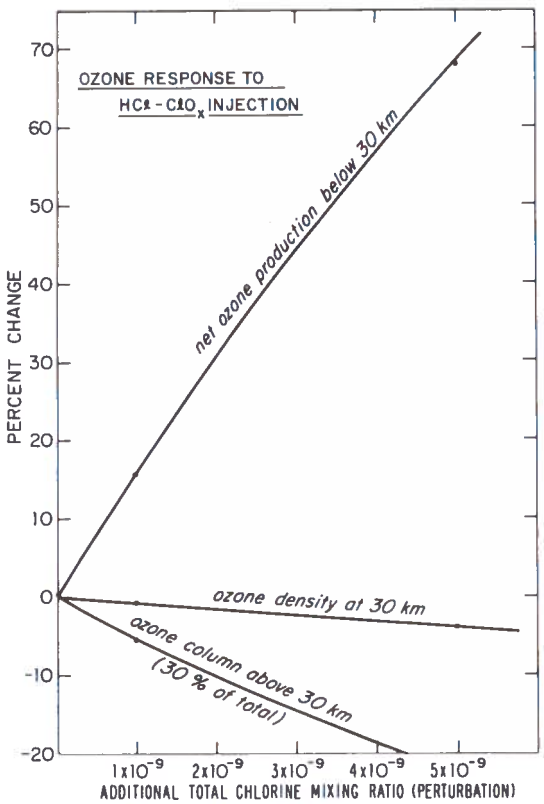

Figure A3. The effect of HCl-ClO_x perturbations is shown for the ozone-column number density above 30 km, for the ozone number density at 30 km, and for the ozone net photochemical production below 30 km. The ClO_x catalytic recombination of O_3 is shown to be restricted to altitudes above 30 km; below that level increased insolation leads to enhanced odd-oxygen production.

In contrast to the NO_x case, ozone below 30 km will decrease weakly, or not at all, in response to artificial chlorine injections. Reliable estimates of this phenomenon are difficult to make, as the results are quite sensitive to details of the chemistry and transport models. However, within a factor of 50%, Figure 7 does reproduce the results of calculations in which the ozone profile is calculated with a one-dimensional "eddy diffusion" model.

REFERENCES

Ackerman, M. and C. Muller (1972), "Stratospheric nitrogen dioxide from infrared spectra," Nature **240**, 300-301.

Ackerman, M., D. Frimout, C. Muller, D. Nevejans, J.C. Fontanella, A. Girard, and N. Louisnard (1973), "Stratospheric nitric oxide from infrared spectra," Nature **245**, 205-206.

Angell, J.K. and J. Korshover (1973), "Quasi-biennial and long-term fluctuations in the total ozone," Mon. Wea. Rev. **101**, 426-443.

Balakhnin, V.P., V.I. Egorov, and E.I. Intezarova (1971), "Elementary reaction kinetics of atomic oxygen in the gas phase by the epr method: II. Reaction O + HCl → OH + Cl," Kinet. Catal. (Eng.) **12**, 258-262.

Basco, N. and S.K. Dogra (1971), "Reactions of halogen oxides studied by flash photolysis," Parts I, II and III, Proc. Roy. Soc. **A323**, 29-68, 401-415, 417-425.

Bates, P. and P.B. Hays (1967), "Atmospheric nitrous oxide," Planetary Space Sci. **15**, 189-197.

Bemand, P.P., M.A. Clyne, and R.T. Watson (1973), "Reactions of chlorine oxide radicals, Part 4 – Rate constants for the reactions Cl + OClO, O + OClO, H + OClO, NO + OClO, O + ClO," J. Chem. Soc. Farad. Trans. **I69**, 1356-1374.

Benson, S.W., F.R. Cruickshank, and R. Shaw (1969), "Iodine monochloride as a thermal source of chlorine atoms: the reaction of chlorine atoms with hydrogen," Int. J. Chem. Kin. **1**, 29-43.

Blanchard, D.C. (1963), "The electrification of the atmosphere by particles from bubbles in the sea," in *Oceanography*, ed. M. Sears, Pergamon Press, Oxford.

Breeding, R.J., J.P. Lodge, J.B. Pate, D.C. Sheesley, H.B. Klonis, B. Fogle, J.A. Anderson, T.R. Englert, P.L. Haagenson, R.B. McBeth, A.L. Morris, R. Pogue, A.F. Wartburg (1973), "Background trace gas concentrations in the central United States," J. Geophys. Res. **78**, 7057-7064.

Broderick, A.J., J. Morley English, and A.K. Forney (1973), "Initial estimate of aircraft emissions in the stratosphere in 1990," AIAA paper 73-508.

Buat-Menard, P. (1970), "Contribution à l'Etude du Cycle Géochimique du Chlore d'Origine Marine," Thesis, University of Paris, 95 pp.

Buat-Menard, P. and R. Chesselet (1971), "Sur la présence de chlore "gazeux" d'origine marine dans l'atmosphère," C.R. Acad. Sci. Paris **272**, 1330-1332.

Chesselet, R., J. Morelli, and P. Buat-Menard (1972), "Some aspects of the geochemistry of marine aerosols," in *The Changing Chemistry of the Oceans*, Wiley Interscience, New York, 93-114.

Crutzen, P.J. (1970), "The influence of nitrogen oxides on the atmospheric ozone content," Quart. J. Roy. Met. Soc. 96, 320-325.

Crutzen, P.J. (1974), "A review of upper atmospheric photochemistry," Can. J. Chem. 52, 1568-1581.

Cunnold, D.M., F.N. Alyea, N.A. Phillips, and R.G. Prinn (1974), "Preliminary results of the MIT photochemical-dynamical ozone model," in this volume.

Davis, D.D., W. Braun, and A.M. Bass (1970), "Reactions of $Cl(^2P_{3/2})$: Absolute rate constants for reaction with H_2, CH_4, C_2H_6, CH_2Cl_2, C_2Cl_4 and c-C_6H_{12}," Int. J. Chem. Kin. 2, 101-114.

Duce, R.A. (1969), "On the source of gaseous chlorine in the marine atmosphere," J. Geophys. Res. 74, 4597-4599.

Durie, R.A. and P.A. Ramsey (1958), "Absorption spectra of the halogen monoxides," Can. J. Phys. 36, 35-53.

Dütsch, H.U. (1946), "Fotochemische Theorie des atmosphärischen Ozons unter Berücksichtigung von Nichtgleichgewichtszuständen und Luftbewegungen," doctoral thesis, Zürich.

Eriksson, E. (1960), "The yearly circulation of chloride and sulfur in nature," Tellus 11, 63-109.

Evans, W.F.J., D.M. Hunter, E.J. Llewellyn, and A. Vallance Jones (1968), "Altitude profile of the infrared atmosphere system of oxygen in the dayglow," J. Geophys. Res. 73, 2885-2896.

Fabian, P. and C.E. Junge (1970), "Global rate of ozone destruction at the Earth's surface," Arch. Met. Geoph. Biokl., Ser. A. 19, 161-172.

Fabian, P. and W. Libby (1974), "The stratospheric residence time of odd nitrogen and the effect of the SST, studied in a two-dimensional model derived from high-altitude sampling of radioactive debris," in this volume.

Farmer, C.B. (1974), "Infrared measurements of stratospheric composition," Canad. J. Chem. 52, 1544-1559.

Galante, T.J. and E.A. Gislason (1973), "Critical reexamination of the reaction $Cl + H_2 \rightleftharpoons HCl + H$," Chem. Phys. Lett. 18, 231-234.

Georgii, H.W. (1963), "Oxides of nitrogen and ammonia in the atmosphere," J. Geophys. Res. 68, 3963-3970.

Gibson, G.E. and N.S. Bayliss (1933), "Variation with temperature of the continuous absorption spectrum of diatomic molecules: Parts I and II," Phys. Rev. 44, 188-192, 193-200.

Hering, W.S. and T.R. Borden (1967), "Ozonesonde Observations Over North America, Vol. 4," Environmental Research Papers, 64-30 (IV), Air Force Cambridge Research Laboratories, Bedford, Mass.

Hilsenrath, E., L. Seiden, and P. Goodman (1969), "An ozone measurement in the mesosphere and stratosphere by means of a rocketsonde," J. Geophys. Res. 74, 6873-6880.

Hippler, H. and J. Troe (1973), "Study of the recombination of chlorine atoms by flash photolysis," Chem. Phys. Lett. 19, 607-609.

Johnson, F.S., J.D. Purcell, R. Tousey, and K. Watanabe (1952), "Direct measurements of the vertical distribution of atmospheric ozone to 70 km altitude," J. Geophys. Res. 57, 157-175.

Johnston, H.S. (1973), "January-February photochemistry in the stratosphere – with applications to supersonic transports," Acta Astron. 1, 135-156.

Johnston, H.S., E.D. Morris, and J. Van den Bogaerde (1969), "Molecular modulation kinetic spectroscopy: ClOO and ClO radicals in the photolysis of chlorine in oxygen," J. Am. Chem. Soc. 91(27), 7712-7727.

Junge, C.E. (1956), "Recent investigations of air chemistry," Tellus 8, 127-139.

Junge, C.E. (1957), "Chemical analyses of aerosol particles and of gas traces on the island of Hawaii," Tellus 9, 528-537.

Junge, C.E. (1963), *Air Chemistry and Radioactivity*, Academic Press, New York, 382 pp.

Junge, C.E. (1973), "Our knowledge of the physicochemistry of aerosols in the undisturbed marine environment," J. Geophys. Res. 77, 5183-5200.

Kaplan, Lewis D. (1973), "Background concentrations of photochemically active trace constituents in the stratosphere and upper troposphere," Pure Appl. Geophys. 106-108, 1341-1345.

Kiang, C.S., D. Stauffer, and V.A. Mohnen (1973), "Possibilities for atmospheric aerosol formation involving NH_3," Nature Phys. Sci. 244, 53-54.

Krueger, A.J. (1973), "The mean ozone distribution from several series of rocket soundings," Pure Appl. Geophys. 106-108, 1272-1280.

Krueger, A.J., D.F. Heath, and C.L. Mateer (1973), "Variations in the stratospheric ozone field inferred from Nimbus satellite observations," Pure Appl. Geophys. **106-108**, 1254-1268.

Loewenstein, M., J.P. Paddock, I.G. Poppoff, and H.F. Savage (1974), "NO and O_3 measurements in the lower stratosphere from a U-2 aircraft" (manuscript, NASA Ames Research Center, Moffett Field, CA 94035).

Mahlman, J.D. (1973), "Preliminary results from a three-dimensional, general-circulation/tracer model," *Proceedings of the Second Conference on the Climatic Impact Assessment Program* (Nov. 14-17, 1972), ed. A.J. Broderick, U.S. Department of Transportation DOT-TSC-OST-73-4, 321-337.

McConnell, J.C. and M.B. McElroy (1973), "Odd nitrogen in the atmosphere," J. Atmos. Sci. **30**, 1465-1480.

McElroy, M.B. and J.C. McConnell (1971), "Nitrous oxide: a natural source of stratospheric NO," J. Atmos. Sci. **28**, 1095-1098.

McElroy, M.B., S.C. Wofsy, J.E. Penner, and J.C. McConnell (1974), "Atmospheric ozone: possible impact of stratospheric aviation," J. Atmos. Sci. **31**, 287-305.

Molina, M. and F.S. Rowland (1974), "Stratospheric sink for chlorofluoromethanes – chlorine atom catalyzed destruction of ozone," Nature **249**, 810-812.

Myer, J.A. and J.A.R. Samson (1970), "Vacuum-ultraviolet absorption cross sections of CO, HCl, and ICN between 1050 and 2100 A," J. Chem. Phys. **52**, 266-271.

Nicolet, M. (1971), "Aeronomic reactions of hydrogen and ozone," in *Mesospheric Models and Related Experiments*, Reidel, Dordrecht, Holland, 1-51.

Nicholas, J.E. and R.G.W. Norrish (1968), "Some reactions in the chlorine and oxygen system studied by flash photolysis," Proc. Roy. Soc. **A307**, 391-397.

Niki, H. and B. Weinstock (1967), "Reaction of oxygen atoms with chlorine," J. Chem. Phys. **47**, 3249-3252.

Norrish, R.G.W. and G.H.J. Neville (1934), "The decomposition of ozone photosensitized by chlorine," J. Chem. Soc., 1864-1872.

Pannetier, G. and A.G. Gaydon (1948), "Band spectrum of ClO in flames," Nature **161**, 242-243.

Porter, G. (1950), "The ClO radical," Disc. Farad. Soc. **9**, 63-65.

Ridley, B.A., H.I. Schiff, A.W. Shaw, L.R. Megill, L. Bates, C. Howlett, and H. LeVaux (1974), "Measurement of nitric oxide in the stratosphere between 17.4 and 22.9 km," Planet. Space Sci. **22**, 19-24.

Robbins, R.C., R.D. Cadle, and D.L. Eckhardt (1959), "The conversion of sodium chloride to hydrogen chloride in the atmosphere," J. Meteorol. **16**, 53-56.

Romand, J. and B. Vodar (1948), "Spectre d'absorption de l'acide chlorhydrique gazeux dans la région de Schumann," C.R. Acad. Sci. **226**, 238-240.

Ruderman, M.A. and J.W. Chamberlain (1973), "Origin of the Sunspot Modulation of Ozone: Its Implication for Stratospheric NO Injection," Institute for Defense Analysis, JSS-73-18-3.

Seery, D.J. and D. Britton (1964), "The continuous absorption spectra of chlorine, bromine, bromine chloride, iodine chloride and iodine bromide," J. Phys. Chem. **68**, 2263-2266.

Stedman, D.H., D. Steffenson, and H. Niki (1970), "The reaction between active hydrogen and Cl_2: Evidence for the participation of vibrationally excited H_2," Chem. Phys. Lett. **7**, 173-174.

Stolarski, R. and R. Cicerone (1974), "Stratospheric chlorine: a possible sink for ozone," Canad. J. Chem. **52**, 1610-1615.

Takacs, G.A. and G.P. Glass (1973), "Reactions of hydroxyl radicals with some hydrogen halides," J. Phys. Chem. **77**, 1948-1951.

Warneck, P. (1972), "Cosmic radiation as a source of odd nitrogen in the stratosphere," J. Geophys. Res. **77**, 6589-6591.

Westenberg, A.A. and N. de Haas (1968), "Atom-molecule kinetics using ESR detection. IV: Results for $Cl + H_2 \rightleftharpoons HCl + H$ in both directions," J. Chem. Phys. **48**, 4405-4415.

Widman, R.P. and B.A. DeGraff (1973), "On the gas phase recombination of chlorine atoms," J. Phys. Chem. **77**, 1325-1328.

Wofsy, S.C. (1974), "On gaseous chlorine and the role of HCl-water aerosols in the earth's lower atmosphere," unpublished work.

Wofsy, S.C. and M.B. McElroy (1973), "On vertical mixing in the upper stratosphere and lower mesosphere," J. Geophys. Res. **78**, 2619-2624.

Wofsy, S.C. and M.B. McElroy (1974), "HO_x, NO_x and ClO_x: their role in atmospheric photochemistry," Canad. J. Chem. **52**, 1582-1591.

Wong, Edgar L. and Frank E. Belles (1971), "Rate Measurements for the Reaction of Hydrogen Chlorine and Deuterium Chloride with Atomic Oxygen," NASA Technical Note D-6495.

Wu, Ching-Hsong and H.S. Johnston (1972), "Molecular modulation mass spectrometry kinetic study of the ClO free radical," Bull. Soc. Chim. Belge **81**, 135-153.

NUMERICAL EXPERIMENTS ON STRATOSPHERIC MERIDIONAL OZONE DISTRIBUTIONS USING A PARAMETERIZED TWO-DIMENSIONAL MODEL

GEORGE F. WIDHOPF AND THOMAS D. TAYLOR
The Aerospace Corporation
Los Angeles, California

ABSTRACT: A time-dependent two-dimensional meridional model of the lower regions of the atmosphere has been developed for calculating the distributions of trace chemical species in the atmosphere. The model incorporates parameterized large-scale eddy transports as well as parameterized mean meridional circulation. Results of calculations run to a steady state for various seasons are compared with available measurements for both the meridional distribution of the total ozone column and vertical profiles of ozone at various latitudes. These detailed comparisons provide an initial assessment of the adequacy of the parameterized-model approach to determine 1) the distributions of trace species in the "natural" atmosphere and 2) the effects which would result from the deposition of pollutants in the stratosphere by the SST. Results obtained for the Chapman-plus-NO_x chemical model are in relatively good agreement with reported ozone observations. Preliminary calculations of the effect of SST exhaust emissions on the meridional total-ozone distribution show a marked meridional variation for the case in which they are injected into a typical North Atlantic flight corridor. The resultant globally averaged decrease in total ozone column is in good agreement with a corresponding one-dimensional result.

INTRODUCTION

With the advent of commercial supersonic flight in the stratosphere, a concerted effort has been initiated to determine what effects, if any, the trace pollutants deposited by these aircraft will have on the state of the "natural" atmosphere. This concern stems from the fact that the stratosphere is a very stable region which is characterized by a residence time on the order of a few years. Thus, the accumulation of pollutants from a fleet of SST's may, through photochemical reactions, alter the concentration of ozone in the stratosphere and, in turn, change the amount of ultraviolet radiation reaching the surface of the earth. Since absorption by ozone of ultraviolet radiation at wavelengths shorter than 310 nm constitutes the main energy source for the upper atmosphere, any alteration of the amount of ozone or its distribution could affect the climate of the upper atmosphere as well.

In order to adequately assess the effect on the ozone layer of pollutants deposited in the lower regions of the atmosphere by future SST aircraft, a consistent numerical model of the existing "natural" atmosphere must initially be developed and verified. State-of-the-art three-dimensional general-circulation models which calculate the entire thermodynamic, hydrodynamic and chemical structure of the lower regions of the atmosphere are very complex and are restricted in scope due to computer limitations. However, two-dimensional meridional models of the lower regions of the atmosphere, which parameterize the meridional thermodynamic structure and the advective and turbulent-eddy transport, while solving for the transient and spatial distributions of the important atmospheric trace species, may be adequate to study the general nature of this specific problem.

Two-dimensional parameterized atmospheric models have been developed in the past using various degrees of sophistication, and have enjoyed various degrees of success in predicting the variation of the total ozone column in the meridional plane (e.g., Prabhakara (1963) and Gebhart et al. (1970)). Various degrees of success have also been achieved in predicting the movement of atmospheric tracers (e.g., Reed and German (1965), and Gudiksen et al. (1968)). Unfortunately, due to the limited number of

quantitative data available for both turbulent-diffusivity coefficients and mean meridional circulation, arbitrary adjustments of the parameterized data were necessary in some cases to obtain reasonable agreement with available observations. However, these numerical experiments did demonstrate that both the large-scale turbulent-eddy transports and the mean meridional circulation must be taken into account in order to adequately model the distribution of species (or tracers) in the lower regions of the atmosphere.

Examples of more recent two-dimensional parameterized models which have been reported include the work of Shimazaki et al. (1973a), Rao (1973), Rao and Christie (1973), and Hesstvedt (1973). Shimazaki et al. (1973a) considered Chapman chemistry and specified spatially invariant values of the components of the diffusivity tensor, together with a harmonic-function parameterization of the meridional circulation. Similarly, Rao (1973) used diffusivities independent of altitude while computing the circulation pattern by solving the steady-state zonal momentum, energy, continuity, and thermal wind equations. Rao investigated Chapman chemistry alone, and Rao and Christie (1973) performed numerical experiments on the effect of NO_x and water vapor on ozone concentration. The results for the oxygen-only atmosphere showed reasonable agreement with data. The results obtained when NO_x and water vapor were introduced were compared only with total ozone column data.

Hesstvedt (1973) has developed a model which incorporates a comprehensive O-N-H chemical model; it uses adjusted values of the data of Reed and German for both the diffusivities and the circulation. These data were adjusted until he obtained results which looked reasonable for the meridional ozone distributions. However, no detailed comparisons with existing observations were presented. All of the above models solve for the steady-state distributions for particular seasons, either by solving the steady-state equations (Rao, 1973; Rao and Christie, 1973; Hesstvedt, 1973) or by relaxing a time-dependent solution (Shimazaki et al., 1973).

It should also be remarked that in each of the models cited the parameterized data were not self-consistent, in that the parameterized transports (advective and diffusive) and thermodynamic data were not obtained from the same set of observations. Thus, they do not satisfy the conservative equations exactly, and therefore any interpretation of their results should be evaluated with this in mind. Obviously, the consistency is directly related to the type of parameterization utilized in the model, and the models are limited by the availability of these data.

Any model which is ultimately to be used to model the effect of aircraft emissions on the distribution of trace species in the atmosphere must initially be able to reproduce the "natural" atmosphere reasonably well, especially in the regions where the effect of the pollutants is likely to be most significant. It is evident that any such model of the atmosphere has to be verified by comparing the numerical results with available experimental data. These comparisons should include detailed examination of the two-dimensional distribution of ozone for each season, together with the meridional variation of the total ozone column. This is necessary since, for example, adjustments made to the parameterized transports can bring the total amount into reasonable agreement with the observed data, whereas the detailed two-dimensional distributions show poor agreement in this respect.

With reference to the evaluation of the effects of aircraft emissions, ultimately only changes in the ozone column are important with respect to the effect on the amount of ultraviolet radiation reaching the surface. However, change in the mean spatial distribution can affect local heat balances, which in turn can affect weather. This effect, coupled with the fact that distributions are important when local injection of pollutants is being investigated, requires that the model yield relatively accurate spatial distributions. Specifically, the transport of some important individual species is controlled by the relative spatial gradients; thus, in order to have confidence in any predictions of the effects of the local introduction of pollutants, a correct prediction of the species distributions is important.

Recently, more detailed information (which is still not entirely consistent) has become available, and can be used to improve the parameterized data necessary for this type of model.

Such a model has been developed in this investigation; together with the parameterization used, it is described in the following sections. Detailed comparisons of the initial results with reported observations are also presented.

GOVERNING EQUATION

The governing species-conservation equation is derived following the general procedure outlined by Reed and German (1965) for representing the turbulent-transport flux due to large-scale eddies. In the meridional plane this equation, written in terms of the mass mixing ratio Y_i, is of the form

$$\rho \frac{\partial Y_i}{\partial t} + \rho w \frac{\partial Y_i}{\partial z} + \frac{\rho v}{r} \frac{\partial Y_i}{\partial \phi}$$

$$= \frac{1}{r} \frac{\partial}{\partial \phi} \left\{ \rho k_{\phi z} \frac{\partial Y_i}{\partial z} \right\}$$

$$+ \frac{1}{r} \frac{\partial}{\partial \phi} \left\{ \frac{\rho}{r} k_{\phi\phi} \frac{\partial Y_i}{\partial \phi} \right\}$$

$$+ \frac{\partial}{\partial z} \left\{ \rho k_{zz} \frac{\partial Y_i}{\partial z} \right\}$$

$$+ \frac{\partial}{\partial z} \left\{ \frac{\rho}{r} k_{z\phi} \frac{\partial Y_i}{\partial \phi} \right\}$$

$$+ 2 \frac{\rho}{r} \left\{ k_{zz} \frac{\partial Y_i}{\partial z} + k_{z\phi} \frac{\partial Y_i}{r \partial \phi} \right\}$$

$$- \frac{\rho}{r} \tan\phi \left\{ k_{\phi z} \frac{\partial Y_i}{\partial z} + k_{\phi\phi} \frac{\partial Y_i}{r \partial \phi} \right\}$$

$$+ \omega_i + S_i \quad (i = 1,2,\ldots NI)$$

where Y_i is the mass mixing ratio ρ_i/ρ of the i^{th} chemical species; ρ is the local mean atmospheric density; t is the temporal variable; $r = z + R_e$, where R_e is the mean radius of the earth and z is the altitude measured from and normal to the earth's surface; ϕ is the latitude; ω_i is the photochemical rate of production or depletion of the i^{th} species; and S_i is the local source/sink effect. The components of the tensor, $k_{\alpha\beta}$, represent the diffusion coefficient in the respective directions arising from large-scale eddy motions, while v and w are the components of the mean circulation in the meridional and vertical directions, respectively. This equation is solved for each of the trace species considered.

CHEMICAL MODEL

It has been shown in other one-dimensional studies that it is necessary to consider an O-N-H chemical system in order to adequately take into account the important chemistry affecting the atmospheric ozone distribution. It was decided that in this investigation a stepwise procedure would be undertaken. Initially the Chapman system (with N_2 as a nonreacting background) will be studied, then the important NO_x reactions which affect ozone will be introduced to determine their effect and, finally, the whole O-N-H chemical system (as recommended in Volume III of the CIAP Monograph Series) will be utilized. This approach permits the determination of the incremental effects of the introduction of different trace species systems (NO_x, HO_x) and simplifies the evaluation of the adequacy of the trace-species transports utilized in the computations. The latter concern is important, since the specification of these transports in certain regions is subject to judgment due to a lack of available data, and therefore the parameterized transports must be evaluated for each season. This approach allows major inaccuracies to be evaluated fairly readily, since most of the gross features of the ozone distribution are determined by the Chapman chemistry. By proceeding in this manner it can readily be determined whether any local underprediction of ozone is a consequence of the presence of too much NO_x or HO_x, or whether instead the transport model provides inadequate local quantities of O_3 before NO_x and HO_x are introduced.

The results reported herein include the $O/O_2/O_3$ chemical model governed by the Chapman chemistry as one chemical subset, as well as the same model with NO and NO_2 added, in order to evaluate their effect on the ozone distribution. The O-N-H system involving $O(^1D)$, $O(^3P)$, O_2, O_3, NO, N_2O, NO_2, OH, H_2O, HO_2, H_2O_2, HNO_3, N, H, and CH_4, governed by

the reaction system suggested by CIAP, is presently being studied. Its results, which will be reported at a later date, will provide a basis upon which the yearly variation of the distribution of trace species can be calculated by permitting the parameterized data to vary temporally.

The specific reactions and reaction rates (Chang, 1973) which were utilized in these computations are listed in Table 1. Since reaction 5 is very fast, the conversion of $O(^1D)$ to $O(^3P)$ was assumed to be instantaneous and thus only $O(^3P)$ was considered in the computations.

Evaluation of the individual chemical production rates involves the calculation of photochemical reaction rates which are of the form

$$J_i(z,\phi,t) = \int_\lambda \Phi_i(\lambda)\, I(\lambda,z,\phi,t)\, \sigma_i(\lambda,T)\, d\lambda$$

where $\Phi_i(\lambda)$ is the quantum yield for photodissociation; $\sigma_i(\lambda, T)$ is the respective absorption cross section for species i; and $I(\lambda, z, \phi, t)$ is the local intensity of solar radiation as a function of wavelength, altitude, latitude, and time of the year. The local value of $I(\lambda, z, \phi, t)$ is given by

$$I(\lambda,z,\phi,t) = I_\infty(\lambda,T) \cdot \exp\left\{-\sum_{i=O_2,O_3} \int n_i(z,\phi,t)\, \sigma_i(\lambda,T)\, \sec\chi\, dz\right\}$$

where $I_\infty(\lambda, T)$ is the intensity of solar radiation at the outer regions of the earth's atmosphere and χ is the incident solar zenith angle at a given latitude and time of the year.

Table 1. Chemical Reactions and Rate Coefficients

(1)	$O(^3P) + O_3$	$\rightarrow 2O_2$	$k_1 = 2(10)^{-11} \exp\left[-2410/T\right]$
(2)	$O_2 + h\nu$	$\rightarrow 2O(^3P)$	J_2
(3)	$O_3 + h\nu$	$\rightarrow O_2 + O(^1D)$	J_3
(4)	$O_3 + h\nu$	$\rightarrow O_2 + O(^3P)$	J_4
(5)	$O(^1D) + M$	$\rightarrow O(^3P) + M$	$k_5 = 4.5(10)^{-11}$
(6)	$O(^3P) + O_2 + M$	$\rightarrow O_3 + M$	$k_6 = 1.11(10)^{-34} \exp\left[+510/T\right]$
(7)	$NO_2 + h\nu$	$\rightarrow NO + O(^3P)$	J_7
(8)	$NO_2 + O(^3P)$	$\rightarrow NO + O_2$	$k_8 = 9.2(10)^{-12}$
(9)	$NO + O_3$	$\rightarrow NO_2 + O_2$	$k_9 = 9(10)^{-13} \exp\left[-1200/T\right]$

The incident solar flux is obtained from the data compiled by Ackerman (1971). The absorption cross-sections for O_2 in the Schumann-Runge bands are obtained from the tabulated values of Hudson and Mahle (1972), while the cross sections in the Herzberg continuum are obtained from data compiled by Ackerman (1972). The cross-sections for O_3 in the Hartley, Huggins, and Chappuis regions are obtained from the data compiled by Ackerman (1972) while the photodissociation cross-sections for NO_2 were obtained from Johnston et al. (1973). The quantum yields for the photodissociation of NO_2 were obtained from Garvin and Hampson (1973).

FINITE-DIFFERENCE EQUATIONS

The finite-difference form of the partial differential equations is obtained by employing the leapfrog/Dufort-Frankel approximation. In this approximation, any function f that can be expressed as

$$f(x,y,t) = f\left(\sum_{\nu=1}^{j-1} \Delta x_\nu, \sum_{\nu=1}^{k-1} \Delta y_\nu, n\Delta t\right) = f_{jk}^n$$

has temporal and streamwise-spatial derivatives of the form

$$\left(\frac{\partial f}{\partial t}\right)_{jk}^n = \frac{\Delta_n f_{jk}^n}{\Delta t} = \frac{1}{2\Delta t}\left\{f_{jk}^{n+1} - f_{jk}^{n-1}\right\}$$

$$\left(\frac{\partial f}{\partial x}\right)_{jk}^n = \frac{\Delta_j f_{jk}^n}{\Delta x_j} = \frac{1}{(1+R_j)R_j\Delta x_j} \cdot \left\{R_j^2\left(f_{j+1k}^n - f_{jk}^n\right) - \left(f_{j-1k}^n - f_{jk}^n\right)\right\}$$

and, in cases where derivatives are required at adjoining points (e.g., for the diffusion terms),

$$\left(\frac{\partial f}{\partial x}\right)_{j+1k}^n = \frac{\bar{\Delta}_j f_{j+1k}^n}{\Delta x_j} = \frac{1}{(1+R_j)R_j\Delta x_j} \cdot \left\{(1+R_j)^2\left(f_{j+1k}^n - \bar{f}_{jk}^n\right) - \left(f_{j+1k}^n - f_{j-1k}^n\right)\right\}$$

$$\left(\frac{\partial f}{\partial x}\right)^n_{j-1k} = \frac{\bar{\Delta}_j f^n_{j-1k}}{\Delta x_j} = \frac{1}{(1+R_j)R_j\Delta x_j} \cdot$$

$$\left\{(1+R_j)^2\left(\bar{f}^n_{jk} - f^n_{j-1k}\right) - R_j^2\left(f^n_{j+1k} - f^n_{j-1k}\right)\right\}$$

where $R_j = \Delta x_{j-1}/\Delta x_j$, and

$$\bar{f}^n_{jk} = \frac{\left(f^{n+1}_{jk} + f^{n-1}_{jk}\right)}{2}$$

In order to eliminate the dependence of the stability of this finite-difference scheme on the local chemical relaxation time, the production term $\omega_i(\rho, T, Y_i)$ is written in the following manner

$$(\omega_i)^n_{jk} = \frac{\left((\omega_i)^{n+1}_{jk} + (\omega_i)^{n-1}_{jk}\right)}{2}$$

where $(\omega_i)^{n+1}_{jk}$ is obtained from a Taylor-series expansion of the form

$$(\omega_i)^{n+1}_{jk} = (\omega_i)^n_{jk} + \left(\frac{\partial \omega_i}{\partial t}\right)^n_{jk} \Delta t$$

and

$$\left(\frac{\partial \omega_i}{\partial t}\right)^n_{jk} = \left(\frac{\partial \omega_i}{\partial \rho}\right)^n_{jk}\left(\frac{\rho^{n+1}_{jk} - \rho^n_{jk}}{\Delta t}\right)$$

$$+ \left(\frac{\partial \omega_i}{\partial T}\right)^n_{jk}\left(\frac{T^{n+1}_{jk} - T^n_{jk}}{\Delta t}\right)$$

$$+ \sum_{\varrho}\left(\frac{\partial \omega_i}{\partial Y_\varrho}\right)^n_{jk}\left[\frac{(Y_\varrho)^{n+1}_{jk} - (Y_\varrho)^n_{jk}}{\Delta t}\right]$$

Thus, the temporal and advective terms are written explicitly, while the diffusion and chemical-rate terms are written semi-implicitly. Solution of the system of NI species-conservation equations is, therefore, an implicit calculation *in time*, at each individual spatial location, involving only ρ^{n+1}_{jk}, T^{n+1}_{jk}, and $(Y_i)^{n+1}_{jk}$ at the mesh point in question, together with information at the two previous time levels. Therefore, at each mesh point an N1 X N1 matrix must be inverted. Thus, the necessity for inverting the system of equations for the entire computational domain simultaneously, as is the case for standard implicit schemes, is relaxed, resulting in substantial savings in computer storage. Also, since the temporal finite-difference approximation is accurate to the second order, there is no need for iterating on the solution, as is necessary in some implicit schemes which are accurate to a lower order. This provides savings in computer execution time.

An analysis of the stability characteristics of this scheme, including numerical experiments, was presented by Widhopf and Victoria (1973), who demonstrated that this finite-difference scheme is stable, independent of the chemical state of the gas mixture, as long as the Courant-Friedrichs-Lewy stability restriction is satisfied. Thus, the stability of this method is independent of the local chemical and diffusive time scales, and the "stiff" nature of the equations is overcome.

This finite-difference approximation is formally spatially second-order-accurate for equal mesh spacing, and is temporally consistent provided the proper temporal-to-spatial step-size ratio is maintained. The consistency and accuracy of this scheme were demonstrated by Victoria and Widhopf (1972).

BOUNDARY CONDITIONS

A schematic diagram of the computational domain considered in this investigation is shown in Figure 1, together with the mesh resolution (Δz = 1 up to 35 km and then Δz = 2.5 to the upper boundary) utilized in the present calculation. The boundary conditions specified for the numerical solution in the domain are described in this section.

A fixed concentration was imposed for ozone at the lower boundary with a value obtained from the meridional distributions compiled by Dütsch (1971). $O(^3P)$ was taken to be in photochemical equilibrium at the lower boundary, whereas both $O(^3P)$ and O_3 were assumed to be in photochemical equilibrium at the upper boundary.

For the calculations which included NO and NO_2, the lower boundary condition was taken to

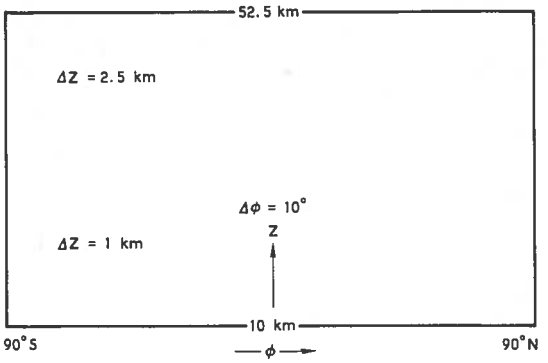

Figure 1. Schematic diagram of computational domain.

be $\partial Y_i/\partial z = 0$ for both species. This was found to be the tendency of the solution when fixed concentrations were imposed at the lower boundary, and agrees in this respect with the NO_x distribution reported by Hesstvedt. The upper boundary conditions for NO and NO_2 were taken to be 5×10^7 and 5×10^5 molecules/cm^3, respectively, as interpreted from one-dimensional studies (e.g., Shimazaki et al. (1973b), Chang and Duewer (1973), Whitten and Turco (1973), and Stewart and Hoffert (1973)).

At the lateral boundaries of the computational domain (80°S and 80°N), the solution for Y_i was analytically continued to the northern and southern poles by a second-order extrapolation in space and time of the form (at 90°S)

$$(Y_i)^{n+1}_{j-1\,k} = 2(Y_i)^{n}_{jk} - (Y_i)^{n-1}_{j+1\,k} + O\left\{(\Delta z)^2, \Delta z \Delta t, (\Delta t)^2\right\}.$$

This method allowed the use of centered spatial differencing at the lateral extent of the computational domain, and was stable. It also eliminated the necessity for specifying any boundary conditions at this location, and was found to give results consistent with the assumption of a zero latitudinal flux at the equinox.

PARAMETERIZATION

As stated in the introduction, the meridional distributions of temperature, density, mean circulation, and the components of the turbulent-diffusivity tensor are parameterized as functions of time and space. Details of the structure of the stratosphere are difficult to obtain because of the paucity of experimental data presently available. The data that are available do not completely encompass the entire region of the atmosphere which is of interest, and knowledge of the large-scale temporal variations is also incomplete. Thus, the accuracy of the parameterization is directly dependent upon the availability and reliability of observational data. The data used in this study are believed to be both the most recent and the most reliable data presently available.

The meridional distributions of both mean density and temperature were specified using the data obtained from ten years of observations which were analyzed and compiled by Louis (1973). These averaged data are specified from the surface to 68 kilometers from the entire meridional plane for each of the four seasons.

Luther (1973a) has recently analyzed the heat-transfer data of Oort and Rasmusson (1971) using the procedure outlined by Reed and German (1965) for defining the components of the anisotropic turbulent-eddy diffusivity tensor. The three components, $k_{\phi\phi}$, $k_{\phi z}$, and k_{zz}, are specified for the northern hemisphere from the surface to 60 kilometers. Values for the components of the diffusivity tensor in regions where observational data were not available were obtained by Luther (1973a,b) by extrapolation, using the results of Wofsy and McElroy (1973) and Newell et al. (1966). These coefficients are specified for each month, as well as seasonally, and were used to parameterize the components of the turbulent-diffusivity tensor. The values for the southern hemisphere were obtained by appropriately applying the northern-hemisphere values of six months later.

The mean meridional circulation was parameterized from the work of Louis et al. (1974), who calculated the circulation patterns by solving the continuity and energy equations using compiled observations of the meridional temperature field and local heat-transfer rates. The circulation patterns are specified for the entire meridional plane for each season from the surface to 50 kilometers.

RESULTS

Computations of the distributions of the trace species were carried out for the entire

meridional plane for the spring, summer, and autumn seasons in the northern hemisphere. Since one objective of this investigation was to ascertain the adequacy of the model by comparing its results with observational data, an average daylight zenith angle at each latitude was used in the computations. Here the calculations were relaxed in time until a steady-state distribution was obtained. It must be remembered that in the troposphere the time scale for changes in the background hydrodynamic structure of the atmosphere is much shorter than the local chemical relaxation time, so a steady-state assumption is not a good approximation in this region. Therefore, the lower boundary for these computations has been selected to be above the surface, but away from the region of primary interest. No modifications were made to the parameterized data in the calculations described.

The results are presented in a similar form for each season. Specifically, the meridional distribution of the total ozone column in Dobson units (10^{-3} cm, STP) is shown together with vertical ozone profiles at selected latitudes in both the northern and southern hemispheres. The numerical results for both the pure-Chapman model and the Chapman-plus-NO_x model are compared with available observations.

Spring in Northern Hemisphere

Figure 2 shows the results for the spring season. The computations for the meridional variation of the total ozone column are compared to the data of Stickel (1970) (southern hemisphere) and London (1963) (northern hemisphere), which are averaged for the spring season. They are also compared to the data of Gebhart et al. (1970), which are average values for the month of April for the entire meridional plane.

Since the data represent the entire ozone column, whereas the computations were carried out for the altitude regime of 10 to 52.5 km (inclusive), the ozone column reported by Gebhart et al. (1970) for the 0-15 km altitude regime was added to the computed results for the 15-52.5 km region to permit a more meaningful comparison. This procedure was followed for all seasons; the bias introduced to the numerical results is relatively small.

As expected, the Chapman model overpredicts the magnitude of the ozone column, but the relative meridional distribution is essentially correct. The introduction of NO_x results in a reduction of the ozone column everywhere, and the calculated result is in relatively good agreement ($\pm$ 23%) with the observed distribution. Here it should be remembered that the upper boundary condition was fixed at a constant averaged level interpreted from one-dimensional results, and thus does not consider any latitudinal variation. This defect should be corrected in subsequent calculations.

Also shown in Figure 2 are comparisons of the vertical ozone profiles with the data of Hering and Borden (1964a, 1964b, 1965, 1967) (as summarized in the data compilation of Wu (1973)) in the northern hemisphere and the data reported by Dütsch (1971) in the southern hemisphere. The comparisons with Hering and Borden (1964a, 1964b, 1965, 1967) at the specified latitudes are in terms of ozone concentration (molecules/cm^3), whereas the data of Dütsch (1971) are in terms of ozone partial pressure (nb), since this is the form in which the data were presented. Comparisons with these data for altitudes below approximately 30 km show relatively good agreement for all the latitudes presented. However, for 60°N latitude the agreement with the data below 20 km is not as good: the Chapman-model result is in agreement with the observations only between 10 and 15 km. This indicates an inadequate transport of ozone at this location, which in turn demonstrates a local inadequacy in the specification of the parameterized transports.

Comparison of the numerical result with ozone observations above 30 km (Hilsenrath et al., (1972) above 30 km is shown for 40°N. Here the numerical results overpredict the local ozone concentration. This is typical of most of the results obtained with these specific chemical models; the problem should be resolved when the CIAP-specified chemical system, mentioned previously, is utilized. Most of the excess in the ozone column in the mid- and lower latitudes is a result of this overprediction of the ozone concentration at the higher altitudes.

Summer in Northern Hemisphere

Figure 3 shows the comparisons of the calculated meridional variation of the total ozone column with the observed data for the summer

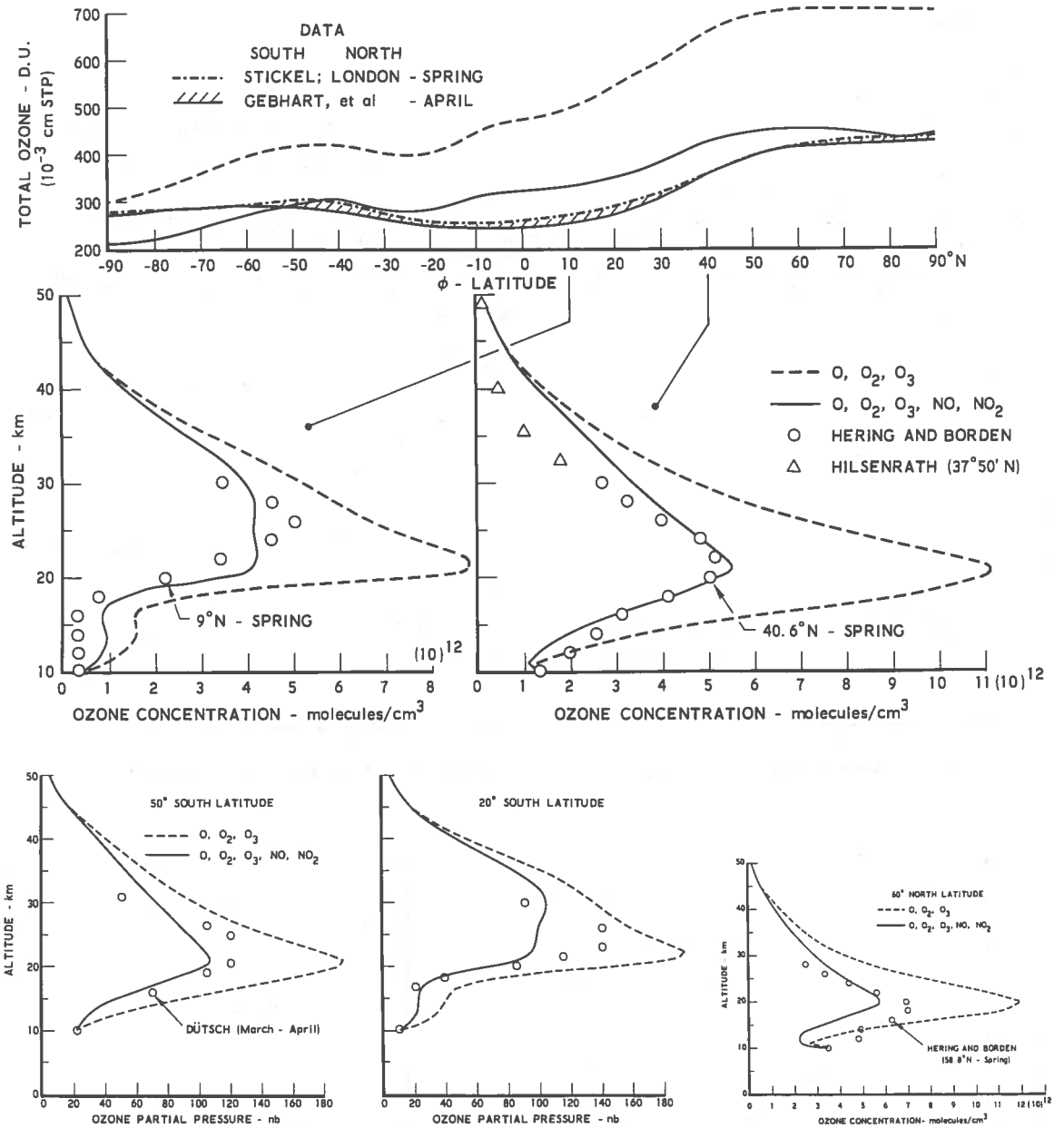

Figure 2. Spring in northern hemisphere: comparison of model results with observations of the meridional distribution of the total ozone column and vertical ozone profiles at selected latitudes.

season in the northern hemisphere. Here it can be seen that the Chapman model underpredicts the ozone column in the northern hemisphere at the higher latitudes, indicating the inadequacy of the transports in this local region. However, the results for the southern hemisphere show good agreement with the observations when NO_x is introduced. Comparisons of the vertical profiles at various latitudes in both hemispheres confirm that the southern-hemisphere ozone distributions are in good quantitative agreement with observations, while the northern-hemisphere ones are not. Since the data of Dütsch (1971) did not include distributions for summer for the southern hemisphere, the results were compared with northern-hemisphere distributions for winter.

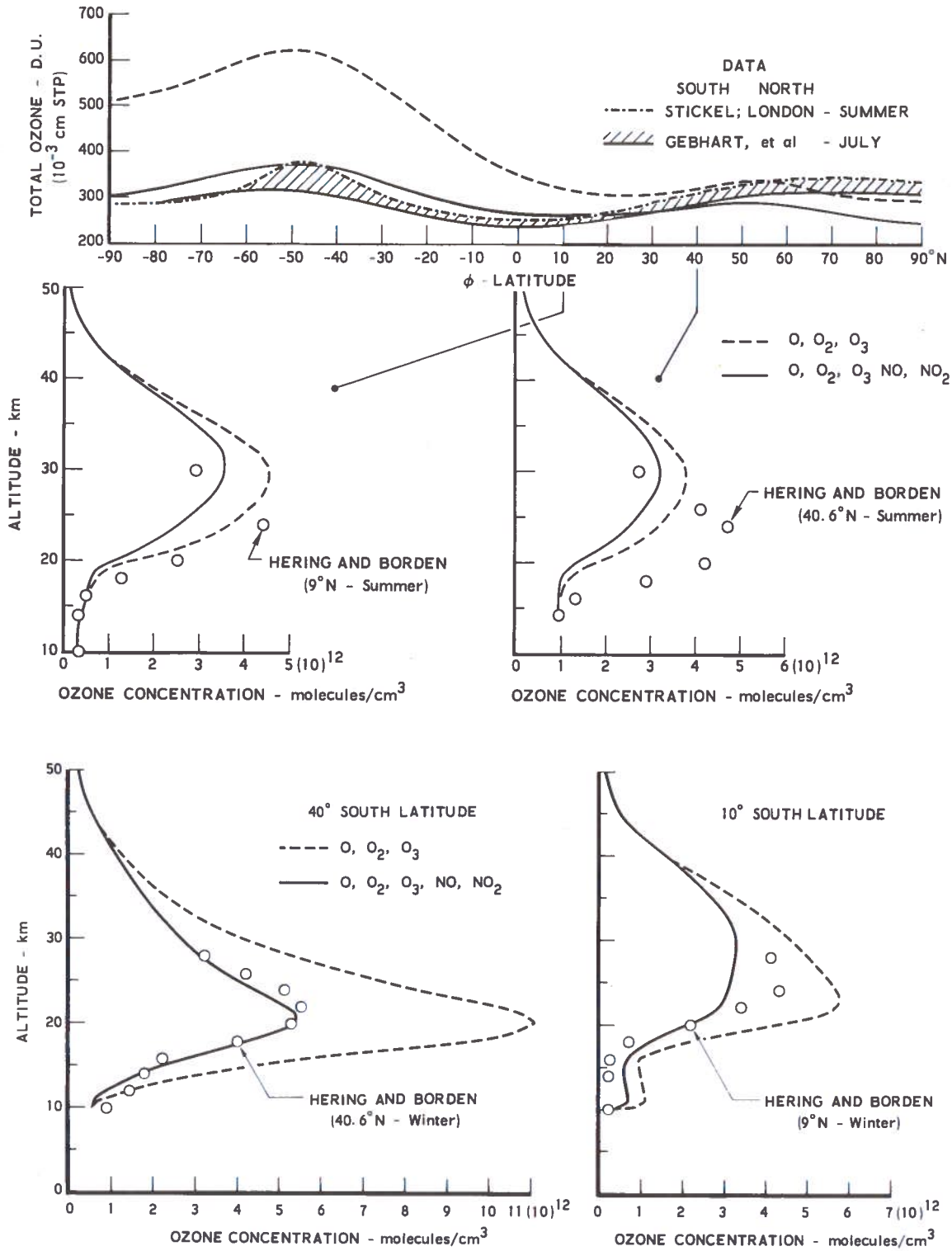

Figure 3. Summer in northern hemisphere: comparison of model results with observations of the meridional distribution of the total ozone column and vertical ozone profiles at selected latitudes.

This assumes that the seasons in one hemisphere can be reflected to the other hemisphere with a six-month time lapse, which is not entirely correct. However, the comparisons are in relatively good agreement for this case.

Fall in the Northern Hemisphere

Figure 4 shows similar comparisons for the fall season in the northern hemisphere. The Chapman scheme overpredicts the total ozone column but gives the correct meridional variation. However, when NO_x is introduced, the distribution is in closer agreement with the data and has the correct latitudinal variation, though the magnitude is still higher than the data's. Comparisons of the vertical profiles show good agreement at all latitudes, and indicate that the discrepancy in the total ozone column is due to the high-altitude overprediction, and also to an insufficient amount of NO_x in some regions. Subsequent results obtained for the CIAP chemical model should clarify this point further. However, the indication is that the parameterized transports are adequate for this season over the entire meridional plane.

Injection of Aircraft Emissions

In order to ascertain the effect of the injection of aircraft emissions on the total ozone column, a numerical experiment, in which a typical amount of effluents was injected into the atmosphere, was performed for the northern-hemisphere spring season. Here a flight corridor was assumed to be centered at 50°N latitude and an altitude of 20 km. NO was injected at this particular spatial point at the rate suggested by SCEP (1970), as modified by Johnston (1971). The computation was run until equilibrium was

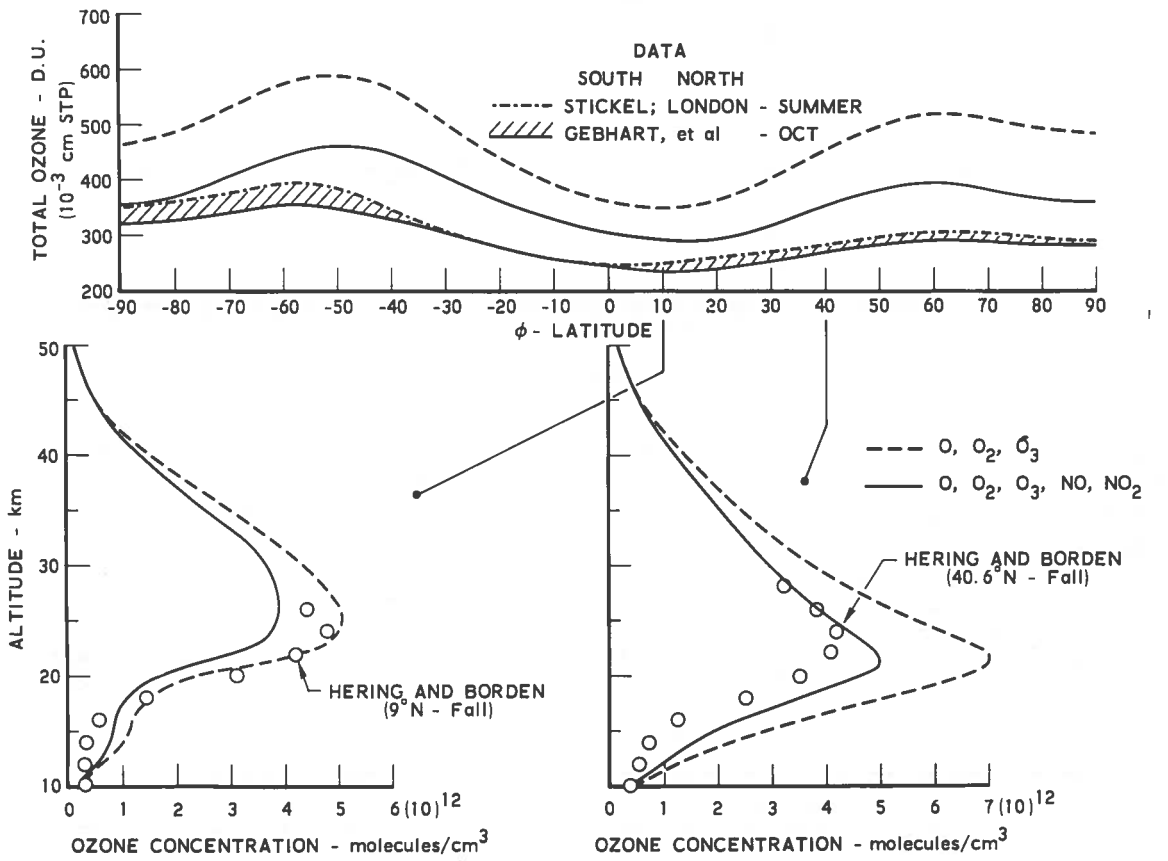

Figure 4. Fall in northern hemisphere: comparison of model results with observations of the meridional distribution of the total ozone column and vertical ozone profiles at selected latitudes.

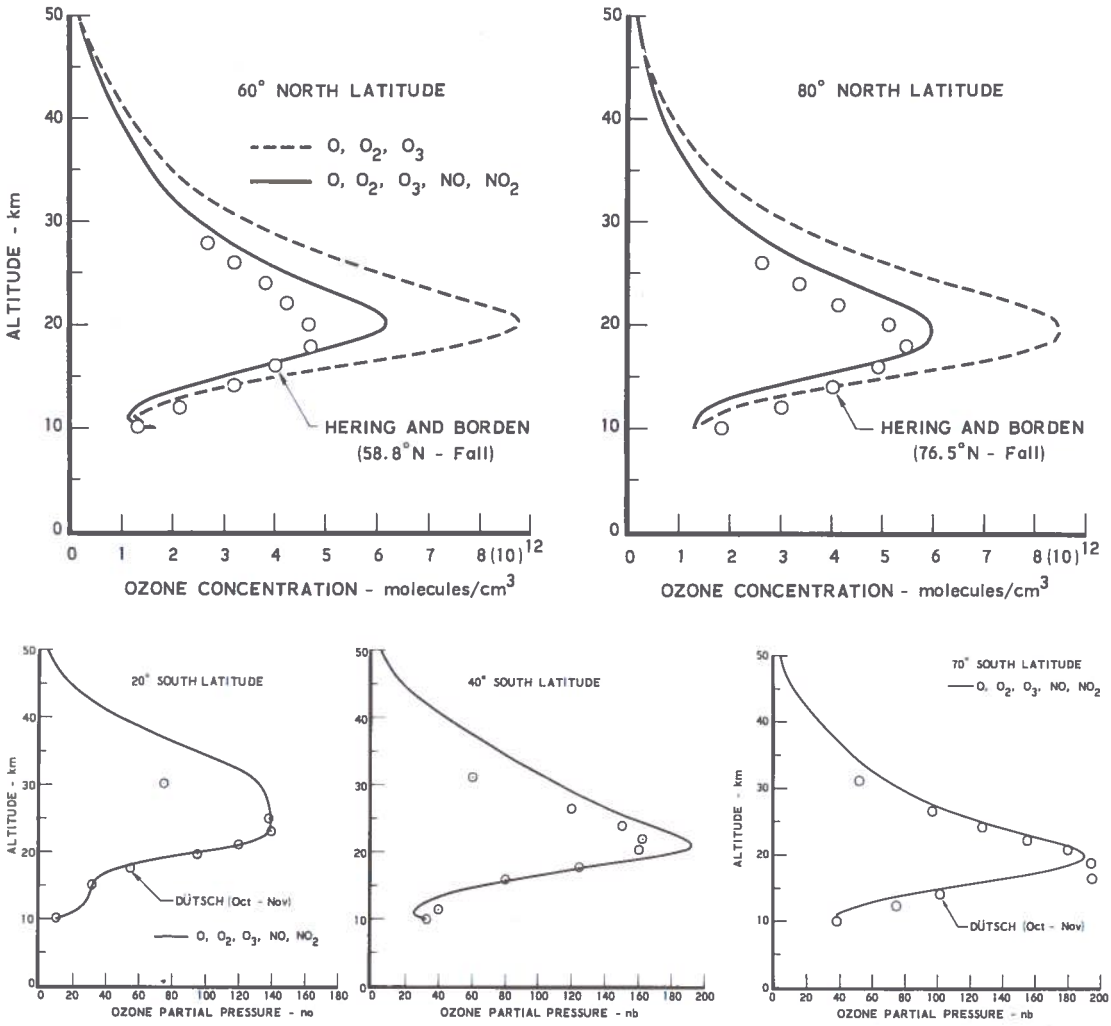

Figure 4 (continued).

attained; the percent decrease in ozone column as a function of latitude is shown in Figure 5. It can be seen that the percent decrease in the ozone column has a marked meridional variation, decreasing from approximately 50% near the flight corridor to approximately 20% in the southern hemisphere. The average global decrease is 32%. This can be compared to the one-dimensional-model result of Chang (1973), who calculated an average decrease of 27.9 percent using an identical chemical model.

In the one-dimensional model the injected NO was assumed to be uniformly distributed in a 1-km-thick global shell, whereas in the two-dimensional model the same total global amount of effluent was injected only in the specified flight corridor. The global averages predicted by both models are seen to be in good agreement;

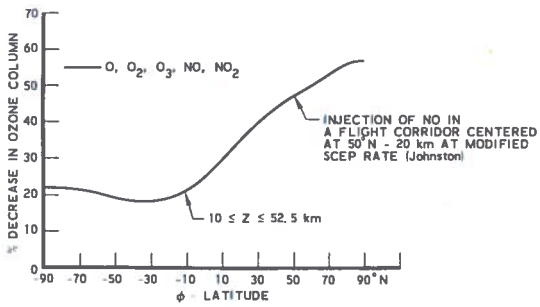

Figure 5. Meridional depletion of the ozone column ($10 \leq z \leq 52.5$ km) resulting from the injection of NO from a fleet of SST's.

however, the two-dimensional model does provide the meridional distribution, which is significant.

It is recognized that the inclusion of HNO_3 in the chemical system will decrease the effect of the injected NO by a factor of 2 to 4, so a similar injection calculation will be performed in a subsequent study which considers the CIAP chemical model.

SUMMARY AND CONCLUSIONS

A time-dependent two-dimensional parameterized-transport model has been developed to model the distribution of trace species in the lower regions of the atmosphere. Preliminary calculations using simplified chemical models have been compared to observed distributions of the total ozone column and also to observed vertical ozone profiles at various latitudes for the spring, summer, and fall seasons. The computations were carried out for the entire meridional plane and good agreement with observations was obtained. In certain areas, the model needs further study, including the northern hemisphere in summer.

Since overall good agreement with published ozone observations was achieved with this simplified chemical model (Chapman chemistry plus NO_x effect), further studies are being pursued with the recommended CIAP chemistry scheme. These steady-state results will be used as a basis for verifying the acceptability of the model parameterization for use in a fully time-dependent calculation.

A numerical experiment was performed to determine the effect on the total ozone column of NO injection in a North Atlantic flight corridor. The average global rate agrees with a corresponding one-dimensional-model global result. However, the meridional variation of the effect of this corridor injection is large; the southern and northern hemispheres differ by approximately a factor of three. Also, the maximum change near the flight corridor is nearly twice the global average.

ACKNOWLEDGMENTS

The authors would like to acknowledge the work of Dr. William S. Helliwell of The Aerospace Corporation, who constructed a very efficient complete code to carry out the numerical calculations. They are also indebted to Mr. Raymond F. Kramer of The Aerospace Corporation who assisted in obtaining these numerical results.

Special thanks are due to Dr. Fred Luther of Lawrence Livermore Laboratory, who graciously made his turbulent diffusivity data available to us in digitized form. Thanks are also due to Mr. Jean-François Louis of the University of Colorado and the National Center for Atmospheric Research, who graciously made his pressure- and temperature-field data, together with his mean meridional circulation results, available to us in digitized form.

This work was supported by the Department of Transportation under the Climatic Impact Assessment Program, and by The Aerospace Corporation's Research Program.

REFERENCES

Ackerman, M. (1971), "Ultraviolet solar radiation related to mesospheric processes," in *Mesospheric Models and Related Experiments*, ed. G. Fiocco, Springer-Verlag, New York, 149-159.

Chang, J.S. and W. Duewer (1973), "On the possible effect of NO_x injection in the stratosphere due to past atmospheric nuclear weapons tests," AIAA Paper No. 73-538 (Denver, June 1973).

Chang, J.S. (1973), "First Annual Report, DOT-CIAP Program," Lawrence Livermore Laboratory, UCRL-51336, B15-B22.

CIAP Monograph Series, Volume 3, U.S. Department of Transportation. NOTE: At present, these monographs exist only in an early draft form. They will be publicly available after completion in September 1974.

Dütsch, H.C. (1971), "Photochemistry of atmospheric ozone," in *Advances in Geophysics*, Vol. 15, ed. H.E. Landsberg and J. Van Mieghem, Academic Press, New York, 219-322.

Garvin, D. and R.F. Hampson (1973), "Atmospherical modeling and the chemical data problem," AIAA Paper No. 73-500 (Denver, June 1973).

Gebhart, R., R. Bojkov, and J. London (1970), "A comparison of observed and computer models," in *Beitrage zur Physik der Atmosphäre*, Vol. 43, 209-227.

Gudiksen, P.H., A.W. Fairhall, and R.J. Reed (1968), "Roles of mean meridional circulation and eddy diffusion in the transport of trace substances in the lower stratosphere," J. Geophys. Res. **73**, 1729.

Hering, W.S. (1964a), "Ozonesonde Observations Over North America, 1," Research Report AFCRL-64-30(I), Air Force Cambridge Research Laboratories, Bedford, Mass.

Hering, W.S. and T.R. Borden, Jr. (1964), "Ozonesonde Observations Over North America, 2," Environmental Research Papers No. 38, AFCRL-64-30(II).

Hering, W.S. and T.R. Borden, Jr. (1965), "Ozonesonde Observations Over North America, 3," Environmental Research Papers No. 133, AFCRL-64-30(III).

Hering, W.S. and T.R. Borden, Jr. (1967), "Ozonesonde Observations Over North America, 4," Environmental Research Papers No. 279, AFCRL-64-30(IV).

Hesstvedt, E. (1974), "Reduction of stratospheric ozone from high flying aircraft, studied in a two-dimensional photochemical model with transport," Canad. J. Chem. **52**, 1592-1598.

Hilsenrath, A.J., D.F. Heath, A.J. Krueger, W. Nordberg, C. Prabhakara, and J.S. Theon (1972), "Observations of the Global Structure of the Stratosphere and Mesosphere with Sounding Rockets and with Remote Sensing Techniques from Satellites," GSFC X-651-72-279, NASA Goddard Space Flight Center, Greenbelt, Maryland.

Hudson, R.D. and S.H. Mahle (1972), "Interpolation Constants for Calculation of Transmittance and Rate of Dissociation of Molecular Oxygen in the Mesosphere and Lower Thermosphere," NASA Technical Memorandum X-58084.

Johnston, H. (1971), "Catalytic Reduction of Stratospheric Ozone by Nitrogen Oxides," Lawrence Radiation Laboratory Report UCRL-20568.

Johnston, H., Shih-Ger Chang, and G. Whitten (1973), "Photolysis of Nitric Acid Vapor," Lawrence Berkeley Laboratory, LBL-1865.

London, J. (1963), "The distribution of total ozone in the northern hemisphere," in *Beitrage zur Physik der Atmosphäre*, Vol. 26, 254-263.

Louis, J.F. (1973), private communication.

Louis, J.F., J. London, and E. Danielsen (1974), "The interaction of radiation and the meridional circulation of the stratosphere," in *Proceedings of the International Conference on Structure, Composition and General Circulation of the Upper and Lower Atmosphere and Possible Anthropogenic Perturbations* (Melbourne, Jan. 1974), pub. IAMAP, 1205-1214.

Luther, F.M. (1973a), "Monthly Values of Eddy Diffusion Coefficients in the Lower Stratosphere," UCRL Report 74616, also AIAA Paper No. 73-498 (Denver, June 1973).

Luther, F.M. (1973b), private communication.

Newell, R.E., J.M. Wallace, and J.R. Mahoney (1966), "The general circulation of the atmosphere and its effects on the movement of trace substances, Part 2," Tellus **18**, 363-380.

Oort, A.H. and E.M. Rasmusson (1971), "Atmospheric Circulation Statistics," Professional Paper 5, National Oceanic and Atmospheric Administration.

Prabhakara, C. (1963), "Effect of non-photochemical processes on the meridional distribution and total amount of ozone," Mon. Wea. Rev. **91** (9), 417-437.

Rao, V.R. Krishna (1973), "Numerical experiments on the steady-state meridional structure and ozone distribution in the stratosphere," Mon. Wea. Rev. **101** (6), 510-527.

Rao, V.R. Krishna and A.D. Christie (1973), "The effects of water vapor and oxides of nitrogen on the ozone and temperature structure of the stratosphere," J. Atmos. Sci. **30**, 667-676.

Reed, R.J. and K.E. German (1965), "A contribution to the problem of stratosphere diffusion by large-scale mixing," Mon. Wea. Rev. **93**, 313-321.

SCEP (1970): *Man's Impact on the Global Environment: Assessment and Recommendations for Action*. Report of the study of critical environment problems (SCEP), MIT Press, Cambridge, Mass.

Shimazaki, R., D.J. Wuebbles, and T. Ogawa (1973a), "A two-dimensional theoretical model for stratospheric ozone density distributions in the meridional plane," AIAA Paper No. 73-541 (Denver, June 1973).

Shimazaki, T., T. Ogawa, and D.J. Wuebbles (1973b), "A theoretical model of minor constituents' distributions in the stratosphere including diurnal variations," presented at Symposium of Aeronomic Processes in the Stratosphere and Mesosphere, International Association for Geomagnetism and Aeronomy, Kyoto, Japan.

Stewart, R.W. and M.I. Hoffert (1973), "Stratospheric contamination experiments with a one-dimensional atmospheric model," AIAA Paper No. 73-531 (Denver, June 1973).

Stickel, P.R. (1970), "The annual variation of total ozone in the southern hemisphere," Mon. Wea. Rev. **98** (10), 787-788.

Victoria, K.J. and G.F. Widhopf (1972), "Numerical solution of the unsteady Navier-Stokes equations in curvilinear coordinates: the hypersonic blunt body merged layer problem," presented at the Third International Conference on Numerical Methods in Fluid Mechanics, University of Paris-Orsay, published in *Lecture Notes in Physics*, No. 19, Vol. II, Springer-Verlag, New York.

Whitten, R.C. and R.P. Turco (1973), "A model for studying the effects of injecting contaminants into the stratosphere and mesosphere," AIAA Paper No. 73-539 (Denver, June 1973).

Widhopf, G.F. and K.J. Victoria (1973), "On the solution of the unsteady Navier-Stokes equations including multicomponent finite rate chemistry," in *Computers and Fluids*, Vol. 1, 159-184.

Wofsy, S.C. and M.B. McElroy (1973), "On vertical mixing in the upper stratosphere and lower mesosphere," J. Geophys. Res. 78, 2619-2624.

Wu, Mao-Fou (1973), "Observations and Analysis of Trace Constituents in the Stratosphere," Environmental Research and Technology, Inc., Annual Report on Contract DOT-OS-20217.

DISCUSSION

CUNNOLD: I'd just like to emphasize that in two-dimensional models one must use coefficients which are consistent with the meridional circulations. If you look at the full-scale dynamical model results, there is a very strong self-cancellation between the two transports, particularly in mid-latitudes.

The other point is that you mentioned comparisons with southern-hemisphere ozone data, but in effect you are using eddy coefficients which are based on northern-hemisphere data.

WIDHOPF: We are limited by the data available for the turbulent diffusivities and meridional circulation in the troposphere and stratosphere. Comparisons with observations should indicate the adequacy of the parameterization used in the model. I have found that the use of another set of mean circulation data gave results which did not agree at all with available ozone measurements.

VUPPUTURI: When you incorporated NO_x, did you compute the NO_x distributions or did you specify them?

WIDHOPF: The NO_x distributions are calculated. The boundary conditions are specified, using the results of one-dimensional models which include the effect of NO_x and HNO_3.

LONDON: There are other southern-hemisphere data available, such as the cross-section of Kulkarni, and a whole host of southern-hemisphere data on vertical ozone distributions.

WIDHOPF: The only data I am familiar with are those of Dütsch.

LONDON: It's very unfortunate that people are starting to use that as a standard model. The data of Hering and Borden are just one longitudinal cross-section. The data of Dütsch were, unfortunately, developed in some cases for just two stations. By now, new cross-sections are being developed that give some improved values.

HOFFERT: Because of the importance of transports in the two-dimensional model, could you comment in a purely formal sense on whether it is possible to isolate the relative importance of diffusion versus advection in producing the high-latitude aspects of ozone? Would it be possible to get essentially the same results just by arbitrarily adjusting them?

WIDHOPF: I have not tried to independently vary the data to achieve good comparisons with observations, so I could not comment on that.

A ZONALLY AVERAGED CIRCULATION MODEL OF THE STRATOSPHERE INCORPORATING RADIATIVE HEATING AND OZONE PHOTOCHEMISTRY IN AN OXYGEN-HYDROGEN-NITROGEN ATMOSPHERE

R.K. RAO-VUPPUTURI
Atmospheric Environment Service
Downsview, Ontario, Canada

ABSTRACT: In the stratosphere, O_3, HO_x, N_2O, and NO_x are not only interdependent among themselves, they are coupled to the radiative and transport properties of the stratosphere. In view of these non-linear effects, it is appropriate to solve the continuity equations for ozone, HO_x, N_2O and NO_x simultaneously in a transport model.

In the study reported here, a zonally averaged model of the stratosphere, incorporating the interactions among ozone, HO_x, N_2O, NO_x, temperature, and the mean circulation, was developed under steady-state assumptions. The model was an extension of the two-dimensional steady-state model developed previously for the photochemical scheme of an oxygen-only atmosphere.

Using the classical photochemical scheme along with new rate coefficients, it was shown in the first experiment that the computed distribution of ozone was quite unrealistic as compared to the observations. However, by incorporating the additional reactions involving hydrogen and nitrogen compounds, a satisfactory agreement was achieved between the computed ozone distribution and the observations.

Along with the computed distribution of ozone, the meridional distributions of HO_x (HO and HO_2), N_2O, NO_x (NO, NO_2, and HNO_3), temperature, and the mean circulation were also derived for the summer and winter seasons. They are in general agreement with the available observations.

Sensitivity tests show that a 100% increase in the mixing ratio of water vapor reduces total ozone by only 2 to 4%, with highest percentage changes occurring in the high-latitude summer. On the other hand, a 100% increase in the NO_x source strength reduces total ozone by 10 to 16%, with the greatest percentage changes again taking place in the high-latitude summer.

INTRODUCTION

The problem of assessing the effects of natural concentrations of HO_x and NO_x, and their perturbation by a potential high-altitude fleet, on ozone balance and other meteorological elements is a complex one. First of all, it should be emphasized that in the normal stratosphere the concentrations of ozone, HO_x, and NO_x are mutually interdependent through the photochemical system of the oxygen-hydrogen-nitrogen atmosphere. In addition, the temperature structure, and consequently the large-scale motions, are largely determined by the ozone distribution through radiative heating, while the motions themselves influence the distribution of radiatively active gases such as ozone and other minor constituents. It seems clear that it is only by treating these non-linear interactions between the atmospheric composition, radiative heating, and air motions in numerical models that one can properly understand the behavior of naturally occurring trace substances in the stratosphere and evaluate their reactions to perturbations, including the feedback effects which may damp or magnify the initial effect of the changes.

The highly sophisticated three-dimensional general-circulation models of the troposphere and stratosphere (those of the GFDL, NCAR, and British Meteorological Office) leave out some of the important coupling effects between chemistry and dynamics because of certain limitations of computer size and availability. Although efforts are under way to introduce the much-needed interactions between atmospheric chemistry and dynamics in a less sophisticated three-dimensional model (that of Cunnold and coworkers at MIT), such a model cannot be expected to produce answers any sooner.

Despite the limitations of having to parameterize large-scale eddy processes, it has been shown recently (Rao, 1973) that the major interactions between atmospheric composition,

temperature, and the transport processes can be incorporated into a two-dimensional model.

This paper discusses the more recent results of a continuing investigation started two years ago, prompted by the general concern over the possible consequences of exhaust gases emitted by a potential fleet of high-altitude aircraft. In the previous paper (Rao-Vupputuri, 1974) the role of HO_x and NO_x in maintaining the ozone balance and the seasonal climate of the stratosphere was discussed in the light of the results of a two-dimensional steady-state model in which the distribution of NO_x has been specified. In the present study the constraint on NO_x is removed and it is allowed to interact freely with ozone and HO_x in the meridional transport model.

The object of this study is twofold. The first objective is to investigate the seasonal and latitudinal variations of ozone, temperature, HO_x, N_2O, NO_x, and the mean circulation in the normal stratosphere, taking into account the mutual interrelationships among them. After a satisfactory agreement between the model results and the observations has been obtained, the model is then applied to investigate the effects of increased HO_x and NO_x on total ozone.

TRANSPORT MODEL

The stratospheric transport model used for this study is the two-dimensional mean-circulation model developed by Rao-Vupputuri (1973). It runs from 10 km to 55 km in the vertical direction and from summer pole to winter pole in the horizontal. The grid spacing is approximately 3 km in the vertical and 10 degrees of latitude in the meridional direction.

The equations used are those governing the zonal momentum and heat balance and the continuity equations for the net mass and ozone, all of which are averaged with respect to time and longitude.

The eddy fluxes of heat and ozone were parameterized using a mixing-length representation on a sloping surface in the meridional plane (Reed and German, 1965). The eddy fluxes of momentum in the horizontal direction, however, were related to the meridional thermal gradients (Williams and Davies, 1965). The diffusion coefficients k_{yy}, k_{yz}, k_{zz} were derived from heat-flux and temperature data in the stratosphere as given by Reed and German. The radiational heating and cooling was incorporated in a form which allows for the major interactions among ozone, temperature, and mean circulation in the model.

The boundary conditions are that both temperature and ozone mixing ratio are specified at the lower and upper boundaries, and the conditions of zero horizontal flux are assumed at both poles. The seasonal values of zonal winds are specified at 10 km altitude, and the vertical components of mean motion based on thermal equilibrium (Murgatroyd and Singleton, 1961) are used at the top boundary. Furthermore, both the zonal wind and the north-south component of mean motion are assumed to be antisymmetric with respect to the poles. The sensitivity of the numerical solution to each of these boundary conditions has been tested and documented by Rao (1973).

PHOTOCHEMICAL CONSIDERATIONS

The only mechanism by which ozone is produced in the earth's atmosphere is photodissociation of molecular oxygen and subsequent recombination of atomic oxygen with the oxygen molecule in the presence of third particles (Chapman, 1930). However, ozone is destroyed not only by photodissociation and by recombination with atomic oxygen but also by the catalytic chains of reactions involving odd-hydrogen and odd-nitrogen compounds. The principal chemical and photochemical interactions leading to the formation and destruction of ozone, odd hydrogen, and odd nitrogen are listed in Table 1. The choice of reactions and rate coefficients is based on the simplified sets of chemical reactions prepared recently by Johnston (1973) and recommended for incorporation into CIAP's transport models. The additional reactions involving hydrogen and nitrogen compounds and their implications for the ozone layer have been discussed rather extensively in the recent literature (Hampson, 1965; Hunt, 1966; Crutzen, 1969, 1971; Leovy, 1969; Johnston, 1971, 1973; Hesstvedt, 1973; Brasseur and Nicolet, 1973; Rao and Christie, 1973; Rao-Vupputuri, 1973; and others). The primary aim in this paper is to highlight the quantitative role played by these additional reactions in the ozone and temperature structure of the stratosphere under the combined influences of radiative-photochemical effects and transport processes.

Table 1. The Important Photochemical Reactions Affecting the Ozone Concentration in the Stratosphere

	Reactions	Rate Coefficients*
R1	$O_2 + h\nu \xrightarrow{\lambda < 0.25\mu} O + O$	J_1 (Solar-flux-dependent, see text)
R2	$O + O_2 + M \rightarrow O_3 + M$	$K_2 = 1.07 \times 10^{-34} \exp(510/T)$
R3	$O + O_3 \rightarrow O_2 + O_2$	$K_3 = 1.9 \times 10^{-11} \exp(-2300/T)$
R4	$O_3 + h\nu \xrightarrow{\lambda < 1.1\mu} O_2 + O$	J_4 (Solar-flux-dependent, see text)
R5	$O_3 + h\nu \xrightarrow{\lambda < 0.31\mu} O_2 + O(^1D)$	J_5 (Solar-flux-dependent)
R6	$O(^1D) + O_3 \rightarrow O_2 + O_2$	$K_6 = 2.5 \times 10^{-10}$
R7	$O(^1D) + M \rightarrow O + M$	$K_7 = 3.2 \times 10^{-11}$
R8	$NO_2 + h\nu \xrightarrow{\lambda < 0.41\mu} NO + O$	J_8 (Solar-flux-dependent, see text)
R9	$NO + O + M \rightarrow NO_2 + M$	$K_9 = 6.9 \times 10^{-32}$
R10	$NO_2 + O \rightarrow NO + O_2$	$K_{10} = 9.1 \times 10^{-12}$
R11	$NO + O_3 \rightarrow NO_2 + O_2$	$K_{11} = 9 \times 10^{-13} \exp(-1200/T)$
R12	$N_2O + h\nu \xrightarrow{\lambda < 0.34\mu} N_2 + O$	J_{12} (Solar-flux-dependent, see text)
R13	$N_2O + O(^1D) \rightarrow N_2 + O_2$	$K_{13} = 6.6 \times 10^{-11}$
R14	$N_2O + O(^1D) \rightarrow NO + NO$	$K_{14} = 6.6 \times 10^{-11}$
R15	$NO + h\nu \xrightarrow{\lambda < 0.19\mu} N + O$	J_{15} (Solar-flux-dependent, see text)
R16	$N + O_2 \rightarrow NO + O$	$K_{16} = 1.02 \times 10^{-14} T \exp(-3130/T)$
R17	$N + NO \rightarrow N_2 + O$	$K_{17} = 5.1 \times 10^{-11} \exp(-170/T)$
R18	$O(^1D) + H_2O \rightarrow 2\,HO$	$K_{18} = 2.8 \times 10^{-10}$
R19	$O(^1D) + CH_4 \rightarrow HO + CH_3$	$K_{19} = 2.4 \times 10^{-10}$
R20	$HNO_3 + h\nu \xrightarrow{\lambda < 0.55\mu} HO + NO_2$	J_{20} (Solar-flux-dependent, see text)
R21	$HO + O_3 \rightarrow HO_2 + O_2$	$K_{21} = 1.3 \times 10^{-12} \exp(-956/T)$
R22	$HO + O \rightarrow O_2 + H$	$K_{22} = 4.2 \times 10^{-11}$
R23	$HO_2 + O_3 \rightarrow HO + 2O_2$	$K_{23} = 1.0 \times 10^{-12} \exp(-1875/T)$
R24	$HO_2 + O \rightarrow HO + O_2$	$K_{24} = 1.0 \times 10^{-11}$
R25	$H + O_2 + M \rightarrow HO_2 + M$	$K_{25} = 2.1 \times 10^{-32}$
R26	$H + O_3 \rightarrow HO + O_2$	$K_{26} = 2.6 \times 10^{-11}$
R27	$HO_2 + HO_2 \rightarrow H_2O_2 + O_2$	$K_{27} = 3 \times 10^{-11} \exp(-560/T)$
R28	$HO + HO_2 \rightarrow H_2O + O_2$	$K_{28} = 1.1 \times 10^{-10}$
R29	$HO + NO_2 + M \rightarrow HNO_3 + M$	K_{29} (height-dependent, see Table 2)
R30	$HO + HNO_3 \rightarrow H_2O + NO_3$	$K_{30} = 1.3 \times 10^{-13}$

* In units of cm^3 $molec^{-1}$ sec^{-1} for second-order reactions, and of cm^6 $molec^{-2}$ sec^{-1} for third-order reactions.

In this study it is more convenient to write the photochemical differential equations by combining the individual species which are in photochemical equilibrium among themselves. By this procedure the photochemical tendency equations for odd oxygen* ($[O_x] = [O(^1D)] + [O] + [O_3]$), odd hydrogen ($[HO_x] = [H] + [HO] + [HO_2]$) and odd nitrogen ($[NO_x] = [N] + [NO] + [NO_2] + [HNO_3]$†) can be written as:

$$\frac{d[O_x]}{dt} = 2J_1[O_2] - 2K_3[O][O_3] + J_8[NO_2] - K_{10}[NO_2][O] - K_{11}[NO][O_3] - (K_{21}[O_3] + K_{22}[O])[HO] - (K_{23}[O_3] + K_{24}[O])[HO_2] - (K_{18}[H_2O] + K_{19}[CH_4])[O(^1D)] - K_6[O(^1D)][O_3] - K_9[NO][O][M] - K_{26}[H][O_3] \quad (1)$$

$$\frac{d[HO_x]}{dt} = 2K_{18}[H_2O][O(^1D)] + K_{19}[CH_4][O(^1D)] + J_{20}[HNO_3] - K_{27}[HO_2]^2 - K_{28}[HO][HO_2] - K_{29}[HO][NO_2][M] - K_{30}[HO][HNO_3] \quad (2)$$

$$\frac{d[NO_x]}{dt} = 2K_{14}[N_2O][O(^1D)] - 2K_{17}[N][NO] - K_{30}[HO][HNO_3] + 2[N_2]J(N_2) \quad (3)$$

The last term in equation (3) represents the production of odd nitrogen through direct or indirect dissociation of molecular nitrogen by cosmic rays, as discussed by Brasseur and Nicolet (1973).

In the real atmosphere O_x, HO_x and NO_x are not in photochemical equilibrium with each other. However, in the sunlit stratosphere, equilibrium relationships are quickly established among individual species in each group. Thus, the following relations are considered valid under daytime conditions.

$$O(^1D) = \frac{J_5[O_3]}{K_7[M]} \quad (4)$$

$$[O] = \frac{J_4[O_3] + J_8[NO_2]}{K_2[M][O_2]} \approx \frac{J_4[O_3]}{K_2[M][O_2]} \quad (J_8[NO_2] \ll J_4[O_3]) \quad (5)$$

$$[N] = \frac{J_{15}[NO] + 2[N_2]J(N_2)}{K_{17}[NO] + K_{16}[O_2]} \quad (6)$$

$$\frac{[H]}{[HO]} = \frac{K_{22}[O]}{K_{25}[O_2][M]} \quad (7)$$

$$\frac{[HO_2]}{[HO]} = \frac{K_{21}[O_3] + K_{22}[O]}{K_{23}[O_3] + K_{24}[O]} \quad (8)$$

$$\frac{[NO_2]}{[NO]} = \frac{K_{11}[O_3]}{J_8 + K_{10}[O]} \quad (9)$$

$$\frac{[HNO_3]}{[NO_2]} = \frac{K_{29}[M][HO]}{J_{20} + K_{30}[HO]} \quad (10)$$

In order to close the photochemical system we still require three more equations for $[H_2O]$, $[CH_4]$, and $[N_2O]$. For the purposes of this study, the concentrations of water vapor and methane are assumed to be known. An additional equation is formed to compute the concentration of nitrous oxide from natural sources and sinks. The photochemical tendency equation for nitrous oxide is:

$$\frac{d[N_2O]}{dt} = -J_{12}[N_2O] - (K_{13} + K_{14}) \cdot [N_2O][O(^1D)] \quad (11)$$

In the stratosphere $d[O_x]/dt$, $d[HO_x]/dt$, and $d[NO_x]/dt$ are essentially equal to $d[O_3]/dt$, $d([HO] + [HO_2])/dt$, and $d([NO] + [NO_2] + [HNO_3])/dt$ respectively because of relatively low concentrations for the chemical species $[O(^1D)]$, $[O]$, $[H]$, and $[N]$. Furthermore, the

* Brackets around chemical species represent concentrations in units of particles per cubic centimeter.

† HNO_3 is treated only as odd nitrogen, although its interaction with the hydrogen system is allowed.

third and last four terms on the right-hand side of equation (1) are small compared to the remaining terms in the equation. The effect of neglecting these terms is negligibly small for the ozone balance in the stratosphere. Making use of these considerations and applying the equilibrium relationships when necessary, equations (1) to (3) and (11) can be rewritten in a form that is more suitable to combine them in a transport model. Thus we have*:

$$\frac{d\chi}{dt} = A J_1 - B J_4 \chi^2 - \chi \left\{ C J_4 \chi(NO_2) + D \chi(HO) + E J_4 \chi(HO) \right\} \tag{12}$$

$$\frac{d\chi(HO_x)}{dt} = F J_5 \alpha_3 \chi + J_{20} \chi(HNO_3) - G \chi^2(HO_x) - \left\{ H \chi(NO_2) + I \chi(HNO_3) \right\} \chi(HO_x) \tag{13}$$

$$\frac{d\chi(NO_x)}{dt} = \frac{2 K_{14} \chi(N_2O) J_5 \alpha_3 \chi}{K_7} - \frac{K_{30} R_1 R_2 [M] \chi(OH) \chi(NO_x)}{R_3} - \frac{2 K_{17} J_{15} \chi^2(NO_x)}{R_3 (K_{17} \chi(NO_x) + \alpha R_3 K_{16})} \cdot 2 \chi(N_2) J(N_2) \frac{\alpha R_3 K_{16} - K_{17} \chi(NO_x)}{K_{17} \chi(NO_x) + \alpha R_3 K_{16}} \tag{14}$$

$$\frac{d\chi(N_2O)}{dt} = J_{12} \chi(N_2O) - \frac{(K_{13} + K_{14}) J_5 \alpha_3 \chi \chi(N_2O)}{K_7} \tag{15}$$

where

$$A = 2 \left(\frac{\rho_2}{\rho_{air}} \right) \frac{m_3}{m_2}$$

$$B = \frac{2}{(\rho_2/\rho_{air})[M]} \frac{K_3}{K_2} \frac{m_2}{m_3}$$

$$[M] = P/RTm$$

$$C = \frac{2}{\alpha[M]} \frac{K_{10}}{K_2}$$

$$\alpha = \frac{[O_2]}{[M]}$$

$$D = 2 K_{21} [M]$$

$$E = \frac{2}{\alpha[M]} \frac{K_{22}}{K_2}$$

$$F = \frac{2 K_{18} \chi(H_2O) + K_{19} \chi(CH_4)}{K_7}$$

$$\alpha_3 = m/m_3$$

$$G = \frac{K_{27} [M] \beta^2 + K_{28} [M] \beta}{(\beta+1)^2}$$

$$H = \frac{(K_{29} [M]) [M]}{(\beta+1)}$$

$$I = \frac{K_{30} [M]}{(\beta+1)}$$

$$\beta = \frac{\chi(HO_2)}{\chi(HO)} = \frac{\alpha K_2 K_{21} [M]^2 + K_{22} J_4}{\alpha K_2 K_{23} [M]^2 + K_{24} J_4}$$

$$\frac{\chi(HO_x)}{\chi(HO)} = 1 + \beta$$

$$R_1 = \frac{\chi(NO_2)}{\chi(NO)} = \frac{\alpha K_{11} K_2 [M]^2 \alpha_3 \chi}{\alpha K_2 [M] J_8 + K_{10} J_4 \alpha_3 \chi}$$

$$R_2 = \frac{\chi(HNO_3)}{\chi(NO_2)} = \frac{(K_{29} [M])[M] \chi(HO)}{J_{20} + K_{30} [M] \chi(HO)}$$

$$R_3 = \frac{\chi(NO_x)}{\chi(NO)} = 1 + R_1 + R_1 R_2$$

χ mass mixing ratio of ozone, or volume mixing ratio of species given

m, m_2, m_3 molecular masses of air, oxygen, and ozone

* From here on all the chemical species will be expressed in units of volume mixing ratio, except for ozone which will be expressed in units of mass mixing ratio.

$[O_2]$, [M]	number densities of molecular oxygen and air
ρ_2	density of molecular oxygen
P	pressure
T	temperature
R	gas constant
$(K_{29}[M])$	height-dependent reaction coefficient of reaction R_{29} (see Table 2)

Table 2. The Rate Coefficient ($K_{29}[M]$) for Reaction R_{29} as a Function of Height

Height (km)	Temperature (°K)	$K_{29}[M]$ (10^{-12} cm^3 sec^{-1})
15	220	3.2
20	217	2.5
25	222	1.6
30	227	0.96
35	235	0.55
40	250	0.27
45	260	0.14

The second term in equation (14) has to be included because of the assumption that NO_3 is a sink for NO_x. There appears to be some doubt as to the validity of this assumption. It can be argued that NO_3 can be converted into NO or NO_2 rapidly by photodissociation. In view of this apparent controversy, this term is deleted in the present experiment, except for one case in which its effect on total ozone is studied.

As one can see from equations (12) to (15), the constituent mixing ratios of O_3, HO_x, NO_x, and N_2O are not only mutually interdependent, but are also coupled to the radiative and transport properties of the stratosphere through the ozone continuity equation. In view of these non-linear effects, it is more appropriate to solve the continuity equations for ozone, HO_x, NO_x, and N_2O simultaneously in a transport model.

SOLAR FLUXES AND PHOTODISSOCIATION PARAMETERS

In order to compute photodissociation rates and the solar heating by ozone in the model, we require spectral data on solar intensities outside the atmosphere, absorption cross-sections and quantum yields for the chemical species under consideration, and the scattering cross-section for air. The data on solar fluxes, absorption cross-sections and quantum yields for ozone and molecular oxygen, and the scattering cross-sections for air were taken from Byron-Scott (1967); the method of computing J_1, J_4 (the dissociation rates for oxygen and ozone), and the solar heating by ozone was described by Rao (1970, 1973). The spectral domain considered covers the wavenumber range from 13,500 cm^{-1} to 59,375 cm^{-1} (168-741 nm). It includes modified spectral data published by Brewer and Wilson (1965) within the 41,237-55,555 cm^{-1} (180-242 nm) wavenumber range.

A more recent data compilation on solar fluxes and absorption cross-sections by Ackerman et al. (1970 shows values of solar intensities and absorption cross-sections for molecular oxygen which are much higher than the values tabulated by Brewer and Wilson (1965), especially around 220 nm (the values differ roughly by a factor of three in solar fluxes and of two in cross-sections of O_2). In view of this discrepancy, the sensitivity of the latitudinal distribution of total ozone column has been tested by using the two sets of spectral data (see Rao-Vupputuri (1974)).

We also require additional spectral data on absorption cross-sections of N_2O, NO, NO_2, and HNO_3 to compute J_{12}, J_{15}, J_8, and J_{20}. The photodissociation cross-sections of N_2O and HNO_3 are taken from Bates and Hays (1967) and Johnston and Graham (1973) respectively. In the case of NO_2, the dissociation rates computed recently by Crutzen (1971) are adopted for this study.

The problem of determining the photodissociation rates of NO is a difficult one, since it requires a detailed knowledge of the absorption spectrum in the Schumann-Runge bands of molecular oxygen. Recently Cieslik and Nicolet (1973) have attempted to calculate J_{15} in the stratosphere using the detailed cross-sections of molecular oxygen determined by Ackerman et al. (1970), and their values are used here.

As far as the production of atomic nitrogen ($2[N_2]J[N_2]$) by cosmic rays is concerned, a value of 5 molecules cm^{-3} sec^{-1} is chosen arbitrarily, on the basis of the study by Brasseur and Nicolet (1973).

As mentioned earlier, H_2O and CH_4 are not treated as variables in this experiment; instead we

have used constant volume mixing ratios of 3×10^{-6} for water vapor and 1.5×10^{-6} for methane.

DISCUSSION OF RESULTS

In order to assess the role of HO_x and NO_x on ozone and thermal balance in the normal stratosphere, experiments were performed under two different photochemical conditions. The first experiment incorporates only the Chapman reaction scheme (O_2-only atmosphere). In the second experiment additional reactions involving water substances and oxides of nitrogen are added. In this paper it is possible only to give preliminary results and discuss them briefly; complete analysis and discussion of the results will be given in a future paper.

Figures 1 and 2 show the computed meridional distributions of ozone and temperature for summer and winter seasons, in the first experiment. As expected from the new reaction coefficients for the classical reaction scheme (Rao-Vupputuri, 1974), the computed ozone is far in excess of that observed, particularly around the level of the ozone maximum (see Figure 1). It is clear from Figure 1 that one cannot explain the observed distribution of ozone by the classical reaction scheme alone using the new reaction coefficients. Like the ozone distribution, the temperature in the middle and upper stratosphere has also been overestimated (see Figure 2) by 5 to 10°K, with the greatest disagreement occurring in the summer upper stratosphere. In view of the present discrepancy between the classical-scheme predictions and the observations, it is of importance to see how much it can be offset by the additional photochemical processes involving water substances and nitrogen oxides.

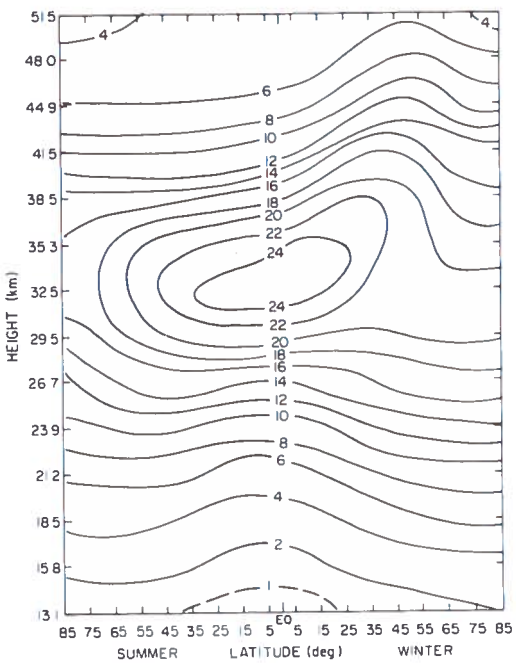

Figure 1. Meridional distribution of ozone mixing ratio ($\mu g\ g^{-1}$) using the classical reaction scheme (O_2-O-M only, experiment 1).

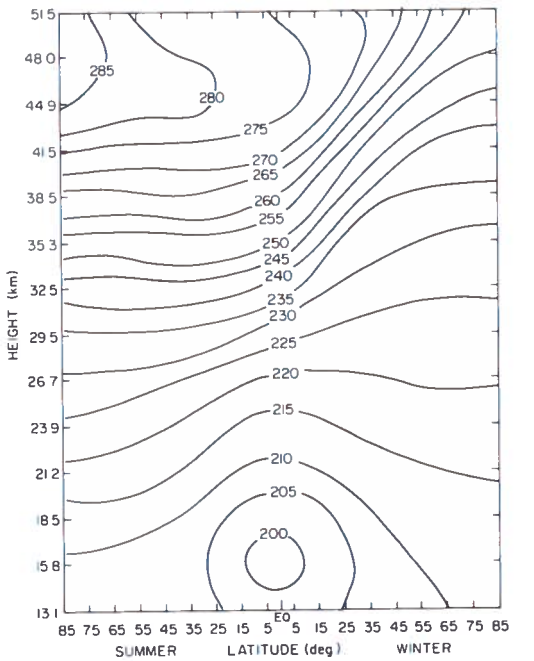

Figure 2. Meridional distribution of temperature (°K) using the classical reaction scheme (O_2-O-M only, experiment 1).

Figures 3 to 11 give the meridional distributions of ozone, temperature, HO, HO_2, N_2O, NO_x, NO, NO_2, and HNO_3, which were derived in the second experiment in a self-consistent manner under the combined influence of photochemistry, radiation, and transport processes. Also derived as a part of the simultaneous solution in the second experiment were the three components of mean circulation which are not shown here. The most significant conclusion that can be drawn from these figures is that the natural sources and sinks of HO_x and NO_x can indeed play a substantial role in the ozone and thermal balances of the stratosphere, and can

contribute to achieving a satisfactory agreement between the computed distributions of ozone and temperature and those observed. Note, for instance, that the distribution of ozone mixing ratio in Figure 3 has several features that are in good agreement with the observations. The height of the ozone maximum and its magnitude are calculated correctly. The ozone ridge in the winter upper stratosphere (which is caused by the inverse temperature dependence of the photochemical-steady-state ozone concentration through the rate coefficients) is also shown by the ozone observations based on BUV data (Krueger et al., 1972). Consistent with the ozone distribution, the computed temperature distribution is also in better agreement with the observations than is that of the classical reaction scheme alone. In this experiment it is rather difficult to separate the individual effects of HO_x and NO_x on ozone and temperature structure because of the complex interactions among them. However, it has been shown previously that the nitrogen oxides have substantial effects on ozone and temperature structure in the middle stratosphere, while the effects of water

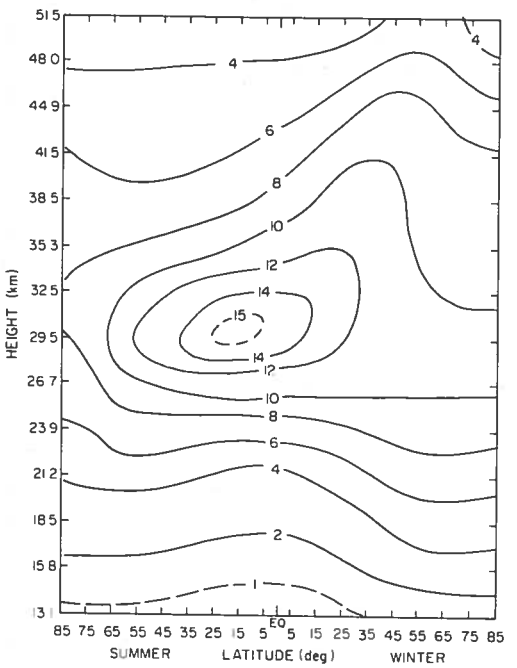

Figure 3. Meridional distribution of ozone mixing ratio ($\mu g\ g^{-1}$) using the reaction scheme of an oxygen-hydrogen-nitrogen atmosphere in a fully interactive transport model (experiment 2).

substances are significant in the upper stratosphere. In addition, both HO_x and NO_x contribute to significant ozone decreases in the lower stratosphere, although their effect on temperature is small.

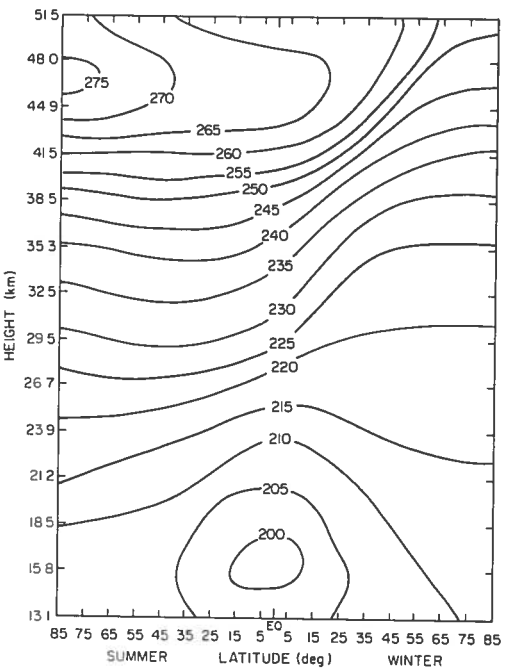

Figure 4. Meridional distribution of temperature (°K) derived in the same model as in Figure 3.

The predominant chemical process leading to the formation of HO_x (HO and HO_2) radicals in the normal stratosphere is the reaction between H_2O and the electronically excited oxygen atom $O(^1D)$, with additional contributions from the reaction between CH_4 and $O(^1D)$ and photodissociation of HNO_3. The termination reactions R_{29} and R_{30}, on the other hand, act as sinks for HO_x radicals. However, the ultimate distribution of HO_x in the atmosphere is determined by the interplay between ozone, HO_x, NO_x, and transport processes.

Figures 5 and 6 show the meridional distributions of HO and HO_2 concentrations for summer and winter seasons. Both these species show strong latitudinal and height variations in the stratosphere. The HO radical shows maximum concentration around 42 km in the summer upper stratosphere, whereas the maximum concentration of HO_2 roughly coincides with the level of the ozone maximum. The time constant

(time to achieve photochemical equilibrium) of the HO_x system is small compared to those of the ozone and NO_x systems in the stratosphere, and thus the transport processes do not appear to play a significant role in the distribution of HO and HO_2 (see Figures 5 and 6).

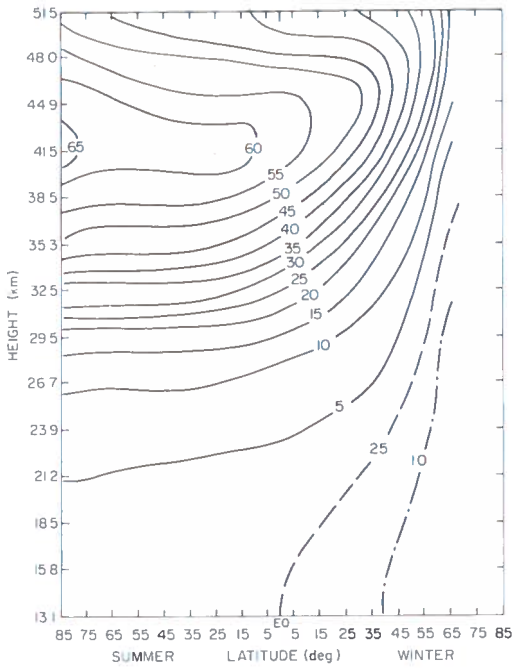

Figure 5. Meridional distribution of hydroxyl radical (OH) concentration (units 10^5 particles cm^{-3}) derived in the same model as in Figure 3.

There are no measurements of HO and HO_2 to compare with the model calculations. However, the computed distributions of HO and HO_2 should be considered reliable, in the sense that these radicals, together with the NO_x distribution, explain the ozone and temperature structure of the normal stratosphere in a self-consistent fashion.

N_2O is created at the earth's surface through biological activity, and it diffuses upward. In the stratosphere its destruction by photodissociation and recombination with $O(^1D)$ provides the predominant source of NO_x. Since both N_2O and NO_x are influenced by ozone (through $O(^1D)$ and photodissociation rates), the concentration of which is in turn controlled by NO_x, the final distributions of N_2O and NO_x again result from the complex mutual interaction between the oxygen-hydrogen-nitrogen photochemical system and the transport processes.

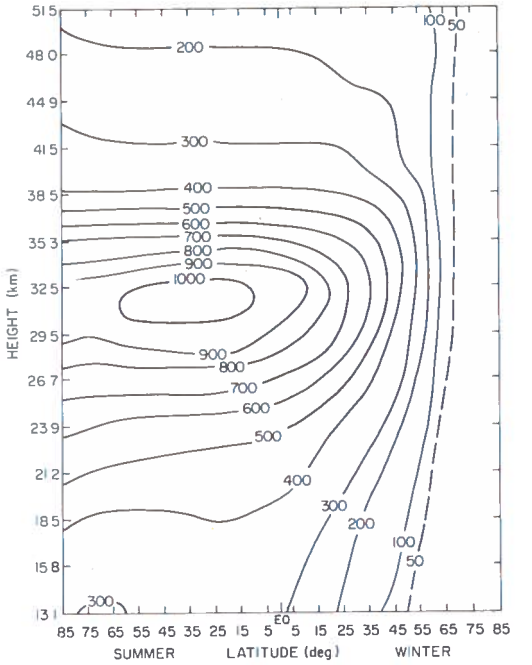

Figure 6. Meridional distribution of hydroperoxyl (HO_2) concentration (units 10^5 particles cm^{-3}) derived in the same model as in Figure 3.

Figures 7 and 8 show the meridional distributions of N_2O and NO_x for summer and winter seasons. The resulting distributions of NO, NO_2, and HNO_3 are illustrated in Figures 9, 10, and 11.

The distribution of N_2O (see Figure 7) shows that in the stratosphere the mixing ratio decreases with height from the lower boundary to ≈ 42 km faster in winter (factor of 8) than in summer (factor of 4). In the horizontal, the N_2O mixing ratio decreases from the tropics to the high latitudes in the lower stratosphere and from the summer pole to the winter pole in the upper stratosphere. The amplitude of variation, however, is small in the lower stratosphere compared to the higher levels. In the case of the NO_x mixing ratio, its distribution in the lower stratosphere resembles that of ozone, although the amplitude of the mixing-ratio increase from tropics to high latitudes is smaller than that of ozone. The height of the NO_x maximum, and its variation above that height, seem to be strongly influenced by the photochemical sink term associated with the reaction R17.

Again, the present observational data on N_2O and NO_x (NO, NO_2, and HNO_3) is insuffi-

cient for making detailed comparison with the model results. However, the computed results for NO, NO_2, and HNO_3 (see Figures 9, 10, and 11)

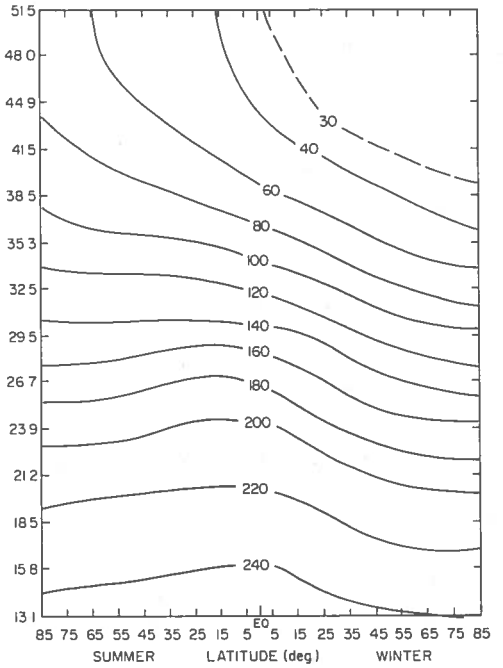

Figure 7. Meridional cross-section of N_2O mixing ratio (ppb) derived in the same model as in Figure 3.

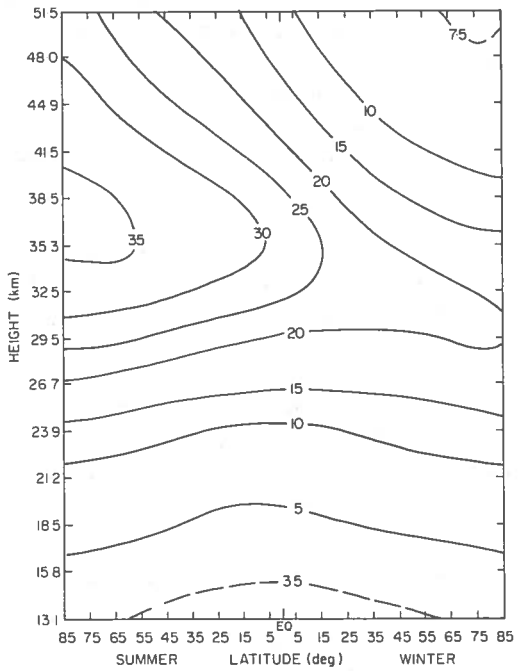

Figure 8. Meridional cross-section of NO_x mixing ratio (ppb) derived in the same model as in Figure 3.

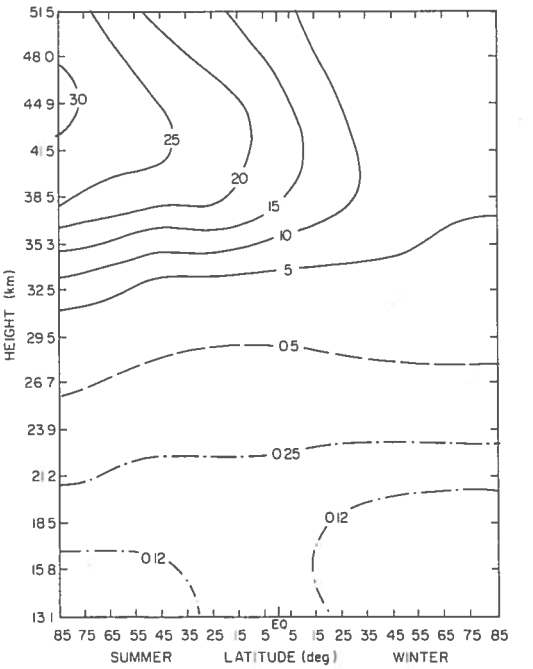

Figure 9. Meridional cross-section of nitric oxide (NO) mixing ratio (ppb) derived in the same model as in Figure 3, and based on the NO_x distribution in Figure 8.

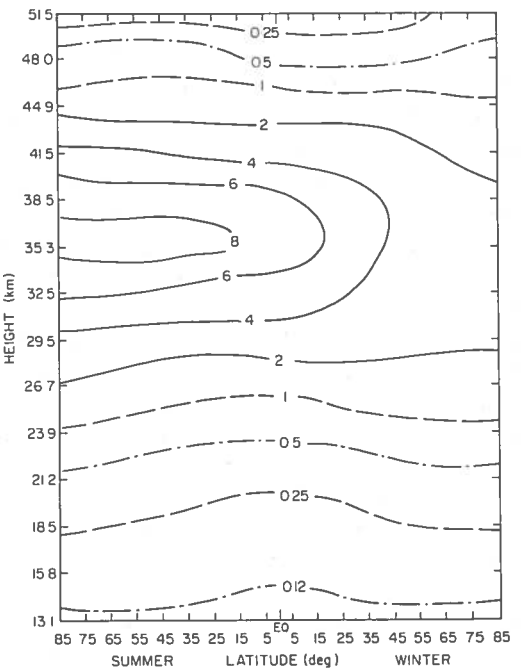

Figure 10. Meridional cross-section of nitrogen dioxide (NO_2) mixing ratio (ppb) derived in the same model as in Figure 3, and based on the NO_x distribution in Figure 8.

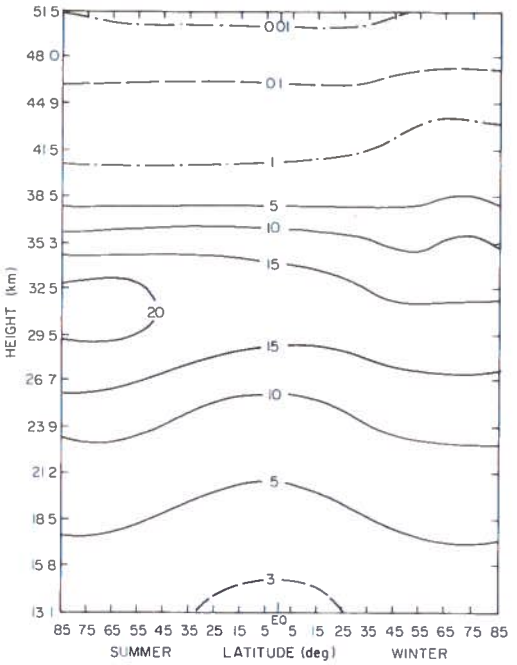

Figure 11. Meridional cross-section of nitric acid (HNO_3) mixing ratio (ppb) derived in the same model as in Figure 3, and based on the NO_x distribution in Figure 8.

are in general agreement with the available observations; for instance, the recent measurements by Ackerman et al. (1973) and Ridley et al. (1973) show that the volume-mixing-ratio values of NO increase from 0.1 to 0.2 ppb in the lower stratosphere to about 3 ppb at 30 km. However, the model calculations show that the bulk of NO is located in the upper stratosphere, and this still remains to be verified by observation. Also, the NO_2 mixing-ratio measurements reported by Ackerman and Muller (1972) (NO_2 increasing from 1 ppb at 22 km to 8 ppb at 27 km) are in fair agreement with the present calculations (see Figure 10), although the computed height of the maximum NO_2 mixing ratio is higher than indicated by the observations.

The distribution of HNO_3 (see Figure 11) shows that its variations in the stratosphere resemble quite closely those of ozone. The seasonal and latitudinal variations of HNO_3 in the lower stratosphere appear to be consistent with the measurements of Lazrus and Gandrud (1973), who reported an increase of HNO_3 from the equator to high latitudes and higher mixing-ratio values in winter than in summer. However, the model predicts the height of the maximum HNO_3 mixing ratio at about 5 km, and its magnitude a factor of two, above the measurements.

The satisfactory agreement between the model results and the observations suggests that the model can be applied with reasonable confidence to assess the perturbing effects of HO_x and NO_x on ozone, the temperature structure, and the mean circulation of the stratosphere. The results of detailed investigation of the perturbed stratosphere will be described in a future paper. In the present paper only the effect on total ozone of doubling the water-vapor mixing ratio and the NO_x source strength is investigated. These results are shown in Figure 12. The total ozone curve of Case 1 (uppermost curve in Figure 12) results from the highly speculative assumption mentioned earlier that R_{30} is a sink for NO_x. This particular effect is, however, excluded in all the other results in this study. It is clear from Figure 12 that a 100% increase in the stratospheric water-vapor mixing ratio has only a small effect on total ozone (2 to 4%, depending upon the latitude). On the other hand, a 100% increase in the NO_x source strength has a substantial effect on the total ozone column (10 to 16%, again depending upon the latitude). Although these results look similar to those obtained previously (Rao-Vupputuri, 1974), they differ in one important respect. In the present experiment the mutual interaction between ozone, HO_x, and NO_x appears to have a stabilizing effect on total ozone reduction, particularly in the tropics, and also in the high latitudes during the summer season.

There are some suggestions in the recent literature that the increase of water vapor in the stratosphere increases the total ozone column (Crutzen, 1974). The results of the present experiment do not show this, although they do indicate that the presence of more HO_x due to increased water vapor may have a restoring influence on the total ozone column by converting NO_x into HNO_3.

SUMMARY AND CONCLUSIONS

A two-dimensional model of the stratosphere, incorporating radiative heating and photochemistry of the oxygen-hydrogen-nitrogen atmosphere, was used to investigate the role of

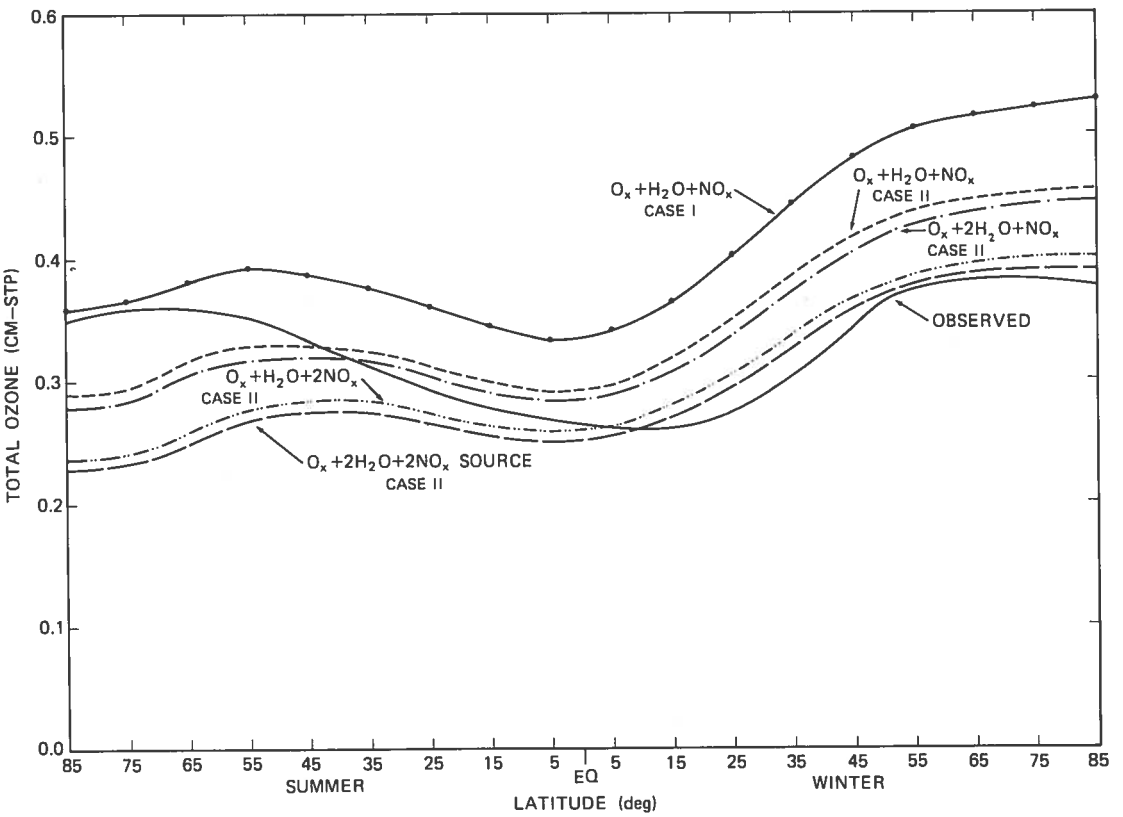

Figure 12. Computed distributions of total ozone using the reaction scheme of the oxygen-hydrogen-nitrogen atmosphere in experiment 2. The uppermost curve (case I) results from the inclusion of an additional sink of NO_x (second term in eq. 14). This sink is excluded in all other curves (case II). Also shown for comparison is the observed total ozone curve.

HO_x and NO_x in the ozone and thermal balances of the normal stratosphere. The meridional distributions of ozone, temperature, HO_x, and NO_x were derived from the model in a self-consistent manner. The results are shown to be consistent with the available observations.

The model has been applied to investigate the perturbing effects of HO_x and NO_x on the latitudinal distribution of total ozone by simply doubling the water-vapor mixing ratio and the NO_x source strength of the normal stratosphere. It is found that even though the latitudinal distribution of total ozone is rather insensitive to the variations in the water vapor (only 2 to 4% reduction in total ozone for 100% increase in the water vapor), the increased water vapor does not lead to increased total ozone as suggested in the recent literature. On the other hand, the total ozone column is highly sensitive to the changes in the NO_x source strength in the stratosphere (10 to 16% reduction in total ozone for a 100% change in the NO_x source strength). It is indicated that an increase in water has the effect of decreasing the NO_x (through conversion of NO_2 into HNO_3), which in turn has a stabilizing effect on ozone reduction.

REFERENCES

Ackerman, M., F. Biaume, and G. Kockarts (1970), "Absorption cross-sections of the Schumann-Runge bands of molecular oxygen," Planet. Space Sci. **18**, 1639.

Ackerman, M. and C. Muller (1972), "Stratospheric nitrogen dioxide from infrared spectra," Nature **240**, 300-301.

Ackerman, M., J.C. Fontanella, D. Frimout, A. Girard, N. Louisnard, C. Muller, and D. Nevejans (1973), "Stratospheric nitric oxide from infrared spectra," Nature **245**, 205-206.

Brasseur, G. and M. Nicolet (1973), "Chemospheric processes of nitrogen oxides in the stratosphere," Planet. Space Sci. **21**, 939.

Brewer, A.W. and A.W. Wilson (1965), "Measurement of solar ultra-violet radiation in the stratosphere," Quart. J. Roy. Meteor. Soc. **91**(390), 452-461.

Byron-Scott, R. (1967), "A stratospheric general circulation experiment incorporating diabatic heating and ozone photochemistry," in Publications in Meteorology, No. 87, Arctic Meteorology Research Group, Dept. of Meteorology, McGill University, Montreal, Quebec, 201 pp. plus appendices.

Chapman, S. (1930), "A theory of upper atmospheric ozone," Mem. Roy. Meteor. Soc. **3**, 103-125.

Cieslik, S. and M. Nicolet (1973), "The aeronomic dissociation of nitric oxide," Planet. Space Sci. **21**, 925.

Crutzen, P.J. (1969), "Determination of parameters appearing in the 'dry' and the 'wet' photochemical theories for ozone in the stratosphere," Tellus **21**, 368-388.

Crutzen, P.J. (1971), "Ozone production rates in an oxygen-hydrogen-nitrogen oxide atmosphere," J. Geophys. Res. **76**, 7311-7327.

Crutzen, P.J. (1974), "A review of upper atmospheric photochemistry," Canad. J. Chem. **52**, 1569-1581.

Hampson, J. (1964), "Photochemical Behaviour of the Ozone Layer," Technical Note 1627/64, CARDE, ValCartier, Quebec, 280.

Hesstvedt, E. (1973), "The effect of water vapor and nitrogen oxides upon the ozone layer," Water Air Soil Pollut. **2**, 49-60.

Hunt, B.G. (1966), "Photochemistry of ozone in a moist atmosphere," J. Geophys. Res. **71**, 1385-1398.

Johnston, H. (1971), "Reduction of stratospheric ozone by nitrogen oxide catalysts from SST exhaust," Science **173**, 517-522.

Johnston, H.S. and R. Graham (1973), "Gas-phase ultraviolet absorption spectra of HNO_3," J. Phys. Chem. **77**(1), 62-63.

Krueger, A.J., D.F. Heath, and C.L. Mateer (1973), "Variations in the Stratospheric Ozone Field Inferred from Nimbus Satellite Observations," preprint of NASA Technical Memorandum X-66108 (NTIS-N73-12379), 13 pp.

Lazrus, A.L. and B.W. Gandrud (1974), "Progress report on distribution of stratospheric nitric acid," in this volume.

Leovy, C.B. (1969), "Atmospheric ozone: An analytic model for photochemistry in the presence of water vapor," J. Geophys. Res. **74**, 417-426.

Murgatroyd, R.J. and F. Singleton (1961), "Possible meridional circulations in the stratosphere and mesosphere," Quart. J. Roy. Meteor. Soc. **87**, 125-135.

Rao, V.R.K. (1973), "Numerical experiments on the steady state meridional structure and ozone distribution in the stratosphere," Mon. Wea. Rev. **101**(6), 510-527.

Rao-Vupputuri, R.K. (1974), "Seasonal and latitudinal variations of N_2O and NO_x in the stratosphere," in *Proceedings of the International Conference on the Structure, Composition, and General Circulation of the Upper and Lower Atmospheres and Possible Anthropogenic Perturbations* (Melbourne, January 1974), ed. IAMAP, 881-905.

Rao-Vupputuri, R.K. (1974), "The role of stratospheric pollutant gases (H_2O, NO_x) in the ozone balance and its implication for the seasonal climate of the stratosphere," in *Proceedings of the International Conference on the Structure, Composition, and General Circulation of the Upper and Lower Atmospheres and Possible Anthropogenic Perturbations* (Melbourne, January 1974), ed. IAMAP, 905-931.

Rao, V.R.K. and A.D. Christie (1973), "The effects of water vapor and oxides of nitrogen on ozone and temperature structure of the stratosphere," J. Atmos. Sci. **30**, 667-676.

Reed, R. and K.E. German (1965), "A contribution to the problem of stratospheric diffusion by large scale mixing," Mon. Wea. Rev. **93**, 313-321.

Ridley, B.A., H.I. Schiff, A. Shaw, and L.R. Megill (1974), "In-situ measurements of NO in the stratosphere using chemiluminescence," in this volume.

Williams, G.P. and D.R. Davies (1965), "A mean motion model of the general circulation," Quart. J. Roy. Meteor. Soc. **91**(390), 471-489.

PRELIMINARY RESULTS OF THE M.I.T. PHOTOCHEMICAL-DYNAMICAL OZONE MODEL

D.M. CUNNOLD, F.N. ALYEA, N.A. PHILLIPS, AND R.G. PRINN
Department of Meteorology
Massachusetts Institute of Technology
Cambridge, Massachusetts

ABSTRACT: This paper reports on a general-circulation model under development, whose ultimate objective is the assessment of the effect of increased stratospheric flight on the atmospheric ozone distribution. The model variables are represented in the spectral domain in terms of 79 spherical harmonics and 26 vertical levels between the ground and 70 km. The results of a three-year integration (run 12) which simulated the unperturbed global ozone distribution are presented in this paper. The model shows the presence of a westerly stratospheric jet in the winter hemisphere with an amplitude similar to those observed in the polar-night jet; easterlies dominate in the summer hemisphere. The model also shows ozone to be transported polewards and downwards. Furthermore, the annual ozone-concentration cycle at mid-latitudes has been simulated. Preliminary comparisons are also made with other features of the dynamics and the ozone distribution in the stratosphere.

INTRODUCTION

This paper reports on a combined photochemical-dynamical (three-dimensional) model of the stratosphere which has been developed with the aims of simulating the observed global ozone distribution and of predicting the changes in that distribution which could result from the introduction of NO_x by a fleet of stratospheric aircraft. The model's calculations of the dynamics of the unperturbed stratosphere, and the ozone distribution therein, are presented. Two three-year integrations have been performed so far. The first integration was reported on at the Melbourne IAMAP meeting (Cunnold et al., 1974). This paper contains the results of the second three-year integration, in which a few minor adjustments were made, resulting in slightly better agreement between the calculated results and the observations of the natural stratosphere.

Stratospheric ozone is produced photochemically; a profile of the time constant for its production is given in Figure 1. Above 40 km the time constant is less than one day, and ozone is essentially in photochemical equilibrium. Below 30 km, however, where most of the ozone in the atmosphere is located, ozone is clearly influenced by both horizontal and vertical motions. This fact is illustrated by the observational data contained in Figure 2, which exhibits the spring maximum in total ozone at high latitudes. Furthermore, the absorption of solar radiation by ozone is an important stratospheric heat source, which thus constitutes a feedback mechanism to the stratospheric climatology. Thus, to successfully simulate the stratospheric ozone distribution, an interactive photochemical-dynamical model is required. Current large general-circulation models are not easily adapted to the ozone problem because of the extensive computing time (currently several hours) required to simulate one day. In dealing with ozone, we must allow the stratosphere several years to adjust, and we should also like to simulate the important seasonal variations. Furthermore, since some stratospheric parameters are poorly known at the present time (e.g., certain chemical reaction rates) several runs of the model can be expected. Our model, which takes only 40 seconds for a one-day simulation on an IBM 360/90, will be run several times, each run consisting of several annual cycles.

Because we are interested primarily in the stratosphere, for which the smaller-scale features appear to be of secondary importance, our model incorporates a fairly limited horizontal resolution (by tropospheric standards). This is accomplished by using a fairly small number (79) of spherical harmonics for the horizontal representation of

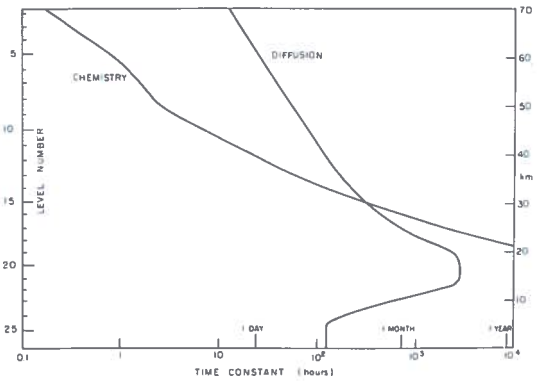

Figure 1. Time constants for the chemistry and vertical diffusion of ozone.

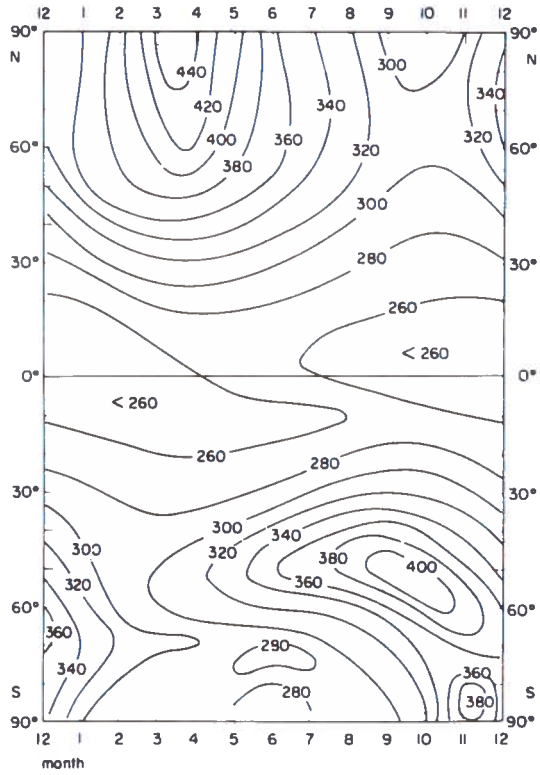

Figure 2. Total ozone distribution with season and latitude (from Dütsch, 1969) (matm-cm or Dobson units).

the dependent variables. In addition, the relative absence of energy in the shorter planetary- and synoptic-scale waves also permits a number of simplifications in the dynamic and the thermodynamic representations. For example, we make use of the differentiated form of the motion equations and invoke the quasi-geostrophic approximation. The large-scale tropospheric motions responsible for driving the stratosphere are included by allowing the model to extend downwards to the ground.

Trenberth (1973) successfully used a model of this type to study stratospheric warmings. Trenberth used only 9 levels in the vertical and 24 horizontal degrees of freedom without any chemistry, but was able to reproduce realistic stratospheric warmings in late winter resulting from tropospheric forcing. A similar model which included a limited set of chemical reactions was used somewhat earlier by Clark (1970). Although Clark's model possessed even poorer resolution than Trenberth's, he was able to reproduce numerically the observed tendency for the large-scale motion field to shift the maximum of vertically integrated ozone poleward from the low-latitude source region.

The principal features of our model consist of the inclusion of NO_x chemistry (together with the potential for adding further chemistry at a later time), and the ability to simulate seasonal variations by running the model over several annual cycles. Without NO_x the model would overpredict the total amount of ozone in the atmosphere. This fact is evident in previous models in which certain assumptions (Hunt, 1969), subsequently proved false, or artificial adjustments (Clark, 1970) had to be made to reduce the total ozone amounts.

MODEL EQUATIONS

Using $\log_e$ (pressure) as the vertical coordinate, the model equations are:

$$R\nabla^2 T = \underline{\nabla} \cdot \left(f \underline{\nabla} \frac{\partial \psi}{\partial Z} \right)$$

$$\frac{\partial \zeta}{\partial t} = \frac{\partial}{\partial t} \nabla^2 \psi = -J(\psi, \zeta + f) - \underline{\nabla} \cdot \left(f \underline{\nabla} \frac{\partial X}{\partial P} \right) + \underline{\nabla} \cdot (\underline{F}_r \times \hat{\underline{k}})$$

$$\frac{\partial T}{\partial t} = -J(\psi, T) - W \left(\frac{d\overline{T}}{dZ} + \kappa \overline{T} \right) + \frac{q}{c_p}$$

$$\frac{\partial \chi_{O_3}}{dt} = -J(\psi, \chi_{O_3}) - W \frac{\partial \overline{\chi}_{O_3}}{\partial Z}$$

$$+\left[\frac{1}{n_m}\frac{dn_{O_3}}{dt}\right]_c+\frac{\partial}{\partial P}\left[-\frac{K_d}{H_0^2}P\frac{\partial \chi_{O_3}}{\partial Z}\right]$$

where

f = Coriolis parameter
R = gas constant for air
$\underline{\nabla}$ = horizontal gradient operator
ψ = streamfunction
T = temperature
Z = $-\log_e$ (P/1000 mb) where P = pressure
ζ = vertical component of vorticity $=\nabla^2\psi$
$\underline{F}_r$ = frictional force
$\underline{\hat{k}}$ = unit vector in the vertical direction

X is related to the rate of change of pressure by $-\nabla^2 X = dP/dt$

W = vertical advection velocity $\left(=\frac{1}{P}\nabla^2 X\right)$
$J(\psi, s)$ = Jacobian operator representing the horizontal advection of the variable "s" by the non-divergent part of the horizontal wind
t = time
κ = $1 - c_v/c_p$
q/c_p = rate of heating (°K/sec)
c_p = specific heat of air at constant pressure
χ_{O_3} = volume mixing ratio of ozone
$\left[\frac{1}{n_m}\frac{dn_{O_3}}{dt}\right]_c$ = net chemical production rate of ozone
K_d = a vertical austausch (exchange) coefficient
H_0 = a scale height (= 7 km)
$(\overline{\ })$ = indicates the horizontal-average value.

These equations have been obtained using a "quasi-geostrophic" balance applied to the horizontal equations of motion in an energetically consistent manner (Lorenz, 1960). The differentiated form of the thermal wind arises out of these quasi-geostrophic balance conditions when hydrostatics are introduced. Mass continuity provides the essential relationship between W and the vertically integrated velocity potential, X. The last terms in the vorticity and thermodynamic energy equations represent dissipation due to frictional stress and diffusion, and forcing through all types of heating.

Computation of the vertical thermal advection has been simplified by replacing the temperature at each level by its global horizontal mean. Thus, the "stability" factor, constructed from observed annual temperatures, becomes a horizontally specified function varying with pressure only. We will no longer interpret the temperature-prediction equation as forecasting global mean temperatures, since we would expect little change, either with season or with changes in the ozone chemistry.

A similar approach has been followed for the prediction of ozone mixing ratios. Here again we have simplified the calculations by using global-mean ozone values but, in contrast to the procedure for temperature, we must allow for time variations in the mean ozone profile. This is accomplished by taking the horizontal average of the ozone-prediction equation written in flux form, giving

$$\frac{\partial \overline{\chi}_{O_3}}{\partial t}=\frac{\partial}{\partial P}\left[\overline{PW'\chi'_{O_3}}\right]+\left[\overline{\frac{1}{n_m}\left(\frac{dn_{O_3}}{dt}\right)}\right]_c+\frac{\partial}{\partial P}\left[-\frac{K_d}{H_0^2}P\frac{\partial \overline{\chi}_{O_3}}{\partial Z}\right]$$

where the primes indicate deviations from horizontal-average values.

These model equations are specified in the vertical direction at 26 levels equally spaced in Z between the ground and approximately 70 km (or at roughly 3-km height intervals). In the horizontal direction, T, ζ, χ_{O_3}, and W are expanded as series of spherical harmonics $Y_n^m(\theta, \phi)$ using planetary waves with maximum wavenumber 6 (m = 0, ±1, ±2, ±3, ±4, ±5, ±6) and 6 degrees of freedom in latitude. Y_7^0 is also included, giving 79 harmonics in all. The equations are solved for $\overline{\chi}_{O_3}$, T, and W at levels 2, 3, 4, . . . , 25 and for ζ (or ψ) at intermediate levels 1.5, 2.5, . . . , 25.5.

Since our model requires that the "quasi-geostrophic" balance condition be maintained at all times, we must generate vertical motions which satisfy this criterion. Therefore, we make use of the spectral form of the three-dimensional

vertical-velocity equation, obtained in the usual manner by eliminating time dependency through substitution among the reduced dynamical set of equations.

FRICTIONAL STRESS, DIFFUSION, AND BOUNDARY CONDITIONS

Horizontal diffusion is neglected, so the frictional force incorporates the effect of vertical stresses ($\underline{\tau}$) with the stress being represented by a vertical eddy viscosity, K_m. At the ground the stress is defined, using a surface drag coefficient in almost the same way that the standard Ekman boundary-layer theory is applied to the lowest layer of the model. These conditions yield expressions of the form

$$\nabla \cdot (\underline{F}_r \times \hat{k}) = \frac{\partial (PF)}{\partial P}$$

$$F_j = -\frac{K_m}{H_0^2} \frac{\partial \nabla^2 \psi}{\partial Z} \qquad 1 \leqslant j \leqslant 25$$

and

$$F_{26} = -k_d \nabla^2 \psi_{25.5}$$

and we set $k_d = 1.6 \times 10^{-6}$ (sec^{-1}). Vertical diffusion of ozone is treated in a mathematically similar way, and at the ground the vertical flux of ozone is specified in terms of the concentration (Galbally, 1971). Thus

$$K_d \frac{\partial \chi}{\partial z} = d\chi_{26}$$

and we set $d = 0.08$ cm/sec, on the basis of the surface-destruction-rate calculations of Fabian and Junge (1970). It is assumed that the vertical diffusion coefficients for momentum and ozone (K_m and K_d) are the same. Two profiles of the diffusion coefficient are shown in Figure 3. Curve A is similar to that used by Wofsy and McElroy (1973) to explain measurements of atmospheric methane in the upper stratosphere and mesosphere. The basis for this profile is largely that gravity waves, which provide a likely mixing process (Lindzen, 1971), increase exponentially with height. At the lower levels of the model the diffusion coefficient was assumed to decrease from a value of 10^5 cm^2/sec at the ground to a value of 2×10^3 cm^2/sec in the lower stratosphere. Preliminary runs of the model indicated that too much ozone was being transported out of the 10-15 km region at high latitudes, thus producing smaller ozone concentrations there than the observational data indicated. This happens in the model because we are using a latitudinally invariant K_d which contains a minimum at about 18 km to account for the effect of the tropopause. However, there is actually a considerable variation of tropopause height with latitude, and we have tried to correct for this deficiency by using diffusion profile B, which contains a 10-km region around the tropopause in which the diffusion coefficient assumes the small value of $4 \times 10^3 cm^2$/sec.

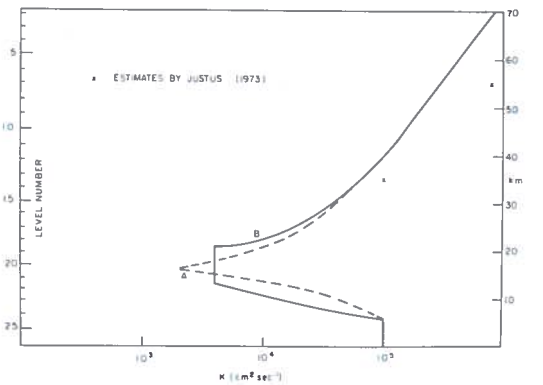

Figure 3. Vertical diffusion coefficients used in the model.

The boundary conditions on W are that W vanishes at level 1 and that it is given by the orographic upslope motion at level 26,

$$W_{26} = \frac{1}{H_0} \hat{k} \times \nabla \psi_{25.5} \cdot \nabla h$$

where h represents the surface orography. Northern-hemisphere orographic patterns are used in the model, together with values defined by reflecting northern-hemisphere heights into the southern hemisphere (see Figure 4). This procedure permits us to obtain statistical results over a shorter stretch of time (e.g., we get two northern-hemisphere winters every year). Additional boundary conditions are that $\overline{W' \chi'_{O_3}}$ is equal to zero at the ground, and that the flux of ozone is equal to zero at the top of the model, where ozone is in photochemical equilibrium.

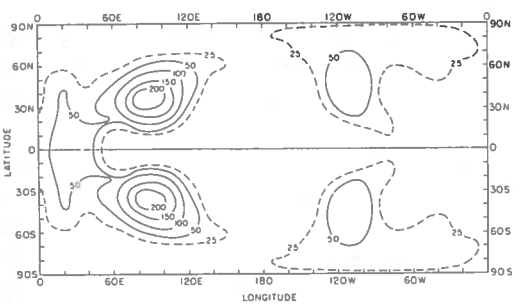

Figure 4. Model surface topography in dekameters, drawn from a spectral representation.

MODEL HEATING

The important heating processes in the stratosphere differ from those in the troposphere. The representation of heating in the model consists of three parts. Method I is used at heights above 30 km, where heating consists of the sum of the absorption of solar energy by ozone and the long-wave cooling by ozone and carbon dioxide. Ultraviolet absorption is computed explicitly in the model as an integral over the solar spectrum and as a function of the ozone column density. It is satisfactorily averaged over the day (to approximately 5% accuracy) using the empirical expression

$$\bar{Q} = \frac{H}{2.05\pi} [Q(\psi_1) + Q(\psi_2)]$$

where 2H radians is the length of the day at any grid point, ψ_1 is the solar zenith angle at the hour angle corresponding to local noon + H/4, and ψ_2 is the solar zenith angle at the hour angle corresponding to local noon + 3H/4. A similar technique is used to evaluate the photodissociation rates. The radiative cooling in the stratosphere above 30 km is parameterized with a Newtonian-cooling approximation using values (see Figure 5) similar to those deduced by Dickinson (1973).

Heating in regions below 20 km, represented as Method II, is more complicated, since in principle it involves both latent-heat release and sensible-heat flux from the ground in addition to solar and infrared radiation. This heating term is parameterized in a linear form

$$\frac{q}{C_p} = h(Z)\,(T^* - T)$$

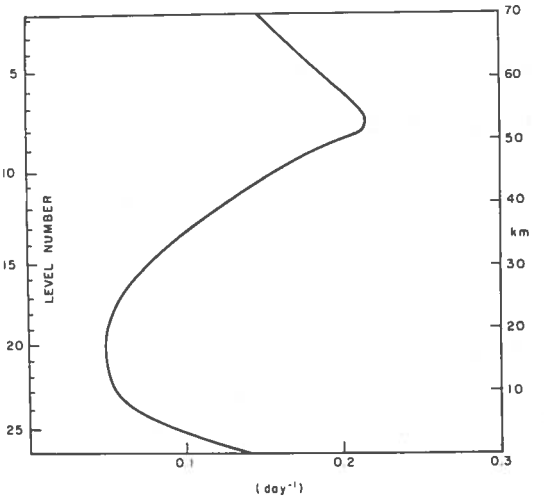

Figure 5. Newtonian cooling coefficients used in the model.

using values consistent with those of Trenberth (1972). The parameter h is essentially a Newtonian-cooling coefficient (values used are indicated in Figure 5) and T* is a hypothetical equilibrium temperature field empirically determined from estimates of the heating rate and observations of temperature in the troposphere and lower stratosphere in the northern hemisphere. The T* field thus determined is permitted to possess non-zonal variations in planetary wave numbers 1 and 2, and furthermore a sinusoidal variation of T* with solar declination is included. In the southern hemisphere the northern-hemisphere T* field is used with a 6-month time lag.

In the 20-30 km region, a linear weighting of methods I and II is used to produce a smooth gradation between the upper and lower regions. An additional term is added to Method I in this region, however, corresponding to the absorption of infrared radiation emitted by the ground and absorbed by ozone in the 9.6-μm band. This corresponds to a heat source of approximately 1°K/day at equatorial latitudes at 25 km (Dopplick, 1970).

MODEL CHEMISTRY

The set of chemical reactions included in our model is very limited. It consists of the Chapman reactions

$$O_2 + h\nu \xrightarrow{J_{O_2}} O + O \qquad \lambda < 245.9 \text{ nm}$$

$$O + O_2 + M \rightarrow O_3 + M$$

$$\ell_1 = 6.6 \times 10^{-35} \exp(510/T) \text{ cm}^6 \text{ sec}^{-1}$$

(Garvin and Hampson, 1973)

$$O_3 + h\nu \xrightarrow{J_{O_3}} O_2 + O \qquad \lambda < 1140 \text{ nm}$$

$$O + O_3 \rightarrow 2O_2$$

$$k_1 = 1.9 \times 10^{-11} \exp(-2300/T) \text{ cm}^3 \text{ sec}^{-1}$$

(Garvin and Hampson, 1973)

and the catalytic cycle of NO_x,

$$NO + O_3 \rightarrow NO_2 + O_2$$

$$k_2 = 1.7 \times 10^{-12} \exp(-1310/T) \text{ cm}^3 \text{ sec}^{-1}$$

(Schofield, 1967)

$$NO_2 + O \rightarrow NO + O_2$$

$$k_3 = 9.1 \times 10^{-12} \text{ cm}^3 \text{ sec}^{-1}$$

(Davis, 1973)

$$NO_2 + h\nu \xrightarrow{J_{NO_2}} NO + O \qquad \lambda < 400 \text{ nm}$$

In order to produce more realistic atmospheric heating rates above 50 km, the pair of reactions

$$\left.\begin{array}{l} OH + O \rightarrow O_2 + H \\ \quad k_4 = 5 \times 10^{-11} \text{ cm}^3 \text{ sec}^{-1} \\ HO_2 + O \rightarrow O_2 + OH \\ \quad k_5 = 6 \times 10^{-11} \text{ cm}^3 \text{ sec}^{-1} \end{array}\right\} J_{O_3}$$

(Kaufman, 1969)

has been added. This set of reactions leads to a net ozone production rate of

$$\left[\frac{1}{n_m}\frac{dn_{O_3}}{dt}\right]_c = 0.42\, J_{O_2} - \left(\frac{2K + d_{OH}}{L}\right) \cdot (\chi_{O_3} J_{O_3} + \chi_{NO_2} J_{NO_2})$$

where

$$K = k_1 \chi_{O_3} + k_3 \chi_{NO_2}$$

$$d_{OH} = k_4 \chi_{OH} + k_5 \chi_{HO_2} \approx 4 \times 10^{-12} (n_m)^{-.5}$$

$$L = 0.21\, \ell_1 n_m.$$

The chemical reactions are temperature-sensitive, particularly that between O and O_3, and thus respond to temperature changes provided by the dynamics.

Many other reactions could have been included in our model, but at the price of additional computer time and of considerable delay in obtaining results. The most significant omission is probably nitric acid, which if included would require the addition of several odd-nitrogen species. We are considering this problem as well as the possibility of adding a prediction equation for NO_x. However, the model results which follow are based upon OH and NO_2 profiles (see Figure 6) which are similar to the results of one-dimensional model calculations by McElroy et al. (1974) and by McConnell and McElroy (1973); they are assumed to be independent of latitude. The OH distribution above 45 km has a significant effect on the ozone distribution, as does the distribution of NO_x between 20 km and 50 km.

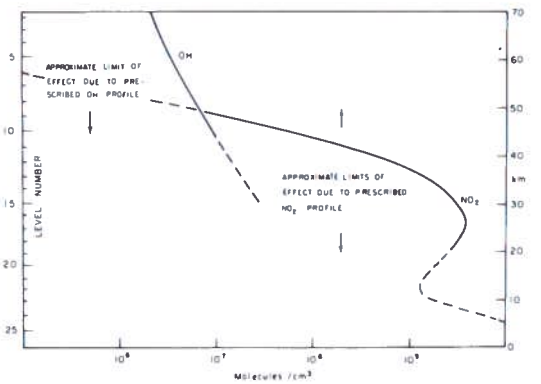

Figure 6. Latitudinally independent OH and NO_2 profiles assumed in the model.

The spectral representation of the ozone generation (and of heating by ozone) is a special problem because of the transcendental functions involved. For this purpose we have designed an especially efficient transform procedure similar to that presented by Machenhauer and Rasmussen (1972). In this procedure, the spectral data representing the predicted temperature and the ozone mixing ratio are transformed to a carefully selected grid mesh. The location and number of these grid points are determined in such a way as to guarantee an exact quadrature transformation to at least the second degree. The heating and generation terms are then calculated

at the grid points and the results are transformed back into the spectral domain, again retaining second-degree accuracy. This procedure also has the property of eliminating aliased modes generated by the grid-point calculation.

INITIAL CONDITIONS AND NUMERICAL PROCEDURE

Initially the temperature field is set equal to a Standard Atmosphere temperature profile and the streamfunctions are set equal to zero. The model is started up from 44 days prior to the spring equinox (i.e., early February) and a model year is 12 months, each month consisting of 30 days. The mean ozone distribution during the first few days of the model run, during which the dynamics has had little time to develop, is shown in Figure 7. This initial ozone distribution is based upon the results of one-dimensional model calculations. Using the chemistry and the vertical austausch coefficient of our global model, an equilibrium calculation was made at several latitudes for a solar declination angle of 0° and with the Standard Atmosphere temperature profile. The resulting profiles were then area-weighted to produce the global-mean ozone profiles depicted in Figure 7. This figure shows the ozone distribution resulting from the prescribed NO_2 profile as well as that from omitting NO_x entirely. It is to be noted that an integration time of the order of two years is required for the tropospheric values to attain the equilibrium values. The figure also shows a mean mid-latitude profile compiled by Krueger and Minzner (1973), based upon the limited number of rocket observations that have so far been made. There is excellent agreement between the predictions of the one-dimensional model and the rocket observations, except below the tropopause, where large-scale transports through the tropopause (which involve tropospheric dynamics) are likely to affect the profiles. At heights above 37 km the predictions of the one-dimensional model for each latitude were inserted in the three-dimensional model as initial conditions, while for heights below 37 km (where large-scale transports are expected to be important) the global mean value of ozone was inserted at each latitude and longitude.

The numerical integration of the global model makes use of the N-cycle time-differencing

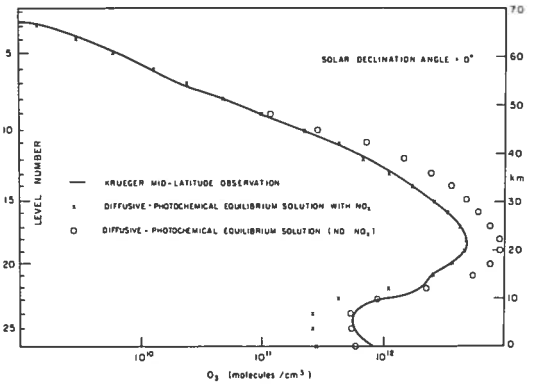

Figure 7. The global-average ozone distribution predicted initially by the model from a one-dimensional calculation.

scheme of Lorenz (1971) with one-hour time steps. N is taken to be 4. At the upper levels of the model, the chemical time constants, as shown in Figure 1, are very fast and would lead to numerical instabilities for our time increment. However, because of these relatively short time constants, photochemical equilibrium can be safely assumed for heights above 50 km. In practice we update χ_{O_3} diagnostically via the photochemical-equilibrium assumption at each time step for levels 9 and above (i.e., above 47 km). This procedure overemphasizes the reaction of ozone to temperature perturbations at the upper levels, but test runs indicate that the dynamics of the stratosphere and mesosphere are little affected by this assumption.

The initial distribution of heating (actually averaged over the first two days) is shown in Figure 8. The long-wave cooling is initially zero because $T = \overline{T}$ (the global mean value of temperature, which has been omitted from the heating because it is not predicted). Thus, in the stratosphere and mesosphere the initial latitudinal heating gradients are due entirely to heating by ozone. In the troposphere the initial heating distribution is in a sense a map of T* at 44 days before the spring equinox (T*, however, also possesses a non-zonal component).

MODEL RESULTS

Several 96-day runs have been made with the model during the past few months in an attempt to discover how the dynamics of the model varied as a function of certain parameters, so as

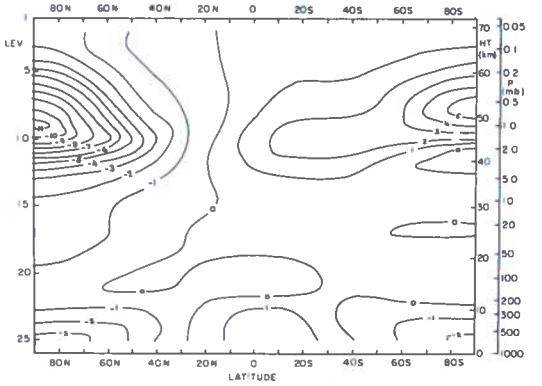

Figure 8. The heating distribution for days 0 to 2 (at 44 days prior to the spring equinox).

to eliminate the need for additional full-scale runs of the model. Two full three-year runs of the model have been made; the initial analysis of the results of the second run is presented as the remainder of this paper. The difference between the second integration (run 12) and the first (Cunnold et al., 1974) is that run 12 contains orographic effects and an adjustment in the static stability to crudely account for the release of latent heat. Also, a coding error related to the frictional drag at the lower boundary has been corrected.

Dynamics

After an initial zonal build-up period of about 28 days, the eddies become active and the kinetic energy begins to stabilize at about 250 m^2/sec^2. The level of available potential energy is about 2.5 times that of the kinetic energy These values are generally in agreement with the results of other models.

Average zonal wind profiles for seasons 10 and 11 are shown in Figures 9 and 10. For comparison, observations analyzed by Newell (1969) for summer and winter have been reproduced on the upper half of Figure 9. We see that for season 10 (the winter-summer situation) the model shows the presence of a high-level wind maximum similar to the polar-night jet in winter and the easterlies in summer. The magnitude of the westerly wind maximum is about 80 m/sec at 50 km, in excellent agreement with Newell's data. At higher levels the failure of this maximum to close off is probably the result of the artificial

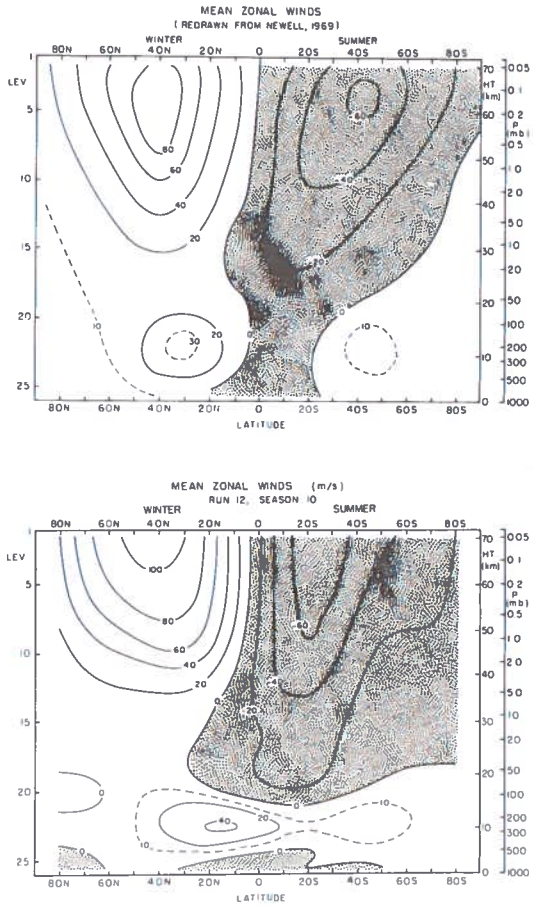

Figure 9. Vertical cross-section of the zonal wind for season 10 (m/sec) compared with the summer-winter observations analyzed by Newell (1969).

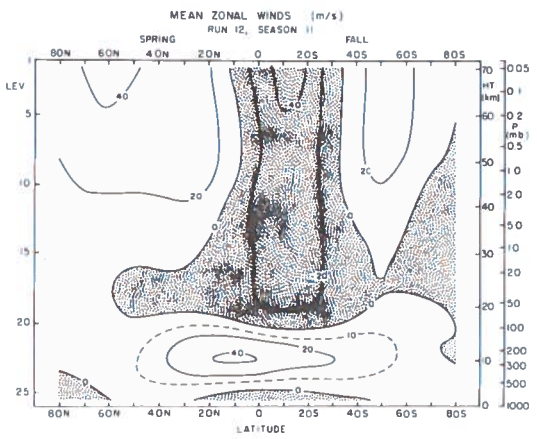

Figure 10. The vertical cross-section of the zonal wind for season 11.

boundary of the model at 70 km. The 50-70 km region in our model is in essence a lid which is needed in order to obtain the correct dynamics at lower altitudes. By forcing W to zero, the artificial lid at 72 km probably prevents the creation of a cold mesosphere over the summer pole, which must be associated with the decrease in zonal wind speeds above 50 km observed in the real atmosphere. (This conclusion agrees with the results of Leovy (1964) in his test of different upper boundary conditions; compare his Figures 5 and 12.)

The location of the wintertime wind maximum at 40°N is in excellent agreement with the observations. The strength and location of the summertime easterlies also agrees well with the observations, except perhaps above 50 km where again the upper boundary may be affecting the results. In the troposphere a jet of the correct amplitude is obtained in the winter. It is located somewhat too close to the equator, however, and in fact extends right across the equator. This result was probably to be expected because our model does not possess the baroclinically active waves of wavenumbers higher than 6, which also transport momentum from equatorial to mid-latitudes. In the lower troposphere our model gives equatorial easterlies and a belt of westerlies in mid-latitudes. The surface winds obtained in run 12 are in much better agreement with the observations than were the surface winds of the earlier run (run 10). This is because run 10 contained a coding error in the computer program which resulted in the use of ψ at level 24.5 rather than level 25.5) in computing F_{26}. During the equinoctial seasons (Figure 10), the zonal wind profile obtained by the model shows the transition state for hemispheric season reversal.

Zonal temperature distributions, both as obtained from observations and as given by our model, are shown in Figure 11. Here it is interesting to note that in the lower stratosphere (about 17-20 km) the model temperature fields exhibit a poleward increase, as do the observations. Elsewhere, as expected, temperature decreases from equator to pole with the exception of the summer upper stratosphere. By comparison with observations, the model seems to slightly overpredict the pole-to-pole temperature gradient in the solstitial stratosphere. This could be related to the "lid" at 72 km, or might be the result of a slightly excessive pole-to-pole ozone gradient in the upper stratosphere caused by our inadequate knowledge of latitudinal distribution of other minor constituents.

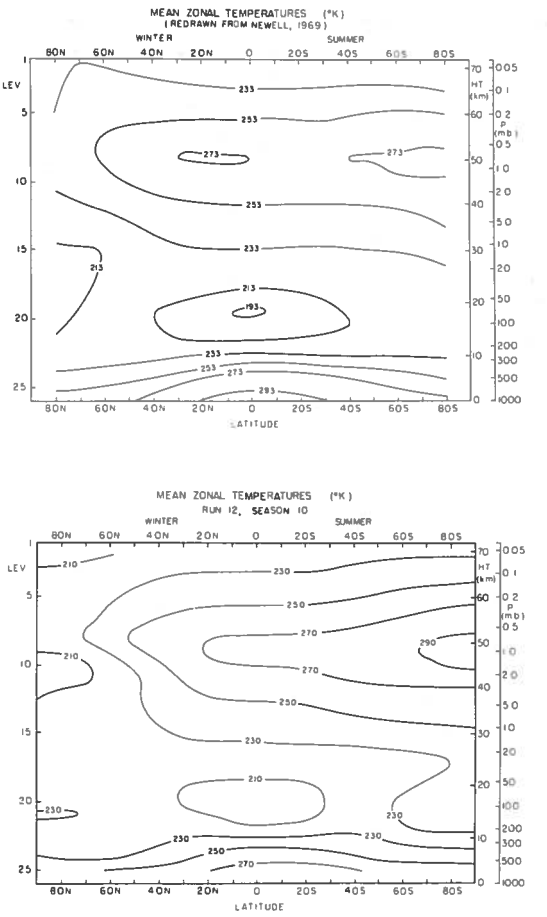

Figure 11. The atmospheric temperature distribution obtained for season 10 compared with the observed atmospheric temperature distribution for summer and winter according to Newell (1969).

The meridional circulations for seasons 10 and 11 are shown in Figure 12. The three-cell hemispheric circulation in the troposphere and the change to a two-cell circulation in the stratosphere are clearly evident at all seasons, except during the summer, when the circulation is very weak and not well established. The strong cross-equatorial transports from the summer to the winter hemisphere should also be noted. Figure 13 shows some mean stratospheric circulations in January and March according to Vincent (1968). Our results are in general agreement with those

of Vincent (except for the January 1965 observations which show a three-cell pattern in the stratosphere at that time). In the troposphere, the inter-tropical convergence zone possesses an annual oscillation whose location varies between 10°N and 10°S. The circulation of the equatorial troposphere has been compared with the flux data of Newell et al. (1972) and found to agree extremely well. For example, in winter the model shows a maximum of just over 200 tons/second being transported equatorward by the equatorial Hadley cell between the ground and 6 km altitude. Corresponding values by Newell average to just under 200 tons/second for the same conditions.

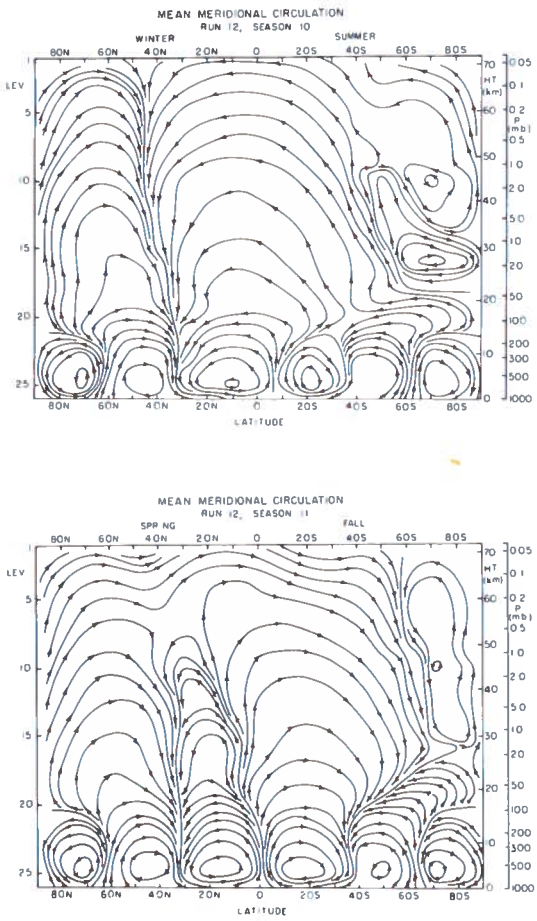

Figure 12. The mean meridional circulations for seasons 10 and 11.

Monthly average maps of geopotential height for September and December at 10 mb are shown in Figure 14. These maps show clearly the lack of standing-wave activity in the summer

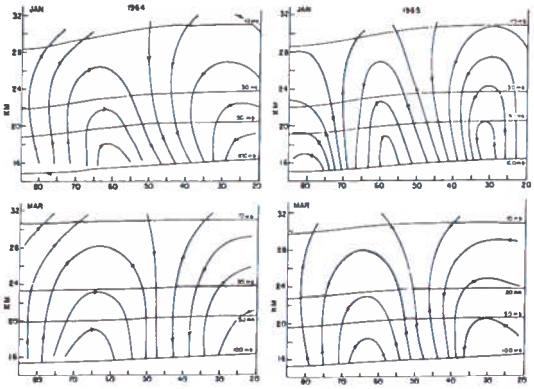

Figure 13. January and March mean meridional circulations in the stratosphere according to Vincent (1968).

(i.e., flow is approximately zonal), the presence of wavenumbers 1 or 2 in the winter, and the existence of an Aleutian high at 180° longitude in December. These features are apparently related to the ability of certain tropospheric standing waves to propagate upwards high into the stratosphere in the presence of westerly flow throughout the troposphere and stratosphere. On

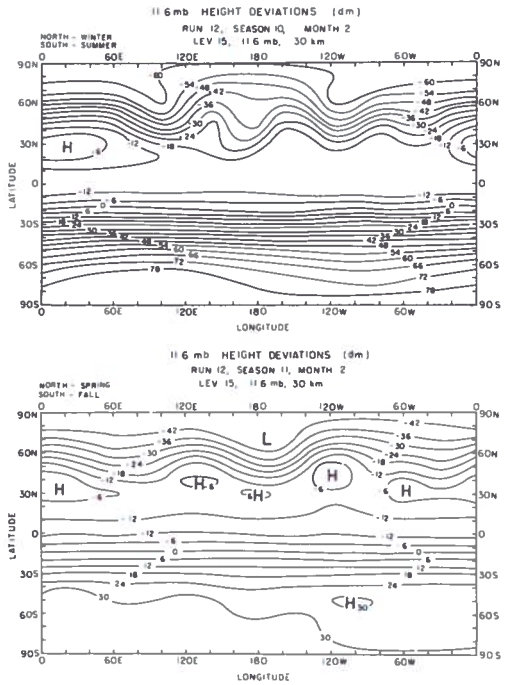

Figure 14. Mean height deviations (dekameters) for seasons 10 and 11, month 2, at approximately 10 mb.

the other hand, these waves cannot propagate through a layer in which low-level westerlies reverse to easterly flow aloft.

There is evidence for the occasional occurrence of large and rapid stratospheric temperature changes in our model. For example, at 2 mb and 70° latitude, temperature changes in excess of 45°K are found to occur during the spring over a period of approximately one week. At 10 mb the amplitude of the temperature changes is approximately 20°K. Although the details are not shown here, the warmings appear to propagate westward with time and may occur at the 10-mb level several days later than at the higher 2-mb level. A full analysis of the stratospheric warmings in our model will be undertaken shortly.

Ozone Results

The global-mean ozone profile calculated for year 3 is shown in Figure 15. During year 2 ozone decays approximately 10% below level 18 (approximately 22 km); in year 3, however, ozone appears to possess only an annual variation.

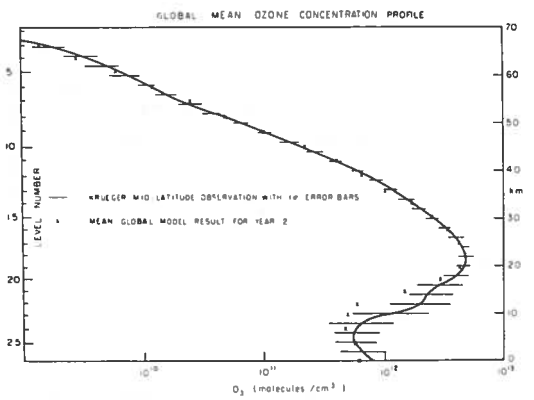

Figure 15. The predicted global-mean ozone profile for year 2 as a function of height and its comparison with mid-latitude rocket data presented by Krueger and Minzner (1973).

The global-average contributions of dynamics and diffusion to the upward flux of ozone for season 10, month 2 (June) are shown in Figure 16. Similar profiles are obtained in equinoctial months. The maximum net production of ozone occurs at level 15, from which the ozone is transported downwards by diffusion, with some compensating upward motion from the large-scale dynamics between levels 15 and 18. There is therefore somewhat less ozone in the lower stratosphere after a two-year integration than there was initially. The large-scale dynamics is apparently able to transport approximately 20 tons/second of ozone through the tropopause, and the total flux of ozone being destroyed at the ground is about 30 tons/second. This is in close agreement with the global surface-destruction estimates by Fabian and Junge (1970). The downward flux in the upper troposphere has considerably reduced the ozone concentration in the 10-15 km region relative to its initial concentration (compare Figure 7) while substantially adding to that below 10 km. It is particularly encouraging that we are obtaining the observed ozone concentration at the ground while using a lower-boundary condition which in no way fixes the value there.

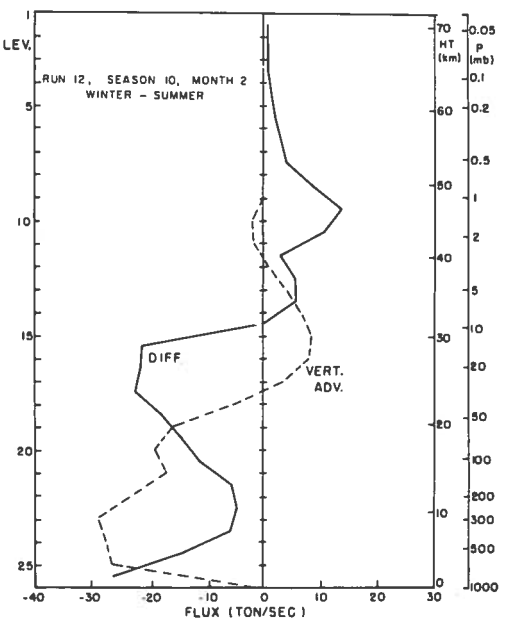

Figure 16. The contributions of diffusion and large-scale dynamics to the vertical motion of ozone for season 10.

The model seems to be ending up with not quite enough ozone in the 10-15 km region. This result may be examined in more detail in the lower parts of Figures 17 and 18, which show the predicted latitudinal distribution of ozone concentration. The figures may be compared with the observations analyzed by Hering and Borden

(1964, 1965, and 1967), presented here in the upper parts of Figures 17 and 18. We note that there is good agreement between the model results and the observations, with ozone being transported poleward and downward. The ozone deficiency between 10 and 15 km now shows up primarily at high latitudes in winter and spring. Calculations suggest that this result could be modified by reducing the diffusion coefficient in the 10- to 15-km height range, which would reduce the tendency for ozone to be diffused out of the polar lower stratosphere. It is also possible that use of a more realistic NO_2 distribution would accomplish this objective.

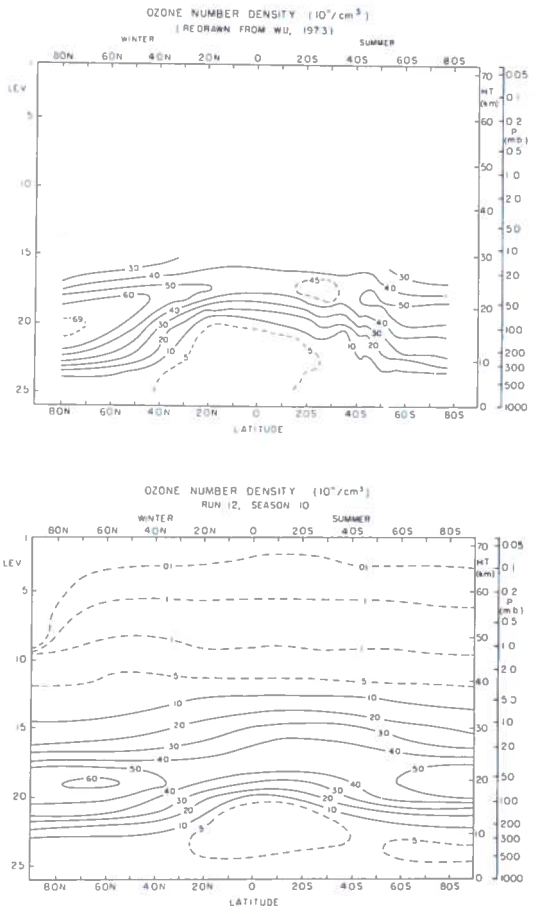

Figure 17. The distribution of ozone as a function of latitude and height predicted for season 10 compared with the mean observed ozone density (10^{11} molecules/cm^3) for summer and winter derived from the ozone profile data obtained by Hering and Borden (1964, 1965, and 1967) (from Wu (1973)).

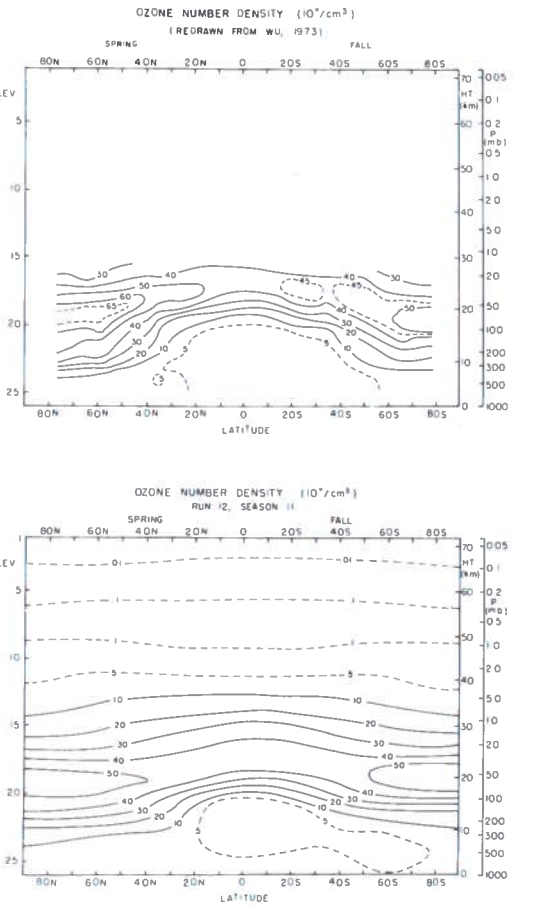

Figure 18. The distribution of ozone as a function of latitude and height predicted for season 11 compared with the mean observed ozone density (10^{11} molecules/cm^3) for fall and spring derived from the ozone profile data obtained by Hering and Borden (1964, 1965, and 1967) (from Wu (1973)).

At altitudes above 30 km, the model predictions regarding ozone may be compared with the satellite observations which are just beginning to appear in print. A sample of that data (Krueger et al., 1973) is shown as Figure 19. Figure 20 shows the predicted distribution of ozone mixing ratios for season 8 (winter-summer). The observed ozone distributions contained in Figure 19 are supposed to be typical of particular seasons, so Figure 20 may be directly compared with orbit 938 (for June 17). Agreement between observations and model results is excellent; the model exhibits peak mixing ratios centered around the subsolar point, and a secondary peak at high altitudes in the winter

hemisphere associated with the cold temperatures there. The model predictions above level 10 at high latitudes of the winter hemisphere are inexact because of the small solar illumination and the diagnostic nature of the ozone prediction there.

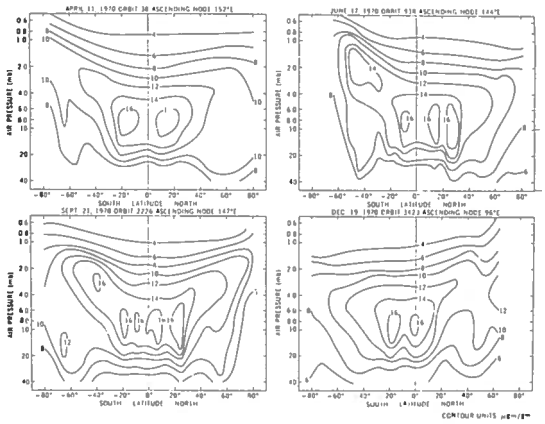

Figure 19. Pseudo-meridional cross-sections of ozone mass mixing ratio derived from BUV data during four orbits of Nimbus 4 (from Krueger et al. (1973)).

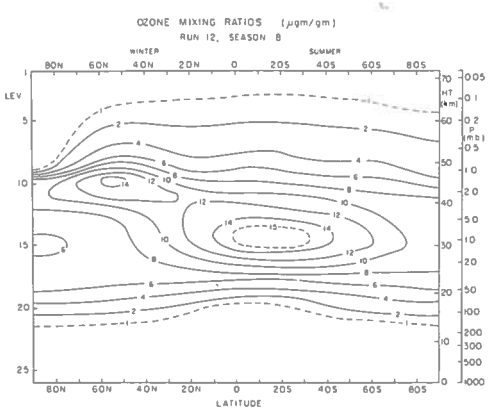

Figure 20. Zonal-mean ozone mixing ratios (μgm/gm) as a function of latitude and height predicted for season 8.

The predicted latitudinal variation of total ozone as a function of the time of year during year 2 is presented in Figure 21. Comparable observed data from Dütsch (1969) are also shown. The model results clearly show a spring maximum in total ozone at all latitudes, with the largest concentrations occurring at high latitudes, in good qualitative agreement with the observations. However, the pole-to-equator gradients and the seasonal variations are somewhat weaker than those observed. This feature is probably also related to the shortage of ozone in high latitudes in the 10-15 km region. Figure 22 depicts the latitudinal distribution of the contributions of the meridional circulation and eddy motions to the horizontal fluxes of ozone for the middle months of seasons 10 and 11 (September and December). At mid-latitudes the meridional transports are always equatorward, while the eddy transports are always poleward, and the largest transports occur in the winter and the spring, with only small transports occurring in the summer. The eddy fluxes appear to possess the anticipated seasonal variation and to have a mean value in good agreement with the observed value of 50 tons/second reported by Hutchings

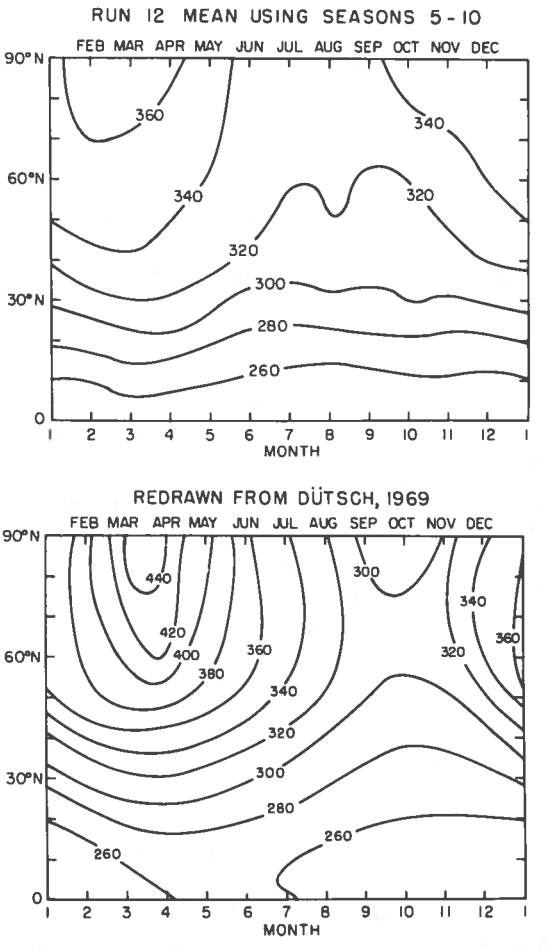

Figure 21. Total-ozone distribution with season and latitude averaged over years 2 and 3 and compared with ozone observations from Dütsch (1969).

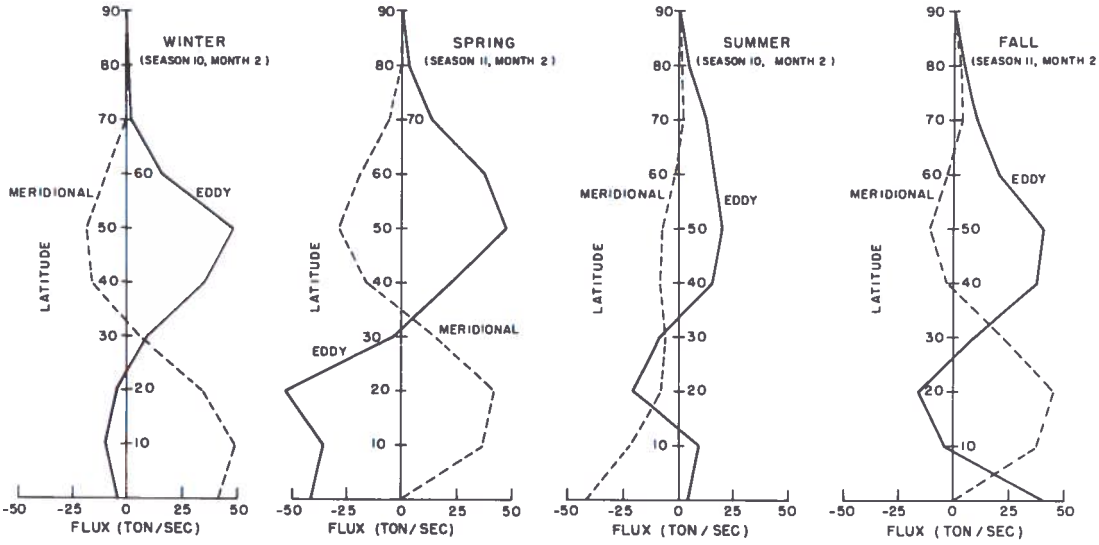

Figure 22. The contributions of the meridional circulation and the eddies to the poleward transport of ozone for the mid-months of seasons 10 and 11.

and Farkas (1971) for a single mid-latitude station. The large transequatorial fluxes due to the meridional circulation during summer and winter may also be noted; they correspond to the large cross-equatorial transports of tropospheric air at that time of year.

The predictions of the model relating to the global distribution of columnar ozone for each season are presented in Figure 23. The results may be compared with the observations analyzed by Wu (1973), of which the monthly mean values for 1960-1969 for the mid-months of each season are given in Figure 24. There is good agreement between theory and observation for the location of the various features of the ozone distribution, particularly during the solstitial seasons. In particular the extensive region of generally low ozone concentrations during summer, centered at approximately 120°E and 70°S, is also present in Wu's charts, as is the region of high ozone concentrations centered at North American latitudes. In the winter the extensive region of high ozone concentrations between approximately 100°E and 30°W bears a remarkable resemblance to the region of high ozone concentrations found in Wu's data, including a peak concentration in approximately the same location. The model also exhibits a small high in the neighborhood of Arosa (20°E).

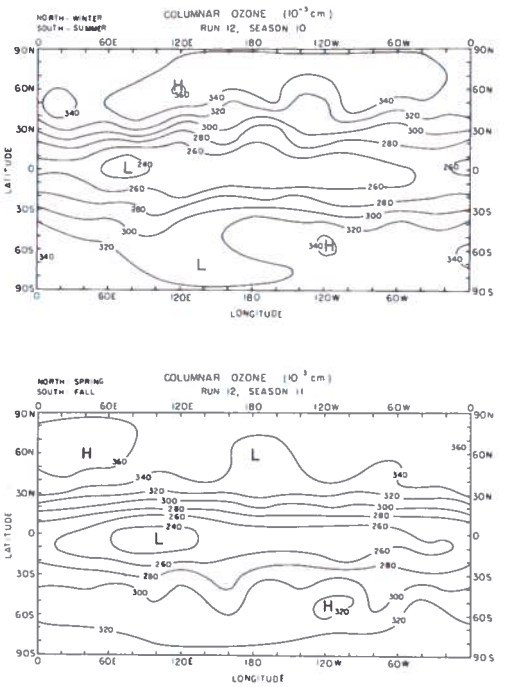

Figure 23. Predicted distribution of total ozone for seasons 10 and 11 (matm-cm).

The magnitudes of the fluctuations in columnar ozone are presented in Figure 25, where they are compared with ground-based

observations in the northern hemisphere summarized by Newell (1963). Both the model results and the observations possess an average standard deviation of 30 matm-cm at mid-latitudes. However, the variation of the predicted fluctuations with latitude is less strong than the variation of the observed fluctuations. This result is almost certainly associated with the weaker pole-to-equator gradient of total ozone that the model results possess. On the other hand, the seasonal variation of the variance is in good agreement with the observations.

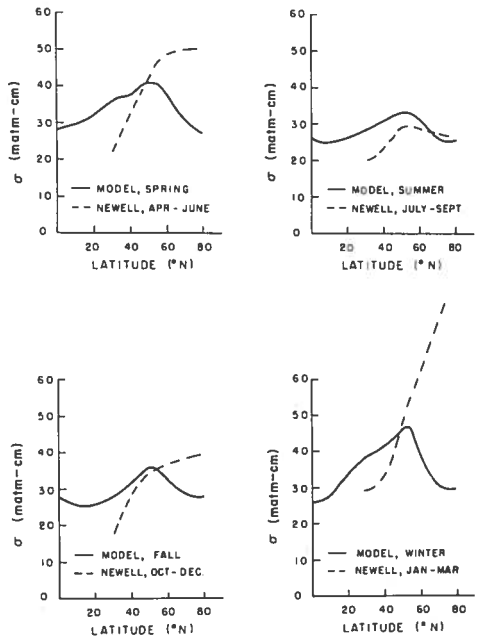

Figure 25. The latitudinal variation of the standard deviations of total ozone as a function of the indicated seasons, compared with observations reported by Newell (1963). Units are matm-cm.

Correlations between total ozone and several other parameters have been calculated. Total ozone is found to be negatively correlated with the 700-mb temperature, with a correlation coefficient of approximately -0.5 at mid-latitudes in winter. By contrast, it is positively correlated with the 100-mb temperature, with a correlation coefficient of +0.4. These correlations are similar to values quoted in Craig's book (1965) that were based upon observations at Oxford. The correlation coefficients between columnar ozone and ozone concentrations at particular pressure levels have also been calculated. The results show a peak correlation of approximately 0.6 at mid-latitudes at around 15 km, in good agreement with the data of Hering and Borden (1967). The model results do not, however, exhibit the fairly rapid decrease of correlation coefficient with height above 15 km. For example, a correlation coefficient of 0.3 is still found in the model results up to 30 km altitude.

CONCLUSIONS

The model appears to be performing well for the purpose for which it has been designed. It simulates the dynamics of the stratosphere very well, giving in the winter a westerly wind maximum whose amplitude and location tally with those observed, and changing over to easterlies in summer. Furthermore, the lower stratosphere is being forced by the troposphere, while the troposphere and the upper stratosphere are largely forced by the in-situ distribution of heating and cooling.

The agreement between observed data on atmospheric ozone and the predictions of the model is generally excellent. In particular, the model correctly shows ozone to be transported polewards and downwards, and the poleward eddy flux is of the same magnitude as that observed. Moreover, the general level of fluctuation of columnar ozone is correctly predicted, as is the seasonal variation in ozone at mid-latitudes. The standing-wave patterns of columnar ozone also seem to agree well with the observations. The only significant deficiency in the model is that the pole-to-equator gradients of ozone are not as large as those observed, particularly during the winter and the spring. An attempt is under way to remove this deficiency by adding a realistic latitudinal distribution of NO_2 and by reducing the diffusion coefficient (perhaps to zero) everywhere except in the atmospheric boundary layer.

ACKNOWLEDGMENTS

This research was supported as part of its Climatic Impact Assessment Program by the U.S. Department of Transportation, under Contract

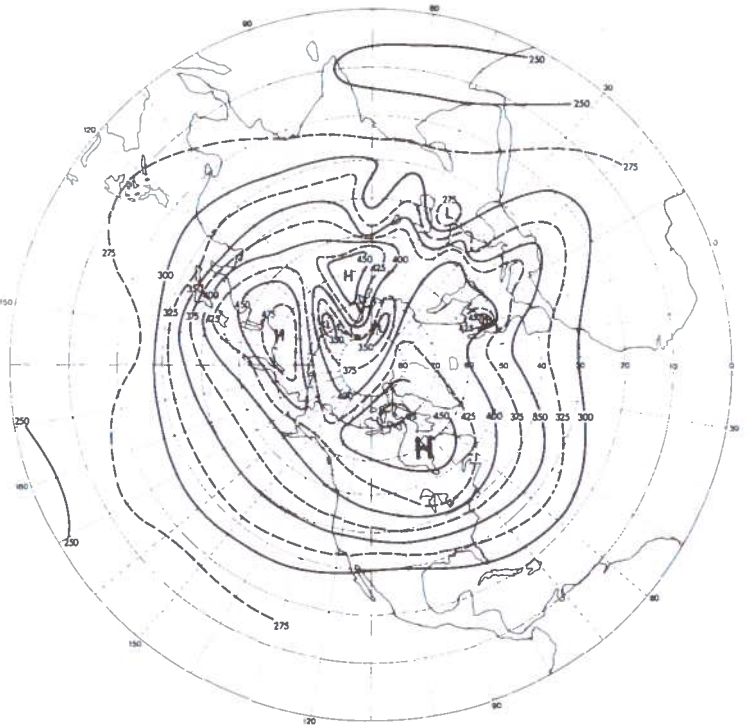

a. March.

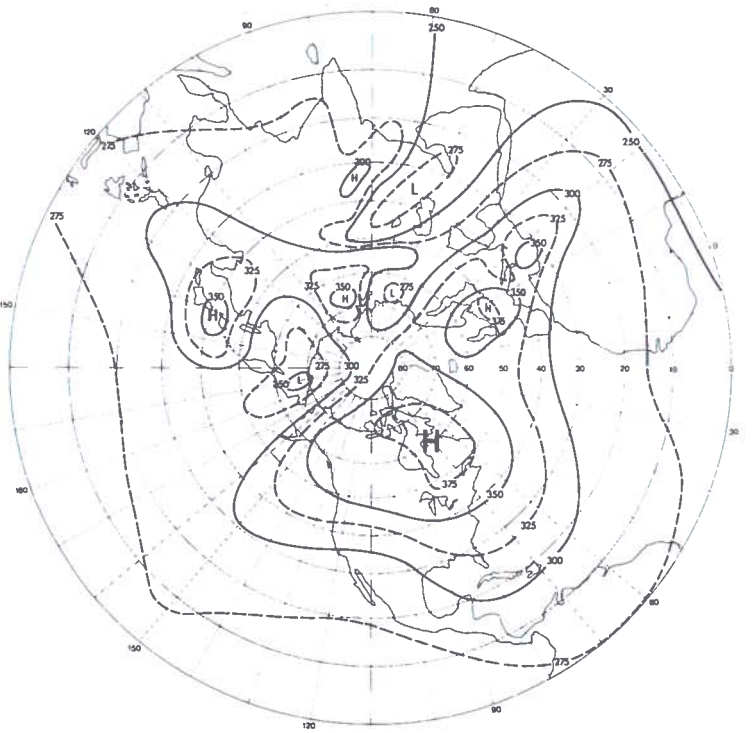

b. June.

Figure 24. Distribution of total ozone in the northern hemisphere, based on 11 years of data, from Wu (1973).

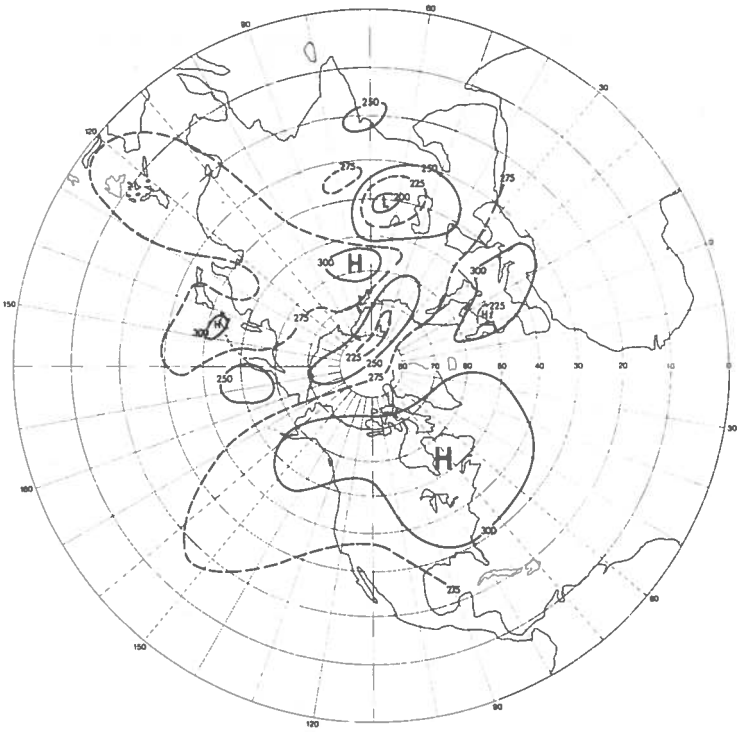

c. September.

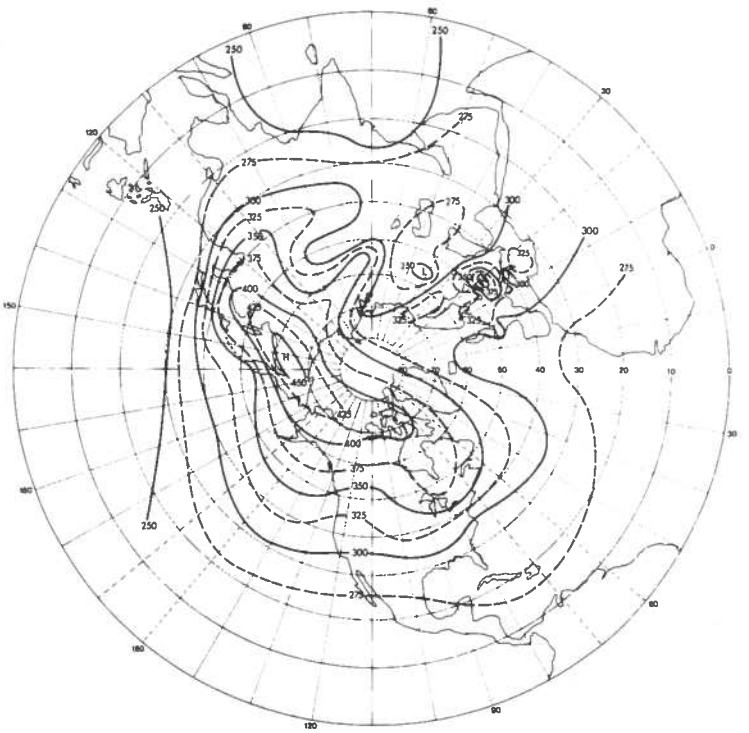

d. December.

Figure 24 (continued). Distribution of total ozone in the northern hemisphere, based on 11 years of data, from Wu (1973).

No. AT 11-1-2249. We also gratefully acknowledge the computer time provided by the Goddard Institute for Space Studies, New York City, through Grant NGR 22-009-727 from the National Aeronautics and Space Administration.

REFERENCES

Clark, J. (1970), "A quasi-geostrophic model of the winter stratospheric circulation," Mon. Wea. Rev. **98**, 443-461.

Craig, R.A. (1965), *The Upper Atmosphere: Meteorology and Physics*, Academic Press, New York, 209 pp.

Cunnold, D., F. Alyea, N. Phillips, and R. Prinn (1974), "A general circulation model of stratospheric ozone," in *Proceedings of the International Conference on Structure, Composition and General Circulation of the Upper and Lower Atmosphere and Possible Anthropogenic Perturbations* (Melbourne, Jan. 14-25), pub. IAMAP, 932-970.

Davis, D.D. (1973), "New rate measurements on the reaction of $O(^3P)$, O_3 and OH," AIAA Paper 73-501 (Denver, June 1973).

Dickinson, R. (1973), "A method of parameterization for infrared cooling between altitudes of 30 and 70 km," J. Geophys. Res. **78**, 4451-4457.

Dopplick, T.G. (1970), "Global Radiative Heating of the Earth's Atmosphere," M.I.T. Meteorology Department, Report No. 24, April 15.

Dutsch, H.U. (1969), *Atmospheric Ozone and Ultraviolet Radiation*, World Survey of Climatology, Vol. 4, ed. H.E. Landsberg, Elsevier Publishing Co., Amsterdam.

Fabian, P. and C. Junge (1970), "Global rate of ozone destruction at the earth's surface," Arch. Meteor., Geo., Bioklimat., (a)-Meteor. u. Geo. **19**, 161.

Galbally, J. (1971), "Ozone profiles and ozone fluxes in the atmospheric surface layer," Quart. J. Roy. Meteor. Soc. **97**, 18.

Garvin, D. and R.F. Hampson (1973), "Atmospheric modelling and the chemical data problem," AIAA Paper 73-500 (Denver, June 1973).

Hering, W.S. and T.R. Borden, Jr. (1964), "Ozonesonde Observations Over North America, Vol. 2," Environmental Research Paper No. 38, AFCRL-64-30 (II) (Air Force Cambridge Research Labs, Bedford, Mass.).

Hering, W.S. and T.R. Borden, Jr. (1965), "Ozonesonde Observations Over North America, Vol. 3," Environmental Research Paper No. 133, AFCRL-64-30 (III).

Hering, W.S. and T.R. Borden, Jr. (1967), "Ozonesonde Observations Over North America, Vol. 4," Environmental Research Paper No. 279, AFCRL-64-30 (IV).

Hunt, B. (1969), "Experiments with a stratospheric general circulation model: III. Large-scale diffusion of ozone including photochemistry," Mon. Wea. Rev. **97**, 287-306.

Hutchings, J. and E. Farkas (1971), "The vertical distribution of atmospheric ozone over Christchurch, New Zealand," Quart. J. Roy. Meteor. Soc. **97**, 249-254.

Justus, C.G. (1973), "Upper atmospheric mixing by gravity waves," AIAA Paper 73-495 (Denver, June 1973).

Kaufman, F. (1969), "Neutral reactions involving hydrogen and other minor constituents," Can. J. Chem. **47**, 1917-1924.

Krueger, A.J., D.F. Heath, and C.L. Mateer (1973), "Variations in the stratospheric ozone field inferred from Nimbus satellite observations," Pure Appl. Geophys. **106-108**, 1254-1263.

Krueger, A. and R. Minzner (1973), "A Proposed Mid-Latitude Ozone Model for the U.S. Standard Atmosphere," Goddard Space Flight Center, X-651-73-72.

Leovy, C. (1964), "Simple models of thermally driven mesospheric circulation," J. Atmos. Sci. **21**, 327-341.

Lindzen, R.S. (1971), "Tides and gravity waves in the upper atmosphere," in *Mesospheric Models and Related Experiments*, ed. G. Fiocco, D. Reidel, Dordrecht, 122 pp.

Lorenz, E.N. (1960), "Energy and numerical weather prediction," Tellus **12**, 364.

Machenhauer, B. and E. Rasmussen (1972), "On the Integration of the Spectral Hydrodynamical Equations by a Transform Method," Report No. 3, Institute for Theoretical Meteorology, Copenhagen University, 44 pp.

McConnell, J.C. and M.B. McElroy (1973), "Odd nitrogen in the atmosphere," J. Atmos. Sci. **30**, 1465-1480.

McElroy, M., S. Wofsy, J. Penner, and J. McConnell (1974), "Atmospheric ozone: possible impact of stratospheric aviation," J. Atmos. Sci. 31, 287-303.

Newell, R.E. (1963), "Transfer through the tropopause and within the stratosphere," Quart. J. Roy. Meteor. Soc. 89, 167-204.

Newell, R.E. (1969), "Radioactive contamination of the upper atmosphere," in *Progress in Nuclear Energy – Series XII, Health Physics*, Vol. 2, ed. A.M. F. Duhamel, Pergamon, Oxford, 535-550.

Newell, R.E., J.W. Kidson, D.G. Vincent, and G.J. Boer (1972), *The General Circulation of the Tropical Atmosphere and Interaction with Extratropical Latitudes*, Vol. 1, M.I.T. Press, Cambridge, Mass. 45.

Schofield, K. (1967), "An evaluation of kinetic rate data for reactions of neutrals of atmospheric interest," Planet. Space Sci. 15, 643.

Trenberth, K. (1972), "Dynamic Coupling of the Stratosphere with the Troposphere and Sudden Stratospheric Warmings," Ph.D. thesis, Dept. of Meteorology, MIT.

Vincent, D.G. (1968), "Mean meridional circulations in the Northern Hemisphere lower stratosphere during 1964 and 1965," Quart. J. Roy. Meteor. Soc. 94, 333-349.

Wofsy, S. and M. McElroy (1973), "On vertical mixing in the upper stratosphere and lower mesosphere," J. Geophys. Res. 78, 2619-2624.

Wu, M.F. (1973), "Observations and Analysis of Trace Constituents in the Stratosphere," Annual Report, Contract No. DOT-05-20217, Environmental Research and Technology (429 Marrett Rd., Lexington, Mass. 02173).

DISCUSSION

CUNNOLD: Yes, it seems to have. The ozone profile changes a lot in year one, and somewhat in year two, but in year three it seems to settle down.

(UNIDENTIFIED): How important is the eddy diffusion coefficient to the time required to reach equilibrium? Some one-dimensional calculations take eight or ten years to get there.

CUNNOLD: The eddy diffusion coefficient is important between twenty and thirty kilometers, but below that the large-scale motions take over, giving you much shorter time constants.

(UNIDENTIFIED): What does a three-dimensional model give you that can't be gotten out of a parameterized two-dimensional model?

(UNIDENTIFIED): Has your model come to equilibrium yet in the 15 to 20 kilometer region?

CUNNOLD: You can simulate a variety of situations with a parameterized two-dimensional model, but when you want to change other conditions or add certain feedbacks you need a three-dimensional model.

SCHAINKER: When you compared your model predictions with observations, did you determine the residual error?

CUNNOLD: We do make a sort of sensitivity study, but nothing that quantitative.

LONDON: In a model, you can simply start with a normal January atmosphere, change the sun condition, say, and then see how close your spring change in ozone distribution is. The difference between your prediction and actuality is a good test for sensitivity.

ZIMMERMAN: Did you use the same NO_2 profile for all latitudes?

CUNNOLD: Yes, because there are no measurements of the meridional distribution. If we can get that distribution from a two-dimensional model, we'll use it.

THE CHANGE IN EARTH-ATMOSPHERE ALBEDO DUE TO STRATOSPHERIC POLLUTION

BENJAMIN M. HERMAN
Institute of Atmospheric Physics
The University of Arizona
Tucson, Arizona

ABSTRACT: This paper presents theoretical calculations of the change in earth-atmosphere albedo for a wide range of aerosol loadings in a perturbed stratosphere. These calculations are based upon a complete solution to the equation of radiative transfer, which includes all orders of multiple scattering by both the aerosol and the molecular constituents.

The aerosols are assumed to be distributed throughout the 15-25 km height interval. Calculations are presented for perturbed-stratosphere loadings up to 3.2 $\mu g/m^3$, and for a wavelength of 0.5 μm. A range of solar-elevation angles and ground albedos is employed to cover all possible conditions. Absorption by the aerosol layer is considered by taking a range of single-scattering albedos for the particulates.

In this paper, we present some results of theoretical calculations of the effects of a perturbed stratosphere on the visible radiation field. Results will be given for a wide range of perturbations, in order to encompass minimal to maximal expected effects.

METHOD OF CALCULATION

The injected particulates are assumed to be sulfates, with a real index of refraction of 1.54. They are assumed to be distributed according to a log-normal distribution given by

$$\frac{dn}{dr} = \frac{1}{2\pi\sigma}\, e\, \exp\left(\frac{\left(\ell n \frac{r}{\bar{r}}\right)^2}{2\sigma^2}\right) \qquad (1)$$

where n is the number of particulates per unit volume of radius r, $\bar{r}$ is the mean radius, and σ is the natural log of the geometrical standard deviation.

The addition of particulates into the stratosphere will cause an increase in atmospheric turbidity. A convenient measure of the turbidity is the optical depth, τ, defined as

$$\tau = \int_0^\infty Q_T\, dz \qquad (2)$$

where Q_T is the volume extinction coefficient, given by

$$Q_T = \int_0^\infty \sigma_T(r)\, \frac{dn}{dr}\, dr \qquad (3)$$

Here $\sigma_T(r)$ is the attenuation cross-section for a particle of radius r, computed from Mie theory, while dn/dr is the size-distribution function, which for the present problem is given by Eq. (1).

By means of Eqs. (1), (2), and (3) above, the optical-depth increase due to the injection of any amount of particulates may readily be computed. Figure 1 presents results from such calculations. For the purposes of these computations, the particulate matter was assumed to be distributed uniformly over a 10-km thick layer, from 15 km to 25 km. The ordinate gives the optical depth increment per microgram (μg) of added mass per m^3 over a 10-km thick layer, with particles distributed in size according to Eq. (1). The abscissa is the mean radius, $\bar{r}$, of the distribution function. Curves are shown for several values of σ. The circled point on the curve for $\sigma = 1.3$, $\bar{r} = 0.3$, pertains to the best fit of the measured stratospheric-aerosol size distribution as reported by Friend (1966). As can be seen on the figure, this particular size distribution implies an optical-depth increase of 0.038 for 1 $\mu g/m^3$ of mass

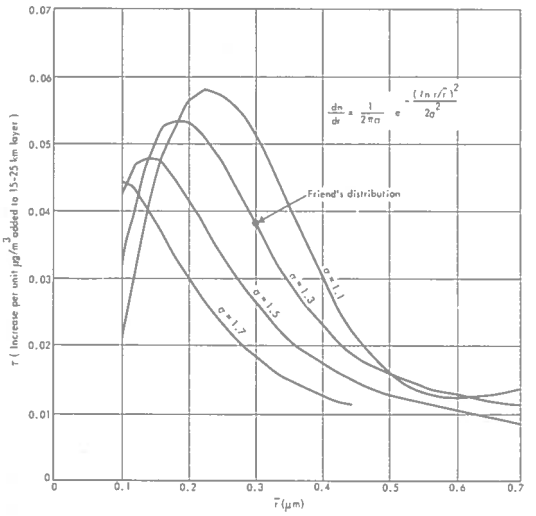

Figure 1. Optical-depth increase due to the injection of different amounts of particulates.

inserted into a 10-km thick layer. If the addition of mass were 0.1 $\mu g/m^3$, say, then this would immediately yield an optical-depth increase of 0.0038. Thus, this figure may readily be interpreted to obtain the optical-depth increase for the addition of any amount of mass per unit volume over a 10-km thick layer.

Since all of the curves in Figure 1 are normalized to a 1 $\mu g/m^3$ mass increase over a 10-km thick layer, they readily demonstrate the variability of the resulting optical-depth increase for different size distributions (i.e., for different values of σ and $\bar{r}$ in Eq. (1)). Thus, for example, values of $\sigma = 1.1$ and $\bar{r} = 2.2$ yield an optical-depth increase of 0.058, while $\sigma = 1.7$ and $\bar{r} = 0.4$ yield an optical-depth increase of about 0.011, both for the same amount of mass increase. It is evident that a knowledge of the size distribution is of considerable importance.

With a given optical-depth increase corresponding to a known mass increase and a known size distribution, one may then compute the perturbation in the radiation field. The particular calculations to be presented here employed a numerical solution to the radiative-transfer equation first described by Herman and Browning (1965), modified to include an expansion of the scattering matrix into a Fourier series in azimuthal angle. This technique makes use of a Gauss-Seidel iteration technique, as described in the above reference. Details of the computational scheme need not be described here; interested readers may refer to the above reference. This particular solution takes into account all significant orders of scattering, polarization of the radiation field, vertical inhomogeneities, absorption and emission (if present), and ground reflectivity.

Certain input parameters must be specified for this model. These are outlined below.

Optical Depth

The optical depth, as previously discussed, is a function of wavelength, particulate size, height distribution, and index of refraction. For the atmospheric model used here, a wavelength of $\lambda = 5000$ Å has been employed. At this wavelength, a molecular optical depth due to the normal gaseous atmospheric constituents is taken to be $\tau_{mol} = 0.145$. For the particulate or aerosol optical depth, a standard atmospheric value of $\tau_{part} = 0.1$ has been assumed. This seems to be a reasonable value for a clear, unpolluted atmosphere, so a total optical depth $\tau = \tau_{mol} + \tau_{part} = 0.245$ is used to represent the standard, unpolluted atmosphere.

Particulate Size Distribution

All stratospheric particulates, whether due to engine emissions or to natural causes, have been assumed to follow a log-normal distribution, given by Eq. (1). In the troposphere, all particulates have been assumed to follow a Junge size distribution, given by

$$\frac{dn}{dr} = Cr^{-(\gamma^* + 1)} \qquad (4)$$

where C is an arbitrary constant which determines the total number density, and γ^* is a shaping parameter. A value of $\gamma^* = 1.5$ has been used for this work.

From the above tropospheric and stratospheric particulate size distributions, the relevant optical properties, such as the scattering phase matrices and the total attenuation cross-sections, were computed from the Mie equations.

Height Distributions

Molecular gaseous species have been assumed to be distributed according to a standard atmospheric profile (U.S. Standard Atmospheric Supplement, 1966). For the unpolluted particulate height distributions, the profile given by Elterman (1968) has been used. Particulate pollutants have been introduced into the 10-km layer from 15 km to 25 km, with uniform mass density throughout the layer. Various amounts of pollutants, in terms of $\mu g/m^3$, have been introduced into this layer, and the total increase converted into an optical-depth increase as computed from Eqs. (1), (2), and (3), with equation (3) first being normalized by means of a multiplicative constant in order to give the proper mass per unit volume.

Index of Refraction

As mentioned earlier, the index of refraction assumed for the particulates, both tropospheric and stratospheric, is m = 1.54. In the troposphere, the absorption by the particulates has been assumed to be zero for all the calculations, while a range of absorption has been assumed for the pollutant aerosols. This absorption has been inserted by means of the single-scattering albedo, ω_0, defined as

$$\omega_0 = \frac{Q_s}{Q_T} \tag{5}$$

where Q_s and Q_T are the scattering and total attenuation cross-sections per unit volume. Physically, the single-scattering albedo represents that fraction of the attenuated radiation which reappears as scattered radiation due to a single-scattering process.

RESULTS

Calculations have been performed for ground albedos A = 0.05, 0.1, 0.3, 0.5, 0.7, and 0.9; for 9 solar zenith angles from 5° to 85° at 10° intervals; and for values of ω_0 = 1.0, 0.95, 0.9, 0.8, 0.7, and 0.6. In addition, calculations were performed for five values of stratospheric aerosol loading, starting with the natural stratosphere (zero pollution) and then adding 0.8, 1.6, 2.4, and 3.2 $\mu g/m^3$ of aerosols over a 10-km-thick layer from 15 km to 25 km. Figure 2 presents results for solar zenith angles of 15°, 45°, and 65°, all for $\lambda = 0.5\mu$. The figure shows the reflected flux as a function of the single-scattering albedo, ω_0, for three values of the ground albedo, A = 0.1, 0.3, and 0.9. For each ground albedo, all five values of the stratospheric aerosol loading are shown.

Let us consider first the sets of curves for a ground albedo A = 0.1. Considering first Figure 2a, for a solar zenith angle of 15°, we see that for $\omega_0 > 0.88$, addition of pollution causes a net increase in the reflected flux out of the top of the atmosphere (i.e., a net cooling), while for $\omega_0 < 0.88$, the reverse is true. Referring to Figure 2b ($\theta = 45°$), we see that this crossover point between heating and cooling occurs for $\omega_0 \approx 0.85$, while for $\theta_0 = 65°$ in Figure 2c, the value is $\omega_0 \approx 0.82$. Referring to the imaginary part of the index of refraction scale, we see the range of values of ω_0 between 0.9 and 0.8 corresponds to an imaginary index near 0.01, which is the value usually used for aerosol absorption. Thus, for ground albedos near 0.1, either heating or cooling may result, depending critically upon the imaginary part of the index of refraction, as well as upon the solar zenith angles.

As the ground albedo is increased, we see that the crossover point between heating and cooling shifts towards smaller values of the imaginary part of the index, such that for ground albedos A = 0.9, a net warming (i.e., decrease of reflected flux) occurs even for non-absorbing aerosols, for any increase of aerosol loading. Thus, over ice- or snow-covered regions, the effect of increased stratospheric pollution is always one of warming, while over bare ground ($A \approx 0.1$) or open water (A = 0.05), the effect could be either warming or cooling, as discussed above.

In order to make some estimate of global effects, the results of the above computations were integrated over time for 10° latitude belts in the following manner. For any given latitude and day of the year, the sun describes a known path in the sky as a function of time. Therefore, at a fixed latitude, and for a given day of the year, the average earth-atmosphere albedo, $\bar{R}$, is given by

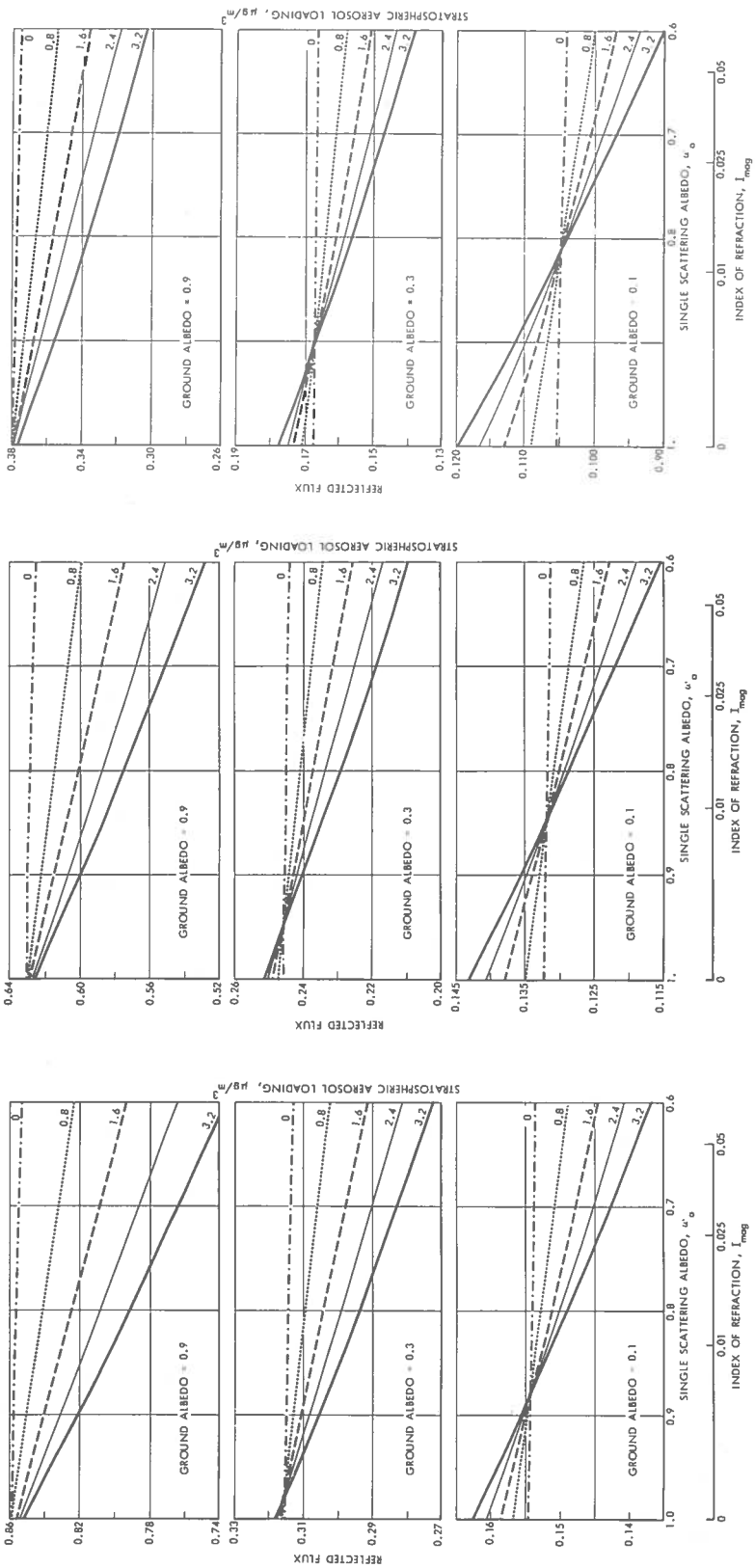

a. Solar zenith angle = 15°.

b. Solar zenith angle = 45°.

c. Solar zenith angle = 65°.

Figure 2. Reflected flux as a function of the single-scattering albedo for three values of the ground albedo for each of three solar zenith angles. Wavelength = 0.5 μm. Five values of the stratospheric aerosol loading are plotted for each ground albedo.

$$\bar{R} = \int_{\text{sunrise}}^{\text{sunset}} \cos\theta_0 F_0 R(\theta_0)\, dt \Big/ \int_{\text{sunrise}}^{\text{sunset}} \cos\theta_0 F_0\, dt$$

where F_0 is the incident solar flux on a plane perpendicular to the solar beam, and $R(\theta_0)$ is the reflected flux at the given solar zenith angle, θ_0. The integration of the above equation was carried out numerically in 5-minute increments. For each increment of time, the value of θ_0 was computed for the latitude and day of the year, and the value of $R(\theta_0)$ was selected from those computed as described above for the nearest value of θ_0 among the nine values used.

The proper value for the ground albedo was determined in the following manner. Ocean was assumed to have an albedo of 0.05, bare ground one of 0.1, and snow and ice one of 0.9. Each 10° latitude belt was weighted as to the percentage of land and ocean. Land areas were assumed to be snow-covered down to 40° latitude in January and February, 50° in March, 60° in April, 70° in May, and 80° in June, and to be bare in July and August; the pattern was reversed in the fall. Ocean areas were assumed to be fractionally covered with ice or snow in accordance with Sellers (1974).

Computations were performed for $\bar{R}$ for the 21st day of each month for each of the 9 latitude belts, and for 0, 0.8 $\mu g/m^3$, 1.6 $\mu g/m^3$, and 3.2 $\mu g/m^3$ pollution through the 15-25 km layer. The calculations were then weighted by the fraction of surface in each latitude belt that was assumed to be bare ground (A = 0.1), open water (A = 0.05), and ice or snow (A = 0.9). In addition, it was assumed that each latitude belt had, on the average, a 50% cloud cover. The cloud cover was approximated by using the results for a ground albedo, A = 0.5.

The results of the above weighting, for the non-absorbing case ($\omega_0 = 1.0$) and for the difference in albedo between a non-polluted stratosphere and a stratosphere containing 0.8 $\mu g/m^3$ pollution between 15 and 25 km, are shown in Figure 3. In this figure, isolines of the change in reflectivity are drawn as a function of latitude (ordinate) and month (abscissa).

Confining our attention first to latitude belts south of 40°N, we see that the pattern is relatively flat; that is, there is little change with season or latitude. The average change for the addition of 0.8 $\mu g/m^3$ in the 10-km layer is about 0.4%. If 0.1 $\mu g/m^3$ were added, this would become approximately 0.05%. For latitudes north of 40°N, the changes are somewhat more pronounced. We see that, during the months of January and February, there is an average change of about 0.7%, or almost 0.1% for the addition of 0.1 $\mu g/m^3$. This is due to the very large change in reflectivity that comes over a water surface (A = 0.05) with very low sun, modified by the very small change that occurs over ice and snow (A = 0.9). As the season progresses into spring, the higher solar zenith angles reduce the reflectivity change over the open-water areas, while the reflectivity change over snow remains very small. As we cross from snow-covered ground into bare ground later in the spring and summer, with relatively high sun, the change levels off near 0.4%, typical of the lower latitudes. As fall progresses, reflectivity changes rapidly increase, peaking out at about 1.1% for 0.8 $\mu g/m^3$ loading near 65°N in early October. This increase is due to the rapid lowering of solar elevation angles in the fall season. As we pass from bare ground to snow cover, the values drop off quickly to 0.7-0.8% for 0.8 $\mu g/m^3$ loading, or approximately 0.1% for 0.1 $\mu g/m^3$ loading. This drop-off is, as before, due to the weighting with the snow and ice cover, which causes very little change in reflectivity with increasing pollution at low solar angles.

We can summarize our results by stating that, for aerosol pollution loadings of 0.1 $\mu g/m^3$ over the 15-25 km height level, the change in earth-atmosphere albedo, for non-absorbing aerosols, ranges from about 0.05% at low latitudes (south of 40°N) and at high latitudes in the summer, to about 0.1 to 0.15% from September through February in high latitudes.

REFERENCES

Elterman, L. (1968), "UV, Visible, and IR Attenuation for Altitudes to 50 km," Air Force Cambridge Research Laboratories (Bedford, Mass.), Environmental Research Papers No. 285, 49 pp.

Friend, J.P. (1966), "Properties of the stratospheric aerosol," Tellus 18, 465-473.

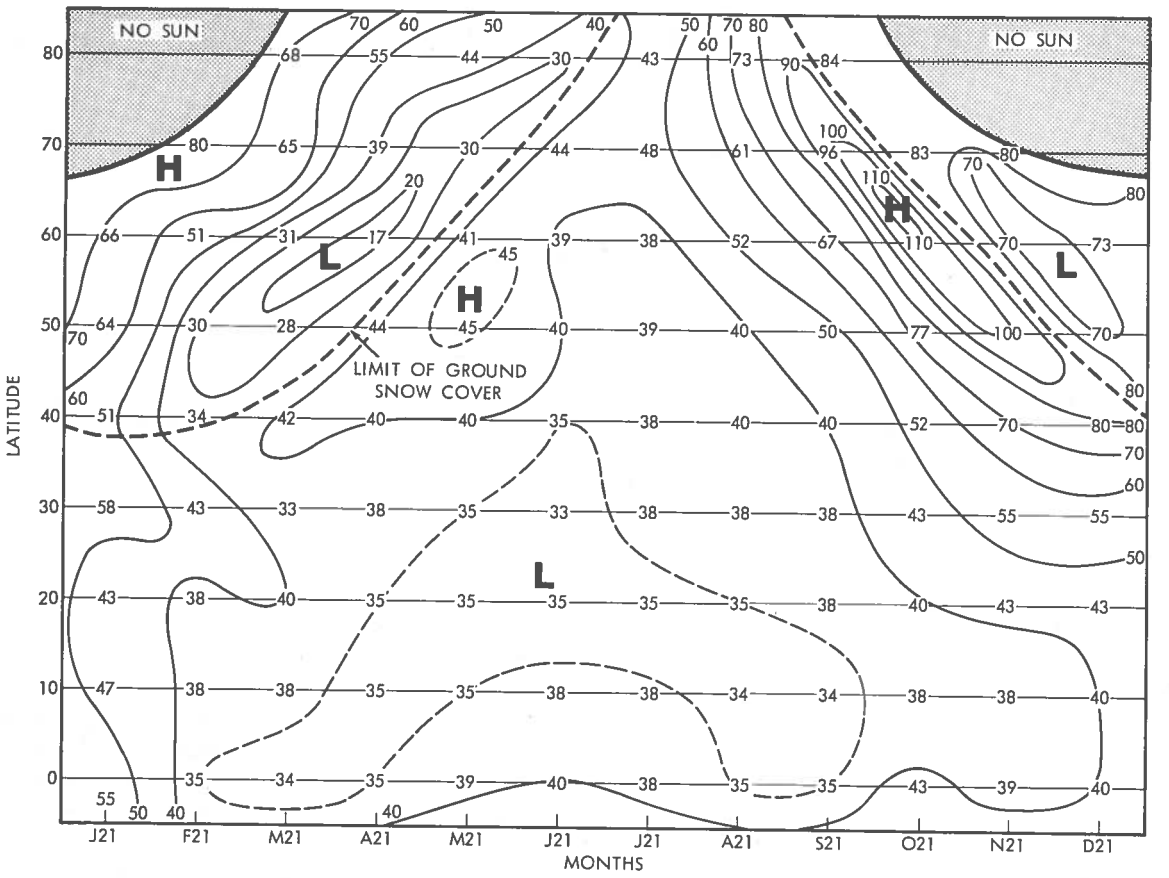

Figure 3. Isolines of reflectivity change as a function of latitude and month. $\lambda = 0.5\ \mu m$; $\omega_0 = 1.0$; Δref = ref (0.8 $\mu g/m^3$ pollution) – ref (0 pollution) in hundredths of 1 percent.

Herman, B.M., and S.R. Browning (1965), "A numerical solution to the equation of radiative transfer," J. Atmos. Sci. **22(5)**, 559-566.

Sellers, W.D. (1974), personal communication.

U.S. Standard Atmospheric Supplement (1966), sponsored by the Environmental Science Service Administration, the National Aeronautics and Science Administration, and the U.S. Air Force.

DISCUSSION

BARRETT: It's worth noting that the adsorption by aerosols tends to stabilize the atmosphere against convection.

HERMAN: Yes, the aerosols do redistribute heating that would otherwise have taken place at the surface. This model calculates the heating rates at all atmospheric levels. The results are available, though I didn't present them here.

(UNIDENTIFIED): Did you include tropospheric aerosols and their observed variations?

HERMAN: We used a constant tropospheric aerosol loading in this study. The real tropospheric variations are quite large, but they may average out. I'm not ready to comment on their importance relative to the stratospheric variations.

SOLAR ULTRAVIOLET RADIATION REACHING THE EARTH'S SURFACE

S.V. VENKATESWARAN
Department of Meteorology
University of California, Los Angeles
Los Angeles, California

ABSTRACT: It is suspected that engine effluents from a fleet of aircraft regularly flying in the stratosphere might deplete the amount of ozone in the atmosphere, and consequently increase the ultraviolet radiation reaching the earth's surface. To estimate the magnitude of this increase, the influence of various factors governing the radiation field is determined by solving the appropriate radiative-transfer equation. It is predicted that a decrease of ozone by 20% at middle latitudes might increase the radiative flux at the biologically effective wavelength of 305.5 nm by as much as 30% for an overhead sun, and between 50-60% for medium solar elevation. Increased stratospheric turbidity is not expected to mask this effect to a noticeable extent.

The ultraviolet solar radiation reaching the earth's surface is confined, for the purposes of this discussion, to the wavelength range 290-340 nm. This radiation is partly absorbed by ozone at stratospheric altitudes. Consequently, any depletion in the stratospheric ozone content will result in an increase in the UV radiation received at the ground. The objective of this paper is to estimate the magnitude of the UV radiation increase as a function of ozone decrease. In addition, the solar UV radiation at the ground will be influenced by several other factors:

- solar flux (as a function of wavelength) incident at the top of the atmosphere
- the obliquity of solar illumination (the solar zenith angle)
- scattering by air molecules
- scattering (and absorption) by aerosols (and clouds)
- planetary reflection

The approach of this paper is to study the influence of these factors in a parametric fashion by solving the appropriate radiative-transfer equation.

DIRECT AND DIFFUSE FLUXES

The quality of interest in photobiological studies is the monochromatic radiative flux at UV wavelengths, i.e., the amount of radiant energy normally incident on unit horizontal area in unit frequency (wavelength) interval and unit time. This quantity (henceforth called simply "flux") has two distinct components: the direct and the diffuse. The origin of these two components is schematized in Figure 1. The direct flux component is associated with the parallel beam of solar radiation which reaches the observer after being attenuated along its atmospheric path, whereas the diffuse flux component is radiation that is scattered several times in the atmosphere and received at the ground from all directions of the sky. The direct flux component can be readily calcualted from the Bouguer-Langley law, if the angle of solar

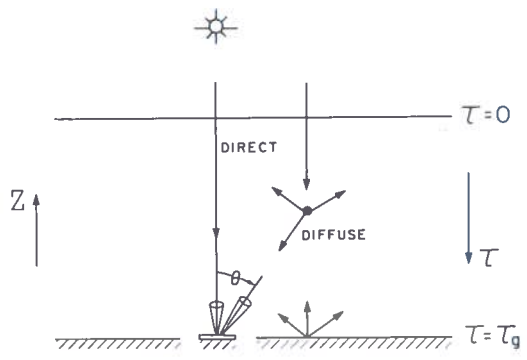

Figure 1. The direct and diffuse components of solar radiation. The sun is assumed to be overhead (0° solar zenith angle or 90° solar elevation) and the ground to be a Lambertian reflector. Z is the height coordinate and τ the total optical thickness whose value at the ground is τ_g.

illumination and the extraterrestrial solar flux are given along with the total extinction (absorption and scattering) optical thickness of the atmosphere at the specified wavelength. The calculation of the diffuse component involves the solution of the complete radiative-transfer equation. The solution is obtained by numerical techniques which are further elaborated in Herman and Browning (1965), Herman and Yarger (1967), Dave and Furukawa (1966), Dave and Gazdag (1970), and Hunt (1971).

The explicit input parameters needed for the problem are: solar zenith angle, the extraterrestrial solar flux, the planetary albedo, the total atmospheric optical thickness (due to Rayleigh scattering, aerosol scattering, molecular and aerosol absorption), albedo for single scattering, and phase matrix elements for turbid air. (The last three are functions of height.) The fundamental quantities involved in these parameters are:

- Optical properties (functions of wavelength)
  - molecular (Rayleigh) scattering coefficient
  - complex index of refraction for aerosols
  - absorption cross-section of ozone
- Atmospheric properties (functions of height)
  - number densities of molecules, aerosols and ozone
  - aerosol size distribution

The basic assumptions are that the atmosphere is plane-parallel, horizontally homogeneous in its scattering and absorbing properties, and bounded by a Lambertian surface of known reflectivity (albedo). For convenience in calculations it is assumed that the incident solar flux (i.e., the rate of energy flow across unit area held normal to the solar beam) at the top of the atmosphere is π units. All ground-level fluxes are given in terms of this relative unit in this paper. Since fluxes scale linearly, they can be converted to absolute amounts by using, for example, Ackerman's (1971) tabulations of the extraterrestrial fluxes, abstracted in Table 1.

Table 1. Ackerman's (1971) Values of the Extraterrestrial Solar Fluxes of UV Radiation Reaching the Ground

$\Delta\lambda$(nm)	$q(m^{-2}\ s^{-1})$ $(\times 10^{18})$
294.1-289.9	3.90
298.5-294.1	3.99
303.0-298.5	3.86
307.7-303.0	5.08
310.0 (± 2.5)	5.92
315.0	6.05
320.0	6.94
325.0	8.12
330.0	9.71
335.0	8.97
340.0 (± 2.5)	9.44

GROUND UV FLUXES FOR MODEL ATMOSPHERES

Diffuse Flux Versus Ozone Amount in Aerosol-Free Atmospheres

For an atmosphere containing no aerosols or clouds, there is revealed (De Luisi and Herman, 1973; Sundararaman, 1973) a simple linear relation between the diffuse UV flux component at the ground (plotted on a logarithmic scale) and the atmospheric ozone content (Figure 2). This relation holds so long as the solar zenith angle is not large ($< 70°$). It was obtained from detailed calculations which used the range of ozone amounts and distributions observed at three sea-level stations which have good records of ozone data: Tateno (Japan), Aspendale (Australia), and Pretoria (S. Africa). This linear relation between diffuse flux and ozone can be explained in terms of an atmospheric model in which the layer of ozone absorption is located entirely above the layer of molecular scattering. However, the ozone layer is not truly devoid of scattering effects, so that the idealization is apparently valid only for the flux calculations. (It may not hold, for example, for calculations of zenith-sky intensities at low solar elevations.)

Effect of Ground Reflection

Multiple reflections between the planetary surface and the atmosphere above it have two distinguishable effects on ground UV radiation

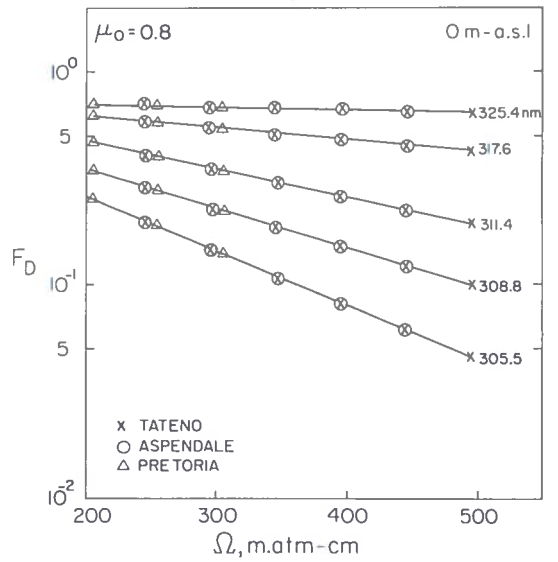

a. Solar zenith angle (θ_0) of 36.9° (μ_0 = 0.8).

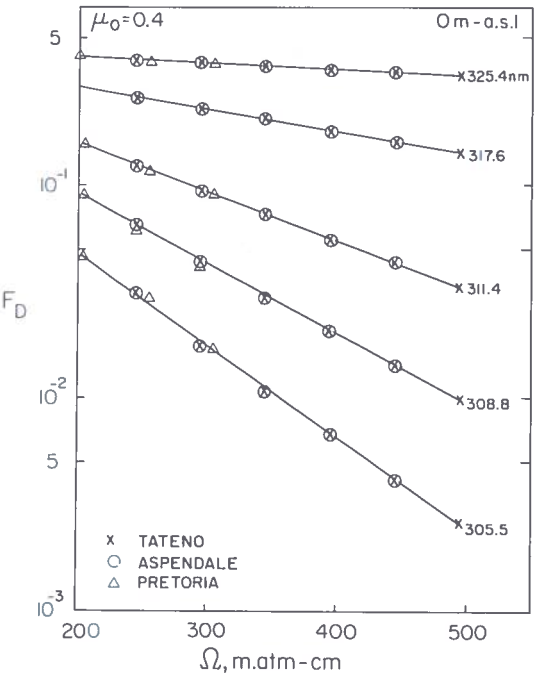

b. Solar zenith angle (θ_0) of 66.4° (μ_0 = 0.4).

Figure 2. The diffuse fluxes F_D (unit: $\pi\,\mu_0$) of solar radiation at sea level are calculated for five wavelengths in the Huggins band of ozone absorption and are plotted as functions of the total ozone amount (in matm-cm) in the atmospheric column. The fluxes are for a pure molecular atmosphere with no ground reflection. Ozone data from three middle-latitude stations – Tateno (36°N, 140°E), Pretoria (25°S, 28°E), and Aspendale (38°S, 145°E) – have been used.

fluxes: 1) they augment the diffuse downward flux, and 2) they produce an upward flux component which, in the case of Lambertian reflection, is related to the total (direct and diffuse) component by $F_U/(F_D + F_S)$ = albedo (reflectivity). The former effect is illustrated in Table 2 for different wavelengths and angles of solar illumination and for three specified values of the ground albedo. The atmosphere is assumed to be free of aerosols and the ozone amount is taken to be 314 matm-cm. Table 2 shows that, for a given wavelength and ground albedo, the ground-reflection effect is most pronounced for an overhead sun. For medium solar elevation, reflection from a snow-covered ground surface with an (assumed) albedo of 0.6 can increase the diffuse flux in the wavelength interval 305.2 to 312.5 nm by about 50 to 60% over the no-reflection value. Notice also that the reflection effect increases with wavelength as well as with the assumed value of the albedo.

Diffuse-to-Direct Flux Ratio in Clear and Turbid Atmospheres

The relative magnitudes of the diffuse and direct UV flux components received from a clear sky depend upon wavelength and solar elevation, as well as upon the value of the ground albedo, as already mentioned. Table 3 shows how the ratio between these components varies with wavelength and solar zenith angle for a selected ozone amount (314 matm-cm) and ground albedo (0.3). As should be expected for a purely molecular atmosphere (with the scattering coefficient varying inversely as the fourth power of wavelength), the diffuse-to-direct flux ratio increases as the wavelength decreases, and also as the slant scattering path of the incident radiation increases. Ozone absorption at shorter wavelengths arrests this increase; consequently, the maximum value of this ratio is obtained at an intermediate wavelength (312.5 nm) for normal incidence of the direct solar beam.

The diffuse-to-direct flux ratio in a turbid atmosphere is critically sensitive to the aerosol properties. To examine this point, Table 4 has been prepared from the extensive tabulations of UV fluxes provided for model turbid atmospheres by Braslau and Dave (1973). Although these authors have studied both absorbing and non-absorbing aerosols, only their results for two atmospheric models consisting of non-absorbing

Table 2. The Effect of Lambertian Ground Reflection on the Diffuse Radiation Fluxes (F_D) Reaching the Earth's Surface at Several Wavelengths in the Near-Ultraviolet Region. The Fluxes are Normalized to the Corresponding Values Obtained for No Ground Reflection, and are given for Three Specified Values of the Ground Albedo (0, 0.3, 0.8) and for Four Values of the Solar Zenith Distance (0°, 30°, 60°, 80°). The Calculations Assume a Pure Molecular Atmosphere with 314 matm-cm of Ozone. Data Taken from Braslau and Dave (1973)

		λ, nm						
θ_0	Albedo	305.2	307.5	312.5	317.5	322.5	330.0	340.0
0°	0.1	1.08	1.08	1.09	1.10	1.10	1.11	1.12
	0.3	1.26	1.29	1.32	1.33	1.35	1.36	1.38
	0.8	1.86	1.98	2.09	2.15	2.20	2.24	2.27
30°	0.1	1.07	1.08	1.08	1.09	1.10	1.10	1.10
	0.3	1.23	1.26	1.28	1.30	1.31	1.32	1.33
	0.8	1.75	1.87	1.96	2.02	2.06	2.09	2.11
60°	0.1	1.04	1.05	1.06	1.06	1.06	1.06	1.06
	0.3	1.14	1.17	1.18	1.20	1.20	1.21	1.21
	0.8	1.46	1.56	1.63	1.68	1.70	1.71	1.71
80°	0.1	1.03	1.03	1.04	1.04	1.04	1.04	1.04
	0.3	1.10	1.12	1.13	1.14	1.14	1.13	1.13
	0.8	1.35	1.41	1.46	1.47	1.48	1.46	1.43

Table 3. The Ratio of Diffuse to Direct UV Radiative Flux (F_D/F_S) in a Pure Molecular Atmosphere with 314 matm-cm of Ozone. Ground Albedo = 0.3. Data from Braslau and Dave (1973)

λ (nm)	$\theta_0 = 0°$	$\theta_0 = 30°$	$\theta_0 = 60°$
302.5	0.89	1.11	3.70
307.5	0.93	1.15	3.27
312.5	0.94	1.14	3.01
317.5	0.91	1.10	2.75
322.5	0.87	1.04	2.49
330.0	0.79	0.94	2.13
340.0	0.68	0.80	1.73

aerosols are included in this table. It is assumed that the aerosols have a refractive index of 1.5, a size distribution corresponding to Deirmendjian's (1969) Haze L model, and modified versions of Elterman's model for their altitude distribution. The total columnar aerosol contents in the models are 1.97×10^{11} and 8.24×10^{11} particles m^{-2}, respectively, which the authors have chosen as examples of "average" and "heavy" aerosol loading.

Table 4 compares the direct and diffuse UV radiative fluxes for the two model turbid atmospheres with those obtained for a pure molecular atmosphere with an ozone amount of 314 matm-cm; also compared are the fluxes in a molecular atmosphere with and without ozone. The comparison is made by expressing the fluxes as ratios: r_{21} and r_{31} are the calculated fluxes for the "average" and "heavy" aerosol models, respectively, given as fractions of the fluxes in a molecular atmosphere with the specified amount of ozone absorption; r_{10} is the ratio of the fluxes in molecular atmospheres with and without absorption.

Table 4 shows that if non-absorbing aerosols are present in the atmosphere, the diffuse component of the UV flux at the ground can increase by as much as 30 percent over its value for a pure molecular atmosphere. The increase is more noticeable for greater aerosol amounts and for smaller angles of the incident solar radiation. For "average" aerosol amounts, the increase is more or less uniform with wavelength.

The increase of the diffuse component is accompanied by a decrease in the direct component of the UV radiative flux. These two effects are not compensatory, however, and the net effect of aerosols appears to be to reduce the total (direct and diffuse) flux of UV radiation reaching the ground. At a wavelength of 302.5 nm, the reduction in total flux might amount to between 2 and 5% of its value for a pure molecular atmosphere. At longer wavelengths, the percentage of reduction is estimated to be even less.

Table 4. Comparison of UV Radiative Fluxes in Molecular and Model Turbid Atmospheres. Ozone 314 matm-cm; Ground Albedo, 0.3. Data from Braslau and Dave (1973). (See text.)

λ (nm)		$\theta_0 = 0°$			$\theta_0 = 30°$			$\theta_0 = 60°$			$\theta_0 = 80°$		
		r_{10}	r_{21}	r_{31}	r_{10}	r_{21}	r_{31}	r_{10}	r_{21}	r_{31}	r_{10}	r_{21}	r_{31}
302.5	F_S	0.12	0.91	0.67	0.08	0.89	0.63	0.01	0.79	0.43	0.00	0.00	0.00
	F_D	0.08	1.00	1.25	0.06	1.00	1.17	0.01	1.00	1.00	0.00	0.00	0.00
307.5	F_S	0.33	0.91	0.67	0.28	0.90	0.63	0.11	0.83	0.45	0.00	0.00	0.00
	F_D	0.25	1.08	1.28	0.21	1.10	1.24	0.09	1.00	1.11	0.01	1.00	1.00
312.5	F_S	0.58	0.91	0.67	0.53	0.90	0.63	0.33	0.83	0.45	0.04	0.57	0.10
	F_D	0.49	1.08	1.29	0.45	1.07	1.24	0.29	1.03	1.10	0.07	1.00	1.00
317.5	F_S	0.75	0.91	0.67	0.72	0.90	0.63	0.57	0.83	0.45	0.20	0.58	0.10
	F_D	0.69	1.07	1.29	0.66	1.08	1.26	0.52	1.06	1.13	0.24	1.00	0.96
322.5	F_S	0.86	0.91	0.67	0.85	0.90	0.63	0.75	0.83	0.45	0.43	0.58	0.10
	F_D	0.82	1.10	1.32	0.80	1.09	1.29	0.71	1.04	1.13	0.46	1.00	0.98
330.0	F_S	0.95	0.91	0.67	0.94	0.90	0.63	0.89	0.83	0.45	0.73	0.57	0.10
	F_D	0.93	1.10	1.34	0.92	1.09	1.32	0.88	1.06	1.17	0.74	1.00	0.96
340.0	F_S	0.98	0.91	0.67	0.98	0.90	0.63	0.97	0.83	0.45	0.91	0.57	0.10
	F_D	0.98	1.11	1.41	0.97	1.11	1.38	0.96	1.07	1.22	0.91	1.00	0.97

If a reasonable amount of aerosol absorption is introduced, model calculations (Braslau and Dave, 1973; De Luisi and Herman, 1973) indicate that the diffuse UV flux component at the ground will be reduced significantly, and that the decrease in the total flux will also be greater. However, the absorptive properties of aerosols, particularly at UV wavelengths, are almost completely unknown.

UV FLUX LEVELS

For a specified amount of ozone decrease in the atmospheric column, the worst effect, in terms of maximum increase in the UV flux levels reaching the biosphere, is expected for a clear and cloudless atmosphere. It is therefore desirable to establish the basic UV flux levels under such atmospheric conditions, for various geographical locations and seasons. Figure 3 and Table 5 give some idea of the expected flux levels during the month of June. (Note that Figure 3 gives noontime fluxes, whereas Table 5 gives the daily average fluxes.) It is clear from both the table and the figure that the diffuse flux component represents a significant part of the total UV radiative flux reaching the earth's surface at all latitudes. It becomes the predominant part at shorter wavelengths, for which molecular scattering effects are greater (provided ozone absorption is not overpowering), and at the high geographic latitudes, where the solar obliquity is larger. Obviously, the diffuse flux component should be included when perturbations of UV flux levels are predicted.

The increase in UV radiation resulting from any decrease in atmospheric ozone can be predicted with greatest confidence when the atmosphere is free of aerosols and clouds. Table 6 gives the calculated increases in the direct and diffuse radiative flux components when the ozone amount of 305 matm-cm in a molecular atmospheric column (a typical value for middle latitudes) is reduced by 2%. It is found that at a wavelength of 305.5 nm both the direct and the diffuse flux components increase by slightly less than 3% for an overhead ($\mu_0 = 1$) sun and less than 5% for medium ($\mu_0 = 0.6$) solar elevation. The calculated percentage increases are smaller for the longer wavelengths, which have less ozone absorption. In Table 7 a range (1-20%) of percentage decreases in ozone is considered, and

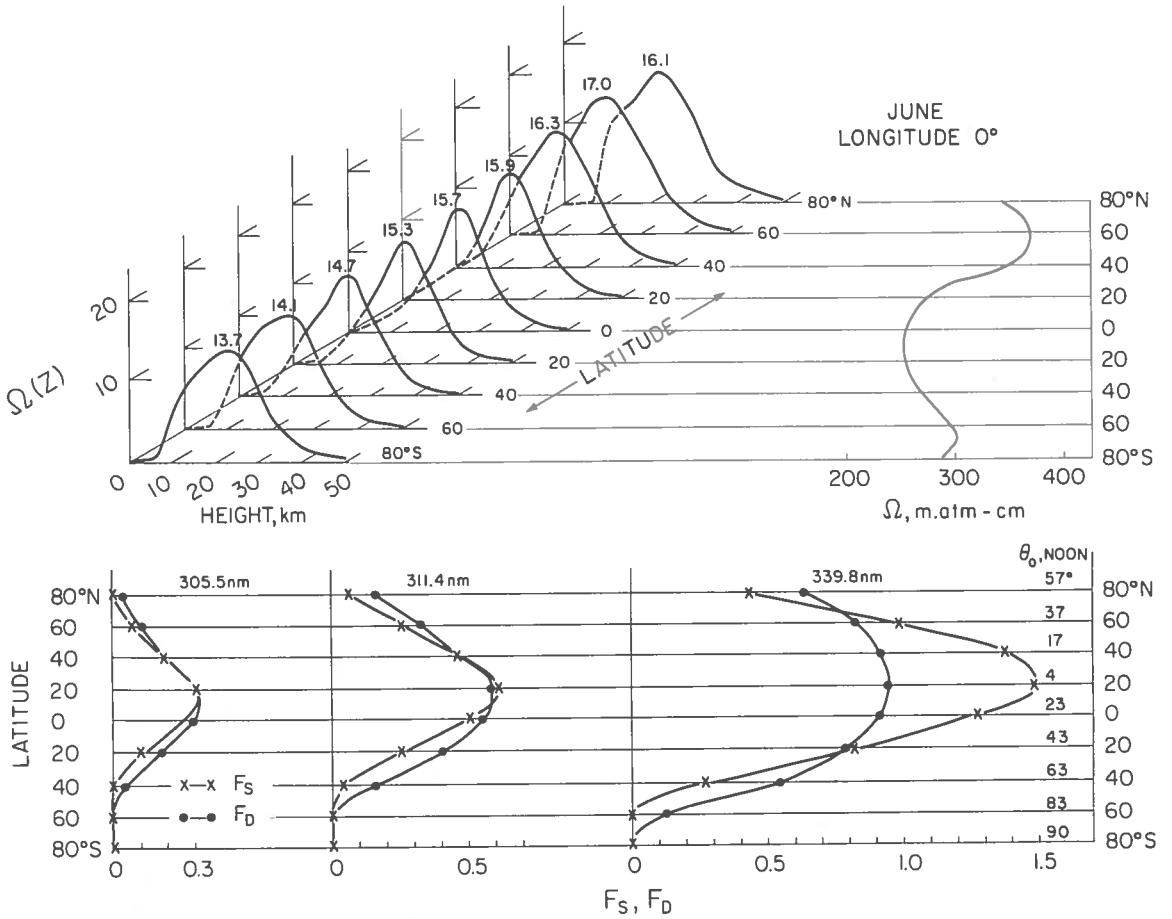

Figure 3. Calculated latitudinal variation of the direct (F_S) and diffuse (F_D) flux of solar ultraviolet radiation reaching the ground along the 0° meridian during the month of June. The monochromatic fluxes are given in units of $\pi \cos\theta_0$ for three wavelengths in the Huggins band of ozone absorption. The height distributions, peak concentrations (in matm-cm/km), and total amounts (in matm-cm) of ozone used in the calculations are shown in the upper part of the diagram. The value of ($\theta_{0,noon}$) given in the lower right-hand corner is the local zenith angle of the sun at noon. The ground is a Lambertian reflector of albedo 0.2.

the corresponding flux increases at a wavelength of 305.5 nm are tabulated. Notice that if the ozone amount decreases by as much as 20%, the flux components can increase by 30% for an overhead sun and between 50 and 60% for medium solar elevation.

In a normally turbid atmosphere, total UV flux reaching the ground is generally smaller, and more of it may be received as diffuse rather than direct radiation. A limited number of model calculations (unpublished) indicates that the consequences of increased stratospheric turbidity on ground UV fluxes may not be significant. Although this result is crucially dependent on the aerosol properties, it is suspected that turbidity effects may mask the increase in UV radiation levels produced by ozone decrease only when the ozone change is quite small.

The influence of clouds on UV radiative fluxes has not been considered in this paper. Bener (1972) finds evidence for decreases as well as increases in UV fluxes under cloudy conditions in Davos, Switzerland. The influence of broken clouds cannot be easily included in radiative-transfer calculations. Co-ordinated measurements of ozone and UV radiative fluxes under cloudy conditions are urgently needed.

Table 5. The Daily Average Values of UV Fluxes at λ = 305.5 nm for Several Stations During the Month of June*

LONGITUDINAL SECTOR -30° to 60° JUNE λ = 305.5 nm ALBEDO = 0.20

				FLUX FOR MEAN MONTHLY OZONE		
STATION	LAT	LONG	OZONE	FD	FS	FD/FS
HEISS ISLAND	81	58	299.9	2.378E-02	5.946E-03	4.000
NY-ALESUND	79	11	352.0	1.620E-02	4.710E-03	3.440
LONGYEAR	78	15	359.1	1.558E-02	4.670E-03	3.335
TROMSÖ	70	18	344.8	2.667E-02	1.208E-02	2.208
MURMANSK	69	33	327.3	3.150E-02	1.444E-02	2.182
PECHORA	65	57	269.6	5.502E-02	2.640E-02	2.084
REYKJAVIK	64	-22	348.4	3.169E-02	1.706E-02	1.858
LERWICK	60	-2	375.8	2.972E-02	1.819E-02	1.634
LENINGRAD	60	30	337.7	3.923E-02	2.334E-02	1.681
OSLO	60	10	360.2	3.361E-02	2.049E-02	1.640
RIGA	57	24	333.6	4.356E-02	2.743E-02	1.588
SVERDLOVSK	57	60	339.4	4.196E-02	2.665E-02	1.575
AARHUS	56	10	354.2	3.834E-02	2.493E-02	1.538
MOSCOW	56	37	317.6	4.979E-02	3.144E-02	1.584
ESKDALEMUIR	55	-4	376.6	3.375E-02	2.286E-02	1.476
KUIBYSHEV	53	50	330.3	4.795E-02	3.196E-02	1.501
POTSDAM	52	11	369.5	3.777E-02	2.669E-02	1.415
OXFORD	52	-2	376.5	3.666E-02	2.642E-02	1.388
BRACKNELL	51	0	378.7	3.628E-02	2.629E-02	1.380
BELSK	51	20	352.6	4.355E-02	3.100E-02	1.405
UCCLE	51	4	383.4	3.572E-02	2.632E-02	1.357
KIEV	50	30	324.8	5.237E-02	3.625E-02	1.445
CAMBORNE	50	-6	359.9	4.182E-02	3.017E-02	1.386
HRADEC KRALOVE	50	15	343.1	4.661E-02	3.301E-02	1.412
VAL JOYEUX-PARIS	49	2	317.9	5.630E-02	3.957E-02	1.423
MAGNY-LES-HAMEAUX	49	2	370.8	4.018E-02	3.002E-02	1.338
HOHENPEISSENBERG	48	11	360.3	4.359E-02	3.258E-02	1.338
BUDAPEST-LORINC	47	19	339.9	4.979E-02	3.645E-02	1.366
AROSA	47	9	347.3	4.803E-02	3.580E-02	1.342
ODESSA	46	30	331.8	5.309E-02	3.896E-02	1.363
KARADAG	45	35	291.5	6.963E-02	4.940E-02	1.410
SOFIA	43	23	310.2	6.350E-02	4.724E-02	1.344
MONT-LOUIS	43	2	353.4	4.865E-02	3.813E-02	1.276
VIGNA DI VALLE	42	12	351.4	4.936E-02	3.869E-02	1.276
ABASTUMANI	42	42	272.7	8.105E-02	5.817E-02	1.393
NAPLES	41	14	300.8	6.847E-02	5.125E-02	1.336
CAGLIARI-ELMAS	39	9	344.2	5.295E-02	4.216E-02	1.256
LISBON	39	-10	317.9	6.253E-02	4.852E-02	1.289
MESSINA	38	15	352.5	5.073E-02	4.109E-02	1.235
ASHKHABAD	38	58	240.4	1.015E-01	7.211E-02	1.408
CASABLANCA	34	-8	341.8	5.545E-02	4.560E-02	1.216
BUNIA	2	30	241.9	7.878E-02	5.275E-02	1.493
PRETORIA	-26	28	254.6	2.734E-02	1.045E-02	2.616

* These values are obtained by summing the instantaneous fluxes during daytime and dividing the sum by the number of records in a mean solar day (86,400). All stations are assumed to be at sea level.

Table 6. Calculated Increases (%) in the Direct (F_S) and Diffuse (F_D) Components of the Solar Radiation Flux Reaching the Earth's Surface at Several Wavelengths in the Near-Ultra-Violet Region when the Total Amount of Ozone (305 matm-cm) in the Atmospheric Column Decreases by 2%. The Calculations are Applicable for a Pure Molecular Atmosphere

		λ (nm)				
μ_0		305.5	308.8	311.4	317.6	325.4
1.0	ΔF_S	2.65	1.91	1.27	0.54	0.16
	ΔF_D	2.92	2.16	1.48	0.68	0.22
0.8	ΔF_S	3.32	2.39	1.59	0.68	0.20
	ΔF_D	3.58	2.64	1.81	0.83	0.23
0.6	ΔF_S	4.45	3.20	2.12	0.91	0.27
	ΔF_D	4.65	3.42	2.33	1.06	0.33
0.4	ΔF_S	6.75	4.84	3.20	1.37	0.40
	ΔF_D	6.34	4.74	3.26	1.48	0.46

Table 7. Calculated Increases (%) in the Direct (F_S) and Diffuse (F_D) Components of the Solar Radiation Flux at λ = 305.5 nm when the Total Amount of Ozone (Assumed to be 305 matm-cm) in the Atmospheric Column Decreases by Various Indicated Percentages. The Calculations are Applicable for a Pure Molecular Atmosphere with No Ground Reflection

		Ozone Decrease (%)							
μ_0		1	2	3	4	5	10	15	20
1.0	ΔF_S	1.32	2.65	4.00	5.37	6.60	14.0	21.7	29.9
	ΔF_D	1.45	2.92	4.41	5.92	7.45	15.5	24.1	33.3
0.8	ΔF_S	1.65	3.32	5.02	6.75	8.51	17.8	27.8	38.6
	ΔF_D	1.78	3.58	5.42	7.30	9.20	19.2	30.2	42.2
0.6	ΔF_S	2.20	4.45	6.75	9.10	11.50	24.3	38.6	54.6
	ΔF_D	2.30	4.65	7.05	9.51	12.00	25.5	40.6	57.5
0.4	ΔF_S	3.32	6.75	10.30	14.00	17.80	38.6	63.2	92.2
	ΔF_D	3.12	6.34	9.70	13.10	16.60	36.0	58.6	84.0

ACKNOWLEDGMENT

I am grateful to Dr. N. Sundararaman and Mr. Dennis St. John for their valuable collaboration.

REFERENCES

Ackerman, M. (1971), "Ultraviolet solar radiation related to mesospheric processes, mesospheric models and related experiments," in *Proceedings of the Fourth ESRIN-ESLAB Symposium* held in Frascati, Italy, 6-10 July 1970, ed. G. Fiocco, Springer-Verlag, New York, 149-159.

Bener, P. (1972), "Approximate Values of Intensity of Natural Ultraviolet Radiation for Different Amounts of Atmospheric Ozone," Final Technical Report DAJA 37-68-C-1017, European Research Office, United States Army, London, 59 pp.

Braslau, N. and J.V. Dave (1973), "Effect of Aerosols on the Transfer of Solar Energy Through Realistic Model Atmospheres, Part III: Ground level fluxes in the biologically active bands 0.2850-0.3700 μm," Rept. RC4308, IBM Thomas J. Watson Research Center, Yorktown Heights, NY, 53 pp.

Dave, J.V. and P.M. Furukawa (1966), "Scattered Radiation in the Ozone Absorption Bands at Selected Levels of a Terrestrial, Rayleigh Atmosphere," Meteor. Monogr., Vol. 7, No. 29, American Meteorological Society, 353 pp.

Dave, J.V. and J. Gazdag (1970), "A modified Fourier transform method for multiple scattering calculations in a plane parallel Mie atmosphere," Appl. Opt. 9, 1457-1466.

Deirmendjian, D. (1969), *Electromagnetic Scattering on Spherical Polydispersions*, American Elsevier, New York, 290 pp.

De Luisi, J. and B.M. Herman (1973), "Radiation in the natural and perturbed troposphere," Chapter 5, Volume IV of the CIAP monograph series, U.S. Department of Transportation. NOTE: At present, these monographs exist only in an early draft form. They will be publicly available after completion in September 1974.

Herman, B.M. and S.R. Browning (1965), "A numerical solution to the equation of radiative transfer," J. Atmos. Sci. **22**, 559-566.

Herman, B.M. and D.N. Yarger (1967), "Multiple scattering from particles in the Mie region," in *Proceedings of the Second Interdisciplinary Conference on Electromagnetic Scattering* held at University of Massachusetts at Amherst, June 1965, ed. R.L. Rowell and R.S. Stein, Gordon and Breach Science Publishers, New York, 99-127.

Hunt, G.E. (1971), "A review of computational techniques for analyzing the transfer of radiation through a model cloudy atmosphere," J. Quant. Spectrosc. Radiat. Transfer **11**, 655-690.

Sundararaman, N. (1973), "Some Consequences of the Absorption of Solar Ultraviolet Radiation by Ozone," Ph.D. Thesis, Department of Meteorology, University of California, Los Angeles, 250 pp.

DISCUSSION

KAROL: You might like to know that Moscow State University has prepared an atlas of maps of the mean monthly fluxes of UV radiation, based on climatological data on ozone and cloudiness, which will be published very soon.

VENKATESWARAN: I'm glad to hear that. It should be interesting to compare our results.

(UNIDENTIFIED): What you have presented here are results of theoretical calculations. Dr. Bener of Davos, Switzerland, has made actual measurements. How do your calculations compare with them?

VENKATESWARAN: I think they agree under clear-sky conditions. Dr. Bener has made measurements for both clear and cloudy skies. I believe he found that UV radiation received at the ground might either decrease or increase under cloud cover, such as, presumably, thin cirrus clouds. We cannot easily reproduce these results in our calculations. At the present time, radiative-transfer theory can treat only horizontally homogeneous conditions.

GREEN: Your first slide showed the DNA absorption curve vanishing at 290 nanometers. We wouldn't have a problem if it did! It changes five orders of magnitude from 260 nm to about 340 nm, and in the solar transmission region it is precisely a little different from zero.

VENKATESWARAN: I didn't draw the curve; I took it from a standard book by Seliger and McElroy. The main point I wanted to make was that there is considerable overlap between the ozone and DNA absorption spectra.

(UNIDENTIFIED): Did you use the integral formulation of the radiative-transfer equation, or the differential formulation? And how did you put in the reflective boundary conditions at the earth's surface?

VENKATESWARAN: As I pointed out, we solved the full integro-differential equation of radiative transfer in a vertically inhomogeneous atmosphere. We adopted a Fourier-series expansion of the elements of the phase matrix. Our vertical integration was carried out using small intervals of optical depth. Our annular resolution was also quite high.

We have also successfully compared results obtained by the iterative technique and by the doubling method. Unfortunately, I can't give the details here.

As far as ground reflection is concerned, the results I have shown here were obtained for Lambertian reflection. However, there is no basic difficulty in adopting some other kind of reflection, say the Fresnel type, if it is more appropriate.

ELLSAESSER: As a resident of Los Angeles and an expert in radiative-transfer theory, what would be your estimate of the effect of increasing UV flux at the ground in L.A. in eliminating the smog?

VENKATESWARAN: I can't deny that I reside in Los Angeles, but let me disclaim being an expert in anything. I would say this: If you have no solar radiation, you won't have much of a smog problem.

(UNIDENTIFIED): You said that aerosol pollution could to some extent cancel out the ozone depletion and protect us from UV. For what percent ozone depletion could this effect compensate?

VENKATESWARAN: I'm fairly certain that if the ozone reduction is greater than five percent, the addition of a reasonable amount of aerosol in the stratosphere will not be able to compensate for it. If the reduction is only about two percent, the effects might cancel out. But the results could be sensitive to the assumed properties of the aerosol.

INITIAL VALIDATION STUDIES FOR ZAM2 RADIATION AND LARGE-SCALE EDDY TRANSPORT MECHANISMS

FREDERICK M. LUTHER AND MICHAEL C. MACCRACKEN
Lawrence Livermore Laboratory
University of California
Livermore, California

ABSTRACT: The second-generation zonal atmospheric model has been undergoing intensive development and validation in order to prepare it for assessing the potential climatic impact of the stratospheric injection of trace species by high-altitude aircraft. Stone's parameterization for the vertical and horizontal eddy fluxes in the troposphere, and Luther's values of the eddy-diffusion coefficients in the stratosphere, are now used. Trace-species transport is included for both radiatively active and radiatively passive species. The radiation prescription has been improved so that ozone absorption is now treated on the basis of the amount of ozone present.

Model validation will include comparison with climatic data and other modeling efforts, as well as sensitivity studies of various modeled processes. Application of this model to the Climatic Impact Assessment Program will involve studying the effects of injection of aerosols, reduction in stratospheric ozone heating, and possible perturbations resulting from water-vapor injection.

INTRODUCTION

Development of the ZAM2 climate model during the past year has emphasized the improvement and validation of many of the individual feedback mechanisms. Since the presentation of the general concept of this second-generation version of the model at the Second Conference on the Climatic Impact Assessment Program (MacCracken, 1972), many of the problem areas have been considered and remedied, including representation of horizontal eddy transport, vertical convection, and atmospheric radiation. With validation of the individual mechanisms nearly complete, we are now running the full model in order to ensure that each mechanism can be balanced by another in a reasonable fashion – rather like constructing a large boundary fence around the climatic state. Our simulation of the average annual climate is indicating climatic stability close to the observed state. Once climatic stability has been established, we plan to perform a broad range of model sensitivity and perturbation studies.

MODEL FORMULATION

The ZAM2 model is a global climate model which uses the conservation equations for mass, momentum, energy, water vapor, and trace species in conjunction with the hydrostatic balance assumption to treat the evolution of a moist atmosphere above an interactive surface consisting of ocean, land, and mountains which can be covered by snow and ice (MacCracken, 1972; MacCracken and Luther, 1974). The model can use either a 5° or 10° latitude grid from pole to pole. The vertical is divided into nine layers reaching up to 10 mb. The time step for the 10° grid is 30 minutes.

One major improvement in the model has been the more detailed treatment of the non-zonal eddy transport terms for energy, water vapor, and trace species. In the troposphere the formulation of Stone (1972, 1973) has been implemented, in which eddy-diffusion coefficients are derived on the assumption that the radiative divergence is balanced by the large-scale eddies. The functional forms developed depend only on zonally averaged values, and are presently being evaluated at every time step. For our model these are the horizontal eddy-diffusion coefficient

$$K_H = 0.144 \frac{p^{1/2} R^{3/2}}{f^2} \cdot \left| \left(\frac{\partial \theta}{a \partial \theta} + \frac{p}{aRT} \frac{\partial \phi}{\partial \theta} \frac{\partial \theta}{\partial p} \right) \right| \left(-\frac{\partial \theta}{\partial p} \right)^{1/2} \quad (1)$$

and the vertical eddy-diffusion coefficient* in terms of pressure

$$K_P = -0.06 \frac{p^{1/2} R^{3/2}}{f^2} \cdot \left| \left(\frac{\partial \theta}{a \partial \theta} + \frac{p}{aRT} \frac{\partial \phi}{\partial \theta} \frac{\partial \theta}{\partial p} \right)^3 \right| \frac{1}{\left(-\frac{\partial \theta}{\partial p} \right)^{3/2}}, \quad (2)$$

where θ is the potential temperature and f the Coriolis parameter for 45°N. Green (1970) developed a similar formulation based on different assumptions, which results in a different lapse-rate dependence. Stone's prescription was chosen because of its applicability to subhemispheric scales and the more reasonable pattern of numerical values resulting when the 5-year circulation statistics of Oort and Rasmusson (1971) were substituted.

Values of K_H and K_P (the latter restated as K_V, in cm^2/sec rather than bar^2/hr) for the months of January and July are shown in Tables 1 through 4. These values were obtained using the temperature and potential-temperature data of Oort and Rasmusson (1971) which were compiled during the five-year period 1958-1963. The tropospheric values of K_H vary by about an order of magnitude latitudinally, with the maximum values approaching 5×10^{10} cm^2/sec in middle latitudes. The values decline sharply near the tropopause because of their strong dependence on the vertical gradient of potential temperature. The high values in the stratosphere emphasize that Stone's assumptions are not valid at those levels. We have therefore adopted the prescription suggested by Reed and German (1965) while using the monthly varying updated values developed by Luther (1973) from the data base of Oort and Rasmusson (1971).

The values of K_V in Tables 3 and 4 which are used to simulate the large-scale eddy transport of energy, water vapor, and trace species show very strong seasonal, latitudinal, and pressure variability, only some of which can be explained by the lack of numerical preciseness of the observation set. We expect that as ZAM2 settles down the computed values of K_V will become much smoother. The tropopause is quite evident, yet in the stratosphere the breakdown of Stone's formulation is evidenced by extreme variability in the values. The mid-latitude cyclogenesis in winter causes values to vary by about two orders of magnitude between the equator and 40°N. In ZAM2, the low K_V vertical transport at equatorial latitudes is made up for by vertical transport by convection.

With the prescribed monthly varying eddy coefficients developed by Luther (using the Reed and German formulation) applied in the stratosphere, and interfaced to the Stone formulation in the troposphere, ZAM2 has a reasonably refined representation for simulation of large-scale eddy transport of potential temperature, water vapor, and trace species. The only developmental task in this area which remains is to implement the cross-term transport K_{yP}.

For momentum transport the situation is not yet satisfactory. Representation of these Reynolds stress terms should ideally be formulated as dependent on internal model variables.

Table 1. Values of K_H (units 10^{10} cm^2/sec) for the Month of January

P (mb)	10°N	20°N	30°N	40°N	50°N	60°N	70°N
50	2.49	4.00	9.68	7.07	0.27	3.86	4.20
100	1.92	5.76	11.06	8.34	0.54	4.14	4.36
200	0.08	0.07	1.51	0.32	0.69	1.68	0.99
300	0.37	1.21	4.56	2.92	1.69	1.19	1.13
400	0.51	1.84	4.10	2.53	1.50	1.08	1.09
500	0.14	2.06	3.58	2.77	1.64	1.18	1.21
700	0.05	2.74	3.52	3.40	2.09	1.52	1.57
850	0.57	2.80	3.05	3.65	2.46	2.18	1.88
1000	0.42	2.04	1.97	3.71	2.36	4.94	4.38

Table 2. Values of K_H (units 10^{10} cm^2/sec) for the Month of July

P (mb)	10°N	20°N	30°N	40°N	50°N	60°N	70°N
50	2.82	1.56	6.41	8.49	7.81	6.68	5.89
100	1.79	3.42	5.03	12.87	7.95	5.01	4.74
200	0.22	1.06	0.01	0.01	0.67	2.14	3.58
300	0.08	0.71	0.68	2.57	1.93	1.08	0.88
400	0.08	0.60	0.91	2.25	1.51	0.94	0.91
500	0.24	0.55	0.67	1.87	1.67	1.10	1.02
700	0.65	0.38	0.48	2.07	1.96	0.98	1.23
850	0.84	0.14	0.51	2.16	1.97	0.96	1.93
1000	0.84	0.22	1.49	2.73	2.07	1.01	3.28

* This formulation is used to simulate the countergradient flux of potential temperature and the downgradient flux of water vapor and trace species.

Table 3. Values of K_V (units 10^3 cm^2/sec) for the Month of January

P (mb)	10°N	20°N	30°N	40°N	50°N	60°N	70°N
50	-0.039	-0.36	-6.7	-4.56	-0.000	-0.66	-1.08
100	-0.79	-10.4	-38.8	-10.4	-0.000	-1.27	-1.90
200	-0.003	-0.002	-0.60	-0.006	-0.012	-0.21	-0.046
300	-0.30	-7.44	-85.6	-16.1	-1.55	-0.43	-0.25
400	-0.28	-12.9	-128.0	-68.6	-10.4	-3.19	-2.16
500	-0.020	-12.9	-88.9	-65.0	-13.6	-4.93	-4.28
700	-0.001	-9.56	-30.8	-33.7	-8.10	-3.06	-3.13
850	-0.21	-11.11	-23.3	-36.5	-9.32	-3.82	-1.34
1000	-0.39	-32.5	-49.9	-104.0	-17.6	-24.9	-4.81

Table 4. Values of K_V (units 10^3 cm^2/sec) for the Month of July

P (mb)	10°N	20°N	30°N	40°N	50°N	60°N	70°N
50	-0.032	-0.040	-1.14	-4.33	-6.16	-3.90	-2.05
100	-0.42	-1.56	-5.12	-41.1	-9.49	-2.07	-1.56
200	-0.081	-1.90	-0.003	-0.001	-0.027	-0.40	-1.35
300	-0.015	-0.92	-1.01	-23.8	-7.44	-0.65	-0.21
400	-0.002	-0.16	-0.99	-20.1	-15.5	-5.46	-4.26
500	-0.011	-0.12	-0.38	-11.1	-7.92	-2.73	-2.54
700	-0.18	-0.038	-0.12	-8.48	-8.80	-1.46	-2.02
850	-0.31	-0.006	-0.10	-4.76	-5.18	-1.13	-4.72
1000	-0.25	-0.008	-0.88	-3.27	-1.25	-0.37	-5.32

The present ZAM2 model, however, still utilizes a constant eddy-diffusion coefficient of 1×10^{10} cm^2/sec to simulate this momentum transport. Implementation of Green's (1970) formulation, in which the meridional eddy-momentum flux can be calculated as a balance between eddy fluxes of potential temperature and potential vorticity, is planned and should improve the model by permitting counter-gradient momentum fluxes.

For vertical momentum transport we are presently using the same vertical eddy-diffusion coefficients described above for potential temperature (with a positive sign), that is, Luther's prescribed values in the stratosphere and Stone's in the troposphere. We have not yet included momentum transport by vertical convection, so in equatorial regions the vertical transport can be expected to be too small. This problem is currently being worked on.

VALIDATION OF PHYSICAL PROCESSES

One of the major goals emphasized during the past year has been validation of the radiation-transport mechanism. This is an especially important aspect of the model because all of the potential perturbations attributed to aerospace utilization of the stratosphere act through the radiation terms. Removing the imposition of unnecessarily restrictive formulations on the radiation is essential if the climatic response is to be capable of sufficient flexibility. We include water vapor, multiple layers of clouds, ozone, and carbon dioxide in the radiation treatment, and are presently using the LLL-modified Dave-Braslau model to develop the parameters appropriate for inclusion of aerosols. Validation of these mechanisms has been pursued for the solar and the long-wave radiation separately.

Solar Radiation

The solar-radiation calculation includes heating due to solar absorption by ozone, water vapor, and clouds. The clouds are assumed to scatter both forward and backward, and the scattered radiation is assumed to be diffuse. The radiative properties of clouds vary with height, reflecting to a limited extent the differences in

cloud type. These parameters are summarized in Table 5.

Table 5. Cloud Albedo and Absorptivity

Pressure level (bars)	Cloud albedo*	Cloud absorptivity*
0.200	0.21	0.01
0.400	0.48	0.04
0.600	0.48	0.04
0.850	0.69	0.06

* Based on values taken from Houghton (1954).

Heating rates due to solar absorption by water vapor are computed using a spectrally averaged transmission function based on an empirical formulation by Luther (1970). A pressure-broadening term is included, and the albedo of the earth's surface is made dependent on the surface type, snow cover, moisture content and, for open oceans, the solar zenith angle.

Atmospheric heating due to solar absorption by ozone becomes a significant energy source above 100 mb. Lindzen and Will (1973) have shown that ozone heating can be accurately modeled by Chapman layers for the Hartley and Chappuis bands, plus a modified Chapman layer for the Huggins bands. Using their expression for the specific heating function, the instantaneous heating rate is computed as a function of ozone concentration and solar zenith angle.

The direct solar-beam calculation is made first; it is followed by an iterative procedure to determine the upward and downward diffuse fluxes at each pressure level. This calculation is performed for each surface type, and the results are averaged proportionally depending upon the fractional surface coverage.

As a part of model validation, results obtained with ZAM2's solar-radiation model have been compared with similar calculations made with a Dave-Braslau (Braslau and Dave, 1973) type of radiation model (RAD1). In RAD1 the radiative-transfer equation for a plane-parallel atmosphere is solved by the successive-iteration procedure of Dave and Gazdag (1970). The model includes Rayleigh multiple scattering (which is not included in ZAM2) along with absorption by ozone, water vapor, carbon dioxide, and oxygen. The solar spectrum from 0.285 μm to 2.500 μm is divided into 83 discrete spectral intervals, and the vertical column is divided into up to 160 layers depending upon the optical thickness of the atmosphere. Direct and diffuse (upward and downward) solar fluxes and the resulting heating rates are computed at 1-km intervals up to 25 km, and then at 5-km intervals up to 50 km. Since clouds are not included in RAD1, comparisons are made only for the clear-sky condition.

The temperature, ozone, and water-vapor profiles which were used in the calculation are shown in Table 6. Calculations were made for

Table 6. Values of Temperature, Water-Vapor Mixing Ratio, and Ozone Mixing Ratio Used for Comparison of RAD1 and ZAM2

Height (km)	Pressure (mb)	Temperature (°K)	Ozone Mixing Ratio (μg/g)	Water-Vapor Mixing Ratio (μg/g)
50	0.951	276	4.52	6.6
45	1.76	270	7.40	10.8
40	3.33	258	12.31	12.9
35	6.52	245	14.11	16.9
30	13.2	234	15.13	27.2
25	27.7	224	7.00	15.6
24	32.2	223	6.38	12.0
23	37.6	222	5.80	9.2
22	43.7	220	5.24	7.4
21	51	219	4.47	6.3
20	59.5	218	3.60	4.8
19	69.5	217	2.88	4.4
18	81.2	216	2.15	3.8
17	95	216	1.56	3.6
16	111	216	1.17	3.6
15	130	216	0.90	3.6
14	153	216	0.73	4.1
13	179	216	0.52	6.2
12	209	222	0.37	18.4
11	243	229	0.30	59.6
10	281	235	0.22	153.9
9	324	242	0.18	257.0
8	372	248	0.15	401.9
7	426	255	0.13	634.6
6	487	261	0.11	940.3
5	554	267	0.09	1387.0
4	628	273	0.08	2376.0
3	710	279	0.07	3730.0
2	802	285	0.06	6047.0
1	902	290	0.06	8611.0
0	1013	294	0.05	11750.0

$\theta = 0°$ and $60°$ and for R = 0.0, 0.10, 0.25, 0.50, 0.75, and 1.00, where θ is the solar zenith angle and R is the albedo of the earth's surface.

Solar heating-rate profiles for $\theta = 0°$ and for R = 0.1 and 0.75 are shown in Figures 1a and 1b, respectively. The stratospheric values of the heating rates generally agree to within 0.4°K/day, with the ZAM2 heating rates being generally smaller in the stratosphere than those of RAD1. The agreement is better for the larger surface albedo. In the troposphere, the ZAM2 heating rates are generally smaller than those of RAD1 in the vicinity of the 10-km level, and generally slightly larger than those of RAD1 in the vicinity of the 4-km level.

Solar heating-rate profiles for $\theta = 60°$ and R = 0.1 and 0.75 are shown in Figures 1c and 1d, respectively. In both figures, the heating-rate profiles show excellent agreement, generally to within ±0.2°K/day. As in the previous figures, the ZAM2 heating rates are smaller than those of RAD1 in the vicinity of the 10-km level.

The net solar flux (total downward flux minus upward flux) at 50 km represents the rate at which energy is being absorbed by the earth-atmosphere system. The net fluxes at 50 km as computed by RAD1 and ZAM2 for $\theta = 0°$ and $60°$ are shown in Figure 2a in langleys per minute (1 Ly = 1 gram-calorie of solar radiation per square centimeter) as functions of the albedo of the earth's surface. The disagreement between the results from the two models is due to differences in the calculation of the upward diffuse flux at 50 km. The upward diffuse flux is underestimated by ZAM2 for small surface albedo because Rayleigh scattering is not included in the model, which results in an overestimate of the net flux. The agreement between the two models is good for surface albedos greater than 0.4.

Figure 2b shows a comparison of the net fluxes computed at 16 km for $\theta = 0°$ and $60°$. Again the differences are due primarily to the Rayleigh scattering which is included in RAD1 but not in ZAM2.

The net flux at the earth's surface represents the rate at which energy is absorbed by the surface. Figure 2c shows that ZAM2 overestimates the energy absorbed at the earth's surface by as much a 0.1 Ly/min for small surface albedo,

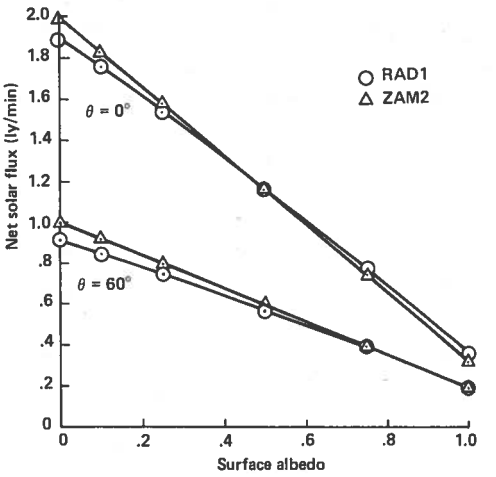

a. At 50 km

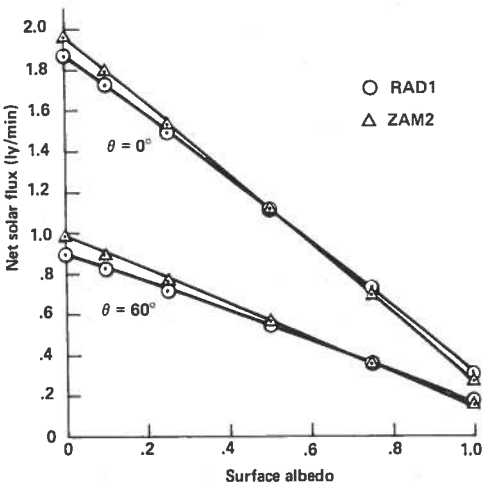

b. At 16 km

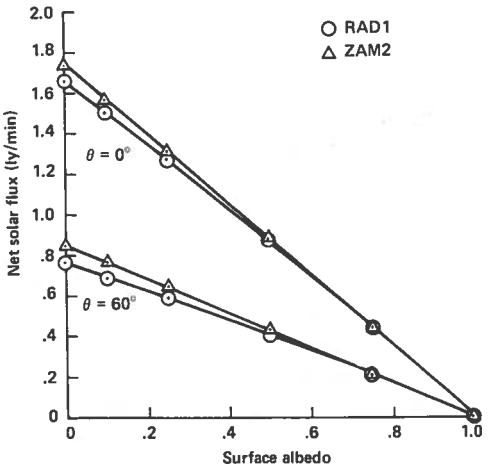

c. At earth's surface

Figure 2. Net solar flux vs. surface albedo.

the error decreasing with increasing albedo. When Rayleigh scattering was taken out of RAD1, the net fluxes at the earth's surface agreed within 1%. The difference between the net fluxes at the earth's surface and at 16 km represents the rate at which energy is absorbed by the troposphere. A comparison between the two models for $\theta = 0°$ and $60°$ is shown in Figure 3a. The agreement between RAD1 and ZAM2 is good at small surface albedo for $\theta = 0°$. There is a significant difference at large surface albedo, but large surface albedoes do not usually occur in ZAM2 for small zenith angles. For $\theta = 60°$, there is excellent agreement for small surface albedo, but the absorption rate is slightly underestimated by ZAM2 at large surface albedo.

A comparison of the energy-absorption rates in the stratosphere (16 to 50 km) is shown in Figure 3b for $\theta = 0°$ and $60°$. Although the curves are similar, ZAM2 systematically underestimates the absorption rate by about 0.007 Ly/min for $\theta = 0°$ and by about 0.004 Ly/min for $\theta = 60°$. Although these differences represent a small fraction of the incoming solar radiation, they represent a significant fraction of the total energy absorbed by the stratosphere. These differences could be reduced by recalibration of Lindzen and Will's specific heating function for ozone.

Long-Wave Radiation

A spectrally averaged transmission function for water vapor is used in the long-wave radiation calculation. Crawford's (1965) empirical formulation for the transmission function is used; it includes the effect of carbon dioxide concentrations of about 0.03 percent. The 0.6-μm band of ozone is not included in the calculation. In order to compute the radiative fluxes at a particular pressure level, the atmosphere above and below the level is divided into slabs, each with a $\Delta\tau$ of 0.05 or less, where τ is the transmissivity. After the radiative fluxes have been determined for each level, the cooling rates are computed by taking the divergence of the net radiation.

In the stratosphere, cooling due to long-wave emission by carbon dioxide is computed by means of an empirical scheme developed by Leovy (1964) and recalibrated with data from Newell (1971). The cooling rate is made proportional to the temperature such that

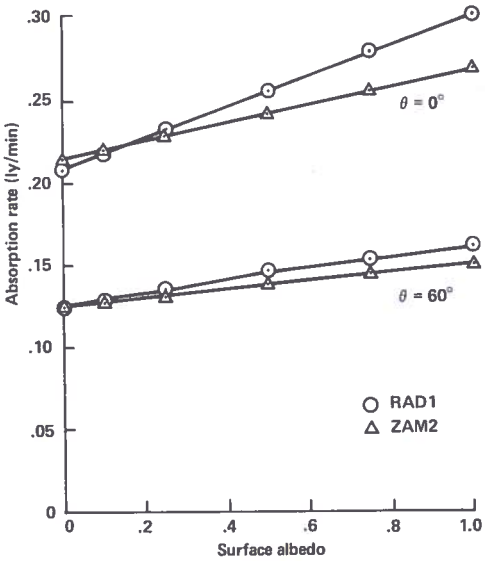

a. Troposphere (0-16 km)

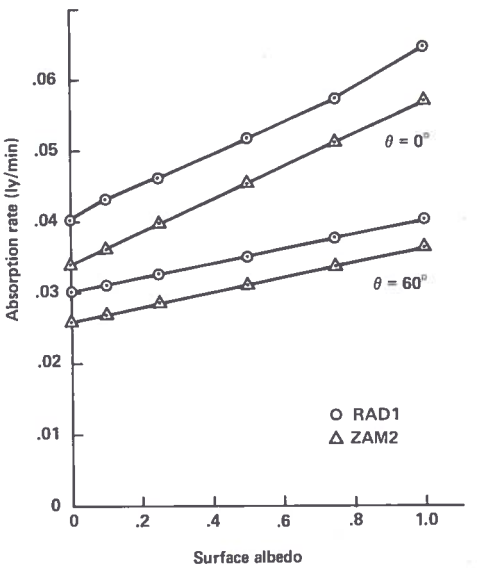

b. Stratosphere (16-50 km)

Figure 3. Energy-absorption rates vs. surface albedo.

$$\frac{\partial T}{\partial t} = k_0 - k_r T$$

where $\partial T/\partial t$ is the rate of change of temperature in °K/sec, T is the local temperature in °K, $k_0 = 2.430 \times 10^{-4}$ °K sec^{-1} and $k_r = 1.160 \times 10^{-6}$ sec^{-1}. This formula is employed only at the 10- and 20-mb levels in the model. The cooling rate at 50 mb is taken to be one-half that at 20 mb.

As in the solar-radiation computation, the calculation is made for each surface type on the basis of its temperature; then the temperature and heating rate are averaged for all layers of the atmosphere but the one next to the surface.

As a part of model validation, results using ZAM2's long-wave radiation model have also been compared with similar calculations made with other methods. Those models used for comparison are the Rodgers and Walshaw (1966) (R-W) model, the Manabe and Strickler (1964) (M-S) model, the NCAR 6-layer radiation model (Sasamori, 1972) and a 25-layer model using Yamamoto's radiation chart (Sasamori, 1972). Among these models, the R-W model is the most complex and is considered the standard for comparison.

The R-W model subdivides the 6.3-μm band, the rotation band, and the continuum of water vapor into 19 subintervals. Two of these subintervals contain the 15-μm carbon dioxide band and the 9.6-μm ozone absorption band. A random model is used to represent the absorptivity for each subinterval, and the Curtis-Godson approximation is used to estimate the effective pressure for absorption.

In the M-S model, the mean transmissivity of water vapor for the entire band is defined according to Yamamoto. The random model is used for the computation of mean transmissivity. The absorptivity of the 15-μm band of carbon dioxide and that of the 9.6-μm band of ozone are determined by means of empirical relationships. The temperature dependence of ozone absorption is neglected, and the pressure effect is approximated on the basis of the laboratory studies.

The NCAR 6-layer radiation model uses empirical formulations for the absorptivities of water vapor and carbon dioxide. The 9.6-μm band of ozone is not included in the NCAR 6-layer model, the 25-layer Yamamoto-chart model, or ZAM2.

The ZAM2 model, the R-W model, the NCAR 6-layer model, and Yamamoto's chart are used in the first comparison. London's (1952) temperature and water-vapor profiles for March and for 0-10°N were used; they are shown in Table 7. The results of the comparison are shown in Figures 4a and 4b for the clear-sky condition. The 9.6-μm ozone band was not included in the R-W model for this calculation.

Table 7. Summary of Distribution of Average Pressure, Temperature, and Total Effective Water Vapor During March for 0-10°N. (Water-vapor content represents total effective optical depth for water vapor up to the tropopause.)

Height (km)	Pressure (mb)	Temperature (°C)	Water Vapor (gm/cm^2)
0	1011	27.7	4.325
1.0	900	22.8	2.575
1.5	856	20.6	2.070
1.8	826	19.2	1.775
2.0	802	18.2	1.560
2.3	780	16.9	1.378
3.0	715	13.3	0.932
4.0	636	7.8	0.541
4.4	602	5.5	0.416
5.0	562	2.0	0.297
6.0	496	- 3.5	0.156
7.0	438	-10.0	0.0797
8.0	385	-16.6	0.0391
9.0	336	-23.2	0.0181
9.8	302	-28.5	0.00967
10.0	293	-30.0	0.00797
11.0	253	-38.6	0.00312
12.0	217	-47.2	0.00121
13.0	185	-55.7	0.00049
14.0	156	-62.3	0.00019
15.0	131	-69.0	0.000052
16.0	112	-75.5	

ZAM2's radiation model agrees well with the other radiation models. The cooling rate at 12 km is somewhat larger than those predicted by the other models, but the cooling rates at other heights agree very closely. In Figure 4b, it can be seen that the upward flux from ZAM2 agrees almost exactly with that of the R-W model. The downward and net fluxes agree well with those of the R-W model below 12 km, but the

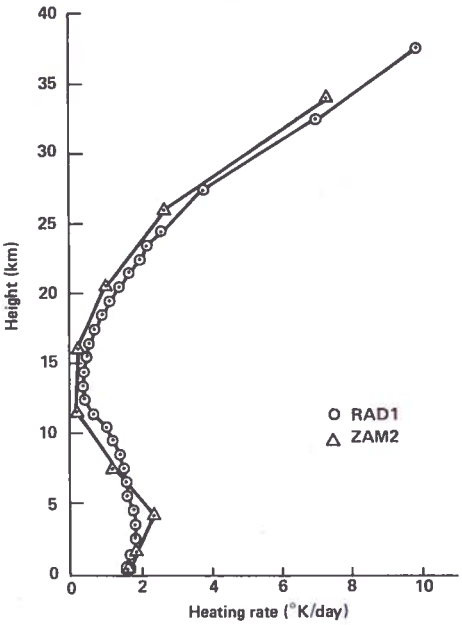

a. $\theta = 0°$, R = 0.1

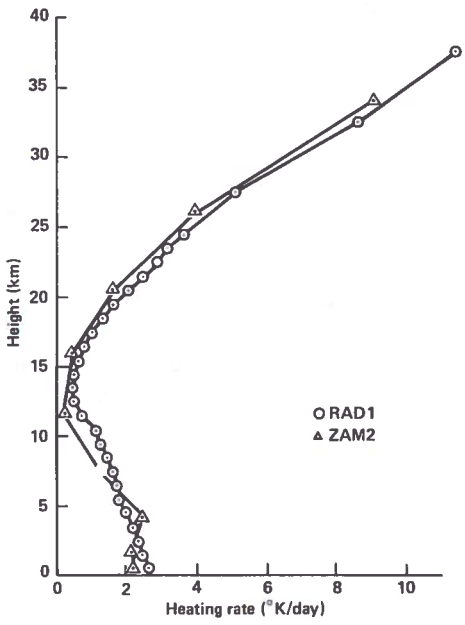

b. $\theta = 0°$, R = 0.25

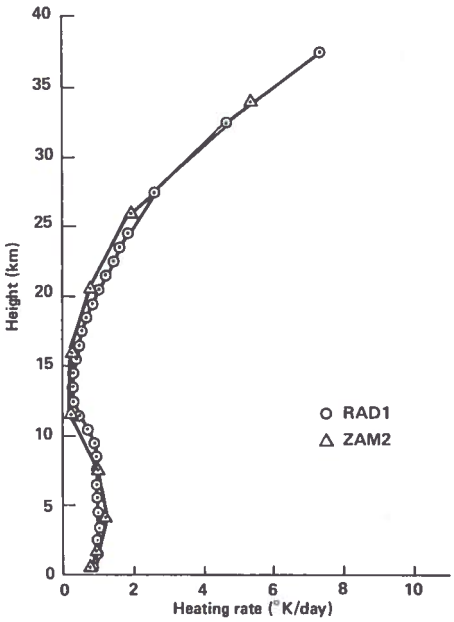

c. $\theta = 60°$, R = 0.1

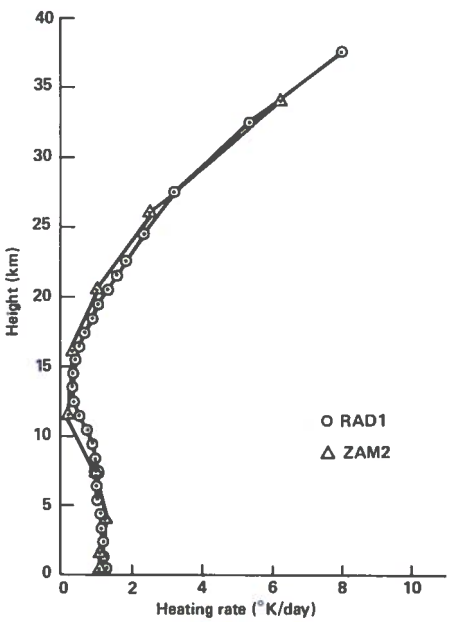

d. $\theta = 60°$, R = 0.75

Figure 1. Solar heating-rate profiles.

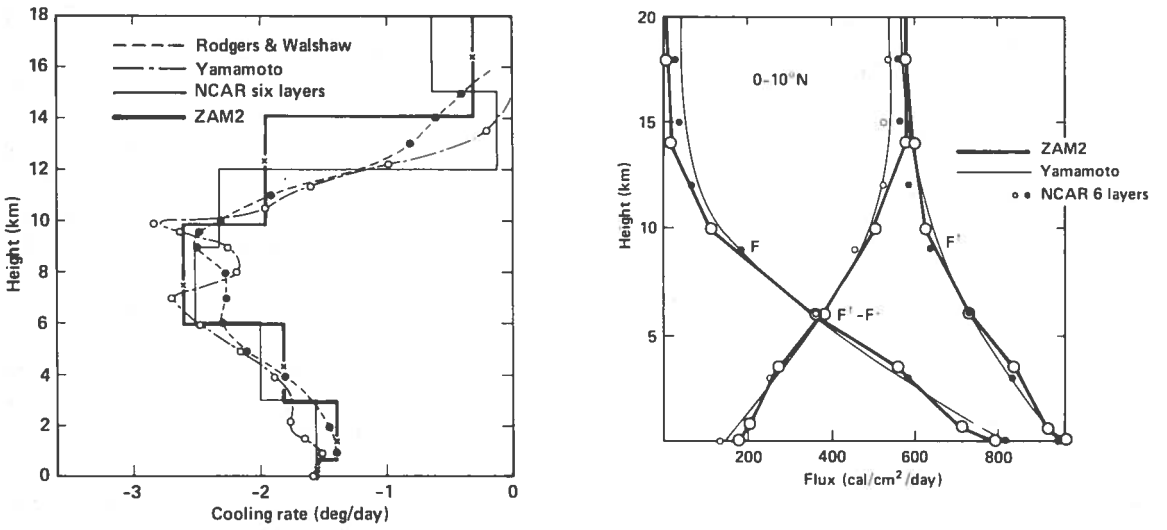

a. Cooling rate

b. Flux

Figure 4. Comparison of various calculations made with London's (1952) data.

downward flux is underestimated above 12 km, thus causing the increase in cooling rate near 12 km.

The ZAM2 radiation model, the R-W model, and the M-S model were used in a second comparison. In this case, the 9.6-μm ozone band was included in both the R-W and M-S models, but not in ZAM2. The vertical distributions of temperature, water vapor, and ozone which were used for the comparison are shown in Table 8. A constant mixing ratio of 0.456 gm/kg for carbon dioxide was used in the M-S and R-W models. The results of the comparison are shown in Figures 5a and 5b.

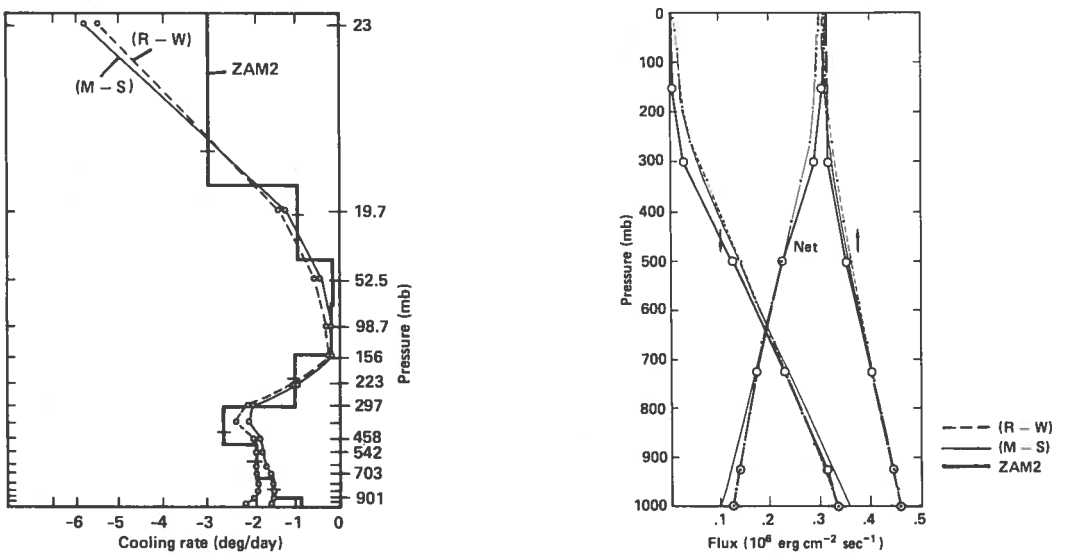

a. Heating rates

b. Flux

Figure 5. Comparison of M-S, R-W, and ZAM2 models.

Table 8. Values of Temperature, Water Vapor, and Ozone Used for Comparison of M-S Model, R-W Model, and ZAM2

Pressure (mb)	Temperature (°K)	Mixing Ratio (gm/kg) R_{Water}	R_{Ozone}
0.0000	251.3879	0.0000	0.000000
2.2719	251.3879	0.0229	0.012436
19.6759	218.1012	0.0105	0.009136
52.2120	218.5738	0.0039	0.002766
98.7226	218.0662	0.0022	0.001148
156.2500	215.9686	0.0050	0.000676
223.0367	226.7878	0.0201	0.000372
297.0250	239.2173	0.0860	0.000290
376.1574	250.0018	0.2930	0.000202
458.3762	259.4072	0.5730	0.000139
541.6238	267.6333	1.0400	0.000139
623.8426	274.8176	1.7700	0.000080
702.9750	281.0544	2.6400	0.000085
776.9633	286.3196	3.4800	0.000062
843.7500	290.8185	4.3700	0.000071
901.2774	294.4844	5.2200	0.000044
947.4880	297.3169	5.9700	0.000058
980.3241	299.2888	6.5700	0.000033
997.7281	300.3594	7.0000	0.000094
1000.0000	300.3594	7.0000	0.000094

The cooling rates again agree well with each other, although ZAM2 overestimates the cooling near 400 mb. The upward radiation flux agrees well with the R-W model's, and the downward and net fluxes agree almost exactly with those of the R-W model below 500 mb. As in the first comparison, the downward flux is underestimated above 500 mb. The results shown in Figure 5a were obtained prior to extending the carbon dioxide cooling-rate calculation down to 50 mb.

MODEL APPLICATION

Faced with the complexity of simulation of the climate, we have sought to represent atmospheric behavior, including as many feedback mechanisms as can be reasonably represented. This has resulted in a model in which atmospheric temperatures can change by about eighteen processes and water-vapor mixing ratio by about twelve processes. For this reason we have sought to validate each process separately before combining them, as evidenced by our studies of the radiation simulation. But like any complex model, this model has been rather stubborn when it comes to working as a unified entity, because of the necessity that each process be balanced by a countering effect. This has required continued inclusion of further processes. As a consequence, we are still working to achieve a satisfactory model climate, and are planning an extensive sequence of model studies to make sure we properly understand model behavior.

The first question we are asking is whether the model climate will come to an equilibrium close to the present climate. In the original ZAM model, the oceans were taken to have a heat capacity equivalent to a depth of 50 m of sea water. Being able to run for only about a year and a half (due to computer time limitations) meant that equilibrium was not truly reached, and significant trends away from the simulated climate might still have been occurring. Schneider and Gal-Chen (1973) have shown, however, that with Sellers' (1969) highly parameterized model the various feedback mechanisms may cause precipitous climatic changes after long times even when they are out of balance by only small amounts at early times. We are therefore now undertaking a specialized model simulation in which we artificially reduce the ocean depth from a typical climatic value of about 50 m to 5 m. Oceanic response time thus becomes weeks rather than months. The rapidness of the approach to climatic equilibrium should offer an early insight into how long a period must be simulated when we later apply perturbations. In addition, in order to remove the annual solar cycle, we are applying only an annual average solar radiation to the top of the atmosphere. To do this without biasing the ozone absorption by use of a large zenith angle, we reduce the solar constant by one half and double the cosine of the zenith angle.

Our early results are indicating that the model will stabilize with meteorological fields approximating observed annual averages. This result contrasts with some preliminary studies with a three-dimensional general-circulation model in which the previously fixed ocean temperatures were instead computed on the basis of the local energy balance (Schneider, 1973). Utilizing ZAM, we expect to start turning off various processes, such as the imposed oceanic

flux term, in order to determine which mechanisms are providing the stabilizing terms.

Once we have achieved a stable climate using annual average solar radiation, we will return to study the seasonal cycle. This variation is perhaps the best understood major climatic change, and model simulation of the annual cycle is of crucial importance. Several studies using a three-dimensional model for climate experiments over a sixty-day period have been reported (Warshaw and Rapp, 1972), but these offer little insight into the net annual effect the perturbation will have. We, on the other hand, are planning to let the model run to as near to cyclic equilibrium as possible.

We are working cooperatively with Warshaw and Rapp at the Rand Corporation to perform statistical analyses on model results, as they have already done using three-dimensional models. This analysis will be considerably easier than in a three-dimensional model because the randomness of eddy transport is not being computed explicitly. Thus, the "noise level" in the model should be lower, and the capability for achieving statistical significance in model perturbation studies should be higher. This hypothesis will be tested in model runs which differ only by the introduction of random noise in the initial field variables.

The importance of the two-dimensional eddy-diffusion approximation will be assessed in several ways. First, by introducing inert tracers to simulate the radioactive debris resulting from atmospheric nuclear testing, we can determine whether the model results reproduce the observed transport rates and artificially injected trace-species depletion times. And second, we plan to vary both the magnitude and dependence of the eddy prescription scheme in order to assess the sensitivity of the results to a particular parameterization. (Weak sensitivity would indicate that the climate is most strongly controlled by other compensating processes, and that our two-dimensional approximation offers a valid basis for climate studies.)

Process sensitivity studies are also planned for such other representations as cloud extent and surface albedo. This latter parameter is of crucial importance, in view of the extreme climate sensitivity evidenced in the simple one-dimensional models (Budyko, 1969; Sellers, 1969, 1973) due to a temperature-albedo feedback which they include (Chapter 6 of CIAP Monograph IV, 1974). We plan a test run with the Sellers or Budyko formulation of the albedo in order to see whether other processes of ZAM2 can counteract the strong tendency toward glaciation which accompanies a change in solar constant. We plan to do this for the cases of both a decreased solar constant and an increased aerosol amount, to see how the results of the two experiments can be related.

The next series of model tests will address the question of climatic transitivity. The original ZAM model indicated that the present climate and an ice-covered earth were both stable states. Whether varying initial conditions will indicate that other stable states exist, as is true for the Sellers model, is not yet clear. This analysis and the random-perturbation study should offer insight into a basic question in climate theory: that is, to what extent is climate change determined by changes in external parameters, such as solar radiation, and to what extent is the variability a function of interactions between internal processes and mechanisms? Clearly, however, since the oceans are represented only as a crudely coupled system, and the actual eddy fluctuations are not included, confirming studies will be needed in later, more sophisticated models.

In conjunction with these basic studies, we want to start model simulations of intentional perturbations to the system. It is not at all clear how large the perturbations in various processes will have to be to cause a signal that is significant. We expect to search for such levels by "sledge-hammer" experiments to see whether a response can be stimulated. One subject which has received considerable previous study is removal of the Arctic Ocean icecap, and this is a likely first candidate.

We are also planning to treat the more subtle perturbations which are expected to occur from operation of supersonic aircraft in the stratosphere. These will include perturbation of the ozone and water-vapor amounts presently in the stratosphere, and introduction of an aerosol layer. Initial studies will take place with the annual-average solar-radiation model, followed by an assessment of the effect of the annual cycle. We hope these can take place during the summer of 1974.

CONCLUSIONS

Despite the many hypotheses as to the causes of major climatic change, a well-structured theory of climate which can be quantitatively verified awaits further research. As a tool in this research, the ZAM2 model stands between the completely deterministic, but not yet achievable, approach offered by three-dimensional general-circulation models, and the quick-running, but highly parameterized, approach available with energy-balance models. With an extensive validation and application sequence of model studies, we are seeking to better understand the interactive processes playing roles in determining the model climate. We also expect to offer insights into both the limitations of simple models and the possibilities which can fruitfully be tested with the more complex models. Together, these results should indicate the directions for further climate model development.

ACKNOWLEDGMENTS

Development of a large and complex numerical model is a time-consuming task, and we would like to acknowledge the assistance of Gerald Potter, who has offered the insights of a geographer while doing much of the actual programming.

This work was performed under the auspices of the U.S. Atomic Energy Commission and was supported by the Climatic Impact Assessment Program, Office of the Secretary, U.S. Department of Transportation.

REFERENCES

Braslau, N. and J.V. Dave (1973), "Effects of aerosols on the transfer of solar energy through realistic model atmospheres," J. Appl. Meteorol. 12, 601-619.

Budyko, M.I. (1969), "The effect of solar radiation variations on the climate of the earth," Tellus 21, 611-619.

CIAP Monograph Series, Vol. IV, U.S. Department of Transportation. NOTE: At present, these monographs exist only in an early draft form. They will be publicly available after their completion in September 1974.

Crawford, T.V. (1965), "The Diurnal Change of Temperature in the Lower Atmosphere," Ph.D. dissertation, University of California, Los Angeles.

Dave, J.V. and J. Gazdag (1970), "A modified Fourier transform method for multiple scattering calculations in a plane parallel atmosphere," Appl. Opt. 9, 1457-1466.

Green, J.S.A. (1970), "Transfer properties of the large-scale eddies and the general circulation of the atmosphere," Q. J. Roy. Met. Soc. 96, 157-185.

Houghton, H.G. (1954), "On the annual heat balance of the Northern Hemisphere," J. Meteorol. 11, 1-9.

Leovy, C. (1964), "Simple models of thermally driven mesospheric circulation," J. Atmos. Sci. 21, 327-341.

Lindzen, R.S. and D.I. Will (1973), "An analytic formula for heating due to ozone absorption," J. Atmos. Sci. 30, 513-515.

London, J. (1952), "The distribution of radiational temperature change in the Northern Hemisphere during March," J. Meteor. 9, 145-151.

Luther, F.M. (1970), "A Numerical Model of the Energy Transfer Processes in the Lower Atmosphere," Contributions in Atmospheric Science No. 2, University of California, Davis.

Luther, F.M. (1973), "Monthly mean values of eddy diffusion coefficients in the lower stratosphere," presented at the AIAA/AMS Meeting, Denver, Colorado, June 11-13, 1973. Available as Lawrence Livermore Laboratory Rept. UCRL-74616.

MacCracken, M.C. (1973), "Zonal atmospheric model ZAM2," in *Proceedings of the Second Conference on the Climatic Impact Assessment Program*, November 14-17, 1972, ed. A.J. Broderick, U.S. Dept. of Transportation, DOT-TSC-OST-73-4, 298-319.

MacCracken, M.C. and F.M. Luther, "Climate studies using a zonal atmospheric model," in *Proceedings of the International Conference on Structure, Composition and General Circulation of the Upper and Lower Atmospheres and Possible Anthropogenic Perturbations* (Melbourne, Jan. 14-25), pub. IAMAP, 1107-1128.

Manabe, S. and R.F. Strickler (1964), "Thermal equilibrium of the atmosphere with a convective adjustment," J. Atmos. Sci. 21, 361-385.

Newell, R.E. (1971), "The global circulation of atmospheric pollutants," Sci. Amer. 224 (1), 32-42.

Newell, R.E., J.M. Wallace, and J.R. Mahoney (1966), "The general circulation of the atmosphere and its effects on the movement of trace substances, Part 2," Tellus 18, 363-380.

Oort, A.H. and E.M. Rasmusson (1971), "Atmospheric Circulation Statistics," NOAA Professional Paper No. 5.

Reed, R.J. and K.E. German (1965), "A contribution to the problem of stratospheric diffusion by large-scale mixing," Mon. Wea. Rev. 93, 313-321.

Rodgers, C.D. and C.D. Walshaw (1966), "The computation of infra-red cooling rate in planetary atmospheres," Q. J. Royal Met. Soc. 92, 67-92.

Sasamori, T. (1968), "The radiative cooling calculation for application to general circulation experiments," J. Appl. Met. 7, 721-729.

Schneider, S.H. (1973), personal communication.

Schneider, S.H. and T. Gal-Chen (1973), "Numerical experiments in climate stability," J. Geophys. Res. 78, 6182-6194.

Sellers, W.D. (1965), *Physical Climatology*, University of Chicago Press, Chicago.

Sellers, W.D. (1969), "A global climatic model based on the energy balance of the earth-atmosphere system," J. Appl. Meteorol. 8, 392-400.

Sellers, W.D. (1973), "A new global climate model," J. Appl. Meteorol. 12, 241-254.

Stone, P.H. (1972), "A simplified radiative-dynamical model for the static stability of rotating atmospheres," J. Atmos. Sci. 29, 405-418.

Stone, P.H. (1973), "The effect of large-scale eddies on climatic change," J. Atmos. Sci. 30, 521-529.

Warshaw, M. and R.R. Rapp (1972), "An Experiment on the Sensitivity of a Global Circulation Model: Studies in Climate Dynamics for Environmental Security," Rand Corporation Rept. R-908-ARPA.

DISCUSSION

ROBINSON: Why don't you use the existing observations of cloud absorption of solar radiation?

MACCRACKEN: Our approach with respect to radiation in the climate model has been to take advantage of the very complicated radiation models, which involve many of the physical processes. With our necessarily simpler models, we are trying to match those complex models rather than actual observations because our models don't include enough of the physical processes for us to expect success in matching observations.

(UNIDENTIFIED): Do I understand correctly that you have a negative vertical coefficient everywhere, and no off-diagonal K_{yz} coefficient?

MACCRACKEN: For potential temperature in the troposphere, the diffusion coefficient is negative, and there is no off-diagonal term. For water vapor and trace species, it is taken as positive, since their transport is not counter-gradient.

RADIATIVE AND DYNAMIC FEEDBACK MECHANISMS COMBINED IN AN ENERGY-BALANCE CLIMATE MODEL

TZVI GAL-CHEN AND STEPHEN H. SCHNEIDER
*National Center for Atmospheric Research**
Boulder, Colorado

ABSTRACT: The semi-empirical climate-modeling approach of Sellers (1969) is formulated as a time-dependent problem in order to study the stability of its asymptotic solutions to perturbation in external and internal conditions. Four dynamical parameterizations have been tried in order to find out what effect, if any, each would have on the climate.

It has been found that a 1% decrease, ΔQ_S, in the solar constant results in a global surface-temperature change ΔT_S, $3.34K < \Delta T_S < 5.38K$, depending upon the particular form of dynamical parameterization.

It has been concluded that the radiation balance is the primary factor in determining the qualitative features of the model's "climate." However, the horizontal and vertical distributions of temperature are influenced by the dynamics. When ice feedback is excluded from the model, the equator-to-pole temperature gradient, $\partial T/\partial y$, behaves as suggested by Stone (1973); this behavior led Stone to conclude that the static stability might be conserved during climatic changes. When ice feedback is included, however, we find that $\partial T/\partial y$ reverses, and that his assumption is not supported by our model. For fixed external conditions the solutions exhibit intransitivity with respect to negative perturbations (i.e., they exhibit different steady-state solutions for different initial conditions). Nevertheless, in order for this intransitivity to occur, an unrealistically large negative temperature perturbation (more than 19K) has to be applied to the initial condition. Numerical experimentation with these models suggests that the radiation balance in equatorial latitudes has a controlling influence on the extent of the polar ice caps.

INTRODUCTION

It is clear that the climate of the earth has sustained dramatic fluctuations in the past (e.g., Dansgaard et al. (1971)) and there is every reason to suspect that it will undergo similarly severe changes in the future. Up until now most changes in climate could hardly be attributed to man's activities. However, man is now altering the face of the earth and the chemical composition of the atmosphere and adding heat to the natural energy budget so much that his influence may soon become, or may already be, comparable to nature's in effecting climatic change. This realization has led to many studies of inadvertent climate change (SMIC (1971) and SCEP (1970), among others).

Since the earth has undergone large climatic fluctuations in the past, one of the major concerns of climatologists studying the possible impact of man's activities on the climate has been the question of the *stability* of the global climate. This question led Budyko (1969) and Sellers (1969) to develop (independently) semi-empirical models of the earth's climate, based on the equations of the zonally-averaged heat balance of the earth-atmosphere system, for the purpose of testing the sensitivity of the equilibrium state of the climate to changes in external conditions (such as the solar constant or the amount of fixed constituents in the earth's atmosphere). One important parametric relationship common to their models is the coupling between the planetary albedo and the temperature of the atmosphere near the earth's surface. This coupling leads to a strong positive-feedback link between a change in surface temperature and a corresponding variation in albedo (e.g., a decrease in temperature would correspond to an increase in albedo – due to the presumed expansion of snow and ice cover). (For a general discussion of climatic feedback mechanisms see Chapter 6 of SMIC (1971) or Schneider and Dickinson (1974).) Thus, Budyko and Sellers found that, because of the positive-feedback albedo-temperature effect included in their models, changes in the global energy budget on the order of 1% could result in extensive changes to the equilibrium climate (e.g., a partial melting of the ice caps or a significant expansion of glaciation). The dramatic results of these models, although they are based only on simplified parameterizations of most atmospheric transport processes, are, nevertheless, sufficiently compelling to indicate the need for further study of climatic stability so that it can be determined just how large a perturbation in the environment would be required, in view of the various climatic feedback processes, to significantly alter our climatic regime (see also Budko (1972)).

The object of this study is to extend the work of Schneider and Gal-Chen (1973), who explored the sensitivity of time-dependent versions of some of the originally time-independent parameterizations of Budyko (1969) and Sellers (1969) to changes in *internal*

* The National Center for Atmospheric Research is sponsored by the National Science Foundation.

(in this case initial) as well as external conditions. Four dynamical parameterizations have been included in this extension in order to examine the effect, if any, of a dynamical parameterization on the model "climate."

MODELING ASSUMPTIONS

A time-dependent version of the zonally-averaged, vertically-integrated equation of the heat balance of the earth-atmosphere system is

$$R \frac{\partial T}{\partial t} = R_e + \mathrm{div}(\vec{F}), \tag{1}$$

where R is the mass-specific heat product (thermal-inertia coefficient) for a zonal column through the land/ocean/atmosphere system (its value was chosen from Sellers (1965, p. 242)), based on a 25-meter mixed layer in the oceans and a linearly varying temperature profile down to zero degrees Celsius at a depth of 125 meters. The value of thermal inertia, R, could also be interpreted as a scaling factor for the time scale, t, if R were to be changed by the same factor at all latitudes ϕ. In these computations $R(\phi)$ is also made proportional to the fraction of the area of the zone covered by oceans. However, the effect of variations in the latitudinal distribution of R on the equilibrium solution is not considered here. T is the zonally-averaged 1000-mb (i.e., sea-level) temperature, R_e is the radiation-balance terms for a zonal column through the earth-atmosphere system,

$$R_e = Q_{SC}(1 - \alpha) - F_{IR}, \tag{2}$$

where $Q_{SC}(\phi)$ is the yearly-averaged, zonally-averaged value of solar-energy input at latitude ϕ, α is the planetary albedo at latitude ϕ, and F_{IR} is the outgoing infrared radiation flux to space,

$$F_{IR} = c(\phi)\sigma T^4[1 - m \tanh(19T^6 \times 10^{-16})], \tag{3}$$

where $c(\phi)$ is a consistency factor which has been discussed thoroughly by Schneider and Gal-Chen (1973). When $c(\phi) = 1$, equation (3) is identical to the infrared-flux formulation of Sellers (1969), and in all cases computed here $c(\phi)$ was found empirically to be in the range $0.87 \leq c(\phi) \leq 1.04$. $\mathrm{div}(\vec{F})$ is the net energy flux transport for latitude ϕ and is parameterized differently for the various models used.

Four models have been constructed. The first one, labeled (S), is:

$$\text{(S):}\quad \mathrm{div}(\vec{F}) = \left(\frac{1}{\sin\theta}\right)\frac{\partial}{\partial y}\sin\theta\,(F_o + F_A + F_q)$$

where

$y = a\theta$
a = radius of earth
$\theta = \frac{\pi}{2} - \phi$
ϕ = latitude belt
F_o = sensible heat transport due to ocean currents
F_A = sensible heat transport due to atmospheric motion
F_q = transport of latent heat energy.

The dynamical parameterization for (S) is:

$$F_o \propto K_o \frac{\partial T}{\partial y}$$

$$F_A \propto K_A \frac{\partial T}{\partial y} - \bar{v}T$$

$$F_q \propto K_q \frac{\partial q(T)}{\partial y} - \bar{v}q(T)$$

where q(T) is proportional to the water-vapor mixing ratio, $\bar{v}$ is some vertically integrated mean meridional velocity and is parameterized as a function of latitudinal temperature gradient, and the K's are eddy-diffusion coefficients. The albedo is:

$$\alpha = \begin{cases} b(\phi) - 0.009\,T_g & T_g < 283.16\text{K} \\ b(\phi) - 0.009(283.16) & T_g > 283.16\text{K} \end{cases} \tag{4}$$

$$(0.25 \leq \alpha \leq 0.85, \text{ all T})$$

T_g, the ground temperature, is determined from the sea-level temperature on the basis of zonally averaged topography (e.g., Sellers (1969)). However, if $\alpha(T)$ turns out to be greater than 0.85, then α is set equal to 0.85, and if $\alpha(T)$ turns out to be less than 0.25, α is set equal to 0.25. Formulation (S) is based on Sellers (1969), from which further details can be obtained.

The second formulation, labeled (SV), is similar to that of (S) except that $\bar{v} \equiv 0$.

The third formulation, labeled (ST), is like (S), except that the K's are non-linear as suggested by Stone (1973), namely,

$$K_i \propto |\Delta T|, \tag{5}$$

where in our case K_i is either K_A, K_q, or K_o.

The fourth formulation, labeled (STV), is similar to (ST), but with $\bar{v} \equiv 0$.

Schneider and Gal-Chen's original paper (1973) discusses the boundary conditions, the crucially important convergence criteria, the initialization (or "consistency") procedure, the method of determining the numerical values of eddy-diffusion coefficients, and the rationale for this approach to climate modeling. Those interested in further detail should consult this reference.

DISCUSSION OF RESULTS

The heat-balance equation, (1), and the boundary conditions, are solved by numerical integration by

means of the fully (time-and-space) centered implicit finite-difference scheme of Crank and Nicholson (see p. 189 of Richtmyer and Morton (1967)). The solution is iterated so that the non-linear coefficients in the finite-difference formulation can also be treated implicitly.

In the introduction it was mentioned that dramatic instability of the climate was found in the steady-state models of Sellers and Budyko when small changes were made in the value of the solar constant. We felt that our time-dependent version of Sellers' model should be able to reproduce his results. That is, the asymptotic equilibrium climate from our model should exhibit the same sensitivity to changes in the value of the solar constant that the Sellers model does, provided that our model is internally consistent (see the discussion in Schneider and Gal-Chen (1973)) and that our initial state is near to the present-day equilibrium or control climate. This agreement of our asymptotic state with the Sellers steady state is indeed found, as can be seen in Figure 1, which is computed for the Sellers dynamical parameterization (S). Curve a on Figure 1 is the asymptotic (after about 10 years of 2-1/2-day time steps) equilibrium climate, with a mean 1000-mb temperature of 287.43K which will be referred to from now on as the *control climate* (in the original paper of Schneider and Gal-Chen (1973), slightly different values were obtained due to the lower precision of the IBM 360/95 that was used then compared to the CDC 7600 which is used now). The initial temperature distribution used to produce the control distribution had a mean temperature of 287.30K, which is quite close to the final steady-state value of 287.43K. The closeness in value between the initial- and final-state mean temperatures is the result of a satisfactory degree of consistency built into the model. Curves b and c result from a 1% increase or decrease, respectively, in the value of the solar constant. We see that a 1% increase in solar input causes an increase in mean global temperature (to 290.25K, shown by curve b on Figure 1) which is significantly larger than the ≈ 1.5K increase which would be obtained if there were no positive feedback between the albedo and temperature. On the other hand, a 1% decrease in solar constant (shown in curve c) yields a mean global temperature of 282.05K – a significant decrease in temperature, caused by the increased planetary albedo arising from the decreased surface temperature – and shows very strong positive feedback. For a decrease in solar constant of more than 1.6%, we obtain a planetary mean temperature of 175.55K, which corresponds to an entirely ice-covered earth. It is results such as these, which are in general agreement with the works of Budyko and Sellers, which have led many climatologists to be concerned with the stability of the present climate. Generally very similar results are obtained by using the other dynamical parameterizations instead of (S); the comparative results for a 1% decrease in solar constant are summarized in Table 1. One can see that the radiation balance is the primary factor in determining the qualitative features of the "climate." However, Table 1 shows that the use of Stone's dynamical formulation reduces the severity of the "ice age." The equator-to-pole temperature gradient is greater in (S) and (SV) than in (ST) and (STV). This is so because in Stone's non-linear eddy-flux parameterization the eddy-diffusion coefficients are increased when the temperature gradient is increased, and therefore the inherent negative feedback (smoothing of gradients) associated with a diffusion is increased. Stone (1973) argued that non-linear eddy-diffusion laws are more realistic, so that Sellers' (1969) value of global decrease of planetary temperature, resulting from a 1% change in the solar constant, is an overestimate. In fact, in a later work Sellers (1973) uses such a non-linear formulation of eddy-diffusion coefficients.

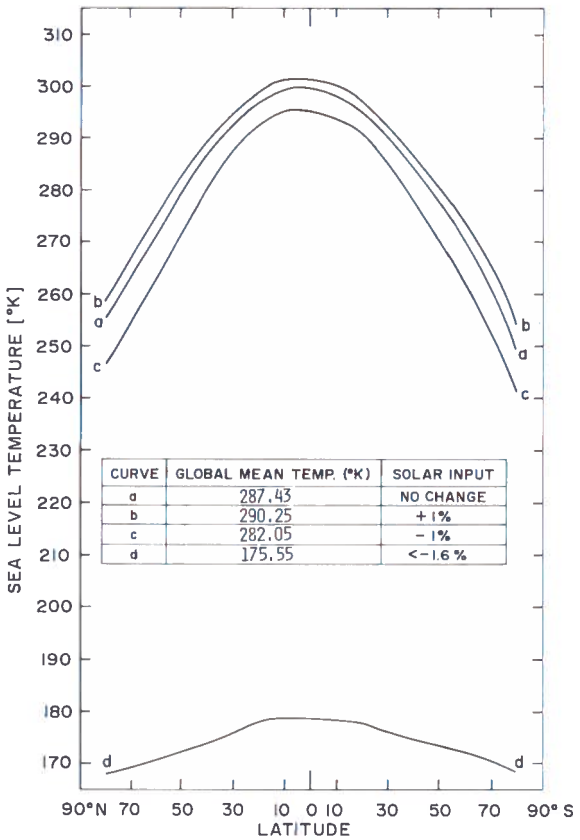

Figure 1. Asymptotic steady-state equilibrium sea-level (1000-mb) temperature distributions computed for parameterizations like Sellers' (1969), as a function of solar input.

One of the most common assumptions in climate modeling is that the static stability remains constant during climatic changes (e.g., Manabe and Wetherald (1967)). Stone (1973) shows this to be valid for a climate model which includes a simplified radiation parameterization and the effects of baroclinic eddy fluxes. He neglects ice feedback and moisture effects, and indeed the results from our model suggest that this assumption can be justified only if ice feedback is

Table 1. Temperature Decrease (in °K) as a Function of Latitude for Four Different Dynamical Parameterizations (see text). The Decreases are Forced by a 1% Reduction in Solar Constant

Latitude (°N)	Sellers (S)	Sellers (SV) ($\bar{v} = 0$)	Stone (ST)	Stone (STV) ($\bar{v} = 0$)
80	-7.70	-6.89	-4.61	-4.14
70	-7.71	-6.87	-4.63	-4.12
60	-7.86	-6.65	-4.58	-4.01
50	-7.32	-6.04	-4.29	-3.87
40	-5.90	-5.10	-3.86	-3.48
30	-4.53	-4.12	-3.29	-3.19
20	-4.08	-3.73	-3.14	-3.05
10	-3.88	-3.66	-3.10	-3.02
0	-3.87	-3.71	-3.18	-2.98
-10	-3.95	-3.48	-3.19	-2.92
-20	-4.18	-3.57	-3.18	-2.98
-30	-4.58	-3.98	-3.34	-3.03
-40	-5.79	-4.81	-3.70	-3.40
-50	-6.97	-5.76	-4.14	-3.72
-60	-8.08	-6.51	-4.47	-3.95
-70	-8.38	-6.79	-4.68	-4.03
-80	-8.06	-7.03	-4.86	-4.05
Global Average Difference	-5.38	-4.68	-3.64	-3.34
Planetary Temperature	282.05	282.82	283.84	284.21
Control Temperature	287.43	287.50	287.48	287.55

excluded. Table 2 shows how the mean horizontal temperature gradient responds to changes in the solar constant, Q_s, for the four dynamical parameterizations, with and without ice feedback. From Table 2 (and from Figure 3 in Stone (1973)) one can see that in the absence of ice feedback a decrease in the solar constant will lead to a decreased equator-to-pole temperature gradient, and therefore to decreased baroclinic activity and less horizontal sensible eddy heat flux ($\overline{v'T'}$). This, in turn, will tend to make the lapse rate more steep, since vertical sensible eddy heat flux $\overline{w'T'}$ is also proportional to equator-to-pole temperature gradient in Stone's theory. However, the radiation will tend to make the lapse rate less steep, because the lower ground temperature leads to a longer radiative relaxation time, which makes the radiation less efficient at destabilizing the atmosphere. According to Stone (1973), these two competing effects almost cancel each other and leave the static stability relatively unchanged over a wide range of values of Q_s. However, when ice feedback is included, both radiation and dynamics work in the same direction, as is evident from Table 2. That is, a decrease in the solar constant will, in this case (with ice feedback), *increase* the horizontal temperature gradient, which, according to Stone, should increase $\overline{w'T'}$ and thus make the lapse rate less steep because of the

Table 2. Average Equator-to-Pole Temperature Gradient, in °K per 100 km, in Response to Changes in Solar Constant for Different Dynamical Formulations, With and Without Ice Feedback

$1 + \frac{\Delta Q_s}{Q_s}$	Sellers (S)	Sellers (SV) $\bar{v} = 0$	Stone (ST)	Stone (STV) $\bar{v} = 0$	Ice Feedback
1	0.28	0.28	0.28	0.28	Yes
1	0.28	0.28	0.28	0.28	No
0.99	0.31	0.30	0.29	0.29	Yes
0.5	0.16	0.15	0.19	0.19	No

increased baroclinic activity. The radiation alone will also make the lapse rate less steep, as mentioned above. Thus, with ice feedback (as specified by equation (4)), radiation, and eddy fluxes included simultaneously, it seems one would be forced to conclude that a decrease in solar input would have the effect of decreasing the lapse rate. (Further experimentation with different formulae for $\alpha(T)$ should be attempted to confirm this statement.) Obviously, the role of moist convection must also be included in a study of the lapse rate (see Section IV.C.4 of Schneider and Dickinson (1974)).

For the stability (transitivity) experiments, a perturbation is added to the initial temperature distribution, while all other parameters in the model are held fixed. It is found that in Sellers' dynamical parameterization cases, as summarized in Table 3, the steady-state control climate can be recovered exactly if the perturbation added to the initial temperature is greater than 0. Perturbations of +2K and +16K are tried (both of which imply a melting of the polar ice caps), and in both cases energy-balance dictates alone produce a return to the control climate – that is, to fully unique, fully stable, transitive control climates.

Table 3. Asymptotic Steady-State Global-Average Temperatures Resulting from Various Perturbations to the Initial Temperature Distribution for the (S) Parameterization (see text for explanation)

Initial Temperature Perturbation P	Latitudes Perturbed	Mean Planetary Temperature (°K) Sellers (S)	Stone (ST)
0		287.43	287.43
$0 < P < 16$	all ϕ	287.43	287.43
$-18.9 < P \leq 0$	all ϕ	287.43	287.43
$P < -18.9$	all ϕ	175.55	175.55
-22 0	$\lvert\phi\rvert \geq 20°$ $\lvert\phi\rvert < 20°$	287.43	287.43
-32 0	$\lvert\phi\rvert \geq 20°$ $\lvert\phi\rvert < 20°$	175.55	175.55

Most interesting, however, is that for initial temperature perturbations less than -18.9K we obtain the ice-covered-earth solution corresponding to curve d of Figure 1 (which was for a 1.6% decrease in solar constant, an *external* parameter). Of course, in these initial-temperature-perturbation experiments the solar constant is held fixed. Thus, it takes an extremely large (more than 18.9K) negative initial temperature perturbation to lead to a highly intransitive alternative climatic regime for these models, namely ice-covered earth. At first this result was quite puzzling, but when Schneider and Gal-Chen (1973) looked carefully at the control temperature distribution, given by curve a in Figure 1, they saw that in the equatorial latitudes the surface temperature is about 300K. If we now look at equation (4) for the albedo formulation, we note that only when the mean zonal temperature is *less than 283K* does the albedo become temperature-dependent. Now if we subtract 18 from 300 we get 282, so it was concluded that the reason the model is relatively insensitive to decreases in initial conditions of less than 18K is that the albedo of the equatorial region has not been changed by the perturbation. But in these experiments the solar input has been held constant, and even though the temperate and polar latitudes could be ice-covered by virtue of the large negative initial temperature perturbation, there is still enough energy available to the tropics (with unaltered albedo since $T \geq 283$) to transport sufficient heat poleward to "melt the ice" and restore the equilibrium climate to a near-present-day value. However, if the equatorial temperature is decreased sufficiently by the initial temperature perturbation (that is, by more than 18.9K) to lower it into the range of the positive-feedback temperature-albedo coupling implicit in equation (4), then climatic instability is evidenced and the ice-covered earth regime results. Thus, the ice-covered-earth solutions of both the Budyko (1969) and Sellers (1969) models, which were obtained by a decrease in the solar constant of more than 1.6%, were a result of the fact that the solar constant was decreased *everywhere*, and thus the energy available to the tropics was also reduced. Therefore, the tropics were no longer able to export the energy necessary to prevent the positive-feedback albedo-temperature coupling in the temperate and polar latitudes (where $T < 283$) from causing a runaway ice age. To further test this hypothesis, we take a very large negative perturbation in initial temperature – namely, -22K – and apply it to all latitudes poleward of 20° while leaving the initial temperature at the equator and at latitude zones 10°N and 10°S fixed. The result is a return to the near-present-day climate. Thus, a fairly extreme initial ice age in temperature and polar latitudes is unable to cause a runaway ice-covered earth because the energy input to the tropics has been maintained. (A -32K non-equatorial perturbation is adequate to lead to instability, however, as can be seen on the table.)

CONCLUSIONS

First, the radiation balance – in particular, the functional relationship between albedo and temperature – seems to control the stability of the semi-empirical models. Therefore, the validity of our conclusions is highly dependent on the level of confidence that can be placed on the Sellers or Budyko radiation parameterizations. Results obtained by Gordon and Davies (1973) seem to indicate that Budyko's model is quite sensitive to different, and, they argue, equally plausible, radiation parameterizations. The dynamic parameterizations seem to play only a secondary part in determining the stability of the global surface temperature, although they may affect the horizontal and vertical distributions of temperature.

Second, the reduction in the average planetary temperature as a result of a 1% decrease in solar

constant is between 5.38K as an upper limit and 3.34K as a lower limit, with these parameterizations. The lower limit seems to be more probable, however, since it is based on Stone's dynamical parameterization, which in turn is based on baroclinic theory. Of course, other processes such as moist convection, direct circulation, or cloudiness (which have not been adequately represented in these simplified theories) could alter these conclusions.

Third, the assumption that static stability remains constant during climatic changes cannot be justified by simplified energy-balance and baroclinic eddy-flux models when strong positive-feedback ice-albedo-temperature effects are also included. Results of models which derive their conclusions on the basis of this assumption should therefore be treated with caution; it is particularly important to assess the sensitivity of these models to changes in static stability. The role of moist convection in changing static stability must also be considered.

Fourth, another conclusion that seems to be justified by these experiments is that if the energy input to the tropics is left nearly constant, then large changes in the temperature and albedo of middle and polar latitudes can eventually be offset by the exporting of sufficient energy from the tropics. This suggests that one possible reason that ice sheets never have proceeded equatorward much below the middle latitudes is that the energy input to the tropics has always been large enough to sustain poleward energy fluxes that prevented the further expansion of the ice sheets, and in fact eventually led to their recession – possibly accelerated by the positive-feedback albedo-temperature coupling.

In conclusion, it must again be repeated that the albedo-temperature formulation used in these models does not explicitly include coupling to the hydrological cycle, nor do the dynamical parameterizations used in some of these models make adequate provisions for a change in the values of effective eddy-diffusion coefficients with changes in climate, which undoubtedly would occur should the climate undergo changes as drastic as those we have been experimenting with in these runs. Also, "eddy fluxes" must include the effects of standing as well as transient eddies; the former were not properly included in these parameterizations. In short, it must be borne in mind that the results obtained with the simplified empirical parameterizations used here should by no means be generalized to explain phenomena observed on earth. Nevertheless, these models do satisfy the energy balance of the earth-atmosphere system, and in the long term it is the energy balance which must determine the surface temperature. Thus these models are, at the very least, a very valuable "educational toy" (as they were described by Robinson (1971)), and their results suggest that climatic stability and sensitivity experiments should be attempted with much more sophisticated models (atmospheric, oceanic, and joint atmosphere/ocean) that explicitly include detailed hydrological cycle and dynamical calculations (see, e.g., the discussions in Schneider and Dickinson (1974)).

REFERENCES

Budyko, M.I. (1969), "The effect of solar radiation variations on the climate of the earth," Tellus **21**, 611-619.

Budyko, M.I. (1973), "The future climate," Trans. Amer. Geophys. Union **53**, 868-874.

Dansgaard, W., S.J. Johnsen, H.B. Clausen, and C.C. Langway (1971), "The Late Cenozoic Glacial Age," symposium edited by K.K. Turekian, Yale Univ. Press, New Haven, Conn.

Gordon, H.B. and D.R. Davies (1973), "The effect of changes in solar radiation on climate," Q.J. Roy. Meteor. Soc. **99**, 123-126.

Manabe, S. and R.T. Wetherald (1967), "Thermal equilibrium of the atmosphere with a given distribution of relative humidity," J. Atmos. Sci. **24**, 241-259.

Richtmyer, R.D., and K.W. Morton (1967), *Difference Methods for Initial-Value Problems*, Wiley, New York.

Robinson, G.D. (1971), "Review of climate models," in *Man's Impact on the Climate*, ed. W.H. Matthews, W.W. Kellogg, and G.D. Robinson, MIT Press, Cambridge, Mass., 205-212.

SCEP (1970), *Man's Impact on the Global Environment: Assessment and Recommendations for Action*, MIT Press, Cambridge, Mass.

Schneider, S.H. and T. Gal-Chen (1973), "Numerical experiments in climate stability," J. Geophys. Res. **78**, 6182-6194.

Schneider, S.H., and R.E. Dickinson (1974), "Climate modeling," Rev. Geophys. Space Phys. (in press).

Sellers, W.D. (1965), *Physical Climatology*, Univ. Chicago Press, Chicago.

Sellers, W.D. (1969), "A global climatic model based on the energy balance of the earth-atmosphere system," J. Appl. Meteor. **8**, 392-400.

Sellers, W.D. (1973), "A new global climatic model," J. Atmos. Sci. **12**, 241-254.

SMIC (1971), *Inadvertent Climate Modification: Report of the Study of Man's Impact on Climate*, MIT Press, Cambridge, Mass.

Stone, P.H. (1973), "The effect of large-scale eddies on climatic change," J. Atmos. Sci. **30**, 521-529.

DISCUSSION

SCHAINKER: How does one validate such a model?

GAL-CHEN: Well, you can get the same results by averaging the energy equation over the latitude and longitude. And the ice age we got was very similar to the last ice age that occurred.

LEITH: It's possible that in the next five or ten years satellites will give us better measurements of the radiation balance of the earth, and of the interannual variation in the heat balance caused by changes in ice cover. Since we really need a knowledge of effects on a much larger time scale, though, and no one has yet made a good measurement of the solar constant, we still have a problem.

GAL-CHEN: You can object to the parameterization of dynamics, but the results turned out not to be particularly sensitive to them. The critical assumption is the functional relationship between ground temperature and albedo.

LONDON: The Kukla and Kukla article that appeared in the February issue of *Science* reports observations that ice cover has been increasing over the last six years, and suggests that there is worthwhile data for the last twenty-five years.

A STUDY OF THE EFFECT OF STRATOSPHERIC AEROSOLS PRODUCED BY SST EMISSIONS ON THE ALBEDO AND CLIMATE OF THE EARTH*

JAMES B. POLLACK
NASA Ames Research Center
Moffett Field, California

and

OWEN B. TOON
Laboratory for Planetary Studies
Cornell University
Ithaca, New York

ABSTRACT: Fleets of aircraft, flying at stratospheric altitudes, could lead to a significant increase in the aerosol content of the stratosphere. We have carried out exact, multiple-scattering calculations to determine the response of the Earth's albedo to an increase of the stratospheric-aerosol optical depth. We find that a tripling of the aerosol content of the stratosphere, which represents an extreme upper limit to the effects of aircraft flying in the stratosphere, results in a 0.6% increase of the Earth's reflectivity and a decrease of the mean surface temperature on the order of 0.3°K. Such changes could be marginally significant.

Much effort has recently been expended in attempting to anticipate the climatic effects of projected fleets of aircraft flying in the stratosphere, particularly SST's. A good fraction of this study has been concerned with determining the effects of gases emitted by such aircraft on the amount of ozone in the atmosphere. A second area of concern is the contribution SST's could make to the aerosol content of the stratosphere. Such an addition will affect the overall heat budget of the Earth, primarily by causing a change in the Earth's albedo. Below we report the initial results of our exact numerical calculations, aimed at obtaining a quantitative estimate for this second problem area.

METHOD

An exact numerical method, based on the doubling principle (Hansen, 1969), was used to calculate the dependence of the Earth's albedo on the optical depth of the stratospheric aerosol layer. The calculations reported here differ in several significant ways from similar calculations made earlier. First, we use the actual optical constants of the dominant aerosol species in the stratosphere and troposphere. Second, allowance for gas absorption is made in an exact fashion. Third, the method permits inclusion of the optically thick water clouds of the troposphere. We now discuss some of these points in somewhat greater detail.

Hansen's doubling method permits one to exactly determine the reflection and transmission of light incident at one interface of a homogeneous scattering layer. In order to model the real atmosphere with some degree of realism, it is necessary to allow for its vertical inhomogeneity. We have done this by dividing the atmosphere into a series of 15 layers, each assumed homogeneous within its extent, and determining the scattering and transmission properties of each layer by the standard doubling technique. We have then generalized the doubling procedure to permit combining the various layers (see Lacis and Hansen (1974)). This procedure yields not only the net albedo of the planet, but also the energy absorbed within each layer.

The dominant aerosol in the stratosphere is apparently an aqueous solution of sulfuric acid, whose concentration is about 75% H_2SO_4 by

* Also presented at the IAMAP meeting in Melbourne, Australia, January 14-25, 1974.

weight (Toon and Pollack, 1973). Aircraft will probably affect the stratospheric aerosol population chiefly through the emission of sulfur-containing gases, which are subsequently converted to sulfuric acid. To calculate the scattering properties of a given aerosol species, it is first necessary to specify its real and imaginary indices of refraction. We obtained the desired optical constants of sulfuric acid from the work of Palmer and Williams (1973) and of Neumann (1973).

In the troposphere there is a ubiquitous, optically thin layer of particles, believed to be composed chiefly of ammonium sulfate, as well as optically thick water clouds, which are present over about 50% of the surface area. The optical constants of water were obtained from Irvine and Pollack (1968), while those of ammonium sulfate came from Neumann (1973), Chermack (1970), and Volz (1973).

Because the near-infrared absorption bands of water vapor contain high-frequency structure, it is difficult to incorporate the effects of water-vapor absorption in an exact fashion into the scattering calculations, which presume monochromatic radiation. However, the present calculations do treat this absorption exactly. We have followed Lacis' and Hansen's (1974) suggestion that the band absorption be expressed in terms of an integral of the probability of having a given absorption coefficient times the usual Beer's-law extinction. Thus we perform calculations for each coefficient, and weight the results by the probability values. This procedure was carried out for all the major water-vapor bands, as well as for the oxygen A band. The shorter-wavelength ozone bands, which do not have this (1969) work. All quantities have been normalized by the amount of solar energy incident at the top of the atmosphere. The second, third, and fourth columns of Table 1 show values of the overall albedo for the cloud-free areas, the cloud-covered areas, and for an appropriate average of cloud-free and cloud-covered results (partly cloudy). All the remaining columns give results for the partly-cloudy case, i.e., the Earth as a whole.
problem, were also taken into account, but no allowance was made in these calculations for CO_2 absorption.

The net albedo of the earth was calculated by averaging calculations performed for model earths having water clouds and those having none. The optical depth of the water clouds was chosen to be 5, so as to give a reasonable net albedo for the earth. The vertical profile of the optical depth of the ammonium sulfate and sulfuric-acid particles was based on the work of Elterman (1969), which was uniformly scaled to give a total optical depth of 0.1 (Herman et al., 1971).

To evaluate the effect of the aircraft, we performed the calculation first for the present optical depth of the stratospheric aerosol layer, and subsequently for several higher values of the stratospheric optical depth. In all cases the optical depth of the tropospheric aerosols was kept constant.

A computer program was written to carry out the calculations. This program included a Mie-scattering subroutine to specify the single-scattering properties of the aerosols. The spectrum was broken into approximately 20 spectral intervals, with the calculations made for each interval weighted by the solar spectrum.

RESULTS

Table 1 summarizes the results of our calculations. It displays the fractional absorption and fractional albedo for several values of the stratospheric-aerosol optical depth at visible wavelengths. The value of 0.01 corresponds to the present value, derived from Elterman's

As might be expected, the effect of adding to the stratospheric aerosol content is more dramatic in the cloud-free case than in the cloud-covered case. Tripling the number of stratospheric aerosol particles, which probably represents a very extreme upper limit to the effects of aircraft flying in the stratosphere (CIAP Monograph III), changes the overall albedo by 0.6%. The surface-temperature change caused by such an albedo variation is estimated below.

Looking at the next two columns, we see that almost all of the absorption in the stratosphere is due to gases, chiefly ozone, and very little to the aerosols themselves. We also see that the amount of gaseous absorption, and hence the ozone dissociation rate, changes by only 0.1% when the optical depth is tripled. Hence, increased aerosol scattering caused by SST emissions will affect the ozone budget in only a very minor fashion.

Table 1. Solar Energy Heat Budget* for the Earth as a Function of the Stratospheric Aerosol Optical Depth (τ) at 0.55μ. Results are for a Partly Cloudy Earth Except Where Indicated

	← Albedo →			Absorption					
				Stratosphere		Troposphere			
τ	Cloud-Free	Cloud-Covered	Partly Cloudy	Gas	Aerosol	Gas	Aerosol	Ground	Ground & Troposphere
0.01	0.14795	0.51455	0.33125	0.052216	4.109×10^{-5}	0.091696	0.022355	0.50244	0.61649
0.015	0.14875	0.51472	0.33174	0.052230	6.143×10^{-5}	0.091591	0.022342	0.50204	0.61597
0.02	0.14955	0.51489	0.33222	0.052244	8.165×10^{-5}	0.091487	0.022329	0.50164	0.61545
0.03	0.15112	0.51524	0.33318	0.052269	1.218×10^{-4}	0.091286	0.022304	0.50084	0.61443

* All quantities listed in the table are ratios of the amount of energy in a given mode to the solar energy incident at the top of the atmosphere.

The remaining columns show the effect of the stratospheric aerosols on the heat budget of the troposphere. The last column shows the fractional sum of the energy absorbed by the troposphere and the ground, and may be used to estimate the overall change in surface temperature. If we crudely assume that the surface temperature changes in proportion to the fourth root of the energy absorbed in the troposphere and the ground, we find that tripling the stratospheric aerosol content implies that the surface temperature will decrease by about 0.3°K. Such a change could be marginally significant; a 4°C change would lead to an ice age. Because of the existence of such positive-feedback mechanisms as the growth of the ice sheets, a primary change of only 1 or 2°C may be amplified to a 4°C change.

In conclusion, we would like to stress the importance of one of the assumptions used in the above calculations. Elterman's (1969) actual value for the stratospheric-aerosol optical depth is about 0.024, which was reduced to 0.01 by requiring that the optical depth of the whole atmosphere be 0.1, as indicated by other measurements. In doing this, we reduced Elterman's profile by a uniform factor. An alternative proposition would have been to reduce the aerosol optical depth only in the bottom part of the troposphere, where Elterman did not directly measure it. Had we done so, the effect of tripling the aerosol population of the stratosphere would have been more dramatic. We are presently carrying out such calculations.

ACKNOWLEDGMENT

Owen B. Toon would like to acknowledge the support of the National Science Foundation for this work, through grant GA 23945.

REFERENCES

Chermack, E.A. (1970), "The Optical Constants (n, k) of Ammonium Sulfate in the Infrared," PhD. thesis, New York University.

CIAP Monograph Series (1974), Volume 3, U.S. Department of Transportation. NOTE: At present, the monographs exist only in an early draft form. They will be publicly available after completion in September 1974.

Elterman, L., R. Wexler, and D. Chang (1969), "Features of tropospheric and stratospheric dust," Appl. Opt. 8 (5), 893.

Hansen, J.E. (1969), "Radiative transfer by doubling very thin layers," Astrophys. J. 155, 565.

Herman, B.M., S.R. Browning, and R.J. Curran (1971), "The effect of atmospheric aerosols on scattered sunlight," J. Atmos. Sci. 28, 419.

Irvine, W.M. and J.B. Pollack (1968), "Infrared optical properties of water and ice spheres," Icarus 8, 324.

Lacis, A.A. and J.E. Hansen (1974), "A parameterization for the absorption of solar radiation in the earth's atmosphere, J. Atmos. Sci. 31, 118.

Neuman, J. (1973), "Radiation absorption by droplets of sulfuric acid water solutions and by ammonium sulfate particles," J. Atmos. Sci. **30**, 95.

Palmer, K. and D. Williams (1973), private communication.

Toon, O.B. and J.B. Pollack (1973), "Physical properties of the stratospheric aerosols," J. Geophys. Res. **78** (30), 7051.

Volz, F.E. (1973), "Infrared optical constants of ammonium sulfate, Sahara dust, volcanic pumice, and fly ash," Appl. Opt. **12** (3), 564.

DISCUSSION

(UNIDENTIFIED): There is a good twelve-year-long record of solar transmission data from the Mauna Loa Observatory in Hawaii at 3.4 kilometers altitude; it shows the increase in optical depth after the Agung and other volcanic eruptions, and the subsequent recovery. It seems to me that this data could be used advantageously for verification.

TOON: The Mauna Loa data is important for following the behavior above 3 kilometers; however, almost all the aerosol optical depth is below 3 kilometers.

AN EXPERIMENT WITH A TROPOSPHERIC AND STRATOSPHERIC THREE-DIMENSIONAL GENERAL-CIRCULATION MODEL

R.L. NEWSON
British Meteorological Office
Bracknell, Berkshire, United Kingdom

ABSTRACT: Under the auspices of the British Committee set up to investigate the meteorological effects of stratospheric aircraft (COMESA), the general-circulation model of the British Meteorological Office has been revised and extended. The model now has 13 levels distributed through the troposphere and stratosphere; in addition to the variables of wind, temperature, and moisture, ozone is carried as a predictive parameter.

The results of the first experiment with a hemispheric version of the model are described, in which an attempt is made to simulate January conditions. For a considerable period, the experimental troposphere and stratosphere seem to be in a state of quasi-equilibrium simulating a characteristic winter state. The polar night jet in the stratosphere is well represented, but it is too strong and temperatures in the polar vortex are excessively low.

There is then a radical change in stratospheric circulation patterns. The polar vortex moves southwards over Greenland and weakens, to be replaced by an upper high which has developed over Eastern Asia and moved northwards. This change is accompanied by rapid temperature rises in the polar stratosphere. The whole phenomenon seems to resemble quite closely the commonly observed stratospheric warmings. A preliminary analysis of the evolution of the model's behavior during this transition is presented.

INTRODUCTION

The difficulties of modeling the stratosphere are apparent from Figure 1, which shows many of the non-linear interactions and feedback mechanisms that take place. Clearly, an understanding of dynamic processes, as well as of the chemical and photochemical ones, is fundamental to giving reliable answers to questions regarding atmospheric structure and the possible effects of aircraft emissions, in particular the distribution of ozone and trace species by atmospheric motions.

From a dynamical point of view, the upward transfer of eddy energy from the troposphere is thought to be of major importance in generating perturbations in stratospheric circulations. The principal source of eddy energy in the atmosphere is eddy available potential energy converted by the baroclinic process, so, for a good representation of stratospheric dynamics, the troposphere and its integral baroclinic process should be adequately described. Three-dimensional numerical general-circulation models (for example, Smagorinsky et al. (1965), Kasahara and Washington (1971), and Gilchrist et al. (1973)) have demonstrated their ability to handle this conversion well and to give a realistic simulation of the overall atmospheric circulation.

In order to simulate the natural stratosphere and troposphere and to study possible effects of perturbations, the British Committee On Meteorological Effects of Stratospheric Aircraft (COMESA) decided to include considerable effort on numerical modeling in its research program.

Its ultimate objective is to produce a full global three-dimensional model of the stratosphere and troposphere, containing all the relevant interactive physics, chemistry, and photochemistry. The first step was more modest, namely, to set up a hemispheric model to simulate stratospheric and tropospheric circulation patterns, and to see how ozone (for example) is redistributed as an inert tracer. This first step has now been accomplished and some of the results obtained are described below. It is of considerable interest to the COMESA program to assess the realism of these first results, to compare them with those of other groups (in particular, Manabe and Hunt (1968)), and to study the dynamics of ozone transport from

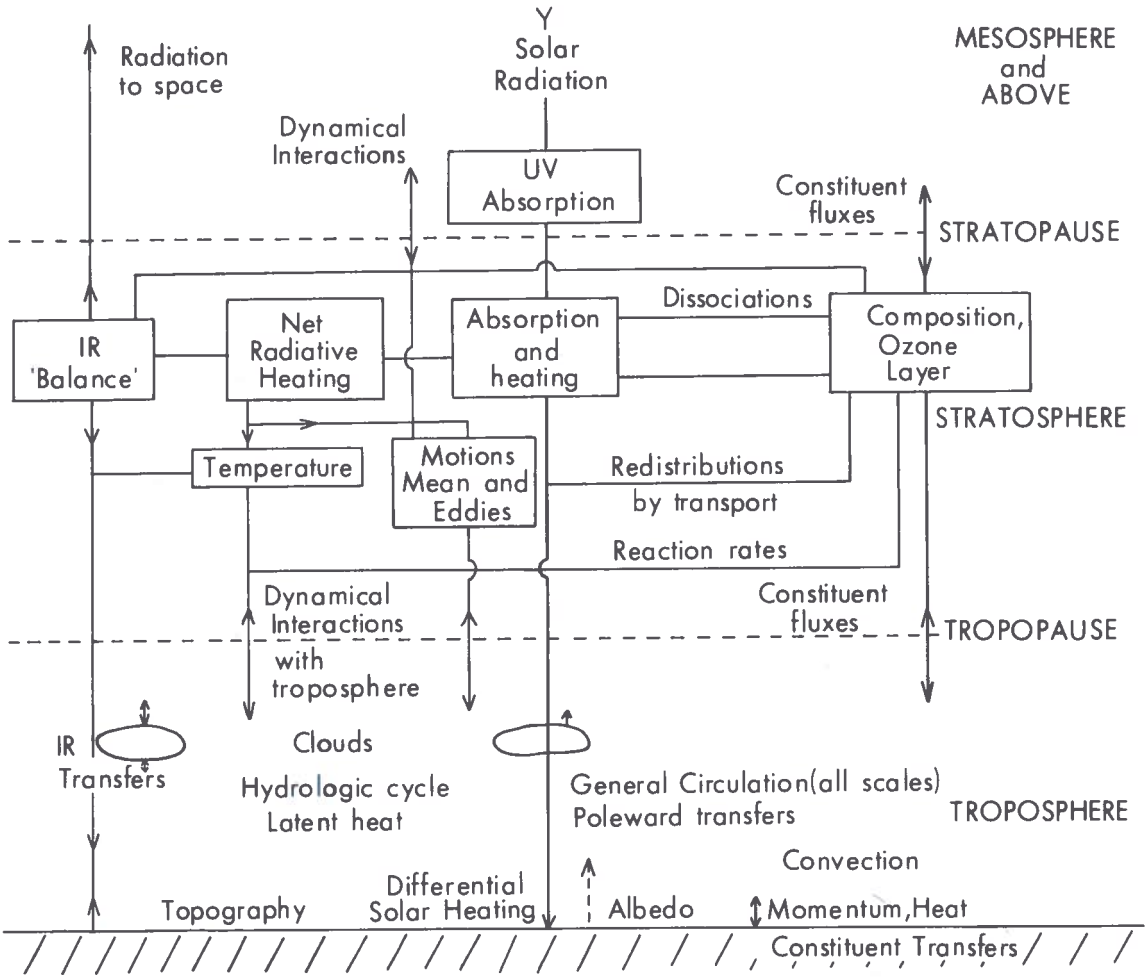

Figure 1. Processes affecting the stratosphere.

equatorial to polar latitudes. The results of the three-dimensional model can also be used to support the parallel two-dimensional modeling work, by providing input such as an array of complete and self-consistent statistics expressing the ozone transport by eddies generated in the three-dimensional model.

In the meantime, progress has been made towards a more comprehensive model, and an experiment with a global version has now been started. In another separate experiment, a fully interactive radiation scheme is being tested. If the latter can be incorporated satisfactorily, the three-dimensional model should provide a means of studying the effect on both the troposphere and the stratosphere of changes in the stratosphere's radiation conditions, e.g. as a result of changes in composition.

STRUCTURE OF THE MODEL

It would be inappropriate in this paper to undertake an extensive discussion of all the technical details involved in establishing a three-dimensional numerical model, or of the representation of all the physical processes. The structure of the model resembles quite closely that described by Corby et al. (1972). However, a number of significant changes and additions have been introduced in an attempt to improve the model's properties and atmospheric simulation, and to represent the additional stratospheric dynamics and physical processes required to meet COMESA objectives.

Of primary importance, of course, is the number and distribution of vertical levels. The

vertical coordinate is the so-called "sigma system" first proposed by Phillips (1957); it takes the form of pressure normalized with respect to surface pressure following the terrain. This vertical coordinate system complicates the equations somewhat, but has the advantage of providing an exact non-linear kinematic lower-boundary condition, which permits proper account to be taken of the dynamical effect of mountains, however high. This may well be of particular significance in the representation of stratospheric circulations.

Thirteen levels, placed at unequal intervals at values of σ as shown in Table 1, have been adopted.

Table 1. Vertical Levels in the COMESA Three-Dimensional Model

Level	σ	Approx. ICAO height in km if surface pressure is 1000 mb
1	0.0015	44
2	0.0058	35
3	0.011	30
4	0.020	27
5	0.032	24
6	0.049	21
7	0.074	18
8	0.117	15
9	0.196	12
10	0.319	9
11	0.493	6
12	0.695	3
13	0.896	1

Horizontally, the grid density is almost homogeneous; there are 2313 points representing the Northern Hemisphere, which gives an average grid-length of about 300 km. The form of the grid is basically irregular, however, and is derived from a grid first used by Kurihara (1965).

On this vertical and horizontal grid, the usual variables of horizontal wind components, temperature, and moisture are carried and predicted. In addition, an ozone mixing ratio is also held at each grid point and its variation predicted as if it were an inert tracer. At present, there is no source or sink term for ozone, save for an empirical one for destruction at the surface by the surface exchange mechanism. In this first version, this destruction leads to a steady decrease in the total ozone content, but in future versions we intend to provide an appropriate photochemical ozone source in the stratosphere.

Another limiting feature of this first experiment is the radiation scheme. As an interim measure, until a full radiative calculation has been developed and tested, a simple linear cooling form has been used to represent long-wave cooling, namely,

$$\frac{\partial T}{\partial t} = aT + b$$

The values for the coefficients a and b, determined as a function of pressure, were based on Dopplick's figures (1970) up to 30 mb; other sources consulted for higher levels were Murgatroyd and Goody (1958) and Kuhn and London (1969). Figure 2 shows the long-wave cooling resulting from the above approximate method, with the zonally averaged mean temperature field used as initial conditions in the first experiment.

For direct heating of the atmosphere by absorption from the solar beam, fixed climatological values (again based on Dopplick and other sources) were used. Figure 3 shows the climatological solar heating field; these values, which are appropriate for January in the winter hemisphere, were used in the experiment described below.

Finally, it should be noted that in addition to the radiation term the model contains a simulation of most of the other physical processes and forcing terms thought to be of importance in determining atmospheric motions. These include representations of large-scale precipitation and latent heating, convective activity driven by static vertical instabilities and the associated convective rainfall, and a surface exchange mechanism. A smoothed version of the Earth's topography is assumed. Three different types of surface are recognized: sea, where the surface temperature is held fixed; land, whose temperature is allowed to vary according to incoming and outgoing heat and radiative fluxes; and sea-ice, whose temperature also varies but is not allowed to exceed 273K. The hemispheric version of the model, with all the physics, runs in 9 minutes of Central Processing Unit time per model day on the British Meteorological Office IBM 360/195 computer.

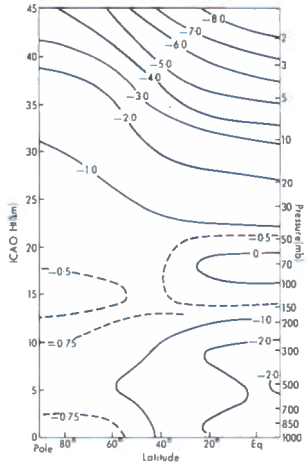

Figure 2. Long-wave radiative cooling of the model atmosphere in °K day^{-1} for the latitudinally meaned initial temperature field.

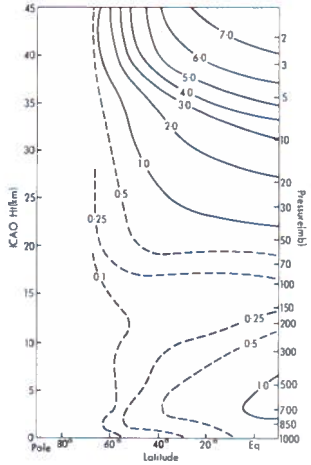

Figure 3. Heating of the model atmosphere in °K day^{-1} by direct solar absorption in January.

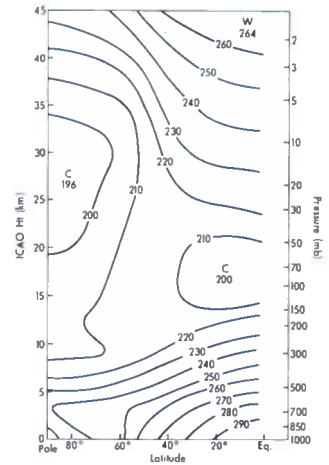

Figure 4. Zonally meaned cross-section of temperature in °K for initial data.

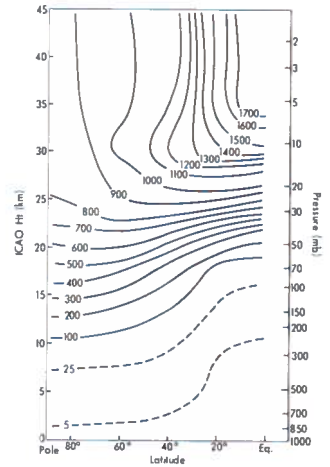

Figure 5. Zonally meaned cross-section of the ozone mixing ratio in g g^{-1} × 10^8 for initial data.

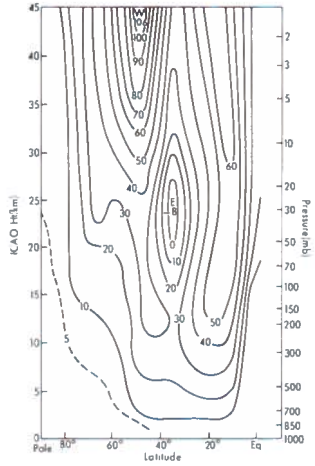

Figure 6. Zonally meaned cross-section of zonal wind in m sec^{-1} for initial data. West-to-east component is positive.

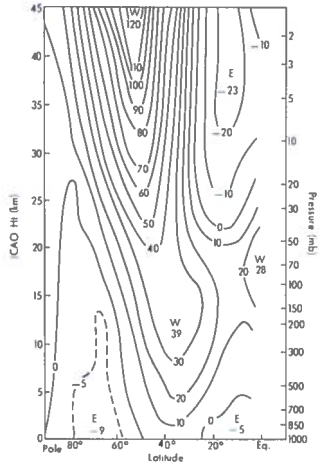

Figure 7. Zonally meaned cross-section of zonal wind in m sec^{-1} for day 70.

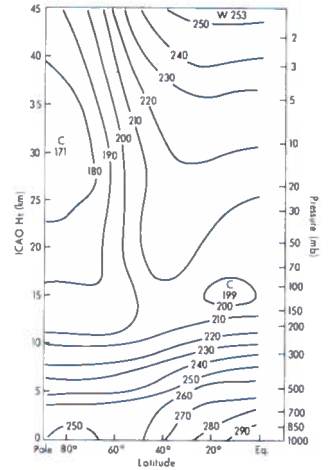

Figure 8. Zonally meaned cross-section of the temperature in °K for day 70.

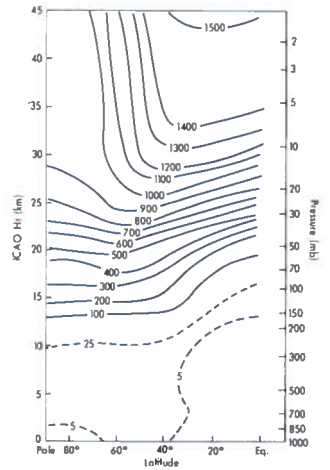

Figure 9. Zonally meaned cross-section of the ozone mixing ratio in g g^{-1} × 10^8 for day 70.

AN EXPERIMENT WITH THE MODEL

Preliminary results of the first experiment with this model are now available.

For initial data the temperature, moisture, and ozone fields were based on the zonally meaned climatological values for January. The temperature and ozone fields are shown in Figures 4 and 5 respectively. The initial wind field was obtained from the temperature field by using a simple geostrophic approximation on the model's sigma surfaces. This generated a virtually zonal wind field, but produced the unrealistic double jet structure shown in Figure 6. This geostrophic initialization took no real account of topography, and this, combined with the spurious strong flow in tropical latitudes, generated gravity waves at the start of the integration. These were well controlled by the model and within a few days of the start had died away.

January values of the sea-surface temperature were used; they were kept constant throughout the integration. The heating rates resulting from direct absorption of the solar beam were set to January values (Figure 3) and held fixed.

This experiment was thus a "perpetual January" simulation for the Northern Hemisphere, and hence somewhat unrealistic. The atmosphere's radiative cooling was offset only by the January solar heating rates throughout the integration period, whereas in reality these winter conditions are sustained only temporarily. However, it was hoped that under these conditions the model would attain some quasi-equilibrium state which could then be taken as its simulation of the January circulation. Such a quasi-equilibrium state, manifested by, for example, fairly steady zonally averaged values of temperature and zonal momentum, might form the basis of a statistical and diagnostic study; comparison with the observed atmospheric circulation at all levels in the troposphere and stratosphere could then be made. Such a comparison should reveal the effectiveness or correctness of the individual factors (particularly the physics such as radiation, surface exchanges, etc.) which entered into the formulation of the model.

The evolution of the model's circulation in broad terms was as follows. Because of forcing by surface heating (especially over the oceans), as well as perturbations induced in the flow by the topography, the initial axisymmetric conditions quickly broke down and by the eighth day realistic tropospheric trough/ridge features had developed. The motions resulted from the release of the baroclinic instability latent in the initial temperature field. After this stage, the strength of the overall flow pattern was maintained by the differential heating between Equator and pole. By 30 days, the mean zonal wind and temperature fields at tropospheric levels of the model seemed to have attained a fairly steady state and subsequently changed very little. They did not differ significantly from the initial fields, except for the disappearance of the spurious double jet structure from the zonal wind component, and substantial heating of the lowest two model levels in polar regions.

In the stratosphere there was a slow intensification of the polar-night vortex, with considerable cooling at upper levels of the model near the pole and associated strengthening of the polar-night jet. This process came to a halt at about 50 days of the model's integration time, however, and from then until about 78 days the whole model seemed to be in a quasi-equilibrium condition, which may represent the model's January simulation. During this period there was little change in the zonal mean winds, temperatures, or ozone mixing ratios. Figures 7, 8, and 9 show these fields at 70 days.

At this time in the troposphere, the zonal mean wind structure (Figure 7) looked to be a reasonable simulation of observed values, with the subtropical jetstream at about the correct latitude, height, and strength. The tropical and polar easterlies near the surface were well represented. In the stratosphere the overall structure was also reasonable, with the polar-night jet well positioned. The intensity of this jet was much too strong, however; 50 m sec^{-1} is a more characteristic observed value for the jet maximum at 45 km. An anomalous feature was the fairly strong westerlies between 16 and 20 km at the equator, but these were suspected to be a result of the equatorial boundary condition.

The mean temperature field (Figure 8) was quite similar to the observed field. In particular, the equatorial tropopause at about 15 km and the temperature minimum there were well represented, and the observed mid-latitude temperature maximum at this level was also reproduced.

The temperature minimum at about 30 km in the stratosphere at the pole was also evident, but the temperature there, as elsewhere at stratospheric levels in polar latitudes, was much too low. Overall, the temperature gradient between 30°N and the pole was too large, giving rise to the excessively strong polar-night jet.

Considering the zonally meaned ozone distribution at day 70 (Figure 9), it can be seen that compared with that of the initial one there has been an increase in the ozone mixing ratio in the polar stratosphere, and a decrease in the equatorial stratosphere. It is apparent that the general circulation has been responsible for transporting ozone northwards to polar regions, and also downwards into the troposphere where it has been destroyed by the empirical sink term at the surface. Figure 10 shows the total (i.e., summed vertically through the atmosphere) meridional ozone transport in the model at day 70 by the eddies and mean motions and their net result. Overall the treatment of ozone by the model appears to have been quite realistic, even though no photochemical processes were included in this experiment to constrain the distribution of ozone in the vertical.

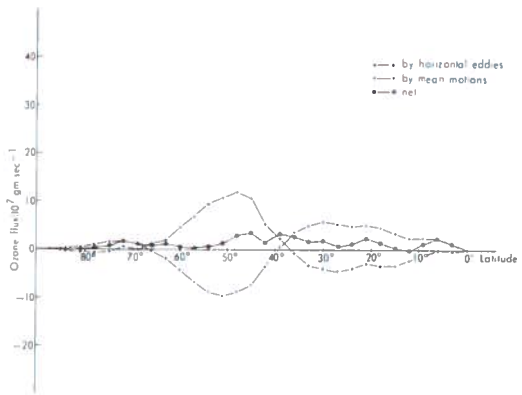

Figure 10. Meridional transport of ozone by horizontal eddies and mean motions and their net result at day 70. Units are 10^7 g sec^{-1}.

Other features of the model's circulation during this quasi-equilibrium period are illustrated in Figures 11, 12, and 13. Figure 11 shows the 500-mb contours and isotherms for day 70, and also some spot wind values. The main features of the tropospheric circulation at this stage were the three vortices over Eastern Canada, Western Europe, and Siberia. There was also a well-marked Atlantic blocking pattern, which was a persistent feature of the model's simulation during this period. However, there were distinct day-to-day variations in the flow in the troposphere, just as might be expected.

Figure 12 shows the total ozone field at 70 days. This is a reasonably realistic pattern with, broadly speaking, an equatorial minimum and high values in middle and northern latitudes. It illustrates one feature that the model represented well – the observed and well-known correlation between tropospheric troughs and ridges and ozone distribution. It can be seen that high values of ozone occurred in association with 500-mb vortices, and low values in the ridges – for example, the mid-Atlantic ridge. Since the bulk of the ozone is in the stratosphere, this correlation encourages the belief that the model was providing a realistic simulation of the dynamical interaction between tropospheric features and the stratosphere.

Figure 13 shows contours and isotherms at 2 mb (about 40 km) for day 70. The characteristic intense polar-night vortex is quite apparent.

Following this quasi-equilibrium period from 50 - 78 days a sudden and dramatic change took place in the stratospheric circulation and temperature field. This change is illustrated by Figure 14, which shows the 2-mb chart for day 90; compare it with the chart for day 70 (Figure 13). It will be seen that a major change in the flow patterns has been produced. The polar vortex has moved a long way from the pole and weakened considerably. A massive upper high has developed over Asia and is moving northwards towards the pole. In association with these developments, there have been very large temperature rises over all northern latitudes – about 60K generally, with some greater local increases. The same disruption of the flow, and temperature rise, occurred at all the stratospheric levels in the model, although the process was less far advanced at lower levels and the temperature changes were smaller. Even at 100 mb there was an area of very warm air over the Bering Strait and a marked ridge over the North Pacific. It is interesting to note that although this change seemed to become apparent almost simultaneously at all stratospheric levels, once initiated it

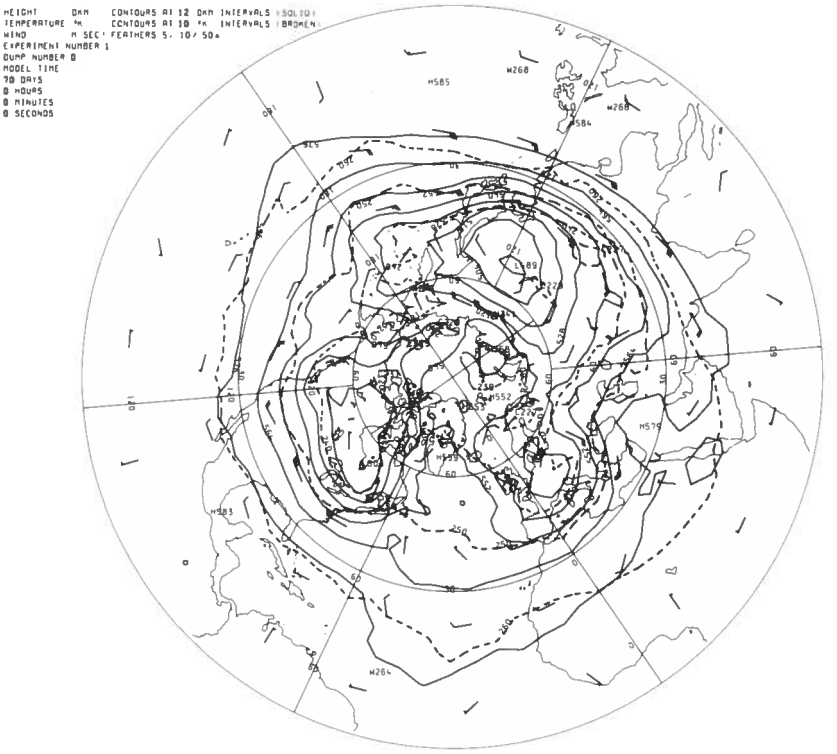

Figure 11. 500-mb chart for day 70.

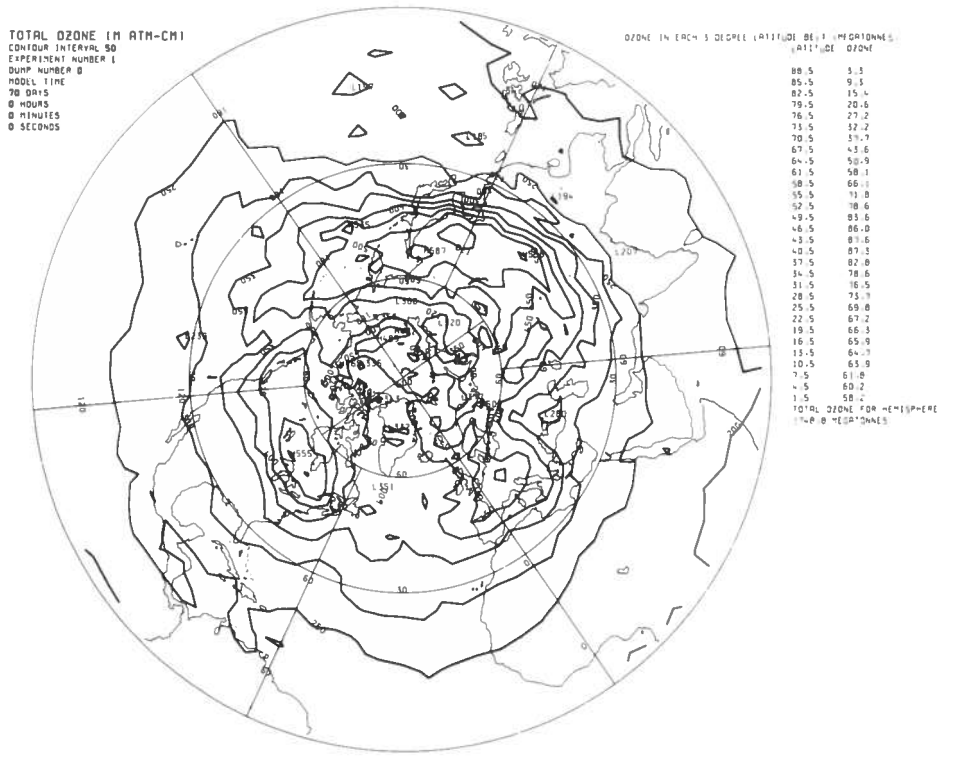

Figure 12. Total ozone field at day 70.

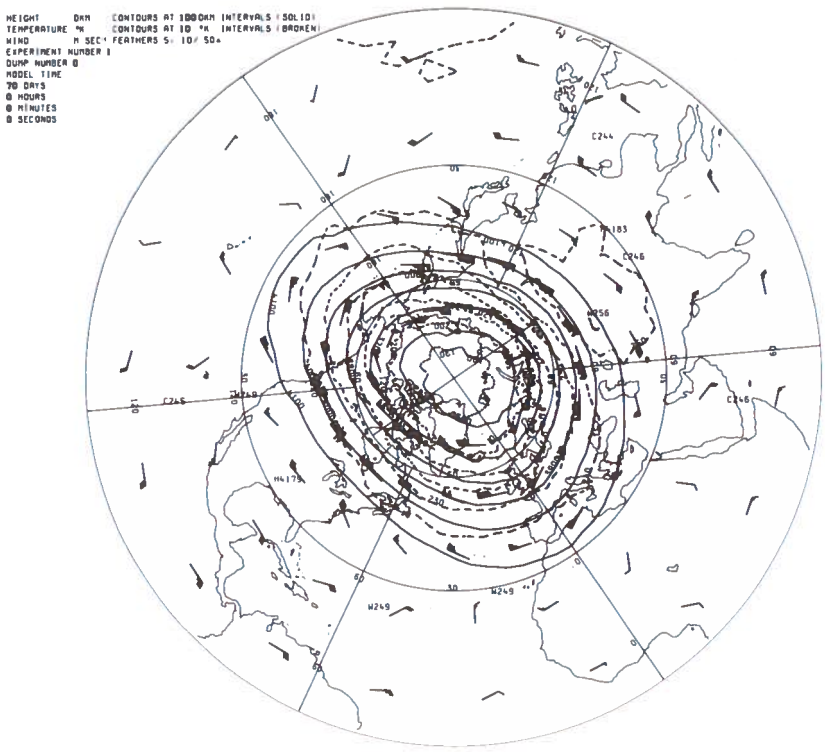

Figure 13. 2-mb chart for day 70.

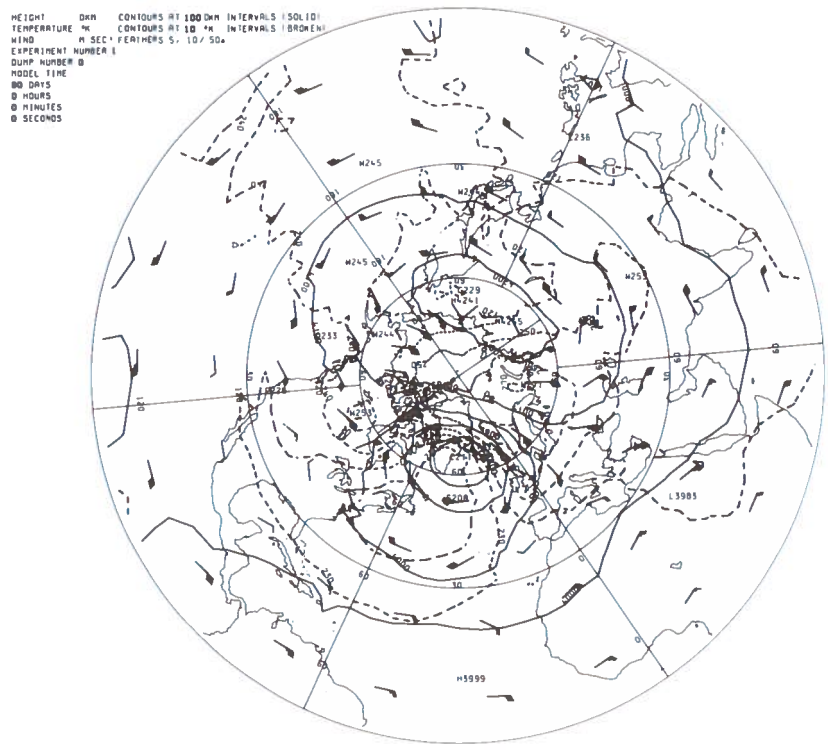

Figure 14. 2-mb chart for day 90.

proceeded much faster at high levels. Another feature of the change was the westward tilt with height of the axis of the warmest air. Overall, the changes that occurred in the model seem to resemble quite closely a stratospheric "sudden warming" event.

The magnitude of the change and circulation disruption can be appreciated by comparing Figures 15 and 16, showing the latitudinally meaned zonal wind components and temperatures at 90 days, with those in Figures 7 and 8, showing them at 70 days. The tropospheric flow below 15 km is virtually unchanged, but a reversal in the stratosphere is clearly evident.

The polar-night jet has completely disappeared and has been replaced by easterlies almost everywhere in the stratosphere. Also, in the temperature field (Figure 16) there has been a complete reversal in the stratosphere, with very large warmings near the pole and some cooling near the equator.

Figure 17 shows the zonally meaned ozone distribution at day 90. It is evident that the circulation reversal has transported very large amounts of ozone poleward and, in agreement

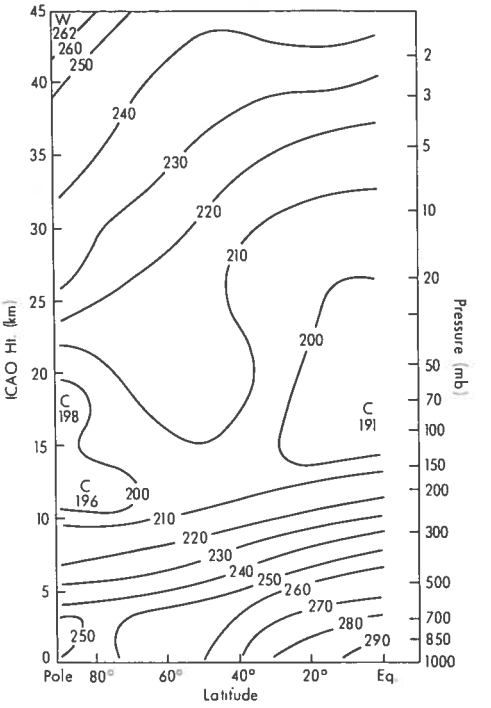

Figure 16. Zonally meaned cross-section of temperature in °K for day 90.

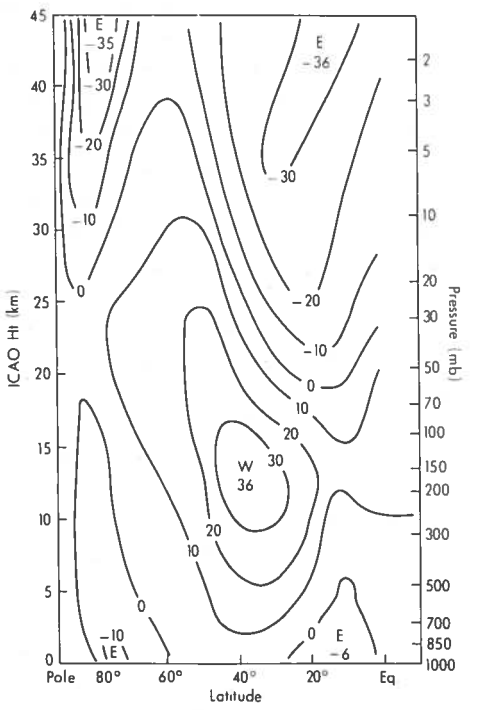

Figure 15. Zonally meaned cross-section of zonal wind in m sec^{-1} for day 90.

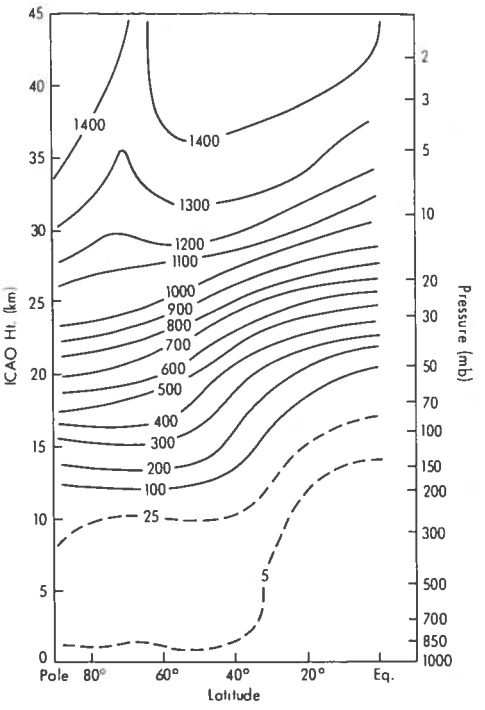

Figure 17. Zonally meaned cross-section of the ozone mixing ratio in g g^{-1} × 10^8 for day 90.

with observation, that this warming event in the model has played a major part in its global ozone budget. This is further illustrated by Figure 18, which shows the meridional transport of total ozone by the eddies and mean motions and their net effect at day 82. This was the stage at which the circulation change was proceeding at its greatest rate, and it can be observed how much larger the mean, eddy, and net fluxes of ozone were during this phase than in the pre-warming period (e.g., day 70 – Figure 10).

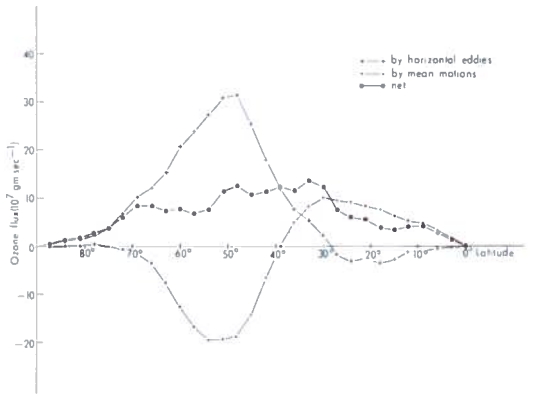

Figure 18. Meridional transport of ozone by horizontal eddies and mean motions and their net result at day 82. Units are 10^7 g sec^{-1}.

After 90 days and the model's simulated warming, at the 2-mb level, the polar-night vortex continued to weaken steadily and drift away southwestwards across Canada, and by day 100 it had completely disappeared. By that time, the upper high was situated close to the pole but was beginning to decline rather quickly. During days 100 to 110, the circulation was weak and ill-defined, but thereafter the polar-night vortex slowly began to reform. Figure 19 shows the 2-mb chart for day 130; although there is a well-marked circulation it is not nearly as intense as the pre-warming vortex. At other stratospheric levels, the circulation was also completely disrupted with a strong upper high over the pole. This high also gradually declined to leave a somewhat indefinite state. Recovery from this state was then extremely slow; at 20 mb, for instance, a well-defined vortex did not re-emerge until about day 160. The time scale of this reassertion of a more characteristic winter regime was much longer than in the real atmosphere. This facet of the model's behavior is somewhat disappointing (bearing in mind that this experiment was a perpetual January simulation), but not entirely unexpected in view of the crude long-wave radiation scheme employed.

ASSESSMENT OF RESULTS

It is encouraging that the first experiment with this tropospheric and stratospheric general-circulation model seems to have simulated an event closely resembling a stratospheric sudden warming. What actually triggered the sudden change in the model circulation, after a period of 30 days with little apparent change, is not yet really clear. However, it is one of the great advantages of a numerical simulation that all the data relating to a simulated event are available in a far more comprehensive and complete form than those for any observed phenomenon. Thus, in time, it should be possible to analyze the transformation of the circulation in considerable detail and to attempt to understand the mechanism of this simulated warming more clearly.

So far, it has been possible to carry out only a relatively superficial analysis, but even so some interesting features have emerged. For example, Figure 20 shows the vertical velocities at the top level of the model (about 1.5 mb) at 82 days. These vertical velocities have been smoothed zonally over a few points to eliminate small-scale roughness induced in the large-scale patterns by the topography. The residual patterns are clearly indicative of the dynamic nature of the phenomenon, with strong descent occurring in the region of warming and associated strong ascent downstream. Generally there is a broad area of descent in mid-latitudes and ascent in equatorial regions.

The essentially baroclinic nature of the circulation changes can be deduced from a study of Table 2, which gives values of energies and conversion terms in the top layer of the model (representing roughly 0 - 3 mb) during the warming period. The value of the baroclinic conversion term reached a maximum at day 80, coincident with rapid development of the warming. It is also evident from a study of values of the eddy kinetic energy that vertical advection of geopotential energy (i.e., the pressure interaction term), and that of eddy kinetic energy, were

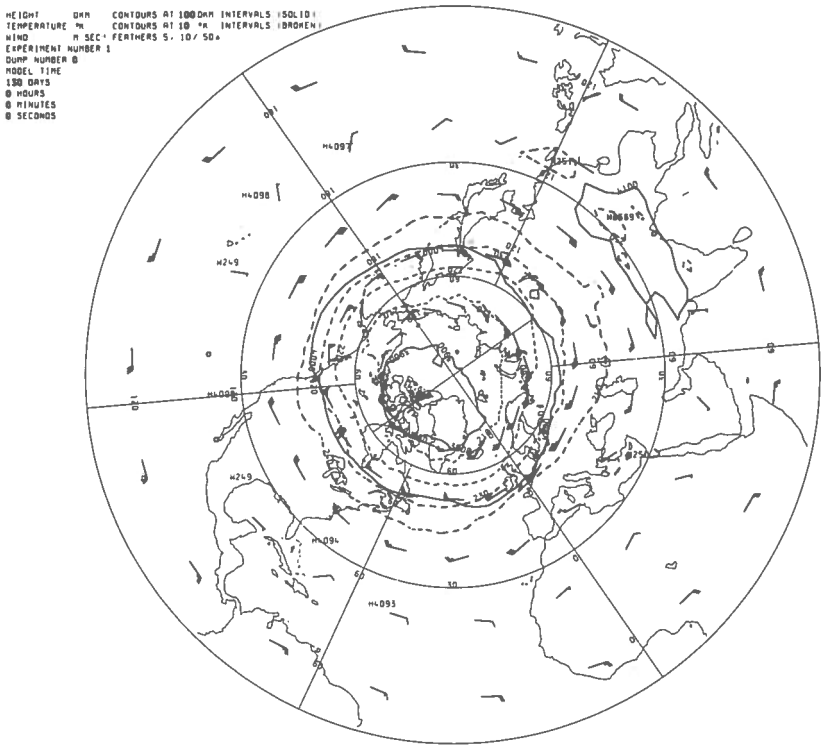

Figure 19. 2-mb chart for day 130.

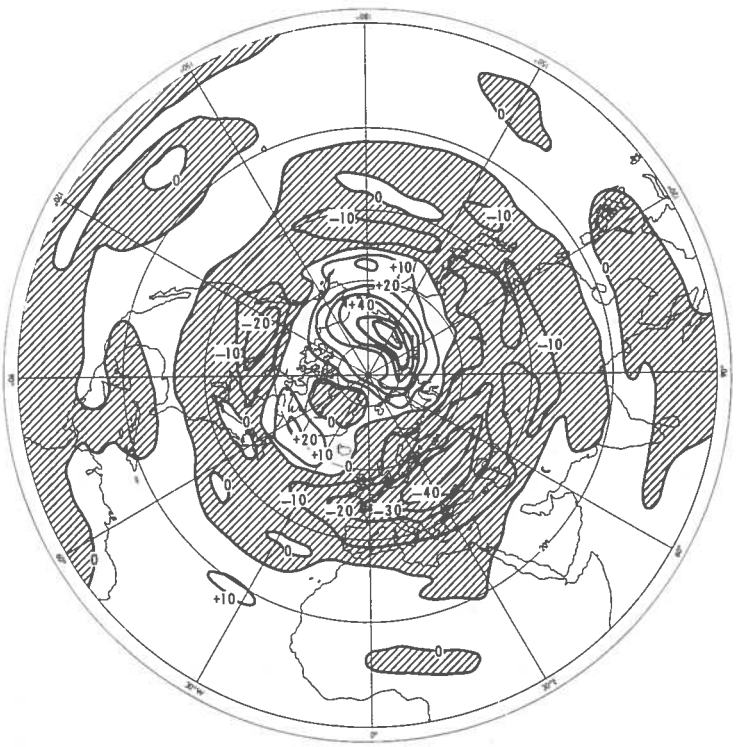

Figure 20. Vertical velocities in dekameters per hour at the top level of the model (about 44 km) at day 82. Hatching indicates areas of descent. Some smoothing has been applied to remove small-scale roughnesses.

Table 2. Energies and Conversion Terms for Top Layer of the Model Atmosphere (representing 0 - 3 mb) During Warming Sequence

Day	P_Z	$C(P_Z,P_E)$	P_E	$C(P_E,K_E)$	K_E	$C(K_Z,K_E)$	K_Z	$C(P_Z,K_Z)$
70	435	138	39	85	308	-245	1760	-85
71	433	156	63	43	378	-175	1716	-80
72	426	155	90	68	476	-258	1656	-103
73	414	269	102	165	572	-449	1614	-146
74	398	258	126	74	613	-460	1601	-134
75	391	215	145	117	593	-472	1638	-150
76	385	199	148	69	543	-431	1693	-139
77	395	242	156	80	458	-494	1757	-158
78	402	320	151	193	387	-598	1795	-230
79	363	430	175	250	561	-653	1643	-285
80	197	564	279	425	1072	-1158	1294	-363
81	53	449	316	264	1527	-1167	1016	-262
82	9	114	300	19	1840	-670	709	-58
83	83	-142	198	-403	1726	-101	467	96
84	92	-222	312	-132	1366	38	349	62
85	54	-145	259	-110	1239	-45	293	55
86	54	-154	213	-178	1027	-126	333	90
87	81	-216	193	-271	854	-50	359	121
88	58	-142	147	-25	703	-190	392	55
89	17	-2	108	-49	681	-36	353	5

P_Z = zonal available potential energy
P_E = eddy available potential energy
K_Z = zonal kinetic energy
K_E = eddy kinetic energy
Units of above terms are 10^{-3} J gm^{-1}

$C(P_Z,P_E)$ = conversion from P_Z to P_E
$C(P_E,K_E)$ = conversion from P_E to K_E (i.e., "baroclinic" conversion)
$C(K_Z,K_E)$ = conversion from K_Z to K_E (i.e., "barotropic" conversion)
$C(P_Z,K_Z)$ = conversion from P_Z to K_Z
Units of above terms are 10^{-3} J gm^{-1} • day^{-1}

fundamental source terms for the eddy kinetic energy of the model atmosphere at this level, and so almost certainly played a major role in the instigation of the warming.

Although a full study has not yet been made, some idea of the importance of the diagnosis of vertical interaction, particularly with relation to wavenumber, is indicated in Figure 21. This shows the time variation of the amplitude of wavenumber 2 in the geopotential field, analyzed zonally at 43.5°N. Lines of maximum and minimum amplitude have been indicated. In general, there were day-to-day variations and maxima and minima in the troposphere and stratosphere, as might be expected, but these variations seemed to be confined to a limited depth of the atmosphere. However, immediately before the warming event, there was a very strong maximum in amplitude of wavenumber 2 in the troposphere, which then seemed to spread

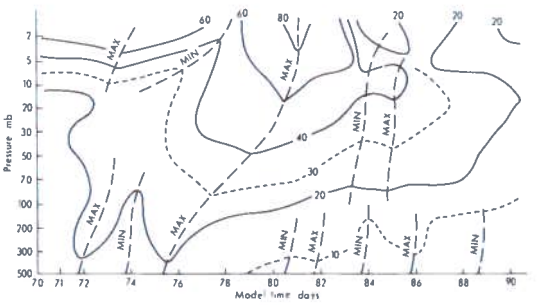

Figure 21. Amplitude of wavenumber 2 in the geopotential height field, analyzed zonally at 43.5°N, as a function of time and height. Trough/ridge lines are indicated. Units are dekameters.

up throughout the entire depth of the atmosphere. Evidently upward propagation of wavenumber 2 energy can be particularly important in affecting the stratospheric circulation, as other

authors have also concluded (e.g., Matsuno (1971)). On the other hand, there seemed to be little change in the troposphere during the model's warming sequence, although this point requires further detailed study too.

CONCLUSION

Only a fairly brief and superficial appraisal of this first experiment with a tropospheric and stratospheric circulation model has been possible. It should be emphasized that this model is a full general-circulation model predicting rainfall, eddy fluxes of heat and moisture, etc., and a complete diagnosis of its various facets is a major task. As yet, for example, the moisture budget has not been examined; like ozone, moisture in the stratosphere and its vertical flux through the tropopause are of great interest in the COMESA and CIAP studies. A more comprehensive analysis of the results of the experiment will thus have to be carried out. However, even from a superficial point of view, the results of this experiment seem to indicate a reasonable degree of success. The progress made so far encourages optimism concerning the results that should soon be available from the second version of the model, which is similar in approach but global in character. Even more comprehensive models are also planned.

ACKNOWLEDGMENTS

Acknowledgment is made to COMESA for the opportunity to carry out this work, to Dr. R.J. Murgatroyd for encouragement and advice, and to R. Smart for programming support.

REFERENCES

Corby, G.A., A. Gilchrist, and R.L. Newson (1972), "A general circulation model of the atmosphere suitable for long period integrations," Quart. J. Roy. Met. Soc. **98**, 809-832.

Dopplick, T.G. (1970), "Global radiative heating of the Earth's atmosphere," Massachusetts Institute of Technology, Dept. of Meteorology Planetary Circulation Project, Report No. 24.

Gilchrist, A., G.A. Corby, and R.L. Newson (1973), "A numerical experiment using a general circulation model of the atmosphere," Quart. J. Roy. Met. Soc. **99**, 2-34.

Kasahara, A. and W.M. Washington (1971), "General circulation experiments with a six-layer NCAR model, including orography, cloudiness and surface temperature calculations," J. Atmos. Sci. **28**, 657-701.

Kuhn, W.R. and J. London (1969), "Infrared radiative cooling in the middle atmosphere (30 - 110 km)," J. Atmos. Sci. **26**, 189-204.

Kurihara, Y. (1965), "Numerical integrations of the primitive equations on a spherical grid," Mon. Wea. Rev. **93**, 399-415.

Manabe, S. and B.G. Hunt (1968), "Experiments with a stratospheric general circulation model," Mon. Wea. Rev. **96**, 477-539.

Matsuno, T. (1971), "A dynamical model of the stratospheric sudden warming," J. Atmos. Sci. **28**, 1479-1494.

Murgatroyd, R.J. and R.M. Goody (1958), "Sources and sinks of radiative energy from 30 - 90 km," Quart. J. Roy. Met. Soc. **84**, 225-234.

Phillips, N.A. (1957), "A coordinate system having some special advantages for numerical forecasting," J. Met. **14**, 184-185.

Smagorinsky, J., S. Manabe, and J.L. Holloway, Jr. (1965), "Numerical results from a nine-level general circulation model of the atmosphere," Mon. Wea. Rev. **93**, 727-768.

DISCUSSION

(UNIDENTIFIED): Have you validated this model against real data?

NEWSON: Naturally I have compared the results with warmings in the real atmosphere; one can find warmings which are similar in evolution. Perhaps I should add that the warming in the model was probably far more intense than that observed in reality, since there were some changes of 60 or 70 degrees Kelvin in a day. This may not be very surprising, however, if one bears in mind the very cold stratospheric vortex from which the warming began.

(UNIDENTIFIED): Do you have any idea why you got a warming fairly easily, when other modeling groups have had a very hard time?

NEWSON: No, none at all. I just selected the model's horizontal and vertical resolution, together with the simple linear radiation scheme; the latter may hold the key. Perhaps in another year, when I have had time to study the results in detail, I'll be able to give you an answer.

LIMITATIONS OF CLIMATE MODELING

PETER H. STONE
Institute for Space Studies
NASA Goddard Space Flight Center
New York, New York

and

Department of Meteorology
Massachusetts Institute of Technology
Cambridge, Massachusetts

ABSTRACT: Climate changes over periods longer than a few years can be studied with current computers only by using one- or two-dimensional models of the ocean-atmosphere system. Recent progress in parameterizing eddy fluxes indicates that such models need not be at a disadvantage compared to general-circulation models in calculating zonal averages. The prime limitation on any model is its ability to parameterize radiation, clouds, moist convection, boundary-layer processes, and ocean transports. Lack of adequate physical models and observations of many of these processes makes climatic predictions using current parameterizations problematic at best. Even the best parameterizations depend on many phenomenological coefficients whose true variability is unknown.

INTRODUCTION

In principle, the behavior of the atmosphere-ocean system is governed by well-known conservation laws which can be expressed as a closed set of mathematical equations and boundary conditions. In practice, the equations are so complex and nonlinear that many compromises must be made if one is to obtain solutions in a finite time. In particular, all models include parameterizations of physical processes which cannot be calculated explicitly because of the limitations imposed by computer speed and capacity. A whole hierarchy of models has been developed, the choice depending on the time scale of the problem of interest. Descriptions of many of these models can be found in Volume 4 of the CIAP monograph series.*

The most sophisticated models are the three-dimensional general-circulation models. Even though these models currently parameterize boundary-layer processes, processes with horizontal scales $\lesssim 300$ km, and the effects of the oceans, they require about one hour of computer time to simulate one day of real time. Consequently they can be used only for investigating changes over periods up to a few years. Next in sophistication are the two-dimensional models, which generally treat the zonal-average state of the atmosphere-ocean system, and therefore have to parameterize eddy processes and topographic effects in addition to those processes parameterized by general-circulation models. These models require about 1 minute of computer time to simulate one day of real time, and can be used only for investigating changes over periods up to a few hundred years. The simplest models are the one-dimensional models, which treat explicitly only the vertical or meridional structure of the atmosphere-ocean system, and must parameterize either the meridional or vertical structure in addition to the other processes cited above. These models are simple enough that equilibrium solutions can be sought without explicit time integrations, and therefore are not limited to studying changes that occur on short time scales.

The ability of any of these models to simulate climate change depends on the adequacy of their parameterizations. This dependence will be lessened as computer technology improves, but it seems unlikely that it can be substantially reduced in the coming decade. In

* At present, these monographs exist only in an early draft form. They will be publicly available after their completion in September 1974.

the immediate future, progress in our ability to model climatic change is likely to proceed from progress in our understanding of the processes which have to be parameterized, and the resulting improvements in the parameterizations. To illustrate the current state of parameterizations and their limitations, we will discuss two particular processes that are important in determining climate – namely, clouds and eddy fluxes.

CLOUDS

Perhaps the most fundamental climatic variable is the global mean temperature. In order to predict the global mean temperature, it is necessary to predict the global albedo. The observed mean global albedo is 0.30 (Vonder Haar and Suomi, 1971), and about two-thirds of this is due to clouds. Consequently any climate model which does not calculate cloud cover cannot predict the most fundamental climatic parameters and must be treated with skepticism.

In fact, many of the models described in Volume 4 of the CIAP monograph series do not calculate cloud cover at all, but merely prescribe current mean values. It has been argued that changes in cloud cover have a negligible effect on climate, because the resulting changes in albedo and long-wave emission compensate for each other (Budyko, 1969). Schneider (1972) calculated the net effect, and found that an increase of 0.08 in cloud cover would lead to a 2K drop in the mean surface temperature. This drop is about one-fourth of what one would expect from the change in albedo alone, so there is a good deal of compensation by the long-wave emissions, but these changes are by no means negligible. More important, Schneider found that changes in cloud cover would cause local changes much larger than the mean changes, and even that the sign of the change was reversed in polar regions. In addition, Schneider showed that a decrease of 0.6 km in the mean cloud height would have as much impact on surface temperatures as an 0.08 increase in the fractional cloud cover. Clearly climate models must calculate cloud covers, heights, and albedos.

The most complex parameterization of clouds used in any of the models described in CIAP Monograph 4 is the one used in the model developed by the Goddard Institute for Space Studies (Somerville et al., 1974). This parameterization is an adaptation of one developed for the UCLA model (Arakawa et al., 1969). It distinguishes two basic cloud types, clouds caused by supersaturation and convective clouds. Supersaturation clouds occur when the relative humidity exceeds 100%, and convective clouds occur when the moist static energy at particular levels exceeds the saturated moist static energy at higher levels. Table 1 lists the properties of the various cloud types and sub-types included in the parameterization. The table gives the layers in which they occur (the model's nine layers are equally spaced in sigma coordinates and are numbered from 1 to 9 from top to bottom), the analogous atmospheric cloud type, the short-wave optical thickness, and the visual albedo. The optical thickness, τ, is specified a priori from observations of the analogous cloud types, and the albedos, a, are derived from an approximate

Table 1. Properties of Clouds in the GISS Model

Cloud Type	Layers	Analogy	Optical Thickness	Albedo
Supersaturation	2	Cirrus	1	0.12
Supersaturation	3	Cirrus	2	0.21
Supersaturation	4	Altostratus	4	0.34
Supersaturation	5 or 6	Altostratus	6	0.44
Supersaturation	7 or 8 or 9	Stratus	8	0.51
Penetrating convection	4-7 or 5-8 or 6-9	Cumulonimbus	32	0.81
Middle-level convection	5 or 6	Altocumulus	8	0.51
Low-level convection	7 or 8	Cumulus	16	0.68

formula based on scattering theory (Lacis and Hansen, 1974),

$$a = \frac{0.13\,\tau}{1 + 0.13\,\tau}$$

So far the most thorough test of this parameterization has been its use in a simulation of the January climatology (Somerville et al., 1974). Figure 1 shows a typical instantaneous picture of cloud cover in this simulation. It has a realistic distribution of cloud cover, with maxima in high latitudes and in the tropics, and minima in the subtropics. The global mean cloud cover was 0.52, and the global mean albedo 0.32, in good agreement with the observed mean values of 0.53 (Sasamori et al., 1972) and 0.31 (Vonder Haar and Suomi, 1971), respectively, for December through February. Figure 2 shows a typical instantaneous picture of the cumulus cloud cover. The convective clouds dominate in low latitudes and the supersaturation clouds dominate in high latitudes, as in the real atmosphere. There is more convective activity in the summer hemisphere and over land, and the most vigorous kind of convection, penetrating cumulus clouds, is sharply peaked in subsolar latitudes. The global cumulus cloud cover is 0.13, a realistic value (Sasamori et al., 1972).

The above results show that current parameterizations of cloud cover can reproduce the most important properties of observed clouds, without these properties' being explicitly specified. What we don't know is whether parameterizations like the above one can predict the correct changes in cloud properties for studies of climate. Many of the important properties are implicitly specified by phenomenological coefficients. For example, the global albedo depends on the optical thicknesses specified for individual cloud types (Table 1). If a sufficient variety of cloud types is included, there is a good deal of scope for changes in global albedo under different climatic conditions, but we don't know whether the optical thicknesses of individual cloud types would themselves change in response to changes in climate. To allow for such possibilities more cloud physics will have to be brought into the parameterizations.

The cloud properties are also strongly influenced by less obvious parameters. For example, the parameterization for mixing of heat and moisture by cumulus clouds in the GISS model involves a relaxation time for the mixing, specified to be one-half hour (Somerville et al., 1974). Although this is a realistic value, it is an important constraint on the cloud properties. Experiments at GISS have shown that doubling this relaxation time doubles the cumulus cloud cover and decreases the global cloud cover by about 0.10. We very much need good models of moist convection which will tell us what factors determine parameters like the relaxation time, so that we can include their variations in climate models.

Another limitation on cloud parameterizations is numerical: moist models have a vertical resolution on the order of 3 km in mid-troposphere. Yet Schneider's calculations showed that changes in cloud height on the order of 1/2 km have a significant effect on ground temperatures. Improved computers or parameterizations will be necessary to include effects like this.

Perhaps the best way we can check the validity of any parameterization is to apply it to seasonal changes. Seasonal changes are really just climate changes on a short time scale, and any parameterization must predict them accurately if it is to be acceptable for use in climate models. The GISS parameterization of clouds has not yet been tested in this way. A similar test of a different parameterization was reported by Schneider and Washington at the AMS Conference on numerical prediction in Monterey in October 1973. They varied the sea-surface temperature in the NCAR general-circulation model to determine the model's response. They found that there was a positive feedback between sea-surface temperature and cloud cover in the NCAR model – i.e., increased sea-surface temperature led to a decrease in cloud cover, which would cause the sea-surface temperature to increase even further. This positive feedback is apparently caused by the close correlation of relative humidity and cloud cover in the NCAR parameterization of clouds (Kasahara and Washington, 1971). However, it appears to contradict observed seasonal changes, which show an increased cloud cover in summer (Sasamori et al., 1972).

We must also be alert to the possibility that our parameterizations do not include all the

Figure 1. Typical distribution of clouds. An "O" indicates the presence of a cloud at at least one level above each location. (From Somerville et al., 1974.)

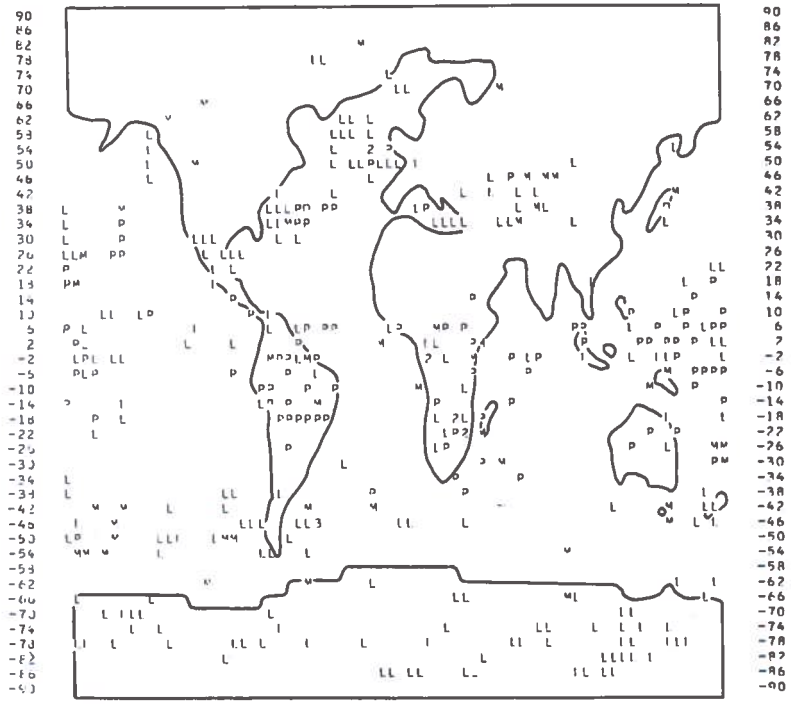

Figure 2. Typical distribution of cumulus clouds. L indicates low-level cumulus clouds, M middle-level cumulus clouds, P penetrating cumulus clouds, and 2 low-level and penetrating cumulus clouds simultaneously. (From Somerville et al., 1974.)

important physical processes. For example, a recent calculation by Holton and Colton (1972) demonstrates that we do not yet understand even the simplest properties of the tropical circulations. They showed that the observed tropical circulations can be explained only by invoking an apparent drag at the 200-mb level in low latitudes. They speculated that this drag is caused by detrainment from the tops of deep cumulus clouds, which would lead to strong momentum mixing in low latitudes. Such momentum mixing by cumulus convection is not included in any of the models described in the CIAP monograph.

EDDY FLUXES

Since studies of climate changes over periods longer than a few years must rely in the near future on two- and one-dimensional models, it is essential that adequate parameterizations of the eddy fluxes be developed. Progress has been made in recent years, and within a few years we may have parameterizations of the eddy fluxes adequate for climate studies. Green (1970), using quasi-geostrophic and mixing-length theory has shown how the eddy fluxes of any conservative quantity and the meridional eddy flux of momentum can be calculated from the meridional eddy flux of sensible heat. Leovy (1973) has shown how the eddy fluxes of latent heat can be related to this same flux. Thus, the meridional eddy flux of sensible heat is the key flux – once it is known, virtually all of the important eddy fluxes can be calculated from it.

Current parameterizations of the eddy flux of sensible heat are based on the theory of baroclinic stability and scaling analysis (Green, 1970; Stone, 1972, 1974). The status of these parameterizations is illustrated by Figure 3, which shows the total meridional eddy flux of sensible heat in the troposphere in January. The solid line is the flux calculated from a parameterization which involves no phenomenological coefficients, and which used as input only the observed mean state of the atmosphere in January (Stone, 1974). The observed fluxes are indicated by x's. Comparison shows one notable discrepancy: the equatorward displacement of the maximum in the calculated flux. However, the cause of this displacement is not hard to find. The derivation of the parameterization does not

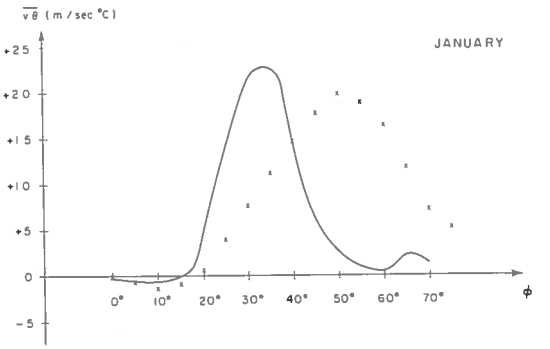

Figure 3. Meridional eddy flux of sensible heat in the troposphere vs. latitude for January. X's are observed values. (From Stone, 1974.)

allow for curvature effects, and the convergence of the meridians would shift this maximum poleward. In principle, this defect should not be hard to correct. The successful features of the parameterization are obvious: it correctly reproduces the sign and magnitude of the observed flux. The parameterization's success on this score is compared in Table 2 with that of some of the major general-circulation models' simulations of January climatology. The parameterization does as well as the models.

Table 2. Maximum Value of the Meridional Eddy Flux of Sensible Heat as Observed, and as Calculated for January by General-Circulation Models

Model	Relative Value
Observed	1.0 ±0.1
Geophysical Fluid Dynamics Laboratory	0.9
Goddard Institute for Space Studies	0.7
National Center for Atmospheric Research	0.7
Eq. (5.19) from Stone (1974)	1.1

Two other tests of this parameterization have been made which go a long way towards establishing its viability for climate models. The first is its successful simulation of seasonal changes. The parameterization correctly predicts a decrease in the northern-hemisphere eddy flux

from January to July by a factor of 5 (Stone, 1974). Rather surprisingly, no simulations of July climatology by general-circulation models have been published yet, so we don't know how they compare on this score.

The second test is an application of the same parameterization of the eddy fluxes to an analysis of the Martian atmosphere. Although we don't have any actual measurements of eddy fluxes on Mars, Mariner 9 has yielded good measurements of the temperature structure, and this structure is very dependent on the eddy fluxes. The adiabatic lapse rate for the Martian atmosphere is 4.9K/km and the mean tropospheric lapse rate measured by Mariner 9 is 2.3K/km (Kliore et al., 1974). These values imply a static stability of 2.6K/km. The static stability predicted using the eddy parameterization is $\approx$ 2K/km (Stone, 1972). This agreement is significant in view of the substantial differences between the terrestrial and Martian atmospheres – e.g., differences in solar constant, atmospheric pressures, composition, gravity, planetary scale, etc.

SUMMARY

The capacity of present computers forces us to rely on two- and one-dimensional models if we are interested in simulating climate changes over periods longer than a few years. Progress in parameterizing the eddy fluxes indicates that, once curvature effects are included, these models need not be at a disadvantage compared to general-circulation models for calculating zonal averages. Rather, the prime limitations on these models are likely to be the same as the limitations on the three-dimensional models, i.e., our ability to parameterize clouds, moist convection, radiation, boundary-layer transports, and ocean transports.

Unfortunately, even the best current parameterizations are strongly dependent on phenomenological coefficients whose true variability is unknown. To improve our parameterizations for climate models we need to develop better physical theories which will enable us to predict "constants" such as the relaxation time for moist convection. Alternatively, observations of seasonal changes and of other planetary atmospheres may provide means of determining empirically the variability of these "constants". Until we have developed reliable methods for calculating fundamental parameters such as cloud cover and sea-surface temperature, the predictions of our climate models will be at best problematical.

REFERENCES

Arakawa, A., A. Katayama, and Y. Mintz (1969), "Numerical simulation of the general circulation of the atmosphere," Proc. WMO/IUGG Symp. NWP, Tokyo, IV-7-IV8-12.

Budyko, M.I. (1969), "The effect of solar radiation variations on the climate of the Earth," Tellus **21**, 611-619.

Green, J.S.A. (1970), "Transfer properties of the large-scale eddies and the general circulation of the atmosphere," Quart. J. Roy. Meteor. Soc. **96**, 157-185.

Holton, J.R., and D.E. Colton (1972), "A diagnostic study of the vorticity balance at 200 mb in the tropics during the northern summer," J. Atmos. Sci. **29**, 1124-1128.

Kasahara, A., and W.M. Washington (1971), "General circulation experiments with a six-layer NCAR model, including orography, cloudiness and surface temperature calculations," J. Atmos. Sci. **28**, 657-701.

Kliore, A.J., G. Fjeldbo, B.L. Seidel, M.J. Sykes, and P.M. Woiceshyn (1973), "S band radio occultation measurements of the atmosphere and topography of Mars with Mariner 9," J. Geophys. Res. **78**, 4331-4351.

Lacis, A.A., and J.E. Hansen (1974), "A parameterization for the absorption of solar radiation in the Earth's atmosphere," J. Atmos. Sci. **31**, 118-133.

Leovy, C.B. (1973), "Exchange of water vapor between the atmosphere and surface of Mars," Icarus **18**, 120-125.

Sasamori, T., J. London, and D.V. Hoyt (1972), "Radiation budget of the southern hemisphere," Meteor. Mono. **13**, 9-23.

Schneider, S.H. (1972), "Cloudiness as a global climatic feedback mechanism," J. Atmos. Sci. **29**, 1413-1422.

Somerville, R.C.J., P.H. Stone, M. Halem, J.E. Hansen, J.S. Hogan, L.M. Druyan, G. Russell, A.A. Lacis, W.J. Quirk, and J. Tenenbaum (1974), "The GISS model of the global atmosphere," J. Atmos. Sci. **31**, 84-117.

Stone, P.H. (1972), "A simplified radiative-dynamical model for the static stability of rotating atmospheres," J. Atmos. Sci. **29**, 405-418.

Stone, P.H. (1974), "The meridional variation of the eddy heat fluxes by baroclinic waves and their parameterization," J. Atmos. Sci. **31**, 444-456.

Vonder Haar, T.H., and V.E. Suomi (1971), "Measurements of the earth's radiation budget from satellites during a five-year period," J. Atmos. Sci. **28**, 305-314.

DISCUSSION

LONDON: You pointed out that Schneider's cloud forecast was the opposite of what one would normally expect in the relationship between surface heating and clouds. I think his model uses an assumption of convective adjustment which almost guarantees that this will happen, due to the relative-humidity link. Such a parameterization needs to be tested against various types of models, since cloud forecasting is a very important part of modeling.

P. STONE: I quite agree. One of the interesting differences between the NCAR and Goddard parameterizations is that we have an Arakawa-type parameterization for convective clouds, so we may not have that problem. It would be very interesting, though, to repeat that sensitivity study for our model.

PLANT RESPONSE TO ELEVATED UV INTENSITIES

M.M. CALDWELL, W.F. CAMPBELL, AND W.B. SISSON
Utah State University
Logan, Utah

ABSTRACT: Field and laboratory experiments were designed to test the response of plants to elevated intensities of global UV-B radiation, such as those which might occur if the amount of stratospheric ozone were reduced. Filter/lamp systems for supplementation of current solar ultraviolet irradiation under field conditions and for simulation of solar ultraviolet radiation under laboratory conditions are described. The growth, development, and productivity of agricultural and native plant species were tested under these enhanced ultraviolet radiation regimes. Under greenhouse conditions, UV supplementation caused significant inhibition of plant growth. Under field conditions, where one finds higher levels of longer-wavelength radiation which might be active in photoreactivation, profound changes in plant growth and productivity were not evidenced. However, under these field conditions more subtle yet important physiological processes were altered. Mutation rates of stamen hairs on a special test line of *Tradescantia* were significantly enhanced by the higher-ultraviolet-radiation regime. Also, ultrastructrual modification of chloroplast membranes (as shown by electron microscopy) was also apparent in soybean leaves exposed to the enhanced UV radiation in the field.

The key question for CIAP is whether or not organisms, including man, can tolerate or repair damage caused by intensities of UV radiation greater than those which currently exist in the normal habitats of these organisms. For higher plants, it appears that the capacity for tolerance and repair of damage caused by ultraviolet radiation at current-day levels may be sufficient in some species to resist the enhanced ultraviolet-radiation regime which would occur with stratospheric ozone depletion. However, through subtle though extremely important physiological alterations, other plants may be damaged by increased ultraviolet-radiation intensities.

INTRODUCTION

To provide experimental evidence germane to the CIAP-posed question of biological response to the elevated ultraviolet-radiation intensities which would occur with stratospheric-ozone depletion, it is necessary to subject organisms to an experimentally enhanced UV-radiation regime. It is apparent that most plants possess natural defense mechanisms to minimize the UV radiation insult under present-day intensities. Absorption of UV radiation in epidermal waxes and cellular compounds, such as flavonoids, reduces the intensities striking sensitive molecular targets (chromatophores). Also, enzymatic repair mechanisms such as photoreactivation seem to be prevalent in many higher plant species (Caldwell, 1971). Therefore, the key question for CIAP is whether or not the absorption and repair capacity of higher plants can tolerate the increased ultraviolet-radiation intensities which would occur if ozone in the stratosphere were depleted. This key question has been addressed in a consideration of higher-plant response in studies at Utah State University.

In a parametric approach to this hypothetical situation, an upper limit of 50% destruction of the total atmospheric ozone column has been assumed, and this upper-limit level has been used in the first series of experiments.

LAMP AND FILTER SYSTEMS FOR UV-RADIATION SIMULATIONS

Because those UV-radiation wavelengths absorbed by ozone within the waveband commonly denoted as UV-B (280-320 nm) are also very effectively absorbed by proteins and nucleic acids, which are important and sensitive components of all living tissues, a careful evaluation of the spectral-irradiance changes of UV-B radiation must be considered in any simulation of an altered terrestrial solar spectrum (Caldwell, 1971, 1973). These considerations were taken into account in devising lamp and filter combinations which would be suitable for studies under CIAP.

Sixty plastic-film products were surveyed as possible candidates for sharp cutoff filters to be used with Westinghouse FS-40 fluorescent lamps

in solar supplementation experiments and with 6000-watt xenon arc lamps in solar-simulation irradiations in controlled environment chambers. Plastic films were chosen because of their low cost and flexibility in field applications.

For ultraviolet supplementation designed to simulate a 50% reduction in stratospheric ozone, the distributions represented in Figure 1 were sought. Assuming an initial ozone concentration of 0.320 atm-cm, which is representative of July concentrations at latitude 40°N, the UV spectrum which is necessary to simulate a global UV spectrum at 0.16 atm-cm ozone is shown in Figure 1. These curves are based upon the calculations of Dr. A.E.S. Green at the University of Florida, which are in turn tied to the measurements of Bener (1973). Using this UV-supplement curve, filters were surveyed; the best-fit filter for the FS-40 lamp was found to be "Kodacel" 5-mil (0.13-mm) plastic film. Figure 2

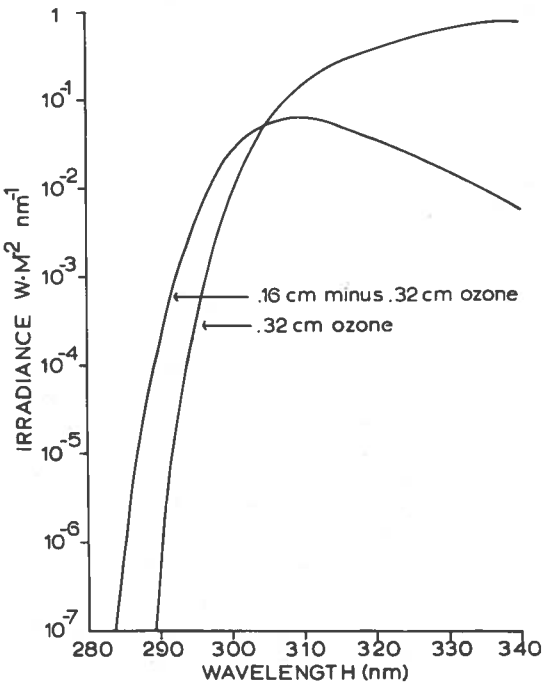

Figure 1. Spectral distribution of global UV radiation for 0.32 atm-cm ozone at a solar altitude of 75°, and the spectral distribution of radiation necessary to supplement the above distribution to simulate the global UV irradiance for 0.16 atm-cm ozone. From formulations of A.E.S. Green et al. (1974). This supplementation curve applies generally for a range of solar altitudes from 40° to 80°.

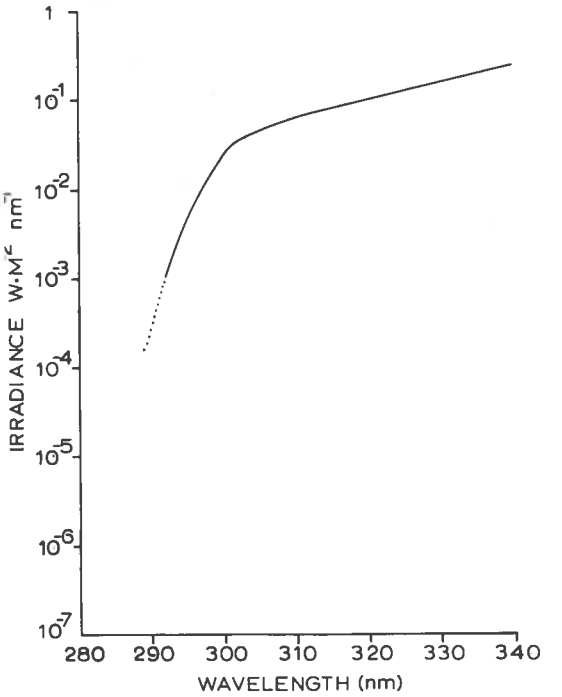

Figure 2. Spectral irradiance of two Westinghouse FS-40 lamps filtered with Kodacel 5-mil (0.13-mm) plastic film in the configuration illustrated in Figure 3. Measurements carried out in absence of solar radiation with a Gamma Scientific Co. spectroradiometer.

shows the irradiance resulting from the combination of this plastic film with two FS-40 lamps in the configuration illustrated in Figure 3. These measurements, taken with a Gamma Scientific Company spectroradiometer in the laboratory, fit remarkably well the desired supplement curve represented in Figure 1. The dotted line on the logarithmic plot in Figure 2 represents an extension of the measurements to an order of magnitude at which scattering normally interferes with detection. Spectroradiometric measurements taken under field conditions for the configuration shown in Figure 3, in both a UV-supplemented plot and in an adjacent plot in the open, are shown in Figure 4. These measurements were taken on a clear day at a solar angle of 48°.

In order to serve as a control for such experiments, it was deemed necessary to have a similar lamp system with filters which would exclude most of the UV-B portion of the spectrum. In this manner any temperature or other microenvironmental effects exerted by the

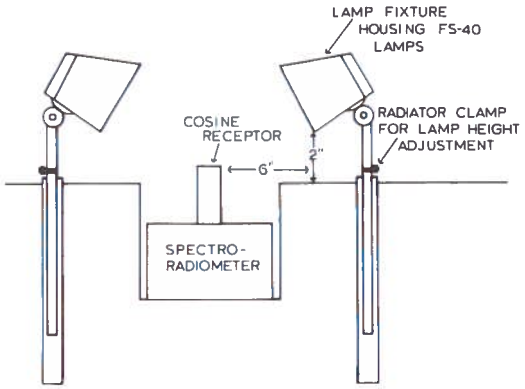

Figure 3. End view of FS-40 fluorescent-lamp configuration used in field solar-UV supplementation experiments. A row of plants replaces the spectroradiometer, with the top of the plant canopy located in the position of the cosine receptor. Lamps are elevated as plants grow.

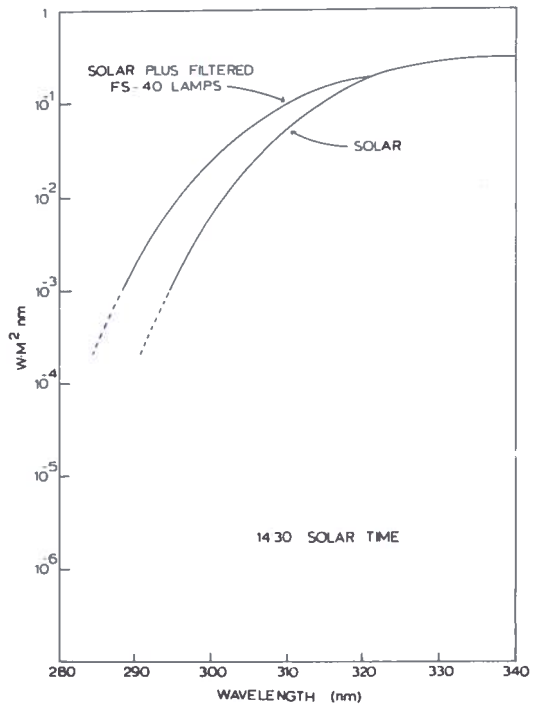

Figure 4. Spectroradiometric measurements of global UV radiation at a solar altitude of 48° in the field, and similar measurements of global UV radiation supplemented by two FS-40 fluorescent lamps filtered with Kodacel plastic in the configuration illustrated in Figure 3.

lamps on the plants, or effects resulting from mercury-vapor emission bands at wavelengths longer than 320 nm (such as 365 nm), would be taken into account. A suitable control system was simulated with the same configuration of lamps as indicated in Figure 3, but with a 10-mil (0.25-mm) "Mylar" type A plastic film. The spectral distribution of this filter/lamp combination is shown in Figure 5.

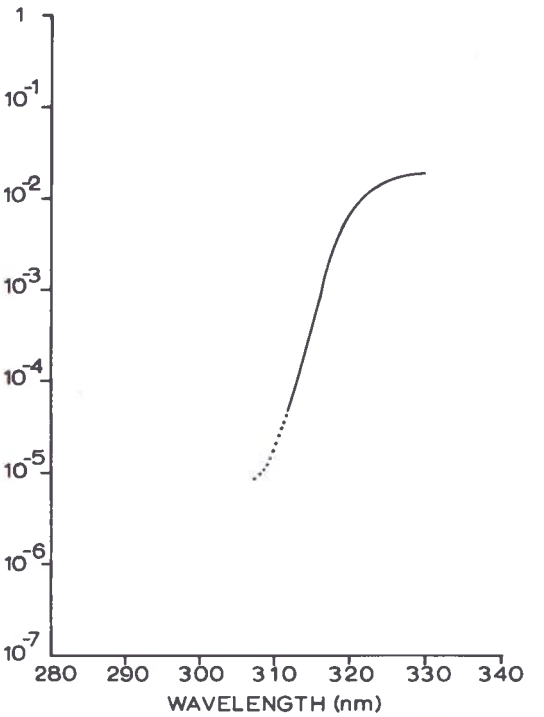

Figure 5. Spectral irradiance of two FS-40 lamps filtered with Mylar type A plastic film (10-mil, 0.25-mm) in the configuration illustrated in Figure 3. Measurements carried out in the absence of solar radiation with a Gamma Scientific Co. spectroradiometer.

In the solar-simulation experiments which used controlled environmental chambers with 6000-watt xenon lamps, similar plastic-film filters were found to be initially successful. For simulation of midday solar irradiation in the month of July at 40°N latitude with an 0.32 atm-cm ozone concentration, the filter/lamp combination shown in Figure 6 was found to be satisfactory. The filter in this case was two sheets of 10-mil (0.25-mm) cellulose acetate. For a solar-ultraviolet radiation regime with a 50% reduction in ozone (0.16 atm-cm), the combination represented in Figure 7 was used. The filter

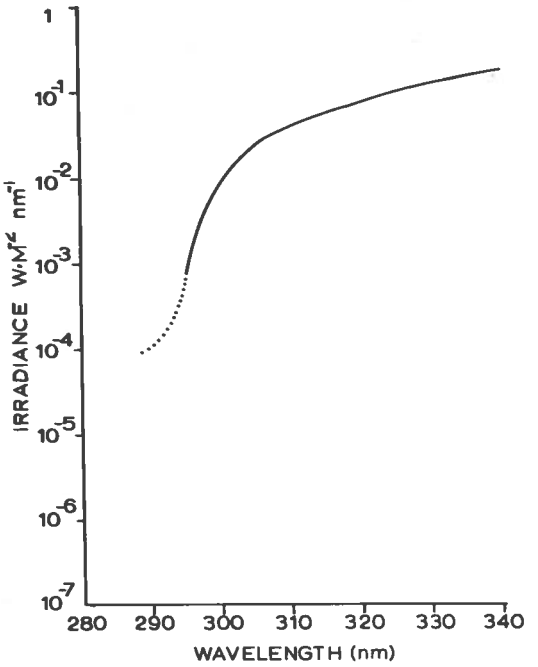

Figure 6. Spectral irradiance of 6000-watt xenon arc lamp filtered with two sheets of 10-mil (0.25-mm) cellulose acetate film measured at 58 cm from the arc. Filter configuration is illustrated in Figure 8.

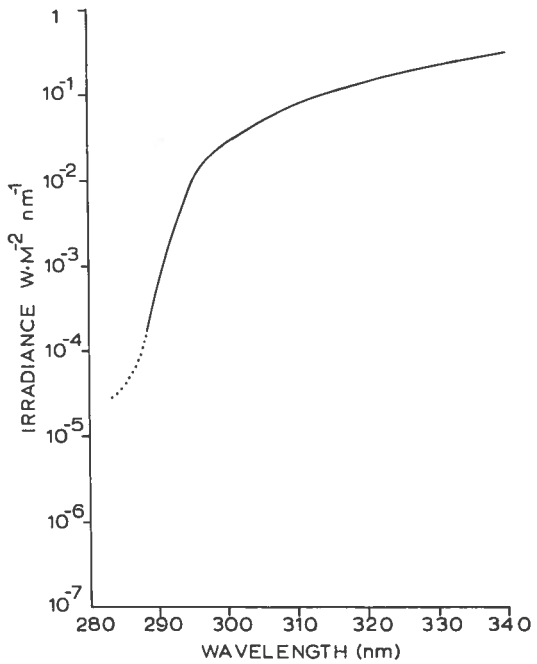

Figure 7. Spectral irradiance of 6000-watt xenon arc lamp filtered with one sheet of 10-mil (0.25-mm) Kodacel plastic film measured at 58 cm from the arc. Filter configuration is illustrated in Figure 8.

employed in this case was 10-mil (0.25-mm) Kodacel, used with the xenon lamp.

In each case, the xenon lamp with quartz filters was surrounded by a "Vycor" cylindrical filter, which absorbs radiation at wavelengths shorter than 250 nm. Nitrogen gas is passed through this cylindrical Vycor filter to prevent ozone formation within the cylinder (see Figure 8). Surrounding the entire assembly is a semi-cylindrical piece of plastic-film filter to provide the desired spectral irradiance to the plant bed below. Unfortunately, the combination of the xenon lamps' intense ultraviolet-radiation output and exceedingly high temperatures cause the plastic films to solarize extremely quickly, and they can be used for only a two-hour period. The lower ultraviolet-radiation intensities and cooler temperatures of the FS-40 lamps present less of a problem, and filters can be used for 30 to 40 hours under present field conditions.

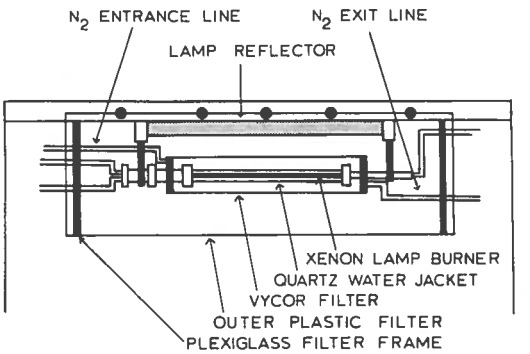

Figure 8. Filter assembly used for 6000-watt xenon arc lamps.

Because of this photochemical-degradation problem, a new filter assemblage for use with Schott Co. glass filters is currently under development.

GROWTH AND MORPHOLOGY: FIELD EXPERIMENTS

The field experiments were designed at Utah State University to simulate the UV-B irradiation regime that would result from a 50% depletion in atmospheric ozone (using 0.32 atm-cm as a base level of ozone for Utah in the summer months).

Because of the low intensity output of these filter/lamp systems, it was not possible to irradiate large areas of vegetal canopies. Therefore,

experiments were concentrated in row-crop situations dealing primarily with the earlier life stages of growth. (However, some plant species were allowed to complete a full growth cycle.) Two sets of experiments were carried out during the course of the 1973 field season, each in a randomized block design. The species used were selected according to their importance as western agricultural crops, and also in part because of known sensitivities to ultraviolet radiation at 254 nm from earlier research (Cline and Salisbury, 1966). Soil nutrient levels and moisture contents were optimized as much as possible for the plant species concerned. Detailed plant-organ measurements were taken at approximately 10-day intervals, and biomass determinations at the end of the experiment were also collected.* Analysis of variance was performed on these data, using as parameters either plant organ dimensions at particular times of the season or relative growth rates, i.e., growth rate per unit size of the organ in question per unit time.

In general, there were no drastic depressions of total dry-weight yield and growth rates, or consistent morphological alterations. There were occasional statistically significant differences between plants exposed to the enhanced UV-B radiation environment and those exposed to a similar control situation (with lamps to provide a comparable alteration of other aspects of the microenvironment apart from UV-B radiation) in these field experiments. The biological meaningfulness of these occasional instances of statistical difference is questionable. Considerable variability in plant size and growth rates was very prominent in these field experiments. This was a reflection of differences in germination time and natural variability in plant vigor among individuals within species groups. This variability, combined with the random appearance of these instances of statistical significance, would warrant considerable caution in attaching much biological significance to these first-season data.

Additional field experiments are being undertaken during the summer of 1974.

* Detailed tabular values of these morphological data are contained in Volume V of the CIAP Monograph Series.

GROWTH AND MORPHOLOGY: GREENHOUSE EXPERIMENTS

Similar growth studies were conducted in November and December 1973 using the same lamp/filter systems employed in the field experiments under greenhouse conditions. These experiments were carried out using tomato (*Lycopersicon esculentum* var. Ponderosa) and a variety of nonagricultural species which grow primarily in exposed habitats in rangelands of the intermountain area.

Under greenhouse conditions, solar UV-B radiation was removed by filtration through the glass. Therefore, the plants were exposed to the UV-B radiation environment depicted in Figure 2 and a control situation with similar lamps filtered to remove UV-B radiation (see Figure 5). Total solar radiation of longer wavelengths was less intense at this time of year, and also partially attenuated in the glasshouse.

The uniformity of plant materials used in these trials, however, was much greater than under field conditions.

In these trials, plant growth rates and morphology were clearly altered by the enhanced UV-B radiation regime. There was considerable species variability in susceptibility to this UV-B radiation exposure. However, in all cases of significant differences there was clearly a depression of relative growth rates by the UV-B radiation. Leaf size was also reduced in most situations. Examples of these effects are shown in Tables 1, 2, and 3.

The pronounced efficacy of UV-B radiation in depressing plant growth under glasshouse conditions, as opposed to the results for field plants, is probably linked at least in part to the lower total solar-radiation intensities in the glasshouse. The potential role of increased photorepair activity in the field as opposed to the glasshouse situation is currently being investigated.

ULTRASTRUCTURE OF LEAF MESOPHYLL CELLS

From soybeans (*Glycine max* cv Hark) growing in the field experiments described in an earlier section, leaf samples were taken to

Table 1. Relative Growth Rates of Non-Agricultural Plant Species Exposed to Enhanced UV-B Radiation Under Greenhouse Conditions

Species	Relative Growth Parameter	Relative Growth Rate (mm mm^{-1} day^{-1}) UV-Irradiated	Control	F ratio
Apocynum pumilum	total height (days 19-38)	0.014	0.028	21.2**
	(days 8-26)	0.010	0.028	11.7*
Aquilegia caerulea	total height (days 8-26)	0.011	0.010	0.04
Aster intergrifolius	total height (days 19-38)	0.032	0.027	0.80
Geum macrophyllum	total height (days 8-26)	0.033	0.053	34.2**
	(days 19-38)	0.027	0.022	1.6
Lepidium perfoliatum	total height (days 19-38)	0.043	0.031	0.88
Melilotus alba	total height (days 19-38)	0.016	0.014	0.85
Potentilla glandulosa	total height (days 19-38)	0.029	0.033	0.12

* Significantly different at 95% probability level
** Significantly different at 99% probability level

Table 2. Relative Growth Rate of Tomato Plants Exposed to Enhanced UV-B Radiation Under Greenhouse Conditions

Relative Growth Parameter	Relative Growth Rate (mm mm^{-1} day^{-1}) UV-Irradiated	Control	F-ratio
Total height (days 5-12)	0.136	0.141	0.42
Total height (days 5-19)	0.088	0.101	10.63*
Total height (days 12-19)	0.040	0.063	10.07*

* Significantly different at the 99% probability level.

Table 3. Biomass of Tomato-Plant Parts Following Chronic Daily Exposure to Enhanced UV-B Irradiation Under Greenhouse Conditions

Plant Organ	Mean Dry Weight Per Plant (grams) UV-Irradiated	Control	F ratio
Leaves	266.8	320.3	0.44
Stems	95.1	159.4	3.00
Roots	41.7	80.9	5.15*

* Significantly different at the 95% probability level.

observe possible UV-B radiation-induced alterations at the ultrastructural level.

Leaf mesophyll samples were harvested after 28, 56, or 112 hours of exposure in the various irradiation treatments. Samples were preserved by standard electron-microscopic techniques. Thin sections were cut with glass or diamond knives on a MT-2 Porter-Blum ultramicrotome. Sections were stained for 12 minutes at 60°C in aqueous uranyl acetate and counter-stained with lead citrate for 5 minutes at 25°C. Samples were examined with a Zeiss EM-9S-2A or JEM 100B electron microscope and significant observations recorded photographically.

Electron micrographs of mesophyll cells from non-treated control soybean leaves exhibited normal organellar structure arranged peripherally within the cells. A large central vacuole, which was bounded by a single membrane, the tonoplast, constituted the major volume of the cell. The plasmalemma appeared as a continuous thin line and was closely appressed to the cell wall.

Chloroplasts were the most conspicuous organelle in the mesophyll cells. They contained a well-organized grana-lamellae system distributed evenly within a homogeneously electron-dense proteinaceous matrix – the stroma. Starch grains of various number, size, and electron density were also present in the stroma of most chloroplasts.

The double-membranous mitochondria were variable in shape and size, usually globular, ellipsoidal, or somewhat elongated. The interior cristae were formed generally by the infolding of the inner membrane, and lay within a moderately electron-dense matrix, presumably proteinaceous in nature.

A nucleus with the double membrane envelopes was often seen in mesophyll cells. The nuclear envelope was discontinuous and broken at irregular intervals by nuclear pores. The nuclear pores generally occupied about 5 to 10% of the nuclear surface and are thought to be the sites of the nuclear-cytoplasmic communication. The nucleolus was embedded in the fibrillar nucleoplasm without a membrane around it. It was usually seen as an aggregate of numerous fibrillar and granular components. In the cytoplasm, rough endoplasmic reticulum (RER) and dictyosomes were not abundant, but were easily detected. The dense ribosome population appeared mostly as free forms.

Cells from plants grown under lamps fitted with the Mylar filters (control with lamps) exhibited no detectable changes from those of the non-treated controls (Figure 9a). Also, the chloroplasts appeared slightly misshapen. However, many mesophyll cells from plants exposed to unfiltered UV radiation from a FS-40 lamp (which exceeds the simulated 50% ozone depletion) exhibited a considerable amount of vesiculation (presumably arising from disruption of the tonoplast), an increased amount of RER, or both (Figure 9b). From leaves under the Kodacel-filtered lamps (UV-B enhancement treatment to simulate 50% ozone depletion), there was a slight aggregation of the plastoglobuli within some choloroplasts (Figure 9c).

The various types of severe cellular damage observed in some cells in both the unfiltered and the Kodacel-filtered lamp treatments are shown in Figure 10. Cells exhibiting these responses could be seen at all sampling times. The amount of injury or the number of cells showing injury did not seem to increase with increased exposure time. An increased amount of RER and an aggregation of the plastoglobuli within the chloroplast are noted in Figure 10a. An increased amount of RER is also noted in Figure 10b; however, this cell has sustained more damage and most of the RER has swollen and formed vesicles. Also, the mitochondria have been damaged. In some cells most of the chloroplasts were totally disrupted, while adjacent cells showed partial to no disruption (Figure 10c). The mitochondria as well as other organelles of the cytoplasm in these cells were also severely damaged. These severe ultrastructural alterations were never found in any samples taken from plants exposed to the Mylar-filtered lamps in the control plots.

In any biological system, concomitantly with growth there will be a certain amount of degradation of organelles. Moreover, a certain amount of disruption of normal organellar structure may be attributed to the harsh treatment of preparative procedures for electron microscopy. The recorded alterations also may have developed secondarily as a result of the UV treatments if the radiation rendered the membranes more susceptible to fixation damage. Furthermore, many of the modifications attributed to UV radiation are known to be produced by mechanical injury (Mollenhauer et al., 1960).

Although statistical analyses were not practical at this time, we feel that the injury noted can be attributed to UV radiation. The degenerative changes observed in the chloroplasts of UV-treated leaves are reminiscent of senescent changes reported in Elodea (Ikeda and Ueda, 1964), in wheat (Shaw and Manocha, 1965) and bean (Barton, 1966) leaves, and in cucumber cotyledons (Butler, 1967). Our studies have indicated that UV radiation enhances the senescent process in some cells, probably by altering membrane permeability, which subsequently leads to altered osmotic potentials. Moreover, since the plant cell vacuole contains a number of hydrolytic enzymes, including proteases, nucleases, phosphatases, and esterases, the continued breakdown of cellular components of the more severely damaged cells could therefore be due partly to the release of these enzymes after rupture of the tonoplast.

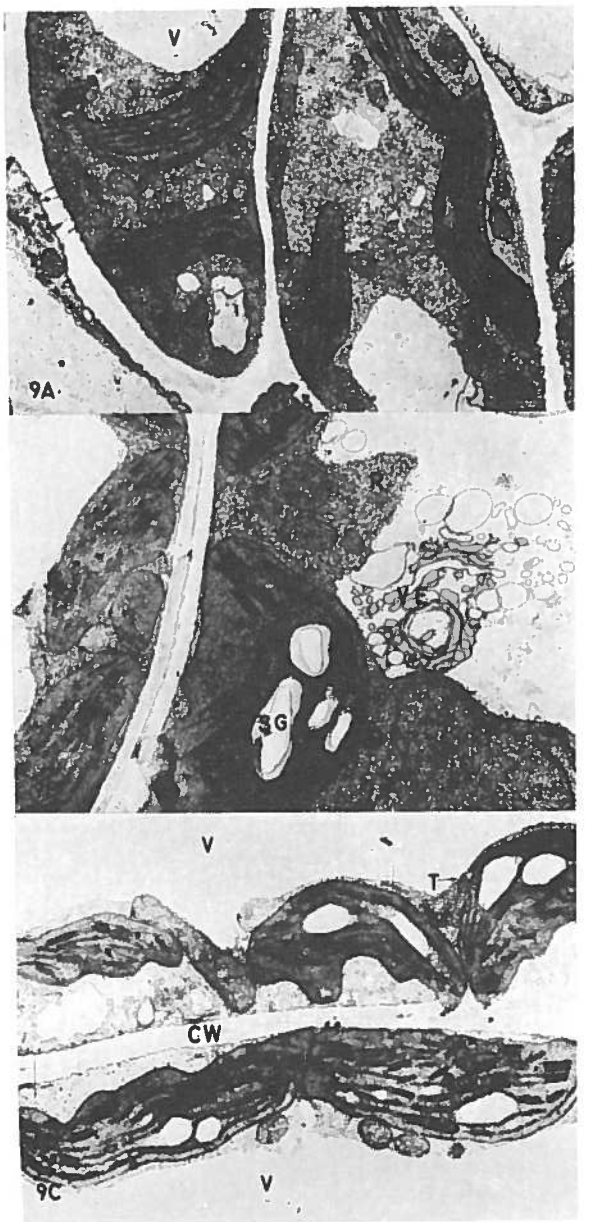

Figure 9. Mesophyll cells from soybean leaves. (a) Exposed to Mylar-filtered light (control). 10,770x. (b) Treated with 56 hours of unfiltered UV radiation from an FS-40 lamp. Note numerous vesicles. 11,298x. (c) Exposed to Kodacel-filtered light for 56 hours. Some vesiculation and misshapen chloroplasts. 10,770x. Legend:

C = Chloroplast
CE = Chloroplast envelope
CW = Cell wall
D = Dictyosomes
G = Grana
M = Mitochondria
N = Nucleus
NU = Nucleolus
PG = Plastoglobuli
PL = Plasmalemma
R = Ribosomes
RER = Rough endoplasmic reticulum
SG = Starch grains
T = Tonoplast
V = Vacuole
VE = Vesicle

Figure 10. Severe damage to mesophyll cells from soybean leaves. (a) Exposed to unfiltered UV from FS-40 lamp radiation for 56 hours. Note increase in amount of RER. 11,540x. (b) Exposed to Kodacel-filtered UV radiation for 28 hours. Note swelling of the RER, damage to the mitochondria, and vesiculation. 11,520x. (c) Exposed to Kodacel-filtered UV radiation for 28 hours. Note the partial to complete disruption of chloroplasts in cells adjacent to those showing relatively little damage. 9,408x.

A conspicuous feature of the disrupting chloroplasts was an accumulation of plastoglobuli. Present in chloroplasts of normal leaves, they are a particularly familiar feature in senescent (Shaw and Manocha, 1965) or damaged (Campbell and Griffin, 1973) leaves. Shakhov and Golubkova (1963) also observed an increase in plastoglobuli in chloroplasts of lettuc following UV radiation at 254 nm. These bodies probably represent the accumulation of lipid components, released on the breakdown of the thylakoids and other insoluble lipid compounds. The increase in RER might signify an increased potential for protein synthesis, since presumably the cell is attempting to repair damage caused by the UV radiation.

NET PHOTOSYNTHESIS

Determinations of net photosynthesis of plants exposed to the enhanced UV-B radiation environment under the greenhouse experiments described in the previous section are indicating that at least part of the depression of plant growth can be attributed to reduced photosynthetic rates.

Not only may chronic exposure to enhanced UV-B radiation be of significance in depressing net photosynthetic rates, but there also now exists limited evidence that acute-dose exposure to increased UV-B radiation may depress photosynthetic rates. The following example will illustrate this.

Net photosynthesis analyses were carried out with four-week-old pea (*Pisum sativum*) seedlings which were grown in a greenhouse without supplemental UV radiation. Rates of photosynthesis were determined with a Siemens Corp. gas-exchange system (Koch et al., 1971). This system facilitates gas-flux-resistance calculations, as well as measurement of transpiration and photosynthetic rates.

Ultraviolet supplementation and global-radiation simulation for these photosynthetic measurements was achieved in the laboratory with four incandescent Sylvania 300-watt lamps and two Westinghouse FS-20 sun lamps, with Kodacel TA 401 (5-mil) plastic-film filters. The control irradiation was identical except that the radiation from these lamps was filtered through a Mylar type A (10-mil) plastic film. Spectral irradiance measurements were made with a Gamma Scientific Company spectroradiometer.

The effects of this acute ultraviolet irradiation within the 280 to 320 nm waveband during photosynthetic measurements are presented in Figure 11. It is apparent that net photosynthesis was inhibited at both 23°C and 33°C with the UV-B irradiation. This acute-dose response exhibited by pea suggests an immediate deleterious effect on the photosynthetic apparatus, since stomatal diffusion resistances did not vary significantly between the test and control situations at any given temperature.

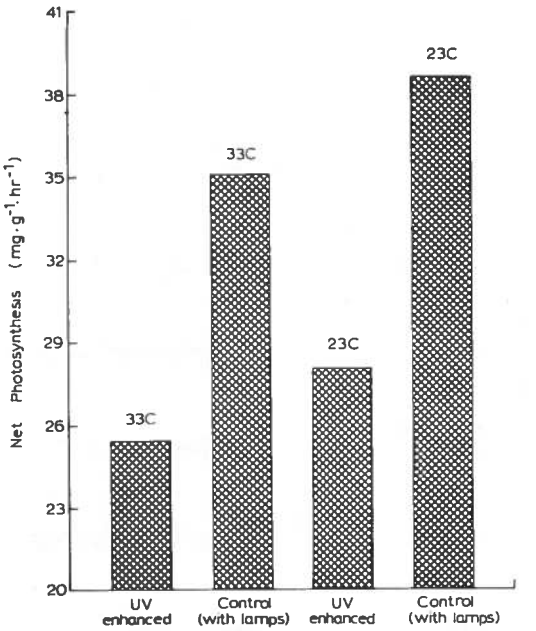

Figure 11. Net photosynthesis of Pea (*Pisum sativum*) for two temperatures under an acute dose of ultraviolet radiation (280 to 320 nm) as compared to controls.

UV-B RADIATION AND MUTATIONS

Apart from possible reductions in plant growth and yield, the likelihood of genetic alterations is of considerable concern to biologists. The stamen hairs of *Tradescantia* species have been shown to be excellent material for mutation studies in general radiobiological studies, and as a test system for chemical

mutagens. We have, therefore, used a test clone of *Tradescantia* as a biological indicator of alteration in mutation frequencies by enhanced UV-B radiation.

Uniformly vigorous plants of *Tradescantia*, clone 4430 (obtained from A.H. Sparrow, Brookhaven National Laboratory), were given seven hours of supplemental UV-B radiation per day under the field conditions described in earlier sections. Non-treated and treated plants were grown under these conditions for one week to equilibrate them, and then somatic aberrations (color changes in the petals and stamen hairs) were scored for 20 days (see Figure 12 for aberration types). Somatic aberrations are expressed as the frequency of events of each type per hair; an event is defined as exhibition of the same aberration or mutation by one cell or any sequence of contiguous cells.

To study the effect of UV radiation on the reproductive integrity of stamen hairs, unrooted vigorous cuttings of *Tradescantia*, clone 02 (obtained from A.H.S., BNL), bearing young inflorescences with immature stamen hairs, were selected on the basis of their being in a similar stage of development. These cuttings were placed in controlled environment chambers (Model PGX-60, Mallory Engineering, Inc., Salt Lake City), and exposed to 10-hour photoperiods. To simulate normal daylight and represent the control, the light (a 6000-watt xenon lamp) in one chamber was filtered with two sheets of 0.010-mil Franklin-fiber cellulose acetate. For the UV-B enhancement treatment, one sheet of 0.010-mil Kodacel plastic film was used (see Figures 6 and 7). Temperatures were held at 35°C (days) and 18°C (nights). After treatment, the plants were placed in a growth chamber (Percival Model E-54U) at 27°C (days) and 16°C (nights) with a 12-hour photoperiod. After a one-week adjustment, data were collected on bud-blasting, number of hairs per stamen, and

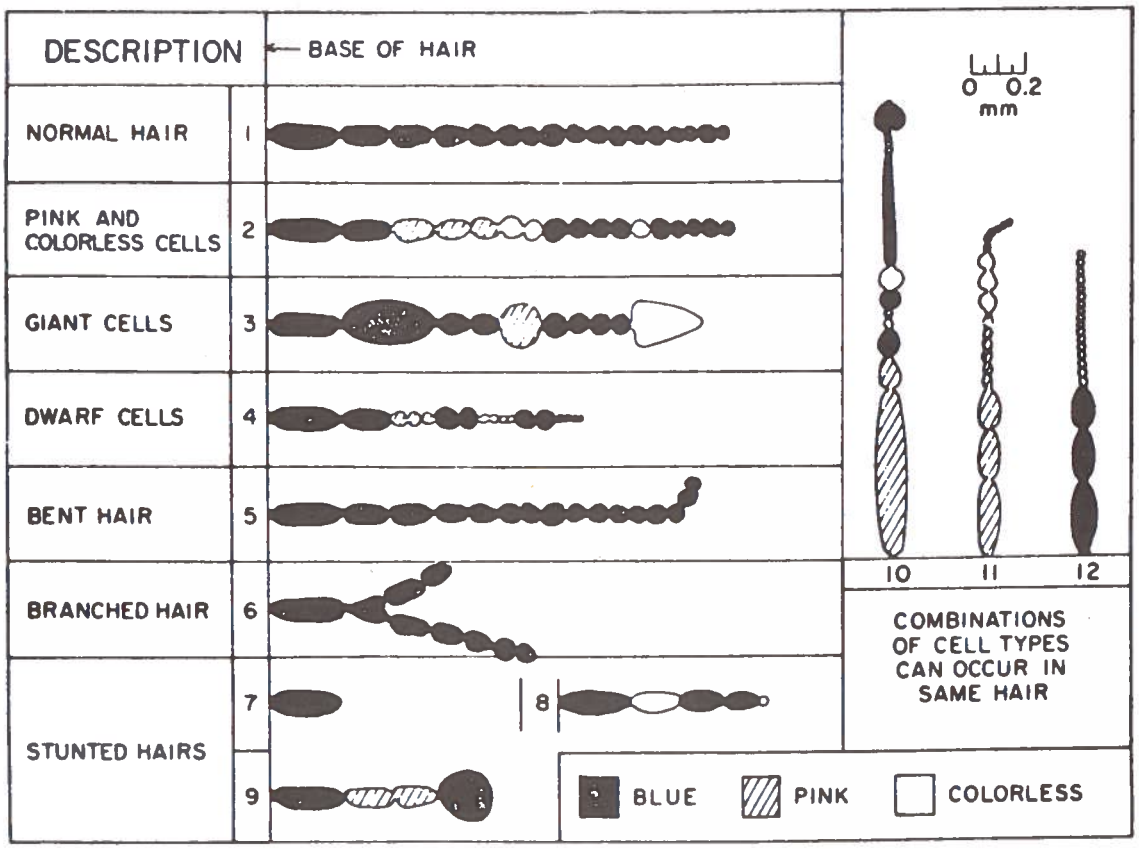

Figure 12. Diagram of a normal *Tradescantia* stamen hair, and examples of aberrant cell and hair types commonly observed.

cells per stamen hair. The hairs at the apex of the filament are the last to form and were considered the most likely to be present as single-cell initials during UV exposure. Therefore, only hairs in this region (denoted as zone 3 in Figure 13) were scored.

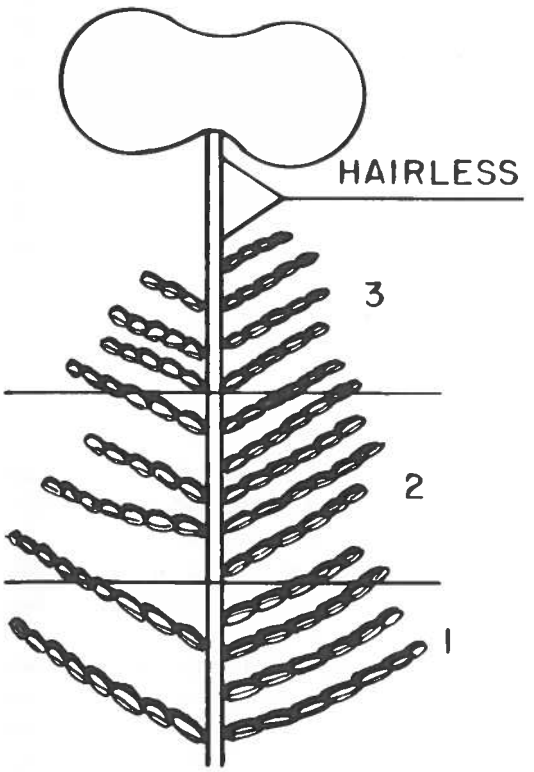

Figure 13. Diagram of a typical stamen divided into three equal hair-bearing regions.

On the basis of our data it appears that the stamen hairs of *Tradescantia*, clone 4430, are sensitive to an environment with enhanced UV-B radiation. The color aberrations noted in the stamen hairs appeared to be all possible combinations, with blue-to-colorless being the most common. Spontaneous aberrations are known to occur in the stamen hairs of clone 4430. However, in the treated-control (Mylar-filtered lamps) or the enhanced-UV-B treatments, such aberrations were significantly increased in number over those occurring in untreated control plants (see Table 4).

According to Sparrow et al. (1968) and Mericle and Mericle (1967), the color changes in stamen hairs are caused by genetic alterations in meristematic cells, with the blue color gene being lost or mutated while the recessive pink allele is expressed. The genetic mechanism for the colorless condition of the stamen hairs is, as yet, undetermined. However, Ichikawa et al. (1969) suggested that these hairs may be genotypically pink homo- or hemi-zygotes (due to mutation or loss of the pink gene), blue hemizygotes (loss of pink gene), or blue/pink heterozygotes (original type), in which some physiological disturbances caused by radiation prevented normal pigmentation production. Whether the mechanism reacts similarly to UV radiation is yet to be determined.

The causes of the other aberrations of stamen hairs are unclear as yet. Because these events occurred infrequently, their value in future studies appears to be limited.

The plants treated with UV-B enhancement evidenced many more aberrant events per stamen hair than did the treated-control and non-treated-control plants (Table 4). The number of aberrant events per stamen hair for the treated controls was significantly higher than that observed for the non-treated-control plants. This may indicate two things: one, an extreme sensitivity to any

Table 4. Effect of Ultraviolet Radiation on the Frequency of Aberrant Events per Stamen Hair and Total Aberrant Events in Stamen Hairs of *Tradescantia* Clone 4430 Grown Under Field Conditions. (Plants were equilibrated for one week and then scored for 20 days.)

Treatment	Aberrant Events per Hair	Total Aberrant Events	Total Number of Stamen Hairs Scored
Control	0.0003	20	58,800
Treated-control (Mylar-filtered lamps)	0.0020	156	79,800
UV-B-enhancement	0.0069	577	84,750

environmental stress, and two, that the additional longer-wave radiation these plants received (at 370-410 nm wavelengths) may have triggered more aberrant events per stamen hair. Further data are needed to confirm the possible effects of longer-wave radiation effects.

According to Sparrow and colleagues (Underbrink et al., 1970), the stamen hairs are shorter at the apex of the filament than at the middle or base in normal, untreated *Tradescantia* species (Figure 13). The terminal cell in the chain is the only one capable of continued division, although the subterminal cell may divide once after it is formed. Thus, the terminal cell gives rise to almost the entire hair, which ranges from 16 to 21 cells in length at maturity. Since no other cell in the chain can become meristematic, sterilization of the terminal cell in an immature hair results in a stunted or deformed mature hair. When we exposed young *Tradescantia* flower buds, with their immature hairs, to UV radiation, and then scored mature filaments for the number of normal hairs, the mean number of cells per hair dropped significantly. The mean number of cells per hair of the non-treated-control plants was 17.0 and 16.7 for 10 and 20 hours, respectively, which agrees with the work of Sparrow and colleagues (see Table 5).

The loss or partial loss of reproductive integrity, i.e., stamen-hair stunting, was established by counting the number of cells in each hair in the distal third of the stamen (Figure 13). A hair was considered stunted if it had fewer than 75% of the number of cells normally occurring in unaffected hairs in control plants. In our study, 11 cells or fewer were counted as stunted. Ten hours of UV-B radiation enhancement induced significant stunting in the stamen hairs, with no further significant changes after 20 hours of exposure.

The average number of hairs per stamen for control plants was 36 and 34 for 10- and 20-hour treatments, respectively. The number of hairs per stamen was significantly reduced, relative to those in untreated control plants, with as little as 10 hours of UV-B enhancement radiation. The 20 hours of UV-B radiation exposure reduced the number of hairs per stamen significantly below those in plants exposed for 10 hours (see Table 5).

These data indicate that the number of cells per hair and the number of hairs per stamen in the distal third of the stamen are sensitive to UV radiation and are useful criteria for future studies. Moreover, with respect to these criteria, *Tradescantia* species respond to UV radiation much as they reportedly respond to ionizing radiation.

INTERACTIONS

In addition to the direct impact of enhanced UV-B radiation on plant processes such as photosynthesis, growth, and mutation, the effects of interaction of this environmental factor with other stress factors on plants may be more than additive.

In studies made by our group at Utah State University, preliminary experiments have tested possible interactions between enhanced UV-B radiation and air pollutants (using fluoride on soybeans as a test case) and plant pathogens (using tobacco-necrosis virus infection on beans). These preliminary trials have not as yet indicated significant interactions between UV-B radiation enhancement and these other stress factors, but such studies are continuing.

Table 5. Effects of Enhanced Ultraviolet Radiation on the Average Number of Cells per Stamen Hair, Number of Hairs per Stamen, and Percent Stunted Hairs per Stamen in *Tradescantia* Clone 02. (Experiments conducted in controlled environment chambers.)

Treatment	Exposure (hrs)	Cells/Hair	Hairs/Stamen	% Stunted Hairs
Control	10	17.0 a*	36.0 a	0.41 a
	20	16.7 a	34.2 a	0.30 a
UV-B enhancement	10	14.5 b	29.9 b	4.00 b
	20	14.9 b	25.9 c	6.00 b

* Those values within a column followed by the same letter are not significantly different at the 5% level.

CONCLUSIONS

The heterogeneity of response of various plant species to enhanced UV-B radiation, and the sizable variation in UV-radiation sensitivity apparent from other studies (Cline and Salisbury (1966) and other studies now under way in CIAP), may at first seem perplexing.

A simple diagram is here presented as a conceptual model of UV-B radiation dose-response relationships.

First, in the absence of radiation-repair mechanisms, a sigmoid dose-response curve has emerged as a most appropriate fit on the basis of experimental studies on a wide variety of organisms.*

Second, to incorporate the effect of molecular repair systems in such a curvilinear model, the postulations of Murphy (1974) have been used for photorepair and dark-repair systems in Figures 14 and 15. For photorepair Murphy concluded that apparently a constant, fixed percentage of the damage resulting from UV-B radiation is repaired. However, this percentage can vary considerably, depending on the organism, and undoubtedly depending on the particular biological phenomenon in question. Figure 14 graphically depicts this relationship. In this case it is assumed that 70% of the damage would be repaired at all UV-B doses. Therefore, with increasing UV dose, the amount of unrepaired photochemical damage would increase proportionately. Photorepair systems are found in many orders of the plant and animal kingdoms, with placental mammals being a notable exception. For dark-repair systems such as excision repair, Murphy (1974) suggests that a large proportion of the damage is repaired up to a certain threshold amount. This is depicted graphically in Figure 15. Dark-repair systems, although not yet documented for photosynthesizing plants, do occur widely among non-photosynthetic organisms.

The critical ecological question for all organisms is where on these dose-response relationship curves the organism is presently situated with respect to UV-B radiation doses received by the organism's physiological targets in its present habitat. Also important is the proportion of damage that can be repaired by molecular repair systems, and whether or not the organism is

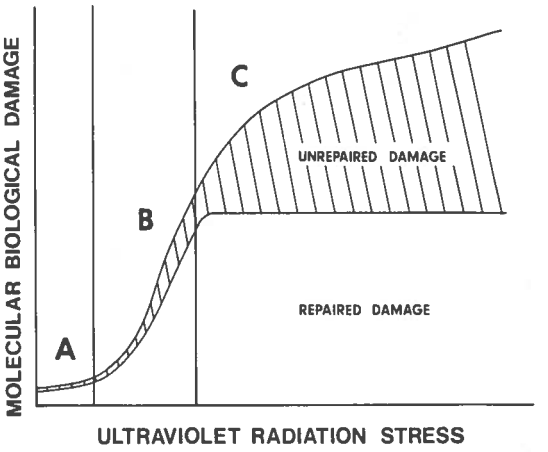

Figure 14. Postulated dose-response curves of molecular damage in organisms exposed to UV-B radiation. The percentage of molecular damage repaired by photorepair systems is depicted as a constant percentage of the total molecular damage, in this case 70%. See text for discussion and assumptions regarding this dose-response relationship and the different segments of the curve labeled as 'A', 'B', and 'C'.

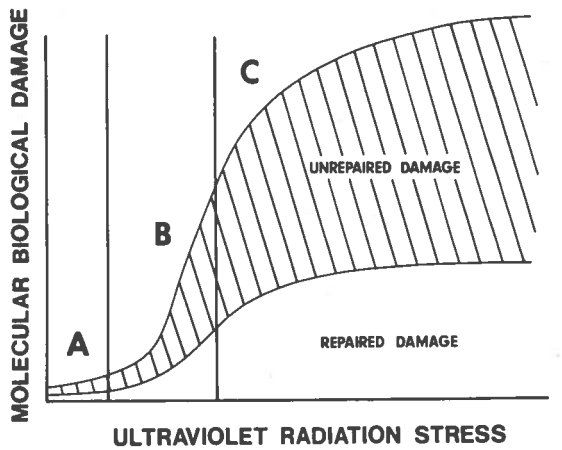

Figure 15. Postulated dose-response curves for molecular damage in organisms exposed to UV-B radiation. The amount of molecular damage repaired by dark-repair systems such as excision repair is depicted as a large percentage of the total damage up to some threshold limit. See text for discussion and assumptions regarding this dose-response relationship and the different segments of the curve labeled 'A', 'B', and 'C'.

* Further details are given in Chapter 7 of Volume V of the CIAP Monograph Series.

already close to a threshold, so that further increases in dose might result in substantially greater quantities of unrepaired damage.

Because of avoidance – whether by behavioral means, habitat selection, or absorption of UV-B in outer tissue layers – many species may be at various positions on part A of this curve as represented in Figures 14 and 15. Other species may be on at least portions B or C of these curves under present-day conditions, so further increases in UV-B irradiance would be expected to have an appreciable effect. More study is certainly warranted to determine the dose-response relationships of a wide variety of domesticated and non-agricultural species in relation to their radiation avoidance and repair capabilities. A consideration of subtle physiological and genetic changes as well as interactions with other stress factors should be included in such studies.

REFERENCES

Barton, R. (1966), "Fine structure of mesophyll cells in senescing leaves of *Phaseolus*," Planta **71**, 314-325.

Bener, P. (1963), "The diurnal and annual variations of the spectral intensity of ultraviolet sky and global radiation on cloudless days at Davos, 1590 m a.s.l.," U.S. Air Force Contract 61(052)-618, Technical Note No. 2.

Butler, R.S. (1967), "The fine structure of senescing cotyledons of cucumber," J. Exp. Bot. **18**, 535-543.

Caldwell, M.M. (1971), "Solar UV irradiation and the growth and development of higher plants," in *Photophysiology*, Vol. 6. ed. A.C. Giese, Academic Press, N.Y., 131-177.

Caldwell, M.M. (1973), "Ecological considerations of solar radiation change," in *Proceedings of the Second Conference on the Climatic Impact Assessment Program* (Nov, 14-17, 1972), ed. A.J. Broderick, U.S. Dept. of Transportation, DOT-TSC-OST-73-4, 386-393.

Campbell, W.F. and G.D. Griffin (1973), "Fine structure analyses of stem nematode-induced white flagging in *Medicago sativa* L.," J. Nematol. **5**, 123-126.

Cline, M.G. and F.B. Salisbury (1966), "Effects of ultraviolet radiation on the leaves of higher plants," Rad. Bot. **6**, 151-163.

Green, A.E.S., T. Sawada, and E.P. Shettle (1974), "The middle ultraviolet reaching the ground," Photochem. Photobiol. **19**, 251-259.

Ichikawa, S., A.H. Sparrow, and K.H. Thompson (1969), "Morphologically abnormal cells, somatic mutations and loss of reproductive integrity in irradiated *Tradescantia* stamen hairs," Radiat. Bot. **9**, 195-211.

Ikeda, T. and R.R. Ueda (1964), "Light and electron microscopical studies on the senescence of chloroplasts in Elodea leaf cells," Bot. Mag. (Tokyo) **77**, 336-341.

Koch, W.L., O. Lange, and E.D. Schulze (1969), "Ecophysiological investigation on wild and cultivated plants in the Negev desert. I. Methods: A mobile laboratory for measuring carbon dioxide and water vapor exchange," Oecologia (Berlin) **8**, 290-309.

Mericle, L.W. and R.P. Mericle (1967), "Genetic nature of somatic mutations for flower color in *Tradescantia*, clone 02," Radiat. Bot. **7**, 449-464.

Mollenhauer, H.H., W.G. Whaley, and J.H. Leech (1960), "Cell ultrastructure responses to mechanical injury: A preliminary report," J. Ultrastruct. Res. **4**, 473-481.

Murphy, T.M. (1974), Section 3.2.2 of Volume V of the CIAP Monograph Series, U.S. Department of Transportation. NOTE: At present these monographs exist only in an early draft form. They will be publicly available after completion in September 1974.

Shakhov, A.A. and B.M. Golubkova (1963), "On chloroplast structure in relation to ultraviolet irradiation," Fiziol. Rast. **10**, 246-252.

Shaw, M. and M.S. Manocha (1965), "Fine structure in detached, senescing wheat leaves," Can. J. Bot. **43**, 747-755.

Sparrow, A.H., L.A. Schairer, and K.M. Marimuthu (1968), "Genetic and cytologic studies of *Tradescantia* irradiated during orbital flight," BioScience **18**, 582-590.

Underbrink, A.G., Rhoda C. Sparrow, A.H. Sparrow, and H.H. Rossi (1970), "Relative biological effectiveness of X-rays and 0.43-MeV monoenergetic neutrons on somatic mutations and loss of reproductive integrity in *Tradescantia* stamen hairs," Radiat. Res. **44**, 187-203.

DISCUSSION

CLAYTON: To what do you attribute the difference between the field and the greenhouse results?

CALDWELL: Enhanced photoreactivation under field conditions may lessen UV-radiation-induced damage; we are testing that hypothesis. We will be doing more greenhouse experiments, and we are also doing some growth-chamber experiments with different levels of visible radiation along with different simulated UV regimes.

(UNIDENTIFIED): Where does the greenhouse glass cut off the shorter wavelengths in the ultraviolet?

CALDWELL: Depending upon the type of glass, greenhouse glass will cut off between about 330 and 370 nm. In our case, it was 325 nm, so the radiation between 285 and 320 nm was supplied by lamps.

(UNIDENTIFIED): Were the lamps raised as the plants grew so as to expose the top of the canopy of the row of plants?

CALDWELL: Yes, we raise them. Unfortunately, we do not have lamps powerful enough that we can irradiate the canopy from a greater distance.

(UNIDENTIFIED): That is the point that troubled me. Perhaps in enhancing the UV you are doing other things that disturb the plant. In particular, there is a natural change of intensity during the day, due to the change of solar angle. Unless you adjust your lamps accordingly, you are certainly considerably altering the ratio of UV to total radiation.

I would like to suggest that a better way to do it might be not to try to enhance the UV, but rather to go to lower latitudes or higher altitudes for higher UV exposure. By using filters you could get the corresponding change that you would like in the environment to make a comparison under those conditions.

CALDWELL: In regard to the first part of your question, UV spectral irradiance between 40 and 80 degrees solar altitude does indeed change. However, the increment needed to supplement the normal global spectrum to simulate a 50% reduction of atmospheric ozone does not change that much, according to extensive calculations made using the semi-empirical formulae of Dr. Alex Green.

In response to the second part of your question, you have to remember that organisms respond to all environmental factors, and you wouldn't know whether the organism was responding only to ultraviolet radiation. The plants you wish to study rarely grow well enough at enough altitudes and latitudes to permit such experimentation.

(UNIDENTIFIED): Have you grown any field plants to full maturity so that you have all the hidden effects showing up?

CALDWELL: In most cases, we have not, mainly because of the limitations on our irradiation scheme. We simply have not been able to get the types of lamps we really need in this short period of time to irradiate large agricultural or native plants to the completion of their specific life cycles.

(UNIDENTIFIED): In your mutation studies, why didn't you use some plants that had some economic significance?

CALDWELL: Well, in this case we were looking at a plant which is a good biological indicator. Plants vary a lot in how easy they are to study. Mutation scoring is difficult under the most ideal circumstances, because mutations are reasonably rare events. So in order to quantify mutation rates, we have been using a test organism which has been used for years in other studies.

(UNIDENTIFIED): That leads to my next question. Would you generalize from this particular organism to organisms which are economically important, which is really what the whole thing is all about?

CALDWELL: Well, this is perhaps in part "what the whole thing is about," but we also have to give careful consideration to organisms which are of no immediate economic value, because they may be of great ultimate value when we consider the roles of such seemingly insignificant organisms in the normal functioning of natural ecosystems.

EFFECTS OF UV RADIATION ON AGRICULTURAL PRODUCTIVITY

J.F. BARTHOLIC, L.H. HALSEY, AND R.H. BIGGS
Institute of Food and Agricultural Sciences
University of Florida
Gainesville, Florida

ABSTRACT: The effects of changes in ultraviolet (UV) irradiation on agricultural productivity were evaluated under field, growth-chamber, and greenhouse conditions. The field-test location was Gainesville, Florida (latitude 30°N), where the UV flux density was expected to be greater during the spring than in areas further north. In the field studies, one check and two shelter treatments were used. One shelter treatment used polyethylene, which has a minimal effect on the incoming radiation; the other used Mylar (type S) which filtered out UV radiation less than 320 nm. The treatments were replicated five times on corn, beans, and tomatoes. Environmental and plant measurements were taken. Fluorescent (FS-40) lights were used in both the greenhouse and growth chamber to enhance the UV irradiation. In the field experiment, although some statistically significant changes were observed in growth characteristics, the total yield produced in each treatment was generally only slightly altered. In the greenhouse experiment, some reduction in growth was observed for most plants, and in the growth chamber, significant changes in growth were measured.

INTRODUCTION

The detrimental effects of ultraviolet (UV) radiation on biological systems have been well documented. For the plant kingdom, it has been shown that UV in the 280-310 nm range (UV-B) can destroy certain key compounds in tissue. In particular, nucleic acids (Setlow and Doyle, 1957), proteins, and chloroplastic pigments (Wu et al., 1973), can be destroyed by UV-B radiation. However, when the studies are conducted in the presence of light in the photosynthetically active band (300-700 nm), some photoreactivation is observed. Unfortunately, no one has reported on alterations in productivity of an entire plant or plant communities as a result of irradiation with UV-B.

Some studies have been conducted by moving plants to a higher elevation at the same latitude. Unfortunately, this experimental technique only enhances the longer-wavelength UV (> 310 nm). The quantity of radiation in this portion of the spectrum received at the earth's surface is affected somewhat by atmospheric particulate matter, haze, etc., but mostly by O_3 in the atmosphere many kilometers above the earth.

UV-B received is generally increased as one moves to lower latitudes (Prabhakara et al., 1971). In May and June, the major growing season for both the southern and the northern portions of the United States, the O_3 concentration is frequently twice as great over the northern states as over areas of Florida and Southern Texas. It would be interesting to find how much the larger amount of UV radiation presently affects yields in the southern states. Unfortunately, no one has yet made such an evaluation, though there is some indirect evidence that it may affect yields. For many crops, yield per acre in the southern states has never reached that obtained in the north. (There are numerous factors that can affect yield, however.)

Because of the direct and indirect evidence of the possible detrimental effects of UV-B, research was undertaken to determine the effect of UV-B on several economically important crops (with an eye to determining the effect on agricultural productivity of a possible increase in UV-B penetration due to increased flight in the stratosphere).

The objectives of this research were: (1) to evaluate the effect of changes in UV-B irradiation on crop productivity under field conditions, (2) to evaluate the effect, under controlled conditions, of increased UV-B, and (3) to conduct a number of selective experiments to aid in understanding how UV radiation affects crops. This paper presents results germane to objectives 1 and 2.

FIELD EXPERIMENT

Methods and Materials

The shelter design, materials used, field plot design, and results are described below.

Construction and Design of UV Shelters

Even the best-designed shelters can to some degree change the natural plant environment, so three treatments were used. They were: (1) check, or open, plots; (2) plots covered with a shelter to filter out UV radiation shorter than 320 nm; and (3) plots with shelters that had a minimal effect on the UV irradiation but otherwise affected the plant environment the same as those of (2).

Numerous shelter prototypes were designed and tested with several basic characteristics in mind. First, the plots had to be large enough to grow the number of plants required for statistical analysis. Second, it was desired to minimize the change in natural air flow over and through the crop, as well as radiation flux. As a result of these factors, plus maintenance and cost considerations, a 3-m X 3-m area was chosen. By building the shelters out of panels, it was possible to leave a space for air movement between the top panel and the two side panels (Figure 1). Poles were used for strength and to make it possible to raise the panels as the crop grew.

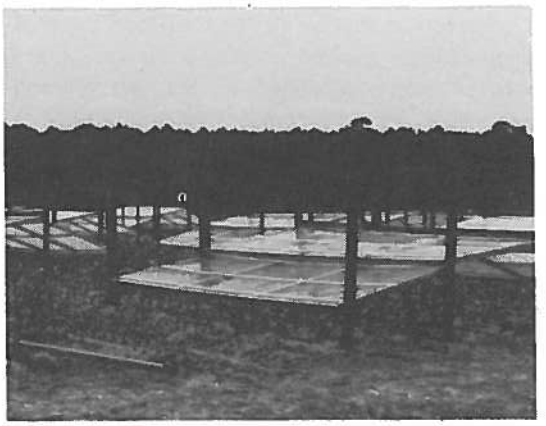

Figure 1. Array of shelter and check vegetable plots.

Materials Used

Over 25 films were evaluated for their filtering properties and durability characteristics. The materials finally selected were 5-mil Mylar (type S), to filter out UV-B radiation (between 290 and 320 nm), and polyethylene, which removed only approximately 7% of the UV-B, as a neutral density filter.

With these two materials it was possible to have a large difference in the amount of radiation between 320 and 280 nm reaching the crop. Figure 2 shows data obtained with a spectroradiometer* placed in the center of the shelters at crop height. The three curves represent the outside radiation (both direct and diffuse) measured at 1355 hours, the radiation reaching the crop in the center of the polyethylene-covered shelter at 1350, and the UV radiation reaching the crop in the center of the shelter under Mylar at 1415. The curves confirm that the Mylar was filtering out UV-B and the polyethylene had little effect on the radiation. (Similar measurements taken within 1 m of the edge of the shelters at midday were not appreciably different.) The materials have been checked for

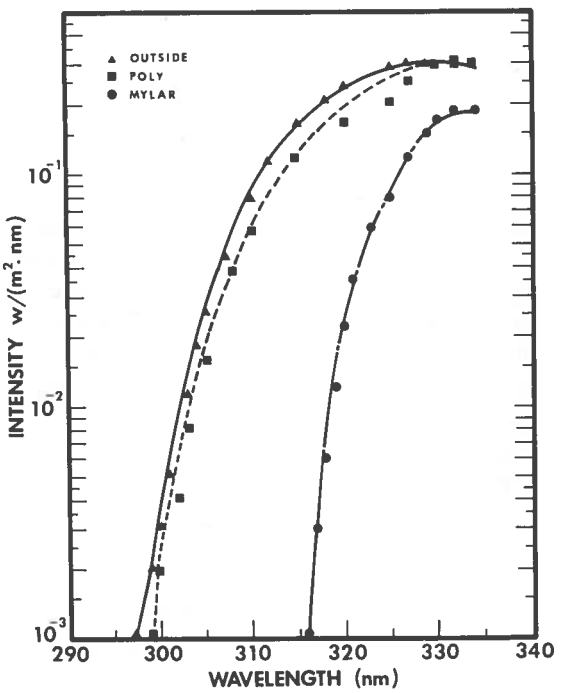

Figure 2. Radiation intensity vs. wavelength as measured with a Gamma Scientific Spectroradiometer in the open and in the center of shelters covered with polyethylene and Mylar filters on April 22.

* Measured with a Gamma Scientific Spectroradiometer, Model 2900.

their effect on the total solar radiation.* The results show that both materials reduce solar radiation as a whole by about 7%.

Field Plots

Treatments were replicated five times each for corn, beans, and tomatoes, to enhance the chance of finding significance between treatments. This number of replications required a total of 30 shelters, 90 panels, and 240 posts. Over 2500 tomato plants were hand-planted. These plants were started in a greenhouse so no UV-B would reach them. They were transplanted at the third leaf stage and shelters were installed over them immediately. Beans and corn were planted mechanically and shelters were installed as the plants emerged. The 'Walters' tomatoes were transplanted on April 2, 'Pioneer 3369A' corn was planted April 4, and 'Harvester' beans were planted April 5, 1973.

Results

Beans

The characteristics of the plants did not vary significantly among treatments. Yields of mature and over-mature pods did not vary, though significant response to treatment was found for under-mature, cull, and total-yield categories. The yields from the checks were higher than those from the covered, with some differential responses measured for plants grown under shelters (see Table 1).

Corn

Plant characteristics did not vary significantly among treatments. Yield of ears varied in dimensions and weight among treatments, with no relation to cover or exposure. Ear weight also varied among treatments, though larger ears were found in the fully exposed check groups (see Table 2).

Table 2. Effect of Ultraviolet Radiation on Corn Yields

Treatment	Ear Dimensions		
	Length (cm)	Diameter (cm)	Ear Weight (kg/ha)
Not covered			
Full UV exposure	21.2 a*	5.6 a	9,683 a**
Covered (polyethylene)			
Transmitted UV	20.3 b	5.3 b	7,500 b
Covered (Mylar S)			
Absorbed UV	19.8 b	5.2 b	6,954 c

*Values with different letters in the same column are significantly different at the .05 level in a Duncan Multiple Range test.

**Values with different letters in this column are significantly different at the .01 level in a Duncan Multiple Range test.

Tomatoes

Statistical analysis of the tomatoes' physical characteristics showed no significant differences between plants subjected to the two filtering treatments, and the tomato yield data (kg/ha) showed very few instances of significant differ-

* Measured with an Eppley Pyranometer, Model No. 8-48.

Table 1. Effect of Ultraviolet Radiation on Bean Yields and Pod Dimensions

Treatment	Yield (kg/ha)					Pod Dimensions (cm)	
	Under-Mature	Mature	Over-Mature	Cull	Total	Length	Thickness
Not covered							
Full UV exposure	377 a*	4203	81	362 a	5023 a	12.4 a	0.96
Covered (polyethylene)							
Transmitted UV	355 a	3885	34	194 c	4468 b	11.0 c	0.91
Covered (Mylar S)							
Absorbed UV	261 b	3640	79	266 b	4246 b	11.7 b	0.92

*Values with different letters in the same column are significantly different at the .05 level in a Duncan Multiple Range test.

ences. For marketable-weight tomatoes (size 7 X 7) from all harvests, yield was highest from the check treatment. Response for total weight of marketable tomatoes was similar to that for size 7 X 7, but to a less significant degree.

With tomatoes of advanced maturity (one of the components of marketable yield), responses of a significant nature were mostly associated with early yields of the larger sizes. Highest yields occurred from the Mylar-shielded treatment (Table 3). (Note, however, that at the fourth harvest the yield of 7 X 7 size tomatoes was highest from the check treatment plots, contrary to the general trend.)

Table 3. Advanced Maturity Yields of Tomatoes (kg/ha) from Various Levels of Ultraviolet Radiation

Harvest Date	Fruit Size*	Uncovered	Covered (Poly)	Covered (Mylar)
June 13	5 X 6	40 a**	1,108 b	2,212 c
	6 X 6	179	145	529
	6 X 7	197	192	264
	7 X 7	23	78	119
	Total	440 a	1,524 b	3,124 c
June 18	5 X 6	490	790	764
	6 X 6	1,102 a	771 b	1,962 c
	6 X 7	1,039	891	873
	7 X 7	333	257	261
	Total	2,965	2,709	3,860
June 25	5 X 6	481	417	1,232
	6 X 6	940	1,233	1,844
	6 X 7	1,810	2,178	2,786
	7 X 7	2,896	2,648	4,251
	Total	6,128	6,477	10,113
July 3	5 X 6	201	264	110
	6 X 6	669	842	326
	6 X 7	1,429 a	1,496 b	546 c
	7 X 7	5,447	4,811	5,111
	Total	7,745	7,413	6,093
All harvests	5 X 6	1,212 a	2,579 b	4,318 c
	6 X 6	2,890	2,991	4,661
	6 X 7	4,475	4,757	4,469
	7 X 7	8,699	7,794	9,742
	Total	17,276	18,121	23,190

*These classifications are determined by diameter as follows:

7 X 7	54-58 mm
6 X 7	58-64 mm
6 X 6	64-73 mm
5 X 6 and up	73 mm and up

**Values with different letters in the same row are significantly different at the .05 level in a Duncan Multiple Range test.

With tomatoes which were mature-green at harvest (the other component of marketable yield), there was only one instance of difference of a significant nature: At the second harvest, fewer tomatoes of the size 5 X 6 were obtained from the polyethylene-covered plots.

Cull tomatoes varied only with respect to misshapen fruit produced at the second harvest; more were found in the open-exposure treatment, a feature reflected in the response for all harvests but to a non-significant extent.

Above-ground plant parts, exclusive of fruit, were analyzed for mineral content. Their content of phosphorus, iron, and manganese varied with treatment.

GROWTH-CHAMBER AND GREENHOUSE EXPERIMENTS

To aid in observing the reaction of plants to UV-B irradiation and parameterizing the responses that should be researched in detail, growth chambers and greenhouses were used to screen a variety of plants. Routine observations included germination, rate of seedling growth, node and date of flowering, fresh vs. dry weights, photosynthetic capacity, and survival. Unusual differences between plants grown with and without UV-B radiation were noted for further tests, e.g., high incidence of a disease, changes in pigmentation, modification in shape and sizes of organs, etc.

Methods and Materials

Plant Material

The plants selected for testing either have an agronomic importance or have been previously reported to respond to ultraviolet light in the UV-C region. They were prepared for the chamber and greenhouse tests in a manner consistent with cultural practices, for example, *Zea mays* by germinating the seeds, coleus by rooting shoot cuttings, and cabbage by transplanting young seedlings.

Test Conditions

Two environmentally controlled chambers were made into growth chambers by the addition of four Westinghouse FS-40 sun lamps per

chamber. The lamps were mounted inside the chambers on adjustable brackets just above the plants. In one chamber the emission from the FS-40 lamps was filtered through 5-mil cellulose acetate, and in the other chamber, through 5-mil Mylar. Ultraviolet irradiance was controlled to approximate a 50% reduction in ozone (cellulose-acetate-filtered) in the UV-B-enriched growth chamber, and a 0% reduction (Mylar-filtered) in the control. Other conditions in the growth chambers were as follows: temperature controlled at 25 ± 2°C, a 16-hr day and 8-hr night, and a daylight intensity of approximately 50 W/m^2.

The greenhouse, which covers 400 m^2, is constructed of Lascolite (Fiberglas). It is equipped with evaporative cooling and natural-gas heaters. The temperature range was 20°C to 32°C. Light conditions for the control are sunlight filtered through the lascolite, with the daylength extended to 16 hours by incandescent lamps (5 W/m^2 at plant height). Ultraviolet-light treatments were provided by FS-40 sunlamps with either cellulose acetate or Mylar filters.

Results and Discussion

Growth-Chamber Tests

Although only limited statistical analysis has been performed, it seems that several reliable observations can be made from inspection. First, agronomic plants do differ in responses to an increase in UV-B radiation. Using the reduction in dry weight/plant as a general index for the six species tested, a ranking of those affected most to least would be 'Early Alaska' peas > cabbage > collard > 'Little Marvel' peas > 'Wando' peas > corn. Second, UV-B seemed to have little effect on germination. Third, flowering in some species may be influenced by UV-B. The data on 'Early Alaska' peas suggest that flowering was delayed. A final point is that the main effect seemed to be one of dwarfing, which was apparent with all six species tested. (None of them showed any signs of leaf "bronzing.")

Adverse reactions were greater in the growth-chamber than the greenhouse tests, though species differed considerably in their response. For example, 'Little Marvel' peas were severely affected by the high levels of UV irradiation (see Table 4). The plants grown under cellulose acetate had a 30% survival rate, compared with 100% survival for those under Mylar. Also, both the fresh weight and dry weight were significantly reduced. In contrast, the 'Wando' peas, under the same conditions, all survived, though the rate of growth was reduced slightly (see Table 5). The 'Little Marvel' peas were bred and developed for northerly latitudes, whereas the 'Wando' peas were developed for more southerly latitudes, and thus may have inadvertently been bred to be less susceptible to high levels of UV irradiation.

Table 4. Data from Growth-Chamber Tests Using 'Little Marvel' Peas*

	Lighting Conditions**	
Parameters	Cellulose Acetate	Mylar
% of germination	100	100
Avg. no. of nodes to youngest mature leaf	8.7	9.3
Fresh wt./plant (g)	5.70	7.10
Dry wt./plant (g)	0.74	1.10
% survival at harvest	30	100

*Planting date, September 7, 1973; dates of seedling emergence, September 15, 1973; date of harvest, October 10, 1973.

**The values for the two treatments are significantly different at the .05 level in a Duncan Multiple Range test for all parameters except germination.

Table 5. Data from Growth-Chamber Tests Using 'Wando' Peas

	Lighting Conditions	
Parameters	Cellulose Acetate	Mylar
% of germination	100	100
Avg. no. of nodes to youngest mature leaf	12.5	13.6
Avg. no. of nodes to first flower	14.0*	12.9
Fresh wt./plant (g)	0.93	1.52
Dry wt./plant (g)	0.11	0.16
% of seedlings surviving at harvest	100	100

*Only 40 percent of plants flowering at harvest.

Greenhouse Tests

Compilations of data from the greenhouse tests of peas, corn, and tomatoes are shown in Tables 6 to 8. When these data are compared to those for plants grown in a growth chamber, the obvious difference is that greenhouse-grown plants demonstrated less of a reaction to UV-B radiation.

As shown in Table 6, there were no significant differences between *Pisum sativum* var. 'Little Marvel' plants grown under the UV-B treatment (cellulose acetate) and those grown under the Mylar-filtered radiation. The differences between the control plants and those under FS-40 sun lamps filtered with either cellulose acetate or Mylar could be attributed to differences in seed lot.

Table 6. Data from Greenhouse Tests Using 'Little Marvel' Peas*

Parameters	Lighting Conditions: Cellulose Acetate	Mylar
% of germination	71	64
Avg. no. of nodes to youngest mature leaf	12.2	12.3
Avg. no. of nodes to first flower	11.6	11.5
Fresh wt./plant (g)	2.11	2.15
Dry wt./plant (g)	0.29	0.28
% survival at harvest	95	90

*Planting date, Sept. 7, 1973; dates of seedling emergence, Sept. 11-12, 1973; date of flowering, Sept. 30, 1973; date of harvest, Oct. 10, 1973.

As shown in Table 7, the fresh weight and dry weight of the *Zea mays* L. 'Pioneer 3369A' seedlings were reduced by UV-B radiation. Except for dwarfing, all the plants looked normal. There were no malformed leaves, bronzing or yellowing, or mineral-deficiency symptoms.

'Walters' tomatoes grown in the greenhouse were found to be significantly affected by the levels of UV irradiation in these tests (Table 8). The control plants and those grown under Mylar were not significantly different in their fresh or dry weights.

Table 7. Data from Greenhouse Tests with 'Pioneer 3369A' Corn

Parameters	Lighting Conditions: Cellulose Acetate	Mylar	Control
% of germination	100	100	100
Fresh wt./plant (g)	17.7 a*	21.2 ab	24.2 b
Dry wt./plant (g)	1.2 a	1.3 a	1.7 b
% survival at harvest	100	100	100

*Values with different letters in the same row are significantly different at the .05 level in a Duncan Multiple Range test.

Table 8. Data from Greenhouse Tests Using 'Walters' Tomatoes

Parameters	Lighting Conditions: Cellulose Acetate	Mylar	Control
% of germination	93.7a*	93.7a	93.7a
Avg. no. of nodes to first flower	9.85a	10.45a	10.40a
Fresh wt./plant (g)	35.78a	48.88b	43.6b
Dry wt./plant (g)	3.5a	4.6b	4.7b
% survival at harvest	100a	100b	100a

*Values with different letters in the same row are significantly different at the .05 level in a Duncan Multiple Range test.

DISCUSSION AND CONCLUSIONS

Considerable effort was made to ensure uniformity in the field experiments, and replication of each treatment five times should have brought out any significant statistical differences. Filtering out the UV-B radiation existing outdoors in Florida during the springtime had few significant effects on growth and development. The most important change may have been the earlier maturity reached by tomatoes under Mylar. The filtering out of UV-B may have made some difference in the pigments, causing the fruit to be pinker and thus in the "advanced maturity" category.

The results of screening studies in the growth chamber showed a dramatic reduction in growth with UV-B exposure. Nearly all crops screened showed some reduction when irradiated

with levels of UV-B comparable to that which could exist for a 50% reduction of ozone. Considerable variations were obtained from different plants, however, and even within varieties of a certain species, as was noted with peas.

When the same species and varieties were grown in the greenhouse with an equal enhancement in UV-B, much less reduction in growth was observed. In the greenhouse there were higher levels of radiation in the 400-700 nm range (photosynthetically active radiation), and more photorepair apparently occurred.

We now need to better understand the degree of growth reduction resulting from different levels of UV-B irradiation. This will be accomplished by additional research in which a variety of UV-B levels will be used and growth and yield will be measured.

REFERENCES

Prabhakara, C., B.J. Conrad, L.J. Allison, and J. Steranka (1971), "Seasonal and Geographic Variation of Atmospheric Ozone Derived from Nimbus III," NASA-TN-D-6443, Goddard Space Flight Center, Greenbelt, Md.

Setlow, R. and B. Doyle (1957), "The action of monochromatic ultraviolet light on proteins," Biochem. Biophys. Acta. 24, 27.

Wu, J.H., T. Skokut, and M. Hartman (1973), "Ultraviolet-radiation acceleration of leaf chlorosis: Prevention of chlorosis by removal of epidermis or by floating leaf discs on water," Photochem. Photobiol. 18, 71.

DISCUSSION

(UNIDENTIFIED): It seems to me that these experiments suggest that an ultraviolet deletion experiment is a very poor substitute for a supplementation experiment. The plants may have developed mechanisms just adequate to deal with the maximum ambient levels that you experienced, and you should get a disturbed response when you go beyond those levels.

BARTHOLIC: This may be correct, and I hope we will soon be able to clarify that point. In the field experiments we will be getting under way this spring, we will be able to use a wide range of UV irradiation levels and see at what level significant reductions in plant growth occur.

(UNIDENTIFIED): I talked with Dr. Borthwick once about his many years of experience at Beltsville with plant growth. He said almost all his experiments were performed under glass to avoid UV.

BARTHOLIC: This is true. However, Mylar turned out not only to be cheaper than glass but to work well, probably since it did keep short-wavelength UV from entering the greenhouse.

(UNIDENTIFIED): How long have these experiments been under way? How much data do we have here?

BARTHOLIC: Well the experiments basically started a year ago. In fact, we got our contract in January and were in the field at the end of February, so the results are still somewhat preliminary, but we think a significant step has been taken toward evaluating the effect of changes in UV irradiation of plants.

A PRELIMINARY ASSESSMENT OF THE EFFECTS OF UV IRRADIATION ON AQUATIC MICROORGANISMS AND THEIR ECOSYSTEMS

JOHN CALKINS
University of Kentucky
Lexington, Kentucky

ABSTRACT: Solar ultraviolet light, especially the shorter wavelengths around 300 nm (UVB) have demonstrable biological effects. Increasing UVB could have significant effects on aquatic biota; in view of the importance of aquatic organisms to man, this aspect of possible effects of modification of stratospheric ozone should be assessed.

Aquatic ecosystems are composed of large numbers of components which are intricately intercoupled in photosynthetic, predative, and degradative food webs. The aquatic system tends to be especially dynamic, since the bases of the photosynthetic and saprophytic food chains are, in general, unicellular microorganisms rather than the more stable multicellular plants and animals of terrestrial ecosystems. Microorganisms may bloom, populations increase by factors of millions or billions, in a matter of hours. The food-web components exert a feedback control on the ecology through predation and competition for the available resources, and thus further complicate the prediction of the consequences of any particular modification of the environment.

Solar UVB is an agent, which (for aquatic microorganisms) lends itself to assessment through the "replacement-limiting model." The central concept of the replacement-limiting model is that a component of the ecosystem will be gradually eliminated by repetitive injury if the individuals killed (inactivated) by the injurious agent are not replaced before the next exposure. Solar UVB can be approximated as an acute exposure repeating every 24 hours.

The critical parameters which must be determined for application of the replacement-limiting model are the lethality from the daily exposure, the amount of growth which can occur before the next exposure, and the delay of growth due to injury. Radiation lethality and division delay have been determined as a function of dose of simulated UVB for a variety of freshwater microorganisms, including bacteria, yeast, protozoans, rotifers, and flatworms. Optimum growth rates at field temperatures of typical individuals have also been determined.

The organisms tested have been collected from various freshwater lakes, streams, and reservoirs. Laboratory study requires asexual growth in culture; the animals under study are relatively common in the collections and in themselves constitute food webs, e.g., flatworms feed on protozoans which feed on bacteria.

Experiments with simulated solar UVB (using FS-20 lamps plus a Pyrex filter) demonstrate that larger aquatic microorganisms are killed by solar UVB (at summer noontime intensity) in a matter of minutes. The UVB also produces a growth delay which is quite significant in the larger organisms. The observations suggest that changed levels of solar UVB could modify freshwater ecosystems and reduce the efficiency of natural water purification. The assessment of the changes caused by impact of increased solar UVB on humans is complicated by the nature of the organisms, the water body under study, and the quality of water which is considered tolerable.

PROBLEM STATEMENT

In most areas of the world, water resources are quite limited. Precipitation is used again and again in its journey to the sea. Between each usage must intervene a natural or artificial purification process. The natural purification of fresh waters may produce fish through complex food webs: the saprophytes, bacteria and other microorganisms metabolize and incorporate dissolved nutrients, and become prey for protozoan and arthropod carnivores which then directly or through further predation feed the edible freshwater fish. Marine food chains supplying substantial parts of the human food supply likewise depend on the microscopic zoo- and phytoplankton. If a change in climatic factors, such as the amount of solar ultraviolet radiation which reaches the aquatic environment, were to significantly modify the functional ecosystems, major social and economic consequences might ensue. A data base adequate for the assessment of this

problem does not yet appear to exist. Therefore, a series of experimental determinations of critical responses of various components of aquatic ecosystems to exposure to simulated increased solar ultraviolet radiation in the 290-315 nm range (UVB) is being conducted.

Agricultural use is the most economically significant application of the American water resources; obviously, it would be little affected by changes in solar UVB. Precipitation and ground water are largely inaccessible to the radiation and cannot be modified by UVB; the salting of irrigation waters with repeated use is an inorganic phenomenon and modification by UVB could proceed only by very indirect pathways.

The multiple use of water for drinking and waste disposal is vital to an urban society such as ours, even beyond the values measured in economic terms. The critical process of urban use of water involves biological steps which may be quite sensitive to changing levels of UVB. Furthermore, aquatic food production and recreational uses of water are, in general, enhanced by the same natural purification processes which improve water quality for urban utilization. (Details on interrelations in aquatic ecosystems are considered in numerous texts on the subject, such as Russell-Hunter (1970).) The organisms which regenerate our pure water are demonstrably sensitive to UVB. But laboratory measurements of sensitivity are only the beginning of the resolution of the problems inherent in assessing the impact of changing levels of solar UVB. Many aquatic organisms can avoid UVB, and perhaps UVB-resistant strains can adequately substitute for the sensitive biota which would be eliminated by increased levels of UVB. Quantitative data and considerable insight into the interrelation of components of the aquatic ecosystems are indispensable in assessing the impact of UVB changes upon our water resources.

Ecosystems are frequently modeled by means of differential equations relating the individual components to their prey and/or predators (Mobley, 1973). A model three-component ecosystem might be approached as schematically illustrated in Figure 1. Even if only the primary carnivore is assumed to be sensitive to solar UVB, the solutions of the appropriate equations are difficult and require accurate data on food-chain relations, data which is almost non-existent. With biologically reasonable assumptions, the detailed analysis of an ecosystem becomes impossibly complex.

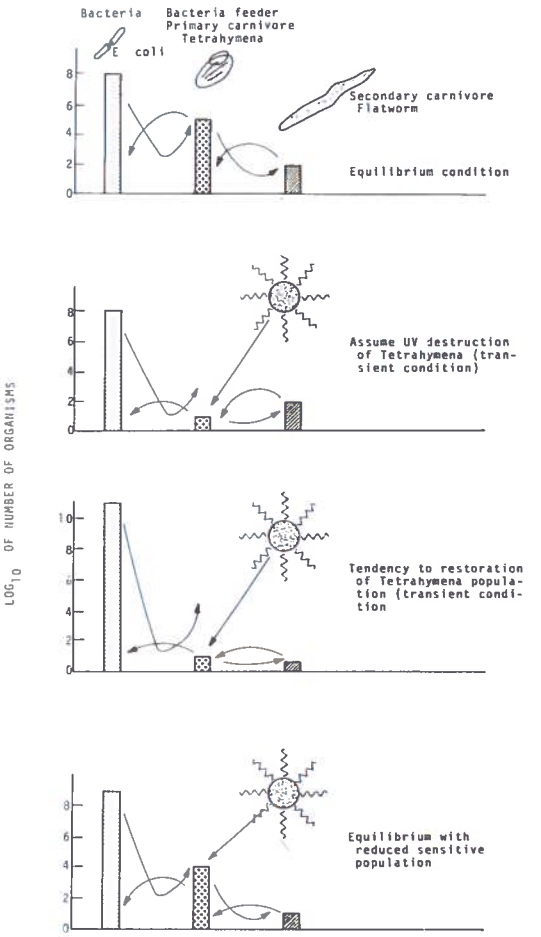

Figure 1. A schematic representation of equilibrium-type modeling of a three-component ecosystem with and without UVB.

Because of the urgency of the need to assess the impact of modified solar UVB on aquatic ecosystems, a new approach has been developed. It is possible to determine the maximum level of a repetitive injury (such as irradiation with solar UVB) which a population of microorganisms (the individual component species of the ecosystem) could withstand. If a population fails to replace those organisms killed by an acute exposure to the repetitive injurious agent before the next exposure occurs, the population will gradually be reduced and ultimately eliminated from the ecosystem. If maximum growth rate and no predation are assumed, the subject species is, in effect, isolated from its normal interactions with

the remainder of the ecosystem. It is obvious that if a species cannot survive a given level of injury under these favorable assumptions, it clearly could not survive under field conditions of high predation and suboptimal growth; i.e., the maximum exposure the species could tolerate would have been established and the actual tolerance would be equal or less. It is implicit in the model that the organism not modify its normal behavior; protective responses are well known, but substantial modification of biology or behavior would have to come at the expense of some evolutionary advantage the organism is currently exploiting. The above considerations have been incorporated into a scheme termed the "replacement-limiting model" (illustrated in Figure 2) for the computation of solar UVB levels which would eliminate common species of organisms from freshwater ecosystems.

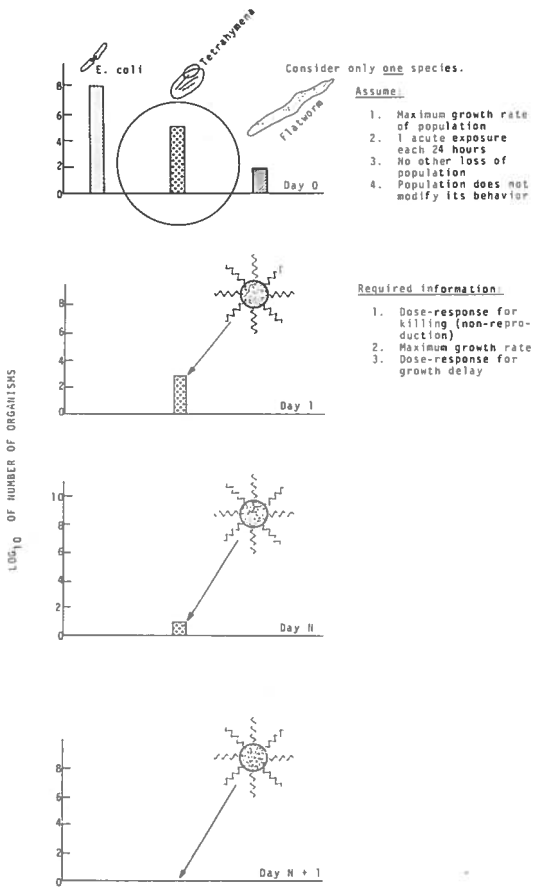

Figure 2. The replacement-limiting model.

As indicated in Figure 2, dose-response data on lethality, growth delay after UVB exposure, and normal growth rates are required for application of the replacement-limiting model. A number of sites have been chosen as typical freshwater situations; the frequencies of a variety of microorganisms in those sites have been determined, and typical species have been subjected to sufficient testing to determine the replacement-limiting dose of simulated UVB.

DESCRIPTION OF THE SYSTEM TO BE STUDIED

Water was collected from a small lake in Kentucky (designated A in Figure 3) and three points (B, C, and D) downstream (along West Hickman Creek) from the lake. Some collections were also made from a relatively "clean" stream (East Hickman Creek) and from a nearby, large, deep lake (Lake Herrington). Each site will be briefly described.

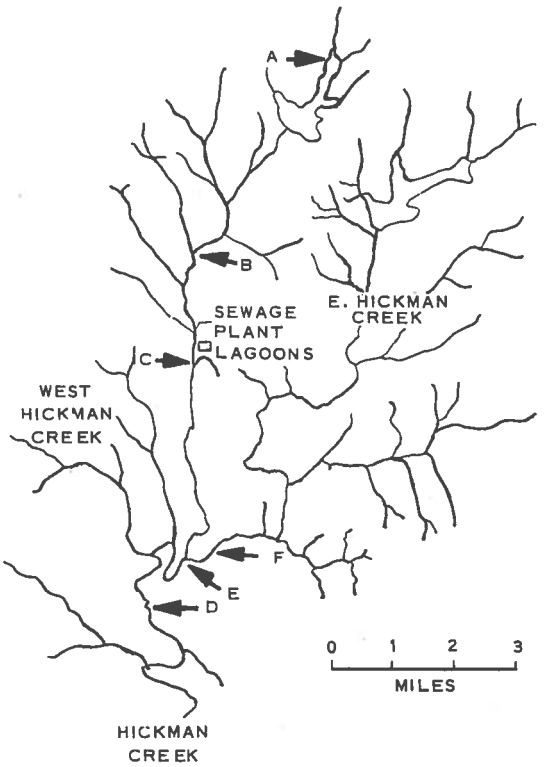

Figure 3. Collection sites.

The small lake is an artificial impoundment belonging to the Lexington Water Company. It is approximately 0.8 km long and is stated to have a maximum depth of 10 m. Although the lake serves as an emergency water reservoir, it is not

regularly used for that purpose. Runoff water from residential and commercial areas flows into the lake with each rainfall; pollution from a leaking sewer line has occurred in the past, but, this is not a current problem. The high quality of the water is evidenced by a large continuous fish population. Collections were made from a water intake structure; the collection point receives almost continual illumination. The intake has not been and probably will not be used during the period of the survey. The water depth at the inlet is approximately 2.7 m; collections were made at the surface and 40-cm intervals to a depth of 2m. (The lake water is relatively turbid, and it is doubtful that significant UVB would penetrate it to depths greater than 2 m.) Also, a shore collection was made from the surface near a permanent stone structure which afforded the location partial protection from sunlight.

The first downstream collection point, B, is approximately 5.6 km below the A collection point. Approximately 1.6 km of the flow is in lakes, there being 3 impoundments in sequence on West Hickman Creek. The flow of the creek to point B includes both urban and rural areas, but no substantial sewage pollution occurs. Point B is exposed to full sunlight for nearly the entire day. As with other points, collections were made from pools, and not a point of rapid or turbulent flow. The flow of West Hickman Creek on a rather typical day was 1.15 m^3/sec. Lexington is subject to extensive and erratic rainfall. After periods of heavy rainfall, it is obvious that flow in West Hickman Creek is several times this amount, and there is extensive washout of biota from the lakes feeding the streams.

The second downstream collection point, C, is approximately 4 km downstream from station B and about 100 m downstream from the outfall of a Lexington municipal sewage treatment plant. The plant includes tertiary treatment, and the outfall is chlorinated.

"Clean" water samples are collected at stations E and F from another tributary, East Hickman Creek, shortly before its confluence with West Hickman Creek. A dam (approximately 9.6 km upstream) on East Hickman Creek provides the major reservoir for the Lexington water supply, the reservoir containing water pumped from the Kentucky River. The flow of East Hickman Creek between the water reservoir and station E is through basically agricultural areas and the creek is considered clean and unpolluted. The collection point is heavily shaded, as is much of East Hickman Creek. Station F is 1 km above station E on East Hickman Creek and is also heavily shaded. It is a pool about 1.3 m deep, and thus useful for UVB-absorption measurements in clean creek water.

Collection station D is on Hickman Creek (below the confluence of East and West Hickman), approximately 8 km below station C. The flow is much larger; East Hickman Creek contributes a substantial addition (4.8 m^3/sec). The collection point is a pool with sides and bottom of limestone rock. The site receives extensive sunlight, being shaded only in early morning and late afternoon.

Collections and absorption measurements were made off a boat dock in Lake Herrington approximately 29 km from Station D. Lake Herrington was formed by damming a deep canyon of the Dix River slightly upstream from the Kentucky River. It is approximately 64 km long, very narrow and deep. At the collection point, the lake is slightly more than 0.4 km wide, has almost vertical banks, and is 61 m deep.

WATER SAMPLES

Water samples were collected in 125-ml bottles. The sample bottles were opened and stoppered at the sampling levels. The samples were cooled during the interval between collection and analysis, but not brought to freezing point. No effort was made to concentrate organisms within the sample.

Counting of Samples

Agar-Plate Colonies

Samples of appropriate size were spread on nutrient agar plates. The plates were incubated at room temperature ($\approx 25^{\circ}C$) for 72 hours before counting. The plating medium was that suggested by the American Public Health Association for water examination. The colonies were counted and clones selected at random for radiation study.

Microorganisms

Samples of appropriate size were scanned with a low-power dissecting microscope. Organisms were removed by freehand micropipettes as they were counted. Samples as small as 0.01 ml (measured by lambda pipette) were used when there were numerous tiny organisms. Larger samples were used to determine the incidence of more rare organisms. Preliminary observations suggested that although there were a great many organisms present in the lake and occasionally in the streams, there was not a large variety of species present in appreciable numbers, so classification of the majority of larger microorganisms such as protozoans, algae, rotifers and arthropods present in a 1-ml sample might be technically possible. Only motile organisms were counted; no large incidence of non-motile organisms (larger than bacteria) has been observed. The accuracy of counting very small organisms such as tiny flagellates or ciliates is, of course, subject to substantial error. After counting, some of the samples were observed under a high-resolution microscope, and the number of non-bacterial organisms remaining uncounted indicated that any errors in the counting procedure were not large.

Preparation of Samples for Further Study

Agar-Plate-Grown Organisms

Pure colonies were removed from the primary field-collection plates and suspended in a cold nutrient medium. The optical density of the suspension was adjusted to 0.1. Using a lambda pipette, 0.01- and 0.001-ml samples were deposited at marked positions on a 150- or 100-mm agar plate. Sixteen colonies were tested per plate; usually eight clones per station were tested. The organisms were irradiated at approximately 8°C on the agar surface. The number of colony-forming organisms deposited in the samples was determined by serial dilution, plating, and counts of viable colonies. After irradiation, the plates were incubated 72 hours and the presence or absence of colonies in the various positions was noted. Since 20 to 1000 viable organisms were originally present, growth of fully viable cells was quickly confluent; however, when radiation had reduced the numbers of viable organisms to low numbers (1-50), individual colonies could often be resolved and counted. Thus, relatively accurate determinations of dose-survival response may be made by what is essentially a screening technique.

Liquid-Cultured Organisms

After the various microorganisms in the samples had been counted, a variety of motile unicellular organisms (excluding bacteria) were removed with a micropipette and deposited in 0.25-ml drops in plastic plates containing 32 depressions. A variety of media were used; food-web relations were used and tested when possible. The organisms were checked for growth at frequent intervals, and those organisms showing substantial growth ability were transferred several times, using an appropriate medium.

Both rotifers and two of the worms demonstrated growth capacity when isolated in large drops in plastic plates with *Tetrahymena* as food organisms. Radiation and re-isolation of larger invertebrates will follow the same general pattern as used for protozoans, but larger volumes, such as quartered plates, may be required for substantial growth.

Organisms were irradiated with UVB in drops of mediums of low absorbance; they were subsequently isolated into suitable mediums, observed, and scored for growth capacity.

It is doubtful that complete growth cycles of arthropods can be sustained within the limitations of this project; therefore, future radiation studies of higher invertebrates and small vertebrates may be limited to determination of the doses required to produce early death of collected organisms which otherwise demonstrate considerable average lifetimes under laboratory conditions.

It has proven difficult to culture many of the organisms collected from the various stations. Some data are included in this report on the response of strains of *Tetrahymena* and *Paramecium* collected in Texas and a strain of *Paramecium* collected in Kentucky prior to the start of this project. Some of the other organisms were grown and tested but died out before complete data were obtained. Since the organisms are common, they will be further tested

when they reappear with warm weather. Other organisms are under test and more complete and diversified data will be available in the near future.

SIMULATION OF SOLAR UVB

A completely experimental assessment of solar UVB effects on aquatic ecosystems would require not only very sophisticated model ecosystems, but simulation of the total solar spectrum to which increments of UVB could be added. Furthermore, the spectral composition of the simulator would need to shift to match the daily variations in UV and visible intensities. Such complex and complete simulations are clearly beyond the scope of the present experimental program. A solar-UVB irradiation system has been designed which provides a spectral output closely resembling the most critical range of wavelengths (290-310 nm) with a zenith angle of 0° and a substantially reduced ozone column. The UVB simulator consists of a bank of eight Westinghouse FS-20 lights, a variable transformer to control the voltage applied to the lamps, and Pyrex plates of nominal 1/4-in. to 1/2-in. thickness which filter the light output to produce the desired spectral relationship (illustrated in Figure 4). The simulator does not attempt to provide the same level of photoreactivating light as would be available in natural sunlight; however, experimental data suggest that maximal photoreactivation does occur, as might be expected from the substantial near-UV and visible light present in the filtered FS-20 output.

The Robertson sensor, a device whose response to UVB is weighted so as to simulate the biological effectiveness of UVB (Robertson, 1972), was used to calibrate the simulation apparatus. Robertson-meter readings are not single-valued functions of either intensity or spectral distribution or their simple combination. The intensity used produced 15 nanoamps of current in the meter; the biological action of 1 minute of exposure at 15 nA would be expected to approximate the effect of 1 minute of summer noontime Kentucky sunshine (Figure 5). (It is recognized, of course, that there will be differences in detail in the action of the two radiation exposures because of details of action spectra, photoreactivation, etc.) 400 counts on the Robertson meter, equivalent to 24 minutes of this noon sunshine, is defined as a sunburn unit (SU); the SU is the principal unit used in reporting the results of these experiments.

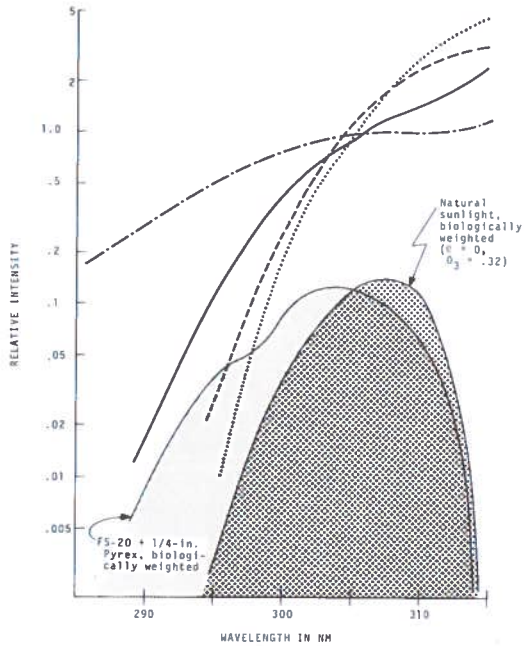

Figure 4. A semilog plot of the characteristics of the simulator system. —·—, FS-20 lamp; ——, FS-20 filtered by 1/4-in. Pyrex; - - - -, $\theta = 0$ and $O_3 = 24$ cm; •••••, $\theta = 0$ and $O_3 = .32$ cm. The various intensities have been normalized to the 305-nm value. The biological effectiveness has been computed by multiplying the relative intensity by Caldwell's (1971) biological weighting factor.

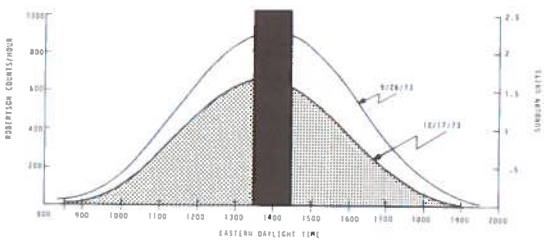

Figure 5. A comparison of weighted UVB doses and rates produced by natural sunlight and the simulation apparatus as measured by the Robertson sensor. The area of the control bar indicates 1 hour of exposure in the simulator (2.5 SU). The areas beneath the curves indicate the exposure on two clear days in Lexington, Kentucky.

The total intensity (IR excluded by a quartz filter) using eight FS-20 lamps filtered by 1/2-in. Pyrex was measured as 40 ergs/mm^2/sec, using a calibrated thermopile. The Robertson sensor indicated the intensity of UVB as filtered by the 1/2-in. Pyrex plate to be only 0.28 of the summer noontime intensity. The 1/4-in. plate provides intensities from 0.7 - 1.6 times the summer noontime intensity, depending on the voltage applied to the FS-20's. The 1/2-in. Pyrex filter provides a good simulation of sunlight UVB, but the low intensity is only minimally biologically effective, and the 1/4-in. filter with a dose rate equivalent to noon sun is most convenient and has been used for almost all simulation studies. When the solar UVB spectrum is weighted for biological effectiveness as suggested by Caldwell (1971) the peak of action occurs between 305 and 310 nm; such weighting of the FS-20 plus 1/4-in. Pyrex gives a peak action somewhat below 305 nm but clearly above 300 nm (see Figure 4).

PRELIMINARY RESULTS

Agar-Plate Colony-Forming Microorganisms

Figure 6 illustrates dose-response relations of a number of microorganisms (primarily bacteria) isolated from the indicated depths in the lakes (stations A and H). These organisms are clearly quite heterogeneous in their resistance to UVB. Observations to date suggest that the distribution of resistance in a natural population is quite variable and complexly dependent upon a number of factors including runoff, nutrients, sunlight, mixing, etc. Resolution of the importance of these variables will be attempted when sufficient data is available.

Figure 7 shows the normal growth, UVB survival, and growth delay of selected bacteria and yeasts at about 50% survival. Growth at 22°C and 10°C were determined, since these temperatures were typical of the lakes in summer and winter. From such data as is illustrated in Figures 2 and 7, the replacement-limiting dose for the indicated organisms (see Table 1) has been computed.

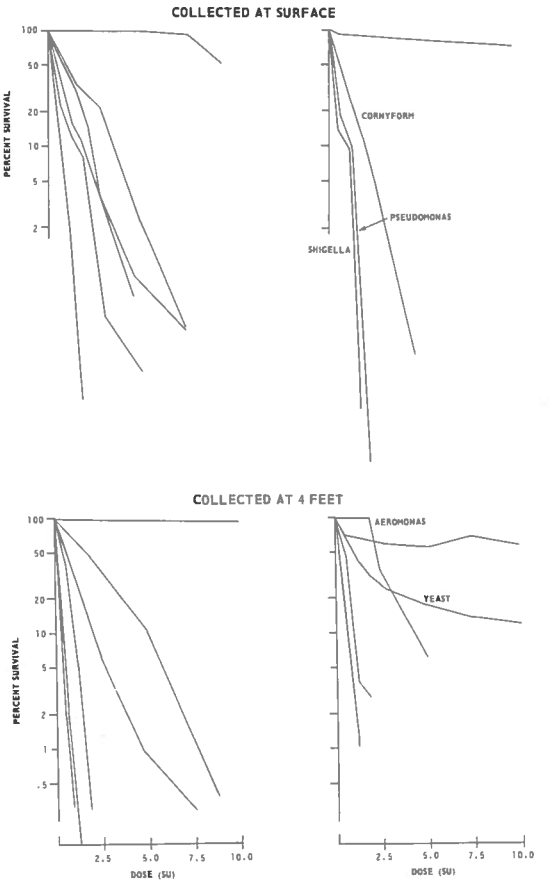

Figure 6. Typical UVB survival of agar-plate colony-forming organisms at a dose rate of 2.5 SU per hour. Those on the left are from reservoir station A; those on the right are from Lake Herrington. Data on numerous other organisms from site A are available; the organisms from Lake Herrington represent the majority of those present in the summer collection.

Liquid-Cultured Invertebrate Microorganisms

Figure 8 shows dose-response relations for killing and division delay, together with normal growth rates for protozoans of a variety of sizes, and some preliminary data on rotifers, roundworms and flatworms. No data on growth at 10°C has been included, since it was observed that the larger microorganisms have virtually disappeared from the winter field collections. The only winter collection with appreciable numbers of organisms larger than bacteria was the one made in the lake outlet after a period of heavy rain, suggesting that the protozoans may overwinter deep in the lake. Bacteria and other

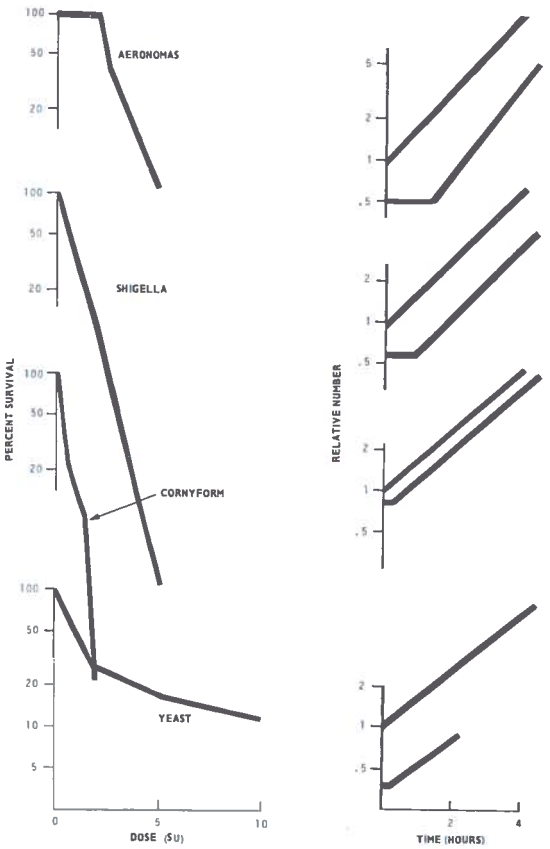

Figure 7. Survival (left) and division delay (right) of bacteria and yeast after UVB irradiation at a dose rate of 2.5 SU per hour. The delay was determined after 50% of the lethal dose; i.e., there is a 1.25-SU difference between the upper and lower lines in each of the right-hand figures.

agar-plate colony-forming units remain high in numbers in winter. The types of data shown in Figure 8 have been used to estimate the RLD values shown in Table 1.

ANALYSIS

A successful biological purification of water polluted through urban uses will render the contaminated water satisfactory for further urban use and should, as a by-product, provide recreational and food-production functions as well. It is possible to compensate for the deficiencies in water quality; with sufficient chlorination, foul water can be made safe to drink, but recreational and food production from fresh waters can be, and have been, extensively sacrificed in our current culture. Nevertheless, improved water resources are an important factor in improving the quality of life in an environment whose degradation threatens the basic values of human existence.

Full assessment of the impact of UVB on aquatic ecosystems is doubtless far in the future, but the urgency and importance of the problem compel an attempt to evaluate at least the general trends of effects which might be expected from increased UVB irradiation. The various problems, and the poor and incomplete data now available, have been generalized into a model situation outlined below.

The biological purification of urban forms of water pollution can proceed along the two distinct pathways, termed photosynthetic and saprophytic, diagrammed in Figure 9. For schematic representation, the two pathways are separated, but in fact they are inextricably interwined. Photosynthesis provides oxygen and nutrients for the saprophytic pathway; detritus decomposed by saprophytes nourishes the photosynthesizers. In the biologically productive areas of the earth, the processes often share the same physical space. It can be assumed that the rate of biological purification of water will be linearly proportional to the number of organisms participating.

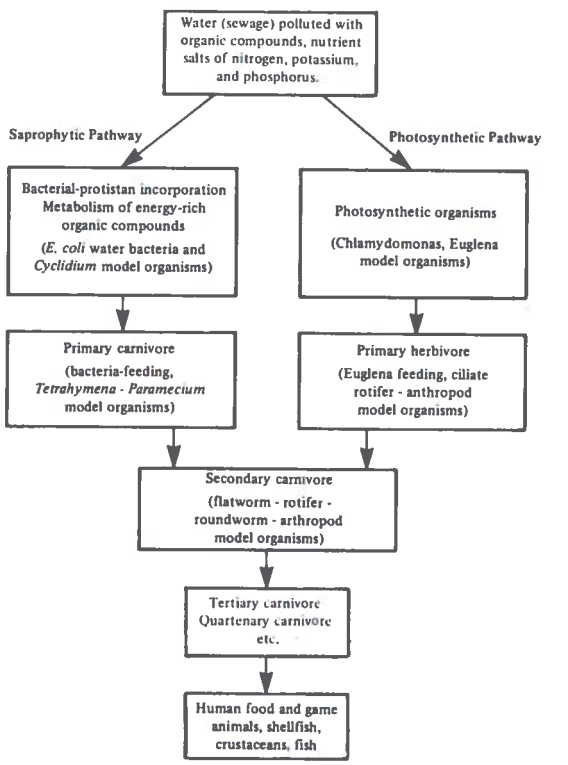

Figure 9. Water purification scheme.

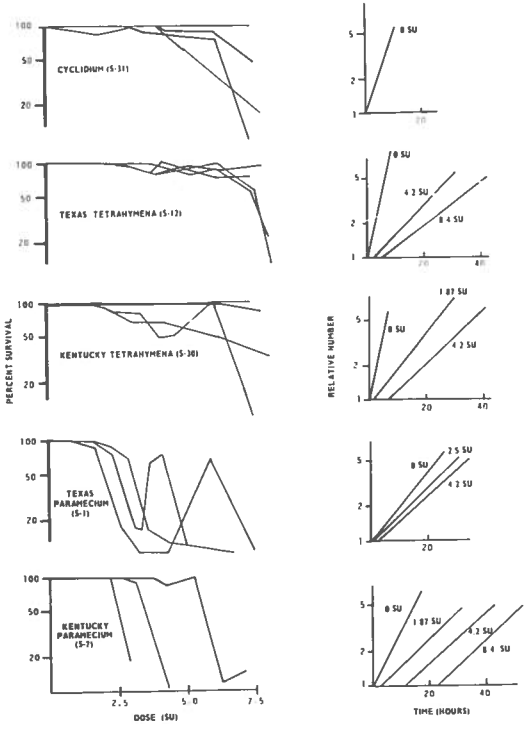

a. Survival (left) and division delay (right) of protozoans after UVB irradiation. Survival is for several typical responses of the organisms at a dose rate of 2.5 SU/hr. (Non-monotonic responses have frequently been observed; the origin of the paradoxical response is under investigation.) The growth delays are for the different dose rates indicated.

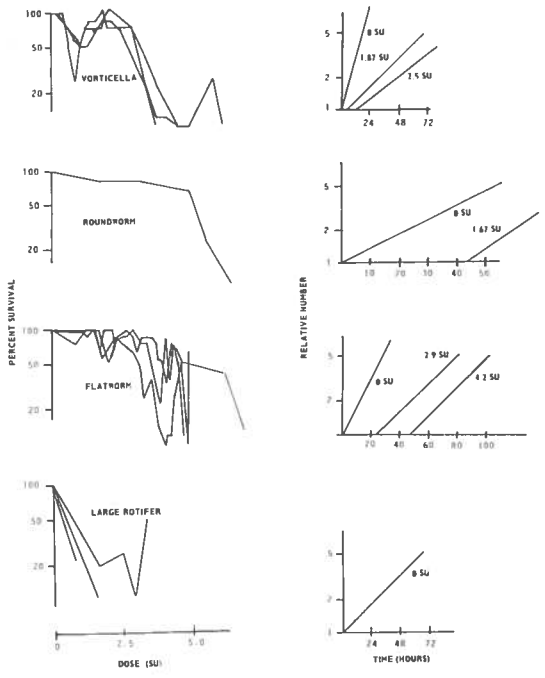

b. Survival (left) and growth delay (right) of vorticella (a large species) and three multicellular microorganisms, under the same conditions as described in (a). These organisms also demonstrate complex survival behavior, which is under study. The two worms feed on *Tetrahymena*; all the organisms grow asexually.

Figure 8. Dose-response relations for liquid-cultured microorganisms.

Table 1. Growth Delay and Replacement-Limiting Dose of Various Microorganisms

Organisms and Collection Point	Summer (24°C) Doubling Time	Estimated Growth Delay at 50% or RLD	RLD in SU	RLD in Minutes of Noon Summer Sunshine
Aeromonas Station H	80 min	2 hr	≈ 12	300
Shigella Station H	80 min	2 hr	≈ 10	240
Cornyform Station H	90 min	≈ 40 min	≈ 5	120
Yeast Station H	90 min	≈ 2 hr	⩾ 10	⩾ 240
Cyclidium Station A	3 hr	–	> 7.5	> 180
Tetrahymena Texas	2.5 hr	6 hr	≈ 10	240
Tetrahymena Kentucky	3 hr	6 hr	≈ 9	210
Paramecium Texas	8 hr	3 hr	≈ 4	96
Paramecium Kentucky	6 hr	12 hr	≈ 4	96
Vorticella Station A	8 hr	12 hr	≈ 2.5	60
Roundworm Station A	24 hr	> 40 hr	< 1.6	< 30
Flatworm Station A	20 hr	> 24 hr	< 2.5	< 60
Large Rotifer Station A	30 hr	–	< 1.25	< 30

Each step in either pathway produces water of higher purity, and the more rapidly the biological purification process proceeds, the more clean, useful water is available. However, since pure, clean water is a commodity in great demand, even at the possible expense of food production, biological purification may be delayed or sacrificed: chlorination of sewage effluent can render receiving waters abiotic for miles downstream, and water reservoirs are often so mineral-rich that they support luxuriant algae growths (the first step in photosynthetic purification beginning where it should have been completed), which leads to expensive, low-quality drinking water.

It might at first appear that UVB affects only a minute volume at the surface of the various natural water bodies. However, further examination of the situation shows that the solar UVB may nonetheless be an important factor in the ecology of fresh waters. The photosynthetic pathway of biological purification cannot be of significance below the euphotic zone, the zone in natural waters in which daily photosynthetic production (of oxygen) equals or exceeds respiration and decompositional utilization. The euphotic zone is commonly estimated as being the layer of water receiving 1% or more of the incident solar radiation (Holmes, 1970). Figure 10 indicates, for the seven collection stations, the euphotic zone (as defined above), the fraction of the euphotic zone which receives 1% of the surface UVB, and the fraction of the euphotic zone which would receive the current 1% if the UVB were increased by a factor of 3 (see Figure 7 in Green, 1974), which approximates the upper limits assumed in the CIAP program. One might expect the stream stations where the euphotic zone extends to the bottom to be the most affected, but planktonic alge are exceedingly rare

in the streams and have occurred in appreciable numbers only as washout from the reservoirs after heavy rains. At the A station, the UVB-affected volume would be increased from 36% to nearly 50% of the euphotic zone if UVB irradiation were tripled. A more comprehensive analysis of the effects of increased UVB on the photosynthetic pathway will be made in the near future when sufficient data on algae survival is available to apply the replacement-limiting model.

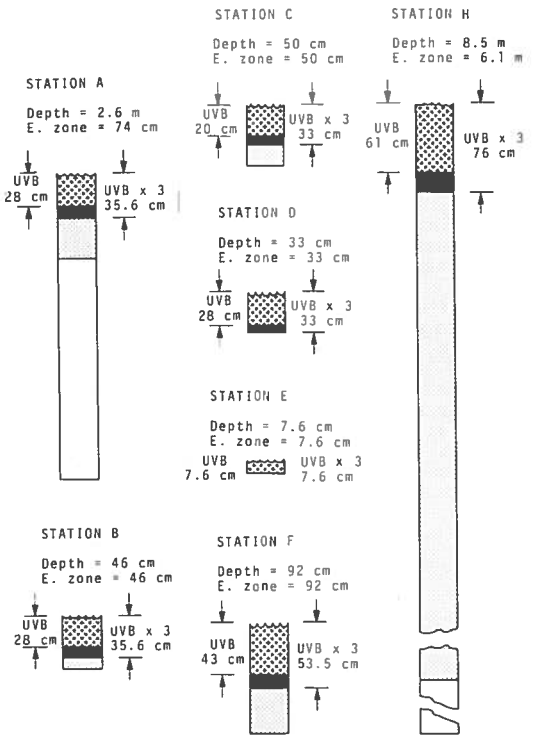

Figure 10. The depth of the euphotic zone (E), the portion of the euphotic zone presently receiving 1% of the surface UVB, and the portion of the euphotic zone which would receive 1% of the surface UVB if the biologically weighted UVB increased by a factor of 3, the approximate maximum value implicit in the CIAP assumptions (see Green (1974)).

Although the photosynthetic zone of natural waters is limited, the saprophytic pathway seems to function throughout the entire volume of natural waters. Again, this may be an erroneous conclusion. The metabolism of energy-rich compounds is complete and efficient only where oxygen is abundant. A rapid, turbulent stream may provide abundant oxygen throughout the water, but placid streams (Noel, 1951), rivers, and lakes (Goulder, 1972) can develop an oxygen gradient and the metabolism of organisms at depth becomes limited by the low level of dissolved oxygen. Data are being assembled to estimate the depths at which the most active purification of water occurs and how these zones, which must be near the surface to obtain large amounts of oxygen, would be affected by increased solar UVB.

The actual concentration of oxygen in waters is exceedingly complex because of the nature of diffusion and turbulent mixing (Phelps, 1944). If oxygen came entirely from diffusion through quiescent water (no photosynthetic or turbulent transport), the transport of oxygen in water would be governed by the following diffusion equation

$$m = \frac{\Delta(d_2 - d_1)\,t}{h}$$

where m is the mass per unit volume, Δ is the diffusion coefficient, d_1 and d_2 are concentrations at the two positions, h is the distance of diffusion, and t is time.

The mass of oxygen transported per unit of time is inversely proportional to the distance between the source (air) and sink (saprophytic organism). If a surface-dwelling organism (at 1 cm, for instance) is presently at its limit of tolerance of solar UVB, then in a typical water body the organisms would have to sink to approximately 9 cm to survive a three-fold increase of UVB. The oxygen transport would then be only 11% of the surface rate, and the rate of oxidation of pollutants would be similarly depressed. The effect in clean lakes such as Lake Herrington (Station H) would be greater, a fifteen-fold reduction in oxidation.

The possibility of driving the natural biological purification processes deeper into the euphotic zone or away from the oxygen supply makes it imperative to assess the resistance of organisms to present levels of UVB and to determine their reserve capacity of tolerance to increased UVB. It is clear that almost all species existing in the current environment must be tolerant to some exposure to solar UVB, but sufficiently high doses of UVB can kill any microorganism tested so far. However, it is essential to specify some exposure in between which would be the limit of tolerance.

As a first approximation we may use the replacement-limiting dose as the limit of tolerance of the various aquatic organisms. Only bacterium No. 1 from Lake Herrington (probably the more resistant bacterial strains from A station), the two *Tetrahymena*, and *Cyclidium* show resistance to solar UVB level exceeding daily surface exposure. (Tetrahymenal resistance may well prove to be overestimated when more accurate determinations of the radiation-induced division delay are available.) The technique used to simulate solar UVB might cause low estimates of resistance, since only a limited amount of photoreactivating light is available in the simulator. However, the source does contain near-UV and visible wavelengths (both effective in photoreactivation), and photoreactivation relative to the UVB effect will be determined for both sunlight and the simulator.

On the other hand, the replacement-limiting model assumes that the growth rate will be maximal and that UVB exposure is the only cause of lethality in the population; if less favorable assumptions were made, it might be found that even small UVB exposures were intolerable. The behavior of the various organisms is in accord with the hypothesis that solar UVB limits the habitat of the various species. The *Cyclidium*-type organisms (resistant) are relatively common in lake collections from all levels. *Tetrahymena* (also resistant) occur less frequently and more often at depth; the large rotifers and the flatworms (sensitive organisms) have been found only at substantial depths. *Paramecia* (relatively sensitive) which in the laboratory live almost exclusively at the surface of the vessel, have never been found in exposed-surface collections, and are quite rarely observed in any collections for this project.

CONCLUSION

If further studies confirm the trend of the observations reported here – that the majority of the microorganisms found in any particular habitat are near the limit of solar UVB which they can tolerate – then increasing UVB levels by 25-300% would profoundly disturb the microorganism ecology. Organisms which compete relatively poorly at present might become dominant in the new situation. Photosynthetic and saprophytic purification of water would tend to be impaired, and further observations and calculations to assess the magnitude of this impairment are in progress.

REFERENCES

Caldwell, M.M. (1971), "Solar UV radiation and the growth and development of higher plants," in *Photophysiology*, VI, ed. A.C. Giese, Academic Press, New York.

Goulder, P. (1973), "The vertical distribution of some ciliated protozoans in the plankton of a eutrophic pond during summer stratification," Freshwater Biology 2, 163.

Green, A. and R.A. Sutherland (1973), "Instrumentation for ground MUV irradiance," in Volume V of the CIAP monographs, U.S. Department of Transportation. NOTE: At present, these monographs exist only in an early draft form. They will be publicly available after completion in September 1974.

Holmes, R.W. (1970), "The Secchi disk in turbid coastal waters," Limnology and Oceanography 15, 688.

Ingraham, J. (1958), "Growth of psychrophilic bacteria," J. Bacteriol. 76, 77.

Mobley, C.D. (1973), "A systematic approach to ecosystems analysis," J. Theoret. Biol. 41, 119.

Noel, J.K. (1951), "Interrelations of certain physical and chemical features in a headwater limestone stream," Ecology 32, 368.

Phelps, E.B. (1944), *Stream Sanitation*, John Wiley and Sons, New York.

Robertson, D.F. (1972), "Solar ultraviolet radiation in relation to human sunburn and skin cancer," Ph.D. Thesis, University of Queensland (unpublished).

Russell-Hunter, W.D. (1970), *Aquatic Productivity*, MacMillan, New York.

DISCUSSION

DANIELS: I think Dr. Calkins made a fine, and indeed conservative, statement of what I think is the most important aspect of all this climatic-change research. I'm here on skin cancer, but an increase in cancer would be minor compared to upsetting the natural ecosystems. About a billion years ago, the oxygen concentration is believed to have increased to the point that it permitted the development of multicelled organisms; I'd rather not reverse the process.

(UNIDENTIFIED): Can your fresh-water results be extended to the oceans – to plankton and the food chains there?

CALKINS: We can only speculate about that; they're kind of far from Kentucky.

NACHTWEY: I have some research on that under way right now. We're studying a single unicellular alga to determine the parameters to use in studying a number of other algae, particularly the ocean phytoplankton. We have found that the UV dose rate is highly critical for this alga; doubling the rate increases mortality by a factor of four.

AN EPIDEMIOLOGICAL INDEX FOR SKIN-CANCER INCIDENCE

A.E.S. GREEN AND T. MO
University of Florida
Gainesville, Florida

ABSTRACT: An epidemiological index, based upon an analytic form of the latitudinal dependence of annual ultraviolet erythema dose, is presented. Allowances are made for variations in cloud cover, cloud and smog thicknesses, ground albedo, and ground elevation. A relationship between this index and skin-cancer incidence is also proposed. The change in the index with a fractional depletion of the ozone thickness is estimated. Finally, simple relationships are suggested for estimating the changes in skin-cancer cases with fractional depletion of the ozone layer.

INTRODUCTION

Recently, a series of investigations of solar ultraviolet (UV) radiation and the associated erythema doses has been undertaken at the University of Florida in connection with the Climatic Impact Assessment Program (CIAP). Figure 1 shows the relationships of these studies with each other and with other studies. In the first of this recent series (Green, Sawada, and Shettle (1974), to be referred to hereafter as GSS) a semi-phenomenological analytic formula for expressing the UV irradiance in the 280-340 nm region is presented.

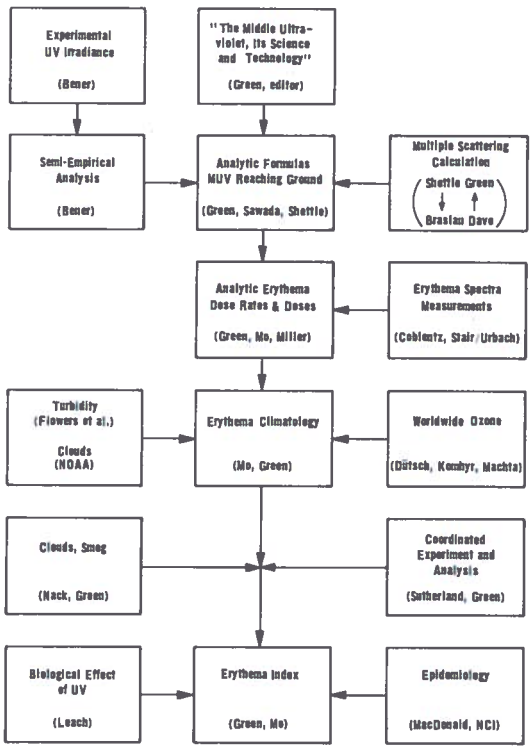

Figure 1. Interrelationships of the studies of solar ultraviolet radiation and the associated carcinogenic erythema dose.

The formula adequately represents the experimental spectral-irradiance results, at various solar zenith angles, accumulated by Bener (1972) over a ten-year period. The GSS paper also encompasses the ab-initio radiative-transfer calculations of Shettle and Green (1974) for a variety of atmospheric conditions, ozone models, aerosol distributions, ground altitudes, and albedos. These calculations are in reasonable accord with the results of Braslau and Dave (1973).

In the study by Green, Mo, and Miller (1974) (GMM), semi-empirical analytical formulas for the erythema dose rates and sizes as functions of geographic latitude, season of year, and ozone concentration are established on the bases of the GSS formulas and an analytic representation of the standard erythema spectrum of Coblentz and Stair (1934). The study by Mo and Green (1974) utilizes the GMM formulas to produce a map of the climatology of daily erythema doses, for the northern hemisphere and for ten metropolitan areas, under various assumed and realistic atmospheric conditions. In addition, an analytic expression for the annual erythema dose (summation of the daily erythema doses over 365 days) as a function of geographic latitude is presented.

The present study is an attempt to use these studies to establish an epidemiological index related to skin-cancer incidence. Its purpose is to provide a basis for making estimates of possible increases in incidence associated with possible changes in the ozone layer.

AN INDEX RELATED TO ANNUAL ERYTHEMA DOSE

Mo and Green (1974) have shown that the annual erythema dose for a cloudless sky can be accurately represented as a function of latitude by the analytic expression

$$AD(L) = \frac{B}{1 + \exp\left(\frac{L - L_0}{L_f}\right)} \qquad (1)$$

where AD(L) represents the annual erythema dose in effective joules/m^2 or (joules/m^2)$_e$ at the latitude L (in degrees). The adjustable parameters B, L_0, L_f are obtained by fitting the numerically calculated results of annual erythema doses. The points in Figure 2 show annual erythema doses calculated with the experimentally determined worldwide ozone distribution (Dütsch, 1969), which depends on the geographic latitudes and seasons of the year, and with an assumed ground albedo of 0.05. The solid curve in Figure 2 represents the fit to these points obtained with Eq. (1) and the following rounded set of parameter values:

B (J/m^2)$_e$	24.1 X 10^5
L_0 (deg)	30
L_f (deg)	15

Calculations with a 5%, 10%, and 20% reduction of this ozone distribution are also exhibited in Figure 2. These enhanced annual erythema doses for various decrements in the amount of ozone will be discussed further on. For the purposes of epidemiological studies of present skin-cancer incidence rates, it would be useful to establish an index which could characterize the relative annual exposure to erythemogenic UV radiation at any location. We would like to include the influence of variations in cloud cover, cloud and smog thickness, ground albedo, and local ground elevation. On the basis of our previous studies, we propose as a relative index

$$I = 100 \frac{1 - \Gamma e^{\theta} C_{\ell}}{1 + \exp\left(\frac{L - L_0}{L_f}\right)} \times \frac{\exp\left(\frac{h}{H_0} - \frac{\tau_s}{\tau_{s_0}}\right)}{1 - r_0 A} \quad (2)$$

where

$$\theta = \left(\frac{\tau_c}{\tau_{c_0}}\right)^{1/2} - 1 \quad (3)$$

The denominator of the first factor allows for the latitude dependence of the annual carcinogenic dose, which is assumed to follow that of the erythema dose. The numerator of the first factor, which allows for the cloud cover (C_{ℓ}) and cloud thickness (τ_c), is based upon the work of Büttner (1938) and of Nack and Green (1974). Values of C_{ℓ} (measured in tenths from 0-10) for many metropolitan areas can be obtained from the Climatic Atlas (NOAA, 1969; see also Mo and Green, 1974). Unfortunately data does not appear to be available on cloud thickness. The denominator $(1 - r_0 A)$ in the second factor corrects for the ground albedo (A); r_0 is an approximate air-ground-air reflection coefficient for the solar radiation in the 300-320 nm interval (see Shettle and Green (1974)). Values of A can be as large as 0.75 for snow conditions. The factor $e^{h/H}$ represents the influence of local ground elevation (h) as suggested by the results of Bener (1972). The factor $\exp^{(-\tau_s/\tau_{s_0})}$, where τ_s is the smog optical depth at $\approx$ 305 nm, is a correction suggested by the results of Nack and Green (1974). The estimated values of the fixed parameters in Eqs. (2) and (3) are as follows:

H (km)	8
τ_{s_0}	4.2
Γ	0.056
τ_{c_0}	15
r_0	1/3

The factor 100 in Eq. (2) is a relative constant, arbitrarily assigned to make the I values fall into a convenient range.

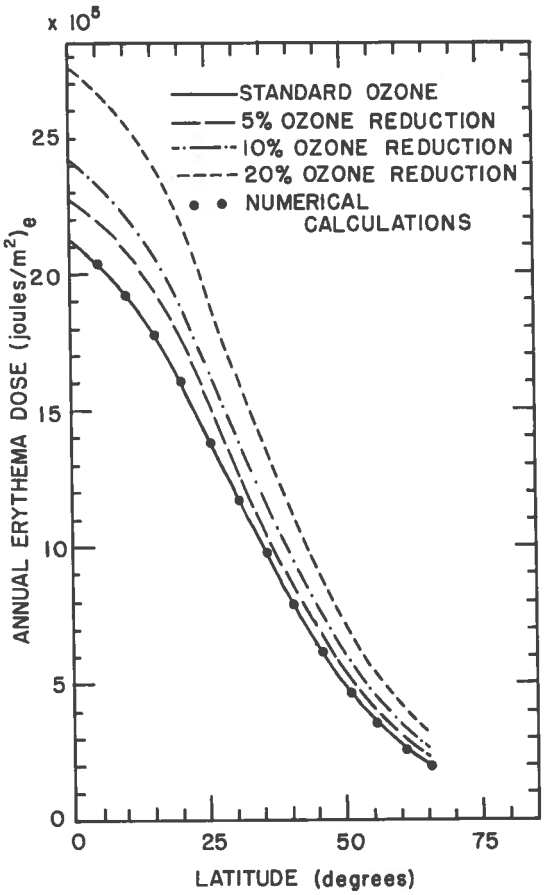

Figure 2. The annual erythema doses in effective joules/m^2 or (joules/m^2)$_e$ calculated for a "standard ozone column" (measured world-wide ozone) along with 5, 10, and 20 percent reduction of this "standard" ozone.

THE ERYTHEMA INDEX AND SKIN-CANCER INCIDENCE

Worldwide data on skin-cancer incidence and melanoma have been assembled by Leach (1974). Figure 3 shows the relationship between these data and a simplified epidemiological index I_s, based entirely upon the first factor in Eq. (2) and with $\theta = 0$. Despite these

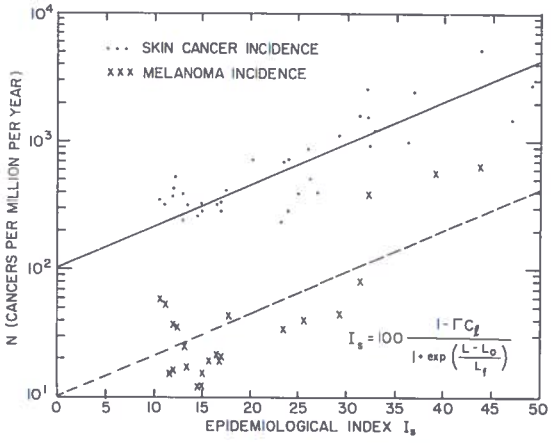

Figure 3. Relationships between the skin cancers (melanoma) and the epidemiological index I_s. The data on skin cancer and melanoma were assembled by Leach (1974). The solid line was drawn through most of the cancer-incidence data (dots), and the dashed line through those of melanoma (x's). The values of I_s were calculated with a "standard" ozone distribution (see the solid curve in Figure 2). An average cloud-cover factor of $(1-0.56\,\overline{C})$, obtained from the $\overline{C}$ data of Leach (1974), was included in this calculation.

simplifications, the skin-cancer incidence (denoted by the dots) generally falls along the solid line and the melanoma data very roughly follows the dashed line. This figure suggests that the skin-cancer incidence increases exponentially with the epidemiological index I according to the formula

$$N = N_0 \exp\left(\frac{I}{I_0}\right) \tag{4}$$

where N is the total number of skin cancers per 10^6 population per year, N_0 is the value of N corresponding to I = 0 ($N_0 \approx 100$ for skin cancer and ≈ 10 for melanoma, according to the data assembled by Leach), and $I_0 \approx 13$. It should be clear that N is an implicit function of L, C_ℓ, τ_c, A, h, and τ_s through the epidemiological index I.

THE INFLUENCE OF CHANGES IN THE OZONE LAYER

Returning to Figure 2, let us consider now the influence of the possible anthropogenic changes in the ozone thickness which are of concern to the CIAP program. To this end, we have numerically generated the expected annual erythema doses for various fractional depletions of the ozone layer ($f = -\Delta w_{O_3}/w_{O_3}$). The additional curves in Figure 2 represent some of these results. Then, using Eq. (1) and a non-linear least-squares fitting routine, we have identified the parameters B and L_0 as given in Table 1. In these fittings, the parameter L_f is kept at the constant value of 15°. We found that the parameters B and L_0 can be expressed accurately as exponential functions of f. On the other hand, the L_0 values shown in Table 1 indicate a small variation in the interval of $f = 0 \rightarrow 0.2$, which is the region of most interest. Therefore, for simplicity in initial application, we have approximated L_0 by the constant value of 30°. With $L_f = 15°$ and $L_0 = 30°$, the only remaining adjustable parameter B can be fitted by

$$B = B_0(1 + \alpha f) \tag{5}$$

where $\alpha \approx 5/3$ and $B_0 = 24.1 \times 10^5$ (joules/m^2)$_e$. This result suggests that we may now use a modified epidemiological index given by

$$I' = I(1 + \alpha f) \tag{6}$$

in conjunction with Eq. (4) to arrive at a modified skin-cancer incidence rate

$$N' = N_0 \exp\left(\frac{I'}{I_0}\right) \tag{7}$$

Eqs. (7), (6), (3), and (2) thus constitute a final epidemiological-index/skin-cancer-incidence relationship which might be useful in estimating modifications to skin-cancer incidence occasioned by anthropogenic changes in the ozone layer.

Table 1. Best-Fit Parameters for the Annual Erythema Doses AD(L), Calculated for 5, 10, 20, and 50% Reductions in f (worldwide ozone distribution)

f (%)	B* (× 10^5)	L_0* (deg)	L_f (deg)	B† { $L_0 = 30°$, $L_f = 15°$ } (× 10^5)
0	24.8	28.9	15	24.1
5	26.2	29.6	15	26.0
10	27.8	30.4	15	28.1
15	31.2	32.0	15	32.7
20	44.3	37.1	15	51.6

NOTES: * The parameters B and L_0 as a function of f (ranges 0-1) can be adequately represented by
$B = B_n \exp(\alpha f) = B_n \exp(1.14f)$
$(B_n = 24.8 \times 10^5)$
$L_0 = 28.9 \exp(\beta f) = 28.9 \exp(0.5f)$

† $B = 24.1 \times 10^5 \exp(1.53f)$. For small f (e.g., 0-0.20), B can be expressed in the linear form $B = 24.1 \times 10^5 (1 + \alpha f)$, $\alpha \approx 5/3$.

At this juncture it must be acknowledged that the chain of assumptions, calculations, data, and analytical representations which leads to our final epidemiological relationship between skin-cancer incidence, the variables (f, L, h, τ_s, τ_c, C_ℓ, A), and the fixed parameters (L_0, L_f, H, Γ, τ_{s_0}, α, r_0, I_0, τ_{c_0}) is an exceedingly long and tenuous one. Thus, recognizing that there may be a number of weak links in this chain, we must use this final relationship with considerable caution.

Since our major objective in the CIAP program is to estimate the change in skin-cancer incidence with respect to f, the fractional reduction in ozone, it might be prudent to express the expected rate for skin-cancer incidence, N', for a finite f in terms of the rate for vanishing f (i.e., the present rate N). By algebra this is simply

$$N' = N \left(\frac{N}{N_0}\right)^{\alpha f} \tag{8}$$

For small values of f, Eq. (8) implies that the change in skin-cancer incidence with f is

$$\Delta N = N' - N = \alpha f N \ell n \left(\frac{N}{N_0}\right) \tag{9}$$

Thus, we can estimate the change in skin-cancer incidence if we have reliable data on the present rate N, the zero-erythema dose limit of the present rate (N_0), and one parameter (α) which is sensitive to our radiative-transfer assumptions and the spectral response curve. *If skin-cancer incidence data is available*, this is probably the best basis at present for estimating changes in skin-cancer incidence rates associated with changes in total ozone-layer thickness.

Unfortunately, global skin-cancer incidence rates gathered using consistent reporting criteria (MacDonald, 1973) are exceedingly difficult to find. One might, however, note that were all other factors (e.g., life style, genetic makeup, skin care, clouds, smog, altitude, ground albedo, etc.) held constant, we would expect N to be very sensitively dependent upon latitude according to

$$N = K_i \exp\left(\frac{K_2}{1 + \exp\left(\frac{L - L_0}{L_f}\right)}\right) \tag{10}$$

where K_1 and K_2 are constants.

CONCLUSION

Our results thus far have been in terms of incidence (rates in cases per million persons per year). To translate these rate changes into people actually affected by skin cancer, we must multiply by the population (P) and allow a weighting factor (w) for skin sensitivity and life style. Thus,

$$\Delta P = wP\alpha f N \ell n \left(\frac{N}{N_0}\right) \tag{11}$$

This formula might be used to establish a "vulnerability measure" for any geographic or political unit, for eventual use in a cost/benefit analysis. (We found that our considerations indicated that Florida is one of the areas most exposed to possible increases in skin-cancer cases due to future anthropogenic changes in the ozone layer in the whole world!)

ACKNOWLEDGMENT

This research was supported in part by the U.S. Department of Transportation in connection with the Climatic Impact Assessment Program.

REFERENCES

Bener, P. (1972), "Approximate Values of Intensity of Natural UV Radiation for Different Amounts of Atmospheric Ozone," European Research Office, U.S. Army, London, Contract No. DAFA37-68-C-1017, 59.

Braslau, N. and J.V. Dave (1973), "Effect of Aerosols on the Transfer of Solar Energy through Realistic Model Atmospheres," IBM T.J. Watson Research Center, Report RC4308 (Yorktown Heights, N.Y.).

Büttner, K. (1938), Physik. Bioklimat., Leipzig.

Coblentz, W.W. and R. Stair (1934), "Data on the spectral erythemic reactions of the untanned human skin to ultraviolet radiation," U.S. Bur. Stds. J. Res. **12**, 13-14.

Dütsch, H.U. (1969), "Atmospheric ozone and ultraviolet radiation," in World Survey of Climatology **4**, 392, Elsevier, N.Y.

Flowers, E.C., R.A. McCormick, and K.R. Kurfis (1968), "Atmospheric turbidity over the United States, 1961-1966," J. Appl. Meteor. **8**, 955.

Green, A.E.S., editor (1966), *The Middle Ultraviolet, Its Science and Technology*, Wiley, New York.

Green, A.E.S., T. Mo, and J. Miller (1974), "A study of solar erythema radiation doses," Photochem. Photobiol., in press.

Green, A.E.S., T. Sawada, and E.P. Shettle (1974), "The middle ultraviolet reaching the ground," Photochem. Photobiol. **19**, 251-259.

Komhyr, W.D. and L. Machta (1973), "The perturbed troposphere of 1990 and 2020," in Volume IV of the CIAP Monograph Series, U.S. Department of Transportation. NOTE: At present, these monographs exist only in an early draft form. They will be publicly available after completion in September 1974.

Leach, J.F. (1974), "Some Biological Effects of UV Radiation," British Aircraft Co. (Box 77, Filton, Bristol).

MacDonald, E.J. (1973), "Cancer of the Skin in Five Regions in Texas, 1962-1966," Department of Epidemiology, University of Texas, Houston, Texas.

Mo, T. and A.E.S. Green (1974), "A climatology of solar erythema dose," Photochem. Photobiol., in press.

Nack, M.L. and A.E.S. Green (1974), "Influence of clouds, haze and smog on the middle ultraviolet reaching the ground," Appl. Opt., in press.

Shettle, E.P. and A.E.S. Green (1974), "Multiple scattering calculation of the middle ultraviolet reaching the ground," Appl. Opt. 13, 7.

Sutherland, R.A., R.D. McPeters, G.B. Findley, and A.E.S. Green (1974), "Sun photometry and spectral radiometry at wavelengths shortward of 360 nm," to be published in J. Atmos. Sci.

Urbach, F. (1974), private communication.

DISCUSSION

ELLSAESSER: I find it difficult to believe that the present distribution of UV on this planet is both the minimum and the maximum we can tolerate, or the optimum. If we want to determine the effect of either increasing or decreasing UV, we have to integrate the good and bad effects over all life forms.

GREEN: Florida is particularly vulnerable to increased UV because it is in low latitudes and has a largely white population. Other states might be differently affected.

ELLSAESSER: As a meteorologist, I can think of many reasons why the decrease in ozone will be less effective at low latitudes. Thus, the problem also concerns northeasterners.

GREEN: These calculations were based on a constant fractional depletion of the global distribution. If a redistribution occurs, then the local value of f should be used.

FIELD MEASUREMENTS OF BIOLOGICALLY EFFECTIVE UV RADIATION AND ITS RELATION TO SKIN CANCER IN MAN

FREDERICK URBACH, DANIEL BERGER, AND RONALD E. DAVIES
Photobiology Program
Skin and Cancer Hospital
Temple University School of Medicine
Philadelphia, Pennsylvania

ABSTRACT: The evidence linking solar ultraviolet radiation to skin cancer production in man has been reviewed. There can be no reasonable doubt, on the basis of animal experiments and human epidemiologic data, that frequent and prolonged exposure to sunlight is the major cause of basal-cell and squamous-cell carcinoma in man, and that the shortest UV wavelengths penetrating the atmosphere are mainly responsible.

The development and construction of a filter-phosphor-phototube instrument with an action spectrum sufficiently close to that of human skin erythema solare is described. Preliminary results from measurements with such instruments at six widely separated stations varying in latitude from 31.8°N to 44.9°N are most encouraging.

On the basis of preliminary measurements and extensive calculations of the probable effect of stratospheric ozone depletion, estimates are made of the magnitude of the effect such an atmospheric perturbation might have on the incidence of skin cancer in man in the USA. The most conservative estimates suggest that a 5% decrease in ozone would result in an eventual increase of from 30,600 to 44,000 additional cases of skin cancer per year (approximately 10 to 15% of the present incidence rate).

INTRODUCTION

Since the end of the 19th century, when the earliest suggestions were made that frequent and prolonged exposure to sunlight is a cause of skin cancer (Unna, 1894; Dubreuilh, 1896; Shield, 1899), substantial experimental, epidemiologic, and clinical observations have changed these earlier suspicions to virtual certainty (Blum, 1959; Urbach, 1966; Gordon et al., 1972).

The evidence for the assumption that exposure to sunlight, particularly the mid-ultraviolet component, is an essential and major factor in the development of most human skin cancers can be briefly summarized as follows:

1. Skin cancer appears on the parts of the body most exposed to sunlight, particularly the head, neck, arms, and hands (Silverstone and Gordon, 1966).

2. Squamous-cell carcinoma in particular (and basal-cell carcinoma to a lesser degree) occur primarily on the skin sites most heavily exposed to solar radiation (Urbach, 1966).

3. There is greater prevalence of skin cancer in outdoor workers (Blum, 1959), and in any particular community greater frequency of skin cancer (and occasionally the only skin cancer) is found in those who have spent the longest periods outdoors (Urbach, Rose, and Bonnem, 1972; O'Beirn et al., 1970).

4. For similar types of skin, the occurrence of skin cancer increases fairly rapidly with decrease in latitude, particularly in the middle latitudes (mid 50's to low 20's). This tendency is not shown by any other cancer except malignant melanoma (Dorn, 1944; Blum, 1959; Gordon et al., 1972).

5. Susceptible racial types, especially those of Celtic origin, are more prone to skin cancer than other whites, and particularly to multiple lesions. The characteristic skin has little pigment, or scattered freckles, and susceptible individuals seem more often to have fair

hair and blue or gray eyes, and to sunburn easily, severely, and often (O'Beirn et al., 1970; Gellin et al., 1966; Silverstone and Searle, 1970; Urbach, Rose, and Bonnem, 1972).

6. In extensive, carefully controlled experiments with UV on animal (primarily mouse) skin, it has been shown without any doubt that skin cancer is produced by repeated exposure to wavelengths between 320 and 250 nm, with the 320 to 280 nm range being most effective (Findlay, 1928; Blum, 1959; Epstein, 1966; Forbes, 1969). Tumors have also been induced by massive single doses of UV (Hsu et al., in press), and tumor cells have been initiated by a single, modest UV exposure and promoted into cancers by chemical substances (Epstein, 1966; Pound, 1970).

7. Regular use of sunscreen lotions, absorbing strongly in the sunburn part of the solar spectrum, has markedly decreased development of new solar keratoses in susceptible patients (Fitzpatrick et al., 1972).

All photobiological responses to irradiation with ultraviolet and visible radiation show a dependence on the energy of the incident photons, with a maximum response at a fairly well defined photon energy, a somewhat limited range, and a "threshold" beyond which the lower photon energies are very much less effective. This is primarily due to the ability of biologically important molecules to absorb appropriate photons, since without such absorption no effect is possible.

The sun, being essentially a very hot blackbody radiator, emits a wide range of wavelengths. The relative intensities of the ultraviolet and visible light which reach the earth's surface depend considerably on attenuation by the atmosphere (due to absorption and scattering). Below 320 nm, the intensity of ultraviolet falls very rapidly because of the absorption by stratospheric ozone, the details of which have been described in other papers in this volume. Virtually no radiation below 288 nm reaches the earth's surface from the sun. The known biological effects of solar radiation are thus confined to the extreme short end of the terrestrial solar spectrum and involve no more than about 1 1/2% of the total solar energy reaching earth.

ACTION SPECTRA FOR SKIN ERYTHEMA AND SKIN CANCER

In order to attempt to predict any change in biologic activity of solar radiation caused by contamination of the atmosphere, it is necessary to know the range of wavelengths effective for the production of sunburn and skin cancer, and, if possible, those wavelengths that give the maximum response.

Johnson, Daniels, and Magnus (1968) have reviewed the many attempts to determine the action spectrum for sunburn. The major differences in shapes of action spectra reported by various investigators were found by Berger et al. (1968) to be dependent on the degree of erythema, the method by which it was judged, and stray light. The action spectrum shown in Figure 1 has been used in the work reported here, for use in calibration of the instruments described below, and in the calculations used for comparisons (Mo and Green, 1973).

On the basis of the present state of the art, and what is known about human skin erythema, it may be stated that:

1. The maximum responsiveness for sunburn in the wavelength range of terrestrial sunlight is within 3 nm of 295 nm.

2. Allowing for the shape of the sun's spectrum, the most effective wavelength in sunlight is within 3 nm of 305 nm.

3. The effective long-wave limit for the major part of sunburn is about 325 nm (although the longer UV wavelengths may be able to enhance the effect of the 290-325 nm region) (Willis, 1972; Forbes, 1973).

In the absence of direct experimentation ending in the appearance of keratoses or skin cancer in human skin, the carcinogenic action

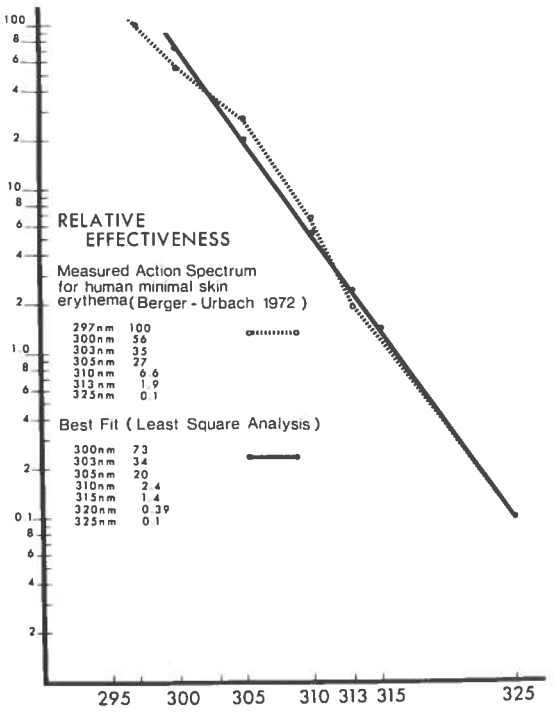

Figure 1. Action spectrum for human-skin erythema produced by ultraviolet light. The solid line represents the calculated best fit to the observed data (dotted line). After Berger et al. (1968).

spectrum must remain somewhat speculative. However, the indirect evidence points to the same part of the spectrum (i.e., below 325 nm), with a caveat similar to that for sunburn erythema, that longer ultraviolet wavelengths may have an intensifying effect on the main (290-320 nm) effective wavelength for carcinogenesis (Epstein, 1966; Magnus, 1971; Freeman, 1970; Forbes, 1973).

For the above reasons, the present working assumption is that the action spectra for human skin erythema and for skin cancer are sufficiently similar that the former can be used as a basis for field ultraviolet measurements, and for calculations of changes in the biological effectiveness of ultraviolet radiation due to changes in its quality and quantity.

MEASUREMENT OF ERYTHEMAL EFFECTIVENESS OF SUNLIGHT

Although extensive basic experimental information on the solar spectrum exists, and elegant mathematical models have been produced in this age of high-speed computers, neither can be applied with any certainty to any one practical exposure to sunlight. The number of atmospheric attenuation processes are too great, and too ill defined, to be simultaneously quantified with any degree of accuracy.

Therefore, alternative approaches have been investigated, utilizing physical and chemical sensors which respond only to the same spectral range of radiation as a particular biologic effect, and, as nearly as possible, have the same variation in relative response for different wavelengths or photon energies within that range. Measurements with such a sensor are applicable only to well-defined biological responses with the same, or very closely similar, action spectra. However, the evaluation of the effectiveness of each photon is made instantly and automatically; physical sensors usually give an instantaneous response which can be expressed as either dose or dose rate, and can be designed for continuous automatic recording. (For detailed review of the problem, see Robertson, 1972.)

Prior to the work of Robertson (1968), continuous records in sunlight for an extended period which would permit comparison with a long-term process such as skin-cancer development had been made only at a few places, and with cells whose action spectra were uncertain, and which were not specifically related to each other (Coblentz and Stair, 1944; Coblentz, 1952.)

The basic requirements for a measuring system which would allow for comparison of the long-term biologically effective exposure at places where clinically significant cancer statistics could be obtained were set forth by Robertson (1972) as follows:

a. The effectiveness of all radiation should be measured on a horizontal surface, including radiation from as much of the sky as possible.
b. The spectral response of the sensor should be as near as possible in form to the average for normal human skin erythema so that its estimate of effectiveness on skin would be automatic.
c. All measuring units at different sites should have essentially the same limits and shape of spectral response.

d. Any drift in sensitivity should be confined to the magnitude of the overall response and should not affect the range and shape of the spectrum.
e. Any other differences from ideal performance should operate in comparable fashion at all sites.
f. Measuring equipment should operate continuously in all weathers.
g. Operation and recording should proceed automatically without action by a trained observer.
h. Reliable operation should not require frequent maintenance and calibration by specially trained attendants. (However, regular cleaning and confirmation that all was well would be desirable.)
i. Records should provide data relative to
   1. clear sky conditions
   2. variation during each day
   3. variation during a number of years
   4. disturbed sky conditions
   5. total exposure

   and should permit comparisons of different sites.

THE SUNBURNING-ULTRAVIOLET METER (ROBERTSON-BERGER)

Based on the extensive work and years of field experience of Robertson (1972), a phosphor-filter ultraviolet integrating instrument was designed and constructed by Robertson and Berger in the spring of 1973. The arrangement of the phosphor (as the sensor) with filters and a phototube, as used in the continuously operating field instruments, is shown in Figure 2.

The desired spectral response (closely similar in wavelength dependence to that for erythema of human skin) is provided by the magnesium tungstate phosphor in a thin, uniform layer bonded to a filter plate (which in use is normally horizontal). On exposure to suitable radiation, the fluorescent emission from the phosphor irradiates the vacuum phototube, the photocurrent from which is proportional to the combined luminescent effect of all photons reaching the phosphor. The operative spectral range of the phototube is limited by a narrow-pass green filter (Corning 4010) which passes part of the fluorescence. The phosphor, green filter, and phototube are protected from the intense visible part of

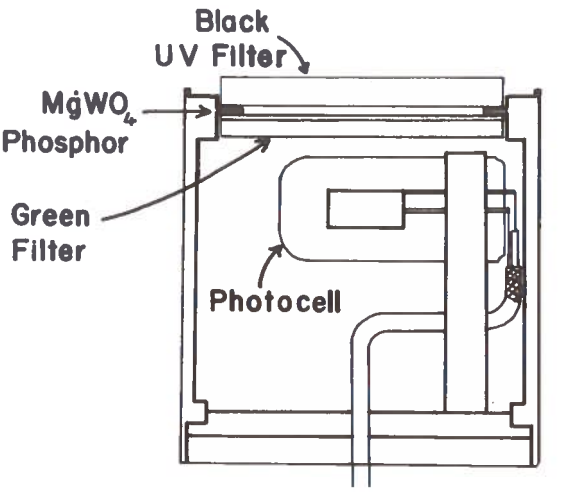

Figure 2. Schematic drawing of the magnesium tungstate sensor. "Black" filter, Schott UG11, 3 mm thick. Green filter, Corning 4010, 6 mm thick. Phototube, RCA 1P39.

sunlight by 3 mm of ultraviolet-transmitting, light-absorbing "black" glass (Schott UG11). Any direct UV or IR which passes the black filter is strongly absorbed by the green filter. If the phosphor layer is omitted, the phototube response to the whole of sunlight is zero. The only photocurrent, when the phosphor is included, comes from fluorescent conversion of wavelengths less than about 330 nm. In terrestrial sunlight there is no radiation shorter than 290 nm, so that the actual response of this tungstate cell is limited to the 290-330 nm band.

The action spectra of the phosphor alone and of the assembled filter-phosphor sensor are shown in Figure 3.

The instruments in use were checked for spectral response with a double monochromator (Berger et al., 1968) and calibrated against each other and a standard meter so as to read out in comparable units.

In the measurement of global radiation, emphasis is usually placed on Lambert's cosine law. Neither the human skin, nor the sunburning UV meter's magnesium tungstate cell, is a true cosine-law detector. As can be seen in Figure 4, the deviation from expected cosine response at sun angles of 20° or more above the horizon is less than 10%. Since at low sun angles the intensity of direct-sun UV is small, and sky UV is not greatly affected, cosine errors are negligible when the sun is high.

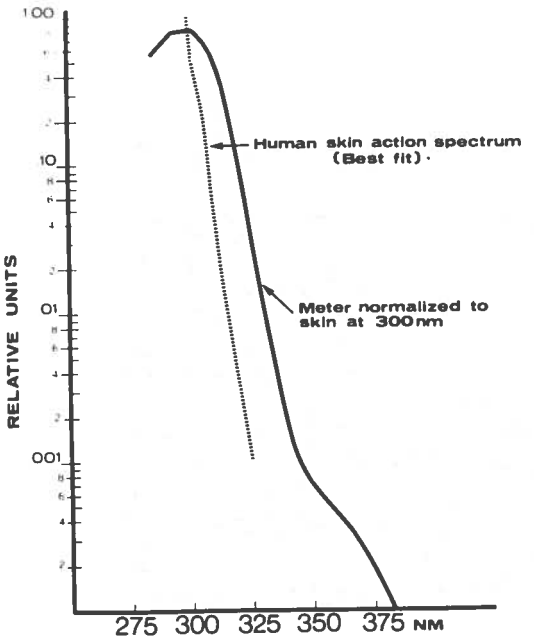

Figure 3. Comparison of action spectra of skin (dashed line, after Berger et al., 1968), and the assembled sensor-filter-phototube as used in the field (solid line).

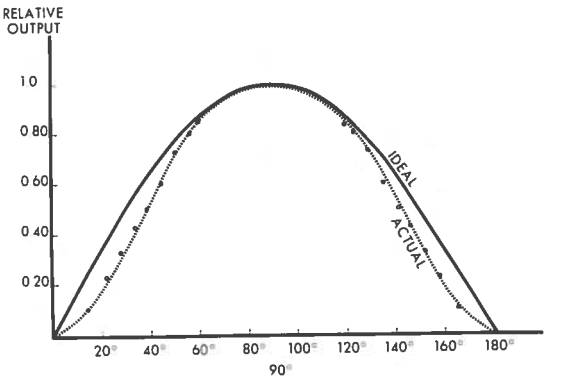

Figure 4. Plot of ideal and actual agreement of the cosine response of the sunburning-UV meter.

At each observing station the sunburning UV meters have been installed permanently above roof level to receive radiation from the whole sky. The polarizing voltage for the phototube and the signal current from the phototube are carried by shielded coaxial cable to the integrating amplifier and printer in the building below. The assembled detector and electronic unit are shown in Figure 5 and the rear of the recorder in Figure 6.

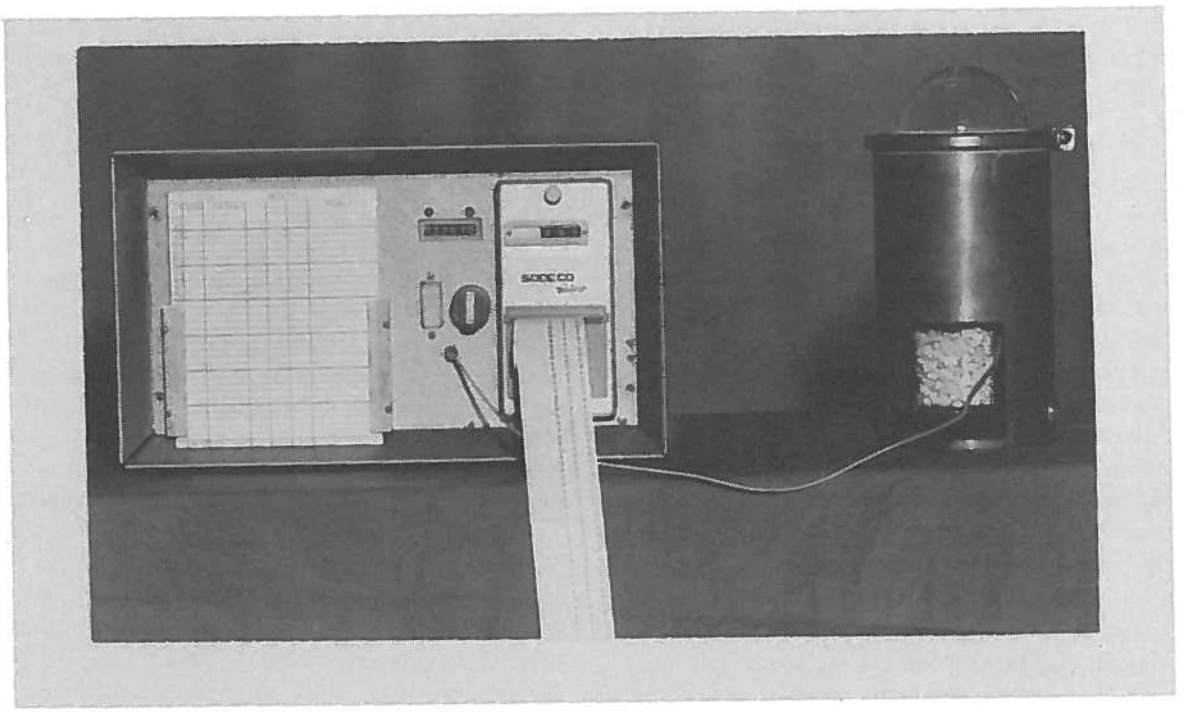

Figure 5. The sunburning-ultraviolet meter (Robertson-Berger). The detector is the cylinder on the right; the amplifier-counter is on the left.

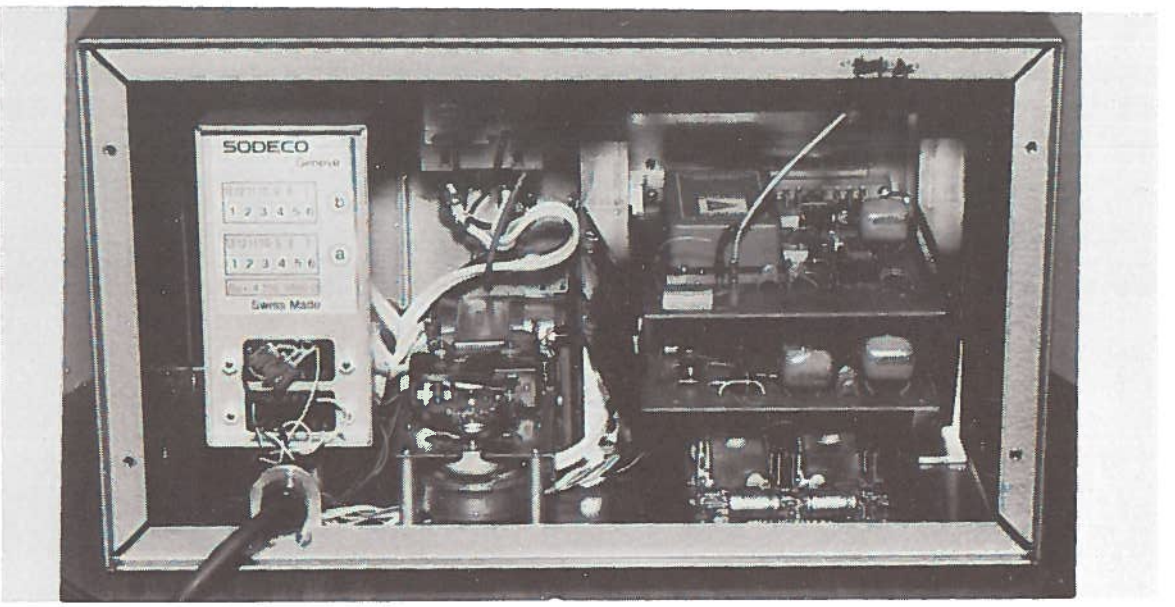

Figure 6. Rear view of amplifier-recorder with rear panel removed.

The amplifier-recorder integrates the signal current coming from the phototube until a preset dose is obtained, then stores a count and resets the integrator. At the end of each half hour a counter prints the number of counts stored in that half hour, and is reset. The paper tape which advances each half hour provides a permanent record of the sunburning effectiveness during the day.

In September and October 1973, calibrated sunburning-UV meters were installed at National Weather Service Stations at Bismarck, North Dakota; Des Moines, Iowa; Minneapolis, Minnesota; Albuquerque, New Mexico; El Paso, Texas; Fort Worth, Texas; Tallahassee, Florida; Oakland, California; and in December 1973 at the Mauna Loa Observatory, Hilo, Hawaii. The National Weather Service scientists at these stations have been caring for the instruments, and sending data to the Skin and Cancer Hospital Laboratories on a regular basis. The authors are extremely grateful for their cooperation and help.

PRELIMINARY RESULTS OF FIELD MEASUREMENTS OF "SUNBURNING" ULTRAVIOLET LIGHT

The major factors affecting transmission of ultraviolet in the 290-330 nm range to a terrestrial observer are sun angle (and thus season and latitude), cloud cover, and aerosols and suspended particles. The importance of atmospheric conditions and their variability from hour to hour and day to day are shown in Figures 7 and 8.

Figure 7 shows half-hourly plots of integrated erythemogenic UV as measured by the meters stationed at El Paso, Texas (latitude 31.8° north) and Tallahassee, Florida (latitude 30.4° north) for the same days of the first week of January 1974. Although Tallahassee is 1.4° further south than El Paso, and thus would be expected to reach higher daily and cumulative total ultraviolet light levels because of latitude, this was the case only on one day, January 5, 1974, when both stations had cloud cover for most of the day. The generally lower UVL totals are due to almost-daily intermittent-to-major cloud cover at Tallahassee, and generally clear weather at El Paso. In Figure 8, a similar plot is given for El Paso and Albuquerque (latitude 35.1° north). Again, repeated cloud cover over Albuquerque magnifies the latitude effect. The sensitivity of the meters to change in local atmospheric conditions is clearly indicated by these figures. During 1973, Dr. Alex Green and his associates performed extensive calculations on systematics of climatic variables and their effects on local ultraviolet erythema dose (Green, 1973). They calculated profiles of ultraviolet erythema radiation doses for the Northern

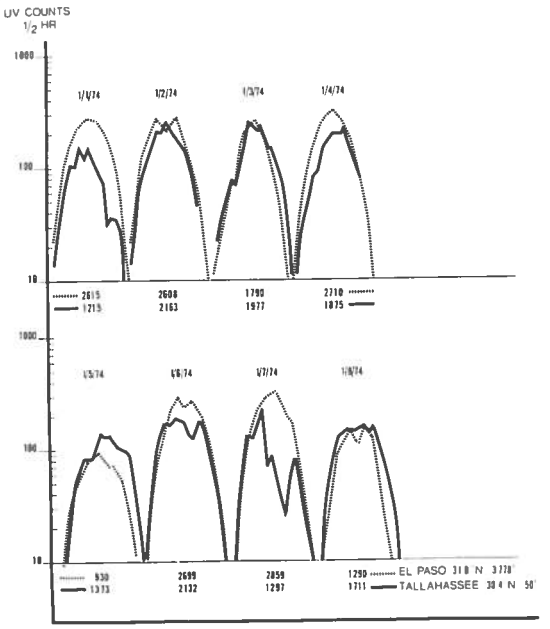

Figure 7. Half-hourly readings taken from sunburning-UV meters in El Paso, Texas and Tallahassee, Florida in January 1974. Note the marked effect of cloud cover at Tallahassee compared to almost daily clear weather in El Paso.

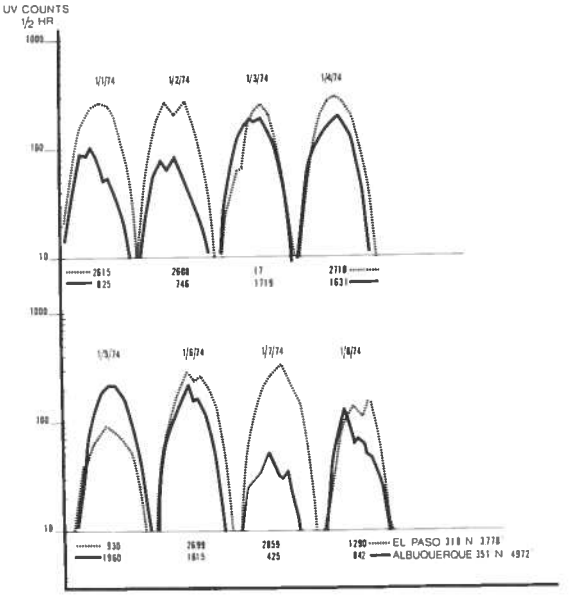

Figure 8. Half-hourly readings taken from sunburning-UV meters in El Paso, Texas and Albuquerque, New Mexico. Again, much more cloud cover in Albuquerque.

Hemisphere at 5° latitude intervals, utilizing a semi-empiric analytic formula for the erythema-spectrum-weighted daily dose of ultraviolet radiation in the effective wavelength region. Their calculation takes into consideration variation in the ozone thickness, aerosol thickness, and seasons of the year (through the solar declination). For the purposes of the discussion below, seasonal variations of ozone concentration were incorporated into the erythema dose calculations (Green, 1973). In Table 1, the monthly total counts per half hour from sunrise to sunset obtained from the sunburning-UVL meters and Green's calculation for erythema-effective UVL (in Jm^{-2}/month) are listed for comparison.

Table 1. Monthly Total Counts from Sunburning UVL Meters Compared with Calculated Values of Erythema-Effective UV

Location	Latitude		Oct '73	Nov '73	Dec '73	Jan '74
El Paso	31.8°	counts:	159,247	99,030	77,066	78,430
		Jm^{-2}:	33,180	14,900	7,400	7,200
Fort Worth	32.8°	counts:	105,617	58,080	52,235	49,662
		Jm^{-2}:	31,200	13,600	6,580	6,460
Albuquerque	35.1°	counts:	134,881	72,300	44,820	53,692
		Jm^{-2}:	27,020	10,800	4,900	4,900
Oakland	37.8°	counts:	87,544	41,820	32,271	33,697
		Jm^{-2}:	23,320	8,580	3,640	3,700
Des Moines	41.6°	counts:	81,003	28,380	20,950	27,683
		Jm^{-2}:	16,460	4,900	1,740	1,860
Minneapolis	45.0°	counts:	52,080	21,300	12,307	18,569
		Jm^{-2}:	12,280	3,040	900	1,000

From these data, it is possible to attempt to derive an estimate of the reliability of the calculated values for erythemogenic UV radiation, and of the accuracy of representation of this factor by the sunburning-UVL meters.

The predicted monthly dose of erythemogenic ultraviolet radiation expressed in Joules meter^{-2} was obtained for each of six stations for four winter months. In Figure 9 these data ($\times 10^{-3}$) are plotted as a function of the recorded measurements, expressed as counts month^{-1} $\times 10^{-3}$. A crude correlation of 0.910 was observed between the two sets of data, indicating that approximately 83% of the measurement differences were predictable. An examination of the distribution of points suggested that the residual variation was not random. In Figure 10, the data are broken down by months, and correlations ranging from 0.882 to 0.968 were observed; the residual variation ranged from 6-22% (average 14.8%), similar to that of the overall comparison (Figure 9, residual variation 17.2%), suggesting that most of the variability was associated with differences between stations. Of interest in Figure 10 is the systematic change in slope between the months of October, November, and December. In contrast, identical slopes were seen in December and January, months which are essentially equivalent with respect to sunlight exposure. The possible significance of the slope change will be discussed later.

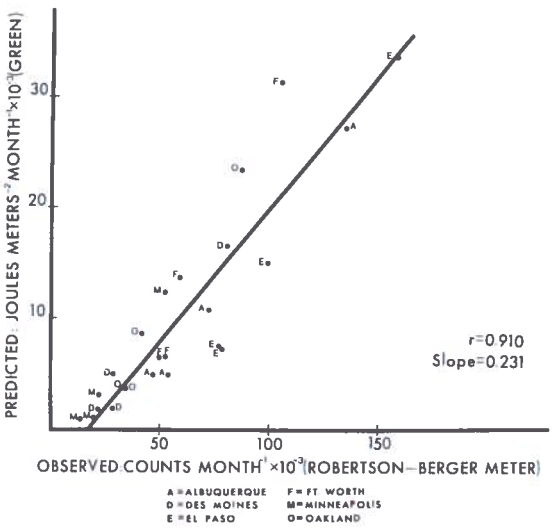

Figure 9. Predicted monthly dose of erythemogenic UV at six stations in the US plotted as a function of actual recorded measurements. The crude correlation is 0.91. (Calculations by Mo and Green, 1973.)

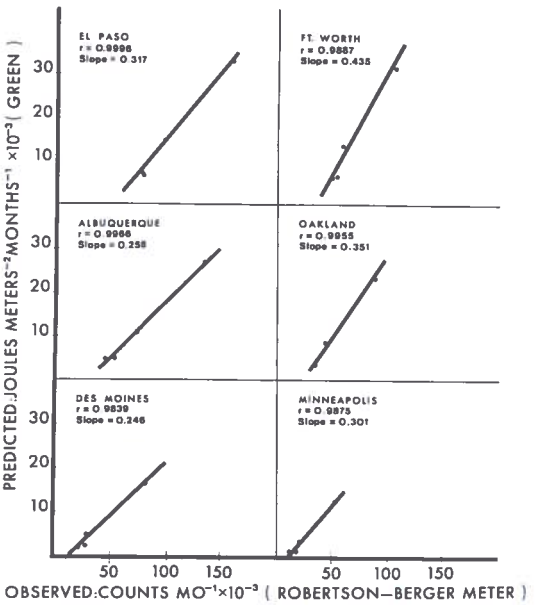

Figure 10. Predicted dose of erythemogenic UV plotted within months by stations. Within stations the correlation is better than 98%. For detailed discussion, see text.

Figure 11 presents four months of data for each of the six stations separately. Three significant observations arise from this presentation. First, the deviation of observation from prediction within a station is very small: residual variation ranged from 0.08 to 3.19% (average 1.60%). Clearly there are systematic differences between the stations with respect to the relationship of observed and predicted data, but within a station the relationship appears highly reproducible, at least over this limited time period. A second observation is the failure of any of the regression lines to approach a 0,0 intercept: all have positive x-intercepts, most of which are too large to be atributable to chance. The third observation concerns the large variation in slopes between stations.

A possible explanation for the positive x-intercepts relates to the difference in action spectra between the sunburning-UV meter and human erythema. Relative to the usual erythema spectra, the sunburning-UV meter overestimates longer-wave (>315 nm) UV and underestimates wavelengths of about 300 nm (see Figure 3). Since the quantity of long-wave UV varies less with such factors as sun angle and ozone concentration than does that of the shorter-wavelength

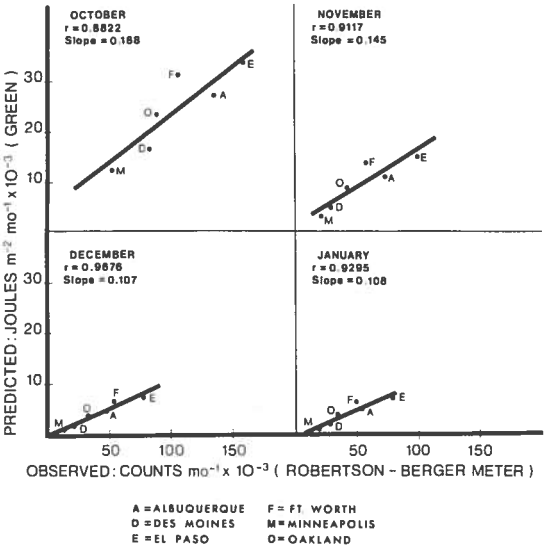

Figure 11. Predicted dose of erythemogenic UV plotted for each month for six stations. Note the systematic change in slope between the months of October, November and December.

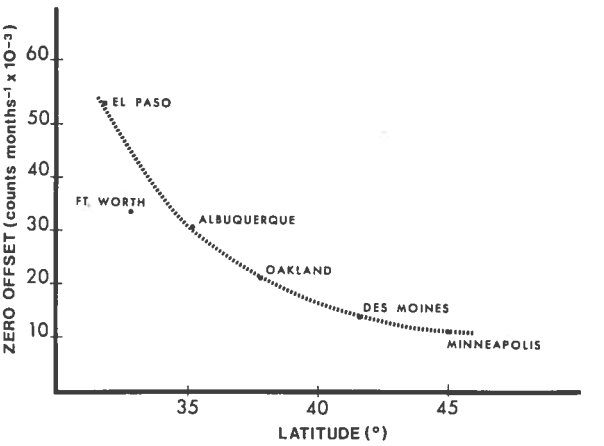

Figure 12. Plot of "zero-offset" by stations and latitude. (For discussion, see text.)

radiation, it might be expected that some counting should occur even at the (extrapolated) point where no erythemogenic UV was predicted. The "zero-offset" would thus represent an estimate of the contribution of longer-wave UV to the meter reading. This explanation is supported by the observation (Figure 12) that the quantity of this offset varies systematically with latitude, being greatest in the more highly insolated areas. It is also supported by the observation (Figure 10) that the slopes of monthly data were minimal in December and January, when the short-wave-to-long-wave UV ratio would also be minimal. It seems appropriate, therefore, to adjust the meter readings by an amount which estimates the unwanted long-wave contribution, namely, the value of the x-intercept. (It is recognized that the appropriate correction will actually be some function of the total flux, and thus will in all cases be greater than the x-intercept value. Since there is no basis at present for estimating the slope of this relationship, and since it should be small relative to the change in short-wave UV flux, we have based our present calculations on the use of the x-intercept.)

The occurrence of station-to-station variation in slope is not unexpected, although its exact basis is not immediately apparent. Since all meters were matched to better than ±5% in sensitivity, and since there is no reason to expect differences in action spectra between meters, it seems reasonable to assign these differences to systematic errors in the predicted values. Such errors could easily result from factors not amenable to direct prediction, such as cloud cover, atmospheric pollution, albedo, etc. Since most of these variables (except winter albedo) would act to reduce the predicted UV exposure (and thus reduce the slope of the plotted data), we chose to normalize the slopes for all stations to that of Des Moines. The normalizing factors were observed to have some tendency to increase with latitude, but there were clearly other major effects of unexplained origin.

The data were adjusted for the two sets of station-specific effects noted above (subtracting the zero offset from the meter readings and normalizing the slopes of the predicted values) and replotted in Figure 13. The resulting correlation of 0.995 indicates that these adjustments accounted for all but about 1% of the variation, and thus offers considerable support for their empirical validity. With a larger number of readings from more stations, and possibly with a finer graduation of the intervals compared, it will be possible to test the general applicability of these corrections and, if appropriate, to refine them. By other techniques it should be possible to estimate the relative contribution of longer-wave radiation to meter readings obtained under specified conditions. Finally, the values of the

slope-normalizing factors, which can initially provide useful station-calibration factors, may eventually offer insights into presently unrecognized components of the variation in UV irradiation.

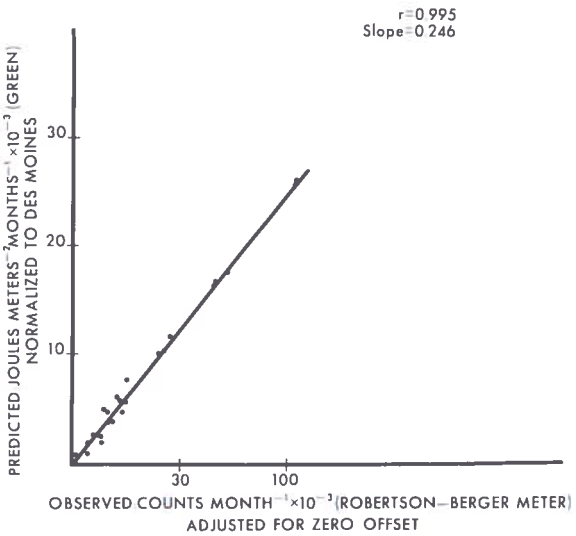

Figure 13. Relationship of predicted (normalized) and observed (adjusted) sunburning-UV radiation. Correlation r = 0.995. (For discussion, see text.)

ESTIMATE OF THE EFFECT OF OZONE REDUCTION IN THE STRATOSPHERE ON THE INCIDENCE OF SKIN CANCER IN THE UNITED STATES

Utilizing the figures for incidence of skin cancer in the US obtained by the Third National Cancer Survey in 1970-71 (Scotto et al., in press) and Green's (1973) calculation for change in biologically effective UV radiation resulting from ozone reduction, it is possible to estimate the probable increase in skin cancer (basal- and squamous-cell carcinoma) that may follow atmospheric perturbation.

The basic assumptions underlying the calculations presented below are:

1. The action spectrum for skin carcinogenesis and sunburn solare are closely similar.
2. The calculations of Mo and Green (1973) (solar energy reaching the earth between 290 and 320 nm multiplied by the relative effectiveness of these wavelengths for erythema production) reasonably represent the natural UV doses at various latitudes.

From the tables of Green the following amounts of erythema-effective energy are obtained:

Annual dose in Joules m^{-2} of relative erythema-effective energy:

Dallas	32.8°N	441,870 Jm^{-2}
Des Moines	41.7°N	332,831 Jm^{-2}
Minneapolis	44.9°N	229,636 Jm^{-2}

The relationship of erythema-effective energy to ozone reduction has been calculated recently by Schulze (1973) and is reported as follows:

$$-5\%\ O_3 = +9\%\ EEE$$
$$-10\%\ O_3 = +19\%\ EEE$$
$$-20\%\ O_3 = +43\%\ EEE$$
$$-40\%\ O_3 = +119\%\ EEE$$

Preliminary data comparing measured ultraviolet values with measured changes in ozone at the National Weather Service Station in Bismarck, North Dakota, suggest that the ratio of percentage rise in erythema-effective radiation to percentage reduction in ozone varies between 1.25:1 at 3 mm ozone to 1.8:1 at 3.6 mm ozone (Machta and Hass, 1974, personal communication). Chavandra and Latarjet (1973) estimate a 2:1 factor.

We utilized a factor of 1.8:1 for the UV:ozone ratio for the subsequent calculations and assumed that there is a linear relationship between skin cancer-incidence and annual erythema-effective ultraviolet radiation reaching the population. Thus, if the skin-cancer incidence is approximately 370/100,000 in Dallas (32.8°N) and 126/100,000 in Des Moines (41.7°N), and if the 109,039 more Jm^{-2} EEE per year accounts for a difference of 244 cases of skin cancer per 100,000 population, then an increase of 1 Jm^{-2} represents an increase of 0.002 cases of skin cancer/100,000 population.

Thus, if no correction for difference in exposure by life style is applied, the probable eventual increase in incidence of skin cancer at Dallas would range from 80/100,000 for a 5%

decrease in ozone to 1052 per 100,000 for a 40% ozone decrease, or 1576 to 20,725 more cases of skin cancer per year in Dallas alone.

For an average of 300,000 new cases of skin cancer per year, the crude incidence of skin cancer would average about 143/100,000 per year in the US (Scotto et al., in press). For a 5% decrease in ozone this would represent an eventual increase of about 60/100,000: 125,800 total cases per year, or a 42% increase in skin cancer in the US.

It can be argued that the exposure of the population is much less in the colder north than in the warmer south. For this reason, a comparison attempting to compensate for this factor is also presented. The assumption is made that in Dallas, a metropolitan southern area, exposure occurs 7 months out of the year (April to October), but in Minneapolis, a northern metropolitan area, exposure will occur principally during 4 months (June to September). Thus, the effective erythema energy will be 380,660 Jm^{-2} in the south and 195,500 Jm^{-2} in the north. The value of a Jm^{-2} becomes 0.00112. The resultant increases for various decreases of ozone can be seen in Table 2.

Table 2. Increases in Skin Cancer per Hundred Thousand of Population for Different UV-to-Ozone Ratios

A: UV-to-Ozone Ratio, 1.25:1

Location		Present incidence	-5% O_3	-10% O_3	-20% O_3	-40% O_3
Dallas	32.8°N	370/100,000	+27.7	+53.3	+106.6	+213
Minneapolis	44.9°N	162/100,000	+13.7	+27.4	+54.7	+109.5
Average US		143/100,000	+14.6	+29.2	+58.4	+116.7

B: UV-to-Ozone Ratio, 1.8:1

Location		Present incidence	-5% O_3	-10% O_3	-20% O_3	-40% O_3
Dallas	32.8°N	370/100,000	+38	+81	+183	+507
Minneapolis	44.9°N	162/100,000	+19.7	+41.6	+94	+260
Average US		143/100,000	+21	+44.3	+100	+278

On the basis of these more conservative estimates, the eventual increase in skin cancer for the US for a 5% decrease in ozone may be expected to range from 14.6 to 21/100,000, or from 30,600 to 44,000 additional new cases of skin cancer per year, representing an increase between 10 and 15%. If the ozone decrease should reach 40%, the eventual increase in skin cancer could range from 116.7 to 278/100,000, or a shocking 244,500 to 582,500 additional cases per year, representing an increase ranging from 81.5 to 194%.

ACKNOWLEDGMENTS

The authors are grateful to Dr. Alex Green, Aeronomy Group, University of Florida, Gainesville, Florida, for use of extensive computations of expected biologically active ultraviolet radiation; to Drs. L. Machta and W. Hass of NOAA for advice and data on ozone measurements performed by the National Weather Service; to meteorologists Lloyd Brown, Ellis Burton, Warren Caldwell, Denzil Davis, Ronald Fegley, Robert Lucas, Robert Orton, William Reed, and Joseph Strub of the National Weather Service for their care of our instruments and faithful recording and forwarding of data; and to Drs. P.D. Forbes and H.F. Blum for valuable advice in the interpretation of these studies. The work was supported by a contract from the Climatic Impact Assessment Program, U.S. Department of Transportation, and by a grant from the National Institutes of Environmental Health Sciences, U.S. Department of Health, Education, and Welfare.

REFERENCES

Berger, D., F. Urbach, and R.E. Davis (1968), "The action spectrum of erythema induced by ultraviolet radiation," in Proceedings of the 13th

Congressus Internationalis Dermatologicae, Munich, 1967. Berlin: Springer Verlag, 112-117.

Blum, H.F. (1959), *Carcinogenesis by Ultraviolet Light*, Princeton, Princeton University Press, 185-204.

Chavandra, T., and R. Latarjet (1973), "Influence des variations de l'ozone atmosphérique sur certaines activités biologiques du rayonnement ultraviolet solaire," Comp. Rendus Acad. Sc. Paris, Series D **276**, 3481-3485.

Coblentz, W.W. (1952), "Summary of correlations of bioclimatic ultraviolet and total solar radiation in Washington, D.C. 1941-1950," Bull Am. Meteorol. Soc. **33**, 158-162.

Coblentz, W.W., and R. Stair (1944), "A daily record of ultraviolet solar and sky radiation in Washington, 1941 to 1943," Bur. Standards J. Res. **33**, 21-44.

Dorn, H.F. (1944), "Illness from cancer in the United States," U.S. Public Health Reports **59**, 33-49. 65-77, 97-115.

Dubreuilh, W. (1896), "Des hyperkératoses circonscrites," Ann. Derm. Syph. (Series 3) **7**, 1158-1204.

Epstein, J.H. (1966), "Ultraviolet light carcinogenesis," in *Advances in Biology of Skin:* VII. Carcinogenesis, ed. W. Montagna and R.L. Dobson. Oxford, Pergamon Press, 215-236.

Findlay, G.M. (1928), "Ultraviolet light and skin cancer," Lancet **215**, 1070-1073.

Fitzpatrick, T.B., M.A. Pathak, and M.M. Lane-Brown (1972), "Prevention of solar degeneration and sun induced carcinoma of the skin," in *Melanoma and Skin Cancer*, ed. W.H. McCarthy. Sydney, N.S.W. Government Printer, 293-298.

Forbes, P.D. (1973), "Influence of long wave UV on photocarcinogenesis," Am. Soc. Photobiol., 1st Annual Meeting, Sarasota, FL.

Forbes, P.D., and F. Urbach (1969), "Vascular and neoplastic changes in mice following ultraviolet radiation," in *The Biologic Effects of Ultraviolet Radiation*, ed. F. Urbach, Oxford, Pergamon Press, 279-289.

Freeman, R.G., H.T. Hudson, and R. Carnes (1970), "Ultraviolet wavelengths in solar radiation and skin cancer," Int. J. Derm. **9**, 232-235.

Gellin, G.A., A.W. Kopf, and L. Garfinkel (1966), "Basal cell epithelioma: A controlled study of associated factors," in *Advances in Biology of Skin*: VII. Carcinogenesis, ed. W. Montagna and R.L. Dobson. Oxford, Pergamon Press, 329-344.

Gordon, D., H. Silverstone, and B.A. Smithhurst (1972), "The epidemiology of skin cancer in Australia," in *Melanoma and Skin Cancer*, ed. W.H. McCarthy, Sydney, NSW Government Printer, 23-37.

Green, A.E.S. (1973), "Expected changes in ultraviolet radiation reaching the ground," Section 2.2 of Chapter 2, Volume 5 of the CIAP monograph series, Department of Transportation, Washington, D.C. *NOTE:* The monographs currently exist in an early draft form only. They will be publicly available after completion in September 1974.

Hsu, T., P.D. Forbes, L.C. Harber, and E. Lakow "Induction of skin tumors in hairless mice following single exposure to ultraviolet radiation," submitted to Photobiol. and Photochem. for publication.

Johnson, B.E., F. Daniels, and I.A. Magnus (1968), "Response of human skin to ultraviolet light," in *Photophysiology: Current topics*, Vol. 4, ed. A.C. Giese, New York. Academic Press, 139-202.

Magnus, I.A. (1971), Personal communication.

Mo, T., and A.E.S. Green (1973), "Systematics of climatic variables and implication on local ultraviolet dose," Section 2.2.3 of Chapter 2, Volume 5 of the CIAP monograph series, Department of Transportation, Washington, D.C. *NOTE:* The monographs currently exist in an early draft form only. They will be publicly available after completion in September 1974.

O'Beirn, S.F.O., P. Judge, F. Urbach, C.F. MacCon, and F. Martin (1970), *Sixth National Cancer Conference Proceedings*, Philadelphia. J.B. Lippincott Co., 489-500.

Pound, A.W. (1970), "Induced cell proliferation and the initiation of skin tumor formation in mice by ultraviolet light," Pathology **2**, 269-275.

Robertson, D.F. (1968), "Solar ultraviolet radiation in relation to sunburn and skin cancer," Med. J. Australia **2**, 1123-1132.

Robertson, D.F. (1972), "Solar Ultraviolet Radiation in Relation to Human Sunburn and Skin Cancer," Thesis submitted to the University of Queensland, Brisbane, Australia, 47-60.

Schulze, R. (1973), "Increase of carcinogenic ultraviolet radiation due to reduction in ozone concentration in the atmosphere" (submitted for publication).

Scotto, J., A.W. Kopf, and F. Urbach "Non-melanoma skin cancer among whites in four areas of the U.S.," Cancer, in press.

Shield, A.M. (1899), "A remarkable case of multiple growths of the skin caused by exposure to the sun," Lancet **1**, 22-23.

Silverstone, H., and D. Gordon (1966), "Regional studies in skin cancer. Second report: Wet tropical and sub-tropical coasts of Queensland," Med. J. Aust. **2**, 733-740.

Silverstone, H. and J.H.A. Searle (1970), "The epidemiology of skin cancer in Queensland: The influence of phenotype and environment," Brit. J. Cancer **24**, 235-252.

Unna, P.G. (1894), *Die Histopathologie der Hautkrank heiten*, Berlin, A. Hirschwald, 725.

Urbach, F. (1966), "Ultraviolet radiation and skin cancer in man," in *Advances in Biology of Skin*: VII. Carcinogenesis, ed. W. Montagna and R.L. Dobson. Oxford, Pergamon Press, 195-214.

Urbach, F., D.B. Rose, and M. Bonnem (1972), "Genetic and environmental interactions in skin carcinogenesis," in *Environment and Cancer*, Baltimore, The Williams and Wilkins Co., 355-371.

Willis, I., A. Kligman, and J. Epstein (1972), "Effects of long wave ultraviolet rays on human skin: protective or photoaugmentative?" J. Invest. Derm. **59**, 416-420.

DISCUSSION

(UNIDENTIFIED): You do not feel that the Cancer Institute figure represents an increase in incidence over that quoted by James McDonald in 1971?

URBACH: McDonald's data are certainly different from those just reported by the Cancer Institute. The reasons for the differences are not clear; they may be due to different methods of data acquisition. I don't believe that the incidence of skin cancer has doubled in five or six years, though it has certainly increased significantly.

(UNIDENTIFIED): Isn't that in conflict with the observation that ozone has also been increasing over the last ten years?

URBACH: No, I think the conflict can be explained by a cultural change. Once upon a time, people of means protected themselves from the sun, and only manual laborers got a tan. Now a tan is a status symbol, and the degree of exposure is unbelievably – or delightfully – high.

CELL-POPULATION GROWTH IN CANCERS INDUCED BY ULTRAVIOLET RADIATION

HAROLD F. BLUM
Skin and Cancer Hospital
Temple University Health Sciences Center
Philadelphia, Pennsylvania

ABSTRACT: This paper presents a model for growth of cancer that takes into account the complementary effects of changes in rate of cell duplication and changes in number of participating clones. Uncertainty regarding the relative weights of these two functions is revealed by experiments with different time relationships for dosage with ultraviolet radiation. A limiting role of metabolite supply is indicated. Study of dose-time relationships for other carcinogens is recommended.

Table 1 illustrates a fundamental difficulty in the study of cancer growth. Increase in number of cells by duplication is described as an exponent of 2, whereas the effect of change in number of clones by death or recruitment of cells cannot be so described. The latter depends upon the moment of addition or subtraction of a cell, but in either case has an effect on the growth of the cell population proportional to the number of duplicating cells. Relationship to cancer growth may be expressed by

$$V/V_0 = e^s\, 2^{r\,(t-t_0)}, \qquad (1)$$

where V_0 and V are the volume of cancer at the beginning and end of the time period $(t-t_0)$, r is the rate of cell duplication (reciprocal of doubling time), e is the base of natural logarithms, and s is a non-duplicating function.

Table 1. The Effect of Recruitment and Deletion of Clones on Cell Population

Cells from original clone	1 (2^0)	2 (2^1)	4 (2^2)	8 (2^3)	16 (2^4)	32 (2^5)
Cells from recruited clone			1	2	4	8
Cells from deleted clone				-1	-2	-4
Cells from recruited clone					1	2
Total cells	1	2	5	9	19	38

The function s describes death and recruitment of cells, production of extra-cellular material, changes in cell volume, or other factors that affect growth in tumor volume. The proportionality of the effect of these non-duplicating factors to growth by cell duplication is expressed as an exponent of e, whereas cell duplication itself is expressed as an exponent of 2. Cancer growth thus involves two complementary exponential functions, but we are confronted with uncertainty because neither can be determined independently of the other. How is this uncertainty to be treated? I propose in my model to get around the difficulty by taking the functions s and r each equal to 1. Thus, after changing to a common base of exponents and taking logarithms, (1) becomes

$$\log_e (V/V_0) = 1 + 0.6932\,(t-t_0), \qquad (2)$$

where $\log_e$ indicates the natural logarithm, and 0.6932 is the conversion factor from exponent of base 2 to exponent of base e.

With this probabilistic dodge the model successfully describes various data on experimental induction of cancers by ultraviolet radiation, although the fundamental uncertainty is, of course, not resolved. I shall give only the final form of the model since the full derivation will be published shortly (Blum, 1974). But first a brief description of the experiments[1]: In a given experiment doses of ultraviolet radiation were given at regular intervals. The size of dose and interval between doses were kept the same until an end-point volume was reached. Different dose sizes and intervals were used in different experiments; the index for comparing results was the time from the first dose to the end-point.

It may be assumed that each dose affects both the non-duplicating function and the rate of cell duplication, the complementary effect of these on growth accumulating with the number of doses. The time between a given dose and the end point diminishes with the number of doses, of course, and the contribution to growth decreases accordingly. Taking these things into account, one may derive from (2)

$$\log_e (V_c/V_1) = (1 + 0.6932i)\, U\, (n_c^2 + nc)/2, \qquad (3)$$

where V_1 is the volume when the first dose is given, V_c the end-point volume, i the interval between doses, U the size of dose, and n_c the number of doses that have been given when the end-point is reached.

[1] These experiments are described in papers in the *Journal of the National Cancer Institute* (1940-50) by Hugh Grady, John Kirby-Smith, and myself. These are summarized in Blum (1959). The model described in the latter reference and hypotheses based thereon are invalidated by the present model.

Since volume of normal tissue is the same for all experiments, and so is the end-point volume, to a close approximation

$$(1 + 0.6932i)\, Un_c^2/2 = K\,, \qquad (4)$$

where K is a constant.

The interval i and dose U are constant for a given experiment, but have different values for each of the experiments, for which the data are plotted in Figure 1 on a log-log grid. In agreement with (4), a straight line with a slope of -1 is followed down to a sharp break to a horizontal line. The break indicates that the growth rate has reached a maximum which cannot be exceeded. Such a maximum limit on overall growth would be imposed by the upper limit of the supply of metabolites to the cancer, without regard for the relative contributions of cell duplication and non-duplicating factors. Circulatory channels adjust as cancers grow, and the diagonal line in Figure 1 may also be explained by feedback that adjusts metabolite supply to the requirements of an increasing cell population. Further evidence of this overall control of growth rate comes from other aspects of these experiments.

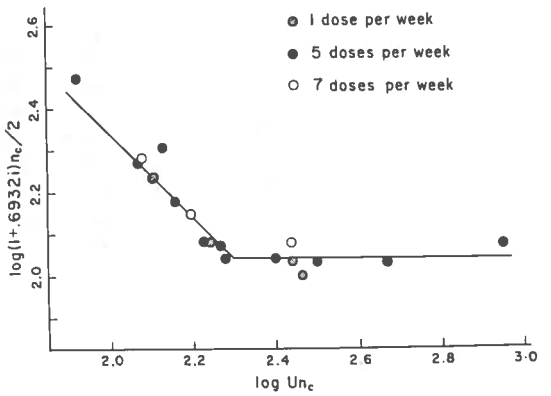

Figure 1. Results of experiments on cancer induction with repeated doses of ultraviolet radiation (see text for details). After Blum (1974).

The cancers were predominantly of two kinds: carcinomas deriving from the epidermis, and sarcomas deriving from the dermis. Often these are mixed in the same tumor. As shown in Table 2, the ratio of these two types of tumor varies randomly with size and intensity of dose, and with the incidence within a given experiment, but is systematically affected by the time schedule of the doses. This would be expected if the distribution of types is correlated with difference in the relative contributions of cell-duplicating and non-duplicating factors, which should vary with interval (4). This is explained if cancer develops in various loci which coalesce; the relative growth rates of carcinoma and sarcoma loci influence the composition of the cancer observed at the end-point. In spite of difference in composition all the cancers follow the quantitative relationship seen in Figure 1, indicating that overall control depends not on tumor composition but on metabolite supply.

Table 2. Summary of Ratios of Tumor Types (after Blum, 1974)

Conditions	Carcinomas/ Sarcomas
Dosage Schedule (various dose sizes)	
1 per week	0.05
5 per week	0.26
7 per week	0.48
Dose Size (5 doses per week, 7 experiments)	Mean = 0.27; S.D. 0.06
Intensity (5 doses per week, 7 experiments)	Mean = 0.27; S.D. 0.06
Percentiles (all experiments)	Mean = 0.27; S.D. 0.08

In other experiments the time relationships were disturbed by stopping the doses early, causing a delay in arriving at the end-point. The distribution of tumor types was not studied in this case, but quantitative agreement was obtained by appropriate adjustment of (4) to describe these conditions, indicating overall limitation of growth regardless of the changed relationships between cell duplication and non-duplicating factors.

In the above findings two things of basic importance stand out: 1), the uncertainty in growth of cell populations; and 2), the limiting role of metabolite supply. To illustrate the first of these I have had Figure 2 drawn to suggest that the cancer growth curve is mushy – I take the word from George Gamov, who used it to describe the Heisenberg uncertainty of position and velocity of an electron in an atom. The mushiness is indicated by the stippled area within which the growth curve may be supposed to lie, but just where we can have no exact idea. The curve drawn by the artist suggests that at one point growth takes a negative direction, which could conceivably happen if there was an excess of cell deaths; but in reality we could not know this if it occurred.

The role of metabolite supply and its control should be kept in mind as regards cancers in general, and it should not be forgotten in this regard that limiting caloric intake delays the appearance of tumors. Induction of tumors by chemical carcinogens may reach a maximum as the dose is increased, indicating similar feedback control. Experiments with different carcinogens may require correction on three parameters to bring them into agreement (Blum, 1974); the relevance of this to testing procedures in general seems worth consideration.

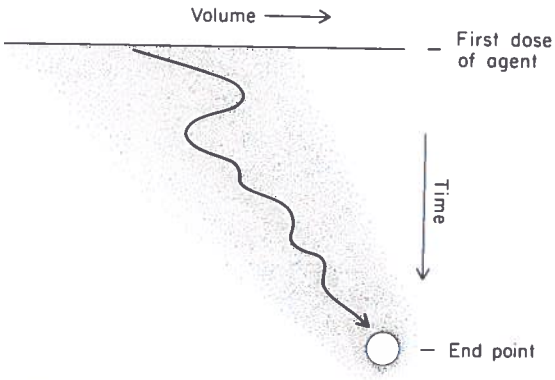

Figure 2. Drawing by Ryland Loos to illustrate the uncertainty of the curve for cancer growth. The curve is imaginary; it might lie anywhere within wide boundaries suggested by the stippled (mushy) area.

We might know more about the cancer process today if more experiments had been carried out with other carcinogens where time relationships were varied, as in those described here, which were carried out a good many years ago.[1] Such studies are laborious and time-consuming, but many more may be needed if we are to answer some of the questions with which we are faced in the study of cancer.

REFERENCES

Blum, H.F. (1959), *Carcinogenesis by Ultraviolet Light*, Princeton University Press.

Blum, H.F. (1974), "Uncertainty of growth of cell populations in cancer," J. Theoret. Biol. (in press).

DISCUSSION

(UNIDENTIFIED): Why do you use the ratio of carcinomas to sarcomas? Aren't the sarcomas caused by the radiation?

BLUM: Yes, but they are in different layers, and apparently have a different rate of growth. At any rate, we get the different ratio when we change the time interval, which of course changes the relationship between the duplicating and non-duplicating functions.

(UNIDENTIFIED): You said for your last slide that you had included three factors to bring the data together. What were they?

BLUM: That slide referred to single doses of chemical carcinogens, not to UV. Those curves, unlike those in the first slide, had to be adjusted on both the ordinate and abscissa, and in slope. I just wanted to point out that there are three ways in which such data can be compared, and I don't think we can be sure which to choose until there have been more experiments in which doses of chemical carcinogens are repeated with the time relations changed.

EFFECT OF CLIMATE ON NON-DOMESTIC WHEAT PRODUCTION

CLARENCE SAKAMOTO
Environmental Study Service Center
NOAA National Weather Service
Auburn University
Auburn, Alabama

ABSTRACT: Phytogeographic boundaries as they relate to historical climatic changes are discussed in assessing the effects of climatic alteration upon agricultural production. This approach is based on the premise that historical events and trends may provide an insight into the future. The effects of climatic change, and its impact on agricultural production in Europe and Asia, are discussed. Reference is made to change in species distribution as affected by length of growing season, droughts, and floods. Illustrations are presented to show climatic variations since about 5000 B.C., as well as vegetational response during later periods.

INTRODUCTION

Phenology is the science that treats periodic biological phenomena in relationship to climate. It is well known that plant distribution is influenced by climate. It seems logical that changes in climate should effect phenological as well as phytogeographical changes. Therefore, one approach to investigating the effects of induced climatic alteration on agricultural production is to study past climatic changes. This approach is based on the premise that historical events and their subsequent effects may provide an insight into the future.

Historical evidence indicates that there have been climatic changes. There is also evidence to indicate that agrarian changes have been influenced by changes in the climate. These climatic changes are not the familiar year-to-year fluctuations, but rather those which have occurred over a period of years, in some cases spanning hundreds of years. With unfavorable climate changes, total abandonment of agriculture may result; if the climate becomes more favorable, new crops (or old ones) may be introduced into old as well as new areas.

One disadvantage of this historical or paleophytological approach is that it is difficult to prove the cause-and-effect relationships by data or material on hand. Climate as a primary factor may not always be a "proven" explanation of an event. For example, archeological explorations have uncovered an ancient agricultural community, presumably abandoned (Braidwood, 1958; Helbaek, 1959). Is the lack of activity there today the result of climatic deterioration, or of an overrun by an enemy invasion, or of other economic factors? In the absence of any detailed written records, one can only piece together a monumental puzzle, the parts of which may not all be present, in an attempt to make inferences concerning the abandoned area.

Although this paper deals with wheat, reference is also made to other crops which have been affected by a change of climate in the past. The principal areas of study are Europe and Asia, where much has been reported on this subject. This literature survey will concern itself primarily with the period since 5000 B.C., the neolithic age, and with that period known as the "climatic optimum." In addition, only temperature and precipitation, two major factors in wheat production, are considered.

CLIMATE SINCE THE "OPTIMUM"

The climatic optimum is a period in history when temperatures were as much as 2-3°C (5°F) higher than today. It is a geologically modern thermal maximum that occurred roughly during the period 5000 to 3000 B.C. (In some parts of the world the climatic optimum occurred earlier, such as in the Bering Straits; there the date is approximately 8000-6000 B.C.) Pollen spectra analysis, carbon-14 analyses, archaeological analyses (including sediment analysis), and historical analyses in connection with vegetative changes, provide evidences for an estimate of temperature regimes.

Figure 1, which is partly hypothetical, shows the temperature-change curve with time since 5000 B.C. The general curve for Europe (Brooks, 1949) shows a gradual drop of temperature to 3000 B.C. Temperature rose after 2000 B.C. and began to fall again near 1000 B.C. There has not been a full recovery since that time. It is generally agreed by investigators (Chu, 1973; Brooks, 1949) that the climate near the end of the first millennium A.D. was similar to what it is today. Fluctuations have occurred since this period, including dry and wet periods as well as the advance and retreat of glaciers. The China curve has been derived from phytological studies by Chu (1973). It, too, shows a warm period to about 800 A.D. interrupted by cooler conditions near 1100 B.C. and 200 A.D. The Norway snow-line change, determined by glaciologists (Schwarzbach, 1963), also suggests a change in temperature regime (assuming that with warming the snow line rises and with cooling it retreats). The very low snow line about 400 B.C. corresponds to a cooler period in Europe and continues the trend to lower elevation since 1000 B.C.

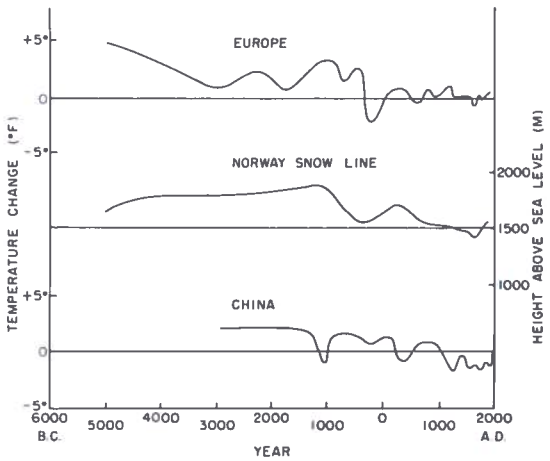

Figure 1. Estimated temperature change with time. The curve for Europe is after Brooks (1949); the curve for China is after Chu (1973); the Norway snow line is after O. Liestol (in Schwarzbach, 1963).

The timing of precipitation change since the climatic optimum for four areas is shown in Figure 2. During the climatic optimum, rainfall was generally higher, as indicated by the curves for Europe, Western Asia, and China. Drier periods have occurred in Europe, Britain, and Western Asia, centered near 2500 B.C., from 2000 to 500 B.C. in Britain, and near 1000 B.C. in China. Trends to increasing precipitation following drier periods were noted from 2500-2000 B.C. in Europe and Britain, near 1500 B.C. in Western Asia, and near 500 to 200 B.C. in all four areas. This description of the major changes of temperature and precipitation provides the background for a discussion of these influences on the vegetative distribution. Three examples follow.

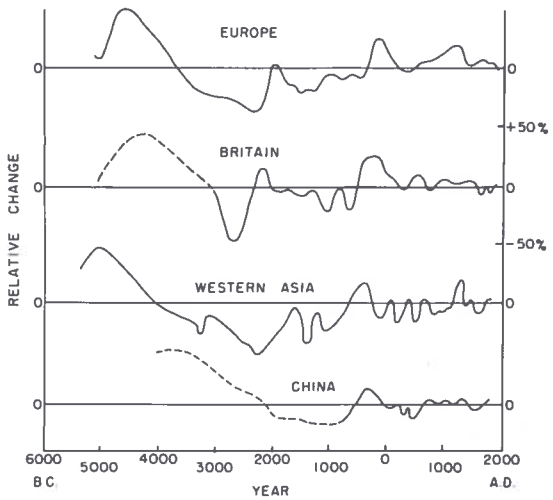

Figure 2. Relative precipitation change with time in four areas. The amount of relative change is approximated by the ±50% spacing indicated for Britain. The dashed lines for Britain and China are hypothetical.

CLIMATIC INFLUENCES IN CHINA

Chinese agriculture had its beginning in the Yellow River Basin. The rich alluvial soil from the higher elevations spread into what is known today as the North China Plain, one of the main agricultural areas of Communist China. From archeological expeditions, historical reports, diaries, and local gazetteers, Chu (1973) has been able to provide some convincing evidences of the changes in climate during the past 5000 years. For example, bamboo groves were found extensively in the Yellow River Basin during the period 3000 to 1000 B.C. Today bamboo groves rarely grow north of the latitudes of Sian (see Figure 3). This northern limit of bamboo coincides with the 0°C January mean isotherm which passes from Sian in the west to Suchow in

the east. This means that the northern limit of bamboo distribution has moved southward approximately three degrees' latitude. If Hopkins' Bioclimatic Law (Hopkins, 1938) is used as a general guide, this corresponds to approximately 12 days of time. That is, phenological events such as sprouting and blooming have been delayed 12 days by the cooler climate. On the basis of his study, Chu (1973) approximated this change as 2°C mean annual temperature change and a 5°C change for January.

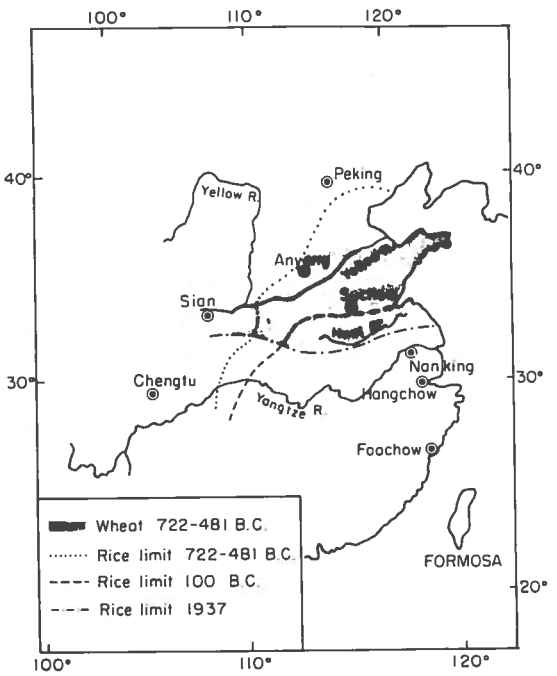

Figure 3. Phytogeographic changes for rice in China. Names of referenced locations are also shown in the figure.

Cultivated wheat was introduced in the Central China Plain in approximately 1100 B.C. (Hermann, 1966) which also corresponds to the time of the Shang or Yin Dynasty (1400-1100 B.C.). This was followed by the Chou Dynasty (1066-256 B.C.). These dynasties occupied the major portion of the Yellow River and Yangtze River basins. The estimated cultivated wheat area for the warm moist period, 722-481 B.C., is shown in Figure 3 (after Hermann, 1966). It is a curious observation that during the 722-481 B.C. period, wheat culture did not extend to the Yangtze Valley. Today, however, it is a major winter-wheat-producing area. It is suggested that the warm tropical climate was unsuitable for this activity during the first millennium. Evidences of tropical climate have been found in the Yellow River Basin. This means that the Yangtze River Valley must also have been tropical and perhaps a bit warmer. Cooling since 400 A.D. and a decrease in rainfall may have opened the new areas further south. (In spite of this observation, it is important to remember that climate is but one of the factors determining the geographical limits of cultivation.)

Rice is another crop whose vegetation boundary limit in China is climatically induced. In Figure 3 are depicted three boundaries for rice: 722-481 B.C., 100 B.C., and 1937, which represents the modern limit. Each of these geographical limits corresponds to cooling trends since 5000 years ago. Rice requires a warmer and slightly longer period for maturity than wheat. Since the first millennium, the northern limit of rice has moved southward approximately six degrees of latitude. This corresponds to a trend toward a cooler climate that began near the end of the 10th century B.C., from which modern climate has never returned to the climatic optimum.

From the Chinese calendar, the first frost in autumn 2000 years ago in the Yellow River Valley was fixed as October 24. In modern times, the first fall frost is the first week in November (Chu, 1926). In more recent history, Chu (1973) has also reported several phenological changes associated with climate. In the sixth century A.D., apricots north of the Yellow River were reported to reach full bloom in the middle of April. Today, they bloom by the end of March, a difference of approximately two weeks. Litchi, a Chinese fruit, grows only as far north along the coast as Foochow today. It was growing abundantly during the Tang Dynasty (618-907 A.D.) when temperatures were about 1° to 2°C warmer than modern times. In the eighth century litchis were grown abundantly further north in Chengtu. Also, during the twelfth century, litchis grew only at the southern boundaries of the province along the Yangtze Valley. Chu (1973) estimates that Hangchow was 1-2°C colder than modern times during the twelfth century. Also at Hangchow, in the seventeenth century, winter wheat was planted two weeks earlier than in the sixteenth century because of the cooler fall temperatures. With the warmer climate of modern times, winter wheat is again sown in late

November. All of these indications are responses of agricultural production to the changing climate.

Radioisotope measurements made on the Greenland ice sheet showed (Dansgaard et al., 1969) remarkable resemblance to Chu's temperature estimates. Although the comparison is for separate land masses, it partially supports the phenological deductions made by Chu. Bishop (1922), in discussing the development of Chinese civilization, noted the overthrow of the ruling dynasties in 1766 B.C. and in 1122 B.C. Great turmoil occurred in 842-771 B.C. In each of these cases, it is curious to note that they followed periods of drought. Such events add to the difficulty in establishing cause-and-effect relationships in historical studies where climate may have been a major factor.

Partly on the basis of past climatic history, and partly on a 1 to 2°C annual temperature decrease, the likely effect of climatic alteration in China seems to be a shift southward of the growing zones. This corresponds to approximately three degrees of latitude, and involves a shortening of the growing season by roughly two weeks in the spring and two weeks in the fall. If this were to occur under present-day conditions, the estimated growing-season length (average number of consecutive days above 0°C) would appear as in Figure 4. Although the length of the season would still be relatively long for wheat cultivation, practices such as double or triple cropping would no longer be practical. Furthermore, unless irrigation is practiced, wheat-growing areas should have a minimum annual precipitation of at least 250 mm – and even this amount is borderline, and often necessitates fallowing practices. Figure 4 also shows the present-day average precipitation in the winter wheat belt of China, and indicates that reduction in precipitation could significantly affect wheat production in the densely populated and intense agricultural areas of China.

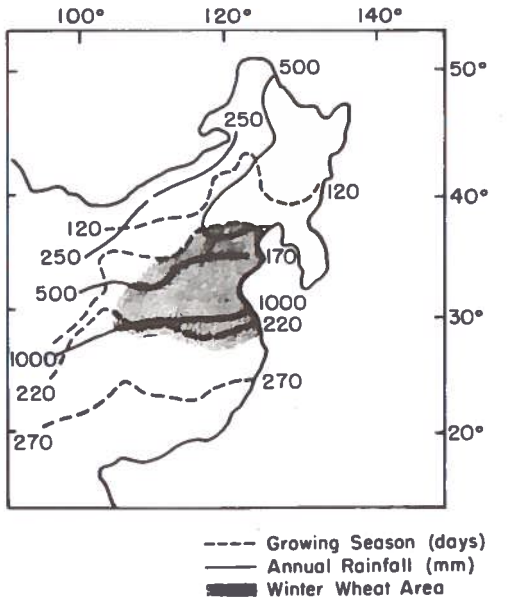

Figure 4. Possible average growing-season length resulting from shortening of the season by approximately four weeks (dashed line), present-day annual precipitation total, and winter-wheat area of China.

CLIMATIC INFLUENCES IN EUROPE

On the basis of botanical evidence, it is estimated that in Europe (including England) the annual average temperatures during the climatic optimum were approximately 2-3°C above modern-day averages. The tree lines were about 175 to 300 meters higher than today (Lamb, 1965; Manley, 1951). Deteriorating weather followed between 5000 B.C. to 1000 B.C. when storms increased, soil moisture increased, and average temperatures dropped about 2°C (Figures 1 and 2). A warm peak was noted near 1000 A.D. Precipitation, however, decreased somewhat from the 500 B.C. era. Change to colder climate began near the thirteenth century and led to the so-called "Little Ice Age" between 1550 and 1850.

Although vegetative changes in response to climatic changes are obscured because of man's intervention, some documentary evidence and archeological evidence do exist, and provide insight into the past weather. Documentary records since Christ are more numerous than those for earlier periods, so much more can be inferred for the more recent periods. Figure 5 is the estimated curve for 1000 years of central England temperature based on 50-year averaging (Lamb, 1966). The estimates show that between 1200 A.D. and 1600 A.D. temperatures decreased between 1 and 2°C. Rainfall changes during the 1000 years have also been estimated by Lamb (Figure 6). Higher amounts are noted from 1100 A.D. to 1300 A.D. Some of the effects of these changes are discussed below.

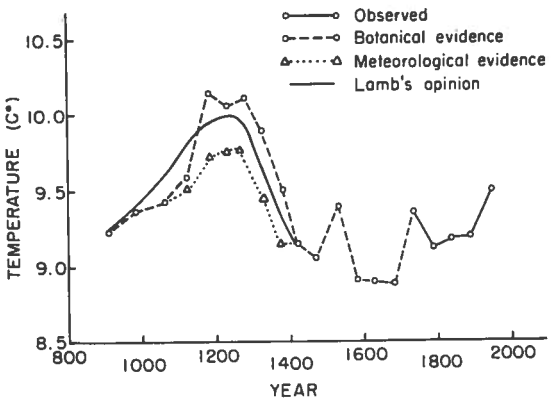

Figure 5. One thousand years of estimated temperature change in central England (after Lamb, 1966).

Because wheat has been and is still a major crop in Europe, human habitation is very dependent upon the success or failure of this crop. This is especially true for the weather-sensitive wheat crop, and where dry-farming is practiced. Much has been written in historical documents, particularly in more recent records, about the impact of climate on the grain harvest. The period about 1300 A.D. was a striking example of this. The impact of crop failures during the years 1309-1323 was felt from France to Sweden (Manley, 1958). In northern France, the wet

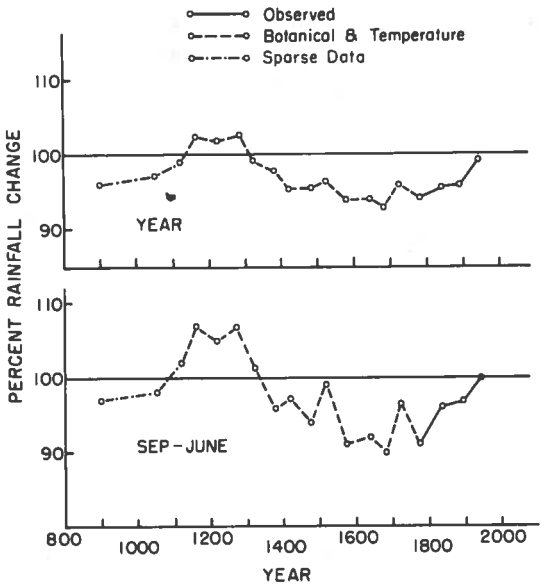

Figure 6. One thousand years of estimated precipitation change in central England on an annual basis (top) and for the September-June period (after Lamb, 1966).

weather of 1315 (see Figure 6) flooded wheat harvests and vineyards. The 1316 wheat harvest was so poor that "ingenious bakers mixed what little flour they had with the droppings of pigeons and pigs" (Ladurie, 1971). (Recycling is obviously not a modern innovation!) It may be significant that Mt. Hekla in Iceland erupted in 1300 and was followed by other eruptions later in the century. This could have made farming difficult or impossible (Utterstrom, 1955).

Growing of wheat was largely abandoned in east and south Scotland, although Lamb (1966) mentions that in 1733, wheat was reintroduced around Dunfermline and was known to have been grown at Kelso in 1290, although not in great quantity (see Figure 7). The late-seventeenth and mid-eighteenth centuries were relatively warmer, which may explain the reintroduction attempt at Dunfermline. Today wheat is grown primarily in eastern England (Figure 7).

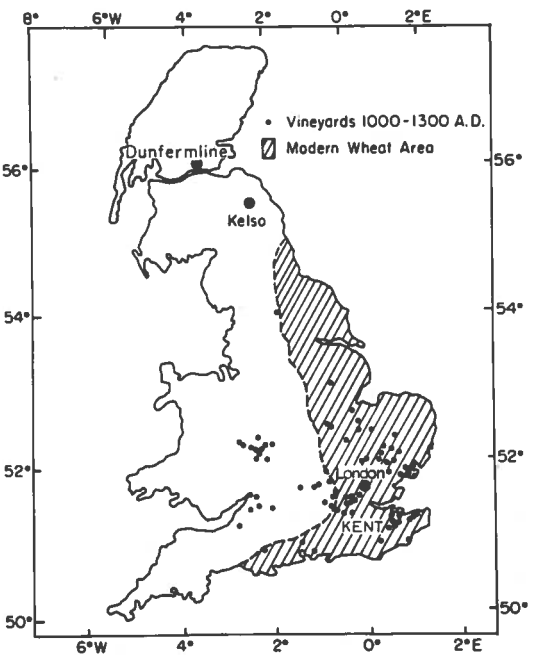

Figure 7. Former vineyards (after Lamb, 1966) and present-day wheat area in England. Names indicated on the figure are referenced in the text.

In England harvest failures were reported in the 1430's, 1550's, and 1590's, periods in the "Little Ice Age." Open-field agriculture was converted in large measure to sheep raising between 1300 and 1600. Interspersed in the Little Ice Age were warm periods, such as the

one from 1500 to 1540. The weather of the 1590's was very cold for wheat (see Figure 5). It was wet much of the year while springs and summers were cool. The wheat crop grew poorly and much was left in the field to rot. Late and poor harvest made wheat both scarce and expensive, and famine occurred in four consecutive years, from 1594 through 1597. Cool weather seems to have lasted through the seventeenth century. Similarly severe conditions were experienced during the decade of the 1690's. Feudal wars followed the harvest failure of 1693. The food supply for the army was foremost and supply to the people dwindled. The year 1816 brought another poor wheat year. The summer was about 2.5 degrees cooler than normal, which led to a late harvest and a wheat shortage. Famine followed the wheat shortage, and once again turmoil and national unrest plagued England. The economy was very sensitive to wheat and its availability.

Grapes are another crop that was affected by the changing climate. During the warm period of 1100-1300, vineyards were widespread in southern England (see Figure 5). In western and middle Europe, vineyards extended 4-5° further north in latitude and 100-200 meters higher on the hills than today (Lamb, 1966). By comparing temperatures at the northern limits of modern commercial vineyards in Europe with those of the locations of the best wine districts of 1150-1300 in England, Lamb (1965) was able to deduce that it was about 1 to 1.5°C warmer than now in the spring and summer months prior to 1300. He concluded that the increasing coolness of spring and May frosts brought an end to most grape-growing in England. More recently, Lamb (1965) estimated that the growing season as measured by the duration of temperatures above 6°C (42°F) had increased approximately two to three weeks during the 1921-1950 period by comparison with the 1840-1910 period. After the moderate success of wine-making from 1948-1954 in Kent, Hyams (1967) introduced in Devon the best French variety that was disease-resistant. After four years (1961-1965) of disease-free vines and abundant vegetative growth with flowers, his efforts to make home-brewed wine failed miserably. The vines rarely flowered before July 2, and the fruits could not ripen sufficiently before the cold set in.

Although Ladurie (1971) admits that the famine decade of the 1310's was the result of climate changes, he does not agree that climatic deterioration influenced the abandonment of vineyards. He attributes the disappearance to economics, and explains that it was simply too expensive to produce wine during this period. This may be something of a chicken-or-the-egg question, however. The plague years, 1378 to 1380, also contributed to the calamity. Historical evidence, however, suggests that famine years resulted from fluctuations in climate, which influenced the wheat crop, the staff of life. Turmoil and unrest seem to follow poor harvest years. (Of course, early farmers were more affected by weather variations than farmers are today. The climatic influences which resulted in poor crop years would have had far less effect on the early farmers had they possessed today's technological knowledge.)

From this literature search, it has been shown that climatological changes in parts of Europe apparently resulted in the movement of the geographical boundaries for wheat and grapes approximately 4-5° south, as well as 100-200 meters lower in elevation. Manley reported that in northern England, the growing season decreases approximately ten days for each 260 feet of increase in elevation. According to Hopkins, phenological events change approximately four days for each 1° change in latitude. From these values, the fluctuations in the growing season of two to three weeks, corresponding to a temperature change of 2° to 3°C, seem fitting. History also indicates that a reduction of precipitation in England during the growing period for wheat is not as serious as a reduction in southern Europe where precipitation amount is not as great. The danger in Great Britain is that rainfall will be excessive (Utterstrom, 1955).

CLIMATIC CHANGES IN SOUTHWESTERN ASIA

One of the most important archeological discoveries with regard to wheat domestication was made in a village called Jarmo in Iraq-Kurdistan (see Figure 8). Archeological evidence suggests that the village of Jarmo was occupied continuously for approximately 250 years after

Figure 8. Area associated with the wild Emmer wheat. The shoreline of the Persian Gulf was once much closer to Ahwaz. Deposits from the river are gradually building out the shoreline at a rate of approximately 1 1/2 miles each century.

about 7000 B.C. (Butzer, 1964). It was here at Jarmo that the oldest known wheat was excavated in the 1950's (Braidwood, 1958; Helbaek, 1959). Today the January mean temperature of Jarmo is about 6.5°C; the July mean is 29°C and the annual rainfall totals about 400 to 500 mm, most of which falls during the winter. These climatic conditions are sufficient for the culture of wheat, which is a present-day crop of the area. More important, wild wheat grows naturally and is believed to be indigenous to this area, including Turkey and Iran. The oldest known wheat, *Triticum dicoccoides* (wild Emmer), and a direct ancestor of *Triticum dicoccum* (Emmer), were found in baked clay and adobe and dated by carbon-14 analysis at 6700 B.C. Helbaek believes that this wild wheat represents the earliest appearance of wheat in a cultural context. The Emmer wheat became the main wheat and spread with human migration into Asia, Africa, and Europe. It maintained its lead position as a staple food crop during the first five millennia of agriculture. The wild Emmer wheat reached the interior of Iran and the Indus Valley during the third millennium B.C., but by late in the period, other variants of the species appeared. Through mutations of *Triticum dicoccum, T. durum* appeared near 300 B.C. in Egypt or the Mediterranean countries. The durum or macaroni wheat became the main wheat near the beginning of the Christian era.

The wild Emmer as well as the wild Einkorn, *Triticum aegilopoides* (also named *Triticum boeticum*), were introduced to the plains of lower Iraq in the fifth millennium B.C., and in the third millennium in France, Switzerland, Spain, Britain, and southern Russia. Einkorn in early times did not adapt well when introduced to less favorable environments. However, the cultivated Einkorn (*Triticum monococcum*) of today, which has been selected through mutations and hybridization, is quite resistant to cold, heat, and drought.

The distribution of these early wheat species is discussed as an example of the first stage of domestication of a species outside its natural limits. As a result of introduction into an unnatural environment, the process of selection for a particular type of grain began. Those strains that survived the harsher northern climate were selected for more advanced types of wheat.

South of Jarmo, an archeological survey was made in the ancient capital of Susa (Figure 8), located in the Khuzestan plain of southwestern Iran. Adams (1962) traced the span of history of this ancient village from about 6000 to 5500 B.C. In earlier times vigorous growth and settlement were indicated, but today rainfall is only approximately 300 millimeters, just barely sufficient for dry wheat farming. Adams suggested that the high early density of settlement can be traced to exceptionally favorable circumstances, including adequate precipitation. The pattern of settlement, which was almost exclusively in the northern portion of the upper Khuzestan plain, also indicated higher rainfall amounts. Agriculture in Susa was highly dependent on rainfall, since irrigation systems were not known until much later.

The number of villages in Khuzestan increased for several centuries after 5000 B.C. This increased population may have been associated with the development of irrigation systems. These systems were localized, however, and the pattern of agriculture still depended on adequate

rainfall. There are suggestions that the outwash channels between the Diz and Karun Rivers (see Figure 8) may have carried a larger and less seasonal flow than today. All of this evidence suggests a higher rainfall during the period several centuries following 5000 B.C., or at least so Butzer (1961) hypothesizes.

During the half-millennium before 3000 B.C., the total number of settlements declined, indicating some instability in the population (Adams, 1962). A period of intense drought followed. The trend continued into the second millennium, so that by 2000 B.C. Susa was the only known settlement in the upper Khuzestan plain. Wheat and barley were the most important crops in Susa. The period during the first millennium was filled with campaign battles which influenced the occupancy of the villages. Efforts to revive the villages were hampered by invasions, possibly droughts, as well as problems related to salinization of the agricultural land.

Brooks (1949) also describes a settlement at Anau in the northern section of Iran (Persia). This settlement was abandoned and resettled from time to time, and no evidence of conquest has been found. The village was reoccupied twice before 5200 B.C. The third reoccupation continued until about 2200 B.C., when a period of intense drought occurred. Anau as well as Susa was abandoned following this period, but reoccupied during the Iron Age, about 600 B.C.

One of the world's largest rain gauges, the Caspian Sea, also provides some evidence of climatic changes, particularly toward the end of the first millennium. From Herodotus' description in 438 B.C., the Caspian probably was joined with the Aral Sea, and its waters were about 45 meters higher than now. In 20 A.D., the height was estimated at 23 meters above the present level. Additional reports have been recorded to indicate large changes in the water level, including lower lake levels from about 300 A.D. to 800 A.D., around 1000 A.D., and in the twelfth century. Rising levels occurred in 1306 to 1307, when it was 11 meters above the present level, and in the fifteenth century, when water covered the city of Baku, on the eastern side of the Caspian Sea in the Soviet Union. The city is 5 meters above the present water level (Brooks, 1949).

More recent comparisons of precipitation in Western Asia, North Africa, the Middle East, and India have been made by Butzer (1961). A precipitation anomaly map of the period 1911-1940, expressed as a percent deviation from the mean of 1881-1910, is shown in Figure 9. Precipitation changes of as much as 30 percent were noted in the analysis. Furthermore, the figure indicates a drying trend for the period 1911-1940 in the Near East. Butzer estimates an annual decrease of 25.3 million cubic meters by comparing the mean for 1871-1900 with the mean of 1901-1945. Agriculture and the ecology of the Nile Valley would have suffered had it not been for the Egyptians' improved technology in dam building and irrigation. Butzer also notes that since 1910 the Caspian Sea has dropped 2-3 meters.

Again, it is difficult to prove that the changing population of villages such as Jarmo and Susa depended directly on climate, but the evidence suggests that climate was probably a major factor. It is certain, however, that microclimate changes have had a major effect on plant communities. Devegetation has been increasingly evident in modern times throughout the mountains of the Near East. Ecologically, this is associated with greater exposure to the sun's rays, higher temperatures, and reduced humidity, which all indicate a drying trend.

We have learned from the study in southwestern Asia that people adapted themselves to changing climate either by migrating in search of more favorable environments, or by introducing selected crop species which adapted to the changed environment. Introduction of the wild wheat to different environments enabled man to adapt the crop to newer and relatively harsher climates, thus expanding land area for production. However, by moving north he moved to areas where the growing season was limited. In Susa, the means of coping with diminishing rainfall was gained when irrigation systems were constructed.

SUMMARY

A study of the association between past climatic changes and agricultural production has provided some insight into changes in the phenologically induced vegetative boundaries in the past. According to Utterstrom (1955), "phenology has taught us that the period of ripening is considerably shortened within continental areas, that dry warmth accelerates the

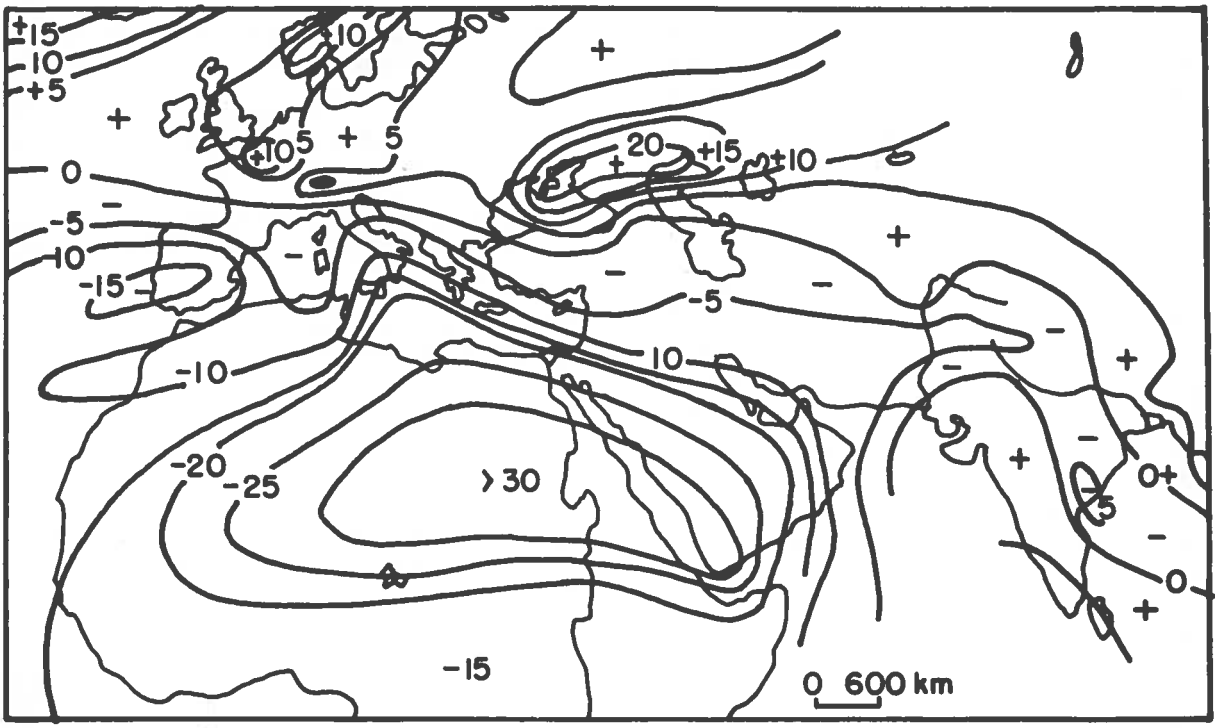

Figure 9. Precipitation anomaly of the period 1911-1940 relative to the period 1881-1910. Values are expressed as a percent deviation from the mean of 1881-1910 (after Butzer, 1961).

phases of flowering and fruition, that sharp changes in temperature cause the buds to open earlier . . . . "

In China, the past indicated that the phenological boundaries fluctuated depending upon the climate. Cooling moved the plant limits further south. In the case of wheat, lowering of the temperature approximately 1 to 2°C may have opened up new suitable areas of the humid south in the Yangtze River Valley. On the other hand, growing-season lengths also decreased. Thus, maturation was delayed in the spring. Furthermore, the sowing of winter wheat in the fall had to be moved ahead approximately two weeks. Rainfall, marginal in much of China where wheat is cultivated, is a major limiting factor. Since agricultural cultivation is so intense in China (with double and triple cropping), even a hectare of land removed from usage because of lowered temperature or reduced rainfall is significant.

Historical European famines have indicated that major crop failures such as wheat can produce chaos in a short time. This is evident even in modern days. It is significant that in the past, poor wheat harvest for several years in a row was usually followed by famine, and later, social upheaval produced by an unstable economy.

The story at Jarmo and Susa is significant because of the domestication of the wild wheat and its subsequent introduction to new areas. It is theorized that drought years in the Near and Middle East could have triggered migration, and this in turn could have led to the introduction of wheat elsewhere. The practice of irrigation came about in the ancient villages because of non-dependable rainfall resulting from climatic change.

Introduction of the wild Emmer wheat and related varieties to harsher climate resulted in mutations and hybridization for better varieties. Selections were made, perhaps unintentionally, for those characteristics that could withstand colder or warmer climate. Today geneticists are capable of breeding desired characteristics, which will be of major importance if climate alterations are effected. The kind of wheat grown in different countries is much affected by climate. Durum (macaroni) wheat favors a special climate, and so does the low-baking-strength, soft-textured wheat of Europe, which prefers higher rainfall and cooler temperatures.

Primitive agriculture was more dependent on favorable weather than modern agriculture with its advanced technology. Today, however, there are more people in the world. The response to any climatic change would therefore probably be more rapid and more intense than in early historical times. Hustich (1952) discusses the mechanism for social changes resulting from historical changes in the climate. With frequent years of poor crop weather, the environment has a direct effect on its inhabitants: "Climatic changes influence the balance within a community and different members react differently to it. This, in turn, leads to a displacement of population boundaries."

Much has been said about how the changes in climate might affect wheat production, but little of a quantitative nature has been mentioned. This numerical prediction awaits a future study; it might be dealt with by means of statistical models. Development of these "forecast" models in itself is a formidable task, although not an unsurmountable one. It is clear, however, that reliable models are urgently needed.

ACKNOWLEDGMENTS

Appreciation is expressed to my colleagues of the Environmental Study Service Center, National Weather Service, for their comments and suggestions regarding the contents of this paper. In particular, acknowledgment is made to Dr. Ray Jensen, Director, for his encouragement in the course of this study. This study was conducted for the Department of Transportation under Contract Number DOT-AS-400006.

REFERENCES

Adams, R.M. (1962), "Agriculture and urban life in early southwestern Iran," Science **136** (3511), 109-122.

Bishop, C.W. (1922), "The geographical factor in the development of Chinese civilization," Geographical Review **12**, 31.

Braidwood, R.J. (1958), "Near east prehistory," Science **127** (3312), 1419-1430.

Brooks, C.E.P. (1949), *Climate through the Ages*, McGraw-Hill Book Company, Inc., New York, 395 pages.

Butzer, K.W. (1961), "Climatic change in arid regions since the Pliocene," in UNESCO, Arid Zone Research XVII, *A History of Land Use in Arid Regions.*

Butzer, K.W. (1964), *Environment and Archeology*, Aldine Publishing Company, Chicago, 524 pages.

Chu, Co-ching (1973), "A preliminary study of the climatic fluctuations during the last 5000 years in China," Scientia Sinica **16** (2), 226-256.

Chu, Co-ching (1926), "Climatic pulsations during historic time in China," Geographical Review **16** (2), 274-283.

Danasgaard, W., S.J. Johnsen, J. Moller and C. Langway (1969), "One thousand centuries of climatic record from Camp Century and the Greenland ice sheets," Science **166**, 377-381.

Helbaek, H. (1959), "Domestication of food plants in the old world," Science **130**, 365-373.

Hermann, A. (1966), *An Historical Atlas of China*, new edition, Aldine Publishing Company, Chicago, 88 pages.

Hopkins, A.D. (1938), "Bioclimatics: A Science of Life and Climate Relations," USDA Miscellaneous Publications, No. 288, 188 pages.

Hustich, I. (1952), "Agricultural production in Finland and the recent climatic fluctuation," Fennia **75**, 97-105.

Hyams, E. (1967), *An Englishman's Garden*, Camelot Press Ltd., London and Southhampton, 160 pages.

Ladurie, E.L.R. (1971), *Times of Feast, Times of Famine:* A History of Climate Since the Year 1000 (translated by Barbara Bray), Doubleday Company, Inc., Garden City, New York, 426 pages.

Lamb, H.H. (1965), "Britain's changing climate," in *Biological Significance of Climatic Changes in Britain*, C.P. Johnson and L.P. Smith, eds., Academic Press, London and New York, 3-31.

Lamb, H.H. (1966), *The Changing Climate*, Methuen and Co. Ltd., London, 236 pages.

Manley, G. (1951), "The range of variation of the British climate," Geographical Journal **117**, 43-68.

Manly, G. (1958), "The revival of climatic determinism," Geographical Review **48** (1), 98-105.

Schwarzbach, M. (1963), *Climates of the Past*, translated and edited by Richard O. Muir, D. Van Nostrand Company, Ltd., Princeton, New Jersey, 328 pages.

Utterstrom, Gustaf (1955), "Climatic fluctuations and population problems in early modern history," Scandinavian Economic History Review **3** (1), 3-47.

DISCUSSION

(UNIDENTIFIED): Do you feel there is any connection between the deforestation in the mountains of the Middle East and the changes in reproduction rates of ponderosa pine in the San Fernando Valley in California?

SAKAMOTO: Well, we do know from the literature that a change in climate in one area frequently coincides with changes in other areas, suggesting that climatic changes tend to be global. So it's quite possible that there is some connection between those changes on opposite sides of the globe.

(UNIDENTIFIED): Have you any idea what the mechanisms for the climatic changes you talked about could be?

SAKAMOTO: This question has been discussed quite a bit. Some of the mechanisms suggested include changes in solar radiation, changes in ocean temperature, and land-mass movements. It seems reasonable to suggest that a combination of factors is at work.

(UNIDENTIFIED): Have you tried to correlate temperature with rainfall?

SAKAMOTO: No, I haven't. There are some data that suggest that decreased temperature is correlated with decreased rainfall. During the climatic optimum, an increase in temperature was associated with an increase in precipitation.

SIMULATION MODELS OF THE EFFECTS OF CLIMATIC CHANGE ON NATURAL ECOSYSTEMS

CHARLES F. COOPER
San Diego State University, San Diego, California

T.J. BLASING AND H.C. FRITTS
University of Arizona, Tucson, Arizona

OAK RIDGE SYSTEMS ECOLOGY GROUP
Oak Ridge National Laboratory, Oak Ridge, Tennessee

FREEMAN M. SMITH AND WILLIAM J. PARTON
Colorado State University, Fort Collins, Colorado

GERARD F. SCHREUDER AND PHILLIP SOLLINS
University of Washington, Seattle, Washington

JON ZICH AND WAYNE STONER
San Diego State University, San Diego, California

ABSTRACT: Five total ecosystem simulation models, developed as a part of the U.S. participation in the International Biological Program, and a statistical model of climate and tree growth were operated with the climatic changes specified by CIAP. The simulation models predicted that primary plant production will decrease linearly with temperature decrease throughout the range of temperatures tested, except in extreme deserts where the effect is expected to be reversed. The predicted decrease is greatest in models of ecosystems more or less well supplied with water, and less or even reversed under moisture-stress conditions characteristic of shortgrass prairies, deserts, or the more arid coniferous forests. Climatic perturbation is predicted to have a nonlinear effect on consumer organisms that is more severe and less regular than the associated effect on primary producers. Rates, pathways, and the seasonal course of microbial decomposition are likely to be altered in relatively complex ways by climatic change; this could significantly influence long-term successional responses. The models suggest that total ecosystem standing crop may be either increased or decreased as a result of climatic change, depending in part on the initial climate and the successional status of the community being investigated. Water stress in vegetation is likely to be slightly reduced by a decrease in temperature even if that temperature decrease is accompanied by a reduction in precipitation. Interactions among climatic variables may generate responses whose signs differ from those which would be predicted from superposition of the independent effects of the several climatic forcing functions. This experiment, apparently the first of its kind that has been made, indicated that simultaneous comparative analysis of several ecosystem models can lead to significant ecological predictions.

Direct experimentation to determine the long-term effects of a sustained climatic change on natural biological communities is clearly impractical. Computer simulation has proved to be an effective surrogate in many instances where time, expense, or uniqueness of the system being investigated preclude direct experimentation. These instances range from testing the effects of novel fiscal and monetary policies on the national economy to designing moon rockets. Ecosystem responses to climatic change can also be simulated by computers, even though ecosystem models have not yet attained the precision characteristic of econometric or aerospace models.

Several simulation models of complex ecosystems have been developed recently, mostly under the aegis of the International Biological Program. Five of these models, each designed for a different purpose, were operated in parallel under perturbations representing the climatic changes assumed by CIAP. Simultaneously, the predictions of a statistical model of climate and tree growth were tested for congruence with

those of the ecosystem models.

This experiment was not intended to yield quantitative predictions of ecological change in natural ecosystems due to climatic change. Rather, it was designed to test whether common qualitative patterns could be discerned in the behavior of the simulated ecosystems as a result of climatic stress. Several consistent trends were in fact observed, not all of which would necessarily have been predicted by the more traditional methods of ecological analysis.

Several major conclusions emerged from the computer simulations:

- Primary plant production is expected to decrease linearly with temperature decrease throughout the range of temperatures tested, except in truly arid regions. This decrease will be greatest in those ecosystems more or less well supplied with water, and will be less under moisture stress conditions characteristic of shortgrass prairies. Plant production in deserts and semi-arid coniferous forests is indicated to be accelerated slightly by temperature decrease.
- Climatic perturbation may have a nonlinear effect on consumer organisms that is more severe and less predictable than the associated effect on primary producers.
- Rates, pathways, and the seasonal course of microbial decomposition are likely to be altered in relatively complex ways by climatic change; this could significantly influence long-term successional responses.
- Total ecosystem standing crop may be either increased or decreased as a result of climatic change, depending in part on the initial climate and the successional status of the community being investigated.
- Water stress in vegetation is likely to be slightly reduced by a decrease in temperature even if that temperature decrease is accompanied by a reduction in precipitation.
- Interactions among climatic variables may generate responses whose signs differ from those which would be predicted from superposition of the independent effects of the several climatic forcing functions.

THE MODELS

Development of ecosystem-simulation models has been a major feature of U.S. participation in the International Biological Program. Since about 1969, many man-years of research effort have gone into construction and testing of ecosystem models. Each of the existing models has been extensively operated and validated, but this is apparently the first time that several comprehensive ecosystem models have been operated in concert to address a single set of questions. The results are therefore of some significance in the development of the science of ecology as well as in the specific task of predicting the ecological consequences of increased stratospheric flight.

The ecosystem models described here have all been developed as a part of the Biome Studies of the U.S. IBP, so called because many separate investigations of ecosystem processes have been grouped to cover the broad groups of ecosystems which are similar in vegetational physiognomy, fauna, and climate, known as biomes. The participating groups include the Deciduous Forest Biome, with headquarters at Oak Ridge National Laboratory, Tennessee; the Coniferous Forest Biome, at the University of Washington, Seattle, and Oregon State University, Corvallis; the Grassland Biome, at Colorado State University, Fort Collins; the Desert Biome, at Utah State University, Logan; and the Tundra Biome, with modeling efforts (but not overall direction of the research program) centered at San Diego State University. One non-IBP group, the Laboratory of Tree-Ring Research at the University of Arizona, Tucson, also participated. The research reported here was supported by a contract from the U.S. Department of Transportation, but the great bulk of the earlier research at the participating institutions which made this study possible was sponsored by the National Science Foundation.

The ecosystem models discussed here are largely comprised of linked sets of non-linear differential or difference equations, often with discontinuities, and subject to constraints im-

posed by biological limitations. The initial state of the ecosystem is described by a large number of variables which express the numbers, weights, age and sex distribution, and composition of each of the major groups of organisms, and similar values which specify the organisms' non-living environment. The model incorporates mathematical specifications of the rates of change of each of the state variables in terms of the various factors influencing them. These factors may be other state variables, or may be variables whose values are not derived from within the model. Values for these exogenous variables, or forcing functions, which normally include local meteorological conditions, must be supplied for the period being simulated. Forcing functions may be entered as constants, as tables with rules for interpolation, as time-dependent functions, or as stochastic functions, but in any case are independent of events within the system. Climatic or other forcing functions may be modified in a specified manner to test the effect of a new assumed condition, such as climatic change. The equations are then solved on a computer. Even though the full complexity of an entire ecosystem may still be beyond the capacity of the current generation of computers, the way has been opened in recent years for a mathematical representation of ecosystem dynamics which can be cast into a form suitable for digital solution. An ecosystem can thus be simulated in the computer (Goodall, 1972).

It is not intended to document here the detailed structure of each of the ecosystem models used in this study, but only to indicate their general nature and probable range of validity. Although all of the models follow the general pattern described above, each has been developed independently and has numerous unique features. All but the University of Arizona model are basically deterministic process models, built up from observations and assumptions about organism responses and interactions in the field. The Arizona Tree-Ring Model is a multivariate statistical model of observed relationships among climatic variables and growth responses of tree rings; it has been described in detail by Fritts et al. (1971).

The tundra simulations were based on two separate models. The first is a model of physical processes affecting primary production in the Arctic (Miller and Tieszen, 1972). It was developed from the energy-budget equation for single leaves. It includes parameters defining the relationships between photosynthesis and light, photosynthesis and temperature, respiration and temperature, and leaf resistances, all calculated from field data collected in 1969 and 1970. The data on single leaves were translated into ecosystem responses by means of a weighted summation based on the relative surface area of leaves of each species in the community, their inclination to the sun, shading and light extinction, and other pertinent structural features. The model has been validated with observational data for 1965 and 1970 from Point Barrow, Alaska.

The other tundra model is a preliminary simulation of the tundra ecosystem developed by Timin et al. (1973). The state variables are a subset of those in the real system. Those of interest for this study include above-ground plant biomass density, and population densities of brown lemmings, least weasels, and pomarine jaegers (Figure 1). The environmental inputs or driving variables are solar-energy flux (global short-wave), mean daily temperature, day length, and fraction of the ground that is snow-free. Photosynthesis and growth rates for the plant community are functions of solar radiation, temperature, and day length. The comprehensive tundra photosynthesis model described above has not yet been coupled into the total ecosystem model. A significant defect of this aspect of the model is that snowmelt, and implicitly the beginning of the growing season, are functions of time and not of temperature. Spring melt occurs at the same time each year regardless of temperature, whereas under a real climatic change it would presumably be delayed by reduced temperature.

Most aspects of lemming population dynamics (birth rates, recruitment rates, death rates, food-consumption rates, etc.) are simulated as functions of food supply. Lemmings are assumed to eat primarily live green plants in the summer and frozen edible plant matter in the winter. The model is programmed to allow for the transfer of an appropriate fraction of material from the live-green to the frozen-edible compartments at the end of the growing season. Least weasels prey on lemmings, and weasel population densities in the model are based primarily on lemming numbers. In-migration and out-migration of weasels are triggered by critical

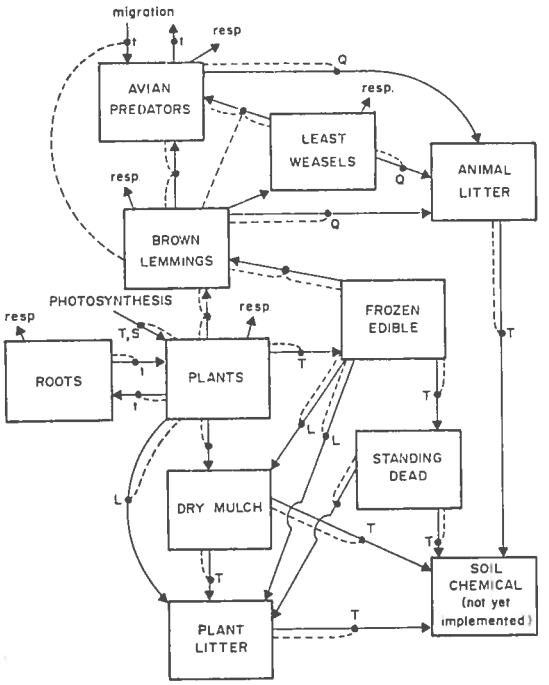

Figure 1. Block diagram of state variables now included in the Barrow simulation model. Solid lines denote flow of matter or energy and dashed lines denote an influence on rate of flow. Denoted by letters are: t, time of year; T, temperature; S, solar radiation; L, lemmings; and Q, various consumption rates.

lemming population densities. Pomarine jaegers immigrate each spring and emigrate each fall. Their summer population densities are modeled as functions of lemming abundance, as is the survival of their offspring. When lemming densities are low enough, jaegers fail to establish territories and mate. The large size of their territories sets an upper limit on their numbers in the simulations regardless of the size of the lemming population.

The tundra ecosystem model includes about 150 separate equations, and a single year can be run in about 0.28 seconds on the 360/91 computer at UCLA. Out of necessity, it contains many simplifying assumptions. An inherent deficiency is the lack of adequate justification for many of the parameter values, simply because of the unavailability of pertinent data. Field research at the Barrow, Alaska site since the model was developed has in fact shown that several of the assumptions about biological interactions are partially incorrect, at least with respect to that location. Nevertheless, the tundra ecosystem model is considered to have significant heuristic value in providing clues about the direction and nature of the probable response of the real system to climatic change, even if it does not yield quantitatively accurate results.

The Coniferous Forest Biome model simulates transfers and accumulation of carbon among biological compartments in a 10.3-hectare watershed dominated by old-growth Douglas fir on the H.J. Andrews Experimental Forest of the U.S. Forest Service in the Cascade Mountains, Oregon. The primary-production model is an outgrowth of one developed earlier by Sollins et al. (1973) for a yellow-poplar stand in the southern Appalachian Mountains of Tennessee as a part of the Deciduous Forest Biome research.

The current model consists of eight nonlinear first-order difference equations operating on a weekly level of resolution. Input variables are mean weekly solar radiation (Ly min^{-1}), mean weekly air temperature (°C), mean weekly daylength, and mean weekly soil water. Flows and compartments are shown in Figure 2. The units of storage are metric tons of carbon per hectare. The entire 10.3 ha is assumed in the present model to be homogeneous spatially and to contain but a single species of vegetation.

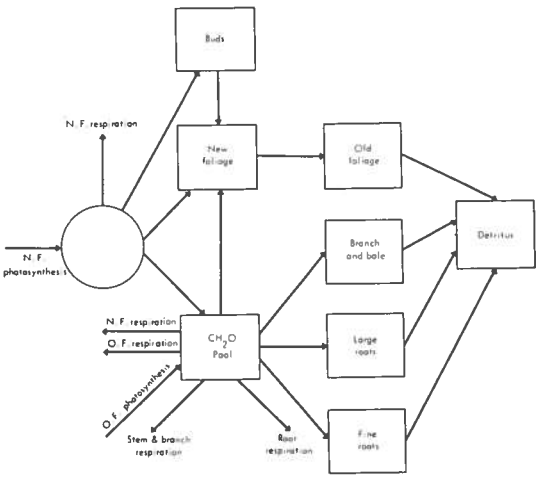

Figure 2. Flows and storages of carbon in Coniferous Forest Biome primary-production model. N.F. – new foliage; O.F. – old foliage.

The other Biome models, which are not described in detail here, are of the same general nature and order of complexity as those previously described. They all have been extensively

validated with field data from the specific ecosystems which they purport to describe.

The models are not designed to predict long-term successional trends or changes in plant and animal community composition; ecological modeling has not yet reached the stage at which meaningful predictions can be made about the potential replacement of one species group by another. The simulation runs are therefore limited to a 5-year period and emphasize changes in primary production and in associated aspects of community structure. It is questionable how far beyond this 5-year period the results can validly be extrapolated.

By definition, all of the conclusions and predictions of the simulations are built into the models, some more explicitly than others. For example, all of the simulated systems are more sensitive to temperature change than to an equivalent change in solar radiation when each is tested separately. This primarily reflects the interplay between the hyperbolic relation of net assimilation to light intensity (at high light intensity the curve is flat) and the exponential effect of temperature on assimilation. Explanations for some other patterns are not so apparent, however. One of the principal values of ecological simulation may be the uncovering of assumed but unrecognized relationships implicit in model structure and their exposure to explicit study and analysis.

Complete comparability was not achieved among all the models. Neither as input driving variables nor as output variables could the same components be included in all of them. Thus, the direct, independent effect of precipitation could not be treated in the tundra model, nor could that of solar radiation alone in the tree-ring model. And, of course, each was designed to deal with a distinct climatic region having plant and animal species quite different from those of the others. Nevertheless, the degree of convergence is encouraging.

In carrying out this experiment, each model was run separately in the respective laboratory; results were synthesized at San Diego State by C.F. Cooper in consultation with the other investigators. The Desert Biome participated only to the extent of providing a simulation of primary production in a desert shrub community.

PRIMARY PRODUCTION

Net primary production – total photosynthesis minus plant respiration, but not including consumption by herbivores or death of plant parts – was simulated in all of the models. This was the only output variable reported by every one of the participating groups. All of the ecosystem simulations except the Desert Biome's predicted a reduction in net primary production as temperature and associated climatic parameters were decreased. This reduction varied from about 18% for each 1°C in the deciduous-forest model to 6%/°C in the grassland model (Figure 3). The Desert Biome model suggested that alleviation of water stress through lowering of temperature might actually increase primary production in extreme deserts by as much as 3%/°C. The University of Arizona statistical model of tree growth demonstrated the same effect in conifers on arid sites.

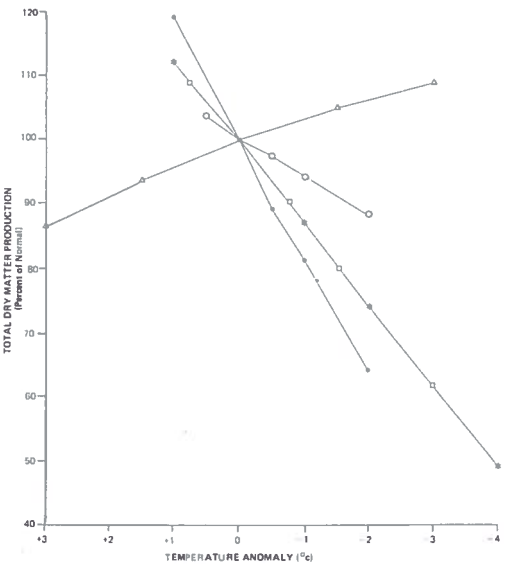

Figure 3. Simulated response of plant productivity in five regional ecosystems to hypothetical climatic change. Associated with the temperature anomalies are the accompanying changes in solar radiation, wind field, and precipitation specified by CIAP. △, desert; ○, grassland; *, tundra; □, coniferous forest; ●, deciduous forest.

The response of primary production to simulated climatic change was essentially linear throughout the range of temperatures investigated. Because of the great differences in productivity among the several ecosystems, all results

are reported as percentage deviations rather than as absolute values.

Several reservations must be taken into account in interpreting the results of the simulations. Temperature and radiation effects on plant production were explicitly built into each of the models. (There was more or less regular interchange among the several modeling groups during the development period; similarity of equations and of some of the results might therefore have been expected.)

Furthermore, many long-term features of the response of plant production to climatic change cannot be predicted from existing models. For instance, some plants may become acclimated to new conditions if the new climate remains stable for some length of time. A change in temperature or water relations may alter physiological processes other than photosynthesis and respiration, and these, by a feedback mechanism, will indirectly affect plant production. Certain threshold values, such as those for temperature induction of enzymes, may be exceeded or not reached – an effect not covered in the models. Finally, long-continued climatic change will influence the outcome of competition among species, leading perhaps to a new community structure with changed productivity patterns. This problem likewise cannot be solved with a model of photosynthesis or primary productivity. Nevertheless, the similarities and differences in the responses of the simulated ecosystems to climatic change may yield significant clues about the possible reactions of real systems to alterations in climate.

The differing slopes of the temperature-response curves can presumably be explained by the climatic conditions of the several biomes, particularly by their differences in water regime. Plant production in the tundra region, for instance, is almost wholly temperature- and radiation-dependent. Apparent soil-water deficiencies of a magnitude likely to inhibit growth are not normally observed on the experimental sites in the wet tundra at Barrow, Alaska. Accordingly, precipitation and soil-water variation were not programmed into the tundra simulation model. These factors were accounted for in the coniferous forest model, but decreases in soil water do not markedly inhibit tree growth in the cool-temperate climate of the high-elevation Douglas-fir forest simulated in this experiment. The slopes of the curves produced by the tundra and the coniferous-forest simulations were almost identical, predicting a relative decrease of 13% in net primary production for each 1°C reduction in mean temperature.

The deciduous-forest model predicted an even sharper decrease in primary production with temperature than the two preceding simulations: 18%/°C. The deciduous-forest region, although well supplied with moisture, does suffer occasional periods of deficiency during the growing season. The TEEM model (O'Neill et al., 1972) used in the deciduous-forest simulation is responsive to variation in temperature and radiation, but includes no explicit dependence on the water cycle or wind velocity. These effects are incorporated in a separate model of atmosphere-soil-plant relations known as PROSPER (Goldstein and Mankin, 1972), but the two have not yet been coupled. Therefore, PROSPER was run separately and subjective observations were made of the biotic response to water stress. The results, as will be discussed in more detail in the later section on evapotranspiration and water stress, indicated that decreased temperature would decrease water stress on the vegetation. The reduced growth due to lower temperature might be partially compensated for by decreased water stress. The subjective judgment of the Deciduous Forest Biome group as a result of running the PROSPER model is that the system changes predicted by the TEEM growth model may be somewhat exaggerated, and would be partially compensated for by changes in water stress which are not incorporated in the TEEM model. If this should prove to be the case, the proportional decrease in primary production with temperature would be lessened, bringing the deciduous-forest line in Figure 3 into closer accord with those for the tundra and the coniferous forest. This points up a significant area for future investigation and for inter-biome comparison.

Plant production in the grassland region, in coniferous forests on relatively arid sites, and especially in the desert, is more dependent upon seasonal and annual patterns of rainfall and soil water than it is in regions of higher precipitation. Grassland plant production is highly sensitive to spring and early summer soil moisture, which in turn is affected by the interplay between air temperature, solar radiation, and precipitation. Reduced temperatures in this moisture-deficient

region may reduce soil-water losses more than they depress photosynthesis. Consequently, the simulated net loss of primary production in the Grassland Biome model is less for a given temperature decrease than it is in those biomes more abundantly supplied with water.

Water deficiency is even more critical in the desert. The Desert Biome model was run for a simulated 100 days during the 180-day main growing season of a single species, *Hammada scoparius*, a native of the Negev Desert of Israel. The growing season of this species extends from about April 1 to September 1. There is normally no rain in the Negev from mid-April to the end of October. Field data for the simulation were collected by E.D. Schultze and associates of the University of Würzburg, Germany, and used by him in development of a photosynthesis submodel as part of the U.S. Desert Biome research.

This series of comparative simulation experiments with ecosystems in different climatic regions suggests that the response of net primary production to changes in temperature and solar radiation, and associated precipitation and wind variables, is likely to be nearly linear within the range of temperature and radiation changes expected from increased stratospheric flight (Figure 3). In regions relatively well supplied with water during the growing season, a 1°C decrease in temperature is likely to reduce net primary production in the neighborhood of 12-15%. The similarity in response of the tundra, coniferous-forest, and deciduous-forest simulations is striking. (A 12% decrease in plant production is of course much larger in a forested region of high production than in the low-production tundra.)

Where water for plant growth is more limiting, the reduction in primary production with temperature will be less, chiefly because lower temperature and reduced solar radiation will result in lowered leaf-water stress. In true desert climates, this effect may be so strong that plant production will actually increase as a consequence of reduced temperature.

The validity of the numerical values suggested here can be established only after additional field research and observation. The qualitative pattern suggested by the comparison is probably valid; logical and reasonable explanations for this pattern can be identified. It is, however, doubtful that this specific prediction of the ecological effects of climatic change could have been made without some sort of comparative modeling effort.

CONSUMER ORGANISMS

When consumer organisms were added to the simulated systems, interactions among trophic levels made the system response appreciably more complex and less predictable than in the relatively simple case of primary production alone. In the Arctic tundra simulation, primary production is reduced so much by a 2°C decrease in mean temperature that the assumed cyclical pattern of lemming population numbers breaks down. Lemming numbers fail to build up enough to support appreciable numbers of predators. The typical crashes in lemming numbers due to predation do not occur. The lemmings thereafter persist in low but essentially constant numbers, determined primarily by their food supply. This food supply is in turn determined by the interplay between reduced primary production and overgrazing. Overgrazing is more or less continuous in the absence of significant predation.

The response of lemming populations to temperature decrease is distinctly nonlinear, in contrast to the nearly linear effect on primary production. At the point where the self-regulating system effectively breaks down, the percentage decrease in lemming numbers is closer to 50% per 1°C decrease in temperature than to the 13%/°C reduction in primary production.

The early version of the tundra ecosystem model used here is more oversimplified and unrealistic than any other of the models tested in this experiment. It is being superseded by an entirely new model. Nevertheless, it is instructive that the simulated system breakdown due to temperature change resulted entirely from differential changes in relationships among system components. The model was initially designed to reproduce an assumed three-year lemming population cycle, but no explicit timing mechanism was incorporated. The emergent property of cyclical behavior resulted from interactions among primary producers, consumers, and predators. The principal state variables and forcing functions in the tundra model were described earlier.

When the simulated mean temperature was increased by 1°C, primary production increased and the peak abundance of lemmings about doubled. The three-year cyclical behavior was retained, and the population dropped between highs to the same very low level as in the control case. When the temperature was reduced by 1°C, primary production decreased proportionately, and the peak lemming population was almost halved. Once again, the three-year cycle remained, but minimum winter population numbers were higher than in the control case. A 2°C temperature decrease, however, completely destroyed the cyclical behavior of the system, primarily because of the loss of significant predation. Net plant production then stabilized at a level considerably lower than would have been predicted from the temperature-induced reduction of 13%/°C in gross primary productivity discussed in the previous section. This, of course, was due to heavy grazing by lemmings.

The significant conclusion from this experiment with the tundra model is not that weasels and jaegers are predicted to be harmed by a moderate decrease in temperature, or even that an apparent system breakdown occurs at a temperature reduction of 2°C but not at a smaller decrease. These quantitative predictions may or may not be vindicated by reality. It is significant, however, that the simulation model predicts an entirely new structural relationship among system components – primary producers, consumers, and predators – as a consequence of a climatic change of relatively modest proportions.

A somewhat similar prediction resulted from the Deciduous Forest Biome simulation. Aphids were the only consumer organisms studied in these model runs. Since no predator was included in implementation of this section of the model, response of aphid populations is dominated by direct temperature effects on aphid metabolism and reproduction and by changes in primary production of the plants upon which they feed.

Aphid populations decreased as temperature was reduced. At moderate reductions, the population stabilized at a lower level commensurate with the reduced primary production. As with the tundra consumers, however, the proportional reduction in aphid population was substantially greater than the reduction in primary production. The most severe perturbation tested in the Deciduous Forest Biome simulation was a 2°C decrease in temperature. This eliminated the aphids entirely in about seven years.

These results definitely do not imply that long-continued temperature reduction is an effective device for controlling noxious insects, including aphids. They do point out the nonlinear nature of second- and higher-order ecosystem responses beyond the initial level of primary production, and the need for additional field analyses to explain some of the simulated results.

The complexity of consumer interactions with other ecosystem components is further illustrated by the Grassland Biome simulation. When warm-blooded consumers (birds and mammals) were added to the control ecosystem, primary production, above-ground production, transpiration, and microbial respiration all increased, perhaps as a result of the greater turnover of nutrients brought about by the consumer activity. Essentially similar results were obtained when consumers were added to the simulated ecosystem under a 2°C reduction in temperature. Almost all response variables were increased slightly over the corresponding case without consumers, although production levels were well below those of the base climate. Interestingly, fixation of carbon in consumer biomass was essentially identical at the control and the reduced temperature.

These results are at variance with observations from long-term grazing experiments. Aspects of this portion of the model will require careful scrutiny before its results can be accepted in their entirety.

DECOMPOSITION AND MINERAL CYCLING

Microbial decomposition of dead plant and animal litter, and the consequent release of bound mineral elements, were studied in several of the models. In the Deciduous Forest Biome simulations, the environmental perturbations had little effect on the total annual turnover of fresh and partly decomposed litter, but the seasonal pattern was significantly affected. The quantity of material and of stored chemical energy in the two litter layers was essentially the same in late autumn under all climatic assumptions. Thereafter, however, microbial respiration rates and

the rate of degradation of fresh litter to partially decomposed litter were inversely related to temperature. Consequently, detritus passed into the partially decomposed state at a slower rate the lower the temperature. By June there was significantly more material in the partially decomposed layer under higher temperatures than under lower. Although the total change in decomposition indicated by the model was relatively slight, the alteration in seasonal patterns could have a profound effect on remineralization in the forest litter. This change in pattern might be expected to cause alterations in the mineral cycling of the forest which are not reflected in the results of the simulations.

In the drier climate of the grassland region, available moisture might be expected to have a significant effect on decomposition. However, microbial respiration is more sensitive to temperature than to rainfall in the grassland simulations. The temperature response was slightly curvilinear. Soil respiration was about 12% less than in the base case with a drop in mean temperature of 2°C. A temperature reduction of 1°C, coupled with the other climatic changes postulated by CIAP, decreased respiration by 7%. A temperature increase of 0.5°C accelerated soil respiration by 4%. Here also, changes in the pattern of mineralization of plant litter may alter long-term successional trends in relatively complex ways.

The Coniferous Forest Biome modeling group independently concluded that the lack of a mineral-cycling component is perhaps the most glaring deficiency in their ecosystem model. They pointed out that the long-term effect of climatic changes would undoubtedly be manifested in changes in rates of mineral release and uptake, but their simulation provides no means for taking account of this process.

TOTAL ECOSYSTEM STANDING CROP

The Coniferous Forest Biome model was the only one to predict the consequences of climatic change on the total standing crop of unharvested old-growth forest stands. In such stands, primary production is normally in rough balance with mortality. This was the case with the coniferous-forest simulation under normal climatic conditions; the system was nearly in balance, with net primary production nearly (if not over-) compensated for by mortality. This is also true of the actual stands on the H.J. Andrews Experimental Forest from which the data for the model were derived.

Temperature change altered simulated detritus production very little. Detritus was defined as the sum of litter fall, wood fall, stem mortality, and root death. Insect consumption was not included in this figure, but was small in all cases. The maximum simulated change in detritus production under the most extreme climatic change was less than 1%, an amount almost undetectable in the field.

It was difficult to establish a ratio of net ecosystem production under perturbed and natural conditions because the natural condition was nearly zero. Since, however, net primary production decreased as temperature decreased (as discussed in a previous section), and detritus production was not materially affected, total ecosystem standing crop had to decrease as temperature was reduced. The coniferous-forest simulation suggests that this reduction would amount to about 0.85 metric tons of carbon fixed per hectare per year in unharvested Douglas fir stands if all plant material is considered. If wood production alone is measured, the reduction amounts to about 0.09 tons of carbon per hectare per year. Since air-dried wood is about 40% carbon, this represents about 0.2 metric tons of wood per hectare per year. Compare this with the normal standing crop of wood in old-growth Douglas-fir stands on the H.J. Andrews Forest: 400-500 tons per hectare.

The predictions of the tundra and grassland simulations concerning standing crop were somewhat contradictory. In these communities dominated by herbaceous vegetation, turnover of biomass is obviously much faster than in forests, and removal by grazing is more important. In the tundra, the pattern of simulated biomass was generally similar to that of the coniferous forest. Both above- and belowground biomass at the end of the growing season are smaller under lower temperatures than under higher. In the grassland, however, the pattern was different. Although aboveground production was reduced by a lowering of temperature, peak aboveground standing crop was slightly increased. The belowground standing crop was smaller at lower temperatures than at higher, a reversal of the

pattern for aboveground biomass. The reasons for this anomaly are not fully understood and are currently being investigated. It is possible that the simulated increase in peak aboveground live biomass may be completely nonbiological, and instead be an artifact of model structure.

TRANSPIRATION, PRECIPITATION, AND WATER STRESS

Water relations are at least as important in natural, noncultivated ecosystems as in agricultural systems. To a considerable extent, natural ecosystems occupy sites unsuitable for cultivation because of deficiencies in either moisture availability or soil properties. Soil deficiencies are as often related to the ability to supply adequate moisture during the growing season as to inherent fertility. Plant-water relations are therefore particularly crucial in assessment of the impact of man-induced climatic change on natural ecosystems.

The PROSPER model of atmosphere-soil-water relations (Goldstein and Mankin, 1972) was run for four years, using observed environmental data from the Walker Branch Watershed on the AEC reservation at Oak Ridge, Tennessee. The environmental perturbations were assumed to occur uniformly throughout the year and were simply added or subtracted from the actual data for each day. For lack of better information, atmospheric vapor pressure was assumed to remain constant.

In accordance with the CIAP assumptions, precipitation was decreased along with temperature. Evapotranspiration was predicted by the model to decrease proportionately more than precipitation. A 5% decrease in precipitation, coupled with a 2°C decrease in temperature, reduced evapotranspiration by 14.5-11.5%, depending upon weather conditions in individual years. The reduction in transpiration was more closely related to the seasonal distribution of precipitation than to its total annual amount. The decrease of evapotranspiration with reduced temperature and precipitation in the simulation can be attributed in part to there being less available water to evaporate, but more to reduced potential evaporation because of lowered temperature and solar radiation.

The balance between precipitation and transpiration largely determines the effect of soil water on vegetation. The Deciduous Forest Biome team estimated that, as a rough approximation, a plant water potential less than -5 bars represents slight water stress, -10 bars represents moderate stress, and -15 bars represents severe water stress. The model did not predict a water stress as severe as -15 bars for any day during the four-year period with any of the climatic perturbations tested, or for the base or normal climate.

The simulation indicated that coupled temperature and precipitation reductions would bring about a small reduction in the number of days with slight water stress, especially in years when water stress was already low. The climatic change reduced water stress the least in the year 1970, when water stress under the normal weather was greatest. These results indicate that the growth declines predicted to occur due to temperature and radiation decreases might be partially compensated for by decreased water stress, particularly in years of good growing conditions when water stress is only moderate. Put another way, man-induced climatic changes are likely to have the greatest impact on vegetation in years when growing conditions are most unfavorable. Bad years will be made considerably worse than they would otherwise have been, whereas in years of relatively good growing conditions the deterioration due to lowering of temperatures may be less. To the extent that successional patterns, species replacement, and other ecological processes are sensitive to the most unfavorable and stressful years, this effect could be serious. This problem requires substantial additional study; simulation modeling is virtually the only feasible way to address it.

The grassland simulation, like the deciduous-forest model, also indicated a decrease in total transpiration when both temperature and precipitation were reduced. The decrease in transpiration was about 4% for each 1°C decrease in temperature, the latter being accompanied by a 2.5% decrease in precipitation. The grassland simulation did not explicitly report on soil-water changes, but the combined result of a decrease in precipitation and a slightly greater percentage decrease in transpiration is likely to be one of relatively little change in total soil-water balance, although there may well be changes in seasonal pattern.

These results are consistent with those reported by J. Ritchie (1974) for agricultural crop-

lands in the central and southern United States. He states, "The compensating effects of cooler weather and less potential evapotranspiration offset the expected decreases in precipitation, and drought probabilities are not expected to increase in a general sense throughout the United States." This is probably true for natural ecosystems as well, although additional investigations are required.

SENSITIVITY TO DIFFERENT FACTORS OF CLIMATE

All of the simulation models were tested with the parameterized climatic changes stipulated by CIAP. These involved coupled reductions in temperature, total solar radiation, precipitation, and wind movement. Several of the groups also varied the input in additional ways, to determine the relative sensitivity of the systems to changes in the several climatic factors.

Temperature change in all instances yielded a greater simulated response than did a comparable change in any of the other climatic variables tested. Several of the models were run with and without a change in solar radiation accompanying the temperature change. The Coniferous Forest Biome model showed a 12-times-greater response to a temperature change of -1°C than to a radiation change of -1.5%. Specifically, the decrease in net primary production attributable to temperature alone was about 12%/°C. When solar radiation was added to temperature, the simulated decrease was 13%/°C. Qualitatively similar conclusions were obtained by the deciduous-forest and tundra modeling groups.

In addition, however, factors other than light for photosynthesis are commonly limiting in natural ecosystems. This is especially true in open communities such as grasslands where soil water and available nutrients commonly limit growth. Even in forests light may often be present in excess during the growing season. Therefore, reduction in solar radiation would not be expected to have as much effect as reduction in temperature.

Independent and simultaneous variations in temperature and in rainfall were simulated with the grassland model. The results indicated that decreasing both air temperature and rainfall will cause a decrease in all the output variables except peak aboveground standing crop, which shows a slight increase. These results show that simultaneously decreasing rainfall and air temperature involves an interaction different from independently adding the effects of air temperature and rainfall. The sign of the change in peak aboveground standing crop and in transpiration when temperature and rainfall were varied together might have been predicted by superposition of the independent effects of air temperature and rainfall. The same does not hold for peak belowground biomass, or for several of the other variables tested. The nature and explanation of these interactions requires additional investigation.

TREE-RING ANALYSIS

The approach used by the Laboratory of Tree-Ring Research at the University of Arizona is substantially different from the simulation models discussed above in that it is an extensive rather than an intensive approach. The model is simple and can be applied readily to a wide variety of sites and habitats. It involves a response function which is a least-squares regression equation to predict ring widths for a group of trees on a particular site by using orthogonal transforms of monthly temperature and precipitation data as predictors. The only requirements are that there be variation in ring width from year to year, and that a significant part of that variation be attributable to limiting conditions of climate. The effects of serial correlation of the ring widths up to lags of three years are also incorporated in the regression.

A reduction in temperature of 2°C (3°C for sites north of latitude 40°N) for each of 14 months was substituted into the regression equation for 26 tree sites including three different species. Calculations also included precipitation changes of +5% and -5% (± 10% for sites north of latitude 40°N). Some of the calculations that were carried out for five successive years are shown in Figure 4. A growth change of more than 30% was obtained for more than half the sites when temperatures were decreased by 2°C (3°C) and precipitation decreased by 5% (10%). More than half these responses were significantly greater than the calibration error of the model at the 95% confidence level. Reversing the sign of

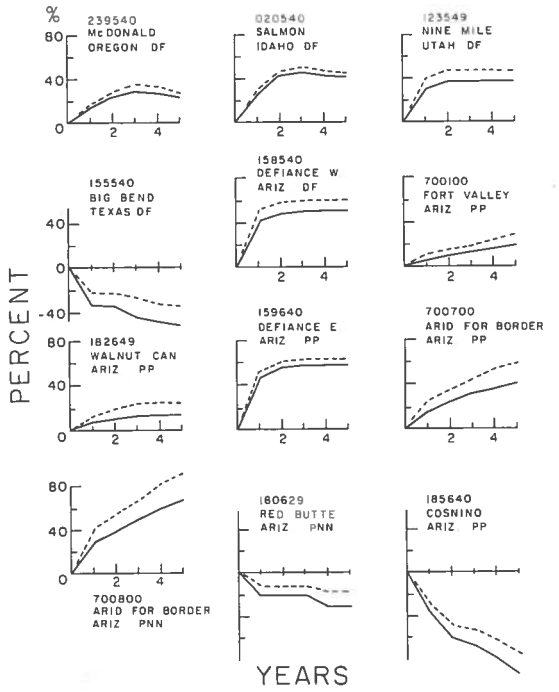

Figure 4. Solid lines represent calculated ring-width response for 1-5 years of persistence of the most extreme climatic conditions postulated by CIAP to result from a fleet of supersonic transport aircraft (temperature decrease of 2°C and 5% precipitation decrease between latitudes 20°N and 40°N, and temperature decrease of 3°C and 10% precipitation decrease between latitudes 40°N and 60°N). Dashed lines show the results obtained when the sign of the precipitation anomaly was changed to positive. Ordinate values are in terms of percentage of present normal ring width at each site. Identification numbers and locations of each site are indicated. Response functions and site data are found in Fritts (in press). The letters DF, PP, and PNN indicate species: Douglas fir (*Pseudotsuga menziesii*), Ponderosa pine (*Pinus ponderosa*), and Pinyon pine (*Pinus edulis*), respectively.

precipitation did not change the sign of, or otherwise substantially alter, the growth response, as the effects of the specified precipitation changes were small compared to those of the specified temperature changes (Figure 4).

The results from 28% of the sites are the same as those obtained from the coniferous-forest and deciduous-forest simulation studies, in that growth declined in response to a reduction in temperature. However, 72% of the sites gave a response opposite to that of the forest simulations, but resembling the growth response for the shrub simulated in the Desert Biome. Considerable variation among the 26 sites was attributed to differences in microenvironments, differences among species, and differences among regional climates (Fritts, in press).

In most of the selected habitats, high rather than low temperatures are naturally limiting. The lowering of temperature may decrease evapotranspiration, which reduces water loss. Lowering of temperature also decreases respiration and favors more rapid net photosynthesis. The result is an increase in accumulation of stored foods and other growth-promoting substances, which leads to increased growth.

The coniferous-forest simulation was for a site where the water budget was not found to be limiting. The McDonald Forest sample used in the tree-ring analysis, though also in Oregon, represented a stand where low moisture and high temperatures are undoubtedly limiting. Thus, it is not surprising that the calculated growth response for the McDonald site was more like that of arid-site trees in the southwest than that of moist-site trees used for the coniferous-forest simulation.

When values specified for changes in temperature and precipitation were reduced to one-half and one-quarter of those used above, there was a proportional reduction in the computed growth changes. When a temperature increase rather than decrease was substituted, and no change in precipitation was specified, there was a reversal in sign of the growth response. As noted previously, reversing the sign of the precipitation had little effect on the growth-response curves, and never resulted in a change in sign of the growth response. However, the precipitation effect on growth response is always in the same direction as the sign of the specified precipitation change. That is, when the precipitation anomalies are positive the growth-response curves tend to be more positive (less negative). It is also seen from Figure 4 that the growth at some sites begins to level off after a few years as the effects of serial correlation appear.

In this analysis the response of the trees was calculated for a temperature change of the same amount during all seasons of the year. The trees, however, respond differently to temperatures in

different seasons (Fritts, in press). If the specified changes in temperature were restricted to one or more particular seasons, such as winter and spring, the nature of the growth responses would be different. Also, it should be noted here that, in terms of the natural climatic variability at a site, the proposed temperature changes were of the order of a standard deviation of monthly temperature, while the proposed precipitation changes were considerably less than that in terms of standard deviation units (particularly for arid regions). This is a likely reason why the effects of the specified temperature changes dominated the effects of the specified precipitation changes in terms of growth response.

CONCLUDING REMARKS

The results reported here have been based on acceptance of the CIAP parameterized climatic changes, with precipitation assumed to decrease with temperature. Although this is presumably true on a global basis, zonal averages may not be applicable to important areas within each latitude band. It may be, for example, that 80% of the area within a given latitude band will undergo changes of 25% in annual precipitation, with the positive changes tending to cancel out the negative ones in such a way that the average anomaly over all longitudes is -5%. Historical evidence, for instance, quite clearly shows that in the Great Plains of the United States, cooler average temperatures have generally been accompanied by higher precipitation, and vice versa. This could materially change some of the predictions made here. In the case of the grassland region, soil-water deficiencies would be appreciably reduced if precipitation were to increase at the same time that mean temperatures were lowered. This question, too, requires additional investigation through simulation modeling and other approaches.

The results of this study point up the need for a variety of models, different approaches, and analyses of many different sites as a basis for large-scale evaluation of environmental impact. The analysis reported here has answered some critical questions, but more work on a greater variety of models, sites, and ecosystem types is needed before these results can be confidently generalized to predict the total ecological impact of man-induced climatic change.

REFERENCES

Fritts, H.C., T.J. Blasing, B.P. Hayden, and J.E. Kutzbach (1971), "Multivariate techniques for specifying tree-growth and climate relationships and for reconstructing anomalies in paleoclimate," J. Appl. Meteor. **10**, 845-864.

Fritts, H.C., in press, "Relationships of Rings in Arid-Site Conifers to Variations in Monthly Temperature and Precipitation," Ecological Monographs.

Goldstein, R.A. and J.B. Mankin, Jr. (1972), "PROSPER: A model of atmosphere-soil-plant water flows," in the *Proceedings of the 1972 Summer Computer Simulation Conference* (San Diego, California), pub. Simulation Councils, La Jolla, California, 1176-1181.

Goodall, David W. (1972), "Potential applications of biome modelling," Terre et la Vie 1, 118-138.

Miller, Philip C. and Larry Tieszen (1972), "A preliminary model of processes affecting primary production in the arctic tundra," Arct. Alp. Res. 4, 1-18.

O'Neill, R.V., R.A. Goldstein, H.H. Shugart, and J.B. Mankin, Jr. (1972), "Terrestrial Ecosystem Energy Model," Eastern Deciduous Forest Biome, Memo Report 72-19, Environmental Sciences Division, Oak Ridge National Laboratory, Oak Ridge, Tennessee, 38 pp.

Ritchie, J. (1974), in Section 4.2.2 of Volume V of the CIAP Monograph Series, U.S. Department of Transportation. NOTE: At present, these monographs exist only in an early draft form. They will be publicly available after completion in September 1974.

Sollins, P., D.E. Riechle, and J.S. Olson (1973), "Organic Matter Budget and Model for a Southern Appalachian *Liriodendron* Forest," USAEC Report EDFB-IBP-73-2, Oak Ridge National Laboratories, Oak Ridge, Tennessee.

Timin, Mitchell E., Boyd D. Collier, Jon Zich, and David Walters (1973), "A Computer Simulation of the Arctic Tundra Ecosystem near Barrow, Alaska," U.S. Tundra Biome Rept. 73-1, Tundra Biome Center, Univ. of Alaska, Fairbanks, Alaska, 82 pp.

DISCUSSION

(UNIDENTIFIED): Would you define high and low moisture stress?

SOLLINS: High-moisture-stress sites are those whose soil moisture reserves are exhausted during the summer. This includes most of the ponderosa-pine areas, much of the Douglas-fir region, and parts of the eastern United States. But, primarily, it includes the desert and some of the grassland areas, while it excludes a large part of the coniferous and deciduous forests.

(UNIDENTIFIED): You mentioned that the total light input has no effect upon growth. Have you tried varying only selected parts of the spectrum?

SOLLINS: What we were measuring was photosynthetically active radiation, and that is what we varied in our simulations. We are also using net radiation as an input to the models for energy-balance considerations. We haven't looked at the effects of changes in that. I can't really say, but I don't think the conclusion would really be different. The effects are probably not noticeable where there is low moisture stress, and I think they would manifest themselves through changes in the hydrologic cycle, not through the production processes directly.

(UNIDENTIFIED): From my experience in agronomy and a study of plant growth, we found exactly the same thing that you are talking about, little effect of variation in light on production. However, when plants were looked at as part of an entire community, we got a different, rather direct relationship with the light input.

SOLLINS: The whole point of the model is to treat the trees as part of an entire system. That is why we include a hydrologic model as an integral part of the overall model. We have also tried this experimentally by enclosing sections of forests in giant plastic bags. Although the results of last summer aren't in yet, the conclusion appears to be the same. Tree species, particularly the coniferous trees of the West, are not very sensitive to changes in light per se. They are on a flat part of the photosynthesis vs. light curve. Agricultural plants, on the other hand, may be better able to take advantage of higher light levels. In both cases, however, I think effects will manifest themselves through other, more subtle pathways such as the hydrologic processes or consumer activity.

CALDWELL: I'd like to emphasize again that when we examine biological effects we have to think about organisms in their environment, whole ecosystems – and to quote one notable ecologist, "Ecosystems tend to be counter-intuitive."

ECONOMIC IMPACT OF CLIMATIC CHANGE: INTRODUCTION AND OVERVIEW

RALPH C. D'ARGE
University of California, Riverside
Riverside, California

ABSTRACT: In a cost/benefit analysis, the stratosphere is conceptualized as being an asset of the earth's population. Included in the services provided by the stratosphere are filtering of UV light and regulation of global climatic profiles. If provision of other services, such as air travel, alters the quality of the services now provided by this asset, the major question is how to value the services so as to impute a value to the change in them. A review of existing methodologies for attaching such a value where no market exists is undertaken. A brief examination is also made of asset utilization when the probabilities of effects of alternative uses are not known, but there are hunches that the effects of certain uses may yield very high negative or positive returns.

INTRODUCTION

Man's fundamental dependence on the atmospheric environment is understood by every human being. His ability to adapt to and live in diverse atmospheric environments without being bound by most of the constraints imposed by natural evolutionary processes is perhaps the dominant characteristic distinguishing man from other animals. As Edholm (1966) has vividly pointed out, man without clothing, heat, or shelter is highly "vulnerable", and restricted in terms of survival to a very few climatic zones of the planet. The pattern of human settlements, location and intensity of agriculture, health, recreational pursuits, and even "moods" are partially the result of the earth's climatic history. Man's adaptation has been to utilize various combinations of resources – clothing, level and timing of exposure, space heating, production methods, and design and location of shelters – to mitigate climatic adversity and extend his range of survival. Natural adaptive mechanisms such as changes in size, body shape, and skin pigmentation have also played a key role. However, until very recent times it was presumed that while the atmospheric environment influenced human activity, human activity had little or no effect on the atmospheric environment. Isolated exceptions to this included periodic air-pollution episodes in the lower troposphere around large human settlements. In recent decades, the observation of "heat islands" around cities, the introduction of radioactive wastes into the stratosphere, the possibility that man's industrial activities may be significantly changing the amount of atmospheric CO_2 and aerosols and thereby inducing a "greenhouse effect" rise (or a possible drop) in global temperature, the increase in use of local or regional weather-modification schemes, and the perception of a generally deteriorating air quality above large cities has led to questioning of the premise that man's activities have no feedback effect on the atmospheric environment. More recently, it has been suggested that large numbers of supersonic aircraft flying without regulation might emit enough aerosols, water vapor, oxides of nitrogen, and other compounds to substantially alter the human environment (SCEP, 1970)*. And Frisken (1973) has suggested that heat generated in energy conversion, given current energy growth rates, may substantially raise temperatures at the earth's surface in 180-250 years. Thus, there appears to be more than mere illusive evidence that man's activities may have substantial repercussions (or feedbacks) on the atmospheric environment, and thereby on man himself. If this is so, man must confront the possibility that both negative and positive atmospheric changes could result from the individual and societal choices that are made. The atmospheric environment may need to be managed, like other social assets, to encourage beneficial uses and dis-

* It is one of the central purposes of CIAP Monographs I through V to provide scientific evidence to test the validity of this conjecture.

courage harmful ones. As long as the atmospheric environment was subject only to natural laws, then human law on rights to use or access were unnecessary. Nature ran its course. But with man-induced changes the need for establishing legal precedents becomes important to all present and potential users. For the troposphere and local atmospheric environments, in most instances, legal control and rights of use on a national scale have been established. For the higher stratosphere, mesosphere, and thermosphere, where impact of use is likely to be multi-national, control and right of use have not been clearly established. By provisions of common law and international treaty, access to the atmospheric environment is under the complete control of the sovereignty directly underneath it. But, since it is impossible to separate the atmospheric environment into physically or biologically unique spaces over each sovereignty, or allot in a meaningful way the atmosphere above the oceans, the atmospheric environment, inclusive of the mesoscale and above, must be viewed as a global common-property resource.

Global common-property resources, or the "commons", are used by all nations but owned – in the sense of having complete exclusionary power – by none. The oceans, atmosphere, and electro-magnetic spectrum are typical examples of global common-property resources where right of access or use is denied by few nations but ownership is subject to dispute by all, since each has a common heritage in terms of established or anticipated access.

The Climatic Impact Assessment Program concentrates on the utilization of one of these "commons", the stratosphere, which is a part of the much larger atmospheric environment, but has at least partially defined boundaries at 10-12 and 55-60 kilometers above the earth's surface.

It is the particular focus of the economic research done for CIAP to initiate a first attempt at assessment of the socioeconomic considerations for evaluating the terrestrial impact of, and potentially necessary controls on, pollutant emissions into the stratosphere. Thus, its focus is more limited than a complete political-economic benefit-cost analysis of the stratosphere as either an intermediate or an ultimate waste sink for anthropogenic pollutants. Its major concern is the analysis of a sequence of "if-then" propositions: 1) If man's use of the stratosphere may markedly alter the natural and thereby the human environments, what are the magnitudes of the obvious and direct monetary costs and benefits? 2) Given these potential economic and social effects, to what extent are various monitoring and control efforts or processes justified? 3) What are the various legal and economic precedents which might allow or preclude the implementation of controls and monitoring efforts, from either a national or multi-national perspective?

This research is aimed not at deriving an answer, since the answer must by its inherent qualities be subjective, but rather at providing objective considerations for a viable *set* of answers on utilizing the stratosphere. Thus, it strives to be both a partial benefit-cost analysis for the questions raised and a map of the ground to be covered in moving toward a reasoned answer.

This introduction to the economics session of CIAP 3 is an attempt to synthesize, discuss, qualify, and place in perspective the research done for CIAP, including the papers which follow. No attempt is made to argue that the results are definitive, for we have quite literally embarked on a new problem for economic and social sciences, one not confronted except in the most isolated circumstances in the past. Thus all results, whether empirically derived or theoretically hypothesized, must be viewed as experimental forays into heretofore uncharted domains of the application of social and economic principles of decision-making.

PARAMETERS AND ASSUMPTIONS

The CIAP economics studies were divided into five interdependent groups. The first goes under the general rubric of research topics in decision analyses and institutional controls. The second is an array of resource impact studies, conducted to partially assess social costs, dietary effects, and sociological and political implications of the parametric climatic changes identified earlier. The third is a preliminary sensitivity analysis of the economic impact analyses, and the fourth is a preliminary examination of the costs of various emission-control possibilities, and of achieving a reasonable monitoring system to identify important shifts or perturbations in the stratosphere.

The starting point for most of these studies was a set of parametric changes in particular climatic measures: mean annual global surface temperature (-2°C to + 0.5°C), amount of annual global precipitation (-12.5 to +12.5%), average wind velocity (0 to -5%), ultraviolet radiation (0 to 50%), and solar radiation (0 to -2.0%), all by latitudinal bands of 20 degrees. These parametric ranges were assumed (but not scientifically validated) to be the probable extreme ranges of man-induced climatic changes resulting from stratospheric aircraft emissions. (This sort of assumption is necessary for parametric study of climatic change during the period of change.) Both temperature and precipitation vary in negative and positive directions, encompassing the range of uncertainty from a dominant "greenhouse effect" to a cooling effect, as well as current uncertainties as to negative, positive, or neutral precipitation effects. It is important to note an extreme qualification for most of the impact studies: economic and social impacts of climatic change have been examined with respect to a shift in mean annual averages of climatic variables, *not* for changes in seasonal, cyclical, or local variations. Since many of man's activities appear to be affected more by climatic variations than by climatic averages (Landsberg, 1972), the scope and thereby completeness of effects examined were of necessity limited.* Future CIAP and other research efforts on the economic and social impacts should shed more light on man's dependence on the variability of the atmospheric environment.

As more accurate forecasts of climatic change evolve through improved climatological models, more precise models of the biological and social uncertainty with respect to range and types of social impacts can be expected to emerge. At present, we can at best say that the chosen set of alternative climatic changes *may* include a portion of the true climatic changes, and the socioeconomic analyses *may* include a portion of the final social impact.

Because of the very long time lags (10-60 years) between inception of a possible climatic change and its adjustment to a new equilibrium, and the further lag in biological and social response (1 to 100 years), the problem of studying social effects becomes speculative, since the types and magnitudes of these effects depend upon values, preferences, and concerns of a future society. In this set of studies, present preferences and concerns were assumed to hold for future societies, for lack of better information.*

A more limiting assumption was that all climatic changes would commence in 1991 and linearly reach a new equilibrium in the year 2025. Thus, an ultimate -1°C change in global average annual temperature was presumed to progress by -1°C/35 = -0.0285°C each year to reach -1°C in 2025 — again for lack of better information.

Ideally, a complete decision analysis of the utilization of the stratosphere as a social asset would consider its highest social value in alternative uses and allocate it to those activities. If the stratosphere could accommodate more than one type of use, then a ranking of uses would have to be devised to include those uses whose social benefits at the margin exceed social costs and exclude those whose costs exceed their benefits. Of course, the utilization of the stratosphere includes comparing current uses with a perturbed or different pattern of utilization. Implicit in these statements of highest utility is the presumption that we now know with perfect certainty the benefits and costs of various uses, *including* the current one of "producing" a certain configuration of both macro- and microclimates, which the individual and society in general have adjusted to. Apparently this is not the case, in that there are large uncertainties as to the role currently played by the stratosphere in determining global climatic patterns. There are also some very substantial uncertainties in our understanding of the interdependencies between climate and evolution of biological communities. Finally, with few isolated exceptions, the interdependency of socioeconomic societies now

* For example, changes in seasonal wind patterns can alter local and regional patterns of precipitation and oceanic nutrient movements, and such changes may turn out to be much more important than those induced by a slight change in trade-wind velocities.

* Since future generations or desires cannot be inferred except through extrapolation of historical trends, and perhaps introspection, an ethically defensible assumption might be that future generations' preferences will be the same as ours. If they are, no error has been committed. If they are not, we have no method of discovering how they differ, but we have the partial defense that future generations were not discriminated against in prospective retrospect.

observed and various aspects of the climate has not been analyzed. Thus, a prominent element in a realistic decision-making analysis must be the current lack of knowledge, along with the recognition that knowledge of the type and extent of possible environmental and social changes, as well as their probabilities, will increase in the future. What must be viewed as the relevant set of social considerations at this time (for preliminary decision on the use of the stratosphere) is the basic uncertainties regarding possible biological and social impacts. To put it very simply, if there are subjective feelings among scientists that there is a high probability of no substantial change, yet a small finite probability of a drastic change (a 1°C reduction in global average temperature, say), then this element of drastic change must be a fundamental consideration in national or international decision-making at this time.*

The CIAP economics group first formulated the following set of assumptions:

1. There are large uncertainties in the climatic effects of various levels of emissions of oxides of nitrogen, oxides of sulfur, particulates, and water vapor, and their effects on surface climate. Some changes may involve irreversibilities in the natural environment, although no substantive evidence of this is now available.
2. There are extremely large uncertainties in the translation of tropospheric climatic changes into quantitative biological effects.
3. There are very high uncertainties as to how social communities and the economic system adjust to large-scale climatic change or even small climatic shifts in the biosphere.
4. None of these substantial uncertainties is likely to become a near-certainty with precision in less than one or two decades.

* A 1°C reduction in mean annual temperature will shift human settlements approximately 60 to 290 km northward, in terms of "average climate," with adjustments for elevation and precipitation. Of course, mean annual temperature differences yield little insight into the other important differences induced by temperature variability, temperature extremes, frost-free days, or chill factors caused by the interaction of wind and temperature.

Given these substantive uncertainties, the group concentrated on defining the decision problem.

The essential economic decision problem is one of analyzing a class of problems in which the relationship between cause and effect is subject to extreme uncertainty at the point of initial decision, but a process of learning over time must inherently be included. The decision process is sequential, in that decisions made in the next decade can be continued or revoked in future times, and not all decisions on the utilization of the stratosphere need be made at one point in time. Impacts of both biological and social consequence may not be observed for one or more human generations after perturbations to the stratosphere occur. The monitoring and emissions-control costs range from extremely low-cost current techniques to very high-cost methods of reducing emissions and detecting subtle climatic changes. The direct economic costs of substantial climatic perturbations are likely to be high when adaptation to environmental changes is not explicitly included in the assessment. With these and other premises in mind, a research methodology was developed. Emphasis was placed in the preliminary investigations on four general areas: 1) improving decision analysis so as to explicitly include dynamic learning processes and finite but small probabilities of events (with or without irreversibilities) with imputed high social costs, 2) a "state of the art" examination of the possibilities and costs of various controls, emphasizing supersonic aircraft, 3) a preliminary examination of the possibility for extensive and agreed-upon international regulations, and 4) an impact analysis centered on economic costs and benefits but examining several other social effects resulting from the parametric climatic changes discussed earlier.

SUMMARY OF THE PRELIMINARY RESULTS

Table 1 shows a set of measures of economic costs and/or benefits for both the human-resource and natural-resource categories. Two specific cases are examined for comparative purposes: a -1°C and a +0.5°C global temperature change with no change in precipitation. (The cost estimates for the various areas are not truly comparable because of their varying assumptions

Table 1. Estimates of Economic Costs of Climatic and Biologic Change (for two changes in mean annual temperature, no change in precipitation, 5% interest rate assumed)

Impact Studied	Investigator(s)	Annualized Cost (Millions of 1971 Dollars)*	
		-1°C Change	+0.5°C Change
Corn production	Schulze, Ben-david	-20.8	14.4
Cotton production	Schulze, Ben-david	11.0	-2.9
Wheat production	Schmitz	2750.0	?
Rice production	Bollman	956.0	-0.0
Forest production	Schreuder	661.4	?
Douglas-fir production	Schmidt	474.6	?
Marine resources	Bell	1,431.0	?
Water resources	Bollman	-1.6	0.5
Health impacts (excluding skin cancer)	Anderson, Lave, Pauly	2,386.0	?
Urban resources			
Wages	Hoch	3,667.2	-1,550.9
Residential, commercial, and industrial fossil-fuel demand	Nelson	175.8	-87.9
Residential and commercial electricity demand	Crocker et al.	-748.0	352.9
Housing, clothing, expenditures	Crocker et al.	506.5	-253.3
Public expenditures	Sassone	23.8	-10.7
Corn-belt investment costs	Niedercorn	51.0-67.0	?

* A negative sign denotes a benefit.

associated with the measurement of economic cost. However, they roughly indicate the important areas.) Tables 2 and 3 show that in some instances, notably in the health impact study, precipitation and temperature decreases tend to be complementary as regards impacts. That is, a temperature decrease and a simultaneous precipitation decrease offset each other, resulting in a minor impact on health (and health costs). On the other hand, a temperature decrease accompanied by a precipitation *increase* has an even greater impact than a temperature decrease in isolation.

Of course, the estimates contained in Tables 1 through 3 are of a very preliminary nature, and are based on a number of assumptions. The estimates are presented for illustrative purposes, since they do indicate which types of economic effects resulting from climatic change might be quite important relative to others, in terms of economic cost. The alternative-cost measures tend to be less than the willingness-to-pay measures of economic loss. This is perhaps most notable in comparisons of economic losses associated with rice production and Douglas-fir production in the Pacific Northwest.

Table 4 gives estimates of the economic costs of skin cancer and for various percentages of ozone depletion in the stratosphere. These costs were measured as the costs of cure and of loss in income, not the cost of prevention. In consequence, the estimate undoubtedly underestimates social costs if prevention is impossible, but may overestimate it if there are low-cost methods of prevention. Table 5 presents materials-weathering costs related to ozone depletion; these are based on the alternative-cost principle, which may overstate the actual social loss, since the possibilities of substituting various types of materials, or of less rapid materials deterioration, are not considered.

While these estimates must be viewed as extremely qualified, and subject to further scientific verification, they do give at least a partial indication of the potential sensitivity of the economy, in both the urban and natural-resources sectors, to long-term, relatively small negative changes in temperature and ozone concentration and relatively slight long-term changes in precipitation. It is too early to conclude that the economy is highly sensitive to perturbations in the atmospheric environment. However, these

Table 2. Sensitivity of Urban Direct Economic Costs to – 1°C Change in Mean Annual Temperature, Together with Changes in Mean Annual Precipitation (in millions of 1971 dollars)

Impact Studied	No Change in Precipitation	12.5% Change in Precipitation	–12.5% Change in Precipitation
Corn production	-20.8	-20.1	-21.6
Cotton production	11.0	10.4	8.6
Wheat production	2,750.0	?	?
Rice production	956.0	1,083.0	918.0
Forest products	1,790.0	?	?
Douglas-fir production	474.6	364.9	582.8
Marine resources	1,431.0	1,785.7	2,434.3
Water resources	-1.6	9.6	105.0
Health impacts (excluding skin cancer)	2,386.0	6,484.6	1,896.2
Urban resources			
Wages	3,667.2	5,445.3	1,861.4
Residential, commercial, and industrial fossil-fuel demand	175.8	175.8	175.8
Residential electricity demand	-41.0	-41.0	-41.0
Commercial electricity demand	-707.0	-707.0	-707.0
Housing and clothing expenditures	506.5	506.5	506.5
Public expenditures	23.8	36.4	15.1
Corn-belt investment costs	51.0-67.0	51.0-67.0	51.0-67.0

Table 3. Sensitivity of Urban Direct Economic Costs to +0.5°C Change in Mean Annual Temperature, Together with Changes in Mean Annual Precipitation (in millions of 1971 dollars)

Impact Studied	No Change in Precipitation	–6.75% Change in Precipitation	+6.75% Change in Precipitation
Corn production	14.4	14.1	14.8
Cotton production	-2.9	-3.7	-2.9
Wheat production	?	?	?
Rice production	0.0	0.0	0.0
Forest production	?	?	?
Douglas-fir production	?	?	?
Marine resources	?	?	?
Water resources	5	53.8	6.2
Health impacts (excluding skin cancer)	?	?	?
Urban resources			
Wages	-1,550.9	-1,550.3	-1,552.0
Residential, commercial and industrial fossil-fuel demand	-87.9	-87.9	-87.9
Residential electricity demand	19.391	19.391	19.391
Commercial electricity demand	333.5	333.5	333.5
Housing, clothing expenditures	-253.3	-253.3	-253.3
Public expenditures	-10.7	-16.9	-5.9
Corn-belt investment costs	?	?	?

Table 4. Projected Increase in Skin-Cancer Cases for Various Percentages of Ozone Depletion, with Costs (5% discount rate)

O_3 Depletion	Cases/ 100,000	Add'l. Cases by 2020	Annualized Cost* (Millions of 1971 U.S. Dollars) Lower Bound	Upper Bound
5%	46	128,000	9	43
10%	97	270,000	18	91
20%	220.6	611,000	41	206

* The lower-bound figure is based on 3.45 hospital days per case and a melanoma incidence rate of 3 per 100,000 (used to derive the rate of non-melanoma skin cancers). The upper-bound figure is based on 0.9 hospital days and a melanoma rate of 6/100,000.

results do contribute to the conjecture that even some of the most rudimentary production and consumption processes of the economy may be temperature-sensitive when shifts in the long-term average of various indicators of climate occur.

Table 5. Projected Costs of Materials Weathering for Various Rates of Ozone Depletion

O_3 Depletion	2020 Costs* (Millions of 1971 Dollars)
5%	200
10%	390
20%	750

* The population projections used in estimating these costs differ from those used in the other CIAP studies.

QUALIFICATION OF RESULTS

In this preliminary effort examining decision methodologies, impacts, and feasible controls and their costs, each area of study must be viewed at present as highly qualified and subject to further scientific verification before definitive conclusions can be stated. There may be synergistic relationships among some of the various areas of study, so an overall set of decision rules or principles of dominance for decision alternatives cannot yet be determined. It must be again emphasized that none of the impact studies contains a set of assumptions that have been adequately tested, scientifically validated, or generally accepted by the scientific community examining them. Consequently, the estimates of impacts and costs must be viewed with extreme caution, both in terms of the adequacy of assumptions and the completeness of coverage on the estimates of social cost. In addition, the appropriateness of the application of the economic measures of social loss employed are subject to some question, as is their acceptability as an adequate measure of change in social value. The cost of our monitoring and control studies are subject to extreme qualification, in that a precise engineering cost analysis has not been worked out for the various control alternatives or monitoring systems. They are at best a first step toward the evolution of a technically feasible and economically viable system embodying both monitoring and control strategies.

Alfred North Whitehead once remarked that definition is the halfway-house toward measurement. It can be added that measurement is perhaps a halfway-house toward a sufficient understanding for implementing public policy. The results of this first effort, although extremely qualified and subject to substantial future revision due to new scientific findings, are perhaps a movement to at least the first halfway-house.

RESEARCH NEEDS AND SUMMARY

The list of research needed to adequately assess the economic and social effects, derive a reasonable decision analysis, and attain substantial certainty as to the costs of various alternative monitoring and control strategies, is almost unending. However, one very important area needing research at this time is the development of a consistent decision methodology

tailored explicitly to a CIAP type of problem, which would provide a more reasoned set of decision rules than a purely "go/no-go" choice on the utilization of the stratosphere. The "go/no-go" approach appears to be the least satisfactory approach to rational management of the stratosphere as a global social asset. It seems appropriate to emphasize research efforts which would examine the social impacts of very slight climatic perturbations, and also the effects of subsonic flight in the lower stratosphere during the next several decades. If these perturbations are extremely slight or unrecognizable, it should be safe to utilize the stratosphere slightly more intensively during the following decades, with accompaniment of a substantial monitoring effort aimed at detecting more-than-minute perturbations. It appears reasonable also to expend a substantial amount of research resources in the area of deriving lower cost-control strategies and "good" to "ideal" monitoring systems. That is, the current estimated control costs, in terms of the desulfurization of jet fuel and slight alterations in flight patterns, seem to be low relative to expected social costs (and thus worth paying) even if the probability of an adverse climatic impact were extremely small, such as 0.01. (Of course, this very tentative conclusion depends substantially on the accuracy of the estimates of social and economic losses and of control costs, both of which are currently subject to extreme qualification.)

In terms of the impact studies, there appear to be two substantial weaknesses of the models tested thus far. The first one (which is unlikely to be resolved) is the so-called partial-equilibrium nature of all the models. Each type of impact is examined, in effect, in *isolation* from other impacts, and yet the various impacts undoubtedly feed back and affect each other. For example, the estimate of economic cost of reduced rice production made in isolation would undoubtedly be substantially less than one for the same reduction if the production of all foods, including substitutes for rice, were simultaneously adversely affected. Thus, the various impact studies must be viewed as partial effects.

This is also a problem in the urban impact studies. For example, a substantial feedback effect not considered in the urban resources area is the possibility that a climatic change may be accompanied by a substantial relocation of existing populations. If this occurred, presumably some of the impacts, such as those on heating costs or health, would be markedly reduced, and many of the human-resource impacts would at least be partially mitigated.

A second serious difficulty is the interaction between the natural-resource impacts and the human-resource impacts. Relocation of individuals in response to climatic changes would undoubtedly affect both the labor supply and the wage rates in the natural-resources industries, and thus their costs of production. However, at this time the state of economic science allows the use of only two rather discrete sets of models for analyzing impacts. One is a very highly aggregated set of models of location shift and movement toward a new spatial equilibrium; the other set involves an examination of large series of partial equilibrium impacts. So far this study has been looking at partial equilibrium impacts, noting that they tend to either overestimate or underestimate actual economic loss. It appears appropriate to suggest a more comprehensive aggregative approach to the effect of climatic change on the economy and its spatial location, and compare and contrast the social cost estimates derived from this macroadjustment process with the assessment of partial-equilibrium impacts developed in this study.

A final and very important component of the impact analyses is a detailed examination of the distributive aspects of climatic change. If a climatic change results in a generally southward movement of crop production, then clearly the northern countries would be harmed, the mid-latitude countries might be partially harmed or benefited, and countries near the equator could receive a gain in terms of their comparative advantage in production and export of agricultural crops. In the partial-equilibrium analyses conducted thus far, these losses and gains by individual countries, or regions within countries, have in many cases been netted out. It appears that in future research into the effects of climatic change, substantial effort should be put into assessing the net intercountry impacts. These distributive impacts appear to be crucially important to devising an adequate international institutional system for implementing a national

management strategy for a resource which is a primary example (and perhaps the first encountered) of a truly global common-property resource.

REFERENCES

Edholm, O.G. (1966), "Problems of acclimatization in Man," Weather **21**, 340-350.

Frisken, W. (1973), *The Atmospheric Environment*, Baltimore: Johns Hopkins Press, Resources for the Future, Inc.

Landsberg, H.E. (1972), "The Assessment of Human Bioclimate: A Limited Review of Physical Parameters," Technical Note No. 123, World Meteorological Organization, Geneva, Switzerland.

SCEP (1970), *Man's Impact on the Global Environment: Assessment and Recommendations for Action*, Report of the study of critical environmental problems (SCEP), MIT Press, Cambridge, Mass.

CIAP PREDICTION UNCERTAINTIES

JOHN L. BARNES
University of California, Los Angeles
Los Angeles, California

The Report of Findings, which is to draw upon the sometimes conflicting results of the many studies CIAP has undertaken, will contain predictions for the years 1990 to 2000 and beyond. If these are not fulfilled in approximately that time interval, it could lead to some embarrassment. Perhaps we should take the advice of Stephen Leacock, the Canadian economist, given many years ago: Having lived to see some of his long-term predictions go unfulfilled, he recommended restricting one's predictions to an era beyond one's lifetime. Since many of us are likely to be alive in 1990, we can't follow Leacock's suggestion. But I recommend an alternative which uses a quantitative but much more acceptable approach to stating a prediction.

By way of background, let us recall a few strict uses of terminology in this field. Figure 1 schematically illustrates the concept of stochastic space. Typical cross-sections at particular times illustrate examples of the essence of probability as a mathematical *deduction*, from an assumed distribution function, of theorems on samples from the subspace described by that function. Statistics, on the other hand, involves mathematical *inference* from samples, leading to an approximation of the distribution function describing the subspace from which the samples were drawn. The two most common methods of inference are (1) the classical or "parametric" approach, and (2) the distribution-free or "nonparametric" approach. In the classical approach, a form of total-set distribution is assumed for a particular subspace; it could be Gaussian ("normal"), exponential, Cauchy, etc. Here, the usual problem involves inferring unknown parameters of the assumed distribution on the basis of a bounded number of experimental sample-values. These unknown parameters may be the mean, the standard deviation, the probable error, etc. In the distribution-free statistical approach, one also assumes statistical regularity (i.e., that some (unknown) distribution exists), and the problem involves inferring this distribution by means of sample-linked characteristics of the experimental observations. In particular, ordinal relations within the set of observations defined by the experimental data (such as ranks or positions in sequence) provide the information used by the test statistic with no *a priori* assumptions about the form of the sample distribution.[1] It is important that we recognize the fundamental difference between these two methods of inference.

The principal object of our studies is to predict what could happen in the real world in the absence of additional flight by aerospace craft in or through the stratosphere, and to use this knowledge to make

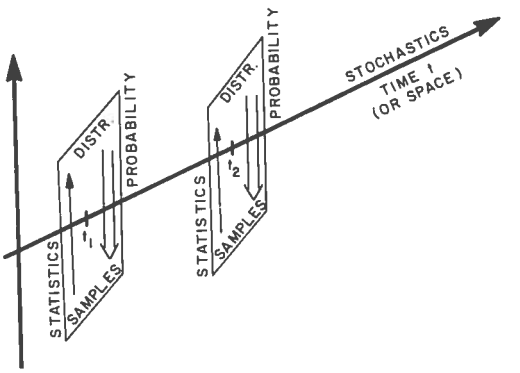

Figure 1. Stochastic space.

important decisions regarding recommended control strategies. The crucial error, then, is the difference between the predicted real courses of events with and without additional stratospheric flight. The major inputs to this decision process may take one of several forms. It can be parameters derived from an assumed distribution or, better, it can be the output of our distribution-free statistical inference. Of course, if we were reckless, we could assume the outcome (prediction) itself. But in any case, it must be remembered that we are dealing with time-varying probabilities – stochastics – in which yet another set of basic concepts (stochastic processes, their stationarity, trends vs. disturbances, etc.) must be brought to bear.

I have two major recommendations with regard to a typical cross-section of our stochastic space. First, we should *predict a distribution* of results in, say, 1990, rather than focusing on a single numerical estimate (such as 500 aerospace vehicles in the stratosphere in 1990). There might be only two points from which we infer the distribution function, as in the case of the upper and lower bounds projected for numbers of aircraft, or a third might be added by including a mean or median value. Second, if only a few (e.g., 30 or fewer) experimental data points have been obtained, we should employ the methods of distribution-free statistics to derive conclusions. Such an approach is especially appropriate with a small data set, where the usually ignored assumptions necessary for use of the relations in classical statistics severely strain the bounds of our knowledge. Such an approach is necessary, lest we fall

[1] James V. Bradley, *Distribution-Free Statistical Tests*, Prentice-Hall, 1968.

into the situation described by Lippmann in an often-quoted remark to Poincaré[2]:

> "Everyone believes in it [the law of errors] however, said Monsieur Lippmann to me one day, for the experimenters fancy that it is a theorem in mathematics and the mathematicians that it is an experimental fact."

[2] H. Poincaré, *Calcul des Probabilités*, 2nd ed., Gauthier-Villars, Paris, 1912, p. 171.

CLIMATIC IMPACT ASSESSMENT PROGRAM: ERROR-VARIANCE ANALYSIS

ROBERT B. SCHAINKER
Systems Control, Inc.
Palo Alto, California

ABSTRACT: This paper describes the status of ongoing efforts to treat the subject of uncertainties in modeling and measurement results as a primary adjunct to the scientific content of the CIAP monographs and Report of Findings. Also presented is the impact these uncertainties have on statistical aspects of monitoring for causal links to stratospheric vehicles.

INTRODUCTION

For interpretation and proper qualification of the CIAP results, the uncertainties in model and measurement results are as important as the results themselves. For this reason, it is necessary to treat the subject of uncertainty analysis (denoted here as error-variance analysis) as a primary adjunct to the scientific content of the final CIAP reports and monographs. To provide ready access to this material, the final version of each monograph will include a separate chapter devoted to the sources and magnitudes of error variances pertinent to the research efforts described therein. At present, the status of this effort is documented in interim reports (Schainker et al., 1973b, 1974) and in chapters of preliminary drafts of the monographs.

This paper presents: first, a definition of terms useful in decomposing and characterizing the various types of uncertainties pertinent to CIAP; second, a statistical methodology useful in quantifying the propagation of uncertainties in a cascade of CIAP models which estimate the effects of stratospheric vehicle emissions; and third, a delineation of statistical tools that can be applied to a sequence of measurement data, and consequently aid in the design of a monitoring program which will investigate changes in the natural conditions which can be causally related to stratospheric vehicle emissions.

DEFINITION OF TERMS

Measurement Uncertainties

The study of error variances in measurement data is directly concerned with identifying the sources and magnitudes of errors associated with experimental and observational results. It is convenient to subdivide the concept of error variances into systematic error variances and random error variances.

Systematic errors are deterministic by definition, and in principle can be eliminated or compensated for, if they are known. They may be constant, or a function of one or more of the system variables and parameters. Constant errors manifest themselves as a bias in the data and are undetectable except by independent measurements and physical-system considerations. If the errors are not constant, they may be detected by testing the data for correlation with the suspected variable or parameter. If a statistically significant correlation is found to exist, it may suggest a physical explanation that will provide a method of compensation.

Examples of systematic errors are those caused by:

1. Incorrect (or an unjustifiably assumed) calibration of an instrument.
2. Construction defects in the measuring apparatus.
3. Inadequate regard to the constancy (or lack of constancy) of experimental and/or environmental conditions.
4. Failure to make necessary corrections, e.g., for the effect of the variation of gravity or pressure with altitude.

Random variations are of the greatest concern in the statistical analysis of measurements. They can be decomposed into two basic categories: variation due to randomness in the process, and variation due to random errors in the measurements.

Instrumentation error variances are described by the deviation in the data attributable to those fundamental errors in the measurement process itself which are not of the systematic type described above. These errors can be quantified by examining the calibration errors and the precision errors of the measurement device itself. The precision error is determined by the reproducibility of a measurement reading, without reference to any true value. The total accuracy of a measurement device is the deviation of a reading from the value of a known input. The accuracy can be improved by proper calibration up to, but not beyond, its precision. A useful approach in quantifying these nonsystematic errors is to place upper and lower bounds (e.g., confidence intervals) on the results derived from raw data, and on the corresponding statistical distribution consistent with these bounds.

Another term associated with measurement data is natural variability. This term refers to the so-called random fluctuations of a set of data about an "average" value. Meteorological variables such as wind velocity, temperature, pressure, and humidity all fluctuate with time and space, even on an "average". Their time-dependent fluctuations may have components with

periods ranging from a fraction of a second to thousands of years. Hence, the natural variability of a variable depends upon the spatial and temporal scale of interest. Once these scales have been defined, the natural variability of a variable can be quantified by statistical analyses of the available data. In general, these analyses provide a statistical description of the data in terms of a trend structure, its parameters, and the residual error accounted for by the trend.

It should be noted that these types of statistical results represent how a variable behaves "on the average". Consequently, a *specific* value of a variable, which is calculated from a statistical trend function, may never be the actual value of the variable at any point in space and time; however, the confidence interval associated with the statistical trend does describe the interval over space and time in which a specific value of the variable will occur. This confidence interval then accounts for the natural variability of the variable.

Modeling Uncertainties

The ultimate test of a mathematical model is its ability to predict accurately the behavior of a given physical system. Its failure to do so may be attributed to two types of errors: systematic or modeling errors, and nonsystematic or statistical errors.

The modeling errors are due primarily to three types of approximations: 1) physical phenomena neglected in order to formulate a model which is usable; 2) mathematical approximations, such as linearization, made in order to make the problems computationally tractable; and 3) numerical approximations made in order to solve the resulting mathematical equations.

The proper ways to understand this type of error are to statistically compare the model predictions with measured data from the process being modeled, and then to augment or extend the model to include a more accurate description of the true physics of the process. For some models the lack of measured data forces the description of the systematic errors to be quite meager. In these cases, the recourse is to include in the model the best physics known, and try to find where nonsystematic errors for a given model can be reduced. When there are data available to compare with those from model predictions, there is a wide body of literature (e.g., Kendall (1966) and Bradley (1968)) that can be used to quantify the "goodness of fit" or systematic error in the model.

Nonsystematic (or random) errors in model predictions are those that affect the statistical mean and variance (uncertainty) of the prediction. They accrue from approximate or uncertain values used for model parameters and/or boundary conditions. The proper ways to understand these types of errors depend on the specific model structure at hand. In general, there are two types of methods, deterministic and statistical. Deterministic methods rely on sensitivity and perturbation analyses of the model prediction with respect to small changes in the parameters and/or boundary conditions. These methods can determine which model variables most influence the model predictions, and, consequently, should be very accurately determined.

Statistical methods employed to understand nonsystematic errors of model predictions rely on determining the statistical properties (mean, variance, and in general the probability-density function) of the model predictions with respect to the statistical properties of the model input variables. Some of the techniques used to quantify these statistical properties, which include statistical distribution propagation analysis, regression/time series analysis, time-dependent covariance analysis, and Monte Carlo analysis, are described in Kendall (1966), Bradley (1969), Schainker et al. (1973a), Papoulis (1965), and Bevington (1969).

Choice of a particular technique depends upon the model structure. These methods can illuminate and give priority measures to those model parameters or boundary conditions that contribute most to the statistical uncertainties in the model predictions. This information can then provide guidance and direction to future work which may modify the model structure (to reduce systematic errors) or adjust the model parameters (to reduce nonsystematic errors).

PROPAGATION OF UNCERTAINTIES THROUGH CIAP'S CASCADED TRANSFER FUNCTIONS

The CIAP study must span many disciplines in order to assess the biological and economic impacts of stratospheric effluents from 1990 aircraft. In predicting these effects, the following types of models are used:

1. Engine-emission models for postulated 1990 aircraft and aircraft engines
2. Jet-engine-wake models including effluent chemistry
3. Radiation models to assess perturbations in the stratospheric radiation balance
4. Aerosol models that describe perturbations in the aerosol content of the stratosphere
5. Climate models that relate climatic variables in the biosphere to changes in the stratospheric radiation balance
6. Biologic survival or production models that relate biologic growth to climate changes
7. Economic-cost models to assess particular costs and benefits of perturbations resulting from 1990 stratospheric aircraft.

Each model can be viewed as one component in a cascade of cause-and-effect transfer functions that relate one type of perturbation (e.g., climatic) to a resulting effect (e.g., biological).

As was described in the first part of this paper, model predictions are subject to two types of modeling uncertainties. The first type of uncertainty, systematic, involves the incorrect choice of the structure of the model. The second type of uncertainty, nonsystematic, involves uncertainties in the choice of the values of the parameters of the selected models. For CIAP these

systematic and nonsystematic modeling uncertainties propagate through the cascade of models, and result in cumulative uncertainties or error variances for each predicted impact.

Because of the diversity of CIAP studies, many cascades are conceivable; however, to date, error-variance analyses have been limited to four perturbation studies: 1) the climatic changes due to increased stratospheric aerosol, 2) the ultraviolet radiation changes due to increased NO_x, 3) the climatic changes due to increased NO_x, and 4) the climatic changes due to increased stratospheric water vapor.

All models used in the cascade analyses have been formulated in one of three ways:

1. The use of the actual model developed by the CIAP researcher in cases where it is in a tractable analytic form.
2. The statistical curve fitting of available data in cases where no model is available at present.
3. The fitting of the results of a complex model into one of a simpler analytic form, over a specified domain of the model variables.

An error-variance analysis of each cascade is performed by calculating the following information at each step in the cascade:

1. The expected value of each model output
2. The variance of the output variables
3. The third statistical moment of the output variables (i.e., the skewness coefficient)
4. The rank-ordering and magnitude of contributing components of the output variance
5. The ratio of the output standard deviation to the output expected value
6. The ratio of the output standard deviation to the output expected value (assuming no error in the model inputs, i.e. all the model uncertainties are due to the parameters).

If it is needed, another item is calculated: the entire probability density function of a model's output variables. Items one through three describe this function and quantitatively represent statistical characteristics of an arbitrary variable. It should be noted that each item above can be calculated using standard statistical techniques (see Papoulis (1965) or the summary in Schainker et al. (1973b)).

This type of analysis is performed on systematic errors by quantifying the "spread" of results from different modelers and by utilizing subjective measures of accuracy that the modelers specify themselves. The analysis of nonsystematic errors is performed by studying the propagation of uncertainties originating from the model parameters in the cascade. Estimates of the uncertainties in these parameters, which act as inputs to the analysis, are acquired from three sources:

1. The error coefficients of statistical regressions for those cases in which a curve fit of data is used as a model.
2. The opinions of the researchers developing the model, which are based on known measurement-data errors and modeling simulation errors.
3. The cumulative estimated uncertainty determined by SCI on the basis of discussions with the researchers, available literature, and plausible error spectra for various assumptions under CIAP consideration.

The results of these error-variance analyses are best interpreted on a relative basis, by comparing the uncertainties at different steps in the cascade. In this manner, attention can be focused on how uncertainties propagate through the cascade of models, and the largest to the smallest components of uncertainty can be identified for later investigations.

STATISTICAL ASPECTS OF A CIAP-ORIENTED MONITORING PROGRAM

One of the planned outgrowths of the CIAP program will be the establishment of a monitoring program focusing upon climatic and biologic indices that may be perturbed by stratospheric vehicle effluents. In the context of nonlinear atmospheric phenomena, the proper design of this program and the proper treatment of the resulting data is a monumental task; however, the statistical literature available today does provide guidelines to properly quantify what can and cannot be inferred from a measurement data base. This section will summarize the three statistical tools which specify the use of the results from the monitoring program, and consequently help in the design of that program. Also presented, where appropriate, will be the interrelationships between the confidence limits of statistical indices and such monitoring parameters as sampling rate and instrumentation accuracy.

Statistical Trend and Confidence-Interval Anslysis

Trend analysis is concerned with extracting from a time sequence of data (i.e., a time series) information about existence of a long-term movement in the data. Specifically:

1. Given Y(t), t = 1, . . . , is there a trend in Y(t)?
2. How can the trend be determined and isolated from the seasonal and random components?
3. How well can we determine the trend:
   - As a function of the number of time periods sampled?
   - As a function of the individual internal variations at each time t?
   - As a function of possible alternative trend structures?

In general, the techniques employed in trend analysis stem from the fields of multiple-regression analysis, correlation analysis, distribution-free statistics,

maximum-likelihood estimation analysis, and goodness-of-fit analysis. The fundamental steps in trend analysis are as follows:

1. Collect data for the time series (making every effort to ensure that the data are reliable). In the collection of data one should always keep in mind the eventual purpose of time-series analysis. In this case, it is essential to document the instrumentation and calibration accuracies of all the measurements, as well as to adjust the data for comparability – e.g., adjust the data for leap years and for the different number of days in each month.
2. Graph the time series, noting the presence of any long-term trend, cyclical variations, and seasonal variations.
3. Determine whether seasonal (i.e., monthly) or cyclical (i.e., non-monthly) variations should be incorporated in the structure of the trend. For example, if the periods of a finite set of trigonometric functions (i.e., sines and cosines) can be identified, then the amplitudes of these functions can be left to be determined by regression analysis.
4. If seasonal or cyclical variations are to be removed from the data, obtain a seasonal index or weighting matrix, and adjust the data for these variations. (There are many procedures for doing this in the literature (see Kendall (1966) or Papoulis (1965)); e.g., divide each month's data by the weighting of the month relative to the yearly average.)
5. Construct the long-term trend function through the data. This is the most important step in the trend analysis; it utilizes the regression techniques described later. In general, this step can be repeated for as many trend model structures as deemed necessary on physical grounds. The residuals associated with different model structures (i.e., the difference between the data and trend-model predictions) can be tested to determine which model structure is most consistent with the statistical uncertainties associated with the measurement equipment and atmospheric variability.
6. Determine the confidence intervals for the trend model. This too is a very important step in trend analysis, for it quantitatively expresses the degree of accuracy the trend model embodies.

If there are N measurement stations of a variable at any one time, Figure 1 illustrates the relationship between the confidence interval for the arithmetic mean of these measurements, the number of measurements, and their standard deviation. (The latter encompasses the instrumentation accuracy and the natural variability in the data.) As can be seen from Figure 1, the confidence interval decreases when the number of measurement stations increases, and the confidence interval increases when the standard deviation of the data increases.

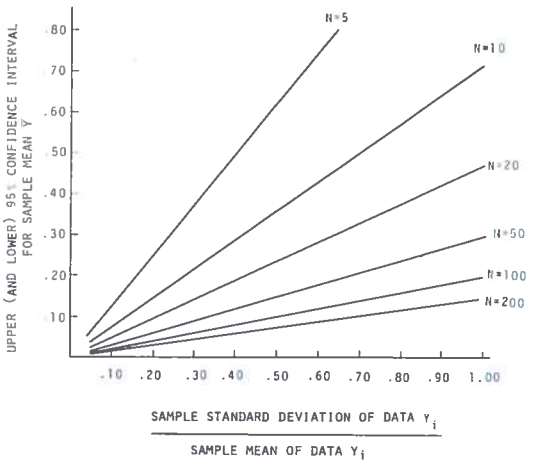

Figure 1. 95% confidence intervals for sample mean ($\bar{Y}$) versus standard deviation of data Y_i divided by the sample mean of Y_i (S/Y) and the number of measurement stations.

$$\frac{S}{Y} = \frac{\text{Sample Standard Deviation of Data } Y_i}{\text{Sample Mean of Data } Y_i}$$

where

$$S^2 = \frac{1}{N-1} \sum_{i=1}^{N} (Y_i - Y)^2$$

$$\bar{Y} = \frac{1}{N} \sum_{i=1}^{n} Y_i$$

Note: S encompasses measurement accuracy and natural variability in data.

If the N stations above take measurements at a sequence of time points, a time-dependent trend can be determined for the variable of interest. Figure 2 illustrates the relationship between the confidence interval for the slope of a linear trend model and the correlation between the time points and the measurements of the variable. (If there is perfect one-to-one correlation, the coefficient r in the figure is equal to 1.) As can be seen in the figure, the confidence interval gets "tighter" as the correlation gets stronger and the number of measurements increases.

To test the validity of the slope parameter calculated in a trend, statistical hypothesis-testing procedures can be used to test the hypothesis that the true slope is zero when in fact the calculations indicate that it is not zero. Figure 3 illustrates the results of such a hypothesis test by showing the relationship between the number of measurements, the correlation coefficient, and the confidence to which we can say that the true slope does not equal zero. By noting that the correlation coefficient in this figure is directly related to the value of the slope parameter, one can determine the number of measurements necessary to identify whether a trend even exists (within a specified confidence). An example of this type of analysis is given in Pittock (1972, 1974).

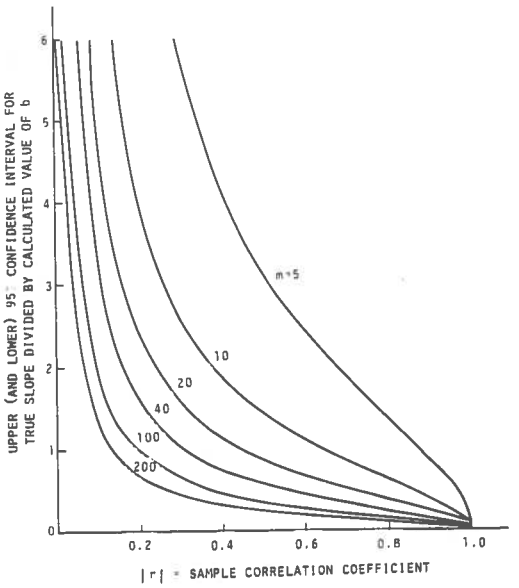

Figure 2. 95% confidence intervals for slope versus correlation coefficient and number of data points.

Note: This plot can be used to determine the confidence interval of a linear correlation between two sampled variables:

- Y vs. time ($Y_i = a + bt_i$)
- Y vs. X ($Y_i = a + bX_i$)

Y and X can be obtained from two monitoring stations.

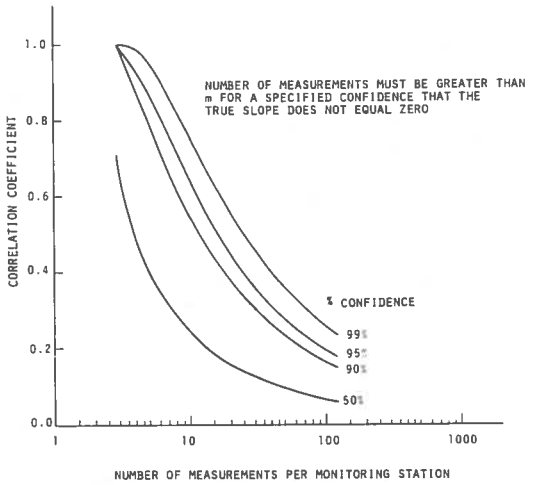

Figure 3. Relationship between number of measurements (m) per monitoring station and correlation coefficient (between t_i and $\bar{Y}(t_i)$, i = 1, . . . , m) for 95% confidence that true slope = 0.

Alarm-Level Analysis Based on A Statistical Trend

This section presents a statistical methodology to establish an alarm condition and a non-alarm condition, for an atmospheric variable of interest (X) defined by the trend-model variables described above. The methodology is based on statistical "Type 1" and "Type 2" errors associated with the decisions to issue an alarm or not to issue an alarm.

Let us define these errors mathematically as follows:

Let

X_{max} = a specified "CIAP threshold value" for an atmospheric variable of interest

X = The true "population" value of the atmospheric variable

$\underline{A}$ = Alarm condition decision

$\overline{A}$ = Non-alarm condition decision

A type 1 error is said to occur if the threshold value X_{max} is truly violated but the CIAP scientist decides that it has not been violated. The probability of this event should be below a specified level, α (e.g., $\alpha = 0.05$), defined as the probability of a type 1 error. Mathematically, this is represented as

$$P\left\{X > X_{max} \text{ if } \overline{A} \text{ is declared}\right\} \leq \alpha$$

A type 2 error is said to occur if the threshold value X_{max} is in fact not violated but the CIAP scientist decides that it has been violated. The probability of this event should also be below a specified level, β (e.g., $\beta = 0.10$), defined as the probability of a type 2 error. Mathematically, this is represented as

$$P\left\{X < X_{max} \text{ if } A \text{ is declared}\right\} \leq \beta$$

For a viable CIAP decision mechanism the above probability conditions should not be satisfied simultaneously. This leads us to the decision procedure given below and illustrated in Figure 4.

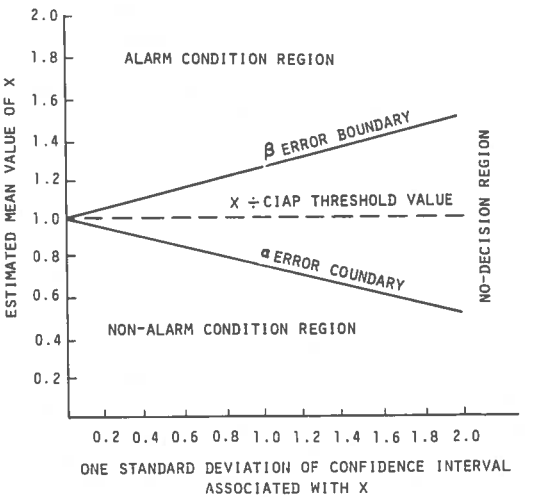

Figure 4. CIAP monograph decision chart for an atmospheric variable X.

1. Decide a CIAP threshold value has been violated (i.e., alarm condition A has been declared) if

$$P\left\{X < X_{max}\right\} \leq \beta$$

and

$$P\left\{X > X_{max}\right\} \geq \alpha$$

2. Decide a CIAP threshold value has not been violated (i.e., non-alarm condition $\bar{A}$ has been declared) if

$$P\left\{X > X_{max}\right\} \leq \alpha$$

$$P\left\{X < X_{max}\right\} \geq \beta$$

3. Decide that no reliable decision can be made within the error levels α and β if none of the above pairs of inequalities holds.

The occurrence of this type of decision means that the CIAP scientist should acquire more measurement data before he can reliably declare A or $\bar{A}$.

A most interesting feature of this nomograph chart is that a placement of only one point on the chart defines the decision to be made by the CIAP scientist. The abcissa of this point is defined by the standard deviation associated with the atmospheric variable X, whereas the ordinate of this point is defined by the estimated mean value of the same atmospheric variable. In practice, this chart can display a "family" of values for α and β (e.g., 0.001, 0.01, 0.05, 0.1), and consequently the placement of a point on the chart can determine the α and β thresholds to which a decision corresponds.

It should also be noted that the nomograph is drawn with linear α and β boundaries, which separate the decision regions. This corresponds to the case where X, as a statistical random variable, is "Student t" or Gaussian-distributed. For those cases in which the statistical distribution of X is not Gaussian or "Student t", the α and β decision boundaries can still be determined by computer and may turn out to be curved lines (Bar-Shalom et al., 1974); however, the decision process will remain as described above.

Causal Discrimination Analysis Based Upon An Alarm Condition

A statistical methodology is used to establish the confidence intervals associated with the causal relationship between two measured variables, e.g., a stratospheric pollutant and a global climatic index. The methodology is divided into two phases. First, one determines whether the two variables are statistically correlated. If they are, then one determines the goodness-of-fit probability associated with the monitoring program measurement data and predictions prescribed by causal CIAP models consistent with basic physics and chemistry. If CIAP scientists prescribe more than one causal model, the second phase above is carried out for each available model and a rank-ordering of the models can be obtained with respect to the goodness of fit index.

Statistical Correlation of Two Variables

This type of analysis can determine when two measured variables exhibit an interdependent relationship. The methods used are analogous to those of trend analysis above, but instead of analyzing one variable against the time axis, one variable is analyzed against another variable (both may be functions of time).

It is important to note that correlation analysis need not be restricted to linear correlation; nonlinear transformations of the variables can also be analyzed.

Tests of Goodness-of-Fit Between Measurement Data and Model Predictions

This type of analysis can determine an index of statistical "significance" for the goodness-of-fit between two sets of data:

- Empirical data from a monitoring program for variable y over n independent stations, $y_{(n)}$
- Model predictions of y, $y_{(m)}$, based on a causal relationship with variable X (e.g., X = stratospheric source emissions of NO_x, and $y_{(m)}$ = model predictions of O_3).

Two methods which address this issue are the chi-square test (see Kendall (1966) or Bradley (1968)) and the Kolmogorov-Smirnov test (see Bradley (1968), Papoulis (1965), or Bevington (1969)). Both methods depend on the distribution functions of $y_{(n)}$ (i.e., a histogram of the monitoring data base) and $y_{(m)}$, which is based on propagating the model input uncertainties into the model output uncertainties. The former is dependent on the structure of the $y_{(m)}$ distribution, whereas the latter does not depend on this structure, and is a so-called non-parametric or distribution-free technique (Bradley, 1968). Because of this distinct advantage, it will be described below.

The Kolmogorov-Smirnov test is based on the cumulative (or integral) distribution functions for $y_{(n)}$ and $y_{(m)}$, $F[y_{(n)}]$ and $F[y_{(m)}]$, respectively.

Let H_0 = hypothesis that the modeled data agrees with the monitoring data base. Since the monitoring data base covers n stations, its cumulative distribution function is a staircase function between 0 and 1. (See Figure 5.)

$$F[y_{(n)}] = \frac{k}{n} \quad k = 1, \ldots, n$$

where k = number of observations with values less than y ($y = 0, \ldots, y_{max}$).

We should expect that if H_0 is true, $F[y_{(n)}]$ will be a fairly good approximation to $F[y_{(m)}]$, and will be better as N increases. In fact, according to the law of large numbers, $F[y_{(n)}]$ will tend to $F[y_{(m)}]$ with a probability of 1. The statistical index to test this hypothesis is defined as $D_{(n)}$, the maximum of the absolute deviation of $F[y_{(n)}]$ from $F[y_{(m)}]$:

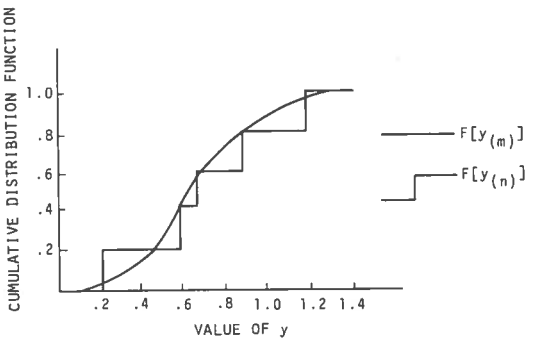

Figure 5. Illustration for Kolmogorov-Smirnov test: Sample cumulative distribution functions for $F[y_{(n)}]$ and $F[y_{(m)}]$, n=5.

$$D_{(n)} = \underset{y}{\text{Max}} \, |F[y_{(n)}] - F[y_{(m)}]|$$

$$P\left\{\underset{y}{\text{Max}} \, |F[y_{(n)}] - F[y_{(m)}]| > D^{T}_{(n)}\right\} = \alpha$$

$$D_{(n)} = \underset{y}{\text{Max}} \, |F[y_{(n)}] - F[y_{(m)}]| > D^{T}_{(n)} = \alpha$$

where α, n, and $D^{T}_{(n)}$ are tabulated values (see, e.g., Bradley (1968)).

The above probability statement can be utilized in the following equivalent ways:

1. Calculate $D_{(n)}$ from the monitoring data $y_{(n)}$ and the modeled prediction $y_{(m)}$. If this value is less than the value given in the table (for a specified α and n), then the two sets of data agree and H_0 is true with probability $1-\alpha$.

2. For a specified n and α, look up the tabulated value, $D^{T}_{(n)}$. We can then expect with probability $1-\alpha$ that if H_0 is true, the step function of monitoring data will lie inside the interval $F[y_{(m)}] \pm D^{T}_{(n)}$.

3. For a specified n and α, look up the tabulated value, $D^{T}_{(n)}$. We can then form a $1-\alpha$ confidence belt for "fittable" modeling functions, $F[y_{(m)}]$, by drawing the "step bands" for $F[y_{(n)}] \pm D^{T}_{(n)}$. Any modeling function which lies wholly in this belt will not be rejected by the monitoring data at the $1-\alpha$ level of confidence.

It should be noted that increasing the number n of monitoring stations will cause the value for $D^{T}_{(n)}$ to decrease for any specified level of confidence $(1-\alpha)$; therefore, to maintain causality agreement with the monitoring data, the predictive models have to produce a $D_{(n)}$ which is smaller and smaller as n increases. The monitoring program will then put stiffer requirements on the models for validating causal relationships between stratospheric emissions and climatic effects.

ACKNOWLEDGMENTS

This work has been supported by the Climatic Impact Assessment Program, Department of Transportation, contract number DOT-OS-40042. It is a product of the efforts of many talented and conscientious people. In particular, I am greatly indebted to R. Lau, J. Patmore, R. Atherton, and J. Wirsching.

REFERENCES

Bar-Shalom, Y., A. Segall, D. Budenaers, and R.B. Schainker (1974), "Statistical Theory for Sampling of Time-Varying Industrial Atmospheric Contaminant Levels," Systems Control, Inc., Final Report HSM 99-73-78, June 1974.

Bevington, P.R. (1969), *Data Reduction and Error Analysis for the Physical Sciences*, McGraw-Hill, New York.

Bradley, J.V. (1968), *Distribution-Free Statistical Tests*, Prentice-Hall, New Jersey.

Kendall, M.G. and A. Stuart (1966), *The Advanced Theory of Statistics*, Vol. 1-3, Hafner Publishing Co., New York.

Papoulis, A. (1965), *Probability, Random Variables and Stochastic Processes*, McGraw-Hill, New York.

Pittock, A.B. (1972), "Evaluating the risk to society from the SST," Search 3 (8), 285-289.

Pittock, A.B. (1974), "Ozone climatology, trends and the ozone monitoring problem," in *Proceedings of the International Conference on Structure, Composition and General Circulation of the Upper and Lower Atmosphere and Possible Anthropogenic Perturbations* (Melbourne, January 14-25), pub. IAMAP, 455-466.

Schainker, R.B., T.R. Ranweiler, and A.J. Tether (1973a), "Sensitivity assessment of parameter uncertainties in climatic forecast models," in *Proceedings of the Sixth Hawaii International Conference on System Sciences*, Western Periodicals Company, January 1973.

Schainker, R.B., J.E. Wirsching, R.W. Lau, J.W. Patmore, and R.P. Brennan (1973b), "Climatic Impact Assessment Program: Error Variance Analysis, Sixth Month Report," Contract Number N00014-73-C-0409, Systems Control Inc., September 1973.

Schainker, R.B., J.E. Wirsching, R.W. Lau, J.W. Patmore, R.P. Brennan, and R.W. Atherton (1974), "Climatic Impact Assessment Program: Error Variance Analysis, Interim Report," Contract Number DOT-OS-40042, Systems Control, Inc., July 1974.

THE HEALTH COSTS OF CHANGING MACRO-CLIMATES

ROBERT J. ANDERSON, JR.
Center for Environmental Policy Studies
Pennsylvania State University
University Park, Pennsylvania

ABSTRACT: The theory, methods, and problems of assessing health costs associated with changing macro-climates are discussed, and preliminary estimates of the range of costs corresponding to the predicted CIAP parametric ranges are presented.

INTRODUCTION

Apparent changes in atmospheric turbidity and in concentrations of carbon dioxide in the earth's atmosphere have led to much speculation about the possible effects of man's recent activities on global climate. Relatively little, in contrast, has been done to evaluate the possible biological and socio-economic consequences of such effects.

This paper summarizes a first effort to assess possible health costs associated with global changes in temperature, precipitation, windspeed, and UV radiation. Medical knowledge of the effects of climate on health is very sparse. Therefore, all estimates presented here are, in fact, the crudest sort of pure empiricism. In particular, the regression results reported in Tables 1 and 2 below can legitimately be viewed only as purely descriptive relationships, pointing up patterns in the historical data on which they are based. What, if any, causal interpretation of them could be made is doubtless a matter of considerable controversy. It is, however, outside the scope of this paper (and most assuredly beyond the competence of its author) to more than note such issues.

All cost estimates in this paper are based on extrapolations from these regressions. Because the basis for their causal interpretation is at issue, and because the legitimacy of extrapolation to other times and other places is always questionable, the numbers reported here must be taken to be purely hypothetical.

COST CONCEPTS

Three different cost concepts have been proposed for CIAP purposes. The purpose of this section is to clarify those concepts. In what follows, the theory of consumer behavior developed by Lancaster and Becker is relied upon heavily. Let U(z) be a twice-continuously-differentiable utility function, increasing in elements of the vector z, and quasi-concave. Following Lancaster, let the vector z represent characteristics or attributes representing the state of the system, insofar as the consumer is concerned. Let characteristics or attributes be associated in an objective way with market and non-market goods and services by the vector function

$$z = H(x)$$

where x is the vector of market and non-market goods and services. (Non-market goods and services are explicitly included so as to admit environmental goods to consideration.) The coordinate functions of H will be termed "consumer production functions".

The problem is to evaluate alternative states — in this instance, alternative macro-climates in 2020. Letting tildes denote values that would obtain in 2020 in the absence of perturbation of the macro-climate through flight in the stratosphere, the problem may be stated as

Problem A: minimize: $y = p'x$
subject to the constraint: $U(z) = U(\tilde{z})$

where $\tilde{z}$ is the solution of

Problem B: maximize: $U(z)$
subject to: $\tilde{p}'x = \tilde{y}$

Letting y^* be the value of the objective function for Problem A at the constrained minimum, define the cost of the perturbation in the macro-climate to be

$$C = y^* - \tilde{y} \tag{1}$$

This amount may be thought of as the additional income needed to make the consumer indifferent to the choice of macro-climates. In the terminology of the CIAP project, it is the opportunity cost measure, since it evaluates the cost which allows complete optimizing adjustment to perturbed external conditions.

Another measure simplifies the cost-evaluation problem (at a cost of making a measurement that is in general incorrect) by focusing on the cost of maintaining a subset of z (say the first r components) at $\tilde{z}$ levels in the face of external change. Technically, this measure may be stated as follows:

Problem C: minimize: $y = p'x$

subject to: $z_i = \tilde{z}_i$ $(i = 1, ..., r)$

where $\tilde{z}$ is the solution to Problem B, as stated in the preceding section. Letting $\hat{y}$ be the value of the objective function for Problem C at the constrained minimum, define the "alternative cost" of perturbations in the macro-climate to be

$$\hat{C} = \hat{y} - \tilde{y} \tag{2}$$

The essential difference between the opportunity-cost and alternative-cost measures is thus seen to be in the applicable constraint. In calculating opportunity cost, the individual is constrained to be indifferent; in calculating alternative cost, he is constrained to the same consumption pattern (or at least to a subset of the same consumption pattern).

Willingness-to-pay and opportunity cost are more closely related. Willingness-to-pay, rather than determining the minimum compensatory income necessary to render a consumer indifferent, seeks to determine the maximum amount the consumer would be willing to pay for the opportunity of remaining in the unperturbed regime. Formally, we may state this problem as

Problem D: maximize: $M = \tilde{y} - \tilde{p}'x$

subject to: $U(\tilde{z}) = U(z)$

$M \geqslant 0$

where z is the solution to

Problem E: maximize: $U(z)$

subject to: $p'x = y$

and where p and y are values that would obtain in a perturbed macro-climate. The value of the objective function of Problem D at the constrained maximum will be said to be willingness-to-pay.

Willingness-to-pay, like opportunity cost, is also a theoretically correct measure of cost. The difference between the two is in the assumption as to whom the burden for compensation is to fall on. Opportunity cost is based upon the assumption that the consumer is to be compensated; willingness-to-pay, conversely, is based upon the assumption that the consumer is to pay to prevent perturbation.

Inasmuch as various measures of costs are to be found in Volume VI of the CIAP monographs, it is of some interest to determine what relationship (if any) the different measures should bear to one another. Such bounding relationships are useful not only for interpreting reported empirical measures, but also for providing some consistency checks on empirical results.

Apparently, the only general bounding relationship that can be established under the conditions set forth above relates the opportunity and alternative-cost measures. This result is set forth below as Lemma 1.

Lemma 1: Consider Problems A, B, and C, and suppose further that in Problem C, $\hat{z} = \tilde{z}$. Then $\hat{C} - C^* \geqslant 0$.

Proof: If $\hat{z} = \tilde{z}$, then $U(\hat{z}) = U(\tilde{z})$. Noting that y^* is the smallest y for which $U(z) = U(\tilde{z})$, it follows that $\hat{y} \geqslant y^*$, which implies $\hat{C} - C^* \geqslant 0$.

Note that this result requires that the *whole characteristics vector* be fixed at its pre-perturbation state, rather than just some subset as specified in Problem C. This is a very restrictive condition, and must be kept in mind when this result is applied as a consistency check on empirical results. In general, the result of Lemma 1 does not necessarily hold for the case in which only a subset of z is held fixed.

There appears to be no general relationship between C and M. Letting y^{**} be equal to $\tilde{p}'x$ in

Problem D at the constrained maximum, $C - M = y^* + y^{**} - 2\tilde{y}$. It is known that $y^* \geq \tilde{y}$ and $y^{**} \leq \tilde{y}$, but this information is not sufficient to yield the sign of $C - M$.

SOME COST ESTIMATES

As is common practice, health costs are divided here into two categories: monetary costs of health care, and non-monetary costs associated with time (or lost output). Monetary costs of health care are costs of physicians' services, hospital services, and medication. They are actual money outlays for treatment. Non-monetary costs, on the other hand, are frequently implicit costs (i.e., time spent in obtaining medical services, in recuperation, or in "moribundity"). Although money never actually changes hands, costs of foregone leisure or income are very real.

Another common way to divide health costs is into costs associated with morbidity and costs associated with mortality. Mortality and morbidity costs can be subdivided, as above, into monetary costs of health care and opportunity costs.

Because exhaustive investigation of all cost categories (as outlined above) was not possible in the time available, comprehensive estimates have had to be pieced together from available data:

1. Additional monetary costs of health care consequent upon a change in climate, whether associated with mortality or morbidity cases, are computed on the basis of regressions provided by Mark Pauly (1973). These regressions, reported in Table 1 below, explain expenditures for both physicians' services and

Table 1. Regression Results, Coefficients, and Standard Errors

Equation No.	Dependent Variable	R^2 (unadj.)	Income per Capita	Population Density	% Over 65	% Black	Hospital Beds/ Capita	GP's/ Capita	Avg. Precipitation	Avg. No. of Days Below 32°
1	Medical practitioner, gross receipts per capita	0.892	1.1 (0.16)	-0.01 (0.02)	-1.1 (1.1)	–	–	0.09 (0.12)	–	-0.07 (0.02)
2	Physician visits	0.847	1.0 (0.15)	–	-1.4 (1.1)	–	–	-0.05 (0.11)	–	-0.07 (0.02)
3	Hospital expense per capita	0.746	0.68 (0.17)	0.06 (0.02)	1.3 (1.2)	–	0.50 (0.14)	–	-0.048 (0.037)	-0.006 (0.02)
4	Avg. hospital census	0.704	0.26 (0.17)	0.03 (0.02)	3.4 (1.3)	65 (0.26)	0.57 (0.13)	0.19 (0.11)	-0.047 (0.037)	0.034 (0.019)

Equation No.	Dependent Variable	Avg. Temp.	Physician Fee Office Visit	Ratio of Tax Returns to AMA Physicians	Hospital Expense per Patient Day	RNP	% of Population with Hospital Insurance
1	Medical practitioner, gross receipts per capita	*	–	0.68 (0.06)	*	*	*
2	Physician visits	*	-0.79 (0.16)	0.67 (0.05)	*	*	*
3	Hospital expense	*	–	*	*	0.14 (0.11)	*
4	Avg. hospital census per capita		-0.25 (0.15)	*	*	–	*

– variable not statistically significant, and so not included
* variable omitted

hospital services. Costs of medication are assumed, for purposes of cost estimation, to change in the same percentage as the sum of the percentage changes in expenditures for physicians' services and hospital services.

2. Additional non-monetary costs associated with use of health-care services are estimated from regressions explaining physicians' visits and from hospital censuses reported in Table 1. It is assumed that 3.3 days are lost for each visit to a physician or hospital day, which is roughly the current ratio between medical-care days and work-lost days.
3. Additional non-monetary costs associated with death are estimated from variations in regressions explaining crude mortality rates as reported in Lave and Seskin (1972). These variations are shown in Table 2.

Table 2. Total Mortality Regression Results

Explanatory Variables	Dependent Variable ln (MR)
Annual arithmetic mean of suspended particulates	0.044 (1.74)
Minimum biweekly sulfation	0.035 (3.17)
Population/mi^2	-0.0004 (-0.39)
% non-white	0.019 (1.97)
% $\geq$ 65 years old	0.544 (13.96)
Total annual rainfall	0.044 (2.60)
Degree days	0.019 (1.26)
Average windspeed	-0.058 (-1.61)
Regression constant	1.456
$\bar{R}^2$	0.790

Note: All log forms are double-log forms. Thus, where the logarithm of a variable is used as the dependent variable, logarithms of explanatory variables are also used.

Comprehensive estimates of costs associated with changes in the macro-climate are then computed as the sum of health-care costs, of non-monetary costs associated with consumption of health-care services, and of non-monetary costs associated with death.

In addition to the kinds of cost estimates described above, special cost estimates are prepared for skin cancer because of the particular interest of the CIAP project in this disease. Cost estimates are based upon the relationship between incidence of non-melanoma skin cancer and UV level given by Urbach et al. (1974), and estimates of health-care and non-monetary costs per skin-cancer case provided by Mark Pauly (1973). These estimated costs per case are shown in Table 3.

Table 3. Estimates of Economic Cost Per Case of Skin Cancer

	High-Cost Case	Low-Cost Case
Medical Costs	$341	$ 62
Work-Loss Costs*	458	93
Work-Loss Costs†	343	70
Total Costs*	799	155
Total Costs†	684	132

* assuming work-loss days = 3.3 X medical-care days
† assuming work-loss days = 3.3 X 0.75 X medical-care days

Total CIAP health-resource costs are, then, the sum of the costs due to additional incidence of skin cancer associated with changed UV level and of the costs of additional morbidity and mortality associated with perturbations in the macro-climate.

It must be kept in mind when reviewing these cost numbers that they are based upon extrapolations from the statistical regression associations reported in Tables 1 and 2.

As has been noted, there is little or no basis for according a causal interpretation to these regressions. (The results from the Urbach data are an exception.) Moreover, even if these regressions did reflect causal relationships, it is not necessarily true that extrapolation of these results to other times and other places would be appropriate. (This qualification holds for the skin-cancer results of Urbach as well.)

In view of these qualifications, *the cost numbers to be reported here can be legitimately viewed only as estimates, which are conditional upon the validity of a causal interpretation of the regression results and conditional upon the validity of extrapolation. Because neither of these conditions is particularly plausible, numbers to be reported here must be viewed as purely hypothetical.*

Costs of Non-Melanoma Skin Cancer

This section presents estimates of the cost associated with possible increases in the incidence of skin cancer (other than melanomas, which are not thought to be associated with UV radiation). For the purposes of this calculation, it is assumed that the populations at risk are those of North America, Europe, and Oceania. Inhabitants of the other continents are presumed, by virtue of protective skin pigmentation, to be at near-zero risk.

Incidence and Case Perturbations

Incidence and case perturbations are calculated on the basis of three predictions: projections of various reductions of ozone in the stratosphere, the effect of these reductions on the level of UV received at the earth's surface, and the relationship between increased UV and skin-cancer incidence.

Potential reductions of ozone in the stratosphere varying from 5% to 40% have been considered in the CIAP Study. For the purposes of calculation, four depletion values have been applied: 5%, 10%, 20%, and 40% of O_3.

The relationship between O_3 reduction and UV increase depends upon latitude. (Assumptions concerning the character of this dependence are based on data given in Urbach et al. (1974).) Table 4 presents estimated increases in skin-cancer-causing UV, given in biological units. (One BU equals 100 J/m^2 of erythema-effective energy; the number of BU's is derived by integrating the solar irradiance between 290 and 320 nm at the earth's surface, multiplied by the relative effectiveness of these wavelengths in producing erythema, which is used as an index of skin cancer.)

For the purposes of this paper, the relationship between increased UV level and increased skin-cancer cases will be assumed to be that given by Urbach et al. (1974):

$$\Delta i = 0.2 \text{ BU} \times \Delta$$

The perturbations in skin-cancer incidence, then, for each of the ozone-depletion levels given above, would be as given in Table 5.

Table 4. Estimated Increases in UV Level (in BU's)

Area	-5% O_3	-10% O_3	-20% O_3	-40% O_3
North America (including USA)	232	490	1109	3070
USA	225	475	1075	2975
Europe	142	300	629	1880
USSR	142	300	629	1880
Oceania	324	684	1548	4284

Table 5. Perturbations in Incidence of Skin Cancer, by 2020, Other Than Melanomas (cases per hundred thousand)

Area	-5% O_3	-10% O_3	-20% O_3	-40% O_3
North America	46	98	222	614
USA	45	95	215	595
Europe	28	60	136	376
USSR	28	60	136	376
Oceania	65	137	310	857

Letting Δ represent the percentage increase in incidence of non-melanoma skin cancers per 100 thousand as set forth above, the increase in numbers of cases may be calculated as

$$AC = \Delta \times N$$

where N is population in 100 thousands, and AC is additional cases per year. The results of this calculation for the projected high and medium populations in 2020 (as specified for CIAP Monograph VI) are set forth in Tables 6 and 7 below.

Table 6. 2020 Projected Annual Additional Cases, Medium Population (1000's of cases)

Area	-5% O_3	-10% O_3	-20% O_3	-40% O_3
USA	128	270	611	1690
North America (less USA)	33	73	166	459
Europe (less USSR)	164	351	796	2200
USSR	108	230	522	1444
Oceania	29	62	140	386
Total	462	986	2235	6179

Table 7. 2020 Projected Annual Additional Cases, High Population (1000's of cases)

Area	-5% O_3	-10% O_3	-20% O_3	-40% O_3
USA	146	309	699	1934
North America (less USA)	79	170	387	1068
Europe (less USSR)	212	454	1028	2843
USSR	146	313	709	1959
Oceania	64	134	304	840
Total	647	1380	3127	8644

Estimates of Costs Associated With Increased Incidence of Skin Cancer

Estimates of total annual costs in the United States associated with perturbations in incidence of non-melanoma skin cancer are set forth in Table 8 (expressed in 1971 U.S. dollars). The calculations are based on the assumption that work-loss days are 3.3 times medical-care days. All costs are morbidity costs. Skin cancer is assumed not to result in death.

Total Non-Skin-Cancer Health Costs of Climate Changes

In this section, estimates of the total health costs associated with possible changes in climate are presented. All populations of the world are presumed to be at risk.

Method of Calculation

The costs reported in this section are based upon extrapolations from the regression results reported in Tables 1 and 2.

In order to extrapolate perturbations consequent upon climatic change, it is necessary to extrapolate values in the absence of such perturbations. It is assumed for purposes of calculation here that the following yearly values would obtain worldwide for variables of interest:

Crude Mortality Rate:	14.5 per 1000
Expenditures for physicians' services per capita:	$68
Expenditures for hospitals' services per capita:	$141
Expenditures for drugs per capita:	$36
Physician visits per capita:	5
Hospital days per capita:	1

Two steps are involved in calculating the costs:

a. Translation of perturbations in climatic variables into perturbations in prices and/or quantities, via the regression relationships cited above.
b. Translation of perturbations in prices and/or quantities into perturbations in total health costs.

Table 8. United States Annual Costs of Additional Non-Melanoma Skin Cancer (in Millions of 1971 U.S. Dollars, Starting 1974)

Assumptions	Case	-5% O_3	-10% O_3	-20% O_3	-40% O_3
Medium Population					
3% discount rate	High-cost	78	164	371	1026
	Low-cost	15	32	74	203
5% discount rate	High-cost	43	91	206	571
	Low-cost	9	18	41	113
8% discount rate	High-cost	19	41	92	256
	Low-cost	4	8	18	51
High Population					
3% discount rate	High-cost	95	201	456	1261
	Low-cost	19	40	90	250
5% discount rate	High-cost	53	112	254	702
	Low-cost	11	22	50	139
8% discount rate	High-cost	24	50	114	314
	Low-cost	5	10	23	62

As has been noted, non-skin-cancer costs calculated here are of two types: value of gross income lost due to additional mortality, and explicit and implicit costs associated with possible changes in the use of health services.

Perturbations in mortality rates affect populations in two ways. First, they may alter the size of the population. Higher mortality rates, other things being equal, result in smaller population sizes than would otherwise obtain. Second, perturbations in mortality rates may alter the age structure of the population. Uniformly higher mortality rates result, in general, in a lesser life expectancy.

For the purposes of the calculations made in this section, it is assumed that natality and mortality are identical, so that perturbations in mortality result only in changes in age structure and life expectancy. That is, natality is assumed to be perturbed simultaneously with mortality so that population size remains constant.

If the crude mortality rate is assumed to apply to all ages, the effect of changes in the crude mortality rate on life expectancy may be easily computed. Letting p be the probability of dying during any given year of one life (= mortality rate × 0.001), the probability of living r years and then dying is given by

$$(1 - p)^r p$$

Average life expectancy is then given by

$$L = p \sum_{r=0}^{\infty} r(1 - p)^r = \frac{1 - p}{p}$$

For a mortality rate of 14 per 1,000, L = 70.4; that is, the average age at death is 70.4 years. Increasing the mortality rate (which is tantamount to increasing p) results in a decrease in average age at death. Let perturbed life-years be given by L′. If the value of a human life per year is equal to per-capita gross national product, the undiscounted value of a shortening of a life from L to L′ on the average is

$$(L - L')y$$

where y is annual per-capita gross national product. If (L – L′) is less than one, this is also the discounted cost per death in the year of death. If (L – L′) is greater than one, however, discounted cost is given by

$$[(L - L') - N]y + \sum_{i=1}^{N} \frac{y}{(1 + r)^i}$$

where N is the largest integer less than (L – L′). Total costs of death computed in this manner are then given by total deaths times cost per death.

Explicit and implicit health care costs in any one year are calculated according to the following formula:

$$\Delta HCC = (\Delta PS \times PS) + (\Delta HS \times HS) + (\Delta PS + \Delta HS)\, D + 3.3\,(\Delta PV \times PV \times W) + 3.3\,(\Delta HC \times HD \times W)$$

where

- ΔHCC = additional health-care costs per capita
- ΔPS = percentage change in expenditures for physicians' services per capita
- PS = unperturbed expenditures for physicians' services per capita
- ΔHS = percentage changes in expenditures for hospitals' services per capita
- HS = unperturbed expenditures for hospitals' services per capita
- D = expenditures for drugs per capita
- ΔPV = percentage change in physician visits per capita
- PV = unperturbed physician visits per capita
- ΔHC = percentage change in hospital census
- HD = unperturbed hospital days per capita
- W = value of a work-loss day

The percentage changes indicated above are extrapolated from climatic data using the regressions in Table 2. Again, the 3.3 factor is the assumed ratio of work-loss days to medical-care days.

Translation of the parametric ranges of change in climate variables specified for CIAP Monograph VI into estimates of changes in the

explanatory variables of the regressions used for extrapolation is relatively straightforward for precipitation and windspeed. This is because average annual values were used for these variables in the extrapolation regressions, and changes in average annual values are specified for CIAP purposes. The relationship between temperature variables used in the regressions and CIAP temperature variables is, unfortunately, much less clear.

CIAP climate projections are projections of changes in mean parameter values, while the climatic variables included in the regressions of Tables 1 and 2 are measures of the prevalence of both "extreme" conditions and average conditions. "Degree days", for example, measure coldness of climate. The other temperature variable, "number of days when maximum temperature exceeds 90°F", measures prevalence of extreme heat.

In theory, calculation of the change in degree days, or change in number of days when the temperature exceeds some critical value, is a simple matter. Letting F(x) be the cumulative density function of the random variable temperature, the expected number of degree days and the probability of temperatures in excess of some critical temperature T* are given, respectively, by

$$E(DD) = \int_{-\infty}^{65} (65 - x)\, dF$$

and

$$1 - F(T^*) = Pr\,(x \geqslant T^*)$$

and changes in the expected number of degree days and expected number of days when temperature will exceed the critical level T* with respect to a vector of distributional parameters, α, are given, respectively, by

$$\left(\frac{dE}{d\alpha}\right) d\alpha$$

and

$$\left(\frac{dF(T^*)}{d\alpha}\right)' d\alpha \times N$$

where N is the number of events under consideration.

Unfortunately, the computations outlined above require fairly detailed knowledge of the temperature distribution and the effect of changes in parameters thereon. The practical problem that arises in translating estimated changes in the mean of the distribution of a variable into estimates of changes in measures of extremes is illustrated in Figures 1a and 1b below. Two different distributions for temperature are shown in the figures. For expository purposes, both are of the form of the rectangular distribution. That in Figure 1a depicts a distribution that assigns relatively little probability to any particular range of temperatures, while that in 1b depicts a distribution that assigns much greater probability to a particular range.

Consider the effect of applying the same shift transformation to both of these distributions or the probability associated with temperatures greater than some critical temperature T*. The effect of one such transformation on these probabilities is given by the shaded areas in Figures 1a and 1b. Note that the same shift in mean and in distribution extrema applied to both distributions results in very different changes and probabilities associated with temperatures greater than T*. In particular, the distribution depicted in Figure 1b produces a much greater reduction in probabilities associated with temperatures in excess of the critical temperature.

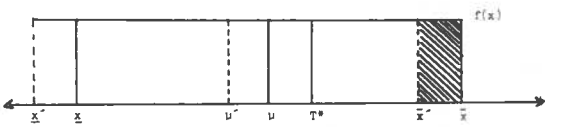

a. Dispersed distribution

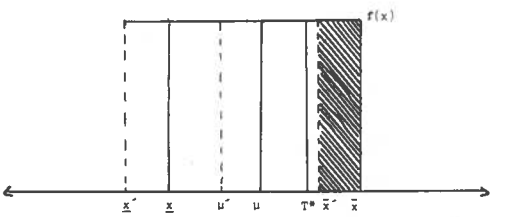

b. Concentrated distribution

Figure 1. Uniform temperature distributions.

It should be noted that although the shifts depicted in the figures below decrease both mean temperature and probabilities associated with temperatures greater than the mean, it is entirely possible that changes in the shape of the distribution could result in a *decrease* in mean temperature and an *increase* in the probability associated with temperatures greater than the mean temperature.

What this very simple example makes clear is that much more information than is presently available on current temperature distributions and changes therein consequent upon flight in the stratosphere is needed, if even logically defensible extrapolations from the regression relationships of Tables 1 and 2 are to be prepared.

Total Non-Skin-Cancer Health Cost Estimates

Hypothetical estimates of additional health costs associated with a perturbed macro-climate in the United States, excluding those for skin cancer, are presented in Table 9. Assumptions about population, population growth rate, per-capita gross national product, per-capita GNP growth rate, the discount factor applied, and the assumed percentage change in average windspeed are arrayed for all calculations. Additional annual costs are projected contingent upon different assumptions about temperature and precipitation. Several different perturbations in temperature are evaluated, due to uncertainty about the relationship between changes in the mean of the distribution and changes in the distribution extremes. It should be noted that although different temperature variables appear in mortality and health-services regressions, the totals presented in Table 9 assume identical percentage changes in both temperature variables.

All costs are expressed as annual costs, starting in the year indicated, in 1971 U.S. dollars. Costs starting in 2000 are simply costs starting in 1974 discounted 26 years. Perturbations in climate are presumed to commence in 1990 and to continue to 2020 in equal annual increments. Conditions specified for the year 2020 are then presumed to persist in perpetuity.

Due to data difficulties and lack of time, none of the costs presented here can be claimed

Table 9. United States Estimated Total Health Costs of Climatic Change, Excluding Skin Cancer

(Additional Costs, Starting 1974, in Billions of 1971 U.S. Dollars)

% Change Precipitation	Percent Change in Degree Days			
	20.0	10.0	5.0	0.0
13.0	7.9	6.7	6.1	5.5
0.0	3.5	2.3	1.7	1.1
-13.0	-0.7	-1.9	-2.5	-3.1

(Additional Costs, Starting 2000, in Billions of 1971 U.S. Dollars)

% Change Precipitation	Percent Change in Degree Days			
	20.0	10.0	5.0	0.0
13.0	2.2	1.8	1.7	1.5
0.0	1.0	0.6	0.5	0.3
-13.0	-0.2	-0.5	-0.7	-0.8

Assumptions:
1990 population = 231 millions
1990 income per capita = $8330 1971 U.S. dollars
Discount rate = 5 percent
Percentage change in windspeed = 2.5%
Population growth = 0.5%
Income growth rate per capita = 2.0%

to correspond precisely to any of the cost concepts set forth in 2 above. Indeed, without knowledge of individuals' utility functions or direct experimentation, it is strictly impossible to evaluate either opportunity or willingness-to-pay cost measures as defined in that section. It is well known that the use of measures of consumers' surplus obtained from empirically-estimated demand functions to estimate willingness-to-pay is only an approximation – and not always a good one.

In concept, the possibilities for empirical estimation of alternative-cost measures seem much greater. Although estimation of this measure requires determination of the ways in which consumers can combine goods and services to produce utility-yielding characteristics (the so-called "consumer production functions"), this appears to be a less difficult problem than learning about consumers' valuations of characteristics.

Most of the estimates presented here are first approximations to alternative-cost measures.

Unfortunately, the estimated "health production functions" presented in Tables 1 and 2 do not include any endogenous economic variables that could be manipulated to modulate the effect of changes in environmental variables. Accordingly, they embody no information about the degree to which use of medical goods and services could be increased to offset possible ill effects of climatic change. For example, it is known that sunscreens can be used to protect against increased exposure to damaging ultraviolet radiation. However, no variable representing "usage of sunscreen" appears explicitly in the relationship between UV radiation and incidence of non-melanoma skin cancer reported by Urbach. Similarly, although it is known that medical goods and services can alter the probabilities of dying, no medical-goods and services variables appear in the mortality equations presented in Table 2.

The procedure followed to generate alternative-cost estimates under these circumstances is to simply *assume* what course of action on the part of consumers will result in least-cost restoration of the vector of characteristics consumed to its pre-climate perturbation state. For example, in the case of skin cancer, it is assumed that a certain treatment regimen – involving physicians' services, hospital services, time, and drugs – will "cure" skin cancer, and is the least-cost way of all methods of prevention and/or treatment for eliminating additional lesions. If it is assumed that this regimen will indeed eliminate additional lesions, and that the costs attached to this regimen are correctly estimated, it follows that the skin-cancer costs presented here are an overestimate of the cost of lesion elimination. This is because there may be some less costly regimen than the one here assumed and costed.

The sense in which the cost estimates for mortality embodied in the estimates in Table 9 may be interpreted as alternative costs wants elaboration. If it had been possible in the time available for this effort to empirically estimate the efficacy of medical resources in reducing mortality rates, the alternative-cost estimate presented would have focused on the minimum additional expenditures necessary to hold constant mortality rates at pre-perturbation levels. Because this was not possible, it is assumed here that there is no course of action to which resort can be had to restore mortality probabilities to pre-perturbation levels. Neither has any attempt been made to determine the cost of a "Lazarus operation," in spite of the obvious lengths to which we have elsewhere gone to produce cost numbers. Rather, alternative cost is evaluated as the cost of the individual's entire consumption bundle (assumed to be equal to the individual's income) if the individual dies.

The medical-care cost estimates embodied in Table 9, based upon regressions presented in Table 1, are very different in concept from the other cost estimates presented in this paper. They are based on regressions of expenditures for medical care resulting from changes in climatic and other variables. As such, these regressions might be interpreted as reflecting actual market adjustments to differences in climatic conditions. Because it is generally true that, even after market adjustment, consumers will fail to achieve pre-perturbation levels of satisfaction, these expenditure estimates understate costs associated with climatic change. If, however, it is assumed that additional expenditures reflect the minimum cost of maintaining health at pre-climatic-perturbation status, these estimates can be given an alternative-cost interpretation.

CONCLUDING COMMENTS

These estimates, notwithstanding their obvious limitations, underscore the need for better understanding of the effects of climate on health. Flight in the stratosphere is only one of many activities with a potential for altering the earth's climate. It seems, therefore, that a much larger and more broadly based research effort than that outlined in this paper is needed.

Estimated costs of increased incidence of skin cancer, which are probably the most realistic numbers reported here, are small in relation to those for other morbidity and mortality. In the United States, estimates of non-skin-cancer costs are about 12 times larger than skin-cancer costs in worst cases. Although the non-skin-cancer costs can be accorded little credibility, they do demonstrate that if climate generally affects health, cost numbers could be quite large.

ACKNOWLEDGMENTS

All regressions and data on which this paper is based were kindly supplied by Lester Lave and Mark Pauly.

REFERENCES

Climatic Impact Assessment Program Monographs, Volume VI, U.S. Department of Transportation. (At present, these monographs exist only in an early draft form. They will be publicly available after completion in September 1974.)

Lave, L. and E. Seskin (1972), "Air pollution, climate, and home heating: their effects on U.S. mortality rates," Am. J. Pub. Health 62, No. 7, 909-916.

Pauly, Mark (1973), private communication.

Urbach, F., D. Berger, D.F. Robertson, and R.E. Davies (1974), "Field measurements of biologically effective UV radiation and its relation to skin cancer in Man," in this volume.

CLIMATIC PERTURBATIONS AND URBAN ECONOMIES

THOMAS D. CROCKER
University of California, Riverside
Riverside, California

and

TERRY A. FERRAR
The Pennsylvania State University
University Park, Pennsylvania

ABSTRACT: This paper assesses the economic consequences for urban places of the climatic perturbations likely to be associated with increased flight in the stratosphere. Variations in incomes, property values, and public and private expenditures are modeled as dependent upon such climatic attributes as precipitation, temperature, and ventilation. The results of an attempt to assess the implications of climatic changes for the structure and location of urban places, in particular with respect to the movement of the urban centers within the corn belt, are also presented.

These different approaches are necessary in order to pick up the wide range of effects, as well as to provide a basis for incidence discussion of the relevant climatic perturbations. Nevertheless, the approaches cannot be considered mutually exclusive. Hence, the theory associated with each method of cost evaluation is considered. Some attention is devoted to the problem of aggregating the estimates established with the three approaches.

The literature dealing with the economics of environmental change is attended by concepts known as benefits and costs. This paper is no exception. The paper is concerned with the benefits and costs of climatic change for locales in which there are substantial densities and numbers of people, i.e., urban economies. Although the circumstances in which the concepts of benefits and costs are meant to apply are not always made explicit in the literature, it is clear that the intent is to characterize the behavior of some measure of value in the presence of progressive change in the environment. When the measure of value and an index of the environmental attribute of interest vary inversely, the pattern of covariation is labelled a cost function. When the value measure and the environmental index vary directly, the result is said to be a benefit function. The first section of this paper presents a theoretical foundation for the various empirical results reported in the second section; it proceeds by comparing and contrasting, in terms of an internally consistent theory, the various reported empirical measures of value, as well as some of the assumptions implicit in any effort to add together the various measures.

A THEORETICAL FRAMEWORK

Let a household's quasi-concave, twice-differentiable utility function be

$$U = U(z_1, z_2, \ldots, z_n), \tag{1}$$

where the z_i $(i = 1, \ldots, n)$ are quantities of objective characteristics to be found in goods over a given time interval. That is,

$$z_i = z(x_i; c) \tag{2}$$

where the x_i are quantities of goods in which the z_i are to be found and over the consumption of which the household is able to exercise discretionary control. For expository purposes, the z's and x's will be viewed in this paper as scalars. However, the reader should remember that the x_i are actually a set of goods, $x_{i_1}, x_{i_2}, \ldots x_{i_m}$, purchased in a market, that are used by the firm or household in producing the z_i. The c is a vector of variables, such as climate, over which the household has no control unless it chooses to relocate. (We will assume for the moment that relocation is out of the question.)

The household's utility function is maximized subject to z(x) and the usual income constraint

$$y = \sum_i p_i x_i \tag{3}$$

where p_i is the unit price of the good, x_i, and y is income. All variables are measured over the same time interval. The Lagrangian may be expressed as

$$L = U[z_1(x_1;c), z_2(x_2;c), \ldots, z_n(x_n;c)] - \lambda(\sum_i p_i x_i). \tag{4}$$

The first-order conditions for maximization with respect to characteristics imply

$$\frac{U_{z_i}}{U_{z_j}} = \frac{p_i x_{z_i}}{p_j x_{z_j}} = \frac{\lambda_i}{\lambda_j} \qquad (i \neq j) \tag{5}$$

where the z subscripts indicate partial derivatives taken with respect to the subscript. In effect, the household behaves so as to equate the ratio of the marginal utilities of any two characteristics to the ratio of their shadow prices. Note that the shadow price of a characteristic is not a constant, but is determined by the prices of the goods that embody the characteristics and by the extent to which the good is capable of providing the characteristic.

When (4) is differentiated with respect to any pair of goods capable of providing the same characteristic, one obtains

$$\frac{p_i}{p_j} = \frac{U_{z_i} x_{z_i}}{U_{z_j} x_{z_j}} . \tag{6}$$

This is the familiar first-order condition of production theory that requires equating the relative prices of two inputs to the relative values of their marginal products. In this case, the value weights for the marginal products are expressed in utility terms rather than explicit market prices. For a single good, i, the condition of (6) can be stated as

$$\frac{p_i}{x_{z_i}} = U_{z_i} . \tag{7}$$

The left-hand side of (7) is the household equivalent of the marginal cost of producing the ith characteristic. Thus when (2) is solved for x and substituted into (7), the marginal cost of producing the characteristic as a function of the characteristic itself and of climate, c, is obtained. If climate is viewed as exogenously determined, from the perspective of the household or firm, a change in climate may affect the prices of goods and/or the marginal products of goods (inputs) with respect to characteristics (outputs). If some index of all characteristics' shadow prices is affected by a change in the shadow price of one or a few characteristics, it is equivalent to a change in the household's cost of living or the firm's cost of production. That is, the utility the household can obtain for a given money income, and the output value the firm can obtain for any given set of good (input) prices and quantities, is affected. In effect, climate is not a good or an input over which the firm can exercise discretionary control. Climate instead operates through a change in the "production function" (2) and thereby affects the level of characteristics or output by changing the productivity of the goods or inputs. In Figure 1, this phenomenon is illustrated by a shift, from MC_0 to MC′, in the marginal cost function for producing a characteristic or output, z.

The right-hand side of (7) can be interpreted either as the marginal utility the household obtains from the availability of an additional unit of a characteristic, or, in the case of a firm for whom the marginal utility of revenues is constant, as the additional revenue the firm obtains from the production and sale of an additional unit of output. In Figure 1, the marginal utility or marginal revenue function is represented by MU. Since we adopt the convention that climate is not an immediate object of preference, a change in climate does not affect the utility function directly. It instead affects utility only insofar as it influences the utility that can be derived from a given income or a given expenditure on inputs. In accordance with the usual caveat, it is assumed that changes in the characteristic (output) are small relative to the inputs over which the individual has discretionary control, so that the amounts and marginal utilities of all other characteristics are not appreciably altered.

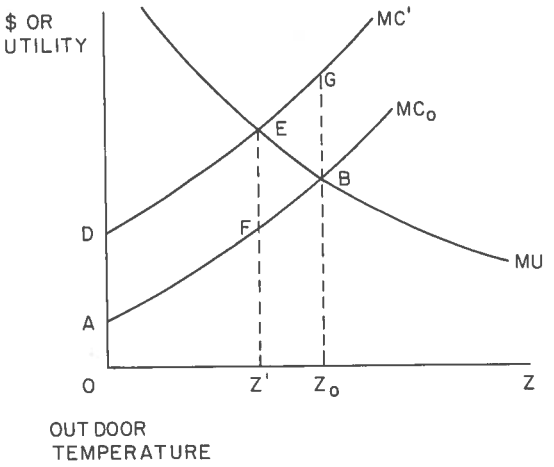

Figure 1. Marginal-utility/marginal-cost diagram.

The z measured along the horizontal axis of Figure 1 could be any one of a number of things about which people care. It could, for example, be the interior temperature of a building, which is influenced by the decision-maker's choice of fuels and building materials as well as by the outdoor climate. Or it could be the volume of traffic passing over a given stretch of road in a given time interval, the skin temperature of an individual, or the quantity of corn grown at a particular location. The approach permits one to consider the decision problems of the firm and the household within the same analytical framework.

Assume, for purposes of discussion, that z in Figure 1 is a scalar measure of the interior temperature of a building. The shift of the marginal cost function from MC_0 to MC' is intended to represent the effects of a change in outdoor temperature that makes it more costly to maintain an interior temperature differing from the outdoor temperature. The positioning of the intercepts of the cost curves on the vertical axis is arbitrary, although it is not implausible that in the case of interior cooling some inputs must be applied to keep interior temperature down to the level of the outdoor temperature. For interior space-heating, the intercepts of the cost curves might go through the horizontal axis, since the interior temperature of most buildings is likely to be warmer than the outdoor temperature even in the absence of any space-heating efforts.

Given the cost functions for maintaining various interior temperatures under the new and old climates, the representative decision-maker of Figure 1 chooses an interior temperature of z_0 under the old climate and z' under the new climate. Under the old climate the cost of attaining the utility maximizing interior temperature is the sum of the incremental costs of attaining z_0. This is given by the area $OABz_0$. The corresponding area with the new climate is $ODEz'$. The difference between these two areas is the change in the individual's interior space-heating expenditures because of the change in climate. Since $OAFz'$ is common to the two areas, the change in expenditure is given by the difference between ADEF and $z'FBz_0$. ADEF is simply the change in cost necessary to maintain the interior temperature at z', and ADGB is the change in cost necessary to maintain the former utility-maximizing temperature of z_0. The latter cost change is the change typically measured by materials damage studies, in which the emphasis is on the outlays necessary to maintain a given performance from a material. It should be noted that the only circumstances in which this would be a correct measure of the actual value of the change would be when the MU function could be disregarded. That is, if and only if the quantity of the output demanded were completely unresponsive to changes in the cost of providing it, so that the MU function exactly coincided with the GBz_0 line, would a measure of this sort actually measure value. Otherwise it neglects the change in value to the individual expressed in the movement along the MU function as the marginal cost functions shift in response to the climate change. If the quantity of output demanded is not completely unresponsive to variations in the cost of producing it, the measure – what is frequently called *the alternative cost measure* – will fail to capture the value of the sum of the excess of the utility of the degrees of temperature no longer maintained over the sum of the costs of producing these degrees.

Simple comparisons of the aforementioned areas of Figure 1 make it clear that it is quite possible to observe zero or quite small changes in expenditures and still have the decision-maker experience substantial changes in utility. All that is required is the equivalence or near-equivalence of ADEF and $z'FBz_0$. By its very nature, an

expenditure measure is a measure of unit costs multiplied by the number of units. With a change in climate and its consequent effects upon marginal costs of production, the individual may adjust the price he is willing to pay for an additional unit of the output, as well as the quantity of the output he desires. If the change in climate is unfavorable, the utility maximizing level of output for the individual will decline, and the value the individual attaches to an additional unit of the output will increase. According to whether the proportionate change in output is greater or less than the proportionate change in willingness to pay, observed expenditures on the output may increase or decrease, respectively. An increase suggests that the demand elasticity for the output is less than unity, while a decrease suggests a demand elasticity greater than unity.

The value to the individual of the change in climate is the sum of consumer and producer surpluses. In Figure 1, this sum is given by the area ADEF plus the area BEF. In the case of an improvement in climate causing MC′ to shift to MC_0, the value of the improvement to the individual would be the area ADEF if and only if no change occurred in the individual's utility-maximizing level of output. A further value of the improvement to the individual is given by the area BEF, representing the sum of the excess of his willingness to pay for the extra output over his extra cost of producing it.

The ambiguities and complexities of interpretation inherent in the expenditures approach and the earlier-mentioned alternative cost approach can be avoided by assessing the effects that changes in the sum of consumer and producer surpluses have upon the demand for the inputs that produce these surpluses. The empirical studies reviewed in the next section that profess to be estimating demand or willingness-to-pay functions are all concerned with measuring the effect of changes in the utility maximizing level of an output upon the demand for an input. Thus, for example, the studies that deal with the demand for fuels are investigating the effect upon the individual's willingness to pay for fuels of changes in utility maximizing levels of interior-space temperatures, quantities of food processed, or a variety of other outputs.* The Marshallian (1961) rules of derived demand apply. Thus the extent to which the demand for an input such as fuel will be responsive to a change in climate that affects the utility to be obtained from a given quantity of an output will vary directly with the (shadow) price elasticity of demand for the output, the price elasticity of supply for substitute inputs, the ease of substitution of these in the production process, and the relative importance of the input in producing the output. Therefore, a change in climate that increases the ease of maintaining a desired interior building temperature with a given type of fuel will cause the relative use of the fuel to increase in order to minimize costs of producing the temperature. Since the relative (shadow) price of the temperature output has decreased, the temperature itself will be increased, or a given desired temperature will be more frequently maintained. However, these effects do not necessarily imply that the absolute quantity demanded of the fuel input will increase. For such an increase to occur, the increase in quantity demanded, generated by the combined effects of the substitution of the input in question for other inputs and the expansion of the output the input produces, must outweigh the saving induced by the enhanced productivity of the input. That is, the utility gained by reducing the use of other inputs and the improved temperature situation must outweigh the utility gained by the improved maintenance capacity of any given quantity of the fuel. If the market price of the input is unchanged, it is easy to see that a given climate change can increase or decrease expenditures on fuels, according to whether the change increases or decreases the quantity demanded.

Many of the complexities of estimating the willingness to pay for inputs can be ameliorated by estimating the payments factors of production must receive in order to be willing to undertake a particular productive activity. Frequently known as the factor-rewards approach, it results in estimates that are in fact measures of opportunity cost. That is, rather

* By referring to willingness to pay, we are assuming that if the individual is to prevent the change in climate, he must pay to do so. His willingness to pay expresses the maximum sum he would pay if costless processes existed by which he could convey this willingness to those causing the change in climate.

than estimating the individual's willingness to compensate others for undertaking an activity that the individual values, opportunity-cost estimates purport to measure the minimum amount the individual must be paid in order to forgo an activity he values. If the activity is a relatively small part of the individual's budget, both measures will provide the same conceptual result. The measures are thus substitutes for one another. However, the differences in factor rewards due to a system perturbation will often be more readily observed and measured than differences in willingness to pay. The reason is that the investigator does not have to discern and evaluate all of the individual decision-maker's adjustment possibilities. The market, through directly observable market prices, does it for him.*

The empirical studies reviewed in the next section include two studies of rewards to factors of production, a study of the effects of climate differences upon rewards to labor, and a similar study dealing with rewards to the owners of land. Only the first provided results useful for the purposes of the CIAP study, although a more detailed and careful investigation might provide similarly useful results in the case of rewards to land. In any case, given knowledge by the individual decision-maker of the effect upon productivity of differences in climate, the area ADEF plus the area BEF of Figure 1 can be expected to show up as a difference in factor rewards.

The fundamental rationale for the differential-wage and differential-rent approaches is similar. The two approaches are in fact better viewed as complements than as substitutes. For simplicity, assume that each individual decision-maker's utility function has only one argument, an output that can be produced using identical types of scarce inputs in fixed proportions at either of two locations. However, perhaps because of a more severe climate, one location requires that the absolute magnitude of each input be increased in order to obtain the same amount of output. In effect, it costs more to produce the output at the location with the more severe climate. If, for some arbitrary reason, wages and rents are initially the same in the two locations, those decision-makers who are first at the more severe location will have an incentive to relocate, since they can produce a greater valuable output at no apparent change in cost. However, the process of relocation tends to drive up relative wages in the less productive location, since the supply of labor has been reduced there while simultaneously increasing in the less severe and more productive location. At the same time, the rent of land in the more productive location will exhibit a relative increase, since, for any particular outlay on other factors of production, a greater valuable output can be produced at that location. In short, relative wages increase and relative rents decline at the less desirable location by an amount just sufficient to compensate those decision-makers who remain for their decision not to relocate. Similarly, wages decline and rents are bid up at the new location by an amount just sufficient to make individuals who do not relocate indifferent to the choice of locations. Thus, viewing returns to immobile and durable capital as a form of rent, for any period shorter than the long run the sum of differential wages and differential rents should measure exactly the value decision-makers place upon the difference in climate.

Whether the approach employed is conceptualized in willingness-to-pay or opportunity-cost terms, it must be remembered that the empirical representations of these conceptualizations are typically no more than partial equilibrium measures. That is, they consist of the enumeration and evaluation of a set of consequences of a particular climatic change, in the context of a much wider economic environment which is presumed to remain completely unaffected. This invariant environment provides the frame of reference in terms of the value of money that permits the desirable and undesirable features of a change to be expressed in pecuniary terms. Otherwise, even a small change in a single value leads to at least a conceptual ambiguity in the use of money as a measuring rod of value. However, where the change being evaluated substantially alters an entire economic system, a general-equilibrium mode of analysis is conceptually called for. The difficulty is that no empirically useful body of general-equilibrium theory for benefit-cost analysis presently exists. Thus, when one sums the results of various

* See Anderson and Crocker (1971), p. 149.

studies of willingness to pay for different outputs, or of studies of the opportunity costs for various inputs in the production of various outputs, one implicitly assumes that the interactive effects among the different outputs and inputs somehow cancel each other.

REPORT OF EMPIRICAL FINDINGS*

This section of the paper summarizes the empirical results of several attempts, employing the various approaches discussed in the previous section, to assess the effect of climatic change upon urban economies. (The full reports on these attempts will be presented in Volume VI of the CIAP monographs.**) Although the authors of the present paper directly participated in some of the summarized efforts, in many cases they had no involvement whatsoever. The following table lists the authors of the separate efforts, as well as the affiliations of these authors.

Study Effort	Authors	Affiliation
Wage Compensation	I. Hoch	Resources for the Future, Inc.
Property Values	T. Crocker, L. Eubanks, R. Horst, Jr., B. Nakayama	University of California, Riverside
Electricity Demand	T. Crocker, L. Eubanks, R. Horst, Jr.	University of California, Riverside
Fossil-Fuel Demands	T. Ferrar, J. Nelson	Pennsylvania State University
Household Budgets	T. Crocker, L. Eubanks, R. Horst, Jr.	University of California, Riverside
Public-Sector Expenditures	B. Booms	Pennsylvania State University
	P. Sassone	Georgia Institute of Technology
Macro-Regional	J. Neidercorn	University of Southern California

As noted in the previous section, the wage-compensation and property-value approaches are conceptually the least ambiguous of the variety of approaches that might be (and have in fact been) employed. However, they also present the greatest difficulty in distinguishing the influences of climatic change from a variety of other influences that might well have similar economic effects. In addition, neither the property-value nor the wage-compensation approach to measurement is capable of giving insight into the economic effects of climatic changes upon various goods or classes of people. Therefore, in order to obtain information with respect to incidence and to provide a check upon the estimates obtained from the income and property-value research, we complemented these approaches with expenditure and demand studies on particular goods and services that appeared likely to be responsive to changes in climate. For example, one might expect the demand for fuels to increase if the climate in a given locale becomes colder; similarly, expenditures on public-road maintenance would be affected by climatic changes. Although such an analysis could hardly be performed for all the urban resources affected by climatic changes, judicious selection of the goods and services studied can provide estimates that are useful in formulating a lower-bound cost for the climatic perturbations under study.

While these two approaches provide useful insights into the impact of climatic changes on existing urban structures, they do not directly examine the long-term consequences in urban and urban-oriented capital stock that are likely to occur. In particular, as shown by research reported in Volume V of the monographs, the assumed temperature and precipitation variations will shift the corn belt significantly to the south. The entire network of central places (urban centers) that has developed in this corn-belt region will be affected. For example, in the more southerly regions, existing central places would necessarily be expanded and new ones developed. Therefore, the influences on capital requirements for construction of the new central places necessitated by this geographical shift in patterns of land use and resource exploitation are also examined.

* Mr. Robert Horst, Jr. participated in the writing and preparation of this section, and Mr. Alan Brownstein assisted in its preparation.

** At present, these monographs exist only in an early draft form. They will be publicly available after completion in September 1974.

Wage Compensation and Property Value Studies

Wage-Compensation Study

Wage rates for the same work vary by locale. This discrepancy can be explained by either possible short-run disequilibrium or long-run differences in the "quality of life" between locales, leading to compensating differences in wage rates. In the case of disequilibrium, workers will move from low-pay to high-pay areas, tending to raise wages in the former and lower them in the latter, until equilibrium ultimately is established. Equilibrium, however, does not necessarily involve equality of wage rates, because additional compensation is needed to retain employees in unpleasant or harsh environments. Therefore, it is conceivable that climate is a factor in quality of life, and hence affects wage rates. Regions with good climate will have lower wages than areas with bad climate. The higher wages in the latter compensate both for increased expenditures necessary to live there, in terms of additional clothing, home heating and insulation, higher transportation costs, etc., and for increased "psychic" or non-market costs, expressing workers' preference about the weather. Everybody not only talks about the weather, but does something about it – specifically, by taking it into account when making locational decisions. Therefore, if climate changes, there should be measurable real-income changes.

In this study the climatic variables varied in significance, with summer temperature by far the most important in terms of explanatory power. It had a negative coefficient in all cases, while its square had the opposite sign when it entered the equations. The winter-temperature coefficient varied between equations, and its magnitude was much smaller in absolute value than that of summer temperature. It usually appeared to be an offset to the effect of the latter.

The effect of precipitation was always negative, and its interaction with summer temperature was positive and important in the equations. Because of the nonlinearity and interaction effect, there was an implication that optimal summer temperature occurred at 74°F for average precipitation, and that the optimal temperature increased as precipitation decreased; furthermore, the net effect of precipitation was beneficial given low summer temperatures (as in the arid West), but harmful to welfare given high summer temperatures (as in the humid South). The effect of wind velocity was always positive, indicating that increased wind signifies increased costs.

These predictive equations were employed to assess the impact of climate changes, given the set of changes in temperature and precipitation that were specified for this CIAP project. Wages for each observation were calculated before and after the specified climate change, and the ratio of wages-after to wages-before was obtained. If the ratio was greater than 1.0, it meant that money wages must increase to compensate for the climate change, thus indicating that the change imposed a cost on workers. The amount of the cost as a fraction of wages could be measured by subtracting 1.0 from the ratio. In similar fashion, if the ratio were below 1.0, this could be interpreted to mean that workers were better off, and would accept lower money wages at equilibrium. The measure of benefits as a fraction of wages then could be calculated by subtracting the ratio from 1.0.

Climate changes were specified to vary by latitude zone. The results obtained for each observation were averaged both within latitude zones and for the entire United States, in order to obtain an estimate of the overall impact. The averages for each sample were then weighted in proportion to the number of occupations covered, to yield a penultimate set of averages. Specified climate change by case (indicated at 40° latitude) and the after-before ratio obtained for United States wages were as shown in Table 1.

Table 1. Effect on Wages of Changes in Temperature and Precipitation

Temperature Change (°C) (At 40° Latitude)	Precipitation Change (%)	Ratio of Wages, U.S. (After/Before)
-2.5	+20	1.0067
	0	1.0132
	-20	1.0196
-1.25	+10	1.0038
	0	1.0061
	-10	1.0083
-0.625	+5	1.0020
	0	1.0029
	-5	1.0038
+0.625	-5	0.9978
	0	0.9974
	+5	0.9967

The maximum effect occurs for a maximum decline in both temperature and precipitation; for this case, the wage loss is two percent. If that percentage were applicable to all income, the estimated 1973 annual cost would be $20 billion, or $100 per person per year.

The temperature decline was specified to increase with increasing latitude, with an additional decline of 1°C for every 20° of latitude. Precipitation change first increased with latitude and then decreased, with a maximum change occurring at latitude 30°. The second and third sets of change were obtained by multiplying the first set by 0.5 and 0.25, respectively, and the fourth set by multiplying by -0.25, thus reversing the direction of change for the other three cases.

The predicted after-to-before wage effects, by latitude zone, are presented in Table 2.

Table 2. Effects of Changes on Wages by Latitude Zone

Temp. Change (°C) At 40° Latitude	Precip. Change (%)	Ratio of Equilibrium Wages: After to Before Latitude Zones 20°-30°	30°-40°	40°+
-2.5	+20	1.0125	1.0159	1.0204
	0	0.9970	1.0121	1.0272
	-20	0.9816	1.0083	1.0340
-1.25	+10	1.0075	1.0086	1.0103
	0	0.9977	1.0050	1.0122
	-10	0.9874	1.0013	1.0141
-0.625	+5	1.0041	1.0045	1.0052
	0	0.9987	1.0022	1.0058
	-5	0.9933	1.0000	1.0063
+0.625	-5	0.9954	0.9953	0.9948
	0	1.0019	0.9984	0.9950
	+5	1.0083	1.0016	0.9952

The costs of decreasing temperature (or the benefits of increasing temperature) increase as latitude increases. In fact, a temperature decline improves welfare in the hottest zone, and an added precipitation decline further increases welfare there. (Compare B and C cases.) Because the ratio of after to before wages was obtained for each observation, it was relatively simple to regress the ratio on latitude, thus making possible general predictions for any latitude classification. (Testing indicated that the ratio-latitude relation was linear.)

Given the predicted change in wages caused by climate change, dollar magnitudes can then be estimated also. First, it was assumed that 90 percent of the percentage change applied to income. Wages account for 70 percent of national income, and if dollar changes were localized to wages only, 70 percent would then be the appropriate percentage to employ. If wage changes applied to all income, regardless of source, 100 percent would be appropriate. The difference is a matter of whether changes occur only with respect to the work place (such as increased costs of the journey to work), or occur with respect to the residence (such as all travel). Although it seemed probable that the latter effect was by far the stronger, 90 percent was imposed as a "conservative" assumption.

Standard capitalization formulas were applied to obtain the present value of climate change (its cost) for various temperature changes, but no precipitation change, for the years 1974 and 2000, given alternative interest rates of 8, 5 and 3 percent. (See Table 3.) The results have been rounded to three significant digits.

The cost of climate change can also be broken down by latitude. Table 4 shows such a breakdown for a 1°C decrease in temperature. (The assumption used is that national income is proportioned 48.8% between 20 and 40° latitude and 51.2% above 40°. Results have been rounded to three significant digits.)

These results indicate that for a 5 percent interest rate the annualized costs associated with wage differentials due to a temperature change of -1°C are 4.72 billion dollars, beginning in the year 1974.

Property Value Study

It has frequently been suggested that many of the psychological and pecuniary costs of living in alternative urban environments might be capitalized into both the value of land and the immobile improvements upon the land. Theoretical studies on the effects of environment on property markets have a long and distinguished history in economic analysis. Employing these theoretical developments, investigators have assessed the effects upon equilibrium property values of a variety of environmental factors that can be altered by public policy. In this analysis, we attempt to determine the extent to which variations in climatic conditions within urban

Table 3. Costs of Climatic Change with Reference to Wages

Temperature Change	Interest Rate (%)	Present Value (Billions of Dollars) 1974	1990	2000	Annualized Costs (Billions of Dollars) 1974	1990	2000
-1°C	8	21.0	71.8	154.9	1.68	5.74	12.39
	5	94.3	205.9	335.3	4.72	10.29	16.77
	3	492.9	791.1	1062.8	14.79	23.73	31.88
-2°C	8	45.5	156.0	336.8	3.64	12.48	26.95
	5	205.0	447.5	729.0	10.25	22.38	36.45
	3	1071.5	1719.8	2310.5	32.15	51.59	69.32
-5°C	8	10.0	34.4	74.2	0.80	2.75	5.94
	5	45.2	98.6	160.6	2.26	4.93	8.03
	3	236.1	378.9	509.1	7.08	11.37	15.27
+5°C	8	8.9	30.4	65.5	0.71	2.43	5.24
	5	39.9	87.1	141.8	1.99	4.35	7.09
	3	208.5	334.6	449.6	6.25	10.04	13.49

Table 4. Cost Latitude Breakdown, with Reference to Wages

Latitude	Interest Rate (%)	Present Value (Billions of Dollars) 1974	1990	2000	Annualized Costs (Billions of Dollars) 1974	1990	2000
20-40°	8	10.2	34.9	75.4	0.82	2.80	6.04
	5	45.9	100.2	163.3	2.30	5.01	8.16
	3	240.0	385.2	517.5	7.20	11.56	15.52
Over 40°	8	10.8	36.8	79.5	0.86	2.95	6.36
	5	48.4	105.6	172.1	2.42	5.28	8.60
	3	252.9	405.9	545.3	7.59	12.18	16.36

areas are capitalized into property values because of psychological and pecuniary costs associated with living in alternative environments.

The key to this micro-oriented study was the existence of significant differences in temperature, precipitation, and other climatic variables within a single standard metropolitan statistical area (SMSA). The "heat island" phenomenon in urban centers introduced the possibility of having the desired wide range of climatological parameters within a single SMSA. Therefore, it was our hope that these variations in climate would in fact be reflected as significant explanatory variables in the determination of property values within a particular city. If our expectations were borne out, it would be possible to relate CIAP's postulated temperature and precipitation changes to changes in property values, and consequently obtain estimates, at a highly disaggregated level, of marginal effects of the climatic change.

Because of the time constraints faced by this study, only one urban area – Washington, D.C. – was examined. Since many other urban areas have been observed to have significant variations in climatic conditions within their boundaries, the results obtained from the Washington study could be expected to provide insights into the marginal effects of climatic changes on property values in other urban areas as well.

The results are very disappointing, in that none of the weather variables proves to be statistically significant at customary levels. They do not necessarily indicate, however, that climate is not capitalized into property values, but merely that data limitations make it impossible to reach any conclusions.

Budget Studies

To gain some insight into the economic effects upon goods and classes of people caused by changes in climate, expenditure and demand studies were performed on particular goods and services. The following are the assumptions and parametric ranges that underlie the analysis (unless otherwise qualified).

1. Cost estimates are discounted using interest rates of 3, 5, and 8 percent. Annualized costs are calculated with two starting dates, 1974 and 2000, continuing to infinity.
2. All prices are evaluated in terms of constant 1971 U.S. dollars and remain unchanged over the relevant time span.
3. Parametric changes in mean annual temperature (except for the electricity-demand study of the "all-electric" portion of the commercial sector, where it is measured in mean monthly temperature changes) of 2.0°C, -1.0°C, -0.5°C, and +0.5°C are examined. In addition, we assume that the temperature change of -1.0°C is effective only below 40° latitude, and that a -1.5°C change occurs simultaneously within the latitude range 41-60°.
4. Population assumptions are given by CIAP for the years 1990 and 2025. This enables us to estimate a trend in the construction of commercial buildings and households.
5. We assume that the total effect of a climate change can be linearly interpolated. For example, given a total impact of -2°C for the years 1990-2025, we take the change per year to be equal to -2/35 = -0.0543°C.
6. Similarly, we assume that the increase in the number of all-electric commercial buildings and households per year from 1990-2025 can be linearly interpolated.
7. The change in temperature can be converted into a change in degree days using the empirical relationships reported in Appendix B to chapters IV and V of the Urban Resources section of CIAP Monograph VI.

Commercial Sector: Electricity

The purposes of the present study are twofold: first, to estimate, using completely disaggregated data, the covariation of electricity demand and climatic indicators; and second, if a significant relationship between these climatic indicators and electricity demand appears, to calculate for these and similar buildings the money costs of climatic modification. The data employed are detailed histories of actual, month-by-month electricity consumption and weather environments over a year for approximately eighty all-electric buildings located throughout the United States. Since a relatively small proportion of buildings in the United States are currently electrically heated, the effects of a change in climate upon the money costs of heating these buildings is not readily extrapolated to building units that are not all-electric. However, since 90 percent of those buildings that have space cooling employ electricity for the purpose, extrapolation of the change in money costs to all space-cooled buildings is likely to give reasonable results.

In the findings to be presented below, the following additional conditions are assumed:

1. The commercial sector is viewed as consisting of the following types of establishments: retail and wholesale outlets, professional office buildings, churches, educational facilities, banks, small industrial plants, and apartment houses.
2. Since the heating (cooling) degree-day variable was not significant at customary levels for April, May, October, and November, we must assume that the total dollar impact of temperature-induced changes in KWH demand is generated entirely from the other eight months.
3. We use the mean value of our degree-day observations as an initial value for our cost calculations.
4. We can ignore changes in the relative prices of fossil fuels and electricity. It has been borne out in our regression studies that the price of natural gas, for example, does not significantly contribute to the demand for electricity in all-electric commercial buildings.

5. Any growth in electric power demand, apart from that induced by climatic changes, is neglected. We cannot gauge potential annual "natural" rates of change in demand for the industry.

The findings relevant to the CIAP effort are reported in Tables 5 and 6.

These results indicate that the annualized costs associated with electricity demand in the residential and commercial sector due to climatic variations (-1°C) are, at minimum, approximately -700 million dollars, beginning in the year 1974 and corresponding to an interest rate of 5 percent.

Table 5. United States Costs of Climatic Change (in billions of dollars)*

Discount Rate	Starting Year	Basis	Temperature Changes -2°C	-5°C	+5°C	-1°C
3%	1974	P.V.	-91.581	-21.210	20.321	-43.429
		A.C.	-2.747	-0.636	0.610	-1.303
	2000	P.V.	-197.500	-45.741	43.824	-93.658
		A.C.	-5.925	-1.372	1.315	-2.810
5%	1974	P.V.	-29.619	-6.926	6.770	-14.141
		A.C.	-1.481	-0.346	0.333	-0.707
	2000	P.V.	-105.315	-24.626	23.715	-50.280
		A.C.	-5.266	-1.321	1.186	-2.514
8%	1974	P.V.	-8.039	-1.904	1.846	-3.872
		A.C.	-0.643	-0.152	0.148	-0.310
	2000	P.V.	-59.459	-14.083	13.655	-28.642
		A.C.	-4.757	-1.127	1.092	-2.291

*Negative cost equals a positive benefit, by definition.

Table 6. Regional* Costs of Climatic Change (in billions of dollars)

Discount Rate	Starting Year	Basis	Temperature Change -1°C	-1.5°C	Total
3%	1974	P.V.	-21.715	-33.408	-55.123
		A.C.	-0.651	-1.002	-1.654
	2000	P.V.	-46.829	-72.046	-118.875
		A.C.	-1.405	-2.161	-3.566
5%	1974	P.V.	-7.070	-10.843	-17.914
		A.C.	-0.354	-0.542	-0.896
	2000	P.V.	-25.140	-38.555	-63.695
		A.C.	-1.257	-1.928	-3.185
8%	1974	P.V.	-1.936	-2.957	-4.893
		A.C.	-0.155	-0.237	-0.391
	2000	P.V.	-14.321	-21.870	-36.191
		A.C.	-1.146	-1.750	-2.895

* Our regional analysis is based on a temperature change of -1°C below 40° latitude, and a temperature change of -1.5°C above 40° latitude.

Commercial Sector: Fossil Fuel

This study presents an econometric analysis of fossil-fuel demand in the residential and commercial sector of the United States for the year 1971. The basic relationship estimated is that between fuel consumption (total or per-capita), as the dependent variable, and several independent variables, including population, income, degree days, fossil-fuel prices, electricity prices, construction costs, and urbanization rates. Data are obtained for a cross-section of the 48 continental states and the District of Columbia.

The objective of the econometric analysis of demand is to isolate the effect of temperature, measured in degree days, on the consumption of fossil fuels. In order to accomplish this, it is necessary to hold constant, or control for, the other independent variables previously mentioned. The statistical technique of ordinary least-squares regression analysis is used to achieve this goal. The resulting estimate is then employed to predict the impact of a given climatic change on consumers under different economic conditions. The final result is a range of cost estimates of the effect of climatic change on the residential and commercial sector.

In the findings presented below, the following conditions are assumed:

1. Only the mean expected elasticity of degree days with respect to Btu/capita will be used. On the basis of the regression results, this value is 0.45.
2. Population and per-capita GNP estimates (in constant 1971 U.S. dollars) are given for the year 2025. Personal income per capita is assumed to be 80 percent of per-capita GNP.
3. Relative prices for fossil fuels, electricity, and construction materials will remain unchanged between 1971 and 2025. We lack a method for estimating future movements of these prices.
4. We ignore the possible higher rates of fuel consumption due to relatively lower heat-loss construction standards in southern climates and, similarly, lower rates in northern climates. This relationship has not been confirmed empirically in this report. If it does exist, our cost estimates are understated for southern climates and overstated for northern climates.
5. The estimated change in heating degree-days per year will be evaluated with respect to normal heating degree-days for 1931-1960. This will tend to overstate the cost estimates, since the percentage change in degree-days would be somewhat smaller in the later years of the forecast period if the reference base were allowed to change.
6. Cost estimates are evaluated using only simple averages for basic data (fuel prices, degree-days) for the entire U.S. or for the two groups of states, those above and those below 40° latitude.
7. It is assumed that changes in temperature affect total commercial consumption of fossil fuels. Since only 75 to 80 percent of consumption is for space heating, this assumption may tend to overstate costs.

An econometric model was constructed for fossil-fuel-energy demand in the commercial sector of the United States. It was found that fossil-fuel demand per capita would change 4.5 percent for every 10 percent change in heating degree-days per year. The model was used to forecast fossil-fuel demand per capita in the year 2025, and then the percentage change in degree-days for different climatic conditions was used to predict changes in demand. These estimated changes were then converted into dollar costs and discounted to the present.

For an interest rate of 8 percent, and a mean annual global temperature change of -1°C by 2025, it was found that the present value of the stream of costs to be incurred by the commercial sector of the U.S. would be 1306.57 million dollars. Cost estimates are presented in Table 7 for (1) three alternative interest or social discount rates (2) four alternative changes in mean annual temperature, and (3) two climatic zones in the U.S.

Personal Budget Study

This section examines the covariation between climate and various categories of household expenditures. Two different studies are

Table 7. Physical and Economic Effects on Fossil-Fuel Demand, U.S. Residential and Commercial Sector (1971 dollars)

a. Under the following assumptions:
Degree-day elasticity = 0.45
U.S. population (2025) = 284 million
Real personal income per capita (2025) = $11,840
Fossil-fuel price (1971) = $1.16/$10^6$ Btu
U.S. 10^6 Btu per capita (1971) = 73.93
U.S. 10^6 Btu per capita (forecast 2025) = 100.00

Global Temperature Change	Degree-Day Change (%)	Physical Impact: Total Btu (× 10^{12})	Physical Impact: Btu/capita (× 10^6)	Cost Impact: Total (Million $)	Cost Impact: $/capita	Incremental Cost/Year (Million $)	Basis	Costs (in Billion $, rounded) at Various Discount Rates: 3%	5%	8%
-2°C	16.4	2102	7.4	2438	8.58	69.7	P.V., 1974	14.525	7.033	2.613
							P.V., 1990	23.307	15.350	8.952
							P.V., 2000	31.440	25.007	19.327
							A.C., 1974-∞	0.436	0.352	0.209
							A.C., 2000-∞	0.943	1.250	1.546
-1°C	8.2	1051	3.7	1219	4.29	34.8	P.V., 1974	7.262	3.516	1.307
							P.V., 1990	11.653	7.676	4.476
							P.V., 2000	15.720	12.504	9.663
							A.C., 1974-∞	0.218	0.176	0.105
							A.C., 2000-∞	0.472	0.625	0.773
-0.5°C	4.1	525	1.8	609	2.15	17.4	P.V., 1974	3.631	1.758	0.653
							P.V., 1990	5.827	3.838	2.238
							P.V., 2000	7.860	6.252	4.832
							A.C., 1974-∞	0.109	0.088	0.051
							A.C., 2000-∞	0.236	0.313	0.387
+0.5°C	-4.1	-525	-1.8	-609	-2.15	-17.4	P.V., 1974	-3.631	-1.758	-0.653
							P.V., 1990	-5.827	-3.838	-2.238
							P.V., 2000	-7.860	-6.252	-4.832
							A.C., 1974-∞	-0.109	-0.088	-0.052
							A.C., 2000-∞	-0.236	-0.313	-0.387

b. Demand *below* 40° latitude, under the following assumptions:
Degree-day elasticity = 0.45
Population (2025) = 142 million
Real personal income per capita (2025) = $11,307
Fossil-fuel price (1971) = $1.01/$10^6$ Btu
10^6 Btu per capita (1971) = 60.20
10^6 Btu per capita (forecast 2025) = 83.66

-1°C (21-40° latitude)	11.8	632	4.45	639	4.50	18.3	P.V., 1974	3.806	1.843	0.685
							P.V., 1990	6.108	4.023	2.346
							P.V., 2000	8.239	6.553	5.065
							A.C., 1974-∞	0.114	0.092	0.055
							A.C., 2000-∞	0.247	0.328	0.405

c. Demand *above* 40° latitude, under the following assumptions:
Degree-day elasticity = 0.45
Population (2025) = 142 million
Real personal income per capita (2025) = $12,372
Fossil-fuel price (1971) = $1.30/$10^6$ Btu
10^6 Btu per capita (1971) = 87.66
10^6 Btu per capita (forecast 2025) = 114.80

-1°C (40-60° latitude)	9.4	690	4.86	899	6.33	25.7	P.V., 1974	5.358	2.594	0.964
							P.V., 1990	8.598	5.663	3.302
							P.V., 2000	11.598	9.225	7.130
							A.C., 1974-∞	0.161	0.130	0.077
							A.C., 2000-∞	0.348	0.461	0.570

reviewed. First, ordinary least-squares semi-logarithmic, cross-sectional regressions are employed to estimate the climatic and household-expenditure covariation. Data on expenditures in various expenditure categories were obtained for typical households in 1960-61 in each of 41 cities across the United States. The appropriate pecuniary values were deflated to 1960 prices using the U.S. Consumer Price Index. The regression results obtained indicate that weather does not significantly influence household consumption patterns. Given the broad categories of household expenditures analyzed, this result is not too unexpected.

The second study briefly summarizes a doctoral dissertation by Kazem Attaran (1973) in which statistically meaningful evidence of a relationship between climate and household expenditures was discovered. Attaran uses stepwise, ordinary least-squares, linear (in the original variables), cross-sectional regression techniques to estimate the effects of various influences upon outlays in the following expenditure categories: food, clothing, housing, transporation, medical-care, and "other" expenditures. The budget cost estimates were taken from a 1971 publication of the U.S. Bureau of Labor Statistics in which detailed data was presented for "low", "moderate," and "high" income, four-person families in 60 cities across the United States.

The cost calculations presented in Table 8 are based on what Attaran terms his "best" regressions for each expenditure category. These categories are defined as follows:

1. Housing outlays include shelter, house furnishings, household operations, and an allowance for lodging when away from home.
2. Clothing (and personal care) outlays represent replacement of clothing inventories.
3. Miscellaneous outlays include allowance for reading and education, recreation, alcohol and tobacco (excluding cigarettes), and other expenses such as bank service charges.

Table 8. Cost Tables for Household Expenditures (Personal Budget Study) (in billions of dollars)

Discount Rate	Basis		-1°C	-2°C	-0.5°C	+0.5°C	Regional (-1°C < 40° lat, -1.5°C > 40° lat)
				a. Housing			
3%	1974	P.V.	15.730	31.461	7.865	-7.865	19.663
		A.C.	0.472	0.944	0.236	-0.236	0.590
	2000	P.V.	33.923	67.847	16.962	-16.962	42.404
		A.C.	1.018	2.035	0.509	-0.509	1.272
5%	1974	P.V.	7.678	15.357	3.839	-3.839	9.598
		A.C.	0.384	0.768	0.192	-0.192	0.480
	2000	P.V.	27.302	54.604	13.651	-13.651	34.127
		A.C.	1.365	2.730	0.683	-0.683	1.706
8%	1974	P.V.	2.833	5.665	1.416	-1.416	3.541
		A.C.	0.227	0.453	0.113	-0.113	0.283
	2000	P.V.	20.951	41.901	10.475	-10.475	26.188
		A.C.	1.676	3.352	0.838	-0.838	2.095
				b. Clothing			
3%	1974	P.V.	3.496	6.991	1.748	-1.748	4.370
		A.C.	0.105	0.210	0.052	-0.052	0.131
	2000	P.V.	7.539	15.077	3.769	-3.769	9.423
		A.C.	0.226	0.452	0.113	-0.113	0.283
5%	1974	P.V.	1.706	3.413	0.853	-0.853	2.133
		A.C.	0.085	0.171	0.043	-0.043	0.107
	2000	P.V.	6.067	12.134	3.034	-3.034	7.584
		A.C.	0.303	0.607	0.152	-0.152	0.379
8%	1974	P.V.	0.629	1.259	0.315	-0.315	0.787
		A.C.	0.050	0.101	0.025	-0.025	0.063
	2000	P.V.	4.656	9.311	2.328	-2.328	5.820
		A.C.	0.372	0.745	0.186	-0.186	0.466
				c. Miscellaneous			
3%	1974	P.V.	1.529	3.059	0.765	-0.765	1.912
		A.C.	0.046	0.092	0.023	-0.023	0.057
	2000	P.V.	3.298	6.596	1.649	-1.649	4.123
		A.C.	0.099	0.198	0.049	-0.049	0.124
5%	1974	P.V.	0.747	1.493	0.373	-0.373	0.933
		A.C.	0.037	0.075	0.019	-0.019	0.047
	2000	P.V.	2.654	5.309	1.327	-1.327	3.318
		A.C.	0.133	0.265	0.066	-0.066	0.166
8%	1974	P.V.	0.275	0.551	0.138	-0.138	0.344
		A.C.	0.022	0.044	0.011	-0.011	0.028
	2000	P.V.	2.037	5.074	1.018	-1.018	2.546
		A.C.	0.163	0.326	0.081	-0.081	0.204

The results indicate that the annualized costs associated with variations in household expenditures due to climatic perturbations (decrease of -1°C) are 506.564 million dollars, beginning in the year 1974 and corresponding to an interest rate of 5 percent.

Industrial-Sector Study

This study presents an econometric analysis of fossil-fuel demand in the industrial sector of the United States for the year 1971. In methodology and scope, this work parallels the Residential and Commercial Sector: Fossil Fuel section of the Urban Resources section of CIAP Monograph VI. This analysis differs in only one significant respect from the analysis contained in the Residential and Commercial Sector Study. The tentative hypothesis tested in that effort was that temperature had a significant effect on the demand for fossil fuels in the residential and commercial sector, while the tentative hypothesis to be tested in this section is that temperature has *no* significant effect on the demand for fossil fuels in the industrial sector. That is, on a-priori grounds one would expect climatic perturbations not to influence industries' demand for fossil fuels, since production rates are rather insensitive to the climatic influences under consideration. Indeed, this hypothesis is reinforced by the failure of our regression coefficients to exhibit values significantly different from zero.

Public Costs of Climate Modification

An investigation of the public sector was conducted to determine the nature and magnitude of the effects of climate change on government expenditures. Federal, state, and local governments were all initially considered as potential impact areas; however, since the range of government activity is extremely diverse, and this work seems to be the ground-breaking effort in this field, a new methodological procedure was dictated. The research strategy which offered the least chance of overlooking an important climate-sensitive government expenditure area was the coupling of deductive and inductive approaches.

The deductive approach centered on the functional expenditures of government. Several climate-sensitive functions were pinpointed, including: (a) space heating of government buildings, (b) snow and sleet removal, salting and sanding of public roads, (c) sanitation and sewerage, (d) fire protection, and (e) public recreation. A regression analysis of local public functional expenditures constituted the first part of the inductive effort; a systematic relation between climate and expenditures was discovered for both recreation and sewerage categories. The second part of the inductive effort was focused on state snow-removal costs. As expected, the climate sensitivity of this relation proved highly significant.

As regards cost projections for CIAP from the identified impact areas, several externally imposed extremes had to be recognized. Among these were the constraints that only "first-round" costs be measured and that costs measured in other CIAP studies not be measured again (i.e., double-counted). These considerations eliminated all but (b) above. Table 9 thus represents a lower-bound estimate of the public costs of climate modifications.

Summarizing Remarks on the Budget-Study Research

As mentioned earlier, these budget studies were conducted primarily to permit an analysis of who would bear the costs of CIAP-relevant climatic modifications. The findings discussed in the preceding pages should supply the materials required for an economic cost-incidence profile.

In order to illustrate how such results could be useful to policy makers, we outline such an incidence analysis. For our example, let us assume a discount rate of 5%, annual costs beginning in the year 2000, and require that the climatic perturbations examined begin in the year 1990 and proceed linearly to the maximum by the year 2025 (which is consistent with the studies reported in this paper.)

First, observe that the fossil fuel consumed directly by the commercial sector tends, as expected, to increase with a decline in ambient temperatures. Specifically, from the findings reported above, a 1°C drop in temperature is associated with a $625.2 million yearly increase in cost for such fuels at current prices.

Table 9. Costs of Highway Maintenance Under Selected Parametric Variations of Climate, Discount Rate, and Base Year (in millions of 1971 dollars)

Temperature Change: -2°C			Precipitation Change (%)* +21	0	-21
Discount Rate	Basis		Snow Change (cm)** 48.95	34.29	19.63
3%	1974	P.V.	4209.0	2877.0	1587.0
		A.C.	126.3	86.3	47.6
	2000	P.V.	8635.0	5904.0	3256.0
		A.C.	259.1	177.1	97.7
5%	1974	P.V.	1454.0	944.0	548.0
		A.C.	72.7	49.7	27.4
	2000	P.V.	4693.0	3209.0	1769.0
		A.C.	234.7	160.5	88.5
8%	1974	P.V.	415.0	284.0	157.0
		A.C.	33.2	22.7	12.6
	2000	P.V.	2538.0	1735.0	957.0
		A.C.	203.0	138.8	76.6

Temperature Change: -0.5°C			Precipitation Change (%) +5.6	0	-5.6
Discount Rate	Basis		Snow Change (cm) 12.50	8.59	4.67
3%	1974	P.V.	980.0	615.0	340.0
		A.C.	29.4	18.5	10.2
	2000	P.V.	2010.0	1263.0	698.0
		A.C.	60.3	37.9	20.9
5%	1974	P.V.	338.0	214.0	118.0
		A.C.	16.9	10.7	5.9
	2000	P.V.	1092.0	688.0	380.0
		A.C.	54.6	34.4	19.0
8%	1974	P.V.	97.0	62.0	34.0
		A.C.	7.8	5.0	2.7
	2000	P.V.	591.0	371.0	205.0
		A.C.	47.3	29.7	16.4

Temperature Change: -1°C			Precipitation Change (%) +10.5	0	-10.5
Discount Rate	Basis		Snow Change (cm) 24.46	17.15	9.33
3%	1974	P.V.	2005.0	1374.0	756.0
		A.C.	60.2	41.2	22.7
	2000	P.V.	4113.0	2820.0	1551.0
		A.C.	123.4	84.6	46.5
5%	1974	P.V.	693.0	475.0	261.0
		A.C.	34.7	28.8	13.1
	2000	P.V.	2235.0	1533.0	843.0
		A.C.	111.8	76.7	42.2
8%	1974	P.V.	198.0	136.0	75.0
		A.C.	15.8	10.9	6.0
	2000	P.V.	1209.0	829.0	456.0
		A.C.	96.7	66.3	36.5

Temperature Change: +0.5°C			Precipitation Change (%) -5.6	0	+5.6
Discount Rate	Basis		Snow Change (cm) -12.50	-8.59	-4.67
3%	1974	P.V.	-980.0	-615.0	-340.0
		A.C.	-29.4	-18.5	-10.2
	2000	P.V.	-2010.0	-1263.0	-698.0
		A.C.	-60.3	-37.9	-20.9
5%	1974	P.V.	-338.0	-214.0	-118.0
		A.C.	-16.9	-10.7	-5.9
	2000	P.V.	-1092.0	-688.0	-380.0
		A.C.	-54.6	-34.4	-19.0
8%	1974	P.V.	-97.0	-62.0	-34.0
		A.C.	-7.8	-5.0	-2.7
	2000	P.V.	-591.0	-371.0	-205.0
		A.C.	-47.3	-29.7	-16.4

* Based on interpolation from Table C.2 in Appendix C of Chapter VIII in the Urban Resources section of CIAP Monograph VI.

** Based on the relation among snow, temperature, and precipitation in Table 2.5.1, page 55 of Chapter VIII in the Urban Resources section of CIAP Monograph VI.

The electricity demand analysis has shown that savings will be realized in the commercial sector via a reduction in air-conditioning demand if ambient temperature is lowered. Specifically, a 1°C drop in average summer temperature will save the commercial sector up to $2,812.8 million per year. Of course, there are also costs associated with an increase in commercial electric space heating. These costs, resulting from a 1°C decrease in average winter temperature, are approximately $298.8 million per year. (It should be noted that because of data limitations, the researchers were unable to obtain results on the effects of a temperature drop on residential electric air conditioning and space heating.)

The research devoted to evaluating the impact of the climatic modifications on personal-budget items indicate that housing, clothing, and miscellaneous personal outlays will increase on an annual basis by $1,801.2 million if ambient temperatures fall by 1°C.

The industrial sector, however, will not be significantly influenced by such climatic perturbations. Apparently, the cost structure of this producing sector of the economy is rather insensitive to the climatic modifications being discussed by CIAP.

Conservatively, we could expect expenditures on roads and road maintenance to be increased as much as $111.75 million per year

for a 10.5% increase in precipitation accompanied by a 1°C temperature drop.

At this point, we will present some aggregate figures derived from the results of the budget studies. The aggregated *costs* associated with a drop in ambient temperature are summarized in Table 10. It is appropriate to mention that the aggregation of these cost figures is subject to some extreme qualifications. First, there are potential overlaps in these studies that are not considered in this summation process. For example, the personal-budget study includes expenditures on utilities when considering housing expenditures. Second, it was impossible to incorporate in this study all aspects of costs of climatic change within urban areas.

The drop in ambient temperature will also result in savings. Table 11 summarizes *net values* when the savings resulting from a decrease in air conditioning are included in the picture. These values are also subject to severe qualification. First, as was previously mentioned, an explicit econometric analysis of the residential consumption of electricity for heating and cooling purposes has been neglected. Specifically, if the

Table 10. Summary of Costs Associated with Climatic Change (in billions of 1971 dollars)

Discount Rate	Starting Year	Basis	-2°C	-0.5°C	+0.5°C	-1°C
3%	1974	P.V.	69.5930	17.3700	-17.4260	34.7315
		A.C.	2.0878	0.5211	-0.5228	1.0419
	2000	P.V.	149.9020	37.5757	-37.6960	74.8188
		A.C.	4.4971	1.1273	-1.1309	2.2446
5%	1974	P.V.	31.5933	7.9089	-7.9246	15.8031
		A.C.	1.5797	0.3954	-0.3962	0.7902
	2000	P.V.	112.0136	28.0440	-28.0998	56.0349
		A.C.	5.6007	1.4022	-1.4050	2.8017
8%	1974	P.V.	11.3393	2.8036	-2.8070	5.6040
		A.C.	0.9071	0.2243	-0.2246	0.4483
	2000	P.V.	83.5368	20.6492	-20.6743	41.2745
		A.C.	6.6829	1.6519	-1.6539	3.3020

Table 11. Aggregate Cost Figures Derived from Budget Study Research (in billions of 1971 dollars)*

Discount Rate	Starting Year	Basis	-2°C	-0.5°C	+0.5°C	-1°C
3%	1974	P.V.	-32.6708	-6.5879	5.6991	-14.0394
		A.C.	-0.9801	-0.1976	0.1709	-0.4212
	2000	P.V.	-70.6361	-14.0909	12.1741	-30.3588
		A.C.	-2.1191	-0.4227	0.3652	-0.9108
5%	1974	P.V.	-1.3305	0.1351	-0.3914	-0.0185
		A.C.	-0.0665	0.0068	-0.0196	-0.0009
	2000	P.V.	-5.0526	0.4030	-1.3139	-0.2217
		A.C.	-0.2526	0.0202	-0.0657	-0.0111
8%	1974	P.V.	2.4636	0.6857	-0.7436	1.3069
		A.C.	0.1971	0.0549	-0.0595	0.1046
	2000	P.V.	17.8887	4.9843	-5.4124	9.4917
		A.C.	1.4311	0.3987	-0.4330	0.7593

*Negative numbers indicate an overall cost savings.

residential sector experiences impacts on electricity consumption similar to those projected for the commercial sector, a significant savings will have been neglected. Second, the two qualifications to Table 10 are also appropriate here.

The net values in Table 11 may lead to suspicion on the part of some readers as to the validity of the magnitude of the savings. Admittedly, the values do seem rather large relative to the estimated costs, until it is realized that these figures imply only a $2.42 savings per commercial building per month, using July as an example. This dollar number is based on a temperature decrease of $(-1.8^{\circ}C/35) \approx -0.05^{\circ}F$, and is expressed in 1974 terms.

Furthermore, estimated elasticities indicate that commercial consumers of electricity are more responsive to changes in temperature during the summer months than during the winter months. In particular, using January and July as examples, the estimated elasticities of heating (cooling) degree days with respect to the demand for kilowatt-hours were 0.262 and 0.591 respectively.

In general, it seems that the dollar magnitudes presented in Table 10 – that is, the *costs* of climatic change – are at least "ballpark" estimates. On the other hand, the single section in this study that obtained an overall savings might be interpreted as an upper-bound dollar estimate. This upper limit would be reflected not only in the total number of commercial electric buildings assumed for space heating and cooling purposes, but also by the changing percentages over time of the buildings with respect to end use. However, since the savings side of the analysis is somewhat incomplete, it is impossible to accurately gauge the entire savings effect, so we cannot yet present a meaningful composite view of the effects of climatic changes on the urban sector.

Macro-Regional Study

Capital Costs Associated with Corn-Belt Effects

Long-term climatic change induced by aircraft of various types flying in the stratosphere is likely to affect the earth and its inhabitants in many ways. One of the most significant potential consequences of a permanent drop in temperature is a massive set of world-wide shifts in patterns of agricultural land use.

As research in the biological area done for CIAP Monograph V has shown, the availability of food, fiber, and wood resources in certain areas is extremely sensitive to small variations in temperature and rainfall. A relatively small lowering of mean temperatures would shift the corn belt significantly to the south and drastically reduce the production of wheat in Canada and the Soviet Union, as well as the grain output of Northern China, while it would also to some extent displace southward the warm-temperature crops such as cotton. Consequently, the whole network of highways and central places (agriculturally oriented urban centers) that has developed in the most northerly regions would be at least partially abandoned, while in the more southerly regions existing central places would be expanded and new ones established. This tendency toward increased labor force, capital stock, and population in southern regions is likely to be accentuated by the continuing long-term increase in world demand for foodstuffs, and the higher world market prices that now appear to be inevitable for agricultural commodities.

Capital Stock Shifts

Earlier volumes have dealt with the estimation of climatic changes, their impact on agricultural productivity, and the concomitant shifts in agricultural land-use patterns. This study attempts to measure the costs of shifts in the network of highways and central places necessitated by the changes in the location of agricultural production. Simply stated, it involves the estimation of capital requirements for the construction of new central places and the expansion of those that already exist. These capital requirements must be understood in a net sense, that is, new capital construction generated by both climatic changes and the resultant land-use changes, minus the construction that would have occurred without these changes.

Since the corn-belt is clearly the most important agricultural region in the United States, this study concentrated on estimating the capital costs necessitated by a shift in the corn belt resulting from a July mean-temperature decrease of $5^{\circ}F$ ($2\ 7/9^{\circ}C$). All cost estimates given in this paper were derived under this assumption, and then multiplied by 0.25 to yield figures based on a $1^{\circ}C$ decrease. A factor of less

than 0.36 (the reciprocal of 2 7/9) is assumed because investment requirements can be expected to increase more than linearly with distance as the fertility of the land decreases.

Even though the corn belt produces only a part of total U.S. agricultural output, and the U.S. accounts for only a fraction of the world's total, it can be argued that the capital costs incurred through a shift in the corn belt can be viewed as a good indicator of whether or not a potential world-wide problem exists. If these costs appear to be small, we can conclude that the likely world-wide costs would not be disastrous; on the other hand, if costs associated with a shift in the corn belt appear to be large, a much more detailed study of capital costs on a world-wide basis would be in order.

Assuming that the net investment costs are incurred in 25 equal annual amounts over the period 2000-2025, these annual costs equal $0.233, $0.272, and $0.311 billion under the low, medium, and high assumptions in the study, respectively. Present values of these net investment costs attributable to climatic change were calculated back to 1974 and 2000 in two separate operations for three different rates of interest. The results appear in Table 12 for the medium assumption.

Table 12. Present Value of Net Investment in the New Corn Belt Attributable to Climatic Change (in billions of 1971 dollars)

Discount Rate	1974 Present Value	2000 Present Value
3%	2.20	4.73
5%	1.08	3.83
8%	0.40	2.90

The present values in 1974 of the net investment costs attributable to climatic change lie in the range of $1.88 to $2.50 billion at a 3% rate of discount, $0.93 to $1.23 billion at a 5% rate of discount, and $0.33 to $0.45 billion at an 8% rate of discount. Thus the costs appear to be significant, although very small relative to gross national product.

However, if the production of food in the more northerly regions of the world is significantly reduced, world prices of foodstuffs are sure to rise rapidly. As a result, it is almost certain that the labor and capital intensity of production in the corn belt would also increase markedly, and the costs attributable to climatic change would be significantly increased. Therefore, the figures presented should be considered as lower bounds of these costs.

In order to obtain an estimate of the annual costs brought about by the climatic change, the present values of the net capital costs have been annualized over the periods 1974-2025 and 2000-2025. These results are as shown in Table 13.

Table 13. Annualized Present Values of Net Investment in the Corn Belt Attributable to Climatic Change (in billions of 1971 dollars)

Discount Rate	Ann. Costs 1974-2025	Ann. Costs 2000-2025
3%	0.085	0.272
5%	0.059	0.272
8%	0.033	0.272

Hence, annualized costs vary from a possible low of $27 million spread over a 51-year period to a high of $311 million spread over a 25-year period.

ACKNOWLEDGMENT

This research was supported by the Climatic Impact Assessment Program of the United States Department of Transportation under Contract No. DOT-OS-400-32.

REFERENCES

Anderson, R.J. and T.D. Crocker (1971), "The economics of air pollution: A literature assessment," in P.B. Downing, ed., *Air Pollution and the Social Sciences*, Praeger, New York.

Attaran, K. (1973), "Inter-Metropolitan Budget Cost Determinants: An Econometric Analysis," unpublished Ph.D. dissertation, Dept. of Economics, University of Southern California.

CIAP Monograph Series, Volumes V and VI, U.S. Department of Transportation. NOTE: At present, the monographs exist only in an early draft form. They will be publicly available after completion in September 1974.

Haworth, C.T. and D.W. Rasmussen (1973), "Determinants of metropolitan cost of living variations," Southern Economic Journal 40(2), 183-192.

Marshall, A. (1961), *Principles of Economics*, 8th ed., MacMillan, London.

THE ECONOMIC EFFECTS OF THE CONSEQUENCES OF STRATOSPHERIC FLIGHT ON LIVING MARINE RESOURCES

FREDERICK W. BELL
Florida State University
Tallahassee, Florida

ABSTRACT: We find every indication that the climatic changes projected for the 1990-2025 period will have an overall adverse impact on living marine resources on a world basis. A change in present environmental parameters as a result of increased discharge of effluents into the stratosphere by aircraft could decrease marine-resource productivity by up to 35% for some species groups by 2025. Groundfish, tuna, salmon, sardines and other food fish would be hardest hit by environmental changes. We considered fourteen fishery groupings, including commercial and recreational fishing. Using consumers' surplus as a measure of loss or gain from a change in environmental parameters, we estimated that the fishing industry could suffer a present-value loss of $92.8 billion on a world basis (1974-2025 at a 3% rate of discount). To assess the sensitivity of the estimates to the long lag between primary cause and effect, we computed the present-value losses starting in 1990 to the year 2025 (at a 3% discount rate). The loss in consumers' surplus was estimated at $148.9 billion for the 1990-2025 period, for an annualized cost of 4.4 billion. These losses would fall primarily on the "developed" countries such as Japan, the U.S.A., and France, which are the main consumers of fishery products. The loss in fishery production due to climatic change is shared between "developed" and "developing" countries. No estimate could be made of the adjustment of these countries to decreased production, since this would depend upon alternative employment opportunities and technological change (i.e., reduced labor impact by 1990-2025), which were outside the scope of this paper.

INTRODUCTION

Over the next several decades, air travel will increase due to rising population and income throughout the world (provided the supply of petroleum remains adequate). If this increased air traffic flies in the stratosphere, the effluents discharged could cause changes in the earth's climate.

The stratosphere (the part of the earth's atmosphere between about 11 and 50 kilometers) is in reality a social asset that provides valuable services – for example, the ultraviolet-shielding function – to man and his environment. More specifically, the existing and potential services rendered by the stratosphere to those traveling in it may seriously conflict with other services provided by the atmosphere as a whole to those on earth, which raises the problem of determining the best use of this common-property resource. A common criterion of economic allocation is that the social gains from increased use of the stratosphere must exceed any associated increases in costs. This report focuses on the estimated economic costs resulting from alterations in the marine environment due to increased use of the stratosphere*.

In order to estimate the external costs, three steps are required:

1. The physical and environmental implications of changes in the stratosphere due to an increase in the stratospheric services allocated to aircraft must be estimated.
2. The biological impact of these changes must be estimated.
3. The biological impact must be translated into social costs.

The Department of Transportation's Climatic Impact Assessment Program (CIAP) has identified four major areas in which environmental change might take place due to increased use of the stratosphere:

* This is a classic case of a technological externality. The stratosphere is a common-property resource available to all at zero price. However, increased use of this resource by aircraft may shift the production functions of industries operating on the earth's surface.

- precipitation (P)
- seawater temperature* (ST)
- ultraviolet radiation (UV)
- wind velocity (WV)

CIAP provided a set of working assumptions to be used in the calculations, thus fulfilling the requirements of Step 1. Steps 2 and 3 were completed as part of this report. This paper briefly discusses the economic status of marine resources today and their future potential under current environmental conditions. It next describes the dimensions of the marine environment and the comparatively small area we are considering in this report. Then it articulates the bioeconomic model used to evaluate the social gains or losses associated with increased use of the stratosphere, and provides the empirical results. Finally, the paper presents basic conclusions and recommendations for future research.

LIVING MARINE RESOURCES TODAY AND IN THE FUTURE

The world fishery resource is not only fixed, but is common property in nature. That is, ocean fishery stocks are generally in the wild state (and available to all nations) and are renewable, although fixed on a sustainable-yield basis for a given level of fishing effort. One aspect of the consumption of world fishery resources (commercially harvested species) has been its propensity to increase at a greater rate (for some periods, at a considerably greater rate) than that of the world population (FAO, 1969). This increase in consumption has meant a considerably augmented per-capita protein allowance.

Over the 1963-71 period, the world commercial catch increased at a rate of 5.4% a year. It has been estimated (Olson and Bell, 1973) that the dockside value of the world's commercially harvested fishery products has increased from $6.1 billion in 1963 to $14.3 billion in 1971. No reliable statistics exist on the world retail value of fishery products. However, a recent study by Penn (1973) indicates that for the United States the fisherman's share of every dollar the consumer spends on fishing products averaged 36.6% for finfish, and 47.4% for shellfish. Using the *value* of world finfish and shellfish as weights, the fisherman would receive approximately 40% of the consumer's fishery dollar. Generalized on a world basis, the estimated retail value in 1971 of the commercial world fisheries might approximate $35.8 billion. Table 1 shows the catch of each of the leading species of the world by its top three harvesting countries. In 1970, the United States, Japan, Canada, France, Italy, and the USSR appeared to be the top fish-catching nations among the "developed countries", while Taiwan, Peru, Chile, Spain, Morocco, India, Pakistan, Korea, and Thailand were the major fishing nations among the "developing" countries. Table 2 ranks the countries on the basis of percentage of the value of the 1971 catch. Clearly, Japan and the USSR overwhelmingly dominate the world commercial fishing scene.

Table 2. Percent of Dockside Value of World Commercial Catch for the Top Ten Countries, 1971 (Olson and Bell, 1974)

Country	Percent
Japan	22
USSR	12
USA	4
Philippines	4
Spain	3
India	2
France	2
Pakistan	2
Italy	2
Korea	2

Since world fisheries have expanded exceedingly rapidly over the last two decades, tremendous pressure has been placed on the resource itself. The Food and Agricultural Organization estimates (FAO, 1969) that the maximum sustainable yield (MSY) for all world fisheries is approximately 120 million metric tons. This figure includes many species that have virtually no market potential at this time. As of 1971, world catches were running about 70 million metric tons. However, for the major species, overfishing is occurring in many areas of the world. Despite the emergence of a number of international commissions to control fishing effort, resource depletion of many stocks is taking place at an alarming rate. Figure 1 illustrates overfishing for Atlantic menhaden (off the U.S.

* CIAP provided a set of assumed surface temperatures only; the equivalent seawater temperature changes (see Table 5) were derived from them by a mechanism explained in CIAP Monograph 2.

Table 1. Rank of Three Leading Fishing Countries, by Catch of Specified Species, 1955 and 1970, in round weight (FAO, 1955, 1970)

	1955		1970	
Species	Country	lb × 10^6	Country	lb × 10^6
Groundfish	USSR	1,884	Japan	5,448
	United Kingdom	1,304	USSR	4,008
	Japan	871	Norway	1,468
	Total world	10,560	Total world	1,942
Tuna	Japan	786*	Japan	1,065
	United States	355*	United States	402
	Peru	214*	Taiwan	219
	Total world	1,659*	Total world	3,338
Salmon	Japan	395	United States	399
	USSR	393	Japan	253
	United States	282	Canada	159
	Total world	1,270	Total world	1,008
Halibut	United States	49	USSR	58
	Canada	34	Canada	43
	Norway	11	United States	35
	Total world	112	Total world	150
Sardines (canned herring)	United States	147	W. Germany	314
	Portugal	109	Morocco	127
	Norway	103	Spain	87
	Total world	1,254	Total world	1,930
Shrimp	United States	244	United States	368
	India	235	India	254
	Japan	107	Thailand	184
	Total world	1,024	Total world	2,050
Lobsters	Canada	48	Chile	89
	South & Southwest Africa	47	United States	47
	United States	32	Canada	37
	Total world	227	Total world	357
Crabs	Japan	152	United States	256
	United States	137	Japan	198
	USSR	83	Thailand	107
	Total world	425	Total world	882
Clams	Japan	232	United States	490
	United States	207	Japan	396
	United Kingdom	17	Spain	70
	Total world	500	Total world	1,168
Scallops	United States	194	Canada	104
	Japan	36	United States	52
	Canada	14	Japan	36
	Total world	247	Total world	331
Oysters	United States	1,061	United States	763
	Japan	216	Japan	421
	Mexico	23	France	128
	Total world	1,376	Total world	1,609
Fish Meal†	United States	750	Peru	4,968
	Norway	438	Norway	1,772
	United Kingdom	199	United States	623
	Total world	2,276	Total world	11,299

*1956 figures
†Product weight

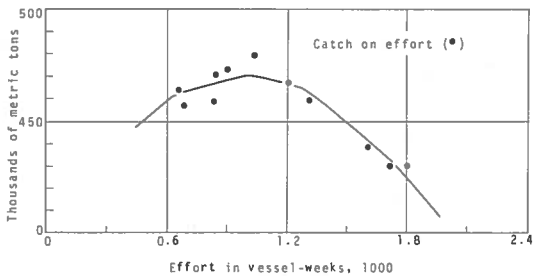

a. Northwest Atlantic menhaden.

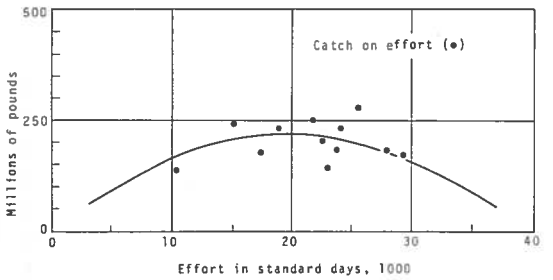

b. Eastern Pacific yellowfin tuna.

Figure 1. Catch per weeks of effort for two commercial fish. (From Bell et al. (1972).)

coast) and Eastern Pacific yellowfin tuna (off the coast of Central and South America). A recent study by Bell et al. (1972) found that of 75 fishery stocks fished by U.S. fishermen, 22 were either fully or over-capitalized. For 28, or a third, of the fisheries stocked, not enough data was available to permit definitive conclusions to be drawn.

Increasing world needs for protein are likely to generate overexploitation of traditional species (shrimp, haddock, lobsters, tuna, etc.). Productivity will decline and the fishing industry in many countries will undoubtedly suffer economically unless enlightened resource management is employed (Bell, 1972). The Bell et al. (1970) projections for the year 2000 for some major species groups indicate that overexploitation of many species has already begun (see Table 3).

Adverse impacts on the environment will influence not only commercial fishing, but also sport fishing. According to the Department of the Interior's 1970 National Survey of Fishing and Hunting, an armada of about 9.5 million saltwater anglers devoted 114 million days to

Table 3. Years in Which World Will Reach Maximum Sustainable Supply for Various Fish

Species*	Year
Salmon[1]	1970
Halibut	1970
Groundfish[2]	1970
Crabs	1980-85
Fish meal (i.e., species for reduction)	1980
Lobsters	1985
Tuna[3]	2000
Shrimp	2000
Sardines	2000+
Scallops[4]	2000+
Clams	2000+

* Aquaculture not assumed in these projections.

1. Does not include the possibility of expanded supply through hatchery operations and stream improvements.
2. Excludes hake and hake-like fish.
3. Excludes Central Pacific skipjack.
4. Includes recent discovery of calico scallops.

marine fishing in the U.S. alone. These anglers incurred expenses for the purpose of marine recreational finfishing in the amount of $1.25 billion, and received additional recreational value (i.e., opportunity cost of time devoted to fishing) of around $1.5 billion, making a total value to society of $2.75 billion in 1970. Statistics on the amount of marine recreational fishing for molluscs and crustaceans are not available; however, marine recreational shellfishing has been estimated to be of such magnitude that the value from all marine recreational fishing might exceed $3.0 billion in 1970 for the U.S. (Wilson and Pfetch, 1973). It would therefore be a serious mistake to overlook this sector in estimating the economic impact and costs of climatic change.

MARINE ECONOMIC SECTORS AND LIVING MARINE RESOURCES

Living ocean resources are economically valuable to all nations, providing both necessities, such as food and foreign exchange, and luxuries, such as recreation and other amenities. The total economic value of marine activities cannot be estimated precisely, since some ocean activities such as sightseeing and aesthetic appreciation cannot be simply quantified. For example, Tihansky (1973) identifies eight sectors of economic activity that depend wholly upon the coastal area of the United States (see Table 4). It

is clear that many of these sectors have expanded rapidly since 1964, the last year Tihansky was able to gather data for *all* sectors. This report will limit its finding to sectors F and R since the latter deal directly with living marine resources. However, there may be significant *indirect* effects on other sectors if there is a decline of living marine resources, since the ecological system is a general-equilibrium one, where everything to a greater or lesser degree depends upon everything else. Within the R sector we will necessarily restrict ourselves to sports fishing which is directly related to productivity of living marine resources. In order to accomplish a complete survey of this area, CIAP would have to consider all the other sectors which are related to the marine environment.

Table 4. Economic Sectors in Coastal Areas of U.S., 1964 (from Tihansky (1973))

Symbol	Economic Sector	Expenditures (Million $)
F	Fishing and Aquaculture	345
R	Recreation	3,855
T	Transportation	11,280
DS	Defense and Space	1,319
HW	Health and Welfare	372
M	Mining and Petroleum	1,704
ME	Marine Engineering	2,320
RD	R and D	232
		$21,427

THE BIOECONOMIC MODEL

The bioeconomic model developed here applies to two sectors:

F = commercial fishing and aquaculture
R_{SF} = recreational sports fishing (fresh and salt)

For sector F, we assume that fishery products commercially harvested are traded internationally under conditions approaching pure competition. The modeling of R_{SF} will be discussed below. Since we are dealing with events that are not likely to take effect for two decades, we need two kinds of bioeconomic projections:

1. *Baseline Projections.* The major economic variables associated with living marine resources (i.e., prices, quantities produced and consumed) must first be forecast *without* the projected expansion of jet travel or changes in the environment. This will give us a bench mark by which to judge the economic consequences of alterations in the environment and their impact on living-marine-resource productivity.
2. *Impact Projections.* The impact of stratospheric travel and its economic consequences on world living marine resources must next be projected.

At the outset, we should state what we mean by a projection. We want to project shifts in the demand for services in sectors F and R_{SF}, which are largely dependent upon future trends in human population and per-capita income. We shall make the simplifying and very plausible assumption that changes in P, ST, UV, and WV will not influence consumer demand projections. Second, to complete our projection, we must know the supply potential of living marine resources, or the "biological production function" – i.e., the relation between catch and economic inputs such as capital, labor, and technology. Baseline projections will give us world equilibrium *price* and *quantity*, assuming no significant changes in P, ST, UV, and WV. The impact projections will consider shifts in supply functions caused by biological changes related to changes in the environmental measures P, ST, UV, and WV.

There are five basic approaches to the biological production function:

Limited Ecological Systems Approaches (Stock by Stock)
- Beverton-Holt yield per recruit (Beverton and Holt, 1957)
- Simplified Schaefer model (Schaefer, 1954)
- Mod. 1: Schaefer model (Carlson, 1969)
- Mod. 2: Schaefer model (Pella and Tomlinson, 1969)

Expansive Ecological System Approach
- Trophic-level or food-chain approach (Schaefer, 1965)

These five identifiable approaches to the biological production function, which underlies the

supply function for fishery products, have various advantages and disadvantages. Some in the first group have no parameters presently available for most fishery stocks, while others such as the trophic-level approach lack specific application (i.e., to individual species) and do not have readily available data. The Beverton-Holt (BH) approach uses nature mortality and fishery growth as parameters to derive a relation between yield (catch) per recruit (fish or biomass available to fishermen to catch) and man-made mortality (i.e., fishing effort). This relation, combined with a stock-recruitment relationship, will produce a biological yield function. From a theoretical point of view, the BH model offers much, since one might relate P, ST, UV, and WV to K (growth), M (natural mortality), and R (recruitment). Unfortunately, these parameters of the BH model are not worked out for most fishery stocks of the world. The simplified Schaefer model postulates a logistic growth function for the biomass that leads to a parabolic relation between catch and fishing effort. Mod. 1: Schaefer is, in the author's opinion, more flexible, in that the function is flatter after maximum sustainable yield has been reached. (This has been verified for some stocks by Carlson et al. (1973).) Mod 2: Schaefer is still experimental, and the parameter m is not readily available for many fishery stocks. Finally, the trophic-level approach is based upon theoretically probable primary productivity (rate of carbon fixation of plants: conversion of carbon from carbon dioxide and carbonates into organic substances) in the ocean, and estimated transfer coefficients among trophic levels of the food chain. The trophic-level approach is appealing because it is specified in terms of photosynthesis, carbon dioxide and carbonates, and energy transfers. These variables might be related to P, ST, UV, and WV, but the model is not specific to a species. Figure 2 shows the various graphical forms of the five biological models. Mod. 1: Schaefer was chosen for the overriding reason that we have *baseline projections* of economic variables available from Bell et al. (1970) to the year 2000 based on this model.

The mechanics of the Mod. 1: Schaefer model are illustrated in Figure 3. Panel A shows supply and demand for a particular fishery

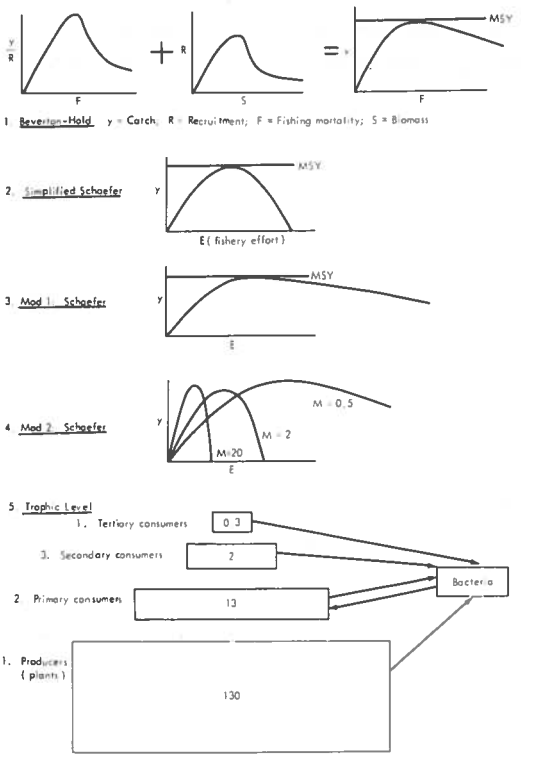

Figure 2. Graphic forms of various biological production functions. The numerical example gives relative nutrient weight at each trophic level.

product. OAC shows the traditional backward-bending long-run average-cost curve for a fishery. The demand curve intersects OAC at point A, giving prices and quantities produced (p_1; q_2).* This point would represent a *baseline projection* for any given year, say 1990. Panel B shows the biological production function (OC) from which the OAC curve can be derived (Bell, 1972). Next, a quantitative estimate was made of the percentage shift in the biological yield function due to CIAP-specified changes in P, ST, UV, and WV. The search of the literature and a survey of selected biologists throughout the nation and world provided us with enough material to make these rough estimates. The shifts estimated

* Notice that market equilibrium for a fishery resource is where AC = P, not at MC = P. This is due to the common-property nature of the resources, atomistic competition, and a decline in catch per unit of fishing effort (capital and labor) as the industry expands (i.e., technological external diseconomy).

(either positive or negative) for our 13 commercial species groups and 1 recreational sports-fishing category are documented in Appendix A.

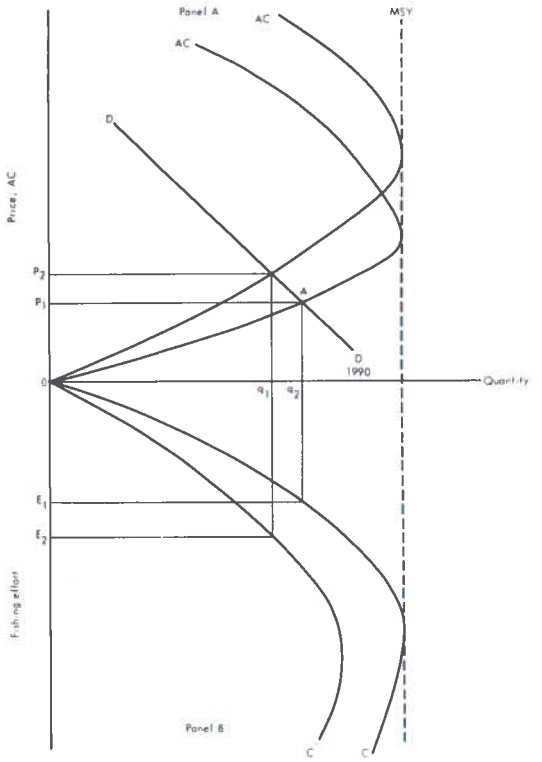

Figure 3. Adjustment of a fishery to shifts in environmental parameters.

In Figure 3, we illustrate a detrimental net influence of P, ST, UV, and WV, in that the biological yield function has shifted downward. This is shown in Panel B as OC′. In effect, factor productivity is lowered throughout the range of output, thereby producing a shift in the supply function or OAC′. This ends our discussion of the market adjustment of a fishery to changes in environmental parameters. In the sample case, output has been lowered to q_1 and price increased to p_2 as a result of environmental changes. Next we want to know the costs of the detrimental impact of changes in P, ST, UV, and WV shown in Figure 3.

ALTERNATIVE MEASURES OF SOCIAL WELFARE

It is virtually impossible to evaluate all the economic aspects of marine resources. The coastal seas, estuaries, and bays provide an abundant food supply, which is only partially assessed in the commercial market. For example, sports fishing as a recreational activity is difficult to assess. However, unless damages to polluted fisheries or gains through external environmental changes are evaluated in terms of social welfare, other competing demands (such as stratospheric flight) may take priority even if they are less valuable. Let us consider alternative measures of social welfare.

Revenue

The valuation of commercial fishing benefits is in many cases based on total gains (losses) in revenue. It is argued that a decline in production (due to environmental changes) will result in a decrease in revenue *valued at present market prices*. A fallacy in this logic is the underlying assumption of constant price. For price-elastic goods, reduced production will result in a decline in revenue. However, if the good (i.e., fish) is price-inelastic, a drop in production will actually increase revenue. Economic efficiency under certain circumstances requires that net gains or losses to commercial fishing be calculated as the increase (decrease) in market value of fish which results from the external variable (i.e., development plan, pollution, etc.), less associated costs. This definition suffers from the fact that the price-elasticity may arbitrarily influence the results. The U.S. Water Resources Council uses revenue as a measure of benefits but widens the definition to final user.

Net Revenue

Another approach defines welfare gains (or losses) as the net value of fish produced. Net benefits are estimated as the difference between gross revenue and costs (i.e., value added or income originated in the fishery sector). However, gross revenue is still influenced by price elasticity, and the underlying assumption here is that resources (i.e., capital and labor) displaced cannot find alternative employment. In the short run, this assumption may be quite valid, especially among isolated fishing regions, but its validity may decrease as the time period under consideration is lengthened. Also, this definition

does not consider willingness-to-pay and social preference by the consumer.

Consumers' Surplus

A third method of measuring social benefits (or losses) is represented by the demand curve shown in Figure 4. The intersection of the demand and supply curves at A determines the equilibrium price under *current environmental conditions*. Each point on the demand curve should reflect what individuals are willing to pay for the associated level of fish consumption.* Obviously, some consumers are willing to pay more than the market price. These customers are thus benefiting from lower prices, and this difference represents a "consumers' surplus". Net welfare for all consumers is measured as the area BAF, or the amount they are willing to pay beyond the social cost of production. A change in environmental variables (P, ST, UV, and WV) may, if detrimental, shift the supply curve up and to the left (i.e., shift the biological-production function downward). There will be a loss in consumers' surplus, or area BAEC. In Figure 4, the supply function is flat up to market equilibrium. This is especially untrue of the fishing industry, where supply functions are usually postulated as being upward-sloping due to diminishing productivity as fish stocks are exploited. Therefore, producers' surplus could be added to consumers' surplus. (See Figure 5.) Producers' surplus is defined as the excess of actual earnings from a given quantity of output over the amount the firm would refuse to accept rather than market its product altogether. It can be expressed as Consumers' Surplus Loss + Net Producers' Surplus Loss = Total Welfare Loss, or $AP_1P_2B + AP_1P_3C - BgP_2 = P_3CAB_g$.

In this study, two decisions were made. First, we would use *consumers' surplus* (CS) as an economic measure of welfare losses (or gains) from changes in P, ST, UV, and WV. Although producers' surplus could be estimated, we made the decision to be conservative. Furthermore, the supply-function approximations used in Bell et

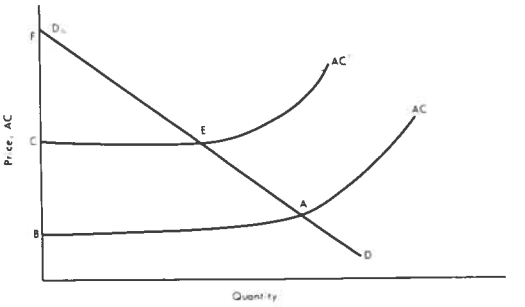

Figure 4. Supply and demand for a fishery product.

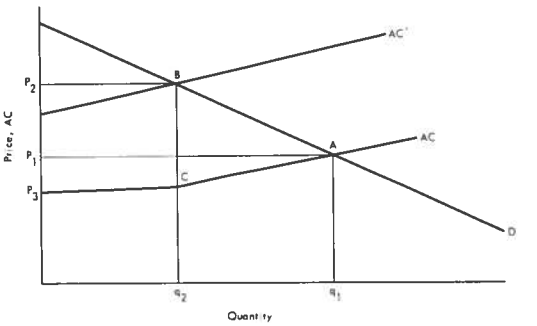

Figure 5. Consumers' and producers' surplus from supply and demand analysis.

al. (1970) were very crude and possibly subject to large error (they were the only ones then available on a world basis). Second, consumers' surplus should be computed at the retail level. Retail prices vary from country to country for most species, but even in the U.S. retail prices are not available for all major species groups. Because of these complexities, landing price (which is fairly uniform throughout the world since there is a large volume of international trade in fishery products) is used in our calculations, which should again lead to a conservative estimate of consumer surplus.*

The same definition of welfare gains or losses will be used for recreational fishing, which

* Figure 4 shows a somewhat flatter supply function (infinitely elastic) up to market equilibrium than Figure 3. This will vary from species to species depending on the parameters of the biological production function. Figure 4 was drawn so as to exclude producers' surplus up to market equilibrium.

* Of course, one of the assumptions behind the measurement of consumers' surplus from a Marshallian demand curve is that real income increases along the demand curve as prices fall. Therefore, an unambiguous measure of consumers' surplus can be derived only from something like a marginal valuation curve that holds real income constant by showing all units purchased at their full marginal prices. For fishery products, we can reasonably conclude that the change in real income is inconsequential.

is a predominantly nonpriced recreational resource.* Most economists would favor the willingness-to-pay approach, which is fundamental to the standard demand curve and consumers' surplus. Tihansky, in a recent paper (1973), used consumers' surplus to evaluate the social loss from water-pollution damages to fishing resources, an approach which is conceptually similar to that of this study. Two recent studies helped us to treat recreational sport fishing in a manner similar to that used for commercial fishing. (This is discussed in the next section.)

In order to measure the loss or gain in consumers' surplus by species group (discussed below), we used the following formula as an approximation

$$CS_t = V_t \left[g - \frac{ng^2}{2(1-g)} \right]$$

where

V_t = (a) Negative impact of environment parameters (dockside value of the fishery (price X quantity) after the shift in the supply function upward)
(b) Positive impact of environmental parameters (dockside value of the fishery (price X quantity) before shift in supply function downward)

g = (a) Negative impact (absolute (i.e., ignoring sign) percent change in price measured from new equilibrium if supply function shifts upward)
(b) Positive impact (absolute percent change in price measured from old equilibrium if supply function shifts downward)

n = estimated arc price elasticity between equilibria (include sign which will be negative in all cases)

After obtaining CS (gains or losses) in year t, the following procedure will be used:

a. *Discounted Present Value from 1974-2025.* For the ith species group, we have the following formula:

$$PV_i = \sum_{t=1974}^{2025} \frac{CS_t}{(I+v)^t} \quad \text{(in 1971 dollars)}$$

where PV = present value and CS_t from 1974-1990 equals zero.* CS was discounted using 3%, 5%, and 8% per CIAP guidelines.

b. *Discounted Present Value from 1990-2025.* A similar formula, in which t = 1990, is used. CS_t in 1990 is assumed to be zero*, and the same discount rates as above are used. Annualized cost was found by multiplying the present value by the approximate interest rate.**

We shall also discuss the loss or gain in production and value by the major fishing nations of the world, under the assumption that they will maintain their relative production and consumption positions from 1970 to 1990.

EMPIRICAL RESULTS

Description of Baseline Projections

Bell et al. (1970) made projections for major fishery products to the year 2000. This study assumed no major changes in the environment, such as changes in P, ST, UV, or WV. The supply of fishery products (i.e., supply curve) was developed using the Mod. 1: Schaefer model in conjunction with 1965-7 statistics of world catch (by species group) and Gulland's (1971) estimates of MSY by stock. Therefore, for each species group, a supply function was developed for many stocks which are or will be exploited. These supply functions were aggregated for each

* In addition to consumers' surplus, other methods such as net market value, option value, existence value, bequest motivation, gross expenditures, induced benefits, and time-spent-in-fishing may be employed.

* Since climatic effects were assumed to take place starting in 1990 per CIAP guidelines, CS was measured from this date. The first year was assumed to be zero because of its negligible impact in all cases.

** Losses in consumer surplus due to environmental pollution are a measurement of a loss in real income for world consumers. Therefore, PV_i could also be expressed as a stream of losses (at a given interest rate) to the PV of world per-capita income, for comparative purposes.

species to obtain a world supply function. Demand functions were estimated by species for each of the major consuming countries, plus a residual.* The assumption of a declining income elasticity was built into these functions (log-linear), which is plausible for food products. The various species demand curves for each country and a residual were aggregated to derive a world demand curve. A world equilibrium was derived (quantity and price) for each five-year interval from 1970-2000, using population and income projections supplied by the U.S. Department of Agriculture (1968).** Projections beyond 2000 were derived by simple extrapolation of trends established by the projections over the 1970-2000 period except in a few cases. It was the author's judgment that the expense of using the Bell et al. computer model to project beyond the year 2000 would not be justified by the results.***

In addition, the data needed to implement the model are expensive to collect. Figure 6 shows graphically the results for a species group, lobsters, from the Bell et al. study.

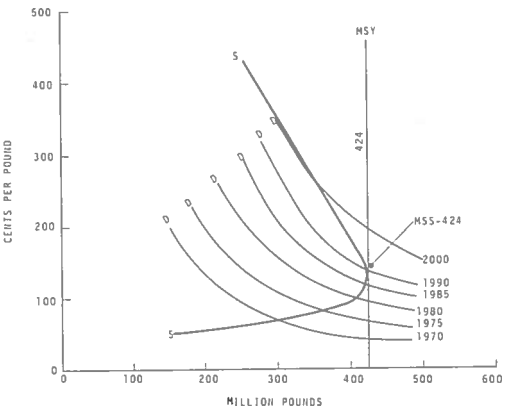

Figure 6. World demand and supply function for lobster, 1970-2000.

Shifts in Biological Production Functions and Corresponding Supply Functions as a Result of Changes P, ST, UV, and WV

CIAP specified four sets of parametric changes in P, ST, UV, and WV. Because of the complexities of handling all four cases and resulting combinations, we selected the case which was indicated as most probable by CIAP specifications.

Table 5 shows the environmental parametric changes used in our study. A massive literature search and national and international surveys were made to link biological productivity to the parametric changes shown in Table 5. Appendix A discusses these relationships. Table 6 is a summary of the results which appear there, in terms of percentage changes in the baseline supply function as a result of the combined influence of changes in ST, T, UV, and WV. The parameters are specified by latitude, so we considered the distribution of each species group by latitude band; if an overlap occurred, the mean of the parameter was used.

To give the reader some familiarity with how we related the biological production function to changes in ST, T, UV, and WV, let us discuss groundfish as a sample case.

1. *Seawater Temperature (ST).* A 26% decrease in groundfish catch compared to baseline was predicted for a 1.5 to 1.75°C seawater temperature decrease by 2025. A large part of this figure

* Per-capita consumption of the ith species group for each of the major consuming countries was specified as being a log-linear function of *real* price (i.e., dockside price divided by consumer price index in each country) and *real* per-capita income. The *constant* income elasticity was decreased over the 1970-2000 project period. After consideration of the reasonableness of the estimated parameters (i.e., a few were changed using other countries' results), these equations were aggregated to obtain a world demand function via a computer model. For the CIAP study and the Bell et al. (1970) report, we felt a declining income elasticity was most appropriate for food commodities over a 55-year period (1970-2025). The decline was based upon statistical studies of species consumed principally in the U.S., and applied to other countries.

** Appendix B compares the CIAP and Bell et al. (USDA) per-capita income projections from 1990-2025. Except for a few regions and countries, the two sets compare favorably. Considering the offsetting (+) and (–) deviations from CIAP projections, it is the author's opinion that the final results would not be appreciably influenced.

*** Even using the Mod. 1: Schaefer model, demand projections for groundfish, lobsters, crabs, and fish meal to the year 2025 would lead to virtual extinction of the resource. The year-2000 projections indicated significant overexploitation for these species groups. Because management usually follows significant overexploitation, we held the supply for these four groups at the year-2000 level assuming a management authority would intervene, but the resource would take many years to recover to maximum sustainable yield.

Table 5. Range of Climatic Parameters for the CIAP Case Chosen[1]

Latitude	Surface Temperature Change	Estimated Seawater Temperature Change[2] (ST)	Precipitation Change (P) A	B	C	Solar Radiation Change[3]	Estimated UV Change[4]	Change in Wind Velocity (WV)
0-20	-0.5°C	-0.5°C	+10 %	0	-10 %	-1 %	+10%	0
21-40	-1.0°C	-1.0°C	+12.5%	0	-12.5%	-1.2%	+10%	-2.5%
41-60	-1.5°C	-1.5°C	+ 7.5%	0	- 7.5%	-1.6%	+10%	-5.0%
61-80	-2.0°C	-2.0°C	+ 7.5%	0	- 7.5%	-3.9%	+10%	-7.5%

[1]Projections for all four CIAP cases would have required extensive biological and economic research, so the Monograph VI chairman authorized us to use only Case 2.

[2]Figures arrived at from O'Brien (1973) and Tabata (1961). Figure 25 of Tabata, reproduced below, shows the correlation of surface and seawater temperature.

[3]For mid-latitude point at vernal equinox, noon.

[4]Per d'Arge (1973).

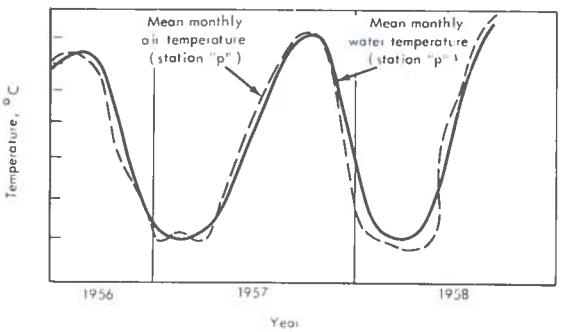

Table 6. Estimated Percentage Changes in the Sustainable Catch by Species Groups for 1991 and 2025 Due to Assumed Climatic Changes

Species Group	Case A* 1991	Case A* 2025	Case B 1991	Case B 2025	Case C 1991	Case C 2025	Three Top Countries Catching Resource 1970	Three Top Countries Consuming Resource
1. Groundfish	-0.38†	-31.19	-0.38†	-31.19	-0.38†	-31.19	Japan-USSR-Norway	USA-UK-Japan
2. Tuna	-0.50	-20.00	-0.50	-20.00	-0.50	-20.00	Japan-USA-Taiwan	USA-Japan-Taiwan
3. Salmon	-0.86	-35.00	-1.4	-50.0	-1.7	-70	USA-Japan-Canada	USA-Japan-Canada
4. Halibut	+0.09	+ 3.25	+0.09	+ 3.25	+0.09	+ 3.25	USSR-Canada-USA	USA-Canada-Norway
5. Sardines	-0.01	-30.00	-0.01	-30.00	-0.01	-30.00	W. Germany-Morocco-Spain	USA-Portugal
6. Shrimp	+0.17	+ 6.0	-0.05†	- 1.0†	-0.59	-20.0	USA-India-Thailand	USA-India-Japan
7. Lobsters	-0.14	- 0.20	-0.14	- 0.20	-0.14	- 0.20	Chile-USA-Canada	USA-UK-France
8. Crabs	-0.01	- 0.20	-0.01	- 0.20	-0.01	- 0.20	USA-Japan-Thailand	USA-Japan-France
9. Clams	+0.16	+ 7.5	0	0	-0.15	- 5.0	USA-Japan-Spain	USA-Japan-Spain
10. Scallops	+0.16	+ 5.0	0	0	-0.15	- 5.0	Canada-USA-Japan	USA-Japan-France
11. Oysters	+0.18	+ 5.0	0	0	-0.18	- 5.0	USA-Japan-France	USA-Japan-France
12. Other Food Fish	-0.50	-15.0	-0.50	-15.0	-0.50	-15.0	Numerous Miscellaneous Countries	Numerous Miscellaneous Countries
13. Fish Meal	-0.23	-10.0	-0.23	-10.0	-0.23	-10.0	Peru-Norway-USA	USA-UK-W. Germany
14. Recreational Fishing	-0.66	-11.0	-0.33	-10.0	-0.66	-11.0	USA-Others Unknown	USA-Others Unknown

†Decline in catch starts 2001

Source: Appendix A

*Case A = $+\Delta P; -\Delta ST; +\Delta UV; -\Delta WV$
Case B = $0\Delta P; -\Delta ST; +\Delta UV; -\Delta WV$
Case C = $-\Delta P; -\Delta ST; +\Delta UV; -\Delta WV$

(20-25%) can be attributed to the difficulties caused by *redistribution*. For example, the final daytime depth of herring is governed by temperature, cooler temperatures being associated with greater depths (Braun, 1960). One study has shown that catches of herring are dependent on a *rise* in surface temperature (which is anomalous) in connection with a given wind component (Craig, 1960). Obviously, cooling will adversely affect this necessary rise in surface temperature, and consequently the catch. Chase (1955) has analyzed a similar wind and temperature interaction as it affects the brood size of haddock. Colton (1972) showed that two out of four species of groundfish had their distributions altered from 1953 to 1967 as seawater temperature decreased.

A small portion (1-6%) of the 26% estimate was based on direct mortality, especially of cod. Cod prefer temperatures of 2-4°C, and the 2°C isotherm is especially critical. Woodhead and Woodhead (1959) discussed the various observations of other authors that cod concentrate at the 2°C isotherm, and suggested a physiological intolerance of temperatures lower than 2°C, except during the summer months. The data of Templeman and Fleming (1956, 1963) suggest that good cod fishing in shallow waters during the summer is dependent on the peculiarities of water warming and wind. Herring, incidentally, migrate along 5-6°C isotherms (Radakov and Soloviev, 1959), and cooling would shift these isotherms, definitely shifting distribution and possibly causing direct mortality.

The overall 26% decrease was estimated on an ad-hoc basis by considering the historical difference between poor and good groundfish landings, due apparently to problems of redistribution (vertical and horizontal), and adding a minor component for direct mortality, which may not become apparent until the end of the projected time period.*

2. *Precipitation (P).* Counted as zero due to (1) lack of information and (2) intuitive feeling that most groundfish, being either benthic or deepwater (and many are boreal) would not be affected by changes in precipitation or consequent variations in salinity.
3. *Ultraviolet Radiation (UV).* Counted as zero, even though Bodvarsson and Jonsson (1961) showed definitely that strong year-classes of cod prefer to emerge during periods of low solar activity. The UV change was thought not to be significant enough to make an appreciable impact.
4. *Wind Velocity (WV).* Counted as a 5% detrimental effect due to the negative effect on upwelling, and the indication in the literature that wind strength, together with temperature trends, is an important indicator of good catches of some species (Chase, 1955; Craig, 1960; Templeman and Fleming, 1963).

Combining the figures for temperature and wind, we get a net impact of -31% by the year 2025. By far the largest component of this is caused by redistribution due to lowered temperature. We may have overestimated this factor, since the details of the effects of redistribution on various aspects of the fishery were not completely analyzed; on the other hand, we may have underestimated mortality, considering that herring and cod concentrate at isotherms (cod: 2°C; herring: 5°C) at which they are "flirting with danger," since temperatures lower than those at the isotherms may cause heavy mortalities.

Yves (1964) provides our strongest support for placing heavy emphasis on the distributional effect with the following statement: "Most species of groundfish undergo seasonal changes in horizontal and vertical distribution that have direct effects on the fishery. The environment

* The historical technique of evaluating temperature changes may not be valid for all species. See Tuna in Appendix A for a discussion of this point.

(mainly temperature) brings about or accompanies these changes."*

This completes our sample case. (The bibliography, however, contains all the references we used to assess the environmental impact of changes in parameters shown in Table 5.) Now, let us turn to the social implications of the parametric changes, in terms of the bioeconomic model developed earlier.

Welfare Gains and Losses in Terms of Consumers' Surplus as a Result of Changes in Environmental Parameters

In computing gains and losses in consumers' surplus, we have essentially three cases. Case A is derived by considering parametric changes in ST, UV, and WV, and an increase in P (precipitation). (This does not mean that precipitation had an impact on every species, just on a few.) Therefore, we developed Case A adjusted for differential precipitation changes as shown in Table 5. Some entries, such as that for groundfish, are the same in Cases A, B, and C. This means that precipitation was not thought to be a significant variable. Case B is derived by considering changes in ST, UV, and WV but no change in precipitation. In short, it considers only three parameters. Notice that clams, scallops, and oysters have zero losses or gains. This means that a change in P was the only variable influencing biological productivity. Changes in ST, UV, and WV were judged to have a negligible impact as specified in Table 5. Finally, Case C considers parametric changes in ST, UV, and WV, and a decrease in precipitation.

The present value and annualized value of consumers' surplus are shown in Tables 7 and 8. The two tables represent two discounting periods. Table 7 discounts the gains and losses in consumers' surplus over the 1974-2025 period. Since CIAP has specified that the environmental impact of stratospheric flight will not be significant until the last decade of this century, no gains or losses were associated with the period 1974-1990. In effect, Table 7 specifies the costs of climatic change in terms of loss in consumer utility (expressed in dollars) to society projected to the year 2025. In terms of present value, the greatest loss as a result of changes in the marine environment (sectors F and R_{SF}) will occur for Case C at a discount rate of 3%.* *The present value of consumers' surplus losses (1974-2025) from sectors F and R_{SF} is approximately $92.8 billion (annualized cost of $2.8 billion) for the world as a result of the assumed climatic changes.*** Case C is by far the most damaging to fisheries, primarily because decreased precipitation affects shrimp, clams, scallops, and oysters.

* In essence, the redistribution will gradually lower the catch per trawl for world fishing fleets.

* Producers' surplus would probably run about 2/3 of consumers' surplus, or $61.9 billion for a total loss of $154.7 billion over the 1974-2025 period (Case C at r=3%).

** One can notice from Table 7 that the sport fishing sector (Recreational Fishing) is extremely large. This was discussed earlier. The Bell et al. baseline projections did not include Recreational Fishing, since it is typically not priced in the marketplace. However, we were able to make baseline projections in the following manner: First, Cicchetti et al. (1969) contained projections of the number of U.S. sport-fishing days to the year 2000. We used the rate of growth projected between 1990-2000 (a somewhat dampened one) to project to the year 2025 for the U.S. From these figures, we obtained the U.S. per-capita sport-fishing days (SFD) to the year 2025. This figure was in turn used as a bench mark for estimating the per-capita sport-fishing days for other countries and parts of the world by using a strict proportionality assumption, explained in Appendix I of Monograph VI, between SFD and per-capita income. (Since sport fishing is essentially a recreational activity, per-capita income seems a reasonable scaling device.) Robert Wilson of the U.S. Department of Interior (1973) estimates that the value (i.e., price) of a U.S. sport-fishing day is $18.00; we scaled this down to $5.00 for the world. At this point, we had the x-axis containing world sport-fishing days, and an average world price for 1974 on the y-axis. This gave us price-quantity coordinates for 1974. Adams (1973) estimated the price elasticity for sport fishing to be -.29. Using this estimate from the U.S. for the world, we were able to derive a demand curve running through the price-quantity coordinates estimated for 1973.

Second, a supply function was developed from the 1974 coordinates, rising to an estimated MSY of 3.3 billion SFD. The MSY was estimated on the assumption that the "developed" countries would reach MSY by the year 2000, and "developing" countries much later in the 21st century. The sum among countries in terms of recreational fishing days gave us a rough estimate of MSY. (This is admittedly crude, but no other data are presently available.) A demand curve was constructed for each year from 1990-2025 to intersect the estimated supply function at a price and SFD consistent with our initial projections. In this way, we made a crude approximation of the welfare loss due to environmental changes for the world recreational fishing sector.

Food fish accounts for approximately 57.6 percent of the discounted present value, and recreational fishing accounts for 41.7% (i.e., Case C at 3%). Although Table 7 indicates that increased stratospheric flight would be economically detrimental to the F and R_{SF} sectors (i.e., technological externality and diseconomy), some species groups such as halibut, shrimp, clams, scallops, and oysters could benefit, although only under Case A (1974-2025) in Table 7.

We should remember that these estimates are very conservative since we are (1) not estimating consumers' surplus at the retail level and (2) not including losses in producers' surplus. In addition, no consideration is given to the *multiplier* effects on sectors that supply F and R_{SF}. The usual multiplier of two or three would make the losses much greater. Also, as was mentioned in

Table 7. World Discounted Annualized Costs and Present Value of Gains and Losses in Consumers' Surplus by Species Group as a Result of Environmental Changes (CIAP Case 2), 1974-2025 (millions of dollars)

Species Groups		Case A			Case B			Case C		
		3%	5%	8%	3%	5%	8%	3%	5%	8%
1. Groundfish	AC	132.9	101.8	54.24	132.9	101.8	54.24	102.9	101.8	54.24
	PV	-4,429.	-2,036.	-678.	-4,429.	-2,036.	-678.	-4,429.	-2,036.	- 678.
2. Tuna	AC	15.3	12.45	7.44	15.3	12.45	7.44	15.3	12.45	7.44
	PV	- 510.	-249.	- 93.	- 510.	- 249.	- 93.	- 510.	- 249.	- 93.
3. Salmon	AC	33	25.55	13.84	65.46	51.9	29.04	119.07	91.2	48.64
	PV	-1,100.	-511.	- 173.	-2,182.	-1,038.	-363.	-3,969.	-1,824.	- 608.
4. Halibut	AC	0.51	0.40	0.24	0.51	0.40	0.24	0.51	0.40	0.24
	PV	+ 17.	+ 8.	+ 3.	+ 17.	+ 8.	+ 3.	+17.	+ 8.	+ 3.
5. Sardines	AC	61.59	43.1	19.76	61.59	43.1	19.76	61.59	43.1	19.76
	PV	-2,053	- 862.	- 247.	-2,053.	- 862.	- 247.	-2,053.	- 862.	- 247.
6. Shrimp	AC	100.5	80.9	46.32	24.93	20.85	12.88	356.31	280.4	157.76
	PV	+3,350.	+1,618.	+579.	- 831.	- 417.	- 161.	-11,877.	-5,608.	-1,972.
7. Lobsters	AC	1.77	1.3	0.64	1.77	1.3	0.64	1.77	1.3	0.64
	PV	- 59.	- 26.	- 8.	-59.	-26.	-8.	- 59.	- 26.	- 8.
8. Crabs	AC	15.12	12.30	7.2	15.12	12.30	7.2	15.12	12.3	7.2
	PV	- 504.	- 246.	- 90.	- 504.	- 246.	- 90.	- 504.	- 246.	- 90.
9. Clams	AC	4.11	3.35	1.42	0	0	0	0.96	0.85	0.56
	PV	+137.	+67.	+ 24.	0	0	0	- 32.	- 17.	- 7.
10. Scallops	AC	1.44	1.05	0.56	0	0	0	4.05	3.35	0.43
	PV	+48.	+21.	+7.	0	0	0	- 135.	- 67.	-25.
11. Oysters	AC	2.34	1.8	0.96	0	0	0		6.1	3.44
	PV	+78.	+36.	+12.	0	0	0	- 257.	-122.	- 43.
12. Other Food Fish	AC	891.45	774.25	501.00	891.45	774.25	501.04	891.45	774.25	501.04
	PV	-29,715.	-15,485.	-6,263.	-29,715.	-15,485.	-6,263.	-29,715.	-15,485.	-6,263.
TOTAL FOOD FISH	AC	1,042.23	883.3	544.24	1,208.0	1,017.6	632.0	1,597.6	1,326.7	802.48
	PV	-34,741.	-17,666.	-6,928.	-40,266.	-20,352.	-7,900.	-53,523.	-26,534.	-10,031.
13. Fish Meal	AC	16.53	13.85	8.48	16.53	13.85	8.48	16.53	13.85	8.48
	PV	- 551.	- 277.	- 106.	- 551.	- 277.	-106.	- 551.	- 277.	-106.
14. Recreational Fishing	AC	1,161.6	888.5	476.8	560.1	399.5	190.4	1,161.5	888.5	416.8
	PV	-38,720.	-17,770.	-5,960.	-18,670.	-7,990.	- 2,380.	-38,720.	-17,770	- 5,960.
GRAND TOTAL	AC	2,220.63	1,758.65	1,039.52	1,784.6	1,431	830.85	2,783.8	2,229.05	1,287.84
	PV	-74,012.	-35,713.	-12,994.	-59,487.	-28,619.	-10,386.	-92,794.	-44,501.	-16,098.

Case A = $+\Delta P; -\Delta ST; +\Delta UV; -\Delta WV$
Case B = $0\Delta P; -\Delta ST; +\Delta UV; -\Delta WV$
Case C = $-\Delta P; -\Delta ST; +\Delta UV; -\Delta WV$

our earlier discussion, more sectors than F and R_{SF} depend on the ocean environment.

Now, let us consider Table 8, which discounts from 1990-2025. This illustrates (in combination with Table 7) the differential losses between the present time and the actual time (1990's) when it is assumed that aircraft travel in the stratosphere could begin to have an appreciable impact on the marine environment. The two tables demonstrate the lag between cause and effect. Again, Case C at a discount rate of 3% dominates, with an estimated loss in consumers' surplus of $148.9 billion dollars.* Tables 7 and 8 can be compared for individual species. They have generally similar trends, since they differ only in years discounted.

* If we add producers' surplus, welfare losses could be as much as $248.2 billion.

Table 8. World Discounted Annualized Costs and Present Value of Gains and Losses in Consumers' Surplus by Species Group as a Result of Environmental Changes (CIAP Case 2), 1990-2025 (millions of dollars)

		Case A			Case B			Case C		
Species Groups		3%	5%	8%	3%	5%	8%	3%	5%	8%
1. Groundfish	AC	213.21	222.25	185.76	213.21	222.25	185.76	213.21	222.25	18
	PV	-7,107.	-4,445.	-2,322.	-7,107.	-4,445.	-2,322.	-7,107.	-4,445.	-2,322.
2. Tuna	AC	24.54	27.2	25.52	24.54	27.2	25.52	24.54	27.2	25.52
	PV	-818.	-544.	-319.	-818.	-544.	-319.	-818.	-544.	-319.
3. Salmon	AC	52.92	55.8	47.56	105.03	113.3	99.36		144.05	165.48
	PV	-1,764.	-1,116.	-594.	-3,501.	-2,266.	-1,242.	-6,369.	-3,981.	-2,081.
4. Halibut	AC	0.78	0.90	0.86	0.81	0.90	0.88	0.81	0.90	0.88
	PV	+26.	+18.	+11.	+27.	+18.	+11.	+27.	+18.	+11.
5. Sardines	AC	98.82	94.05	67.76	98.79	94.05	67.76	98.82	94.05	67.76
	PV	-3,294.	-1,181.	-847.	-3,293.	-1,881.	-847.	-3,294.	-1,881.	-847.
6. Shrimp	AC	161.25	176.55	158.64	39.99	45.55	44.08		612.15	540.40
	PV	+5,375.	+3,531.	+1,983.	-1,333.	-911.	-551.	-19,059.	-12,243.	-6,756.
7. Lobsters	AC	2.85	2.90	2.24	2.85	2.90	2.24	2.85	2.90	2.24
	PV	-95.	-58.	-28.	-95.	-58.	-28.	-95.	-58.	-28.
8. Crabs	AC	24.27	26.9	24.72	24.27	26.01	24.72	24.27	26.4	24.72
	PV	809.	-538.	-309.	-809.	-538.	-309.	-809.	-538.	-309.
9. Clams	AC	6.6	7.25	6.56	0	0	0	1.56	1.85	1.8
	PV	+220.	+145.	+82.	0	0	0	-52.	-37.	-23.
10. Scallops	AC	2.28	2.30	1.92	0	0	0	6.51	1.25	6.80
	PV	+76.	+46.	+24.	0	0	0	-217.	-145.	-85.
11. Oysters	AC	3.75	3.95	3.28	0	0	0	12.36	13.35	11.84
	PV	+125.	+79.	+41.	0	0	0	-412.	-267.	-148.
12. Other Food Fish	AC	1,430.52	1,690.05	1,716.56	1,430.52	1,690.05	1,716.56	1,430.52	1,690.1	1,716.56
	PV	-47,684.	-33,801.	-21,457.	-47,684.	-33,801.	-21,457.	-47,684.	-33,802.	-21,457.
TOTAL FOOD FISH	AC	1,672.47	1,928.1	1,898.8	1,938.45	2,221.25	2,157.12	2,576.97	2,896.05	2,741.20
	PV	-55,749.	-38,562.	-23,735.	-64,615.	-44,425.	-26,964.	-85,889.	-57,921.	-34,265.
13. Fish Meal	AC	26.55	30.25	24.12	26.55	30.25	29.12	26.55	30.25	29.12
	PV	-885.	-605.	-364.	-885.	-605.	-364.	-885.	-605.	-364.
14. Recreational Fishing	AC	1,864.20	1,939.0	1,634.4	899.1	872.	652.8	1,864.20	1,939.0	1,634.4
	PV	-62,140.	-38,780.	-20,430.	-29,970.	-17,440.	-8,160.	-62,140.	-38,780.	-20,430.
GRAND TOTAL	AC	3,563.22	3,897.35	3,562.34	2,864.1	3,123.5	2,847.12	4,467.42	4,865.3	4,448.0
	PV	-118,774.	-77,947.	-44,529.	-95,470.	-62,470.	-35,589.	-148,914.	-97,306.	-55,060.

Case A = $+\Delta P$; $-\Delta ST$; $+\Delta UV$; $-\Delta WV$
Case B = $0\Delta P$; $-\Delta ST$; $+\Delta UV$; $-\Delta WV$
Case C = $-\Delta P$; $-\Delta ST$; $+\Delta UV$; $-\Delta WV$

Principal Countries Affected by Social Losses in Commercial and Recreational Fishing

Referring to Table 6, we see that the United States is the leading consumer of the first 11 species groups and number 12, Fish Meal. Statistics are not readily available on other food fish or recreational fishing, but it would be safe to say that the USA ranks high in terms of consumption for these sectors. Japan follows a close second. The other top three consuming nations are generally highly developed (i.e., industrialized with a relatively high per-capita income). Therefore, the loss in consumers' surplus (or increased price) will fall mainly upon *highly developed* countries, assuming they maintain their 1970 rankings in the consumption of marine resources (F and R_{SF}) into the 1990-2025 period.*

One measure of losses often advocated is that of income (value added) and employment. The countries producing fishery products include both "developed" and "developing" countries. Although the estimated declines in production shown in Table 6 cannot be generalized to percentage declines in value added or employment because of technological change (i.e., reducing labor requirements as well as capital requirements per unit of output), they give the reader some indication of the possible magnitude of projected lost employment and income for the major fish-harvesting nations.

In essence, Japan, the USA, and West Germany would be heavily hit in terms of reduction in production (i.e., 31%, 20%, 35%, and 30% reduction in sustainable production for groundfish, tuna, salmon, and sardines respectively). Taiwan, Morocco, and Spain, which are "developing" nations, would also be greatly affected. If our estimates are correct, these countries would probably experience the greatest loss in income and employment. However, these resources may be utilized elsewhere within the countries, though it is highly unlikely that this would be true for capital and labor employed in fishery sectors *in the short run*. Since our period of analysis is 35 years (1990-2025), and reduction in output is assumed to be gradual (CIAP assumption by linear interpolation of changes in environmental parameters), resources (capital and labor) may adjust with minimum unemployment and resulting loss in income.

* Although losses in consumers' surplus may fall on the developed countries, the loss in yields of protein-rich fish to less developed nations may be of greater importance due to their insufficient protein production and its impact on nutrition, etc.

CONCLUSIONS AND RECOMMENDATIONS

Conclusions

After consideration of various biological yield functions, that of the Mod. 1: Schaefer catch-effort function was judged to be the most effective in evaluating the relationship between environmental parameters and resource productivity.

Consumers' surplus appears to be the most theoretically defensible measure of losses or gains due to environmental changes that influence resource productivity. Other measures, such as change in revenue or value-added, suffer because they do not adequately consider consumer substitution effects or price adjustments.

Fourteen categories of fishery products were selected for evaluation. These included Recreational Fishing, which is sizable in terms of economic value. After relating the environmental parameters to fishery productivity, we found that, in most cases, *the projected increase in stratospheric flight would be detrimental to living marine resources* in terms of sustainable productivity. The effects ranged from a 35% decrease in productivity in salmon by the year 2025 to a slight increase in productivity for oysters (in Case A).

The present value (for Case C at a discount rate of 3%) of consumers' surplus losses (1974-2025) from commercial and recreational fishing as a result of the assumed climate changes is estimated at $92.8 billion for the world.* The annualized cost is $2.8 billion. The most critical environmental parameters in terms of resource productivity are seawater temperature and precipitation.

The present value (for Case C at a discount rate of 3%) of consumers' surplus losses (1990-2025) from commercial and recreational fishing as a result of the assumed climate changes is estimated at $148.9 billion ($4.5 billion annualized cost) for the world.**

* If we add producers' surplus to our conservative estimate, welfare losses may run as high as $154.7 billion.

** If we add producers' surplus, welfare losses may run as high as $248.2 billion.

Because the "developed" countries consume most of the fishery products of the world, the loss in consumers' surplus will fall most heavily upon them. However, these same countries will probably make the most use of both sub- and supersonic jet aircraft traveling in the stratosphere.

On the producers' side, Japan, the USA, and West Germany will be heavily hit in terms of reduction in production, especially for groundfish, tuna, salmon and sardines. However, the picture is more mixed for producers than for consumers, since many "developing" countries such as Taiwan, Morocco, and Spain will experience significant declines in catch. Depending on technological change and factor mobility, the estimated decline in fishery production cannot easily be translated into employment and value-added changes for these countries.

Recommendations

In addition to commercial and sport fishing analyzed here, the uses of the oceans include navigation, mining, and swimming, to mention just a few. CIAP-type studies should explore the economic consequences of the assumed climatic changes on the various sectors shown in Table 4, developed by Tihansky (1973).

It is recommended that a substantial amount of further interdisciplinary research by economists, population dynamicists, and marine biologists be started immediately to place the various findings on stronger grounds, or at least give them quantitative justification or qualification.

The Bell et al. (1970) baseline projections should be extended, using the actual model, to the year 2025.

Because of our concern that leaving out recreational fishing would seriously bias the losses in living marine resources downward, we made a crude estimate of losses in this area. It is highly recommended that this estimate can be confirmed by obtaining data from other countries and by a more intensive search of the literature.

Finally, we recommend that a much more detailed analysis be done for individual countries to assess the distribution effects of this technological diseconomy on living marine resources. That is, would the rich nations prosper by polluting the stratosphere at the expense of the poor countries who depend on fishing resources for protein, and in some cases (e.g., Iceland and South Korea) for survival?

ACKNOWLEDGMENTS

This report was requested by the University of California at Riverside under a general contract with the U.S. Department of Transportation. It was prepared under the general supervision of Dr. Frederick W. Bell. Valuable consulting services were obtained from Dr. William Schaaf, Fishery Population Dynamicist of the National Marine Fisheries Services' Beaufort Laboratory. We would like to express our especial gratitude to Chris Goodwin, supervisory research assistant, who performed valuable services in coordinating the work of Randy Martin and William Lueck, Marine Biologists, in their extensive research and survey of the biological literature pertaining to the impact of climatic changes on resource productivity. William Gaynor, economist and programmer, helped process the raw data so that we could compute the social costs or gains associated with these changes in the environment. Finally, we want to acknowledge the contribution of more than fifty marine scientists who shared their opinions and data with us in the course of the investigation.

DISCUSSION

(UNIDENTIFIED): It seems to me that economists are prisoners in a world where there are no negative values.

BELL: Prices and quantities are inherently non-negative, and the variables used in the regressions were all positive, such as number of days below 32 degrees Fahrenheit.

(UNIDENTIFIED): Somewhere in this temperature curve there must be an optimum. Couldn't we locate that and make a symmetric distribution of the variations about it? Also, I'd like to point out that this increase in fishery costs with temperature decrease makes an interesting contrast to the ideas of the people concerned with thermal pollution.

APPENDIX A

AN ANALYSIS OF THE RELATION BETWEEN CHANGES IN ENVIRONMENTAL PARAMETERS AND RESOURCE PRODUCTIVITY BY SPECIES GROUP

1. GROUNDFISH

Parameter Analyses

Seawater Temperature (ST)

A 26% decrease in groundfish catch from baseline was predicted for a 1.5 to 1.75°C seawater temperature decrease by 2025. A large part of this figure (20-25%) is due to the difficulties caused by redistribution. For example, the final daytime depth of herring is governed by temperature, cooler temperatures being associated with greater depths (Braun, 1960). One study has shown that catches of herring are dependent on a *rise* in surface temperature (which is anomalous) in connection with a given wind component (Craig, 1960). Obviously, cooling will adversely affect this necessary rise in surface temperature, and consequently the catch. Chase (1955) has analyzed a similar wind and temperature interaction affecting the brood size of haddock. Colton (1972) showed that the distribution of two out of four species of groundfish altered from 1953 to 1967 as seawater temperature decreased.

A small portion (1-6%) of the 26% estimate was based on direct mortality, especially of cod. Cod prefer temperatures of 2-4°C, and the 2°C isotherm is especially critical. Woodhead and Woodhead (1959) discussed the various observations of other authors that cod concentrate at the 2°C isotherm, and suggested a physiological intolerance of temperatures lower than 2°C, except during the summer months. The data of Templeman and Fleming (1956, 1963) suggest that good cod fishing in shallow waters during the summer is dependent on the peculiarities of water warming and the wind. Herring, incidentally, migrate along 5-6°C isotherms (Radakov and Soloviev, 1959), and cooling would shift these isotherms, definitely shifting distribution and possibly causing direct mortality.

The overall 26% decrease was estimated on an ad-hoc basis by considering the historical difference between poor and good groundfish landings, due apparently to problems of redistribution (vertical and horizontal), and adding a minor component for direct mortality, which may not become apparent until the end of the projected time period.

Precipitation (P)

Counted as zero due to (1) lack of information, and (2) intuitive feeling that most groundfish, being either benthic or deepwater (and many are boreal) would not be affected by changes in precipitation or consequent variations in salinity.

Ultraviolet Radiation (UV)

Counted as zero, even though Bodvarsson and Jonsson (1961) showed definitely that strong year-classes of cod emerge, preferably during periods of low solar activity. The UV change was thought not to be significant enough to make an appreciable impact. As Dr. Doug Martin of the Puerto Rico Nuclear Center has pointed out (1973), "Since UV is absorbed by this top 1-2 mm and because the oceans represent such a vast heat sink we are talking about fractions of degree increase over a thousand years. On this basis, such an increase could be safely ignored. The majority of all dissolved or suspended organic compounds are present in the microlayer at the surface film. This *would* be directly available to the increased UV. It is well known that UV can provide the energy to increase rates of chemical reactions and can cause photoalteration of organic compounds. The increase in UV at the microlayer could cause an increase in rates of flowthrough of chemical reactions without a change in quantities of compound in any given pool; an increase in compounds of one type with a resultant decrease in some others, or some combination of the two for the whole system. However, since our analytical procedures are not good enough for us to say with certainty what is present in this microlayer for sure, how much is there, or how dependent various ecosystems are on this as an energy source, we cannot make any predictions." We have relied upon this analysis for all the species groups.

Wind Velocity (WV)

Counted as a 5% detrimental effect due to the negative effect on upwelling, and the indication in the literature that wind strength, together with temperature trends, is an important indicator of good catches of some species (Chase, 1955; Craig, 1960; Templeman and Fleming, 1963).

Net Effect on Sustainable Yield

Combining the figures for temperature and wind, we get a net impact of -31% by the year 2025. By far the largest component of this is due to redistribution caused by lowered temperature. We may have overestimated this factor, since the details of the effects of redistribution on various aspects of the fishery were not completely analyzed; on the other hand, we may have underestimated mortality, considering that herring and cod concentrate at isotherms (cod: 2°C; herring: 5°C) at which they are "flirting with danger", since temperatures lower than those at the isotherms may cause heavy mortality.

Yves (1964) provides our strongest support for placing heavy emphasis on the distributional effect with the following statement: "Most species of groundfish undergo seasonal changes in horizontal and vertical distribution that have direct effects on the fishery. The environment (mainly temperature) brings about or accompanies these changes." In essence, the redistribution will gradually lower the catch per trawl for world fishing fleets. (For all the species groups, the bibliography contains all the references we used to assess the environmental impact of changes in parameters shown in Table 5.)

2. TUNA

Parameter Analyses

Seawater Temperature

Of the voluminous tuna literature, papers dealing with skipjack, yellowfin, albacore, and bluefin tunas were scrutinized, since these four species are the most important commercial ones. Of special interest were the data of Seckel (1972) and Seckel and Austin (1962) showing that the landings of skipjack tuna off Hawaii were related to the time of the winter reversal from cooling to warming of surface waters. Early reversals were predictive of better-than-average landings, whereas late reversals heralded poor catches. The strongest case of relationship of the distribution of a tuna species with seawater temperature has been made for albacore (Alverson, 1961; Inoue, 1962; and Johnson, 1962). Slight cooling of Pacific coast waters will shift albacore populations to the south; Inoue (1962) reported that southward shifting of the spring migration of albacore off Japan due to abnormally cold water intruding from the north resulted in poor summer catches of albacore.

Yellowfin is the warmest-water tuna, preferring temperatures of 21.5-28°C. 80% of the tuna catch in the mid-Atlantic grounds is yellowfin (Hatheway, 1961).

Bluefin tuna are reported to occur off the northwest Atlantic slope where feeding grounds are rich due to mixing of deep and surface waters (Mather and Bartlett, 1962). Surface temperature of "bluefin water" ranged from 9.5° to 17.7°C. With these and other data in mind, we concluded that a 1-2°C temperature decrease between 1990 and 2025 could cause significant redistribution of three of the four most commercially important species of tuna, e.g., albacore, bluefin, and skipjack. This conclusion was based on the data of the effects of cooling off Hawaii, Japan, and the northwestern coast of North America. Yellowfin would probably not be affected, given their tropical distribution and rather wide temperature tolerance range.

Thus, counting the effect of temperature on yellowfin as zero, and the effects on bluefin, albacore, and skipjack as 20-25% each, we obtained an overall reduction of 15% due to declining temperature. (The 20-25% figure was a rough estimate based on the differences between good and poor landings of the three species considered (FAO, 1969).)

Precipitation

Counted as zero due to lack of information and to intuitive feeling that its effect would be negligible in the open ocean.

UV Radiation

Counted as zero due to insignificant increase in UV.

Wind Velocity

Since tuna concentrate in areas of rich nutrients (verified for bluefin: see Mather and Bartlett (1962)), various decreases in wind velocity were counted as a 5% negative effect due to the adverse effect on upwelling.

Net Effect on Sustainable Yield

The combined effect of temperature and wind velocity was a decrease in catch of 20%. It should be noted that the conclusion regarding temperature is directly counter to statements by researchers at the Southwest Fisheries Center (Lamarz, 1973) that cooler temperatures may increase fish stocks for non-temperature-sensitive species, but the latter refers to a possible direct effect, whereas our estimate is based on a more indirect effect due to redistribution.

The possibility of an overestimate of the effect of temperature is counteracted by the possibility of an underestimate for wind velocity. The detrimental effect of decreased winds may be much greater than we think; Dr. Robert Owen of the SFC feels that a 0-15% reduction in the potential yield of the tuna fishery might occur for a 2-3% reduction in trade winds (Owen, 1973).

3. SALMON

Parameter Analyses

Seawater Temperature

Much research on the eggs, embryos, and larvae of various salmon species indicates an extreme temperature susceptibility (Bailey and Evans, 1972; Combs, 1965; Combs and Burrows, 1957; Efimov, 1962; Johnson and Brice, 1953; Kazakoz, 1971; and Reingold, 1968). The optimum incubation temperatures for most species are above 4.5°C; temperatures lower than this begin causing mortality, especially during early gastrula stages, the period of highest temperature sensitivity (Efimov, 1962). Assuming that the 1.75°C decrease in seawater temperature would also occur in the freshwater streams where salmon spawn, it was calculated that the yield of salmon could be decreased by as much as 50% by 2025 due to mortality during egg and early developmental stages. The suggestion of Dr. Anthony Novotny (1973), that a 1.75°C temperature decrease would *increase* the fishery because the population would shift southward is arguable, since salmon return to their areas of birth when preparing to reproduce (see, e.g., Hasler (1966)).

Precipitation

The increase in precipitation proposed for the latitude bands of the major salmon stocks was assumed to have a beneficial effect because it would increase the available spawning area (Glude, 1973). This effect was estimated to be 15%, due not only to increased area but increased nutrient flow, leaching, etc. Decreased precipitation was assumed to have a stronger negative effect due to the obvious problem of drying out of spawning areas. The overall negative effect was estimated at 20%.

UV Radiation

As with all other fisheries, a 10% increase was counted as having a zero effect. Bodvarsson and Jonsson (1961) noticed that strong year classes of salmon emerged during periods of low solar activity, but the significance of this in terms of change in UV radiation is not known.

Wind Velocity

Decreased wind velocity was counted as having a zero effect, since it was assumed not to affect spawning areas.

Net Impact on Sustainable Yield

Three cases were considered: With increased precipitation, a net detrimental effect of 35% was predicted; with no change in precipitation, a net detrimental effect of 50% was calculated; and with decreased precipitation a 70% detrimental effect was foreseen. The last case (70% decrease in yield) is the gloomiest prediction for any fishery, but the problems of decreased temperature *and* decreased precipitation greatly exacerbate the precarious situation in salmon spawning grounds.

4. HALIBUT

Parameter Analyses

Seawater Temperature

A cooling of seawater would theoretically cause halibut to move south from the Bering Sea to the Gulf of Alaska where 90-95% of the catch of Pacific halibut is located (Skud, 1973). The potential stock in the Bering Sea is estimated to be four million pounds. The total northeast Pacific stock is 76 million pounds; thus, the catch rate may rise as much as 5.26% (four million divided by 76 million).

For the first ten years, it was estimated that gradual movements southward would cause a 1% increase in mortality. Thus, the net effect on the Pacific halibut would be +5.25% – 1%, or +4.25%, for 1990-2000.

The only information available on the Atlantic halibut was that a resource potential of 37 million pounds exists. Thus, the total halibut resource is 113 million pounds worldwide. Assuming that temperature would not affect Atlantic halibut, the net effect worldwide for 1990-2000 would be a 2.85% increase in yield (the Pacific stock is 2/3 of the total; 2/3 × 4.26% = 2.85%); and the effect for 2001-2025 would be 3.52% (2/3 of 5.26%). The overall impact for 1990-2025 would thus be +3.33%.

Precipitation

The effect of increased or decreased precipitation on a benthic organism such as the halibut was counted as zero.

UV Radiation

Counted as zero; would have practically no direct effect on a bottom-dweller.

Wind Velocity

Also counted as zero because a change would have little or no effect on a bottom-dweller.

Net Impact on Sustainable Yield

The predicted beneficial impact of 3.33% (due entirely to a temperature effect) was the only case of a beneficial impact predicted for a finfish group. The two main reasons for this are the following;

1. "Halibut" as a group consists of only two species of fish, the Pacific and Atlantic halibut. These are unusual fish which live completely on the bottom in the cold northern waters, and cooling would cause a redistribution which would make the fish easier to catch. In other finfish groups, many species make up the groups, and none are as unusual in their distribution or habits as halibut. Halibut are a unique case, and are exceptions to the generalizations that apply to the other groups.
2. The prediction was based largely on a personal communication, and thus may be less firmly founded than the other predictions. Little information on the effects of our specific environmental variables on the halibut exists in the literature.

5. SARDINES

Parameter Analyses

Seawater Temperature

Lasker (1964) observed that the maximum development of Pacific sardine embryos and larvae occurred at 16-17°C. Below 13°C development failed. Bogdanov (1968) observed that lower-than-average spring temperatures resulted in low survival rates of sardines. Murphy

(1961) stated that a temperature difference approximately equal to that between spring and fall temperatures (warmest to coldest) in the California current resulted in a ten-fold variation in survival of larval sardines. Taking these and other references (Ahlstrom, 1943; Overko, 1962; Vincent and Kurc, 1969) into account, we predicted a 25% decrease in sardine yield function by 2025 for a 1.25°C decrease. This estimate was based largely on data for the Pacific sardine, which has an optimum range of 12-16°C but a critical threshold of 13°C for development, as mentioned above.

Precipitation

All cases of precipitation change were counted as zero effects due to a lack of information, and the presumed minimal effect of precipitation on salinity in the open ocean.

UV Radiation

No possible effect could be visualized, so it was counted as zero.

Wind Velocity

The importance of nutrients furnished by upwelling, which in turn is dependent on winds, led us to estimate that a decrease of approximately 10% in wind velocity could account for a 5% decrease in sardine yield by 2025. In certain critical areas, such as the western coast of South America, this may be a gross underestimate, due to the almost complete dependence of fish stocks on the wind *El Niño*.

Net Impact on Sustainable Yield

Combining the temperature and wind components, we obtain a net impact of -30% on the sardine yield. We believe this figure is in the realm of possibility even if the effect of decreasing temperature has been overestimated, because the wind component was, if anything, underestimated.

6. SHRIMP

Parameter Analyses

Seawater Temperature

Due to the large number of species which comprise the world shrimp catch, no indicator species was chosen. Attention was focused on the family Penaeidae in general. Hedgpeth and Gonor (1969) state that small oceanic temperature fluctuations may alter the distribution and abundance of species, especially those that occur in large populations (as shrimp do). Although Dow (1964) found that the catch of *Pandalus borealis* in the Boothbay Harbor area fell to essentially zero after the high temperatures of 1953, and concluded that spawning is depressed by high temperatures, both Olsen (1973) and Raye (1973) state that a temperature drop would slow shrimp growth rates. Raye specifically mentioned the brown shrimp *Penaeus aztecus*. Crozier (1973) offers a third view – that shrimp would acclimate to a gradual temperature change, and thus it would have little effect. In consideration of these views, and realizing that a temperature decrease is predicted for the chosen case, the conclusion arrived at was that a decrease of 1% due to temperature effects could be expected.

Precipitation

Because of nutrient enrichment of estuaries from land drainage, the effects of a change in precipitation would probably be rather large. Olson (1973) stated that shrimp are affected by nutrient flow. Direct salinity effects also play a role. Parker (1955) observed that the *Penaeus setiferus* population in a Texas estuary decreased during a Texas drought in which the salinity of the estuary often exceeded that of open sea water, fluctuating between 25 and 40%. Reid (1955, 1956) found fewer brown shrimp (*Penaeus aztecus*) in an estuary in which salinity had approximately doubled over a one-year period. Copeland (1966) states that peak migration of postlarval *Penaeid* shrimp through Arkansas Pass Inlet, Texas, corresponds to times of high river flow in the spring and fall. He also showed that an increase or decrease in precipitation (rainfall) is followed by a similar fluctuation in shrimp catch. From an analysis of these data, precipitation increase was assigned an effect of +7.0%, no precipitation change a zero effect, and precipitation decrease an effect of -19.0%.

UV Radiation

Although Sick et al. (1973) showed that juvenile shrimp can be stimulated to consume more food when illumination intensity is increased, there is no basis for a quantitative prediction of this effect. Furthermore, Crozier (1973), Frolander (1973), and Raye (1973) all agree that ultraviolet penetration into seawater is so small that the predicted increases would have little effect on organisms. Therefore, a negligible effect would seem to be a reasonable prediction of the impact of an ultraviolet-radiation increase.

Wind Velocity

Although wind-velocity alterations may affect currents and thus larval distribution and nutrient mixing, no information was located which allowed any prediction to be made. It has been assumed that a simple velocity-only increase would have a negligible impact.

Net Impact on Sustainable Yield

The following tabulation summarizes the effects of individual parameters and also total impact on sustainable yield.

parameter	effect, % change Case A	Case B	Case C
temperature	-1.0	-1.0	-1.0
precipitation	+7.0	0	-19.0
UV radiation	0	0	0
wind velocity	0	0	0
total impacts	+6.0%	-1.0	-20.0%

The total impacts represent the variation from baseline projections, assuming no change in parameters.

7. LOBSTERS

Parameter Analyses

Seawater Temperature

The representative lobster species for the purposes of this study is *Homarus americanus*, the American lobster. The effect of temperature variations on lobster catch is discussed by Dow (1969) and McLeese and Wilder (1958). Dow relates increased catch at higher temperatures to an increased molting (growth) rate in *H. americanus* (shorter length of instars). McLeese and Wilder stress increased activity of the species as temperature increases as playing a role in increased catches. No doubt both factors are involved. Flowers and Saila (1972) analyzed several equations relating such factors as previous catches and temperature data to present-year catch. However, due to the unavailability of certain input data for these equations, they could not be employed in predictions of temperature effects on catch for the 35-year period 1990-2025. It seems that lobsters should generally be less subject to drastic effects due to temperature, since they have a significant rate of locomotion which allows at least short-term escape to deeper and more thermally stable waters. Also, Crozier (1973) has indicated that many marine species would be able to compensate for small environmental changes distributed over time. For the purposes of this study a value of 0.2% yield reduction by 2025 was arrived at, an effect due to slower growth rate of lobster resulting from the predicted general decrease in worldwide temperature.

Precipitation

The literature made little mention of the relationship between *H. americanus* and salinity variations; however, Copeland (1966) mentions that the blue crab's reproductive cycle is closely tied to salinity. Even if the lobster's is too, it should be noted that lobster adults and, to a certain degree, larvae are capable of locomotion, and can thus escape from suboptimal conditions. Also, the predicted maximum precipitation variations, in the latitude band 20-40° north, are +12.5% and -12.5%. On a yearly basis, this is only a 0.36% increase (decrease) per year. It seems quite possible that over the period 1990-2025 nongenetic adaptation to such a factor could occur. For these reasons, and because lobsters are to a degree less dependent on estuaries than some other organisms, a negligible effect was ascribed to salinity, and thus precipitation, changes.

UV Radiation

Both Frolander (1973) and Raye (1973) state that ultraviolet penetration into ocean water is very small, and that the predicted radiation increase would probably have a negligible effect.

Wind Velocity

Due to the lack of available information concerning the possible effects of wind-velocity changes and subsequent current alterations on lobsters, either directly or through food-chain alteration, no predictions could be made. A negligible effect was therefore ascribed to this parameter.

Net Impact on Sustainable Yield

The total impacts of the various parameters on sustainable yield, and a summary of the individual effects, are given in the following table:

parameter	effect, % change Case A	Case B	Case C
temperature	-0.2	-0.2	-0.2
precipitation	0	0	0
UV radiation	0	0	0
wind velocity	0	0	0
total impacts	-0.2%	-0.2%	-0.2%

8. CRABS

Parameter Analyses

Seawater Temperature

The effects of seawater temperature variations on crabs can be expected to be similar to those discussed in the section on lobsters. Due to the relatively short time span involved, and since crabs and lobsters are similar in that they are highly motile crustaceans living in similar environments, the effect of temperature was assumed to be not significantly different for crabs. As with lobsters, a decrease of 0.2% is predicted.

Precipitation

It is here assumed that the effect of altered salinity on crabs will also not vary significantly from that on lobsters. Copeland (1966) found that the blue crab, *Callinectes sapidus*, decreased in numbers in Mesquite Bay, Texas, during the Texas drought. But Parker (1955) found that *C. clanae* numbers increased in Arkansas Bay during roughly the same time. Also, Reid (1955, 1956) found that blue-crab numbers increased in a Texas estuary in which salinity values doubled because

of the influx of ocean water through a newly opened pass. From this, it seems that although different crab species may vary in population size, variations in one might well be offset by reverse variations in others, resulting in essentially no effect. (Also, crabs are often regarded as rather hardy animals from an environmental viewpoint.) The effect of salinity variations due to precipitation changes is thus concluded to be negligible, as for lobsters.

UV Radiation

The reader should refer to the discussion of UV effects on lobsters and other fish such as groundfish. A negligible effect is assumed due to lack of penetration of ultraviolet light into ocean water.

Wind Velocity

Reference should be made to the discussion of the effects of this parameter on lobsters, which for the same reasons is here assumed to be negligible.

Net Impact on Sustained Yield

Following is a tabular summary of individual effects for each case, showing also total impacts:

	effect, % change		
parameter	Case A	Case B	Case C
temperature	-0.2	-0.2	-0.2
precipitation	0	0	0
UV radiation	0	0	0
wind velocity	0	0	0
total impacts	-0.2%	-0.2%	-0.2%

The total impacts represent the final change in sustainable yield over the baseline by the year 2025.

9. CLAMS

Parameter Analyses

Seawater Temperature

Gulland (1971) breaks down the world clam catch by species. From this source it was found that there are many species involved, with no one species accounting for a high percentage of the total catch, so we did not select an indicator species. Temperature-related effects on clam catch should be similar to the effects on oysters, since both are filter-feeding, primarily estuarine, essentially sessile organisms. The effect is more fully discussed in the section on oysters; it was determined that temperature variation would have a negligible impact. (Even the largest projected temperature variation is only -2.0°C for the 35-year period 1990-2025.) Also, while Hedgpeth and Gonor (1969) state that small oceanic temperature changes may influence population size and species distribution of many marine animals, they quote examples of the often quite large temperature variations which are apparently tolerated by estuarine organisms. Thus, the impact of the predicted temperature changes on the clam biomass of the world is expected to be negligible.

Precipitation

Again, it is reasonable to assume that the effect of a parametric change on clams will be similar to that determined for oysters. However, Reid (1955, 1956), in two studies of vertebrate and invertebrate changes in a Texas estuary following the introduction of high-salinity waters by a cut at Rollover Pass, found two bivalve species apparently existed in the same numbers before and after the salinity increase. The mussel *Brachidontes recurvus* and the pelecypod *Macoma mitchelli* were found, even after the change in salinity, to have increased approximately twofold throughout the bay. Goodwin (1973), while stating that embryos of *Panope generosa* require a rather limited salinity range for development, also states that adults and juveniles probably have wider tolerance limits. He also points out that the coot clam, *Mulinia lateralis*, a clam sympatric with *P. generosa*, has wider salinity tolerance. Thus, for precipitation increase an increase in production would be seen, since the organisms can tolerate the salinity and make use of whatever nutrient enrichment may occur from increased freshwater influx; a 7.5% increase is projected. For no precipitation change no effects are predicted. A precipitation decrease would probably have a small negative effect on clam biomass, however, say 5%, for the same reasons cited for oysters elsewhere in this paper. However, the effect would probably be rather small relative to that on oysters, given the apparently wider salinity tolerance of clams.

UV Radiation

See the discussion of this parameter for oysters and groundfish (negligible effect).

Wind Velocity

See the discussion of this parameter for oysters (negligible effect).

Net Impacts on Sustainable Yield

Negligible effects were assigned to all parameters except for precipitation; the latter thus determines the final impact. Summarizing the effects of each parameter:

	effect, % change		
parameter	Case A	Case B	Case C
seawater temp.	0	0	0
precipitation	+7.5	0	-5
UV radiation	0	0	0
wind velocity	0	0	0
total impacts	+7.5%	0%	-5%

10. SCALLOPS

Parameter Analyses

Due to the insufficient time available for this study, the effects of climate changes on scallops were assumed to be not significantly different from those on oysters, and the reader is referred to that discussion. This seems to be a reasonable assumption, since both scallops and clams are bivalves (pelecypods) which are estuarine, benthic, and filter feeders. It is true that scallops can locomote somewhat, but they cannot move over significant distances and thus are also essentially sessile with regard to the environment.

Net Impacts on Sustainable Yield

	effect, % change		
parameter	Case A	Case B	Case C
seawater temp.	0	0	0
precipitation	+5	0	-5
UV radiation	0	0	0
wind velocity	0	0	0
total impacts	+5%	0%	-5%

The total impacts reflect the effect on sustainable yield at the end of the 35-year period 1990-2025.

11. OYSTERS

Parameter Analyses

Seawater Temperature

According to Gulland (1971), approximately 46.01% of the world commercial oyster catch is comprised of *Crassostrea virginica*, which was adopted as the identicator of this study. *C. virginica* is found primarily in the latitude band 20-40° north. For this latitude band, the assumed temperature change is -1.0°C over the 35-year period 1990-2025. As Collier (1965) has pointed out, within the estuarine environment, where most oysters are found, seawater temperature follows air temperature closely. While it has been demonstrated that a lower temperature may decrease mortality in shallow waters (Collier, 1965), Crozier (1973) has indicated that estuarine organisms would acclimate to a gradual temperature change, with no measurable effect on population structure. Given an incremental temperature decrease of 0.028°C per year, it would seem that *C. virginica* would show little change in total biomass. Therefore, for the purposes of this study, it is considered that the impact of temperature on the world's oyster stocks will be negligible.

Precipitation

For the latitude band 20-40° north, the assumed precipitation changes over the period 1990-2025 are: increased precipitation, +12.5%; unchanged precipitation, no change; decreased precipitation, -12.5%. It was assumed that for no change there will be no effect on oysters. Concerning salinity variations caused by precipitation changes and the effect on *C. virginica*, Copeland (1966) mentions that many oyster parasites can tolerate only relatively high salinity conditions. Copeland also mentions that a parasitic fungus of oysters, *Dermocrystidium marinum*, may be controlled by fresh-water influx. However, Dawson (1955) showed that *D. marinum* infections may be rather heavy even under low-salinity conditions. Parker (1955) reported that during a drought in Texas, with accompanying high-salinity conditions in the estuaries, the oyster population seemed to shift toward more *Ostrea equestris* and fewer *C. virginica* (*O. equestris* being a less desirable, high-salinity oyster). It should be pointed out that the drought conditions experienced involved a larger precipitation decrease than the -12.5% assumed for this study. Amemiya (1926) states that the most favorable salinities for *C. virginica* larval development are in the range 22-33 parts per thousand, a rather wide range. Concerning the direct effect of salinity on oysters, Glude (1973) has indicated that little effect will be noted for the variations in precipitation. Olsen (1973) has pointed out, however, that increased nutrient flow due to increased precipitation would increase productivity and perhaps stimulate oyster growth. (The converse should also be true.) Thus, for a precipitation increase of 12.5%, the effect on oyster yield would be positive due to increased phytoplankton and growth from nutrient influx, and decreased mortality from high-salinity parasites. Conversely, a decrease of 12.5% would have a negative effect. Due to the lack of quantitative studies in this area, it was difficult to arrive at a percentage biomass increase and decrease, but +5% for increased precipitation and -5% for decreased precipitation seem to be justified.

UV Radiation

Little data concerning ultraviolet radiation and the effect of an increase in it on shellfish was found except the general analysis under groundfish. Crozier (1973) has stated that ultraviolet penetration into seawater is small and would probably have little effect, either directly on individuals or indirectly by affecting the food chain. It has been assumed for this study that UV radiation levels will have a negligible effect on the oyster population.

Wind Velocity

No information correlating wind velocity with effect on oysters, through possible alterations of current patterns and velocities, was found. Thus, this parameter was assumed to have no effect of significant proportions.

Net Impact on Sustainable Yield

In the three cases considered, all parameters, and thus all effects on the *C. virginica* indicator species population, are the same, except for precipitation. Since

negligible effects were assigned to all parameters except precipitation, the net impact on sustainable yield predictions are due to precipitation. Summarizing the individual impacts for each case gives:

	effect, % change		
parameter	Case A	Case B	Case C
temperature	0	0	0
precipitation	+5	0	-5
UV radiation	0	0	0
wind veolcity	0	0	0
total impacts	+5%	0%	-5%

These figures reflect the effect at the end of the 35-year period 1990-2025.

12. OTHER FOOD FISH

Parameter Analyses

Temperature

Much miscellaneous data was collected on various groups of fishes not included in other finfish categories to come up with an estimate of the effect of temperature. For example, trout literature was considered (Hazzard, 1933; Timoshina, 1972; Seegrist and Gard, 1972), as well as saury literature (Norikov, 1972; Sokolovskiy, 1972) and references to groups of fishes (Hubbs, 1948; Needham and Jones, 1959; Schmidt, 1959; Templeman, 1965; Uda, 1961). Also, general references on the effects of temperature (Brett, 1956) were read. In addition, the various effects on other species groups (groundfish, -26%, tuna -15%, fish meal, -5%, etc.) were all averaged to determine the net effect. Finally, an admittedly tenuous estimate of a negative 10% effect was used.

Precipitation

Counted as zero on the basis of previous species analysis and composition of category.

UV Radiation

Counted as zero, as argued under groundfish.

Wind Velocity

Many of the other food-fish species are dependent on upwelling to provide a source of food, so a negative 5% effect of decreased wind velocity was arrived at.

13. FISH MEAL

Parameter Analyses

Seawater Temperature

A drop of 1.5°C at latitudes 40-60° would adversely affect many species caught for fish meal which are dependent on estuaries for the larval stage of the life cycle. For example, Lewis (1965, 1966) and Lewis and Hettler (1968) studied the effects of various experimental temperatures on larval menhaden after it became known that menhaden were absent from plankton net tows at temperatures less than 3°C. Basically, Lewis' group discovered that menhaden would suffer mass mortalities if water temperature dropped below 3°C for several days, or if it chilled rapidly to 4.5°C. Lowered salinity exacerbated this effect.

In addition to the above, Fore and Baxter (1972) cited a statistical relationship between falling water temperature at night and increased catch of larvae ($r = 0.54$). Westman and Nigrelli (1955) indicated that mass mortalities of menhaden off the eastern coast of the United States were due to low temperature.

Thus, primarily because of direct mortality effects in the estuaries, as well as a slight possible effect on adults in the open ocean, a 5% negative effect was estimated.

Precipitation

The indirect effect of precipitation on salinity was assumed to be zero, since most species caught as fish meal are relatively euryhaline.

UV Radiation

Counted as zero, as argued under groundfish.

Wind Velocity

Due to the dependence of species of fish used as meal on nutrients for feeding, the adverse effect on upwelling of decreased wind velocity was counted as 5%.

Net Impact on Sustainable Yield

The overall effect on fish meal was estimated to be a 10% detrimental impact. This may be an underestimate if anything, since this species group as a whole is extremely vulnerable to environmental vagaries during the larval stage of the life cycle, and massive kills of the adults can be caused by a variety of factors.

14. RECREATIONAL FISHING

Parameter Analyses

Seawater Temperature

An estimate of a 5% detrimental effect was used, on the basis of the analyses of related commercial fish and fish that are used for both sports and commercial purposes.

Precipitation

Since Hanson (1972) showed that pileworms could tolerate a salinity high enough to cause collapse of the

sport fishery, we estimated that decreased precipitation, which would increase salinity, could have a very slight negative effect. We did not believe that the increase in salinity would reach the levels reported by Hanson, so we estimated the effect at -1%.

We also estimated a -1% effect for increased precipitation, due to the detrimental effect of flooding on the many sport species dependent on freshwater areas (e.g., Seegrist and Gard (1972)) as mentioned under "other food fish".

UV Radiation

Counted as zero, as argued under groundfish.

Wind Velocity

An effect of -5% was used because of the negative effect on upwelling.

Net Impact on Sustainable Yield

Three changes in yield were projected: -11% with increased precipitation, -10% with no change in precipitation, and -11% with decreased precipitation. Our temperature estimate is based largely on the effects of temperature on similar types of fish in other groups. Moore and Frisbee (1972) found no correlation between water temperature and the number of fish caught per man-hour of effort in a winter sport fishery in Maryland, but this is an extremely isolated example, of course, useless for worldwide extrapolation.

APPENDIX B

GROWTH PROJECTIONS OF GROSS NATIONAL PRODUCT PER CAPITA

The CIAP rates of growth are medium estimates supplied for use in the monograph studies. The rates of growth used in the Bell et al. (1970) study to year 2000 are taken from projections of a United States Department of Agriculture working paper, "World Population and Income by Countries and Projection to 1980". Extrapolations beyond 1980 to the year 2000 are based upon the same rate as 1965-1980. Extension of the Bell et al. study to 2025 took into consideration the CIAP projection (medium) for part of the second period, 2000-2025.

	1970-1990		1990-2025	
Area	CIAP %	USDA %	CIAP %	USDA %
Asia	2.7	2.6	2.2	2.4
Europe (less USSR)	3.2	3.7	2.5	3.0
Oceania	2.3	2.2	2.3	2.2
North America	2.5	2.6	1.6	2.1
Africa	2.7	2.3	2.6	2.3
Latin America	1.6	2.0	1.4	2.0
USSR	4.6	4.4	2.8	3.0
Japan	4.0	6.5	3.0	5.0
China	3.6	2.2	3.7	2.2
USA	2.6	2.7	2.0	2.5
Brazil	5.0	4.0	3.0	4.0
West Germany	3.5	3.6	2.4	3.0
United Kingdom	1.5	2.4	1.5	2.4
France	3.0	3.7	2.4	3.0
World	2.3	2.6	1.7	2.0

Stanley, J.G. and P.J. Colby (1971), "Effects of temperature on electrolyte balance and osmoregulation in the alewife *(Alosa pseudoharengus)* in fresh and sea water," Trans. Amer. Fish. Soc. **100**, 624-638.

Templeman, W.T. (1965), "Mass mortalities of marine fishes in the Newfoundland area presumably due to low temperature," Intern. Commn. N.W. Atl. Fish. Spec. Publ. **6**, 137-148.

Timoshina, L.A. (1972), "Embryonal development of rainbow trout *Salmo gairdneri irrideus* Gibb. at different temperatures," J. Icthyol. **12**, 471-478.

Uda, M. (1961), "Fisheries oceanography in Japan, especially on the principles of fish distribution, concentration, dispersal, and fluctuation," Calif. Coop. Oceanic Fish. Invest. Rept. **8**, 25-31.

13. Fish Meal

Fore, P.L. and K.N. Baxter (1972), "Diel fluctuations in the catch of larval Gulf menhaden, *Brevoortia patronus*, at Galveston Entrance, Texas," Trans. Amer. Fish. Soc. **101**, 729-732.

Henry, K.A. (1971), "Atlantic Menhaden *(Brevoortia tyrannus)* Resource and Fishery – Analysis of Decline," Technical Report NMFS SSRF-642, National Oceanic and Atmospheric Administration.

June, F.C. and J.L. Chamberlin (1959), "The role of the estuary in the life history and biology of Atlantic menhaden," in *Proceedings of the Gulf and Caribbean Fisheries Institute, 11th Annual Session, 1958*, 41-45.

Kramer, D. and J.R. Zweifel (1970), "Growth of anchovy larvae (*Engraulis mordax* Girard) in the laboratory as influenced by temperature," Calif. Coop. Oceanic Fish. Invest. Rept. **14**, 84-87.

Lewis, R.M. (1965), "The effect of minimum temperature on the survival of larval Atlantic menhaden, *Brevoortia tyrannus*," Trans. Amer. Fish. Soc. **94**, 409-412.

Lewis, R.M. (1966), "Effects of salinity and temperature on survival and development of larval Atlantic menhaden, *Brevoortia tyrannus*," Trans. Amer. Fish. Soc. **95**, 423-426.

Lewis, R.M. and W.F. Hettler, Jr. (1968), "Effect of temperature and salinity on the survival of young Atlantic menhaden, *Brevoortia tyrannus*," Trans. Amer. Fish. Soc. **97**, 344-349.

Reintjes, J.W. and A.L. Pacheco (1966), "The relation of menhaden to estuaries," Amer. Fish. Soc. Spec. Publ. **3**, 50-58.

Westman, J.R. and R.F. Nigrelli (1955), "Preliminary studies of menhaden and their mass mortalities in Long Island and New Jersey waters," J. N.Y. Fish Game **2**, 142-153.

14. Recreational Fishing

Hanson, J.A. (1972), "Tolerance of high salinity by the pileworm, *Neanthes succinea*, from the Salton Sea, California," Calif. Fish Game **58**, 152-154.

Moore, C.J. and C.M. Frisbee (1972), "A winter sport fishing survey in a warm water discharge of a stream electric station on the Patuxent River, Maryland," Chesapeake Science **13**, 110-115.

BIBLIOGRAPHY AND REFERENCES

A. General

Adams, Robert (1973), *The Demand for Recreation in the U.S.*, U.S. Department of Interior.

Bell, F.W., R. Fullenbaum, E. Carlson, F. Waugh, R. Kinashita, and D. Nash (1970), "The Future of the World's Fishery Resources: Forecasts of Demand, Supply and Prices to the Year 2000 with a Discussion of Implications for Public Policy," File Manuscript No. 65-1, National Marine Fisheries Service, U.S. Department of Commerce, 289 pp.

Bell, F., E. Carlson, W. Schaaf, and G. Hershorn (1972), "The Extent of Capitalization in United States Fisheries," File Manuscript No. 125, National Marine Fisheries Service, U.S. Department of Commerce, 419 pp.

Bell, F. (1972), "Technological externalities and common property resources an empirical study of the U.S. northern lobster fishery," J. Polit. Econ. **80**, 148-58.

Beverton, R. and S. Holt (1957), *On the Dynamics of Exploited Fish Populations*, Her Majesty's Stationery Office, Vol. XIX, 533 pp.

Carlson, E. (1969), "Bioeconomic Model of a Fishery," File Manuscript No. 12, National Marine Fisheries Service, U.S. Department of Commerce, 35 pp.

Carlson, E. (1973), "Production from the Sea," Technical Report NMFS CIRC-371, National Oceanic and Atmospheric Administration, 72-91.

CIAP (1971), Volumes 2 and 6 of the CIAP Monograph Series, U.S. Department of Transportation. NOTE: At present, these monographs exist only in an early draft form. They will be publicly available after completion in September 1974.

Cicchetti, Charles J., Joseph Seneca, and Paul Davidson (1969), *The Demand and Supply of Outdoor Recreation*, Bureau of Outdoor Recreation of the U.S. Department of Interior under contract to the Bureau of Economic Research, Rutgers – The State University, New Jersey, 301.

d'Arge, Ralph (1973), personal communication (University of California, Riverside).

FAO (1955), *Yearbook of Fishery Statistics*, U.N. Food and Agricultural Organization, Rome.

FAO (1969), *The Prospects for World Fishery Development in 1975 and 1985*, Food and Agricultural Organization Indicative World Plan.

FAO (1970), *Yearbook of Fishery Statistics*, U.N. Food and Agricultural Organization, Rome.

Gulland, John (1971), *The Fish Resources of the Ocean*, Fishery News (Books) Ltd. for the FAO. 255 pp.

Martin, Doug (1973), personal communication (Southwest Fisheries Center, U.S. Dept. of Commerce, La Jolla, California).

O'Brien, James (1973), personal communication (Florida State University).

Olson, F. and F. Bell (1974), "Apples, oranges and fish," to be published in Marine Fisheries Review, National Marine Fisheries Service, U.S. Department of Commerce.

Pella, Jerome and Patrick Tomlinson (1969), "A Generalized Stock Production Model," Inter-American Tropical Tuna Commission, Bulletin **13** (3), 421-458.

Penn, E. (1973), "Price spreads of fish products among producers and distributors," Marine Fish. Rev. **35** (7), U.S. Department of Commerce, 1-9.

Schaefer, Milner B. (1954), "Some aspects of the dynamics of populations important to the management of the commercial marine fisheries," Inter-american Tropical Tuna Commission, Bulletins 1 and 2, 1-56.

Schaefer, M. (1965), "The potential harvest from the sea," Am. Fish. Soc. Trans. **94**, 123-128.

Tabata, Susumu (1961), "Temporal changes of salinity, temperature, and dissolved oxygen content of the water at Station 'P' in the Northeast Pacific Ocean, and some of their determining factors," J. Fish. Res. Bd. Can. **18**, 1073-1124.

Tihansky, Dennis P. (1973), "An economic assessment of marine water pollution damages," in the proceedings of the International Association for Pollution Control, Third Annual Conference (Montreal), 41.

USDA (1968), "World Population and Income by Countries, 1950-65 and Projections to 1980," (working paper), U.S. Department of Agriculture Economic Research Service.

USDI (1970), *National Survey of Fishing and Hunting*, U.S. Department of Interior, Bureau of Outdoor Recreation.

Wilson R. and M. Pfetsch (1973), "Executive Summary of the Importance of Marine Recreational Fisheries," File Manuscript No. 157, National Marine Fisheries Service, U.S. Department of Commerce, 4 pp.

Wilson, Robert (1973), personal communication (U.S. Department of the Interior).

B. Species Groups

1. Groundfish

Bodvarsson, G. and J. Jonsson (1961), "Fluctuations in marine populations in Icelandic waters," Nature **192**, 768-769.

Braun, V.M. (1960), "Seasonal and diurnal vertical distribution of herring (*Clupea harengus* L.) in Passamaquoddy Bay, N.B.," J. Fish. Res. Bd. Can. **17**, 699-711.

Chase, J. (1955), "Winds and temperatures in relation to the brood-strength of Georges Bank haddock," in Fifth Annual Report of the International Commission for the Northwest Atlantic Fisheries.

Colton, J.B., Jr. (1972), "Temperature trends and the distribution of groundfish in continental shelf waters, Nova Scotia to Long Island," U.S. Nat. Mar. Fish. Serv. Fish. Bull. **70**, 637-657.

Craig, R.E. (1960), "A note on the dependence of catches on temperature and wind in the Buchan pre-spawning herring fishery," J. Conseil Inter. Explor. Mer **25**, 185-190.

Harding, D. (1967), "Larval survival of the plaice in the North Sea and the Irish Sea," Rep. Challenger Soc. **3**, 55-56.

Pechenik, L.N. (1959), "Sirievaia baza proliva Devisa (Fish Resources of the Davis Straits)," Ryb. Khoz. **35**, 9-17, in Russian, abstract in English in FAO World Fish. Absts. Mar./Apr. 1960, 3.

Radakov, D.V. and B.S. Soloviev (1959), "Pervyi opyt primienienia podvodnoi lodki dlia nabliudenii za poviedieniem seldi," (First experiment with submarine for observing the behavior of herring), Ryb. Khoz. **35**, 16-21, in Russian, English abstract in FAO World Fish. Abst. Mar./Apr. 1960, 3.

Solonitsyna, L.R. and L.Ya. Kaverna (1970), "The distribution of herring in the Norwegian Sea as related to hydrological and biological factors," Tr. Polyarn. Nauchno-Issled. Proektn. Inst. Morsk. Rybn. Khoz. Okeanogr. **27**, 227-235, in Russian.

Templeman, W. and A.M. Fleming (1956), "The Bohavista longlining experiment, 1950-53," Fish. Res. Bd. Can. Bull. **109**, 1-55.

Templeman, W. and A.M. Fleming (1963), "Longlining experiments for cod off the east coast of Newfoundland and southern Labrador, 1950-55," Fish. Res. Bd. Can. Bull. **141**, 1-65.

Woodhead, P.M.J. and A.D. Woodhead (1959), "The effects of low temperatures on the physiology and distribution of the cod, *Gadus morhua* L., in the Barents Sea," Proc. Zool. Soc. London **133**, 181-199.

Yves, J. (1964), "Seasonal distribution of cod (*Gadus morhua* L.) along the Canadian Atlantic coast in relation to water temperature," J. Fish. Res. Bd. Can. **21**, 429-460.

2. Tuna

Alverson, D.L. (1961), "Ocean temperatures and their relation to albacore tuna (*Thunnus* genus) distribution in waters off the coast of Oregon, Washington, and British Columbia," J. Fish. Res. Bd. Can. **18**, 1145-1152.

Blackburn, M. (1962), "Distribution and abundance of eastern tropical Pacific tunas in relation to ocean properties and features," U.S. Fish. Wildl. Serv. Spec. Sci. Rept. **415**, 25-26.

Brown, R.P. and K. Sherman (1962), "Oceanographic observations and skipjack distribution in the North central Pacific," U.S. Fish. Wildl. Serv. Spec. Sci. Rept. **415**, 22.

Clemens, H.B. (1962), "The distribution of California bluefin tuna in the eastern north Pacific," U.S. Fish. Wildl. Serv. Spec. Sci. Rept. **415**, 22.

DeOliveira Neves, A. (1960), "A pesca de atum – suas posibilidades en Angola," Boletim da Pesca **12**, 79-87.

FAO (1969), *Yearbook of Fishery Statistics*, U.N. Food and Agricultural Organization, Rome.

Hatheway, M. (1961), "The world-wide tuna fishery," Trade News **14**, 16-19.

Inoue, M. (1962), "Relation of sea condition and ecology of albacore in the northeast Pacific Ocean," U.S. Fish. Wildl. Serv. Spec. Sci. Rept. **415**, 25-26.

Iwamoto, T. (1965), "Summary of tuna observations in the Gulf of Mexico on cruises of the exploratory fishing vessel *Oregon*, 1950-63," Commer. Fish. Rev. **27**, 7-14.

Johnson, J.H. (1962), "Sea temperatures and the availability of albacore off the coasts of Oregon and Washington," U.S. Fish. Wildl. Serv. Spec. Sci. Rept. **415**, 26.

Lamarz, William (1973), personal communication (Southwest Fisheries Center, U.S. Department of Commerce, La Jolla, California).

Lane, R.K. (1965), "Wind, nearshore ocean temperature, and the albacore tuna catch off Oregon," Research Briefs **II**, 25-28.

Mather, F.J. III and M.R. Bartlett (1962), "Bluefin tuna concentration found during a longline exploration of the northwestern Atlantic slope," Commer. Fish. Rev. **24**, 1-7.

McGary, J.W. J.J. Graham, and T. Otsu (1961), "Oceanography and north Pacific albacore," Calif. Coop. Oceanic Fish. Invest. Rept. **8**, 45-53.

Murphy, G.I. and R.S. Shomura (1972), "Preexploitation abundance of tunas in the equatorial central Pacific," U.S. Natl. Mar. Fish. Serv. Fish. Bull. **70**, 815-913.

Owen, Robert (1973), personal communication (Southwest Fisheries Center, U.S. Department of Commerce, La Jolla, California).

Rosa, H., Jr. and T. Laevastu (1962), "World distribution of tunas and tuna fisheries in relation to environment," U.S. Fish. Wildl. Serv. Spec. Sci. Rept. **415**, 34-35.

Seckel, G.R. (1972), "Hawaiian-caught skipjack tuna and their physical environment," U.S. Nat. Mar. Fish. Serv. Fish. Bull. **70**, 763-787.

Seckel, G.R. and T.S. Austin (1962), "The association between Hawaiian skipjack landings and the oceanographic climate," U.S. Fish. Wildl. Serv. Spec. Rept. **415**, 35-36.

3. Salmon

Bailey, J.E. and D.R. Evans (1972), "The low-temperature threshold for pink salmon eggs in relation to a proposed hydroelectric station," U.S. Natl. Mar. Fish. Serv. Fish. Bull. **69**, 587-593.

Bodvarsson, G. and J. Jonsson (1961), "Fluctuations in marine populations in Icelandic waters," Nature **192**, 768-769.

Combs, B.D. (1965), "Effect of temperature on the development of salmon eggs," Prog. Fish.-Cult. **27**, 134-137.

Combs, B.D. and R.E. Burrows (1957), "Threshold temperatures for the normal development of Chinook salmon eggs," Prog. Fish.-Cult. **19**, 3-6.

Efimov, V.I. (1962), "Vyzhivaemost' gorbush v period embrional'nogo razvitiya (Survival rate of pink salmon, *Oncorhynchus gorbrischa*, during embryonic development)," Polyarn. Nauchno-Issled. Inst. Morsk. Rybn. Khoz. Okeanogr. Nauchn. Tekhni. Byul. **4**, 25-26.

Glude, John (1973), personal communication (National Marine Fisheries Service, NW Region).

Hasler, A.D. (1966), *Underwater Guideposts: Homing of Salmon*, Univ. Wisconsin Press, 155 pp.

Hurley, D.A. and W.L. Woodall (1969), "Responses of young pink salmon to vertical temperature and salinity gradients," Prog. Rep. Inst. Pacific Salmon Fish. Comm. **19**, 1-80.

Johnson, H.E. and R.F. Brice (1953), "Effects of transportation of green eggs, and of water temperature during incubation, on the mortality of Chinook salmon," Prog. Fish. Cult. **15**, 104-108.

Kazakoz, R.V. (1971), "Experimental verification of the effect of the temperature regime of egg incubation on the condition of embryos and larvae of the Neva River population of Atlantic salmon *(Salmo salar L.)*" J. Ichthyol. **11**, 123-128.

McInerney, J.E. (1964), "Salinity preference: an orientation mechanism in salmon migration," J. Fish. Res. Bd. Can. **21**, 995-1018.

Novotny, A. (1973), personal communication (National Marine Fisheries Service, Seattle).

Reingold, M. (1968), "Water temperature affects the ripening of adult fall Chinook salmon and steelhead," Prog. Fish. Cult. **30**, 41-42.

Sullivan, C.M. and K.C. Fisher (1953), "Seasonal fluctuations in the selected temperature of speckled trout, *Salvelinus fontinalis* (Mitchill)," J. Fish. Res. Bd. Can. **10**, 187-195.

Sylvester, J.R. (1973), "Effect of light on vulnerability of heat-stressed sockeye salmon to predation by Coho salmon," Trans. Amer. Fish. Soc. **102**, 139-142.

4. Halibut

Skud, Bernard (1973), personal communication (International Pacific Halibut Commission).

5. Sardines

Ahlstrom, R.H. (1943), "Studies on the Pacific pilchard or sardine *(Sardinops caerulea)*. IV: Influence of temperature on the rate of development of pilchard eggs in nature," U.S. Fish. Wildl. Serv. Spec. Sci. Rept. **23**, 1-26.

Bogdanov, G.A. (1968), "Factors governing the reproduction of certain sardines," J. Ichthyol. **8**, 695-704.

Lasker, R. (1964), "An experimental study on the effect of temperature on the incubation time, development, and growth of Pacific sardine embryos and larvae," Copeia **1964**, 399-405.

Murphy, G.I. (1961), "Oceanography and variations in the Pacific sardine population," Calif. Coop. Ocean. Fish. Invest. Rept. **8**, 55-64.

Overko, S.M. (1962), "New fishing objects – South Atlantic sardine," Rybn. Khoz. **6**, 21-23, English translation in U.S. Joint Publications Research Services No. 19.

Vincent, A. and G. Kurc (1969), "Les variations de la situation thermiques dans le Golfe le Gascogne et leur incidence sur l'écologie et la pêche de la sardine en 1968," Revue Trav. Inst. Scient. Tech. Pêche Marit. **33**, 203-212.

6. Shrimp

Copeland, B.J. (1966), "Effects of decreased river flow on estuarine ecology," J. Water Poll. Cont. Fed. **38**, 1831-1839.

Crozier, G. (1973), personal communication (University of Alabama, Dauphin Island Marine Laboratory).

Dow, R.I. (1964), "A comparison among selected marine species of an association between seawater temperature and relative abundance," Jour. du Conseil **28**, 425-431.

Frolander, H. (1973), personal communication (Oregon State University).

Hedgpeth, J.W. and J.J. Gonor (1969), "Aspects of the potential effect of thermal alterations on marine and estuarine benthos," in *Biological Aspects of Thermal Pollutions: Proceedings of the National Symposium on Thermal Pollution,* ed. Krenkel and Parker, Vanderbilt U. Press, Nashville, Tenn., 80.

Olsen, D. (1973), personal communication (Marine Resources Development Foundation, Puerto Rico).

Parker, R.H. (1955), "Changes in the invertebrate fauna, apparently attributable to salinity changes, in the bays of central Texas," J. Paleont. **29**, 193-211.

Raye, S. (1973), personal communication (Texas Agricultural and Mechanical University, Galveston Marine Laboratory).

Reid, G.K. (1955), "A summer study of the biology and ecology of East Bay, Texas. Part 1: Introduction, description of area, methods, some aspects of the fish community, the invertebrate fauna," Texas J. Sci. **7**, 316-343.

Reid, G.K. (1956), "Ecological investigations in a disturbed Texas coastal estuary," Texas J. Sci. **8**, 296-327.

Sick, L.V., D. White, and G. Baptist (1973), "The effect of duration of feeding, amount of food, light intensity, and animal size on rate of ingestion of pelleted food by juvenile penaeid shrimp," Progress. Fish Cult. **35**, 22-25.

7. Lobsters

Copeland, B.J. (1966), "Effects of decreased river flow on estuarine ecology," J. Water Poll. Cont. Fed. **38**, 1831-1839.

Crozier, G. (1973), personal communication (University of Alabama, Dauphin Island Marine Laboratory).

Dow, R.L. (1969), "Cyclic and geographic trends in sea water temperature and abundance of American lobster," Science **164**, 1060-1063.

Flowers, J.M. and S.B. Saila (1972), "An analysis of temperature effects on the inshore lobster fishery," J. Fish. Res. Bd. Can. **29**, 1221-1225.

Frolander, H. (1973), personal communication (Oregon State University).

McLeese, D. and D.G. Wilder (1958), "The activity and catchability of the lobster *(Homarus americanus)* in relation to temperature," J. Fish. Res. Bd. Can. **15**, 1345.

Raye, S. (1973), personal communication (Texas Agricultural and Mechanical University, Galveston Marine Laboratory).

8. Crabs*

Copeland, B.J. (1966), "Effects of decreased river flow on estuarine ecology," J. Water Poll. Cont. Fed. **38**, 1831-1839.

Parker, R.H. (1955), "Changes in the invertebrate fauna, apparently attributable to salinity changes in the bays of central Texas," J. Paleont. **29**, 193-211.

Reid, G.K. (1955), "A summer study of the biology and ecology of East Bay, Texas. Part I: Introduction, description of area, methods, some aspects of the fish community, invertebrate fauna," Texas J. Sci. **7**, 316-343.

Reid, G.K. (1956), "Ecological investigations in a disturbed Texas coastal estuary," Texas J. Sci. **8**, 296-327.

* See also references listed for lobsters.

9. Clams*

Goodwin, L. (1973), "Effects of salinity and temperature on embryos of the geoduck clam (*Panope generosa* Gould)," Proc. Nat. Shellfish. Assoc. **63**, 93-95.

Gulland, J.A. (1971), *The Fish Resources of the Ocean*, Fishing News (Books) Ltd., Surrey, England, 255 pp.

Hedgpeth, J.W. and J.J. Gonor (1969), "Aspects of the potential effect of thermal alteration on marine and estuarine benthos," in *Biological Aspects of Thermal Pollution: Proceedings of the National Symposium on Thermal Pollution*, ed. Krenkel and Parker, Vanderbilt U. Press, Nashville, Tenn., 80.

Reid, G.K. (1955), "A summer study of the biology and ecology of East Bay, Texas. Part I: Introduction, description of area, methods, some aspects of the fish community, the invertebrate fauna," Texas J. Sci. **7**, 316-343.

Reid, G.K. (1956), "Ecological investigations in a disturbed Texas coastal estuary," Texas J. Sci. **8**, 296-327.

10. Scallops

The references applicable to oysters were also utilized for scallops.

11. Oysters

Amemiya, I. (1926), "Notes on experiments on the early developmental stages of the Portuguese, American, and English native oysters, with special reference to the effect of varying salinity," J. Marine Biol. Assoc. U.K. **14**, 161-175.

Collier, A.W. (1967), "A study of the responses of oysters to temperature, and some long range ecological interpretations," *Proceedings of the National Shellfish Association*, 13-37.

Copeland, B.J. (1966), "Effects of decreased river flow on estuarine ecology," J. Water Poll. Cont. Fed. **38**, 1831-1839.

Crozier, G. (1973), personal communication (University of Alabama, Dauphin Island Marine Laboratory).

Dawson, C.E. (1955), "Observations on the incidence of *Dermocystidium marinum* infection in oysters of Apalachicola Bay, Florida," Texas J. Sci. **7**, 47-56.

Glude, J. (1973), personal communication (National Marine Fisheries Service, Seattle, Washington).

Gulland, J.A. (1971), *The Fish Resources of the Ocean*, Fishing News (Books) Ltd., Surrey, England, 255.

Olsen, D. (1973), personal communication (Marine Resources Development Foundation, Puerto Rico).

Parker, R.H. (1955), "Changes in the invertebrate fauna, apparently attributable to salinity changes, in the bays of central Texas," J. Paleont. **29**, 193-211.

12. Other Food Fish

Brett, J.R. (1956), "Some principles in the thermal requirements of fishes," Quart. Rev. Biol. **3**, 75-87.

Hazzard, A.S. (1933), "Low water temperature, a limiting factor in the successful production of trout in natural waters," Trans. Amer. Fish. Soc. **63**, 204-207.

Hubbs, C.L. (1948), "Changes in the fish fauna of western North America correlated with changes in ocean temperature," J. Marine Res. **7**, 459-482.

Joseph, E.B. (1972), "The status of the sciaenic stocks of the middle Atlantic coast," Chesapeake Science **13**, 87-100.

Needham, P.R. and A.C. Jones (1959), "Flow, temperature, solar radiation, and ice in relation to activities of fishes in Sagehen Creek, California," Ecology **40**, 465-474.

Novikov, Yu.V. (1972), "Distribution of the spawning portion of the saury population (*Cololabis saira* Brev.) in the Pacific Ocean and Sea of Japan in relation to the temperature of the surface water layer," J. Ichthyol. **12**, 572-576.

Schmidt, U. (1959), "Zur frage neuer Fangmöglichkeiten auf dem Schelfund im offenen Ozean. Gibt es neue Fangmöglichkeiten auf dem Schelf?" (On the problem of new fishing prospects on the continental shelf and in the high seas. Are there new fishing prospects on the continental shelf?), Inform. Fischwirt **6**, 33-39.

Seegrist, D.W. and R. Gard (1972), "Effects of floods on trout in Sagehen Creek, California," Trans. Amer. Fish. Soc. **101**, 478-482.

Silliman, R.P. (1943), "Thermal and diurnal changes in the vertical distribution of eggs and larvae," U.S. Fish. Wildl. Serv. Spec. Sci. Rept. **24**, 1-32.

Sokolovskiy, A.S. (1972), "Reproduction of the saury (*Cololabis saira* (Brevoort)) in the central and mixed waters of the North Pacific," J. Ichthyol. **12**, 716-720.

* See also references listed for oysters.

LIST OF PARTICIPANTS

Ralph Abbott
American Science and Engineering
955 Massachusetts Ave.
Cambridge, MA 02139

Marcel Ackerman
Institut d'Aéronomie Spatiale de Belgique
Avenue Circulaire 3
B-1180 Brussels, Belgium

Frederick N. Alyea
Meteorological Laboratory
Massachusetts Institute of Technology
Cambridge, MA 02139

J.G. Anderson
Department of Physics
University of Pittsburgh
Pittsburgh, PA 15210

Larry Anderson
Lockheed Palo Alto Research Laboratory
3251 Hanover Street
Palo Alto, CA 94304

Robert J. Anderson
Mathematica, Inc.
P.O. Box 2392
Princeton, NJ 08540

Capt. Randolph W. Ashby
Edwards Air Force Base
California 93523

Thomas E. Ashenfelter
NOAA Air Resources Laboratory
8060 13th St.
Silver Spring, MD 20910

Walter Baginsky
Air Force Cambridge Research Laboratories
Hanscom Field
Bedford, MA 01730

Charles E. Baker
NASA Lewis Research Center
21000 Brookpark Rd.
Cleveland, OH 44135

Emanuel M. Ballenzweig
DOT Federal Aviation Administration
800 Independence Ave., SW
Washington, DC 20591

Morton L. Barad
Air Force Cambridge Research Laboratories
Hanscom Field
Bedford, MA 01730

John L. Barnes
Department of Engineering
University of California, Los Angeles
Los Angeles, CA 90024

Marcel Barrère
Office National d'Etudes et de Recherches
Aérospatiales
29, avenue de la division Leclerc
92320 Châtillon, France

Earl W. Barrett
Atmospheric Physics and Chemistry Laboratory
NOAA Environmental Research Laboratories
Boulder, CO 80302

Jon Bartholic
Institute of Food and Agricultural Sciences
University of Florida
Gainesville, FL 32601

William C. Bartley
National Academy of Sciences
2100 Pennsylvania Ave., NW
Washington, DC

Ernest Bauer
Institute for Defense Analyses
400 Army-Navy Drive
Arlington, VA 22202

Robert W. Beadle
U.S. Atomic Energy Commission
Washington, DC 20545

W. Boynton Beckwith
United Air Lines
Box 66100
Chicago, IL 60666

Frederick W. Bell
Department of Economics
Florida State University
Tallahassee, FL 32304

A.D. Belmont
Research Division
Control Data Corporation
Box 1249
Minneapolis, MN 55418

G.T. Best
Air Force Cambridge Research Laboratories
Hanscom Field
Bedford, MA 01730

Jacques E. Blamont
Centre National d'Etudes Spatiales
129, rue de l'Université
75007 Paris, France

Harold F. Blum
612 E. Durham St.
Philadelphia, PA 19119

M.H. Bortner
Building 100
GE Valley Forge Space Center
P.O. Box 8555
Philadelphia, PA 19101

William J. Borucki
NASA Ames Research Center
Moffett Field, CA 94035

Robert E. Boughner
NASA Langley Research Center
Hampton, VA 23665

Guy Brasseur
Institut d'Aéronomie Spatiale de Belgique
Avenue Circulaire 3
B-1180 Brussels, Belgium

Jean Bricard
Laboratoire de Physique des Aérosols
Tour 25, 5e étage
11, quai St.-Bernard
75005 Paris, France

Anthony J. Broderick
DOT Transportation Systems Center
Kendall Square
Cambridge, MA 02142

Edward M. Brooks
Department of Geology and Geophysics
Boston College
Chestnut Hill, MA 02167

Bernard D. Brown
British Aircraft Corporation (U.S.A.) Inc.
399 Jefferson Davis Highway
Arlington, VA 22202

C.M. Brown
Naval Research Laboratory
Washington, DC 20375

A. Edmond Brun
COVOS
8, place du Commerce
75015 Paris, France

William J. Burroughs
British Embassy
3100 Massachusetts Ave., NW
Washington, DC 20008

Martyn M. Caldwell
Ecology Center
Utah State University
Logan, UT 84321

George Caledonia
Physical Sciences, Inc.
18 Lakeside Office Park
Wakefield, MA 01880

John Calkins
Department of Radiation Medicine
University of Kentucky Medical Center
Lexington, KY 40506

Lin B. Callis
NASA Langley Research Center
Hampton, VA 23665

Capt. Joseph M. Calo
Air Force Cambridge Research Laboratories
Hanscom Field
Bedford, MA 01730

Morton Camac
Aerodyne Research
Tech/Ops Building
South Ave.
Burlington, MA 01803

Norman T. Campbell
Pratt & Whitney Aircraft
400 Main St.
East Hartford, CT 06111

Robert H. Cannon, Jr.
Chairman, Department of Engineering
California Institute of Technology
Pasadena, CA 91103

A.W. Castleman
Department of Applied Science
Brookhaven National Laboratory
Upton, NY 11973

Robert Center
AVCO Everett Research Laboratories
2385 Revere Beach Parkway
Everett, MA 02149

J.W. Chamberlain
Space Physics and Astronomy
Rice University
Houston, TX 77001

Bill Chameides
Department of Geology and Geophysics
Box 2161, Yale Station
New Haven, CT 06520

K.W. Champion
Air Force Cambridge Research Laboratories
Hanscom Field
Bedford, MA 01730

Julius S. Chang
Lawrence Livermore Laboratory
P.O. Box 808
Livermore, CA 94550

M.L. Chanin
Service d'Aéronomie
Centre National de la Recherche Scientifique
91370 Verrières-le-Buisson, France

Tom Chesworth
Ionosphere Research Laboratory
Pennsylvania State University
University Park, PA 16802

R.J. Cicerone
University of Michigan
2455 Hayward Ave.
Ann Arbor, MI 48105

Roderick K. Clayton
Department of Genetic Development
Cornell University
Ithaca, NY 14850

Robert N. Coltharp
Lockheed Electronic
16911 El Camino Real
Houston, TX 77508

Marcel Compagna
DOT Transportation Systems Center
Kendall Square
Cambridge, MA 02142

Samuel C. Coroniti
Deputy Manager, CIAP
Department of Transportation
2100 Second St., SW
Washington, DC 20590

Thomas Crocker
Department of Economics
University of California, Riverside
Riverside, CA 92505

Harold L. Crutcher
NOAA EDS National Climatic Center
Asheville, NC 28801

Derek Cunnold
Department of Meteorology
Massachusetts Institute of Technology
Cambridge, MA 01239

R. Bruce Curry
Department of Agricultural Engineering
Ohio Agricultural R&D Center
Wooster, OH 44691

Pythagoras Cutchis
Institute for Defense Analyses
400 Army-Navy Drive
Arlington, VA 22202

R.J. Cvetanović
National Research Council of Canada
Ottawa, Ontario, K1A 0R9 Canada

Farrington Daniels, Jr.
New York Hospital
525 East 68th St.
New York, NY 10028

Ralph d'Arge
Department of Economics
University of California, Riverside
Riverside, CA 92505

Eric R. Davies
Rolls-Royce Aero Engines, Inc.
551 Fifth Avenue
New York, NY 10017

Douglas D. Davis
Department of Chemistry
University of Maryland
College Park, MD 20742

William O. Davis
National Oceanic and Atmospheric Administration
6010 Executive Blvd.
Rockville, MD 20852

A. Neal de Gaston
Douglas Aircraft Company
3855 Lakewood Blvd.
Long Beach, CA 90846

Thomas C. Degges
Visidyne, Inc.
19 Third Ave.
Burlington, MA 01803

Frank P. DelGreco
Air Force Cambridge Research Laboratories
Hanscom Field
Bedford, MA 01730

John J. DeLuisi
National Center for Atmospheric Research
P.O. Box 3000
Boulder, CO 80303

Edmond M. Dewan
Air Force Cambridge Research Laboratories
Hanscom Field
Bedford, MA 01730

Col. Currie S. Downie
2212 Wakefield St.
Alexandria, VA 22308

S. Roland Drayson
Department of Atmospheric and Oceanic Science
University of Michigan
Ann Arbor, MI 48104

Maurice W. Dumais
DOT Transportation Systems Center
Kendall Square
Cambridge, MA 02142

Lawrence Dunkelman
NASA Goddard Space Flight Center
Greenbelt, MD 20771

David Edelson
Bell Telephone Laboratories
600 Mountain Ave.
Murray Hill, NJ 07974

H. Frank Eden
Aeronomy & Meteorology Programs
National Science Foundation
Washington, DC 20550

Dieter H. Ehhalt
National Center for Atmospheric Research
P.O. Box 3000
Boulder, CO 80303

Hugh W. Ellsaesser
Lawrence Livermore Laboratory
P.O. Box 808
Livermore, CA 94550

Louis Elterman
Air Force Cambridge Research Laboratories
Hanscom Field
Bedford, MA 01730

J. Morley English
School of Engineering and Applied Science
University of California, Los Angeles
Los Angeles, CA 90024

David Escoe
Department of Transportation
2100 Second St., SW
Washington, DC 20590

W.F.J. Evans
Atmospheric Environment Service
4905 Dufferin St.
Downsview, Ontario, Canada

J.J. Ewing
AVCO Everett Research Laboratories
2385 Revere Beach Parkway
Everett, MA 02149

P. Fabian
Institute of Geophysics and Planetary Physics
University of California, Los Angeles
Los Angeles, CA 90035

C.B. Farmer
Jet Propulsion Laboratory (CIT)
4800 Oak Grove Drive
Pasadena, CA 91103

Robert W. Fenn
Air Force Cambridge Research Laboratories
Hanscom Field
Bedford, MA 01730

Frederick G. Fernald
National Center for Atmospheric Research
P.O. Box 3000
Boulder, CO 80303

Terry A. Ferrar
Center for Study of Environmental Policy
Pennsylvania State University
University Park, PA 16802

Antonio Ferri
Advanced Technology Laboratory
Merrick and Stewart Avenues
Westbury, Long Island, NY 19590

Guy V. Ferry
NASA Ames Research Center
Moffett Field, CA 94035

Giorgio Fiocco
University of Florence
Largo E. Fermi 2
50125 Florence, Italy

A.K. Forney
DOT Federal Aviation Administration
800 Independence Avenue, SW
Washington, DC 20591

D.E. Freeman
Air Force Cambridge Research Laboratories
Hanscom Field
Bedford, MA 01730

Johnny Freiberg
Aeronautical Research Associates of Princeton
50 Washington Rd.
Princeton, NJ 08512

James P. Friend
Department of Chemistry
Drexel University
Philadelphia, PA 19104

Tzvi Gal-Chen
National Center for Atmospheric Research
P.O. Box 3000
Boulder, CO 80303

Robert J. Gelinas
Lawrence Livermore Laboratories
P.O. Box 808
Livermore, CA 94550

Michael Gersh
Aerodyne Research
20 South Ave.
Burlington, MA 01803

Arthur C. Giese
Department of Biological Sciences
Stanford University
Stanford, CA 94305

John C. Gille
National Center for Atmospheric Research
P.O. Box 3000
Boulder, CO 80303

André Girard
Office National d'Etudes et de Recherches Aérospatiales
29, avenue de la division Leclerc
92320 Châtillon, France

Russell D. Glenn
Air Force Weapons Laboratory
Kirtland AFB, NM 87116

Arnold Goldburg
The Boeing Company
P.O. Box 3707
Seattle, WA 98124

Aharon Goldman
Denver Research Institute
University of Denver
Denver, CO 80210

Harold W. Goldstein
Building 100
GE Valley Forge Space Center
P.O. Box 8555
Philadelphia, PA 19101

Daniel Golomb
Air Force Cambridge Research Laboratories
Hanscom Field
Bedford, MA 01730

R.E. Good
Air Force Cambridge Research Laboratories
Hanscom Field
Bedford, MA 01730

Philip Goodman
Panametrics, Inc.
221 Crescent Street
Waltham, MA 02154

Gerald W. Grams
National Center for Atmospheric Research
P.O. Box 3000
Boulder, CO 80303

Donald D. Grantham
Air Force Cambridge Research Laboratories
Hanscom Field
Bedford, MA 01730

Carlton R. Gray
MIT Draper Laboratory
75 Cambridge Parkway
Cambridge, MA 02142

Alex E.S. Green
Department of Physics and Astronomy
University of Florida
Gainesville, FL 32601

William B. Green
Concorde 1-A
Department of Trade and Industry
Monsanto House, 10 Victoria St.
London SW1 HONQ, England

Reynold Greenstone
Department of Transportation
2100 Second St., SW
Washington, DC 20590

L.R. Greenwood
NASA Langley Research Center
Hampton, VA 23665

M. Griggs
Science Applications Inc.
P.O. Box 2351
La Jolla, CA 92037

Alan J. Grobecker
Manager, CIAP
Department of Transportation
2100 Second St., SW
Washington, DC 20590

Jack Grobman
NASA Lewis Research Center
21000 Brookpark Road
Cleveland, OH 44135

William L. Grose
NASA Langley Research Center
Hampton, VA 23665

Thomas J. Gross
U.S. Atomic Energy Commission
Washington, DC 20545

Paul R. Guthals
Los Alamos Scientific Laboratories
P.O. Box 1663
Los Alamos, NM 87544

Joseph J. Gwiazdowski
Department of Transportation
2100 Second St., SW
Washington, DC 20590

J. Brooks Haberl
General Electric Ordnance Systems
100 Plastics Ave.
Pittsfield, MA 01201

L.C. Hale
Ionosphere Research Laboratory
Pennsylvania State University
University Park, PA 16802

L.A. Hall
Air Force Cambridge Research Laboratories
Hanscom Field
Bedford, MA 01730

Robert F. Hampson
National Bureau of Standards
Washington, DC 20234

Frederick A. Hanser
Panametrics, Inc.
221 Crescent St.
Waltham, MA 02154

Thomas M. Hard
DOT Transportation Systems Center
Kendall Square
Cambridge, MA 02142

Alan B. Harker
Science Center
Rockwell International
1049 Camino Dos Rios
Thousand Oaks, CA 91360

Richard H. Hart
USDA Agricultural Research Service
Building 046A, BARC-West
Beltsville, MD 20705

Curtis L. Hemenway
Dudley Observatory
100 Fuller Rd.
Albany, NY 12205

Benjamin M. Herman
Institute of Atmospheric Physics
University of Arizona
Tucson, AR 85721

John T. Herron
Chemistry Building
National Bureau of Standards
Washington, DC 20234

Henry Hidalgo
Institute for Defense Analyses
400 Army-Navy Drive
Arlington, VA 22202

Ernest Hilsenrath
NASA Goddard Space Flight Center
Greenbelt, MD 20771

Arthur Hilsenrod
DOT Federal Aviation Administration
2100 Second St., SW
Washington, DC 20590

Glenn R. Hilst
Aeronautical Research Associates of Princeton, Inc.
50 Washington Road
Princeton, NJ 08540

Martin Hoffert
NASA Goddard Institute for Space Studies
2880 Broadway
New York, NY 10025

Herbert Hoffman
Air Force Cambridge Research Laboratories
Hanscom Field
Bedford, MA 01730

David J. Hofmann
Department of Physics and Astronomy
University of Wyoming
Laramie, WY 82070

Patrick Hogan
Chemistry Department
University of Maryland
College Park, MD 20742

Hiroshi Hoshizaki
Lockheed Palo Alto Research Laboratory
3251 Hanover St.
Palo Alto, CA 94304

John N. Howard
Air Force Cambridge Research Laboratories
Hanscom Field
Bedford, MA 01730

Joseph Howell
Department of Transportation
2100 Second St., SW
Washington, DC 20590

Joseph Huang
Scripps Institute of Oceanography
P.O. Box 109
La Jolla, CA 92037

Frank Hudson
Sandia Laboratories
P.O. Box 5800
Albuquerque, NM 87115

R.D. Hudson
NASA Manned Space Flight Center
Houston, TX 77058

Robert E. Huffman
Air Force Cambridge Research Laboratories
Hanscom Field
Bedford, MA 01730

Ivar S. A. Isaksen
Institute of Geophysics
University of Oslo
P.O. Box 1022, Blindern
Oslo 3, Norway

Haruji Ishikawa
Institute of Atmospherics
Toyokawa, Aichi 442
University of Nagoya
Nagoya, Japan

John R. Jasperse
Air Force Cambridge Research Laboratories
Hanscom Field
Bedford, MA 01730

René C. Joatton
Société Nationale Industrielle Aérospatiale
37 boulevard de Montmorency
75016 Paris, France

Francis S. Johnson
Center for Advanced Studies
University of Texas at Dallas
Dallas, TX 75230

Norman Johnson
Block Engineering
19 Blackstone St.
Cambridge, MA 02139

R.E. Johnson
Engineering Department
United Air Lines
San Francisco International Airport
San Francisco, CA 94128

Harold S. Johnston
Department of Chemistry
University of California, Berkeley
Berkeley, CA 94720

Richard Eric Jones
Aviation Research
Ministry of Transport
Tower C, Floor 8C, Place de Ville
Ottawa, Ontario, Canada

William L. Jones
National Center for Atmospheric Research
P.O. Box 3000
Boulder, CO 80303

Robert S. Kandel
Department of Astronomy
Boston University
Boston, MA 02215

Arthur J. Kantor
Air Force Cambridge Research Laboratories
Hanscom Field
Bedford, MA 01730

B.J. Kaplan
American Science and Engineering
955 Massachusetts Ave.
Cambridge, MA 02139

Igor L. Karol
Main Geophysical Observatory
7 Karbyshev
Leningrad, USSR 194018

D. Katayama
Air Force Cambridge Research Laboratories
Hanscom Field
Bedford, MA 01730

Frederick Kaufman
Department of Chemistry
University of Pittsburgh
Pittsburgh, PA 15213

George Keller
Ballistic Research Laboratories
Aberdeen Proving Ground, MD 21005

J.B. Kerr
Atmospheric Environment Service
4905 Dufferin St.
Downsview, Ontario, Canada

James King, Jr.
Jet Propulsion Laboratory (CIT)
4800 Oak Grove Drive
Pasadena, CA 91103

Sidney Kirschner
Department of Physics
Ohio State University
Columbus, OH 43210

George D. Kittredge
Mobile Sources Pollution Control Division
Environmental Protection Agency
Waterside Mall
Washington, DC 20460

Teodor Kopcewicz
University of Warsaw
Warsaw, Poland

Col. Earl R. Kreins
Meteorology Program Office
NASA Goddard Space Flight Center
Greenbelt, MD 20771

Philip W. Krey
Health and Safety Laboratory
U.S. Atomic Energy Commission
376 Hudson Street
New York, NY 10014

Arlin J. Krueger
NASA Goddard Space Flight Center
Greenbelt, MD 20771

Ralph H. Kummler
Research Institute for Engineering Sciences
College of Engineering
Wayne State University
Detroit, MI 48202

Jacob Kuriyan
University of California, Los Angeles
Los Angeles, CA 90029

Michael J. Kurylo
National Bureau of Standards
Washington, DC 20234

Dr. Emanuel Landau
Bureau of Radiological Health
HEW Public Environmental Health Service
5600 Fishers Lane
Rockville, MD 20852

Ronald Lau
Systems Control, Inc.
260 Sheridan Ave.
Palo Alto, CA 94306

Vernon J. Laurie
5610 Haddon Dr.
Lanham, Md. 20801

J.A. Laurmann
ODSI
Monterey, CA 93940

Allan Lazrus
National Center for Atmospheric Research
P.O. Box 3000
Boulder, CO 80303

J.F. Leach
British Aircraft Corp.
P.O. Box 77
Filton, Bristol, England

W.Z. Leavitt
DOT Transportation Systems Center
Kendall Square
Cambridge, MA 02142

Francis J. LeBlanc
Air Force Cambridge Research Laboratories
Hanscom Field
Bedford, MA 01730

Dr. John A.H. Lee
Royal Ottawa Hospital
University of Ottawa
Ottawa, Ontario K1Z 7K4, Canada

Richard L. Lehman
Office of Ecology
National Oceanic and Atmospheric Administration
DOC Building, Room 5813
Washington, DC 20230

Cecil E. Leith
National Center for Atmospheric Research
P.O. Box 3000
Boulder, CO 80303

Howard A. LeVaux
Center for Research in Aeronomy
Utah State University
Logan, UT 84322

Robert S. Levine
Building 1219
NASA Langley Research Center
Hampton, VA 23365

Hiram Levy II
NOAA ERL Geophysical Fluid Dynamics Laboratory
Princeton University
P.O. Box 308
Princeton, NJ 08540

Lawrence H. Linden
Department of Mechanical Engineering
Massachusetts Institute of Technology
Cambridge, MA 02139

Bernard A. Lippman
New York University
4 Washington Place
New York, NY 10003

Ernest V. Loewenstein
Air Force Cambridge Research Laboratories
Hanscom Field
Bedford, MA 01730

Max Loewenstein
NASA Ames Research Center
Moffett Field, CA 94040

Julius London
Department of Astro-Geophysics
University of Colorado
Boulder, CO 80302

Jean-François Louis
National Center for Atmospheric Research
P.O. Box 3000
Boulder, CO 80303

D.J. Lovell
Barton Road
Stow, MA 01775

James E. Lovill
Lawrence Livermore Laboratory
P.O. Box 808
Livermore, CA 94550

Walter S. Luffsey
DOT Federal Aviation Administration
800 Independence Ave.
Washington, DC 20591

Iver A. Lund
Air Force Cambridge Research Laboratories
Hanscom Field
Bedford, MA 01730

Gen. Gustav E. Lundquist
Associate Administrator for Engineering
and Development
DOT Federal Aviation Administration
800 Independence Avenue, SW
Washington, DC 20591

Hylan B. Lyon, Jr.
Office of Science and Technology
Executive Office of the President
Washington, DC 20506

Michael C. MacCracken
Lawrence Livermore Laboratory
P.O. Box 808
Livermore, CA 95440

Eleanor J. Macdonald
M.D. Anderson Hospital
University of Texas at Houston
Houston, TX 77025

Lester Machta
Director, Air Resources Laboratory
National Oceanic and Atmospheric Administration
8060 Thirteenth Street
Silver Spring, MD 20910

Guy J. Madelaine
Centre d'Etudes Nucléaires
B.P. 6
Fontenay-aux-Roses 92, France

Jerry D. Mahlman
NOAA ERL Geophysical Fluid Dynamics Laboratory
Princeton University
P.O. Box 308
Princeton, NJ 08540

Harvey L. Malchow
MIT Draper Laboratory
75 Cambridge Pkwy.
Cambridge, MA 02142

Donald W. Male
Arnold Engineering Development Center
Arnold Air Force Station, TN 37389

R. Carroll Maninger
Lawrence Livermore Laboratory
P.O. Box 808
Livermore, CA 94550

William G. Mankin
National Center for Atmospheric Research
P.O. Box 3000
Boulder, CO 80303

Oscar P. Manley
Visidyne, Inc.
19 Third Ave.
Burlington, MA 01803

Frederick F. Marmo
DOT Transportation Systems Center
Kendall Square
Cambridge, MA 02142

Walter F. Martin
Office of Naval Research
800 N. Quincy St.
Arlington, VA 22217

Ronald J. Massa
Dynatrend, Inc.
131 Middlesex Turnpike
Burlington, MA 01803

R.A. McClatchey
Air Force Cambridge Research Laboratories
Hanscom Field
Bedford, MA 01730

John C. McConnell
Physics Department
York University
Downsview, Ontario M3J 1P3, Canada

Billy M. McCormac
Lockheed Palo Alto Research Laboratory
3251 Hanover Street
Palo Alto, CA 94304

C. Thomas McElroy
Department of Physics
University of Toronto
Toronto, Ontario M5S 1A7, Canada

Charles H. McLellan
NASA Langley Research Center
Hampton, VA 23365

Robert J. McNeal
The Aerospace Corporation
P.O. Box 92957
Los Angeles, CA 90009

John W. Meyer
Lockheed Palo Alto Research Laboratory
3251 Hanover St.
Palo Alto, CA 94304

Stanislaw Michnowski
Polish Academy of Sciences
Ul. Swietokrysko
Warsaw, Poland

Thomas Mikus
Department of Mechanical Engineering
Massachusetts Institute of Technology
Cambridge, MA 02139

René H. Miller
Department of Aeronautics and Astronautics
Massachusetts Institute of Technology
Cambridge, MA 02139

Masao Misaki
Meteorological Research Institute
4-35-8 Koenji-kita, Suginami-ku
Tokyo, Japan

Kenneth Moe
McDonnell Douglas Astronautics Co.
5301 Bolsa Ave.
Huntington Beach, CA 92647

Mario J. Molina
Department of Chemistry
University of California, Irvine
Irvine, CA 92664

John Mormino
Department of Transportation
2100 Second St., SW
Washington, DC 20590

James M. Morris
DOT Transportation Systems Center
Kendall Square
Cambridge, MA 02142

Demetrios J. Moschandreas
GEOMET, Inc.
50 Monroe St.
Rockville, MD 20850

Edmond Murad
Air Force Cambridge Research Laboratories
Hanscom Field
Bedford, MA 01730

D.S. Nachtwey
Radiation Center
Oregon State University
Corvallis, OR 97331

Rocco S. Narcisi
Air Force Cambridge Research Laboratories
Hanscom Field
Bedford, MA 01730

Murali Natarajan
State University of New York at Stony Brook
Stony Brook, NY 11790

Arthur W. Nelson
Pratt & Whitney Aircraft Division
United Aircraft Corporation
400 Main Street
East Hartford, CT 06108

Reginald E. Newell
Department of Meteorology
Massachusetts Institute of Technology
Cambridge, MA 02139

R.L. Newson
British Meteorological Office
12 London Rd.
Bracknell, Berkshire RG12 2SZ, England

Marcel Nicolet
Institut d'Aéronomie Spatiale de Belgique
Avenue Circulaire 3
B-1180 Brussels, Belgium

George F. Nolan
Air Force Cambridge Research Laboratories
Hanscom Field
Bedford, MA 01730

Toshihiro Ogawa
Geophysics Research Laboratory
University of Tokyo
Hongo, Bunkyo-ku
Tokyo, Japan

Toshio Ogawa
Geophysics Institute
Kyoto University
Kyoto, Japan

Robert C. Oliver
Institute for Defense Analyses
400 Army-Navy Drive
Arlington, VA 22202

Fritz Ostherr
Dynatrend, Inc.
131 Middlesex Turnpike
Burlington, MA 01803

Hans-Karl Paetzold
Institut für Geophysik und Meteorologie
Universität zu Köln
Albertus-Magnus Platz
5 Köln 41, West Germany

Hans A. Panofsky
Department of Meteorology
Pennsylvania State University
University Park, PA 16802

Jae H. Park
Department of Astro-Geophysics
University of Colorado
Boulder, CO 80302

Frederick G. Parsons
Institute for Defense Analyses
400 Army-Navy Drive
Arlington, VA 22202

James W. Patmore
Systems Control, Inc.
260 Sheridan Ave.
Palo Alto, CA 94306

C.W. Patten
Department of Transportation
2100 Second St., SW
Washington, DC 20590

John F. Paulson
Air Force Cambridge Research Laboratories
Hanscom Field
Bedford, MA 01730

Rudolf Penndorf
148 Oakland St.
Wellesley Hills, MA 02181

Theodore J. Pepin
Department of Physics and Astronomy
University of Wyoming
Laramie, WY 82070

Porter J. Perkins
NASA Lewis Research Center
21000 Brookpark Road
Cleveland, OH 44135

Capt. Jerry J. Perrizo
Department of Physics
Ohio State University
Columbus, OH 43210

Millard Fillmore Perry
Perry Associates, Inc.
RD #2
Cumberland, RI 02864

Robert W. Peterson
Los Alamos Scientific Laboratories
Box 1663
Los Alamos, NM 87544

Norman A. Phillips
Department of Meteorology
Massachusetts Institute of Technology
Cambridge, MA 02139

Stephen A. Piacsek
Naval Research Laboratory
Washington, DC 20375

R.G. Pinnick
Department of Physics and Astronomy
University of Wyoming
Laramie, WY 82071

Walter G. Planet
NOAA National Environmental Satellite Service
FOB 4
Suitland, MD 20235

Charles Polk
Department of Electrical Engineering
University of Rhode Island
Kingston, RI 02881

John A. Polutchko
Dynatrend, Inc.
131 Middlesex Turnpike
Burlington, MA 01803

I.G. Poppoff
NASA Ames Research Center
Moffett Field, CA 94040

William M. Porch
Lawrence Livermore Laboratories
P.O. Box 808
Livermore, CA 94550

Jerome Pressman
Pressman Enterprises
4 Fessenden Way
Lexington, MA 02173

Ronald Prinn
Meteorology Department
Massachusetts Institute of Technology
Cambridge, MA 02139

Larry A. Pugh
Department of Physics
Ohio State University
Columbus, OH 43210

A.F. Quesada
Air Force Cambridge Research Laboratories
Hanscom Field
Bedford, MA 01730

Alain Quillévéré
SNECMA
Centre d'Essais de Villaroche
77550 Moissy-Cramayel, France

Boris Ragent
NASA Ames Research Center
Moffett Field, CA 94035

Elliot Raisen
Illinois Institute of Technology Research Institute
10 W 35th St.
Chicago, IL 60616

V. Ramanathan
NASA Langley Research Center
Hampton, VA 23665

Juanito M. Ramirez
Department of Soils
North Dakota State University
Fargo, ND 58102

K. Narahari Rao
Physics Department
Ohio State University
Columbus, OH 43210

R. Robert Rapp
RAND Corporation
1700 Main Street
Santa Monica, CA 90406

Gregory M. Reck
NASA Headquarters
600 Independence Ave., SW
Washington, DC 20546

Elmar R. Reiter
Department of Atmospheric Science
Colorado State University
Fort Collins, CO 80521

Ellis E. Remsberg
LIDAR Applications Section
NASA Langley Research Center
Hampton, VA 23665

Joseph Ritchie
USDA Agricultural Research Service
Box 748
Temple, TX 76501

Donald E. Robbins
NASA Johnson Space Center
Houston, TX 77058

George D. Robinson
Center for Environment & Man, Inc.
275 Windsor Street
Hartford, CT 06120

Aidan E. Roche
Lockheed Palo Alto Research Laboratories
3251 Hanover St.
Palo Alto, CA 94304

James M. Rosen
Department of Physics and Astronomy
University of Wyoming
Laramie, WY 82070

N.W. Rosenberg
Air Force Cambridge Research Laboratories
Hanscom Field
Bedford, MA 01730

Larry Rothman
Air Force Cambridge Research Laboratories
Hanscom Field
Bedford, MA 01730

John N. Rowe
Pennsylvania State University
University Park, PA 16802

Richard A. Rudey
NASA Lewis Research Center
21000 Brookpark Road
Cleveland, OH 44135

James M. Russell III
NASA Langley Research Center
Hampton, VA 23365

Philip B. Russell
Stanford Research Institute
Menlo Park, CA 94025

Clarence Sakamoto
NOAA Environmental Science Service Center
Auburn University
Auburn, AL 36830

Edward S. Sarachik
Center for Earth and Planetary Physics
Harvard University
Cambridge, MA 01238

Doyne Sartor
National Center for Atmospheric Research
P.O. Box 3000
Boulder, CO 80303

Howard Savage
NASA Ames Research Center
Moffett Field, CA 94035

Boris I. Sazonov
Main Geophysical Observatory
Karbysheva 7
Leningrad, USSR

Robert B. Schainker
Systems Control, Inc.
1801 Page Mill Rd.
Palo Alto, CA 94304

Harold I. Schiff
Centre for Research in Experimental Space Science
York University
Downsview, Ontario M3J 1P3, Canada

Burton G. Schuster
University of Missouri
Rolla, MO 65401

C. John Scott
Bristol Engine Division
Rolls Royce (1971) Ltd.
P.O. Box 3
Filton, Bristol B512 7QE, England

Noelle Anne Scott
CNRS Laboratoire de Physique Moleculaire
et d'Optique Atmospherique
Campus d'Orsay, Bat. 220
9145 Orsay, France

Michael Scotto
DOT Transportation Systems Center
Kendall Square
Cambridge, MA 02142

C.F. Sechrist
Aeronomy Laboratory
University of Illinois
Urbana, IL 61801

William A. Sedlacek
Los Alamos Scientific Laboratories
Box 1663
Los Alamos, NM 87544

John Selby
Air Force Cambridge Research Laboratories
Hanscom Field
Bedford, MA 01730

F. Bach Sellers
Panametrics, Inc.
221 Crescent St.
Waltham, MA 02154

Ralph Shapiro
Air Force Cambridge Research Laboratories
Hanscom Field
Bedford, MA 01730

Alan W. Shaw
Center for Research in Aeronomy
Utah State University
Logan, UT 84322

Eric P. Shettle
Air Force Cambridge Research Laboratories
Hanscom Field
Bedford, MA 01730

Tatsuo Shimazaki
Aeronomy Laboratory
NOAA Environmental Research Laboratories
Boulder, CO 80302

P. Simon
Institut d'Aéronomie Spatiale de Belgique
Avenue Circulaire 3
B-1180 Brussels, Belgium

R.V. Simonaitis
Ionosphere Research Laboratory
Pennsylvania State University
University Park, PA 16802

Tom G. Slanger
Stanford Research Institute
Menlo Park, CA 94025

Ronald Smelt
Vice President, Lockheed Aircraft Corporation
2555 Hollywood Way
Burbank, CA 91504

Col. Francis J. Smith
Environmental Protection Office
HQ AFSC
Andrews Air Force Base, MD 20334

Cdr. William L. Smith
Office of Naval Research
800 N. Quincy St.
Arlington, VA 22217

Donald E. Snider
Concepts Analysis Laboratory
U.S. Army Ballistic Research Laboratories
Aberdeen Proving Ground, MD 21005

Deborah F. Sola
ORI
Department of Transportation
2100 Second St., SW
Washington, DC 20590

Phillip Sollins
Coniferous Forest Biome
University of Washington
Seattle, WA 98195

Kenneth C. Spengler
American Meteorological Society
45 Beacon Street
Boston, MA 02108

A. Fred Spilhaus, Jr.
American Geophysical Union
1707 L Street, NW
Washington, DC 20036

V.J. Stakutis
Mitre Corp.
Route 62
Bedford, MA 01730

Christos G. Stergis
Air Force Cambridge Research Laboratories
Hanscom Field
Bedford, MA 01730

Charles B. Stewart
Commercial Airplane Group
The Boeing Company
Box 3707
Seattle, WA 98124

Richard W. Stewart
NASA Goddard Institute for Space Studies
2880 Broadway
New York, NY 10025

Richard S. Stolarski
Space Physics Research Laboratory
University of Michigan
Ann Arbor, MI 48105

N.W.B. Stone
National Physical Laboratory
Teddington, Middlesex TW11 0LW, England

Peter Stone
Meteorology Department
Massachusetts Institute of Technology
Cambridge, MA 02139

Daryl F. Strobel
Naval Research Laboratory
Washington, DC 20375

Joseph C. Sturm
DOT Transportation Systems Center
Kendall Square
Cambridge, MA 02142

Jack A. Suddreth
National Aeronautics and Space Administration
600 Independence Ave., SW
Washington, DC 20546

Ed Sullivan
NASA Langley Research Center
Hampton, VA 23665

Joel Susskind
NASA Goddard Institute for Space Studies
2880 Broadway
New York, NY 10025

William Swider, Jr.
Air Force Cambridge Research Laboratories
Hanscom Field
Bedford, MA 01730

C.D. Tackett
Dudley Observatory
100 Fuller Place
Albany, NY 12205

Sanzo Takezawa
Air Force Cambridge Research Laboratories
Hanscom Field
Bedford, MA 01730

Yoshio Tanaka
Air Force Cambridge Research Laboratories
Hanscom Field
Bedford, MA 01730

Raymond L. Taylor
Physical Science, Inc.
18 Lakeside Office Park
Wakefield, MA 01880

John Tigue
DOT Federal Aviation Administration
2100 Second St., SW
Washington, DC 20590

Shelby G. Tilford
Naval Research Laboratory
Washington, DC 20375

Takao Tohmatsu
Geophysics Research Laboratory
Faculty of Science
University of Tokyo
Yayoi 2-11-16, Bunkyo-ku
Tokyo 113, Japan

Robert Toolin
Air Force Cambridge Research Laboratories
Hanscom Field
Bedford, MA 01730

Owen B. Toon
Laboratory for Planetary Studies
Cornell University
Ithaca, NY 14850

Daniel W. Trainor
AVCO Everett Research Laboratories
2385 Revere Beach Parkway
Everett, MA 02149

Joseph Robbins Tucker, Jr.
DOT Federal Aviation Administration
800 Independence Ave., SW
Washington, DC 20591

Paul Twitchell
Office of Naval Research
495 Summer St.
Boston, MA 02210

Robert L. Underwood
TRW Inc.
10880 Wilshire Blvd.
Los Angeles, CA 90024

Dr. Frederick Urbach
Skin & Cancer Hospital
Temple University Health Science Center
3322 North Broad St.
Philadelphia, PA 19140

Gregg Van Volkenburgh
Intra-Space International, Inc.
285 Wildcat Rd.
Downsview, Ontario M3J 2N5, Canada

S.V. Venkateswaran
Department of Meteorology
University of California, Los Angeles
Los Angeles, CA 90024

Douglas T. Vickery
Commercial Aircraft Division
British Aircraft Corporation
GOP Box No. 77
Filton, Bristol BS99 7AR, England

William Viezee
Stanford Research Institute
Menlo Park, CA 94025

Jerome Vigil
Block Engineering
19 Blackstone St.
Cambridge, MA 02139

Fred Volz
Air Force Cambridge Research Laboratories
Hanscom Field
Bedford, MA 01730

V.R. Krishna Rao Vupputuri
Atmospheric Environment Service
4905 Dufferin St.
Downsville, Ontario, Canada

Stacy Walters
Space Physics Research Laboratory
University of Michigan
Ann Arbor, MI 48105

John J. Walton
Lawrence Livermore Laboratory
P.O. Box 808
Livermore, CA 94550

Peter Warneck
Max Planck-Institut für Chemie
Postfach 3060
Mainz D-6500, West Germany

Velvin R. Watson
NASA Ames Research Center
Moffett Field, CA 94035

L.H. Weeks
Air Force Cambridge Research Laboratories
Hanscom Field
Bedford, MA 01730

Michael P. Weinreb
NOAA National Environmental Satellite Service
Suitland, MD 20233

Billy E. Welch
SAFIL, OST
Department of the Air Force
The Pentagon
Washington, DC 20330

Raymond Wexler
Atmospheric and Hydrospheric Applications Division
NASA Goddard Space Flight Center
Greenbelt, MD 20771

John L. Whitesides, Jr.
Joint Institute for Acoustics and Flight Sciences
NASA Langley Research Center
Hampton, VA 23669

R.K. Whitford, Deputy Director
DOT Transportation Systems Center
Kendall Square
Cambridge, MA 02142

Cynthia K. Whitney
Draper Laboratory
75 Cambridge Pkwy.
Cambridge, MA 02142

James R. Whittaker
DOT Federal Aviation Administration
2100 Second St., SW
Washington, DC 20590

Robert C. Whitten
NASA Ames Research Center
Moffett Field, CA 94040

George F. Widhopf
The Aerospace Corporation
3450 E. El Segundo Blvd.
El Segundo, CA 90245

M.R. Williams
Bristol Engine Division
Rolls Royce (1971) Ltd.
P.O. Box 3
Filton, Bristol BS12 7QE, England

J.E. Wirsching
Systems Control, Inc.
3364 Marina Avenue
Livermore, CA 94550

Steven C. Wofsy
Center for Earth and Planetary Physics
Harvard University
Cambridge, MA 02138

Mao-Fou Wu
Environmental Research and Technology, Inc.
3 Militia Dr.
Lexington, MA 02173

Donald J. Wuebbles
Lawrence Livermore Laboratory
P.O. Box 808
Livermore, CA 94550

Samuel Yee
Air Force Cambridge Research Laboratories
Hanscom Field
Bedford, MA 01730

T.M. York
Pennsylvania State University
University Park, PA 16802

Robert A. Young
Intra-Space International
286 Wildcat Rd.
Downsview, Ontario M3J 2N5, Canada

Martin Zabielski
United Aircraft Corp. Research Laboratories
400 Main Street
E. Hartford, CT 06108

A. Zachor
Honeywell Radiation Center
2 Forbes Rd.
Lexington, MA 02173

Samuel P. Zimmerman
Air Force Cambridge Research Laboratories
Hanscom Field
Bedford, MA 01730

AUTHOR INDEX

☆U.S. GOVERNMENT PRINTING OFFICE: 1974—A 0004/60